

NASA Contractor Report 3974

# Development and Application of Linear and Nonlinear Methods for Interpretation of Lightning Strikes to In-Flight Aircraft

Terence Rudolph, Rodney A. Perala,  
Calvin C. Easterbrook, and Steven L. Parker  
*Electro Magnetic Applications, Inc.*  
*Denver, Colorado*

Prepared for  
Langley Research Center  
under Contract NAS1-17748



National Aeronautics  
and Space Administration

**Scientific and Technical  
Information Branch**

1986



## TABLE OF CONTENTS

Chapter	Title	Page
<hr/>		
1	INTRODUCTION	1
2	DATA INTERPRETATION	4
	2.1 Introduction	4
	2.2 Data Classification	4
	2.3 Simultaneity	7
	2.4 Analysis of D-dot Peak Ratios	28
3	LINEAR MODELING USING TRANSFER FUNCTIONS	35
4	APPLICATION OF THE TRANSFER FUNCTION TECHNIQUE	41
5	NONLINEAR TRIGGERED LIGHTNING PARAMETER STUDY	52
6	RESPONSE OF THE F106B AIRCRAFT TO A HIGH CURRENT LIGHTNING STRIKE	55
7	RESPONSE OF AIRCRAFT OTHER THAN THE F106B TO TRIGGERED LIGHTNING	63
8	ENHANCED NONLINEAR AIR BREAKDOWN MODELING	102
9	SUBGRID DEVELOPMENT AND APPLICATION	118
	9.1 The Effect of Finite Difference Grid Resolution on Field Enhancements	118
	9.2 Subgrid Application	122
10	THUNDERSTORM ENVIRONMENT FOR IN-FLIGHT AIRCRAFT	127
	10.1 Introduction	127
	10.2 Meteorological Terminology and Definitions	127
	10.3 Storm Generation	135
	10.4 Storm Electricity	138
	10.5 The Hydrometeor Environment	142
	10.6 Simplified Hydrometeor Environment for Modeling	142
	10.7 The Role of the Thunderstorm Environment in Modeling	148
11	FIELD ENHANCEMENT FACTORS FOR TYPICAL ICE CRYSTALS	149

## TABLE OF CONTENTS

Chapter	Title	Page
12	SUMMARY AND CONCLUSIONS	156
	REFERENCES	160
	APPENDIX A (D-dot)	A-1 thru 17
	- Plots of the 1983 In-Flight Lightning Data	
	APPENDIX B (B-dot)	B-1 thru 20
	- Plots of the 1983 In-Flight Lightning Data	
	APPENDIX C	C-1 thru 67
	- Linear Transfer Function Modeling Results	
	APPENDIX D	D-1 thru 110
	- Skewed Angle Parameter Study	
	APPENDIX E	E-1 thru 43
	- Partial Principal Angle of Incidence Parameter Study	
	APPENDIX F	F-1 thru 9
	- Bibliography of the Thunderstorm Environment Literature Search	



## LIST OF FIGURES

Figure	Title	Page
1.1	Block Model of the F106B Indicating Approximate Sensor Locations	2
2.1	Simultaneous Waveforms from Flight 83-011	8
2.2	Simultaneous Waveforms from Flight 83-013	9
2.3	Simultaneous Waveforms from Flight 83-013	10
2.4	Simultaneous Waveforms from Flight 84-016	11
2.5	Simultaneous Waveforms from Flight 83-020	12
2.6	Simultaneous Waveforms from Flight 83-021	13
2.7	Simultaneous Waveforms from Flight 83-024	14
2.8	Simultaneous Waveforms from Flight 83-024	15
2.9	Simultaneous Waveforms from Flight 83-029	16
2.10	Simultaneous Waveforms from Flight 83-029	17
2.11	Simultaneous Waveforms from Flight 83-030	18
2.12	Simultaneous Waveforms from Flight 83-030	19
2.13	Simultaneous Waveforms from Flight 83-030	20
2.14	Simultaneous Waveforms from Flight 83-036	21
2.15	Simultaneous Waveforms from Flight 83-036	22
2.16	Simultaneous Waveforms from Flight 83-036	23
2.17	Simultaneous Waveforms from Flight 83-036	24
2.18	Simultaneous Waveforms from Flight 83-036	25
2.19	Overlay of D-dot Data Collected on the F106B Lightning Research Aircraft During Flight 83-013 (SOLID LINE) with Results of Nonlinear Code for Initial Electric Field of 170 kV/m Oriented Along the X, Z Axes and Initial Aircraft Charge of $-1/2 Q_m$ (DASHED LINE)	26

## LIST OF FIGURES (continued)

Figure	Title	Page
2.20	Overlay of B-dot Data Collected on the F106B Lightning Research Aircraft During Flight 83-013 (SOLID LINE) with Results of Nonlinear Code for Initial Electric Field of 170 kV/m Oriented Along the X, Z Axes and Initial Aircraft Charge of $-1/2 Q_m$ (DASHED LINE)	27
3.1	Typical Model Geometries for (a) Natural Lightning, and (b) Triggered Lightning	38
4.1	Measured Aircraft Responses for Flight 84-017 (3 pages)	42-44
4.2	Overlay Showing the Difference in Response Between the Previous Location on the Tail (Incorrect) and the New Location (Correct). The Solid Line is the Measured Data, the Dashed Line the Response at the Incorrect Location, and the Dotted Line the Response at the Correct Location	48
4.3	Overlay of Measured and Calculated Nose Currents for the Case of a 10 cm Radius Channel and Resistances Per Unit Length of 1 ohm/m, 10 ohm/m, and 50 ohm/m. The Measured Data is the Solid Line. Note that the Calculated Responses are Virtually Identical	49
4.4	Overlay of Measured and Calculated Nose Currents for the Case of a 1 cm Radius Channel and Resistances Per Unit Length of 1 ohm/m, 10 ohm/m, and 50 ohm/m. The Measured Data is the Solid Line. Note that the Calculated Responses are Virtually Identical	50
6.1	Current Waveform Used to Determine the Response of the F106B to a Large Current Lightning Strike	56
6.2	Nonlinear D-dot Forward Response of the F106B for the Injected Current of Figure 6.1	58
6.3	Nonlinear D-dot Left Wing Response of the F106B for the Injected Current of Figure 6.1	59

# **LIST OF FIGURES** **(continued)**

<b>Figure</b>	<b>Title</b>	<b>Page</b>
6.4	Nonlinear D-dot Tail Response of the F106B for the Injected Current of Figure 6.1	60
6.5	Nonlinear B-dot Longitudinal Response of the F106B for the Injected Current of Figure 6.1	61
6.6	Nonlinear B-dot Left Wing Response of the F106B for the Injected Current of Figure 6.1	62
7.1	Block Model of the F106B without Delta Wing, Indicating Approximate Sensor Locations	65
7.2	Block Model of the C-130 Indicating Approximate Sensor Locations	66
7.3	Calculated Sensor Responses for the Half Size F106B Aircraft, Nose to Tail Orientation, Net Charge of -.245 Millicoulombs, Electric Field Magnitude of 100 kV/m (3 pages)	69-71
7.4	Calculated Sensor Responses for the Half Size F106B Aircraft, Top to Bottom Orientation, Net Charge of -.245 Millicoulombs, Electric Field Magnitude of 250 kV/m (3 pages)	72-74
7.5	Calculated Sensor Responses for the Double Size F106B Aircraft, Nose to Tail Orientation, Net Charge of -3.95 Millicoulombs, Electric Field Magnitude of 100 kV/m (3 pages)	75-77
7.6	Calculated Sensor Responses for the Double Size F106B Aircraft, Top to Bottom Orientation, Net Charge of 3.95 Millicoulombs, Electric Field Magnitude of 250 kV/m (3 pages)	78-80
7.7	Calculated Sensor Responses for the F106B with Delta Wing Replaced by Straight Wing, Nose to Tail Orientation, Net Charge of -1.0 Millicoulomb, Electric Field Magnitude of 120 kV/m (3 pages)	81-83

## LIST OF FIGURES (continued)

Figure	Title	Page
7.8	Calculated Sensor Responses for the F106B with Delta Wing Replaced by Straight Wing, Top to Bottom Orientation, Net Charge of -1.0 Millicoulomb, Electric Field Magnitude of 240 kV/m (3 pages)	84-86
7.9	Calculated Sensor Responses for the C130 Aircraft, Nose to Tail Orientation, Net Charge of -3.45 Millicoulombs, Electric Magnitude of 190 kV/m (3 pages)	87-89
7.10	Calculated Sensor Responses for the C130 Aircraft, Top to Bottom Orientation, Net Charge of -3.45 Millicoulombs, Electric Field Magnitude of 210 kV/m (3 pages)	90-92
7.11	Calculated Sensor Responses for the Normal Size F106B Aircraft, Nose to Tail Orientation, Net Charge of -.895 Millicoulombs, Electric Field Magnitude of 130 kV/m (3 pages)	93-95
7.12	Calculated Sensor Responses for the Normal Size F106B Aircraft, Top to Bottom Orientation, Net Charge of -.895 Millicoulombs, Electric Field Magnitude of 310 kV/m (3 pages)	96-98
8.1	Ionization Rate as a Function of Scaled Electron Temperature $\sigma$ and Scaled Electric Field $\eta$ . Electron Drift Velocity Is Held At Zero (From Fowler [6]). Note that Fowler's $\beta$ Is Equivalent To $g$ In The Text.	107
8.2	Diagram of the Experimental Configuration Modeled by the Enhanced Nonlinear Air Chemistry Model. The Plates are Held at Constant Potential to Produce the Electric Field.	109
8.3	Axial Electric Field at the Tip of the Ellipsoid	111
8.4	Radial Electric Field Near the Tip of the Ellipsoid	112
8.5	Electron Density at the Tip of the Ellipsoid	113
8.6	Positive Ion Density at the Tip of the Ellipsoid	114
8.7	Negative Ion Density at the Tip of the Ellipsoid	115
8.8	Electron Energy Density at the Tip of the Ellipsoid	116

## LIST OF FIGURES (continued)

Figure	Title	Page
9.1	Three Cylinder Configurations Used in the Finite Difference Numerical Experiment	119
9.2	Field Variation Along the Axis Away From the Tip for Each of the Cylinders Shown in Figure 9.1	121
9.3	Electric Field at the Center of the End of the Bar in the Subgrid. The Solid Line is In the Factor of 2 Subgrid and the Dashed Line In the Factor of 6 Subgrid	124
9.4	D-dot Forward Response of the F106B for the Case with a Subgrid Around the Nose	126
10.1	Example of a Typical Sounding Plotted on a Skew T-Log P Thermodynamic Diagram. The Thick Solid Line Represents the Temperature Profile; the Thick Dashed Line Represents the Moisture Profile. The Flags On the Right of the Diagram Indicate Wind Direction and Speed	131
10.2	Fundamental Shapes of Ice Crystals	134
10.3	Partial Classification of Natural Ice Crystals (from Magano and Lee [7])	134
10.4	Structure of Air-Mass Convective Storm	136
10.5	Structure of Severe Convective Storm, [9]	137
10.6	Cloud Physics Processes Which Can Occur in a Convective Storm	139
10.7	Thunderstorm Penetration and Strike Statistics for "Storm Hazards," 1980-82	144
10.8	Aircraft Strike Statistics for Low Altitude Flights	145
10.9	Altitude Distribution of VLF Sources for Storm I, 6/19/80	145
10.10	Possible Lightning Strike Scenarios for High and Low Flight Paths	146
11.1	Fundamental Ice Crystal Shapes For Which the Electric Field Enhancement Factors Have Been Determined	150

## LIST OF FIGURES (continued)

Figure	Title	Page
11.2	Maximum Electric Field Enhancement Factors for the Hexagonal Column Ice Crystals for Three Different Electric Field Orientations	152
11.3	Maximum Field Enhancements for Hexagonal Plate Ice Crystal	153
11.4	Maximum Field Enhancement for the Hexagonal Dendrite Ice Crystal	154

## LIST OF TABLES

Table	Title	Page
2.1	Waveshape Categories for Data Classification (2 pages)	5-6
2.2	Measured D-dot Ratios	29
2.3	D-dot Forward to D-dot Tail Ratio for Principal Angle Parameter Study	30
2.4	D-dot Forward to D-dot Left Wing Ratio for Principal Axis Parameter Study	31
2.5	D-dot Forward to D-dot Tail Ratio for Skewed Angle Parameter Study	33
2.6	D-dot Forward to D-dot Left Wing Ratio for Skewed Angle Parameter Study	34
7.1	Variable Parameters in Triggered Lightning Investigation	67
7.2	Summary of Initial Peak Responses for the Multi-Aircraft Study	99
10.1	Key to Figure 10.6	140
10.2	Summary of Hydrometeor Parameters	143

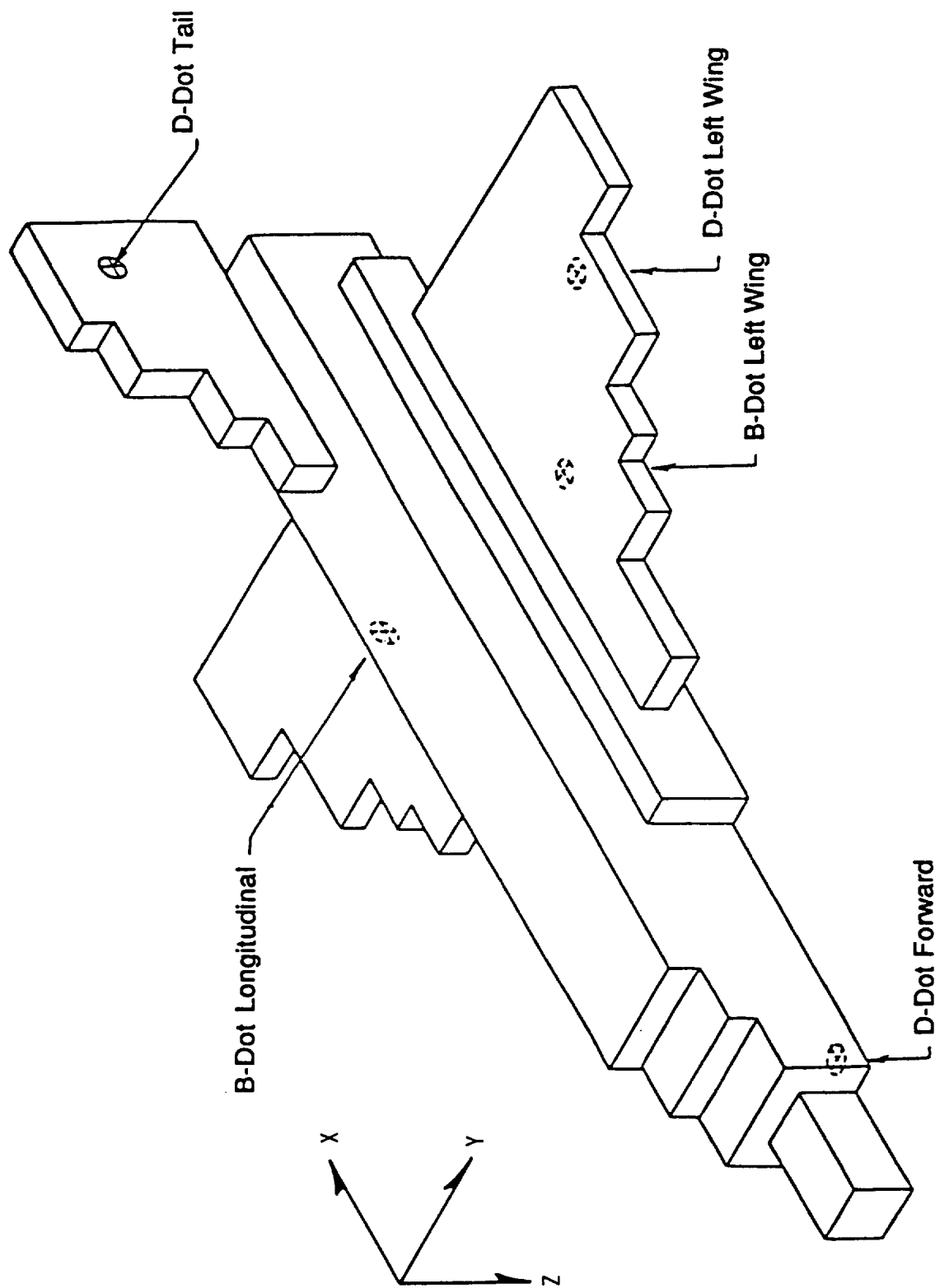
## CHAPTER 1

### INTRODUCTION

Since 1980, NASA has been collecting data on thunderstorm and lightning environments by flying an instrumented F106B aircraft into thunderstorms. The program has been increasingly successful in that more direct lightning strikes to the aircraft and more sensor data have been recorded as the program progressed. This report concentrates on the analysis of the data recorded from the F106B, and on the development and application of analytical tools designed to better analyze that data.

The basic mathematical model utilized throughout the work reported here is the three dimensional, time domain, finite difference model. This model, documented in detail in previous reports [1,2], finite differences Maxwell's equations in a three dimensional cartesian grid to solve transient and static electromagnetic problems. The finite difference "block" model of the F106B is shown in Figure 1.1, along with relevant sensor locations. The spatial resolution in the model is one meter in the direction along the fuselage, and one-half meter in the other two coordinate directions. The temporal resolution, required by the Courant condition, is one nanosecond. Throughout this report, the basic finite difference model has been modified and enhanced in various ways. The addition of thin wires to simulate lightning channels, air chemistry for calculating nonlinear air breakdown, and a subgrid to model sharp points of the aircraft in greater detail, all increase the capabilities of the basic model.

Following this introduction, Chapter 2 concentrates on the direct interpretation of the inflight sensor data, including categorization of the entire 1983 data set. Chapter 3 develops a linear approach to triggered lightning modeling, using frequency domain transfer functions. In Chapter 4, the concepts developed in Chapter 3 are applied to a particular multi-sensor lightning event, with emphasis on the lightning channel impedance. Chapter 5 presents a continuation of the nonlinear parameter study of triggered lightning on the F106B, concentrating on "skewed" angles between the electric field vector and the principal axes of the aircraft. In Chapter 6, the nonlinear air chemistry model is used to determine the response of the F106B to a large current lightning strike, presumably a cloud to ground return stroke. Chapter 7 explores the response of aircraft other than the F106B to a triggered lightning strike. The other aircraft include a C130 transport, which is similar in shape to a commercial



**Figure 1 Block Model of F106B Indicating Approximate Sensor Locations**



aircraft. Enhancements to nonlinear air chemistry modeling are presented in Chapter 8. The addition of a temperature dependent electron avalanche rate and molecular vibrational energy states are documented there, and the enhanced model is applied to a particular two dimensional object. Final testing of the subgrid, which allows increased spatial resolution in selected portions of a problem space, and its first application to the nose of the F106B are presented in Chapter 9. Chapter 10 documents a literature search of the thunderstorm environment, focusing on the particles present in a thunderstorm. The field enhancement effects of typical ice crystals are calculated in Chapter 11. Chapter 12 presents a summary and conclusions. Computational results are provided in the appendices.

## **CHAPTER 2**

### **DATA INTERPRETATION**

#### **2.1 Introduction**

The data collected on the NASA F106B Lightning Research Aircraft during the 1983 season is presented in Appendices A and B. Appendix A contains D-dot forward data records and Appendix B contains B-dot longitudinal records.

In all, some 368 time domain records were available for analysis from the 1983 season. Of these, 161 were D-dot forward and 207 were B-dot longitudinal sensor records.

#### **2.2 Data Classification**

In a continuing effort to identify trends in in-flight lightning measurements, the D-dot and B-dot data have been classified into categories according to waveshape. The categories are intended to highlight waveforms with similar behavior, which may be indicative of similar physical phenomena. Descriptions of the eleven D-dot and eight B-dot categories are given in Table 2.1, along with the number of waveforms in each category. In addition, the number of waveforms in each category from the analysis of the 1982 data are presented. These waveforms were classified in a previous report [3].

It should be noted that the last three D-dot and the last two B-dot categories are new, representing waveshapes not seen previously. On a percentage basis, the 1983 data also does not distribute among the categories in the same manner as the 1982 data. This could be due to the evolutionary nature of the aircraft sensor recording system or varying flight patterns between seasons. In fact, Category 11, the predominant category for the 1983 data, may be simply a variant of Category 6, a primary category from 1982.

The data falls into the previously identified categories quite well. The "double-hump" structure of the F106B aircraft signature identified by Trost, et al., [unpublished report on NASA Grant NAG-1-28, August 1985], from the 1981-82 data, is visible throughout the 1983 data as well.

**TABLE 2.1    Waveshape Categories for Data Classification**

---

		1983	1982
<b>D-Dot</b>	<b>Category</b>		
1.	Slow positive, then negative, bipolar pulse	6	35
2.	Double bipolar pulses separated by ~ 200-400 ns, initially >0, with $\int \dot{D} dt \approx 0$ .	6	11
3.	Single negative pulse with little structure	4	15
4.	Bipolar pulses, first negative, then positive	0	3
5.	Fast Bipolar pulses, initially positive	24	21
6.	Initial large fast pulse with much structure and having a late time tail, mainly unipolar	4	24
7.	Simple unstructured positive pulse	12	6
8.	Miscellaneous	4	8
9.	Multiple events. 3-5 fast initially positive bipolar pulses separated by 200-400 ns. Much structure	5	0
10.	Slow, low structure, negative unipolar pulse, with fast negative spike	3	0
11.	Multiple fast unipolar pulses, arranged in a triangular shape ~1 $\mu s$ wide at the base. Usually preceded by or including a fast bipolar pulse	30	0

**TABLE 2.1    Waveshape Categories for Data Classification  
(continued)**

---

<b>B-Dot</b>		<b>1983</b>	<b>1982</b>
	<b>Category</b>		
1.	Initially positive pulse with much later time structure	64	7
2.	Slow positive and negative half cycles, usually small	3	1
3.	Initially positive single cycle followed by low amplitude structure	43	15
4.	Unstructured single positive cycle	2	5
5.	Single negative slow pulse	6	3
6.	Fast double pulses, separated by 200-500 ns, initially positive	31	19
7.	Fast monopolar negative pulse, followed by low structure tail	12	0
8.	Fast monopolar negative pulse, followed by high structure and a fast bipolar pulse, negative-positive, after 200-750 ns.	6	0

## 2.3 Simultaneity

In order to further identify trends seen in the data collected on the F106B Lightning Research Aircraft, an analysis has been performed to determine simultaneity between the D-dot forward and B-dot longitudinal sensor records. Simultaneous data, recorded not only on the same trigger, but also at nearly the same time on the record, provides an opportunity to more accurately find correlations between the experimental and analytical data.

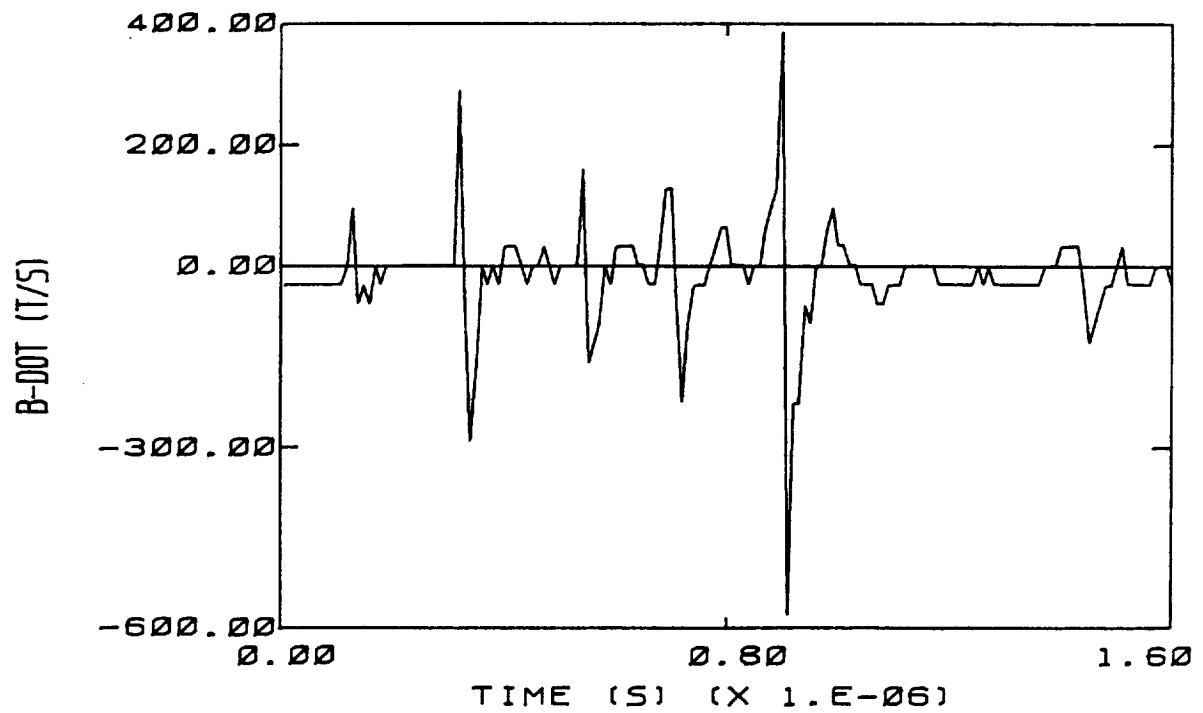
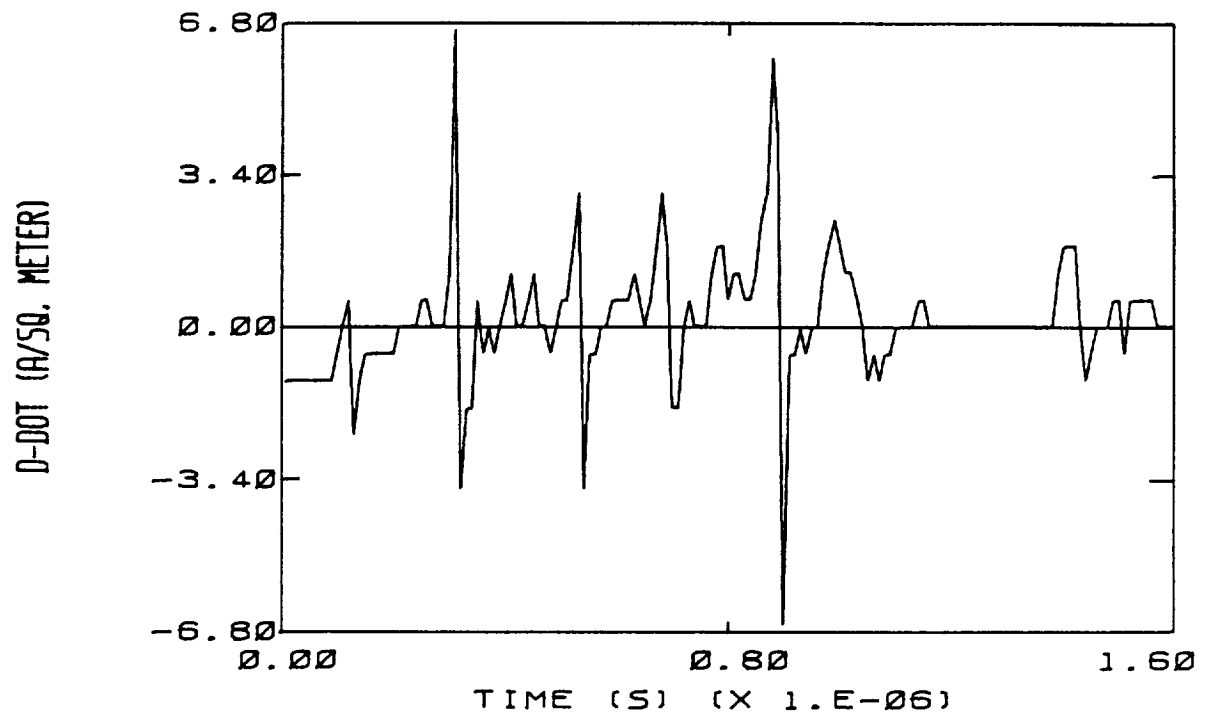
Eighteen pairs of D-dot and B-dot records have been identified as probably simultaneous. The pairs were evaluated for simultaneity based on timing, structure and level. These pairs are presented as Figures 2.1 - 2.18.

Of these pairs, one event from Flight 83-013 has been found to show a high degree of structural similarity to the results of a run from the nonlinear skewed angle parameter study. Overlays of these data are presented in Figures 2.19 and 2.20. In order to accelerate breakdown in the nonlinear code, reasonably high initial electric fields were imposed on the problem. As a result, the magnitudes of the resultant waveforms are somewhat higher than those of the experimental results, but the structure is retained. Assuming that a X, Z incidence on the aircraft produces a nose attachment and a tail detachment in the nonlinear model, it is concluded that this event from Flight 83-013 resulted in a similar attachment.

If this conclusion is extended to the data classification performed earlier (section 2.2), it is possible that all Category 5 D-dot forward waveforms and Category 3 B-dot longitudinal waveforms resulted from a nose attachment - tail detachment lightning stroke.

Although the database is small, some other possible conclusions may be drawn from the simultaneous data. A possible correlation may be seen between D-dot Category 11 and B-Dot Category 6. In addition, a relationship may exist between D-dot Category 5 and B-dot Categories 1 and 3. This last correlation seems to be supported by the comparison made with the nonlinear model above.

(Text continued on page 28)



**Figure 2.1 Simultaneous Waveforms from Flight 83-011**

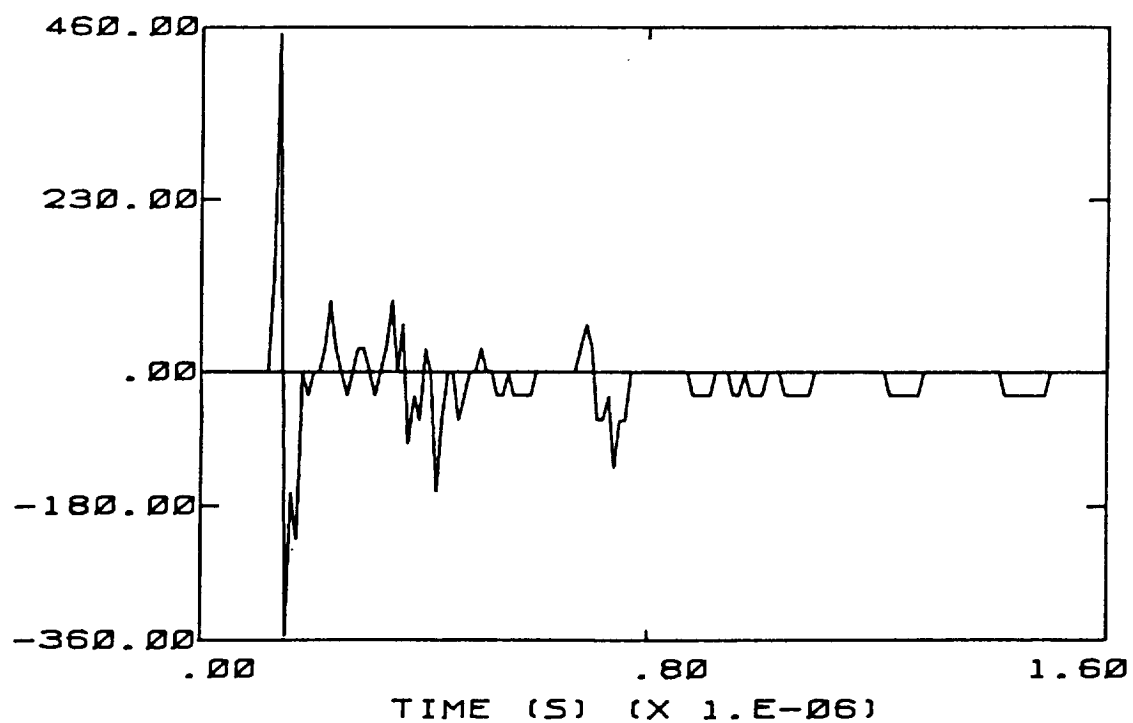
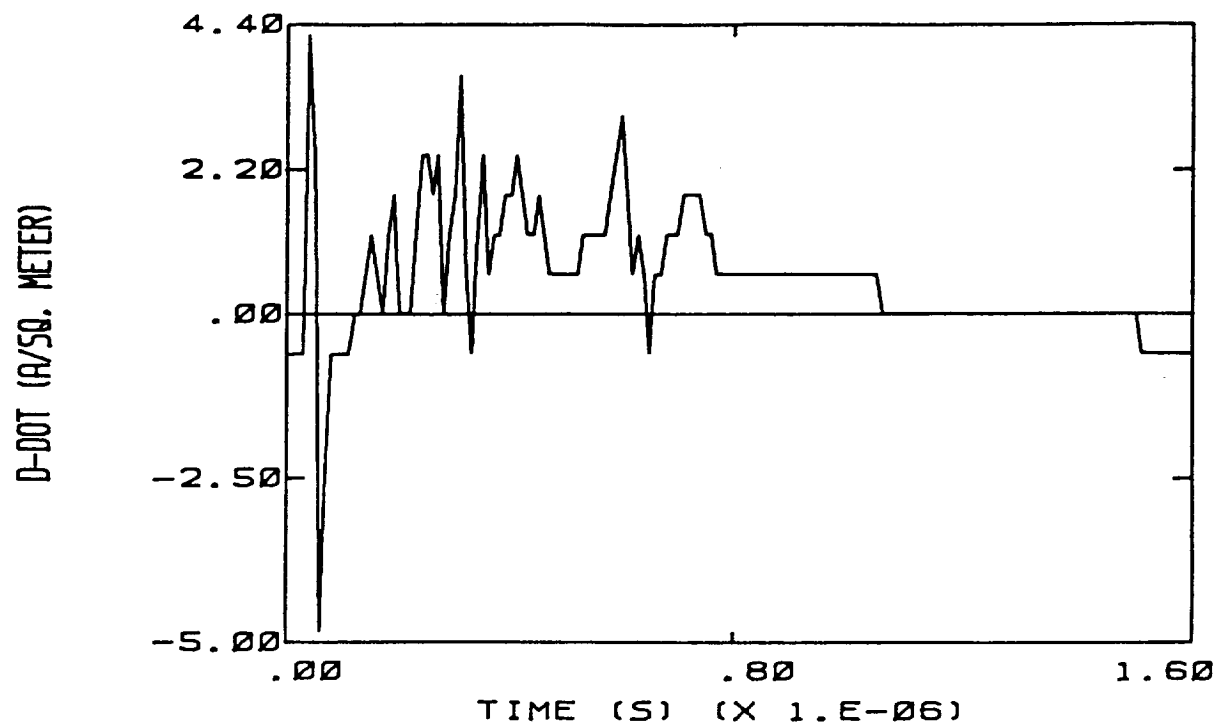


Figure 2.2 Simultaneous Waveforms from Flight 83-013

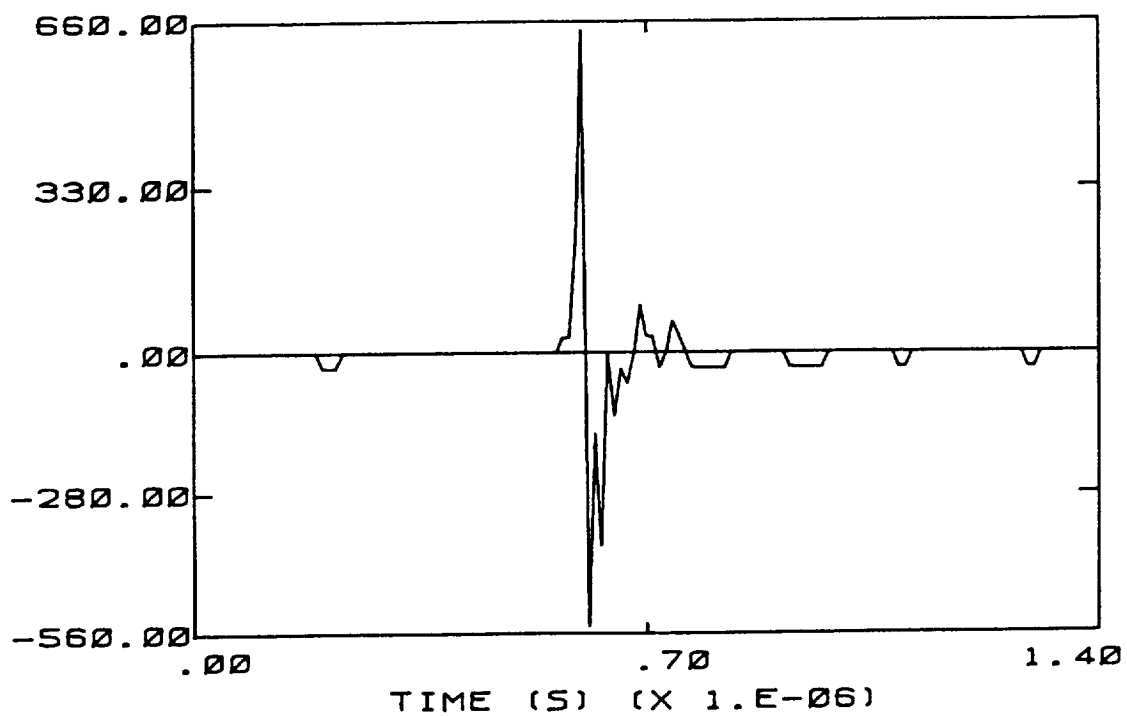
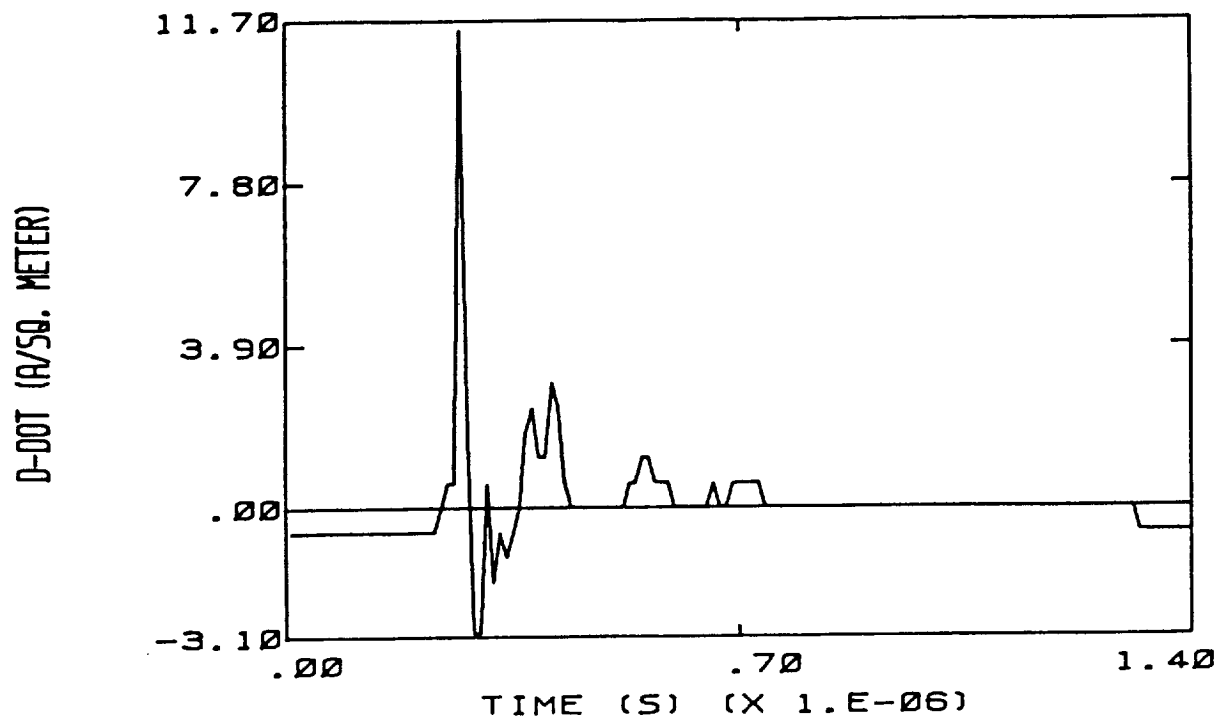


Figure 2.3 Simultaneous Waveforms from Flight 83-013



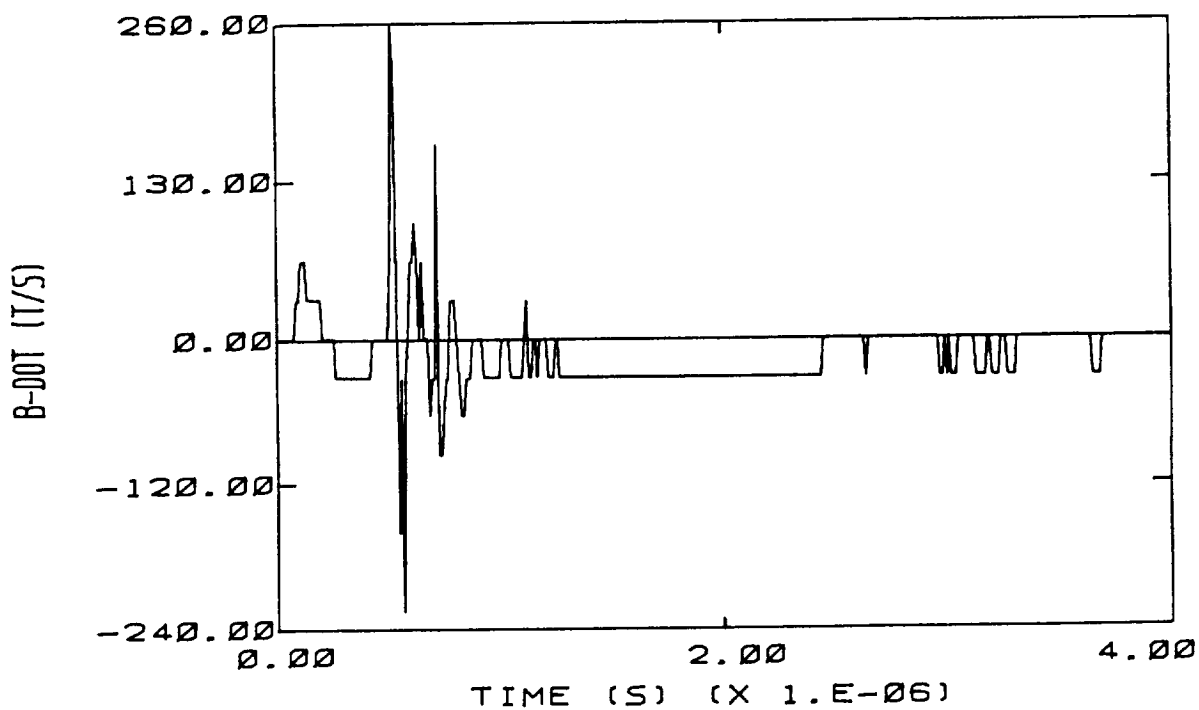
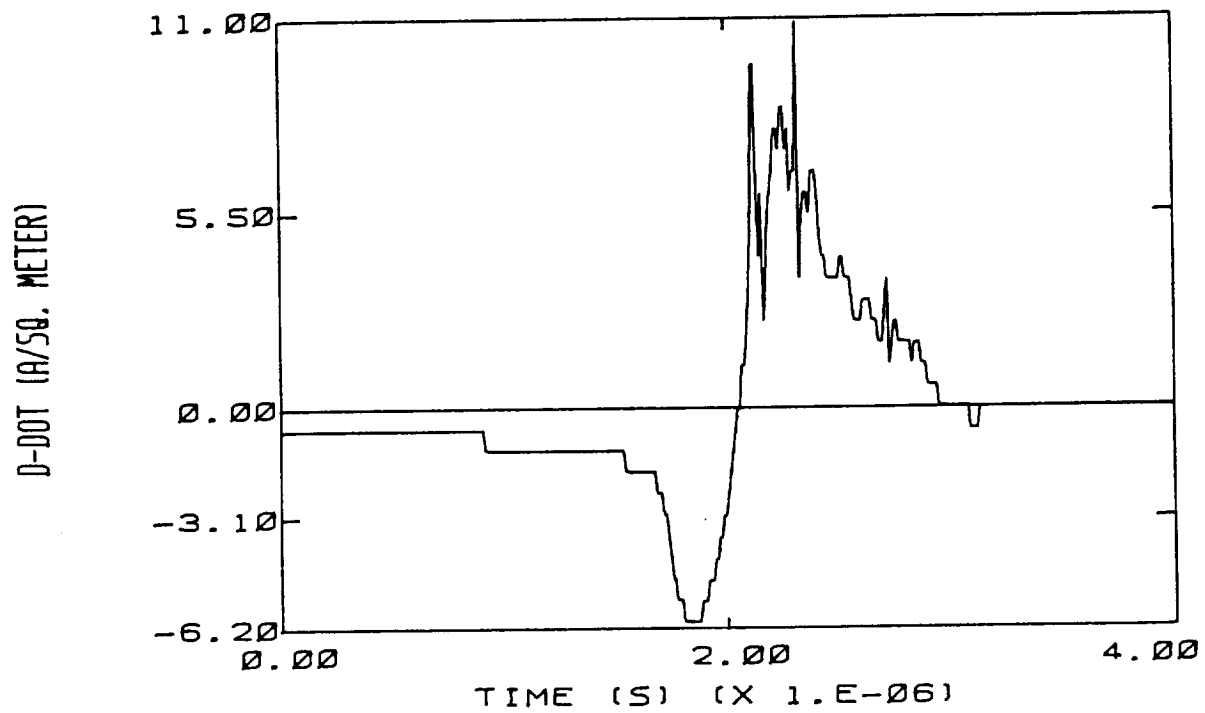


Figure 2.4 Simultaneous Waveforms from Flight 83-016

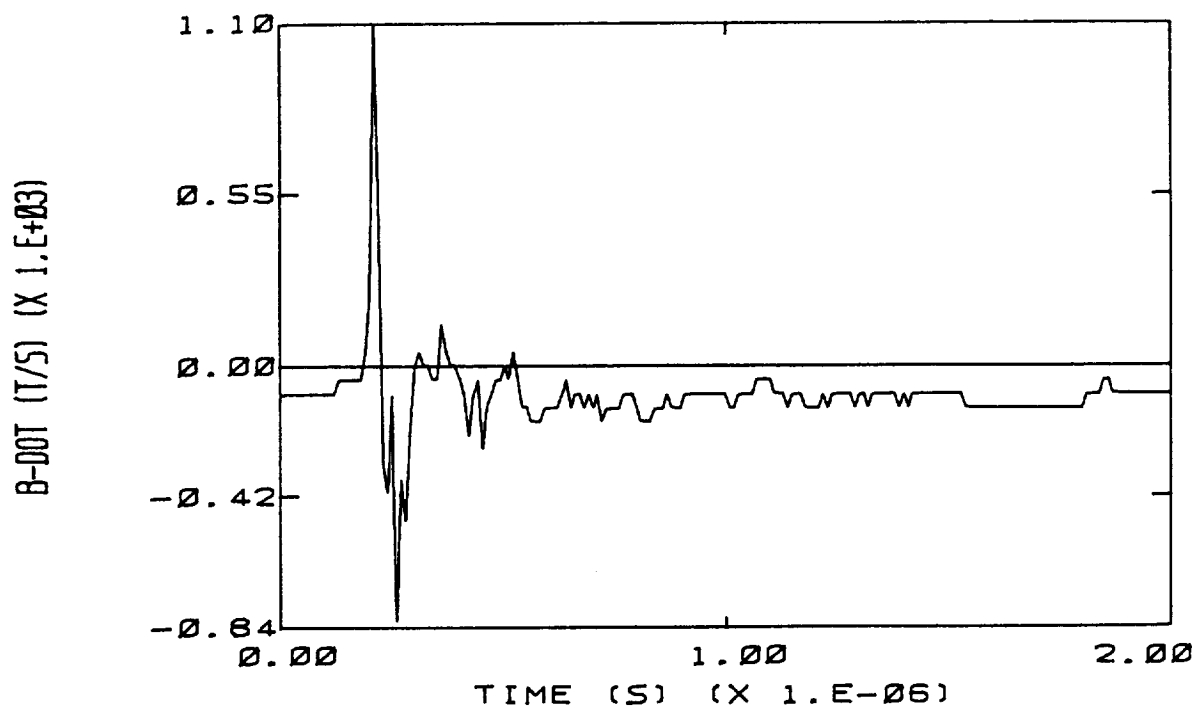
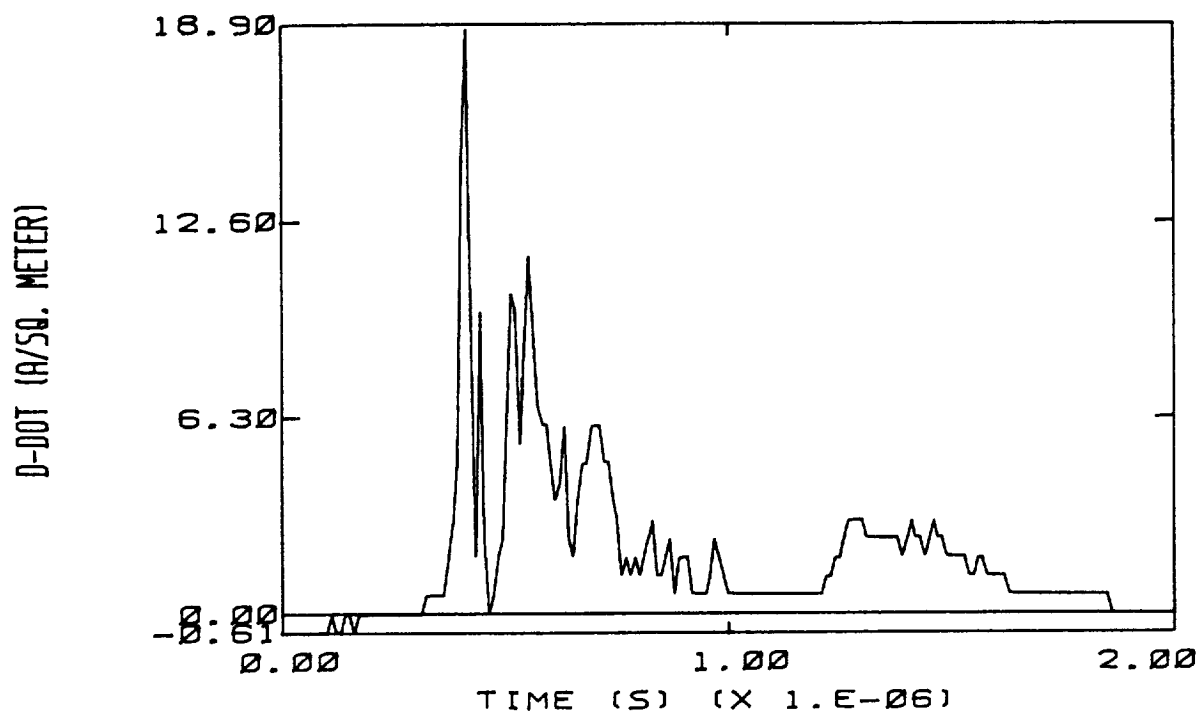


Figure 2.5 Simultaneous Waveforms from Flight 83-020

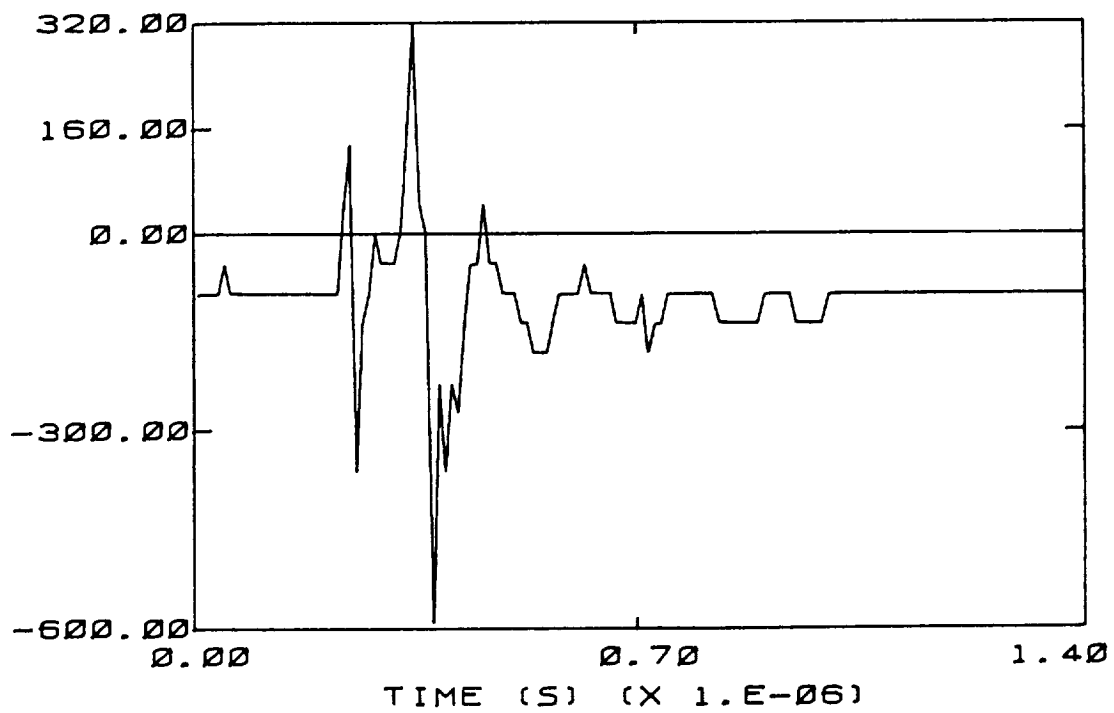
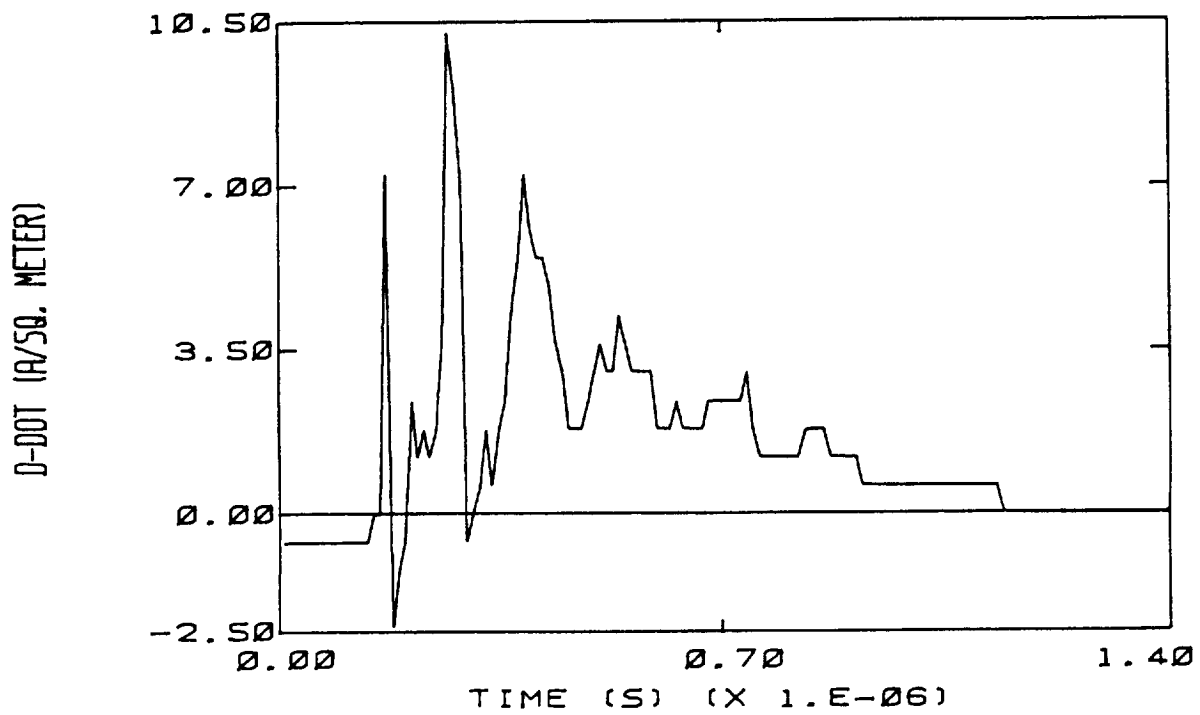


Figure 2.6 Simultaneous Waveforms from Flight 83-021

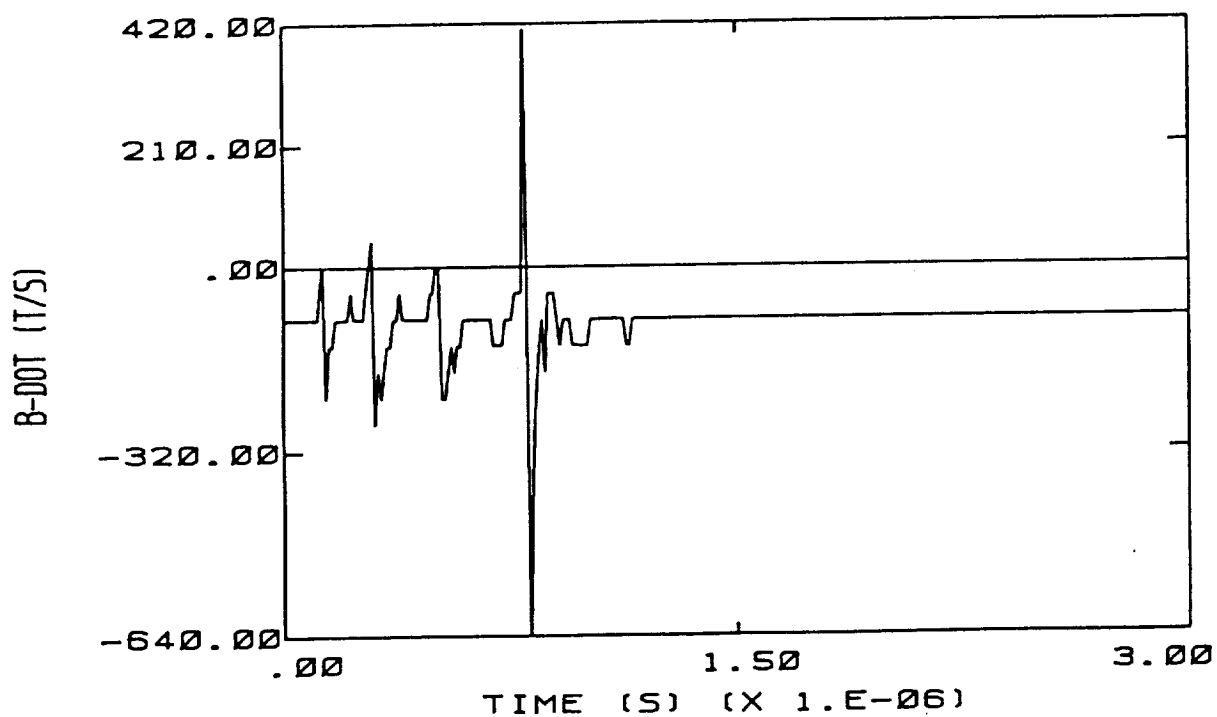
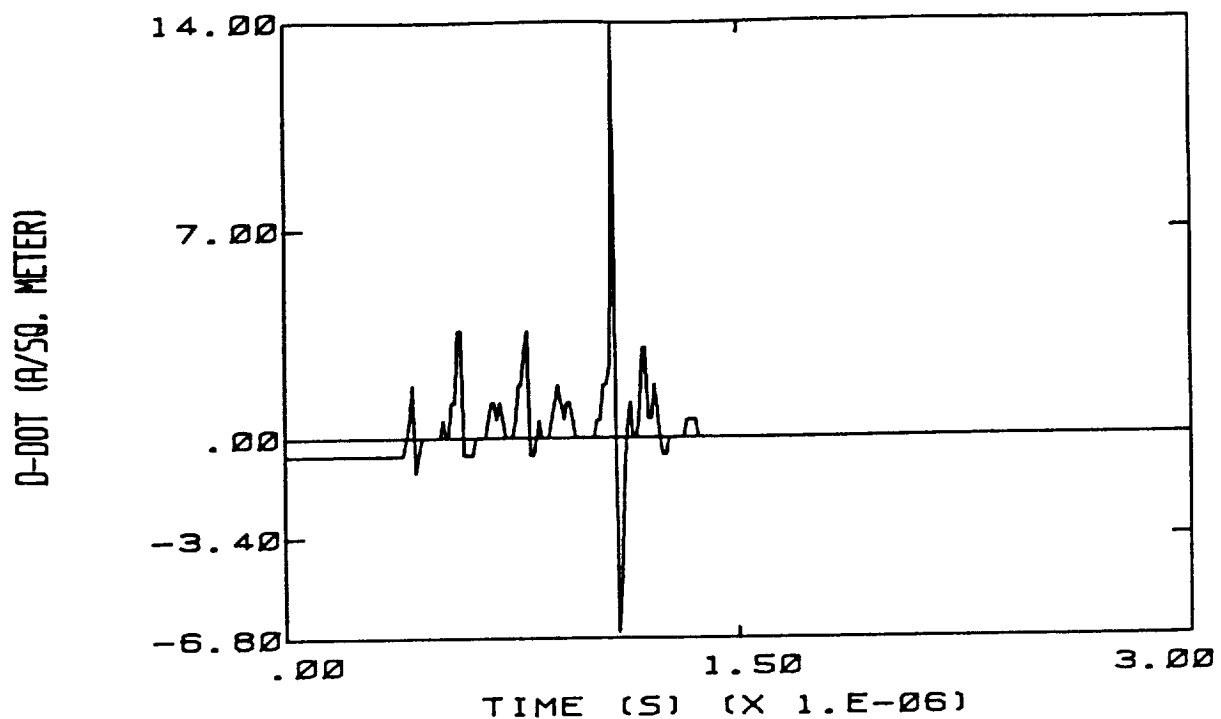


Figure 2.7 Simultaneous Waveforms from Flight 83-024

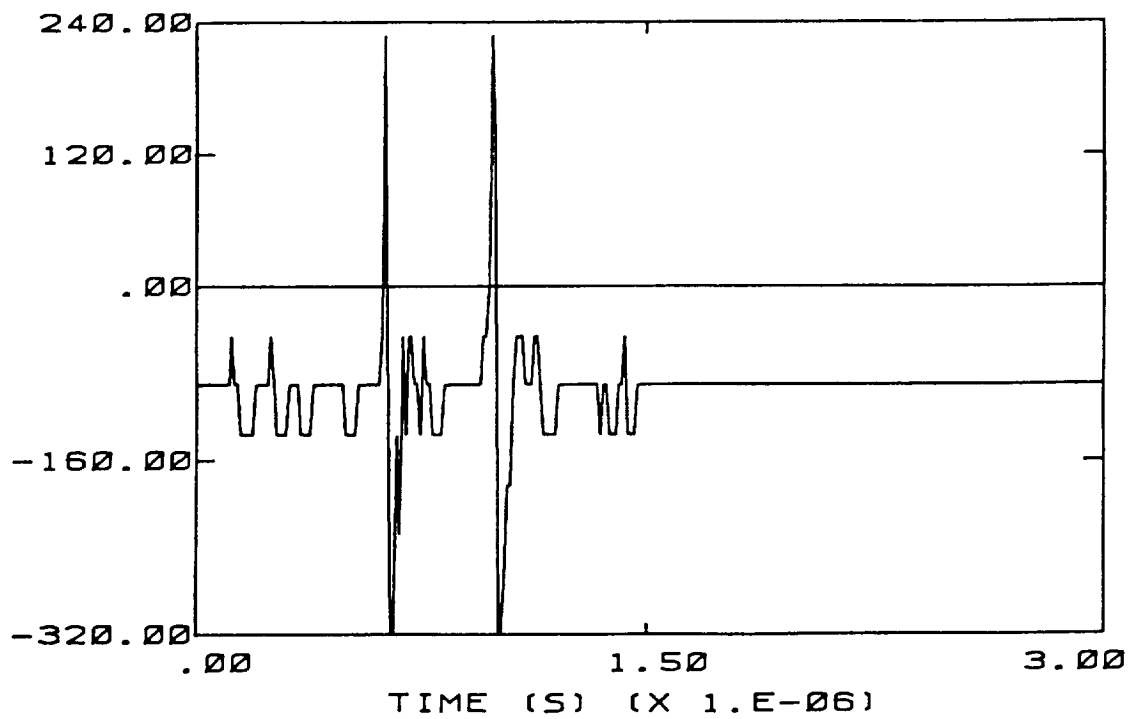
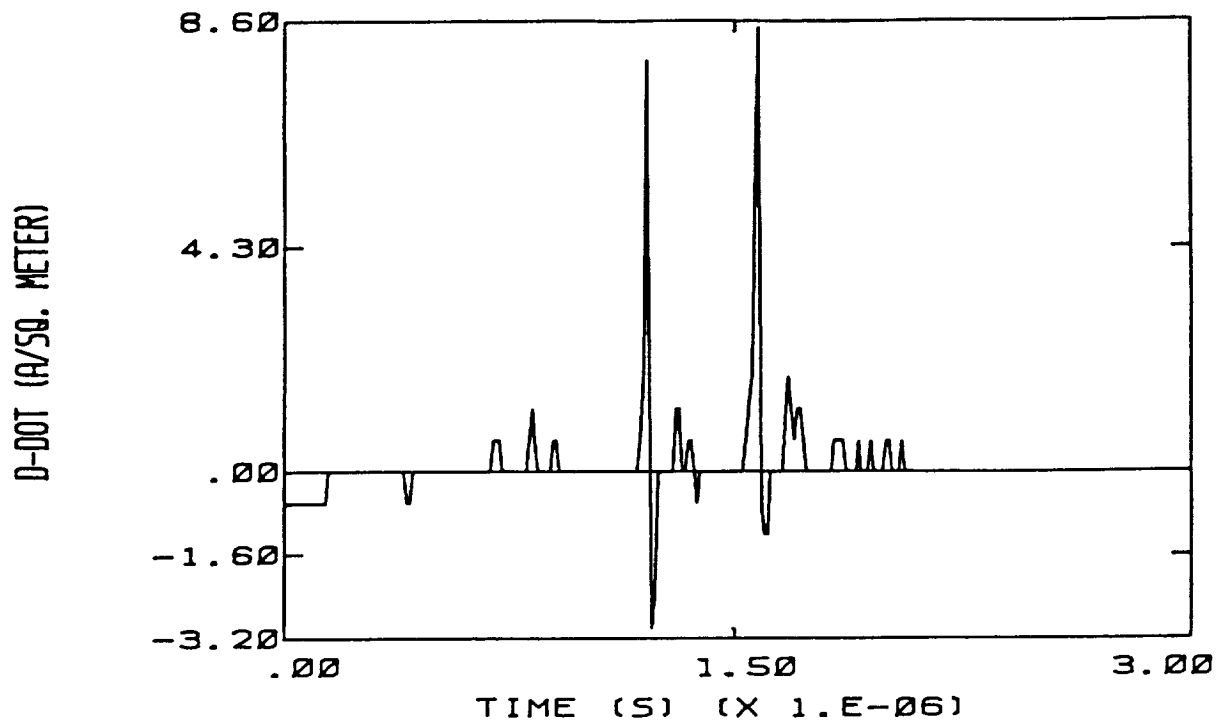


Figure 2.8 Simultaneous Waveforms from Flight 83-024

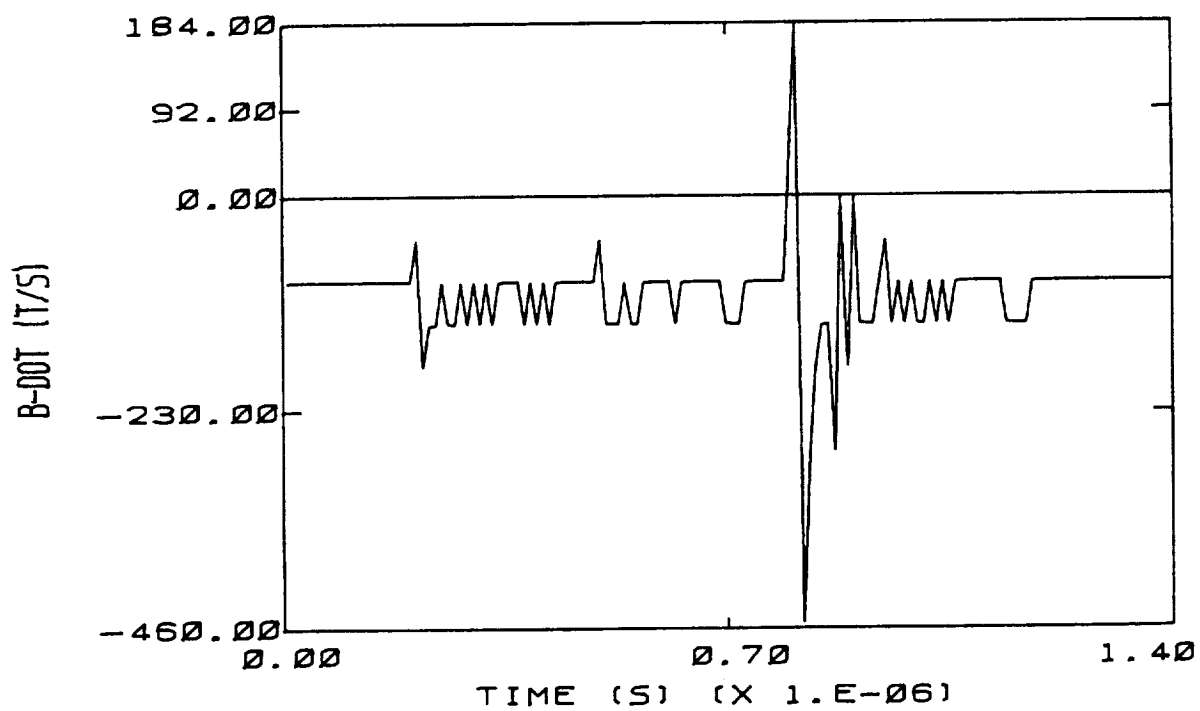
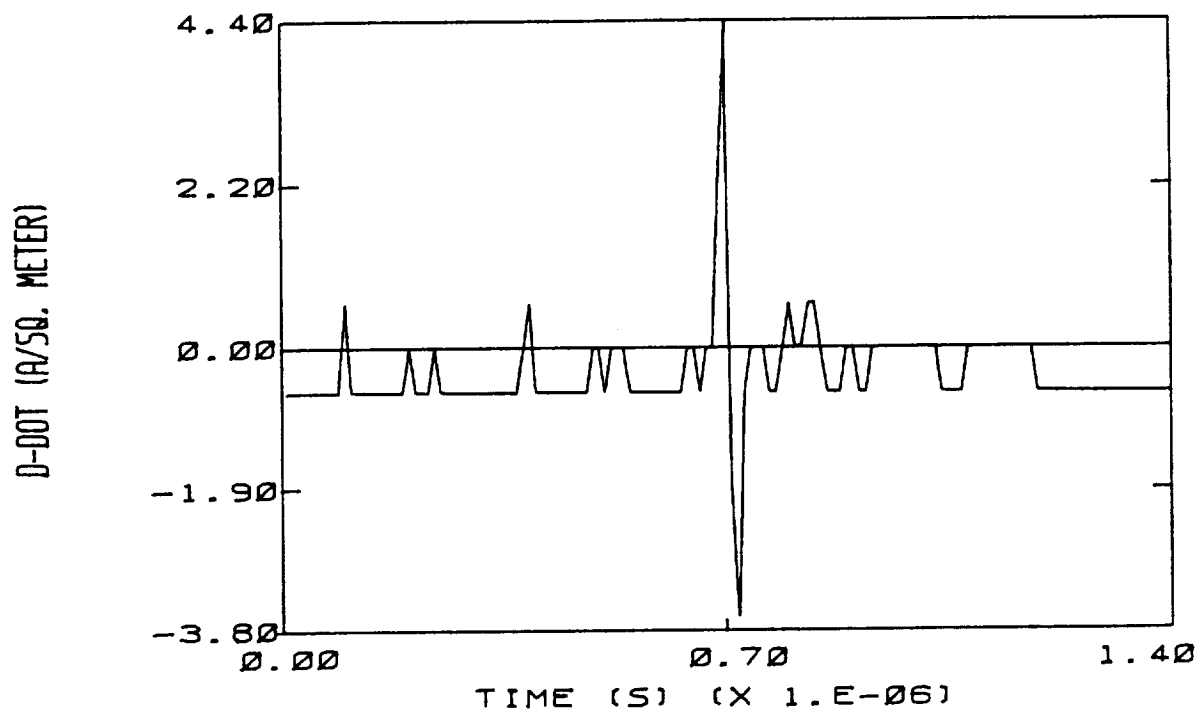


Figure 2.9 Simultaneous Waveforms from Flight 83-029

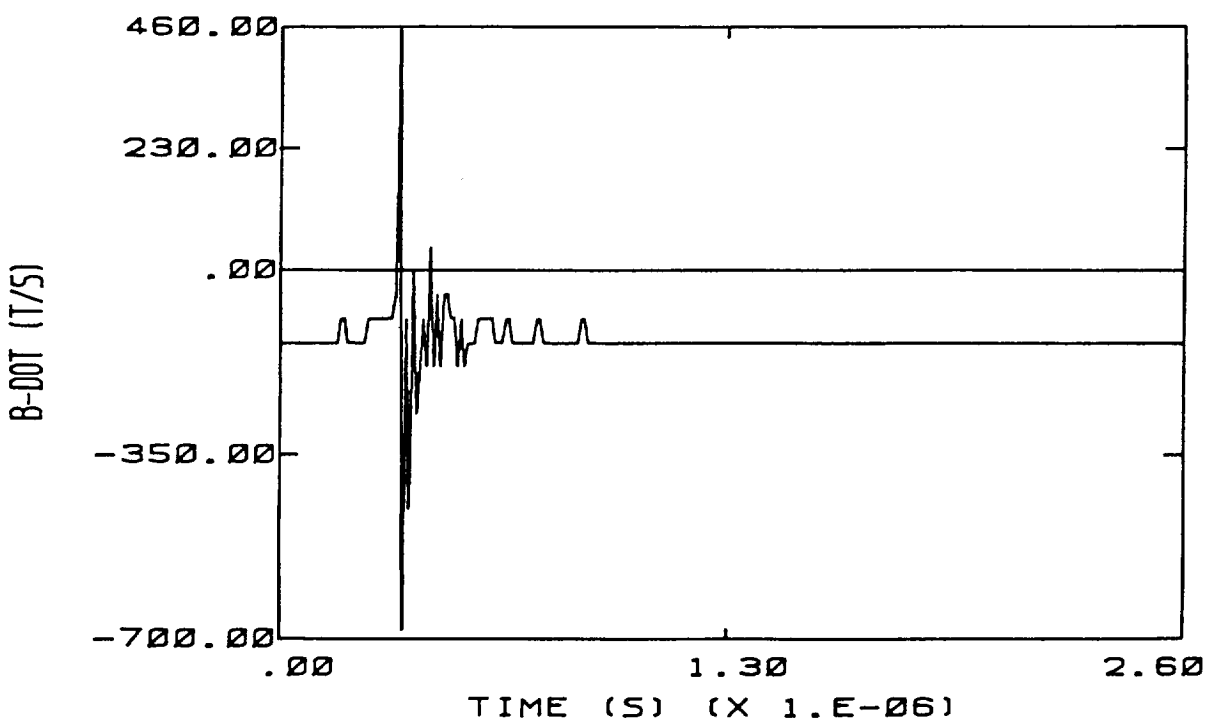
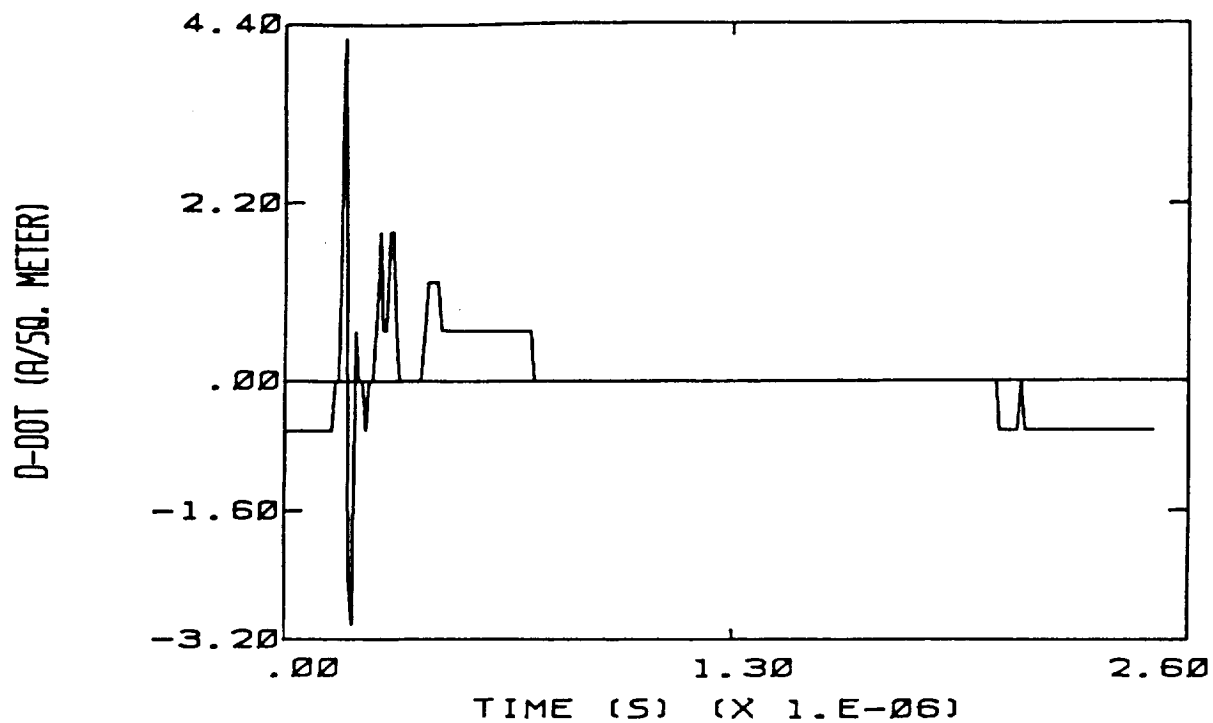


Figure 2.10 Simultaneous Waveforms from Flight 83-029

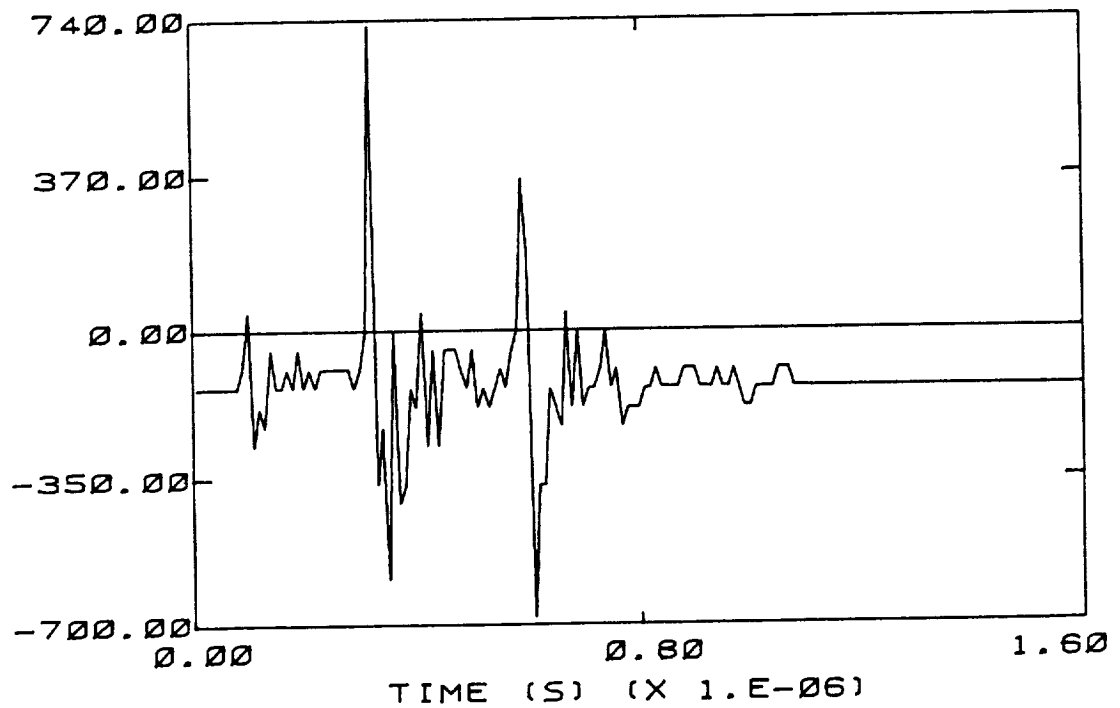
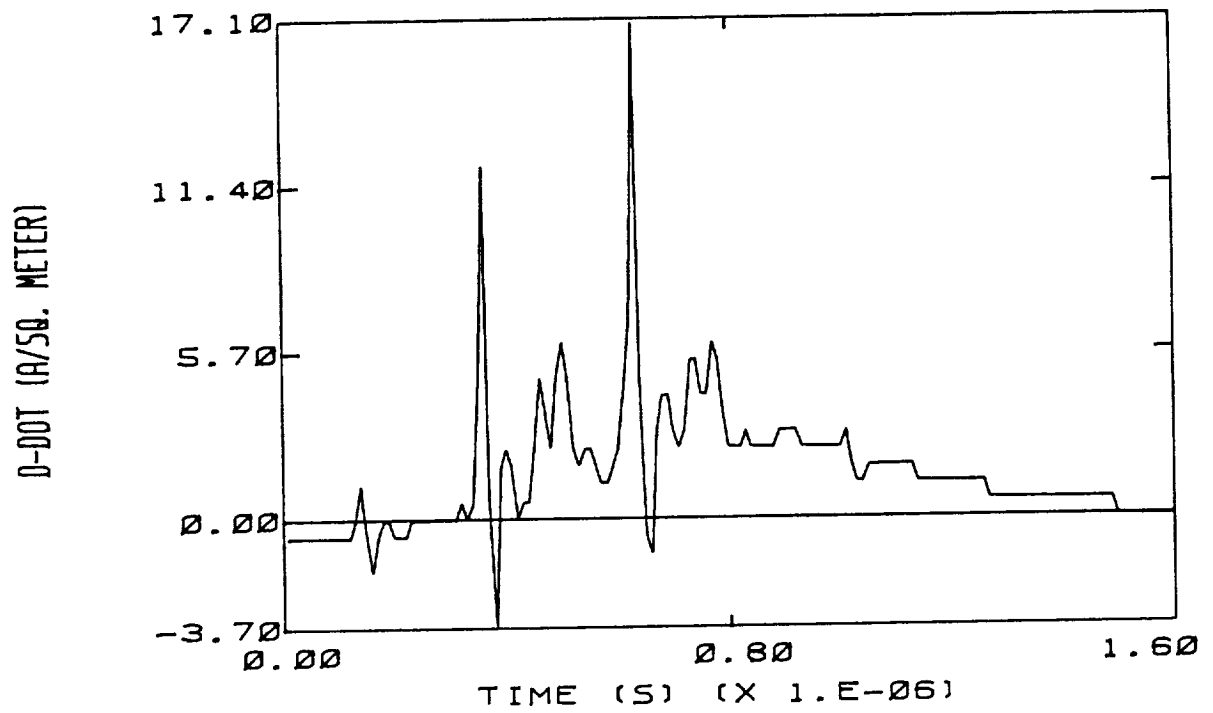


Figure 2.11 Simultaneous Waveforms from Flight 83-030



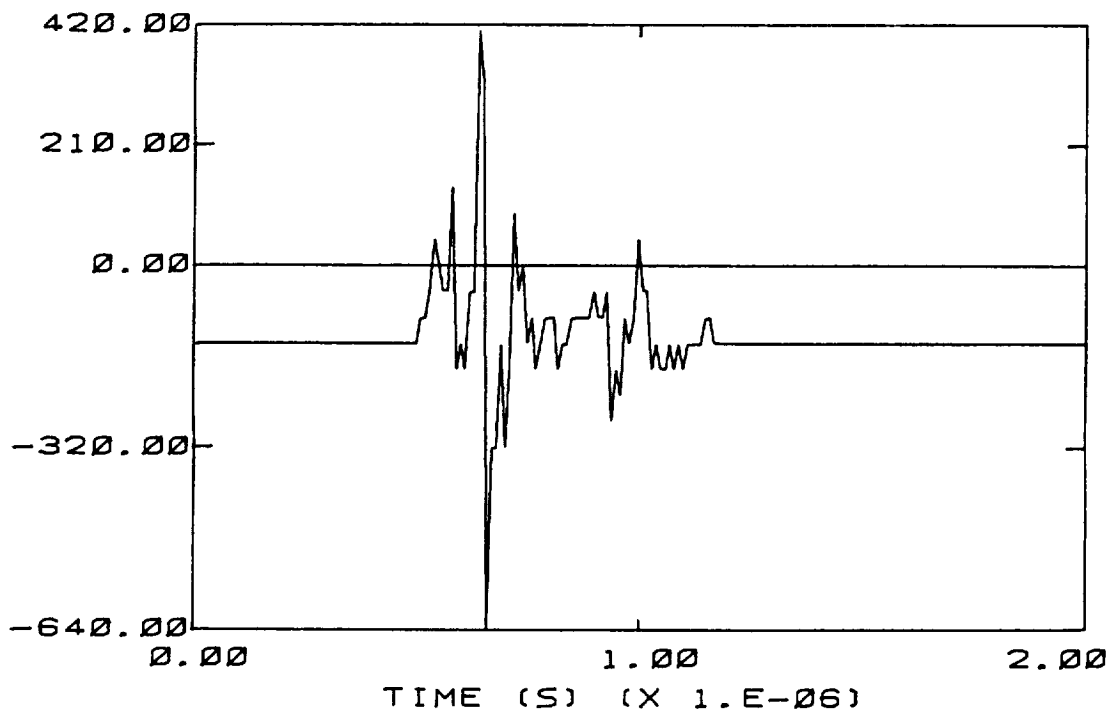
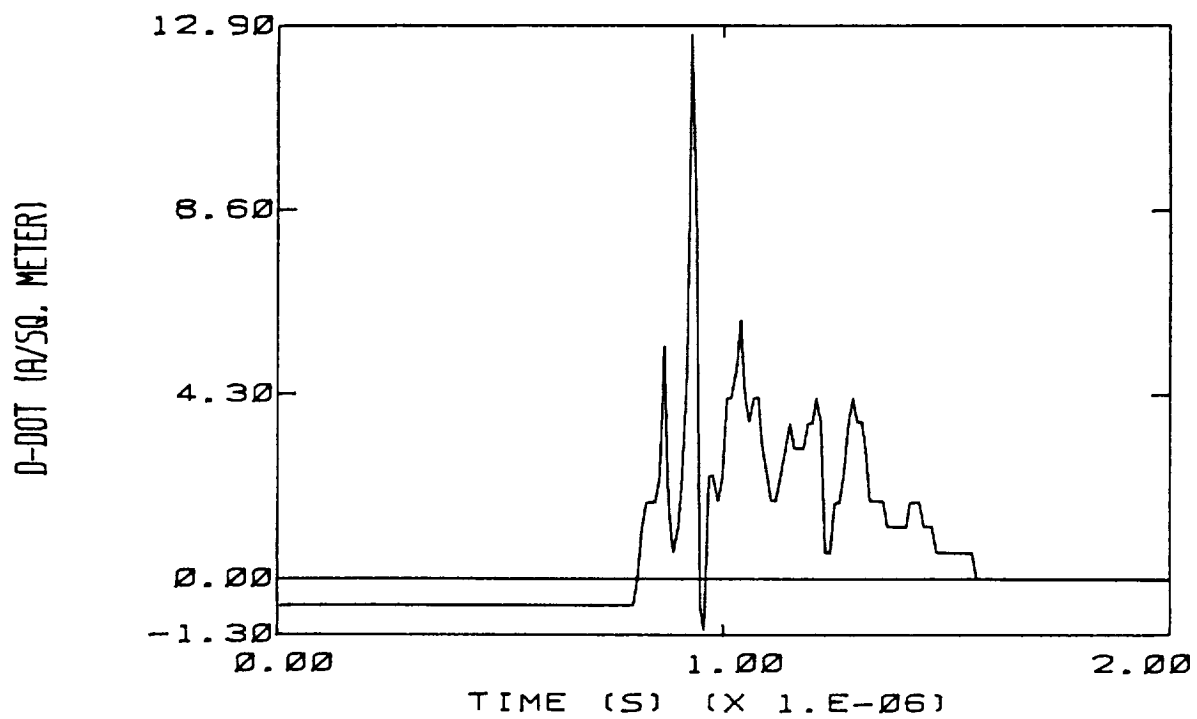


Figure 2.12 Simultaneous Waveforms from Flight 83-030

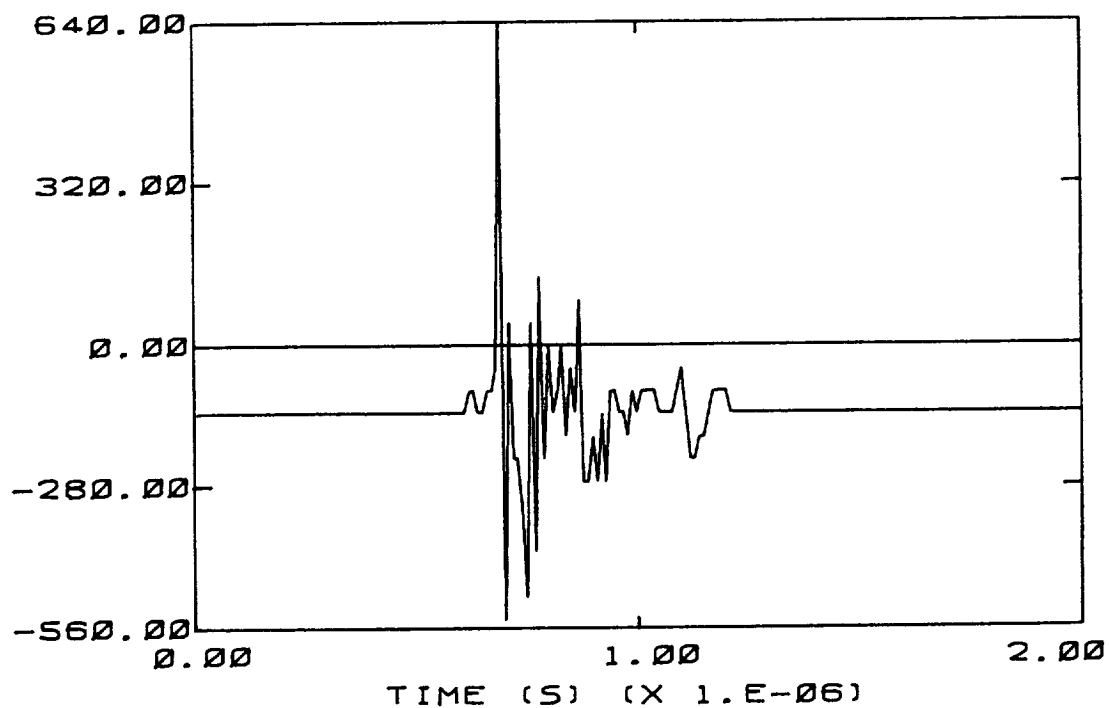
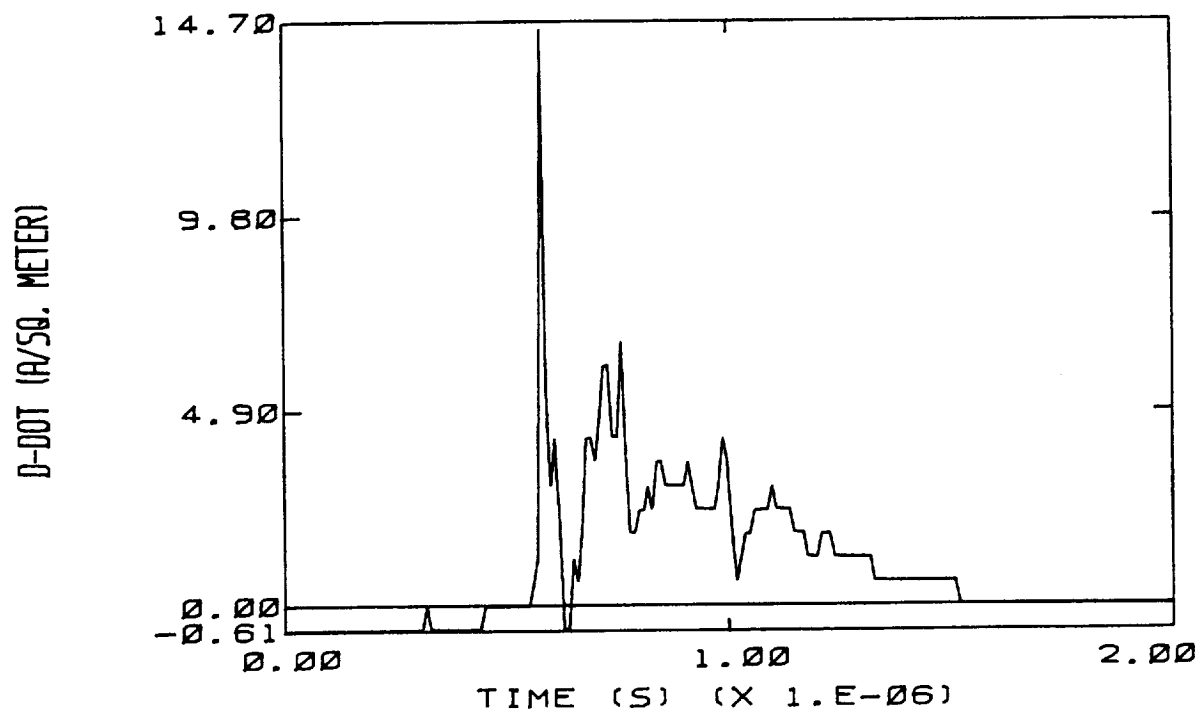


Figure 2.13 Simultaneous Waveforms from Flight 83-030

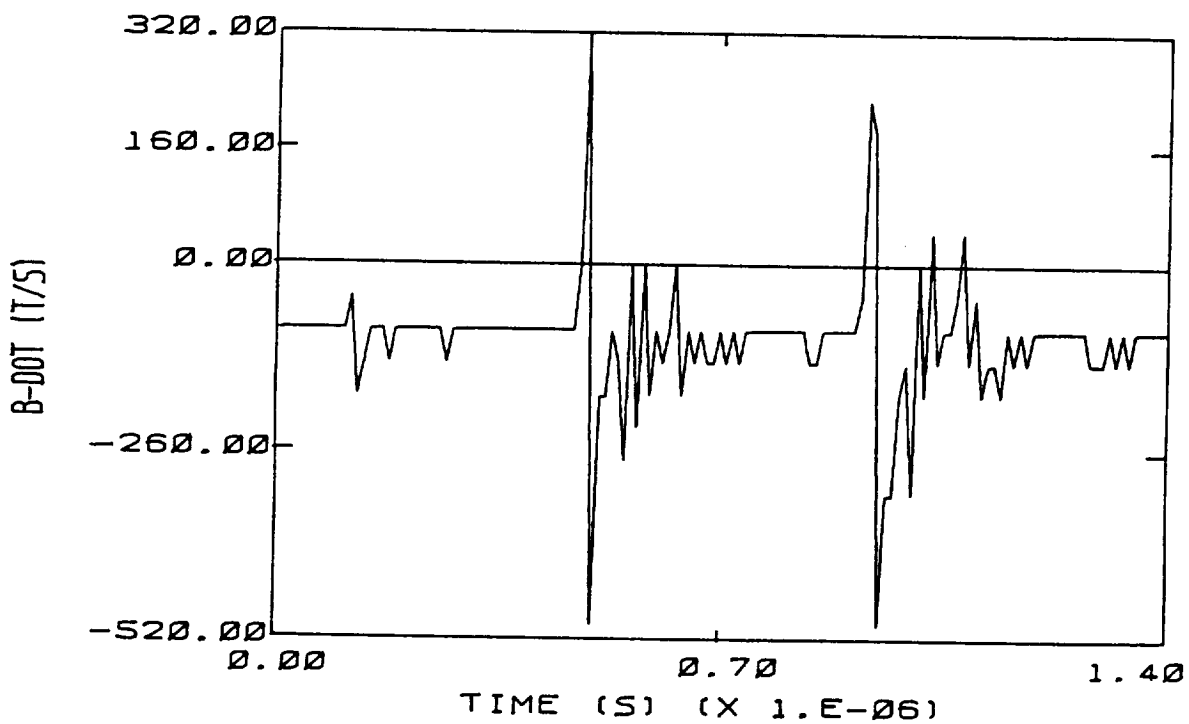
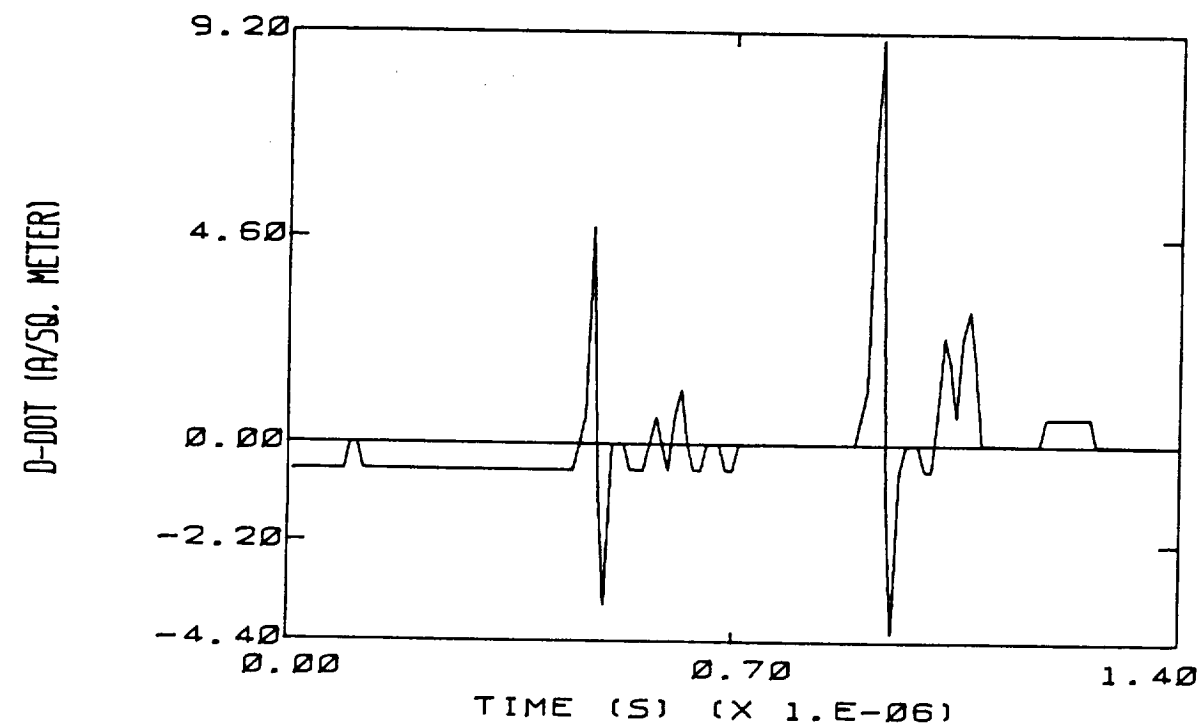


Figure 2.14 Simultaneous Waveforms from Flight 83-036

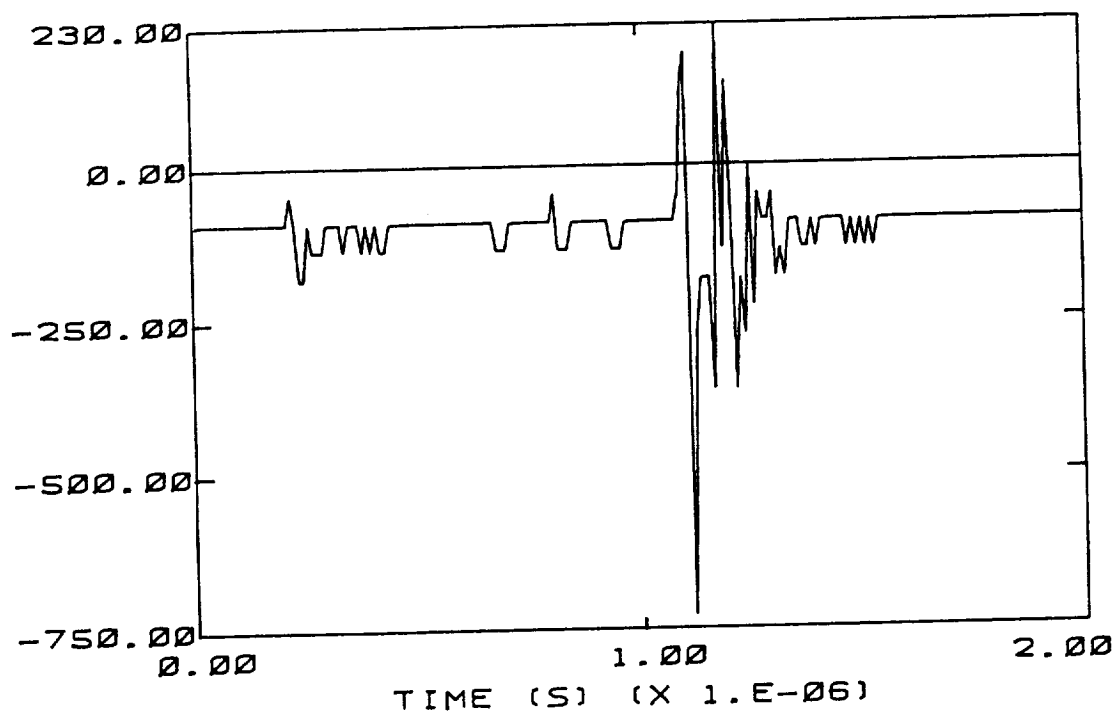
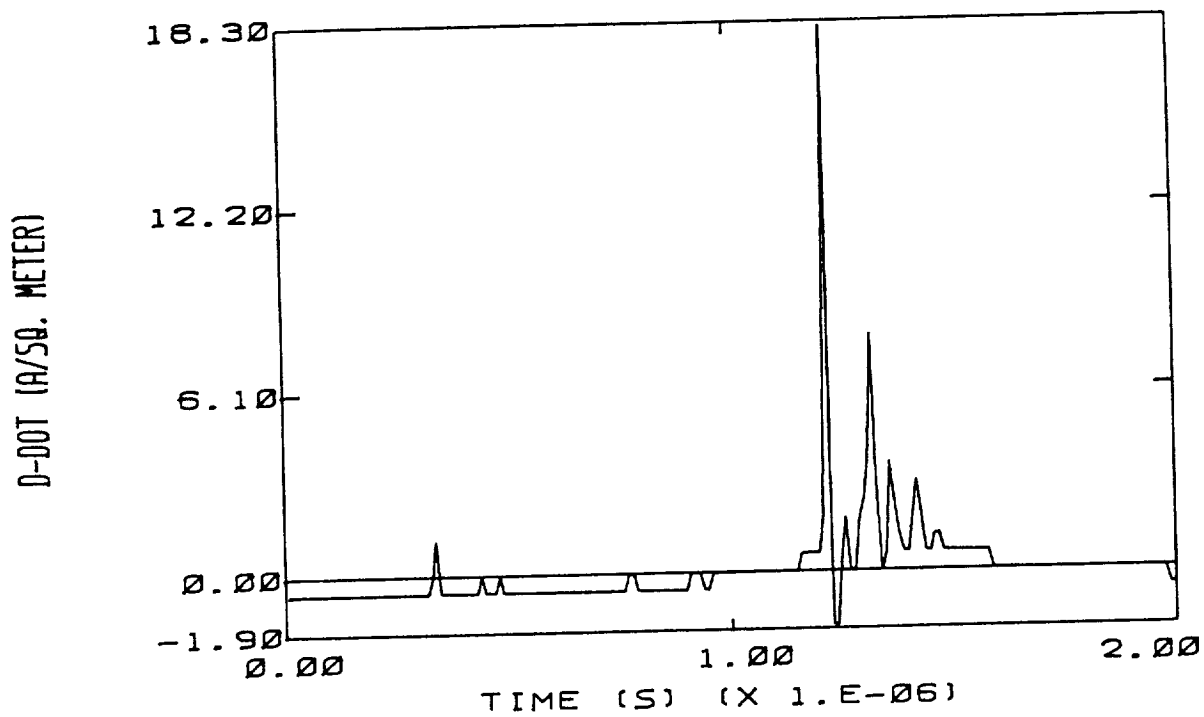
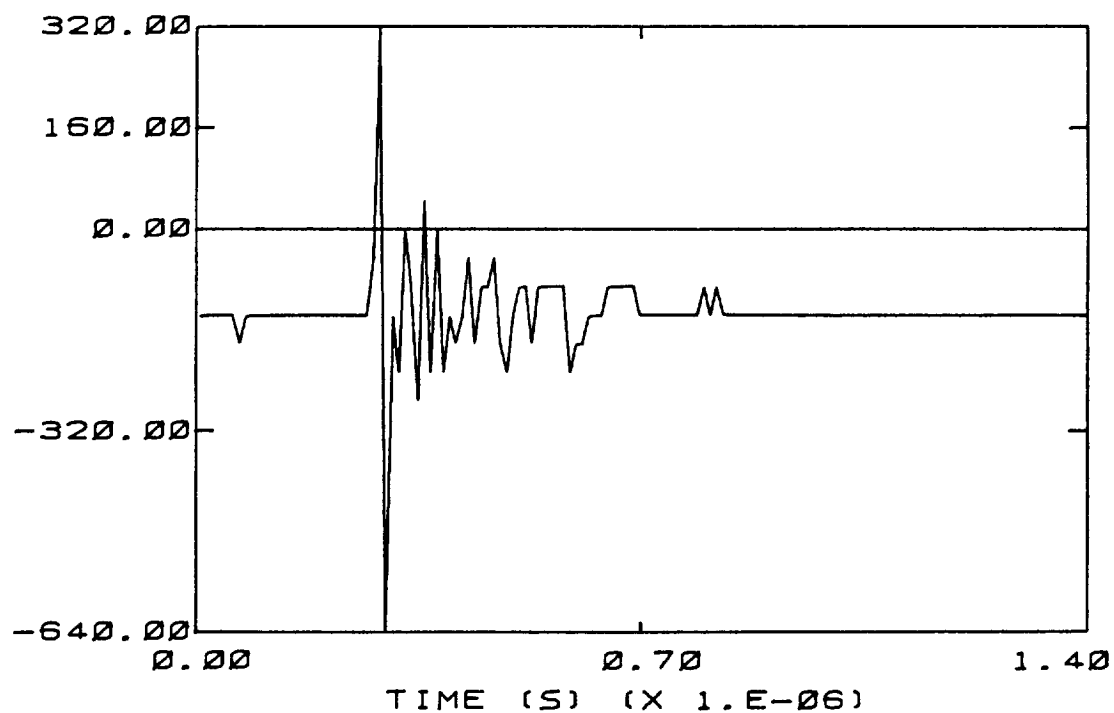
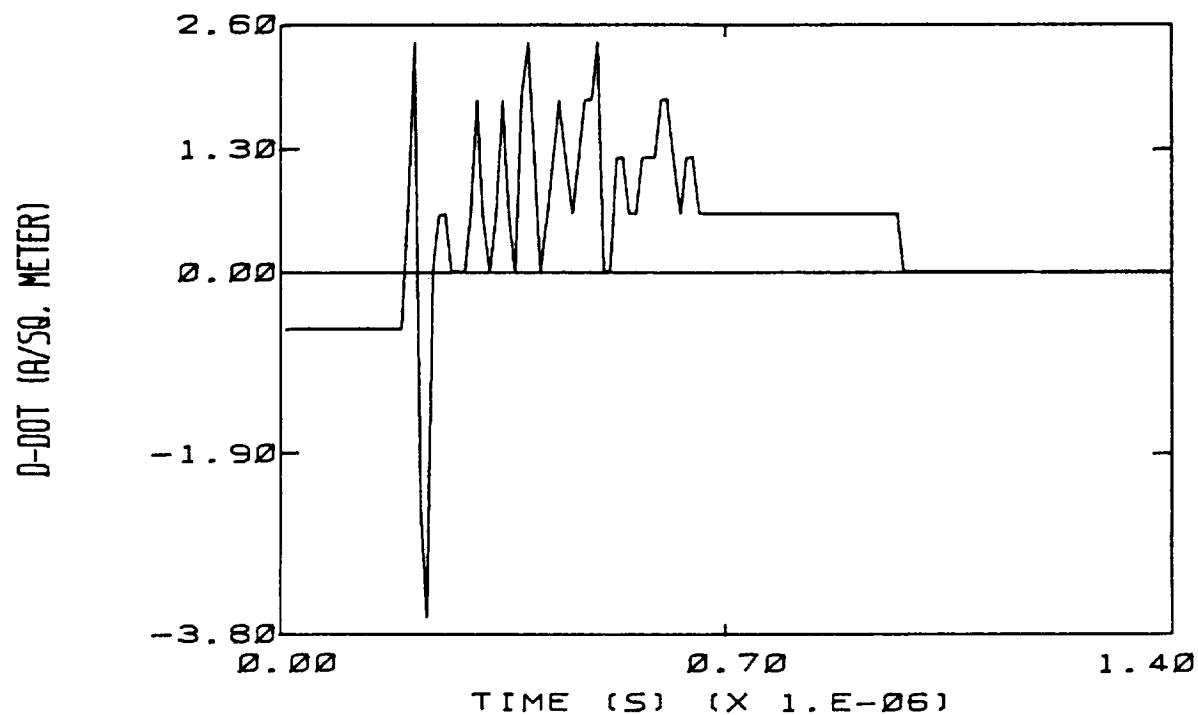


Figure 2.15 Simultaneous Waveforms from Flight 83-036



**Figure 2.16 Simultaneous Waveforms from Flight 83-036**

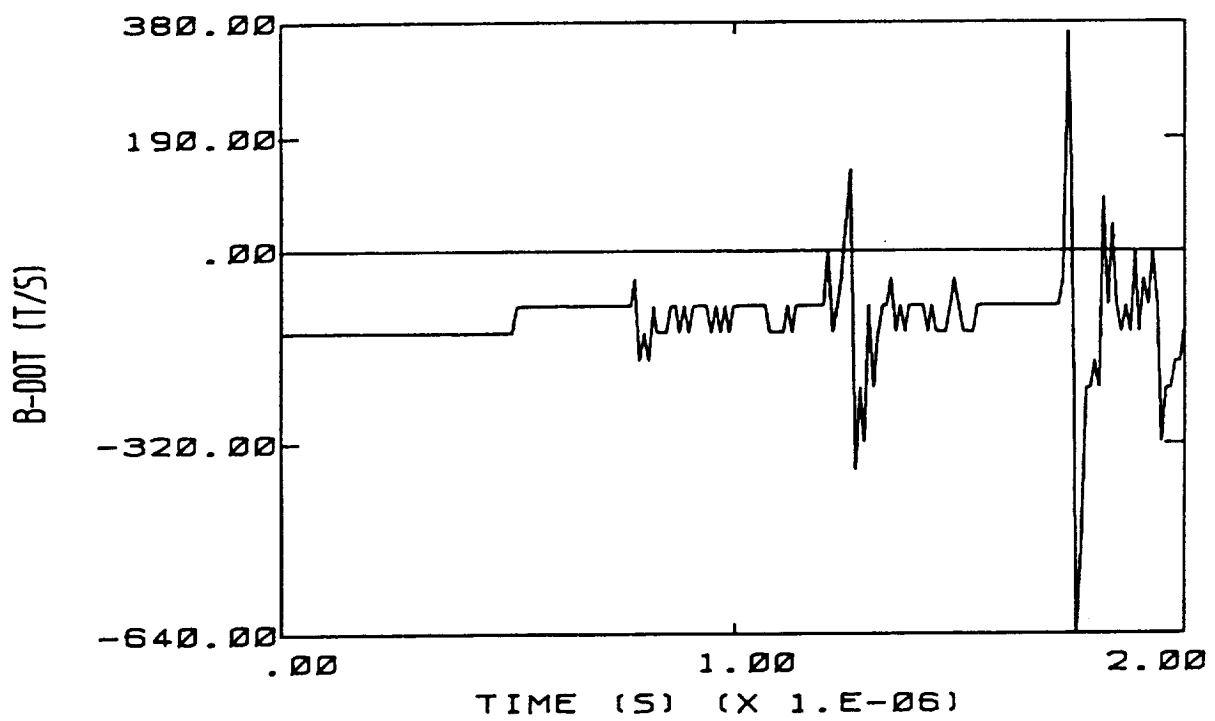
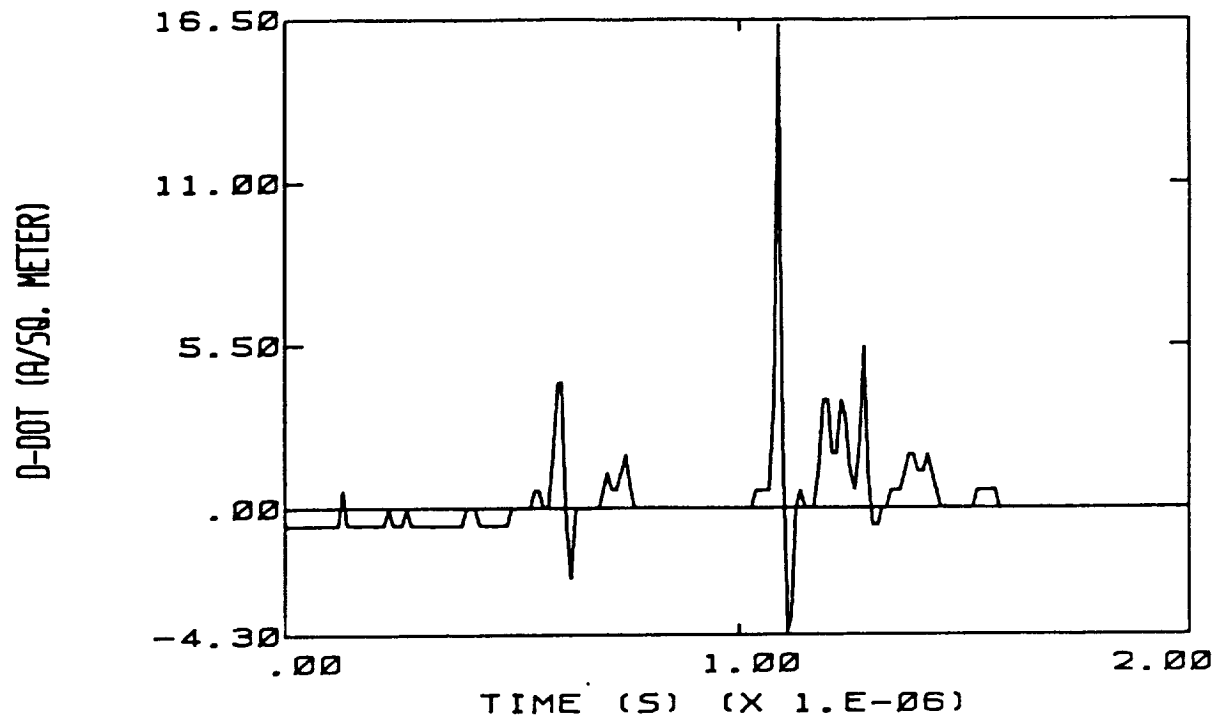


Figure 2.17 Simultaneous Waveforms from Flight 83-036

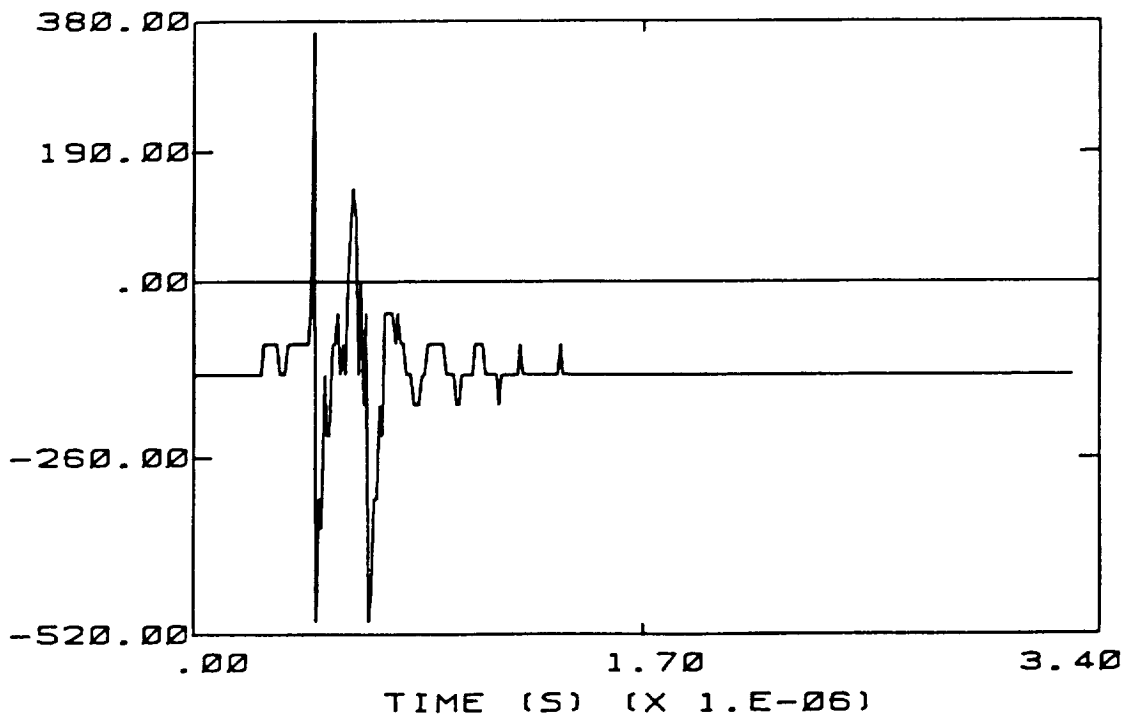
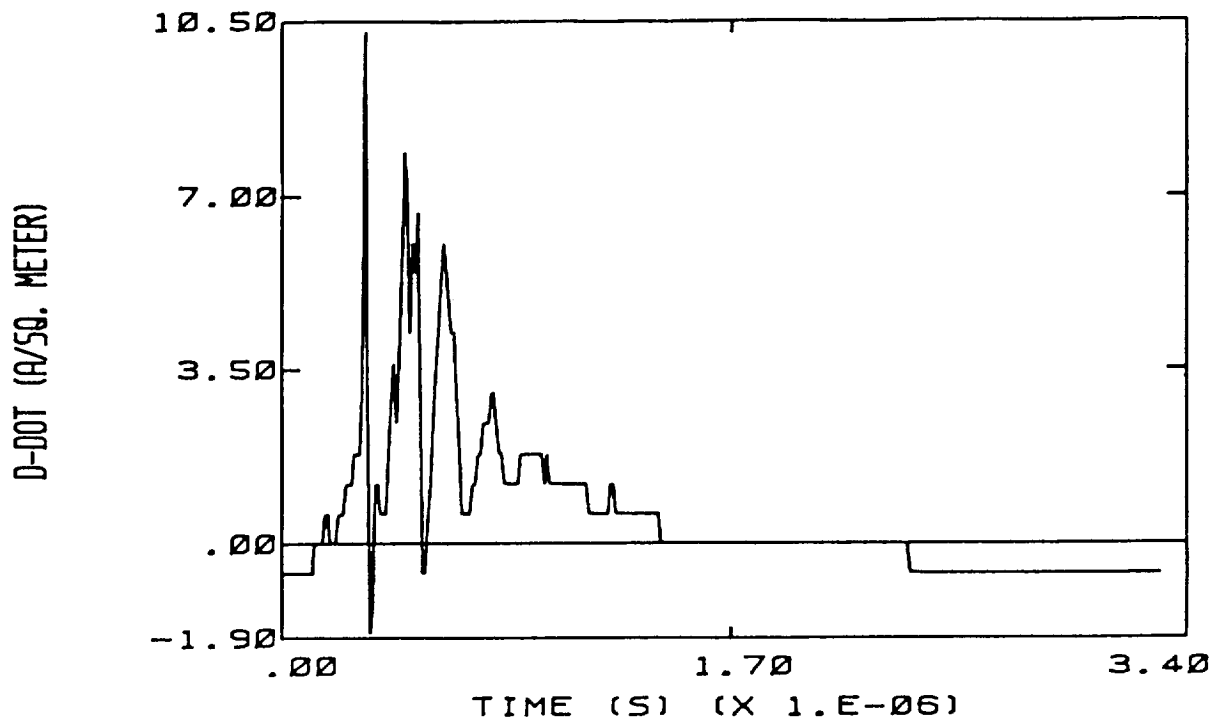
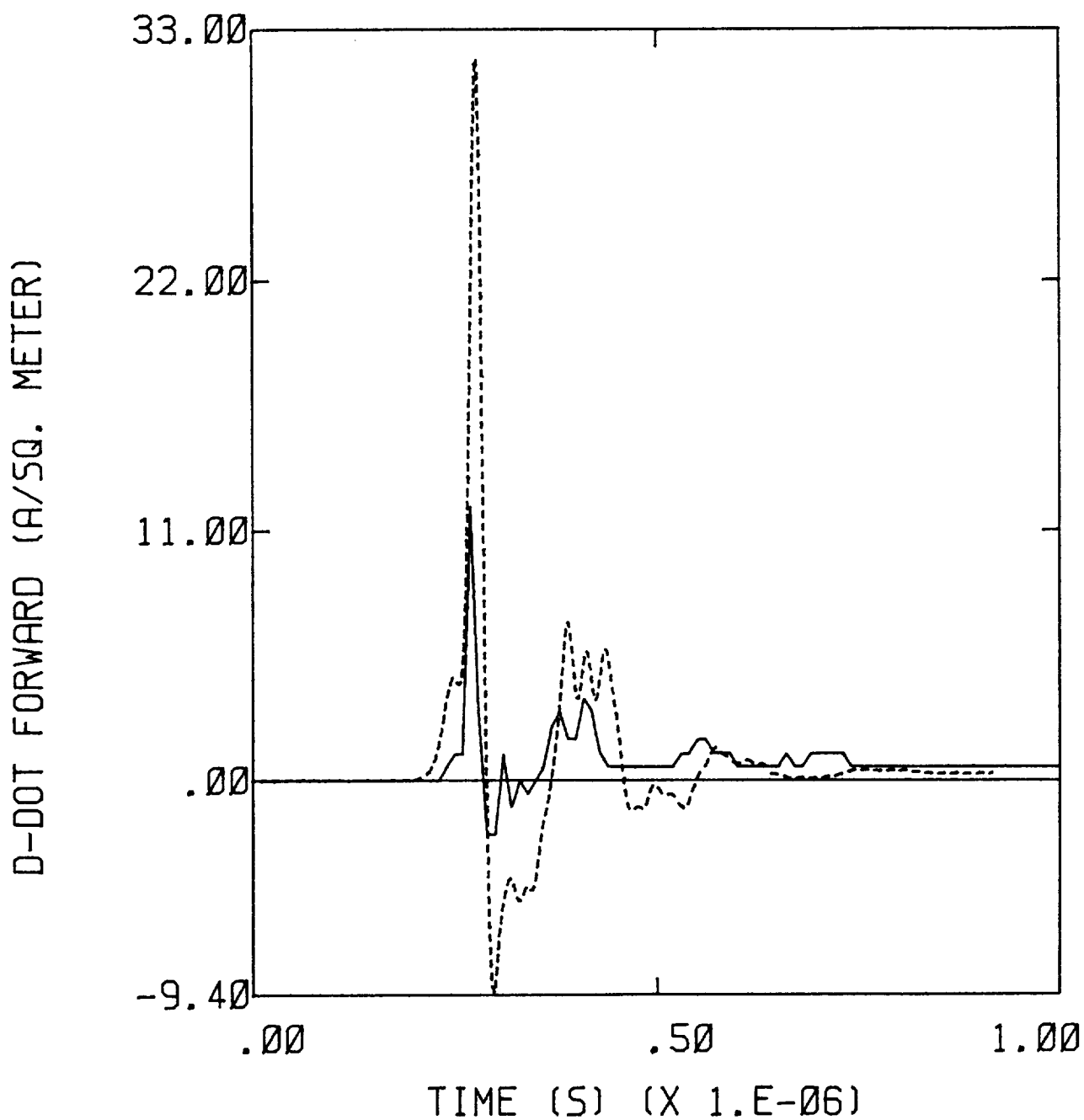
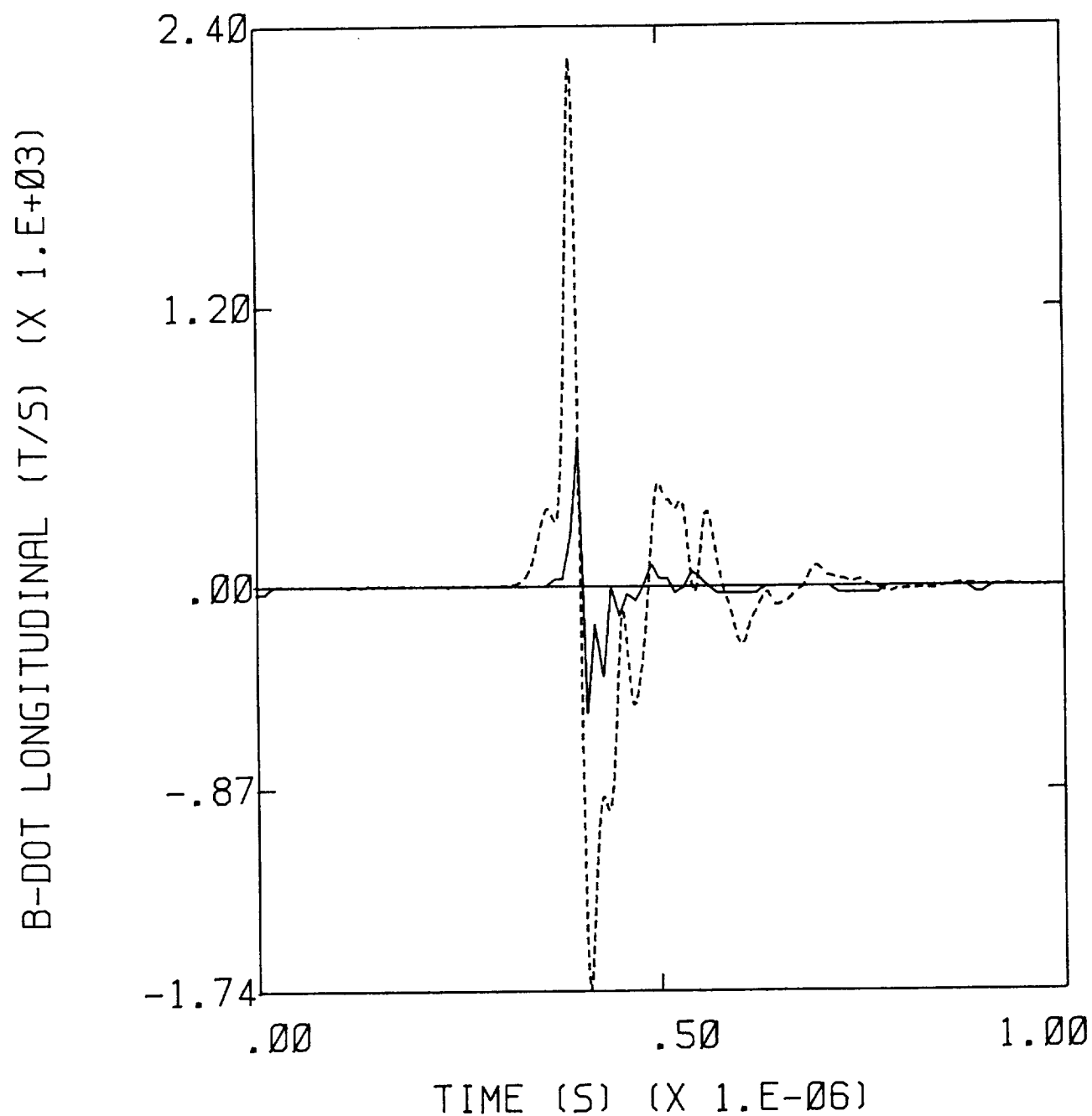


Figure 2.18 Simultaneous Waveforms from Flight 83-036



**Figure 2.19** Overlay of D-dot Data Collected on the F106B Lightning Research Aircraft During Flight 83-013 (SOLID LINE) with Results of Nonlinear Code for Initial Electric Field of 170 kV/m Oriented Along the X,Z Axes and Initial Aircraft Charge of  $-1/2 Q_m$  (DASHED LINE)





**Figure 2.20** Overlay of B-dot Data Collected on the F106B Lightning Research Aircraft During Flight 83-013 (SOLID LINE) with Results of Nonlinear Code for Initial Electric Field of 170 kV/m Oriented Along the X,Z Axes and Initial Aircraft Charge of  $-1/2 Q_m$  (DASHED LINE)

## **2.4 Analysis of D-dot Peak Ratios**

The F106B carries three D-dot sensors, under the forward part of the fuselage, under the left wing, and on the left side of the vertical stabilizer. During the 1984 thunderstorm season, all three of these sensors were active. The ratios of the peak responses of these sensors is of some interest, in that the ratios should be indicative of attachment points. The ratios also allow better comparison to calculated responses, because the amplitude information has been normalized away. Hence ratio comparisons can be used to determine possible ambient field orientations for triggered lightning events. This can be done by comparing measured ratios with calculated ratios found from nonlinear triggered lightning parameter studies.

Part of the motivation for the analysis is the persistent large ratio of the D-dot forward to D-dot tail response which is usually seen in the measured data. The large ratio can also be found in some of the calculated responses, but much less frequently. The reason for this discrepancy is somewhat unclear, but two possibilities are most probable. The first and less likely possibility is that the calibration of the D-dot tail sensor on the F106B is inaccurate. However, the calibrations are performed repeatedly and are unlikely to be consistently wrong. The better possibility is that there is some inaccuracy in the finite difference model of the F106B. This in fact was found to be the case. It was discovered that the location of the D-dot tail sensor about halfway up the vertical stabilizer was incorrect. In actuality, the sensor is located near the base of the tail where the presence of the fuselage can act to reduce the level of the D-dot tail sensor. Hence, the calculated ratios involving D-dot tail are undoubtedly smaller than they should be. This deficiency in the model has been corrected for future work.

In order to compare ratios of all three D-dot sensors, multi-sensor simultaneous data must be used. The 1984 data records are the only records which meet this criterion. As of this writing, eight multi-sensor events were available. The D-dot records from these events were used to create Table 2.2. The ratios were calculated by using the amplitude of the first major peak in the record without regard to sign.

**TABLE 2.2**  
**Measured D-dot Ratios**

<u>Event</u>	<u>D-dot Fwd/D-dot LW</u>	<u>D-dot Fwd/D-dot Tail</u>
84-017	1.42	5.44
84-014	1.33	3.92
84-015 (1)	1.65	6.91
84-015 (2)	1.5	---
84-015 (3)	1.37	4.68
84-028 (1)	1.2	3.75
84-028 (2)	1.25	5.00
84-028 (3)	.68	2.00

In Table 2.2 under the event column the flight number is listed first. If there was more than one trigger during a flight, the number of the trigger is added in parentheses. Note especially the consistency of the ratios, with the exception of the third trigger on Flight 84-028. This leads one to believe that the events were similar in the sense that initial attachment was in almost the same location. Also note that the D-dot forward over D-dot tail ratio is quite large. This is a characteristic that appears frequently in the measured data, but much less frequently in the parameter study to be presented later. Table 2.3 shows the D-dot forward to D-dot tail ratios calculated from the principal angle of orientation parameter study presented in a previous report [4]. This parameter study analyzed the F106B response to triggered lightning with the ambient electric field oriented along principal axes of the aircraft: nose to tail (N-T), tail to nose (T-N), left wing to right wing (LW-RW), right wing to left wing (RW-LW), top to bottom (T-B), bottom to top (B-T). Also varied was the net charge on the aircraft, in units of  $Q_m$ , where  $Q_m$  is the amount of charge necessary to produce air breakdown on the aircraft in the absence of any ambient field ( $Q_m = 1.79 \text{ mC}$ ).

Table 2.4 presents the same data for the calculated D-dot forward to D-dot left wing ratios.

The circled numbers in each of the Tables 2.3 and 2.4 compare favorably to those which have been measured. It is immediately apparent that locations of circled numbers in the two tables do not coincide. Hence none of the elements from the principal angle parameter study reproduce the ratios from the measured data.

**Table 2.3**

D-dot Forward to D-dot Tail Ratio For Principal Angle Parameter Study

Charge Orientation	0	.5Q <sub>m</sub>	-.5Q <sub>m</sub>	Q <sub>m</sub>	-Q <sub>m</sub>
T - N	4.77	5.00	0.17	5.11	1.14
N - T	3.29	0.27	4.64	0.95	3.75
RW-LW	1.00	0.90	1.00	1.28	0.92
LW-RW	0.81	0.79	1.13	0.95	1.24
B - T	0.29	0.28	4.00	0.32	3.43
T - B	0.43	5.69	0.32	5.25	0.58

**Table 2.4**  
D-dot Forward to D-dot Left Wing Ratio For Principal Axis Parameter Study

Charge Orientation	0	.5Q <sub>m</sub>	-.5Q <sub>m</sub>	Q <sub>m</sub>	-Q <sub>m</sub>
T - N	6.36	6.35	0.95	6.40	0.84
N - T	4.06	1.08	4.64	0.97	4.71
RW-LW	1.07	1.82	0.66	1.39	0.59
LW-RW	0.42	0.43	1.43	0.57	1.38
B - T	1.18	1.09	4.29	1.66	3.93
T - B	1.13	5.89	1.00	5.38	1.53

A skewed angle of orientation parameter study has also been partially completed, and is described in detail in Chapter 5. The D-dot ratios calculated from that study are shown in Tables 2.5 and 2.6. The notations for the orientation of the field are described in the preface to Appendix D, but basically refer to axis of the aircraft along which a component of the field is present. The axes chosen for this study are shown in Figure 1.1.

The circled items in the two tables again represent cases which correspond roughly to measured values. Note that this time, there are two circled cases which are colocated in each table. These two cases are doubly circled in the tables. They are possible candidates for the ambient field orientation and net charge present for the measured lightning events. Of course, this cannot in any sense be considered definitive, as there are many possible sources of error, and also other possible parameter variations. It should be considered, however, as worthy of further investigation.

It is significant to observe that the nonlinear parameter study with principal axis E fields did not produce the observed D-dot ratios, but that the ratios were observed for skewed angles. This fact emphasizes the nonlinear behavior of the response and its sensitivity to details of the initial conditions. Thus, the nonlinear parameter study should be continued to include more variety in the initial conditions.

**Table 2.5**

D-dot Forward to D-dot Tail Ratio For Skewed Angle Parameter Study

Charge Orientation	0	$-0.5Q_m$	$-Q_m$
X,Y	3.95	4.19	4.23
-X,Y	4.05	4.19	4.23
X,-Y	4.15	1.03	1.08
-X,-Y	4.91	0.71	0.74
X,Z	0.92	1.00	3.64
-X,Z	0.69	0.72	3.61
X,-Z	0.79	0.92	1.34
-X,-Z	1.03	0.58	0.93
Y,Z	3.81	4.35	4.21
-Y,Z	2.41	0.82	0.79
Y,-Z	6.04	3.37	3.93
-Y,-Z	4.85	0.24	0.40
X,Y,Z	3.66	4.29	4.44
-X,Y,Z	3.75	3.75	4.44
X,-Y,Z	1.37	1.01	1.18
X,Y,-Z	3.14	3.50	3.67
-X,-Y,Z	0.96	0.70	0.83
-X,Y,-Z	3.14	3.50	3.72
X,-Y,-Z	5.05	0.61	1.33
-X,-Y,-Z	5.05	0.24	0.89

**Table 2.6**

D-dot Forward to D-dot Left Wing Ratio For Skewed Angle Parameter Study

Charge Orientation	0	$-0.5Q_m$	$-Q_m$
X,Y	3.75	4.62	4.39
-X,Y	3.57	4.50	4.39
X,-Y	4.15	0.95	0.93
-X,-Y	1.26	0.26	0.27
X,Z	1.05	1.00	4.44
-X,Z	0.44	0.42	1.54
X,-Z	0.41	0.96	1.21
-X,-Z	1.50	0.58	0.30
Y,Z	4.36	4.35	4.35
-Y,Z	2.56	4.52	0.56
Y,-Z	4.29	3.06	4.58
-Y,-Z	5.98	1.30	1.08
X,Y,Z	4.05	4.17	4.28
-X,Y,Z	4.05	4.46	4.28
X,-Y,Z	1.56	0.98	1.03
X,Y,-Z	3.29	3.18	4.26
-X,-Y,Z	0.35	0.34	0.29
-X,Y,-Z	3.14	3.09	4.32
X,-Y,-Z	5.97	1.34	1.23
-X,-Y,-Z	6.07	0.40	0.29



## CHAPTER 3

### LINEAR MODELING USING TRANSFER FUNCTIONS

Nonlinear lightning modeling, although more physically complete than linear methods, is costly and time-consuming. It is therefore quite useful to develop linear modeling techniques which allow one to investigate certain aspects of the lightning event without resorting to the complexity of a nonlinear model. One such technique is the use of transfer functions to determine the lightning current which caused a given set of measured electromagnetic responses on the F106B aircraft. The transfer function is a functional relationship in the frequency domain between a source function and a response function. The use of a transfer function requires that the system under consideration be linear. This requirement is satisfied by a linear finite difference code, but is, of course, not satisfied by a real lightning-aircraft system. The justification for using the transfer function technique is that the nonlinearity in the real system is confined mostly to the lightning channel itself. The electromagnetic responses on the aircraft are quite often approximately linear functions of the lightning current which flows onto the aircraft at the lightning attach point. That is, although the formation of the lightning channel, its evolution, and the lightning current are complicated nonlinear functions of geometry and initial conditions, the aircraft responses usually depend in a linear fashion only on the current at the attach point.

There are a number of assumptions which must be made when using the transfer function technique. These are discussed individually below.

#### (1) Lightning Attachment Locations Must be Known

These locations constitute part of the initial conditions and as such are necessary to define the problem. In addition, the attachment locations cannot change with time (e.g., swept stroke), as this violates the conditions for linearity. Also, if there are multiple channel attachments, only one of these can act as a source, while the others just drain charge from the aircraft. Although having more than one source does not violate linear constraints, the problem no longer has a unique solution if more than one source is involved.

(2) Relative Formation Times of Multiple Channels Must Be Known

Because it is likely that exit channels for lightning current form later than entry channels, it is necessary to have knowledge of their formation times. In a sense, these channels which appear during the course of a problem constitute boundary conditions which change with time. This does not violate the linearity requirement as long as the formation times are fixed and do not vary with the time evolution of the problem. For all the transfer function analysis presented in this report, all lightning channels, both entry and exit, are in place at the beginning of the problem. That is, the relative formation times are always assumed to be zero; all channels form at the same time. This is done for simplicity because no information is available about relative formation times in the observed lightning events on the F106B. For informational purposes, it may be stated here that the formation times of exit channels may be calculated using nonlinear techniques.

(3) Lightning Channel Geometry Should Be Known

Although less important than the first two requirements above, it is desirable to know the orientation of the lightning channel with respect to the aircraft. This also constitutes boundary conditions which can affect aircraft responses to some extent. The responses are affected because electromagnetic radiation from current in the channel also produces some response on the aircraft, in addition to the current which flows onto the plane. The contribution of the current is much larger, however, so the channel radiation can be considered as a perturbation.

(4) Lightning Channel Impedance Should Be Known

Again, this is of lesser importance than the first two requirements, but can affect the linear relationship between source and response somewhat. The reason for this is that the back effect of the aircraft on the lightning current is different depending on the channel impedance. For example, a channel with infinite impedance is completely unaffected by the presence of the aircraft. In this case, whatever current is flowing in the channel is the current which is injected onto the plane, and reflections and responses on the plane behave as if the channel were nonexistent. For any other impedance, the response of the aircraft can affect the current in the channel, more so the lower the impedance. This, in turn, then alters the responses on the plane slightly. Hence it is desirable to know the channel impedance as a boundary condition on the problem. It is even possible to handle a time-varying impedance, as long as the

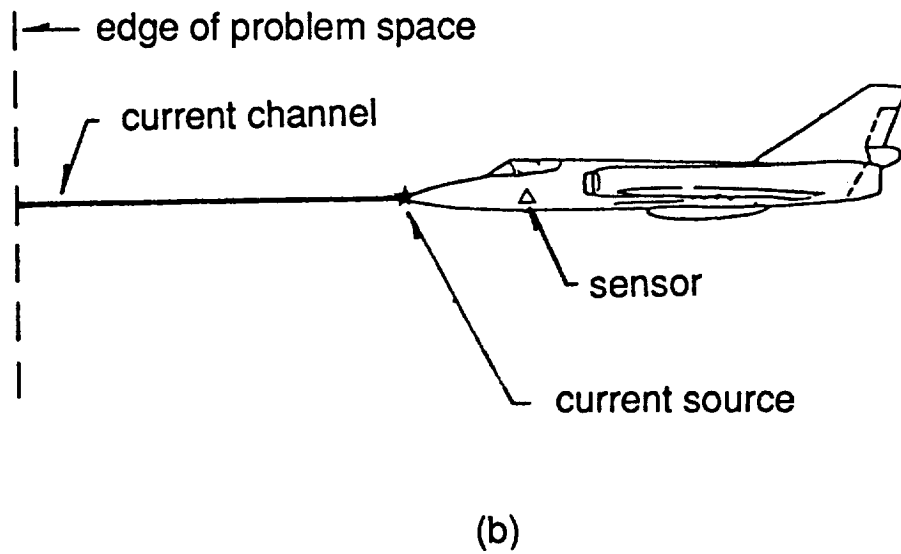
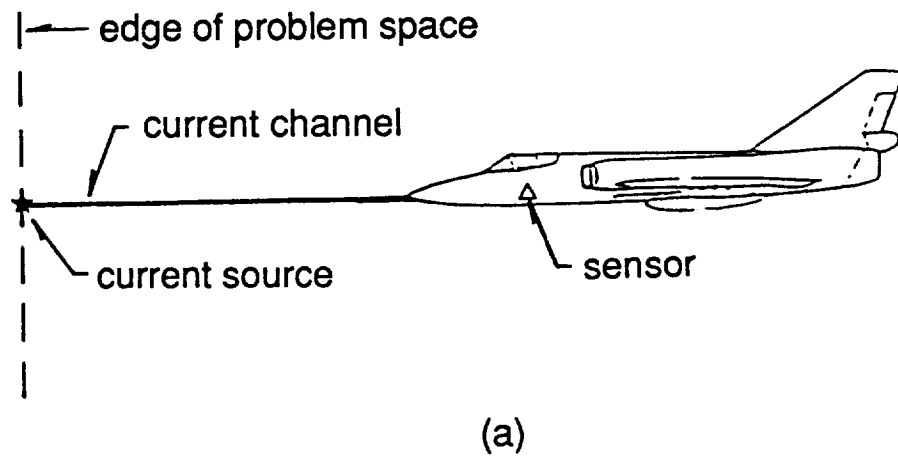
variation is specified in advance, and does not depend on the evolution of the problem.

The transfer function technique can be used either for triggered or natural lightning. The distinction between the two here is that triggered lightning begins at the aircraft and moves away, while natural lightning begins away from the aircraft and moves toward it. Typical geometries for each of these cases are shown in Figure 3.1. The case for natural lightning is shown in Figure 3.1a. A current channel having a specified impedance and velocity of propagation is attached to the nose of the F106B. The impedance and velocity of propagation are determined from the per unit length inductance and capacitance of the channel, which are in turn determined from the physical diameter of the channel. Therefore, in the linear model, the size of the lightning channel determines all of its electrical properties. The attachment to the nose depicted in Figure 3.1 is simply a concession to the point at which many lightning strikes attach to the F106B. The model allows attachment at any point on the aircraft and, in fact, allows multiple channels as long as there is only one current source in the problem. The sole difference between Figures 3.1a and 3.1b is in the location of the current source. For natural lightning, it is located at the edge of the problem space, as far from the aircraft as possible. This is done in an effort to model the fact that the initiation and driving forces for a natural lightning strike occur away from the aircraft, and the lightning current propagates toward the plane. The current source in Figure 3.1b is located near the point where the channel attaches to the F106B. This models the phenomenon of initiation at the surface of the aircraft with propagation outward.

The mathematics of the model are handled identically in the two cases. A transfer function is determined from the Fourier transforms of the current source and the response waveforms.

$$T(\omega) = R(\omega) / I(\omega) \quad (3.1)$$

Here  $T(\omega)$  is the transfer function in the frequency domain,  $R(\omega)$  is the Fourier transform of the calculated response waveform, and  $I(\omega)$  is the Fourier transform of the current source waveform. Because the model is linear  $T(\omega)$  is source independent; that is, changing  $I$  will change  $R$  in such a way as to keep  $T$  the same. Note that there can be as many transfer functions as there are separate responses on the aircraft. If there are



**Figure 3.1 Typical Model Geometries for (a) Natural Lightning, and (b) Triggered Lightning**

N sensors on the aircraft, there will be N different transfer functions for a single current source.

To determine the current source necessary to produce a given measured response, the measured response waveform must be Fourier transformed. Then the transfer function for the particular sensor is used to calculate the Fourier transform of the current source necessary to produce the measured response.

$$I(\omega) = R_{\text{measured}}(\omega) / T(\omega) \quad (3.2)$$

The current is then transformed into the time domain. It can then be used in the linear model as a check, to make sure the measured response is reproduced.

The transfer function technique is most useful in the events where multiple simultaneous sensor responses have been recorded. Then several current sources can be derived, one for each of the multiple responses. In principle, if the model geometry chosen is correct, all of the current sources should be the same. This is virtually never the case, however, for several reasons. First, the channel geometry may be incorrect. Attachment points are usually determined by direct observation of the strike, or examination of pit marks after a flight. If this information is unavailable, ratios of sensor response amplitudes can be used to give a crude idea of attachment locations.

In addition to the uncertainty of attachment locations, the presence of multiple channels, and the timing of their appearance is often unknown. Also, the orientations of the attached channels are uncertain. Even if the channel orientation were known precisely, it would probably be difficult to model accurately if a significant amount of bending or tortuosity were present. The electrical properties of the channel are generally unknown, too, so an estimate must be made.

Another source for error in the model is the gridding of the F106B itself. Because of the .5m x 1m x .5m cell size, the aircraft cannot be represented in the problem space to arbitrary precision. This results in slight differences between the responses of the real aircraft and the model aircraft even if channel properties and

attachment locations are known exactly. The differences are largest in places where the grid resolution is most inadequate, such as wing tips, nose, tail tip, and sharp leading and trailing surfaces. In most cases, the F106B sensors are located away from these regions, but some inaccuracy is expected.

The procedure then, in view of these difficulties, is to calculate all of the current sources for a given geometry, and then to analyze the differences found. If all of the sources are similar, it may be that the geometry chosen is close to the physical situation of the actual lightning strike. If large differences are present, the model geometry must be changed significantly.

In practice, the derived sources are heavily dependent on attachment point and much less dependent on all other factors. Hence, if the attachment point is accurately chosen, it is very likely that the derived current sources will all be similar. This is evidence that the aircraft responses are strong functions of the injected lightning current, and weak functions of all other relevant parameters.

In Chapter 4, the analysis of real measured data using the transfer function technique will be presented.

## CHAPTER 4

### APPLICATION OF THE TRANSFER FUNCTION TECHNIQUE

The linear transfer function technique described in the previous chapter has been applied in some detail to the multiple simultaneous data records from Flight 84-017. The usable simultaneous records from that flight include D-dot forward, D-dot tail, D-dot left wing, B-dot longitudinal, B-dot left wing, and current flowing onto the nose boom. Examination of the records indicates that the strike (probably triggered) attached at the nose of the F106B. The exit point for the current is more speculative, and in fact, the exit channel may have appeared later in time. The measured time domain records from the strike of Flight 84-017 are shown in Figures 4.1 a-f. The relatively large value of the nose boom current is the reason that the strike is thought to have initially attached at the nose. A similar current sensor attached to the vertical stabilizer measured only noise during the event, so it is known that there was no attached channel near that point, at least during the part of the strike while the sensors were recording.

The linear model used to analyze this strike had a thin wire current channel attached to the nose of the F106B. It extended directly outward along the fuselage line to the boundary of the problem space. The current source was placed at the junction of the channel and the model aircraft to simulate a triggered strike. No exit channels were included in the model, because of uncertainty in their possible location and time of appearance. Lightning channels with three different radii were used, 10cm, 5cm, and 1cm. The velocity of propagation of all the channels was kept at  $3 \times 10^8$  m/sec. This is not necessary in principle, and it is certainly more reasonable physically to use a slower velocity of propagation. However, the transfer function technique works somewhat better for a speed of light propagation, because of requirements of the linear finite difference code thin wire formalism. Because the aircraft responses are largely dependent on the injected current at the attachment point anyway, the velocity of propagation is not critical to the solution of the problem. In addition, two cases were done with resistively loaded channels. These were done with transfer functions calculated for the B-dot longitudinal sensor, and channel radii of 10cm and 1cm. The resistances per unit length investigated were 1 ohm/m, 10 ohm/m, and 50 ohm/m.

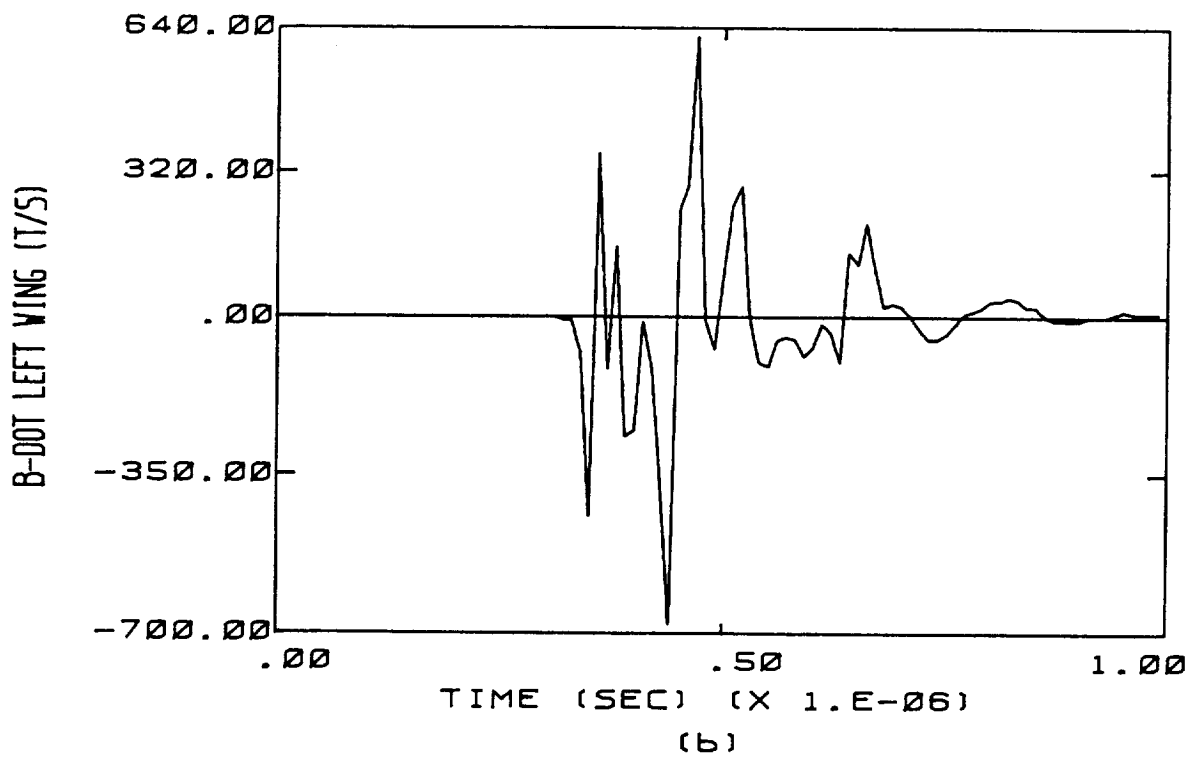
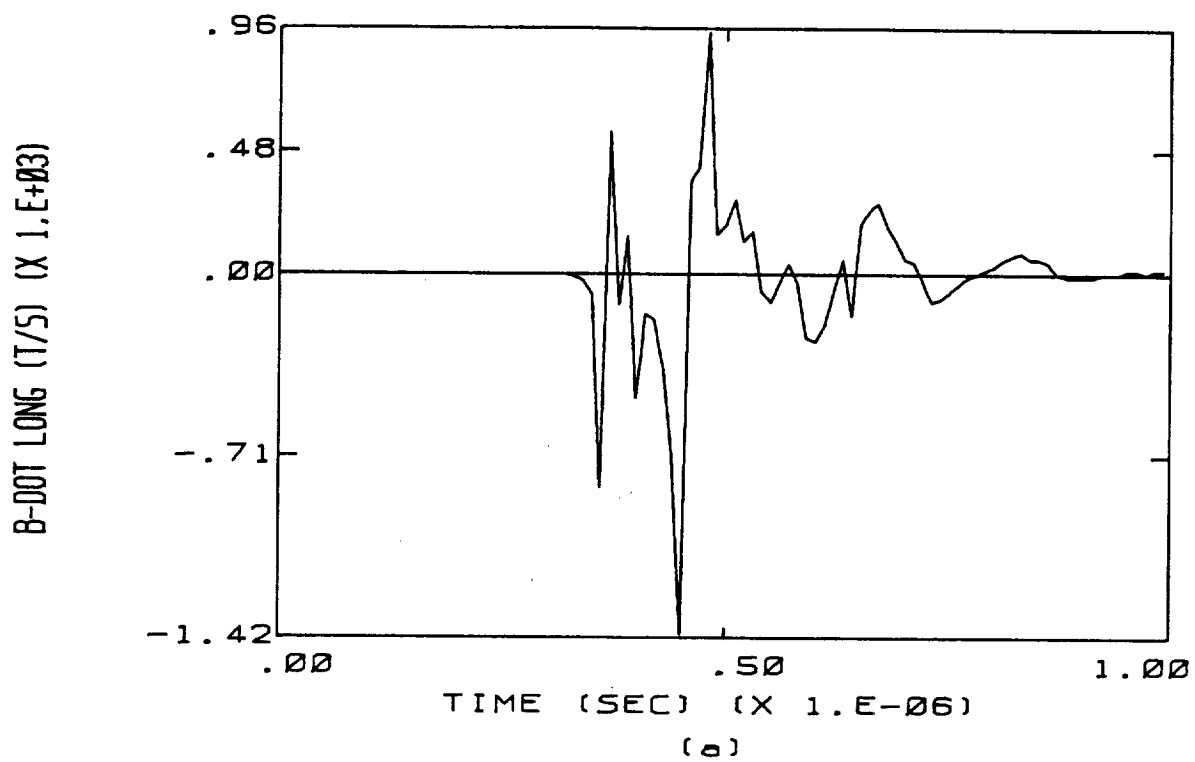
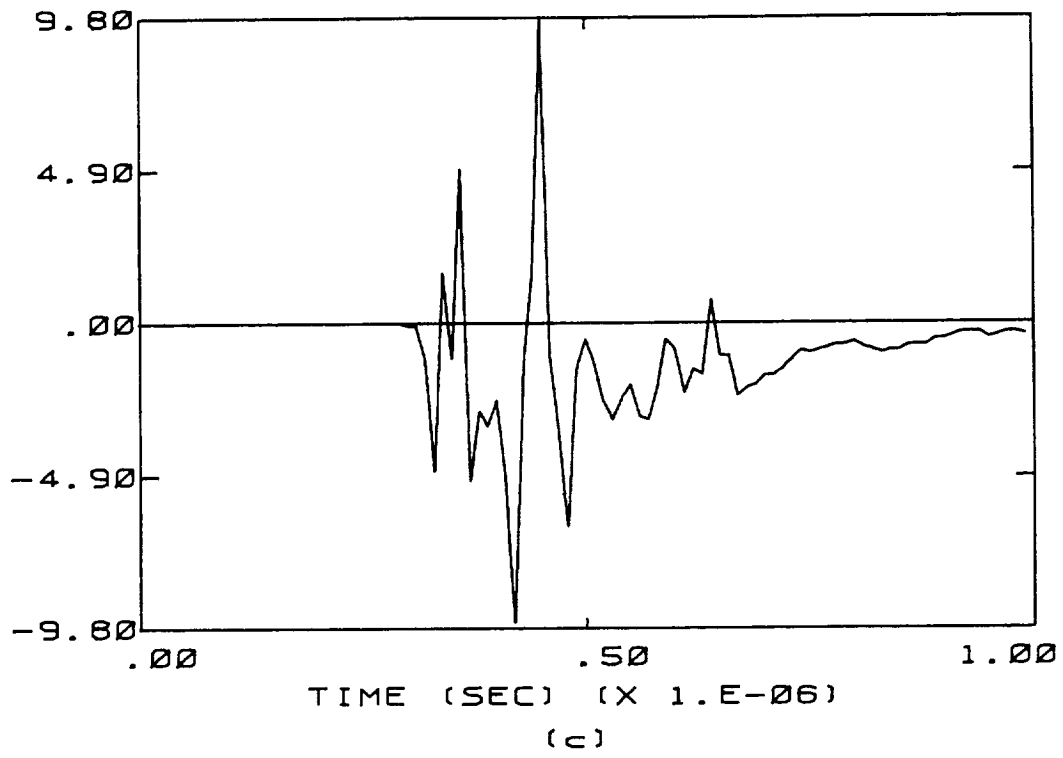


Figure 4.1 Measured Aircraft Responses for Flight 84-017



D-DOT FORWARD (A/SQUARE METER)



D-DOT LEFT WING (A/SQUARE METER)

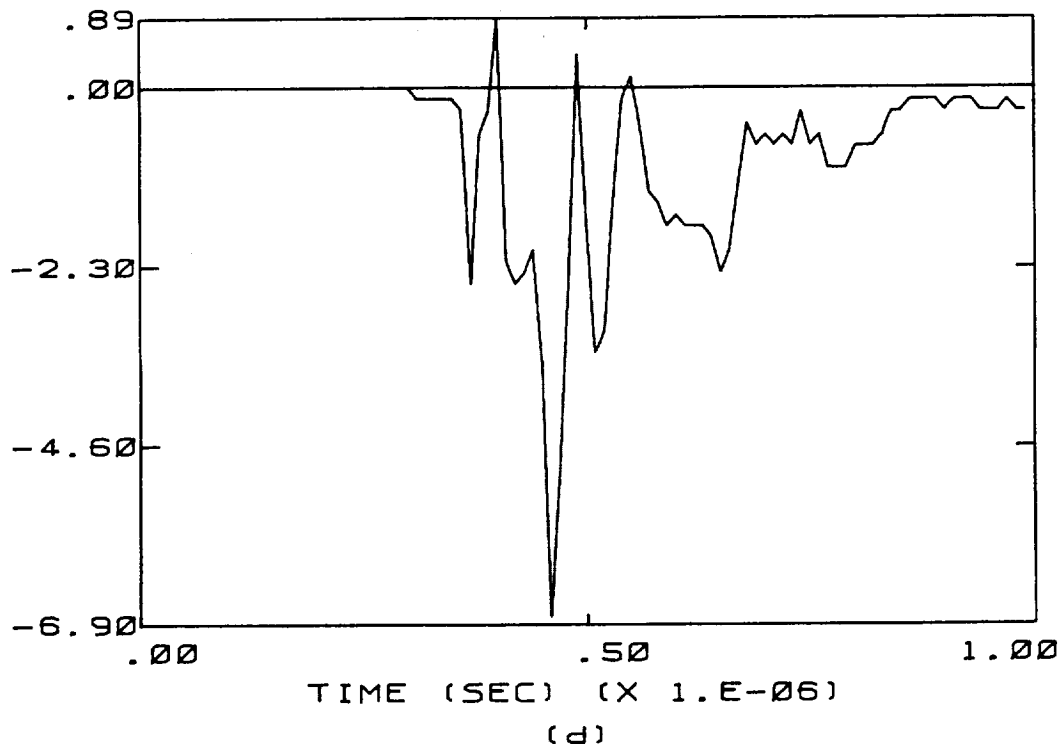


Figure 4.1 (continued)

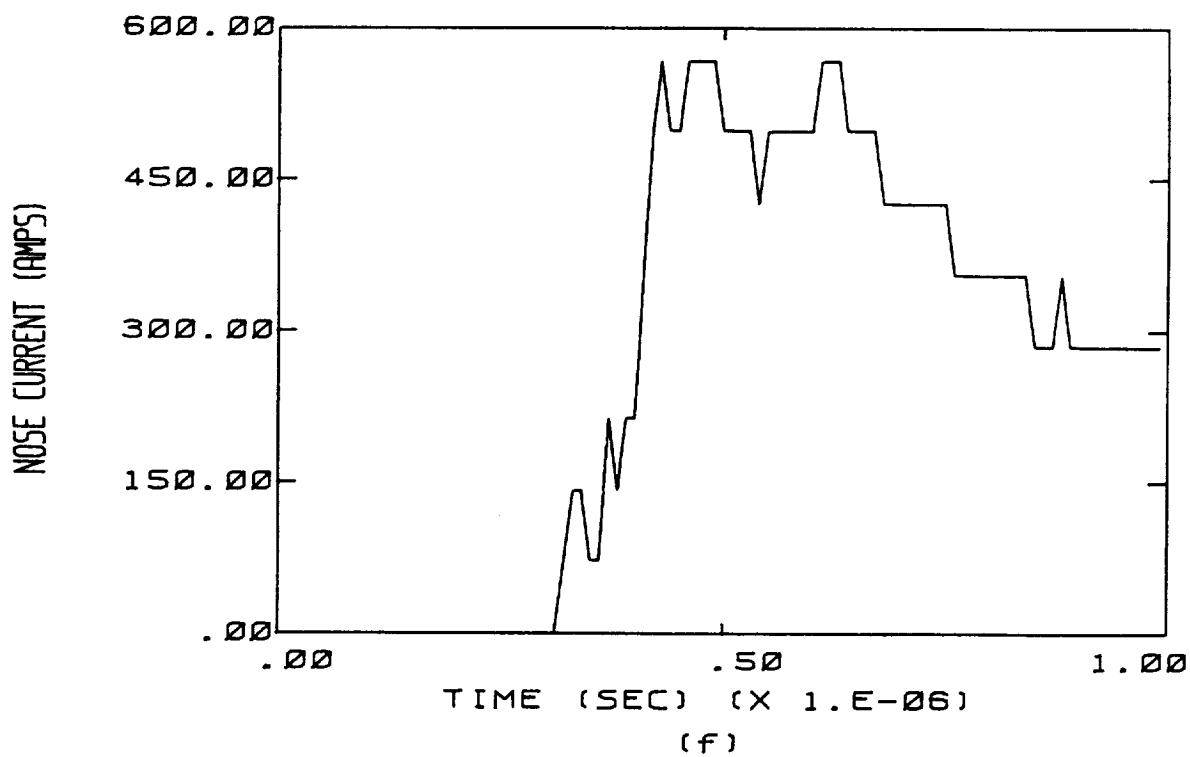
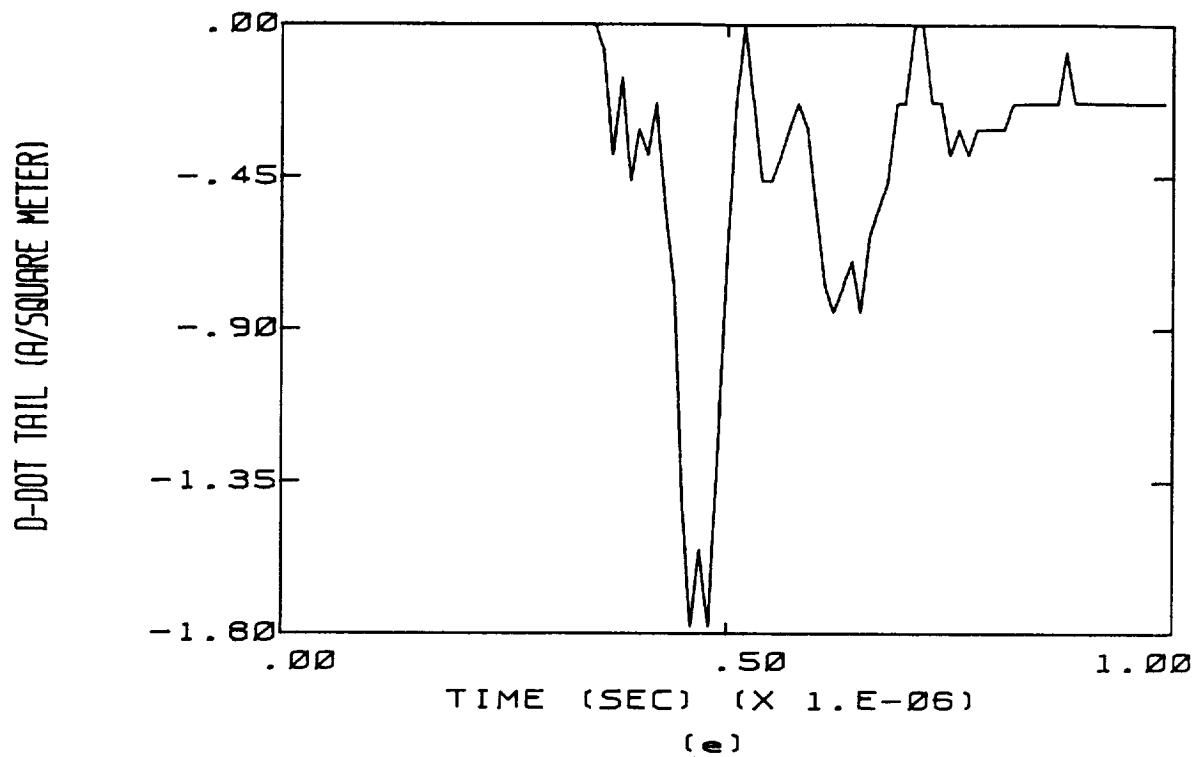


Figure 4.1 (continued)

For each of the current channels described above, a computer run of the finite difference code was done using a current source with a sine squared waveform. The source extended over one period of the sine squared, and was a pulse of 40 nanoseconds duration. The computer runs computed the aircraft responses at all of the sensor locations. The computations were extended far enough in time so that all of the sensor responses had decayed to zero. Next, transfer functions were calculated between the current source and each of the calculated responses. This resulted in five transfer functions per computer run, representing the linear relationship between the current source and the three D-dot and two B-dot sensor responses for each channel radius.

The next step was to transform the measured responses from Flight 84-017 into the frequency domain. The transformed responses were then divided by the appropriate transfer functions to give frequency domain current sources which presumably would reproduce a particular measured aircraft response. The current sources were then transformed back into the time domain.

The last step in the analysis was to use each of the derived current sources in the linear finite difference model of the aircraft and lightning channel. This was done first to check the analysis, to make sure that the particular measured response for which the current source was derived was reproduced by the model. Secondly, the other calculated responses were compared with the measured responses. In principle, if the model were physically accurate, these responses would also compare favorably.

Because of the number of plots, the response comparisons are presented in Appendix C. There, a set of six overlays is shown for each derived current source, of which there are twenty-one. Each set of six plots is identified as to the channel radius for which it applies, and the particular transfer function from which it was calculated. Figures C.1-C.15 use a channel with zero resistance per unit length. Figures C.16-C.21 specify the resistance used. The plots overlay the calculated aircraft response with the corresponding measured response. The calculated nose boom current is also overlaid on the measured current in each set. In addition, Figure C.22 overlays the frequency domain measured and calculated waveforms for the case of a zero resistance channel. This is the frequency domain analog of Figure C.1.

Several things may be noticed from the data presented in Appendix C. First, in any given set of overlays, the measured and calculated responses which are expected to match exactly are quite close. Slight differences can generally be attributed to a lack of frequency resolution in the discrete Fourier transforms used. These differences tend to appear mostly in the amplitude of large peaks in the data where better resolution at high frequencies is needed. Hence the technique is proven to be working properly.

An important part of the analysis of the overlays in Appendix C is to compare the waveforms in each set which are not forced to match by the transfer functions. These give an indication of whether the physical model chosen for the strike is close to being correct. Two criteria can easily be used for comparison, peak values and waveshape. The comparison between peak amplitudes is obvious. Comparison of waveshapes includes the start time of the record, the time it takes to die away, and the time placement of major maxima and minima in the waveform. It also could include the amplitude ratio between two peaks in a waveform.

In general, comparisons of waveshape in the overlays of Appendix C are good. The onset times of all responses match with measured values, meaning that the attachment point at the nose boom is correct. The decay times of calculated and measured responses also match quite well. This indicates that the duration of the current source has been accurately predicted. The time placement of major features in the calculated and measured waveforms is also good, indicating the same resonance effects are active in the calculated and measured data.

The worst correspondence between measured and calculated data is undoubtedly in the amplitude comparison. The calculated and measured responses are usually at worst separated by a factor of two, except for the D-dot tail response. For that sensor, the measured response is about four times smaller than the calculated response except, of course, when the current source is chosen to reproduce that response. When that current source is used, the other four sensor responses and the nose boom current are well below the measured values. Hence, it appears that the model chosen for this strike cannot match both the D-dot tail response and the other responses simultaneously.

The reason for the large discrepancy of the D-dot tail sensor is at least partly because of its location in the finite difference model. It was found late in the contract work that the physical location did not correspond to its location in the model. The physical location is near the base of the tail, while the model placed the sensor about halfway up the tail. This change in location significantly affects the sensor's response. A preliminary test to determine the difference was done using a 10 cm radius channel with a 50 ohm/m resistance per unit length. The desired transfer function was appropriate to reproduce B-dot longitudinal. Thus it was exactly the same case as shown in Figure C.18, except for the altered location of the D-dot tail sensor. The results showing measured response overlaid on both calculated responses, is given in Figure 4.2. Note that the calculated response for the correct sensor location is much closer to the measured response amplitude. Remaining differences can be attributed to a lack of adequate resolution in the model at the point where the tail joins the fuselage.

The best comparison of calculated and measured responses appears to be when the B-dot longitudinal sensor is used to determine the transfer function. This is probably because that sensor is located far from the current source and also away from sharp points and edges of the aircraft. Hence the response is more dependent on the aircraft structure as a whole and less dependent on local details. In terms of channel radius, there is little to choose from among the models, except that the 1cm radius channel may give marginally better comparisons. It is noteworthy that in the resistively loaded channels, there is virtually no difference between responses. Figures 4.3 and 4.4 overlay the measured nose current and the calculated nose currents for different resistances per unit length and different channel radii. Figure 4.3 is for the 10cm radius channel and Figure 4.4 for the 1cm radius channel. In both cases, the calculated currents are nearly identical, and the overlays cannot be separated. This occurs because the linear model requires the same injected current to produce the B-dot longitudinal response from which the currents were derived. It implies that the interaction between the channels modeled and the aircraft is very similar, regardless of channel resistivity.

In summary, the linear transfer function technique appears to work well when the physical geometry associated with a lightning strike is known. For the strike modeled here, all the measured sensor responses were well represented with the

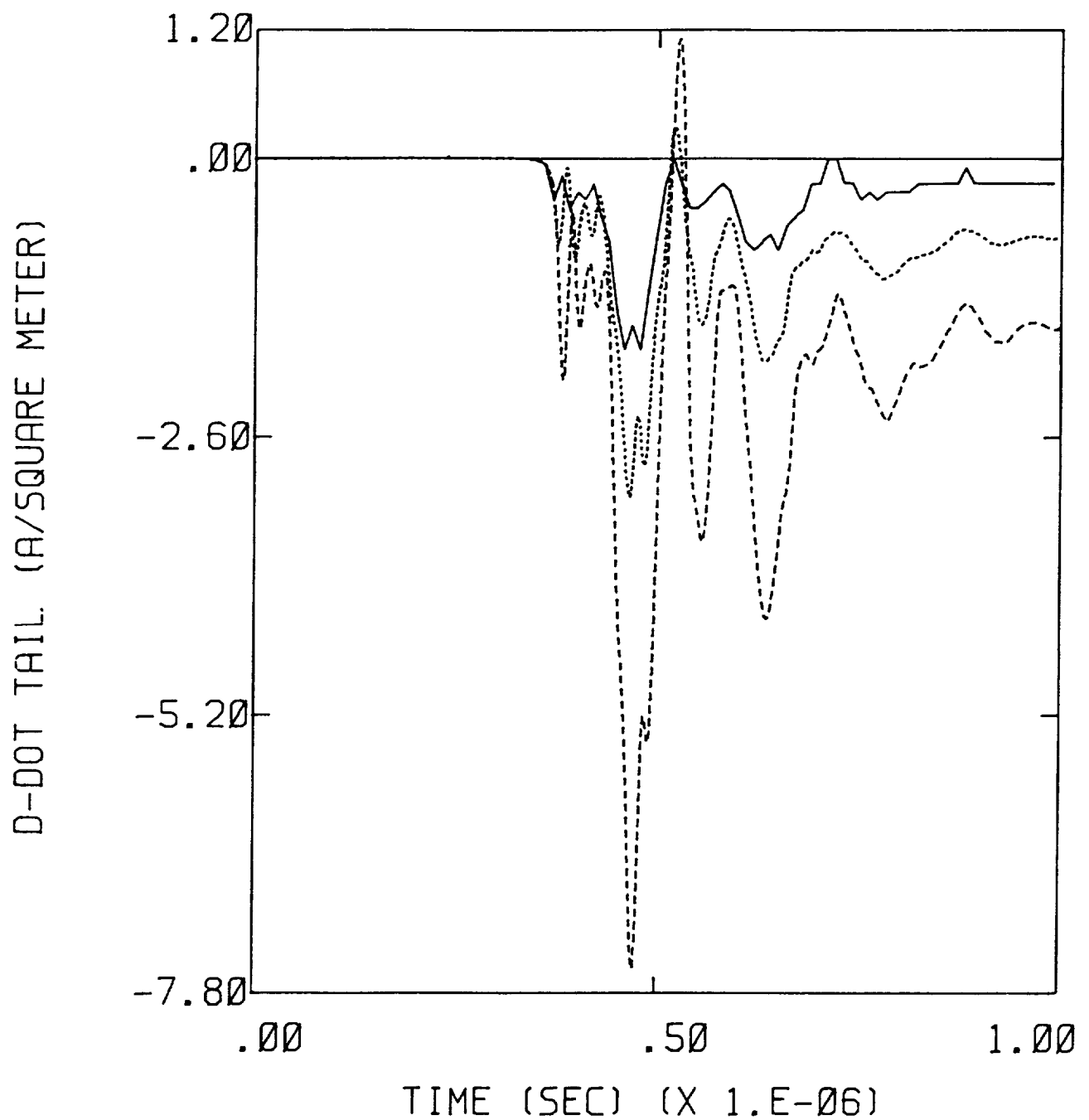


Figure 4.2 Overlay Showing the Difference In Response Between the Previous Location on the Tail (Incorrect) and the New Location (Correct). The Solid Line Is the Measured Data, the Dashed Line the Response at the Incorrect Location, and the Dotted Line the Response at the Correct Location.

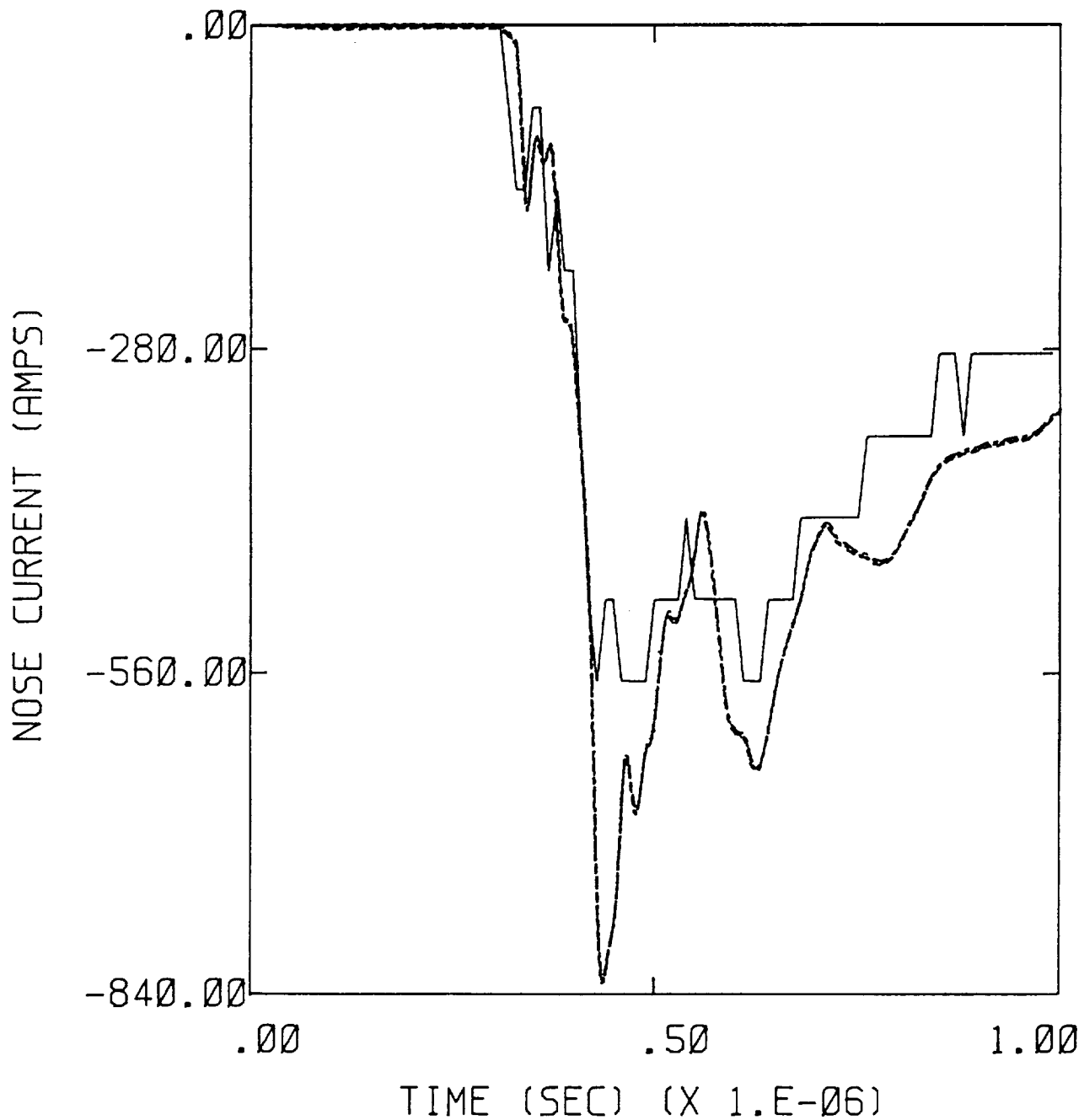


Figure 4.3 Overlay of Measured and Calculated Nose Currents for the Case of a 10 cm Radius Channel and Resistances Per Unit Length of 1 ohm/m, 10 ohm/m, and 50 ohm/m. The Measured Data Is the Solid Line. Note That the Calculated Responses Are Virtually Identical.

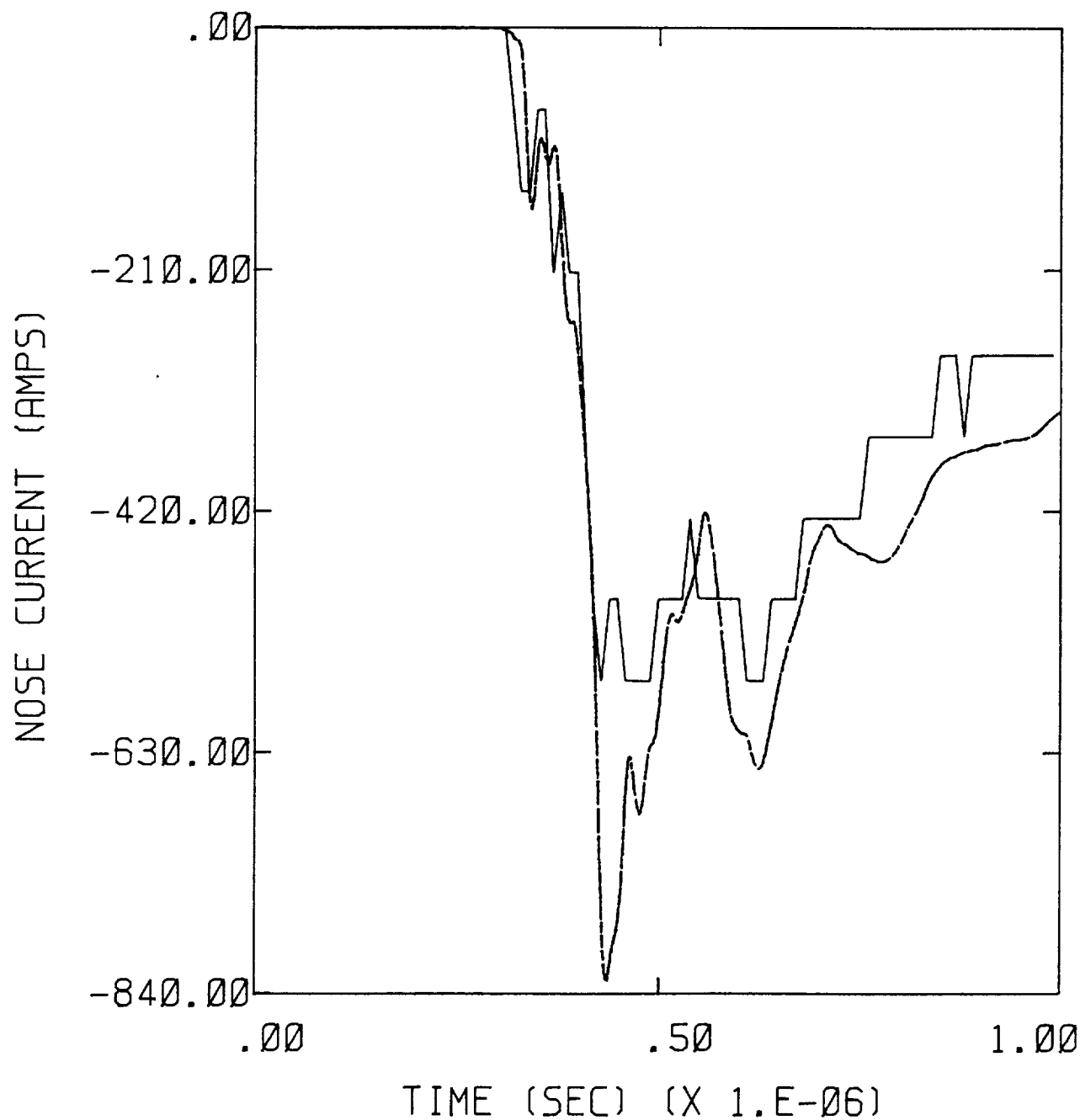


Figure 4.4 Overlay of Measured and Calculated Nose Currents for the Case of a 1 cm Radius Channel and Resistances Per Unit Length of 1 ohm/m, 10 ohm/m, and 50 ohm/m. The Measured Data Is the Solid Line. Note That the Calculated Responses Are Virtually Identical.



exception of the D-dot tail response. The failure at that sensor point is almost certainly due to the error in the location of the D-dot tail sensor as mentioned earlier.

The significance of the linear model is that for the first time, six simultaneous measured responses have been self-consistently reproduced numerically. The largest difference, in the amplitude of the D-dot tail sensor, is greatly reduced by the corrected location of the sensor. Hence, for the first time, a numerical explanation for the responses measured during a lightning event has been achieved. That is, the attach point and lightning current have been numerically identified. It should be kept in mind, however, that only the relevant parameters of the strike itself have been determined, and not the actual thunderstorm environment that caused the strike (e.g., ambient field, net charge, etc.). A nonlinear model is required for that task.

## **CHAPTER 5**

### **NONLINEAR TRIGGERED LIGHTNING PARAMETER STUDY**

The prevalence of triggered lightning strikes among the measured data recorded on the F106B has been confirmed by direct observation [5]. The purpose of this chapter is to report the progress in the ongoing effort to produce a catalog of calculated aircraft responses to triggered lightning. The responses are calculated nonlinearly by placing the F106B in a uniform static electric field oriented at a given angle with respect to the aircraft. A specified net electric charge is also placed on the aircraft. The static solution to Maxwell's equations for this problem is constructed from a basic set of solutions as described in a previous report [4]. A brief description of the construction of the solution is presented here.

The static solution for the electric field distribution around a conducting object can be found from a finite difference model. It is found by first specifying a uniform field in a finite difference problem space with no object present. The conducting object is then introduced into the space by slowly increasing the conductivity in the part of the space that the object occupies. The conductivity is raised slowly to avoid resonance effects associated with the size of the object. After the object has become perfectly conducting, and all resonance behavior has died away, the fields which remain are the desired solution. If this procedure is carried out with the ambient field oriented along each of the cartesian coordinate axes, a general solution for any ambient field orientation and magnitude can be obtained by superposition of the three basic solutions. This can be done because the solutions are each linear in character. If, in addition, the static solution for the object with a net charge on its surface is obtained, then the problem of an object in a uniform field with a net charge can be solved, also by superposition, by adding the charge solution to the basic set of solutions.

The linear solution for the charged F106B in a uniform field is used as an initial condition for the nonlinear triggered lightning model. The linearly enhanced fields around sharp points of the aircraft produce corona and air breakdown nonlinearly, and the currents flowing onto the plane are calculated by the nonlinear model.

A large parameter study has been undertaken using the technique just described to catalog the nonlinear sensor responses on the F106B for various initial conditions. The parameters varied in the study are the orientation of the ambient electric field with respect to the aircraft and the net charge on the aircraft. In this chapter are presented the responses from the "skewed" orientation angles; that is, those angles for which the field is not along a principal axis of the F106B. For example, the ambient field may have equal components in the nose-tail, and wing-wing directions, resulting in an electric field vector oriented at a 45° angle with respect to the fuselage. Also presented are a few cases from the previous principal angle parameter study. These cases were redone because the responses were much larger or smaller than typical measured responses.

The net charge values used for the portion of the parameter study presented here were 0,  $-1/2Q_m$ , and  $-Q_m$ , where  $Q_m$  is the charge needed to cause corona to form on the aircraft in the absence of any external field. In the case of the F106B finite difference model,  $Q_m$  was 1.79 millicoulombs. These signs of charge (no charge and negative charge) were deemed to be most likely on the F106B flying at high altitude (> 20,000 feet) and were therefore completed first.

The responses from the skewed angle portion of the parameter study are presented in Appendix D. The format of the legend below each of the plots is explained in the foreword to Appendix D. Essentially, the legend specifies the orientation of the ambient field with respect to the aircraft and the net charge on the aircraft. The sensor response shown in each plot is indicated along the left side of the plot itself. Also specified in the legends is the ambient electric field magnitude which was present for that case.

Parameters which were not varied were the relative air density and the water content of the air. The relative air density was fixed at .5, meaning that the air density was half that found at sea level. This corresponds to approximately 27,000 feet in altitude. The water content of the air was set at 0% after consultation with Dr. John Helsdon [unpublished data], who confirmed that this is near the correct value, even in the center of a thunderstorm.

Analysis of the calculated responses is in a preliminary state, because the full parameter study, including positive charge values, has not been completed.

However, some simple comparisons of calculated to measured data and early statistical analysis were reported in Chapter 2 of this report.

The principal angle cases which were redone are presented in Appendix E. They were done on the NASA Langley VPS computer. The original report of the principal angle parameter study was reported in Reference 4. The new waveforms in Appendix E are somewhat more representative of measured responses, although some are still larger. Differences still exist because of the difficulty in estimating nonlinear response amplitudes in advance of a calculation.

The nonlinear parameter study is not yet finished. Future work involves the calculation of responses for positive net charge values. Another possibility is the addition of more orientation angles for the ambient field, because of the variety of responses found with the skewed angle portion of the study.

## CHAPTER 6

### RESPONSE OF THE F106B AIRCRAFT TO A HIGH CURRENT LIGHTNING STRIKE

Direct lightning strikes to the F106B aircraft have, to date, been mostly low current strikes (of the order of a few kiloamps injected current), and have been confined to high altitudes. Because of this, very little information is available about the response of the aircraft to a large direct strike. The probability of the F106B intercepting a large amplitude lightning stroke appears to be small, so data on this type of event may be sparse. Even if the aircraft were to intercept such a strike, minimal information might be gained, because the range of response levels is not well known. If sensors saturate or fail to trigger because of improperly adjusted sensitivities, nothing is achieved. In addition, estimates of the required sensitivity settings are difficult to make, because of the strongly nonlinear character of a large amplitude lightning strike.

Currently, the best way to estimate the effect of a large amplitude strike on the F106B is to make use of the nonlinear air breakdown computer model. This has been done using the model described in a previous report [3]. The model assumed that a large amplitude lightning strike attached to the nose boom of the aircraft. The current channel extended directly away from the aircraft along the line of the fuselage. The injected current had a step function waveform with a rise time of one microsecond. The amplitude of the step was 200 kiloamps. The current waveform is shown in Figure 6.1. This was meant to simulate a large return stroke intercepting the F106B. Although the entry channel for the current was specified in advance, no exit channels were predefined. The nonlinear air chemistry incorporated in the code allowed the charge from the lightning current to flow off the aircraft at appropriate exit points.

The main results obtained from the model were the approximate sensor response amplitudes. These are almost certainly upper limits for the amplitudes achieved in any possible interaction of the F106B with lightning. Hence, in future flights in which the intent is to intercept large cloud to ground return strokes, approximate responses will be known. This will allow the sensitivity of the sensors to be adjusted appropriately, to eliminate the possibility of saturation.

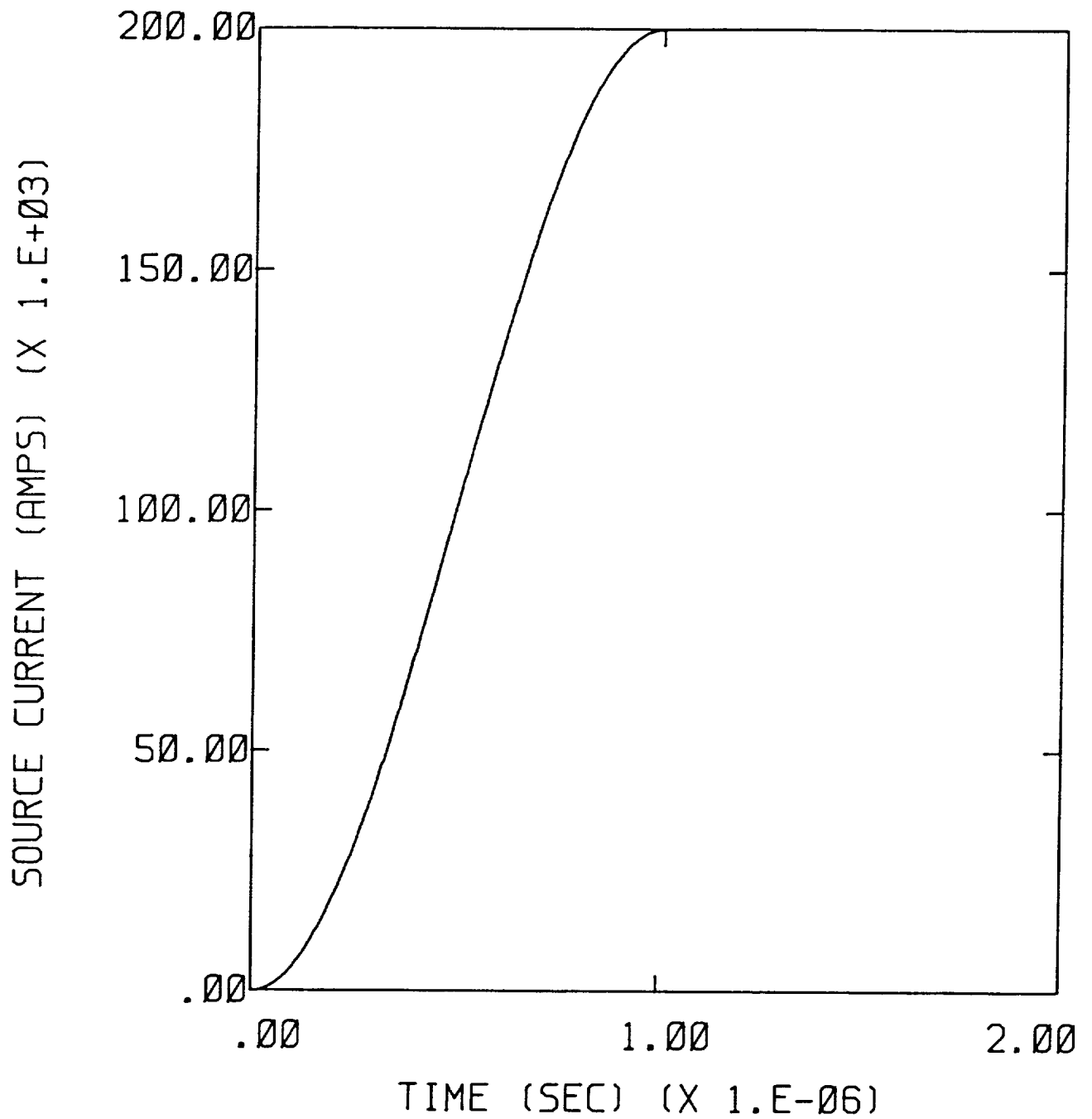


Figure 6.1 Current Waveform Used to Determine the Response of the F106B to a Large Current Lightning Strike

The calculated sensor responses are shown in Figures 6.2 to 6.6. It is interesting to note that they are a factor of about thirty larger than any responses seen in the measured data to date. This is not too surprising, because most strikes so far have been aircraft triggered lightning at high altitude with currents much less than the 200 kiloamp current used in the model. In all cases, the extremely large part of the response waveform lasted only for a few tens of nanoseconds, and was then rapidly damped. The rapid damping occurred most likely because of the nonlinear effects of the electrical corona which formed around the aircraft. Because the aircraft is immersed in conducting air, the resonances which would normally be seen are masked. The electrical corona in the model was found to extend a distance of about two meters from the plane even over flat surfaces, such as above and below the delta wing. This is easily sufficient to strongly damp any of the aircraft's resonances which would be present in a linear model. Shielding of the sensors also occurs because of the presence of the corona. Resonances which would normally be recorded are not because the corona acts to isolate sensor points with its conductivity.

Although no exit points were defined in the model, the lightning current exited the aircraft at the points one would expect. The largest exit currents were seen at the tip of the vertical stabilizer and the wing tips. Smaller but still significant currents were seen exiting the leading and trailing edges of the wings. Still smaller currents existed even over flat portions of the aircraft, because the corona's conductivity allowed charge to flow at all locations. These latter currents, however, did not remove a significant percentage of the entering current.

To summarize, the response of the F106B to a large lightning current has been calculated using a nonlinear air breakdown model. The responses can be used to estimate response levels for flights which intend to intercept cloud to ground return strokes. The calculated responses are seen to be pulselike in character and strongly damped.

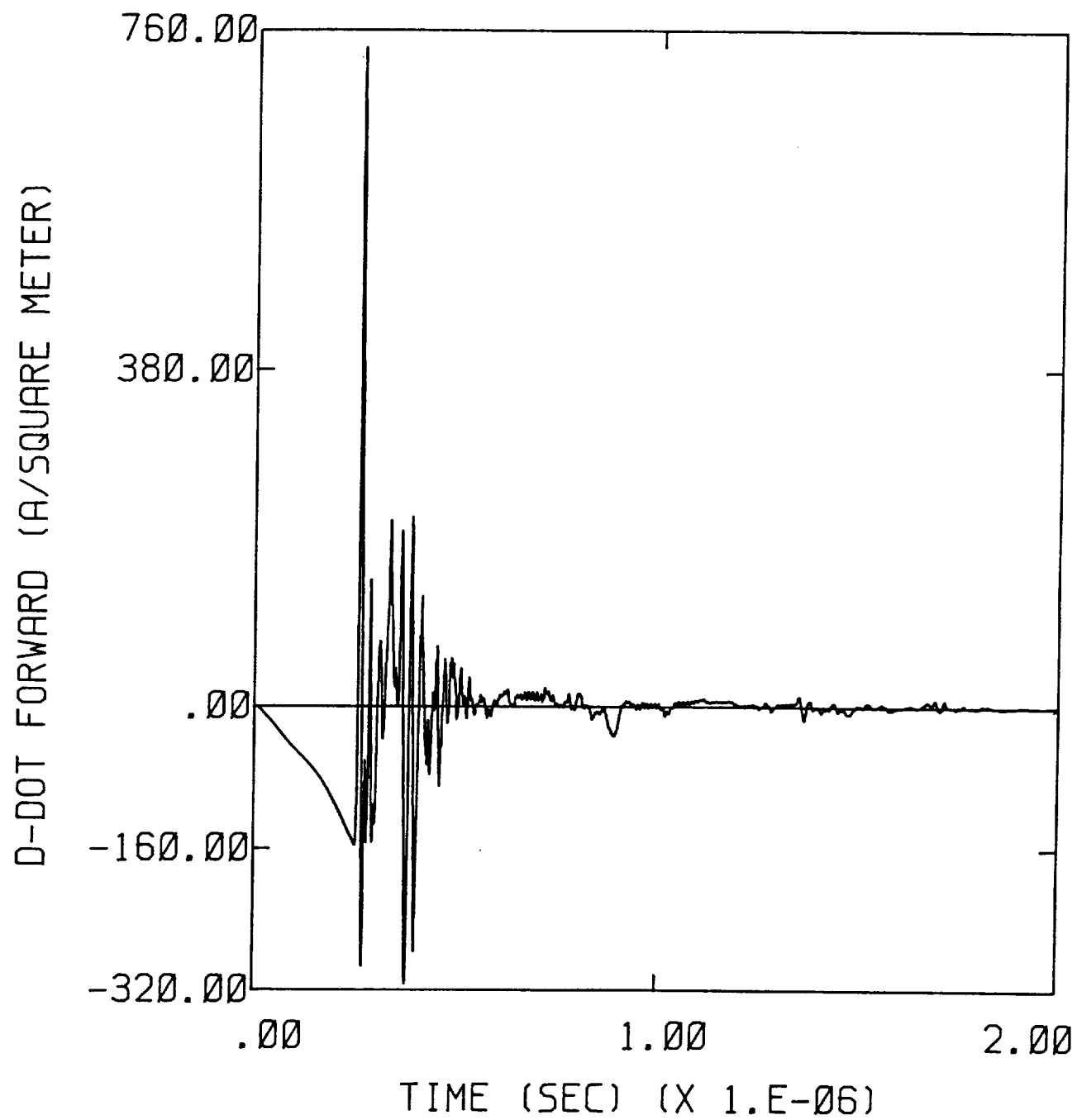


Figure 6.2 Nonlinear D-dot Forward Response of the F106B for the Injected Current of Figure 6.1



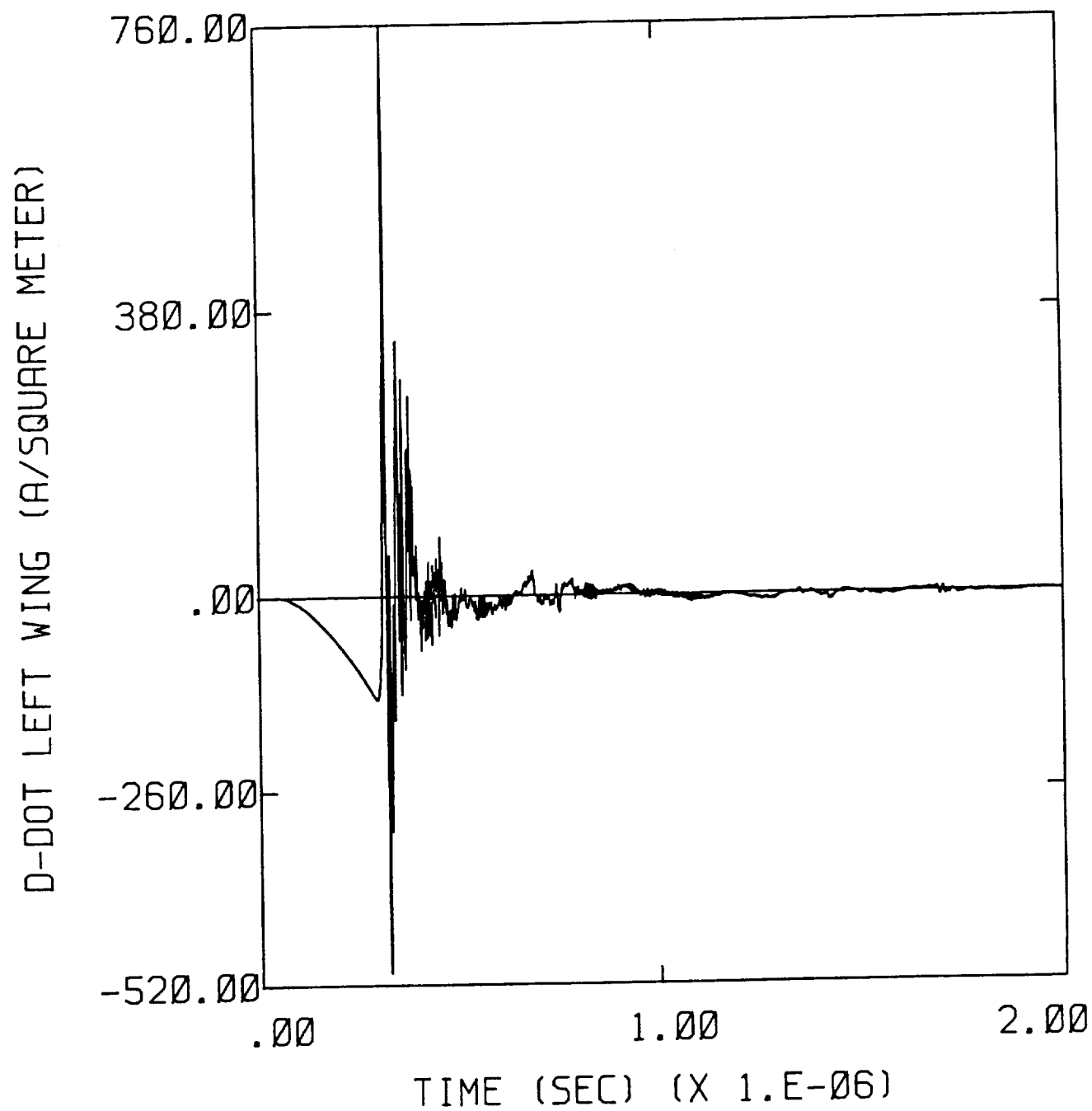


Figure 6.3 Nonlinear D-dot Left Wing Response of the F106B  
for the Injected Current of Figure 6.1

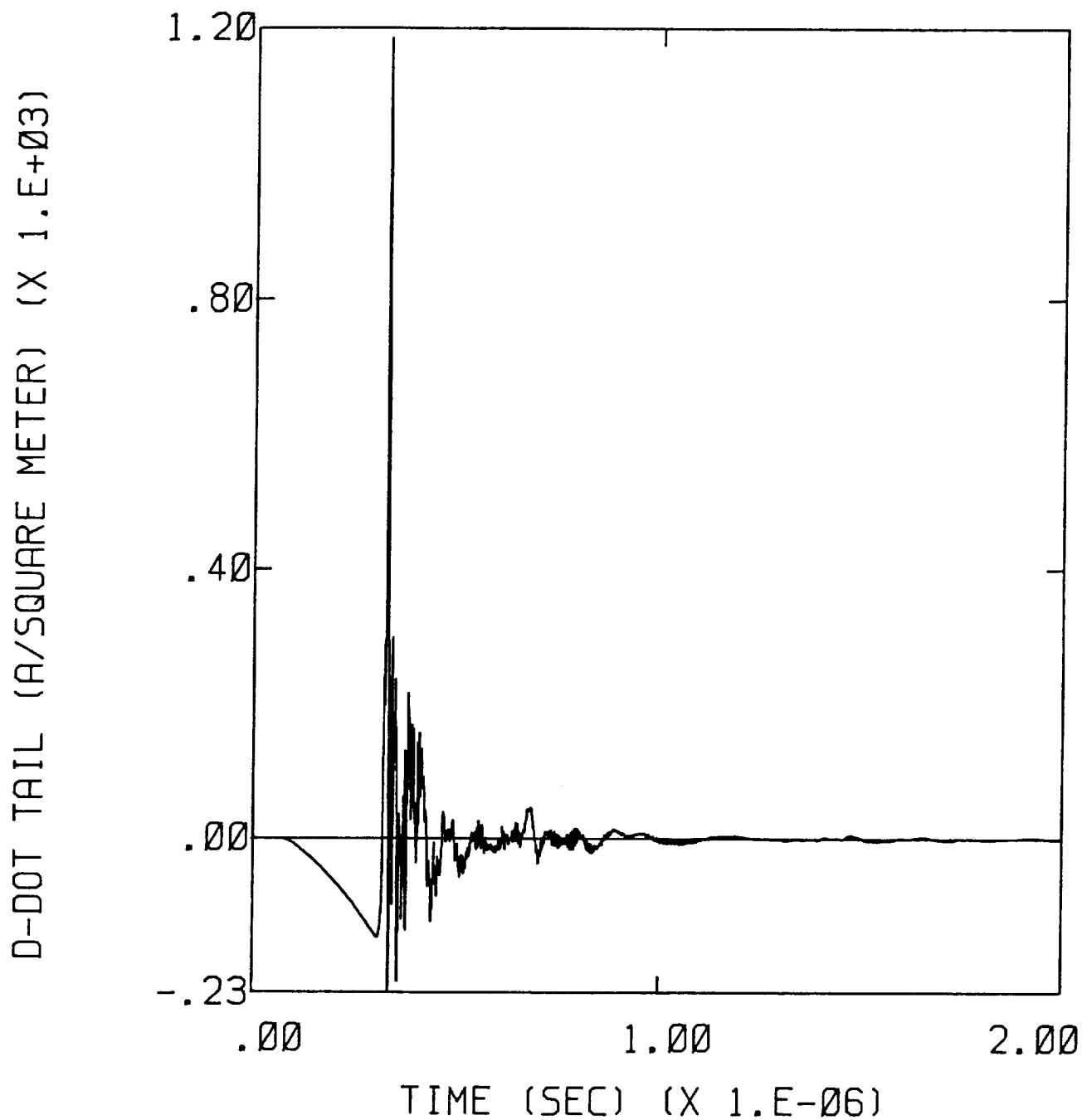


Figure 6.4 Nonlinear D-dot Tail Response of the F106B for the Injected Current of Figure 6.1

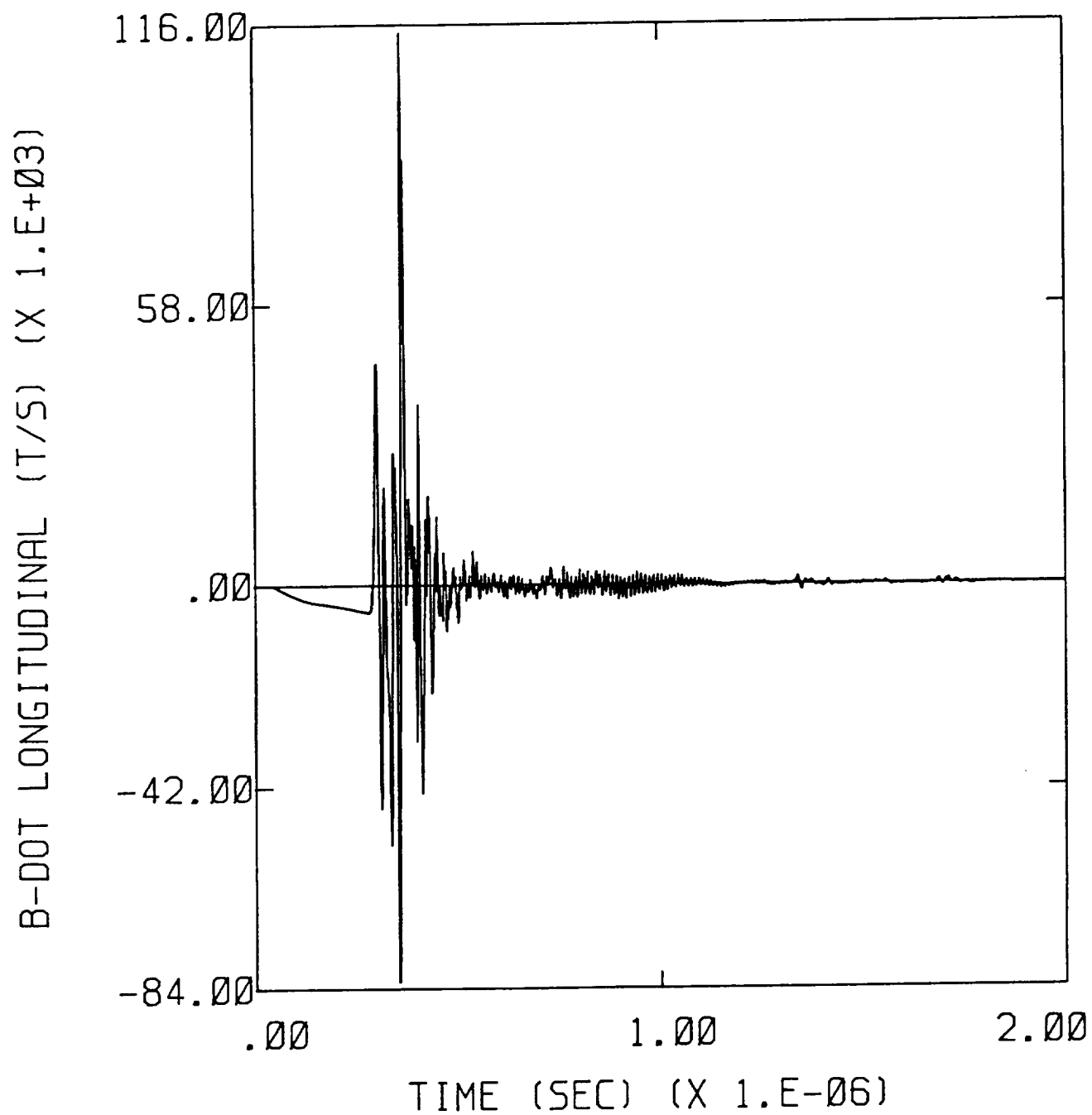


Figure 6.5 Nonlinear B-dot Longitudinal Response of the F106B for the Injected Current of Figure 6.1

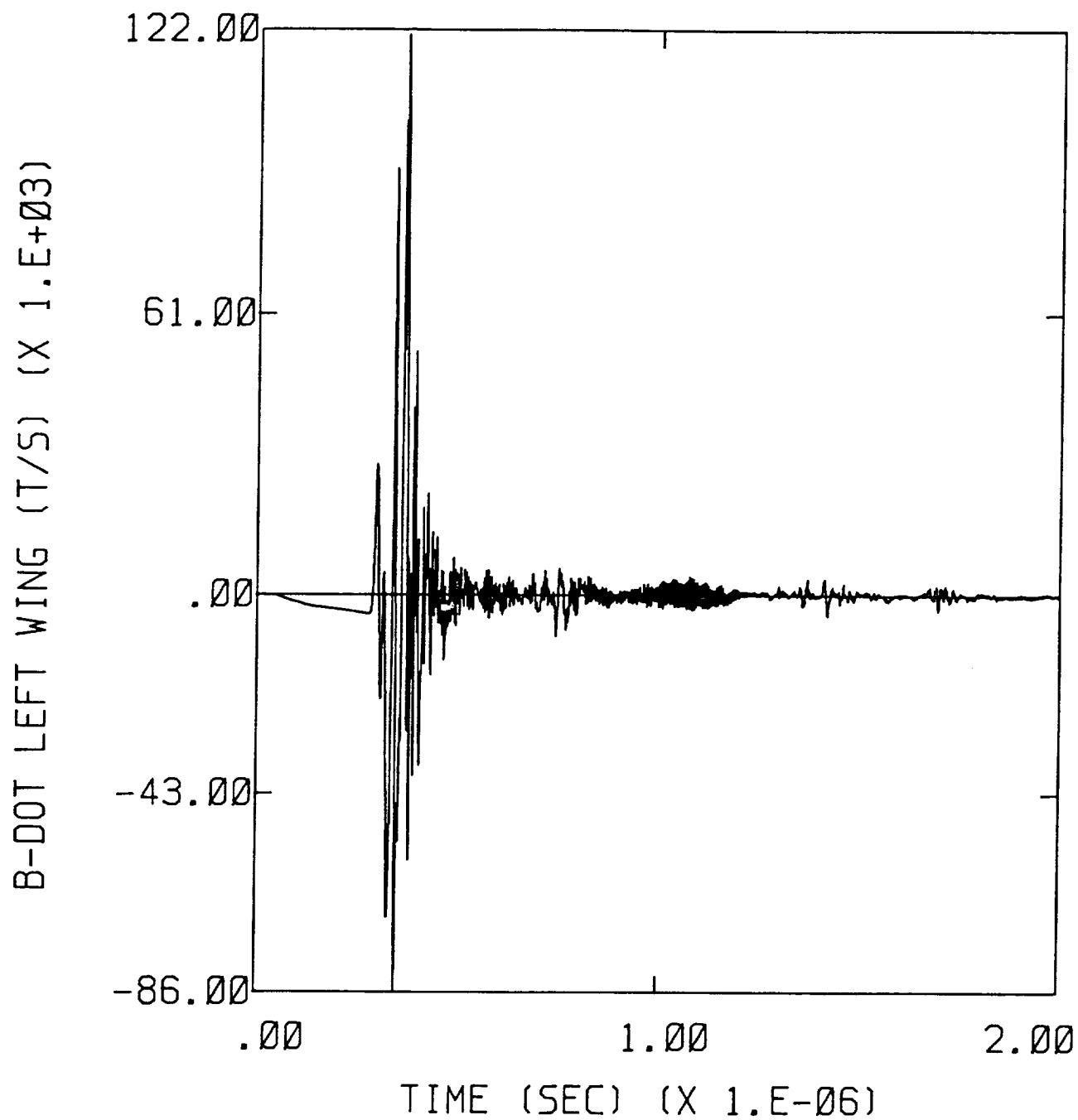


Figure 6.6 Nonlinear B-dot Left Wing Response of the F106B  
for the Injected Current of Figure 6.1

## **CHAPTER 7**

### **RESPONSE OF AIRCRAFT OTHER THAN THE F106B TO TRIGGERED LIGHTNING**

The overall objective of the F106B thunderstorm research program is to determine lightning environments for any size or type of aircraft. To date, nonlinear analysis in this program has concentrated on the F106B itself. But the thunderstorm environment necessary for a direct strike may be different for different types of aircraft. That is, for an identical thunderstorm environment, one aircraft may encounter a direct strike, while a second differently shaped or sized aircraft will not. For this reason, it is desirable to look at the environment in somewhat more generality. In this chapter, four different aircraft will be placed in a thunderstorm environment (i.e., ambient electric field, charge on the aircraft, particular altitude, etc.) and the conditions necessary to produce a triggered lightning strike determined. The electromagnetic responses present on the aircraft as a result of that strike will also be presented.

The four aircraft investigated here are listed below:

- (1) half size F106B,
- (2) double size F106B
- (3) normal size F106B with delta wings replaced with more conventional straight wings,
- (4) normal size C130,
- (5) normal size F106B.

The first two aircraft above afford a size range from approximately 35 feet to 140 feet. Although the field enhancements around these two aircraft are, of course, the same, the effect of a given net charge on the plane is much different. Also, the responses of electromagnetic sensors on the planes are different because of the significantly different resonance characteristics.

The F106B with the straight wing is meant to test the effect of the delta wing on field enhancements, resonant response, and charge storage properties. These are all expected to be changed to greater or lesser degrees. In particular, charge storage

could be significantly affected, because the large flat delta wings act as a large capacitance.

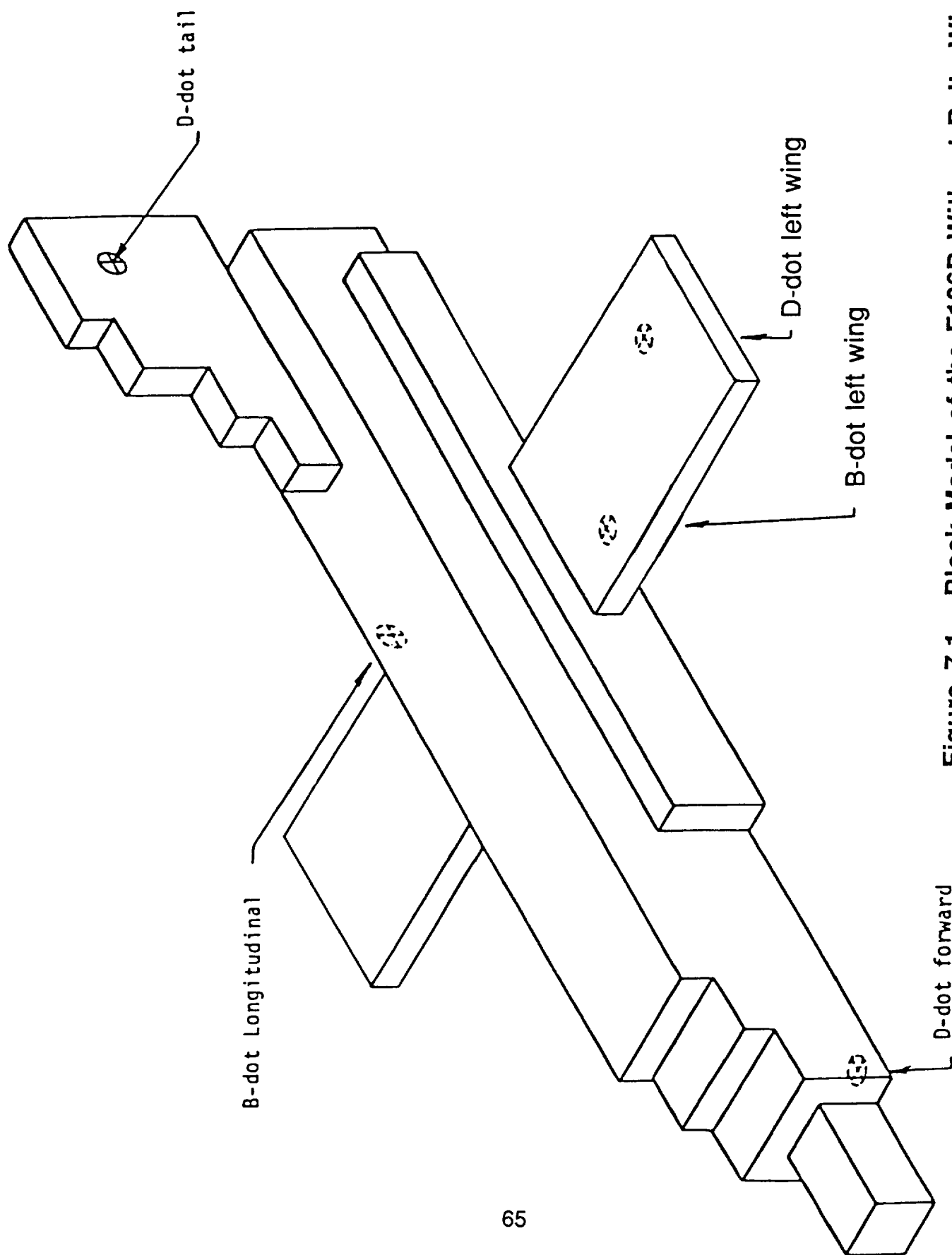
The C130 is included as a non-fighter type of aircraft. It has more rounded contours, particularly at the nose, and is representative of the shapes found in large passenger aircraft. It should give an idea of the environment necessary to generate triggered strikes on that type of aircraft.

The normal size F106B is included for comparison purposes.

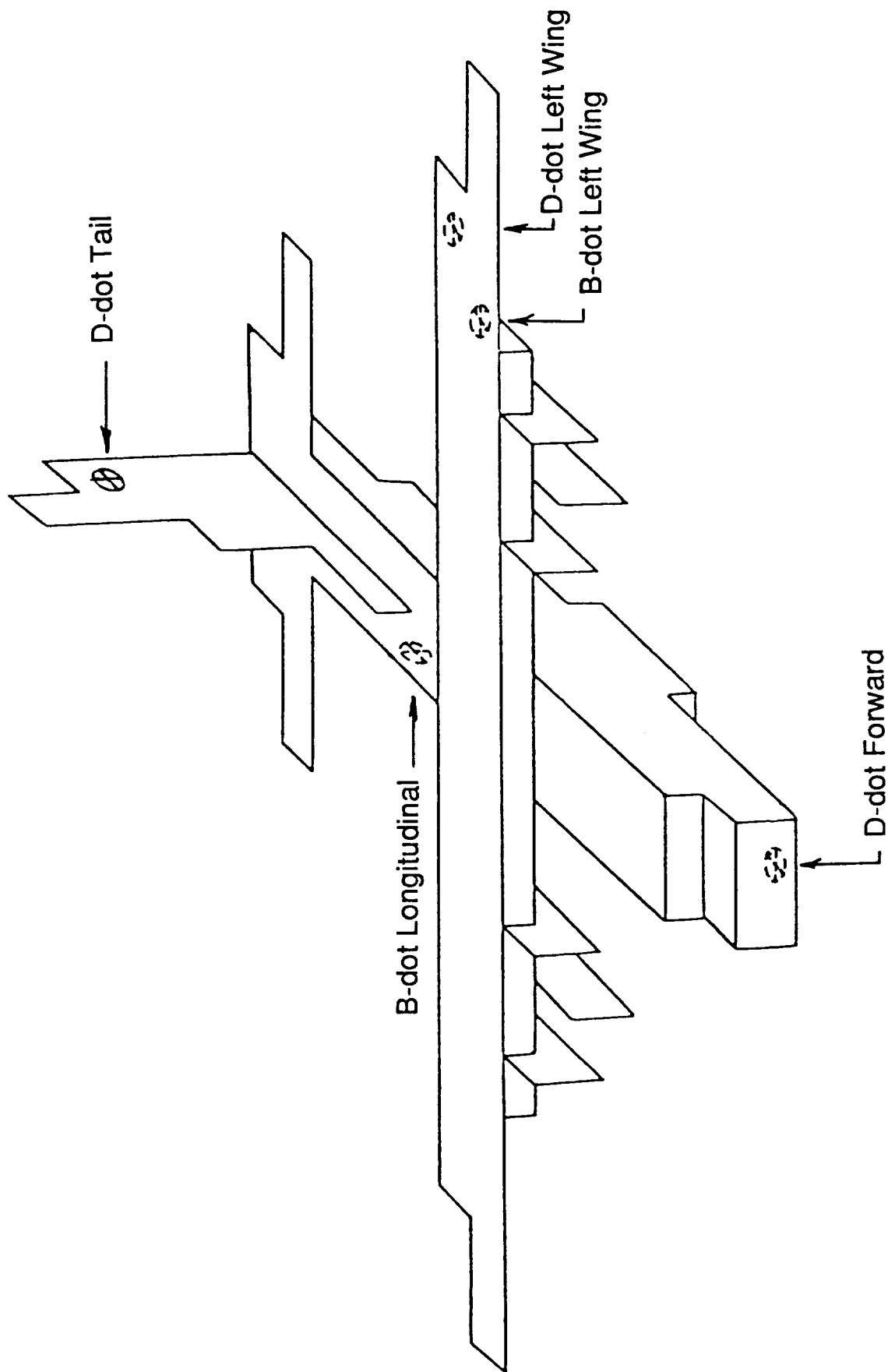
The finite difference models of the first two planes look identical to the normal size F106B shown in Figure 1.1; only the scale is different. The electromagnetic sensors are located in the same position. The finite difference models of the F106B without delta wing and the C130 are shown in Figures 7.1 and 7.2, respectively. Sensor locations are indicated on the figures. These locations are intended to be analogous to the locations on the normal size F106B.

For each aircraft, two different environments were used. In both the net charge on the aircraft was fixed at  $-1/2 Q_m$ , where  $Q_m$  is the maximum charge which can be on the plane without causing immediate corona formation. It should be kept in mind that  $Q_m$  is different for each aircraft. Two separate ambient field orientations were used, one with the field oriented from nose to tail, and the other oriented from top to bottom. These orientations were chosen, because they produce the most interesting sensor responses as determined from full parameter studies on the normal size F106B. The initial conditions for each of the nonlinear finite difference computer runs were determined using the same technique as described in Chapter 5. For consistency, all runs were done at a simulated altitude of 27,000 feet (relative air density of .5) and with a water vapor percentage of zero.

The variable parameters for each of the computer runs are shown in Table 7.1. The field values,  $E_{mag}$ , also represent the minimum field necessary to produce a triggered strike on the given aircraft model for the given orientation and  $Q_m$ . In the table, aircraft number refers to the numbers assigned in the listing earlier in this chapter. The codes NT and TB refer to nose-tail and top-bottom ambient field orientations, respectively.  $Q_m$  is listed in millicoulombs and  $E_{mag}$  in kilovolts per meter.



**Figure 7.1** Block Model of the F106B Without Delta Wing, Indicating Approximate Sensor Locations



**Figure 7.2 Block Model of the C-130 Indicating Approximate Sensor Locations**



**TABLE 7.1****Variable Parameters in Triggered Lightning Investigation**

Aircraft Number	Field Orientation	$Q_m$ (mC)	$E_{mag}$ (kV/m)
1 (1/2 x F106B)	NT	.49	100
	TB	.49	250
2 (2 x F106B)	NT	7.90	100
	TB	7.90	250
3 (straight wing F106B)	NT	2.00	120
	TB	2.00	240
4 (C-130)	NT	6.90	190
	TB	6.90	210
5 (normal F106B)	NT	1.79	130
	TB	1.79	310

Several noteworthy items are apparent from Table 7.1. First of all, note that size is by far the determining factor for  $Q_m$ . For aircraft with similar shapes, one would expect  $Q_m$  to scale as the square of a typical dimension, along with the surface area. This is seen to be true, as  $Q_m$  varies by a factor of 16.1 for the factor of four scale difference between the half size and double size F106B. A second thing to notice in the table is the effect of the delta wing, exemplified by aircraft #3.  $Q_m$  for the normal size F106B with delta wing is 1.79 millicoulombs and is 2 millicoulombs without the delta wing. This is a somewhat surprising result, as one would expect that the large surface area of the delta wing would allow it to hold a large amount of charge. However, the presence of the delta wing changes the static electrical characteristics of the plane considerably. Because of the delta wing at the rear of the aircraft, field enhancements are significantly larger around the nose. In fact, a nose to tail oriented field has an enhancement factor of 6.3 for the aircraft without delta wing, and 7.4 for

the aircraft with a delta wing. The same type of phenomenon occurs for a given charge on the plane. That is, the charge arranges itself on the delta wing plane in such a way that it takes less charge to bring about corona formation.

One final thing to notice about Table 7.1 is the magnitude of the field required for a lightning strike on the C130 model (aircraft #4). For the nose-tail field direction, it is nearly twice that required for the F106B. This is mostly because of the bluntness of the nose of the C130. In actual practice, the triggering fields may differ by even more. The reason for this is that the C130 is quite accurately represented near the nose by the finite difference model, so its maximum enhancement should be correct. However, the sharp nose boom on the F106B is less accurately represented, so real enhancements on the F106B are likely to be larger than the model predicts.

The aircraft sensor responses for each of the models and orientations are presented in Figures 7.3 to 7.12. Each figure contains six plots including the following:

- (1) B-dot longitudinal,
- (2) B-dot left wing,
- (3) D-dot forward,
- (4) D-dot left wing,
- (6a) nose current if field orientation is nose to tail,
- (6b) tail current if field orientation is top to bottom.

The legend of each gives the type of aircraft model, the ambient field orientation and magnitude, and the net aircraft charge. The sensor for each plot is indicated along the vertical axis of the plot. The peak values for the various sensors for the different cases studied are summarized in Table 7.2.

Examination of the sensor responses reveals several interesting things. First, the air breakdown for each case was approximately the same, meaning that the frequency content of the entering currents was similar. The magnitude varied somewhat because of the size of the area of corona formation. Because of this the larger aircraft, having lower characteristic resonances, were more strongly excited by the current. In fact, the half size F106B shows almost no resonant behavior because its lowest resonant frequencies are at the upper limit of those present in the current.

(Text continued on page 100)

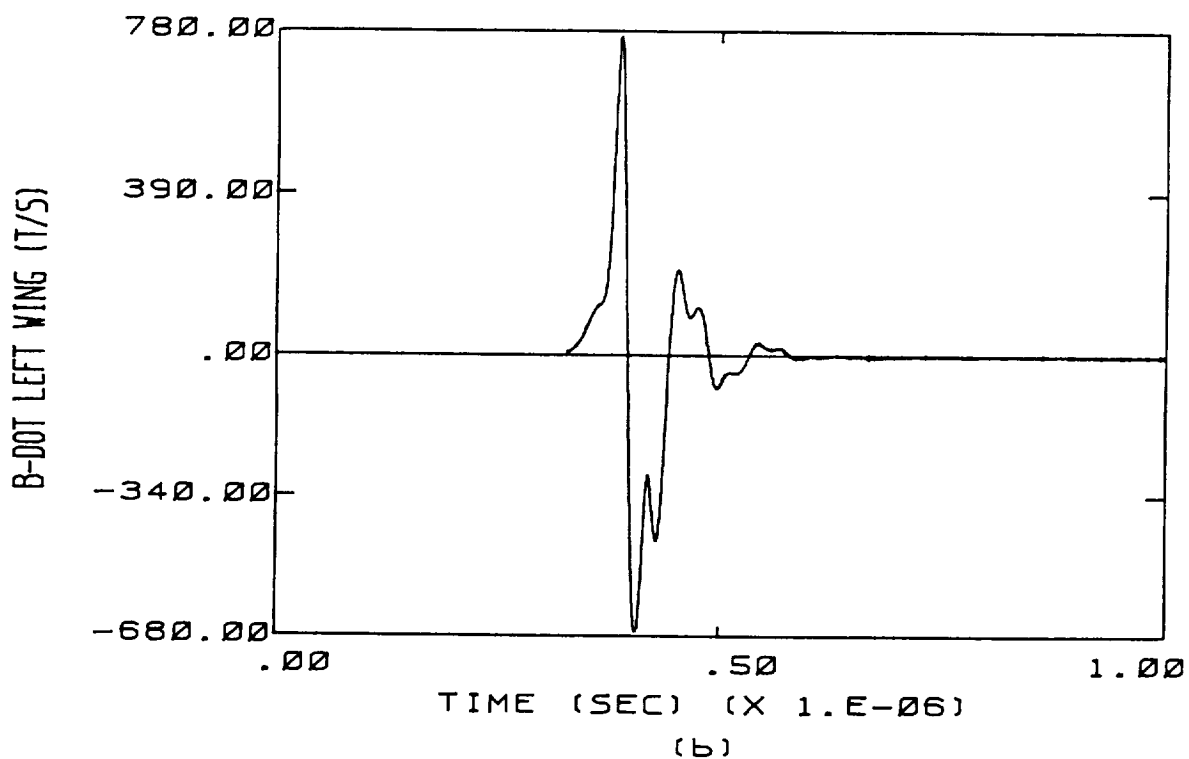
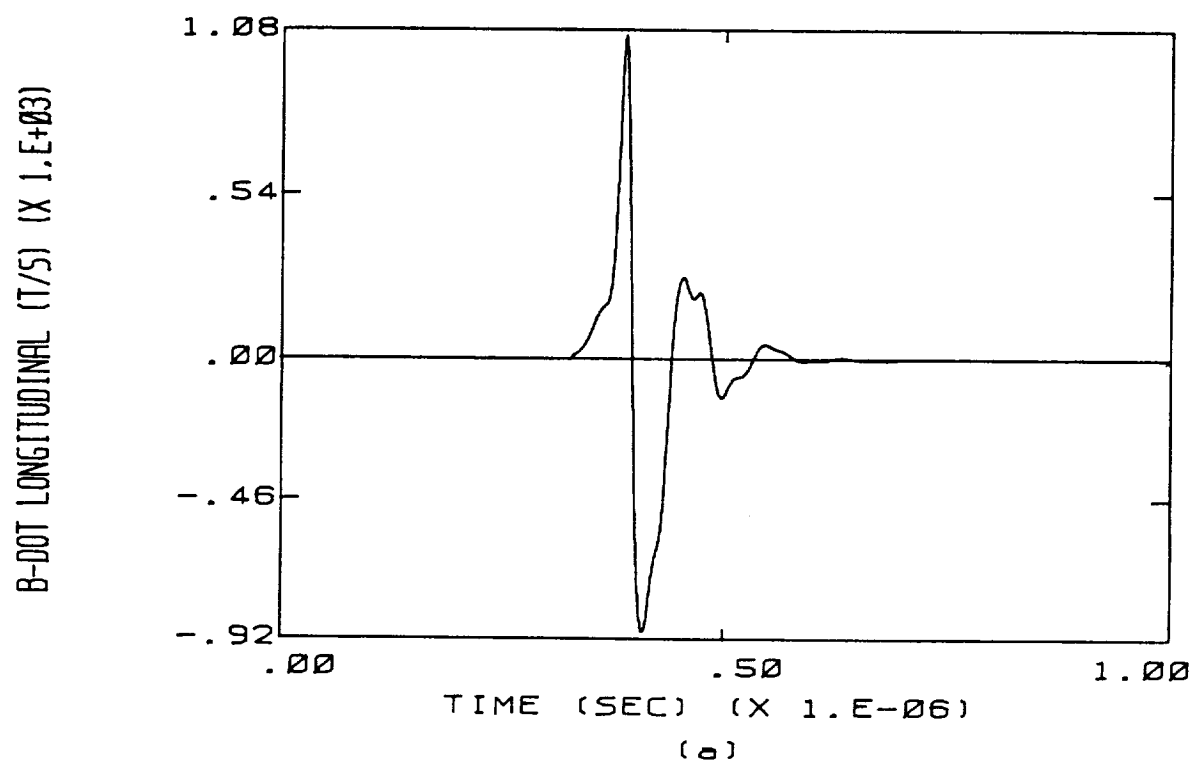
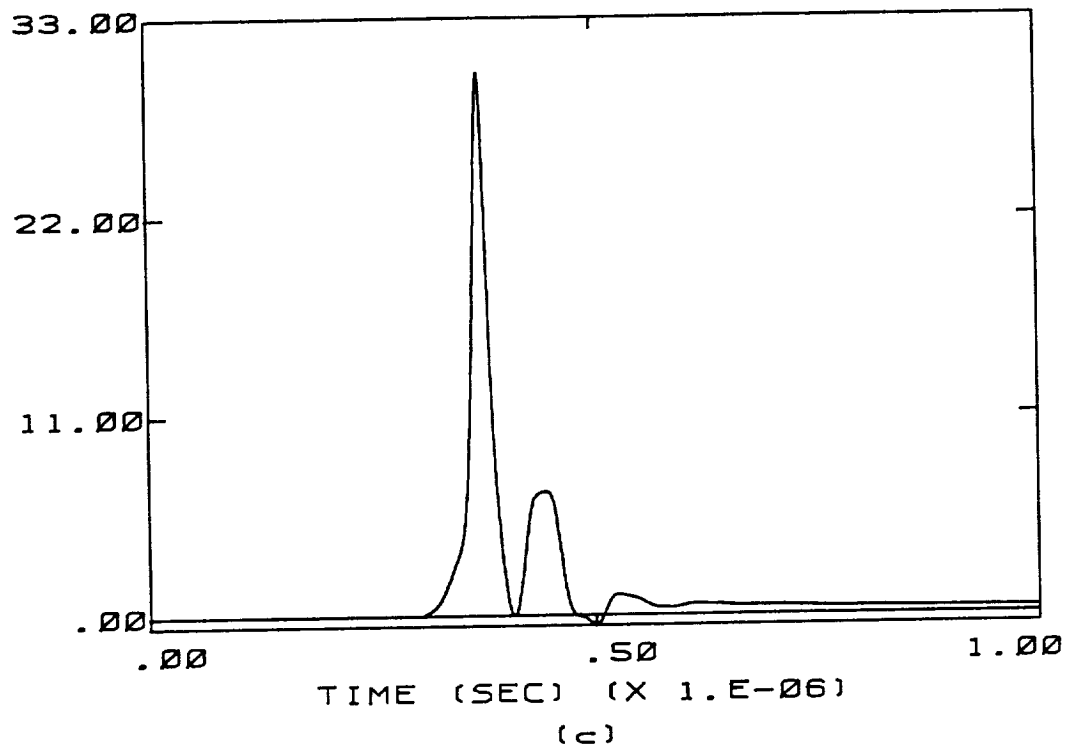


Figure 7.3 Calculated Sensor Responses for the Half Size F106B Aircraft, Nose to Tail Orientation, Net Charge of  $-.245$  Millicoulombs, Electric Field Magnitude of  $100$  kV/m

D-DOT FORWARD (A/SQUARE METER)



D-DOT LEFT WING (A/SQUARE METER)

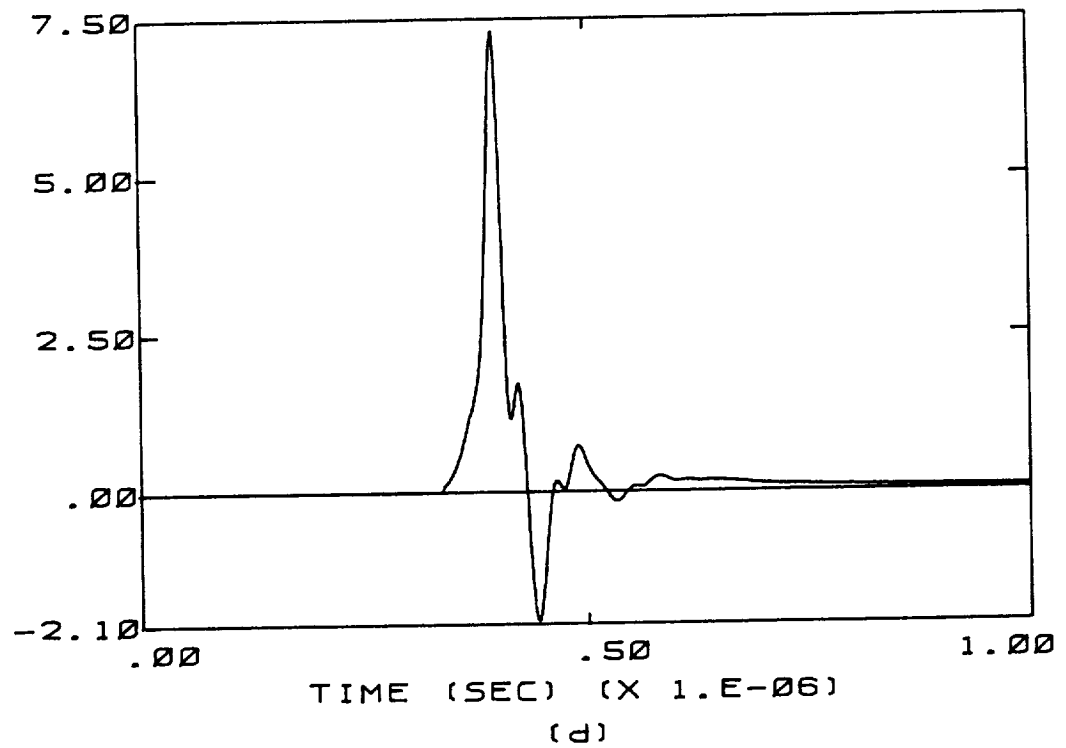


Figure 7.3 (continued)

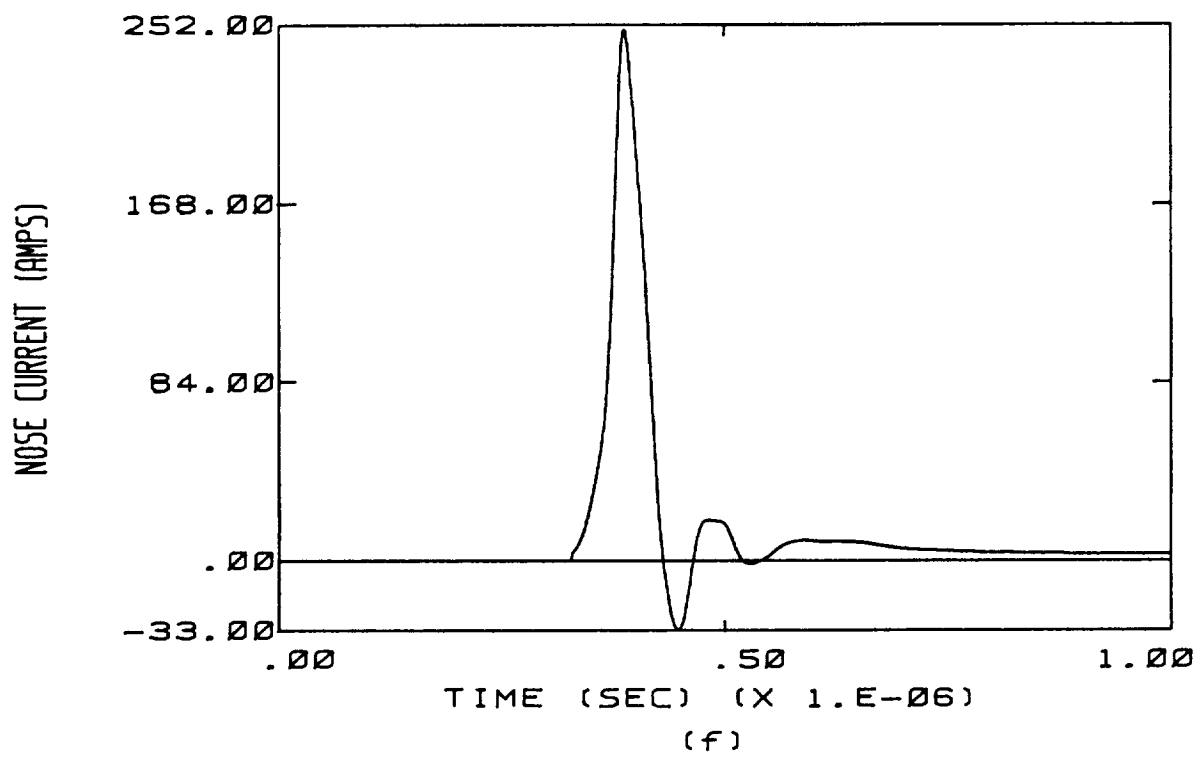
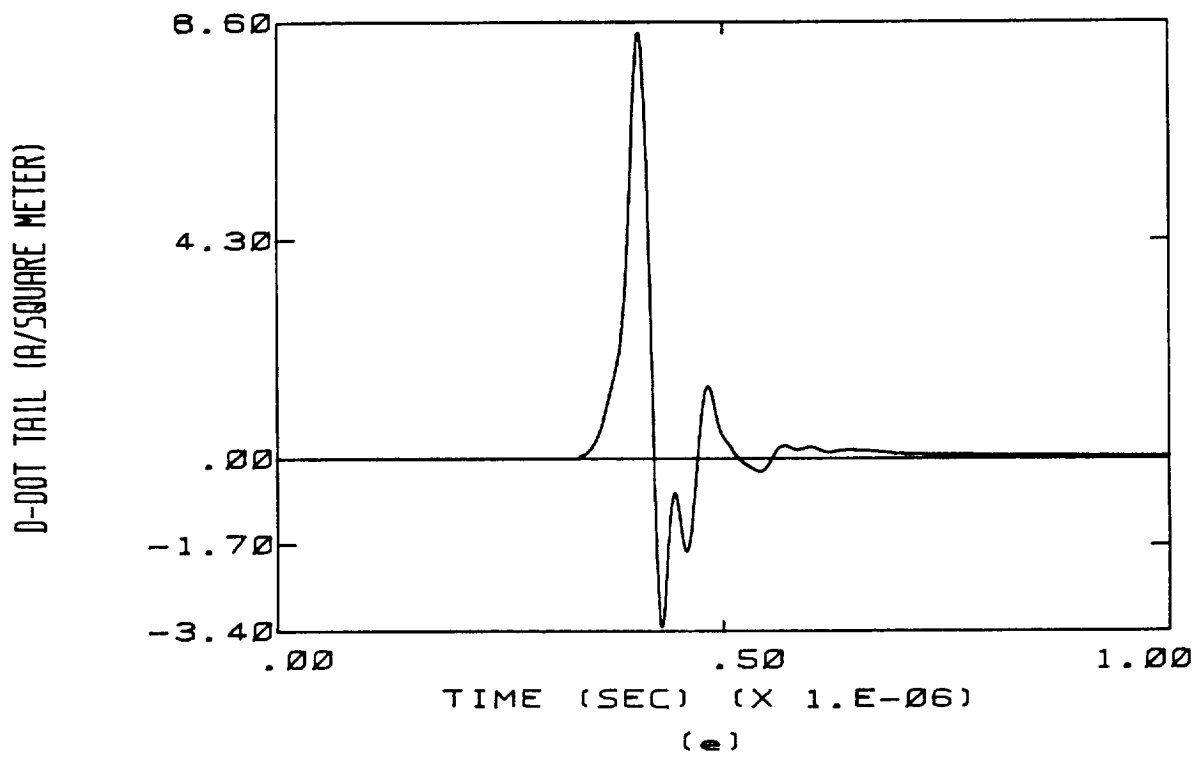


Figure 7.3 (continued)

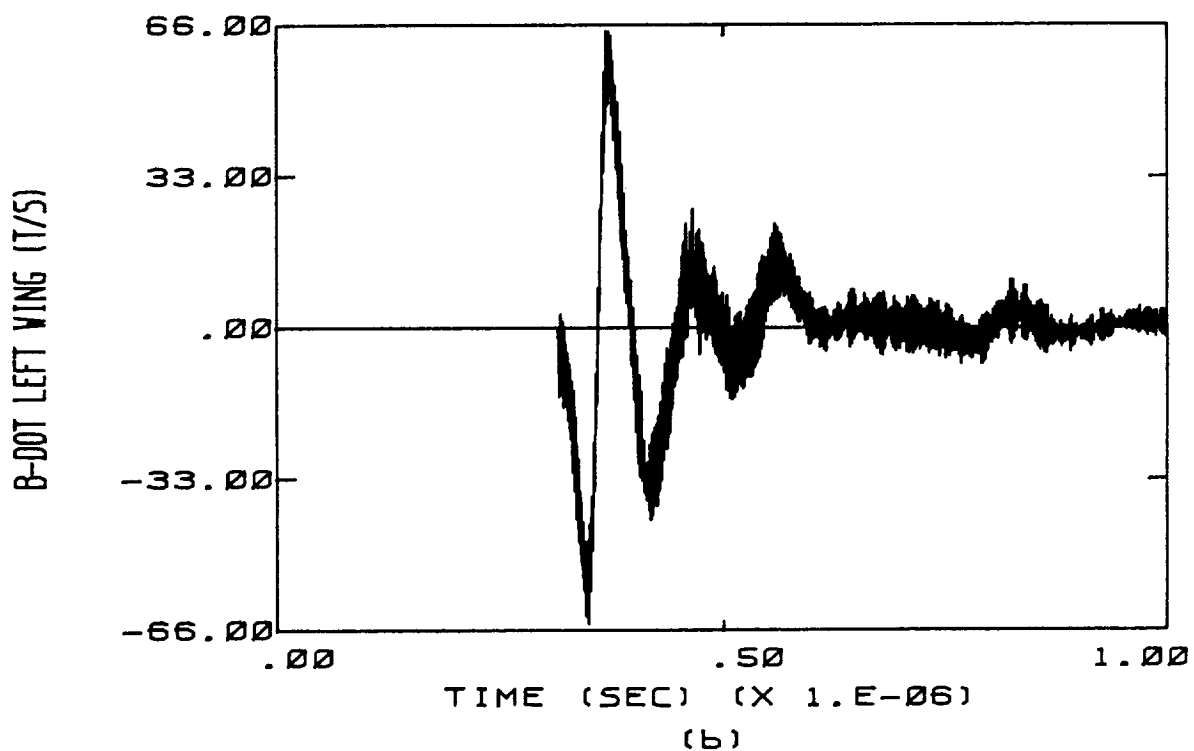
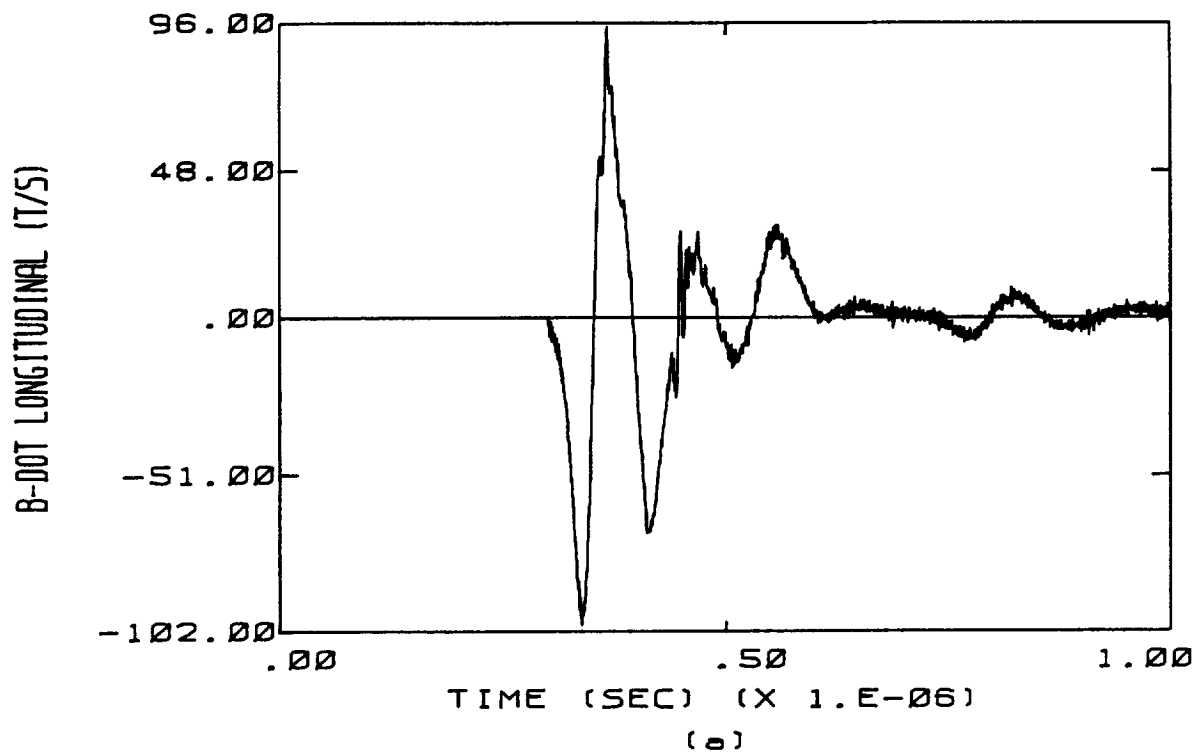


Figure 7.4 Calculated Sensor Responses for the Half Size F106B Aircraft, Top to Bottom Orientation, Net Charge of  $-.245$  Millicoulombs, Electric Field Magnitude of  $250$  kV/m

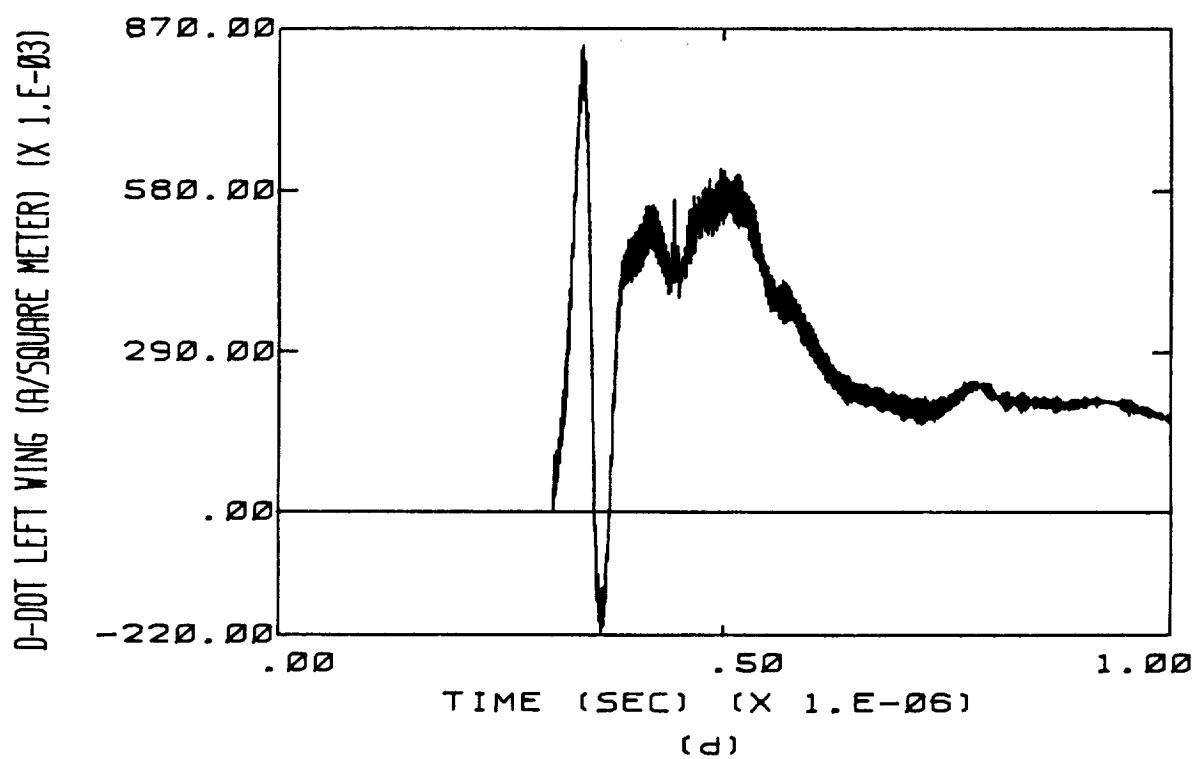
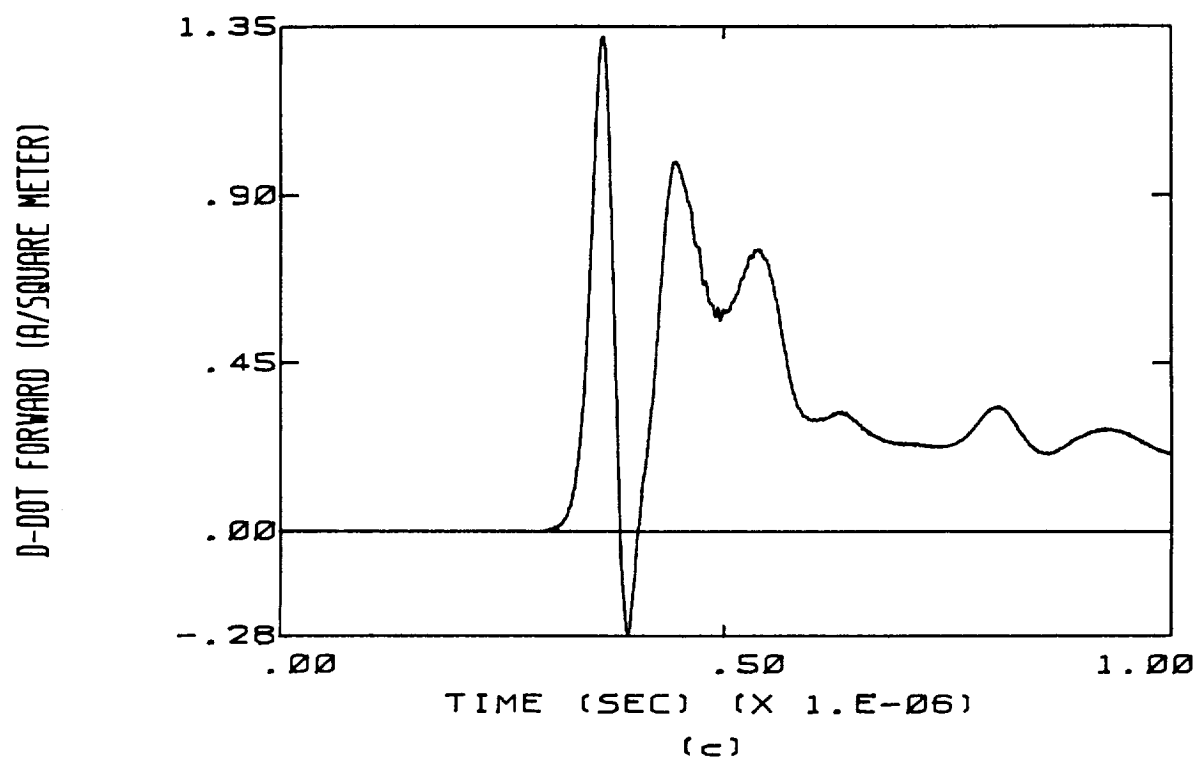


Figure 7.4 (continued)

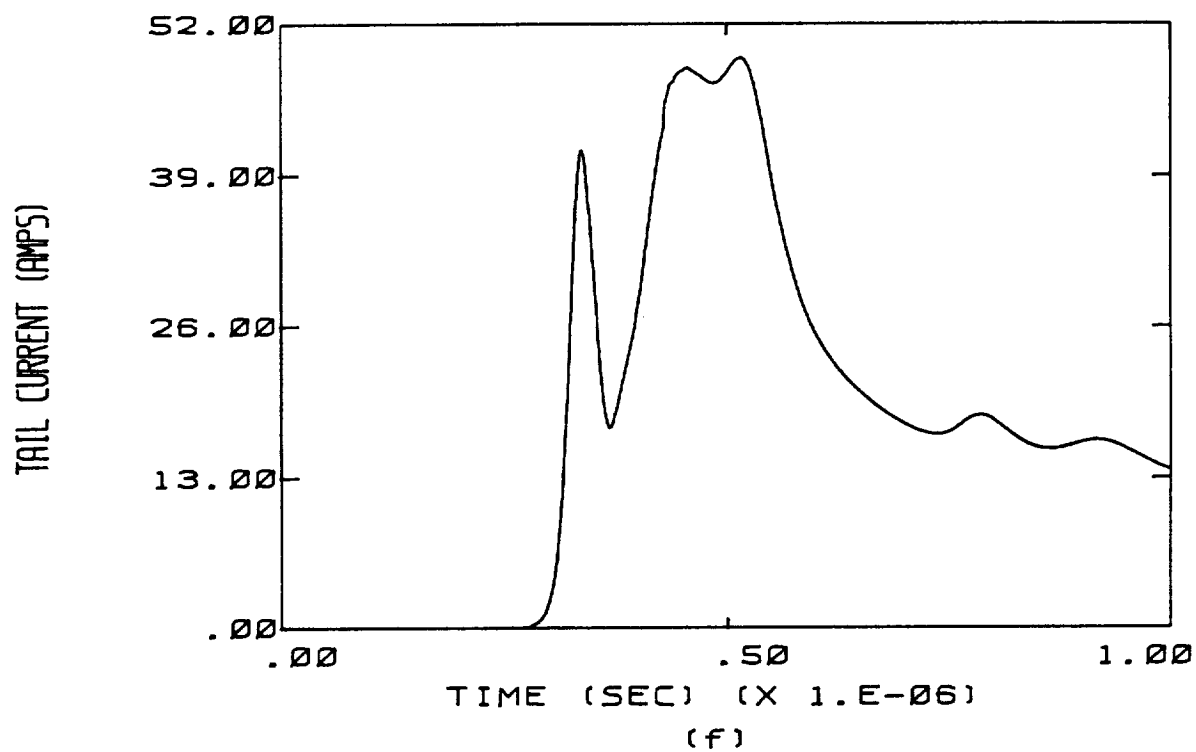
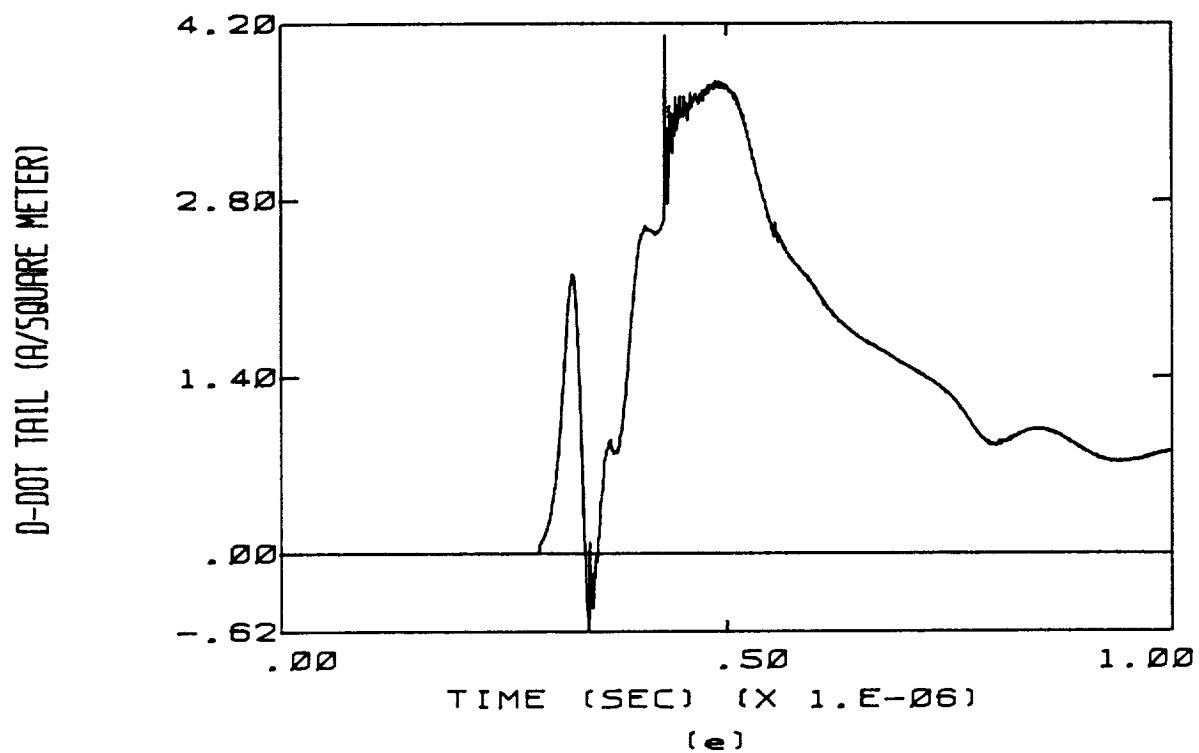


Figure 7.4 (continued)



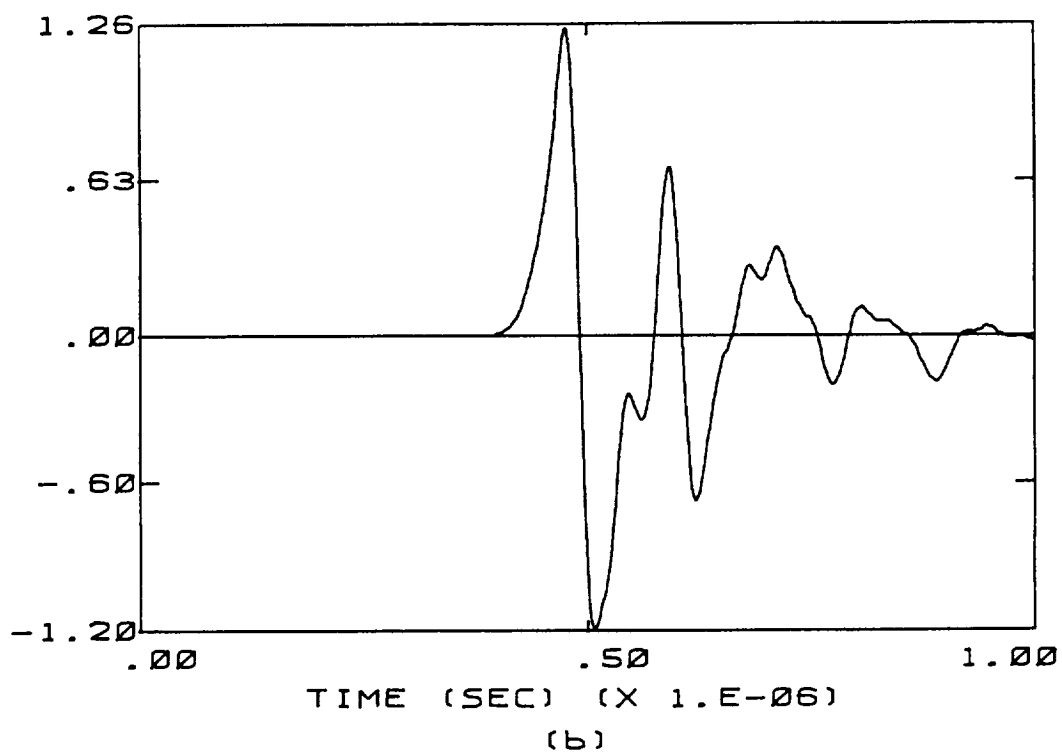
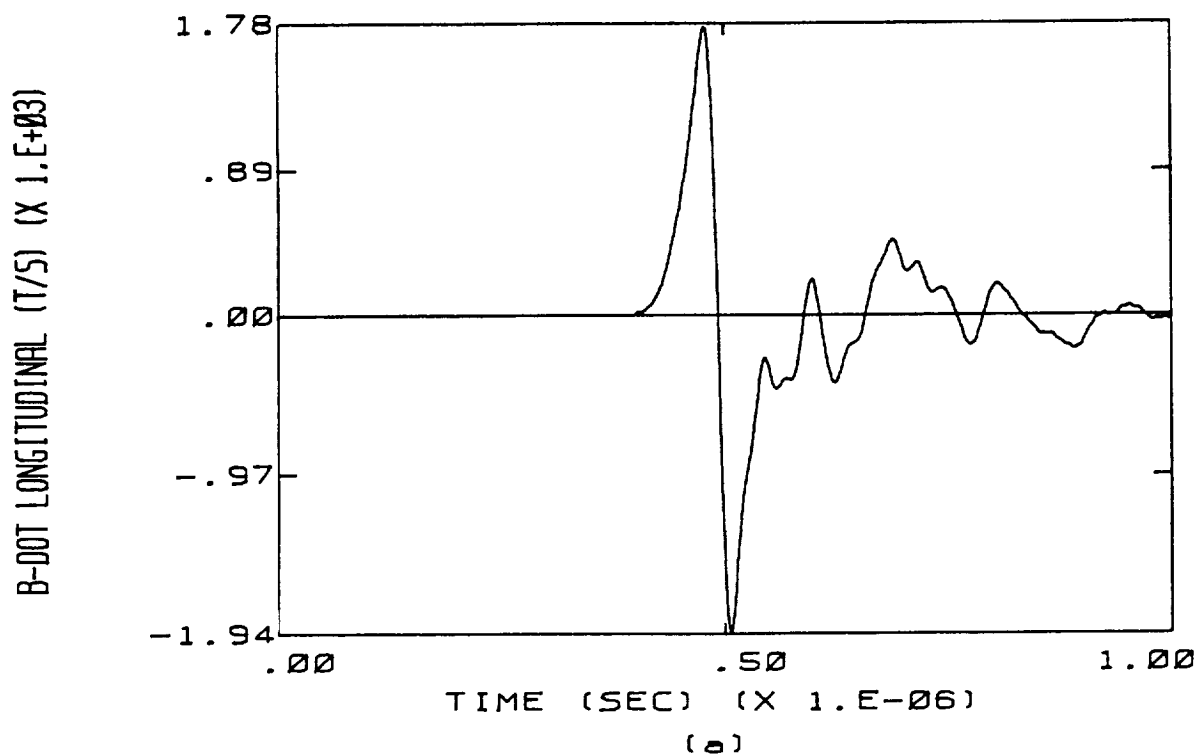


Figure 7.5 Calculated Sensor Responses for the Double Size F106B Aircraft, Nose to Tail Orientation, Net Charge of -3.95 Millicoulombs, Electric Field Magnitude of 100 kV/m

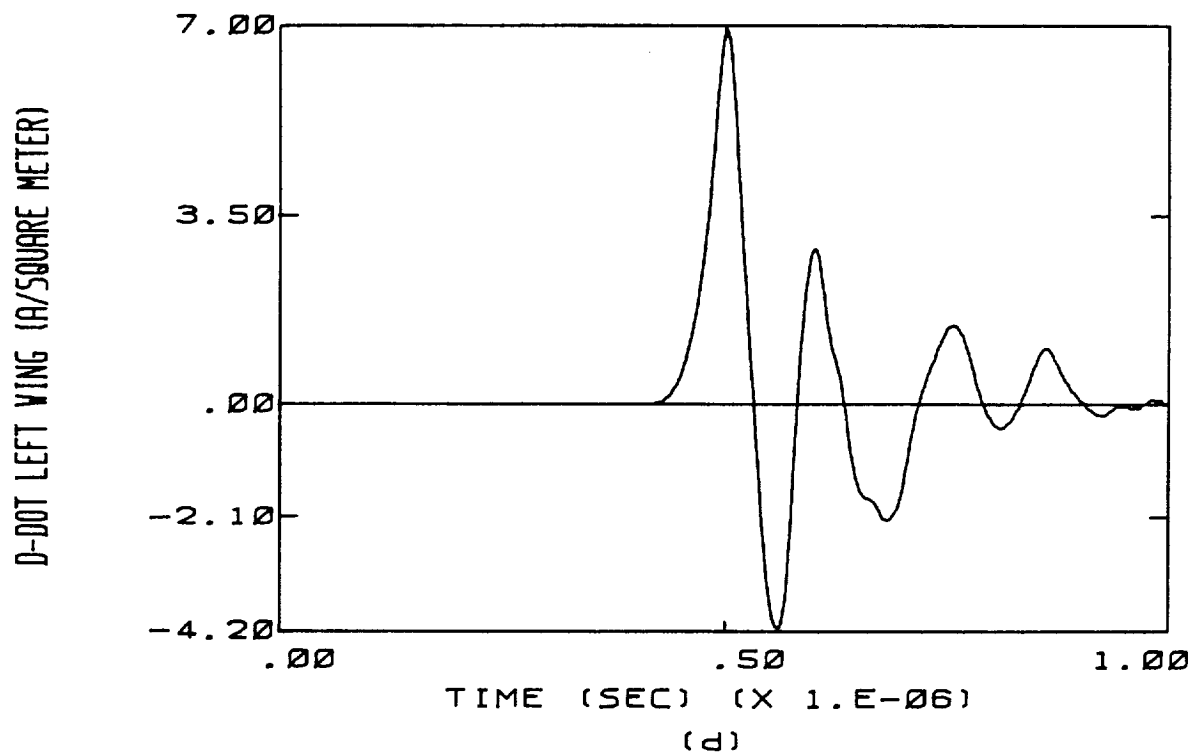
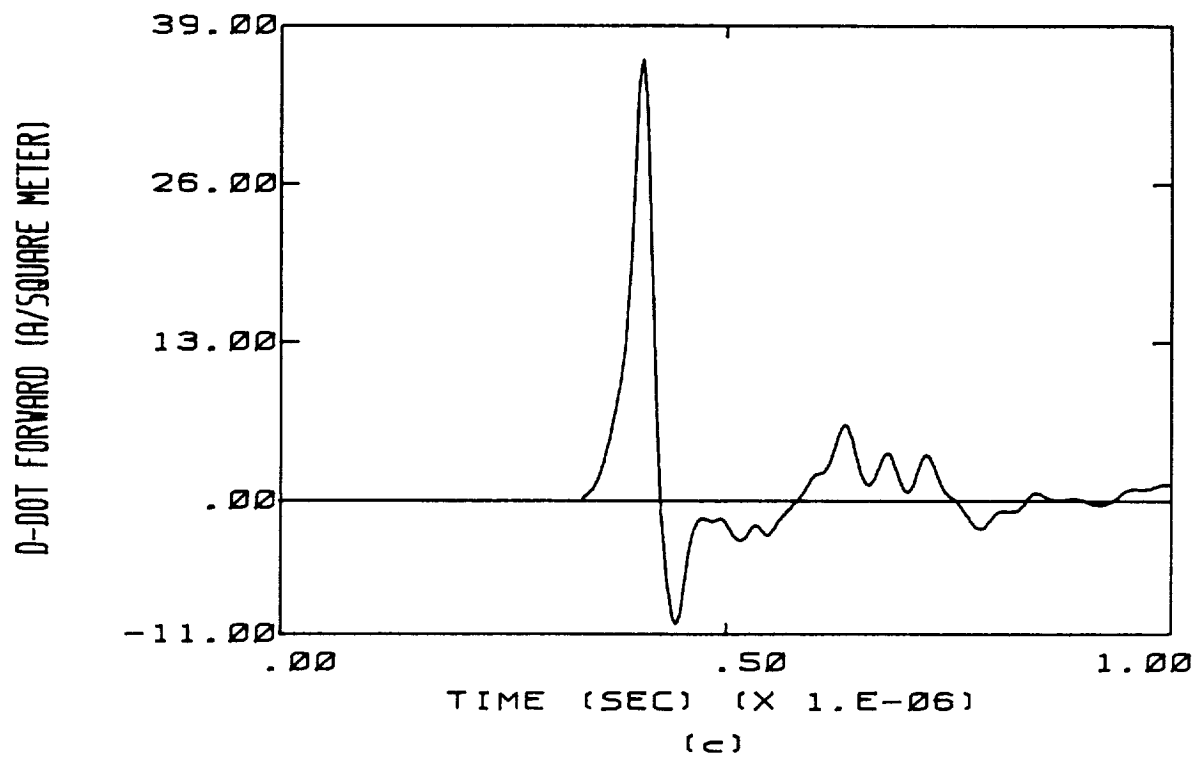


Figure 7.5 (continued)

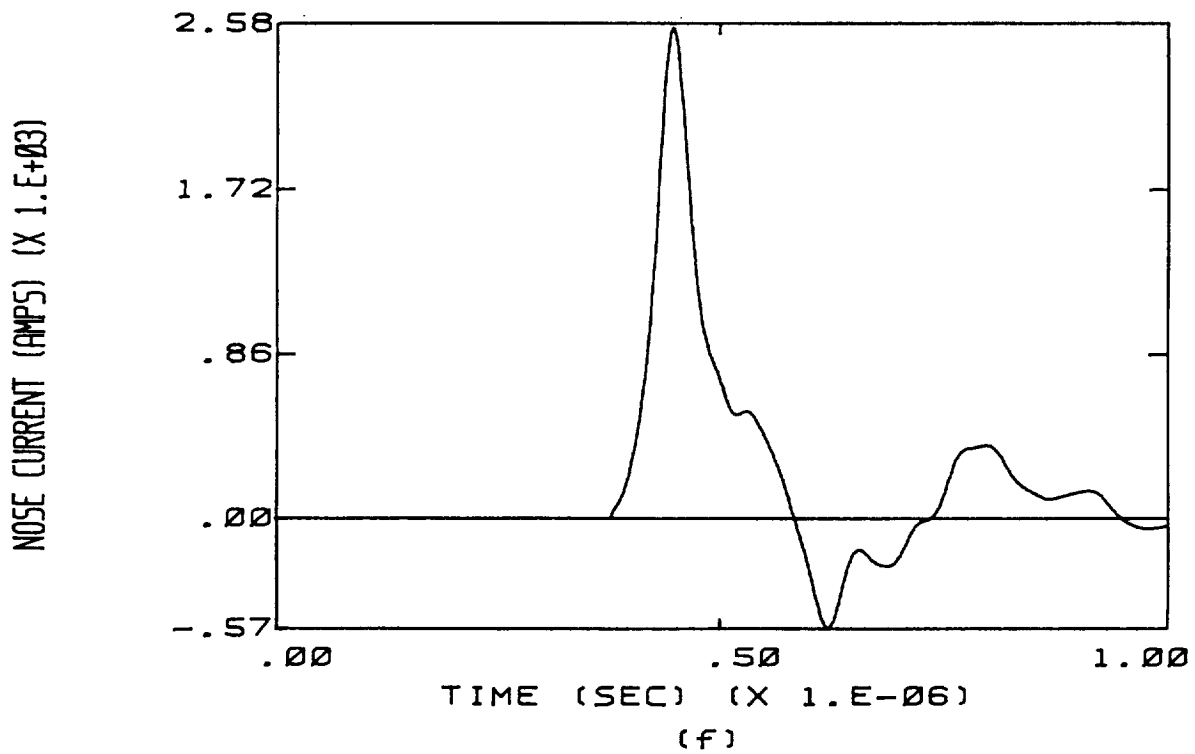
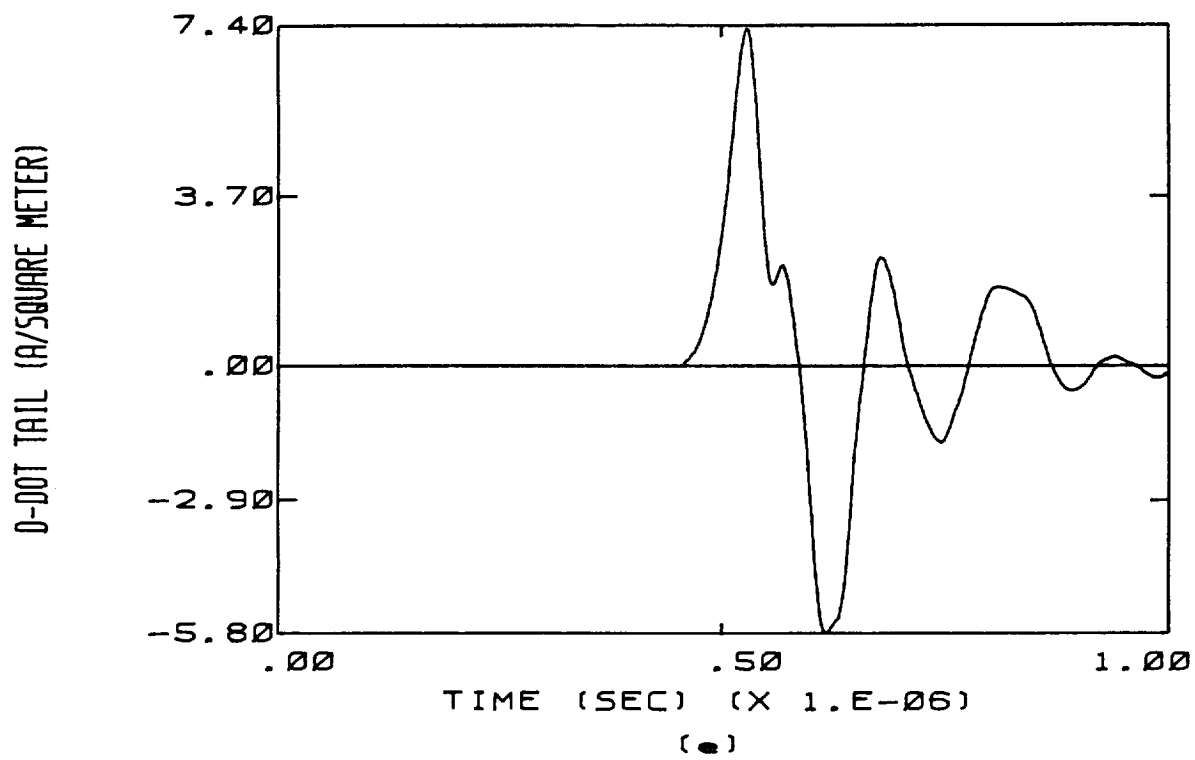


Figure 7.5 (continued)

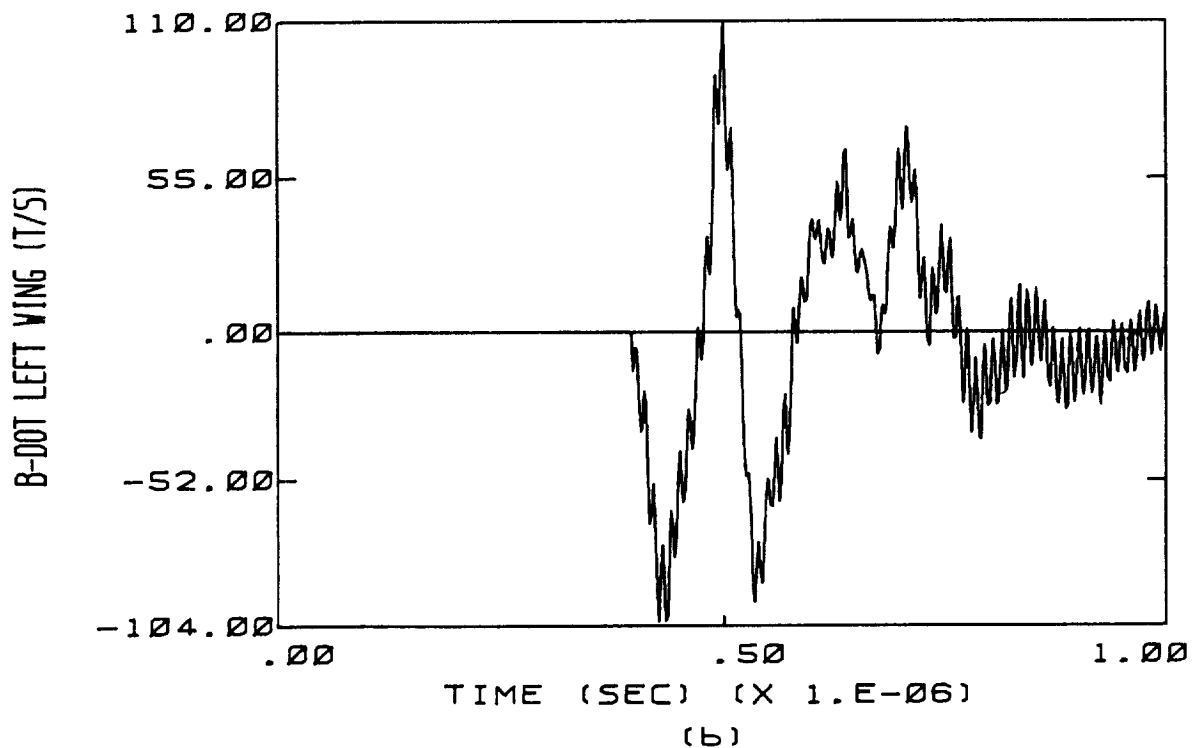
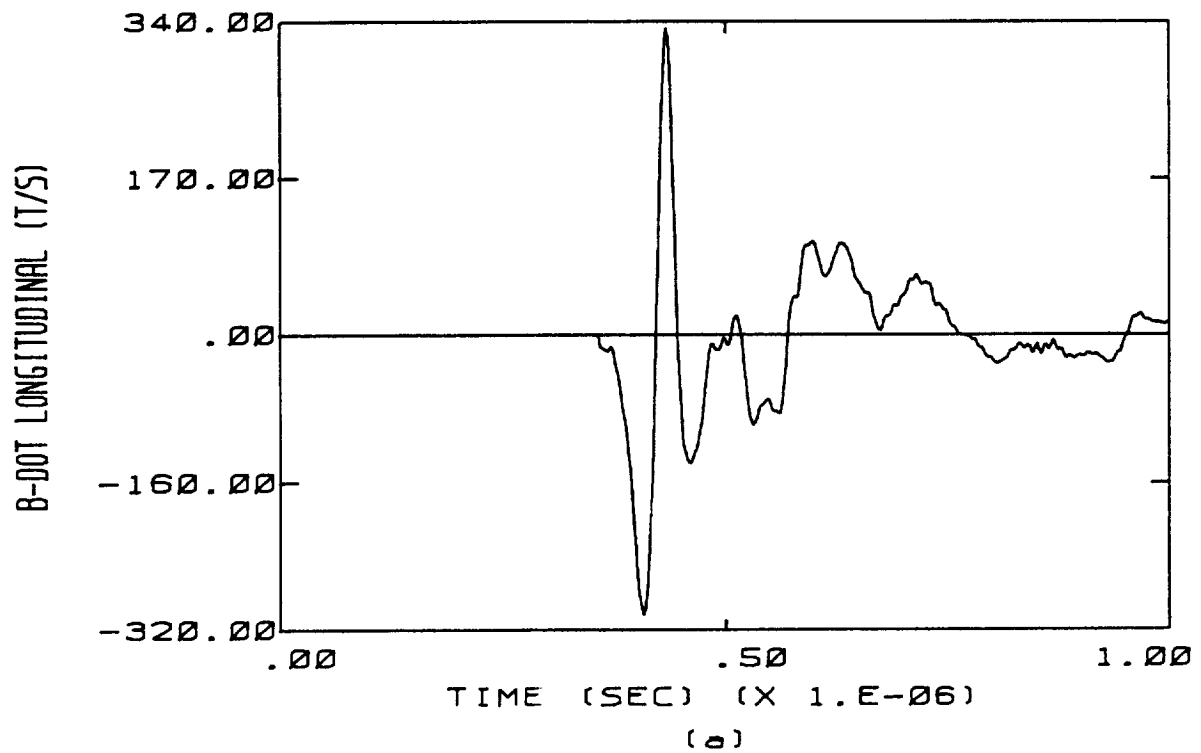
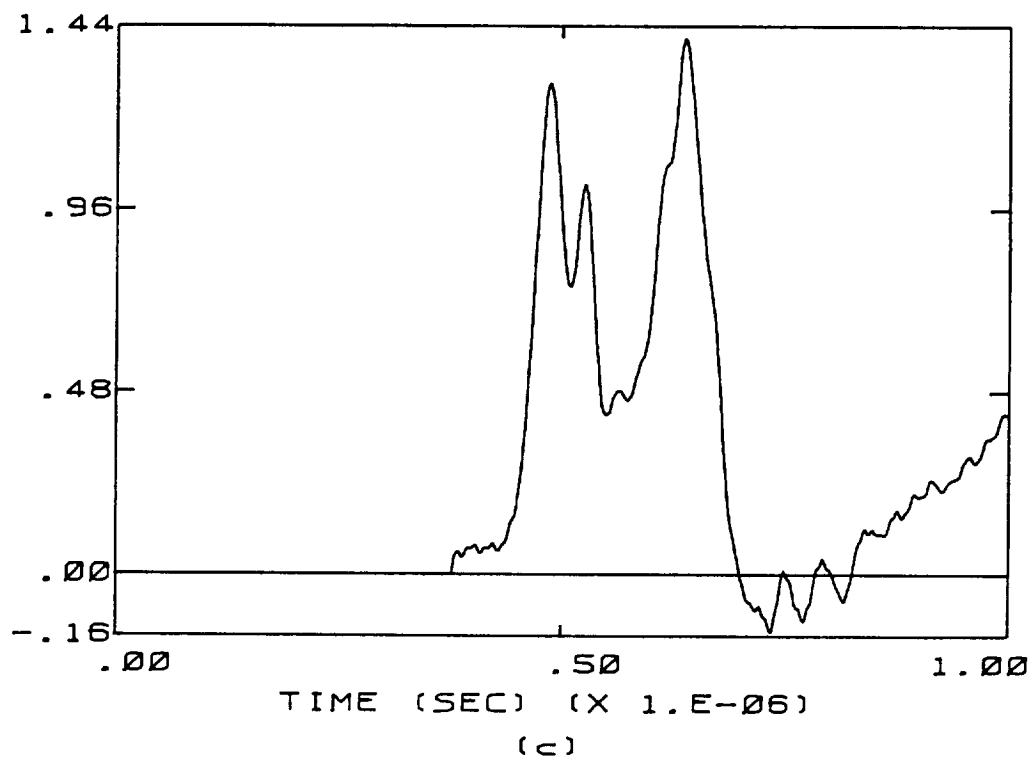


Figure 7.6 Calculated Sensor Responses for the Double Size F106B Aircraft, Top to Bottom Orientation, Net Charge of -3.95 Millicoulombs, Electric Field Magnitude of 250 kV/m

D-DOT FORWARD (A/SQUARE METER)



D-DOT LEFT WING (A/SQUARE METER)

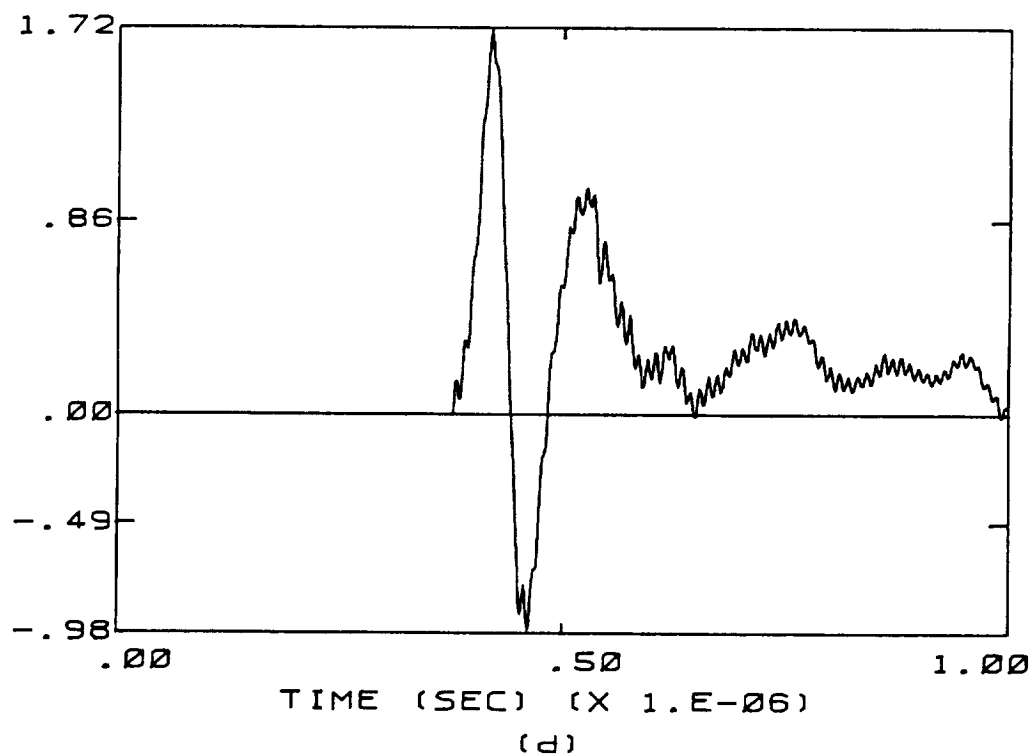


Figure 7.6 (continued)

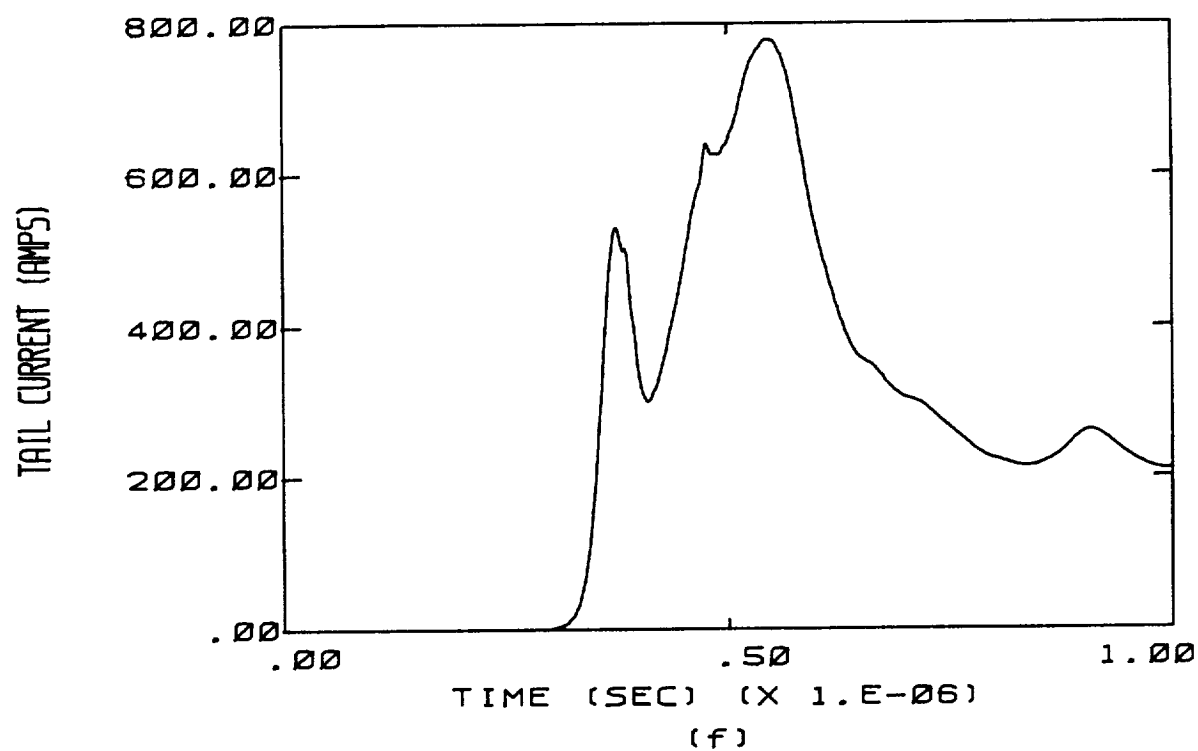
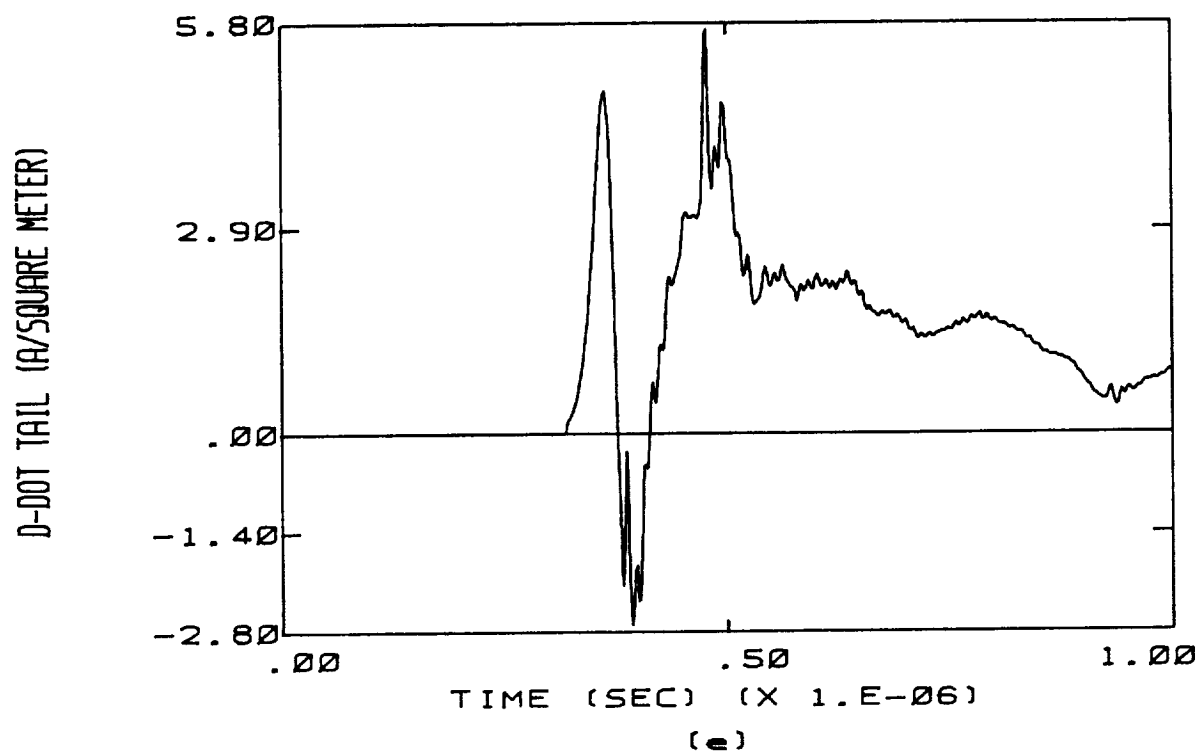
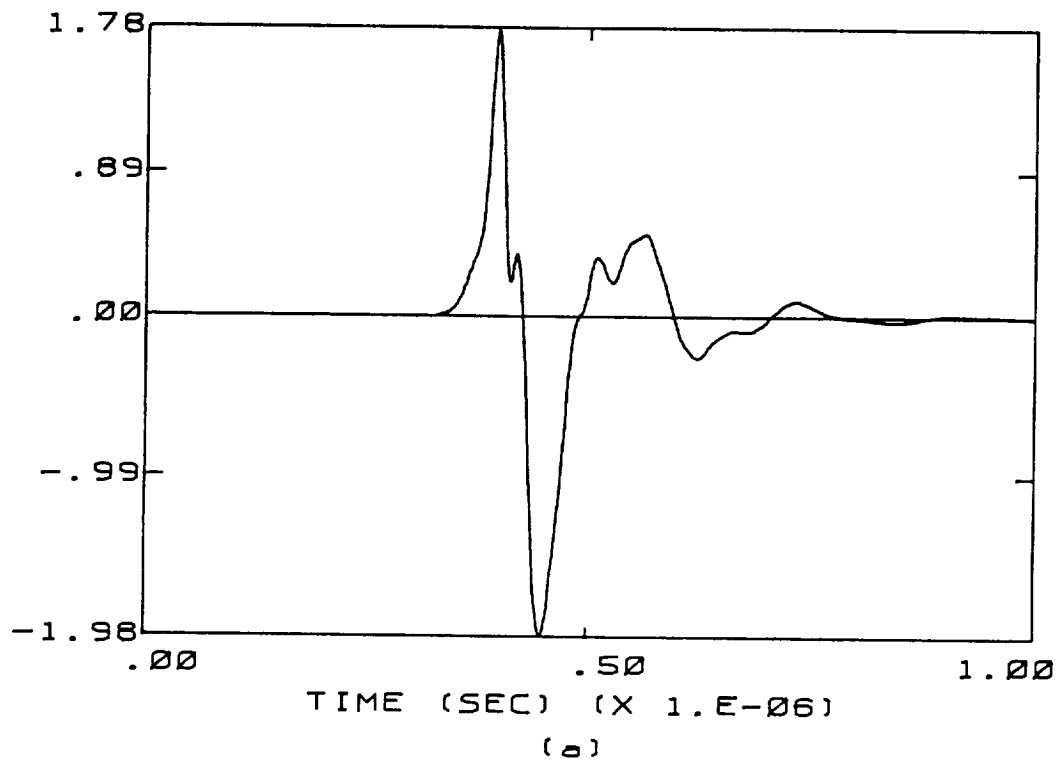


Figure 7.6 (continued)

B-DOT LONGITUDINAL (T/5) (X 1.E+03)



B-DOT LEFT WING (T/5) (X 1.E+03)

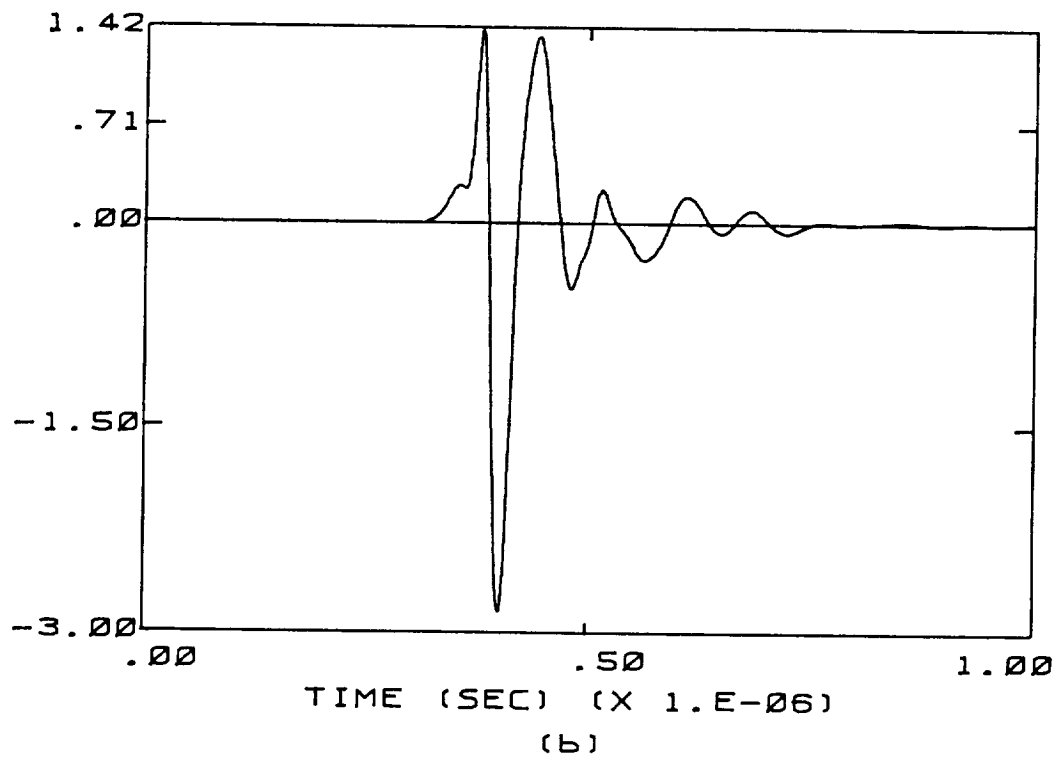
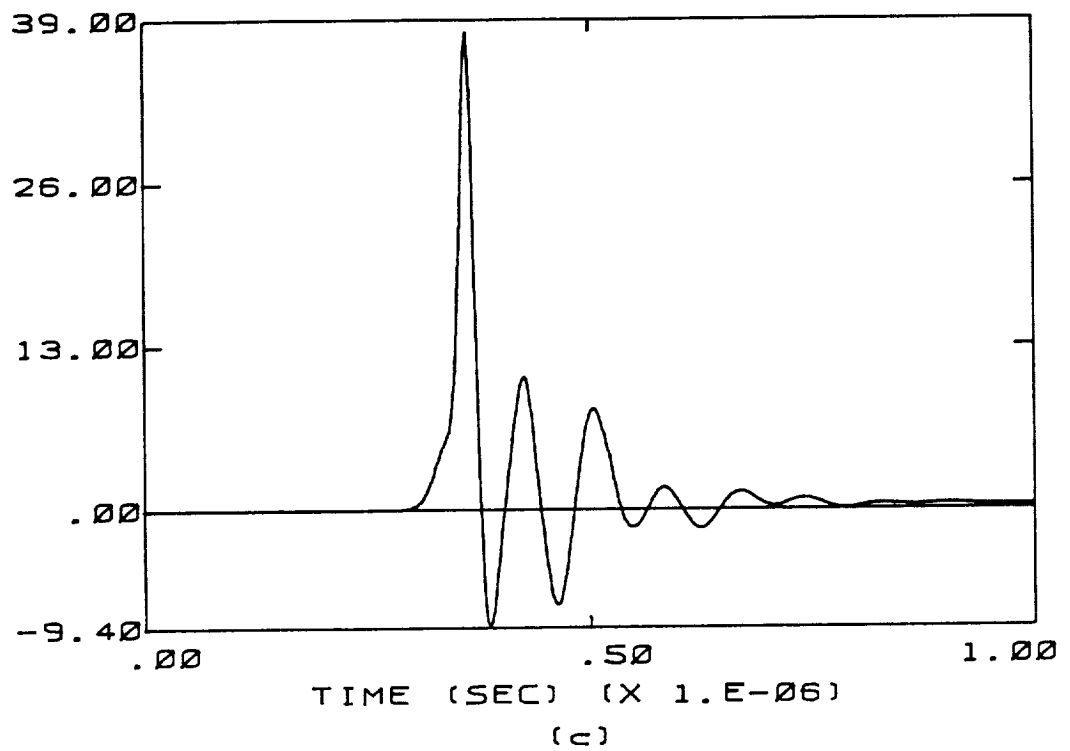


Figure 7.7 Calculated Sensor Responses for the F106B With Delta Wing Replaced By Straight Wing, Nose to Tail Orientation, Net Charge of -1.0 Millicoulomb, Electric Field Magnitude of 120 kV/m

D-DOT FORWARD (A/SQUARE METER)



D-DOT LEFT WING (A/SQUARE METER)

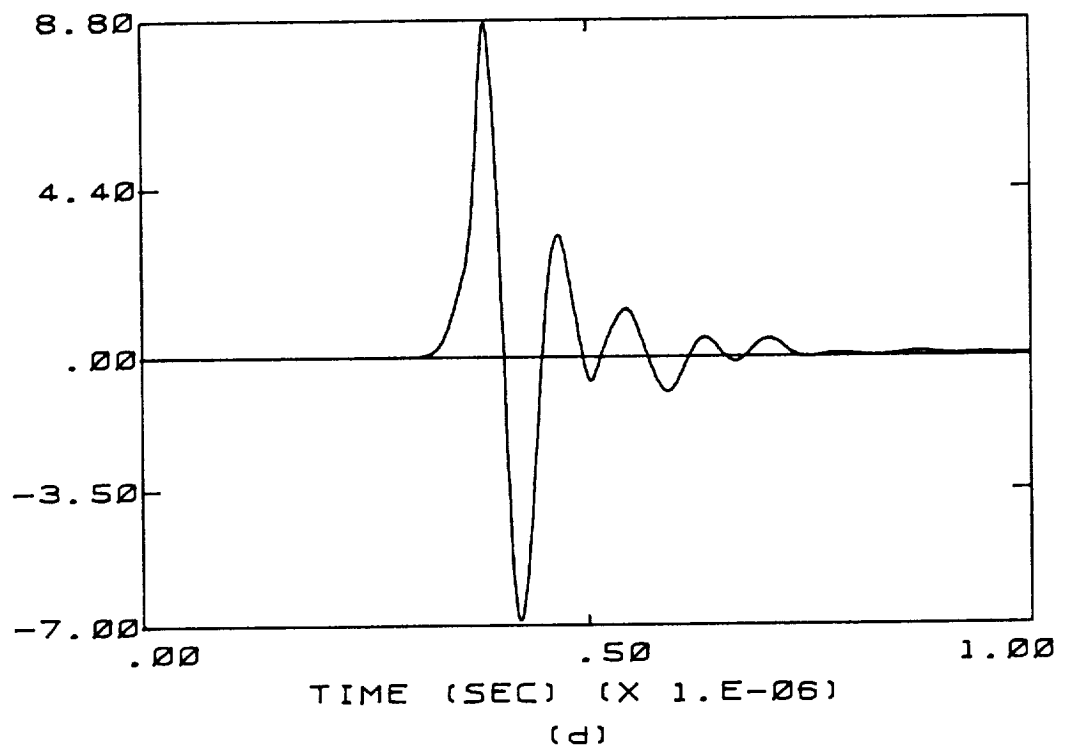


Figure 7.7 (continued)



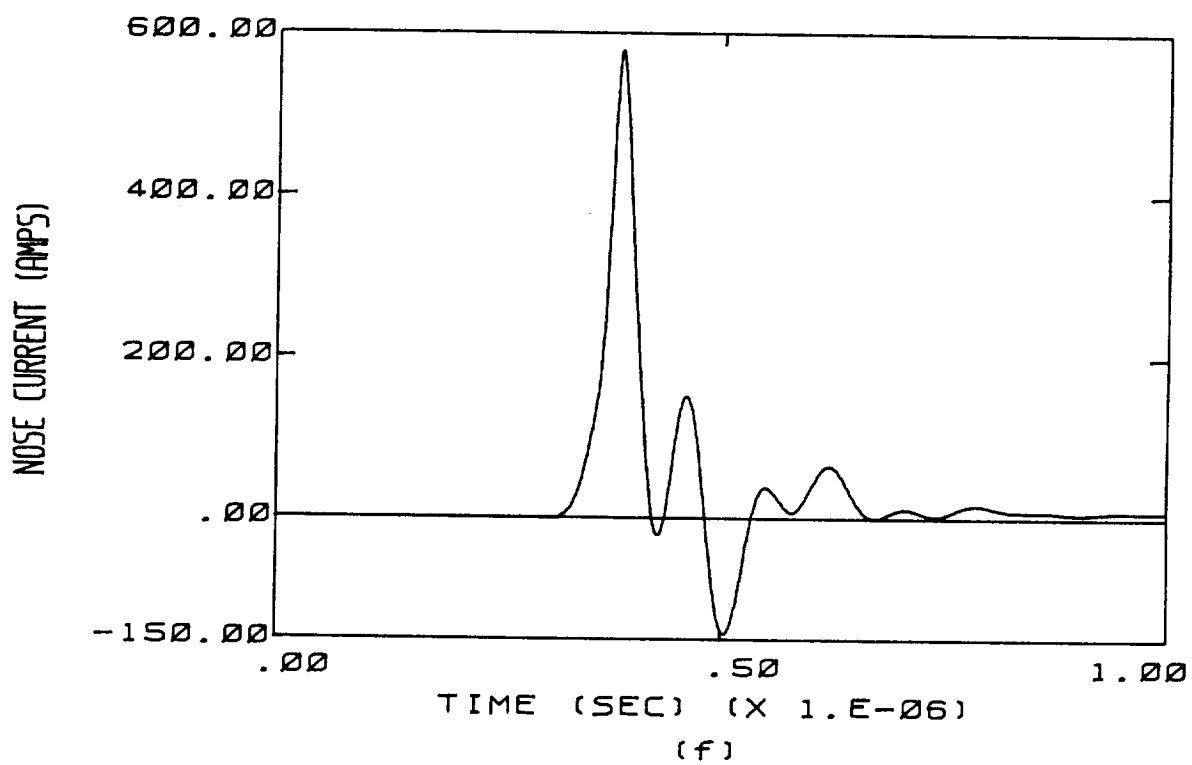
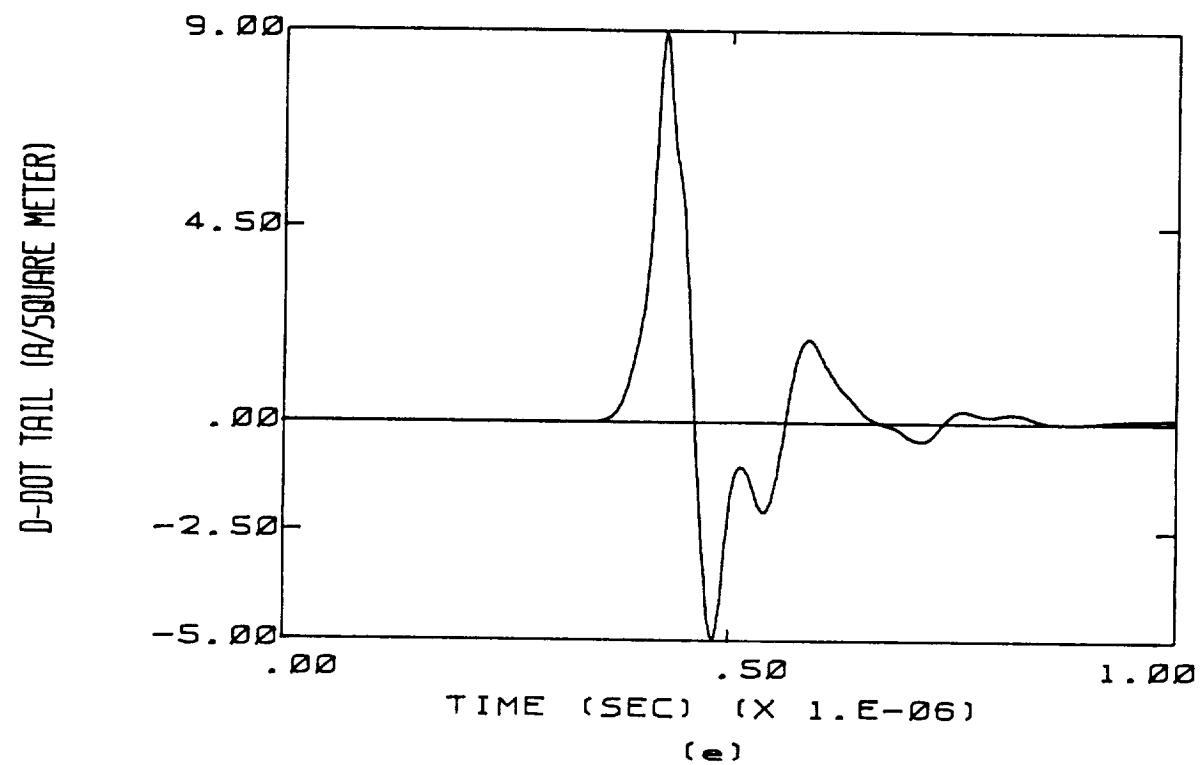


Figure 7.7 (continued)

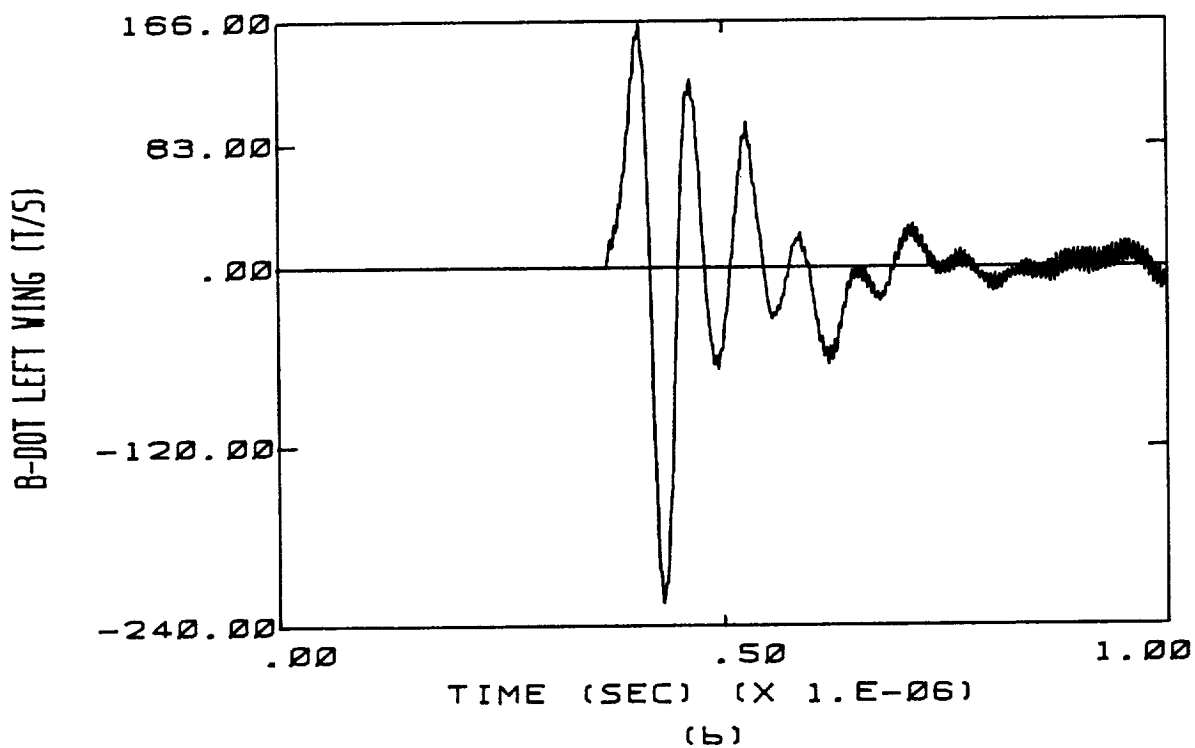
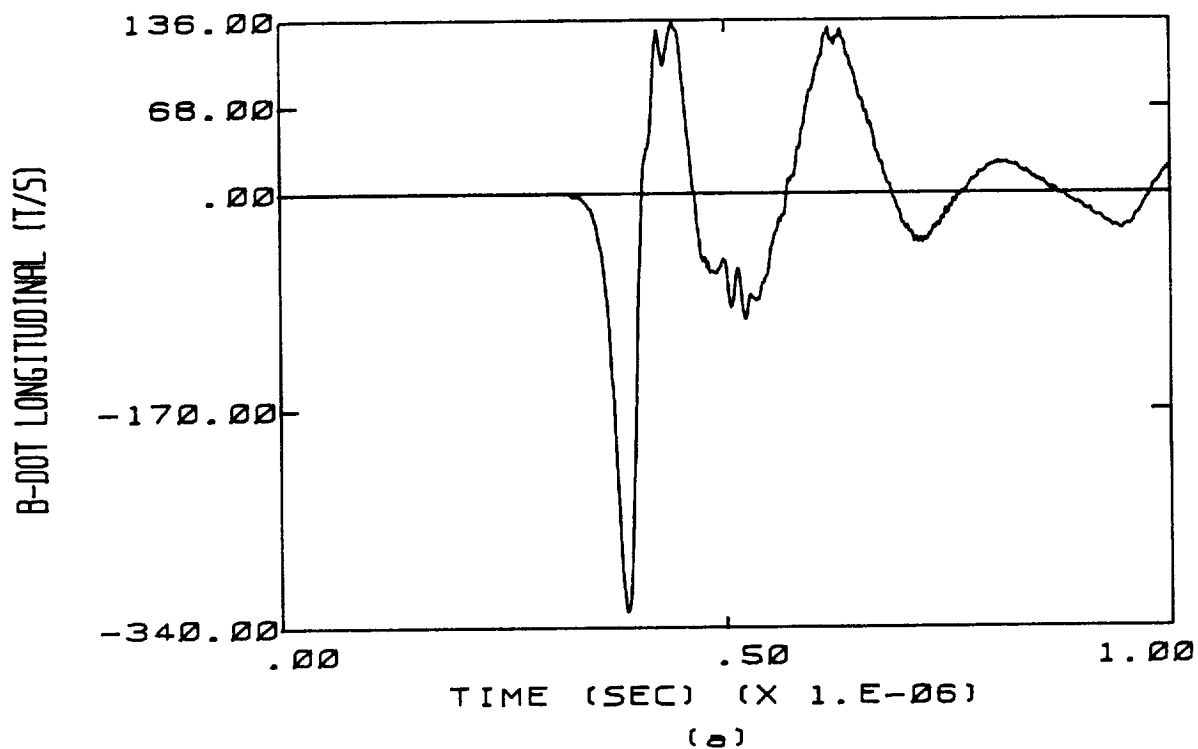


Figure 7.8 Calculated Sensor Responses for the F106B With Delta Wing Replaced By Straight Wing, Top to Bottom Orientation, Net Charge of -1.0 Millicoulomb, Electric Field Magnitude of 240 kV/m

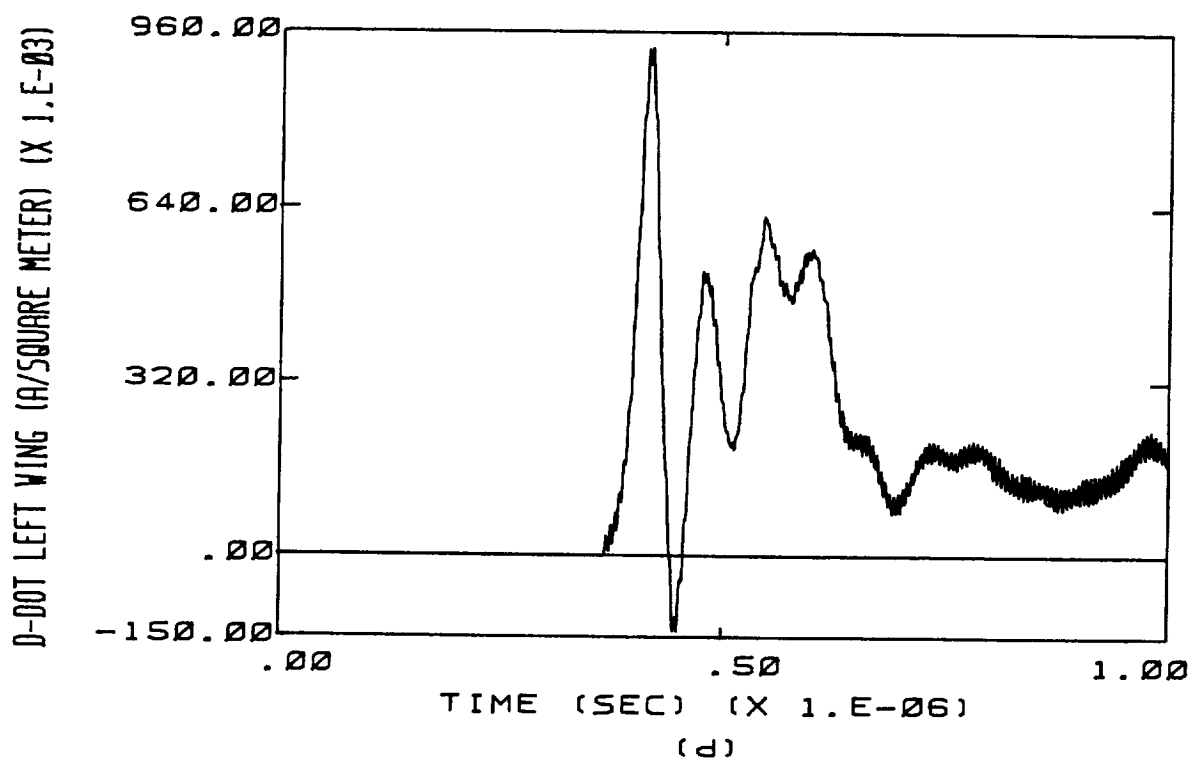
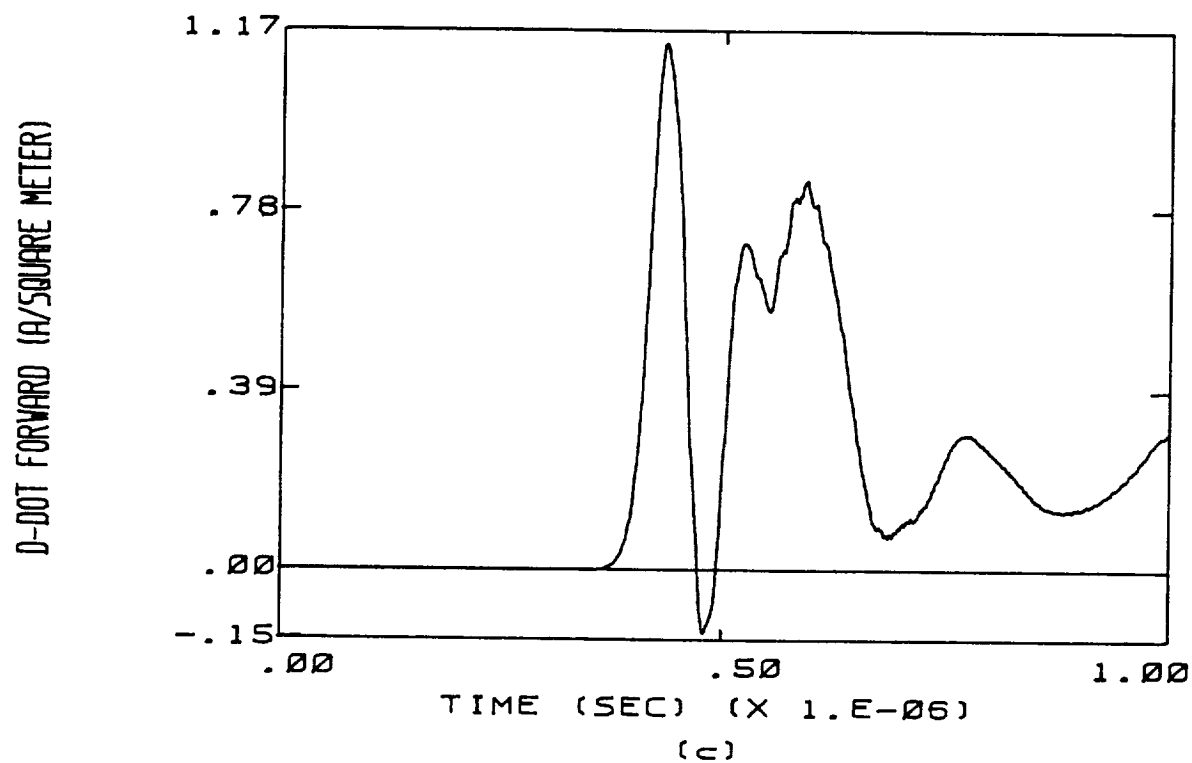
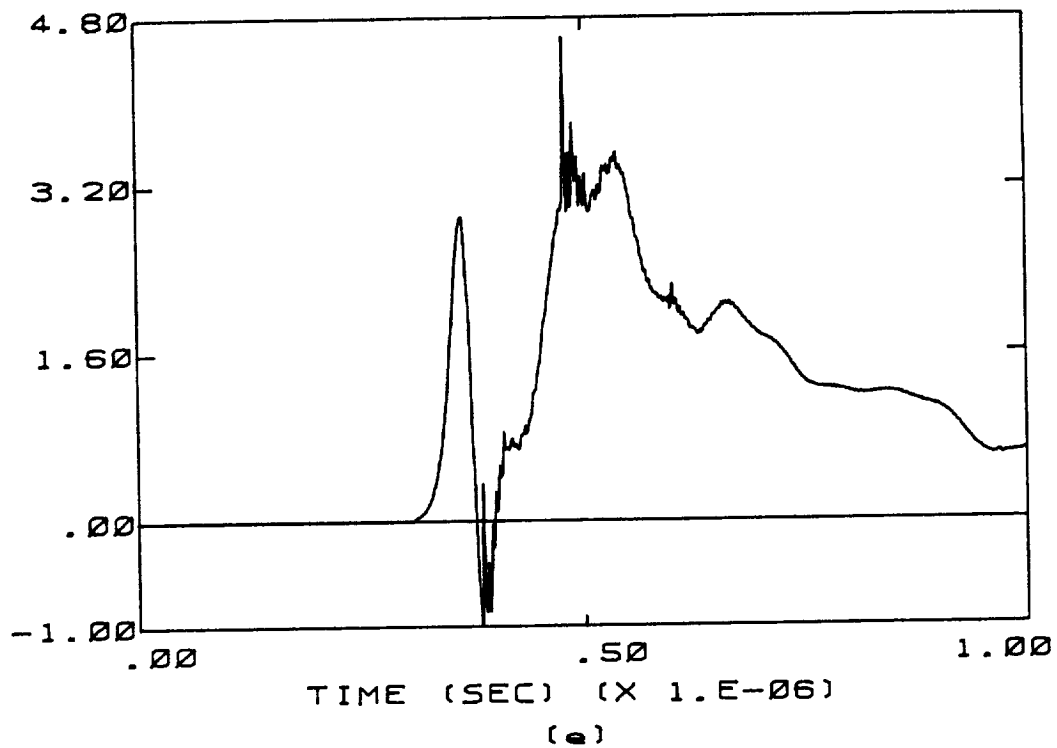


Figure 7.8 (continued)

D-DOT TAIL (A/SQUARE METER)



TAIL CURRENT (AMPS)

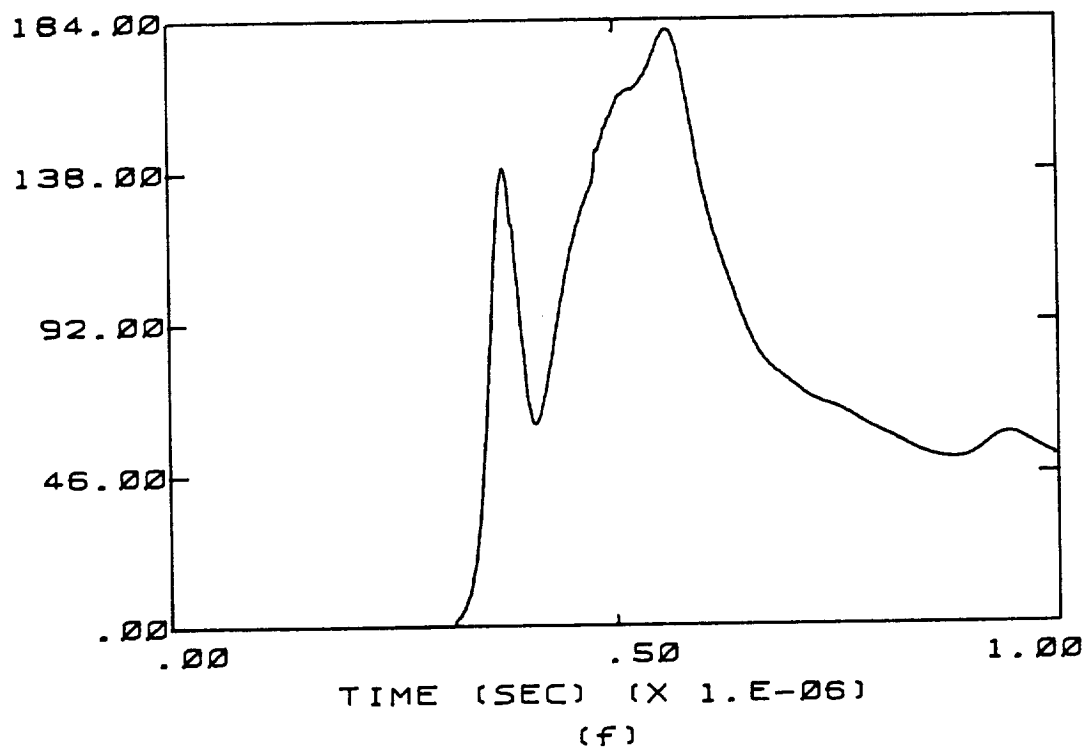
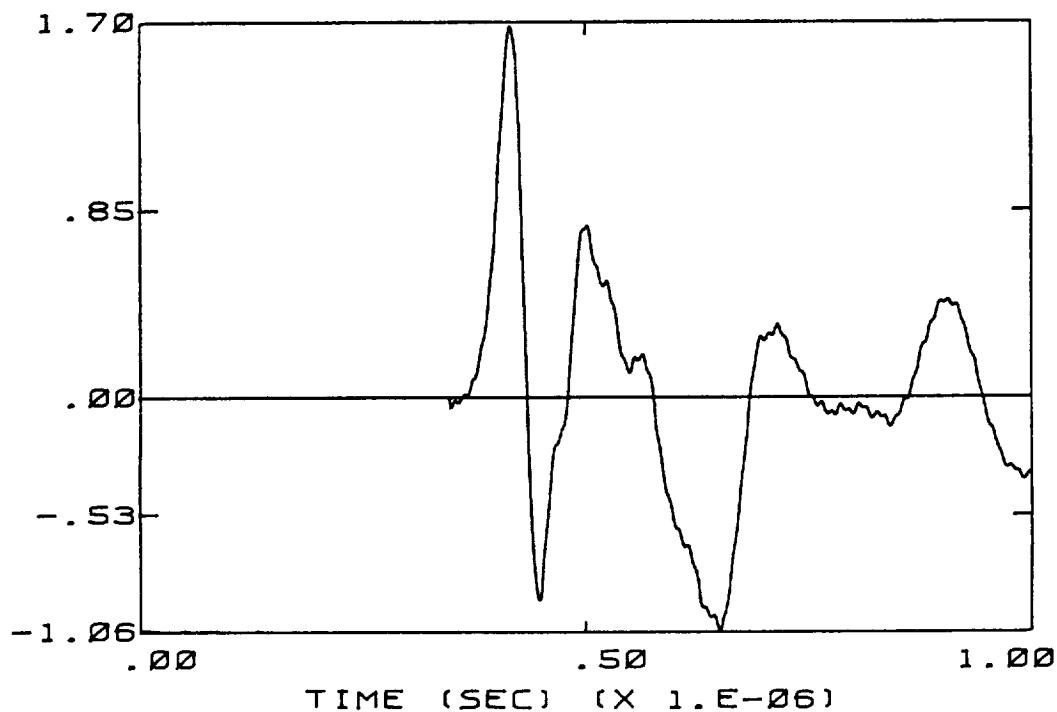


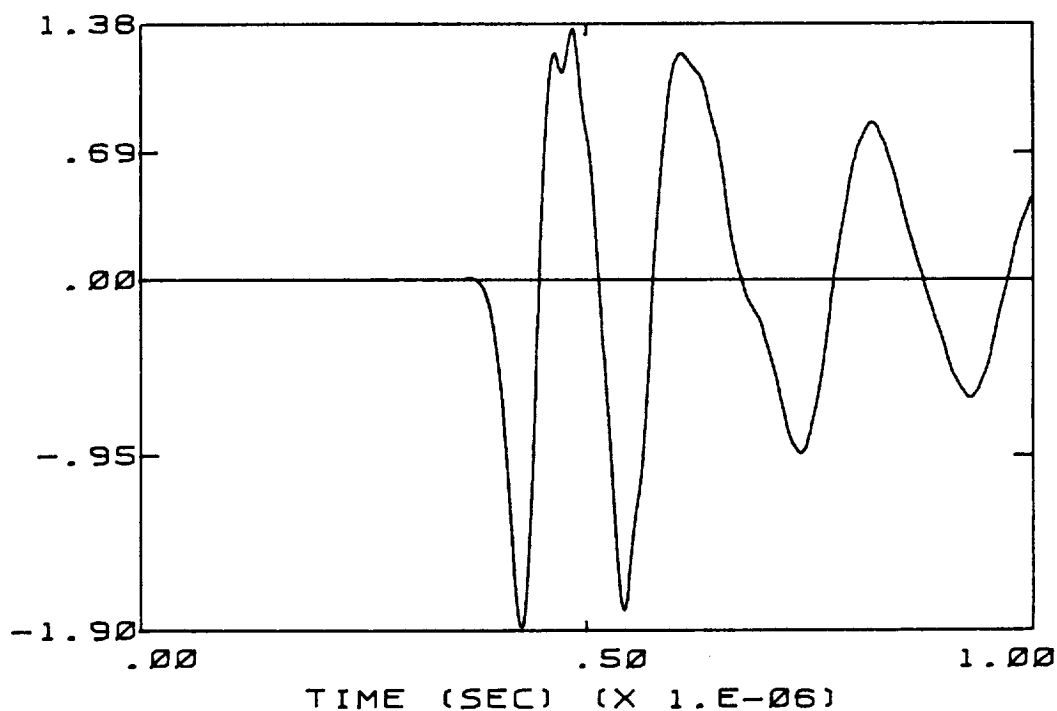
Figure 7.8 (continued)

B-DOT LONGITUDINAL (T/S) (X 1.E+03)



(a)

B-DOT LEFT WING (T/S) (X 1.E+03)



(b)

Figure 7.9 Calculated Sensor Responses for the C130 Aircraft, Nose to Tail Orientation, Net Charge of -3.45 Millicoulombs, Electric Field Magnitude of 190 kV/m

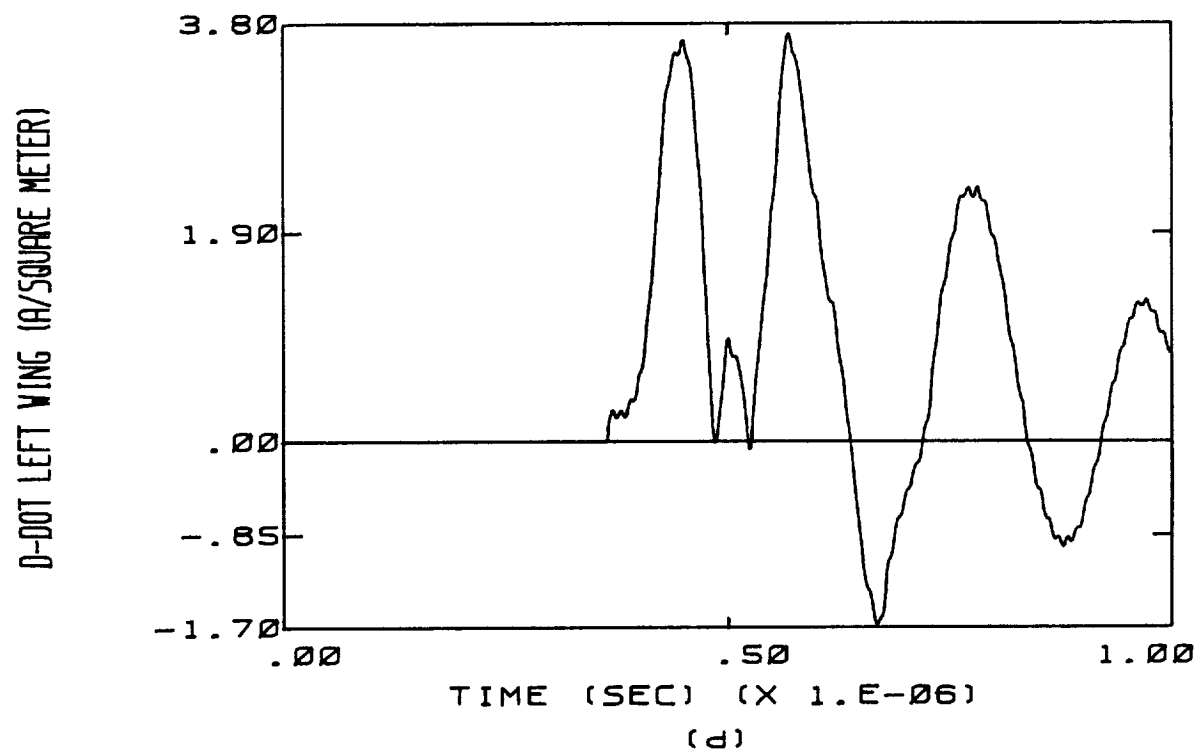
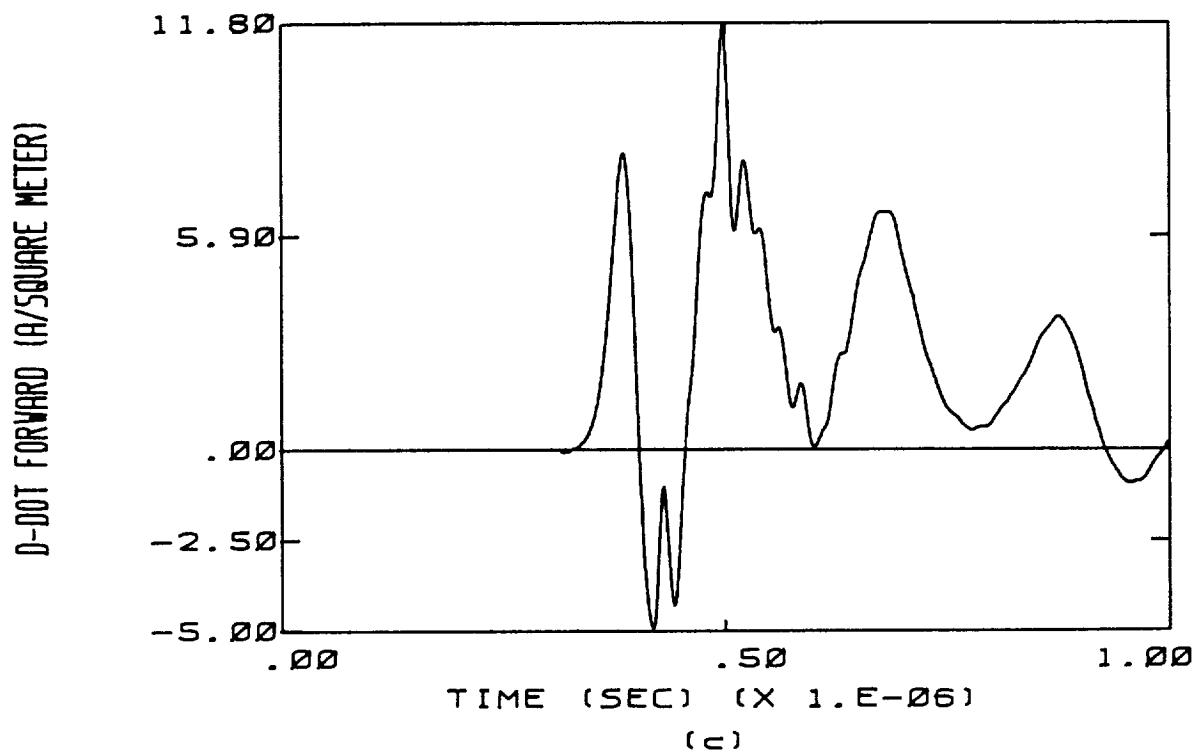
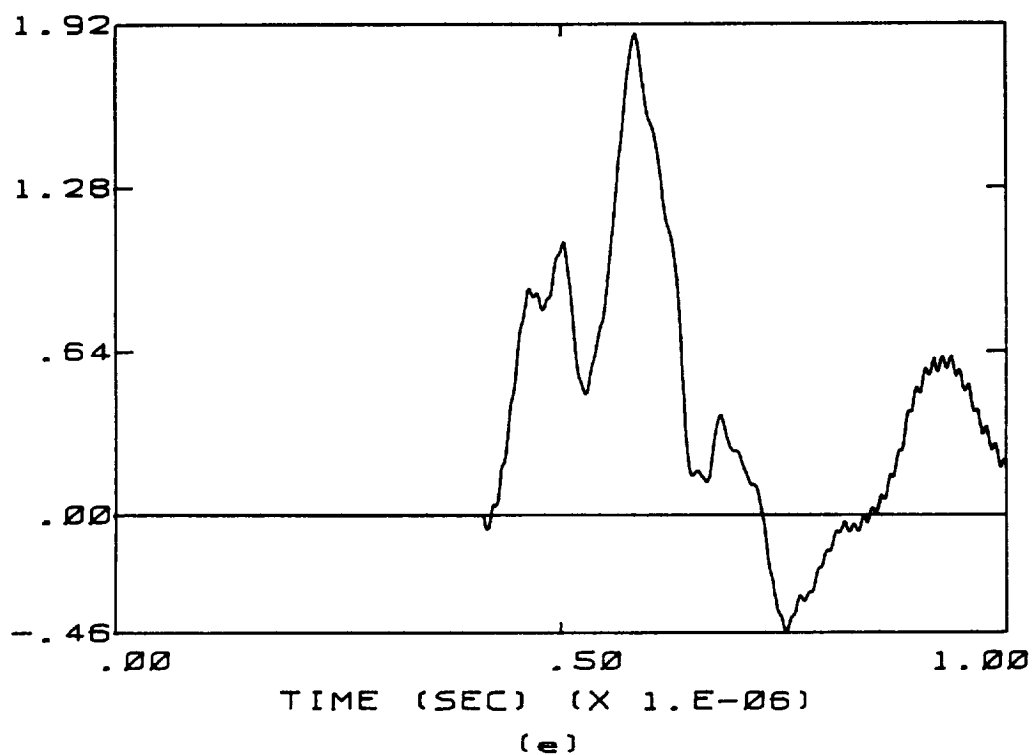


Figure 7.9 (continued)

D-DOT TAIL (A/SQUARE METER)



NOSE CURRENT (AMPS) (X 1.E+03)

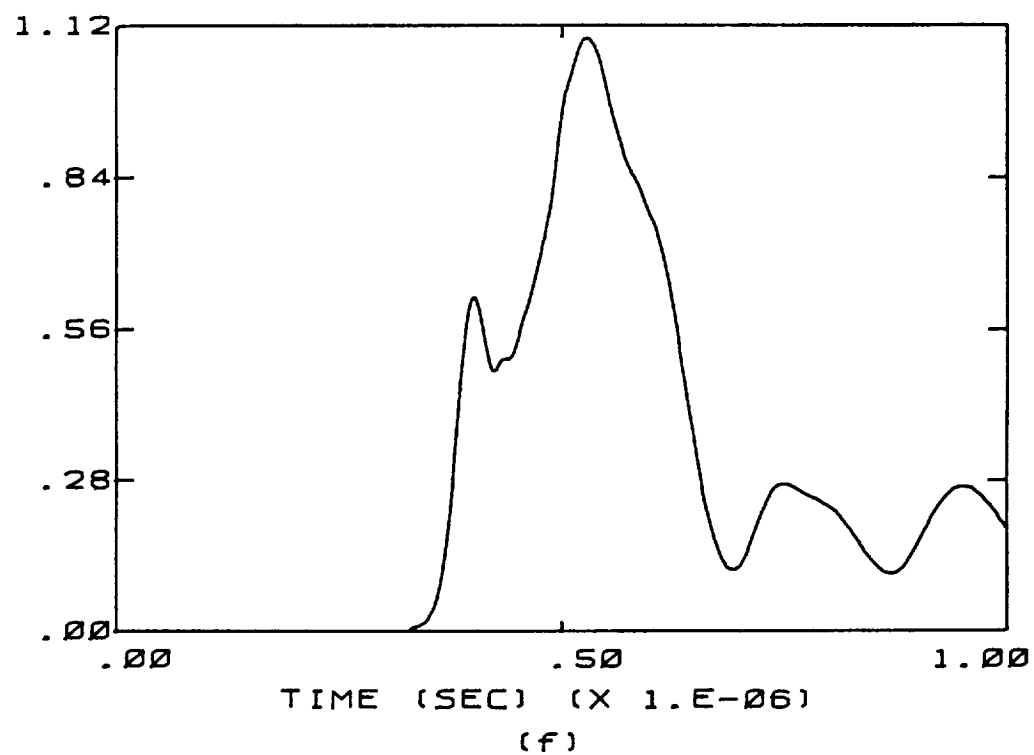


Figure 7.9 (continued)

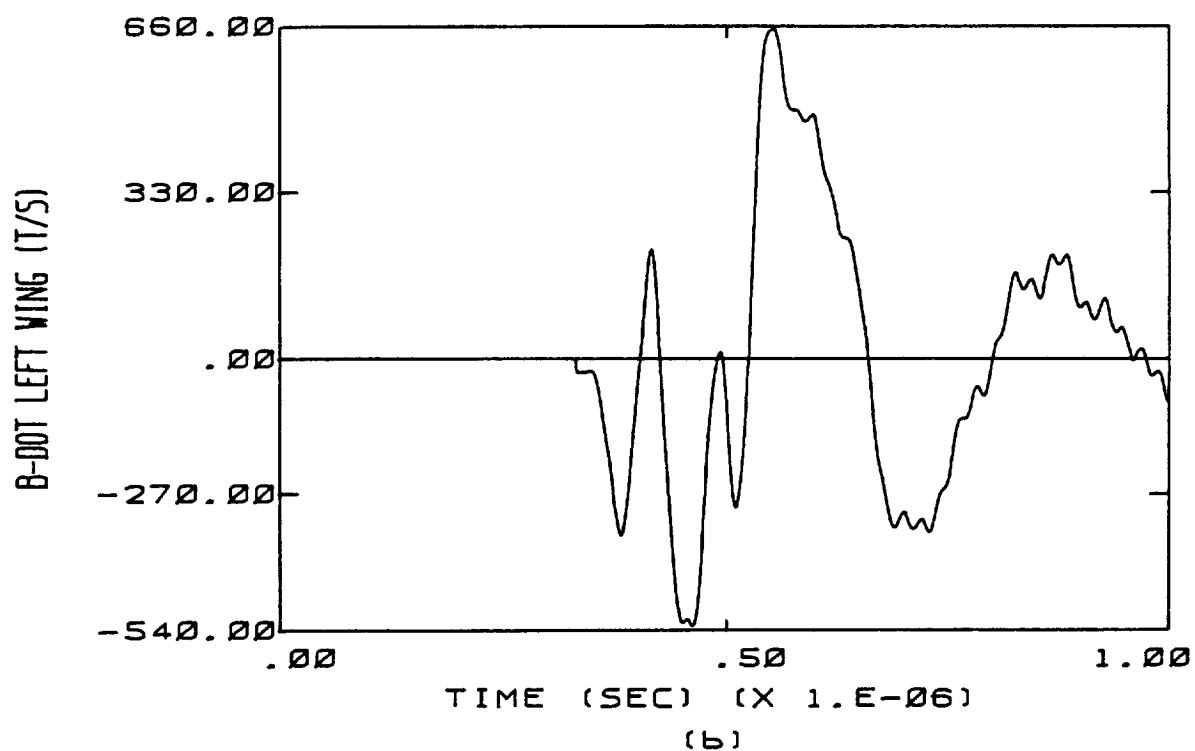
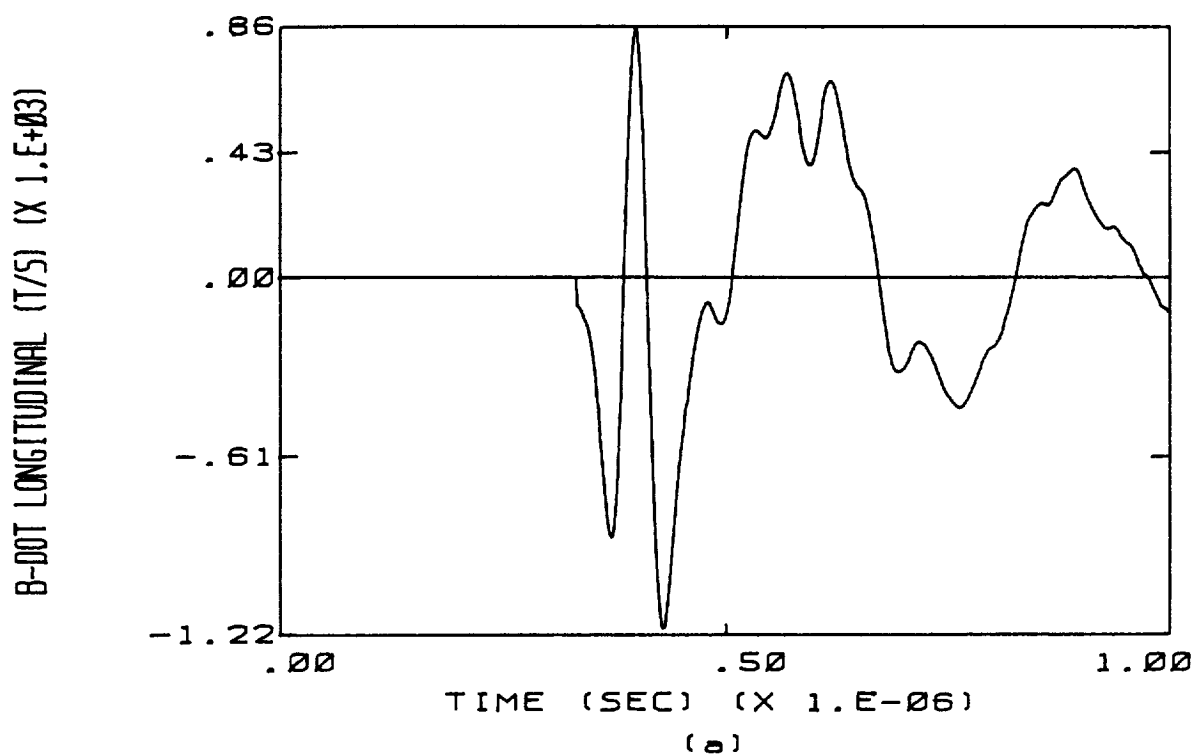
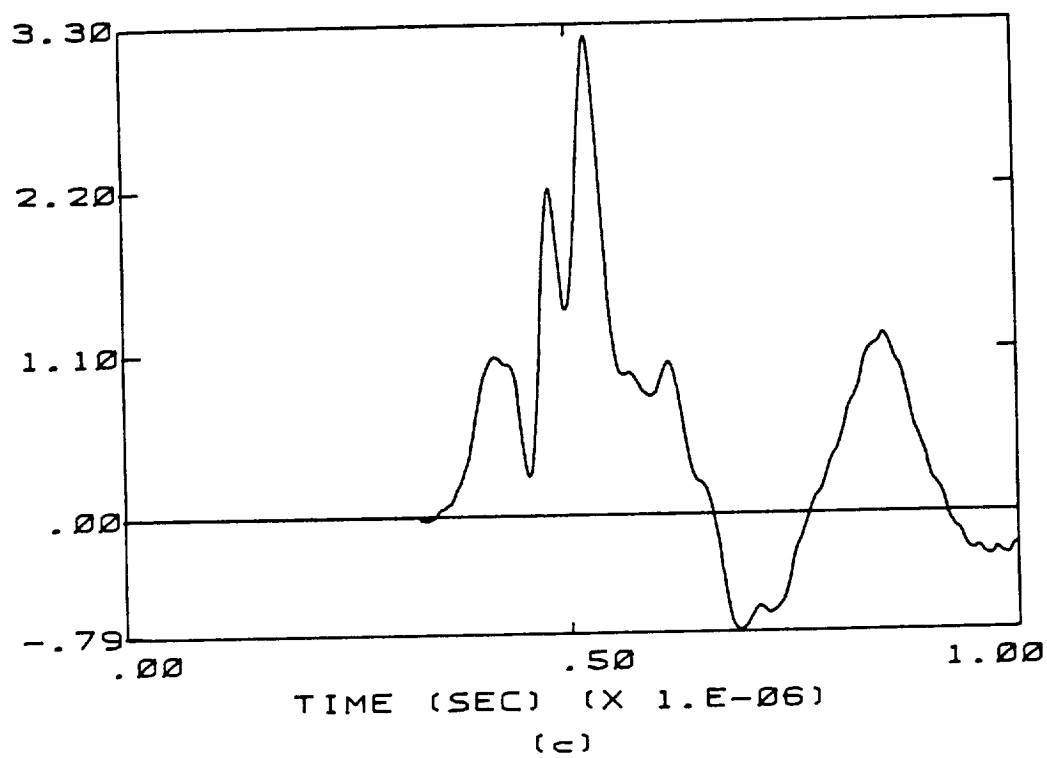


Figure 7.10 Calculated Sensor Responses for the C130 Aircraft, Top to Bottom Orientation, Net Charge of -3.45 Millicoulombs, Electric Field Magnitude of 210 kV/m



D-DOT FORWARD (A/SQUARE METER)



D-DOT LEFT WING (A/SQUARE METER)

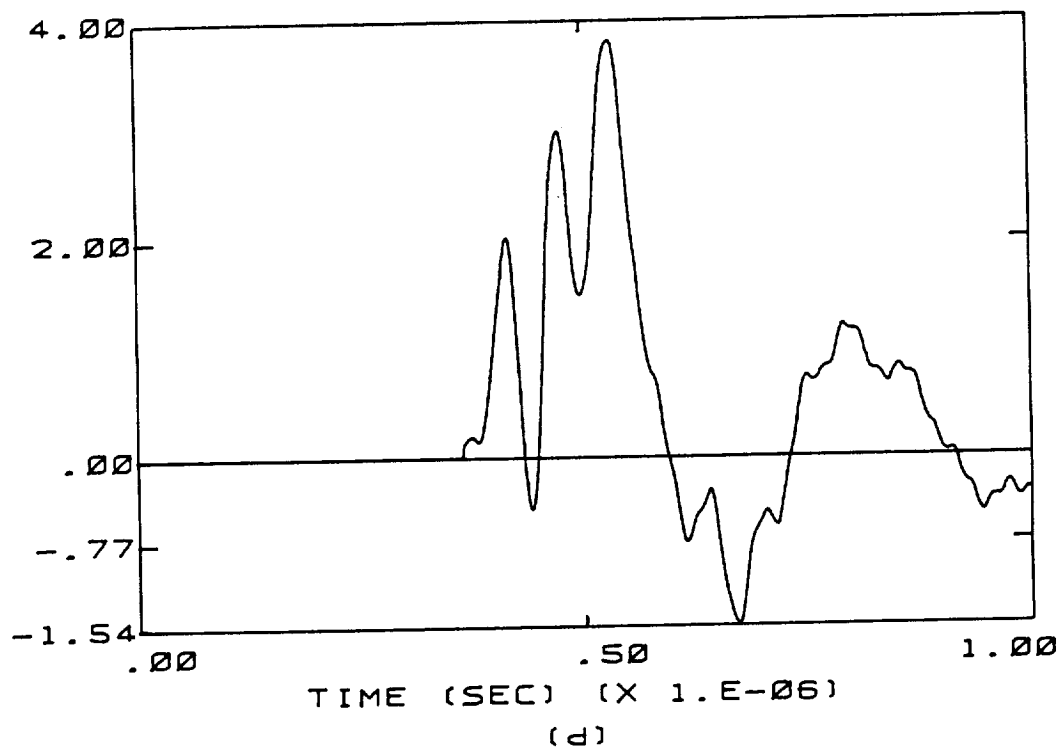
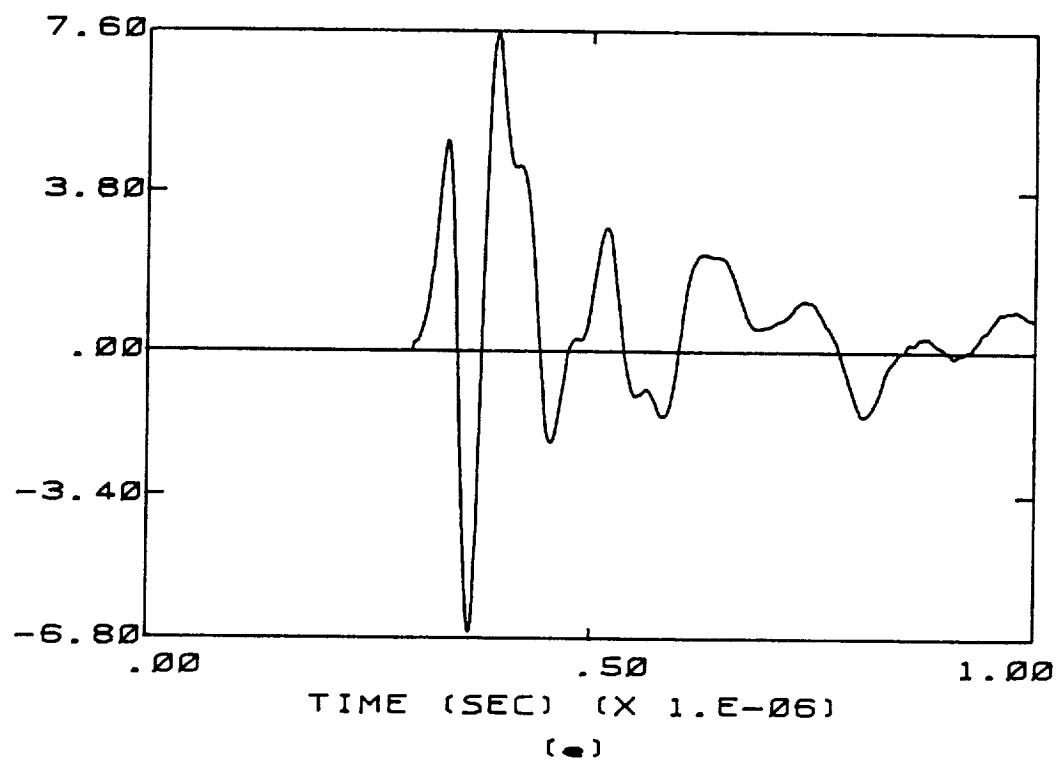


Figure 7.10 (continued)

D-DOT TAIL (A/SQUARE METER)



TAIL CURRENT (AMPS) (X 1.E+03)

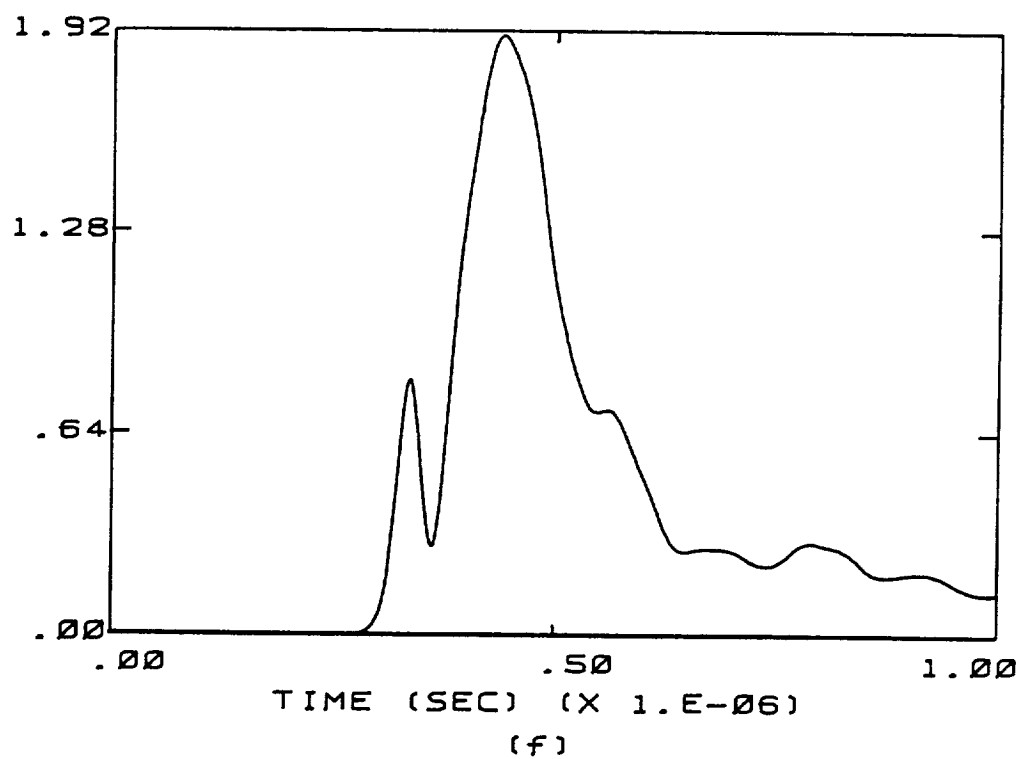
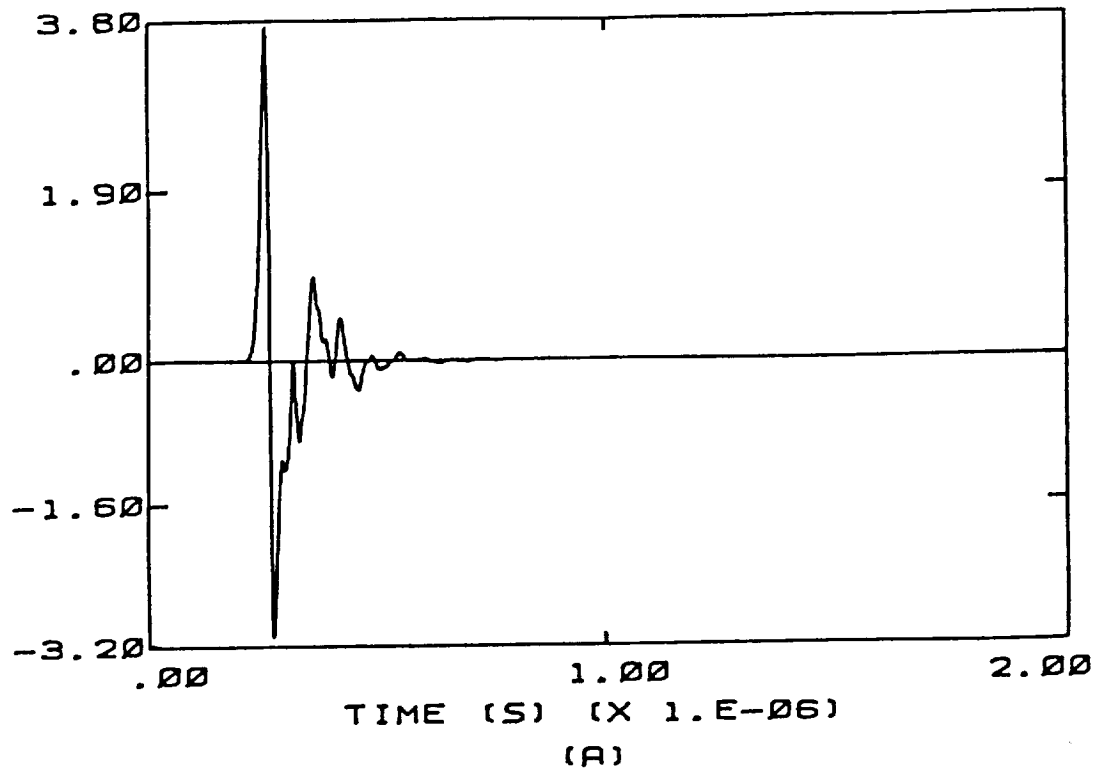


Figure 7.10 (continued)

B-DOT LONGITUDINAL (T/S) (X 1.E+03)



B-DOT LEFT WING (T/S) (X 1.E+03)

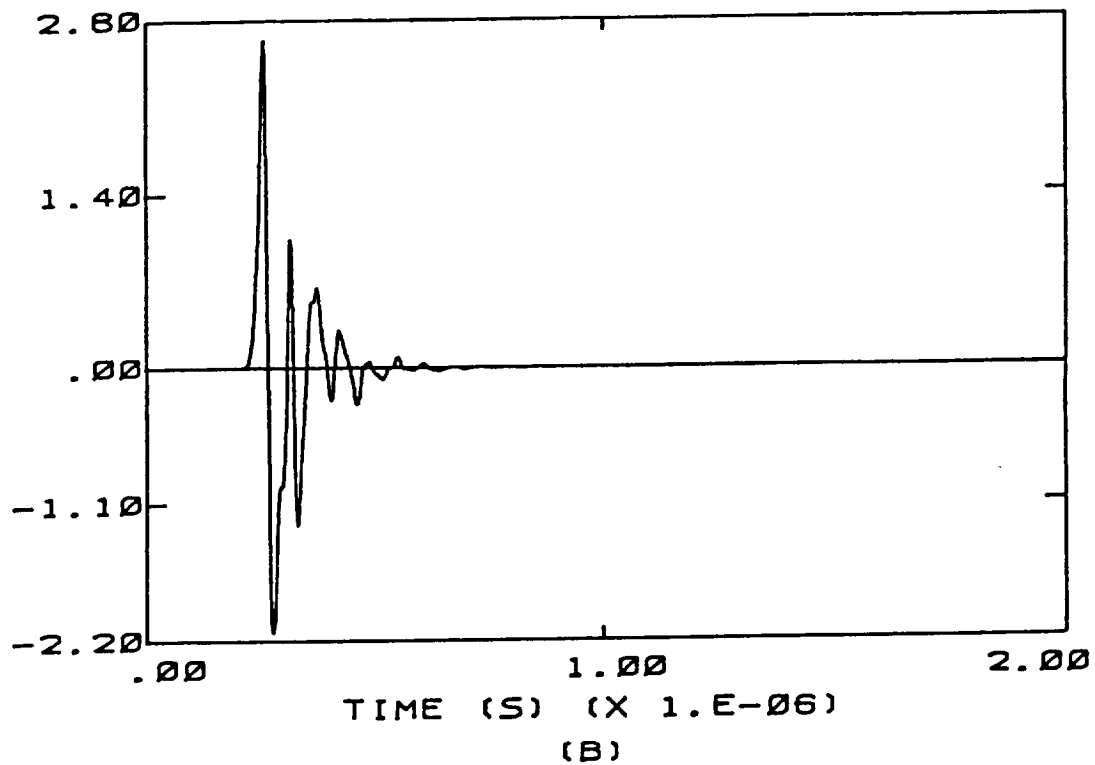
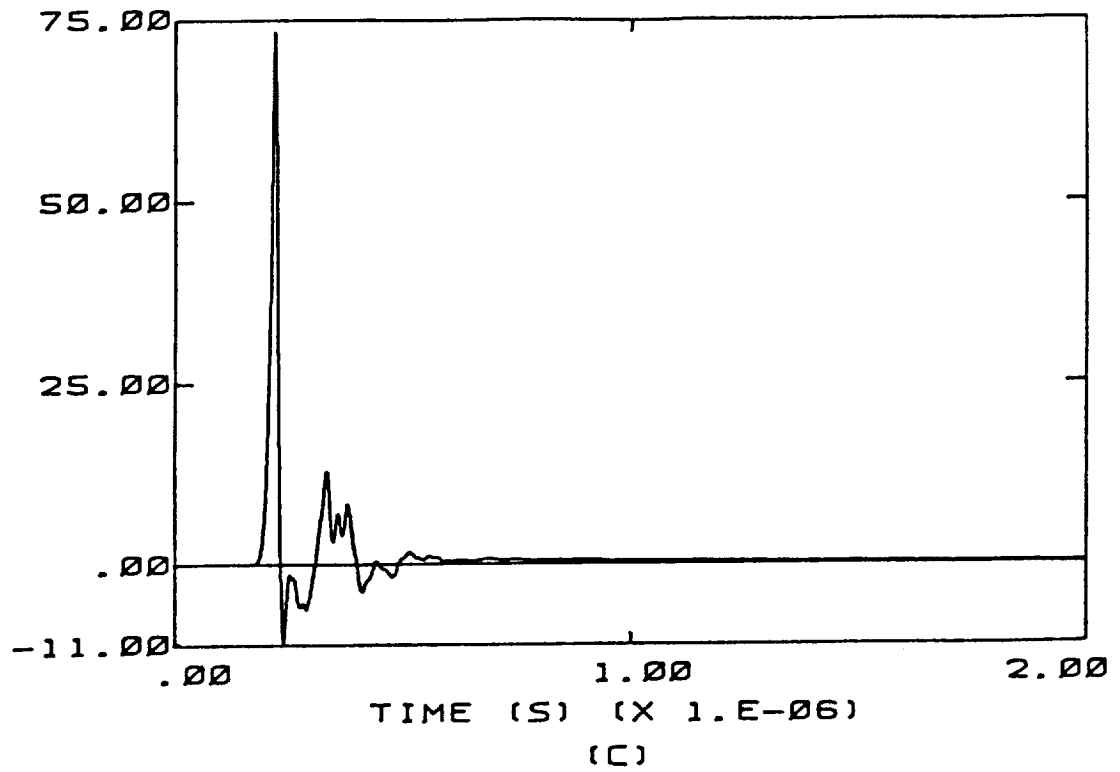


Figure 7.11 Calculated Sensor Responses for the Normal Size F106B Aircraft, Nose to Tail Orientation, Net Charge of -.895 Millicoulombs, Electric Field Magnitude of 130 kV/m.

D-DOT FORWARD (A/SQ. METER)



D-DOT LEFT WING (A/SQ. METER)

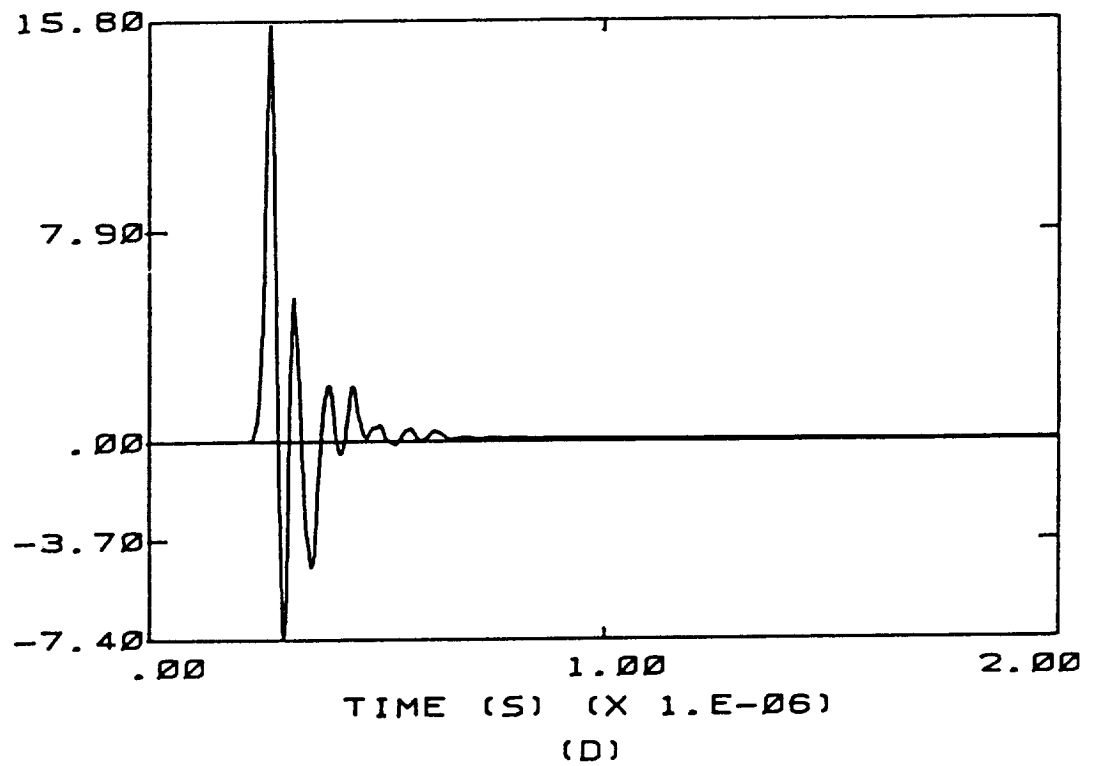
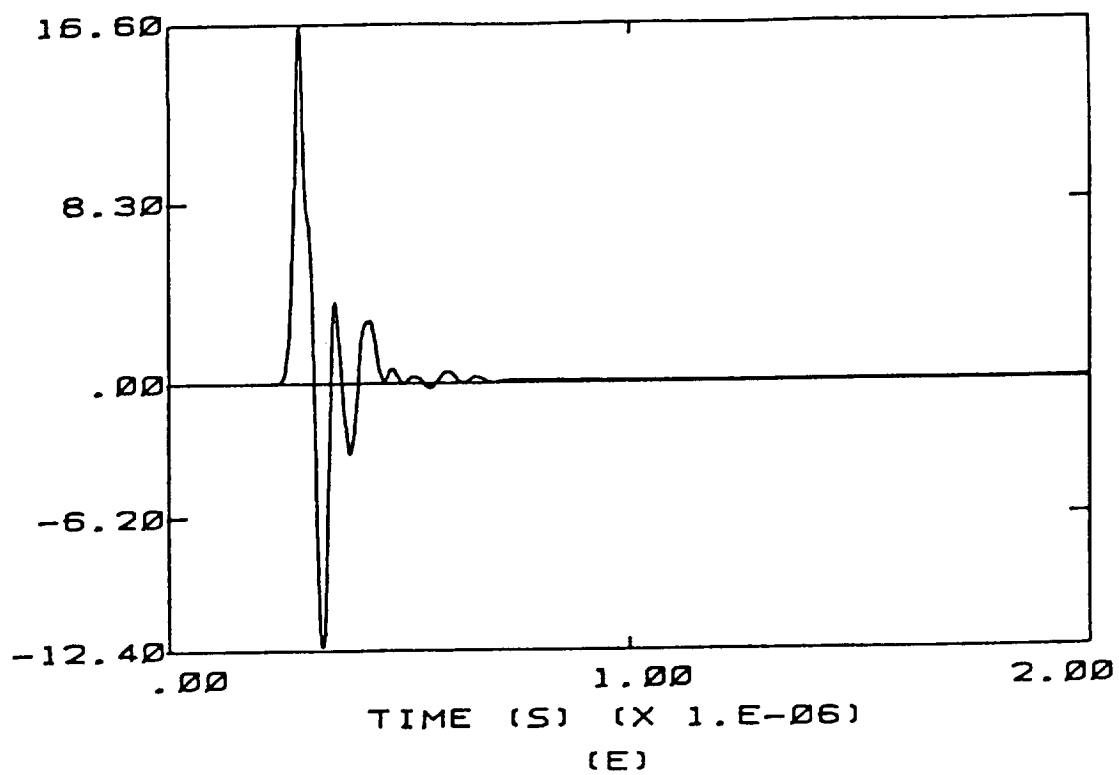


Figure 7.11 (continued)

D-DOT TAIL (A/50. METER)



I NOSE (A) (X 1.E+03)

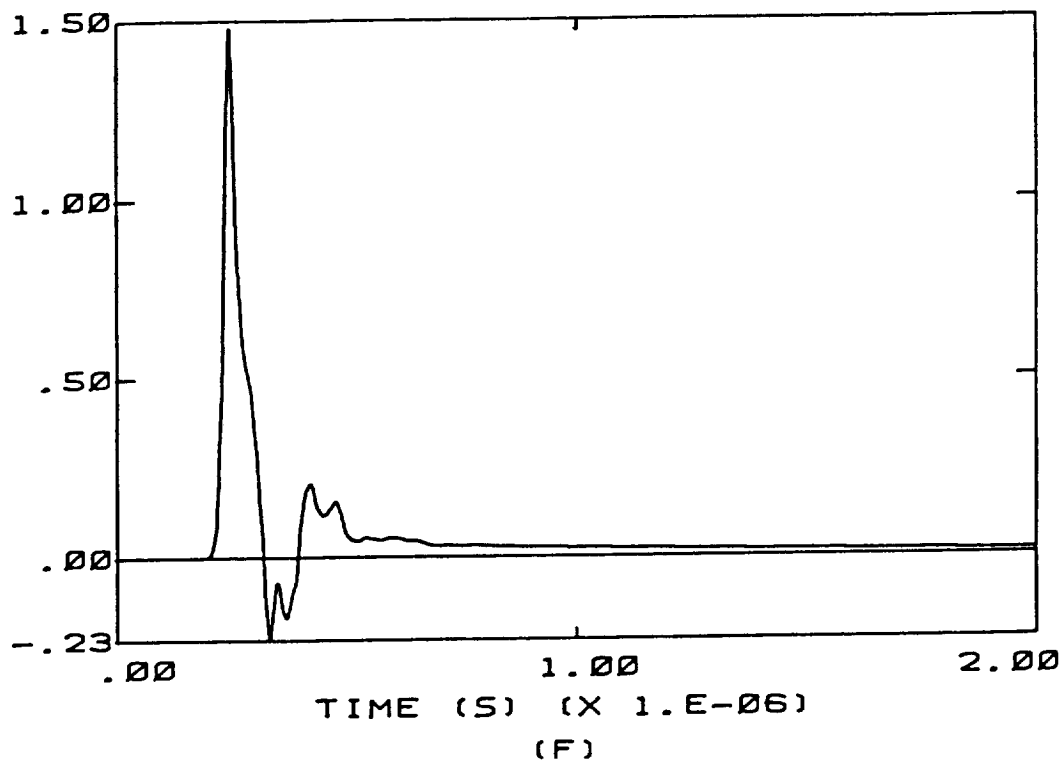


Figure 7.11 (continued)

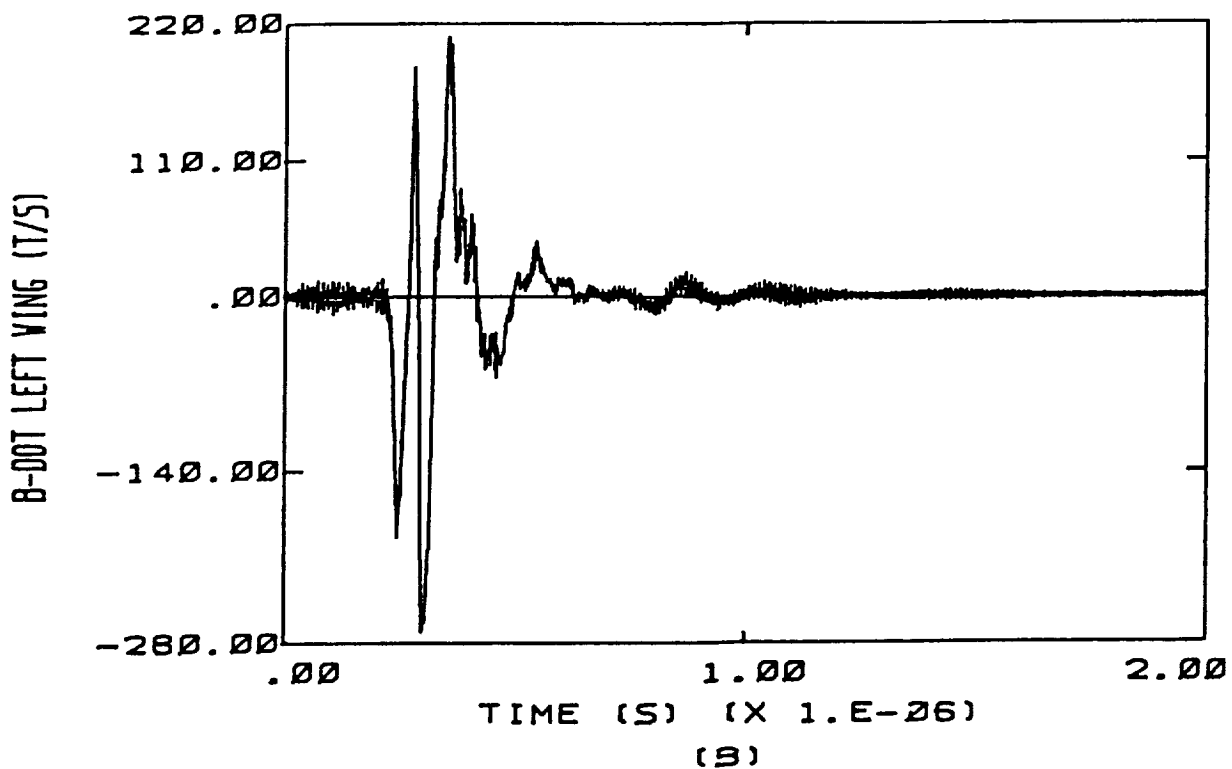
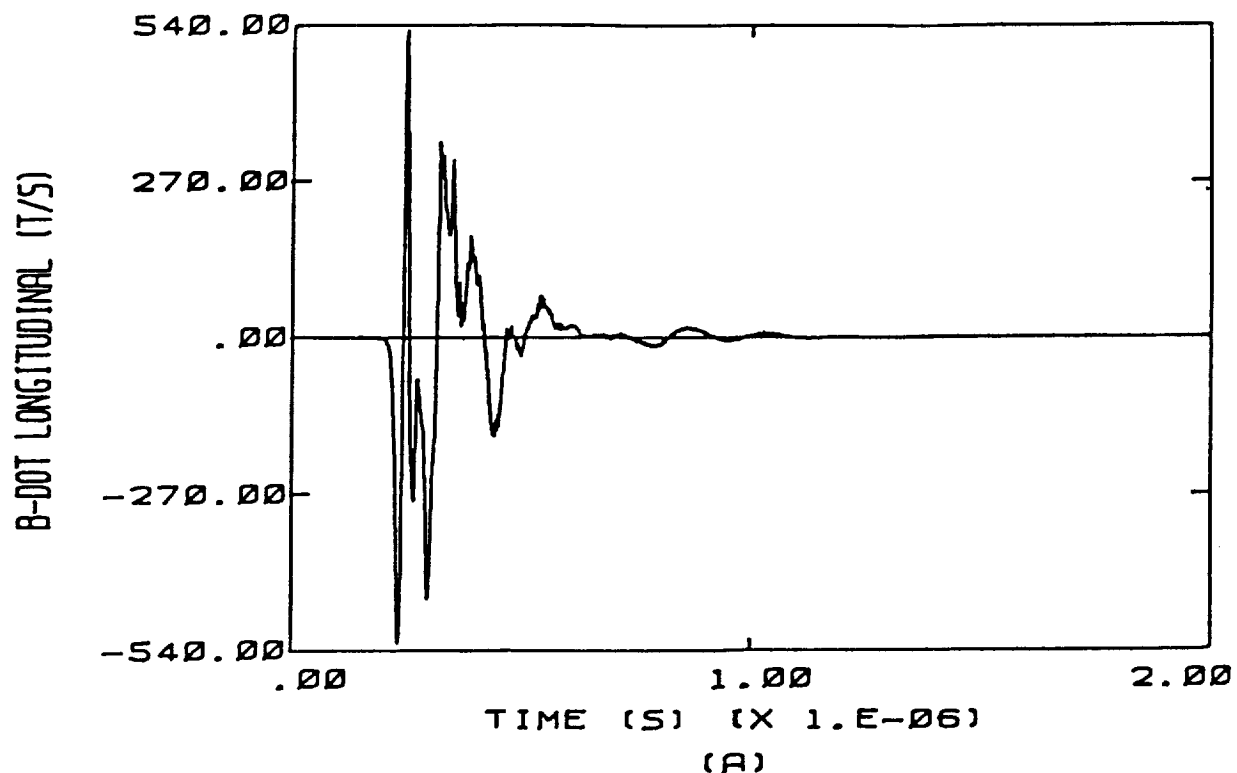
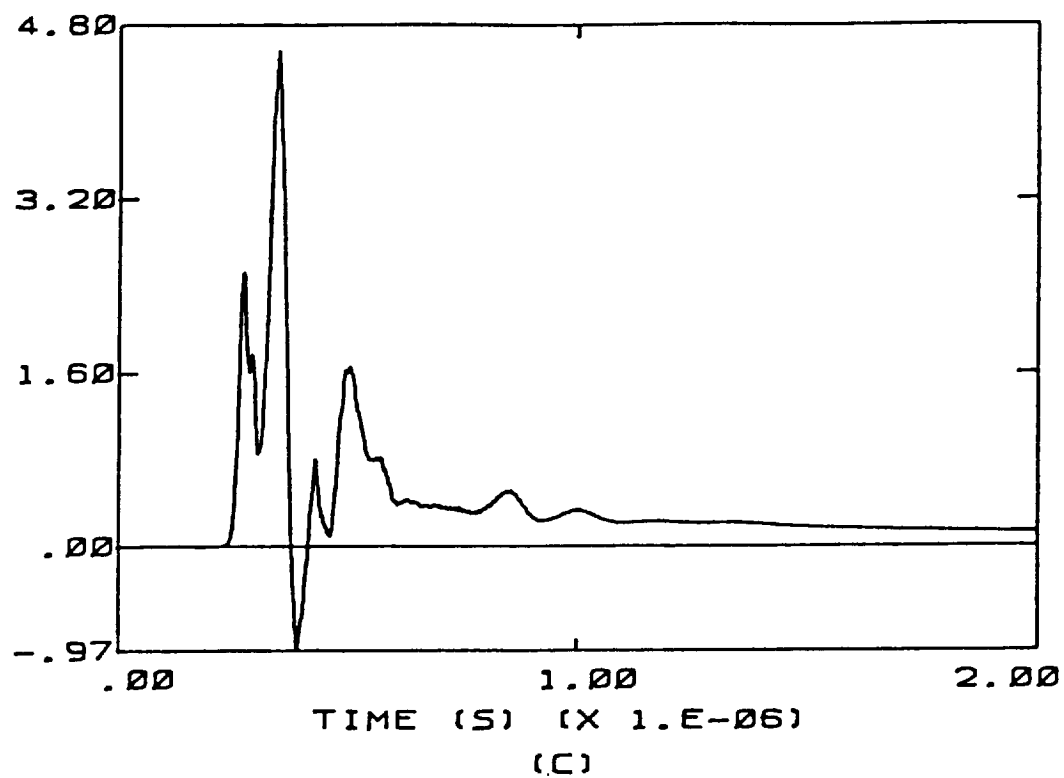


Figure 7.12 Calculated Sensor Responses for the Normal Size F106B Aircraft, Top to Bottom Orientation, Net Charge of  $-.895$  Millicoulombs, Electric Field Magnitude of  $310$  kV/m.

D-DOT FORWARD (A/SQ. METER)



D-DOT LEFT VING (A/SQ. METER)

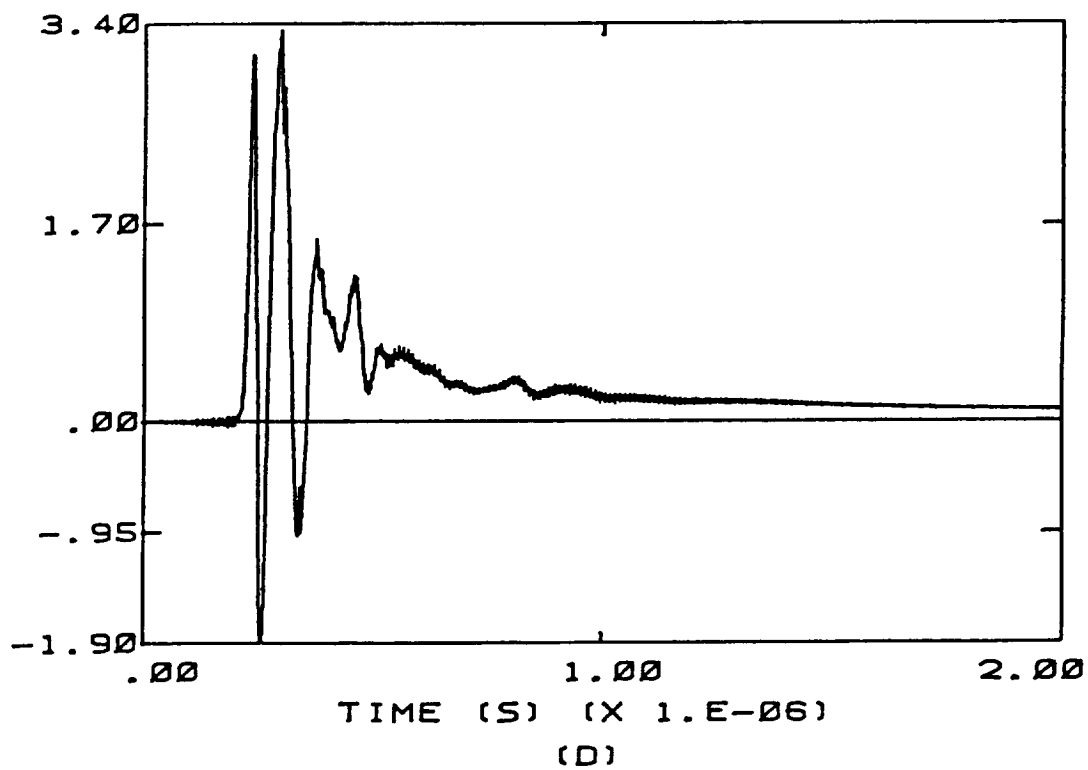


Figure 7.12 (continued)

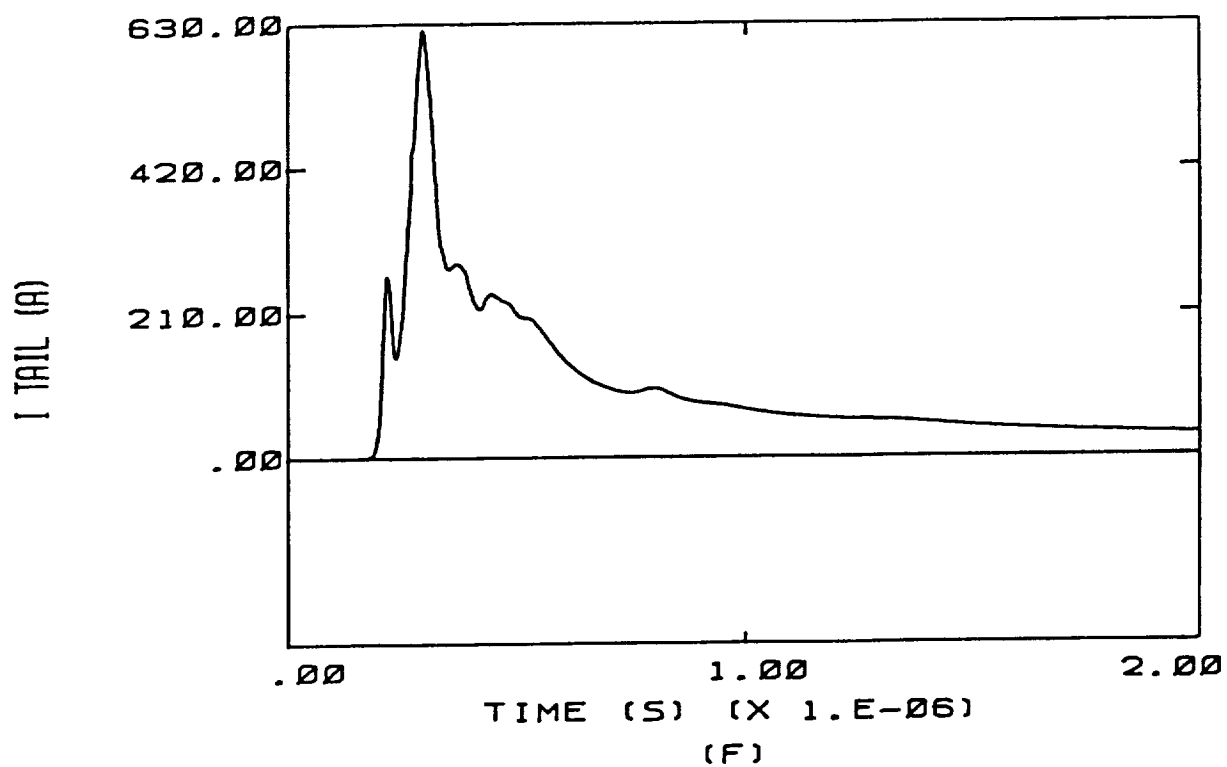
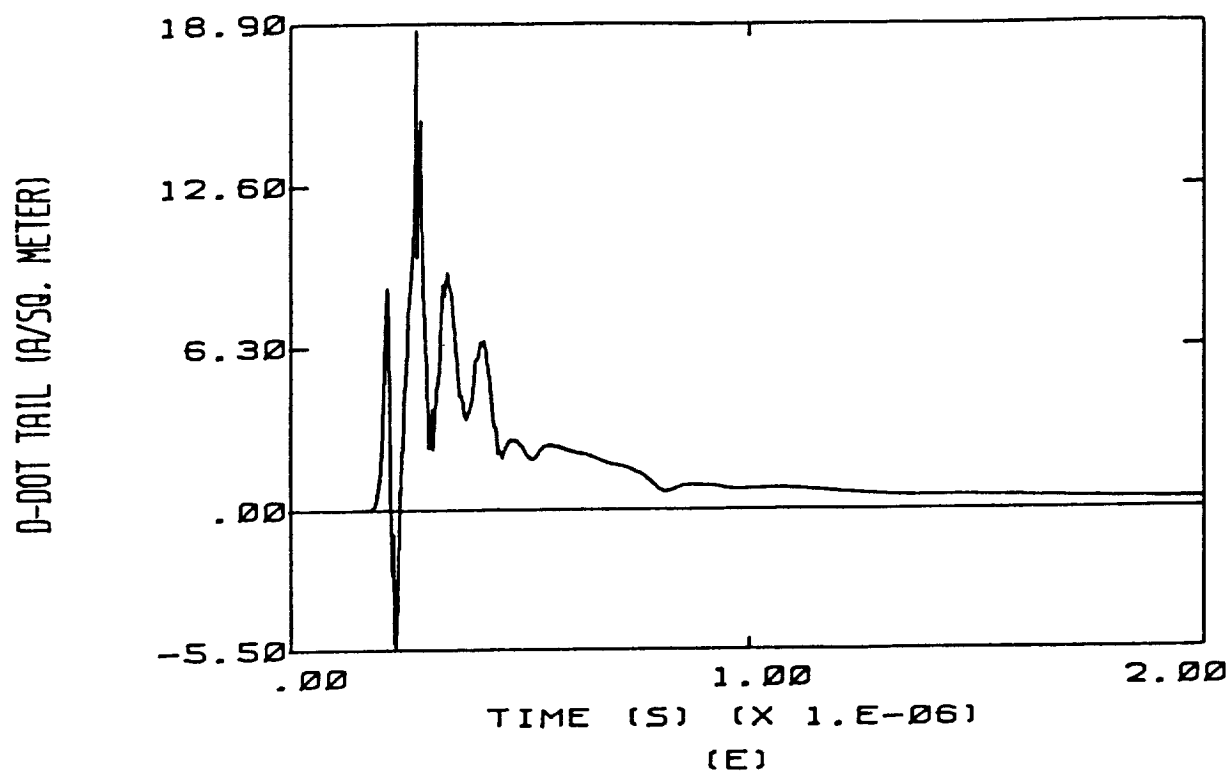


Figure 7.12 (continued)



**TABLE 7.2**  
**SUMMARY OF INITIAL PEAK RESPONSES FOR THE**  
**MULTI-AIRCRAFT STUDY**

**Nose-tail orientation,  $Q = -1/2 Q_m$**

<u>Aircraft</u>	<u>D-dot tail</u>	<u>D-dot LW</u>	<u>D-dot F</u>	<u>B-dot L</u>	<u>B-dot LW</u>	<u>I</u>
1/2 x F106B	8.5	7.4	30	1070	760	250
2 x F106B	7.4	7	34	1750	1250	2570
straight wing F106B	9	8.7	37	1750	1900	580
C-130	1.9	3.6	8	1700	-1900	1100
normal F106B	16.6	15.6	72	3700	2600	1500

**Top-bottom orientation,  $Q = -1/2 Q_m$**

<u>Aircraft</u>	<u>D-dot tail</u>	<u>D-dot LW</u>	<u>D-dot F</u>	<u>B-dot L</u>	<u>B-dot LW</u>	<u>I</u>
1.2 x F106B	4	.85	1.3	-100	-65	50
2 x F106B	4.5	1.7	1.3	-300	-100	780
straight wing F106B	4.7	.9	1.1	-320	165	180
C-130	5	3.8	3	-800	-400	1900
normal F106B	18.8	3	4.5	-530	-200	620

Note: I for the nose-tail orientation refers to current entering the nose.  
For the top-bottom orientation, it refers to current entering the tail.

Also, the F106B without the delta wing seems to show somewhat increased resonance behavior. The increase occurred because the filtering effect of the low Q delta wing was removed.

Second, it is of interest to consider the ambient field required for breakdown on each aircraft. This information can be used to roughly predict the response of each aircraft in a given ambient field. For example, if all of the models were given an equal net surface charge, and were placed in a nose to tail oriented field, there is a range of field magnitudes through which the C130 could fly uneventfully, while the F106B models would all experience triggered lightning events. Conversely, the C130 is more likely to trigger lightning if placed in a vertically oriented field. This indicates that the detailed geometry of any aircraft and its orientation with respect to the ambient field is important in avoiding environments which can cause triggered lightning.

The contents of Table 7.2 are interesting, in that they show some of the nonlinear aspects of the lightning-aircraft interaction. For example, note that the currents entering the nose for the nose-tail oriented field is ten times larger for the double size F106B than for the half size F106B. Because the two aircraft differ in size by a factor of four, linearly one would expect this current to also scale by that same factor. The nonlinear calculations show this to be untrue. In addition, the calculated peak  $\dot{D}$  values are very similar for the two aircraft, despite the big difference in current. This too is unexpected linearly, because the  $\dot{D}$  responses, and in particular  $\dot{D}$  forward, would linearly scale with the current and the inverse of the aircraft radius at the sensor location. The point to be noticed here is that in a general way, the aircraft responses do behave in the way that is expected linearly. That is, the peak responses increase as the peak current increases, and decrease as the aircraft size increases. However, the scaling factors that would apply linearly are not accurate when nonlinearities are included.

In summary, this chapter has examined the environment necessary to produce a triggered lightning strike on aircraft other than the standard size F106B. It has also examined the electromagnetic responses to be expected on those aircraft when involved in a triggered strike. The usefulness of this is that some knowledge is gained of the environments which are likely to cause lightning on non-fighter aircraft, such as large commercial jets and transports. Also, response comparisons allow one to more easily generalize the types of responses which would be expected on aircraft of similar

sizes and shapes. This is valuable in extending the lightning environment to general aircraft which have not been explicitly modeled.

## CHAPTER 8

### ENHANCED NONLINEAR AIR BREAKDOWN MODELING

To model the development of a lightning strike from first corona formation to a fully developed channel is a difficult task. The growth of the channel encompasses many regimes in plasma physics, from very weakly conducting air to fully ionized or even doubly ionized regions. It also includes many different physical and atomic processes, involving many different species of particles, which are active at different times in the channel development.

One way to describe mathematically the growth of the lightning channel, at least in its early stages, is with the use of fluid conservation equations. These equations, which include particle conservation, momentum conservation, and energy conservation for the most important species present in a lightning environment, were discussed extensively in a previous report [3]. The equations are shown again below for convenience:

Particle conservation:

$$\begin{aligned}
 \frac{\partial n_e}{\partial t} + \nabla \cdot (n_e \vec{v}_e) &= Q + g n_e - \alpha_e n_e - \beta n_e n_+ + k_e \\
 \frac{\partial n_+}{\partial t} + \nabla \cdot (n_+ \vec{v}_+) &= Q + g n_e - \beta n_e n_+ - \gamma n_+ n_- \\
 \frac{\partial n_-}{\partial t} + \nabla \cdot (n_- \vec{v}_-) &= \alpha_e n_e - \gamma n_+ n_-
 \end{aligned} \tag{8.1}$$

Momentum conservation:

$$\begin{aligned}
 n_\alpha \frac{\partial \vec{v}_\alpha}{\partial t} + n_\alpha (\vec{v}_\alpha \cdot \nabla) \vec{v}_\alpha &= \frac{n_\alpha q_\alpha}{m_\alpha} (\vec{E} + \frac{1}{c} \vec{v}_\alpha \times \vec{B}) - \frac{1}{m_\alpha} \nabla p_\alpha \\
 &\quad - n_\alpha \vec{v}_\alpha v_c
 \end{aligned} \tag{8.2}$$

Energy conservation:

$$\begin{aligned}
 \frac{\partial \epsilon_e}{\partial t} + (\vec{v}_e \cdot \nabla) \epsilon_e &= q_e n_e \vec{E} \cdot \vec{v}_e - \frac{m_e}{m_H} \nu_c (\epsilon_e - \epsilon_e^0) + g n_e \left( \frac{1}{2} m_e v_+^2 - \epsilon_{ion} \right) \\
 &\quad + \epsilon_Q - \alpha_e \epsilon_e - \beta n_+ \epsilon_e + H_e - k_{excitation} \\
 \frac{\partial \epsilon_H}{\partial t} + (\vec{v}_+ \cdot \nabla) \epsilon_H &= q_+ (n_+ + n_-) \vec{E} \cdot \vec{v}_+ + \frac{m_e}{m_H} \nu_c (\epsilon_e - \epsilon_e^0) \\
 &\quad - \frac{1}{2} g m_e n_e v_+^2 + k_{excitation} \cdot
 \end{aligned} \tag{8.3}$$

The previous report discussed each of the terms in these equations individually, so only a few added comments will be made here. The particle conservation equations include only positive and negative ions, along with electrons. Note that the neutral background gas is not considered. The implicit assumption is that the neutral gas remains unchanging throughout the event under consideration. This is a good approximation during the early stages of growth, but will need to be modified if the model is ever expected to handle the situation of a fully ionized gas. In fact, to fully model a lightning channel, it may be necessary to include a larger set of particle conservation equations, one equation for each ionic species, rather than lumping them all together into positive and negative ions.

In the momentum conservation equations, the  $\alpha$  subscript represents species type, so Equation 8.2 really corresponds to three equations. Also note that  $q_\alpha$  is a signed quantity which determines the direction of drift of each species. The collision frequency,  $\nu_c$ , represents collisions with neutral particles, and is at present a constant value. With increasing model sophistication, this quantity can be made temperature dependent. Also, for a strongly ionized plasma, this term should include coulomb collisions between charged particles as well as charged particle-neutral interactions.

In the energy conservation equations, only electrons and heavy particles are considered. By heavy particles are meant all air constituents other than electrons. Because the heavy particles all have similar masses (within an order of magnitude), energy transfer between them can take place efficiently, and they are all strongly coupled. That is, equipartition of energy can occur in a few collision times, which is of necessity less than the fluid equations' time scale. Hence the energy in the heavy particles is assumed to be equally divided among all the species, including neutrals.

The new features of the model which have been incorporated since the last report are a temperature dependent ionization rate and the presence of molecular vibrational modes. The temperature dependent ionization rate will be discussed first.

The new ionization rate,  $g$  in Equations 8.1, comes from the work of Fowler [6]. It includes the effects of electron temperature and electron drift into the ionization rate. The expressions Fowler derives for the ionization rate are given below.

For  $B > 0$ ,

$$g = .5g_0 \int_A^\infty (z^2 T_i) dz \int_B^\infty \frac{1}{u} \left\{ \exp[-(z-u)^2] - \exp[-(z+u)^2] \right\} \exp(-2Cu) du, \quad (8.4)$$

and for  $B < 0$ ,

$$g = .5g_0 \int_A^\infty (z^2 T_i) dz \int_{-|B|}^\infty \frac{1}{u} \left\{ \exp[-(z-u)^2] - \exp[-(z+u)^2] \right\} \exp(-2Cu) du.$$

Because a full discussion of all of the terms in Equations 8.4 is given in [8], only the highlights will be treated here.

The multiplicative factor  $g_0$  outside the integral is a function of several quantities. It depends on the neutral particle density, the ionization energy of the heavy particles ionized in an electron avalanche (in this case, mostly nitrogen), the electron temperature, the collision frequency, and the electric field. The lower limit of the first integral,  $A$ , may be written:

$$A = \left( \frac{mV_i^2}{2kT} \right)^{\frac{1}{2}} \quad (8.5)$$

Here,  $mV_i^2/2$  is the kinetic energy necessary to cause an ionization,  $k$  is Boltzmann's constant, and  $T$  is the electron temperature. Hence as the electron temperature increases,  $A$  decreases, and the limits of the first integral encompass a larger integration path, in this case leading to a larger avalanche ionization rate. The limit of the second integral,  $B$ , can be written,

$$B = \left( \frac{m}{2kT} \right)^{\frac{1}{2}} V \quad (8.6)$$

Here,  $m$  is the electron mass and  $V$  is the electron drift velocity. As  $T$  increases,  $B$  decreases, and again the integration includes a larger range leading to an increased avalanche rate. Note that  $V$  is a signed quantity, so  $B$  can be positive or negative.

More temperature dependence is contained in  $\tau$ ; the cross section for ionization by electron collisions. This parameter is represented in the model by a numerical fit to experimental data.

The last factor to contain temperature dependence is the quantity  $C$  in the exponential of the second integral. It can be written,

$$C = \frac{1}{2} \left( \frac{2kT}{m} \right)^{\frac{1}{2}} \frac{K}{a} \quad (8.7)$$

In this equation,  $K$  is the collision frequency, and  $a$  is the acceleration produced on an electron in the electric field.

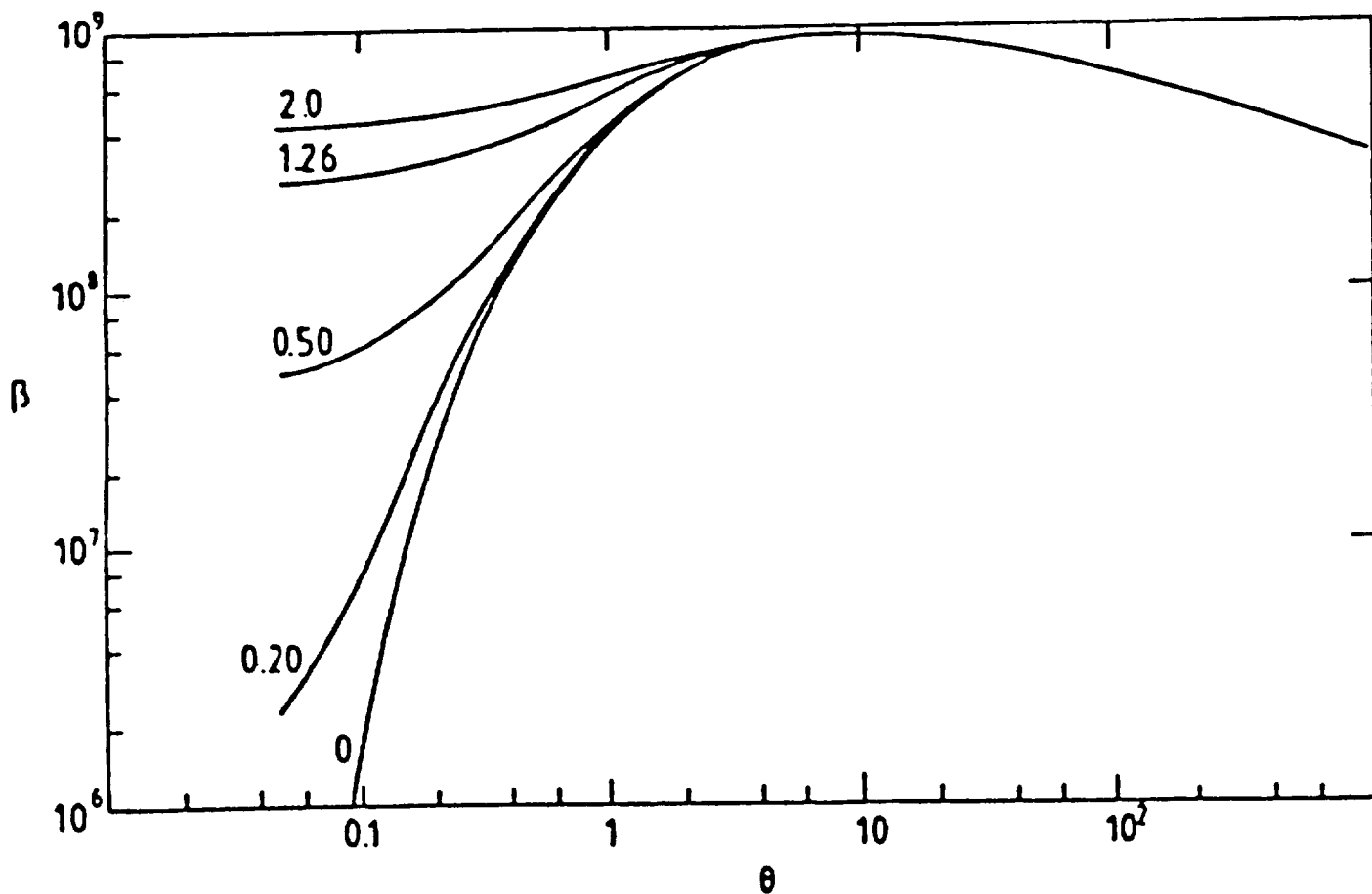
The forms for the ionization rate given by Equations 8.4 are inconvenient for use in a finite difference code. Evaluation of the integrals must be done numerically and is quite time-consuming, particularly when they must be evaluated at every spatial point at every time step. The problem was circumvented by generating a three

dimensional lookup table from which interpolations were done in the model. The variable parameters were electric field, electron drift velocity, and electron temperature. The lookup table was generated by choosing nitrogen as the constituent of air which is ionized in an electron avalanche, and then evaluating Equations 8.4 for ranges of the variable parameters which include all reasonable physical values. The interpolation is done exponentially because of the rapid variation of  $g$  in some areas of the table.

A graph of the ionization frequency as a function of electron temperature and electric field is shown in Figure 8.1. The figure has the electron drift velocity fixed at zero. Although the values in that figure are appropriate for a helium gas, the behavior is similar for nitrogen. Note that the ionization rate rises rapidly with increasing field, and also with increasing electron temperature to a certain point. Also notice that there appears to be a limiting value for the avalanche rate, such that increasing the temperature or the electric field do not change  $g$  very much. For increasing temperature,  $g$  even falls after a certain point. Also notice that the avalanche rate is large even for a low electric field if the electron temperature is large.

The second enhancement to the nonlinear model is in the addition of molecular vibrational energy states. These act as an efficient conduit for energy transfer between electrons and heavy particles. Elementary physics shows that in a collision between a light particle (e.g., an electron) and a heavy particle (e.g., a neutral gas molecule), very little energy can be transferred from the light to the heavy particle. This can lead to a situation in which the electrons in a gas can get very hot while the neutral gas temperature stays close to ambient levels. This is physically real to a point, but it is an observational fact that the electrons in a lightning strike have temperatures of the order of 20,000°K and the background gas temperature is much above the ambient temperature. Elastic collisions alone are inadequate to produce a sufficient transfer of energy. The excitation of molecular vibrational energy states provides a means of transfer. At approximately 20,000°K, an individual electron has enough energy to excite a vibrational energy state, and the cross section for the interaction is very high. Hence many molecules are excited, and the electrons are constrained from going higher than the limiting temperature. The molecular vibrational states subsequently decay by releasing their energy into kinetic energy of the neutral gas. Depending on the lifetimes of the vibrational states, kinetic energy is quite rapidly transferred from the electron gas to the neutral gas.





**Figure 8.1** Ionization Rate as a Function of Scaled Electron Temperature  $\sigma$  and Scaled Electric Field  $\eta$ . Electron Drift Velocity Is Held At Zero (From Fowler [6]). Note that Fowler's  $\beta$  Is Equivalent To  $g$  In The Text.

$$\sigma = .5kT/e\phi$$

$$\eta = eE/mKV$$

$$e\phi = \text{ionization energy}$$

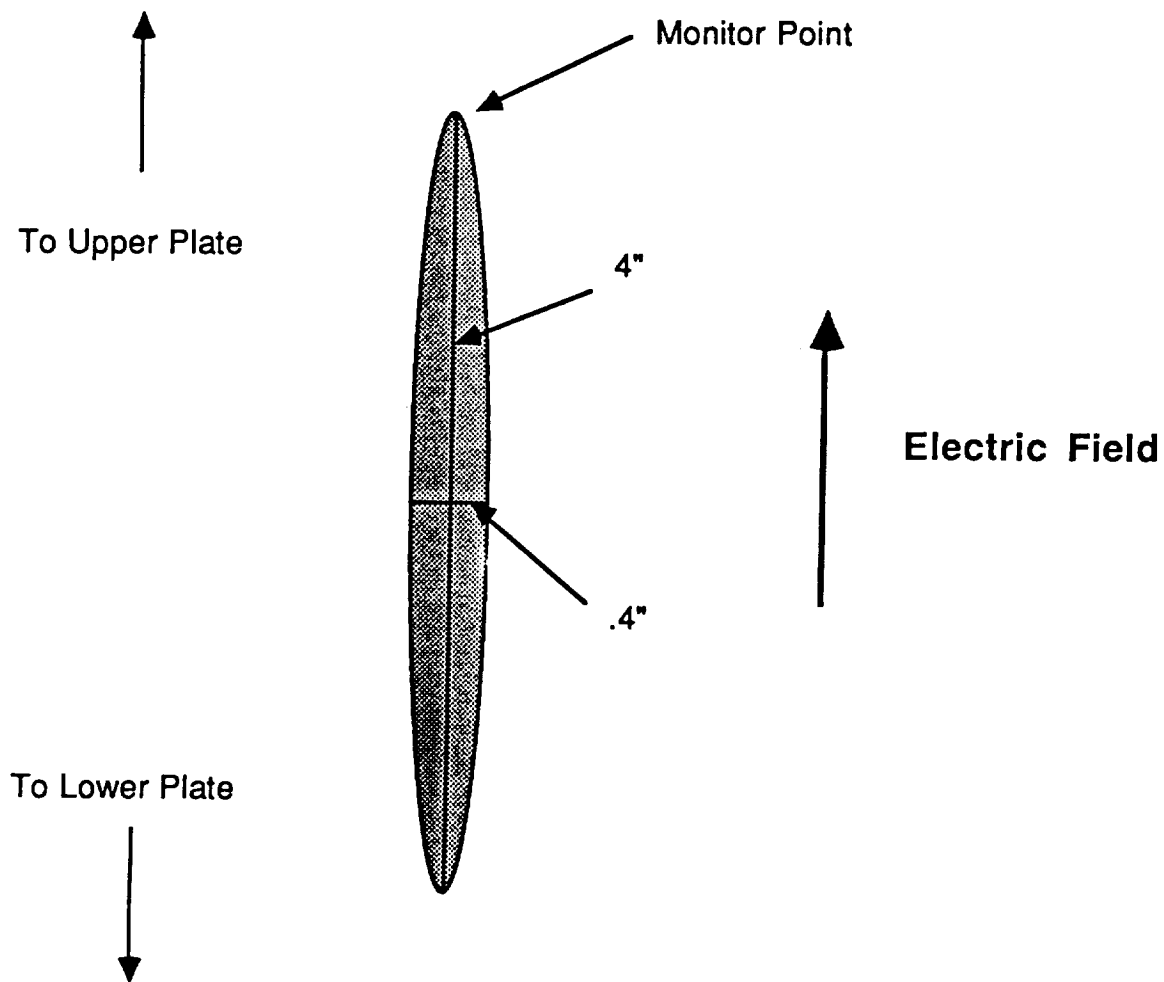
$$K = \text{collision frequency}$$

$$V = \sqrt{2e\phi/m}$$

Implementation of the vibrational states in the nonlinear finite difference model is quite heuristic. The electron fluid in a given cell is not allowed to rise above the 20,000°K limiting temperature. If the temperature does go higher, all of the excess energy is immediately transferred to the heavy particles. This is the meaning of the  $k_{\text{excitation}}$  term in Equations 8.3.  $k_{\text{excitation}}$  is the excess energy density in the electron fluid in a finite difference cell for one time step. It is subtracted from the electron energy conservation equation and immediately added to the heavy particle energy conservation equation. This implicitly assumes that the lifetime of the vibrational states is less than the time step in the finite difference code. For cases in which this is not true, an energy conservation equation for the vibrational states may be added to the model.

The first application of the new model has been to an experiment performed by Dr. Trost at Texas Tech [unpublished data]. His experimental setup is diagrammed roughly in Figure 8.2. He placed a conducting prolate ellipsoid between two plates maintained at a constant potential difference. This produced a uniform electric field in which the ellipsoid was immersed, with its long axis along the direction of the field. The potential difference between the two plates was increased until the air broke down at the ends of the ellipsoid, and a spark was seen to cross the gap between the ellipsoid and the plates. Sensors included a D-dot recorder mounted on the lower plate and an imaging camera which recorded the formation of the sparks at the ends of the ellipsoid.

Although Dr. Trost's experiment was much too large to model in its entirety, the central problem of the ellipsoid in a uniform field has been modeled in two dimensions. The model ellipsoid was four inches long and four-tenths of an inch in diameter. In order to model adequately the ends of the ellipsoid, it was necessary to use a grid size of one-tenth inch in the long axis direction and one-fiftieth inch in the radial direction. This spatial gridding required a time step of one picosecond. The magnitude of the ambient electric field was increased until air breakdown occurred at the ends of the ellipsoid. The model was run for sea level air density and dry air. Air breakdown was seen for an ambient field of 300 kV/m. The model was run to ten nanoseconds, which constitutes ten thousand time steps.



**Figure 8.2 Diagram of the Experimental Configuration Modeled by the Enhanced Nonlinear Air Chemistry Model. The Plates Are Held at Constant Potential to Produce the Electric Field.**

Time domain waveforms of pertinent quantities at the positively charged end of the ellipsoid are shown in Figures 8.3 to 8.8. The axial electric field behavior at the ellipsoid tip is shown in Figure 8.3. The electric field drops very rapidly to a stable value at about one-third of its original value. The same is true of the radial electric field near the tip as shown in Figure 8.4, except that the later time value is slowly drifting. The electron density shown in Figure 8.5 rises rapidly and then decays slowly, presumably approaching asymptotically some quasi-steady state level. Figure 8.6 shows the positive ion density which rises rapidly along with the electron density, and then falls very slowly as recombinations occur. Recombination is a comparatively slow process, so the positive ion density can remain large for a long time. The negative ion density is shown in Figure 8.7. It lags behind the positive ion density because the major source for negative ions is attachment of electrons to neutrals, so the negative ions appear as the electron density decays. Figure 8.8 is the electron energy density, which rises and falls with the number density of the electrons. The temperature of the electron gas has not been plotted but can be approximately derived from the ratio of the electron energy density to the electron number density. When this is done, the temperature is seen to rise very rapidly to the limiting temperature of 20,000°K and remain at that value. Also not plotted is the heavy particle energy density, which was unchanged over the ten nanoseconds that the model was run.

The problem of the ellipsoid in a uniform field was also modeled in two dimensions using an older nonlinear model which did not include momentum and energy conservation equations. This model has been documented in an earlier report [3]. The model used an experimentally derived mobility in place of the momentum conservation equations and ignored energy conservation entirely. This older model predicted no air breakdown at all for the ten nanoseconds that the model was run. However, the electron density was rising at the end of the run, and breakdown would have occurred slowly at some later time. The difference between the two models is therefore substantial. Comparison to experimental situations is still necessary to determine whether the newer model is substantially more accurate.

The biggest flaw in the enhanced nonlinear model is its inefficiency. At four hundred time steps per hour of computer time, it can not realistically be used to model time scales of the order of microseconds. However, the model has not yet been optimized with respect to the physical processes that it contains. That is, many

(Text continued on page 117)

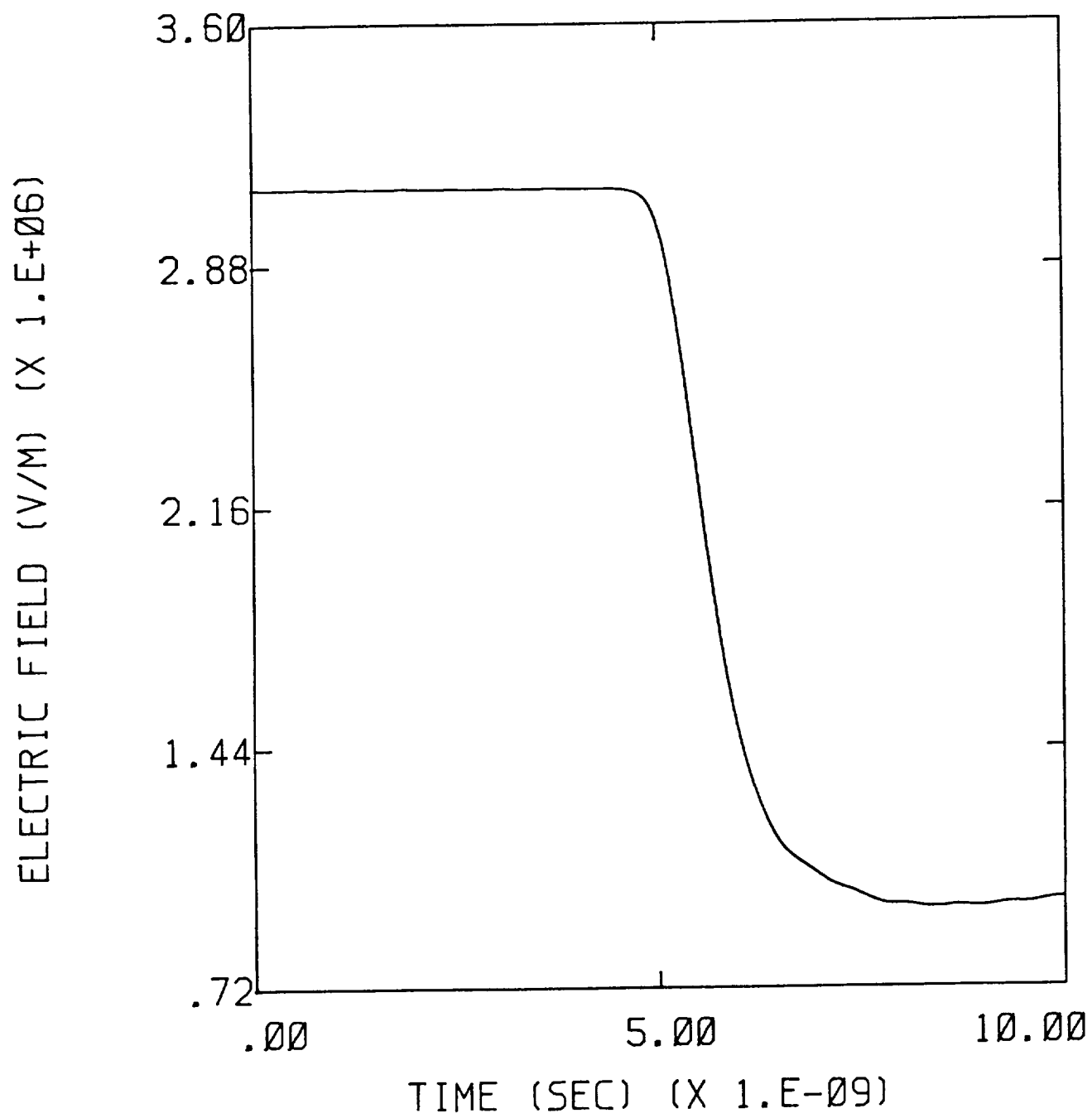


Figure 8.3 Axial Electric Field at the Tip of the Ellipsoid

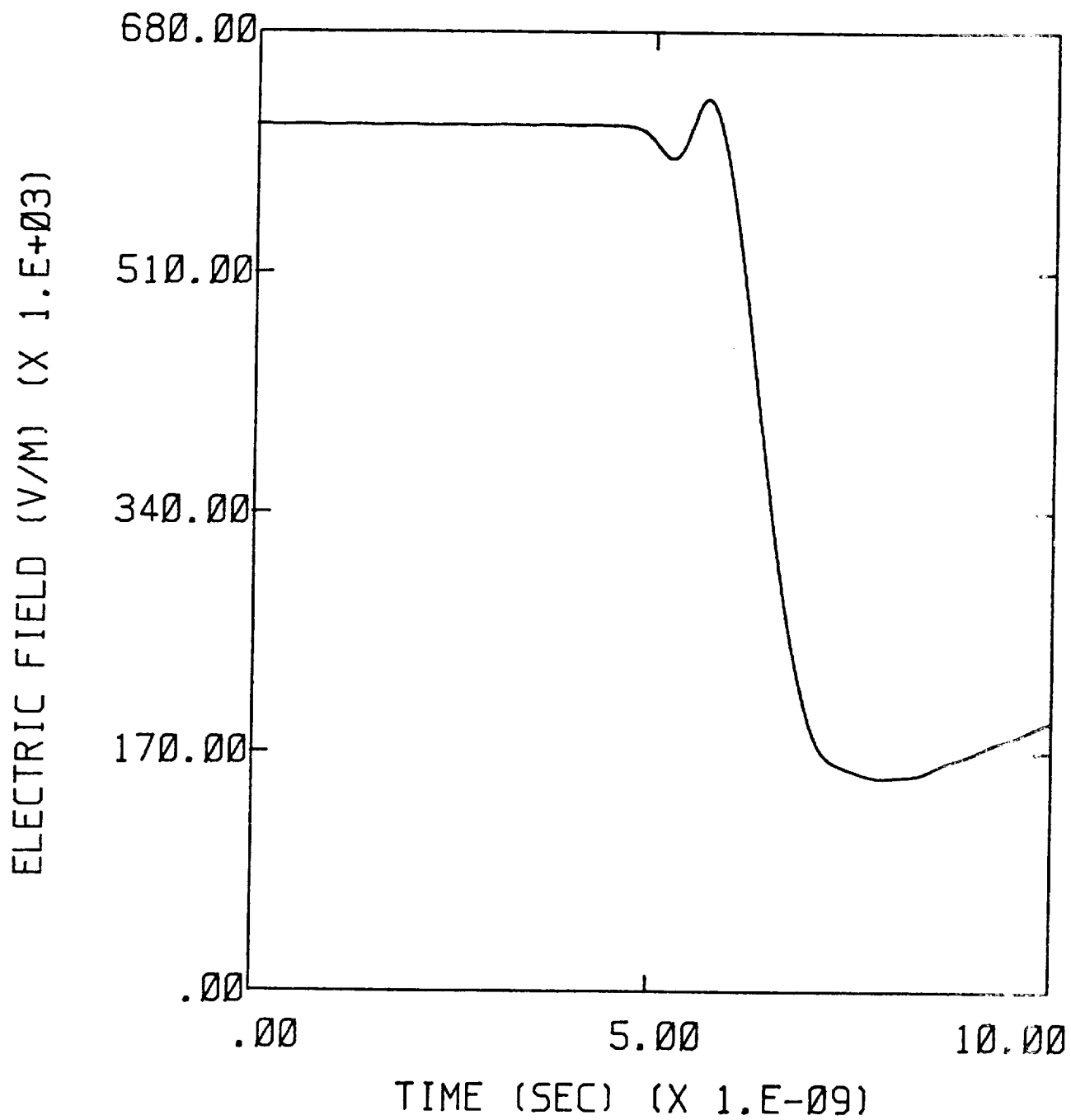


Figure 8.4 Radial Electric Field Near the Tip of the Ellipsoid

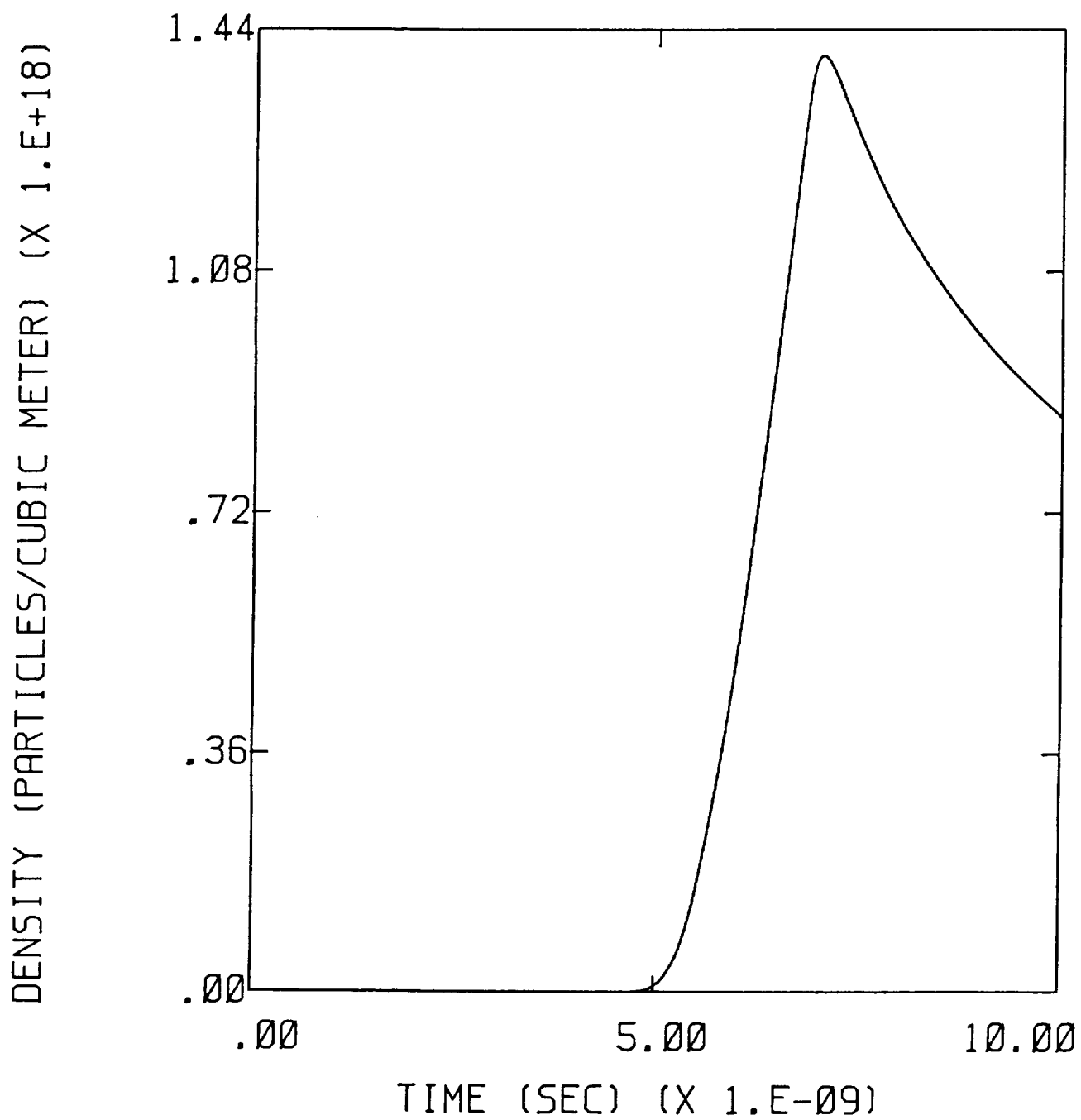


Figure 8.5 Electron Density at the Tip of the Ellipsoid

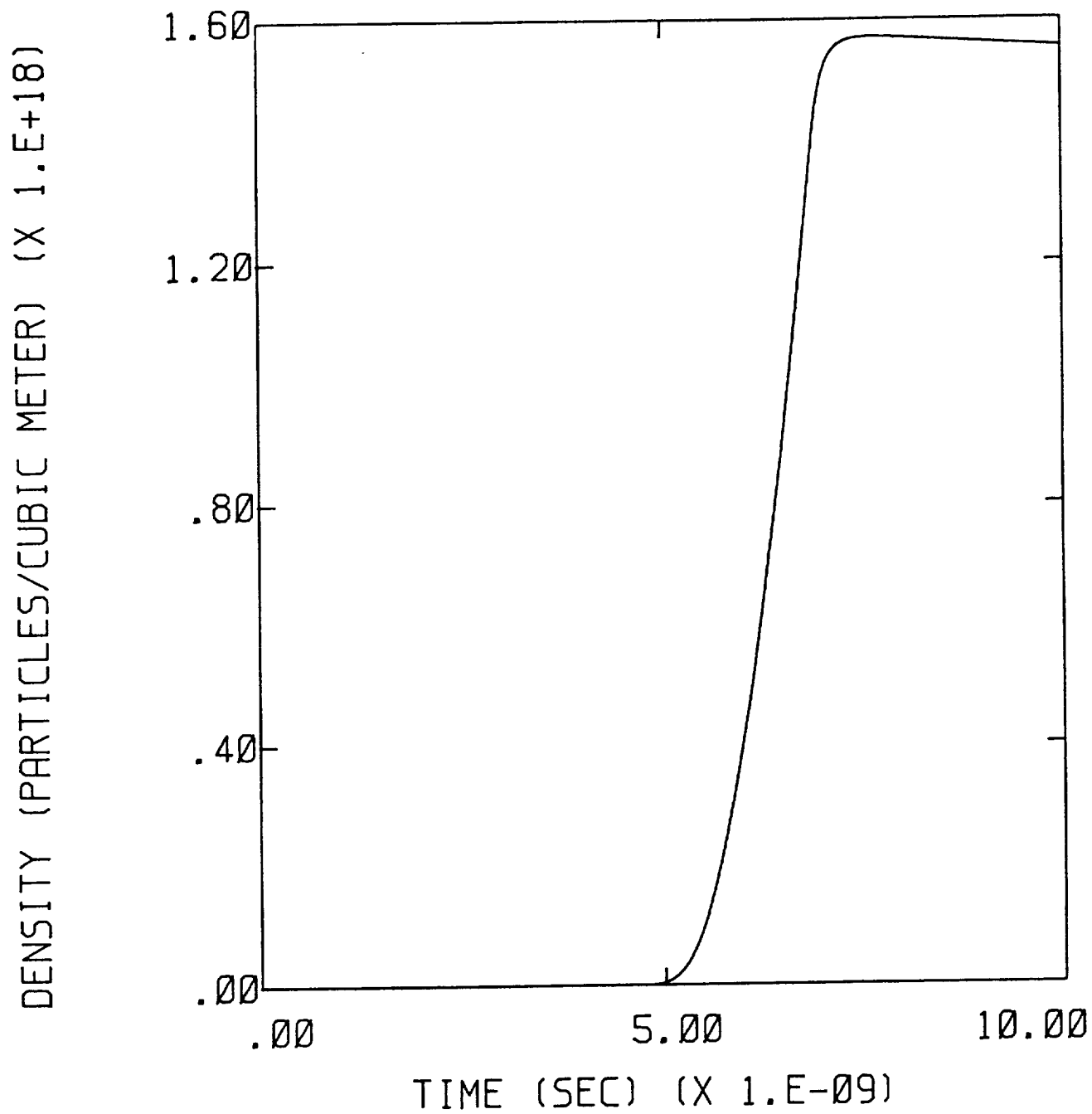


Figure 8.6 Positive Ion Density at the Tip of the Ellipsoid



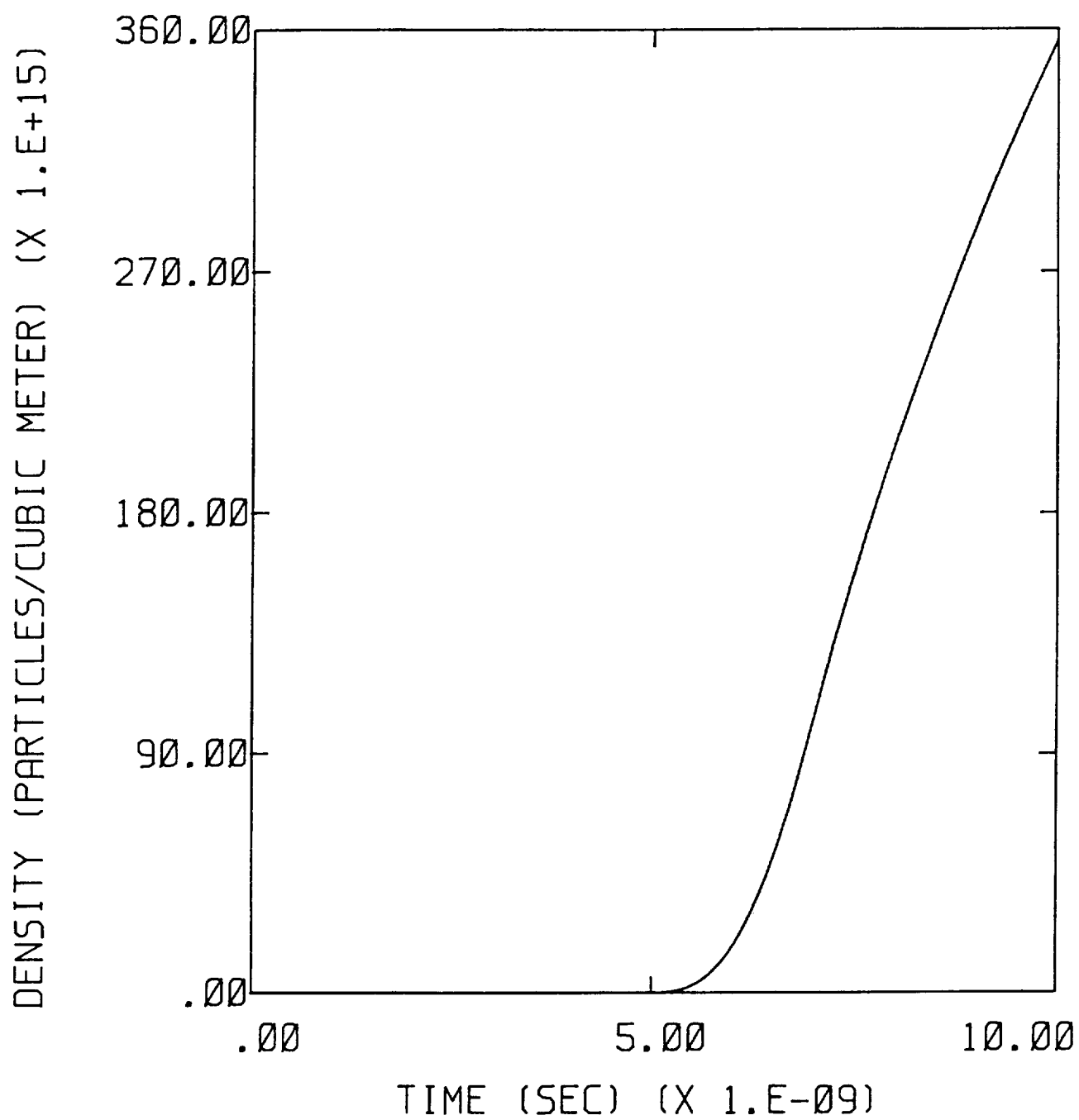


Figure 8.7 Negative Ion Density at the Tip of the Ellipsoid

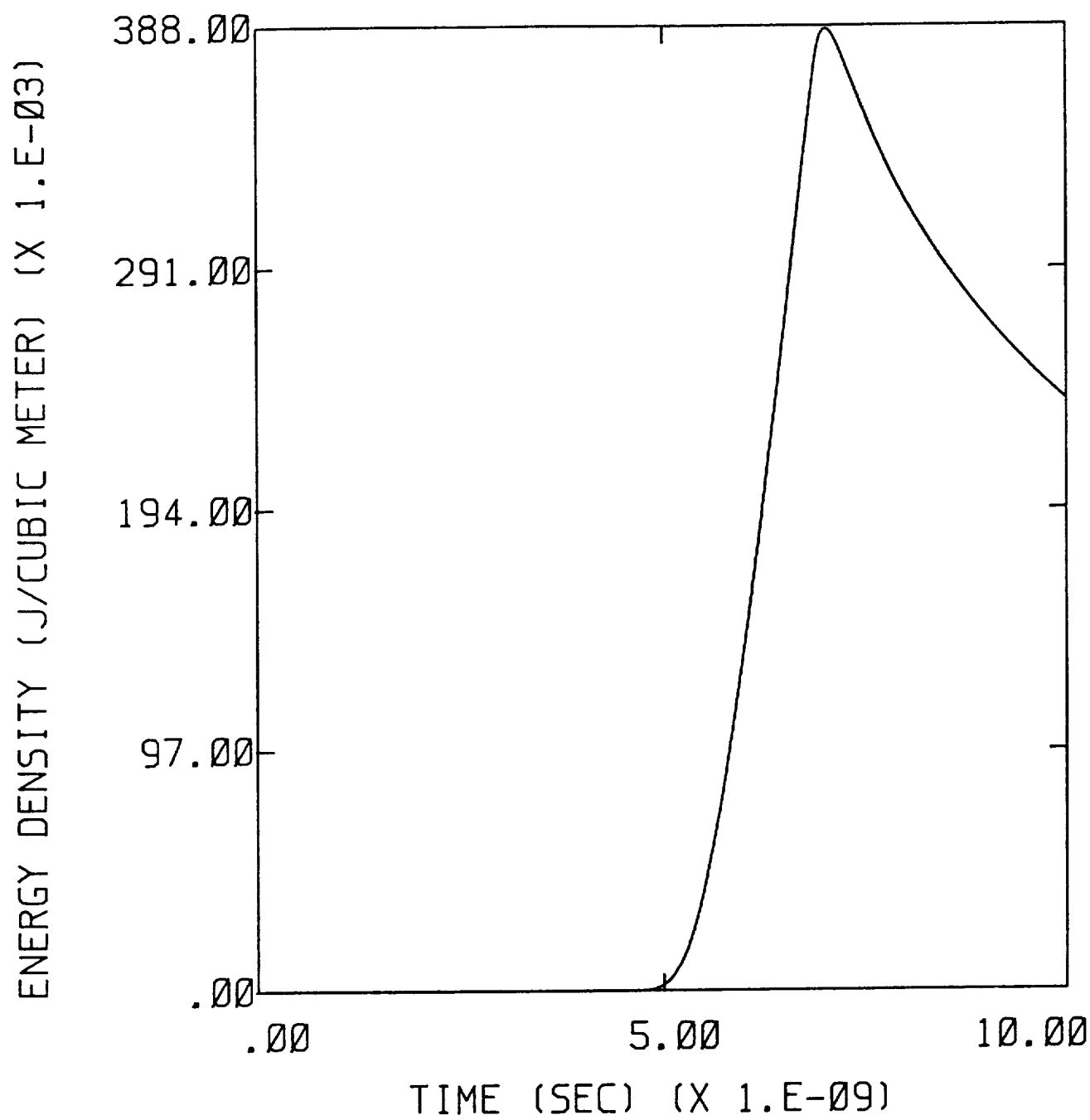


Figure 8.8 Electron Energy Density at the Tip of the Ellipsoid

processes have been added to the model without regard for whether they are effectively changing the results. It is possible that some of this physics could be dropped from the model without serious loss of accuracy, but with a great savings in computer time. This subject is expected to be addressed in future work.

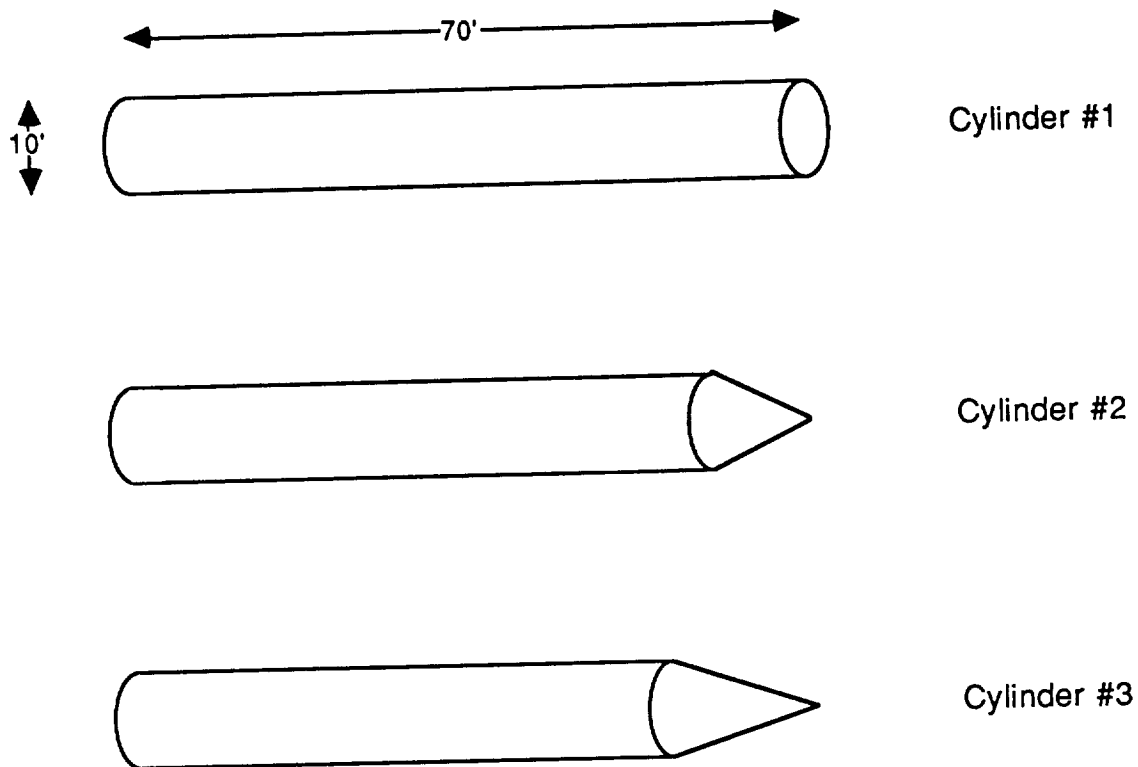
## **CHAPTER 9**

### **SUBGRID DEVELOPMENT AND APPLICATION**

#### **9.1 The Effect of Finite Difference Grid Resolution on Field Enhancements**

Any cartesian finite difference model of Maxwell's equations has a limit on its resolution equal to the cell size used. This means that small features of the object being modeled cannot be included in the model. Unfortunately, it is often around such small features (sharp points, nose booms, etc.) that interesting electromagnetic field behavior is seen. In particular, local field enhancements are usually largest near these areas. The effects of these small features, although significant locally, normally do not extend very far from the feature. A reasonable rule of thumb is that the perturbing effect on an electromagnetic field of a conducting object will extend approximately a single dimension of the object in any direction. If this is true, then field perturbations from small features unresolved in a particular finite difference model should extend one or at most two cells from the object. Restating this in different words, the finite difference solution should be accurate everywhere except in the cell where the small feature exists, and possibly one more cell away from it.

To investigate the effect of lack of resolution in a finite difference model, a numerical experiment was undertaken. Three different two dimensional cylinders were gridded. These are shown in Figure 9.1. Two dimensional cylinders were used for efficiency, and because the nose of the F106 can be represented quite accurately in two dimensions. For the field directions used in this study, the third dimension, the azimuthal direction, is superfluous. The dimensions of the cylinders are shown in the figure, and were chosen to roughly represent the dimensions of an F106B fuselage. The first cylinder has a blunt end, illustrating the situation in a finite difference model with very coarse resolution. The other two cylinders have tapered ends, representing the situation in models with better resolution. The tip angles are 53 degrees for cylinder #2 and 37 degrees for cylinder #3. Each of the cylinders was placed in an ambient electric field of one volt per meter oriented along the cylinder axis, and the solution was allowed to settle to its static value. The field distributions around the tapered ends of the cylinders were then compared. The largest difference between the solutions was, as expected, at the tip of the cylinders. The calculated fields at that point are shown below:



**Figure 9.1 Three Cylinder Configurations Used in the Finite Difference Numerical Experiment**

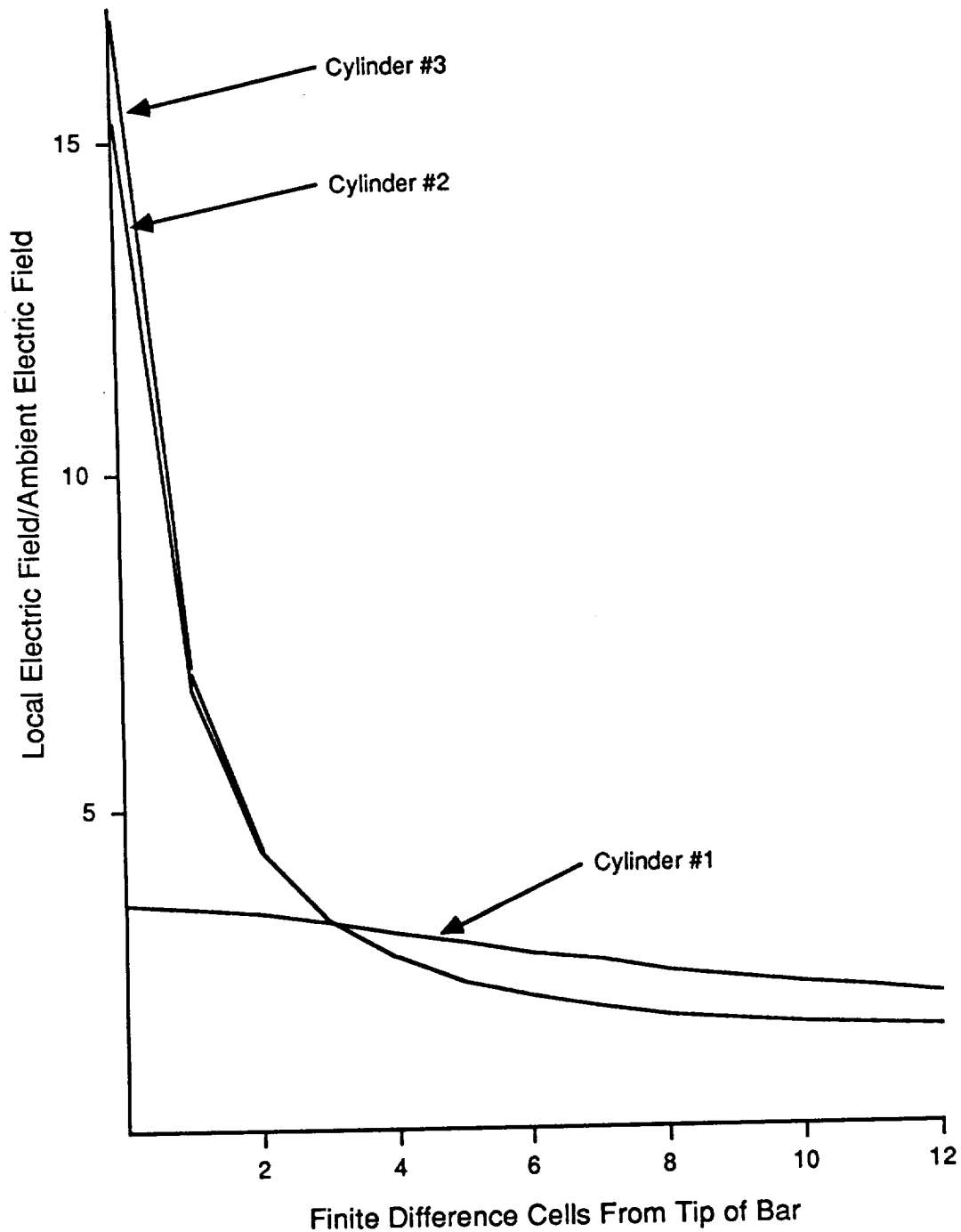
Cylinder #1:  $E_{\text{tip}} = 3.56 \text{ V/m}$   
Cylinder #2:  $E_{\text{tip}} = 15.35 \text{ V/m}$   
Cylinder #3:  $E_{\text{tip}} = 16.97 \text{ V/m}$ .

This shows a 477% change in the local field from the bluntest cylinder to the most pointed. It is indicative of the error in a finite difference model when the local field in the vicinity of a nonresolvable small feature is calculated.

The numerical experiment also calculated the manner in which the electric field varied as one moved away from the tip of the cylinders along their axes. This allows one to determine how far from the tip one must move to lose the effect of the tapering in the field distribution. The field distribution along the axes of the cylinders is shown in Figure 9.2. Note from the figure that the enhancement effect of the tapering extends only three cells from the tip of cylinders #2 and #3. From that point outward, the tapered cylinders show less enhancement than the blunt cylinder. This occurs because the blunt cylinder occupies more volume than the tapered cylinders and therefore alters the ambient field slightly more at a distance of several cells.

To apply the lessons learned here to a concrete example, consider the finite difference model of the F106B. The  $1/2\text{m} \times 1\text{m} \times 1/2\text{m}$  cell size used in that model does not allow direct gridding of the nose boom, where strongly enhanced local fields are expected. The numerical experiment reported in this chapter indicates that the finite difference model's fields at the tip of the nose boom may be incorrect by as much as a factor of ten. However, the high field region is very small, and the model accurately predicts the field distribution at most a cell or two away from the nose. The implication of this for nonlinear modeling is that predicted field levels for triggering lightning by the F106B are probably too high, especially for ambient fields oriented along the fuselage. However, because the fields away from sharp points are accurately calculated, the nonlinear development of a lightning event should be correctly modeled.

It is even possible that in the case of triggered lightning, it is not necessary to model the nose boom of the F106B. That depends on the answer to the question of how a full-fledged lightning strike is initiated. That is, is it possible to begin a channel from a small enhanced field region a few centimeters in radius, or is it necessary to



**Figure 9.2 Field Variation Along the Axis Away From the Tip for Each of the Cylinders Shown in Figure 9.1**

have a larger volume of enhanced fields to actually get the channel started? It is clear that corona can exist on the scale of centimeters, but it is not yet clear that a volume of that size can initiate a lightning event. It is entirely possible that more energy must be available than exists in a tiny volume surrounding a sharp point on the F106B. This question will be investigated in more detail in future work, in which the conditions required for initiation of a lightning strike will be studied. At present, it is unknown whether the resolution of the standard finite difference model of the F106B is adequate to model the initiation of lightning.

## **9.2 Subgrid Application**

To model the fine details of aircraft in a finite difference code, two techniques are possible. The first and most straightforward is to use a spatial grid which is fine enough to resolve the smallest detail throughout the problem space. This results in very large computer programs which are wasteful of resources, because areas where fine resolution is not needed are nevertheless gridded in great detail. The second method, which avoids this difficulty, is to embed within a coarse resolution model a fine resolution volume around the small details of the aircraft. The techniques for doing this have been reported previously [3]. In this chapter are presented examples of the applications of two different subgrids to the end of a conducting bar and the first application of the subgrid model to the F106B.

The biggest obstacle which was found in the development of a subgrid model was a late time numerical instability. This instability, which became evident after approximately two thousand time steps, would cause the numerical solution to diverge exponentially from the correct solution. In addition, the instability was worse for larger expansion factors in the subgrid. That is, the finer the resolution in the subgrid compared to the coarse grid, the worse the instability was. This severely limited the usefulness of the subgrid methodology. In particular, the solution to static problems used as initial conditions for nonlinear triggered lightning models was impossible. The instability was eliminated by a modification of the way in which electric field averaging in the subgrid was accomplished. This modification was documented in a previous report [3].

To illustrate the stability of the new technique, a numerical experiment with a conducting bar was undertaken. The bar was ten meters long and two meters square.



One end of the bar was surrounded by a subgrid, but the cross section of the bar was unchanged in the subgrid. Two different subgrids were tested, one with a resolution increase of two times, and the other with a resolution increase of six times. The coarse grid in both cases had a spatial resolution of one meter, so the subgrids had spatial resolutions of one-half meter and one-sixth meter, respectively.

The solution desired in both cases was the electric field distribution around the bar when it is immersed in an ambient electric field oriented along its length. This was accomplished by using a plane wave electromagnetic field incident on the side of the bar. The plane wave electric field was a step change with a rise time of fifty nanoseconds to an amplitude of one hundred volts per meter. The result of this is that the fields around the bar oscillated for a few cycles as resonances in the bar decayed, and then the solution settled down to the static solution. Of course, the magnetic field from the plane wave was still present, but in the static case the electric and magnetic fields are decoupled, so the presence of the magnetic field is unimportant.

The time behavior of the electric field at the center of the subgrid end of the bar is shown in Figure 9.3 for the factor of two subgrid, overlaid with that from the factor of six subgrid. Note the lesser enhancement of the field for the factor of six subgrid. The enhancement is less because the field from the factor of six subgrid represents a small area near the center of the bar cross section, whereas the factor of two field represents a much larger area extending closer to the edge of the bar, where the enhancement is naturally larger.

The ultimate application for the subgrid is to better resolve the sharp points on the F106B, especially the nose, where many direct lightning strikes are known to have attached. The subgrid may be utilized both in linear codes, to better determine enhanced fields around a sharp point or edge, and in nonlinear codes, to better resolve a particular air breakdown event and its effect on aircraft sensors. The first step in this utilization has been taken by placing a subgrid around the nose of the F106B. The spatial resolution in the standard finite difference model of the F106B is one meter in the direction along the fuselage, and one-half meter in the other two coordinate directions. The subgrid around the nose was given a factor of four expansion in the fuselage direction and a factor of two in the other directions resulting in a cubic lattice of resolution one-quarter meter within the subgrid. Although this resolution is still not adequate to resolve features like the pitot boom, it is good enough

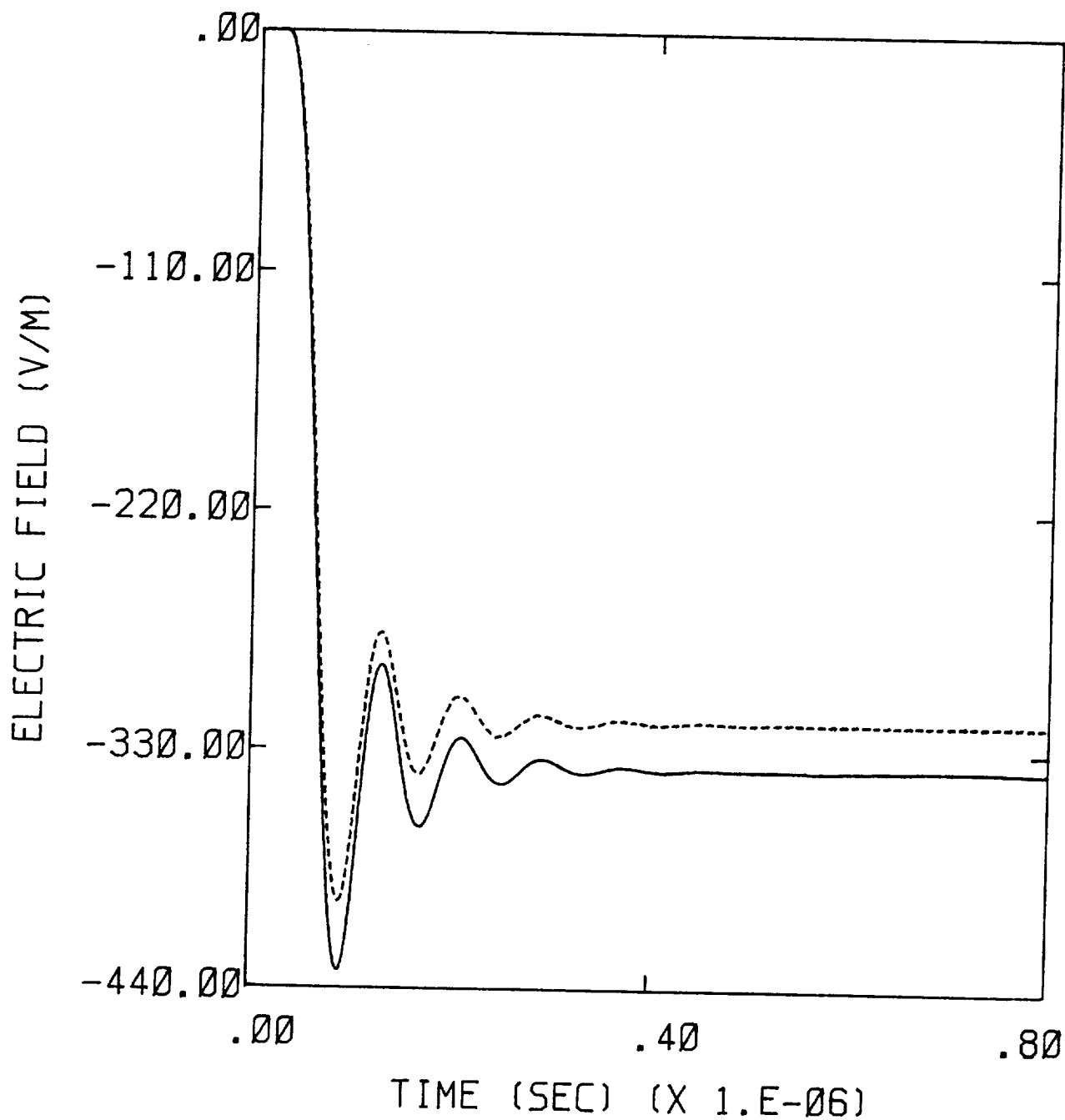


Figure 9.3 Electric Field at the Center of the End of the Bar in the Subgrid. The Solid Line is in the Factor of 2 Subgrid and the Dashed Line in the Factor of 6 Subgrid.

to better resolve the tapering of the nose and to better determine the enhanced electric fields existing there. The new enhanced fields then give a better understanding of the ambient fields necessary to produce a triggered lightning strike at the nose of the F106B.

The static solution for the field distribution around the F106B was achieved in essentially the same way as the fields around the bar described earlier. A plane electromagnetic wave with a step change waveform was propagated across the problem space from bottom to top. The electric field was oriented along the fuselage and rose to a value of one volt per meter in four hundred nanoseconds. The rise time was chosen to minimize the intrusion of aircraft resonances into the static solution.

The D-dot forward response from the aircraft is shown in Figure 9.4 to illustrate the stability of the solution. The more interesting result from the model is the magnitude and location of the largest local electric field value around the more detailed nose of the aircraft. The standard finite difference model of the F106B gave a maximum enhancement of 8.9 under the nose of the plane. This translates to an ambient electric field of 157 kV/m needed to produce a triggered lightning strike to the nose at 27,000 feet. The new maximum field enhancement calculated from the subgrid model was found to be 19.2, which translates to a necessary ambient field of 73.9 kV/m. This reduction will probably be larger when subgrids of greater resolution are placed around the nose. In principle, using subgrids of greater and greater resolution should allow the calculated ambient field necessary to produce a triggered strike to asymptotically approach that seen in nature. In practice, however, the computer resources necessary for arbitrarily good spatial resolution in the subgrid make the use of very large resolution increases impractical.

Application of the subgrid to the F106B finite difference model is just beginning, and it is expected that greater resolution subgrids will be used in future work. In addition, the inclusion of nonlinearities in the subgrid volume is a subject for future work. The subgrid will also be necessary to investigate the conditions under which lightning is initiated. This will allow a determination of whether there exists a lower limit to the volume of high electric field which must exist before a lightning event begins.

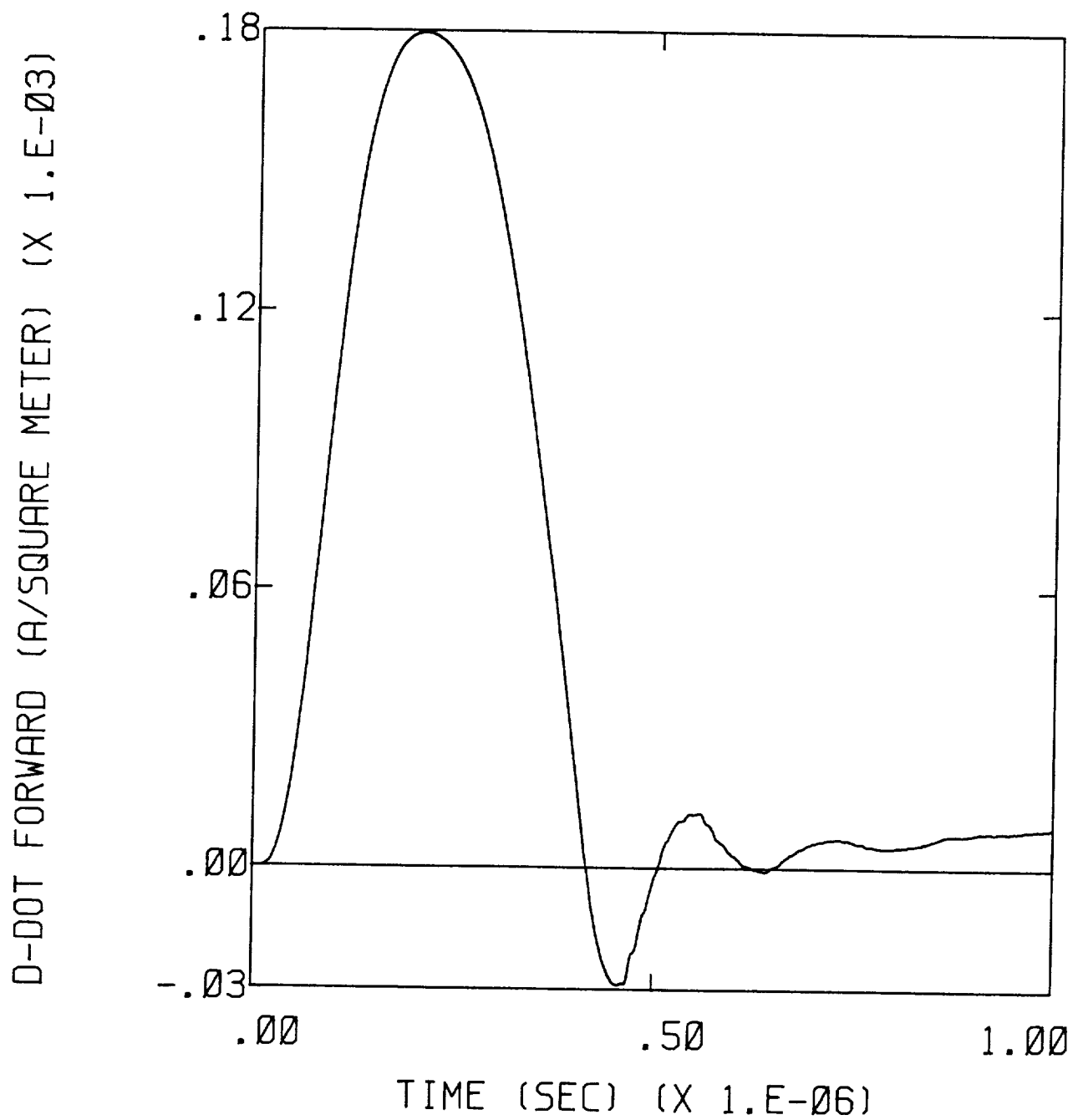


Figure 9.4 D-dot Forward Response of the F106B for the Case with a Subgrid Around the Nose.

## CHAPTER 10

### THUNDERSTORM ENVIRONMENT FOR IN-FLIGHT AIRCRAFT

#### 10.1 Introduction

Real thunderstorm environments are extremely complex and have considerable variability in both space and time. In addition to the ambient atmosphere, the storm environment includes water vapor and a vast array of hydrometeors (cloud and precipitation particles), all of which are moving relative to one another. Some of the hydrometeors are charged through various mechanisms, and relative motion between different sized particles leads to charge separation and the generation of multiple charge centers in the storm.

It is the purpose of this chapter to identify a realistic set of thunderstorm environmental parameters that can be utilized in modeling the initiation of a lightning strike to a penetrating aircraft. In order to accomplish this objective, the thunderstorm environment is first discussed in general terms. Then some specific environmental conditions are chosen which lie within the broad range of possibilities, but which are simple enough to simulate in the mathematical corona model being utilized.

#### 10.2 Meteorological Terminology and Definitions

The discussion of the thunderstorm environment that follows is not intended to be an exhaustive tutorial on the subject but is a short review for non-meteorologists. Therefore, a list of commonly used terms and definitions is in order. The list below is given in the order of ready information flow rather than in alphabetical order.

Atmospheric Pressure: The ambient pressure in the atmosphere results from the weight of the column of air (including any water) existing above the observing point. Obviously, as the observing point moves upward in the atmosphere, this column becomes shorter and hence the pressure decreases with height. The mathematical expression that describes the change of pressure with height is called the hydrostatic equation and is given by,

$$\frac{dp}{dz} = -\rho g \quad (10.1)$$

where  $\rho$  = air density  
 $g$  = acceleration due to gravity

Integration of equation 10.1 provides the information utilized in altimetry.

Relative Humidity: This parameter is not utilized in cloud physics for the most part but is included here as a familiar reference point. Relative humidity is generally expressed in percent, and is a measure of the moisture content in the atmosphere relative to total saturation conditions. The relative humidity is defined as,

$$RH = 100 \frac{e}{e_s} \% \quad (10.2)$$

where  $e$  = ambient partial pressure due to water vapor  
 $e_s$  = saturation vapor pressure (depends only on temperature)

Specific Humidity: This is a measure of the mass of water vapor present per unit mass of ambient air. The specific humidity is given by,

$$q = \frac{.622 e}{p - .378 e} \approx \frac{.622 e}{p} \text{ g/g} \quad (10.3)$$

$p$  = atmospheric pressure

Specific humidity is often expressed in g/km.

Mixing Ratio: The mixing ratio is the moisture parameter most utilized in cloud physics. It is the mass of water vapor contained in a unit mass of dry air and is given by,

$$w = \frac{.622 e}{p - e} \text{ g/g} \quad (10.4)$$

Note that if  $e = e_s$ , then equation 10.4 defines the "saturation mixing ratio". The saturation mixing ratio is a function of temperature and pressure only and therefore

can be plotted as constant curves on a thermodynamic diagram. This parameter is also often expressed in g/kg.

Adiabatic Process: An adiabatic process is one in which heat is neither absorbed or rejected by the system being considered. In the atmosphere, the systems generally being considered are moving parcels of air. For example, if a parcel of dry air is moved upward in the atmosphere without exchanging heat with its surroundings, the temperature of the parcel will decrease with height in a characteristic manner as discussed under lapse rate.

Lapse Rate: Lapse rate refers to the decrease of temperature with height and is a direct result of the vertical pressure change. If a dry parcel of air is caused to move upward under adiabatic constraints, its temperature will change in accord with the pressure change and the applicable ideal gas laws. The resulting change in temperature with height is called the "dry adiabatic lapse rate". This parameter is nearly constant at approximately  $10^{\circ}\text{C/km}$ .

If an air parcel which is saturated with water vapor is moved upward, the water vapor begins to condense into liquid water droplets as the parcel cools. The latent heat given up in the condensation process is retained in the parcel, thereby reducing the cooling rate. The resulting change in temperature with height in this case is called the "moist adiabatic lapse rate". The moist adiabatic lapse rate depends on both temperature and pressure. At standard temperature and pressure, the moist lapse rate is about 35% of the dry lapse rate, whereas at  $-30^{\circ}\text{C}$  and 10 km elevation, the two lapse rates are nearly equal.

Note that the moist adiabatic lapse rate generally applies to upward moving parcels. If saturated air moves downward, the warming process causes immediate unsaturation and the parcel temperature will follow the dry adiabatic lapse rate unless liquid water is present in the parcel.

Sounding: A sounding or atmospheric sounding is the term utilized for a plot of the vertical profile of temperature and moisture content of the atmosphere on a thermodynamic diagram. The data utilized to make these plots are generally obtained by balloon-borne "radiosonde" equipment. The sounding is a most important tool for

describing the state of the atmosphere and for predicting potential for the formation of clouds, storms and precipitation. A sample sounding is shown in Figure 10.1.

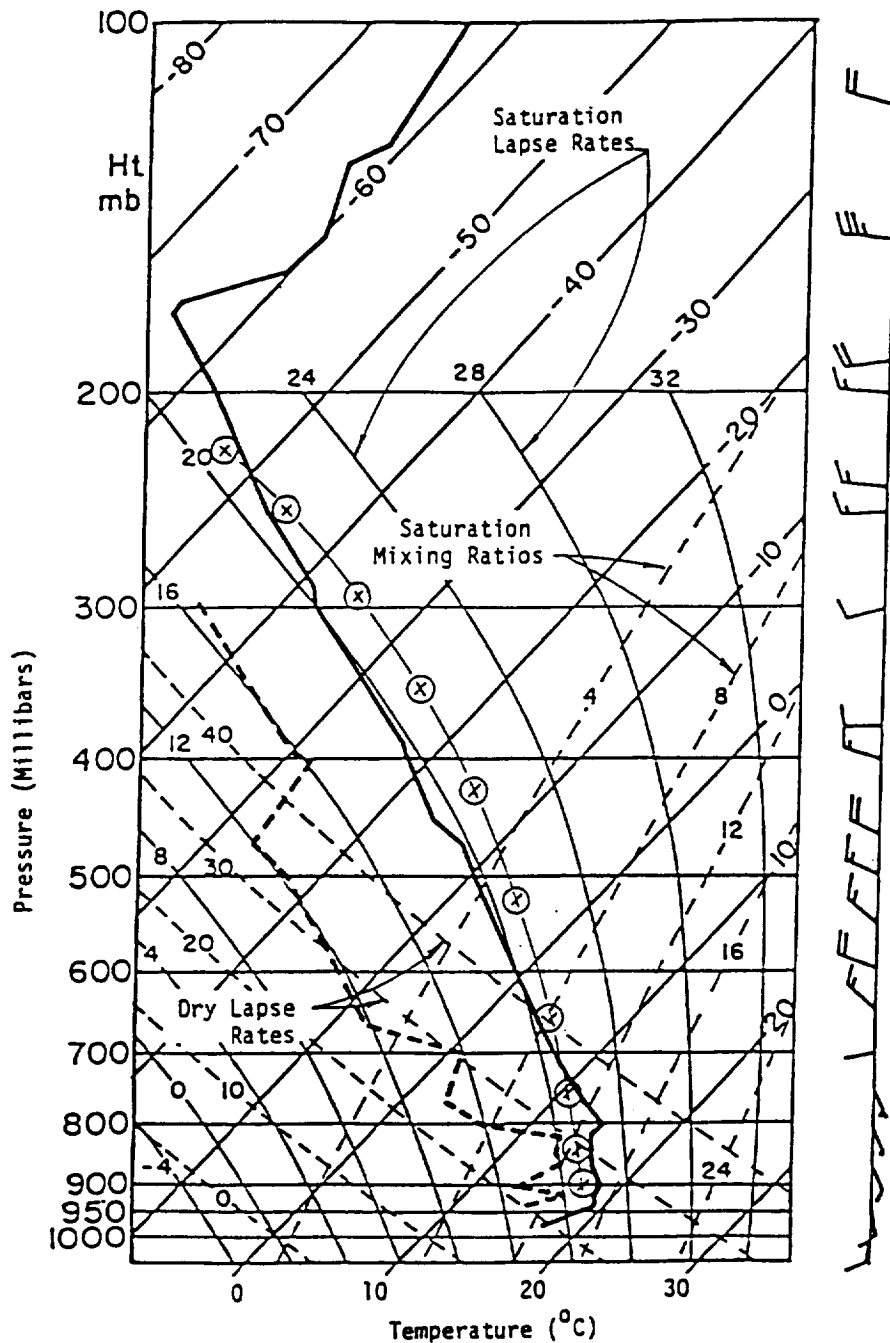
The Thermodynamic Diagram: This diagram generally takes the form of a graphic coordinate system with pressure plotted on the ordinate and temperature on the abscissa. In one standard form, the pressure lines are plotted on a logarithmic scale such that the ordinate is linear in height while the abscissa is linear in temperature. This T-log P diagram has the advantage that the dry lapse rate and mixing ratio lines are straight lines. However, it has the disadvantage that typical soundings are not readily plotted on a single sheet of paper.

Another commonly used diagram is shown in Figure 10.1. This is a skew-T, log p diagram. Here the temperature lines are skewed almost  $45^\circ$  so that atmospheric soundings can be plotted on a single sheet. In the skew T, log p diagram, both the dry and saturated lapse rates as well as the saturation mixing ratio lines are curved lines. Note that the lapse rate curves are labelled with the temperature values they intercept at 1000 millibars pressure. These values are called the wet bulb and dry bulb "potential temperatures", and represent the temperature a parcel of air would have if caused to move to the 1000 mb along the appropriate lapse rate curves (typically these curves are called moist and dry "adiabats"). The dotted curves with positive slope in Figure 10.1 are the saturation mixing ratio lines. They are labelled with values in gms/kgm.

Atmospheric Stability: Atmospheric stability is a term which is applied to the potential of the atmosphere to support vertical motion. It is directly related to the ambient lapse rate and to the moisture content. For example, if the lapse rate in the atmosphere is less than the moist adiabatic lapse rate, any local vertical motion will be suppressed because buoyancy forces will tend to return any displaced air parcel back to its original level. For this lapse rate condition, the atmosphere is in stable equilibrium. If the actual ambient lapse rate is greater than the dry adiabatic lapse rate, the atmosphere is unstable. Under these conditions, any small vertical displacement of air will be accelerated, leading to large vertical displacements.

When the actual ambient lapse rate lies somewhere between the moist and dry adiabatic lapse rates, the atmosphere is said to be conditionally stable or unstable.





**Figure 10.1** Example of a Typical Sounding Plotted on a Skew T/Log P Thermodynamic Diagram.

**Note:** The Thick Solid Line Represents the Temperature Profile; the Thick Dashed Line Represents the Moisture Profile. The Flags On the Right of the Diagram Indicate Horizontal Wind Parameters. The Barbs on Each Flag Represent Wind Speed With Each Full Length Barb Being 10 Knots. Shorter Barbs Indicate Some Fraction of 10 Knots. For Example, the Second Flag From the Top Has 3-1/2 Barbs, or 35 Knots. Wind Direction is Represented by the Orientation of the Flag. Upright Flags Indicate a North Wind, and Upside-Down Flags a South Wind. Flags Pointing Directly to the Left of the Line Indicate an East Wind, and to the Right a West Wind.

The condition for stability in this case is the moisture content of the air. Most general storms and widespread precipitation occur under conditions of conditional instability.

**Entrainment:** Entrainment is the term used for the injection of environment air into a vertically moving air column. Entrainment occurs through turbulent exchange at the boundaries of the moving vertical column or through horizontal convergence generated by vertical acceleration in the column. Entrainment leads to nonadiabatic processes, since heat is exchanged between the vertical moving air and its surroundings.

**Condensation Nuclei:** The aerosol particles that act as nuclei for the formation and growth of cloud droplets are called cloud condensation nuclei. Without these particles being present in the atmosphere, water vapor would not convert to liquid water when small supersaturation conditions occurred. Furthermore, the type, size, distribution, number, density, and chemical content of the existing condensation nuclei play a direct role in determining the characteristics of the clouds and precipitation that forms when supersaturation takes place.

**Ice Nuclei:** Without the presence of ice-forming nuclei, water can be cooled to beyond  $-40^{\circ}\text{C}$  without converting to ice. The aerosol particles active in initiating the ice formation process when the temperature falls below the freezing mark are called ice nuclei. These are a different set of particles from condensation nuclei and are generally highly insoluble in water.

**Hydrometeors:** This term applies to all forms of liquid and solid water in the atmosphere. It includes cloud drops, rain drops, ice crystals, snowflakes, hail particles, etc.

**Cloud Drops:** Cloud drops are the basic form of liquid water in a cloud and are formed by condensation of water vapor on appropriate nuclei. Stable sizes are generally in the range of 10 to 20  $\mu$  in diameter, although they can be larger in convective type clouds.

**Rain Drops:** Rain drops are formed through growth of cloud drops by coalescence, by melting of large ice forms, or by a combination of both processes. Liquid cloud

particles are called rain drops when they have reached sufficient size to fall relative to the cloud updraft.

Ice Crystals: Ice crystals are the basic forms that are generated from cloud water when temperature falls below 0°C. They occur in a large number of shapes or "habits". Since the fundamental ice crystal has a hexagonal form, the basic ice crystal habits are hexagonal. Some basic ice crystal shapes are shown in Figure 10.2. The most fundamental of those shown are simple plates (a), and the solid column (b). Another common form but much more complex is the dendrite (c). Dendrites can be planar as shown or they can be three dimensional (spatial dendrites). The habits shown are only the simplest of a large array of observed forms (see Magano and Lee [7]). A few examples are shown in Figure 10.3.

Snow Flakes: These are formed by the joining together of ice crystals (an ice crystal aggregate). Size is determined by the type of crystal and the length of the growth process.

Ice crystals and snow flakes coexisting with cloud drops can become "rimed". Riming is the process whereby supercooled drops are collected and freeze on contact. Heavily rimed snow flakes have high liquid water content relative to dry flakes.

Graupel: Graupel is a precipitation form which is like spongy hail. Graupel is formed by heavy riming of some embryo such as a frozen rain drop, large ice crystal or a snow flake. Continued riming produces a sponge-like ice particle with a great deal of entrapped air. Densities can range from .1 to .8 gm/cm<sup>3</sup> depending upon the growth process.

Hail: Hail is similar to graupel except that in the coalescence process, the liquid water flows around the embryo before freezing. Long trajectories under appropriate conditions can generate very large diameter precipitation. The long effective trajectories required for hail generation are made possible by the strong updrafts which exist in the convective storm. Hail embryos are carried to high levels in the updraft, growing in the process. They can then continue to grow as they fall through regions of high liquid water content until they finally reach the ground.

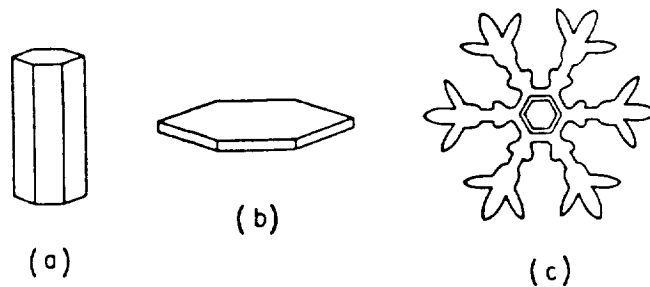


Figure 10.2 Fundamental Shapes of Ice Crystals












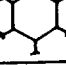





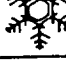


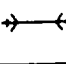


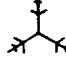

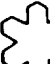
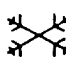




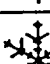


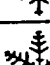
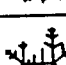
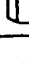
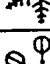
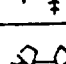
	<b>H1a</b> Elementary needle		<b>C1f</b> Hollow column		<b>P2b</b> Stellar crystal with sectorlike ends
	<b>H1b</b> Bundle of elementary needles		<b>C1g</b> Solid thick plate		<b>P2c</b> Dendritic crystal with plates at ends
	<b>H1c</b> Elementary sheath		<b>C1h</b> Thick plate of skeleton form		<b>P2d</b> Dendritic crystal with sectorlike ends
	<b>H1d</b> Bundle of elementary sheaths		<b>C1i</b> Scroll		<b>P2e</b> Plate with simple extensions
	<b>H1e</b> Long solid column		<b>C2a</b> Combination of bullets		<b>P2f</b> Plate with sectorlike extensions
	<b>H2a</b> Combination of needles		<b>C2b</b> Combination of columns		<b>P2g</b> Plate with dendritic extensions
	<b>H2b</b> Combination of sheaths		<b>F1a</b> Hexagonal plate		<b>P3a</b> Two-branched crystal
	<b>H2c</b> Combination of long solid columns		<b>F1b</b> Crystal with sectorlike branches		<b>P3b</b> Three-branched crystal
	<b>C1a</b> Pyramid		<b>F1c</b> Crystal with broad branches		<b>P4c</b> Four-branched crystal
	<b>C1b</b> Cup		<b>F1d</b> Stellar crystal		<b>P6a</b> Broad branch crystal with 12 branches
	<b>C1c</b> Solid bullet		<b>F1e</b> Ordinary dendritic crystal		<b>P6b</b> Dendritic crystal with 12 branches
	<b>C1d</b> Hollow bullet		<b>F1f</b> Fornlike crystal		<b>P5</b> Half-formed crystal
	<b>C1e</b> Solid column		<b>P2a</b> Stellar crystal with plates at ends		<b>P6c</b> Plate with sector plates

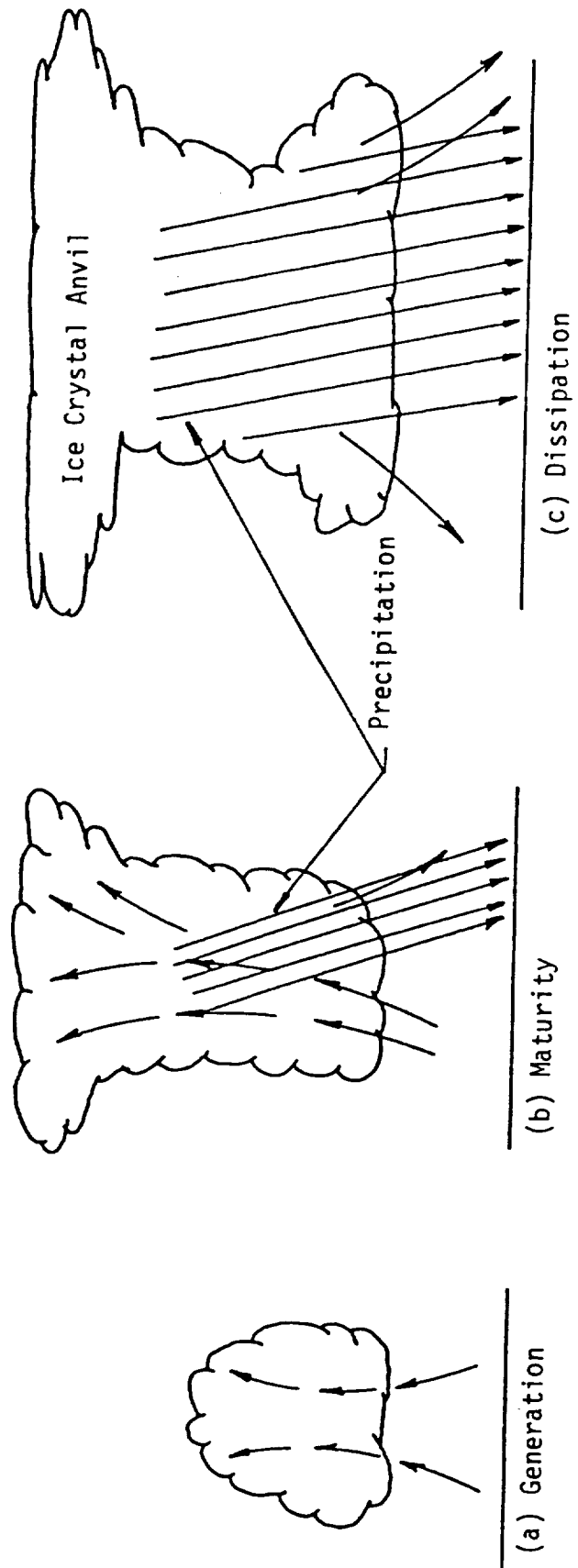
Figure 10.3 Partial Classification of Natural Ice Crystals (from Magano and Lee) [7])

### 10.3 Storm Generation

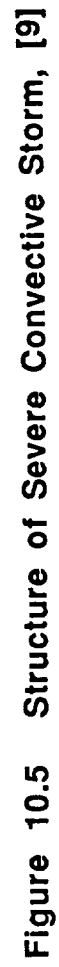
Convective storms are generated when latent instability in the atmosphere is triggered by the onset of local vertical motion. Initiation of this vertical motion may be due to local surface heating or to mechanical lifting by orographic features or frontal surfaces. Whatever the triggering mechanism, the results are the same. Moist air from lower levels is caused to rise until the air parcels find themselves in colder surroundings. The parcels then accelerate upward by virtue of the buoyancy forces, converting water vapor to liquid water and subsequently liquid water to ice. Tremendous quantities of energy are released (of the order of  $10^{15}$  Joules in a single cell [8]). The potential for storm generation is demonstrated in the sample sounding shown in Figure 10.1. If the moist air in the layer between 950 and 850 millibars were caused to move upward as shown, saturation would occur quickly and the temperature of the rising air parcels would then follow the moist adiabat (saturation lapse rate). At the level just below 750 millibars, the rising air would become warmer than the environment air and therefore begin to accelerate upward, converting water vapor to liquid water and ice in the process. When the ascending air approaches the 200 millibar level, it again encounters an environment that is warmer than itself and hence begins to decelerate and form the cloud top. Just as upward accelerating air causes horizontal convergence (entrainment), decelerating air leads to horizontal divergence. This latter process generates the characteristic "anvil" tops characteristic of severe convective storms.

Since cloud tops are generally above 30,000 feet, they consist mostly of ice crystals which give the anvil tops a fuzzy, diffuse appearance. The structure of a typical air-mass type convective storm is shown in Figure 10.4. This type of storm has a life cycle depicted by the three stages shown. The generation stage (a) is triggered by local surface heating or by surface features such as a mountain. It is characterized by an increasing updraft and a rapidly building vertical cloud. The mature stage (b) is reached when the cloud top spreads out to form a typical "anvil" and a heavy column of precipitation penetrates the updraft to the ground. In this type of storm, the precipitation column broadens as the storm matures and eventually quenches the updraft. The dissipation stage (c) is characterized by fairly broad precipitation and generally downward moving air.

The typical structure of a severe convective storm is shown in Figure 10.5. Important features of the severe storm are the tilted updraft and the quasi steady state



**Figure 10.4 Structure of Air-Mass Convective Storm**



flow pattern. This type of storm can persist for several hours with individual cells being continuously generated and regenerated. It is easily seen how this type of storm can produce large hail by virtue of the long trajectories of the hail embryos in regions of high liquid water content.

As a result of the complex dynamics of the storm operating through a deep layer of atmosphere, water vapor is converted to liquid water and then to various ice forms. Conversion in the opposite direction is also occurring because of downward motion. The cloud physics processes taking place are numerous and complex, and a number of different types of hydrometeors may be formed. Several forms can exist together. A detailed discussion of the physical processes involved is beyond the scope and intent of this report. However, Figure 10.6 shows a flow diagram of the known convective storm processes. A brief description of each process is given in Table 10.1.

#### **10.4 Storm Electricity**

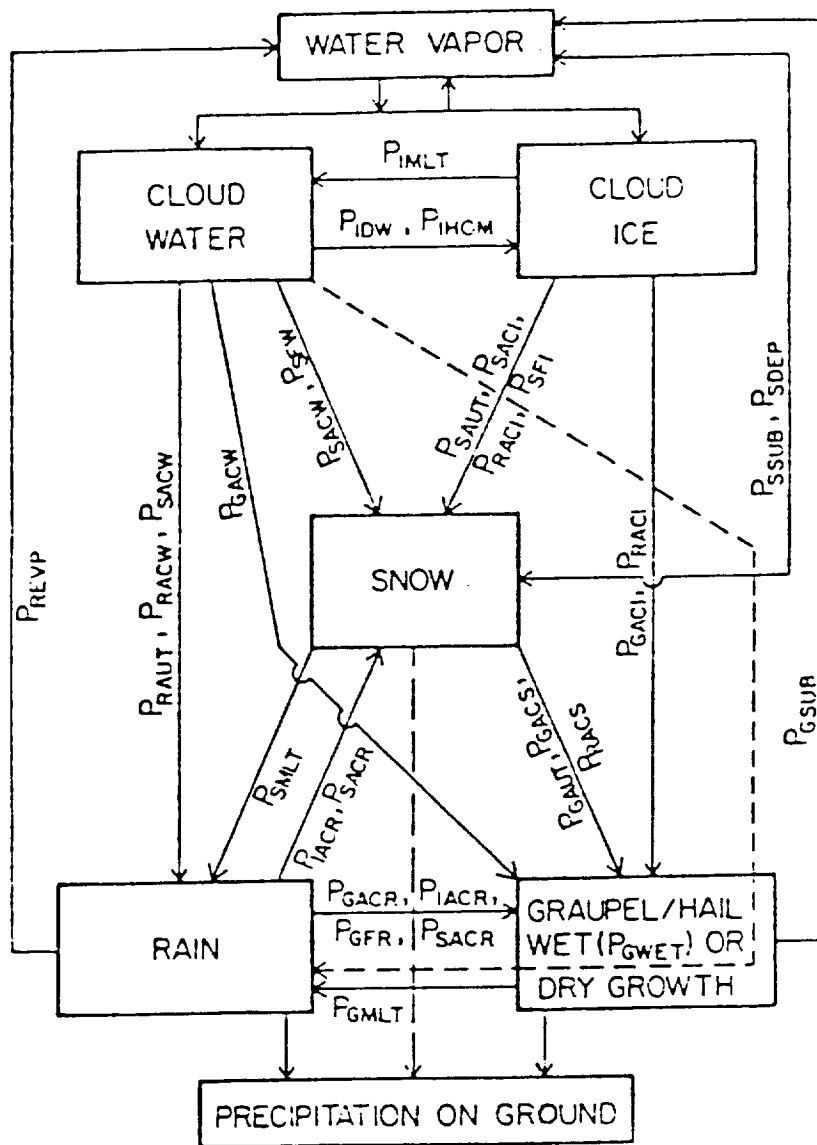
In addition to the heavy precipitation and violent air motions, convective storms generate a great deal of static electricity. The coexistence of strong vertical motion, differential particle terminal speeds and various particle charging mechanisms turn the storm into an effective electrostatic generator. Charge centers of opposite signs develop and intensify until an electrical breakdown or discharge takes place from the cloud to ground or between charge centers within the cloud.

The mechanisms that separate charges in a storm are the strong vertical motions and the differential terminal velocities of the various particles present. Cloud droplets and ice crystals have low terminal velocity and are carried upward in the cell, whereas rain drops, graupel and hail have high terminal velocities and are left behind or fall out, thereby creating the separated charge centers.

In combination with the differential motion of the hydrometeors, several charging mechanisms are operating to produce the charged particles. Investigations into these mechanisms continue as most are still not well understood. However, a list of possible mechanisms is as follows:

Selective Ion Capture [11]. This mechanism involves the existence of different mobilities of electrons and positive ions. Selective capture of electrons by cloud





**Figure 10.6 Cloud Physics Processes Which Can Occur in a Convective Storm**

**Table 10.1**  
**Key to Figure 10.6**

Symbol	Meaning
$P_{\text{MILT}}$	Melting of cloud ice to form cloud water, $T \geq T_0$ .
$P_{\text{IDW}}$	Depositional growth of cloud ice at expense of cloud water.
$P_{\text{IHOM}}$	Homogeneous freezing of cloud water to form cloud ice.
$P_{\text{IACR}}$	Accretion of rain by cloud ice; produces snow or graupel depending on the amount of rain.
$P_{\text{RACI}}$	Accretion of cloud ice by rain; produces snow or graupel depending on the amount of rain.
$P_{\text{RAUT}}$	Autoconversion of cloud water to form rain.
$P_{\text{RACW}}$	Accretion of cloud water by rain.
$P_{\text{REVP}}$	Evaporation of rain.
$P_{\text{RACS}}$	Accretion of snow by rain; produces graupel if rain or snow exceeds threshold and $T < T_0$ .
$P_{\text{SACW}}$	Accretion of cloud water by snow; produces snow if $T < T_0$ or rain if $T \geq T_0$ . Also enhances snow melting for $T \geq T_0$ .
$P_{\text{SACR}}$	Accretion of rain by snow. For $T < T_0$ , produces graupel if rain or snow exceeds threshold; if not, produces snow. For $T \geq T_0$ , the accreted water enhances snow melting.
$P_{\text{SACI}}$	Accretion of cloud ice by snow.
$P_{\text{SAUT}}$	Autoconversion (aggregation) of cloud ice to form snow.
$P_{\text{SEW}}$	Bergeron process (deposition and riming)—transfer of cloud water to form snow.
$P_{\text{SEI}}$	Transfer rate of cloud ice to snow through growth of Bergeron process embryos.
$P_{\text{SDWP}}$	Depositional growth of snow.
$P_{\text{SSUB}}$	Sublimation of snow.
$P_{\text{SMILT}}$	Melting of snow to form rain, $T \geq T_0$ .
$P_{\text{GAUT}}$	Autoconversion (aggregation) of snow to form graupel.
$P_{\text{GFR}}$	Probabilistic freezing of rain to form graupel.
$P_{\text{GACW}}$	Accretion of cloud water by graupel.
$P_{\text{GACI}}$	Accretion of cloud ice by graupel.
$P_{\text{GACR}}$	Accretion of rain by graupel.
$P_{\text{GACS}}$	Accretion of snow by graupel.
$P_{\text{GSUB}}$	Sublimation of graupel.
$P_{\text{GMILT}}$	Melting of graupel to form rain, $T \geq T_0$ . (In this regime, $P_{\text{GACW}}$ is assumed to be shed as rain.)
$P_{\text{GWET}}$	Wet growth of graupel; may involve $P_{\text{GACS}}$ and $P_{\text{GACI}}$ and must include $P_{\text{GACW}}$ or $P_{\text{GACR}}$ , or both. The amount of $P_{\text{GACW}}$ which is not able to freeze is shed to rain.

droplets creates a negatively charged region. Precipitation particles falling through this region can carry away negative charge leaving a positively charged region.

Induction Charging [12], [13]. Induction charging involves non-coalescing collisions between particles in an electric field. Precipitation particles are polarized by the field. If relative motion occurs between particles in the direction of the field, opposite charge is carried away by each particle involved in a glancing or non-coalescing collision.

Freezing Potential Charging [14], [15]. When water begins to freeze, it has been shown that a potential develops between the water and ice, the ice being negative. Therefore, when a water droplet impacts an ice particle and water fragments are shed from the ice surface, the ice particle is left with a negative charge and the water fragments carry away positive charge.

Charging During Riming of Graupel [16], [17], [18]. When an ice crystal impacts a graupel particle in the riming process, positive charge is left on graupel and negative charge is carried away by the ice crystal. It is possible that the two different ice surfaces possess different work functions because of the differing growth mechanisms, i.e., vapor diffusion for the ice crystal and capture of supercooled water in the case of the graupel. Charging may also occur when ice splinters are shed as riming takes place. The sign of the charge carried away appears to be a function of the cloud liquid water content as well as temperature.

Evaporative Charging by Ice Crystals [19]. This mechanism involves the release of positive ions by the complete evaporation of small ice crystals near cloud tops, while larger ice forms retain negative charge. The evaporation process cools the air parcel and the parcel sinks through the cloud carrying the negative charged particles with it. During this sinking process, the positive ions migrate to the surrounding cloud, leaving a negative charge region at lower levels.

The above list of charging mechanisms is not necessarily complete but does include most of the processes believed to be active in storm electrification. At one time, it was thought that the inductive charge transfer mechanism played the major role in storm charging. However, it is now believed that this mechanism cannot produce the electrification typical of thunderstorm conditions on its own. The main charging mechanisms presently considered to be responsible for strong electrification are those

dealing with ice particles interacting with water drops and with other ice crystals. Mechanisms other than those listed certainly exist and the whole subject of cloud electrification is the source of much debate at present.

### **10.5 The Hydrometeor Environment**

From the previous discussions, it is clear that the water and ice environment in a severe storm can be quite complex, and a multitude of different shapes, sizes and water forms is possible. In many cases, several different particles can coexist in a storm region. In most cases, the possible range of particle parameters spans orders of magnitude. Table 10.2 gives a condensed summary of possible cloud particles with nominal ranges given for each parameter as well as typical mean values where possible.

### **10.6 Simplified Hydrometeor Environment for Modeling**

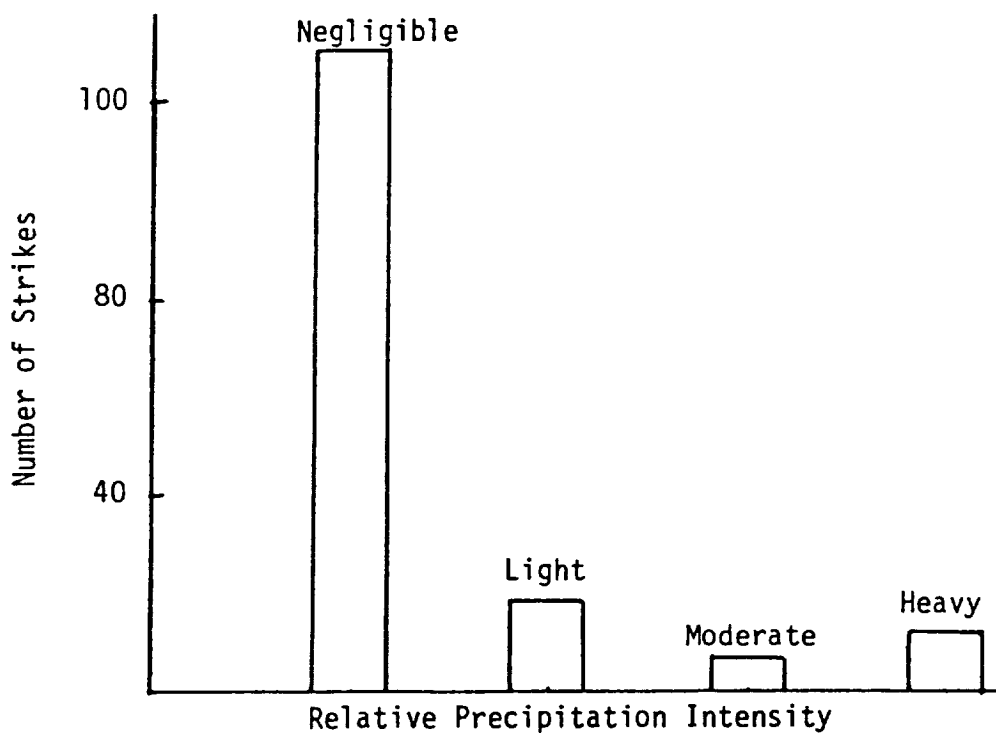
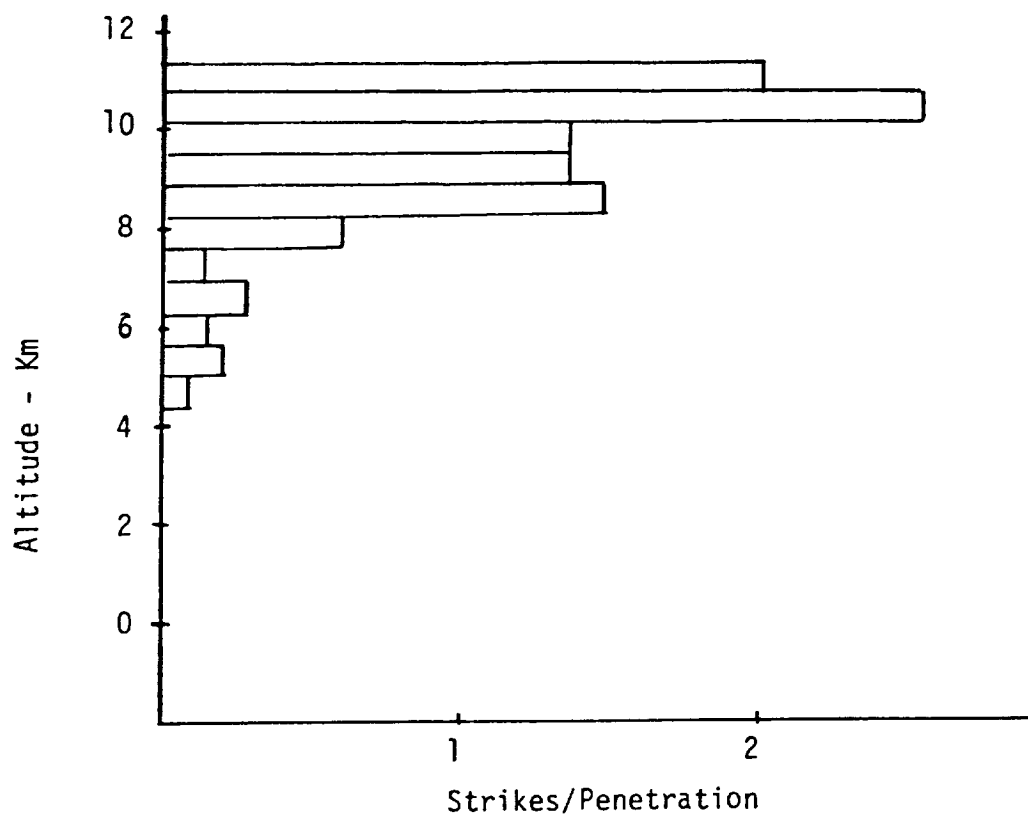
It is seen from the preceding discussions that actual precipitation particle environments can be relatively complex, highly variable in space and time, and can differ greatly from storm to storm. Fortunately, some selection criteria are available that permit considerable simplification of the hydrometeor environment for penetrating aircraft strikes. First, statistics for lightning strikes on penetrating aircraft show two distinct maxima relative to flight altitude. These data are shown in Figure 10.7, and in Figure 10.8 [20]. Second, experimental storm penetration flights for the purpose of measuring lightning are directed clear of high radar reflectivity zones. Thus, regions of heavy precipitation such as heavy rain, hail or graupel are avoided. Indeed, the strike statistics for the NASA F106B flights given in Figure 10.7 indicate that the majority of strikes were encountered in regions of zero or negligible precipitation. Finally, measurements made of lightning sources by NOAA/National Severe Storms Laboratory [21] utilizing VHF mapping techniques show two very marked source maxima centered at 12 km and at about 6 km. These data are shown in Figure 10.9.

Utilizing the above criteria, two relatively simple environments can be established. The first region is at an altitude of about 10 km and the second at an altitude of about 3.5 km. Several strike scenarios are possible within these two regions as shown in Figure 10.10. The aircraft may encounter a branch of the discharge as in (a) or (b), or may become part of the main channel as in (c) or (d).

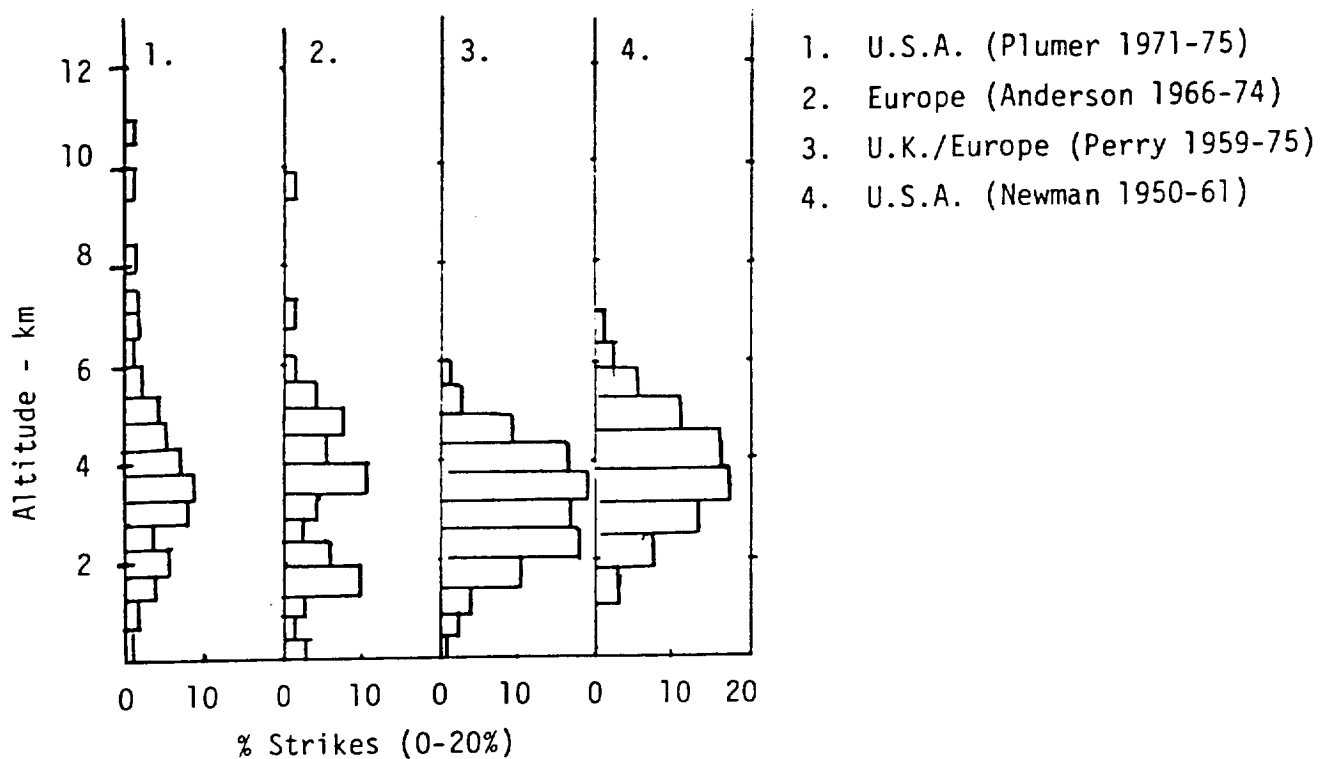
Table 10.2

## SUMMARY OF HYDROMETEOR PARAMETERS

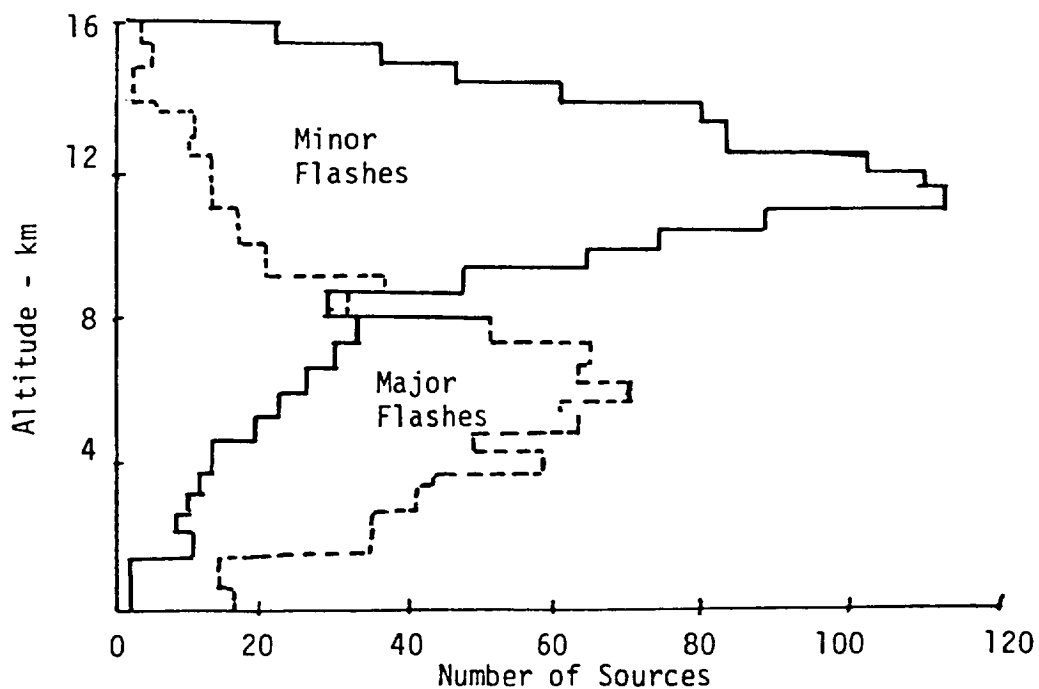
Particle	Diameter Range	Particle Concentration	Conductivity	Dielectric Constant	Possible Charge
Cloud Droplet	1 - 50 $\mu$ (10 $\mu$ )	$10^8 - 10^9/\text{cm}^3$ ( $5 \times 10^8$ )	$10^{-4} - 10^{-3}$ mho/m	80	0-50 pC
Rain Drop	.1 - 5 mm (1 mm)	$10^2 \times 10^4/\text{m}^3$ ( $10^3$ )	$10^{-4} - 10^{-3}$ mho/m	80	0-250 pC
Ice Crystal	1 - 1000 $\mu$ (300 $\mu$ )	$10^4 - 10^6/\text{m}^3$ ( $10^5$ )	$2 \times 10^{-7} - 1 \times 10^{-5}$ mho/m	100-200	0-150 pC
Snow Flakes	1 - 20 mm (5 mm)	.01 - 100/ $\text{m}^3$			Unknown
Graupel	1-20 mm (5 mm)	.01 - 100/ $\text{m}^3$			0-250 pC
Hail	.5 - 8 cm (1 cm)	.01 - 100/ $\text{m}^3$			0-250 pC



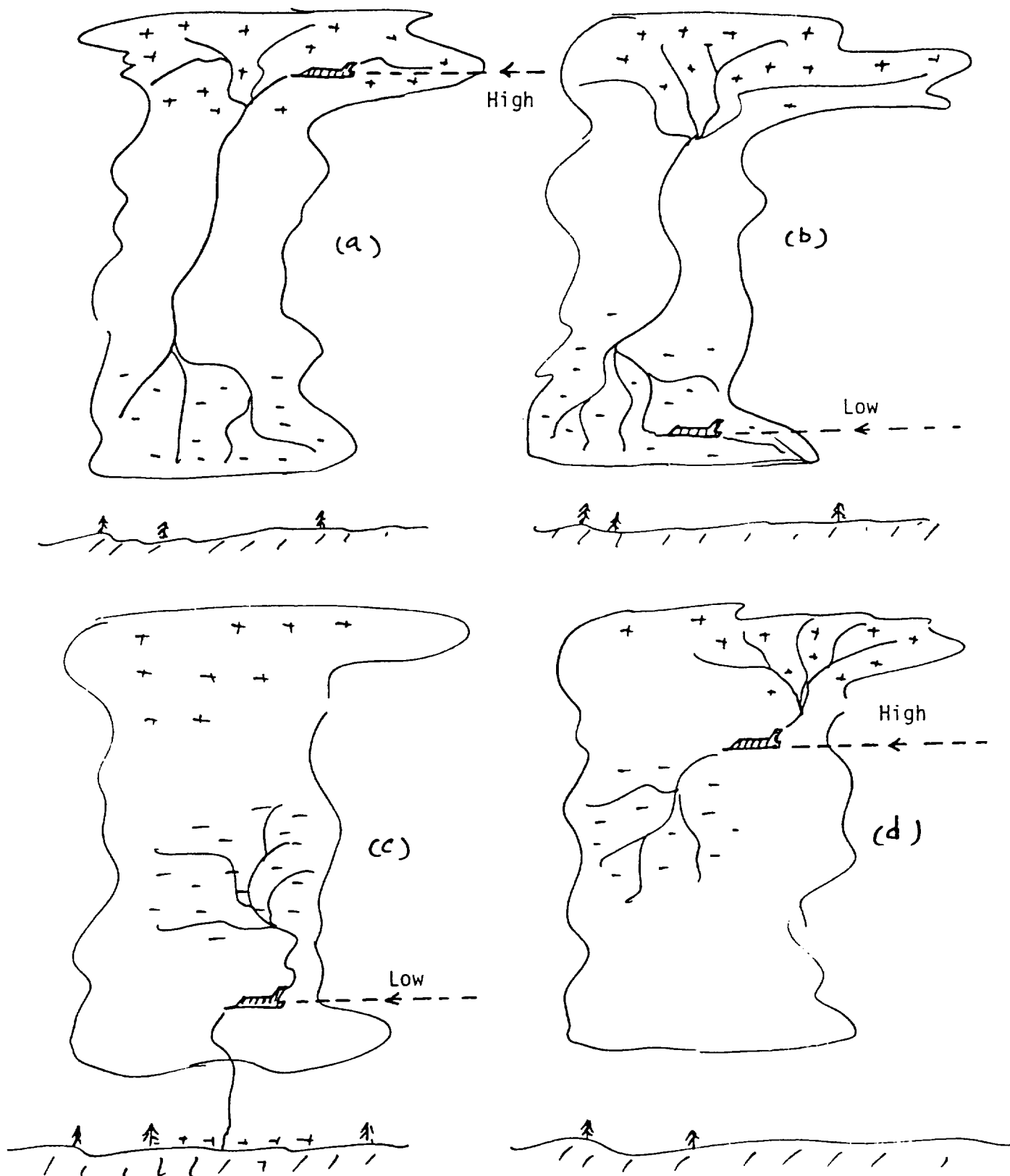
**Figure 10.7 Thunderstorm Penetration and Strike Statistics for "Storm Hazards", 1980-82.**



**Figure 10.8 Aircraft Strike Statistics for Low Altitude Flights**



**Figure 10.9 Altitude Distribution of VLF Sources for Storm I, 6/19/80**



**Figure 10.10 Possible Lightning Strike Scenarios for High and Low Flight Paths**



The specific particle environments for the high and low altitude cases chosen are as follows:

1. The High Altitude Environment

Altitude	10 km
Temperature	-45°C
Pressure	260 mb ( 195 mm Hg)
Air Moisture Content	0.17 g/kg (.065 g/m <sup>3</sup> )
Particle Type	Ice Crystals (a) Hexagonal Plates (b) Hexagonal Columns
Particle size	.1-1.0 mm (large dimension)
Particle Shape Factor	(a) Plates - $\frac{\text{Diameter}}{\text{thickness}} = 25$ (b) Columns - $\frac{\text{Length}}{\text{Diameter}} = 4$
Particle Concentration	10 <sup>4</sup> /m <sup>3</sup> to 10 <sup>5</sup> /m <sup>3</sup>
Ice Dielectric Constant	100 - 200 (static)
Ice Conductivity	2 x 10 <sup>-7</sup> mho/m - 1 x 10 <sup>-5</sup> mho/m
Particle Charge	0 to 150 pC (positive)

2. The Low Altitude Environment

Altitude	3.5 km
Temperature	+ 5°C
Pressure	900 mb ( 675 mm Hg)
Air Moisture Content	6.0 g/kg (6.0 g/m <sup>3</sup> )
Particle Type	Cloud water droplets
Particle Shape	Spherical
Particle Size	5 - 20μ dia.
Particle Concentration	10 <sup>8</sup> /m <sup>3</sup> - 10 <sup>9</sup> /m <sup>3</sup>
Particle Dielectric Constant	80 static
Particle Conductivity	10 <sup>-4</sup> mho/m - 10 <sup>-3</sup> mho/m
Particle Charge	0 to 150 pC (negative)

## **10.7 The Role of the Thunderstorm Environment in Modeling**

The previous sections in this chapter describe the thunderstorm environment in some detail. The last question to be considered is the use of this environment in the lightning aircraft interaction modeling. The most important new item to be added to the modeling process is the presence of particles. These particles, because they have finite conductivity, alter the electric field distribution locally. Factors of three to ten are likely for local field enhancement factors, depending on shape and orientation of the particles. Because of this local field enhancement, the presence of particles in the environment makes the propagation of a lightning channel (especially the leader) easier. That is, the channel may propagate from particle to particle faster than it could move through clear air. A particle may even act as the initiating trigger of a lightning event if it happens to be in a high field region, and enhances the field locally enough to produce corona and air breakdown in its vicinity.

Where modeling is concerned, the most important parameters from the thunderstorm environment are the density, size, shape, and electrical characteristics of the particles. These parameters vary as a function of position in a storm, mainly because of temperature variation with altitude. The goal of future modeling efforts is to incorporate the information reported here of the thunderstorm environment into linear and nonlinear lightning aircraft interaction models. The first step in this direction is reported in the next chapter, where the field enhancements around typical ice particles are determined.

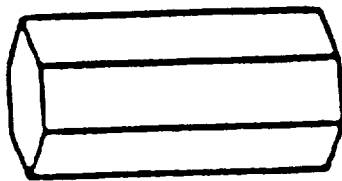
## CHAPTER 11

### FIELD ENHANCEMENT FACTORS FOR TYPICAL ICE CRYSTALS

In the high altitude, low temperature thunderstorm environment in which the F106B has encountered most of its direct lightning strikes, the most prevalent particle is the ice crystal. Because these ice crystals have a finite conductivity, enhanced electric fields exist in their immediate vicinity. Also, since the crystals can have quite irregular shapes, the field enhancements can be quite large. The enhancement does not extend very far from the crystal, only about one crystal dimension. However, it is possible that the small volume field enhancements produced by an ice crystal could aid in the propagation of a lightning channel. It is therefore of some interest to investigate the field enhancements which exist around typical ice crystals.

The electromagnetic properties of ice crystals were discussed in some detail in Chapter 10, so only the most pertinent will be repeated here. The ice relative dielectric constant for static fields varies from 100 to 200 and the conductivity from  $2 \times 10^{-7}$  mho/m to  $1 \times 10^{-5}$  mho/m. These quantities allow one to calculate the relaxation time constant for the ice. This is approximately the time that it takes for the charge on an ice crystal to reach a static distribution when the crystal is placed in an external electric field. The time constant is given by  $\epsilon / \sigma$ , where  $\epsilon$  is the dielectric constant and  $\sigma$  the conductivity. Using the numbers above, the time constant is seen to vary from approximately one microsecond to ten milliseconds. This is the time in which an enhanced field will be created around an ice crystal. For times longer than this, the enhanced fields can be expected to exist around the crystals. The relaxation time constant is important because of the turbulence which generally exists within a thunderstorm. The ice crystals are continually changing their orientation with respect to the ambient electric field because of the turbulence. The time scale for these changes of orientation must be longer than the previously calculated time constant in order for enhanced fields to exist around the ice crystals.

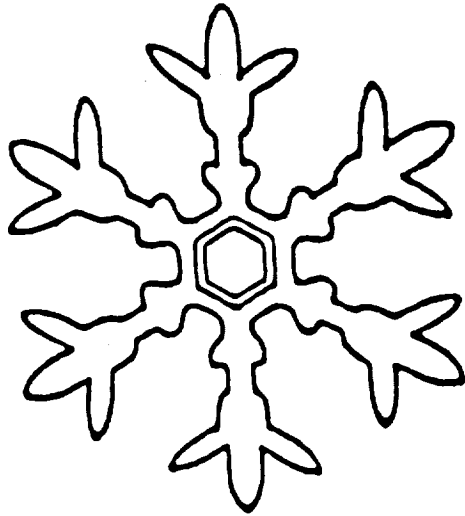
If one postulates an uncharged ice crystal at rest in an ambient electric field, the only things important to the calculation of the enhanced fields are the shape of the crystal and its orientation with respect to the field. The shapes analyzed in this chapter are the fundamental shapes shown in Figure 11.1. The first is a six sided column and has a length to diameter ratio of six. The second is a six sided plate with a diameter to



(a)



(b)



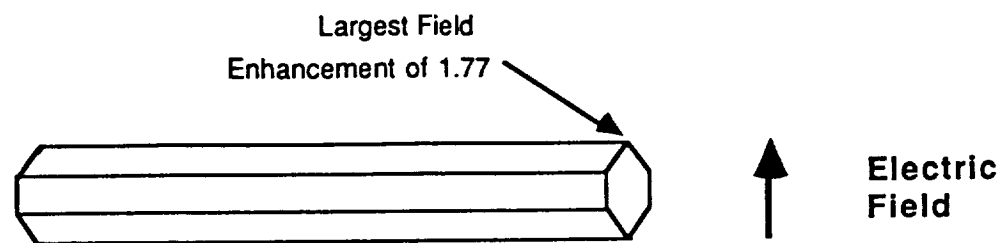
(c)

Figure 11.1 Fundamental Ice Crystal Shapes For Which the Electric Field Enhancement Factors Have Been Determined

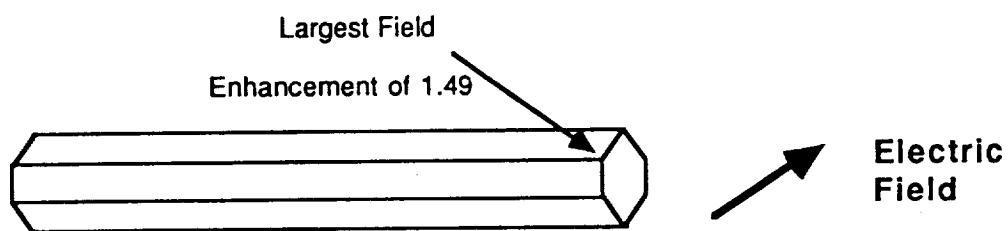
thickness ratio of twenty-five. The third is a somewhat more unusual shape and is included to give some indication of the enhanced field around a typical crystal. Its diameter to thickness ratio is also twenty-five.

The enhanced fields around each crystal were calculated by placing the crystal in a finite difference problem space containing a uniform ambient electric field of one volt per meter. The crystal itself was assumed to be perfectly conducting, because the static field distribution around finitely conducting and perfectly conducting objects is the same. Three orientations of each crystal with respect to electric field were investigated. The first orientation had the field oriented along the axis of the crystal; that is, along the long axis of the column and perpendicular to the plane of the plate. The second orientation had the field perpendicular to the first orientation, across the diameter of the column and in the plane of the plate. The third orientation had the field perpendicular to the first two orientations, also across the diameter of the column and in the plane of the plate. The third orientation is different from the second because of the asymmetry of the six sided crystals in a cartesian coordinate system. However, the enhanced fields are only slightly different for the second and third orientations. The maximum local fields for each of the crystals at each orientation are presented in Figures 11.2 to 11.4. Note in particular that the largest field always occurs near an edge or point of the crystal, as expected. Note also that the field orientation perpendicular to the planes of the plate-shaped crystals produces no field enhancement. This latter result is an artifact of the finite difference model of the crystals, which used only one cell for the thickness. In reality, there would be some enhancement of the fields, and the largest field would be slightly greater than one volt per meter and located around the edges of the plate.

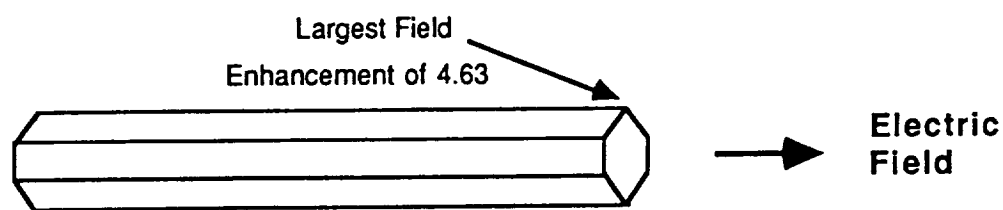
It is significant that the magnitude of the enhanced field is comparable to that on the F106B when it is flying in an ambient field. This implies that when corona exists around the F106B, it will also exist around the ice crystals in the environment. Hence the presence of polarized ice crystals near the F106B could aid in the initiation of a triggered lightning discharge to the aircraft. It should be clearly understood, however, that the enhanced field around an ice particle is a purely local phenomenon, because of the average separation between particles. Particle sizes range from .1 to 1 millimeter, so enhanced fields cannot exist outside of a sphere about three millimeters in diameter centered on the particle. The average separation of the particles varies as the cube root of the particle density, which peaks at about  $10^5$  particles per cubic meter



(a)

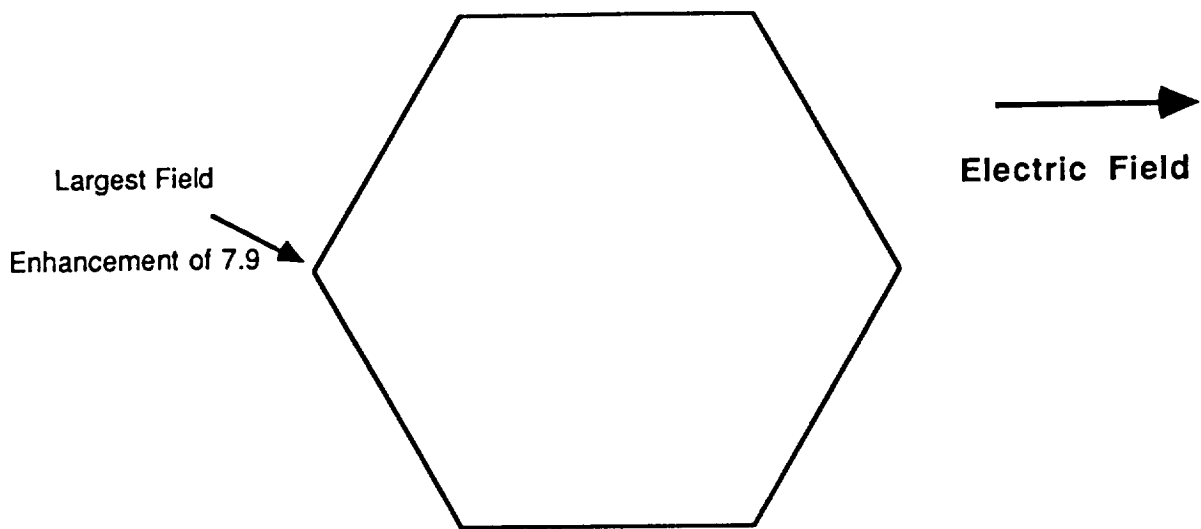


(b)

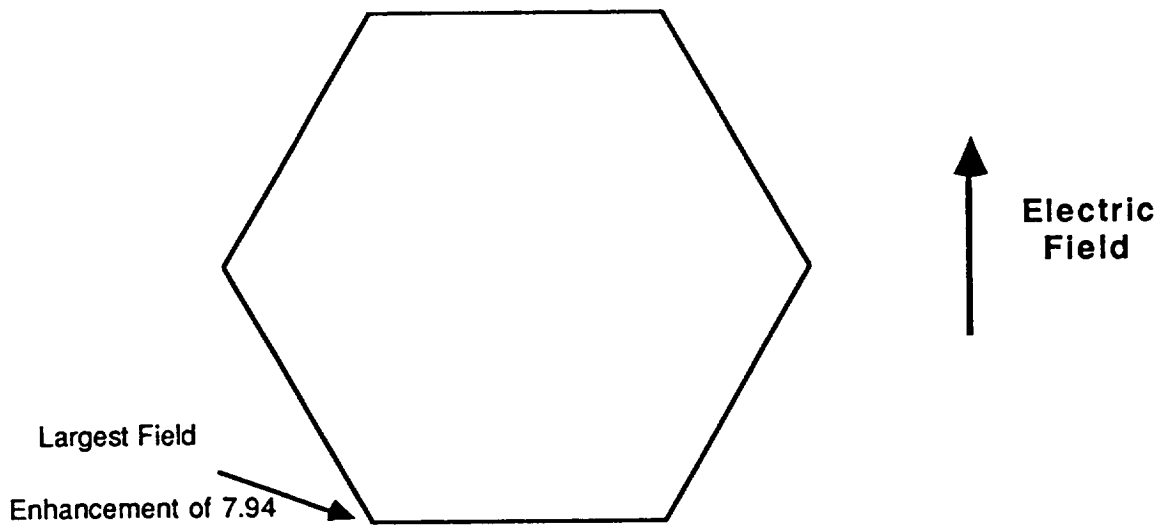


(c)

**Figure 11.2 Maximum Electric Field Enhancement Factors for the Hexagonal Column Ice Crystals for Three Different Electric Field Orientations**

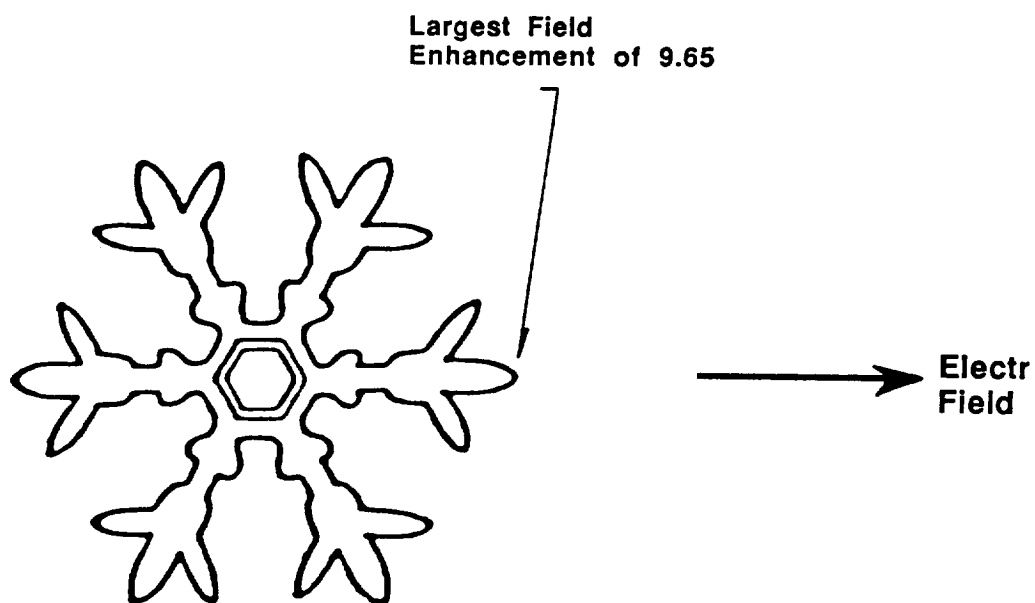


(a)

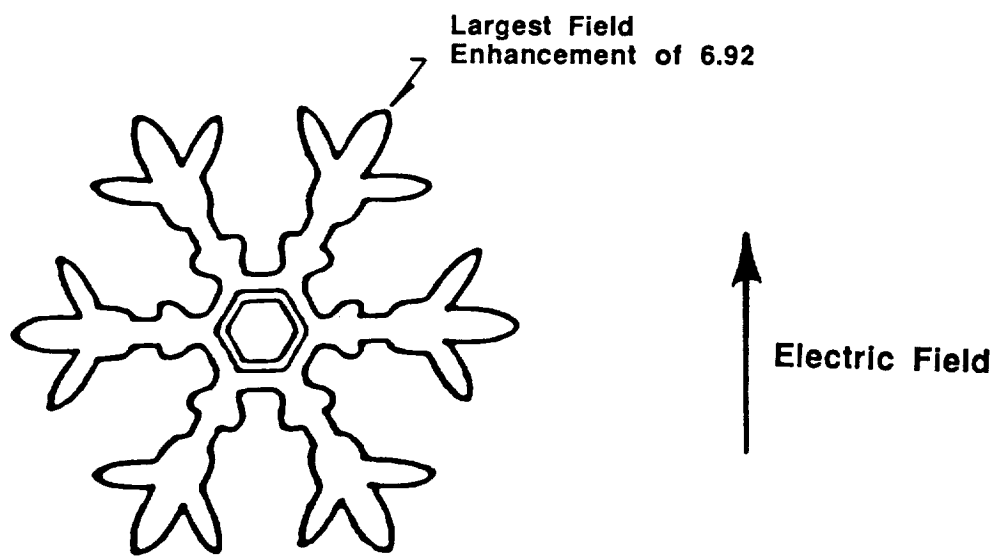


(b)

**Figure 11.3 Maximum Field Enhancements for Hexagonal Plate Ice Crystal**



(a)



(b)

**Figure 11.4** Maximum Field Enhancement for the Hexagonal Dendrite Ice Crystal



at high altitude. Therefore, the average separation is approximately two centimeters, or a factor of almost ten larger than the enhanced field region. Collective processes involving the interaction of enhanced fields should then be rare, at least previous to a lightning event. After discharge initiation, the much larger local electric fields around the discharge may make collective effects more likely.

To understand the importance of particle field enhancements, consider first the F106B flying in clear air in an ambient electric field. Enhancements of about ten times the ambient field are seen locally around the nose for a field oriented along the fuselage. Next assume a particle drifts into the volume where the enhanced field exists. The particle, if properly oriented, can produce another field enhancement of up to ten above the already enhanced field. This results in a local field around the particle which can be a factor of one hundred larger than the ambient field magnitude. Therefore, corona and possible air breakdown could conceivably occur in ambient field magnitudes as low as 10 to 30 kilovolts per meter, depending on altitude. Because particles can act to enhance already enhanced fields, they could possibly act as triggers for the initiation of triggered lightning strikes to the F106B. This possibility will be investigated in future work on the initiation of lightning.

## CHAPTER 12

### SUMMARY AND CONCLUSIONS

The present effort has concentrated in large part on inflight data gathered during the 1983 and 1984 thunderstorm seasons. Only a minimum amount of data from 1984 has as yet been analyzed in the depth of detail desired, but the multisensor character of the data holds great promise for future understanding. Classification of measured data from two years of flights has been completed, and the division into distinct categories, when coupled with linear and nonlinear modeling, allows some conclusions to be drawn. In particular, certain categories of waveshape can be shown to correlate with particular lightning attachment patterns. Ratios of peak response amplitudes can also give information on attachment points, and in addition, provide a quick and easy way to compare measured to calculated data.

The linear lightning model developed and applied in Chapters 3 and 4 is very useful in an engineering sense. It gives the analyst a way to systematically determine the shape and amplitude of the lightning current based on a few simple assumptions. The great utility lies in the fact that the model is linear, and is therefore much more easily and quickly used in investigating a lightning event than the more powerful, but cumbersome, nonlinear models. The linear model has been used to determine that lightning channel impedance (as determined by channel diameter) and resistance per unit length are relatively unimportant when dealing with sensor responses on the F106B. That is, the sensor responses are very strongly dependent on the entering current waveform, but only weakly dependent on the actual channel characteristics.

A skewed angle nonlinear parameter study has been partially completed, with electric field orientations not along principal aircraft axes. The study has been completed only for zero and negative net charges on the aircraft. The results are quite different from those in which the electric field is oriented along a principal axis. This implies that field orientation is important in the types of responses expected on the F106B. This may be true even for relatively small angle differences, such as twenty degrees or less.

A skewed angle nonlinear parameter study has been partially completed, with electric field orientations not along principal aircraft axes. The study has been completed only for zero and negative net charges on the aircraft. The results are quite different from those in which the electric field is oriented along a principal axis. This implies that field orientation is important in the types of responses expected on the F106B. This may be true even for relatively small angle differences, such as twenty degrees or less.

One goal of the NASA program is to intercept lightning strikes at low altitude. Lower altitude strikes are likely to be of larger amplitude, and if a main cloud to ground channel were to be intercepted, could range to as high as 200 kiloamps. To determine approximate response levels for this type of strike, a nonlinear model was developed in which a large current was injected at the nose of the F106B. The calculated response levels can be used as a guide in setting sensor sensitivity for possible cloud to ground strikes. It is also important to notice from the results that corona shielding and damping effects make any linear extrapolations from one aircraft to another questionable.

The ultimate goal of the NASA program is to characterize the lightning environment for all types of aircraft. Therefore, it is necessary to understand the responses of various aircraft to a triggered lightning environment. In this report, the triggering environment has been investigated for five aircraft. The results show that the shape of the aircraft and its orientation with respect to the ambient electric field are the major determining factors in whether the aircraft will trigger a lightning strike. The shape of the aircraft determines the minimum field necessary to produce lightning, and the orientation determines how far above the minimum field the actual strike will occur. Comparisons have also been done of the response amplitudes and waveshapes calculated for the different aircraft. The results show that linear scaling arguments are useful only in a qualitative sense, and that nonlinear calculations are necessary to get quantitative comparisons.

In an effort to model the initiation of a lightning strike beyond the first microsecond, an enhanced two dimensional nonlinear model has been developed. It includes the effects of electron temperature and molecular vibrational energy states in a fluid model containing charge, momentum, and energy conservation equations. The model has been applied to only one experimental situation, and needs more

verification. It also needs more analytical work to make it as computer efficient as possible. It is hoped that the model will eventually be able to follow the glow to arc transition in a lightning discharge.

The importance of enhancement factors in determining the ambient field levels at which triggered lightning will occur has motivated the development of the three dimensional subgrid model. This model allows one to resolve in greater detail sharp points (such as the nose) of an aircraft. Because the sharp points are often the places where a discharge originates, the resolution there is important. In this report, the final development and testing of the subgrid is documented. The first application, around the nose of the F106B, is also documented. The results show a significant increase in the field enhancement factor over the model without the subgrid. This leads one to believe that even more resolution may be necessary to finally determine maximum enhancement factors.

The thunderstorm environment has also been investigated. The particle characteristics at various altitudes will be used in the future to better determine the conditions required for triggered and natural lightning. As a first step, the field enhancement factors around typical ice crystals have been calculated. These factors are similar to those found on the F106B, and can cause large local enhancements when placed in the already enhanced fields existing around the F106B. Future work involves incorporating the effects of these particle enhancements in linear and nonlinear models.

Future application of the work presented here includes several objectives. The nonlinear parameter study will be completed for the positive net charge values. It may also be extended to a finer matrix of field orientations, because of the great variety seen in the responses with the orientations used to date.

The enhanced nonlinear model will be examined in detail in order to determine ways in which it can be made more efficient. Physical processes which have little effect will be eliminated or approximated in less detail to increase computational speed. The model will then be applied to physical problems and experiments to ascertain its range of validity.

The subgrid will be applied in both linear and nonlinear models. This will provide an answer to whether the nose boom of the F106B is important to the responses seen on the aircraft. It will also determine whether there is some threshold volume of high electric field necessary to initiate a lightning discharge.

The thunderstorm environment, and in particular the particle environment, will be incorporated into lightning models to determine its effect on trigger levels and responses. It will also be investigated in connection with the lightning initiation conditions, because particles may play a significant role in this process.

## REFERENCES

- [1] Rudolph, T., and R.A. Perala, "Interpretation Methodology and Analysis of Inflight Lightning Data," NASA CR-3590, October 1982.
- [2] Merewether, D.E. and R. Fisher, "Finite Difference Solution of Maxwell's Equation for EMP Applications," Report EMA-79-R-4 (Revised), Electro Magnetic Applications, Inc. (EMA), P.O. Box 8482, Albuquerque, NM 98198, April, 1980.
- [3] Rudolph, T., and R.A. Perala, "Linear and Nonlinear Interpretation of the Direct Strike Lightning Response of the NASA F-106B Thunderstorm Research Aircraft," NASA CR-3746, March 1983.
- [4] Rudolph, T., and R.A. Perala, "Studies in Increasing the Probability that the NASA F-106B Thunderstorm Research Aircraft Will Be Struck By Lightning at Low Altitudes," EMA-85-R-24, February, 1985.
- [5] Le Vine, D.M., and V. Mazur, "Correlated Measurements of UHF Radar Signatures, R.F. Radiation, and Electric Field Changes from Lightning," Proc. of the 8th Int. Aerospace and Ground Conf. on Lightning and Static Electricity, June 1983.
- [6] Fowler, R.G., "A Trajectory Theory of Ionisation in Strong Electric Fields," J. Phys. B: At. Mol. Phys. **16**, 1983, p. 4495-4510.
- [7] Magono, C., and C.W. Lee, "Classification of Natural Snow Crystals," J. Fac. Sci., Hokkaido University, Ser. 7, 2, No. 4, 1966.
- [8] Braham, R.R. Jr., "The Water and Energy Budgets of the Thunderstorm and Their Relation to Thunderstorm Development," J. Meteorol., **4**, 1952.
- [9] Orville, Harold D., and Fred J. Kopp, "Numerical Simulation of the Life History of a Hailstorm," J. Atmos. Sci. **34**, No. 10, October 1977.
- [10] Lin, Yuh-Lang, Richard D. Farley, and Harold D. Orville, "Bulk Parameterization of the Snow Field in a Cloud Model," J. Climate and Applied Meteorology, **22**, No. 6, June 1983.
- [11] Wilson, C.T.R., "Some Thundercloud Problems," J. Franklin Institute, **208**, 1929.
- [12] Sartor, J.D., "Calculations of Cloud Electrification Based on a General Charge Separation Mechanism," J. Geophys. Res., **66**, 1961.
- [13] Paluch, I.R., and J.D. Sartor, "Thunderstorm Electrification by the Inductive Charging Mechanism: I. Particle Charges and Electric Fields." J. Atmos. Sci., **30**, 1973.

## REFERENCES - continued

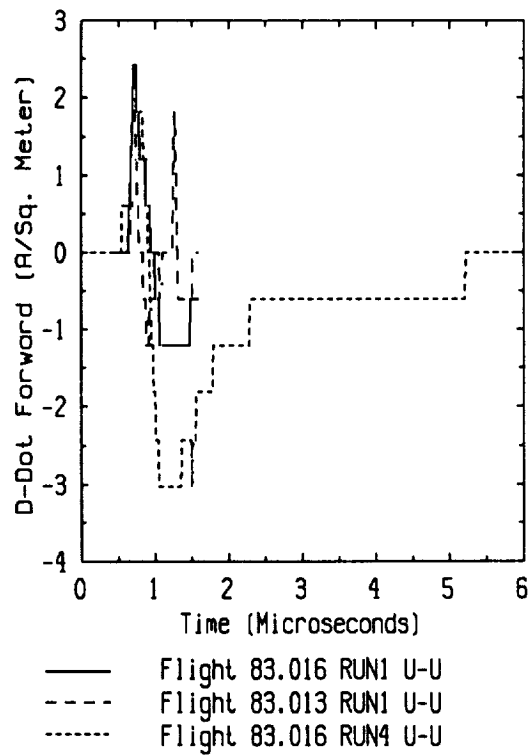
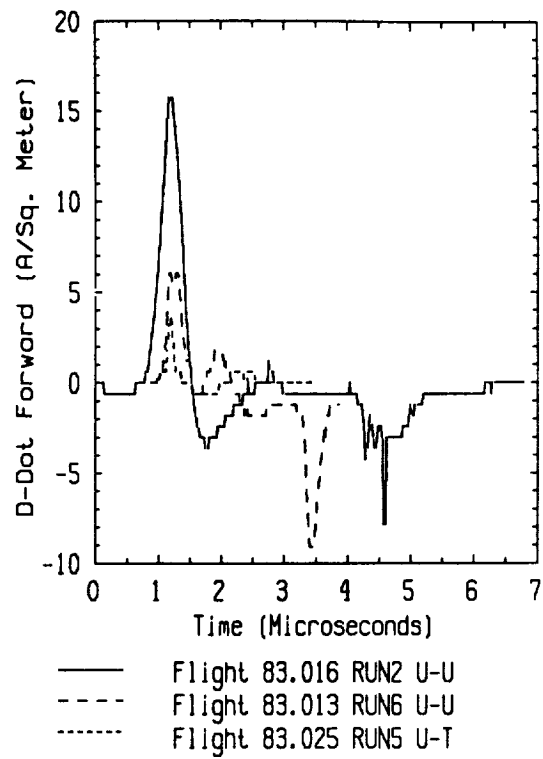
- [14] Workman, E.J., and S.E. Reynolds, "A Suggested Mechanism for the Generation of Thunderstorm Electricity," *Phys. Rev.*, 74, 1948.
- [15] Latham, J., and R. Warwicker, "Charge Transfer Accompanying the Splashing of Supercooled Raindrops on Hailstones," *Quart. J. Roy. Meteor. Soc.*, 106, 1980.
- [16] Latham, J., and B.J. Mason, "Generation of Electric Charge Associated with the Formation of Soft Hail in Thunderclouds," *Proc. Roy. Soc.*, A260, 1961.
- [17] Hallett, J., and C.P.R. Saunders, "Charge Separation Associated with Secondary Ice Crystal Production," *J. Atmos. Sci.*, 36, 1979.
- [18] Saunders, C.P.R., M.F.S. Wheeler, N. Jallo, and E.R. Jayaratne, "Ice Crystal Interaction With a Riming Target: Charge Transfer and Collection Efficiencies." VII International Conference on Atmospheric Electricity, American Meteorological Society, June, 1984.
- [19] Telford, J.W., and P.B. Wagner, "Electric Charge Separation in Severe Storms," *Pure Appl. Geophys.*, 117, 1979.
- [20] Fisher, Bruce D., J.A. Plumer, and J. Anderson, "Lightning Attachment Patterns and Flight Conditions Experienced by the NASA F106B Airplane," *Proc. Eighth Inter. Aero. and Gnd. Conf. on Lightning and Static Elec.*, Ft. Worth, Texas, June 1983. DOT/FAA/CT-83-25 Supplement.
- [21] MacGormon, D.R., W.L. Taylor, and W.D. Rust, "Some Characteristics of Lightning in Severe Storms on the Great Plains of the United States," VII International Conference on Atmospheric Electricity., American Meteorological Society, June 1984.
- [22] Thomas, M.E., "1983 Direct Strike Lightning Data," NASA TM-86426, August 1985.



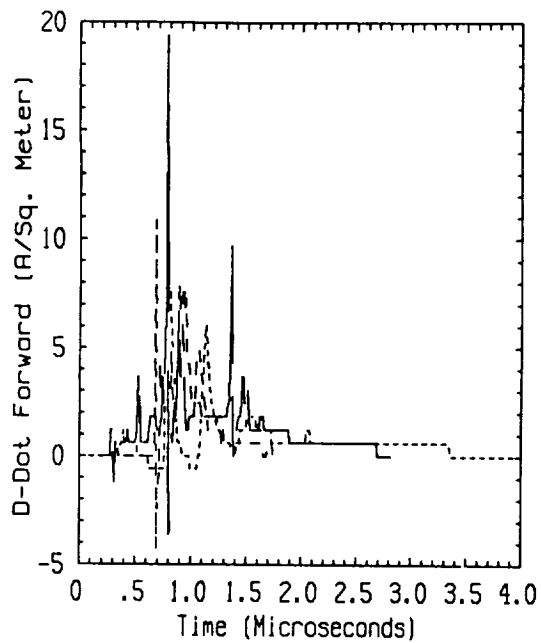


## **APPENDIX A (D-dot)**

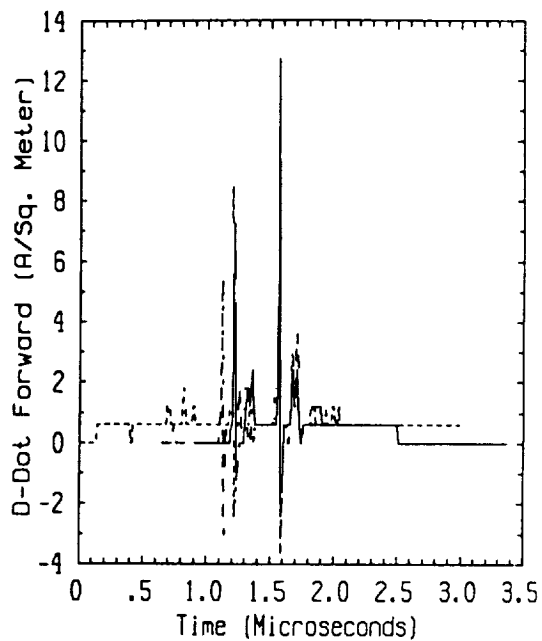
### **PLOTS OF THE 1983 IN-FLIGHT LIGHTNING DATA**



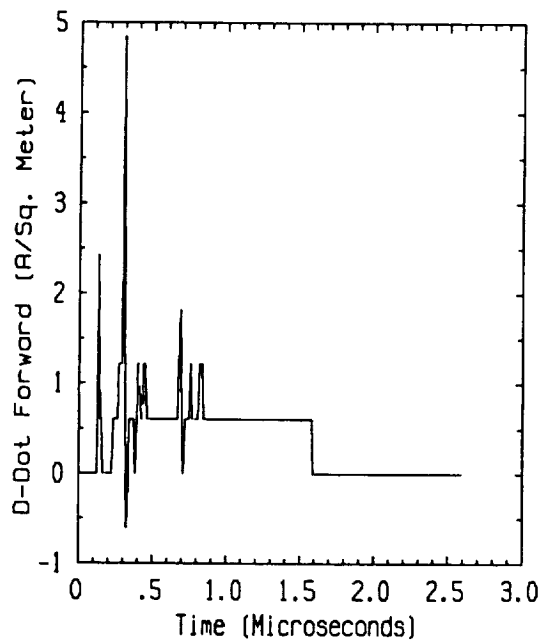
**Figure A.1 D-dot Category 1**



— Flight 83.036 RUN7 NEAR  
 --- Flight 83.013 RUN7 U-U  
 ..... Flight 83.032 RUN6 U-M

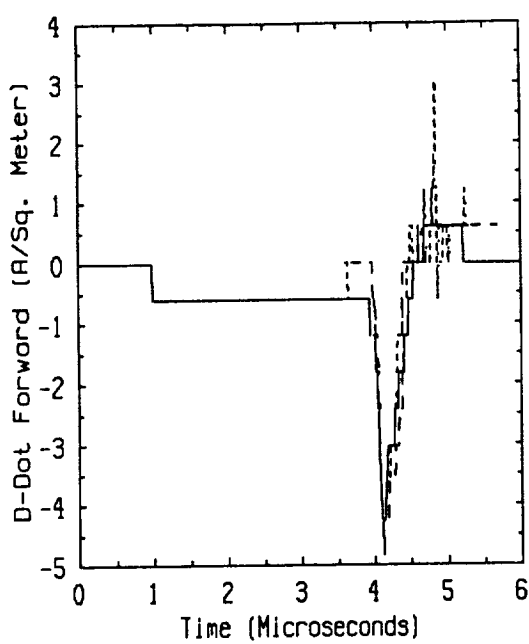


— Flight 83.036 RUN1 NEAR  
 --- Flight 83.036 RUN3 U-T  
 ..... Flight 83.024 RUN4 U-U

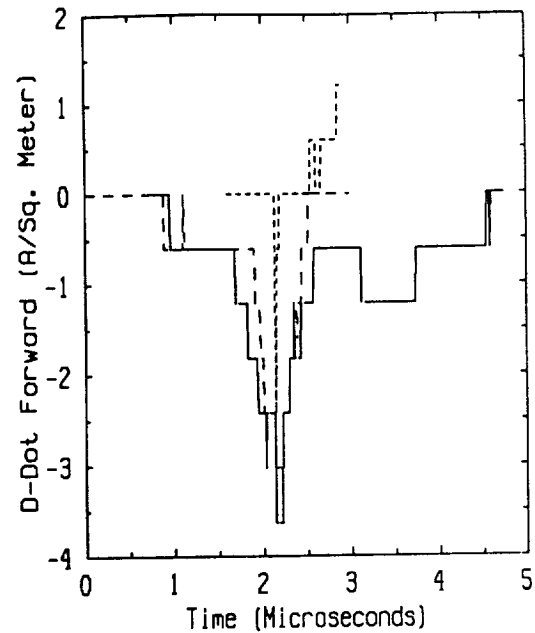


Flight 83.032 RUN1 U-T

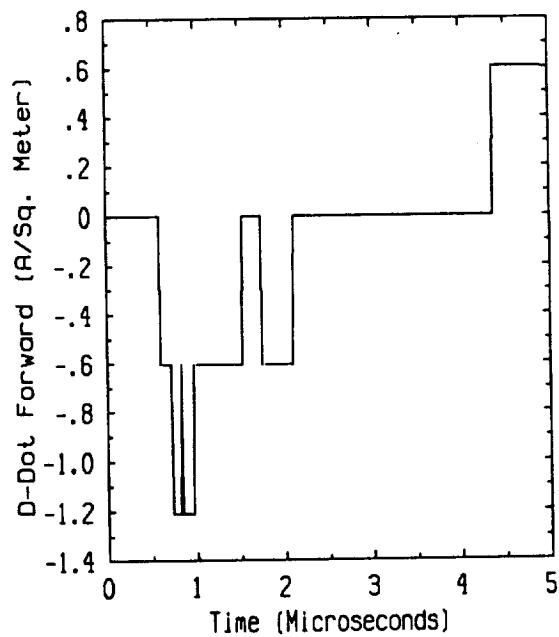
**Figure A.2 D-dot Category 2**



— Flight 83.016 RUN4 U-U  
 --- Flight 83.033 RUN1 U-U  
 ..... Flight 83.015 RUN2 U-U



— Flight 83.016 RUN2 U-U  
 --- Flight 83.016 RUN1 U-U  
 ..... Flight 83.013 RUN1 U-U

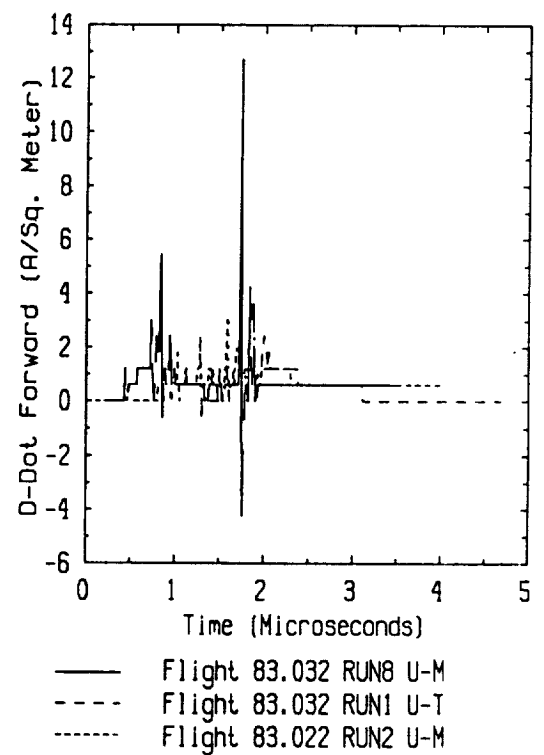
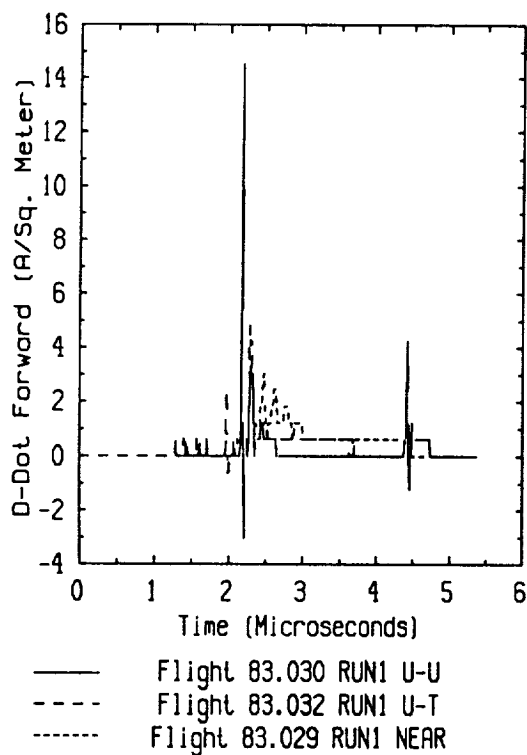
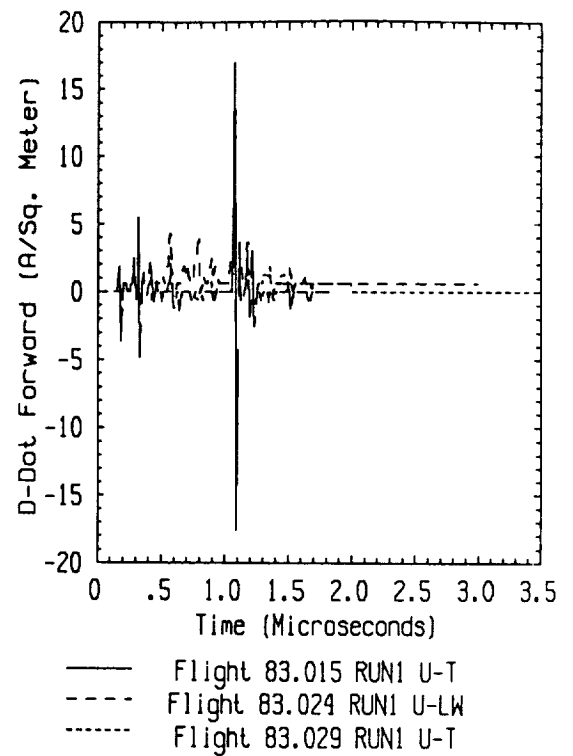
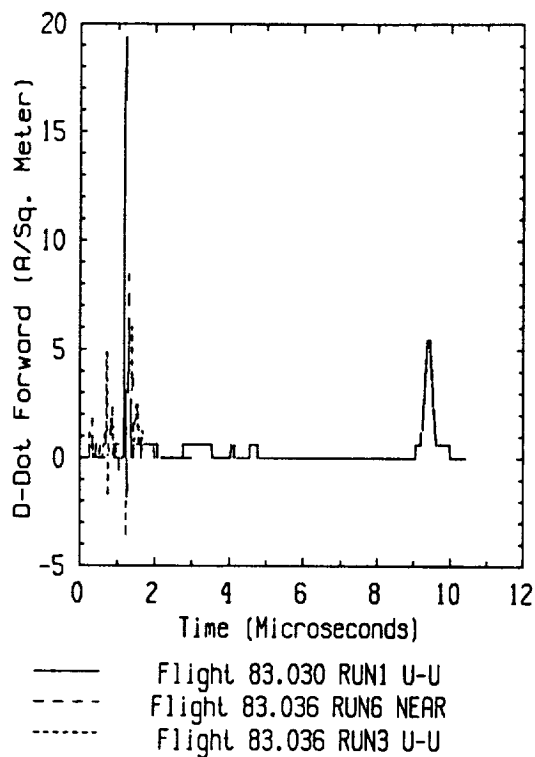


Flight 83.016 RUN1 U-U

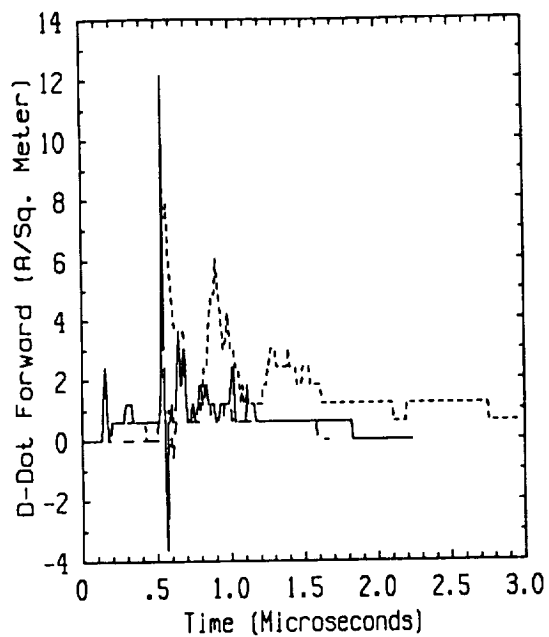
**Figure A.3 D-dot Category 3**

**No Data From the 1983 Thunderstorm Season  
Was Classified in This Category**

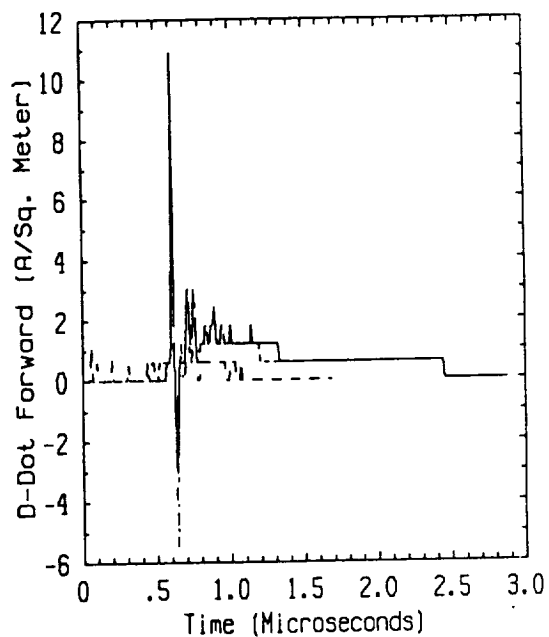
**Figure A.4 D-dot Category 4**



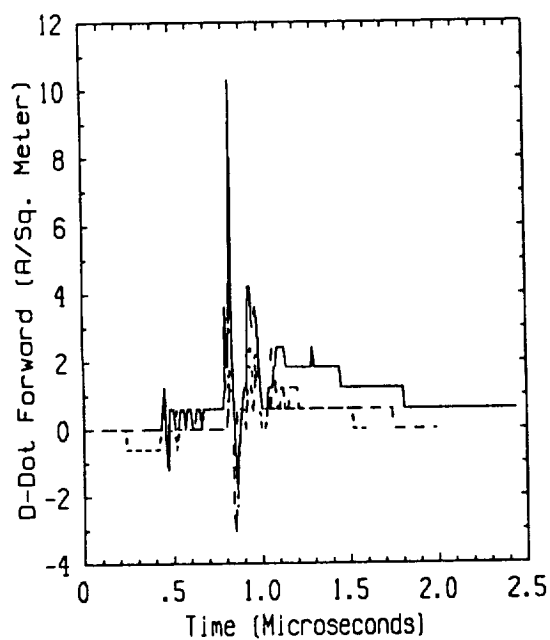
**Figure A.5 (a) D-dot Category 5**



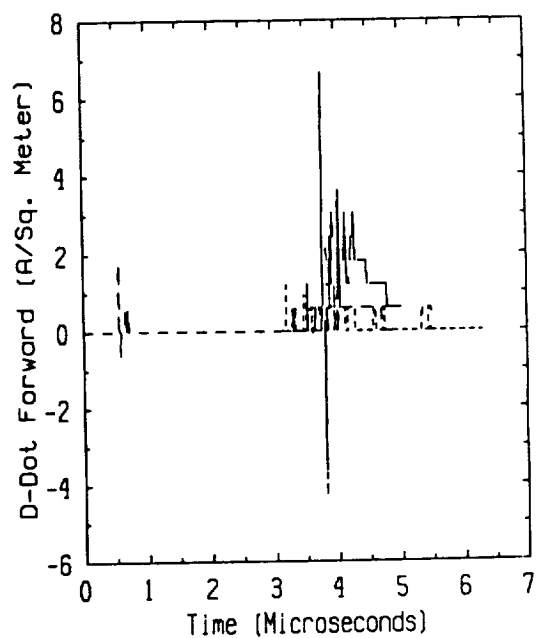
— Flight 83.033 RUN1 U-U  
 --- Flight 83.013 RUN4 U-T  
 ..... Flight 83.016 RUN1 U-U



— Flight 83.029 RUN9 U-U  
 --- Flight 83.030 RUN9 U-U  
 ..... Flight 83.033 RUN1 NEAR

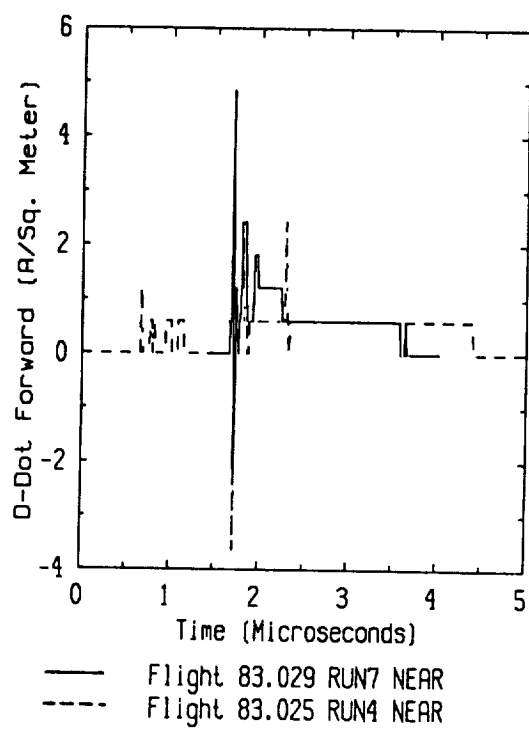


— Flight 83.036 RUN5 NEAR  
 --- Flight 83.025 RUN8 U-M  
 ..... Flight 83.020 RUN1 U-T



— Flight 83.030 RUN2 NEAR  
 --- Flight 83.030 RUN4 U-LW  
 ..... Flight 83.029 RUN1 NEAR

**Figure A.5 (b) D-dot Category 5 (continued)**



**Figure A.5 (c) D-dot Category 5 (continued)**



ORIGINAL PAGE IS  
OF POOR QUALITY

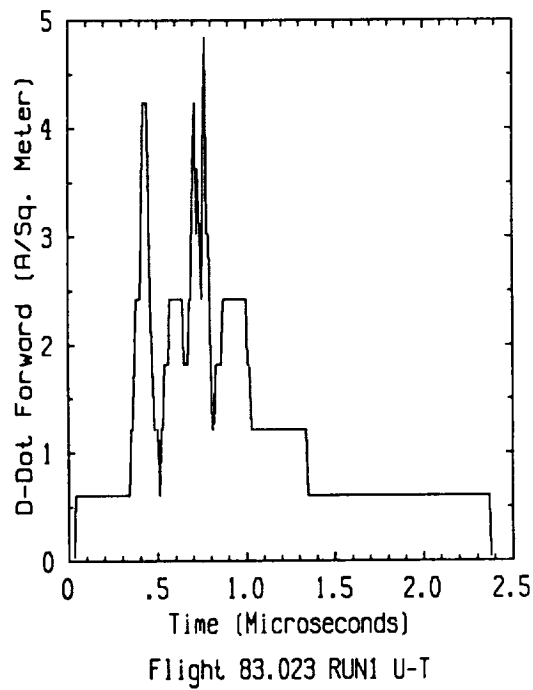
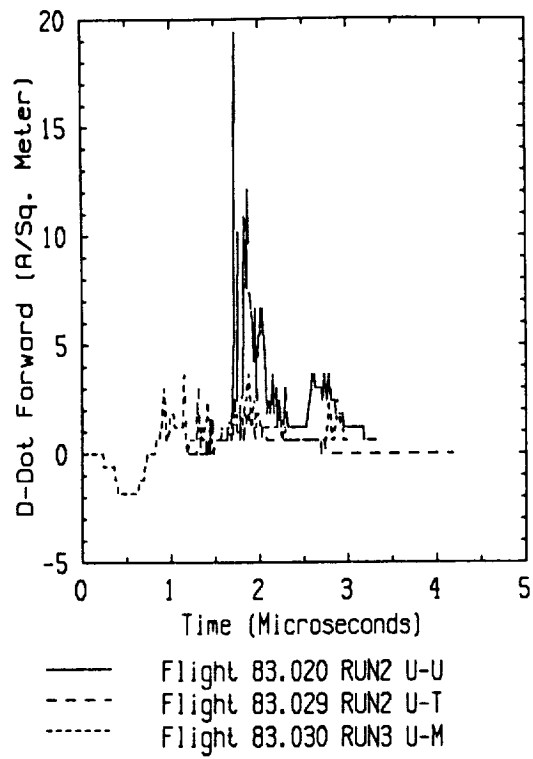
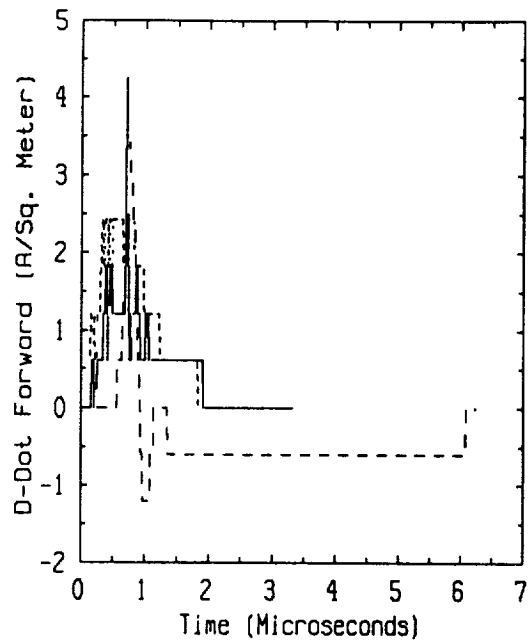
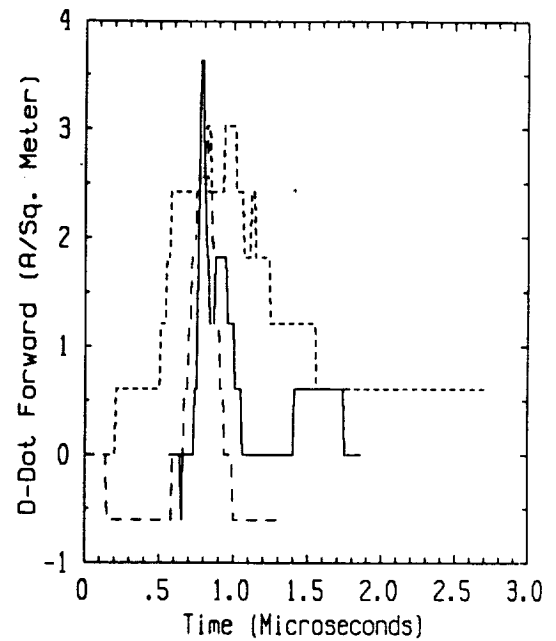


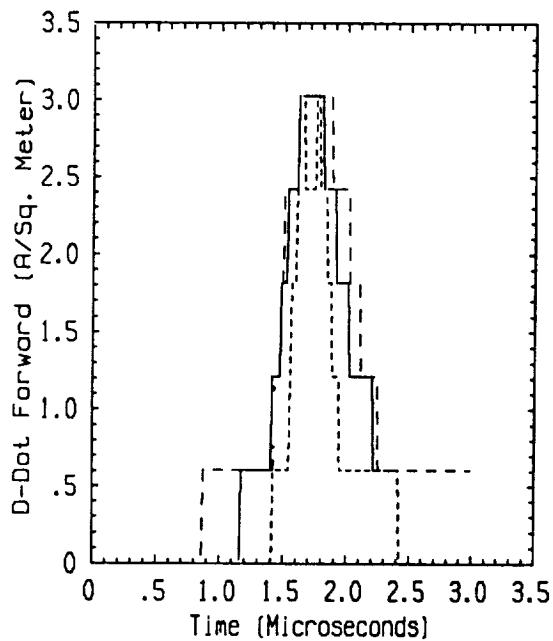
Figure A.6 D-dot Category 6



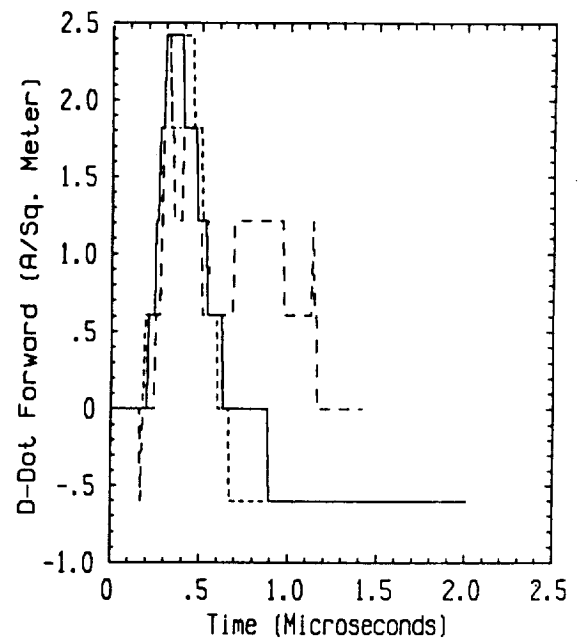
— Flight 83.036 RUN2 U-U  
 --- Flight 83.015 RUN2 U-U  
 ..... Flight 83.032 RUN6 U-M



— Flight 83.015 RUN2 U-U  
 --- Flight 83.030 RUN1 U-U  
 ..... Flight 83.021 RUN3 U-U



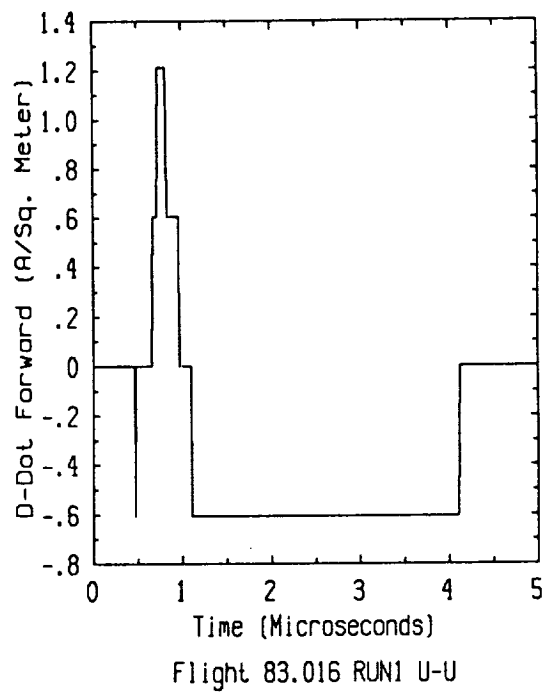
— Flight 83.029 RUN4 U-U  
 --- Flight 83.032 RUN1 U-T  
 ..... Flight 83.033 RUN1 U-U



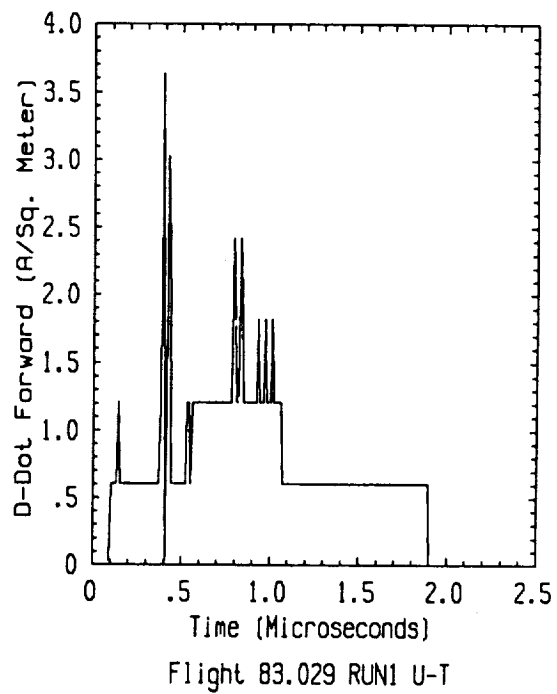
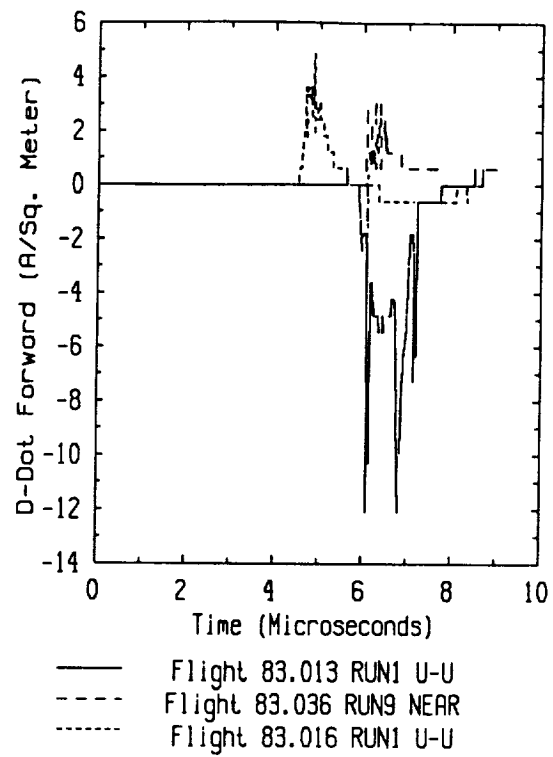
— Flight 83.030 RUN3 U-M  
 --- Flight 83.015 RUN2 U-U  
 ..... Flight 83.016 RUN1 U-U

**Figure A.7 (a) D-dot Category 7**

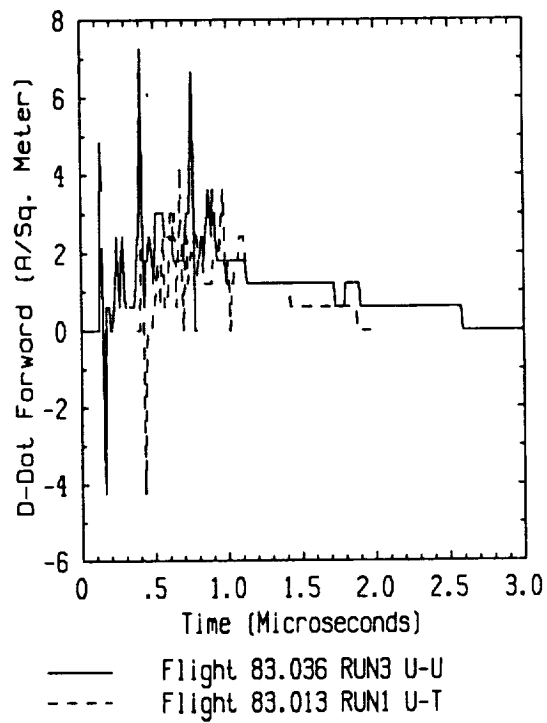
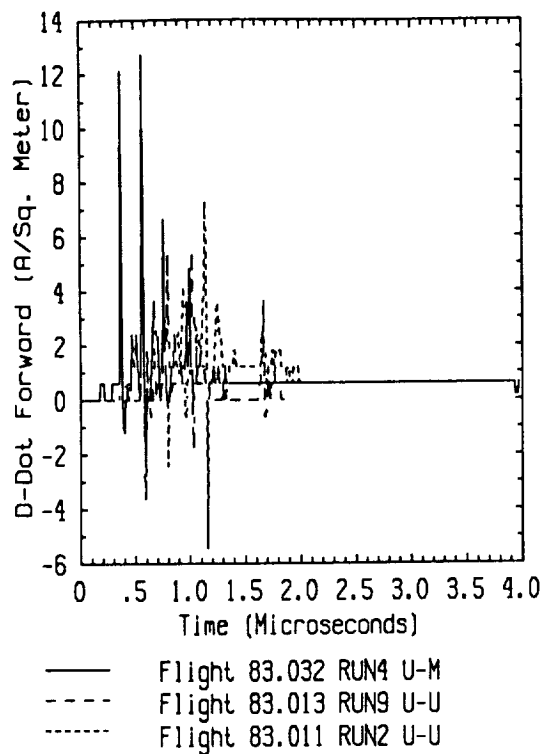
**ORIGINAL PAGE IS  
 OF POOR QUALITY**



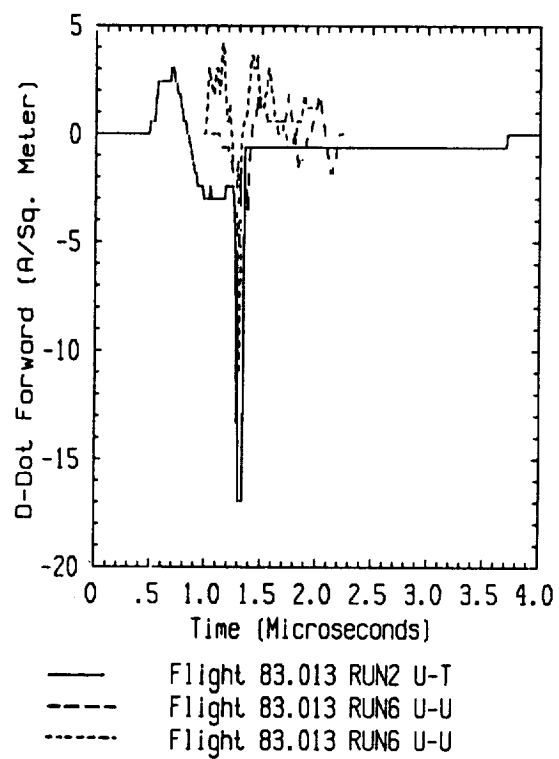
**Figure A.7 (b) D-dot Category 7 (continued)**



**Figure A.8 D-dot Category 8**



**Figure A.9 D-dot Category 9**



**Figure A.10 D-dot Category 10**

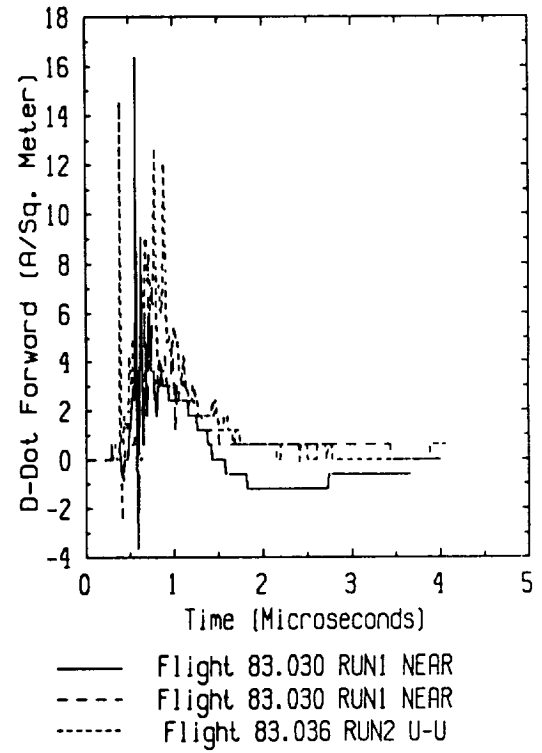
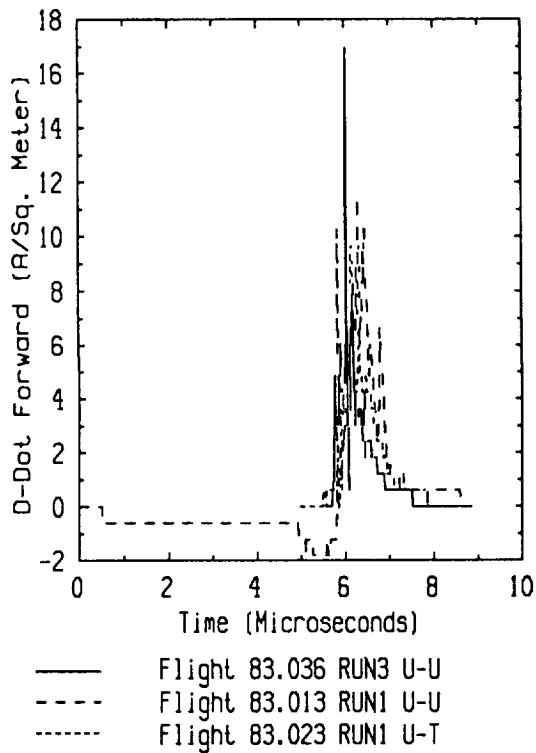
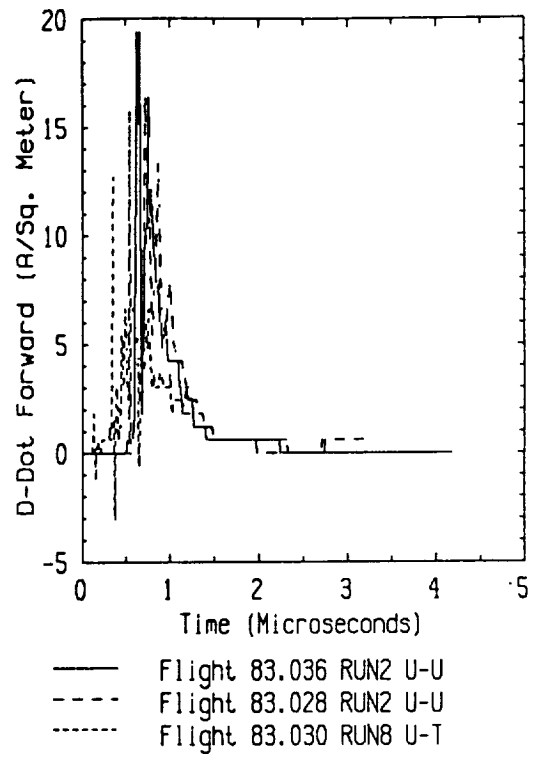
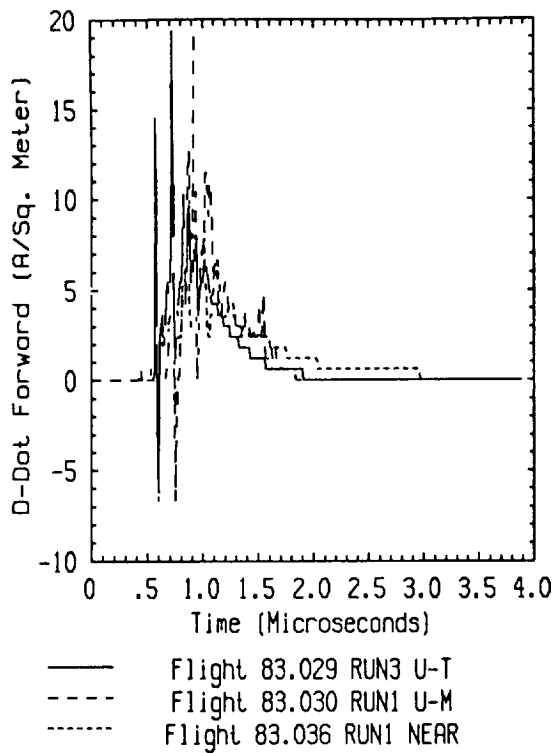
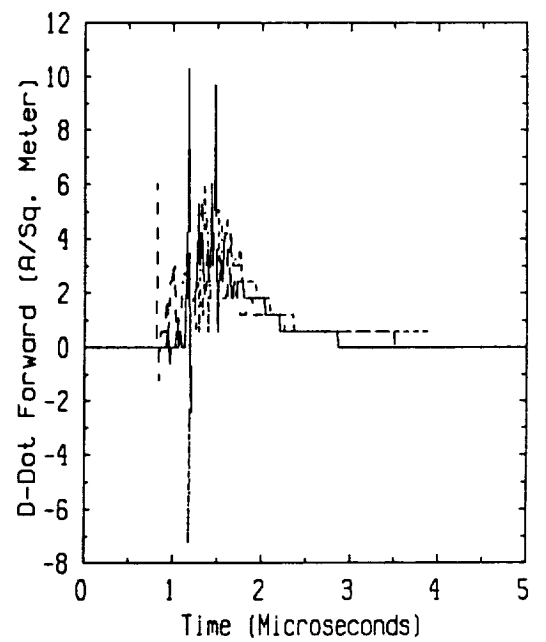
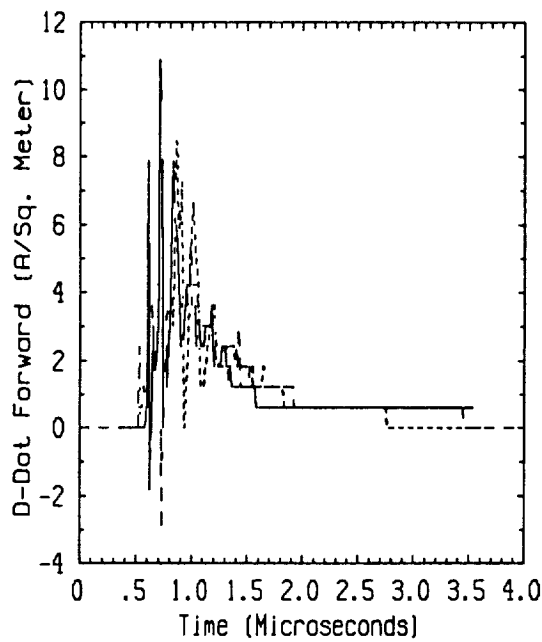
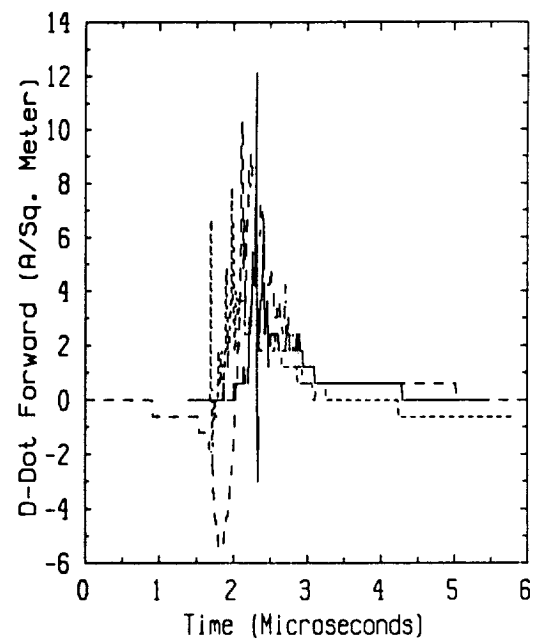
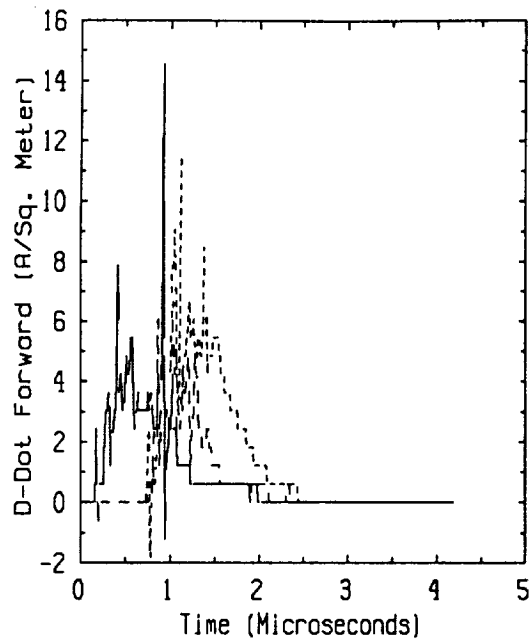
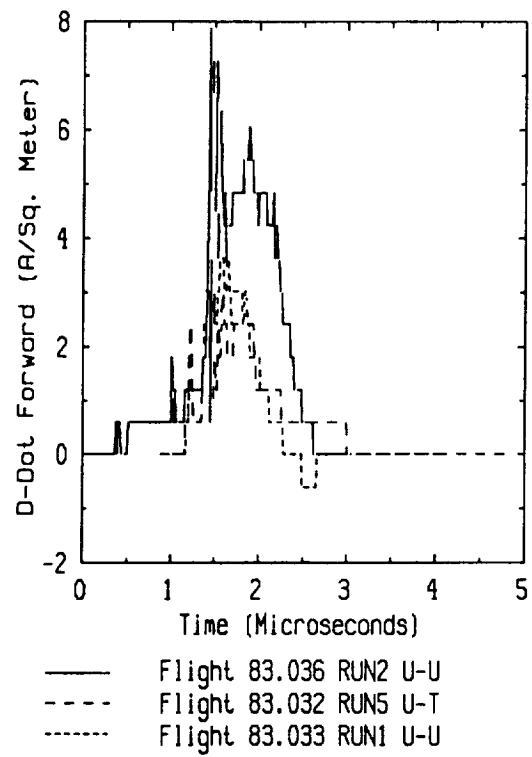
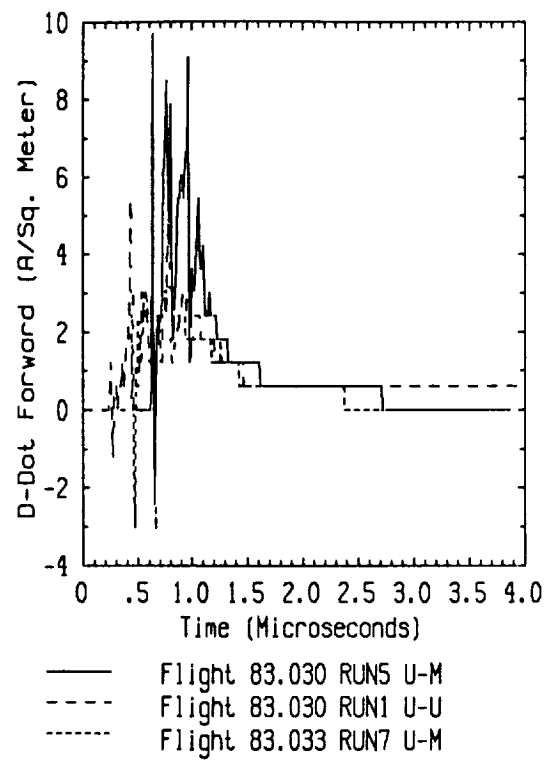


Figure A.11 (a) D-dot Category 11



**Figure A.11 (b) D-dot Category 11 (continued)**

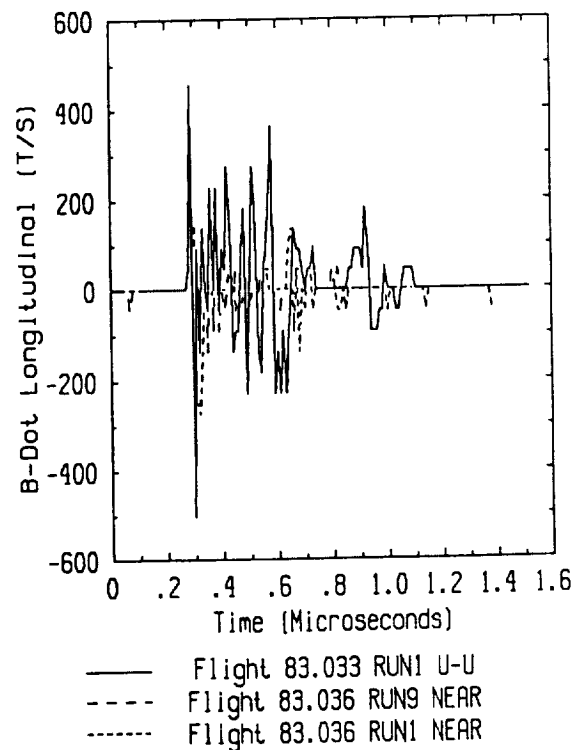
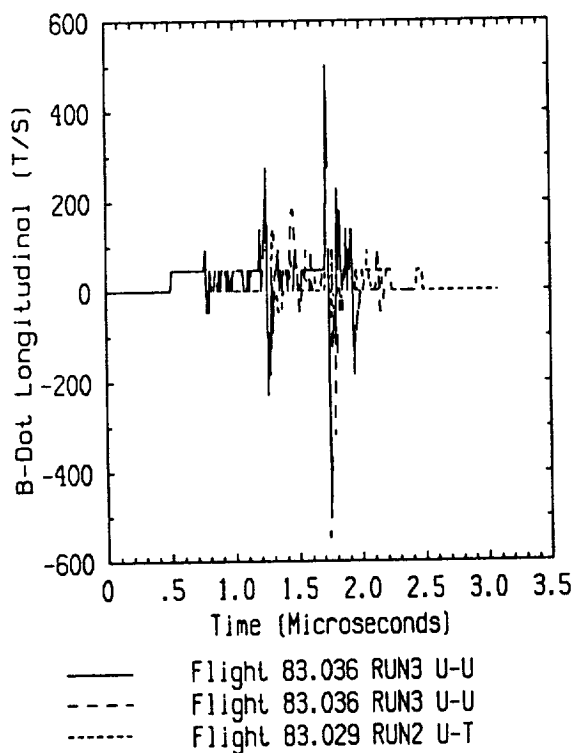
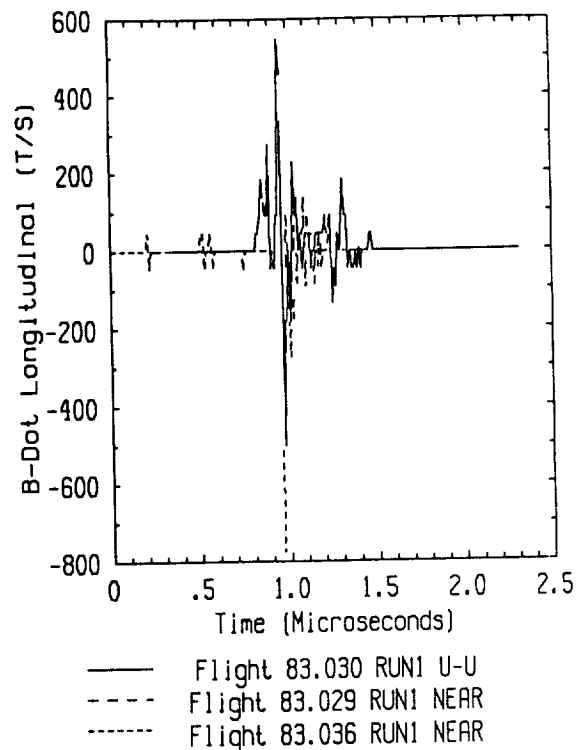
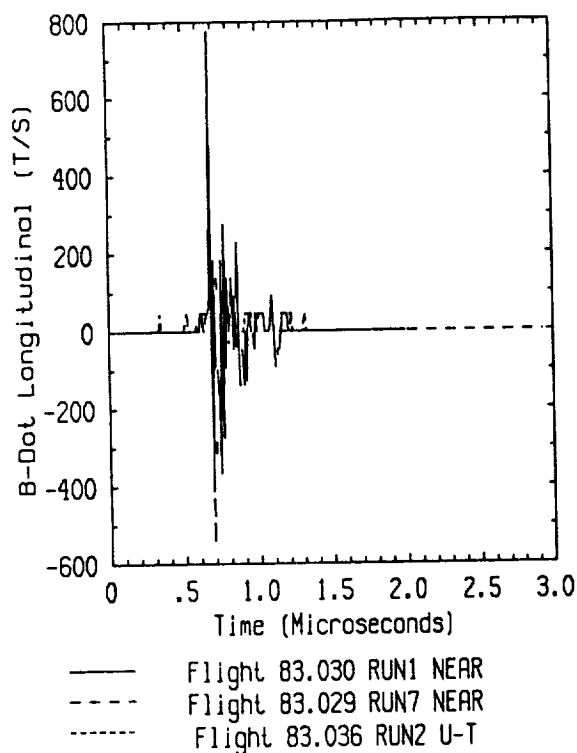




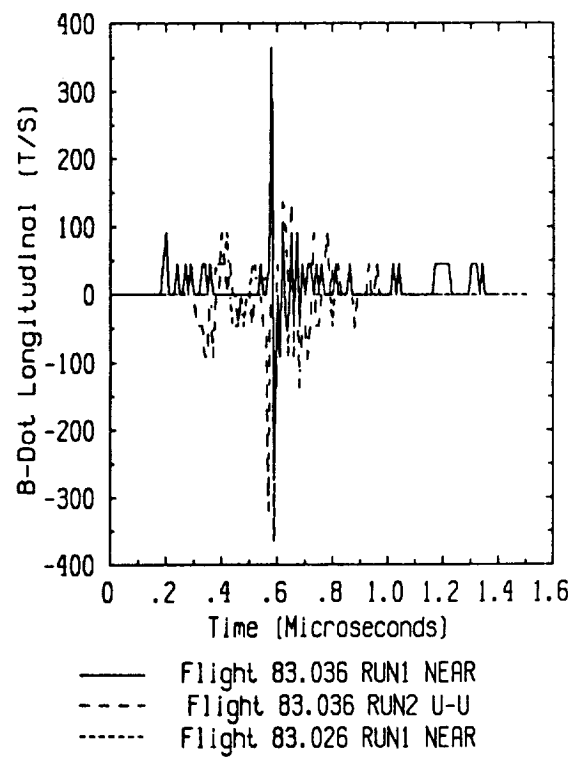
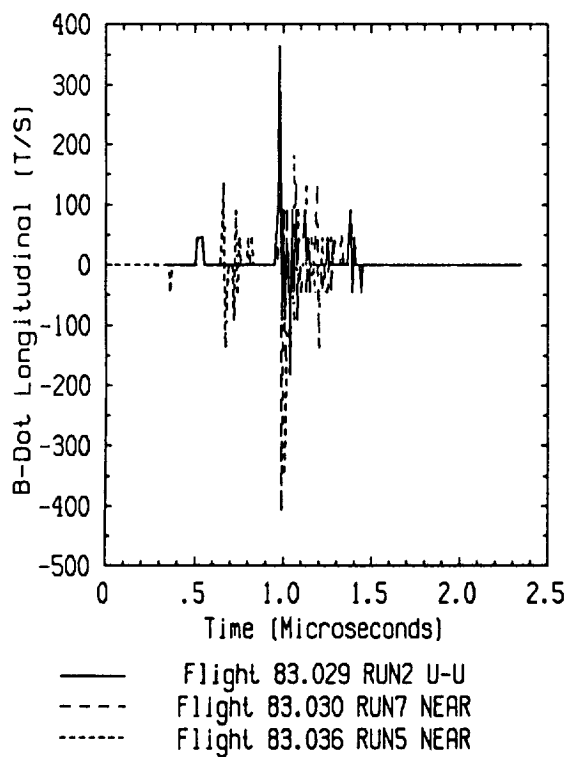
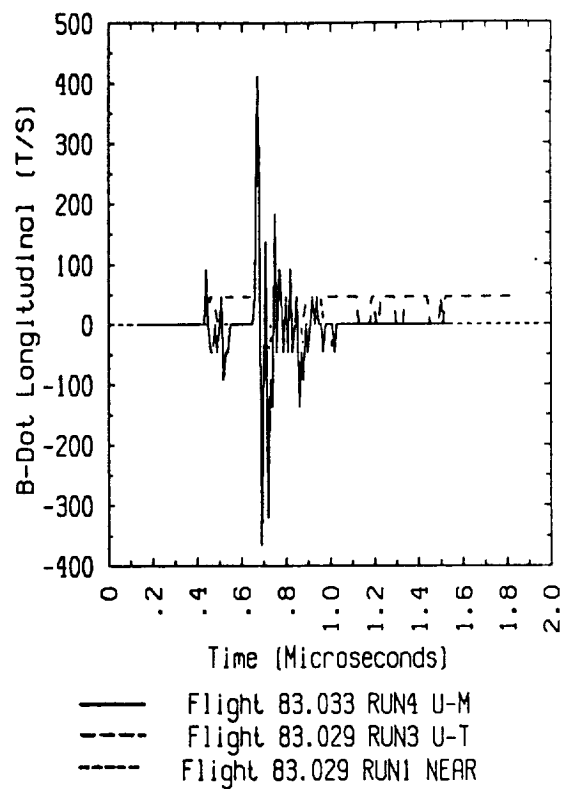
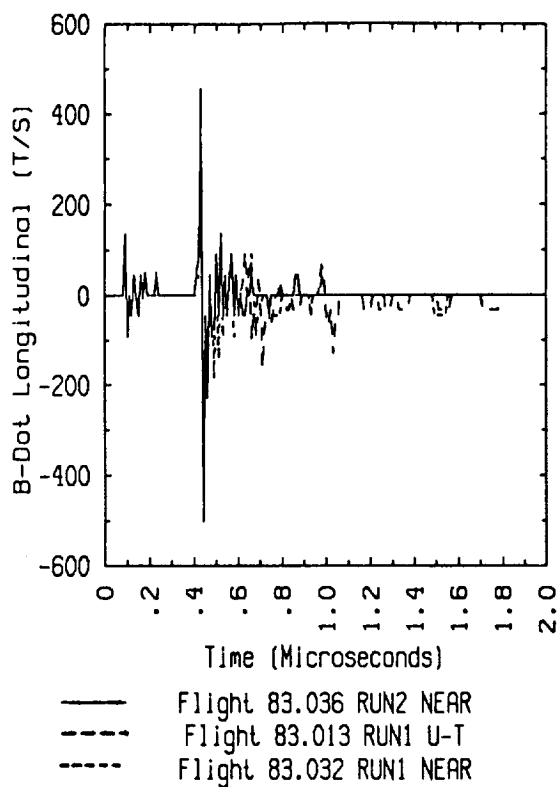
**Figure A.11 (c) D-dot Category 11 (continued)**



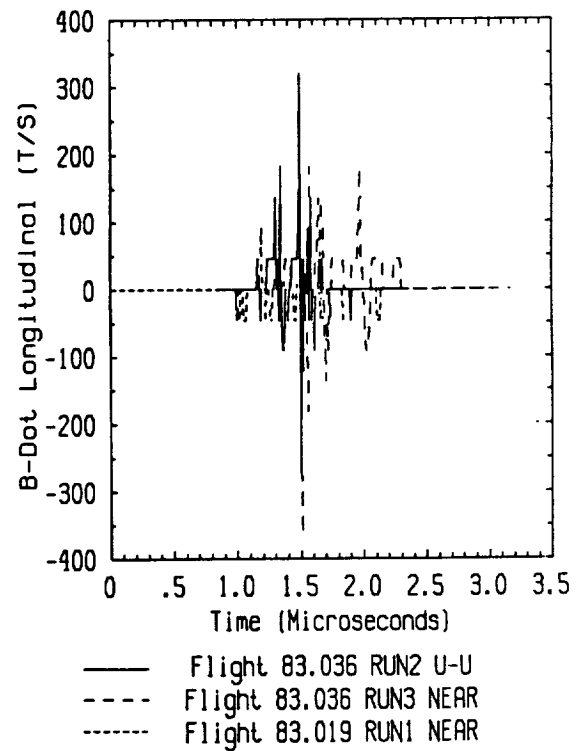
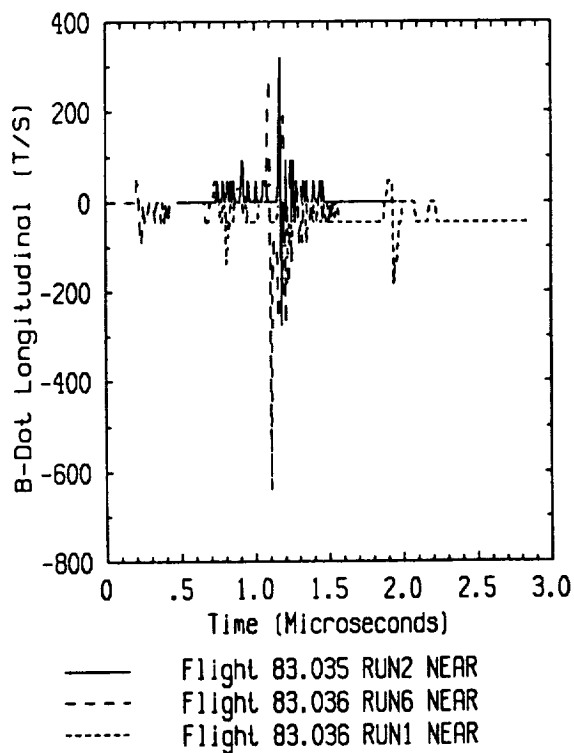
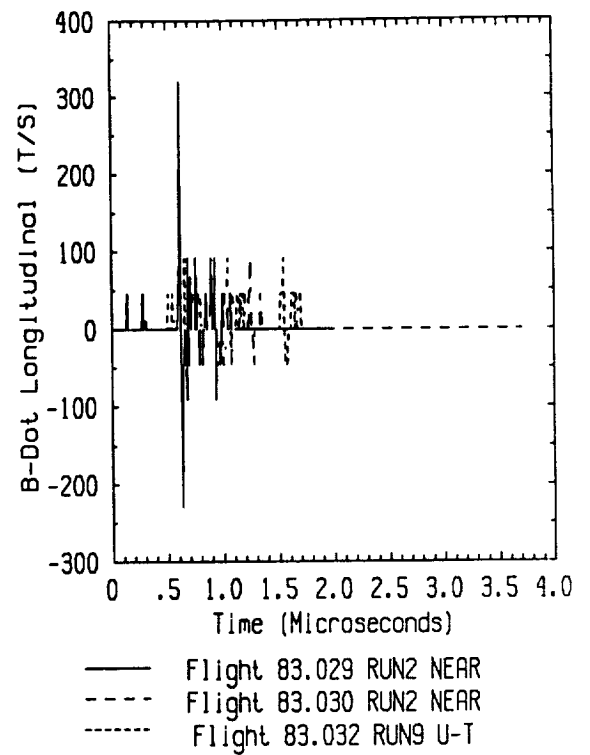
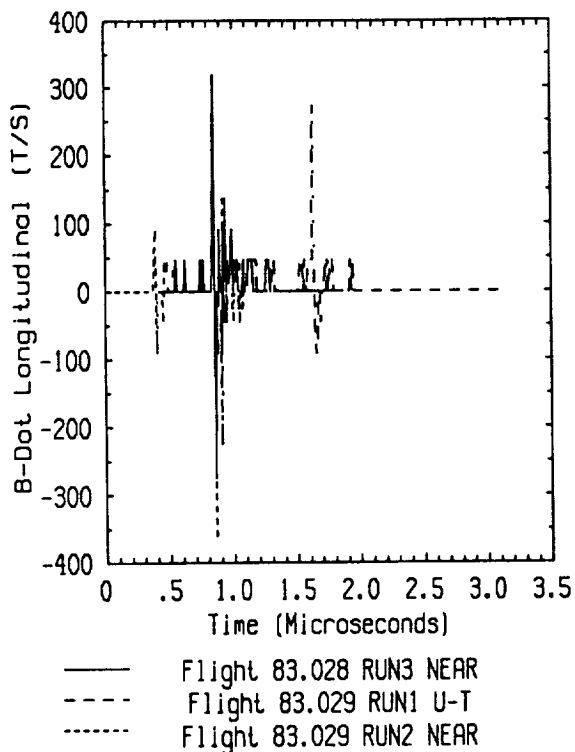
**APPENDIX B (B-dot)**  
**PLOTS OF THE 1983 IN-FLIGHT LIGHTNING DATA**



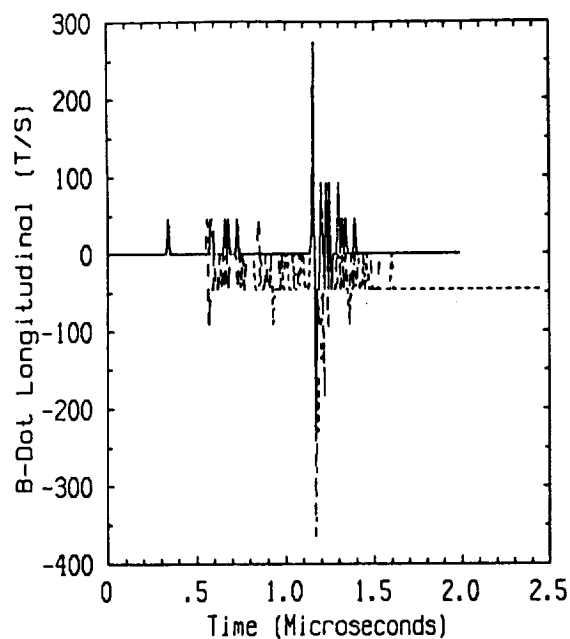
**Figure B.1 (a) B-dot Category 1**



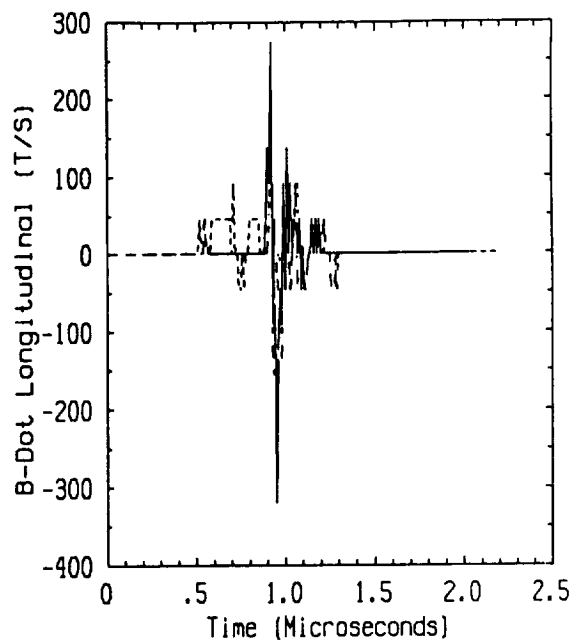
**Figure B.1 (b) B-dot Category 1 (continued)**



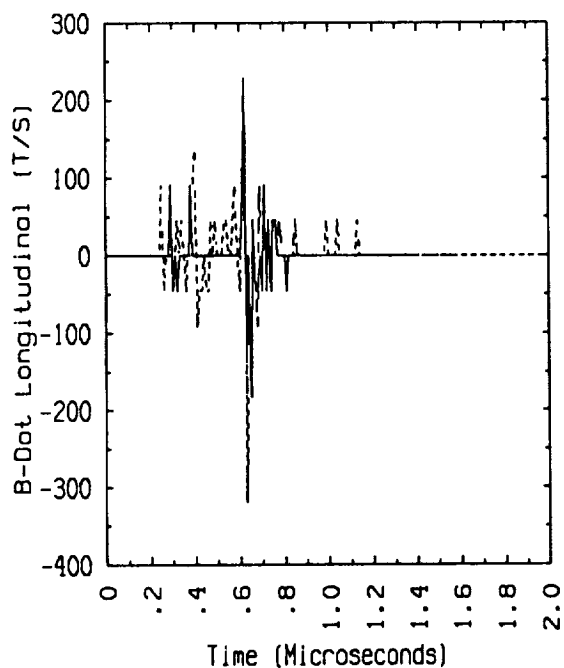
**Figure B.1 (c) B-dot Category 1 (continued)**



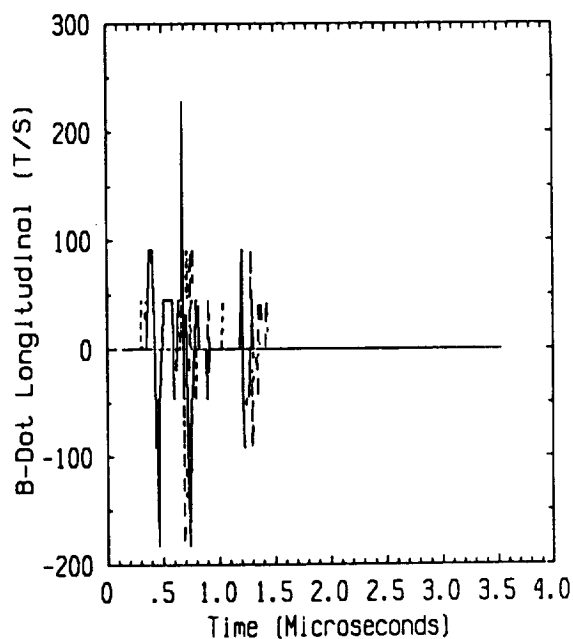
— Flight 83.028 RUN2 U-U  
 --- Flight 83.029 RUN1 NEAR  
 - - - Flight 83.029 RUN2 NEAR



— Flight 83.032 RUN1 NEAR  
 --- Flight 83.025 RUN9 NEAR  
 - - - Flight 83.028 RUN1 NEAR

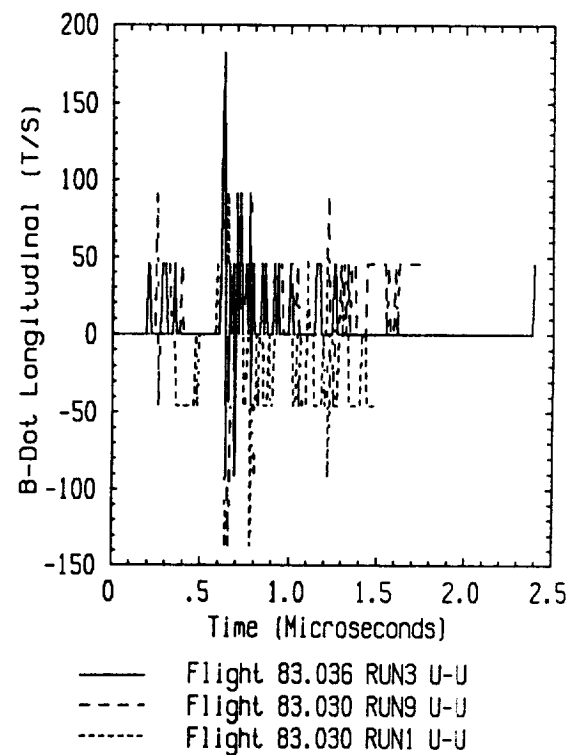
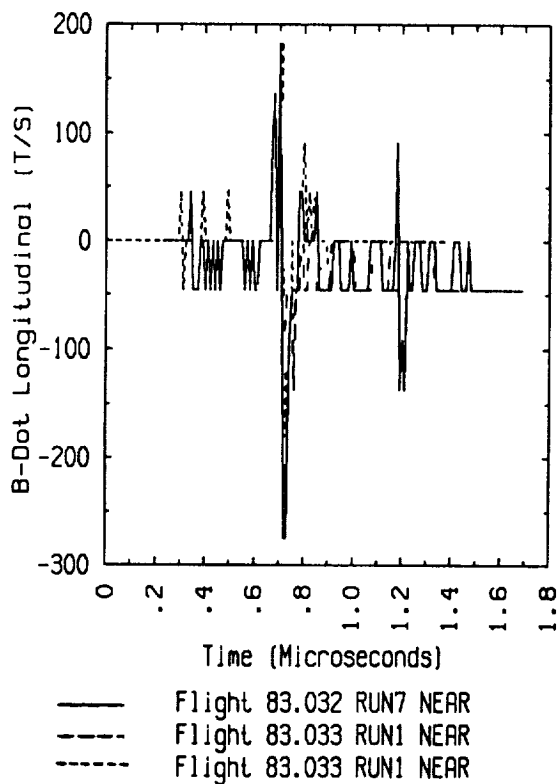
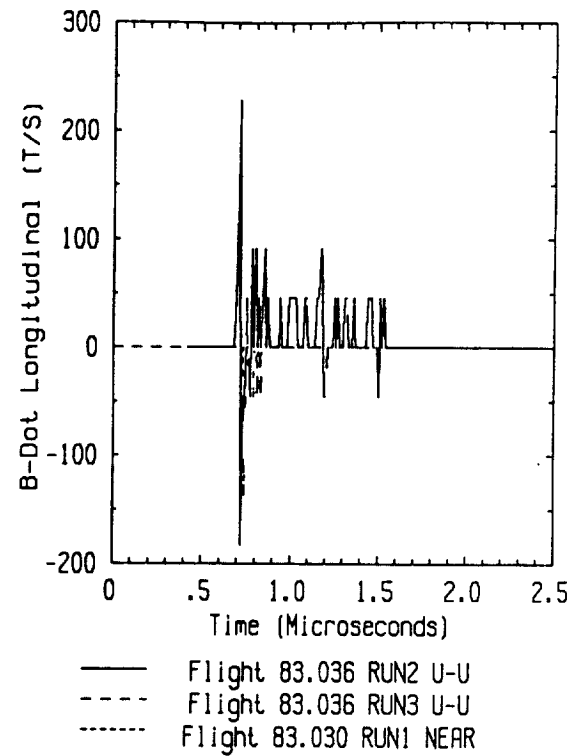
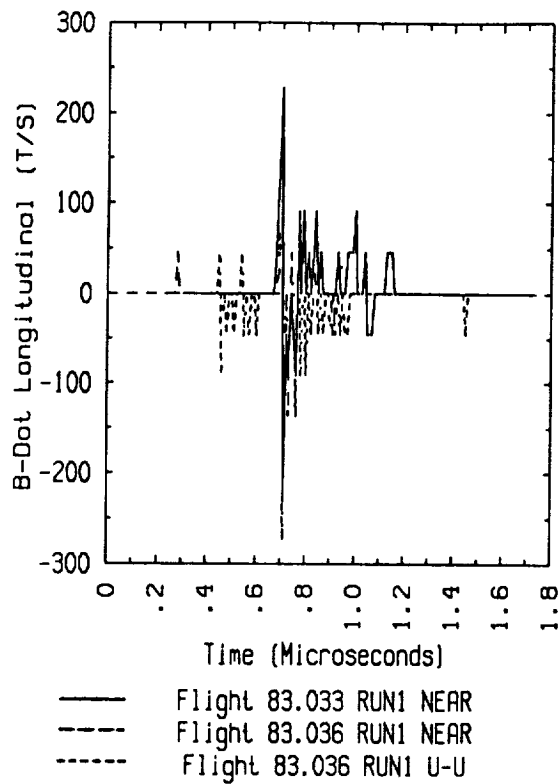


— Flight 83.029 RUN1 NEAR  
 --- Flight 83.029 RUN1 NEAR  
 - - - Flight 83.029 RUN2 NEAR



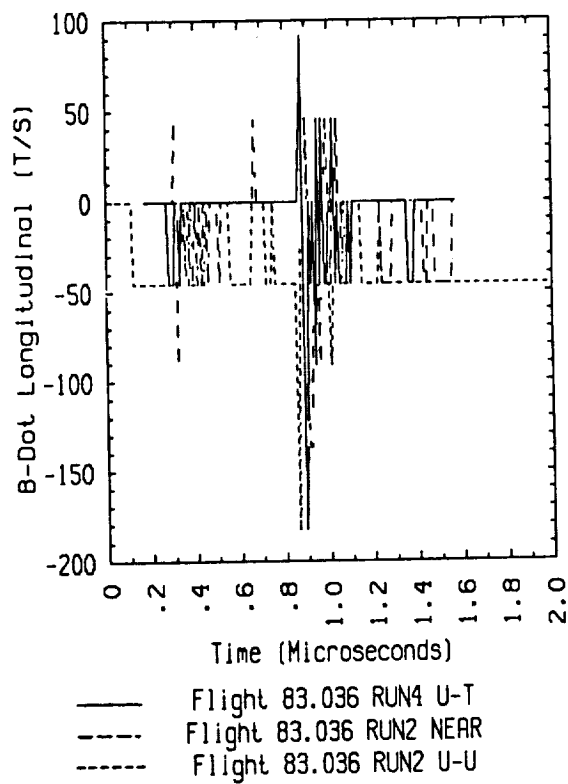
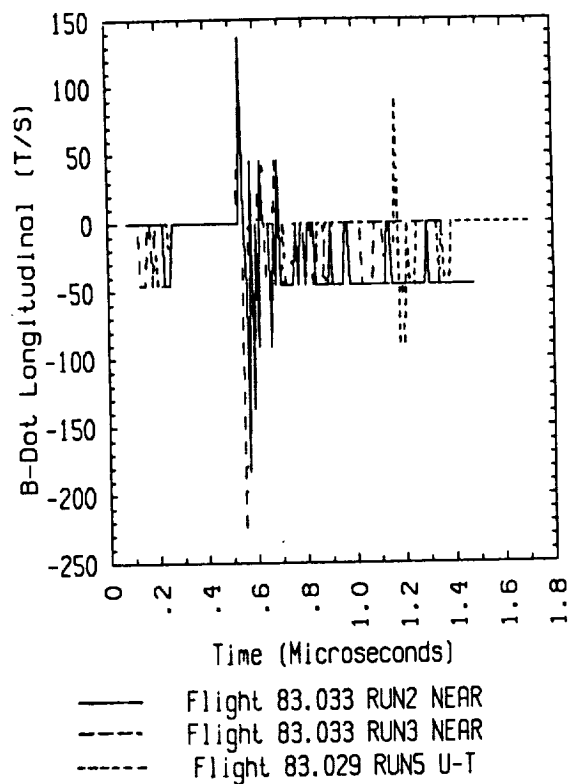
— Flight 83.030 RUN1 U-M  
 --- Flight 83.030 RUN1 U-U  
 - - - Flight 83.032 RUN1 NEAR

**Figure B.1 (d) B-dot Category 1 (continued)**

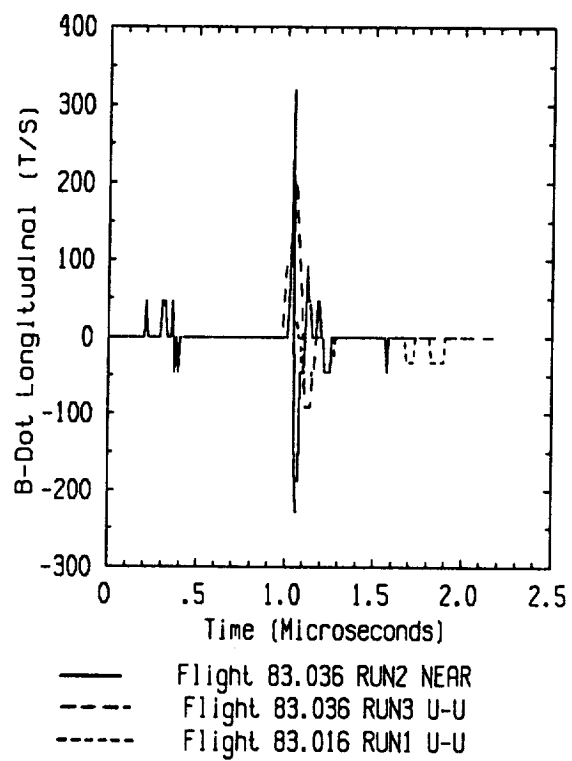


**Figure B.1 (e) B-dot Category 1 (continued)**

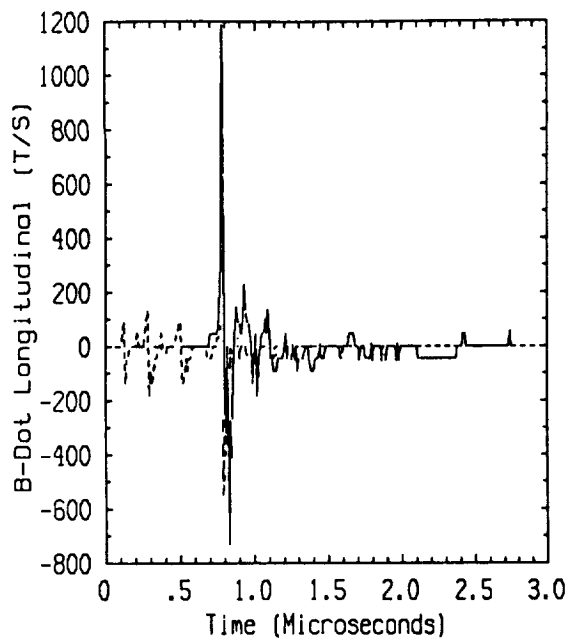




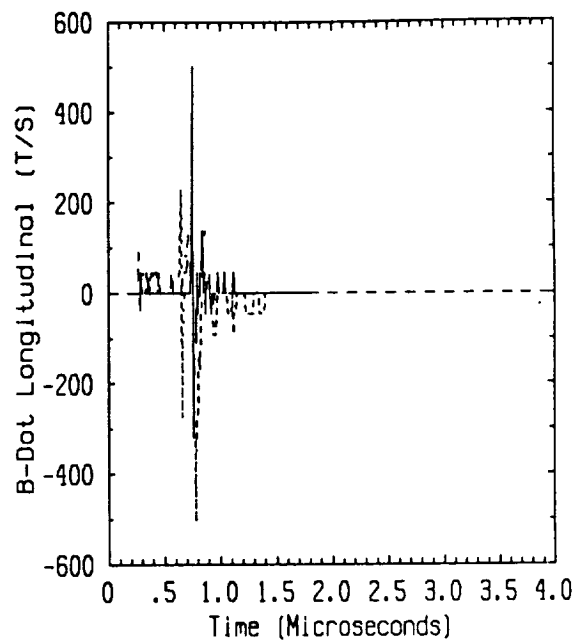
**Figure B.1 (f) B-dot Category 1 (continued)**



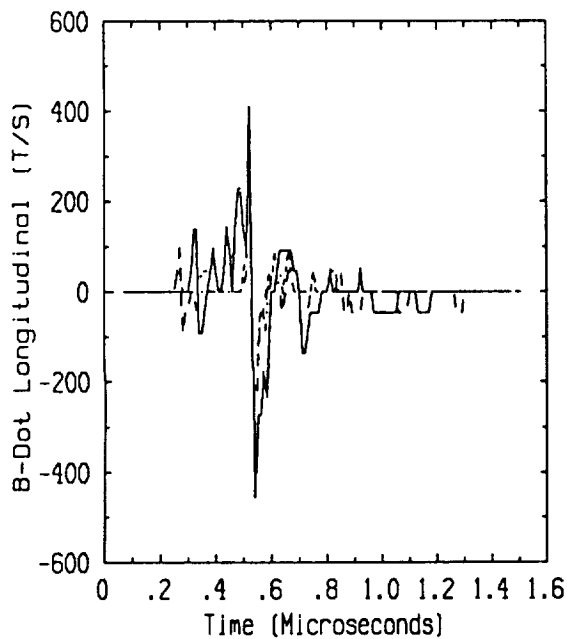
**Figure B.2    B-dot Category 2**



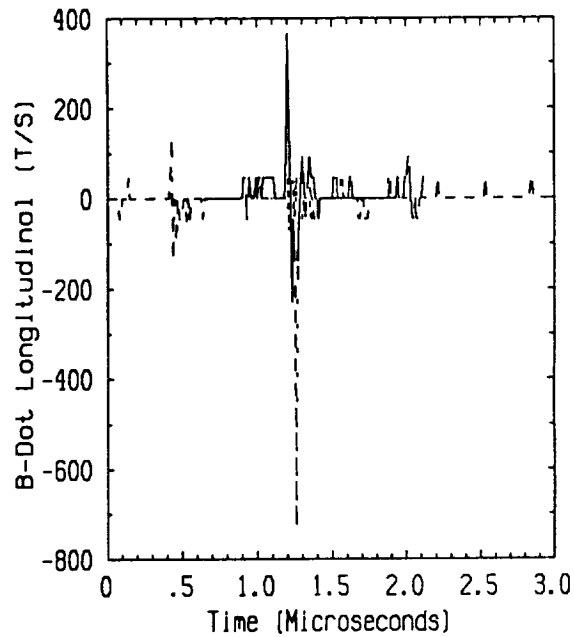
— Flight 83.020 RUN2 U-U  
 --- Flight 83.013 RUN4 U-T  
 ..... Flight 83.024 RUN1 U-LW



— Flight 83.030 RUN1 NEAR  
 --- Flight 83.030 RUN5 U-M  
 ..... Flight 83.021 RUN3 U-U

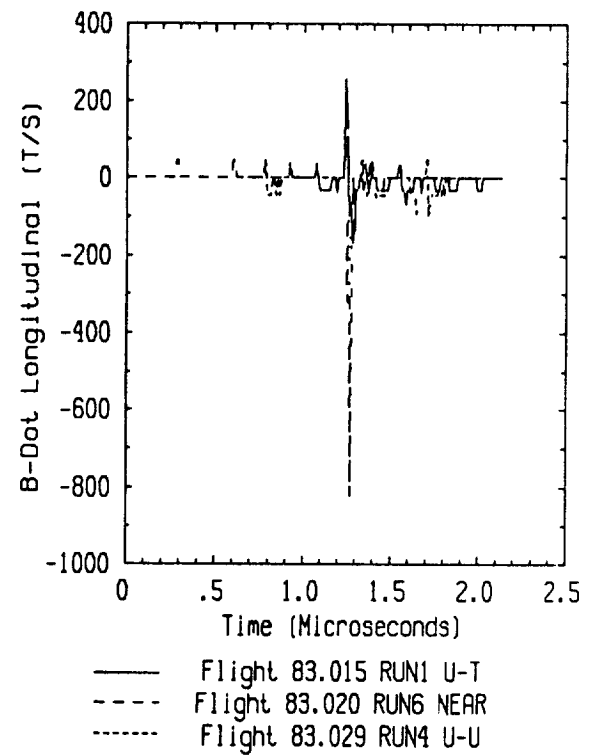
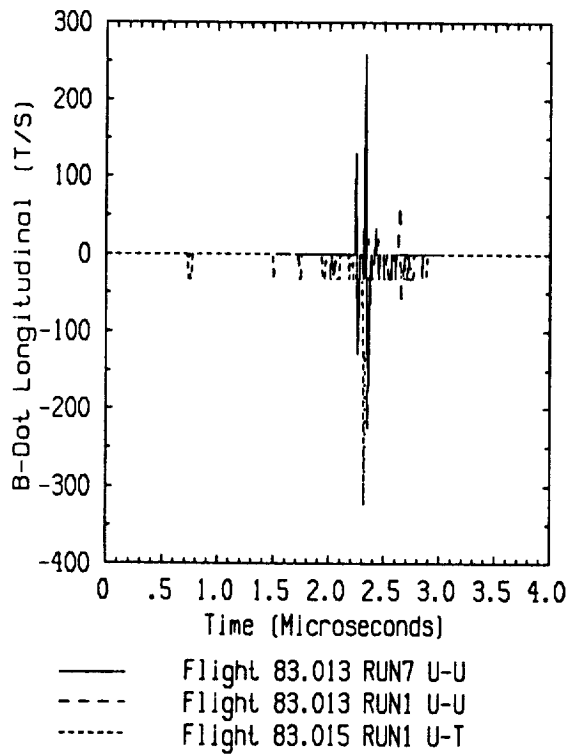
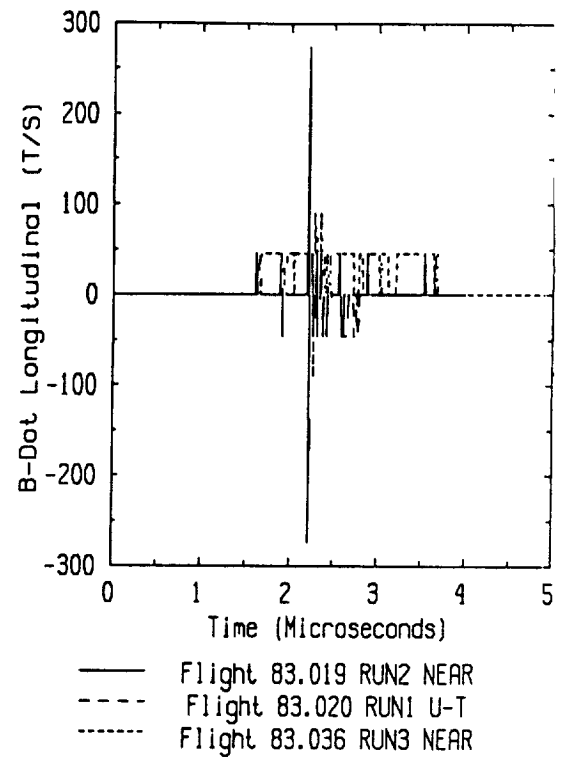
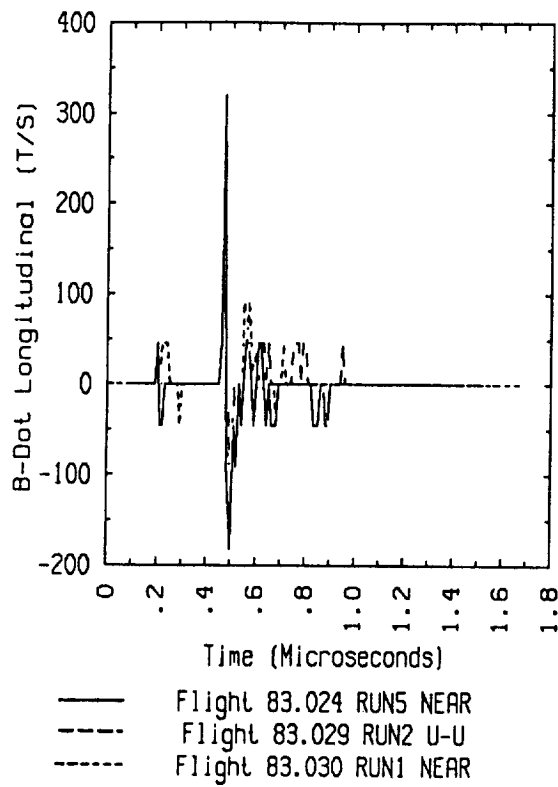


— Flight 83.023 RUN1 U-T  
 --- Flight 83.022 RUN3 NEAR  
 ..... Flight 83.032 RUN6 U-M

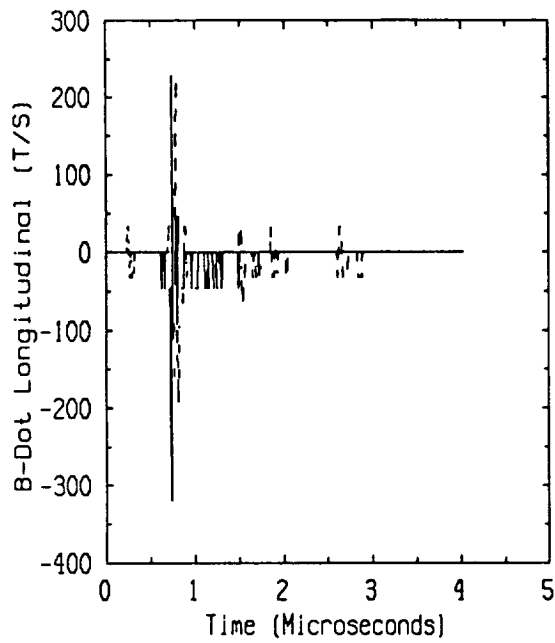


— Flight 83.033 RUN1 U-M  
 --- Flight 83.020 RUN3 NEAR  
 ..... Flight 83.020 RUN4 NEAR

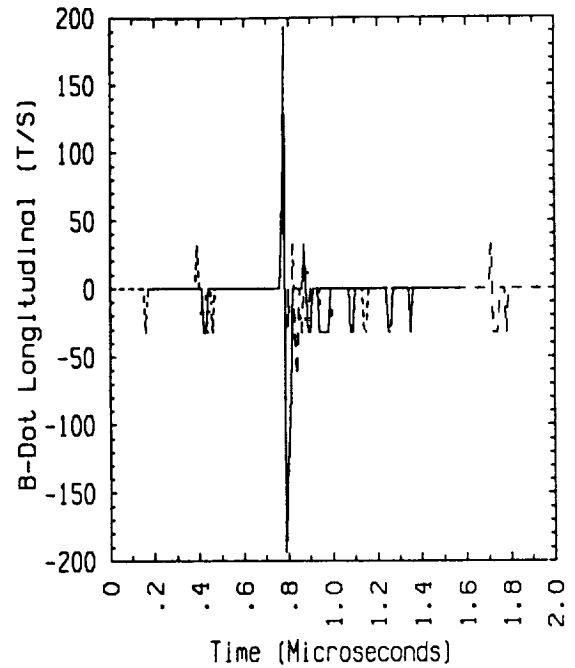
**Figure B.3 (a) B-dot Category 3**



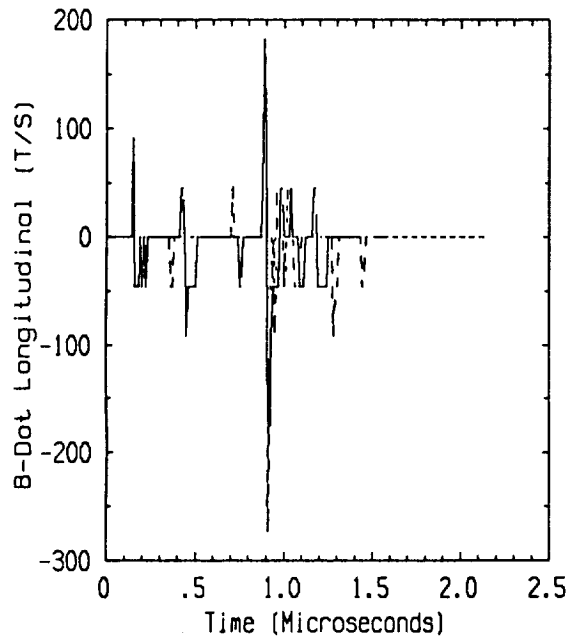
**Figure B.3 (b) B-dot Category 3 (continued)**



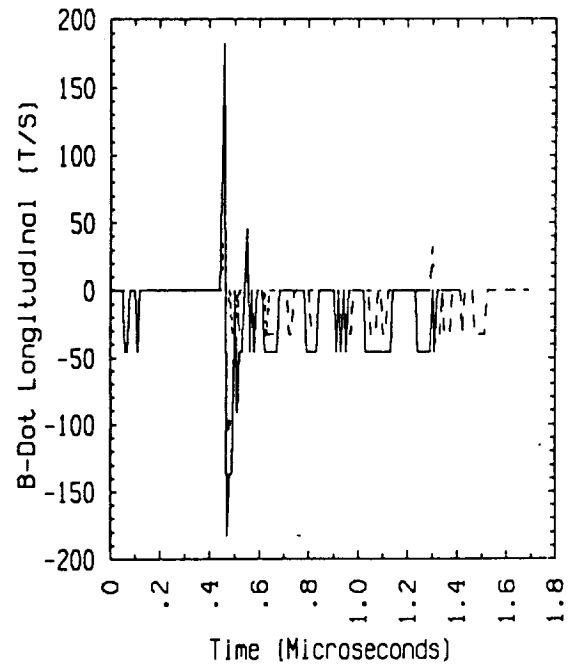
— Flight 83.030 RUN1 U-U  
 --- Flight 83.013 RUN5 U-U  
 - - - Flight 83.013 RUN1 U-U



— Flight 83.013 RUN9 U-U  
 --- Flight 83.013 RUN1 U-U  
 - - - Flight 83.013 RUN1 U-U

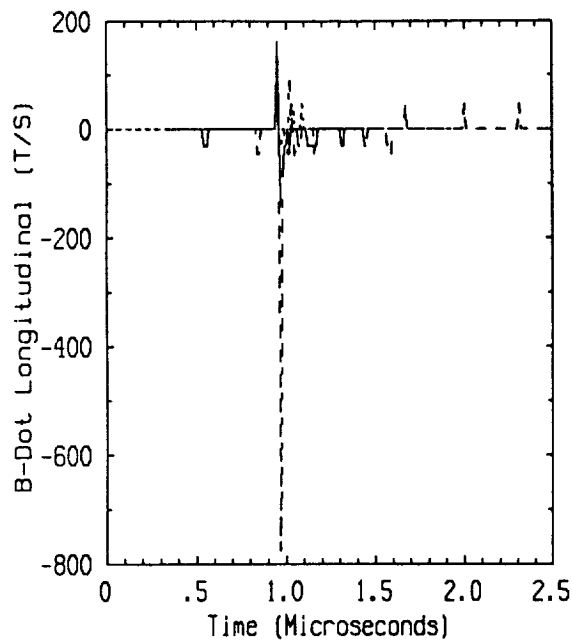


— Flight 83.022 RUN2 U-M  
 --- Flight 83.029 RUN2 NEAR  
 - - - Flight 83.030 RUN1 U-U

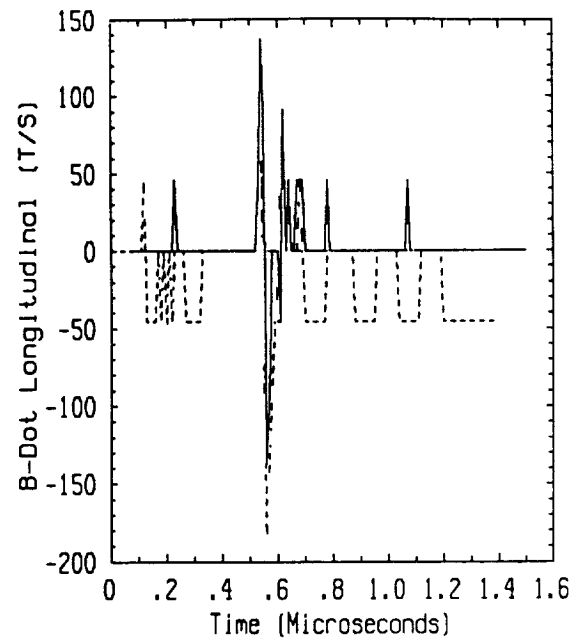


— Flight 83.033 RUN5 NEAR  
 --- Flight 83.013 RUN2 U-T  
 - - - Flight 83.013 RUN1 U-U

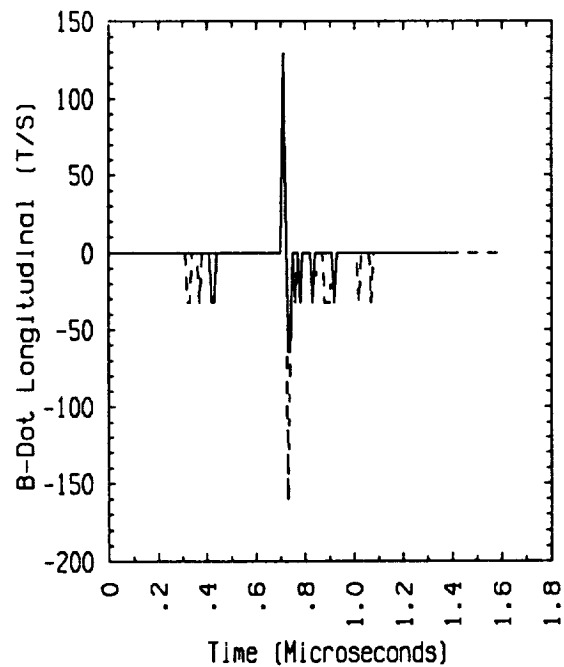
**Figure B.3 (c) B-dot Category 3 (continued)**



— Flight 83.016 RUN3 U-U  
 --- Flight 83.020 RUN4 NEAR  
 - - - Flight 83.025 RUN8 U-M

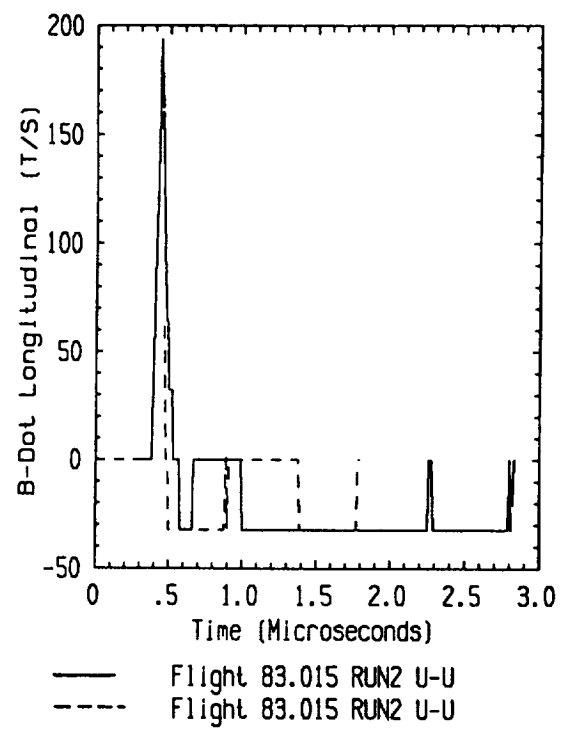


— Flight 83.029 RUN9 U-U  
 --- Flight 83.029 RUN2 U-T  
 - - - Flight 83.036 RUN1 NEAR

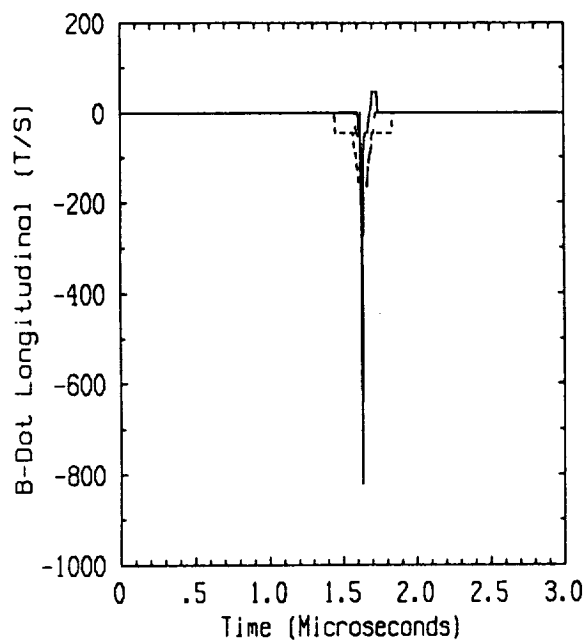


— Flight 83.013 RUN1 U-U  
 --- Flight 83.013 RUN8 NEAR

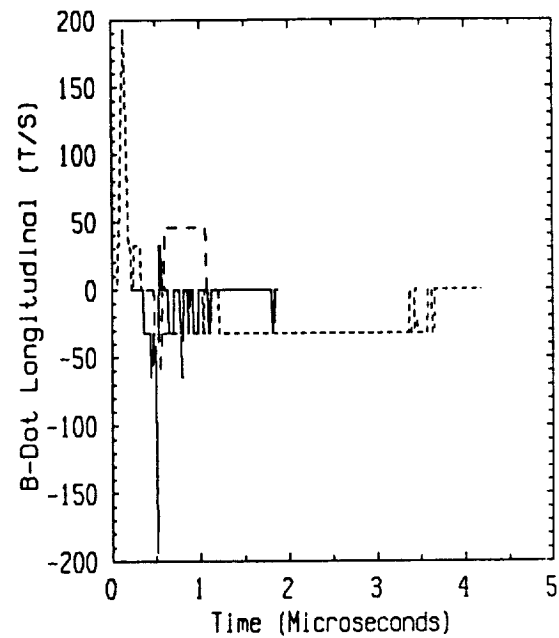
**Figure B.3 (d) B-dot Category 3 (continued)**



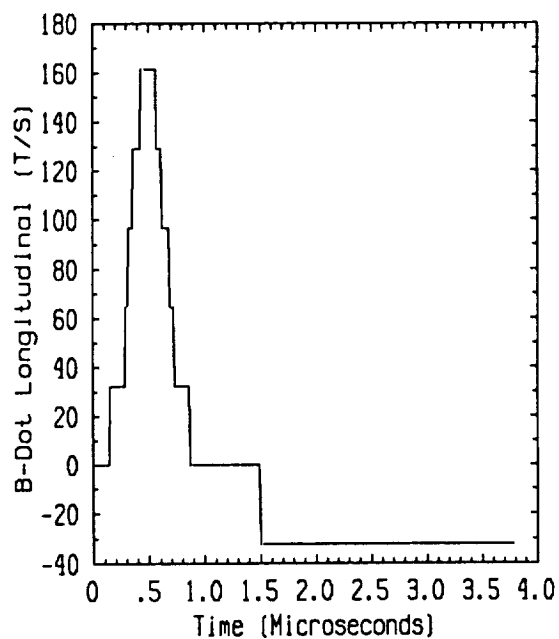
**Figure B.4 B-dot Category 4**



— Flight 83.019 RUN1 NEAR  
 - - - Flight 83.021 RUN2 U-T  
 . . . Flight 83.036 RUN1 NEAR



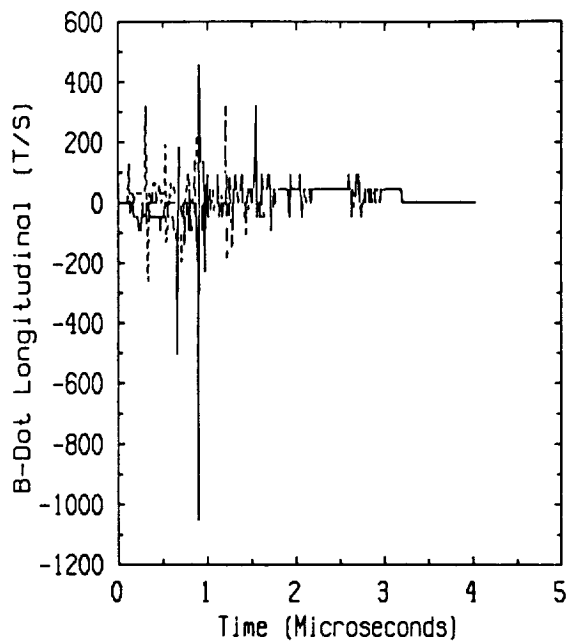
— Flight 83.015 RUN1 U-T  
 - - - Flight 83.033 RUN1 U-M  
 . . . Flight 83.016 RUN4 U-U



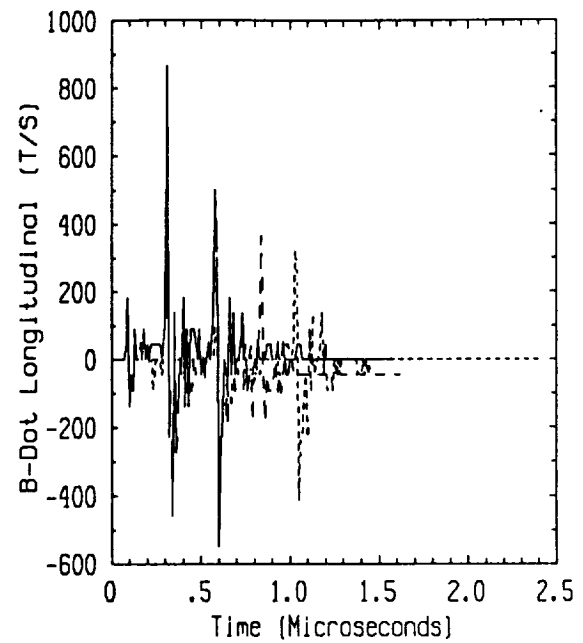
Flight 83.016 RUN4 U-U

**Figure B.5 B-dot Category 5**

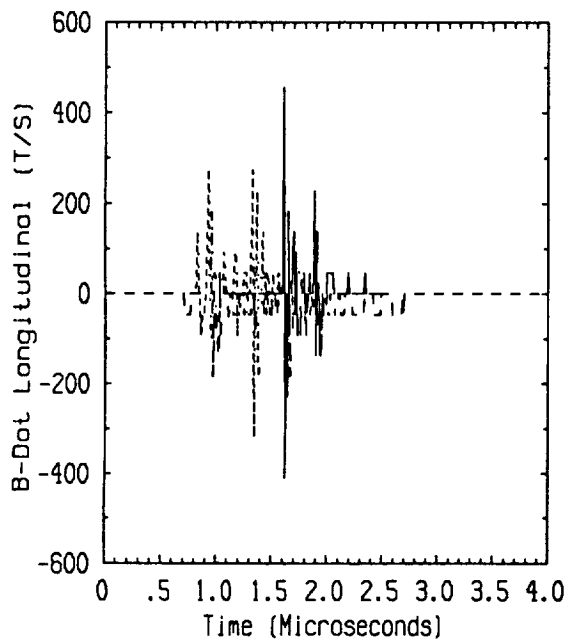




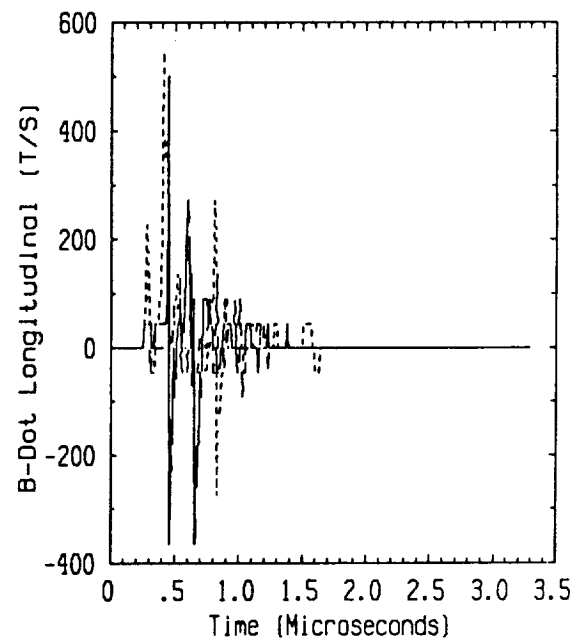
— Flight 83.030 RUN3 U-M  
 --- Flight 83.020 RUN5 U-T  
 ..... Flight 83.011 RUN2 U-U



— Flight 83.030 RUN8 U-T  
 --- Flight 83.036 RUN8 NEAR  
 ..... Flight 83.036 RUN3 U-T

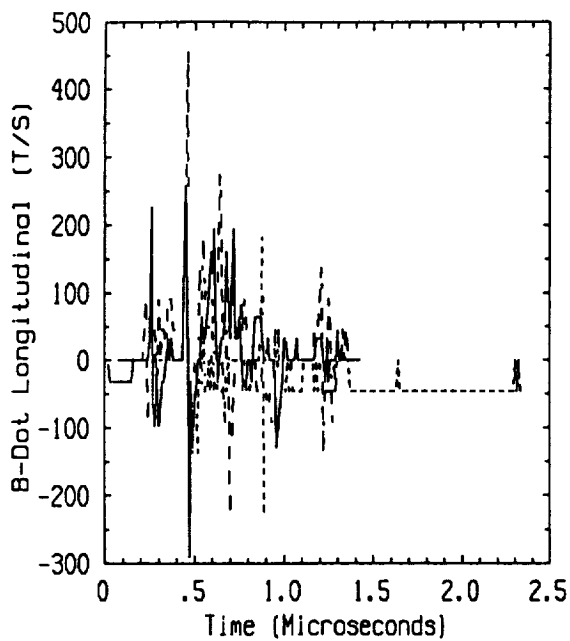


— Flight 83.036 RUN2 NEAR  
 --- Flight 83.029 RUN1 U-T  
 ..... Flight 83.029 RUN2 U-U

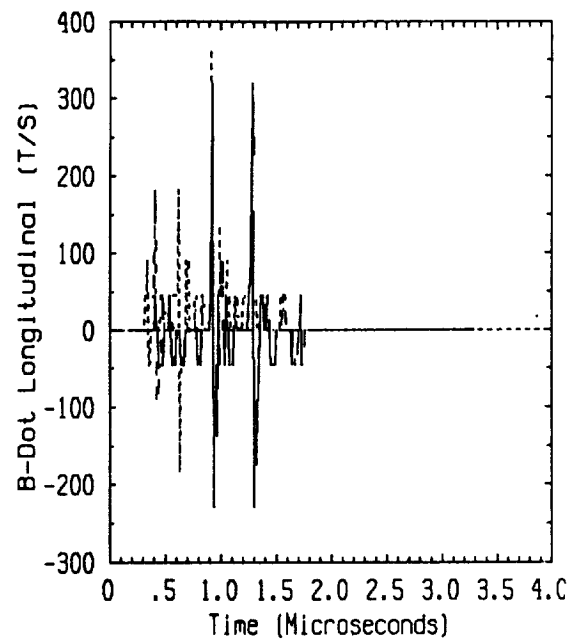


— Flight 83.036 RUN3 NEAR  
 --- Flight 83.036 RUN1 NEAR  
 ..... Flight 83.036 RUN3 U-U

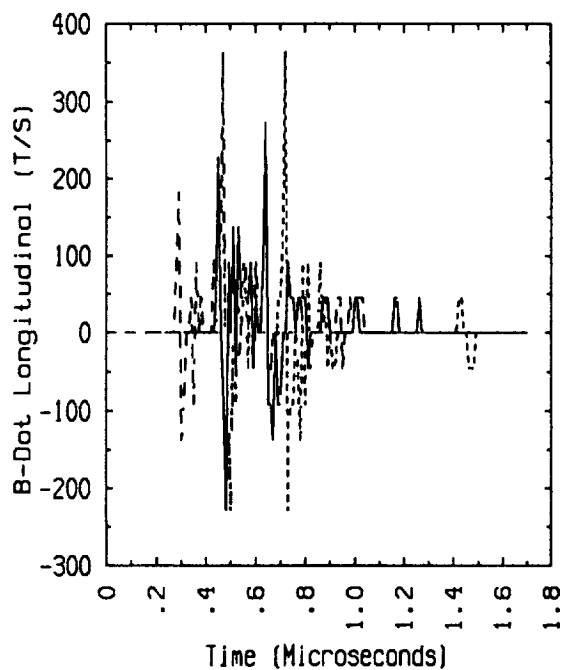
**Figure B.6 (a) B-dot Category 6**



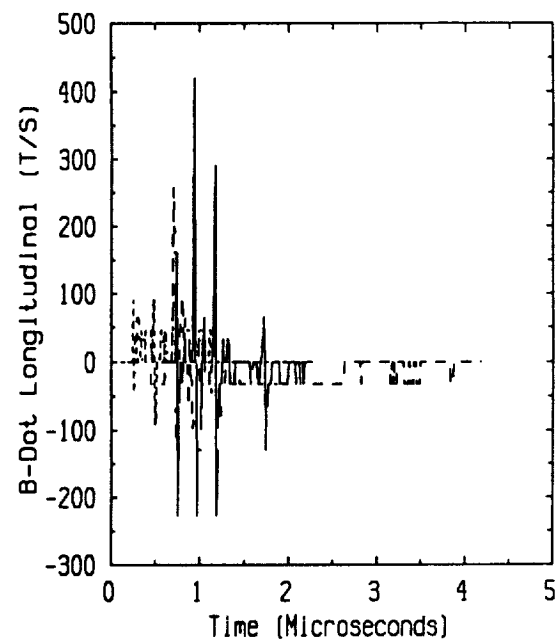
— Flight 83.013 RUN1 U-U  
 --- Flight 83.032 RUN8 U-M  
 ..... Flight 83.035 RUN3 U-U



— Flight 83.024 RUN4 U-U  
 --- Flight 83.025 RUN7 U-T  
 ..... Flight 83.030 RUN4 U-LW

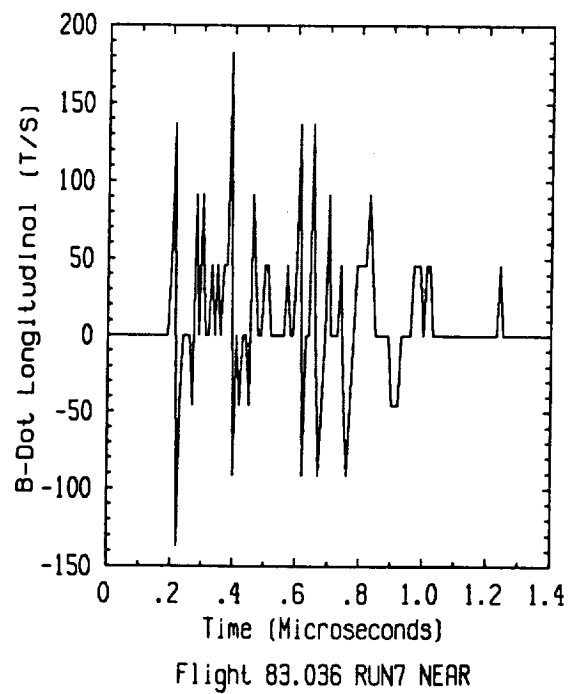
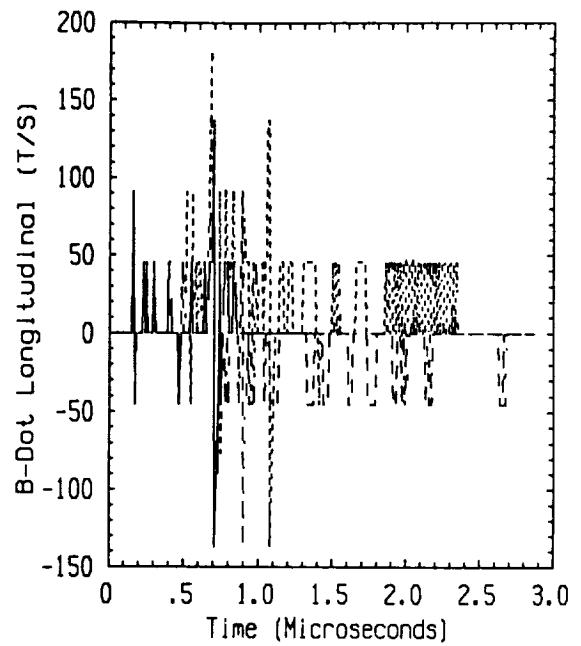
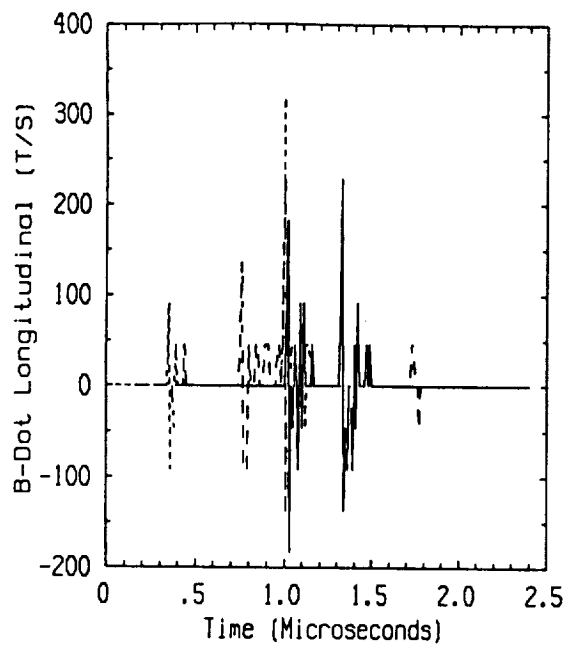


— Flight 83.033 RUN7 U-M  
 --- Flight 83.036 RUN2 U-T  
 ..... Flight 83.036 RUN1 U-T

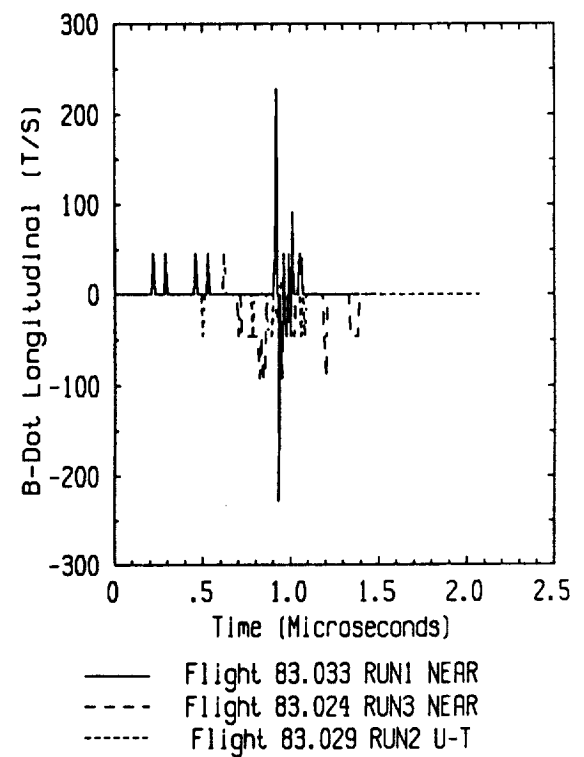
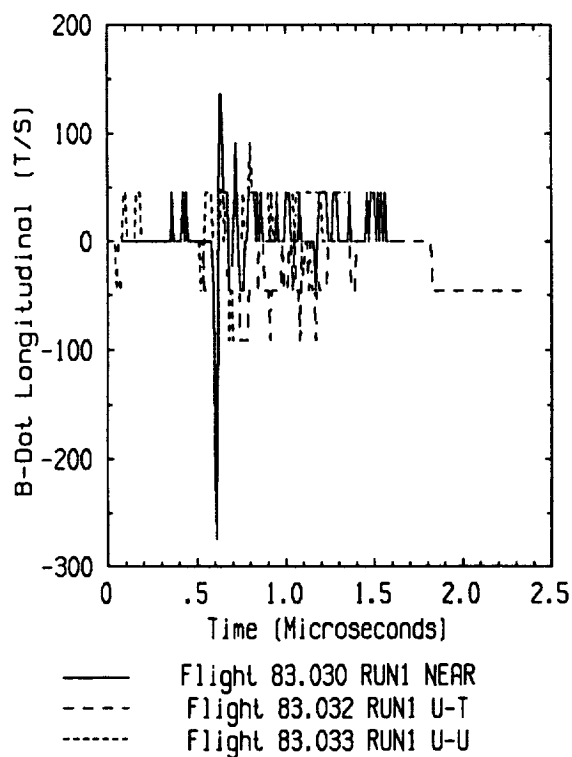
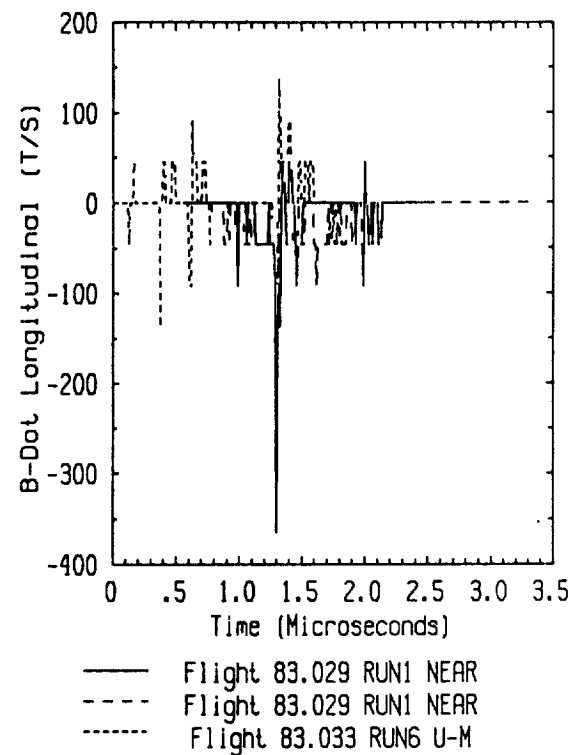
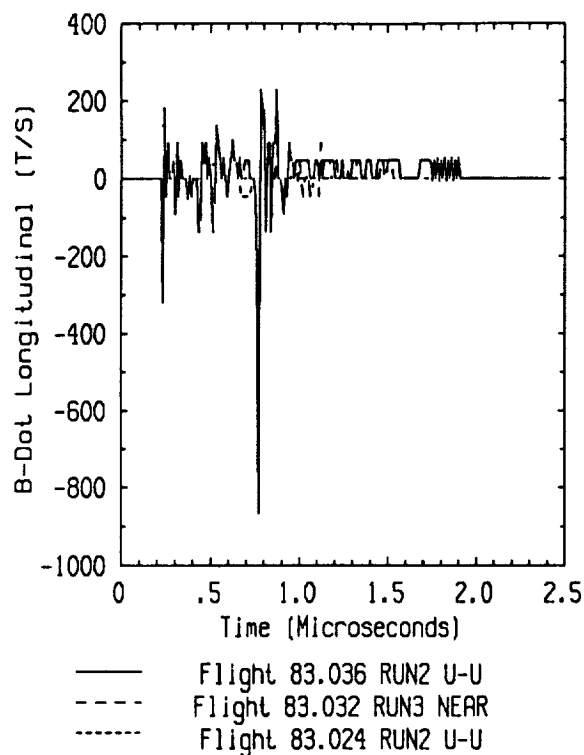


— Flight 83.013 RUN3 U-LW  
 --- Flight 83.016 RUN1 U-U  
 ..... Flight 83.029 RUN1 NEAR

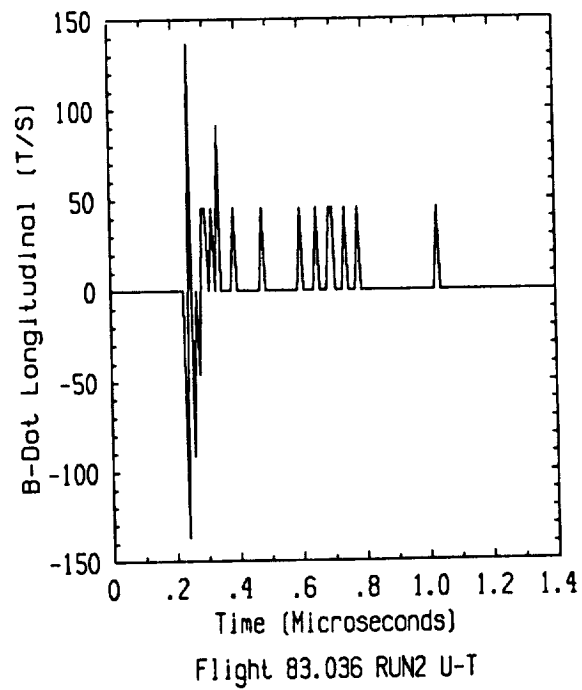
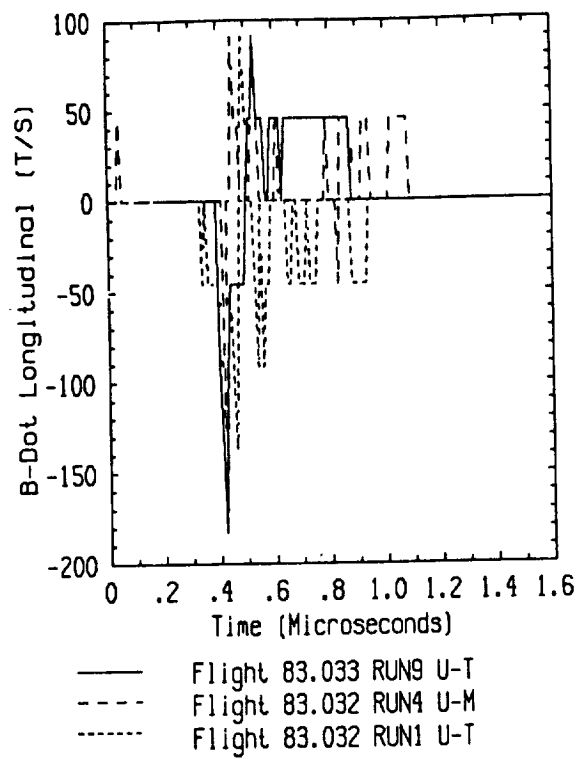
**Figure B.6 (b) B-dot Category 6 (continued)**



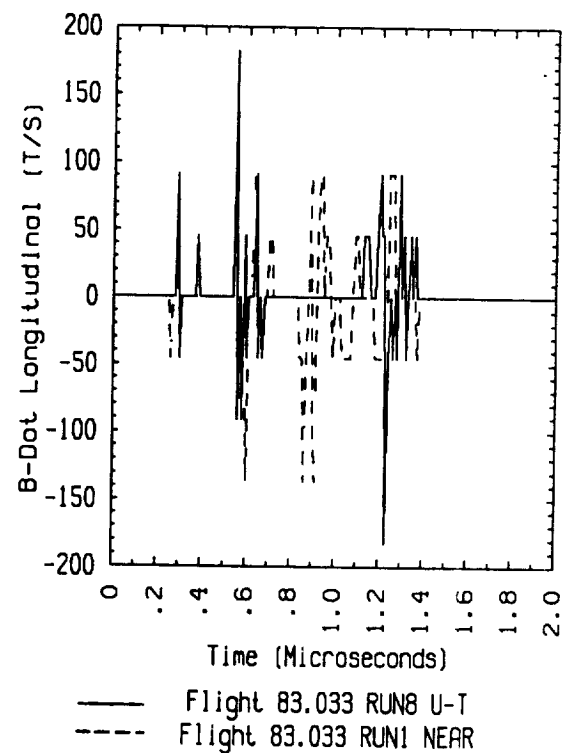
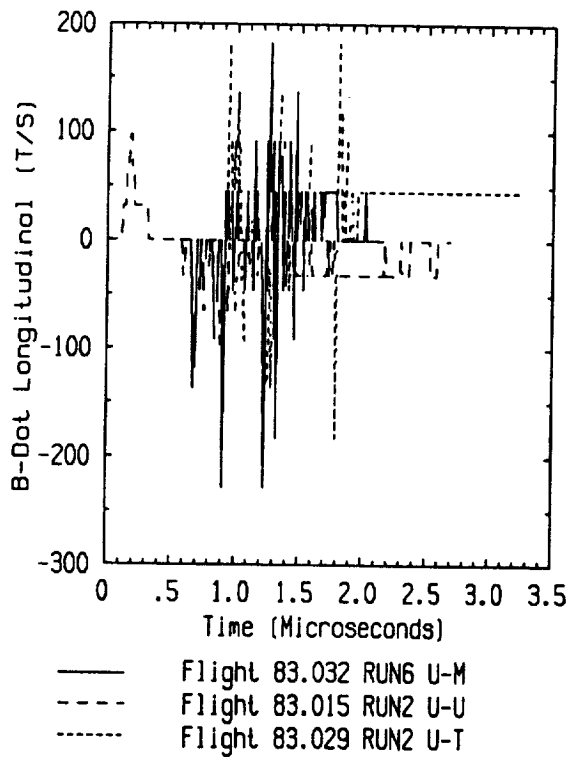
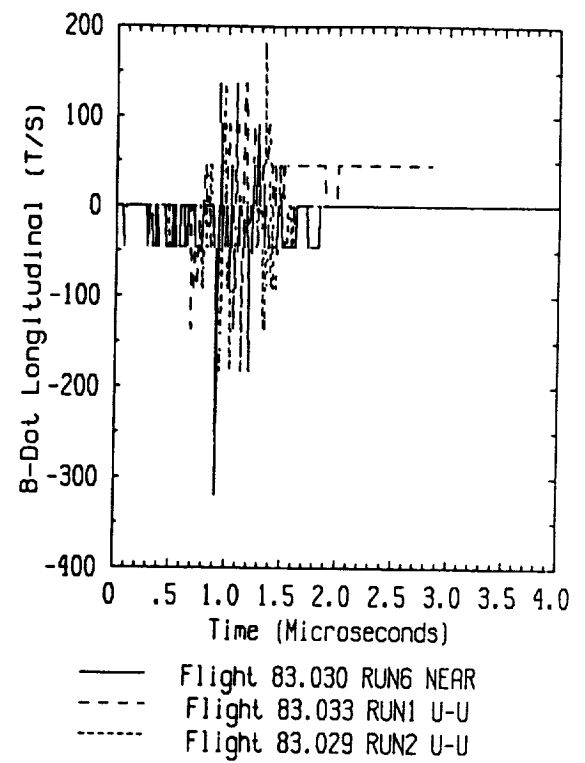
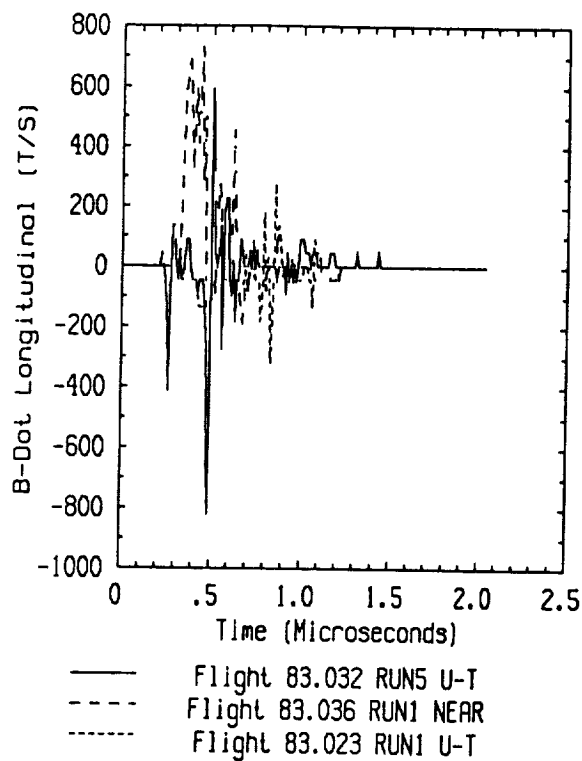
**Figure B.6 (c) B-dot Category 6 (continued)**



**Figure B.7 (a) B-dot Category 7**



**Figure B.7 (b) B-dot Category 7 (continued)**



**Figure B.7 (c) B-dot Category 7 (continued)**

## **APPENDIX C**

### **LINEAR TRANSFER FUNCTION MODELING RESULTS**

The overlays in this appendix are discussed in Chapter 4. They are in sets of six plots with the calculated data (solid line) overlaid on the measured data from Flight 84-017 (dashed line).

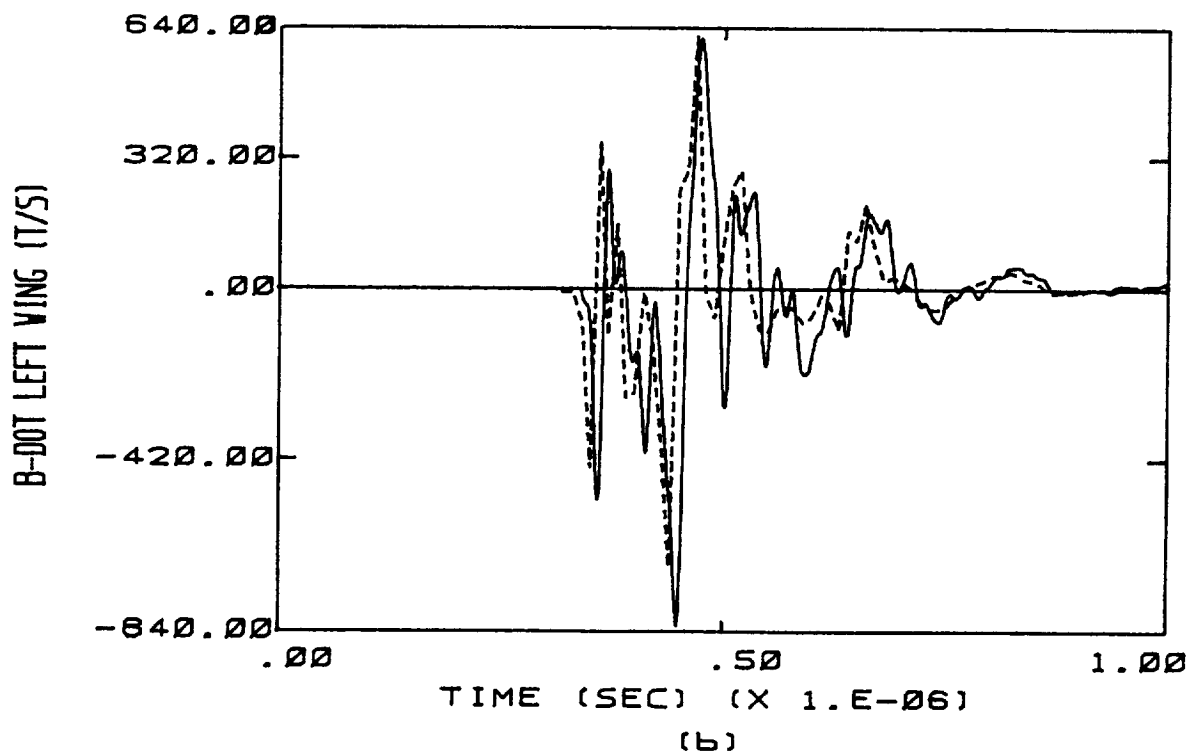
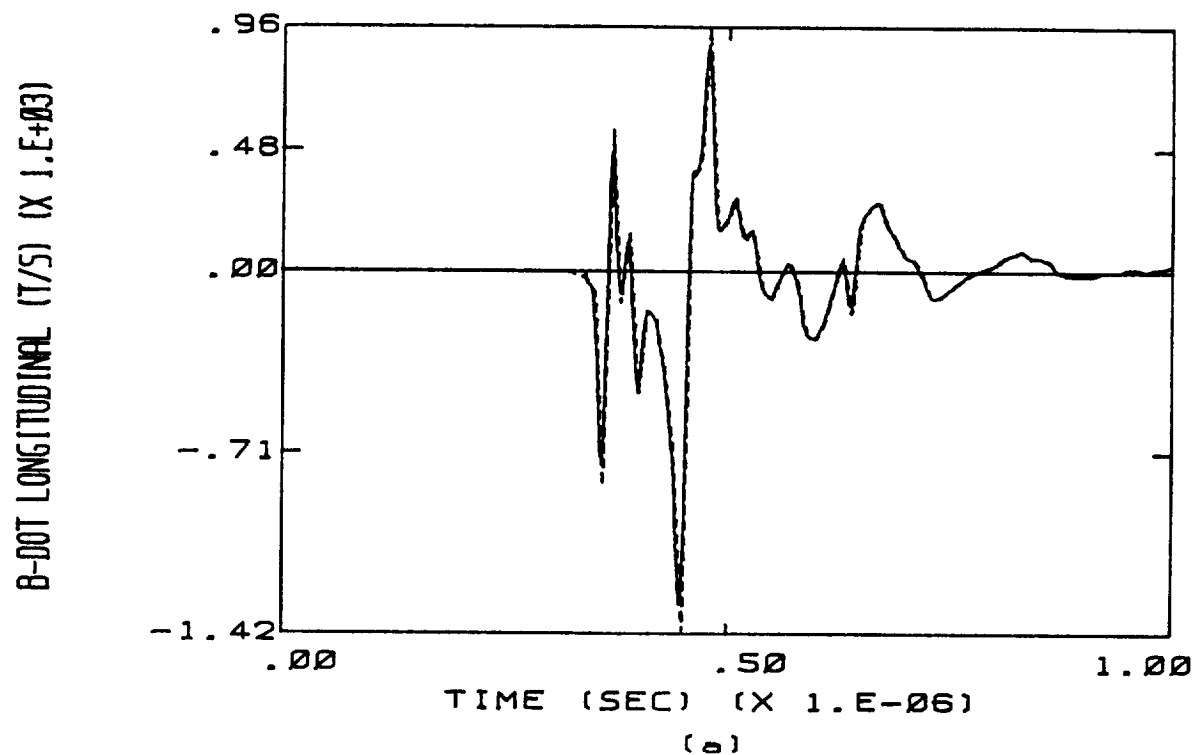
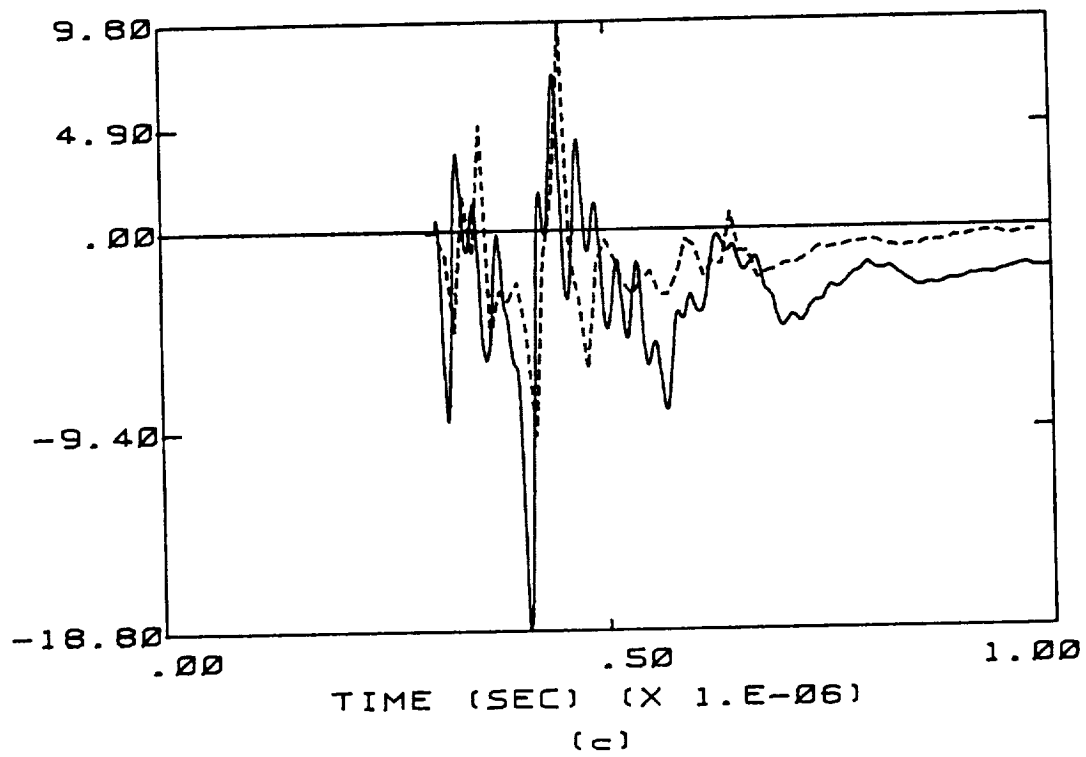


Figure C.1 Calculated Responses Overlaid on Measured Responses of Flight 84-017 for the Case of a 1 cm Radius Channel. The Transfer Function Used Is Appropriate to B-dot Longitudinal. The Dashed Line Indicates the Measured Data.



D-DOT FORWARD (A/SQUARE METER)



D-DOT LEFT VING (A/SQUARE METER)

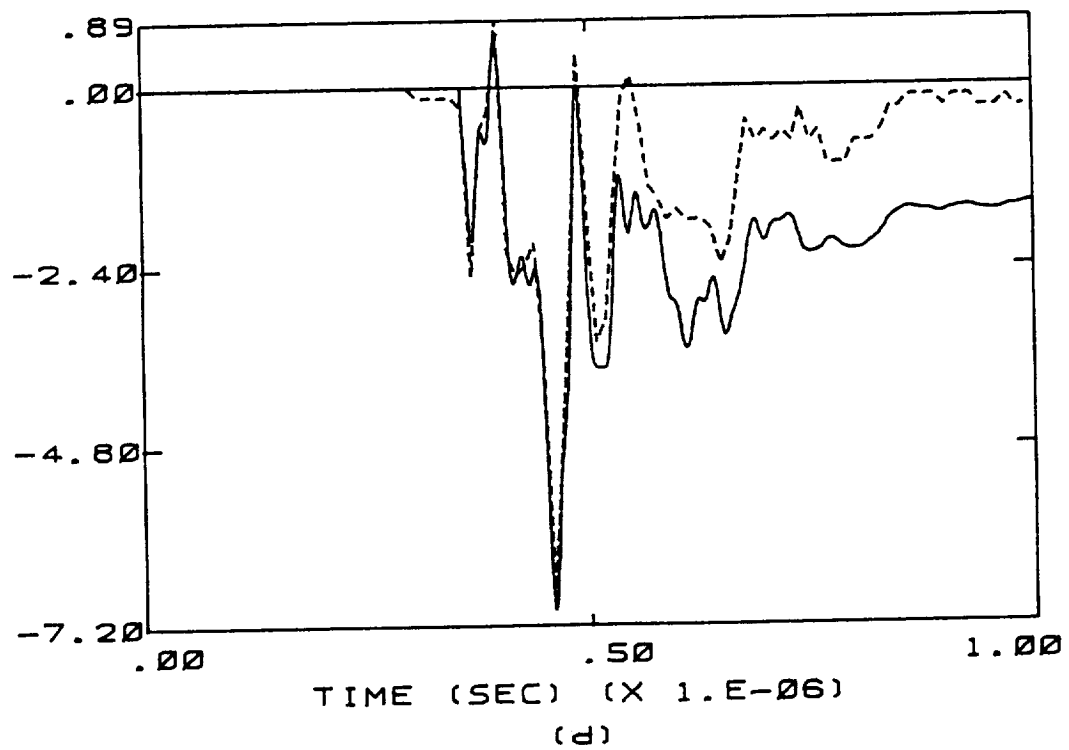


Figure C.1 (continued)

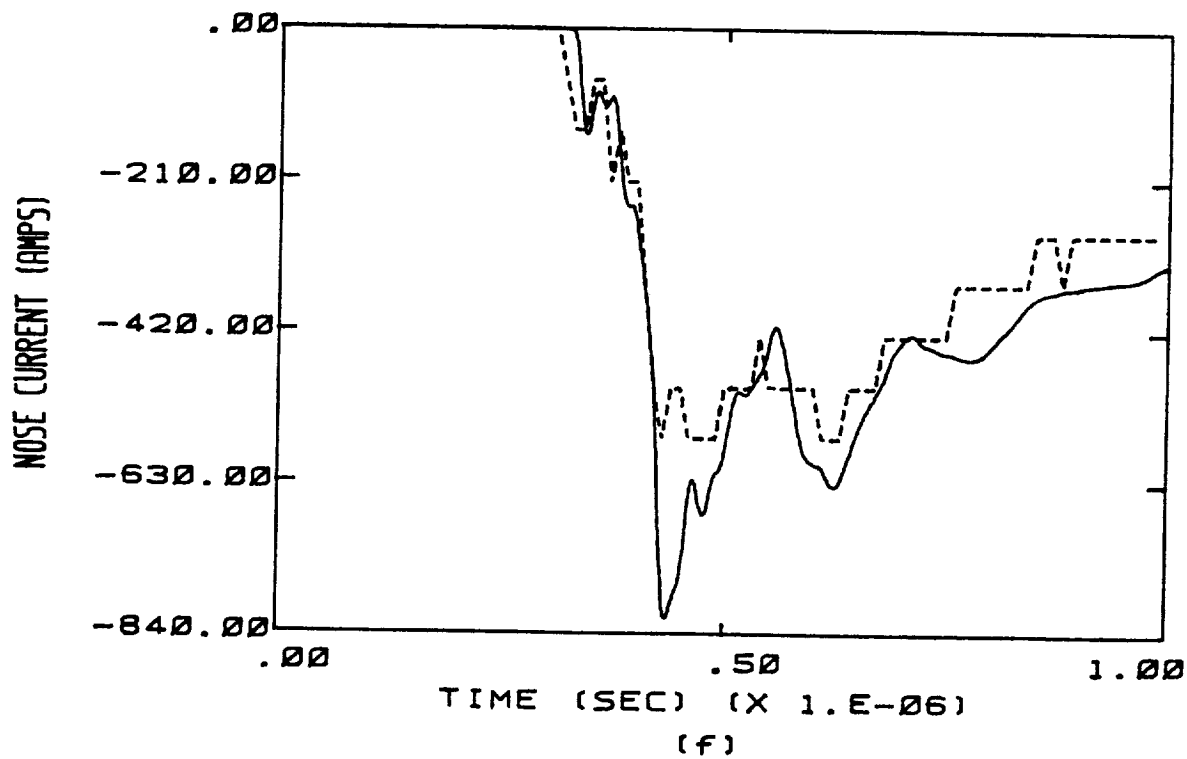
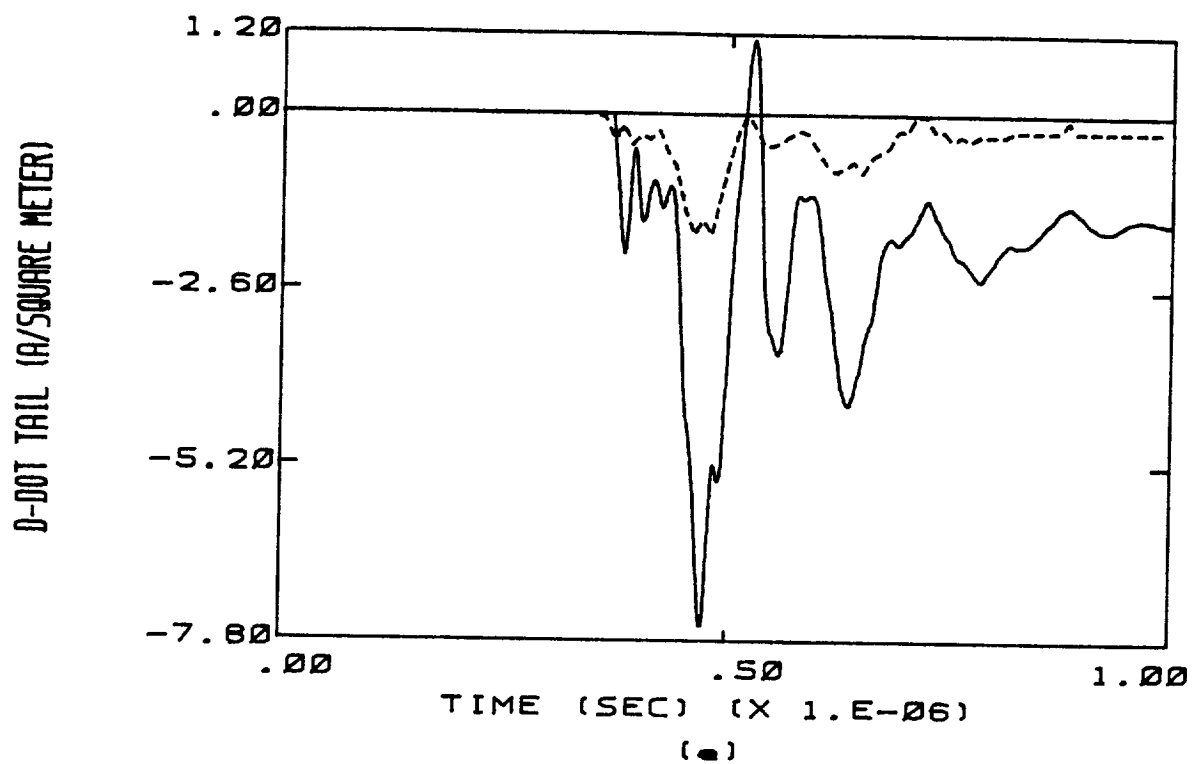


Figure C.1 (continued)

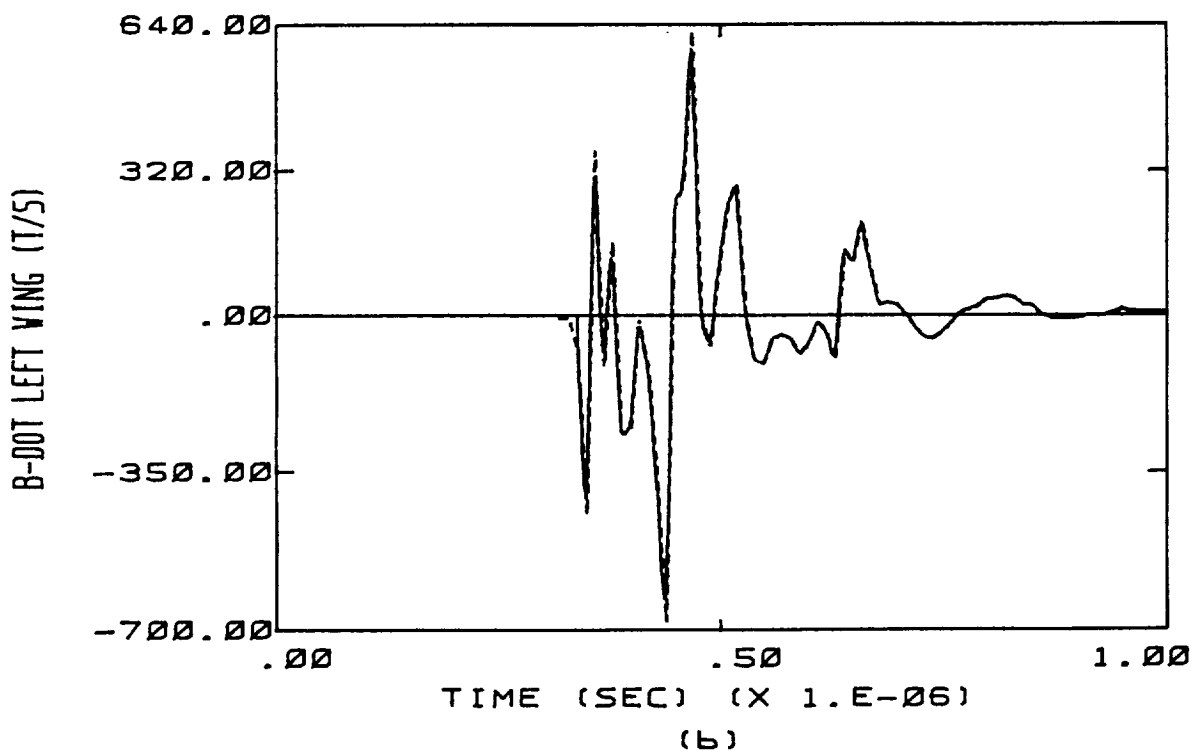
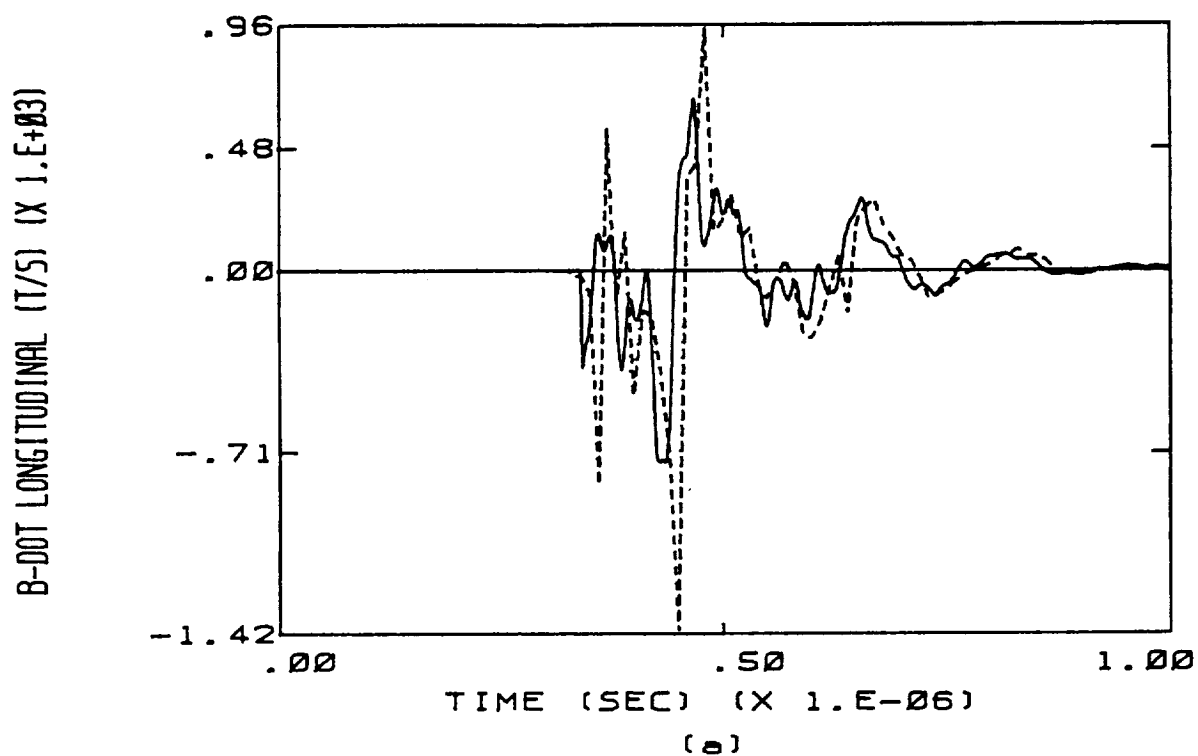
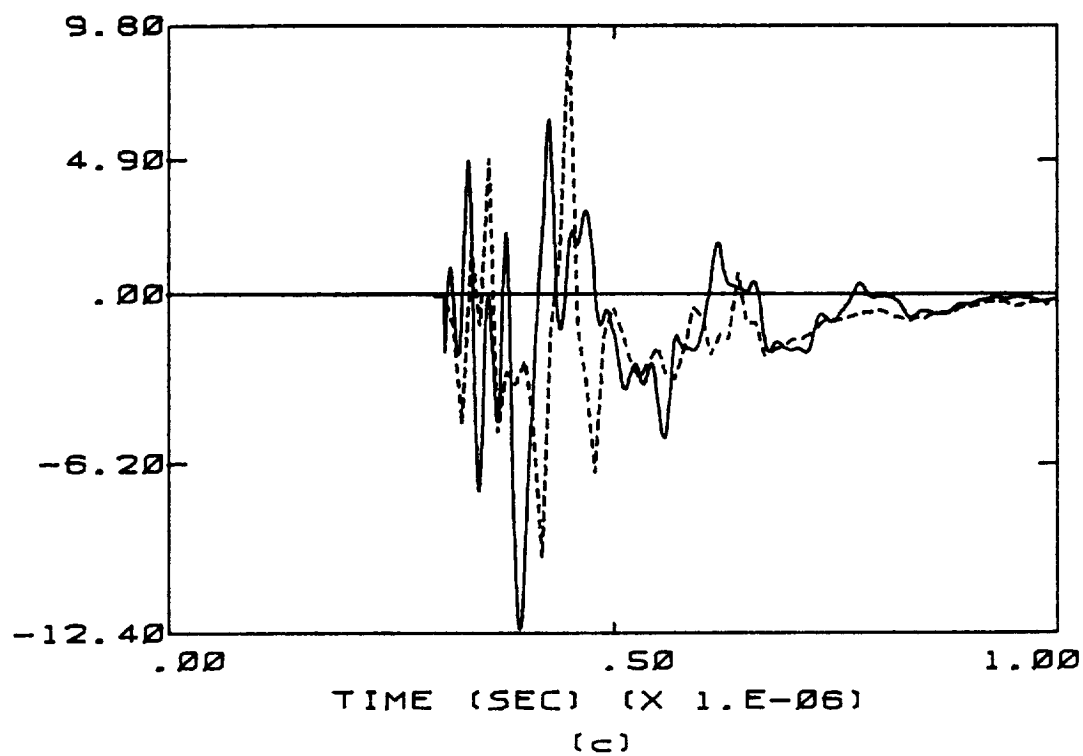


Figure C.2 Calculated Responses Overlaid on Measured Responses of Flight 84-017 for the Case of a 1 cm Radius Channel. The Transfer Function Used Is Appropriate to B-dot Left Wing. The Dashed Line Indicates the Measured Data.

D-DOT FORWARD (A/SQUARE METER)



D-DOT LEFT WING (A/SQUARE METER)

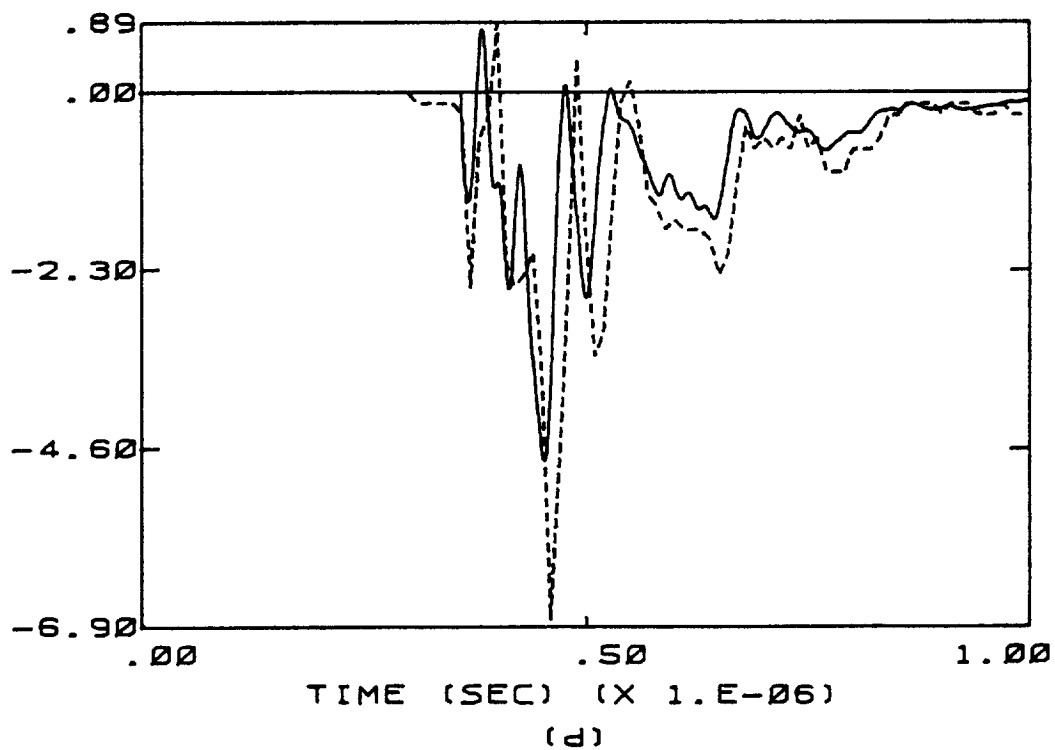


Figure C.2 (continued)

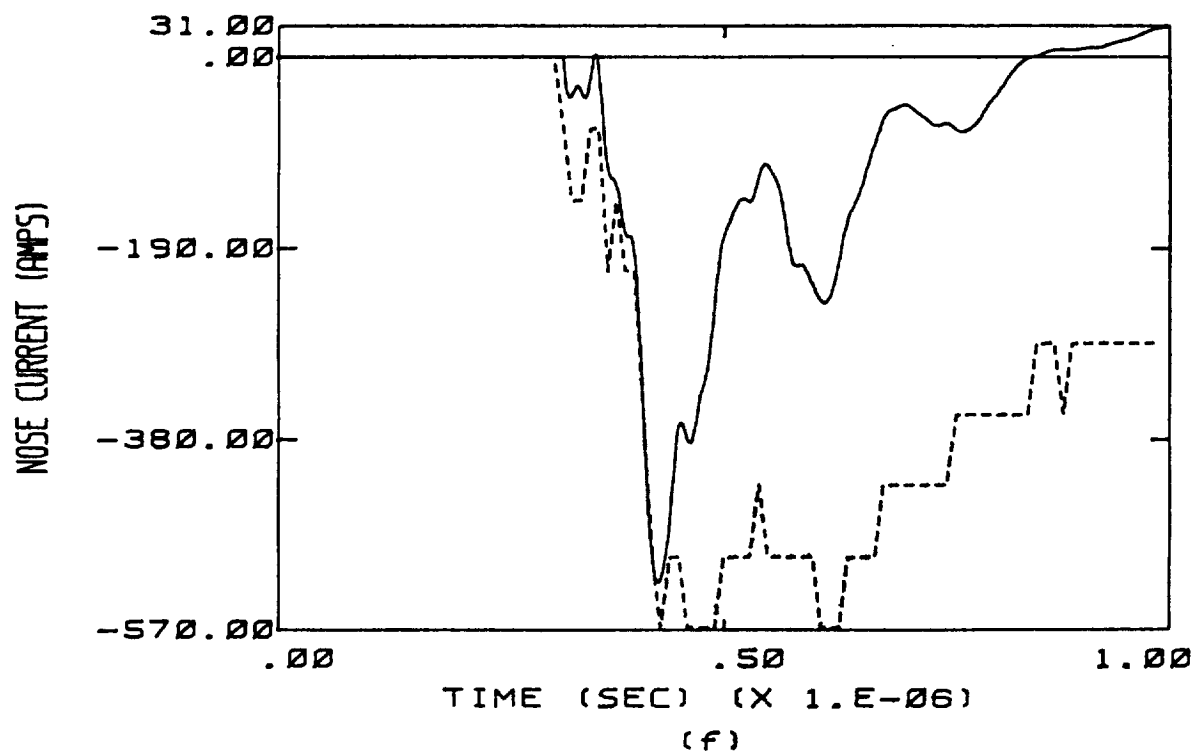
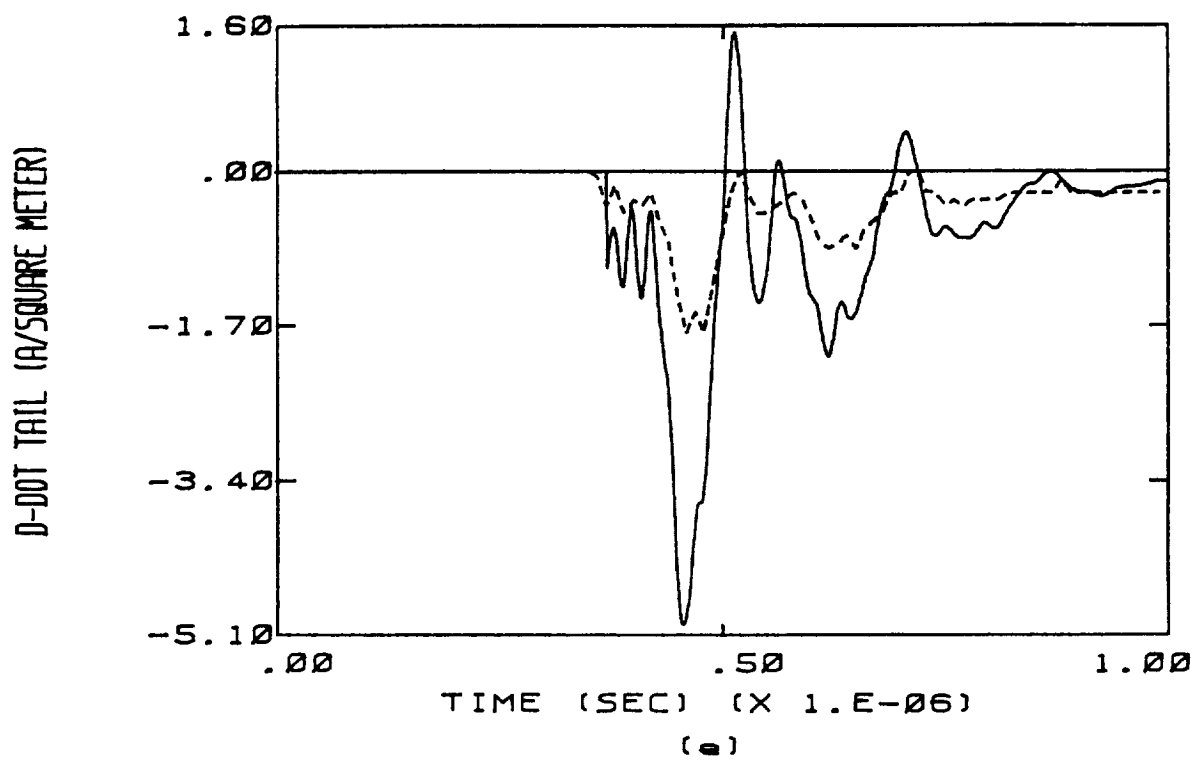


Figure C.2 (continued)

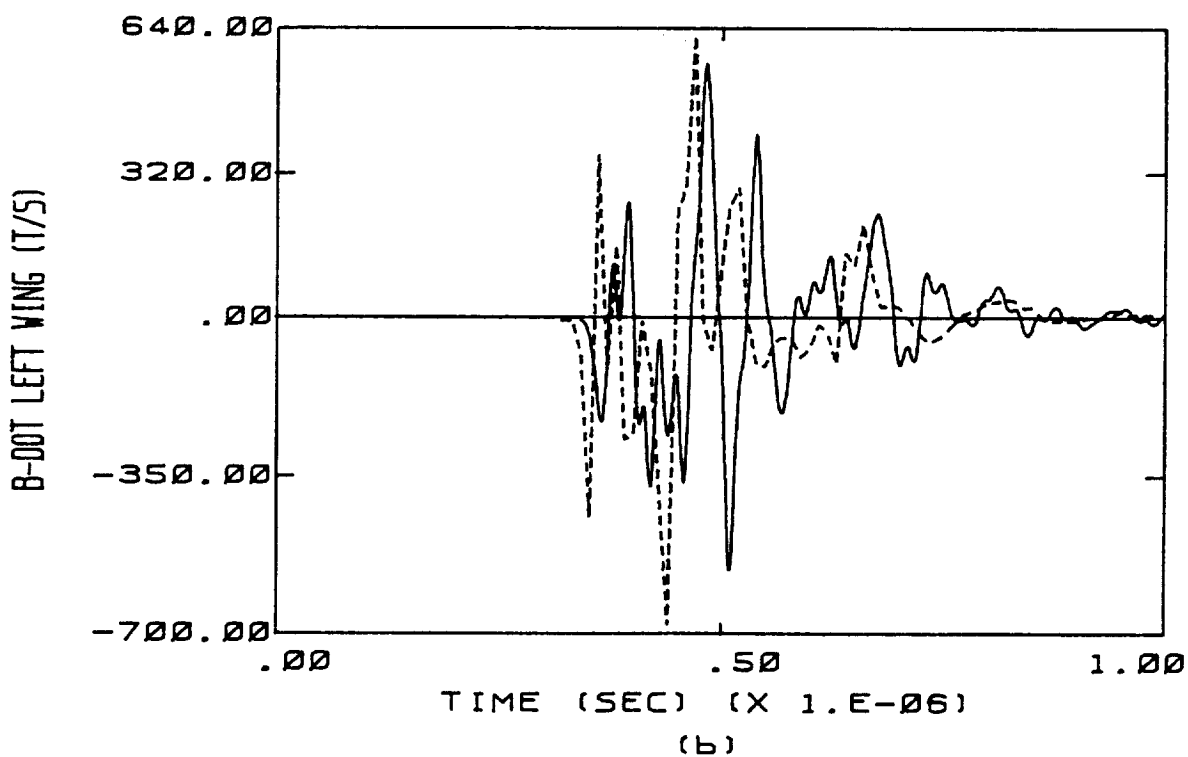
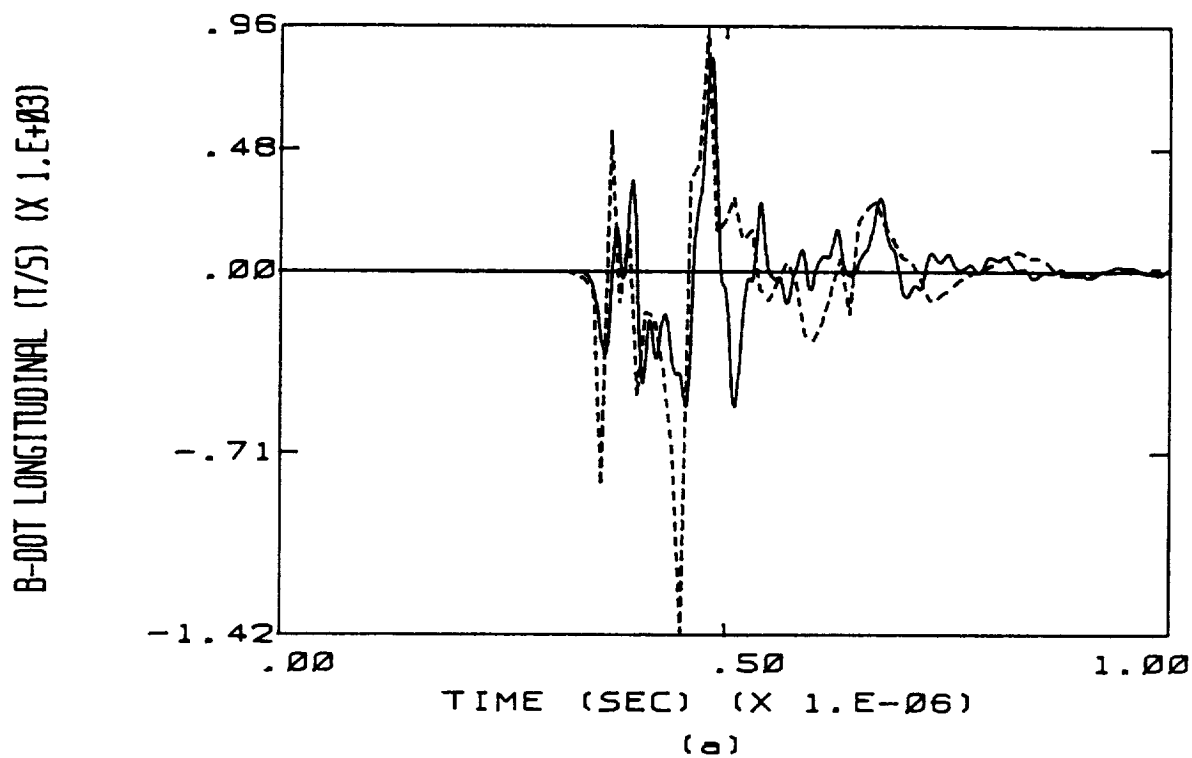
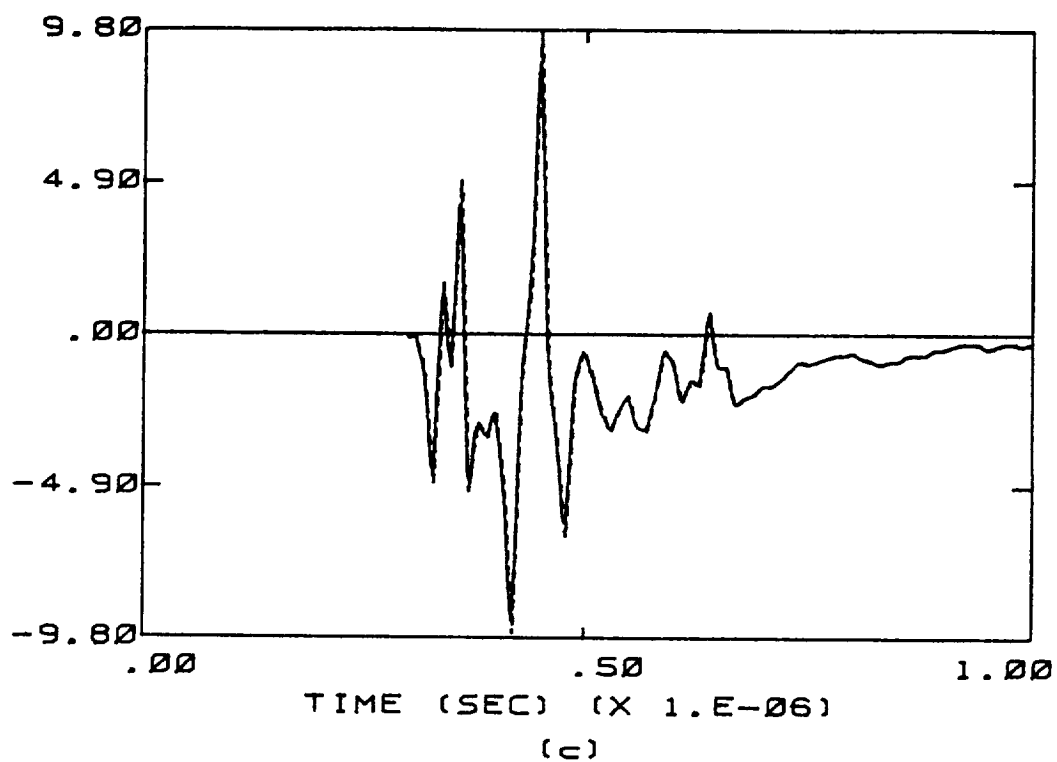


Figure C.3 Calculated Responses Overlaid on Measured Responses of Flight 84-017 for the Case of a 1 cm Radius Channel. The Transfer Function Used Is Appropriate to D-dot Forward. The Dashed Line Indicates the Measured Data.

D-DOT FORWARD (A/SQUARE METER)



D-DOT LEFT WING (A/SQUARE METER)

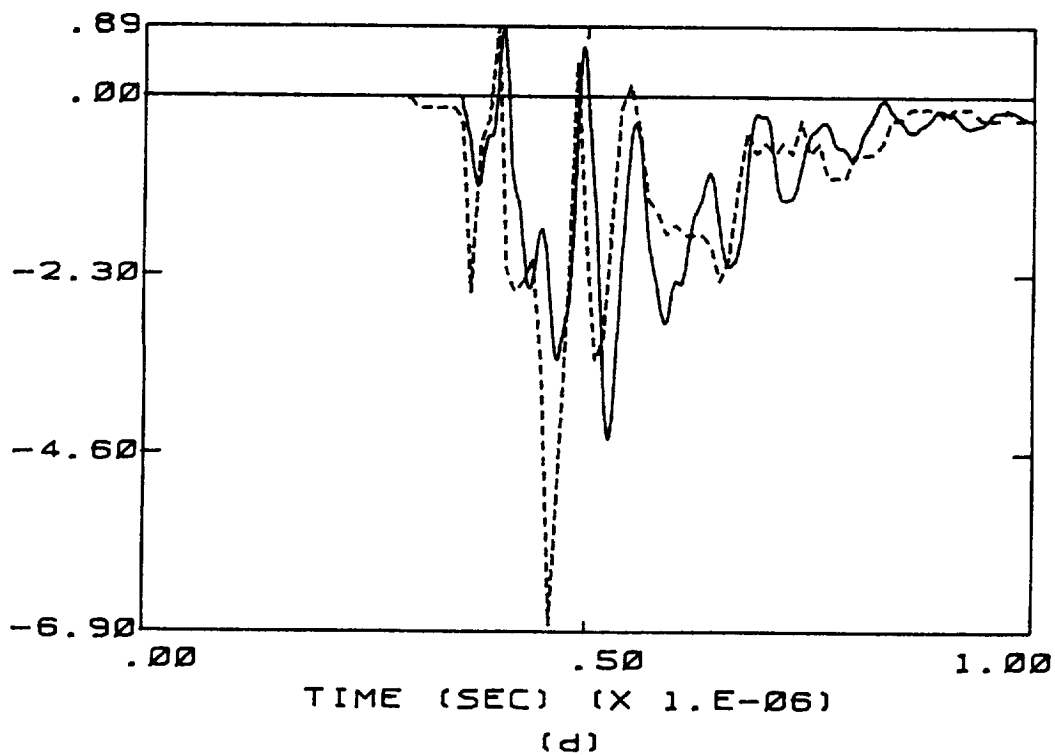


Figure C.3 (continued)

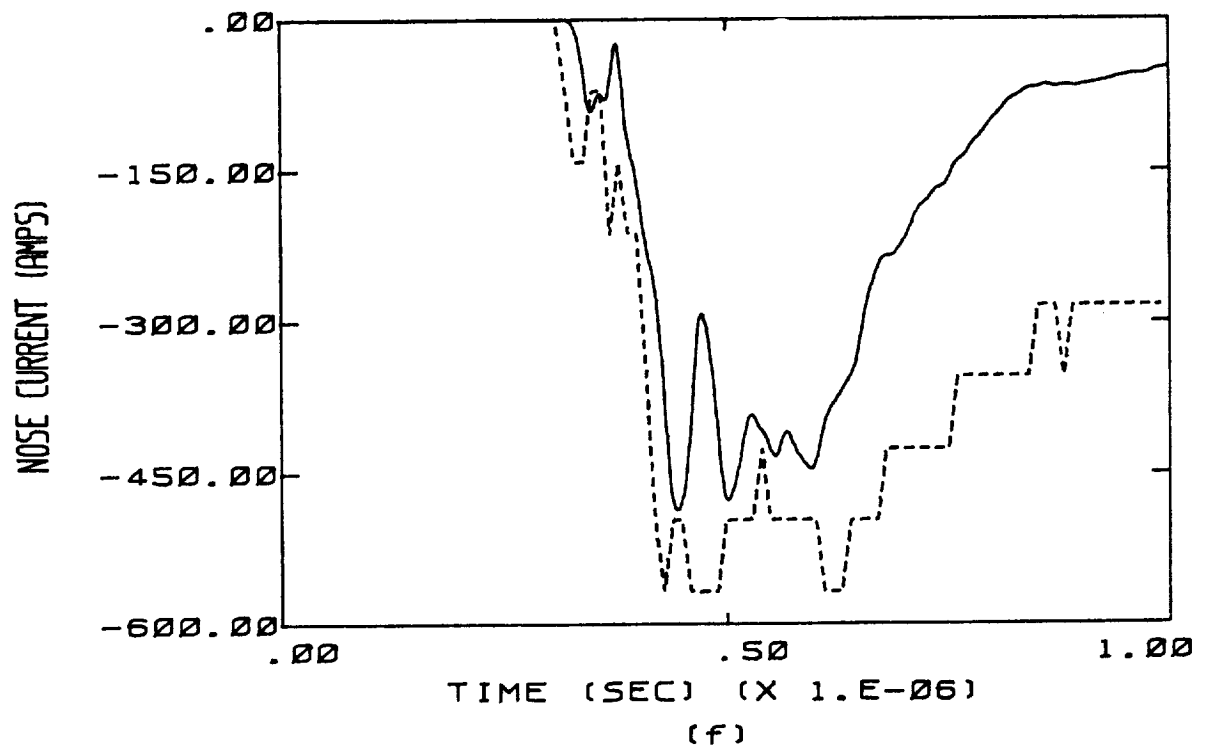
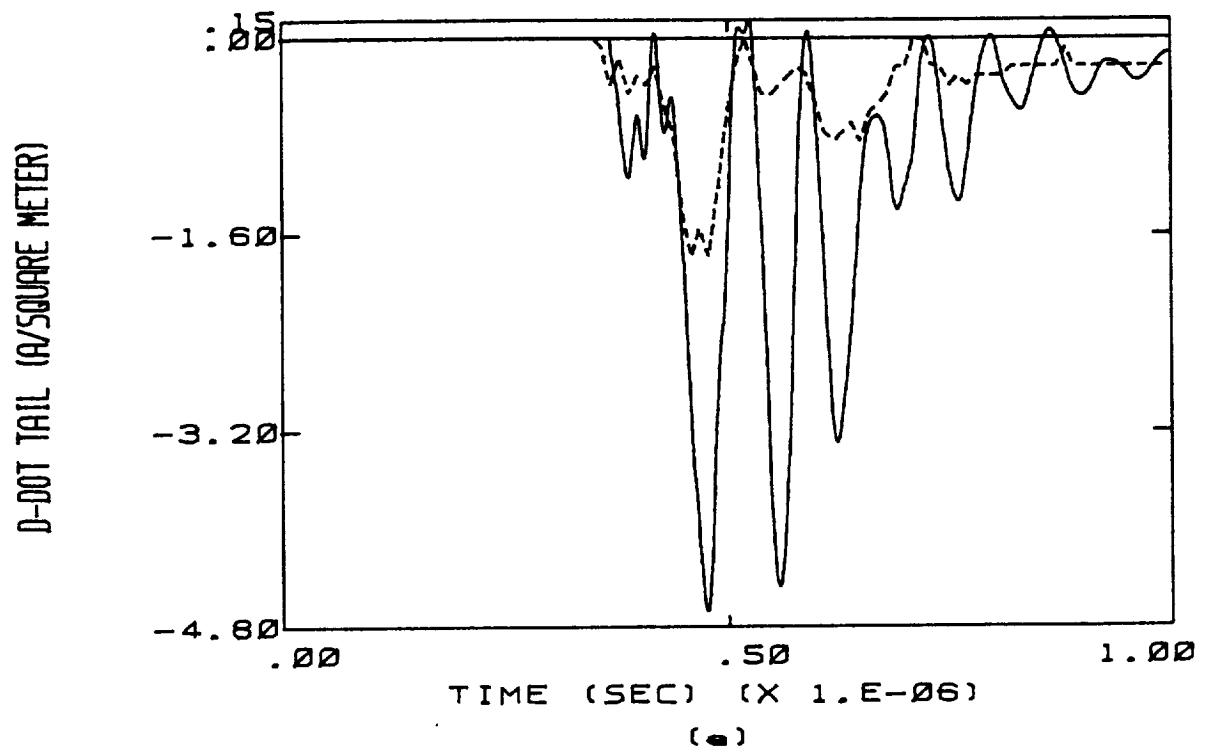
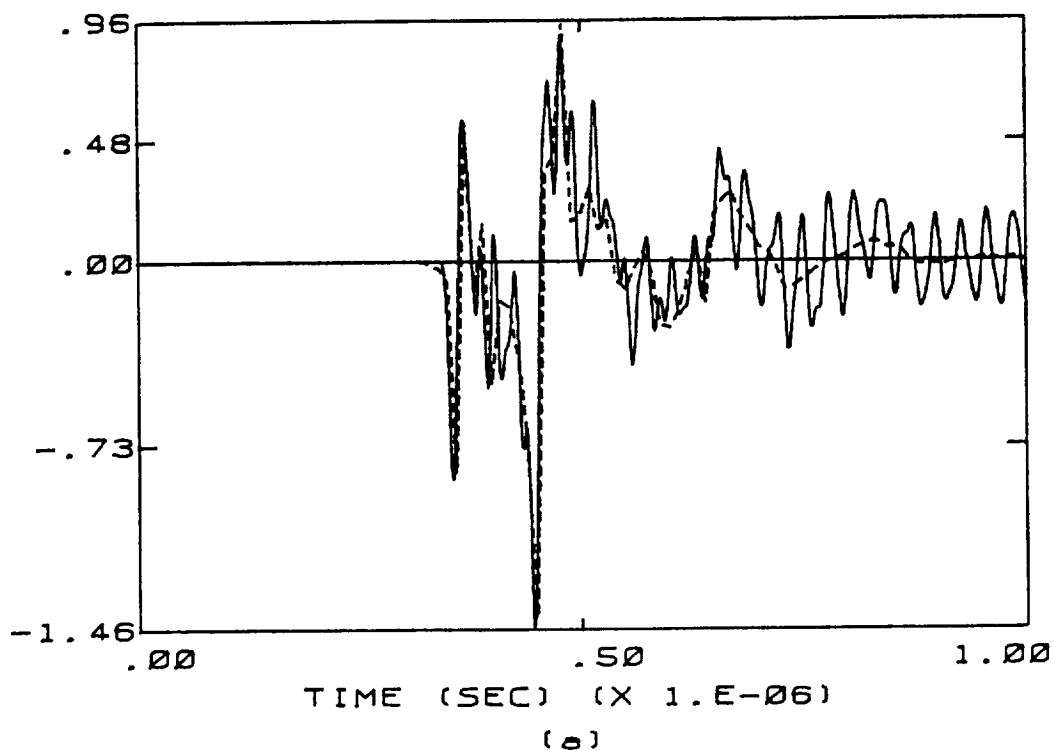


Figure C.3 (continued)



B-DOT LONGITUDINAL (T/S) (X 1.E+03)



B-DOT LEFT WING (T/S) (X 1.E+03)

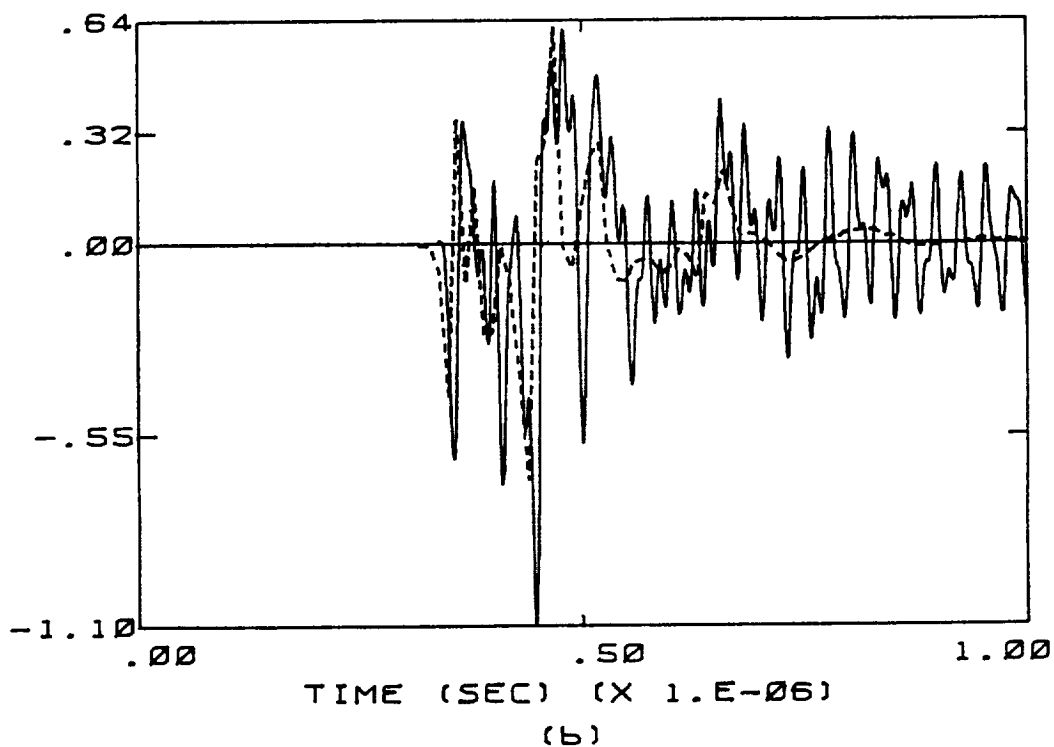


Figure C.4 Calculated Responses Overlaid on Measured Responses of Flight 84-017 for the Case of a 1 cm Radius Channel. The Transfer Function Used Is Appropriate to D-dot Left Wing. The Dashed Line Indicates the Measured Data.

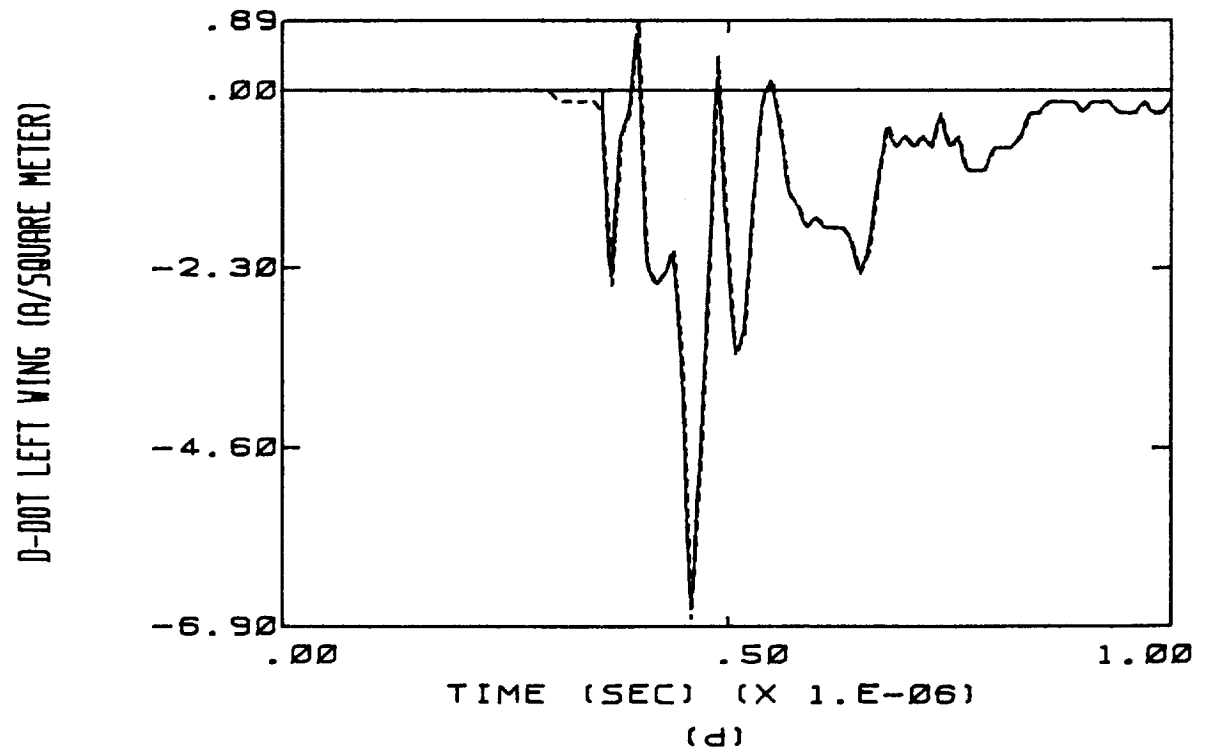
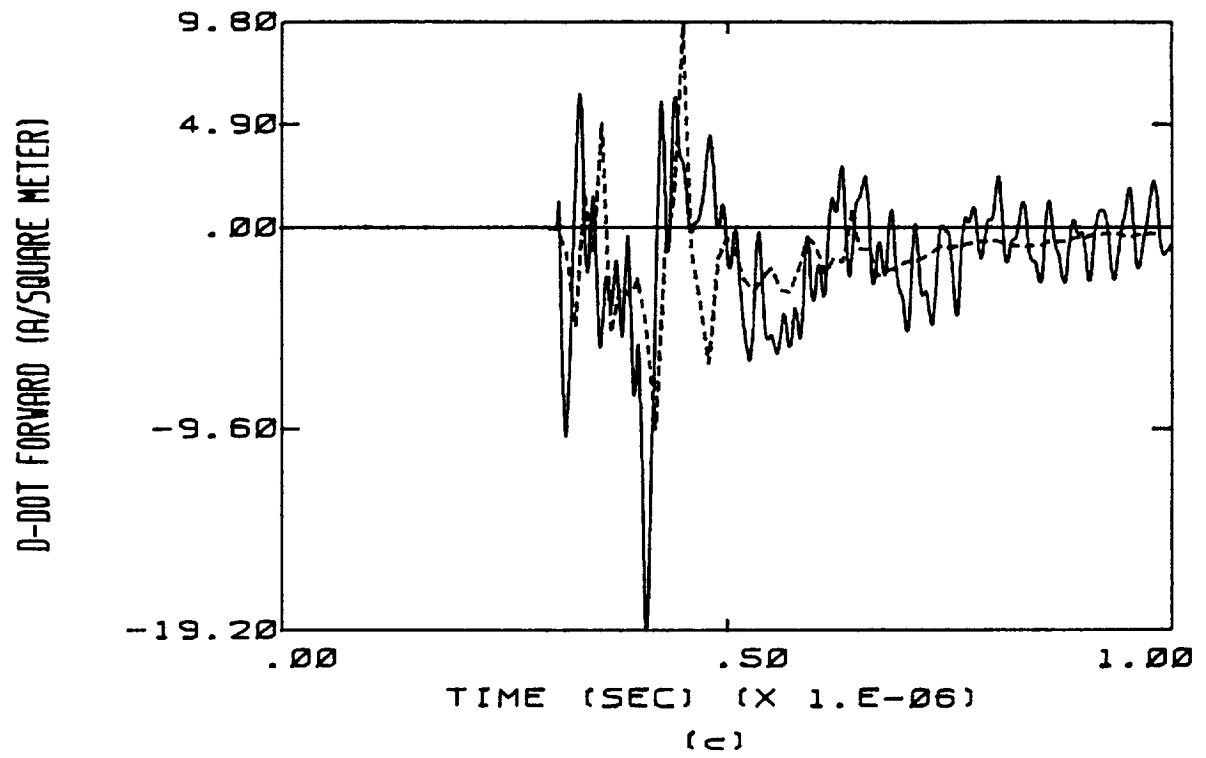


Figure C.4 (continued)

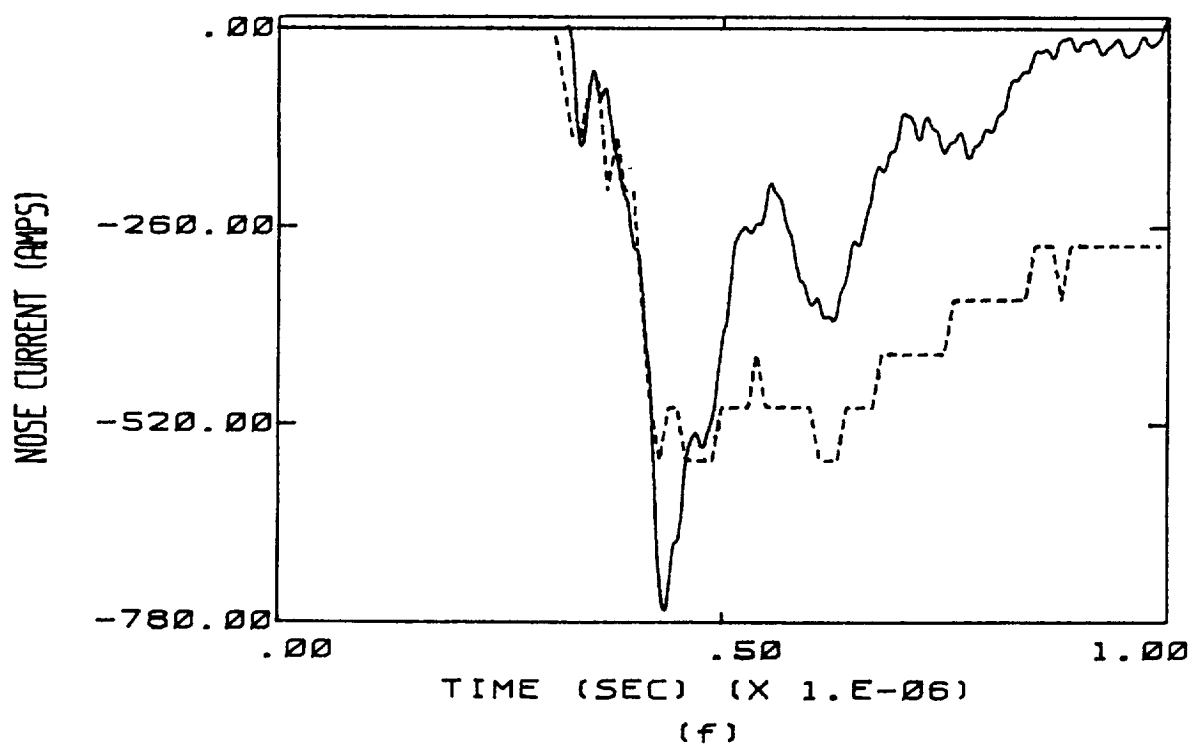
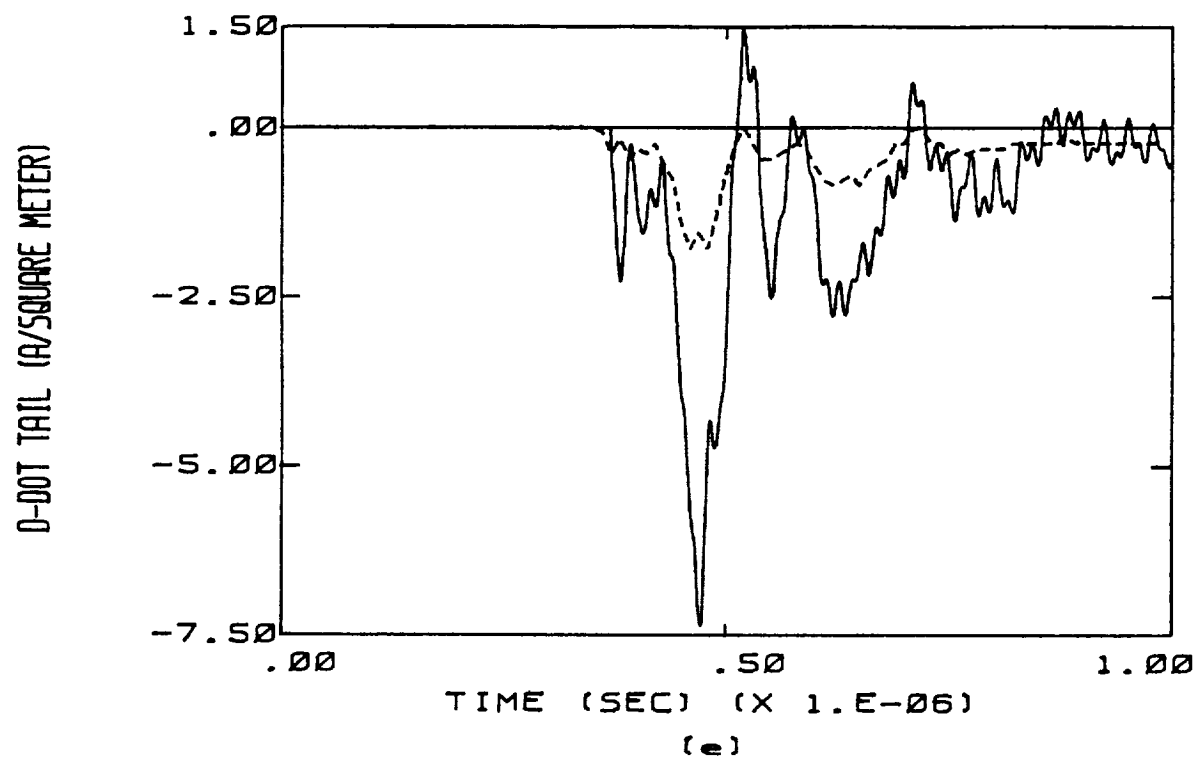


Figure C.4 (continued)

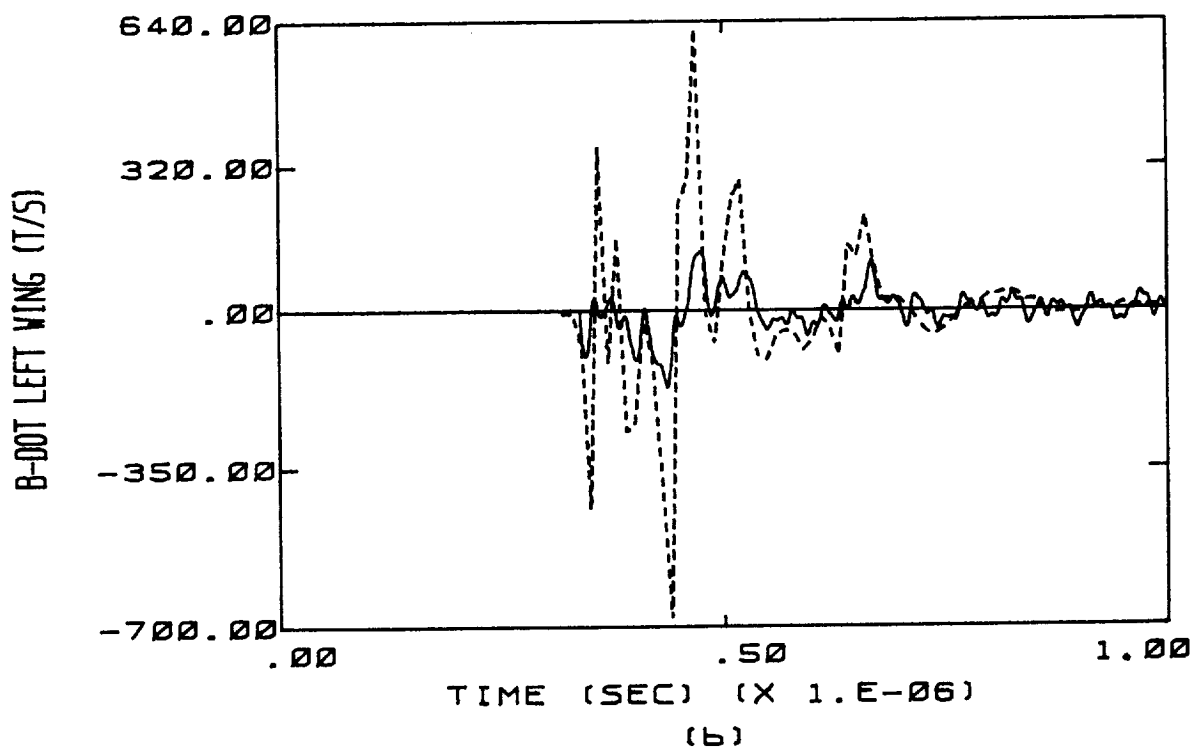
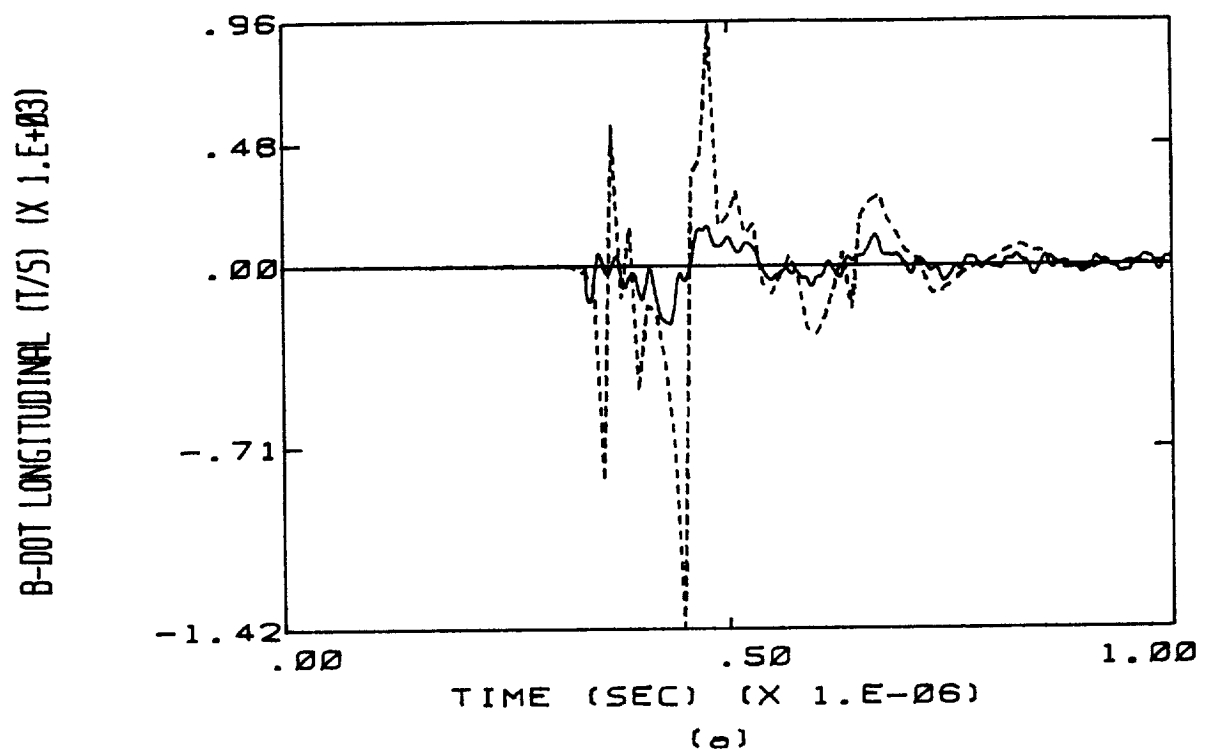
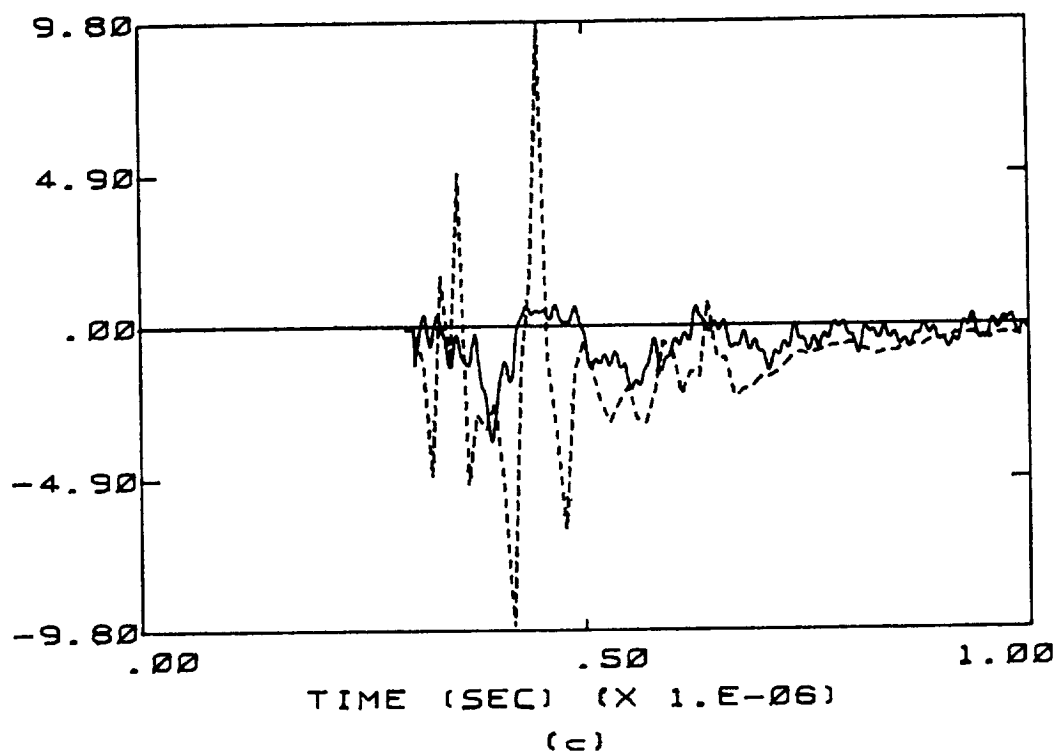


Figure C.5 Calculated Responses Overlaid on Measured Responses of Flight 84-017 for the Case of a 1 cm Radius Channel. The Transfer Function Used Is Appropriate to D-dot Tail. The Dashed Line Indicates the Measured Data.

D-DOT FORWARD (A/SQUARE METER)



D-DOT LEFT WING (A/SQUARE METER)

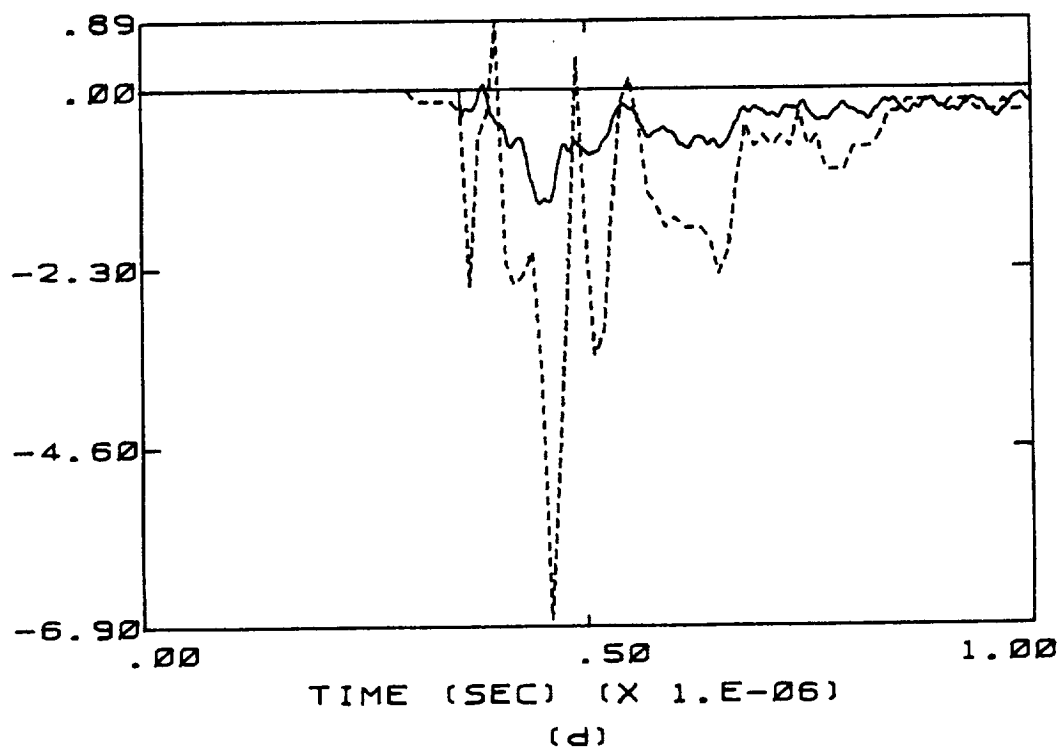


Figure C.5 (continued)

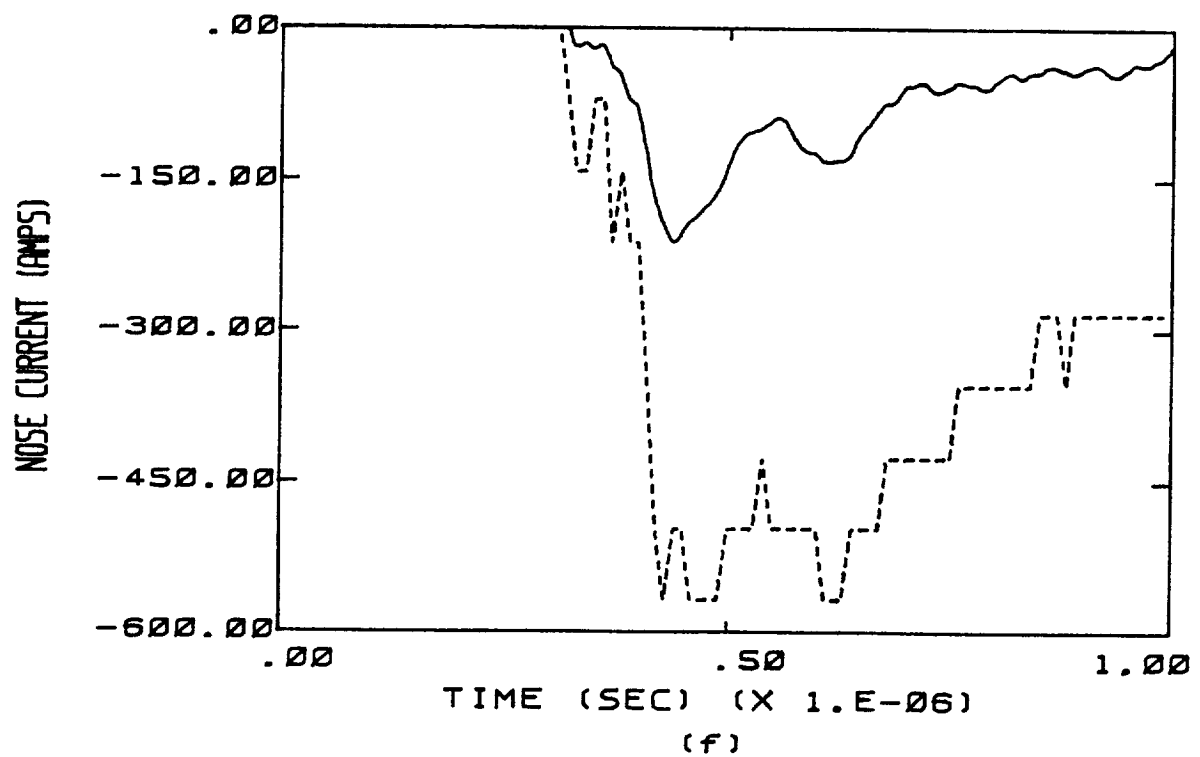
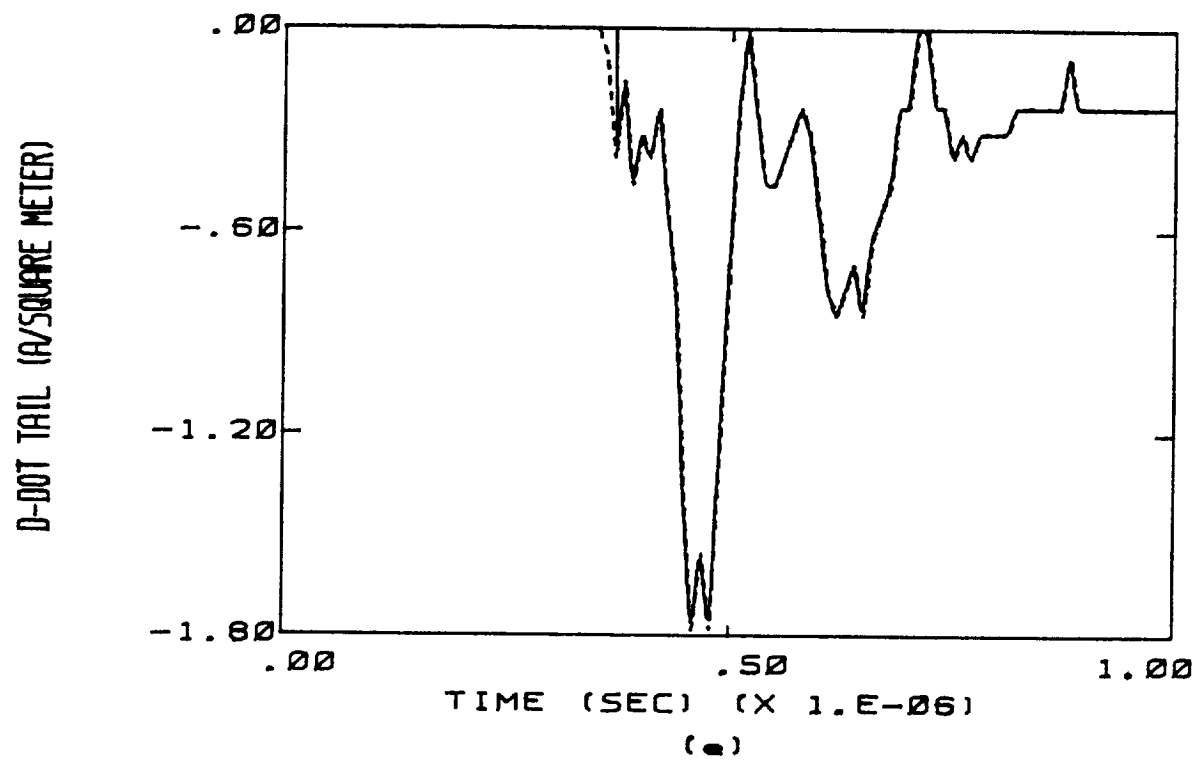


Figure C.5 (continued)

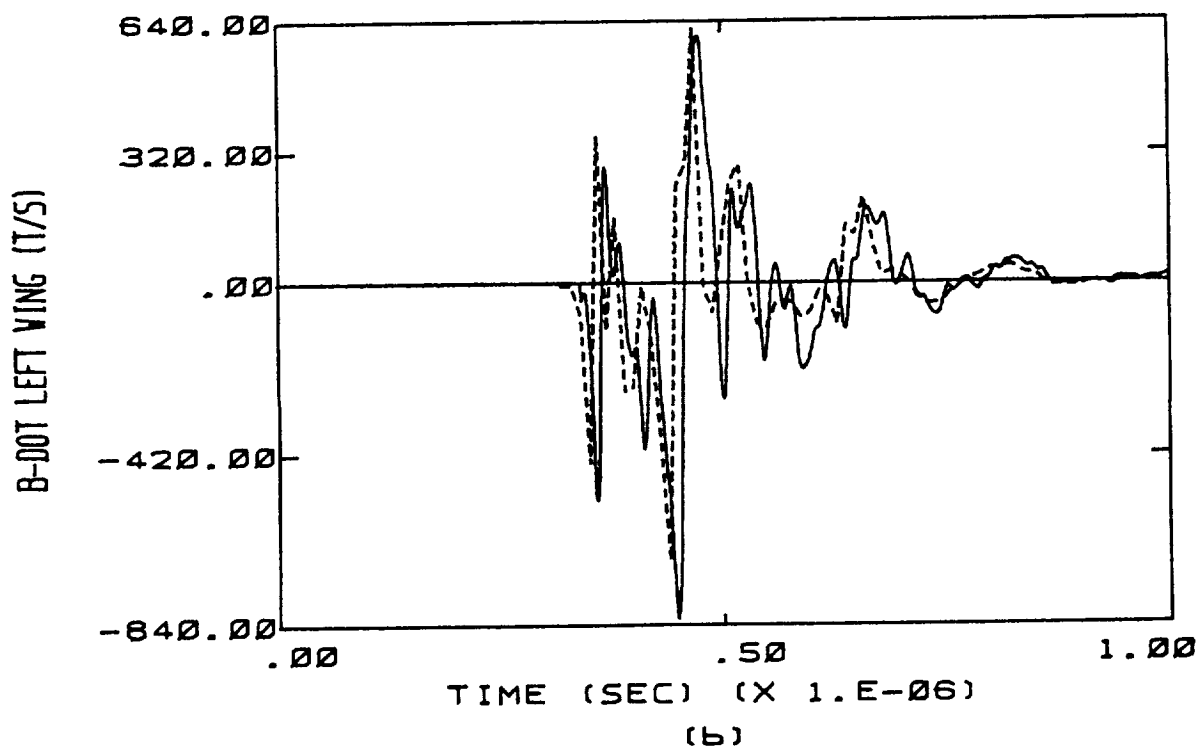
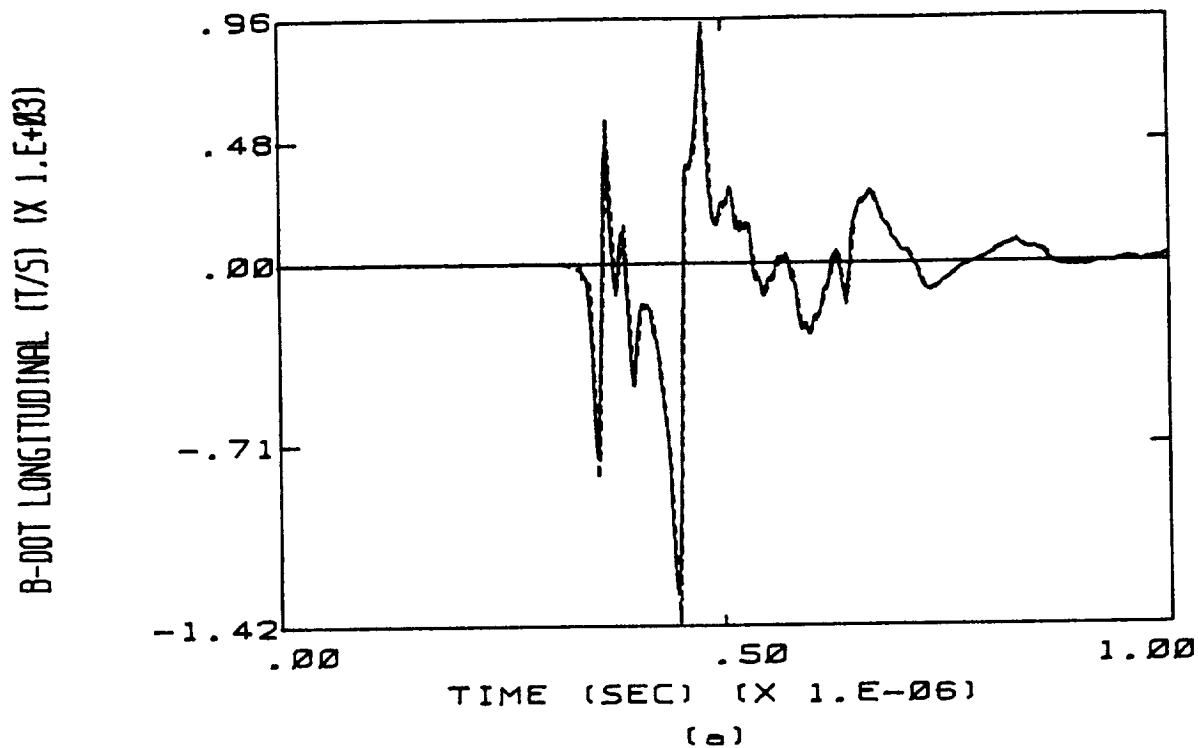
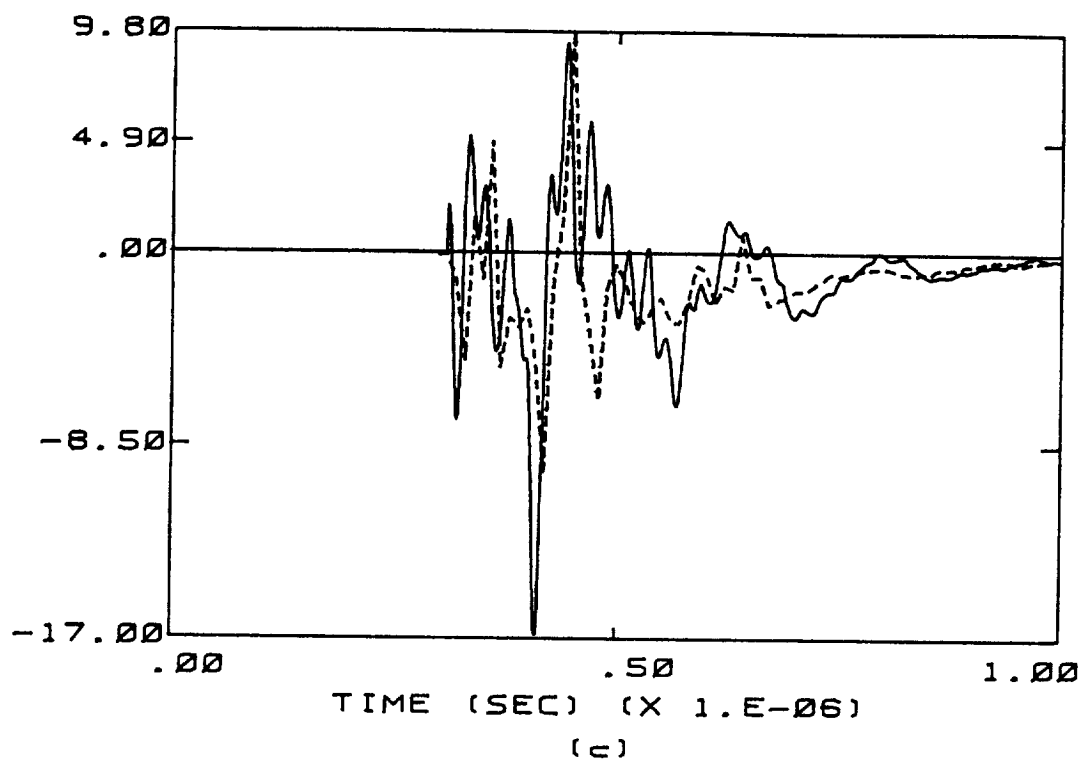


Figure C.6 Calculated Responses Overlaid on Measured Responses of Flight 84-017 for the Case of a 5 cm Radius Channel. The Transfer Function Used Is Appropriate to B-dot Longitudinal. The Dashed Line Indicates the Measured Data.

D-DOT FORWARD (A/SQUARE METER)



D-DOT LEFT WING (A/SQUARE METER)

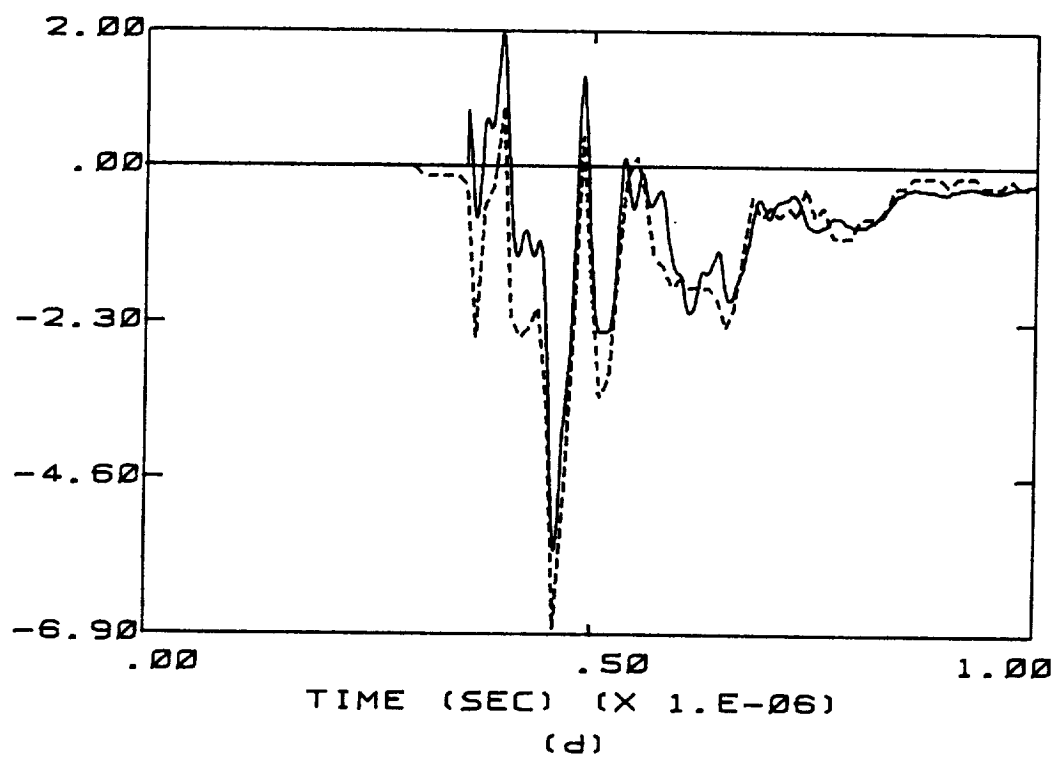


Figure C.6 (continued)



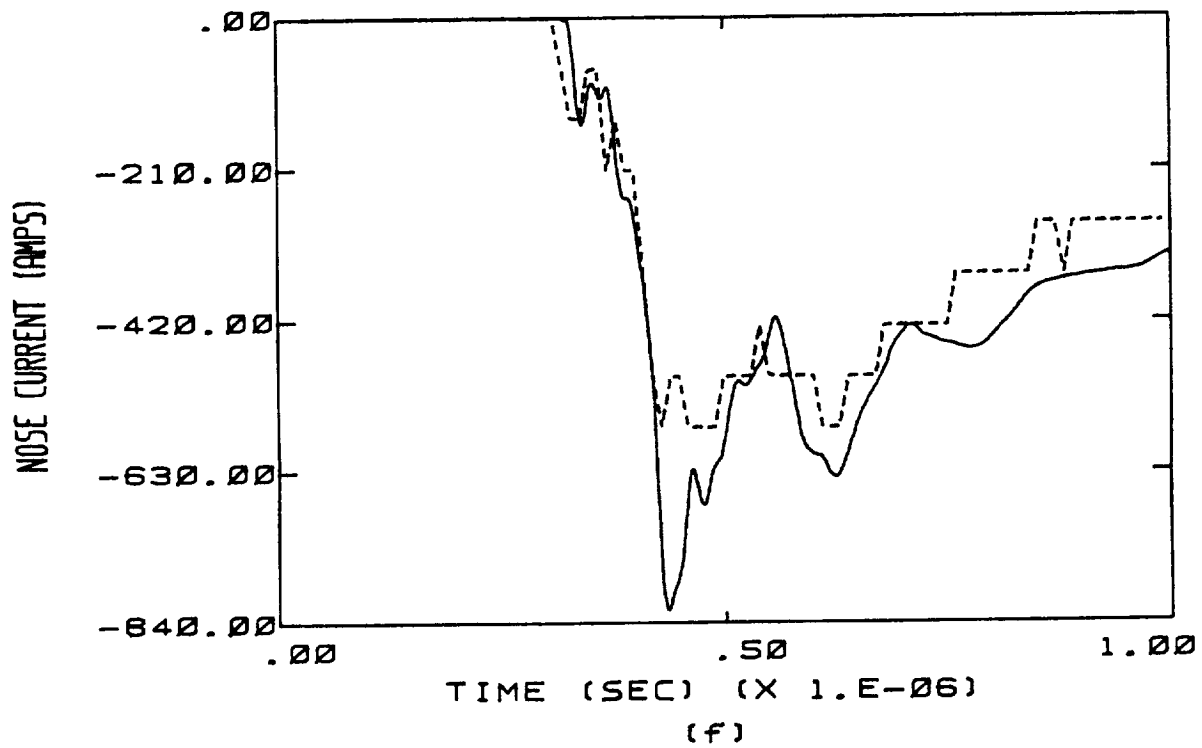
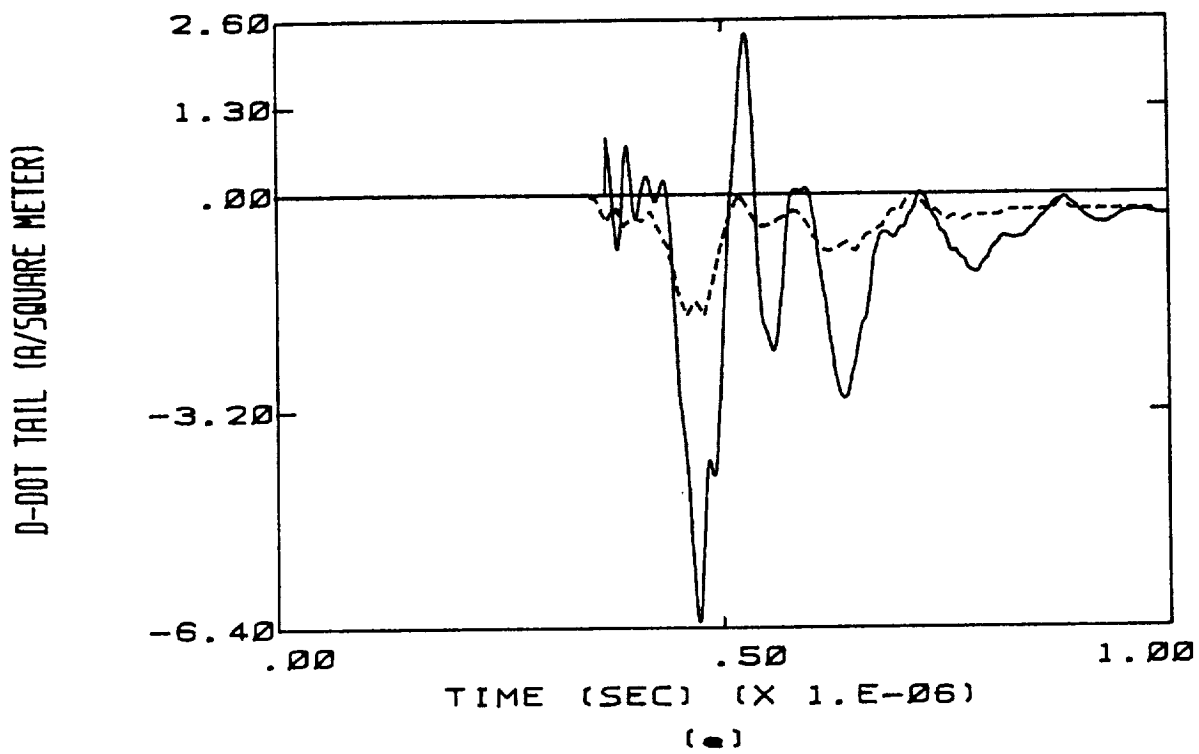


Figure C.6 (continued)

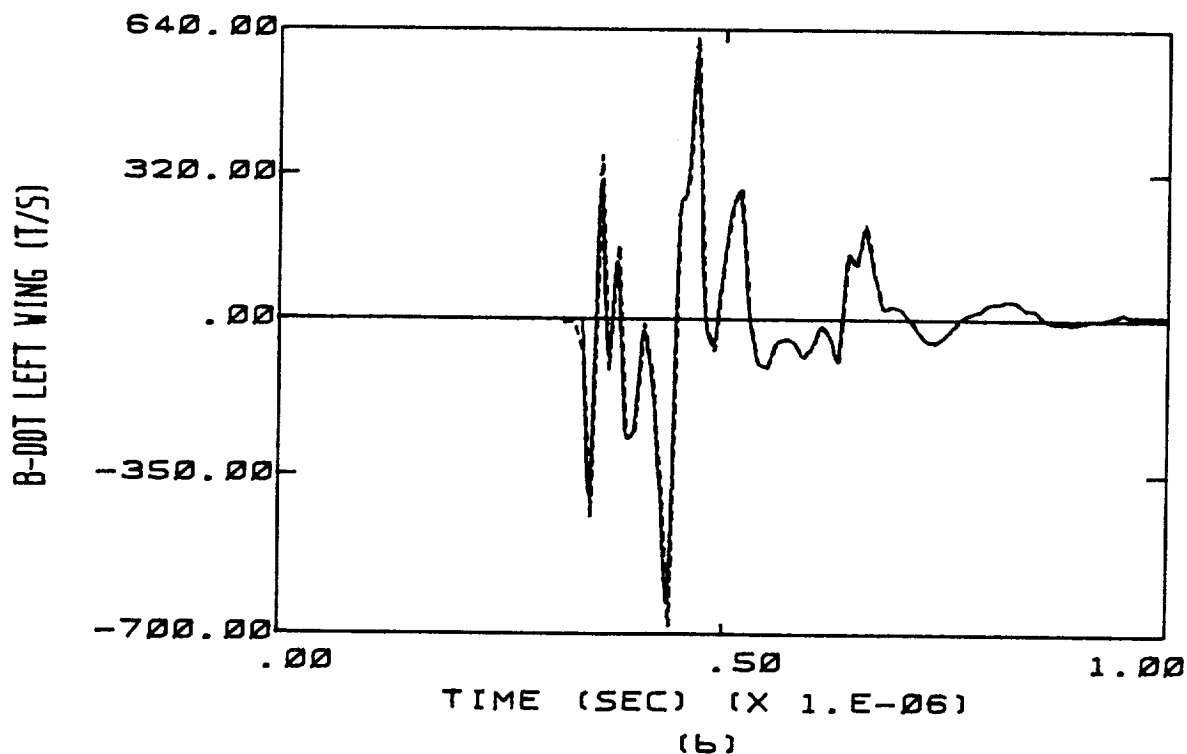
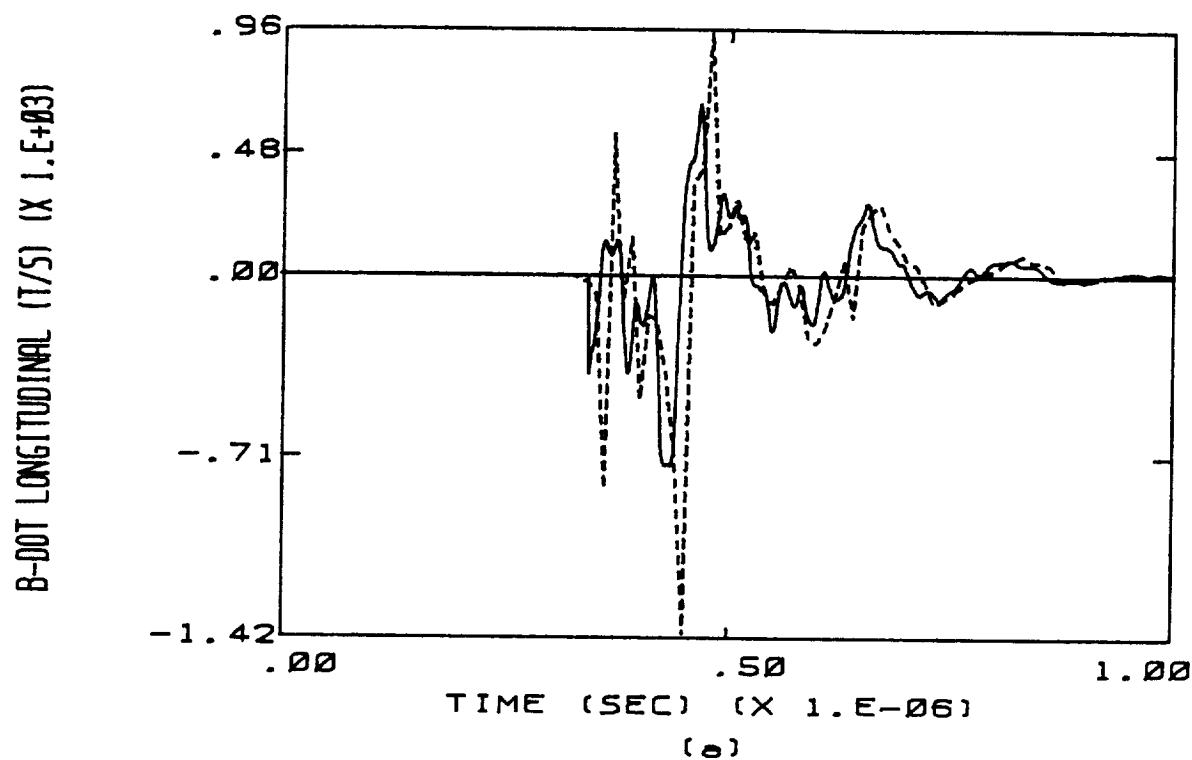
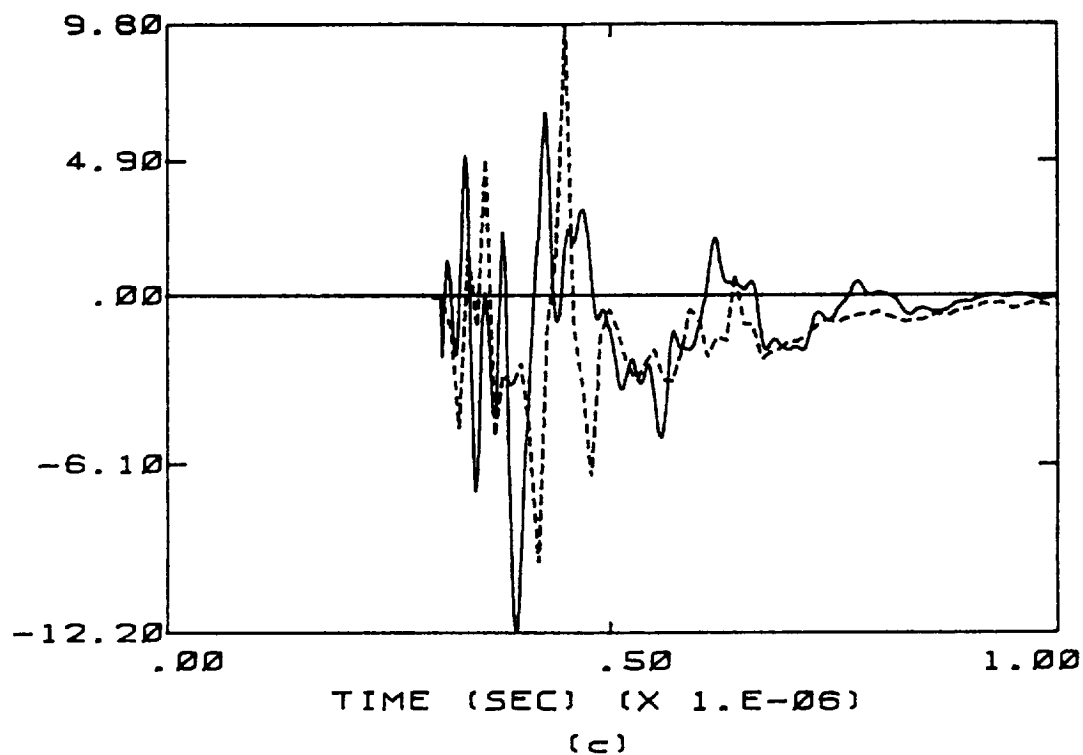


Figure C.7 Calculated Responses Overlaid on Measured Responses of Flight 84-017 for the Case of a 5 cm Radius Channel. The Transfer Function Used Is Appropriate to B-dot Left Wing. The Dashed Line Indicates the Measured Data.

D-DOT FORWARD (A/SQUARE METER)



D-DOT LEFT WING (A/SQUARE METER)

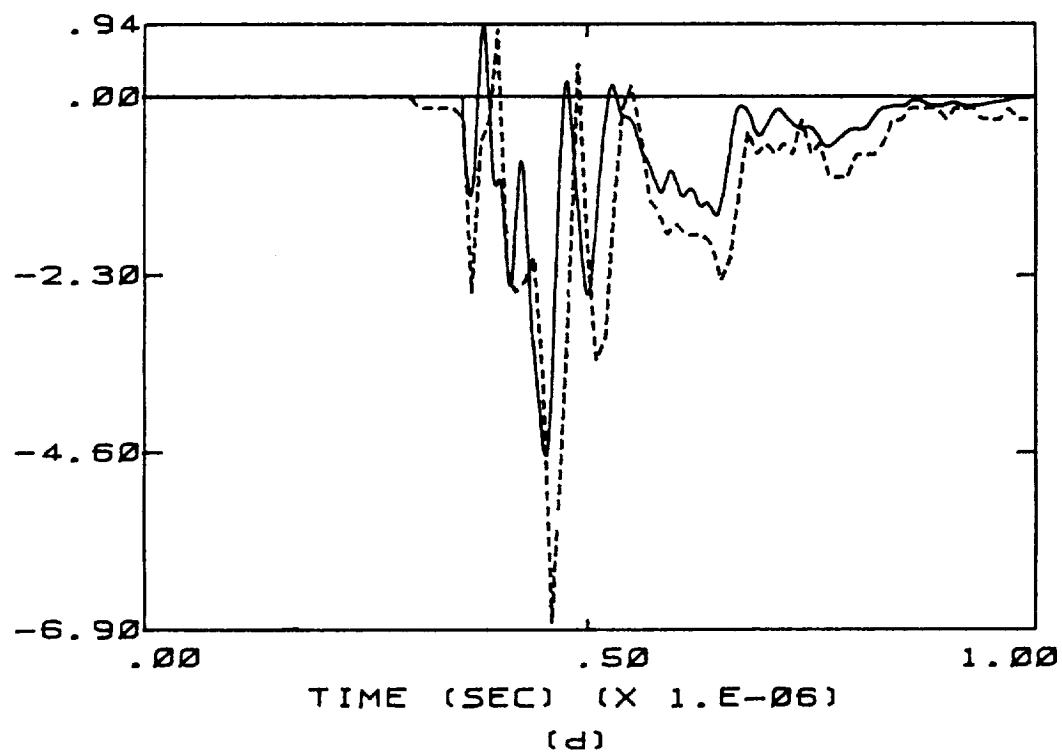


Figure C.7 (continued)

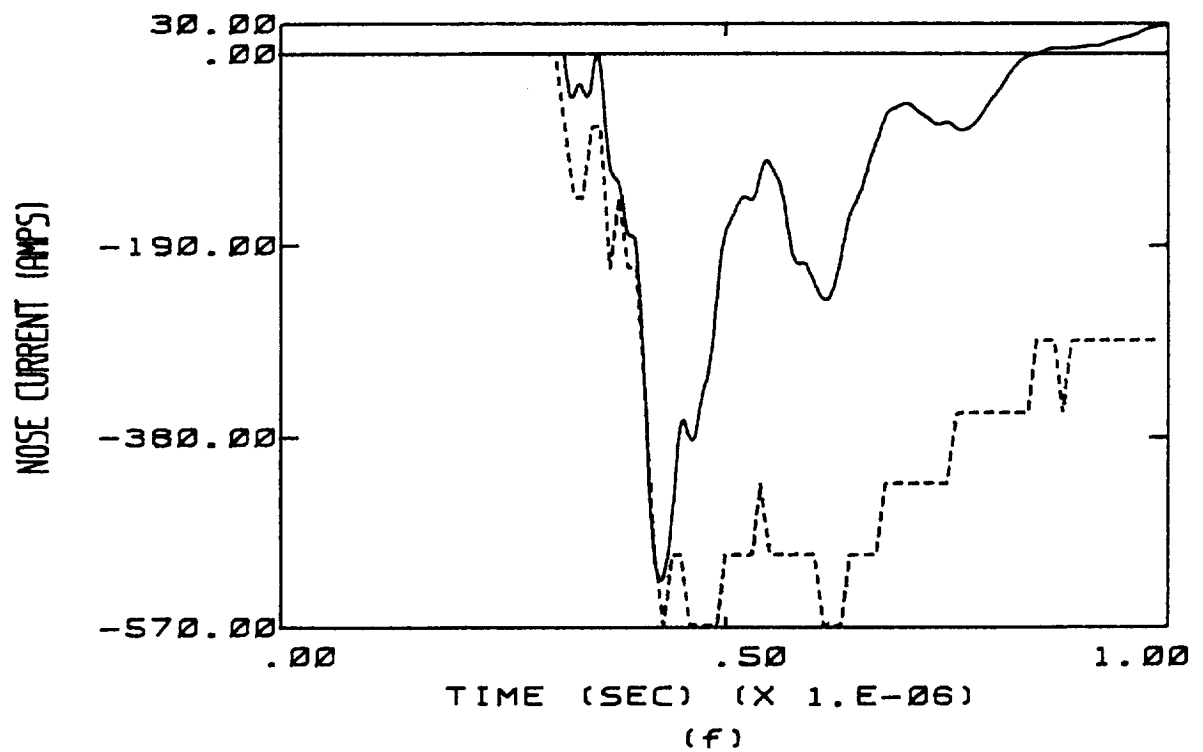
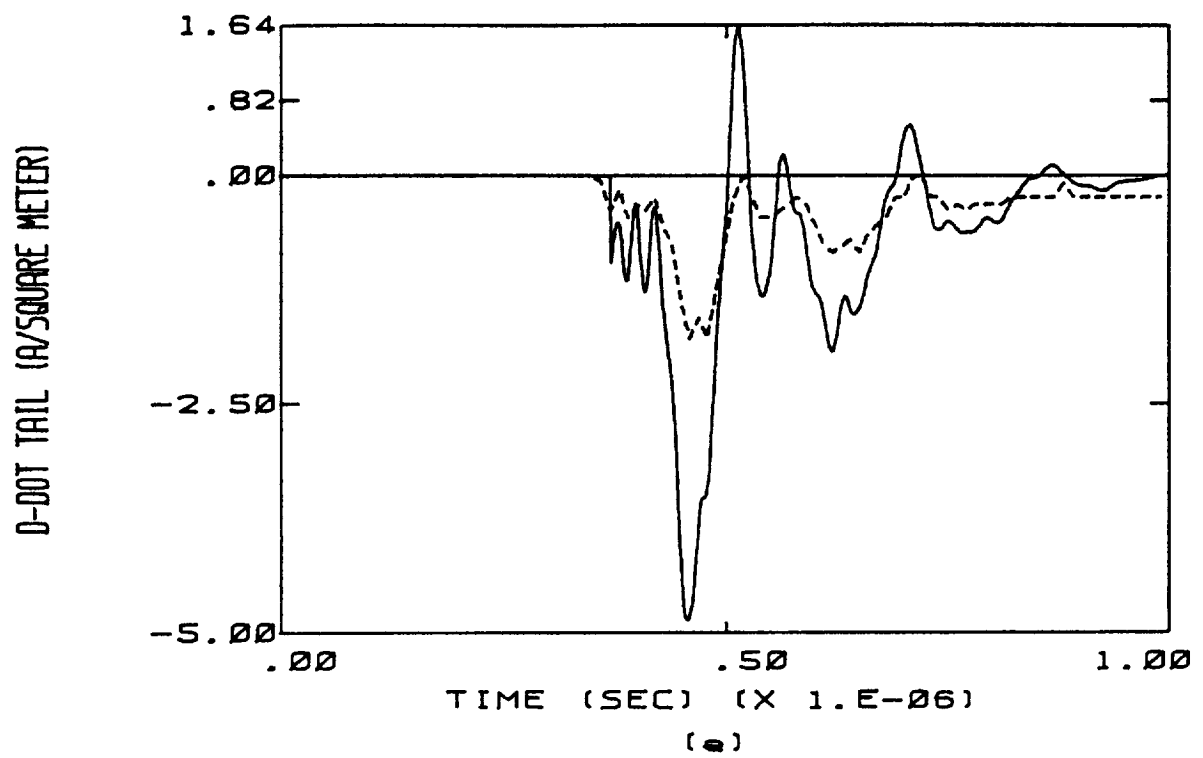


Figure C.7 (continued)

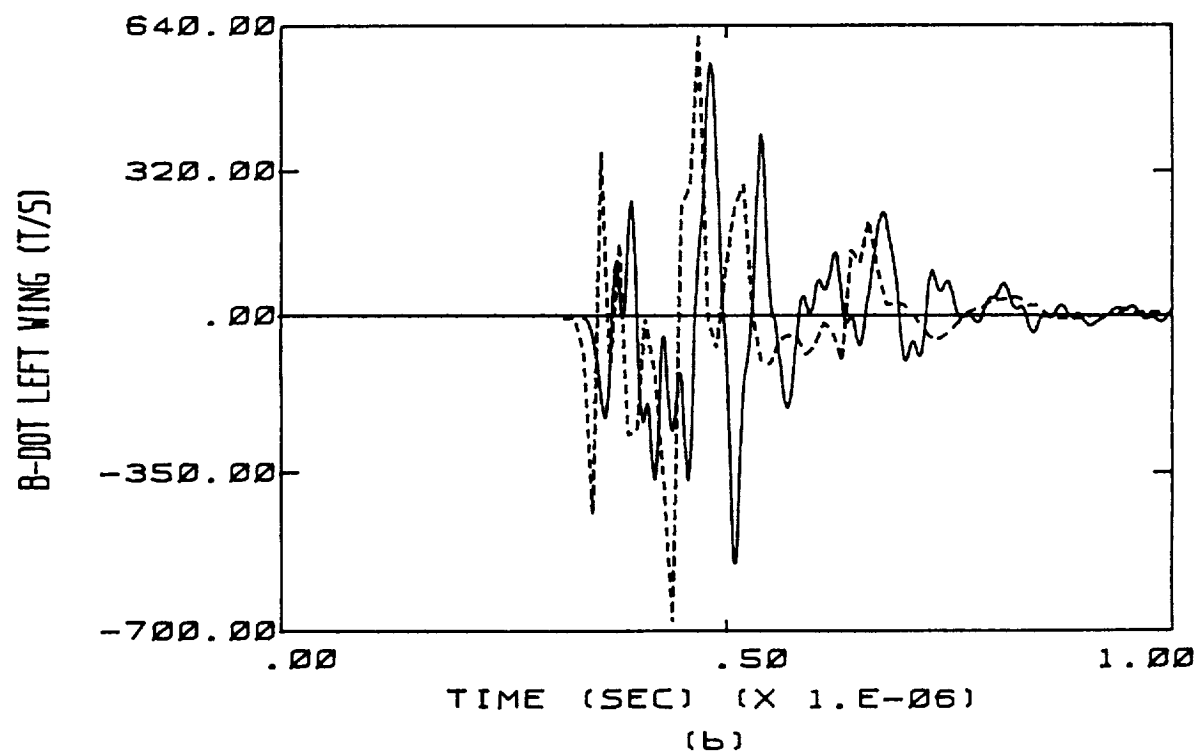
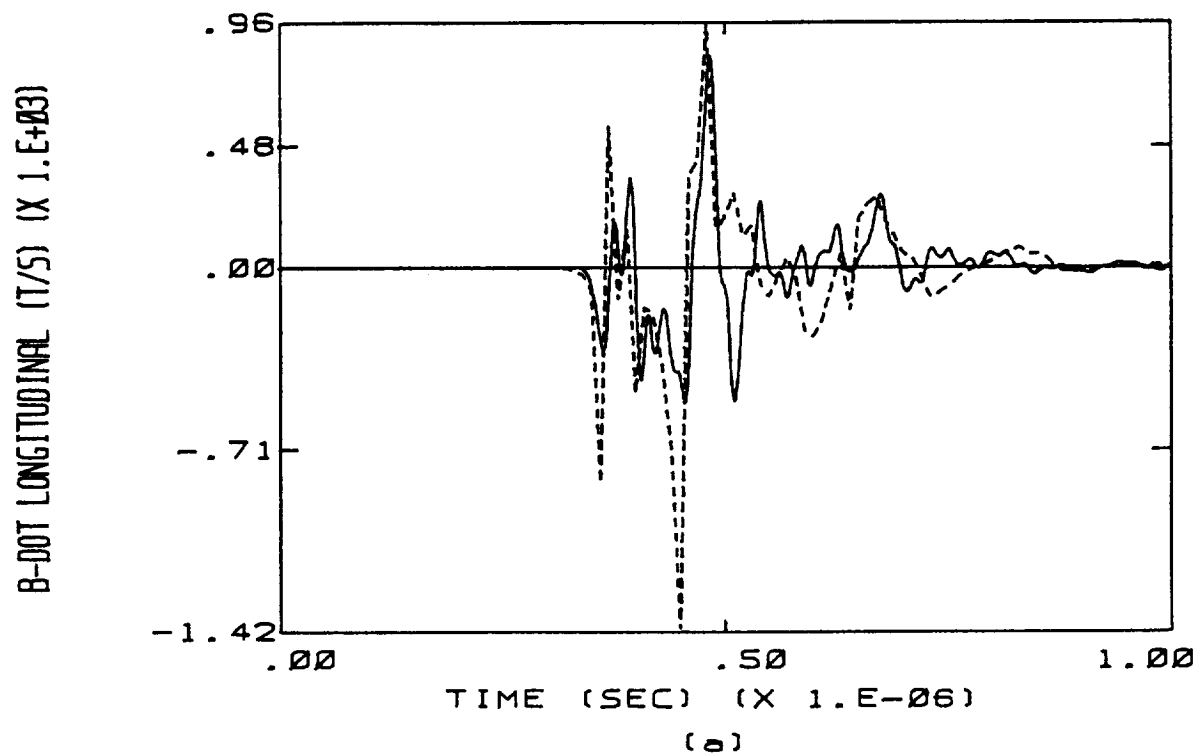
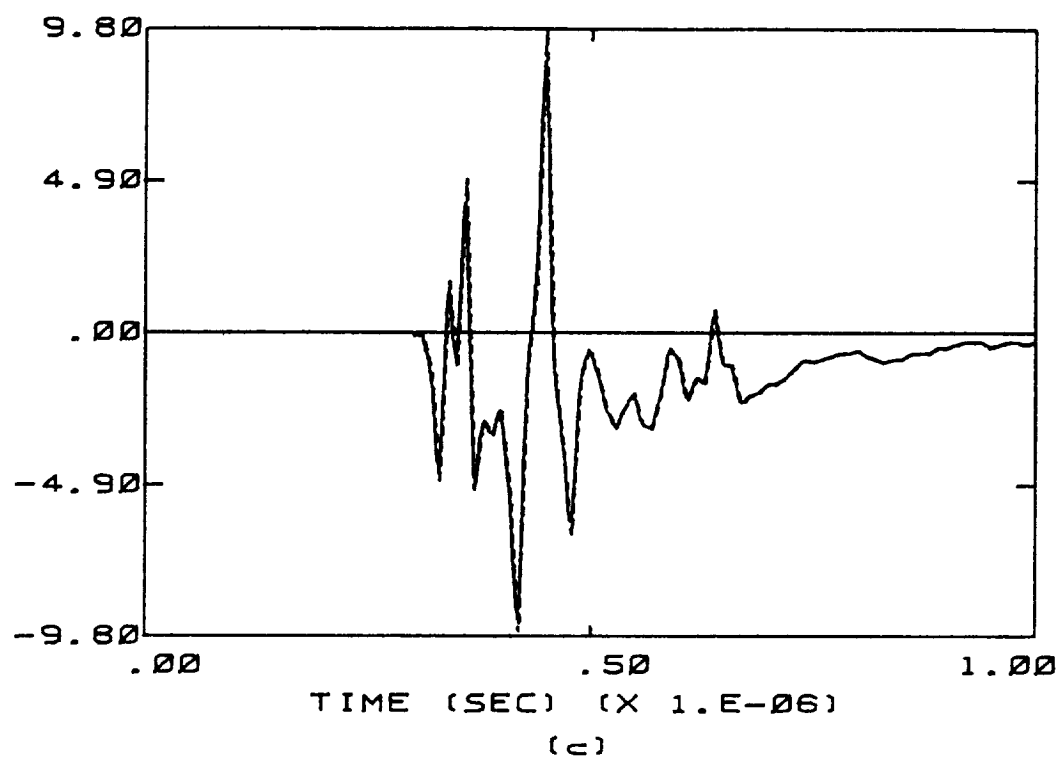


Figure C.8 Calculated Responses Overlaid on Measured Responses of Flight 84-017 for the Case of a 5 cm Radius Channel. The Transfer Function Used Is Appropriate to D-dot Forward. The Dashed Line Indicates the Measured Data.

D-DOT FORWARD (A/SQUARE METER)



D-DOT LEFT VING (A/SQUARE METER)

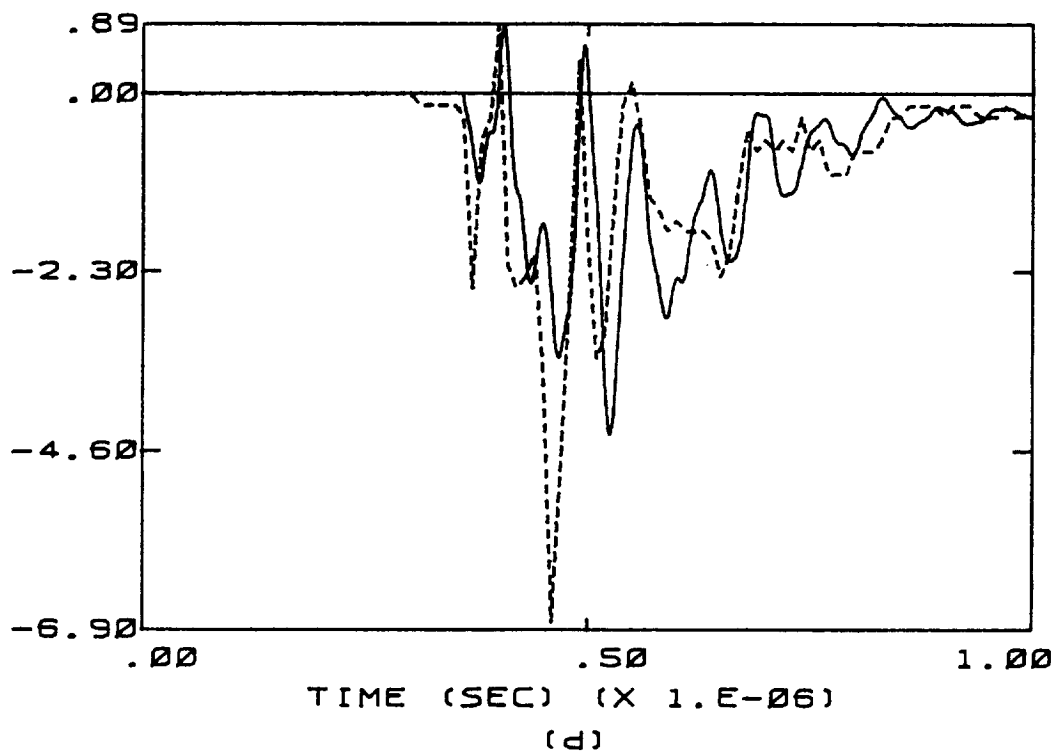


Figure C.8 (continued)

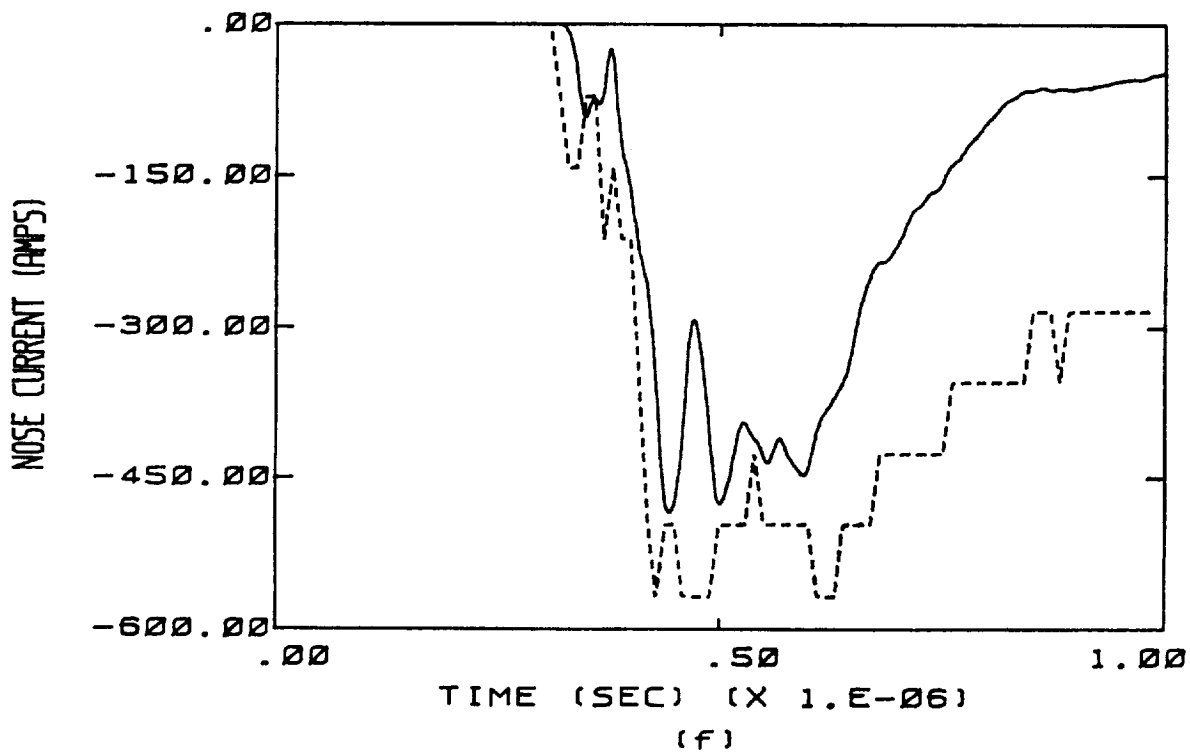
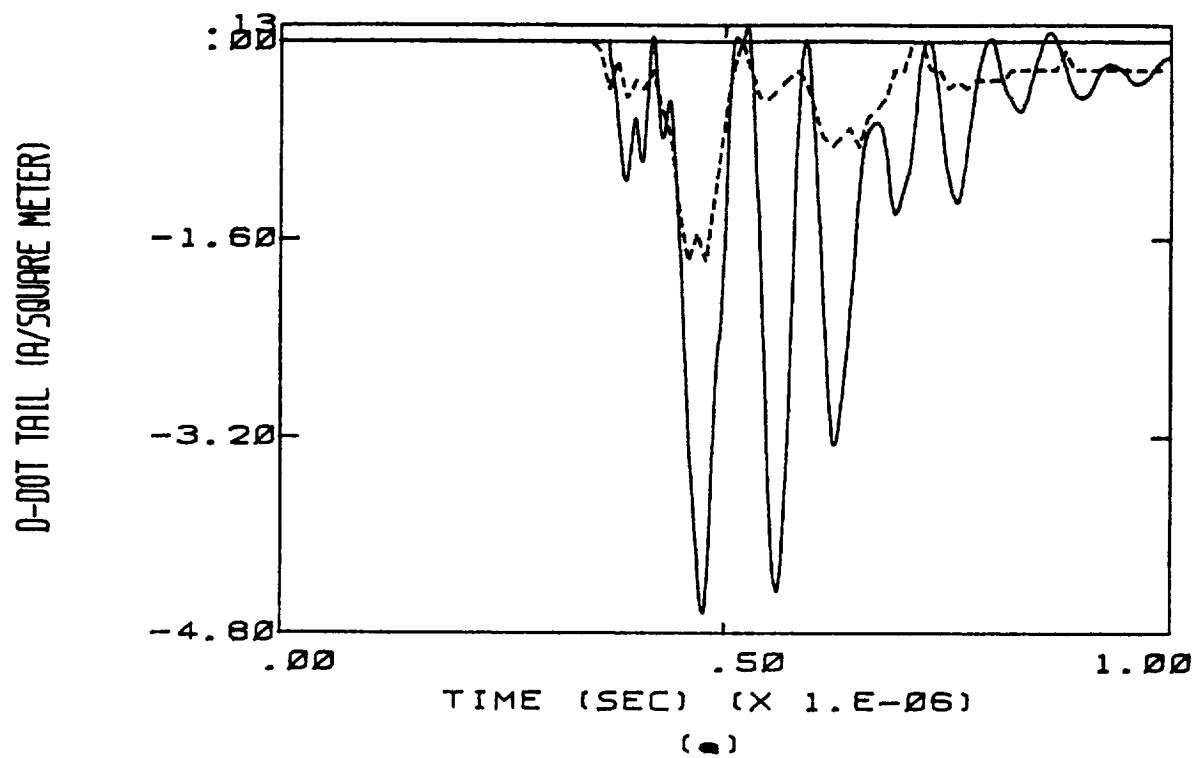


Figure C.8 (continued)

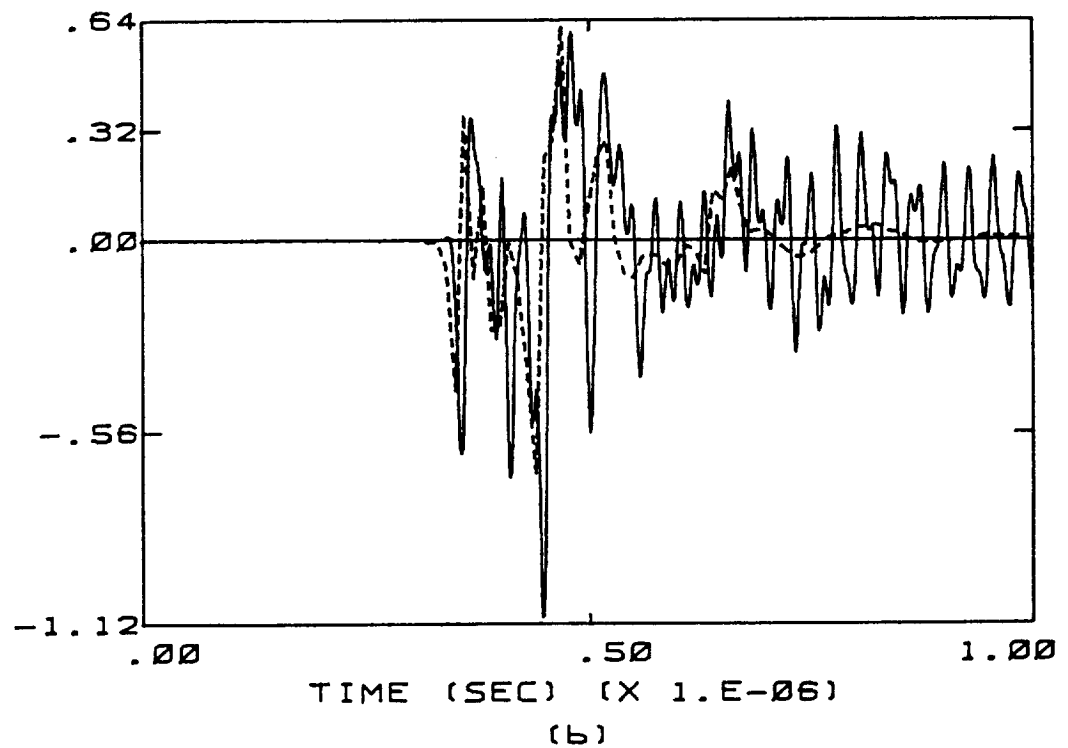
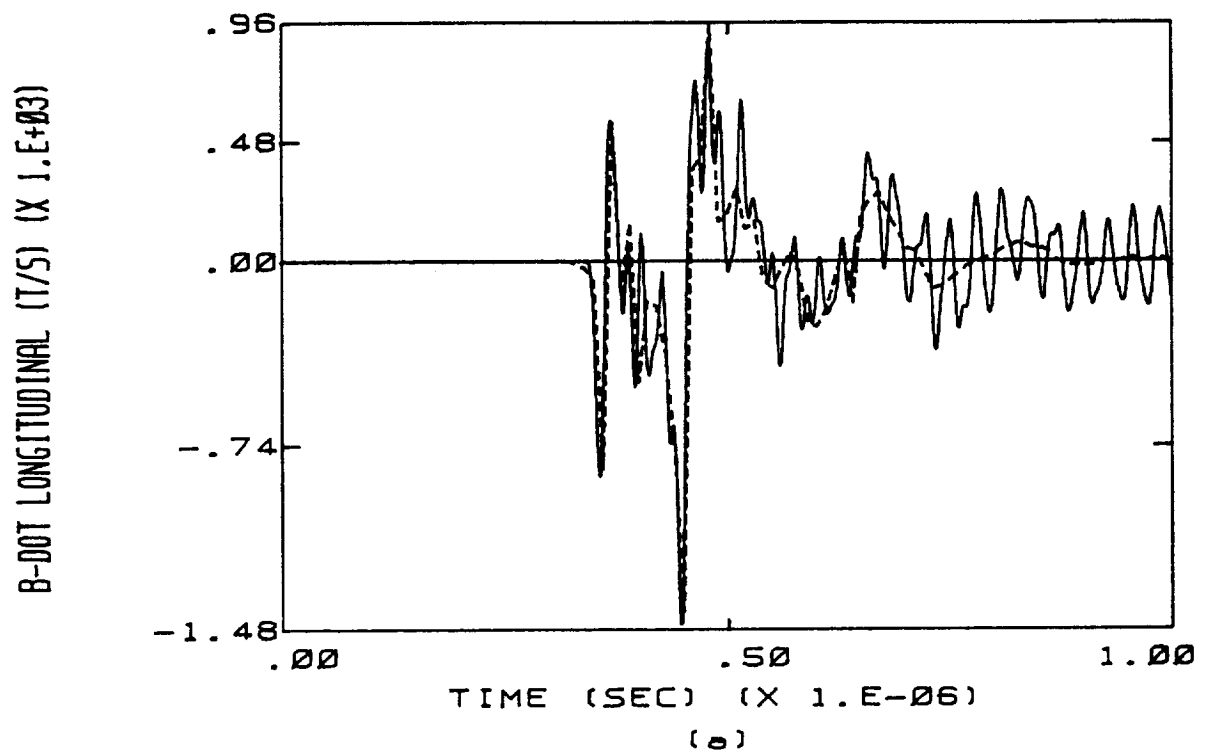
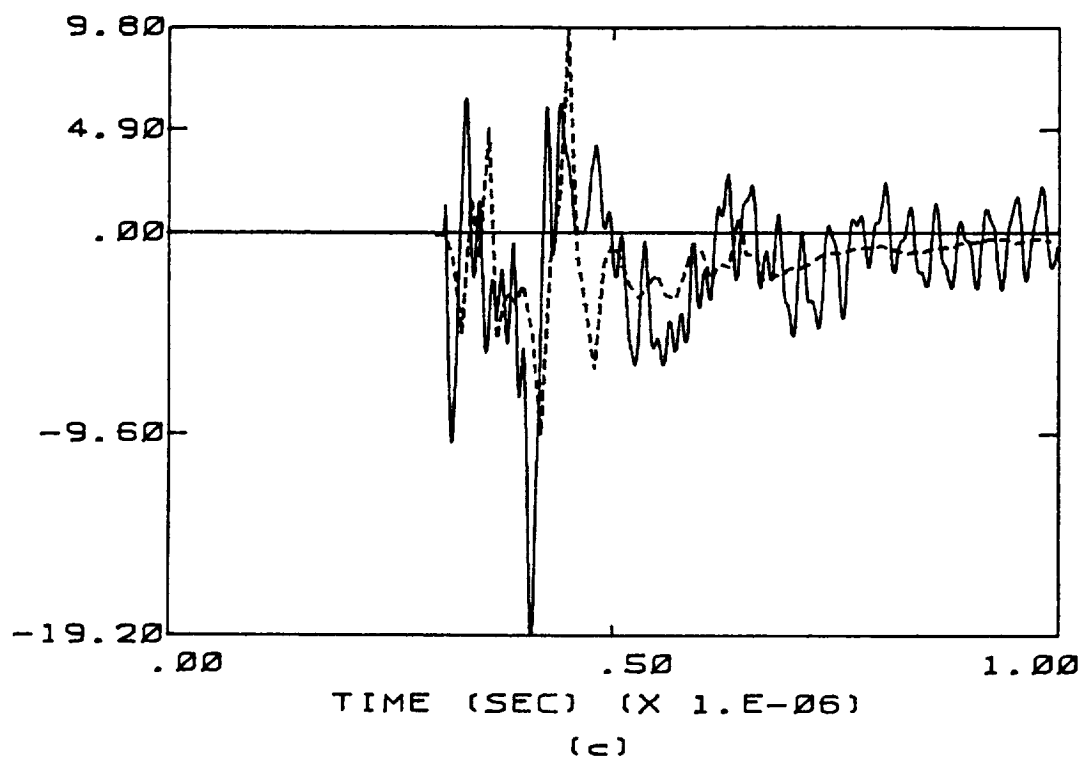


Figure C.9 Calculated Responses Overlaid on Measured Responses of Flight 84-017 for the Case of a 5 cm Radius Channel. The Transfer Function Used Is Appropriate to D-dot Left Wing. The Dashed Line Indicates the Measured Data.



D-DOT FORWARD (A/SQUARE METER)



D-DOT LEFT WING (A/SQUARE METER)

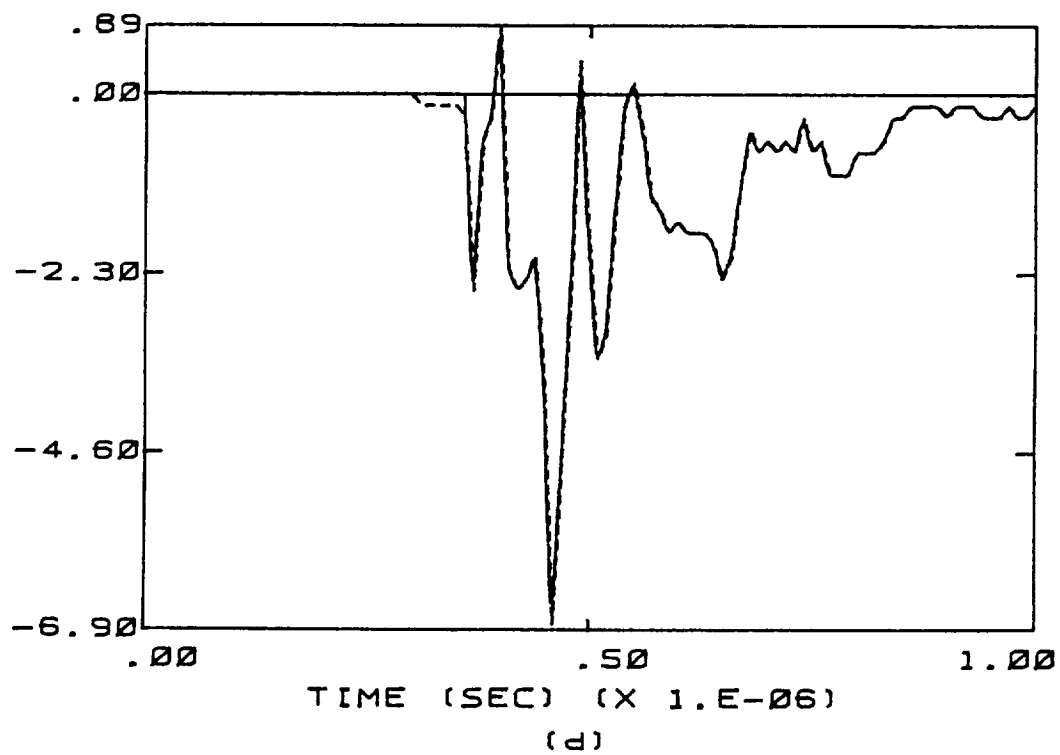


Figure C.9 (continued)

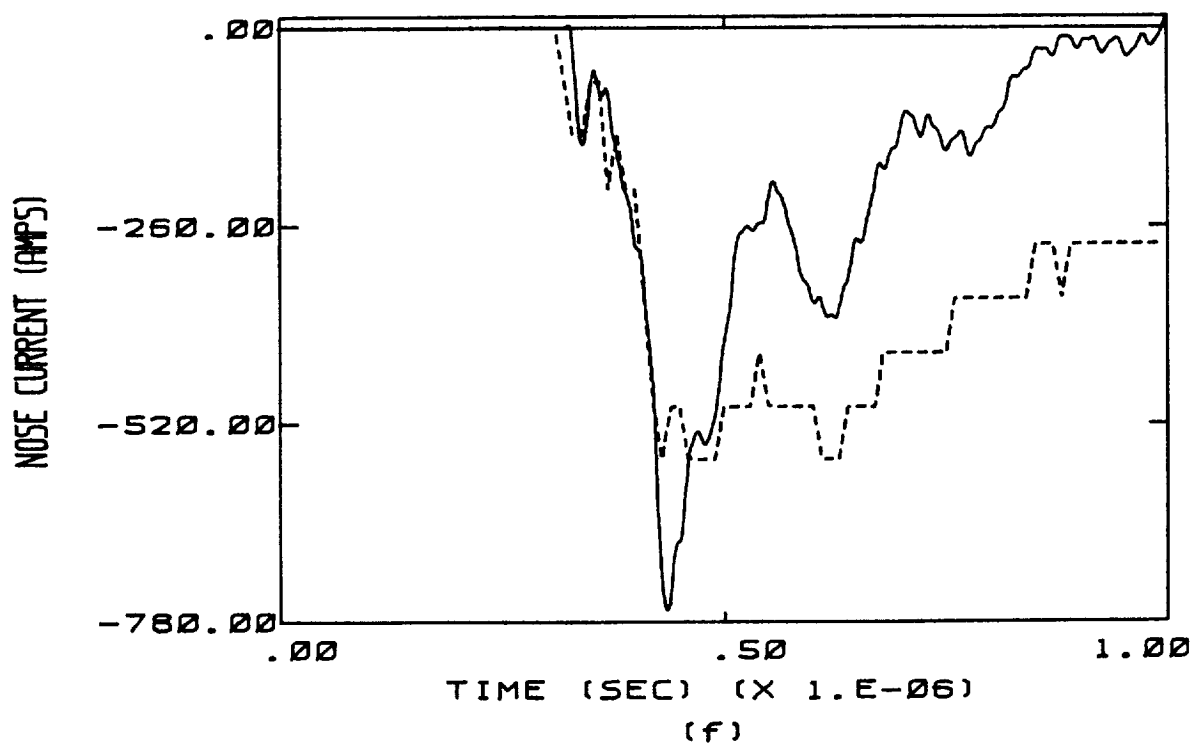
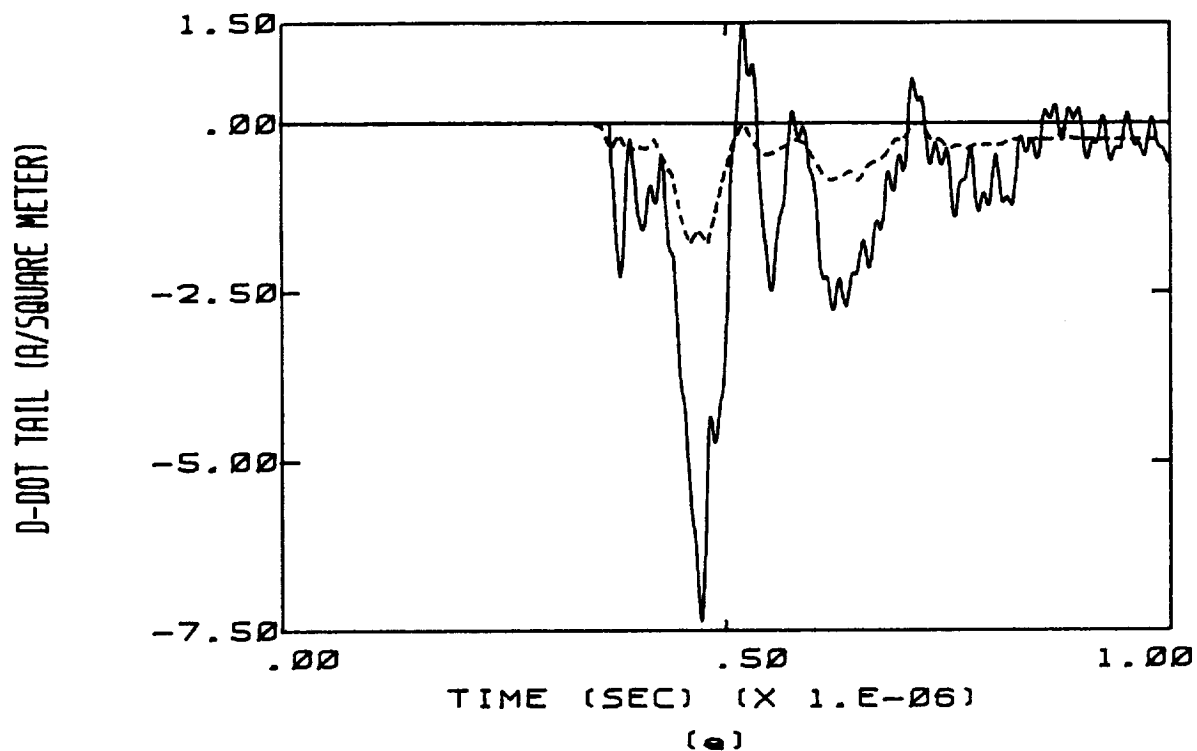


Figure C.9 (continued)

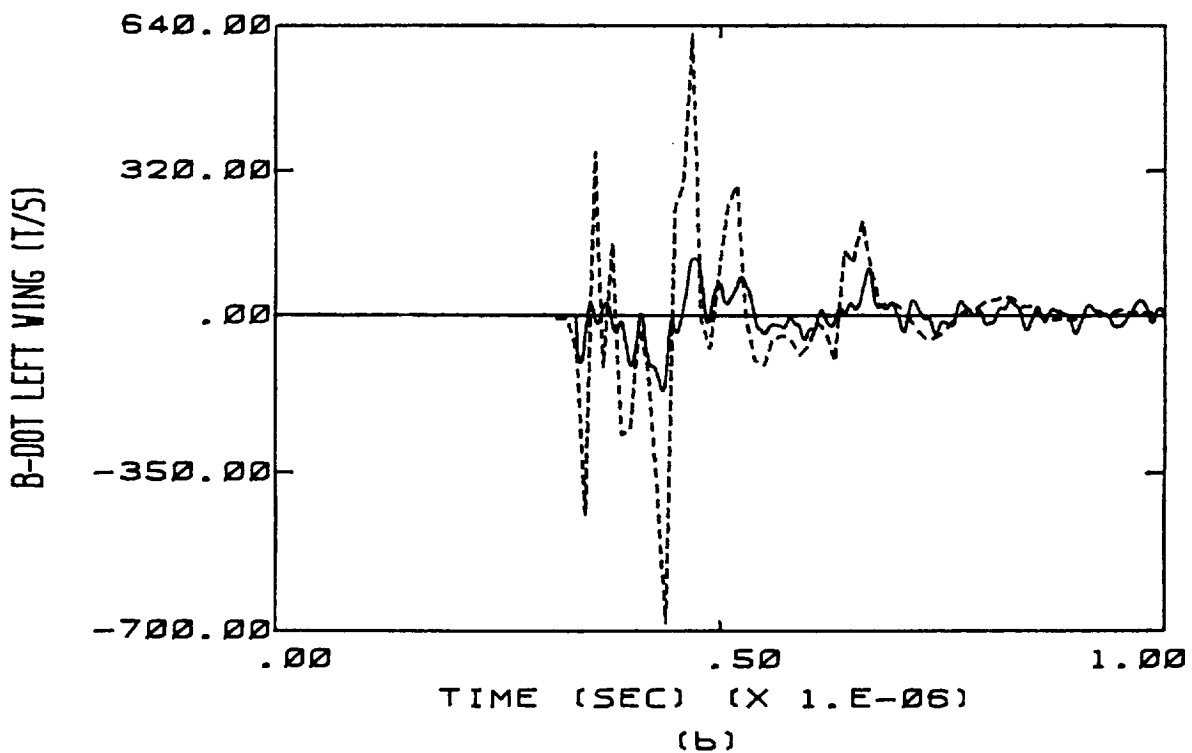
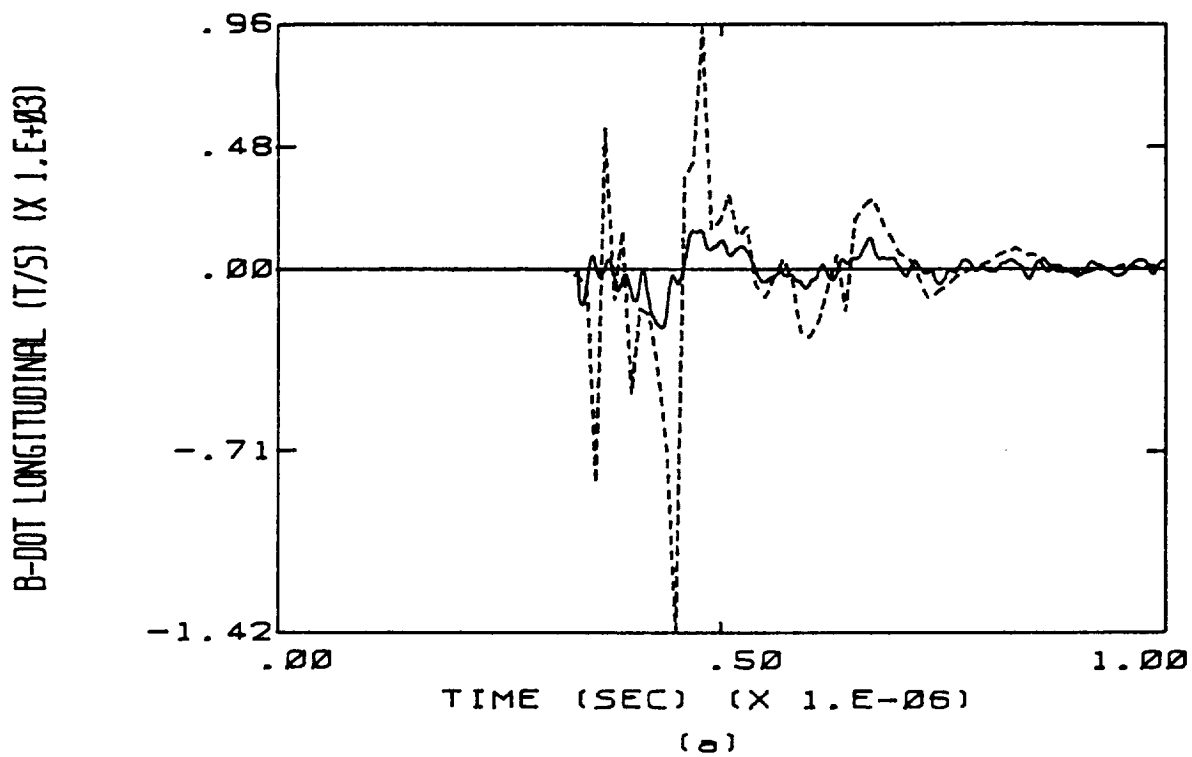
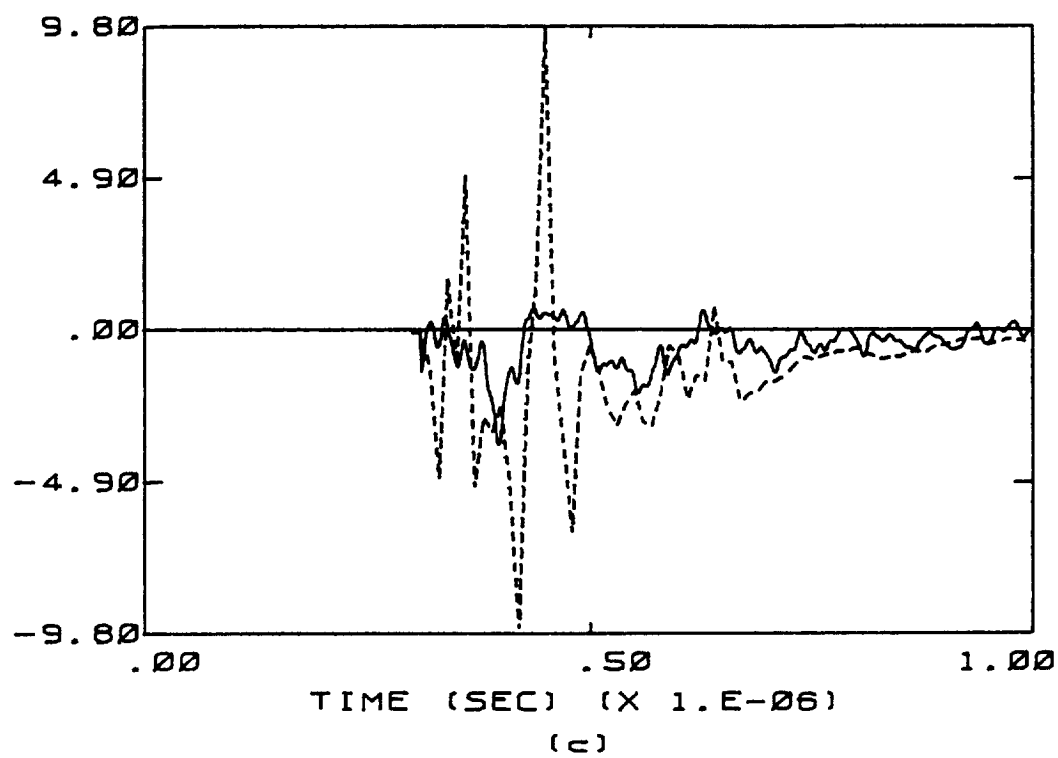


Figure C.10 Calculated Responses Overlaid on Measured Responses of Flight 84-017 for the Case of a 5 cm Radius Channel. The Transfer Function Used Is Appropriate to D-dot Tail. The Dashed Line Indicates the Measured Data.

D-DOT FORWARD (A/SQUARE METER)



D-DOT LEFT VING (A/SQUARE METER)

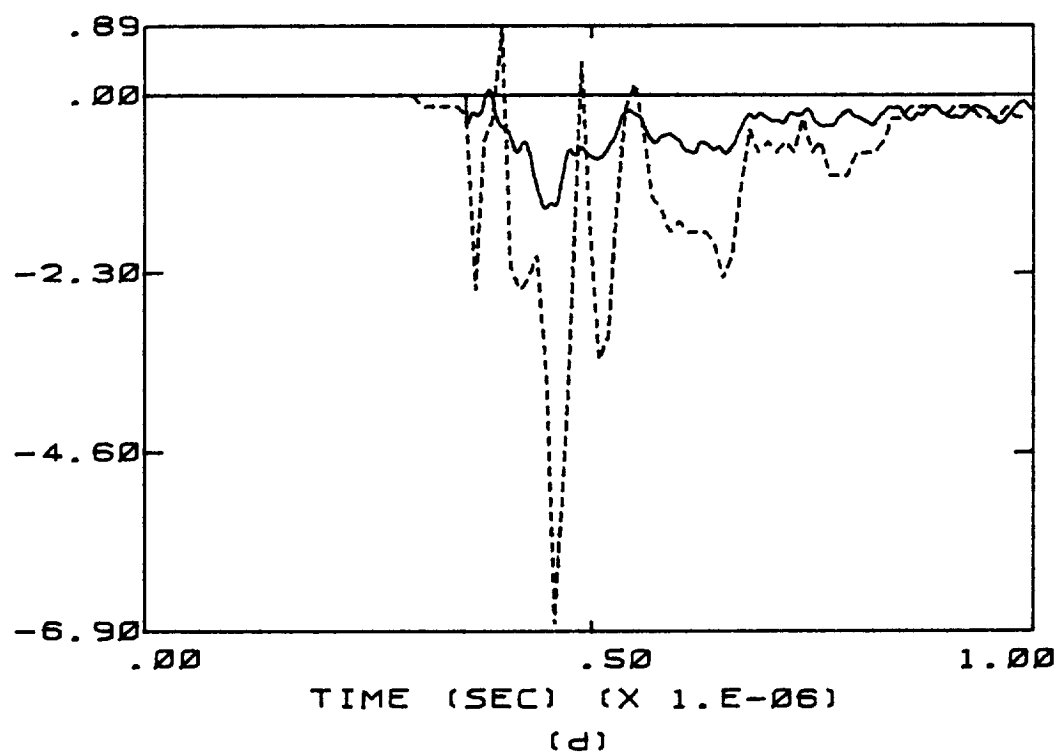


Figure C.10 (continued)

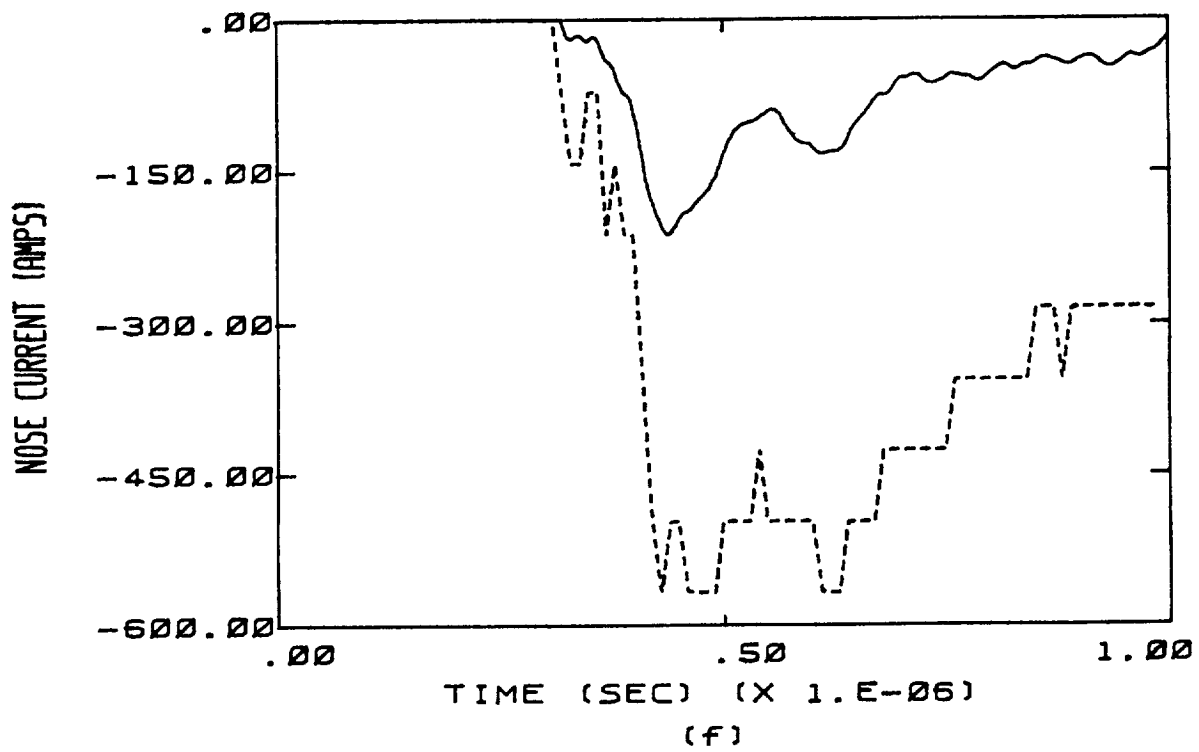
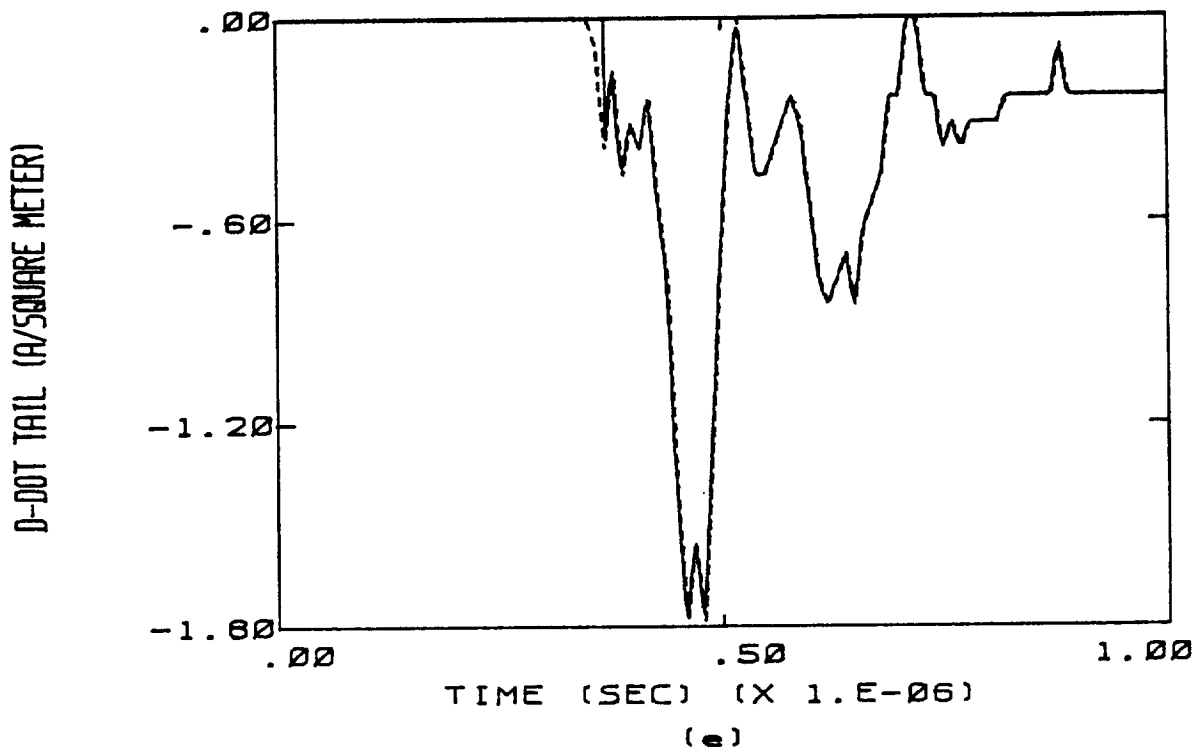


Figure C.10 (continued)

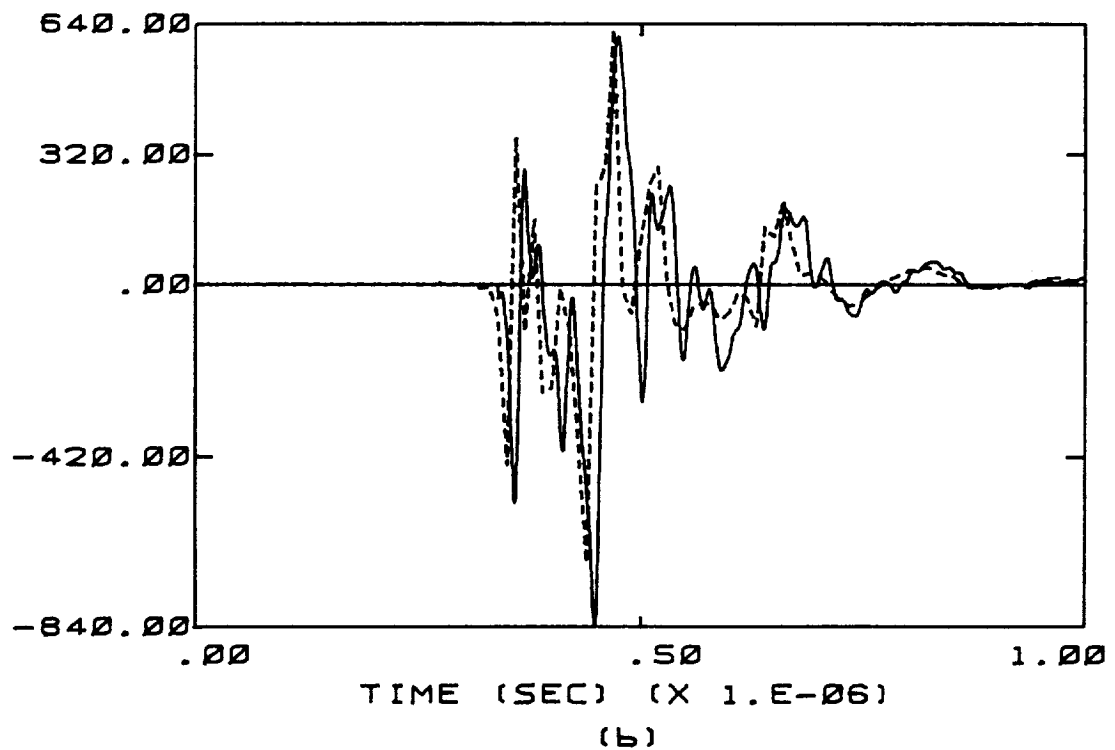
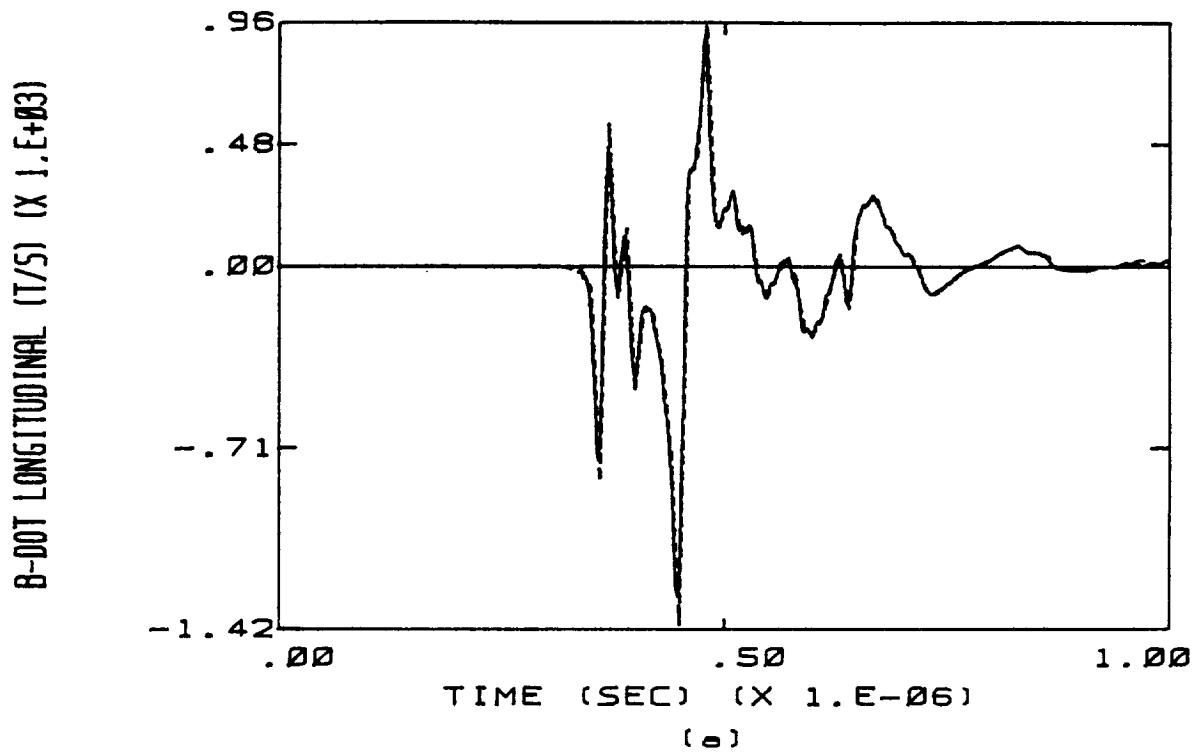
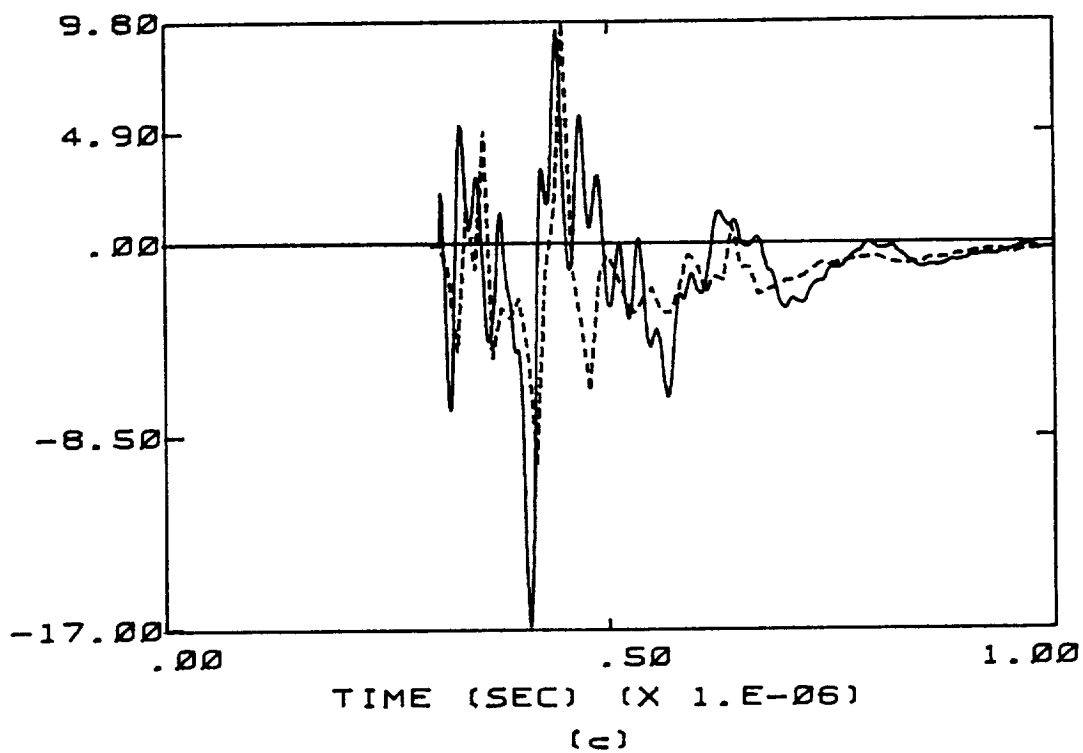


Figure C.11 Calculated Responses Overlaid on Measured Responses of Flight 84-017 for the Case of a 10 cm Radius Channel. The Transfer Function Used Is Appropriate to B-dot Longitudinal. The Dashed Line Indicates the Measured Data.

D-DOT FORWARD (A/SQUARE METER)



D-DOT LEFT WING (A/SQUARE METER)

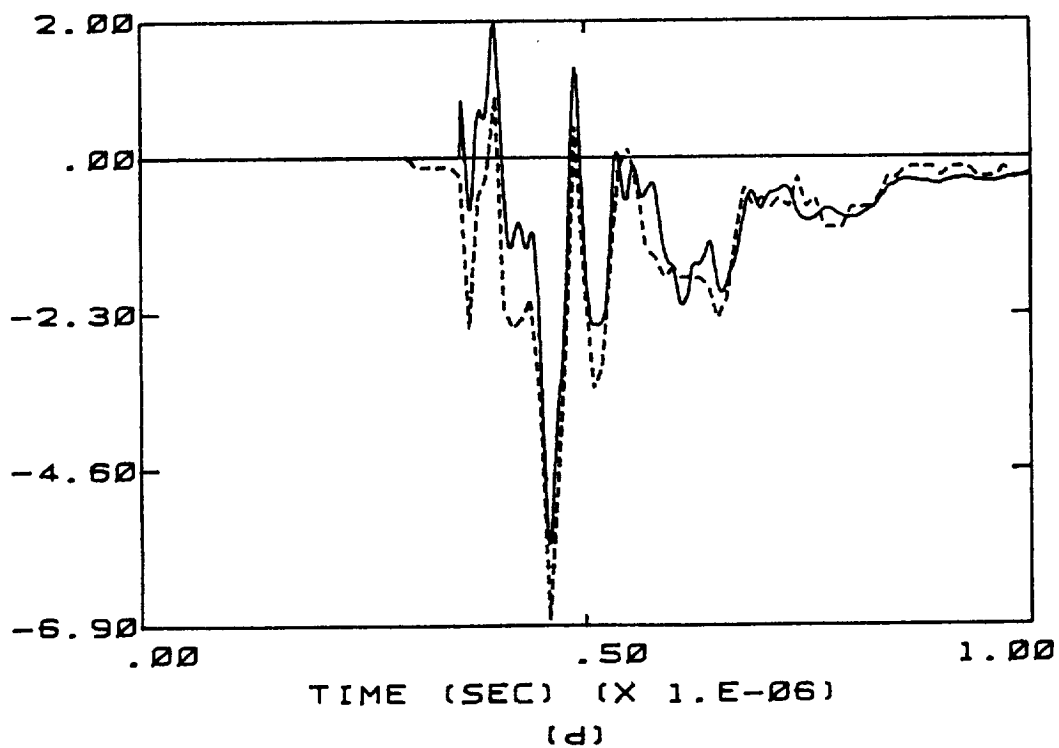


Figure C.11 (continued)

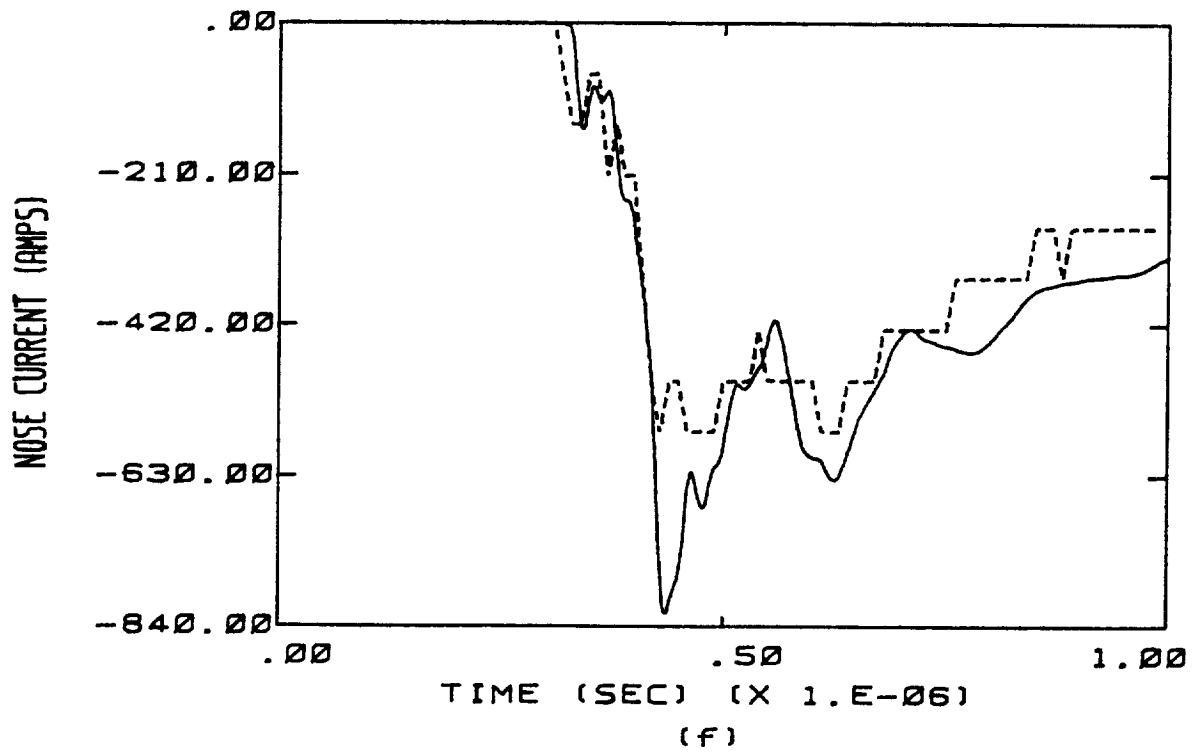
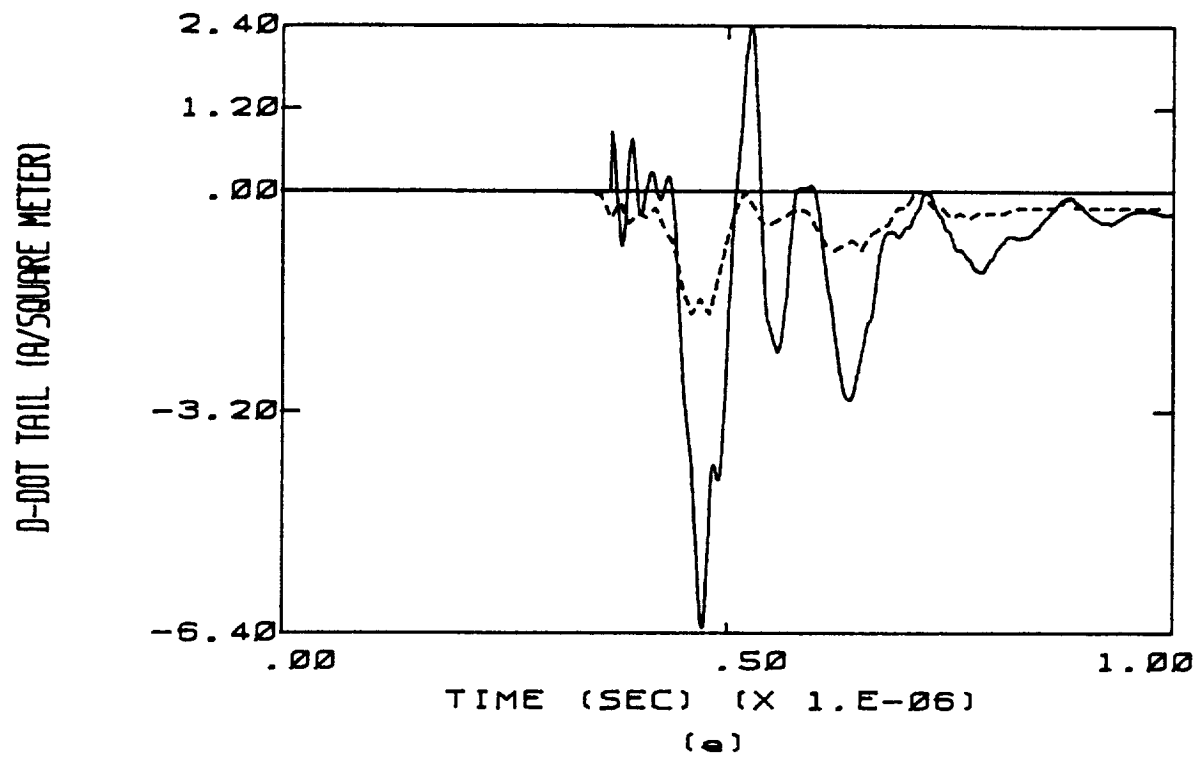


Figure C.11 (continued)



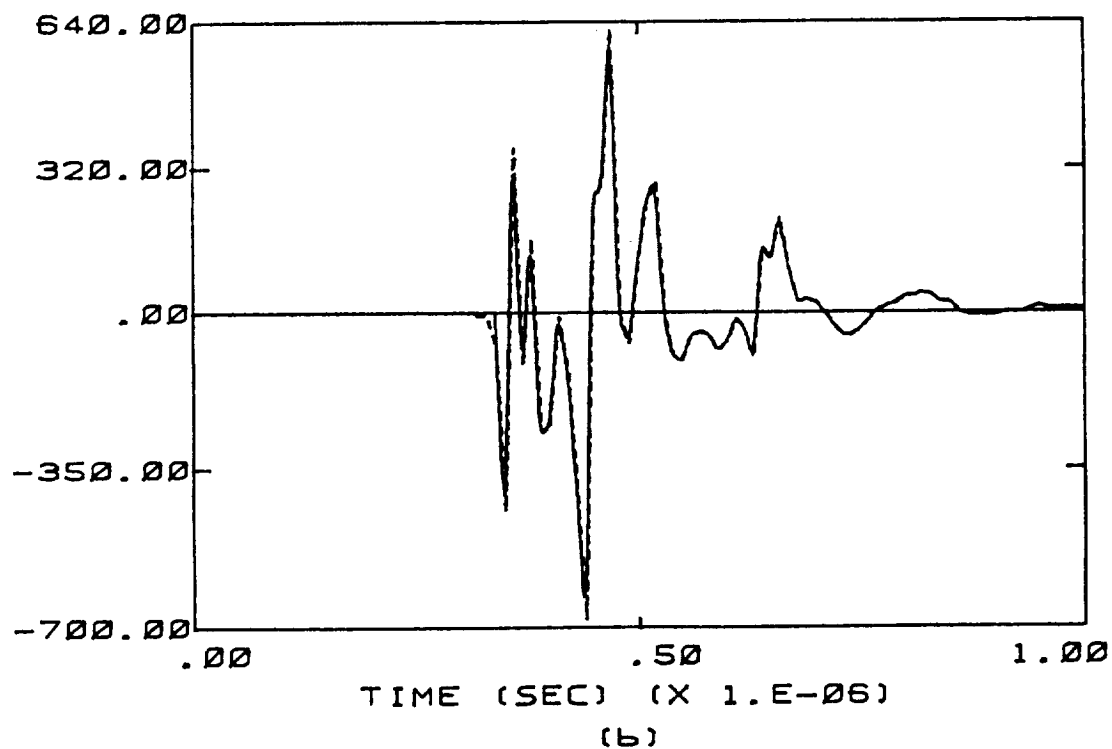
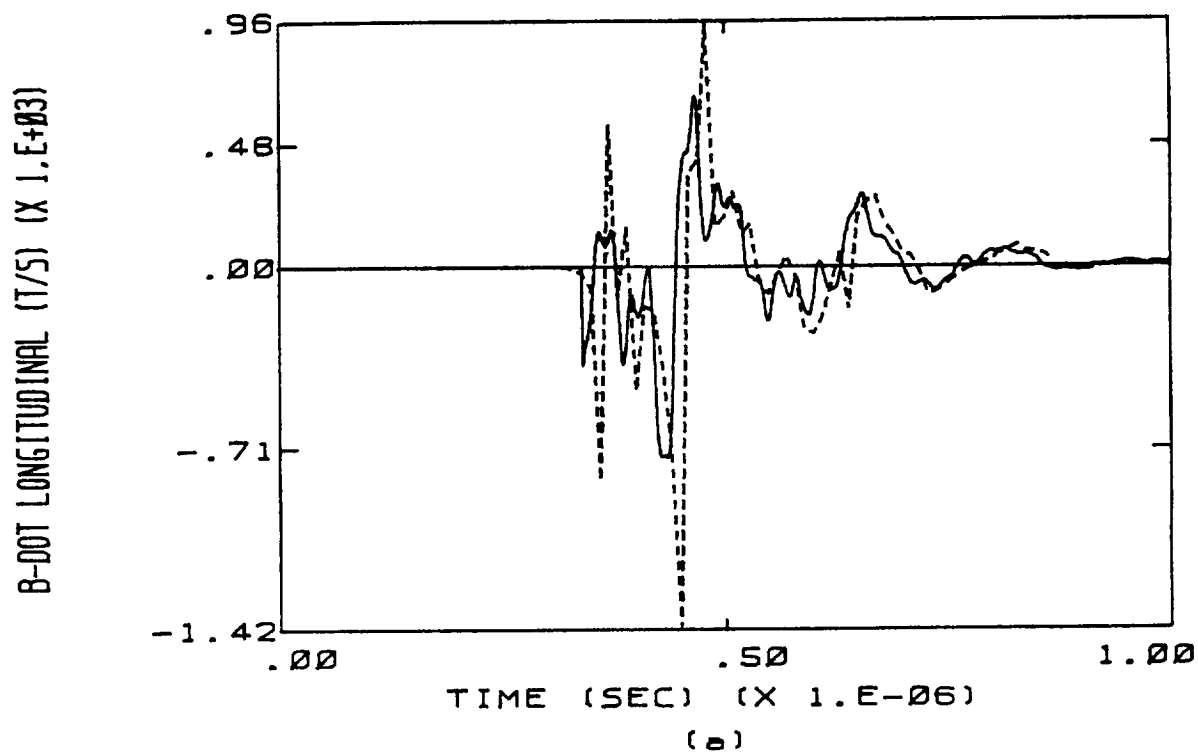
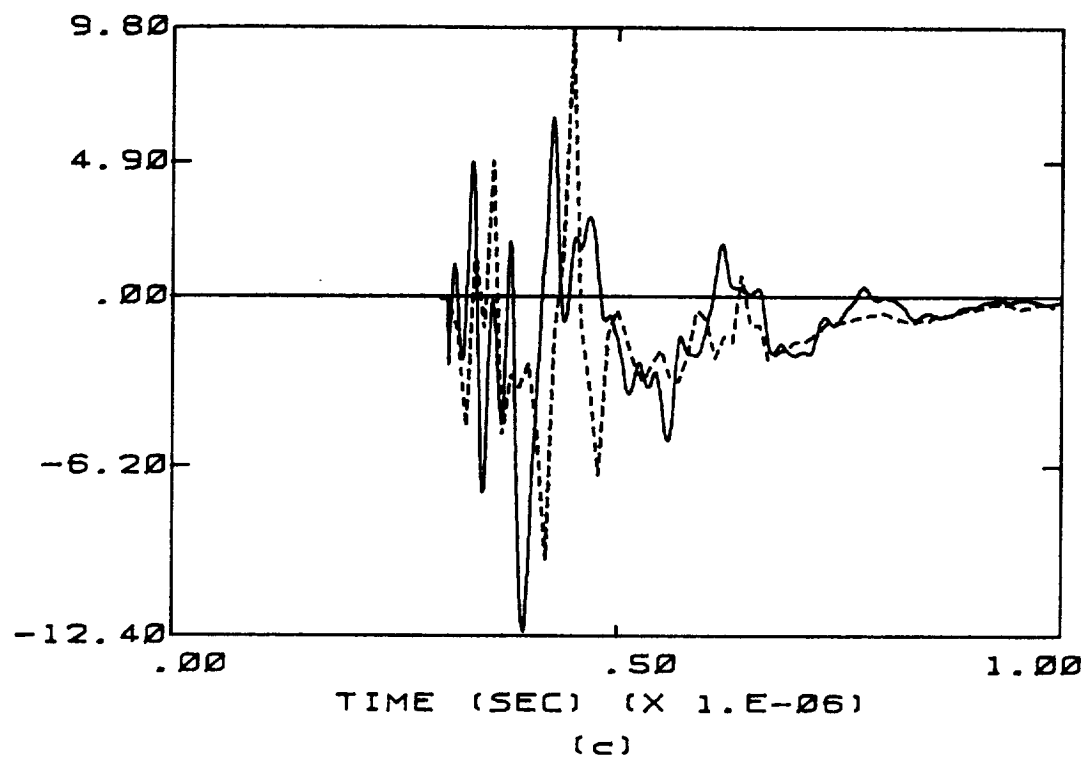


Figure C.12 Calculated Responses Overlaid on Measured Responses of Flight 84-017 for the Case of a 10 cm Radius Channel. The Transfer Function Used Is Appropriate to B-dot Left Wing. The Dashed Line Indicates the Measured Data.

D-DOT FORWARD (A/SQUARE METER)



D-DOT LEFT WING (A/SQUARE METER)

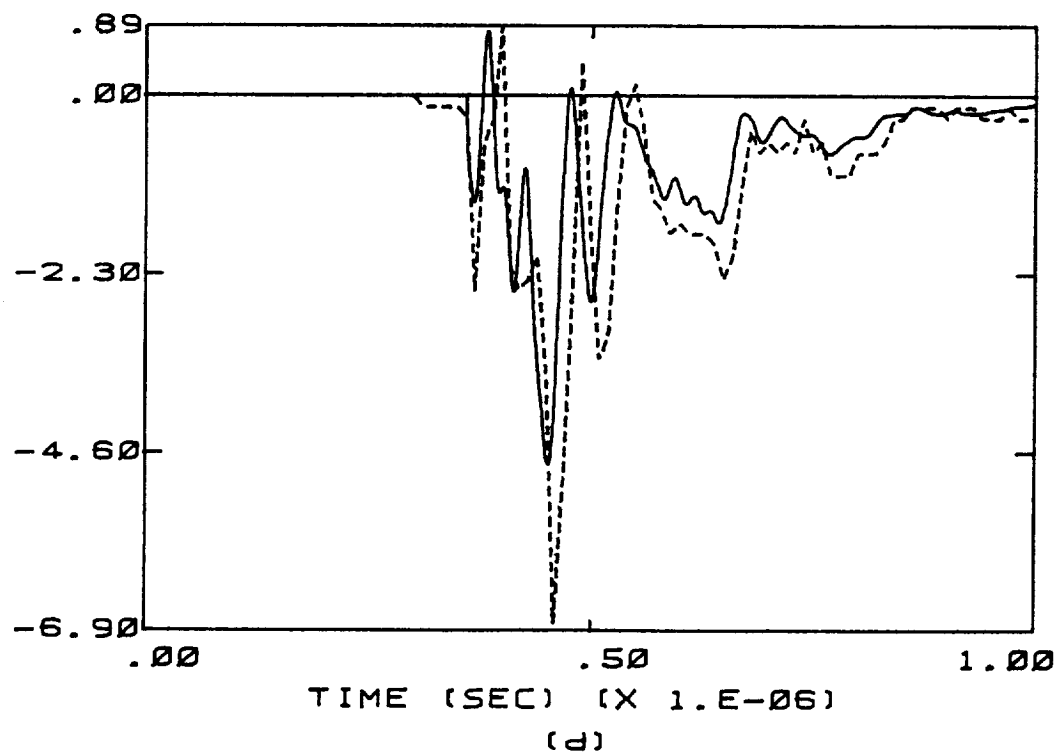


Figure C.12 (continued)

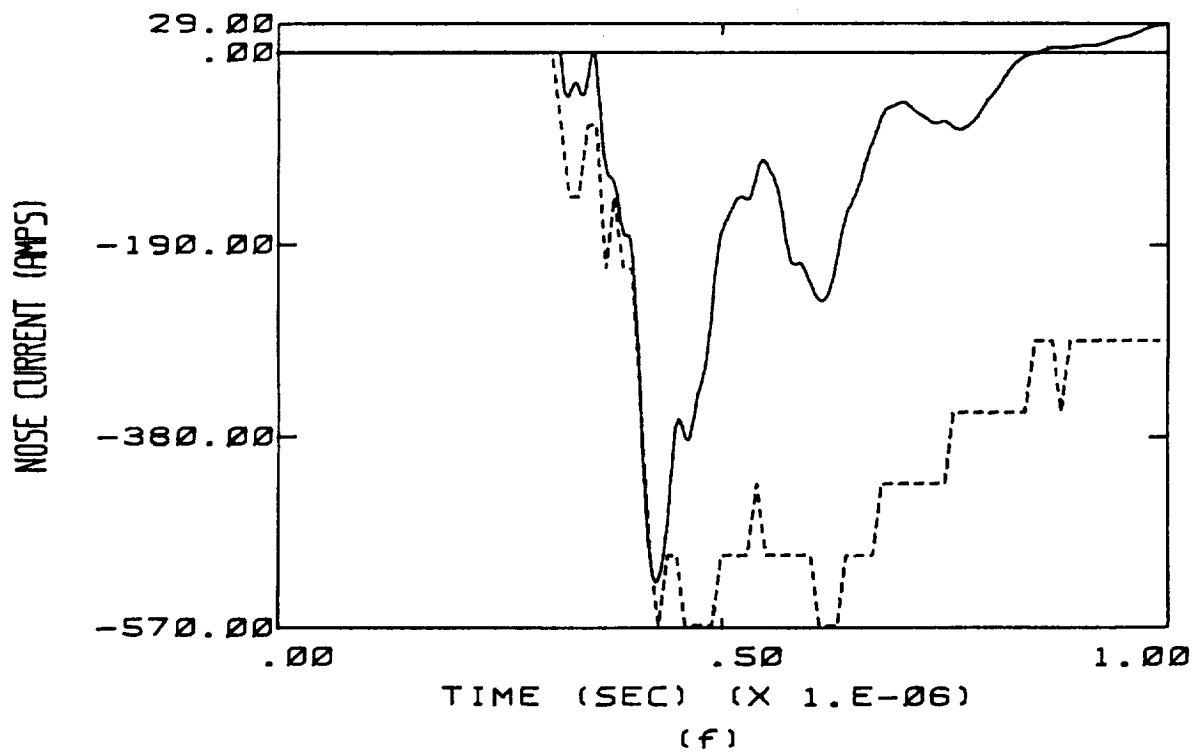
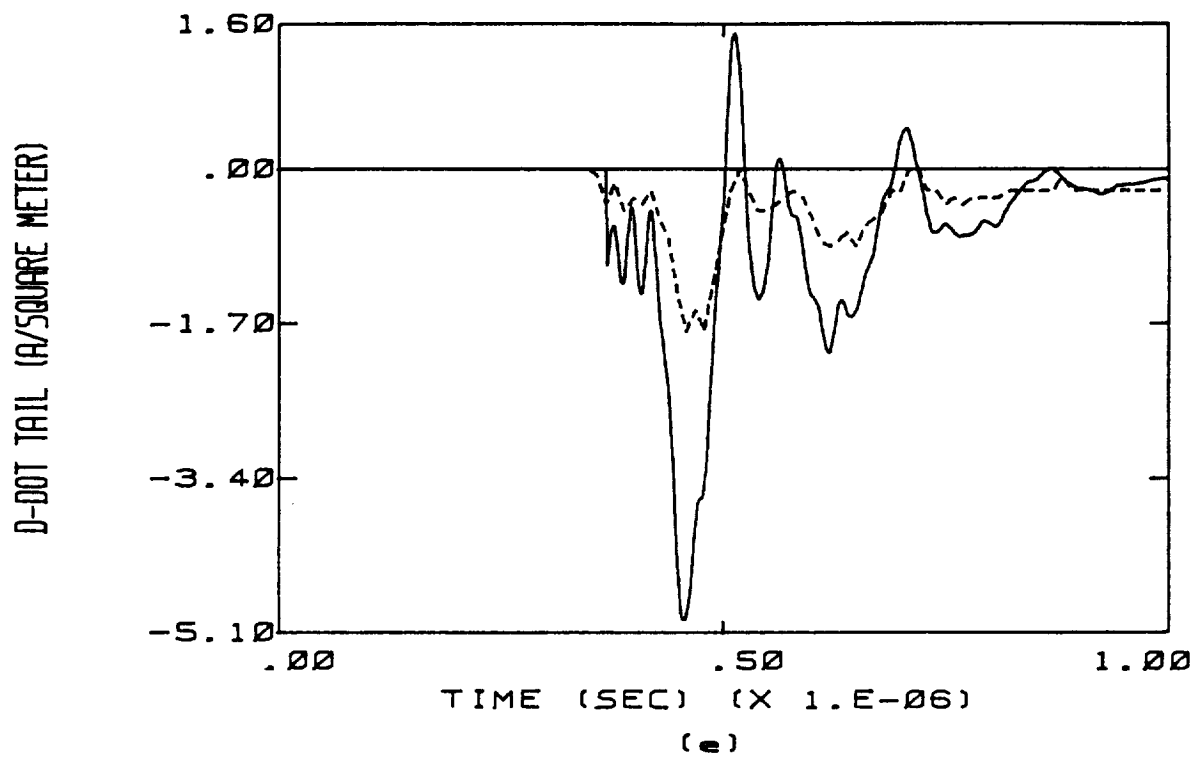


Figure C.12 (continued)

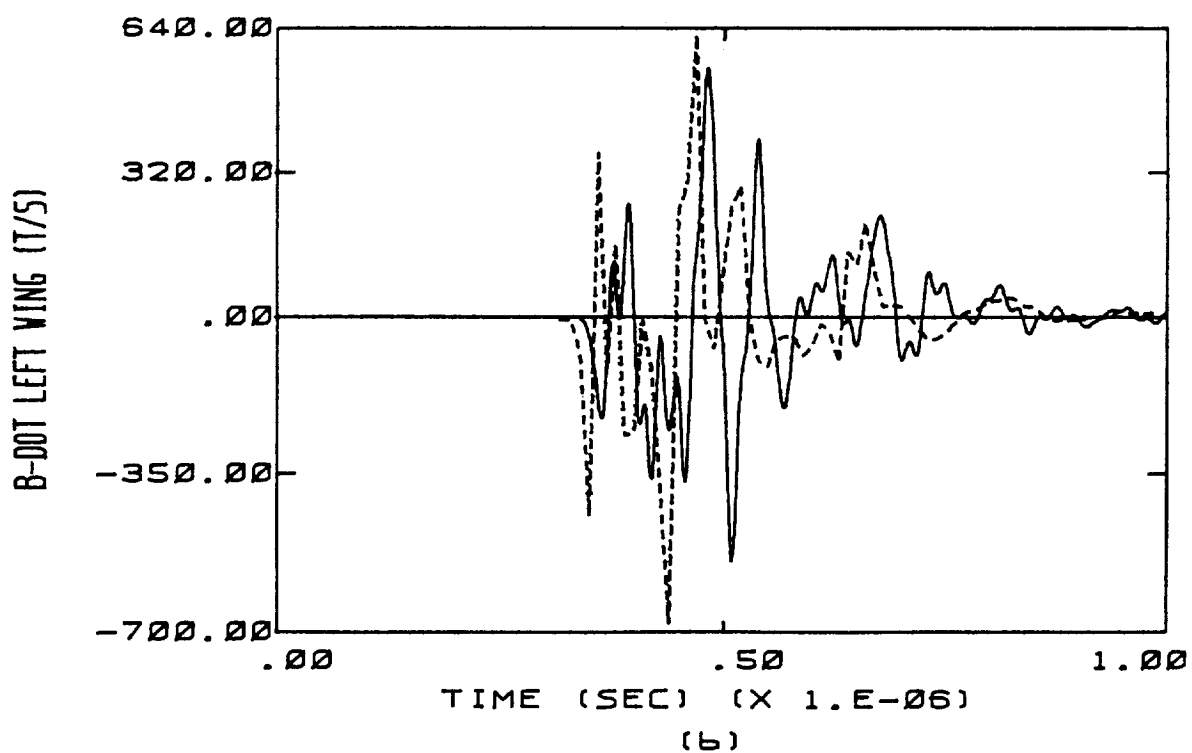
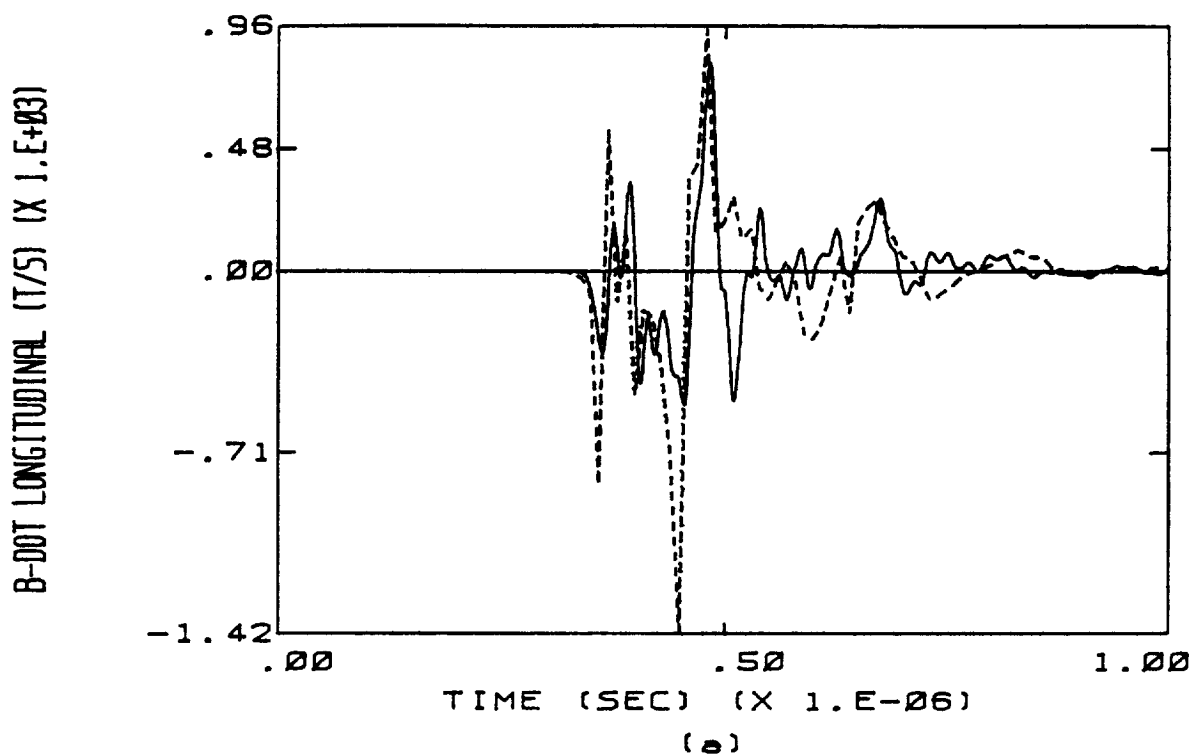
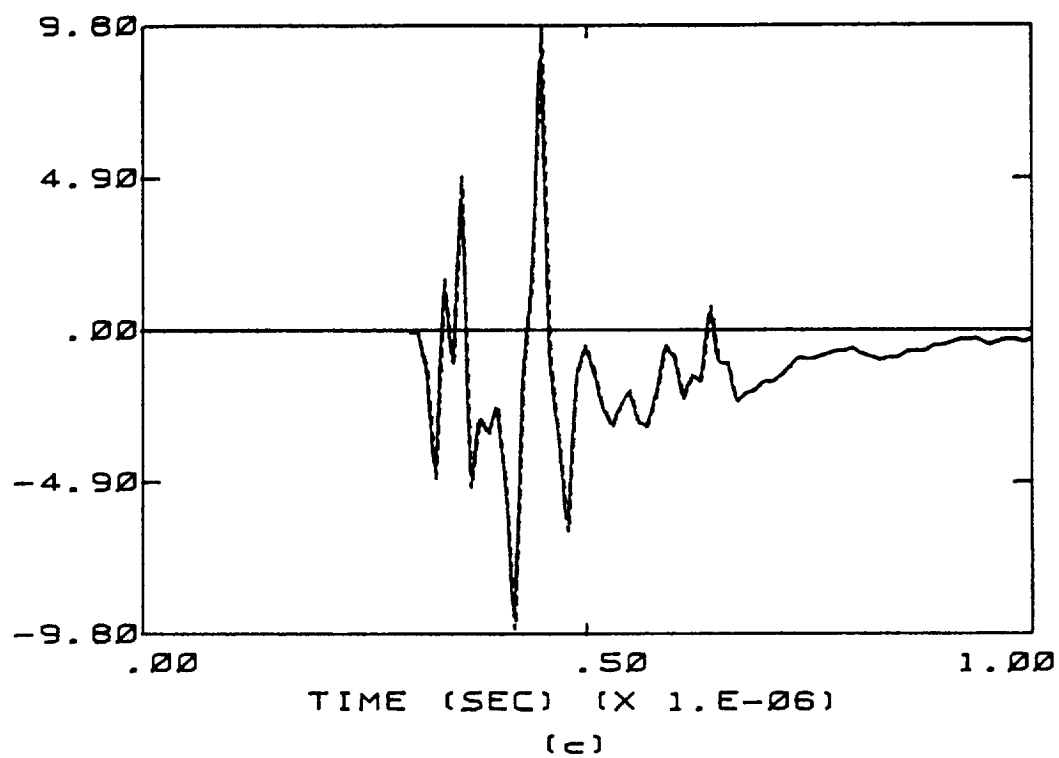


Figure C.13 Calculated Responses Overlaid on Measured Responses of Flight 84-017 for the Case of a 10 cm Radius Channel. The Transfer Function Used Is Appropriate to D-dot Forward. The Dashed Line Indicates the Measured Data.

D-DOT FORWARD (A/SQUARE METER)



D-DOT LEFT VING (A/SQUARE METER)

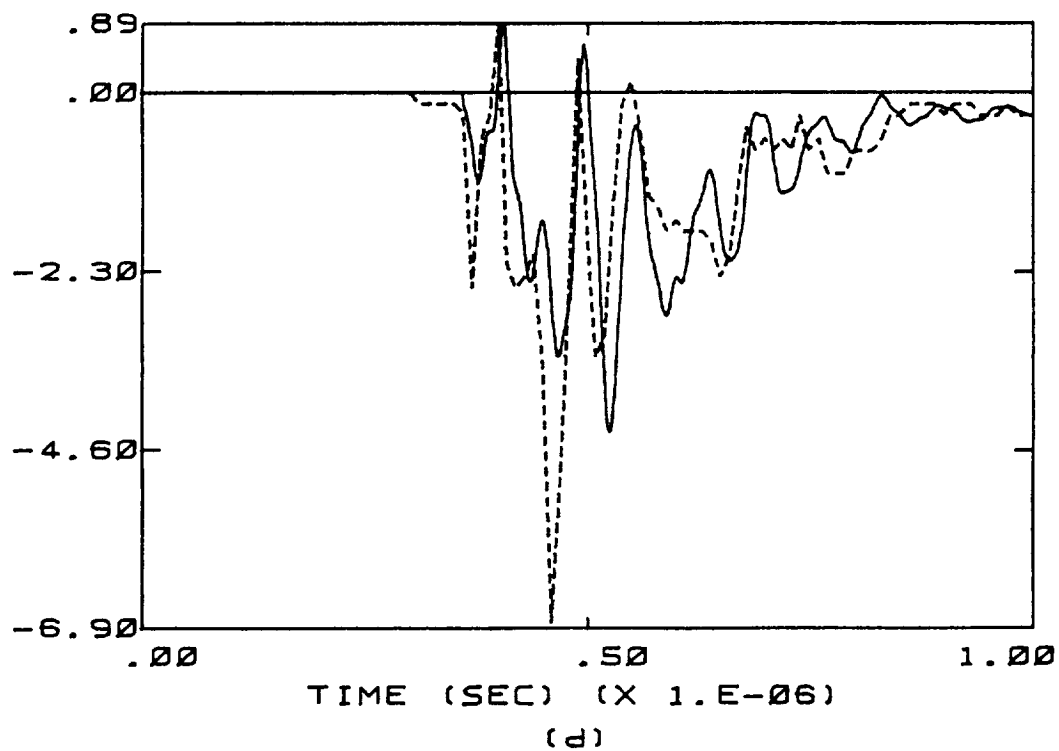


Figure C.13 (continued)

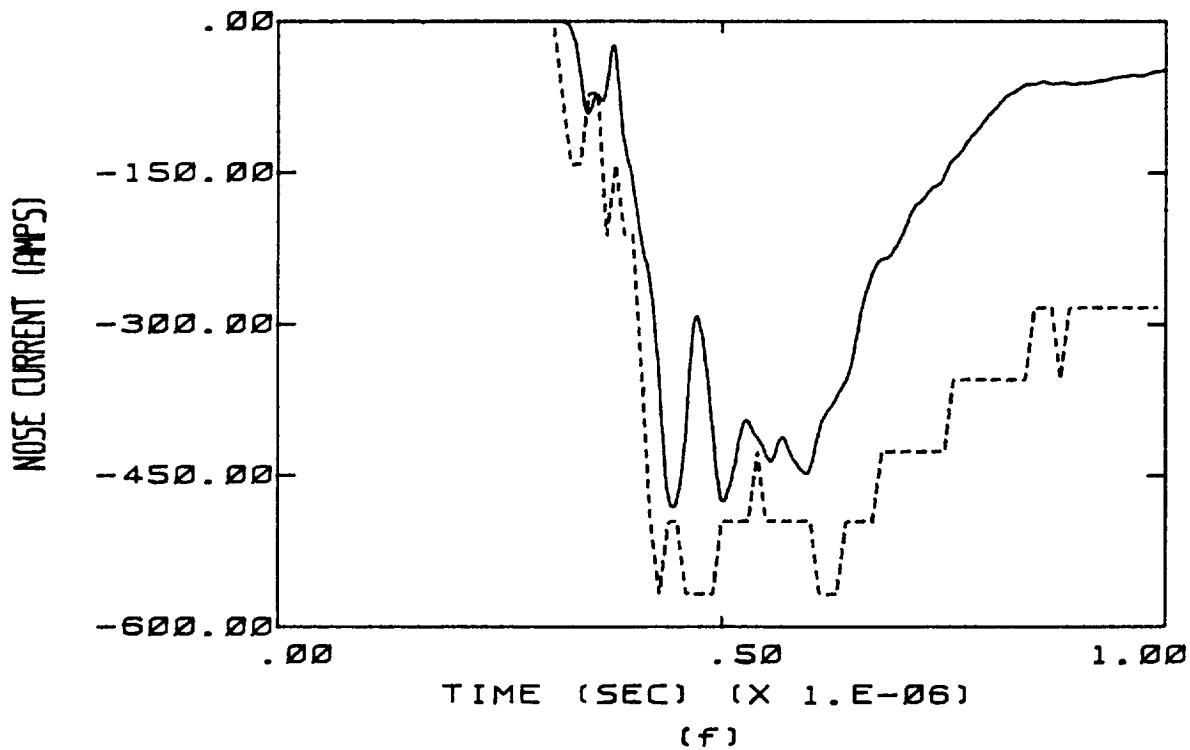
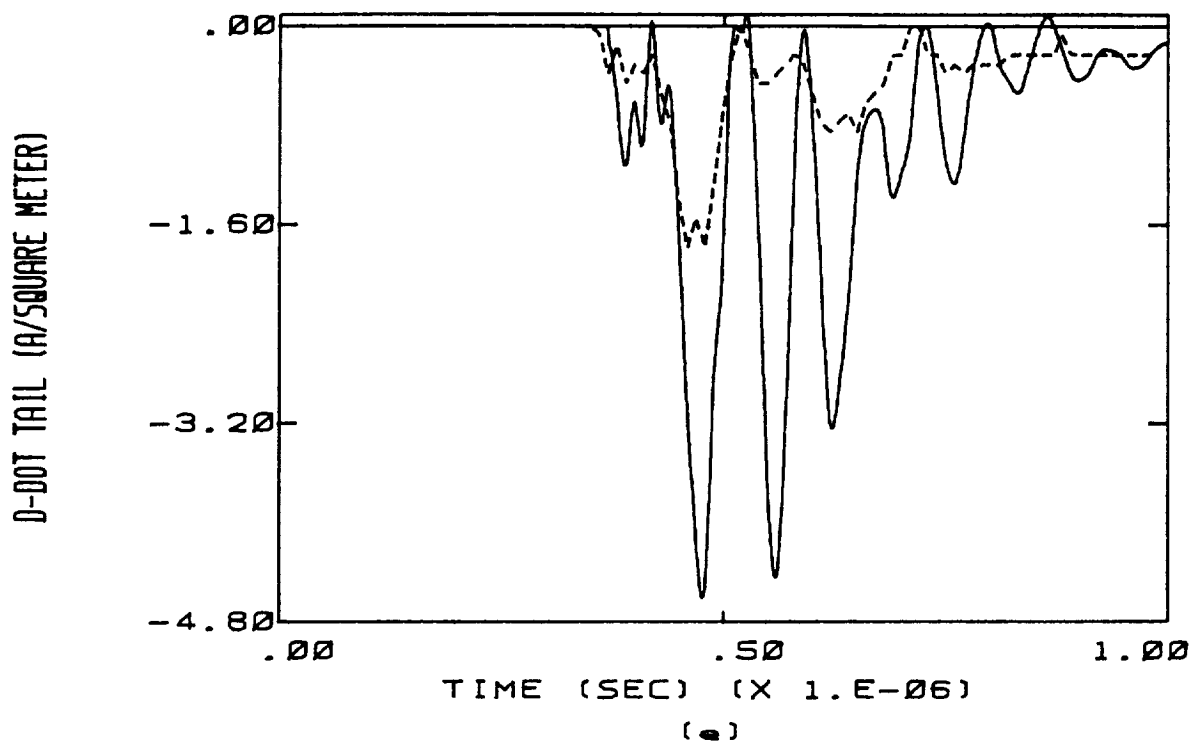
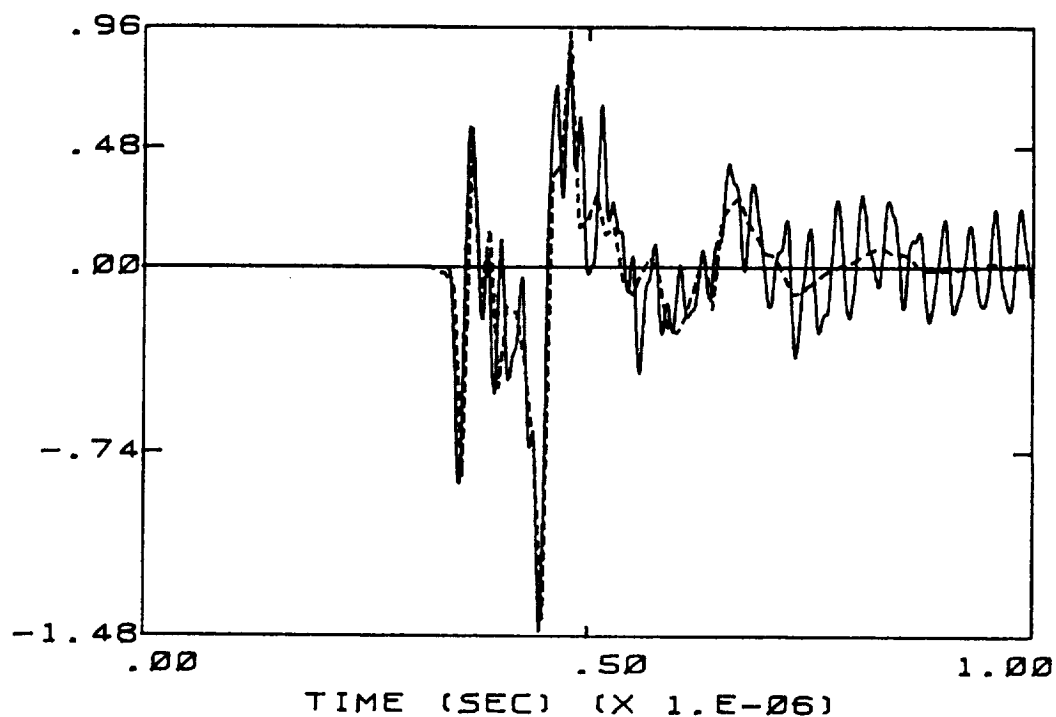


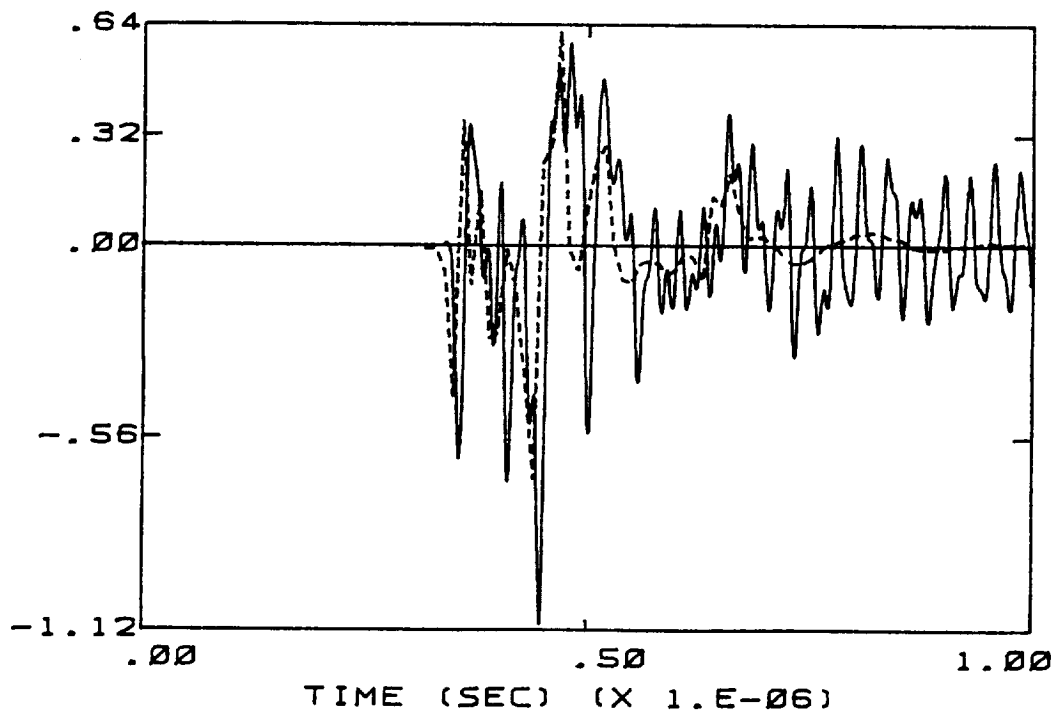
Figure C.13 (continued)

B-DOT LONGITUDINAL (T/S) (X 1.E+03)



(a)

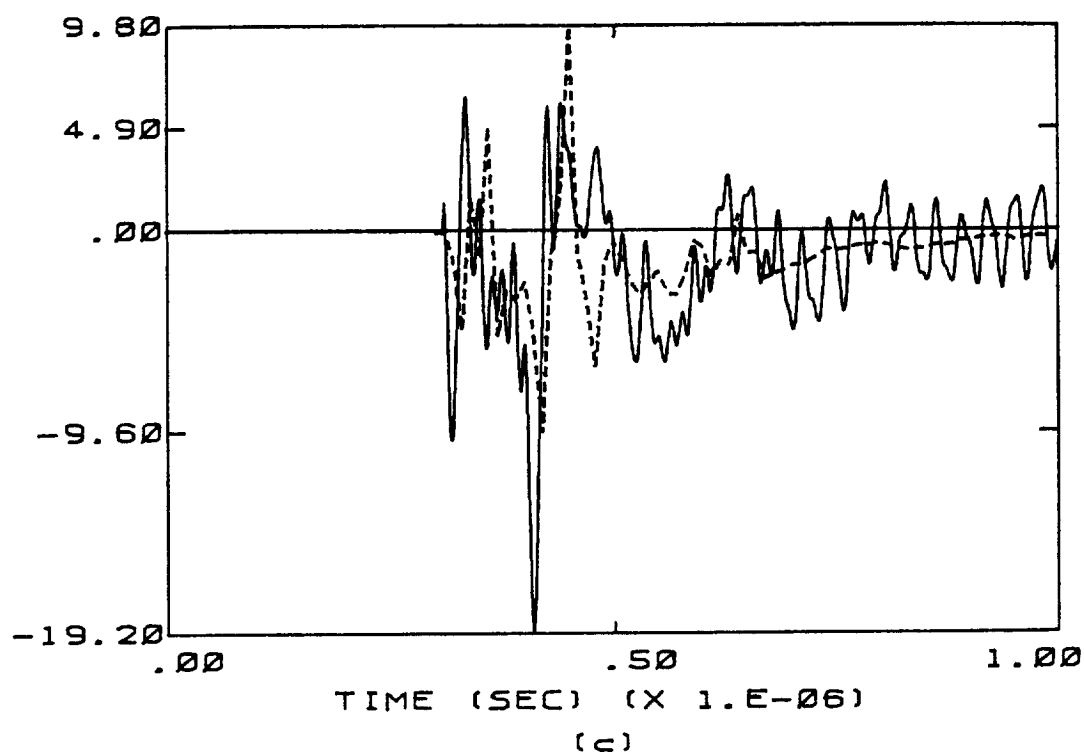
B-DOT LEFT WING (T/S) (X 1.E+03)



(b)

Figure C.14 Calculated Responses Overlaid on Measured Responses of Flight 84-017 for the Case of a 10 cm Radius Channel. The Transfer Function Used Is Appropriate to D-dot Left Wing. The Dashed Line Indicates the Measured Data.

D-DOT FORWARD (A/SQUARE METER)



D-DOT LEFT WING (A/SQUARE METER)

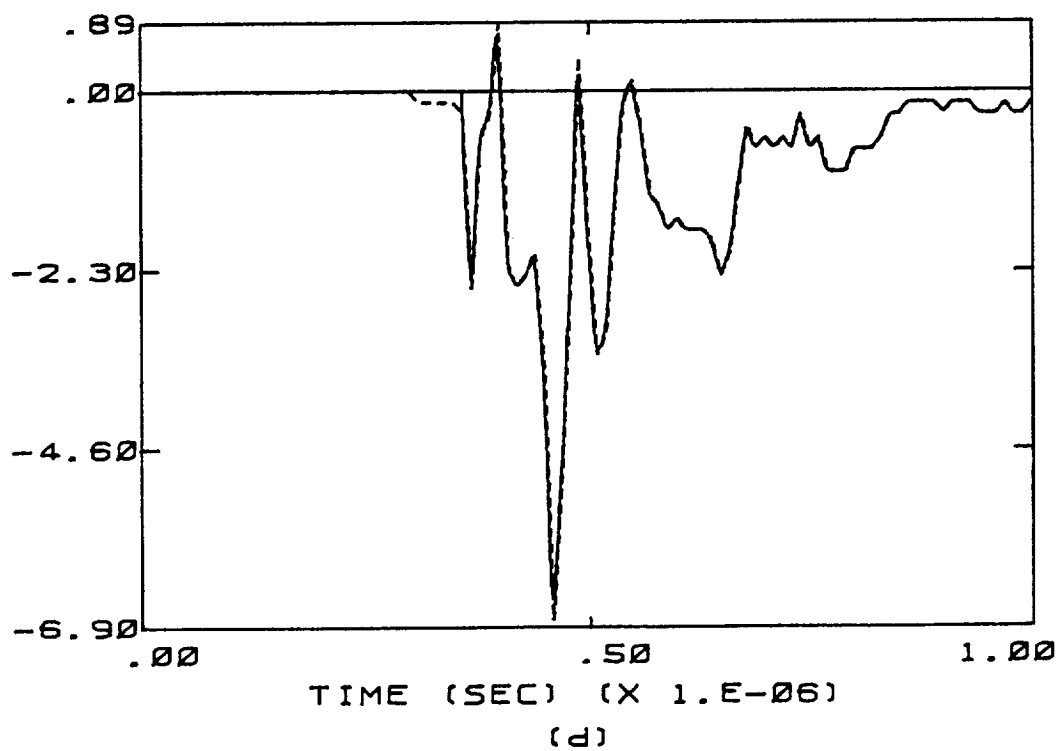


Figure C.14 (continued)



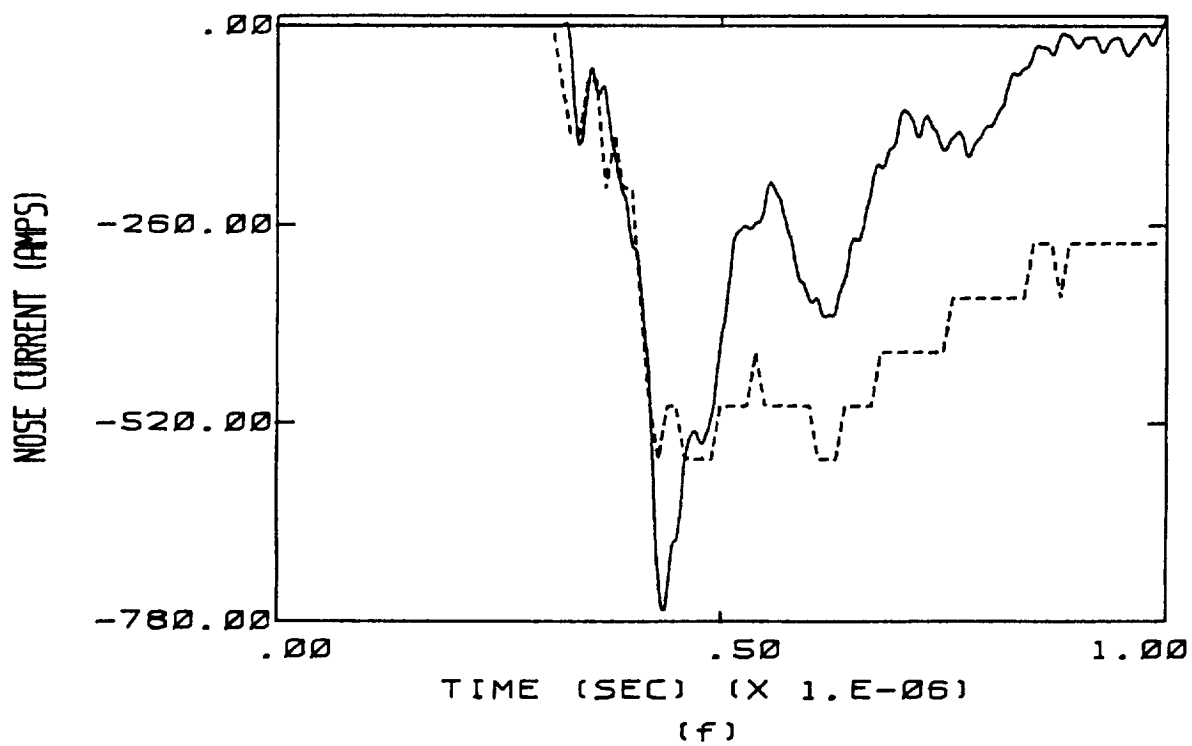
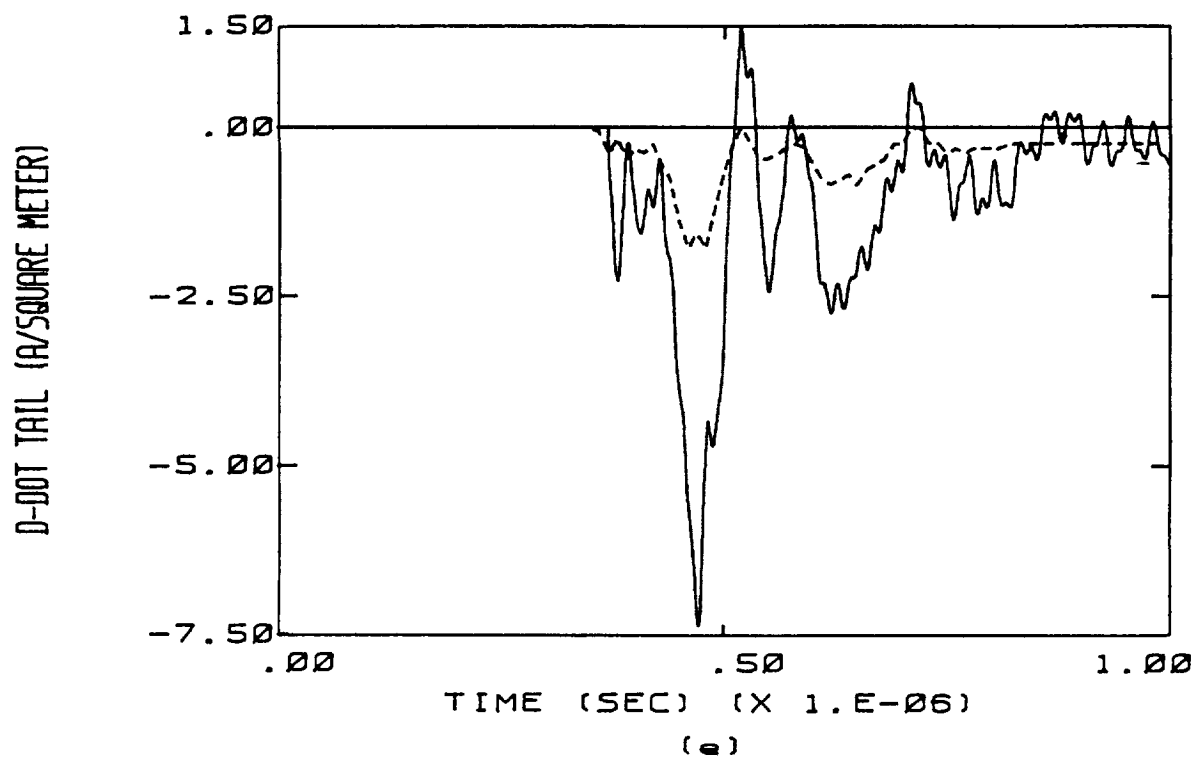


Figure C.14 (continued)

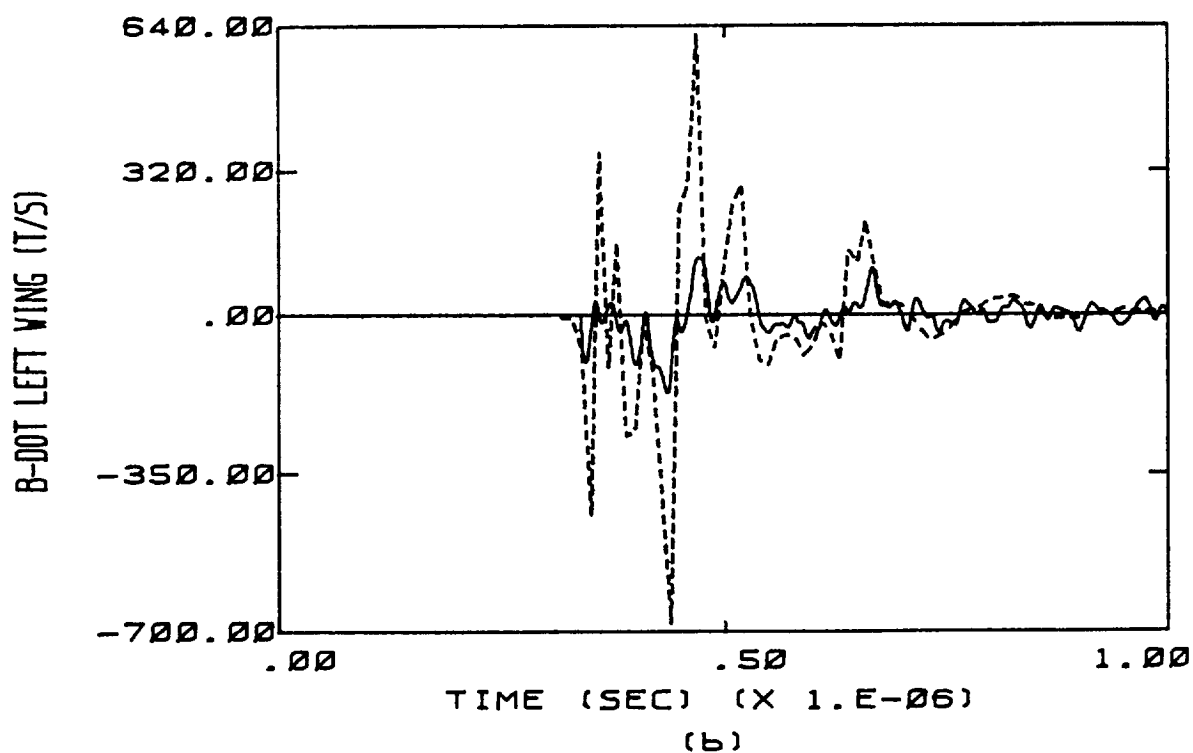
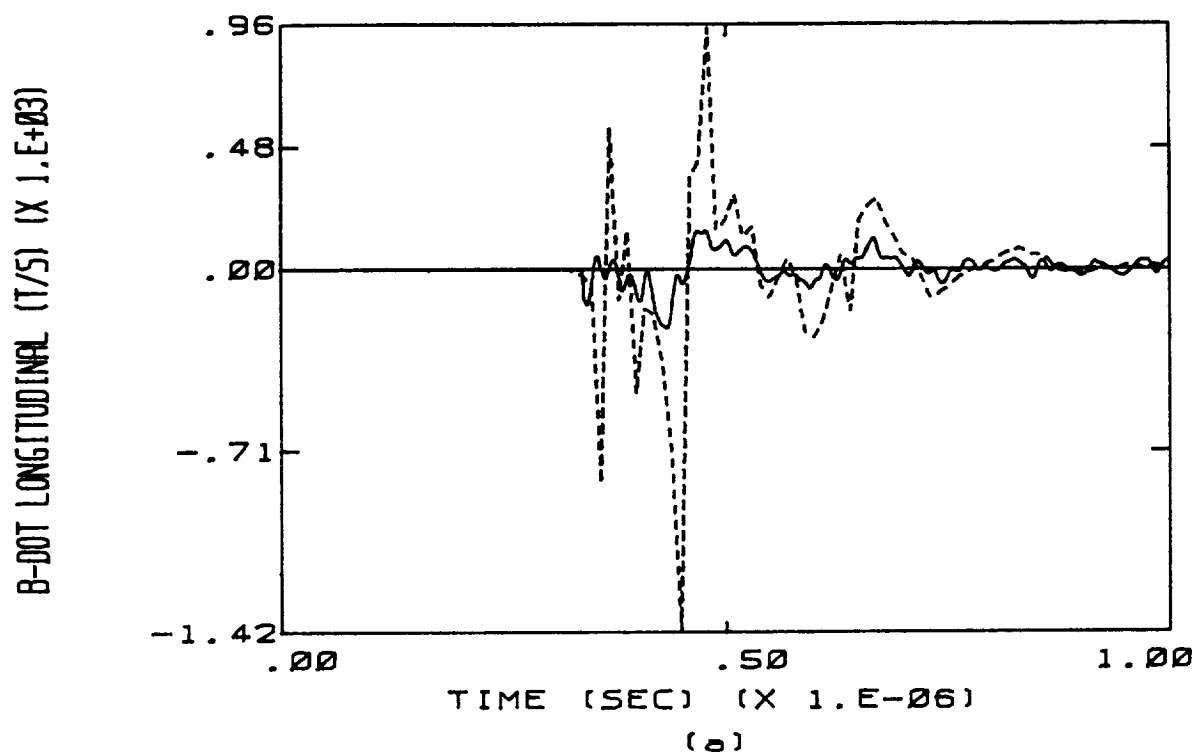
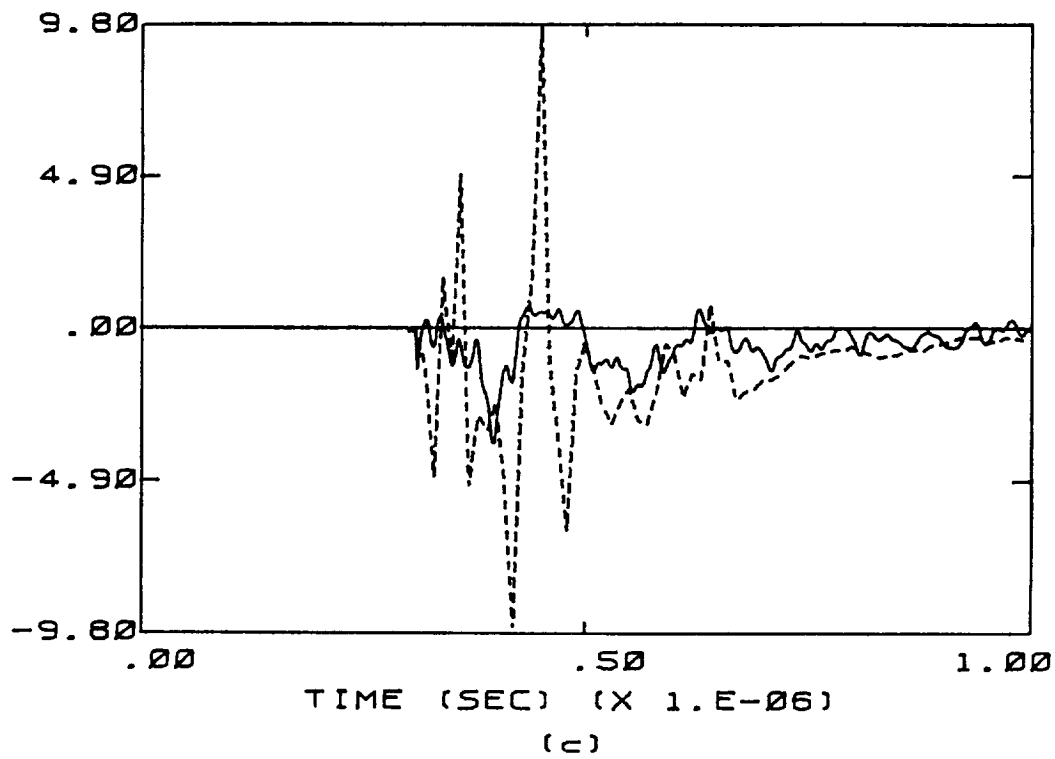


Figure C.15 Calculated Responses Overlaid on Measured Responses of Flight 84-017 for the Case of a 10 cm Radius Channel. The Transfer Function Used Is Appropriate to D-dot Tail. The Dashed Line Indicates the Measured Data.

D-DOT FORWARD (A/SQUARE METER)



D-DOT LEFT WING (A/SQUARE METER)

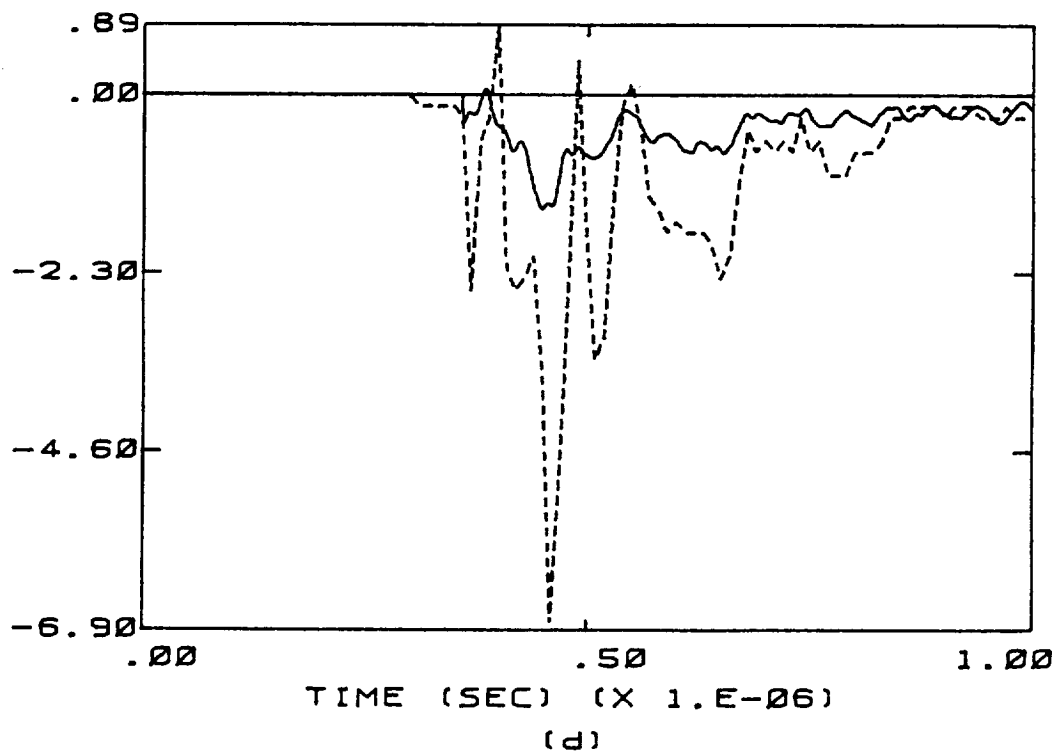


Figure C.15 (continued)

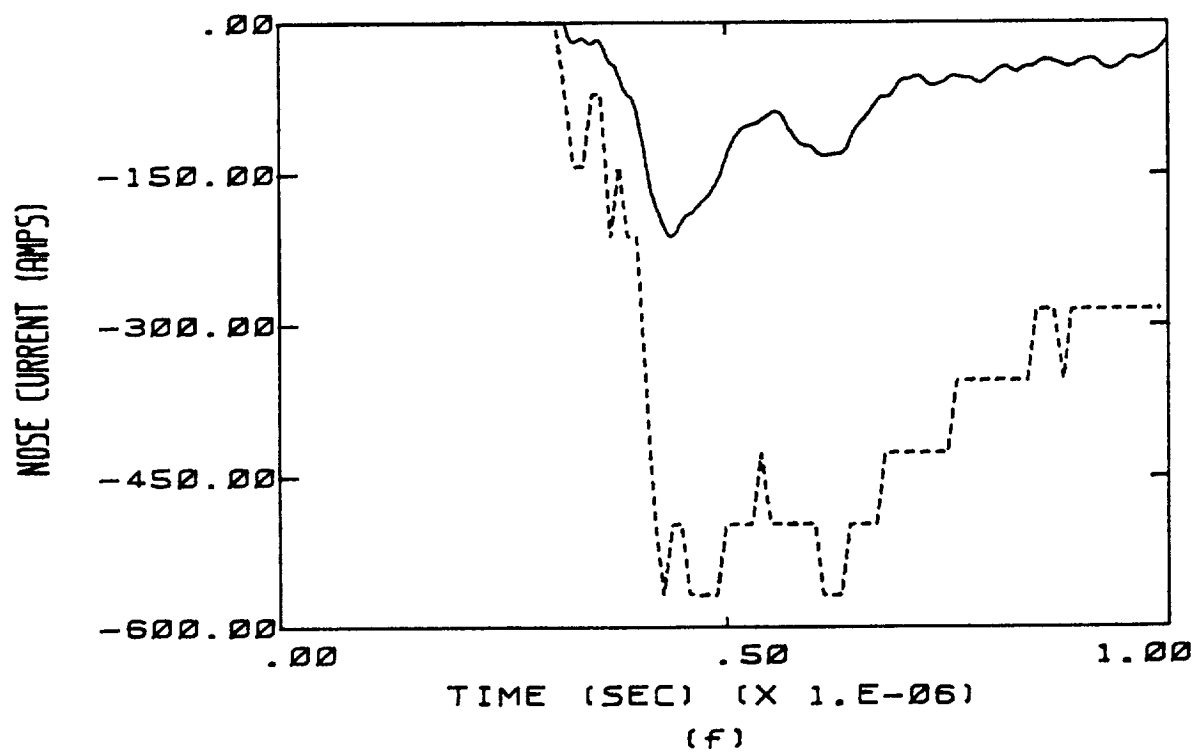
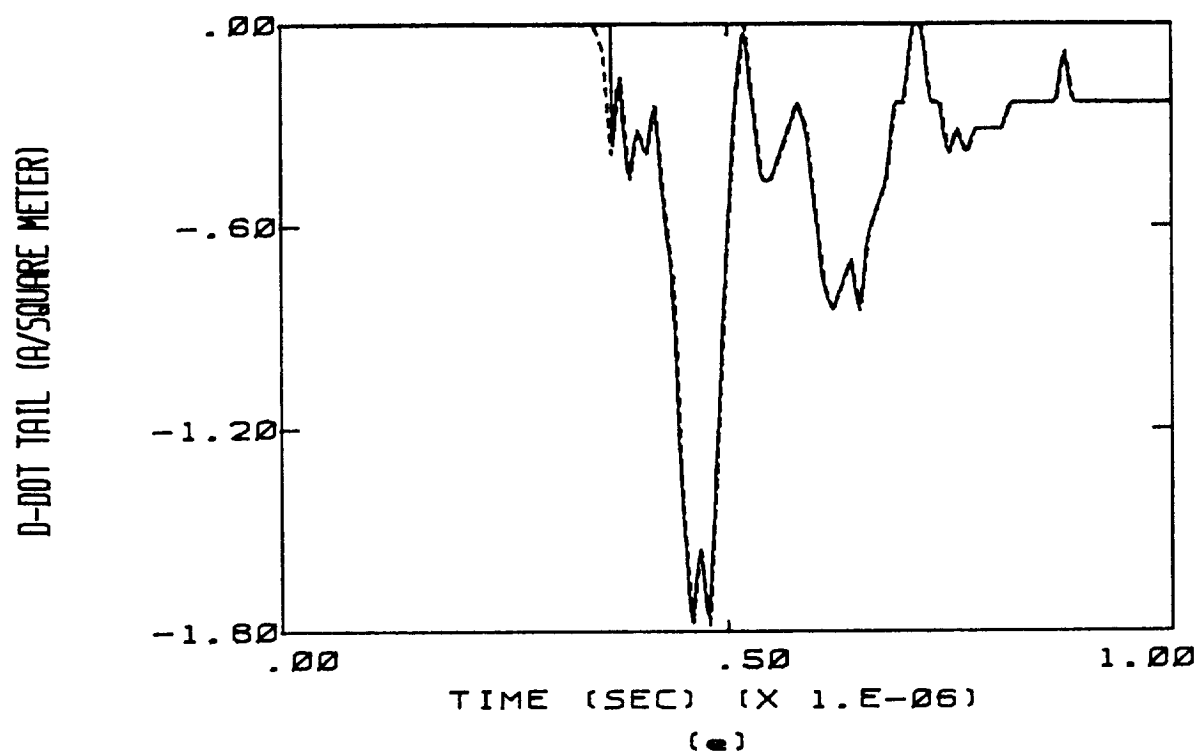
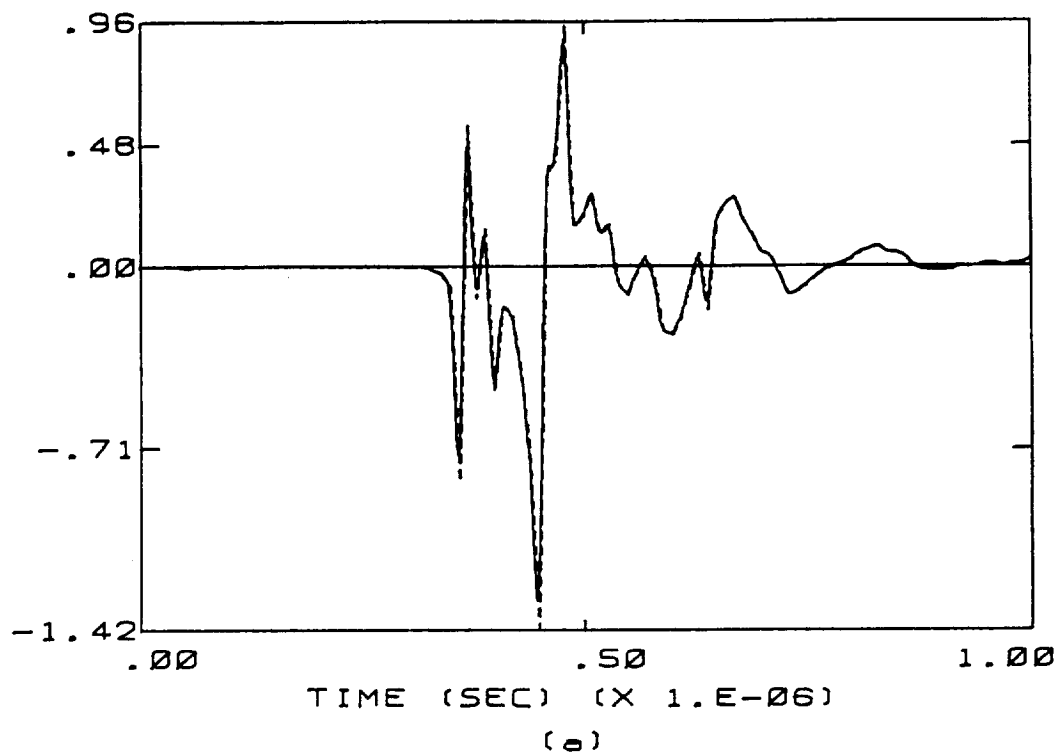


Figure C.15 (continued)

B-DOT LONGITUDINAL (T/S) (X 1.E+03)



B-DOT LEFT WING (T/S)

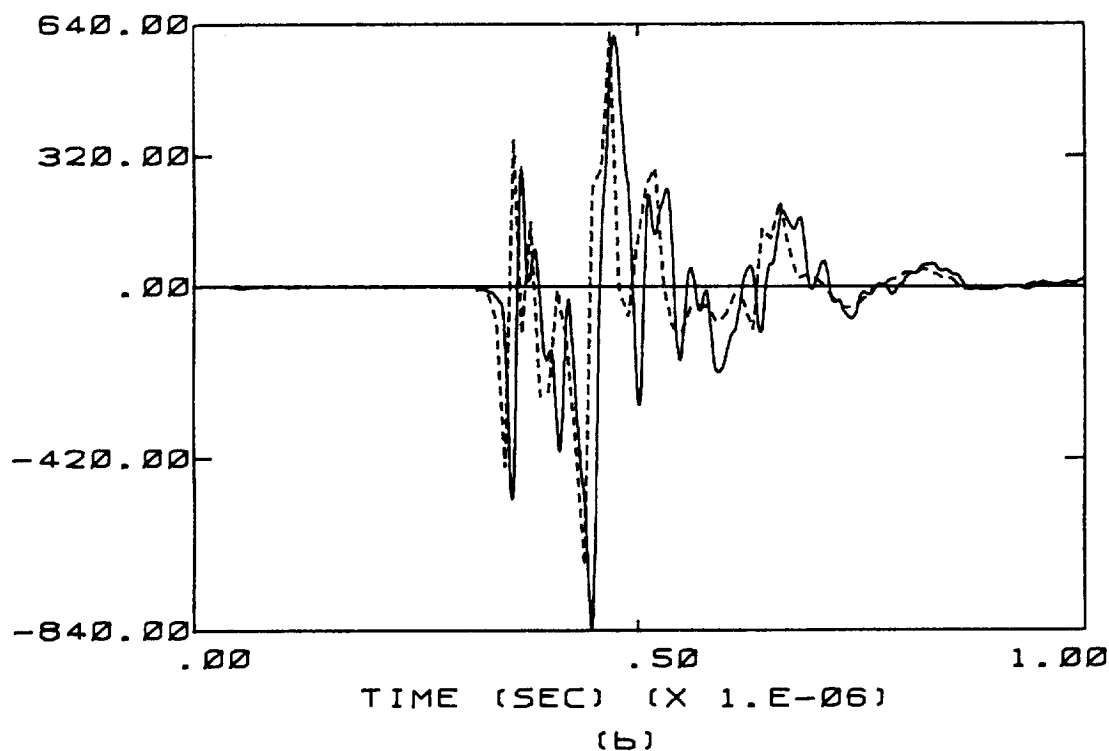
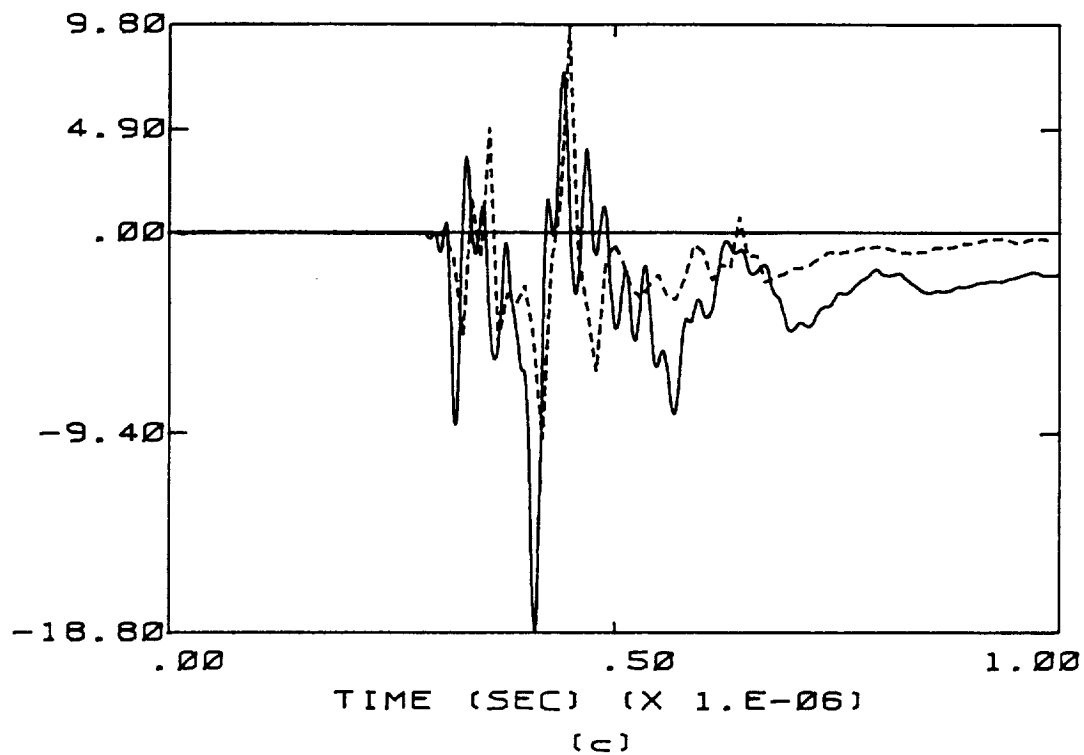


Figure C.16 Calculated Responses Overlaid on Measured Responses of Flight 84-017 for the Case of a 10 cm Radius Channel. The Transfer Function Used Is Appropriate to B-dot Longitudinal. The Resistance Per Unit Length Is 1 ohm/m. The Dashed Line Indicates the Measured Data.

D-DOT FORWARD (A/SQUARE METER)



D-DOT LEFT VING (A/SQUARE METER)

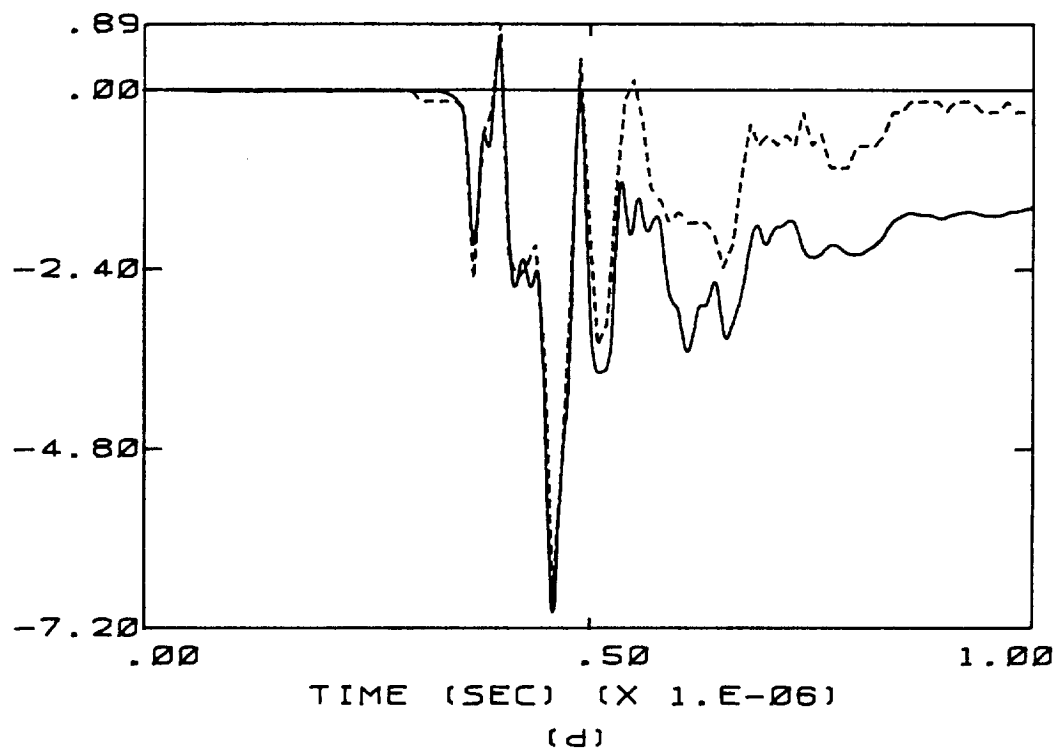


Figure C.16 (continued)

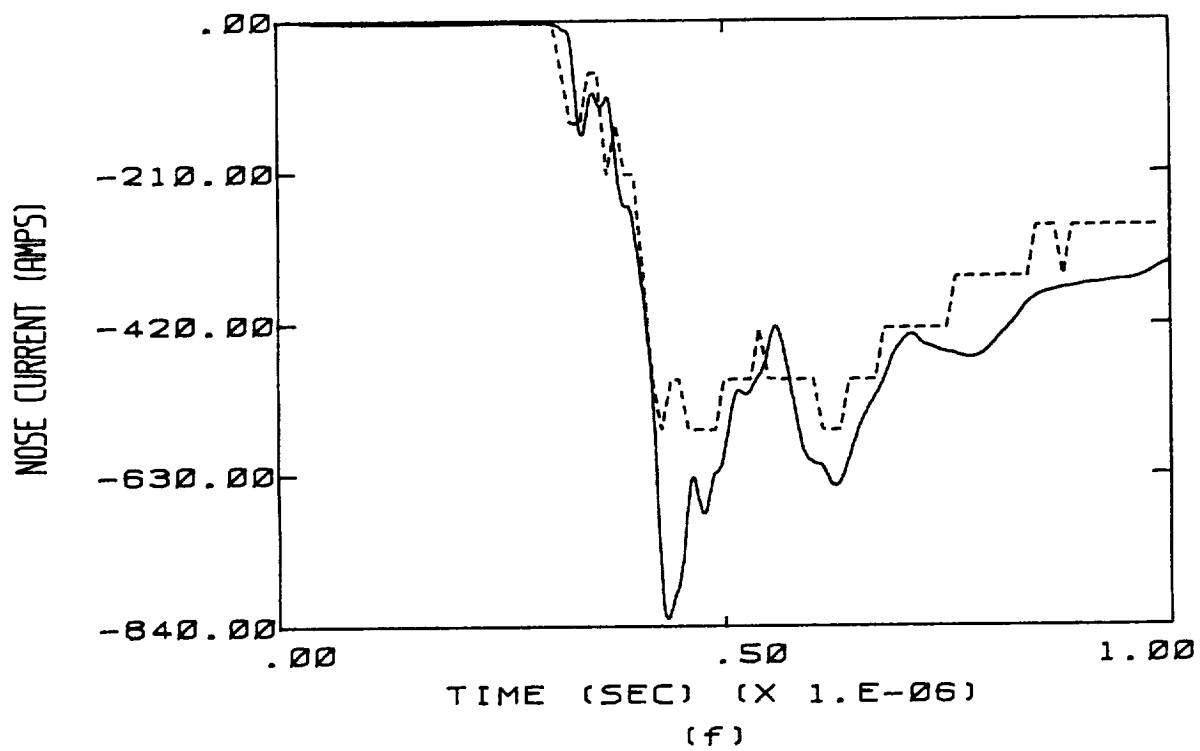
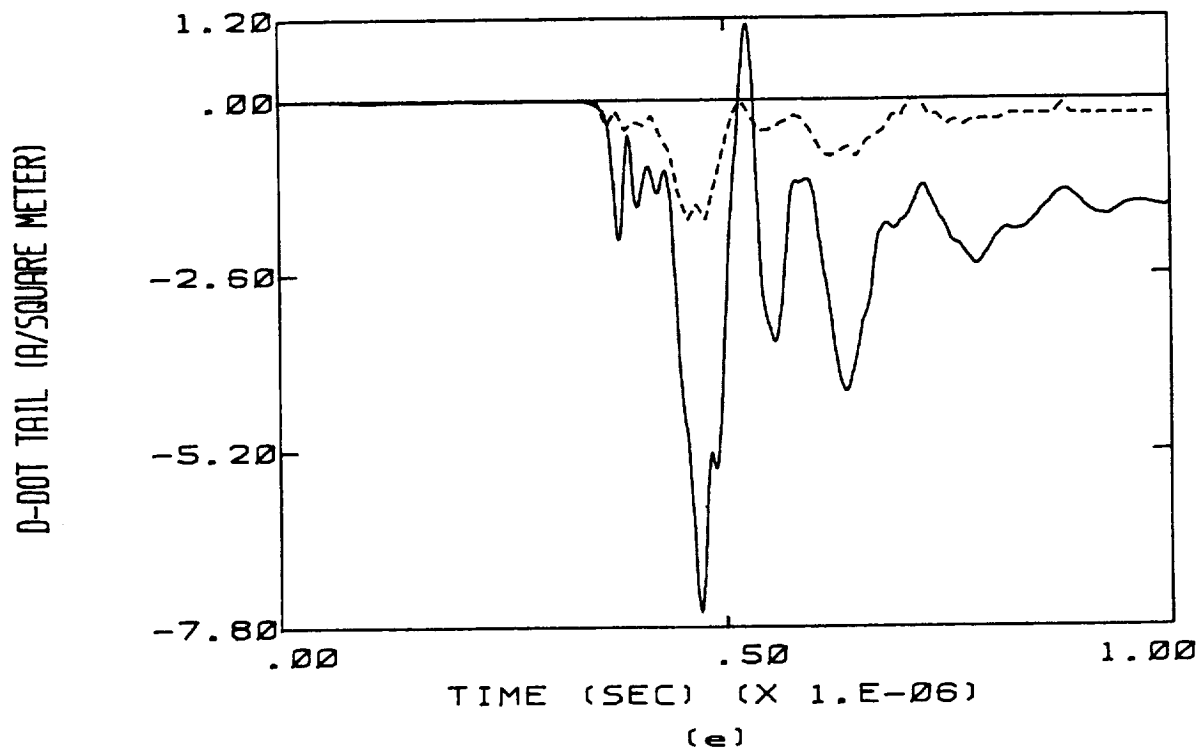


Figure C.16 (continued)

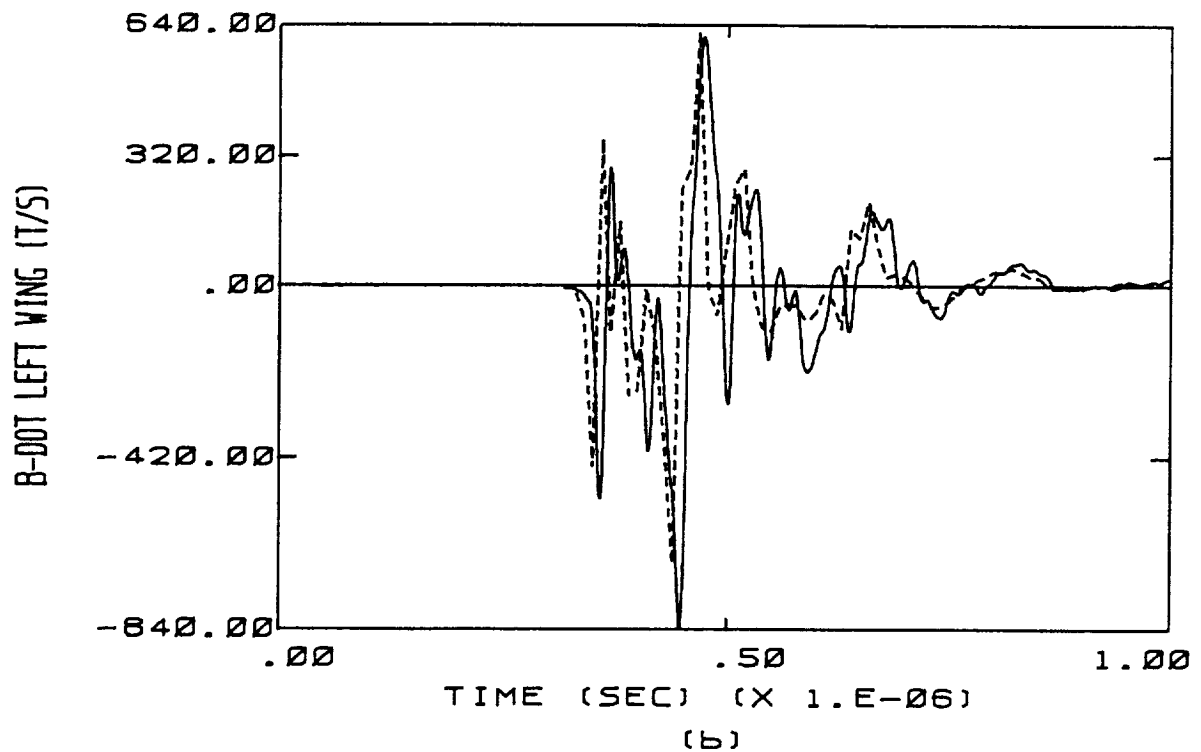
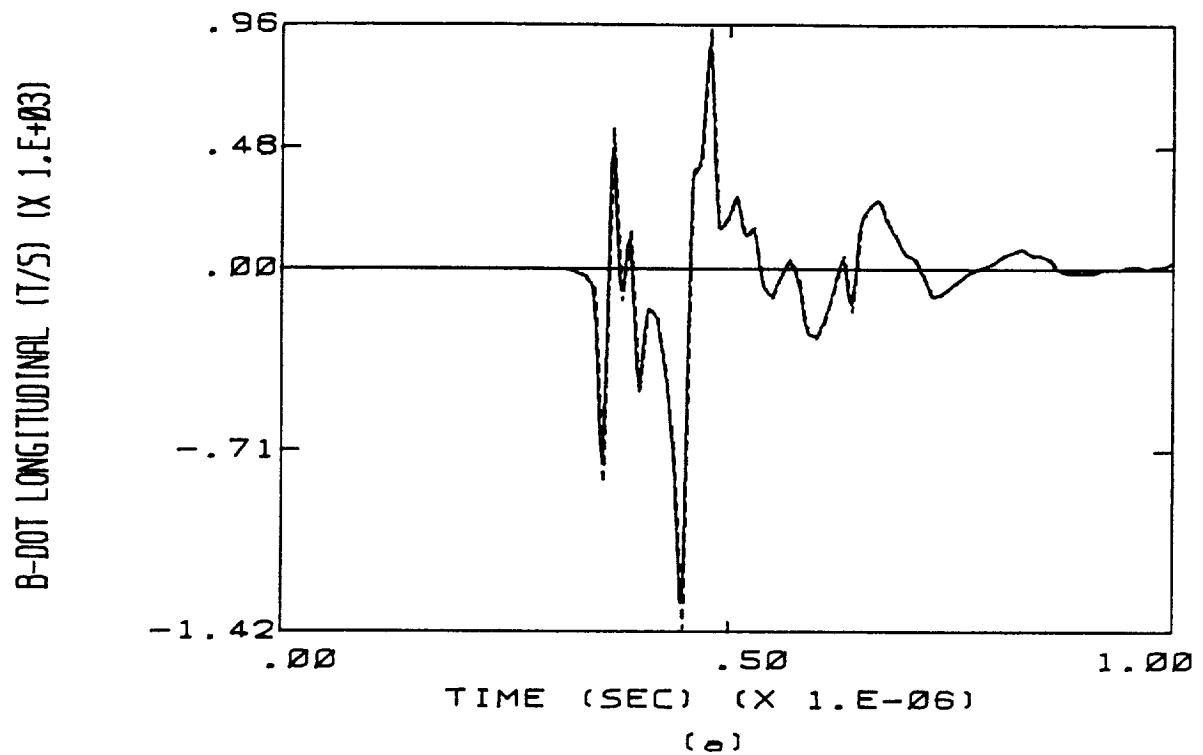
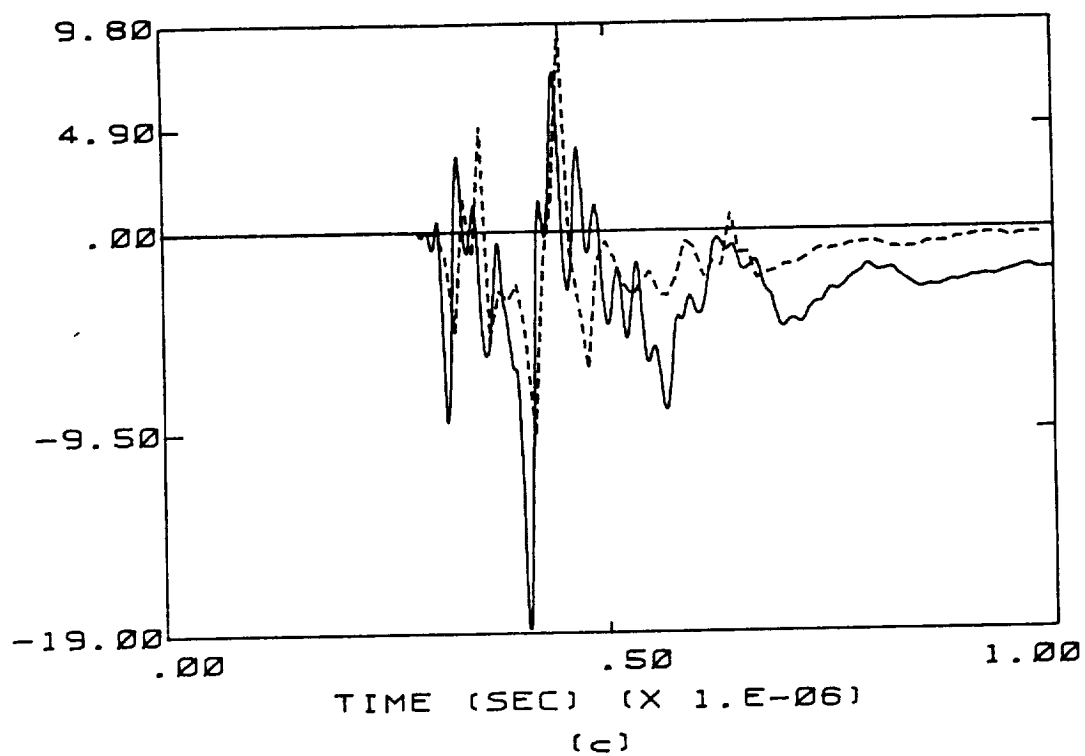


Figure C.17 Calculated Responses Overlaid on Measured Responses of Flight 84-017 for the Case of a 10 cm Radius Channel. The Transfer Function Used Is Appropriate to B-dot Longitudinal. The Resistance Per Unit Length Is 10 ohm/m. The Dashed Line Indicates the Measured Data.



D-DOT FORWARD (A/SQUARE METER)



D-DOT LEFT WING (A/SQUARE METER)

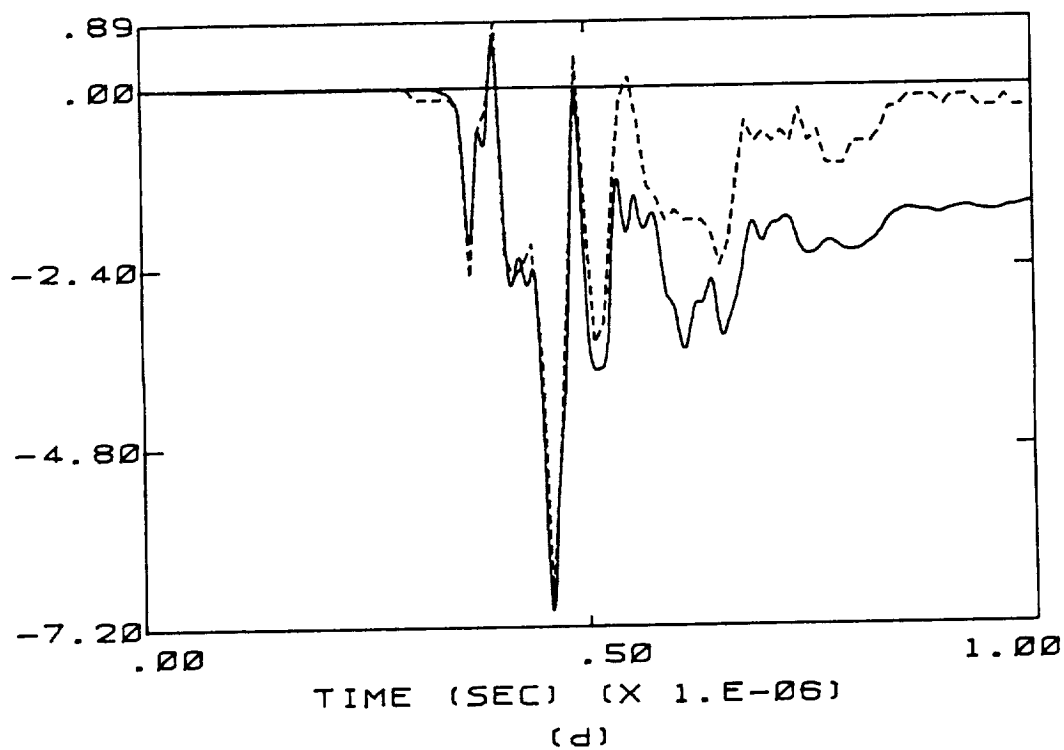


Figure C.17 (continued)

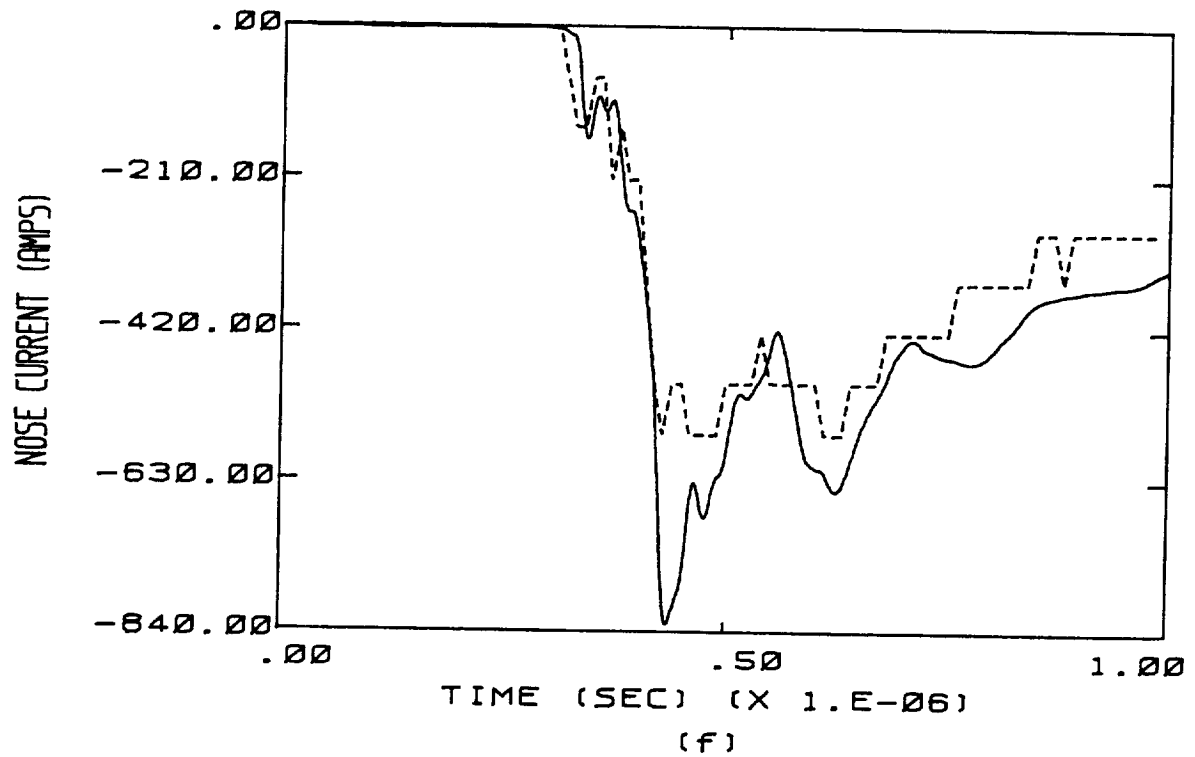
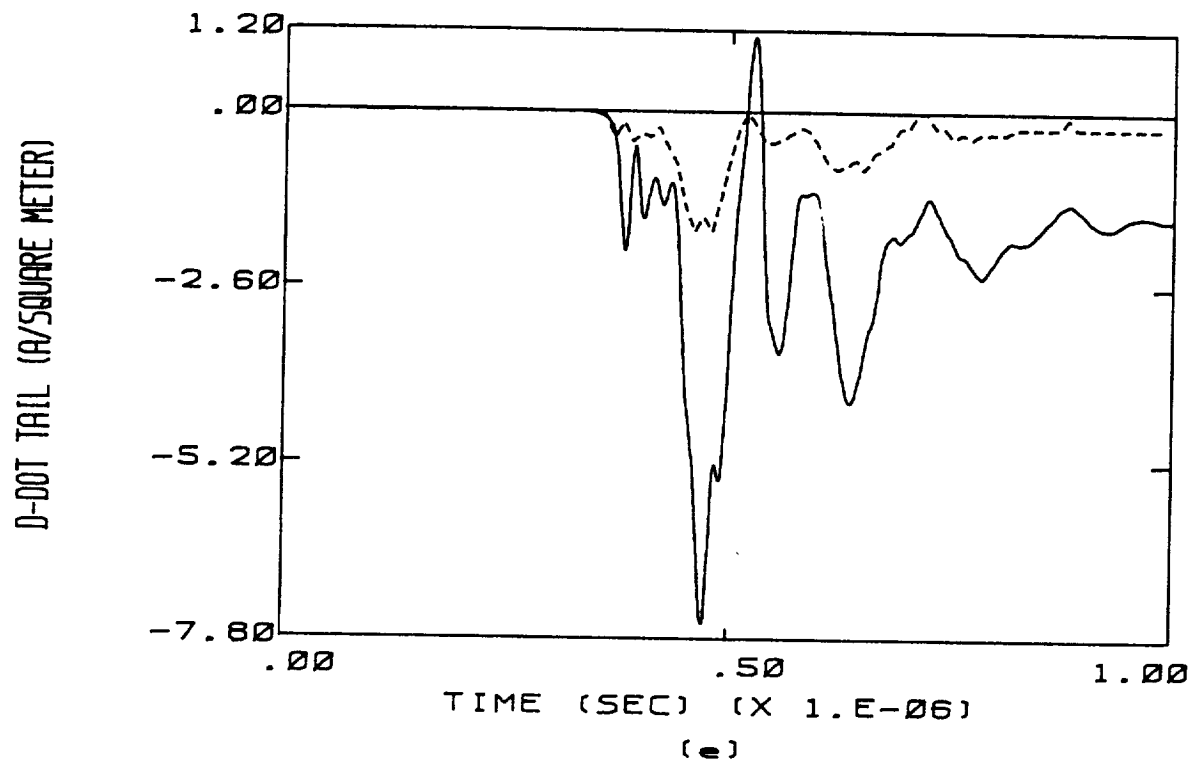


Figure C.17 (continued)

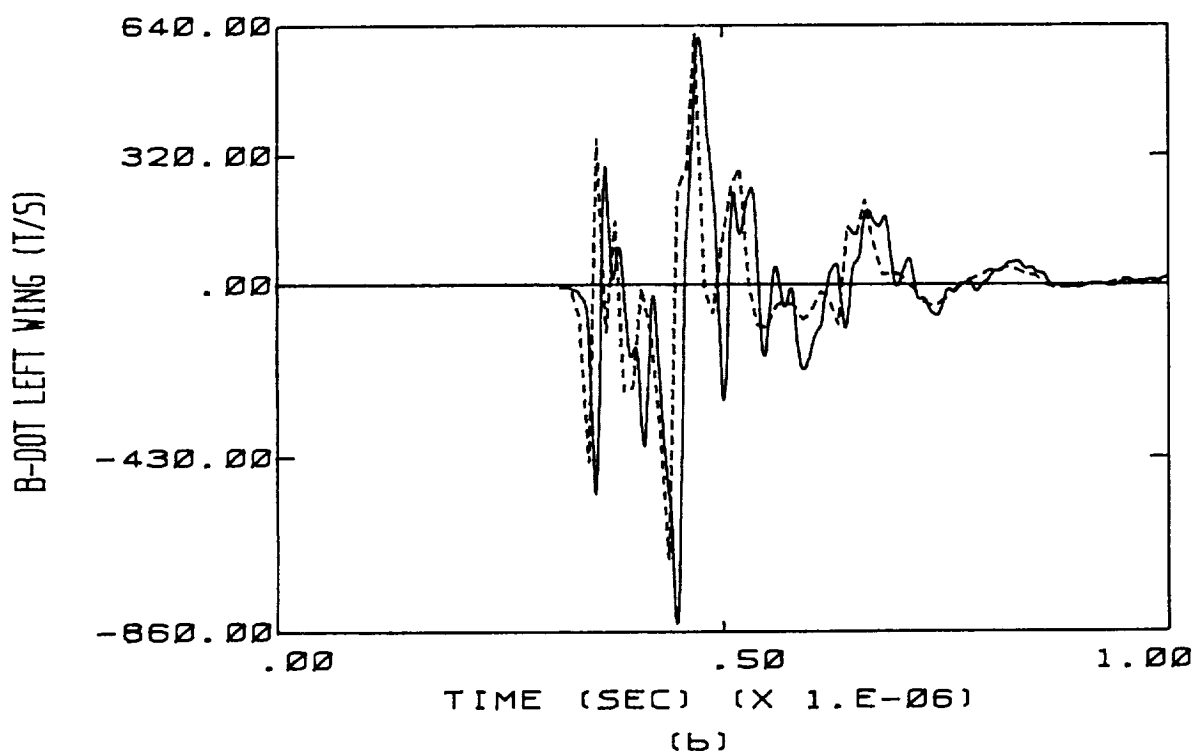
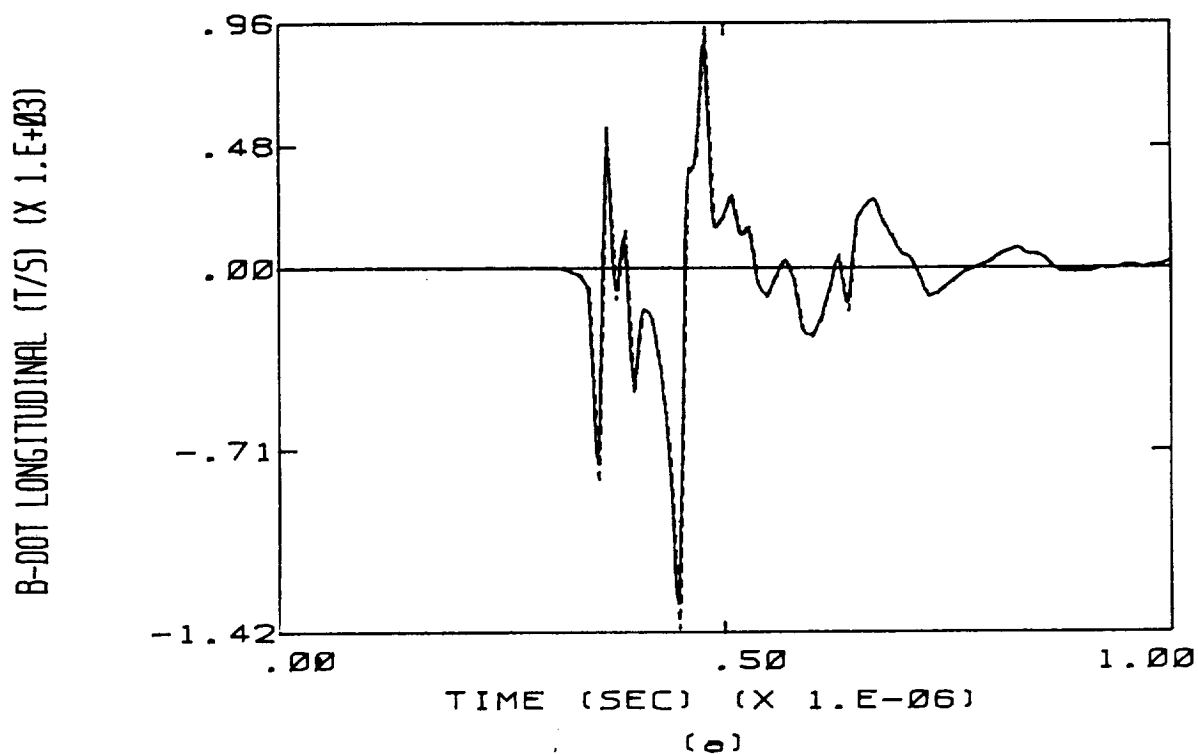
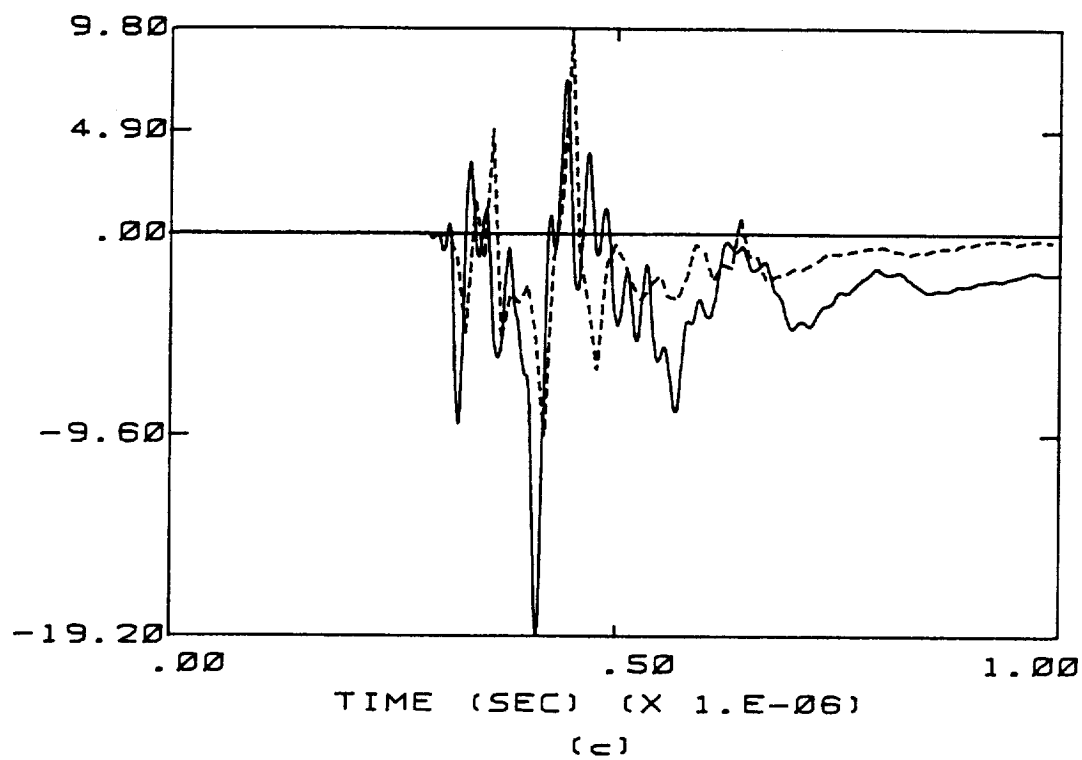


Figure C.18 Calculated Responses Overlaid on Measured Responses of Flight 84-017 for the Case of a 10 cm Radius Channel. The Transfer Function Used Is Appropriate to B-dot Longitudinal. The Resistance Per Unit Length Is 50 ohm/m. The Dashed Line Indicates the Measured Data.

D-DOT FORWARD (A/SQUARE METER)



D-DOT LEFT WING (A/SQUARE METER)

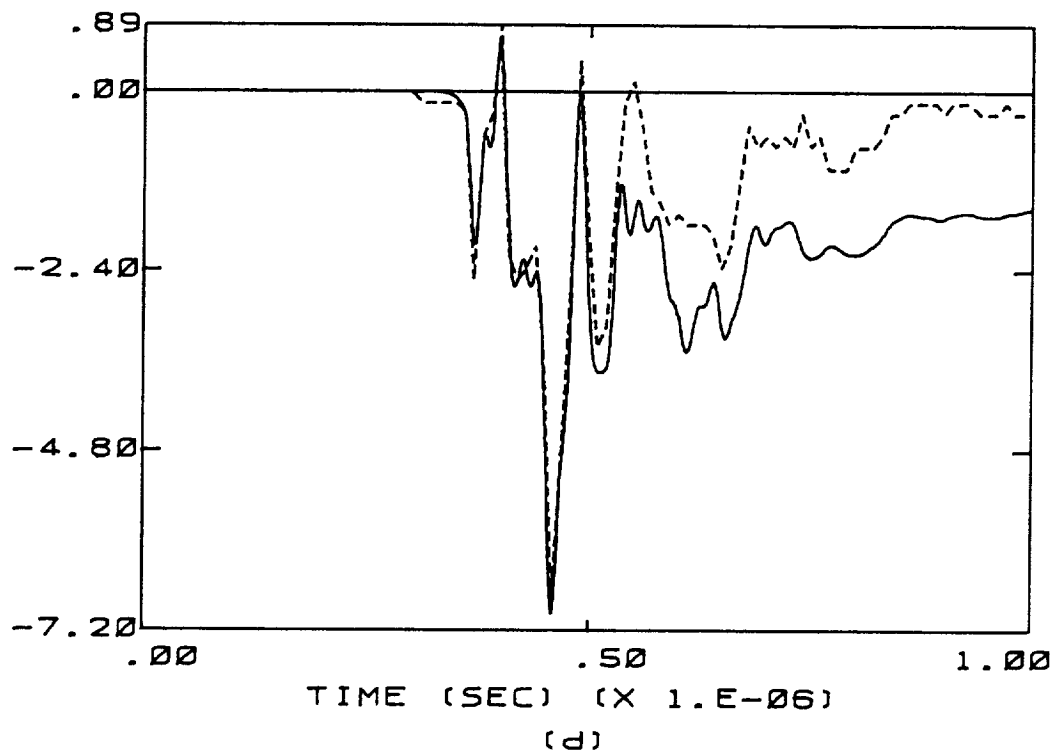


Figure C.18 (continued)

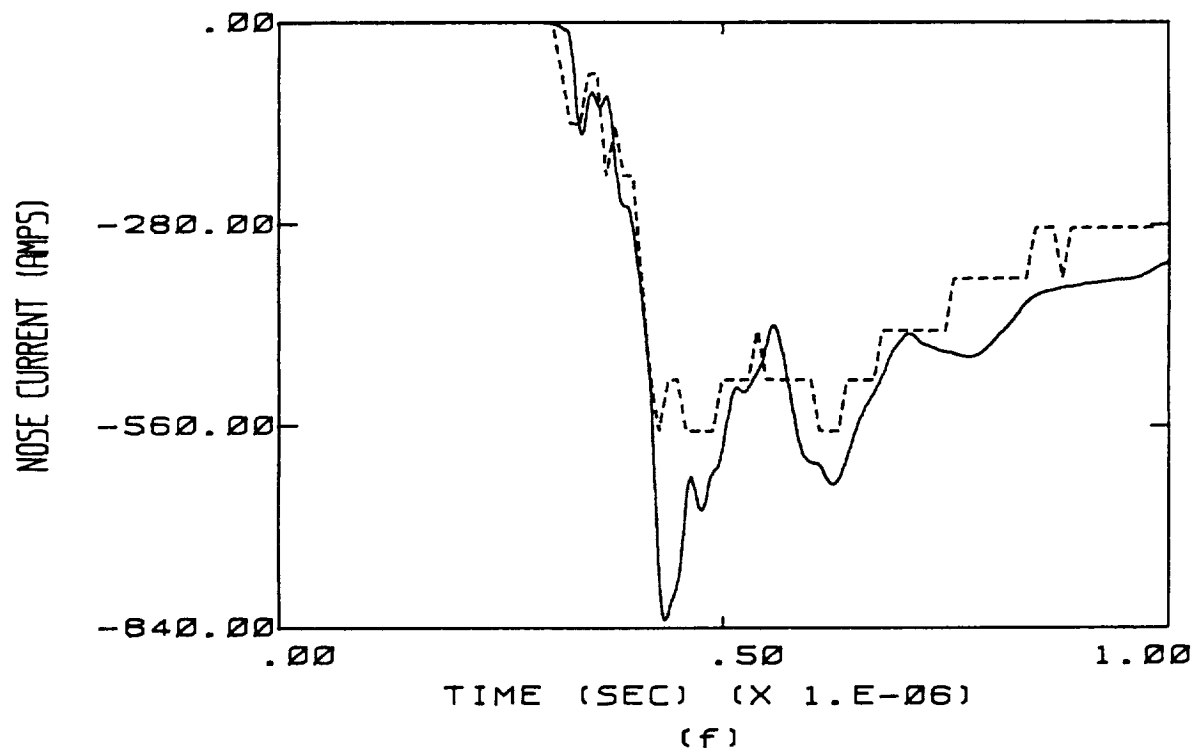
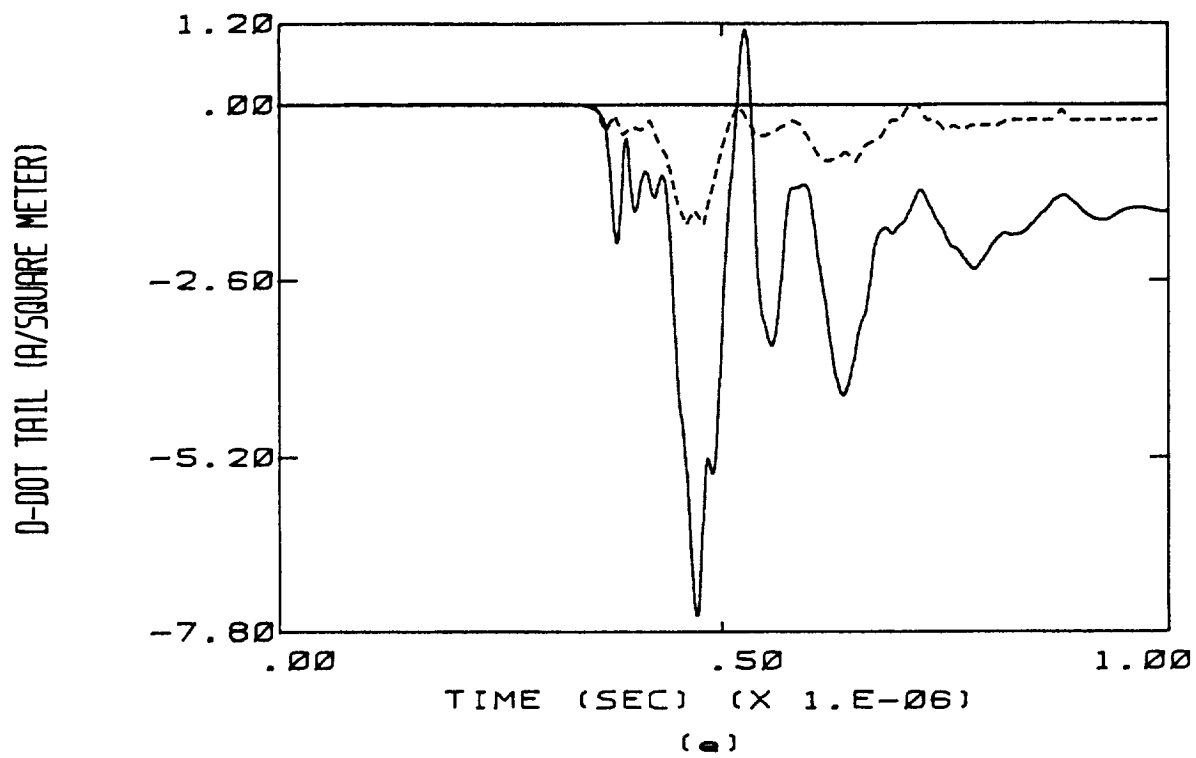


Figure C.18 (continued)

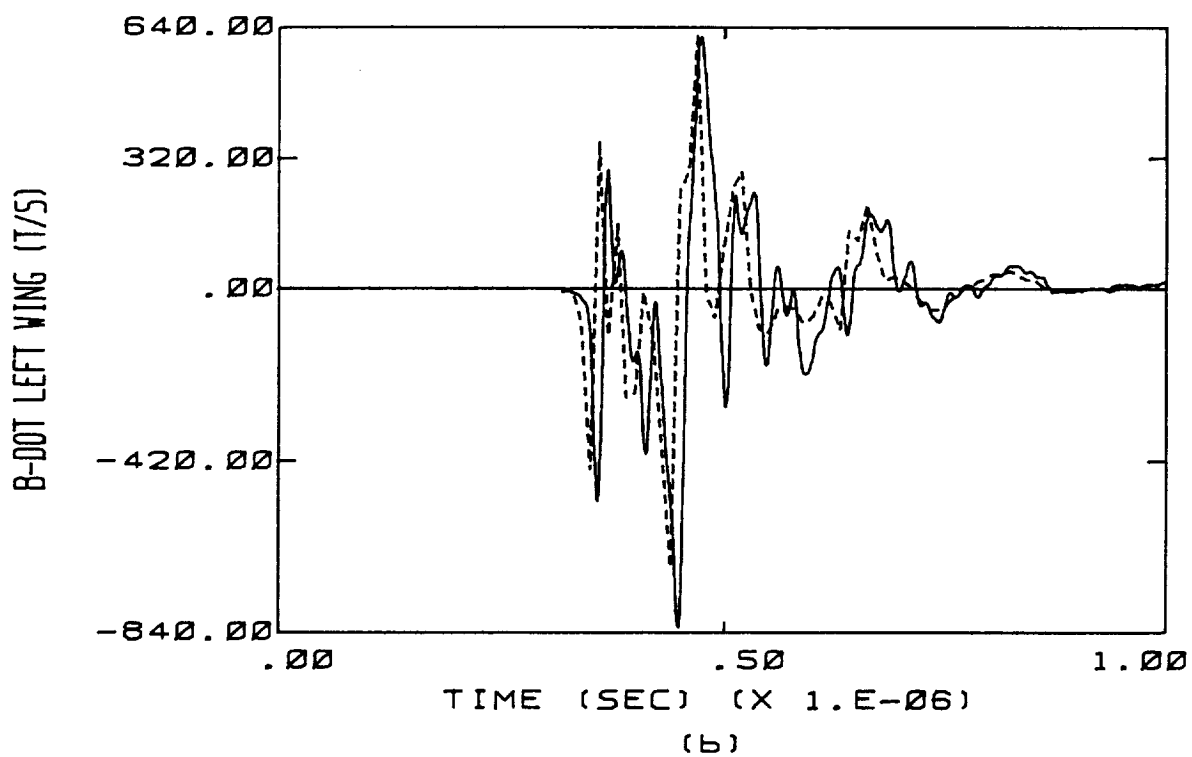
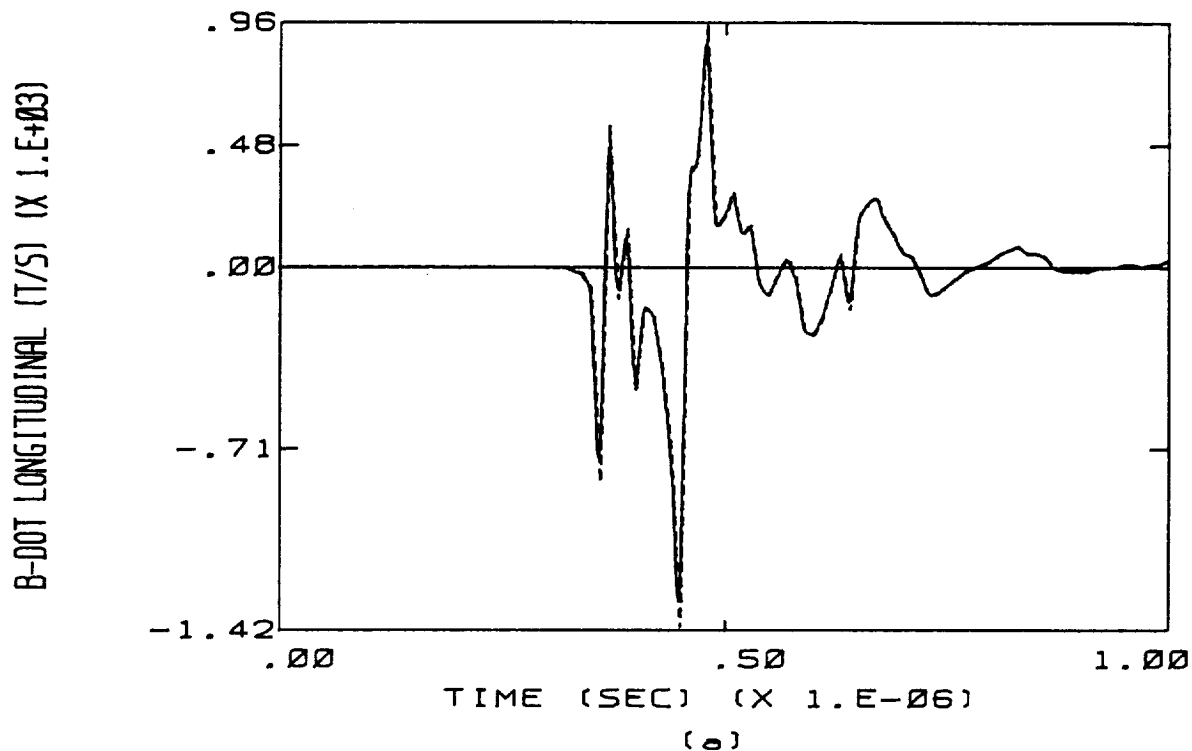
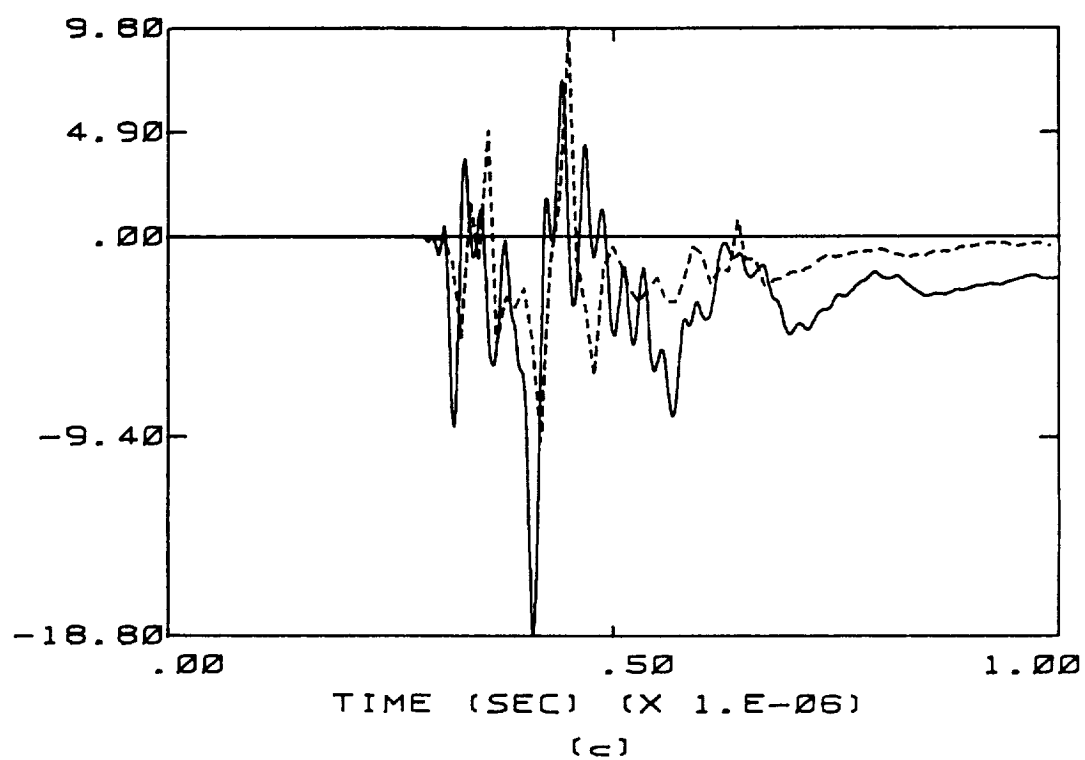


Figure C.19 Calculated Responses Overlaid on Measured Responses of Flight 84-017 for the Case of a 1 cm Radius Channel. The Transfer Function Used Is Appropriate to B-dot Longitudinal. The Resistance Per Unit Length Is 1 ohm/m. The Dashed Line Indicates The Measured Data.

D-DOT FORWARD (A/SQUARE METER)



D-DOT LEFT WING (A/SQUARE METER)

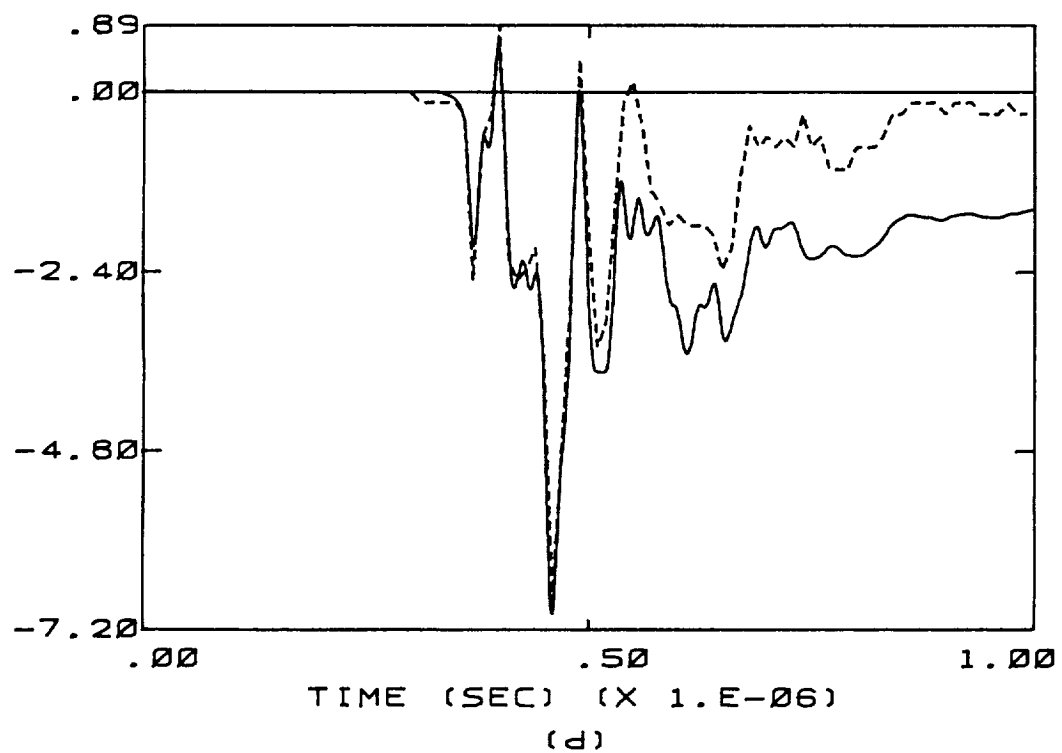


Figure C.19 (continued)

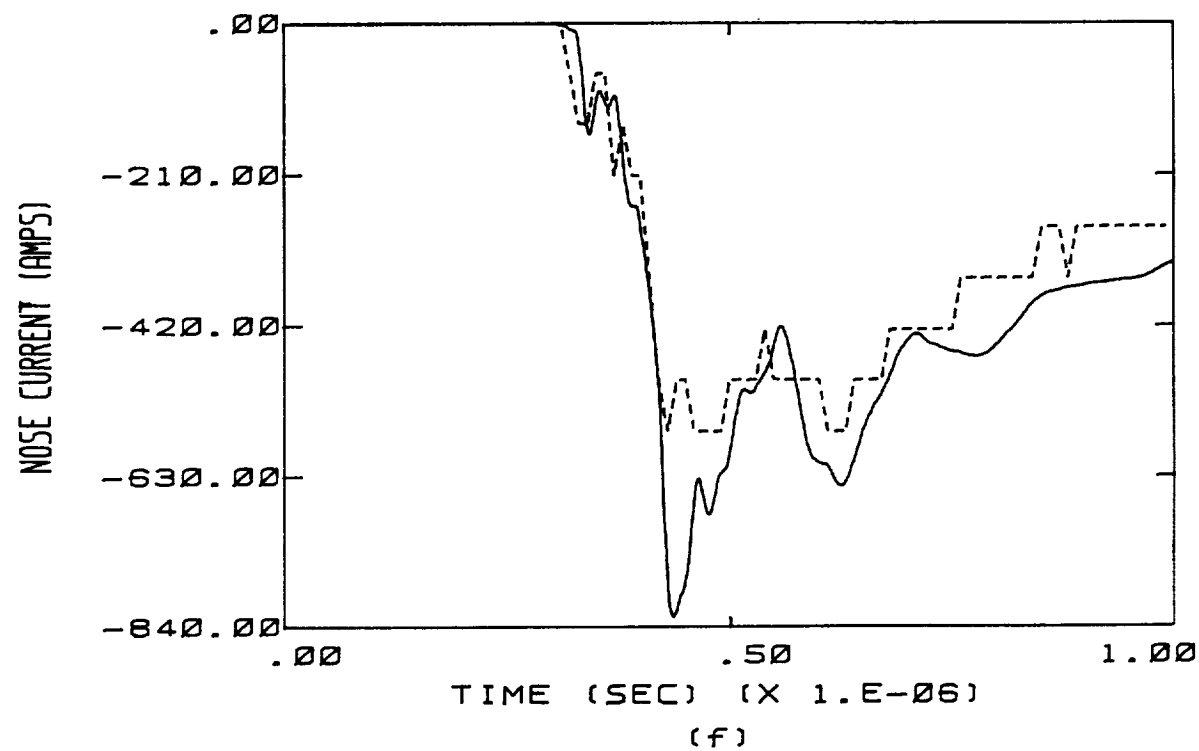
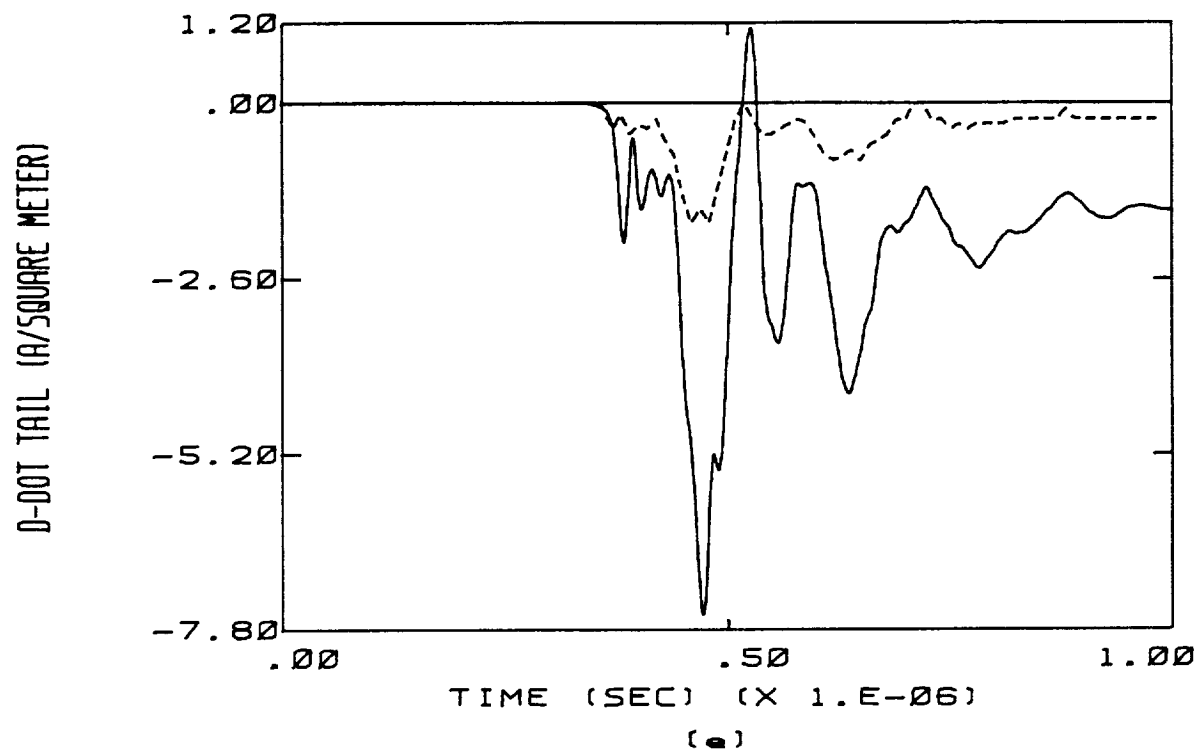


Figure C.19 (continued)



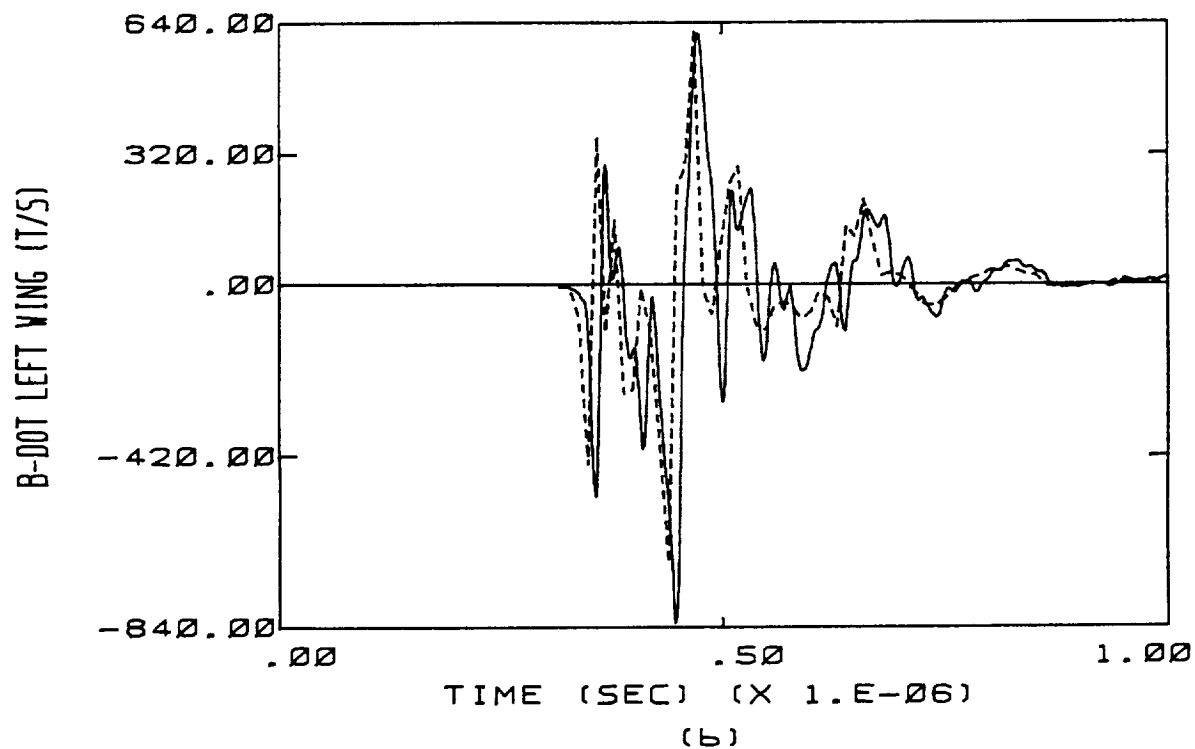
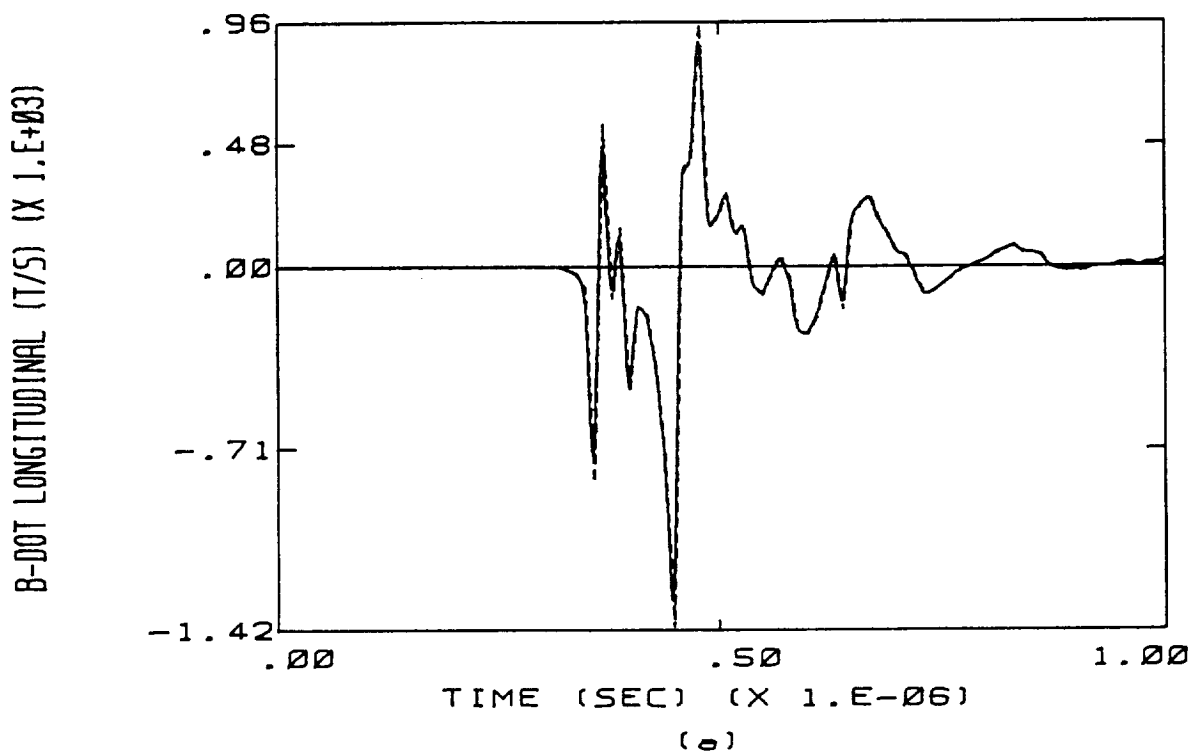
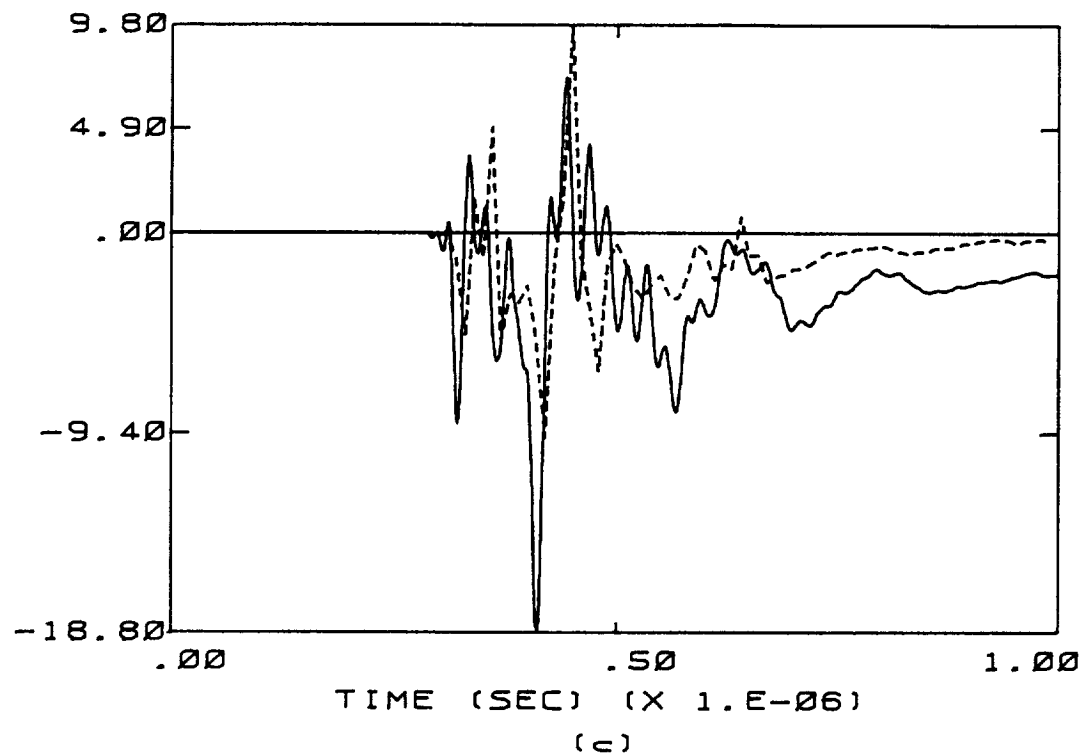


Figure C.20 Calculated Responses Overlaid on Measured Responses of Flight 84-017 for the Case of a 1 cm Radius Channel. The Transfer Function Used Is Appropriate to B-dot Longitudinal. The Resistance Per Unit Length Is 10 ohm/m. The Dashed Line Indicates the Measured Data.

D-DOT FORWARD (A/SQUARE METER)



D-DOT LEFT WING (A/SQUARE METER)

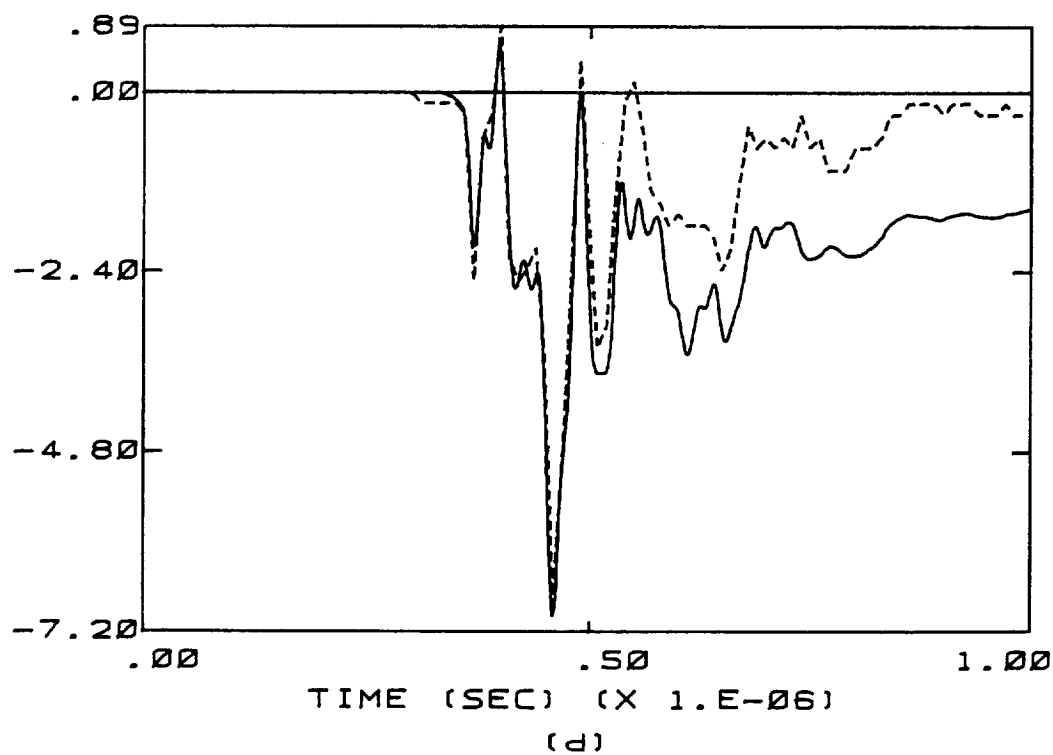


Figure C.20 (continued)

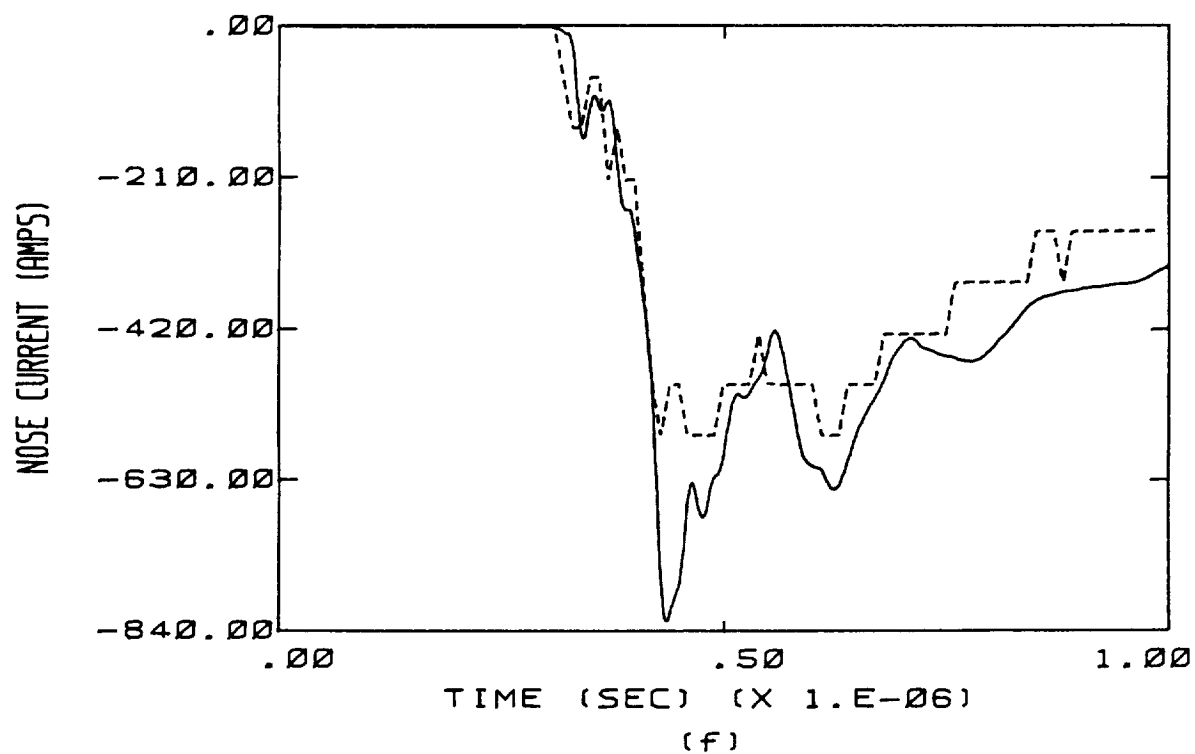
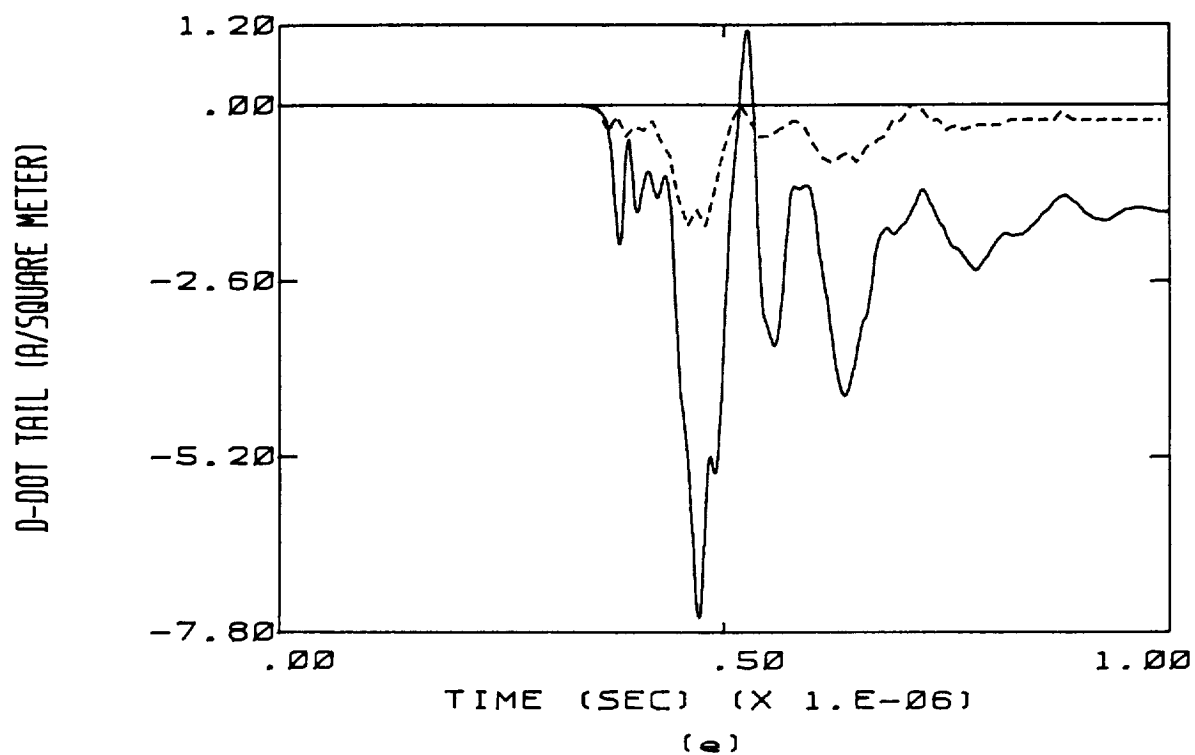


Figure C.20 (continued)

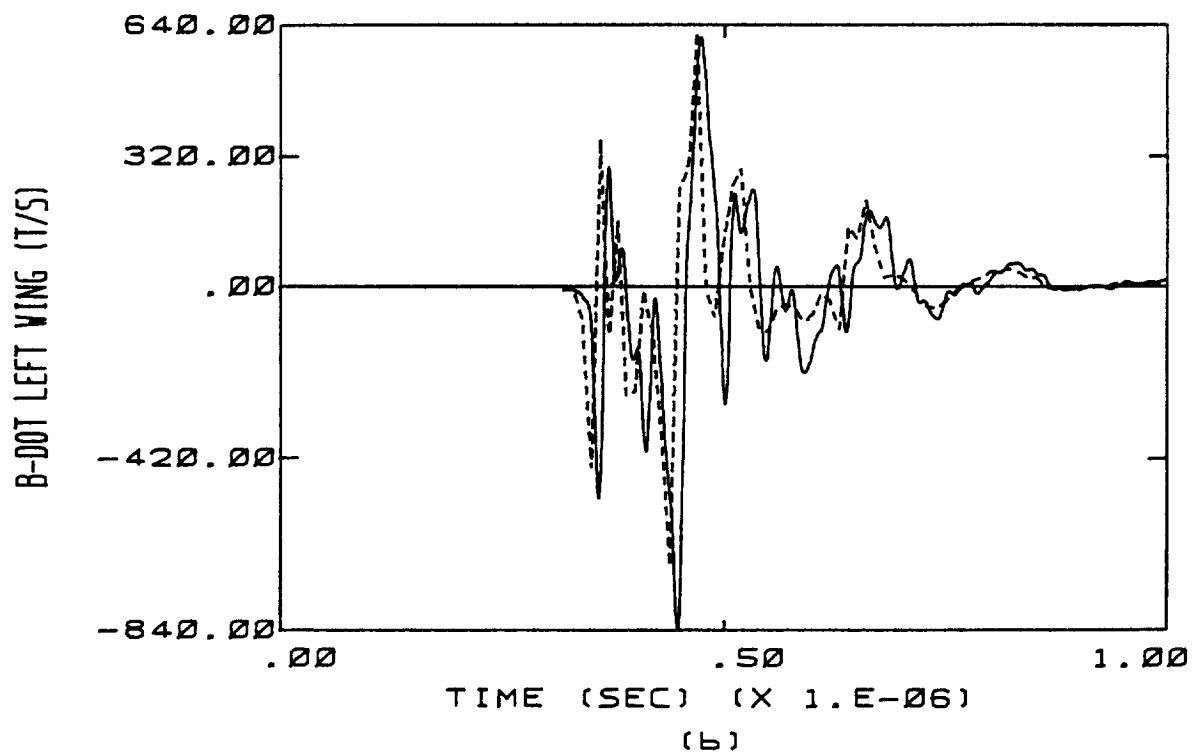
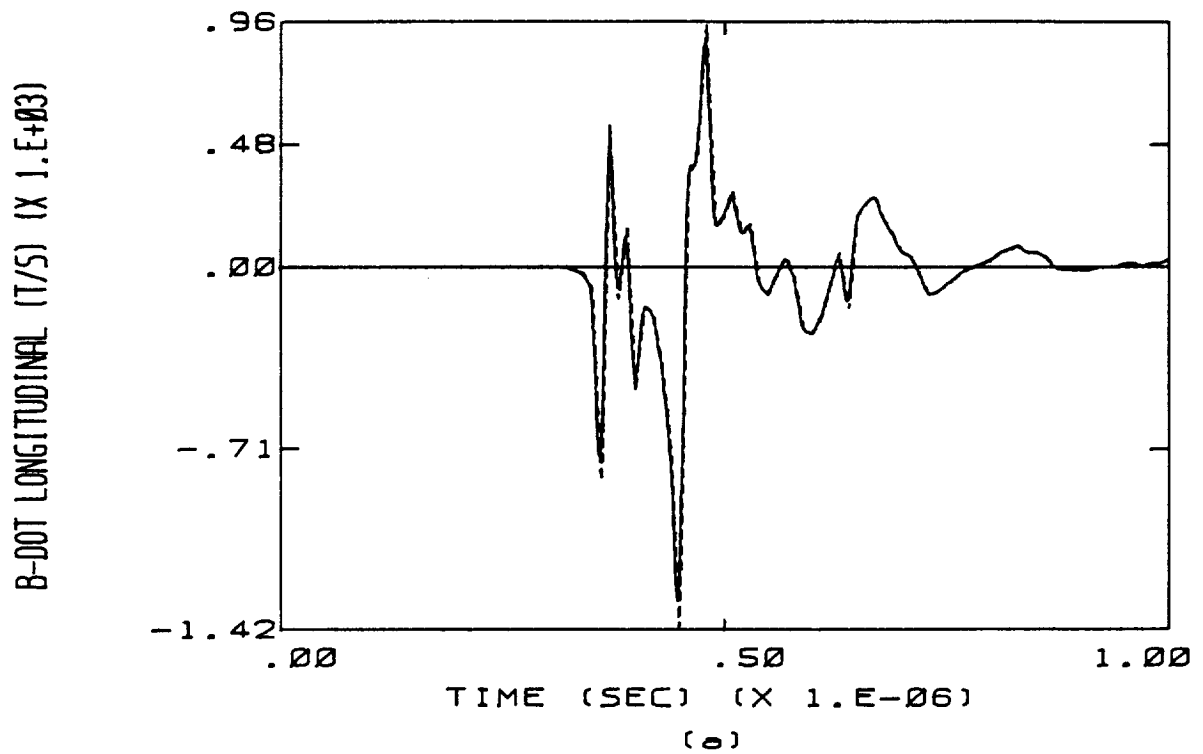
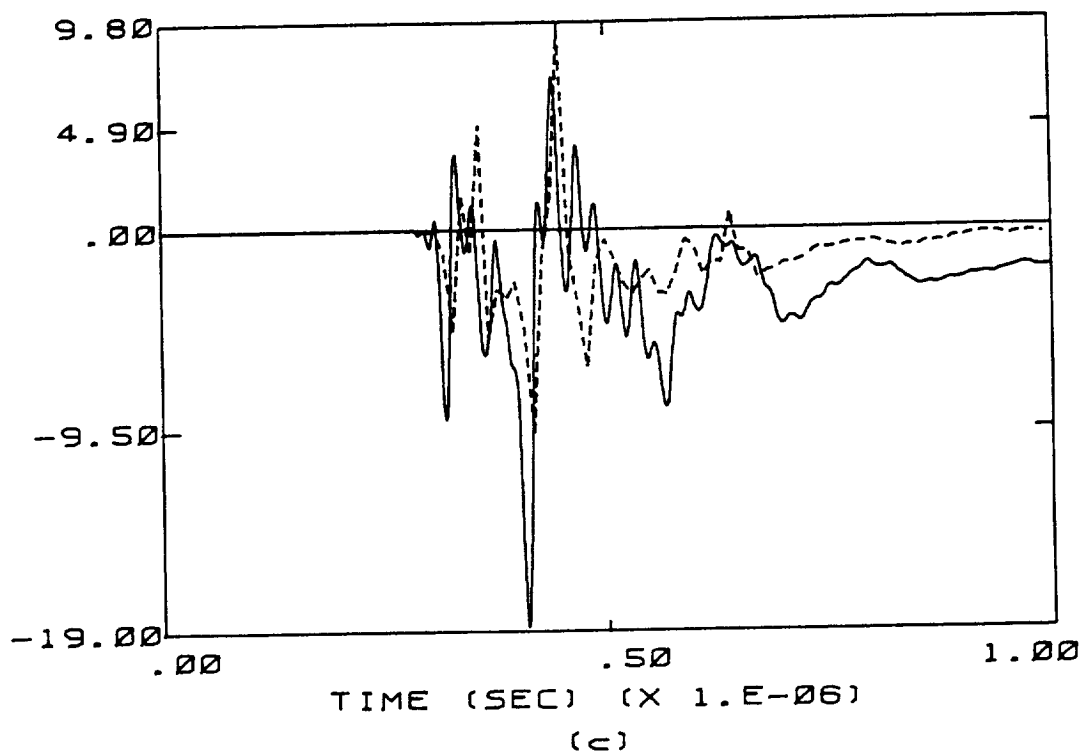


Figure C.21 Calculated Responses Overlaid on Measured Responses of Flight 84-017 for the Case of a 1 cm Radius Channel. The Transfer Function Used Is Appropriate to B-dot Longitudinal. The Resistance Per Unit Length Is 1 ohm/m. The Dashed Line Indicates the Measured Data.

D-DOT FORWARD (A/SQUARE METER)



D-DOT LEFT WING (A/SQUARE METER)

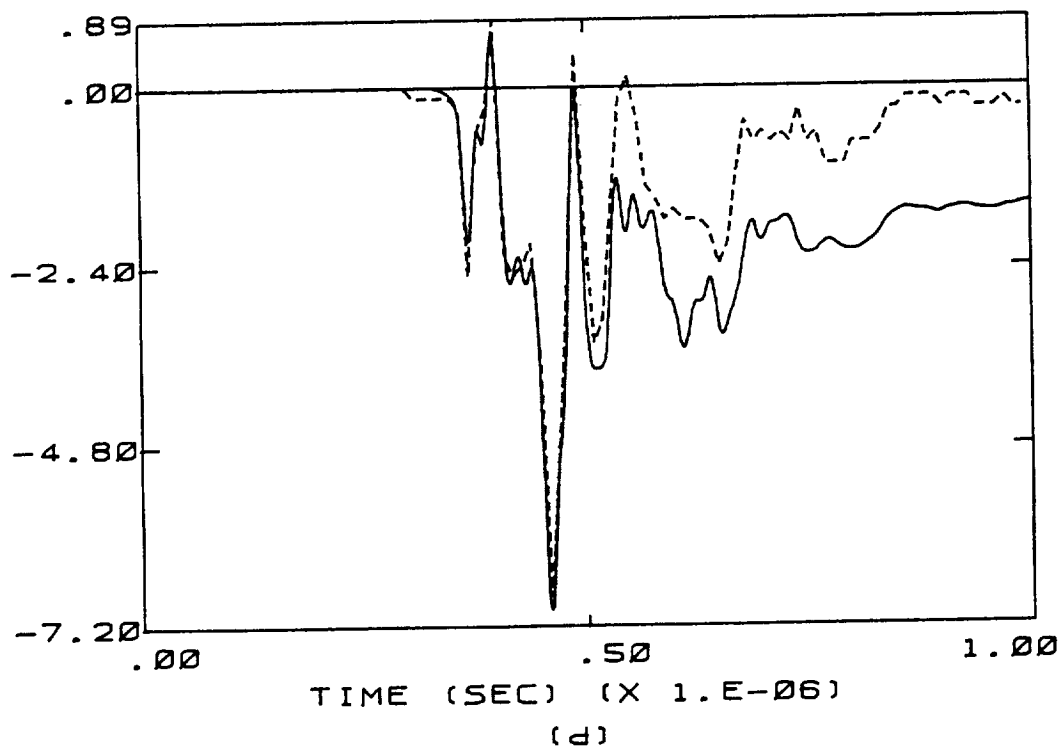


Figure C.21 (continued)

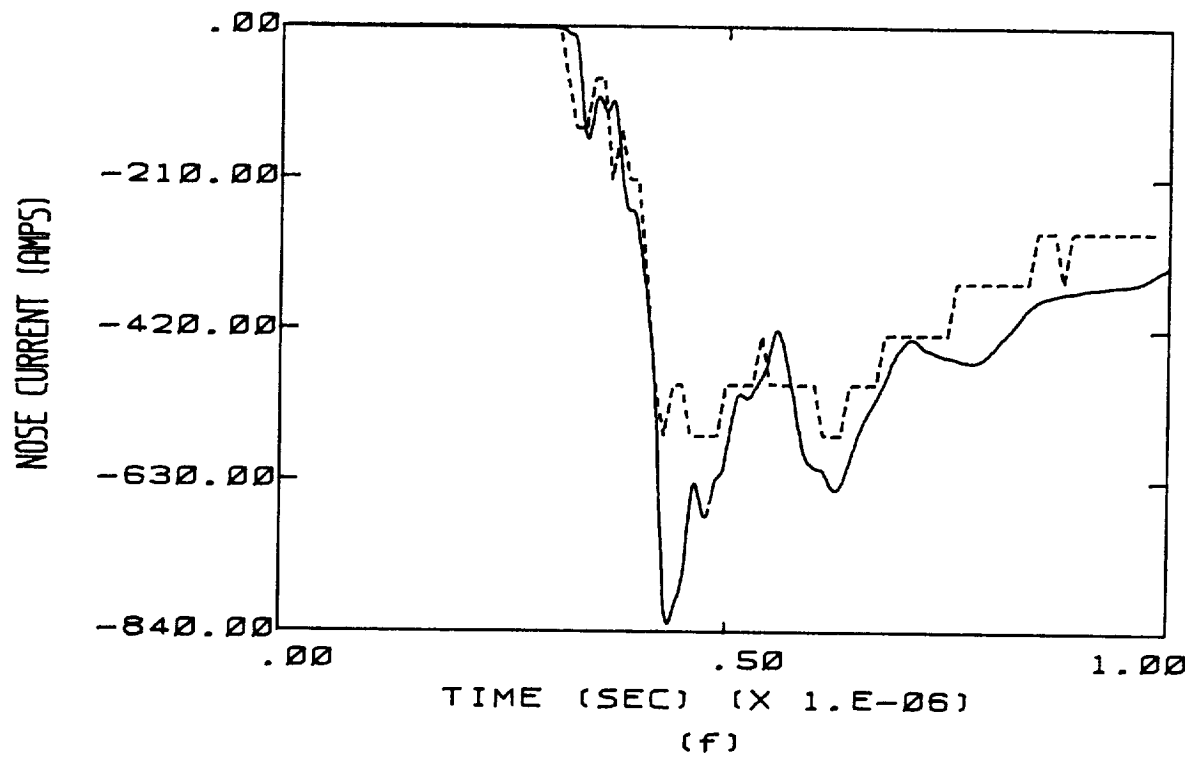
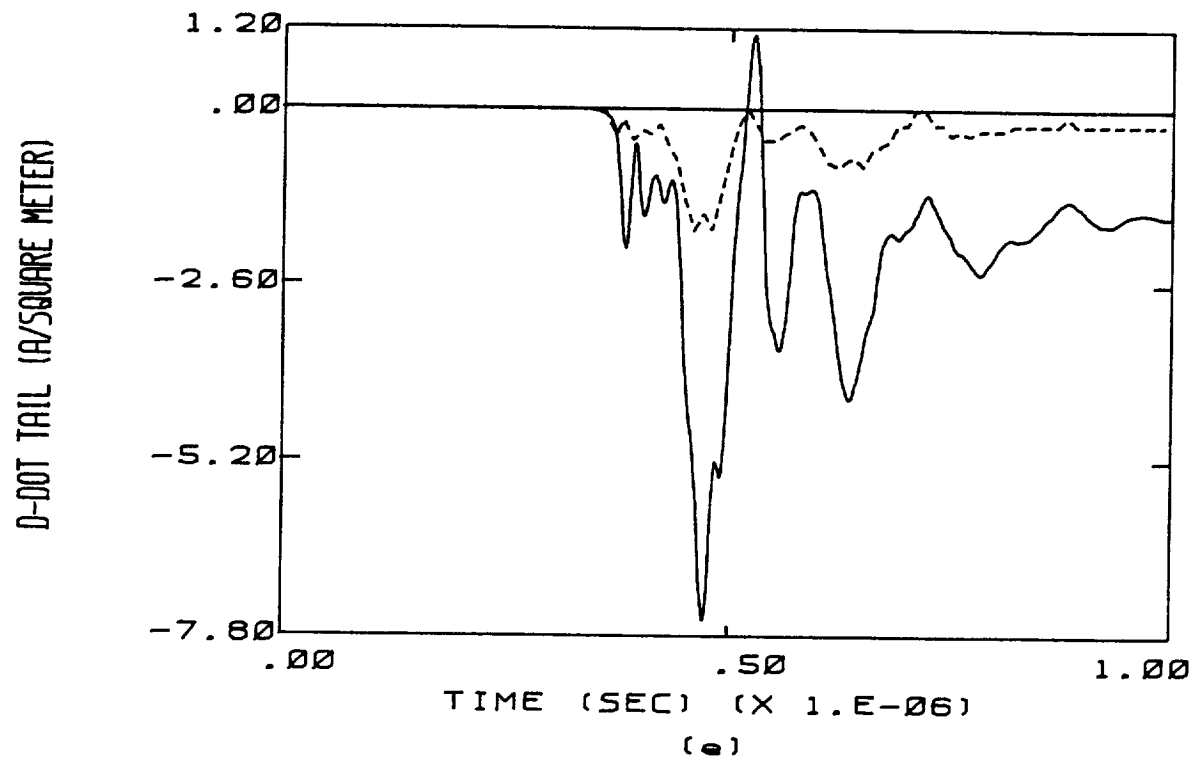


Figure C.21 (continued)

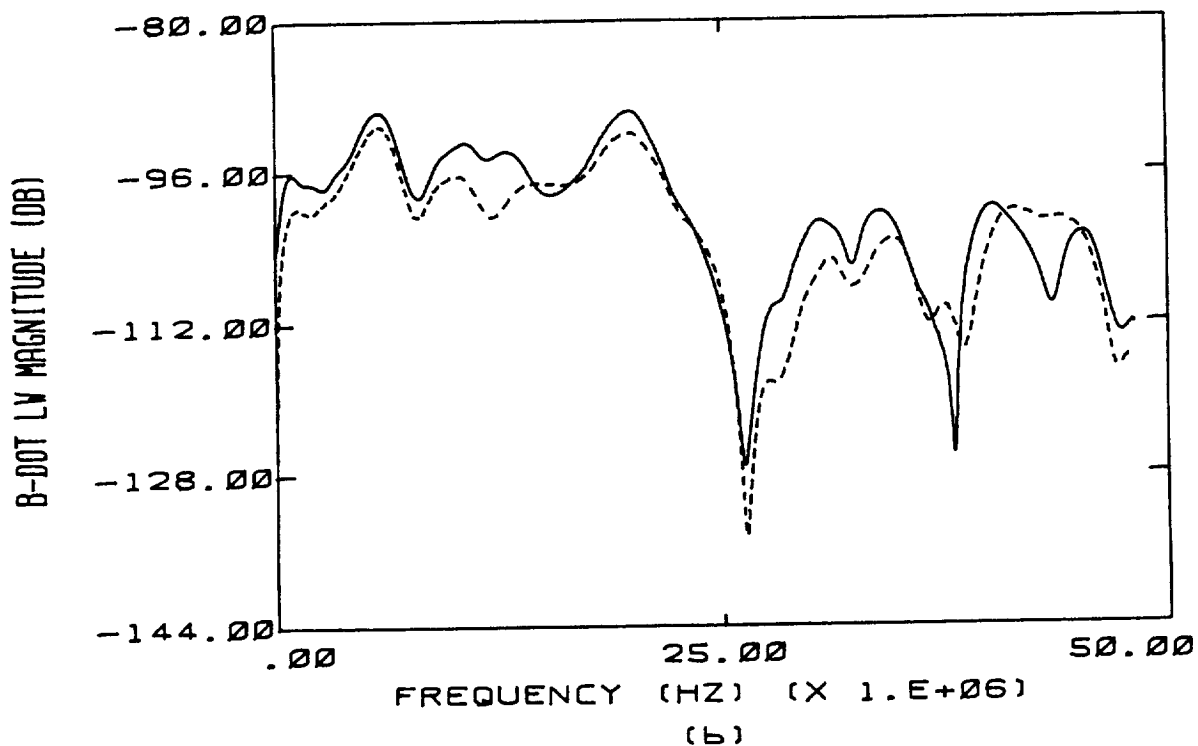
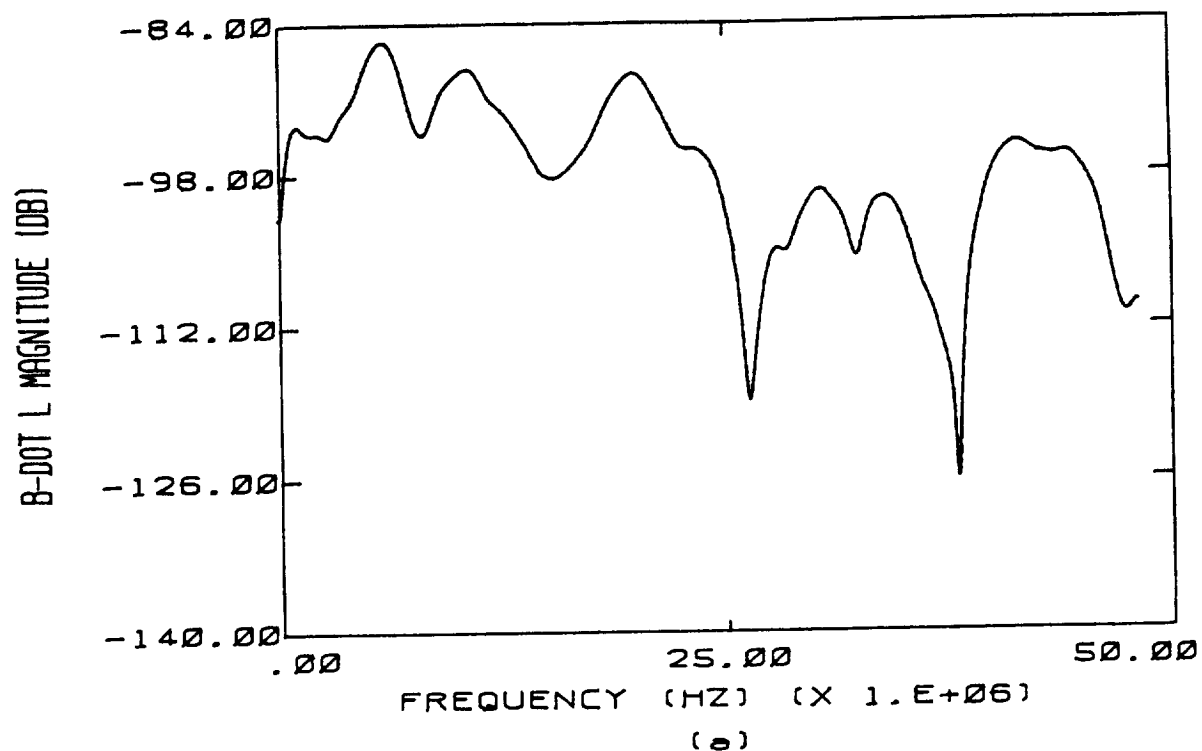


Figure C.22 Frequency Domain Calculated Responses Overlaid on Measured Responses of Flight 84-017 for the Case of a 1 cm Radius Channel. The Transfer Function Used Is Appropriate to B-dot Longitudinal. The Dashed Line Indicates the Measured Data.

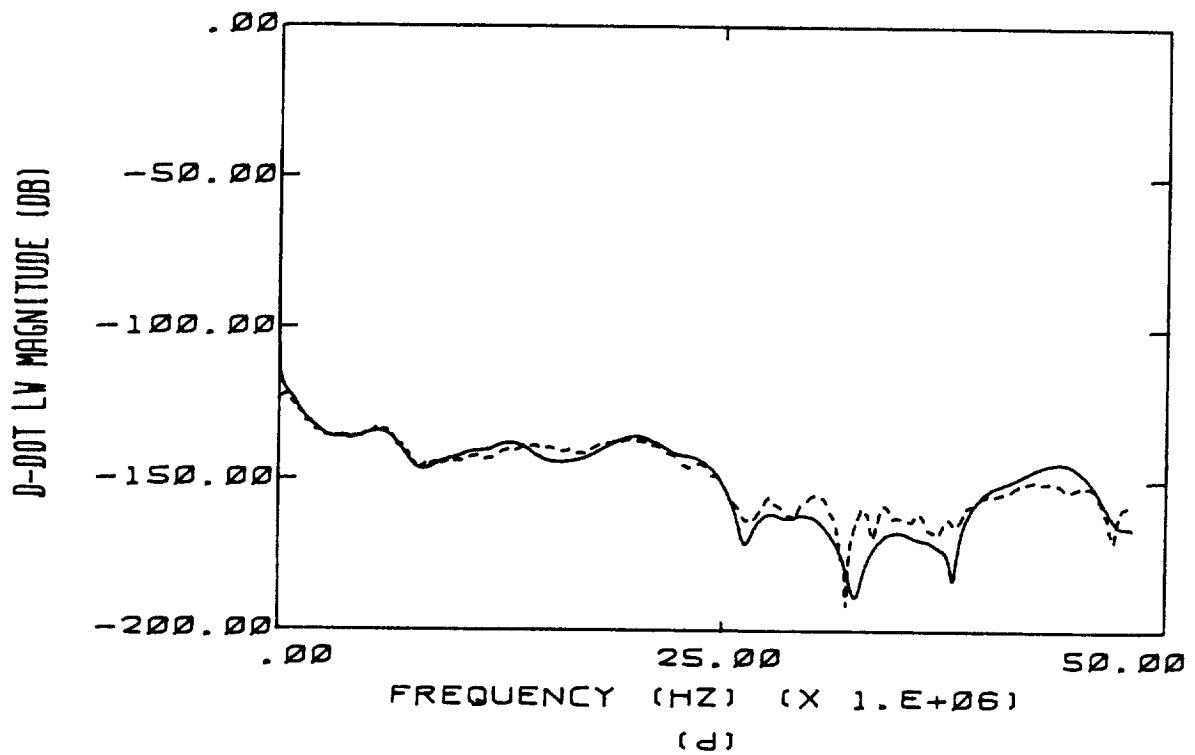
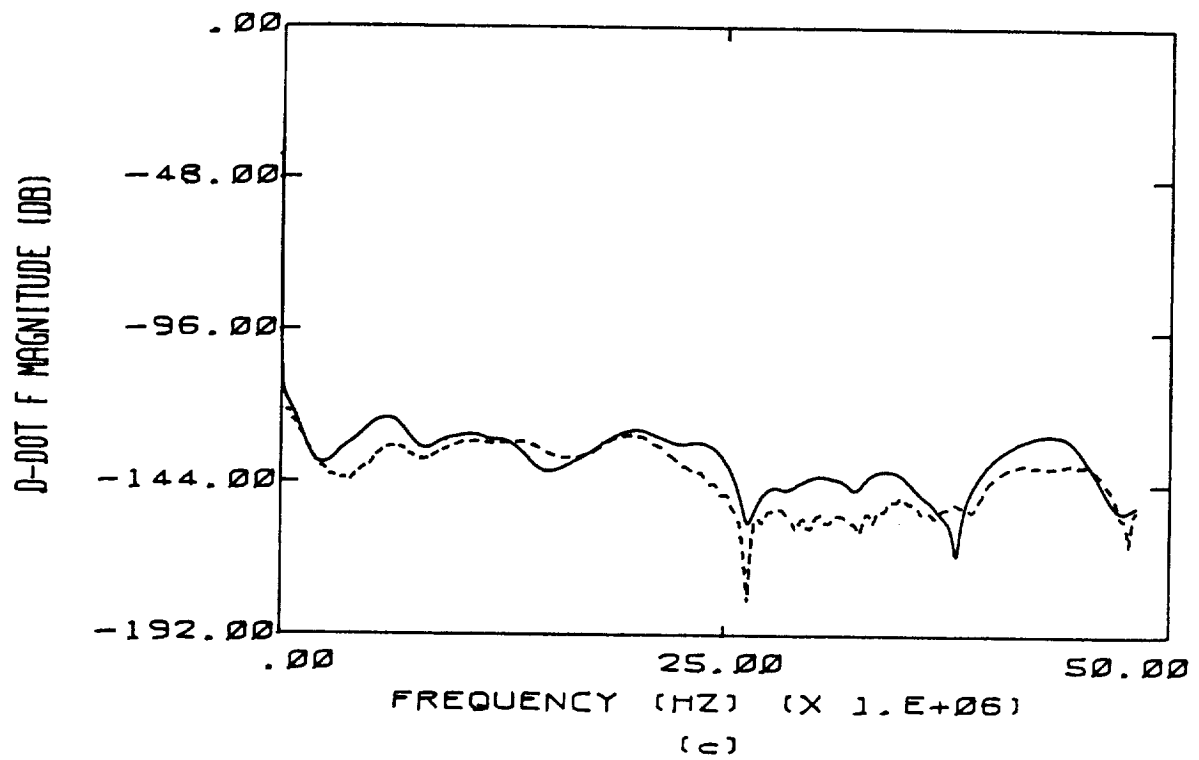


Figure C.22 (continued)



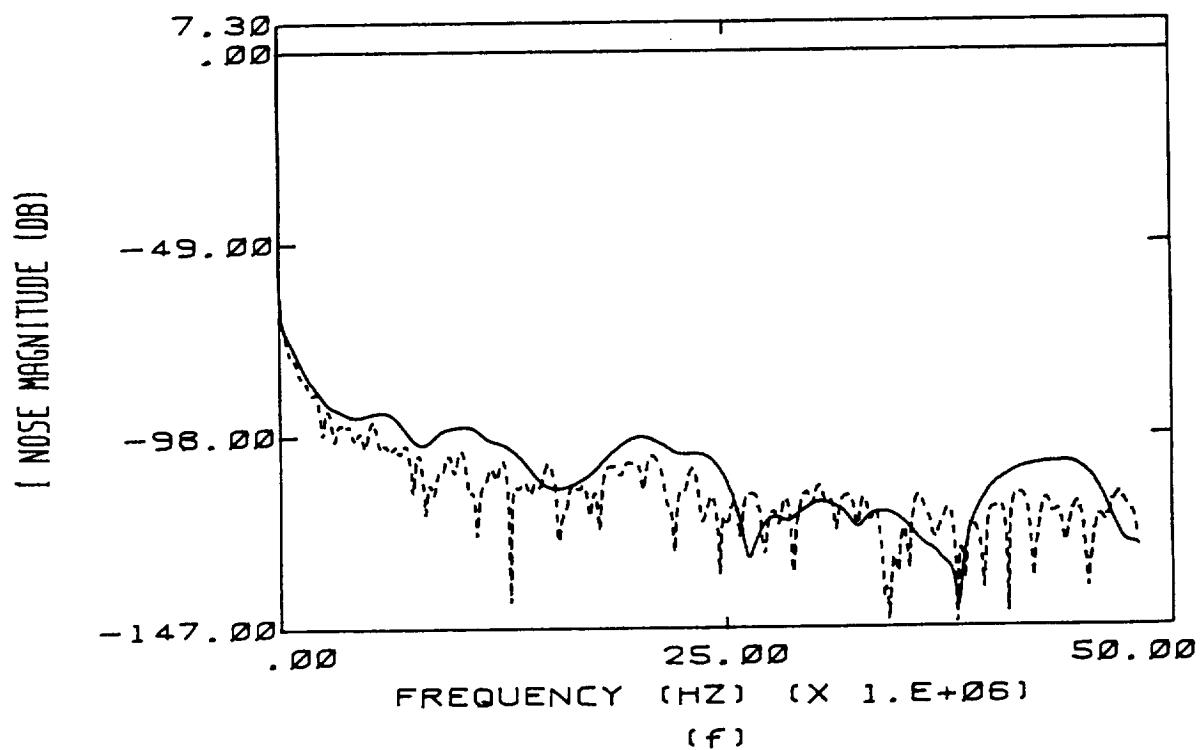
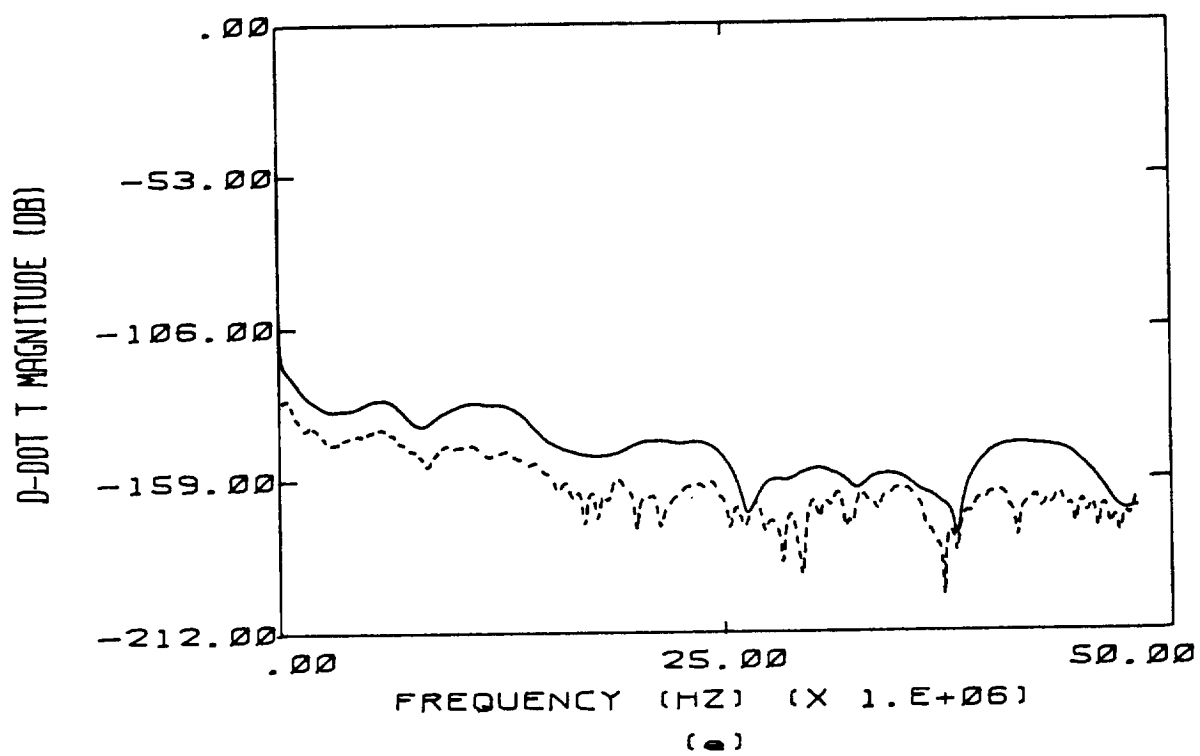


Figure C.22 (continued)



## **APPENDIX D**

### **SKEWED ANGLE PARAMETER STUDY**

The plots in this appendix were discussed in Chapter 5. The legend beneath each plot gives the magnitude of the electric field, the net charge on the aircraft, and the orientation of the field. The field orientation is specified by the letters X, Y, and Z. These refer to coordinate axes as shown in Figure 1.1. For each letter that is present (X, Y, or Z), the ambient field has a component along that direction. All of the components present are equal in magnitude. For example, the notation X, -Y, Z means that the ambient field has components along the X axis, the negative Y axis, and the Z axis. All these components are equal in magnitude and combine to give a resultant magnitude shown in a particular legend.

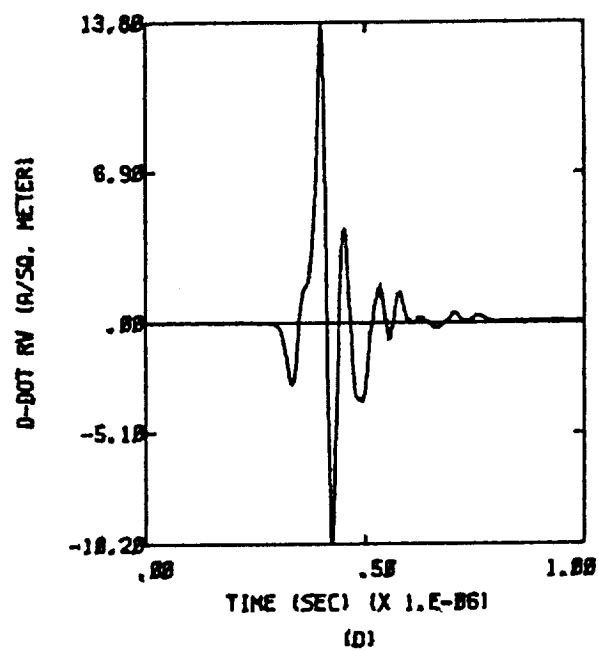
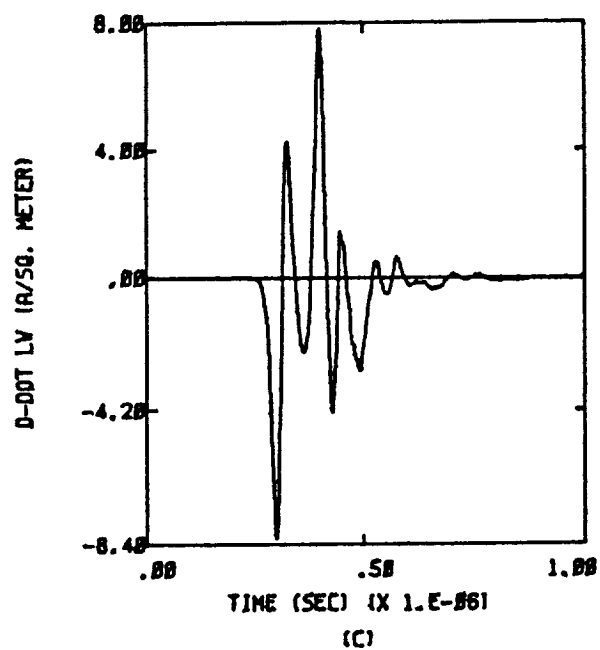
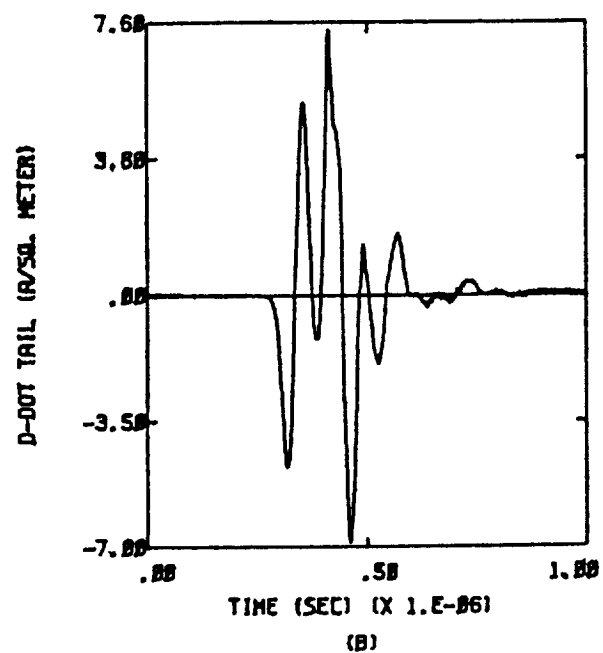
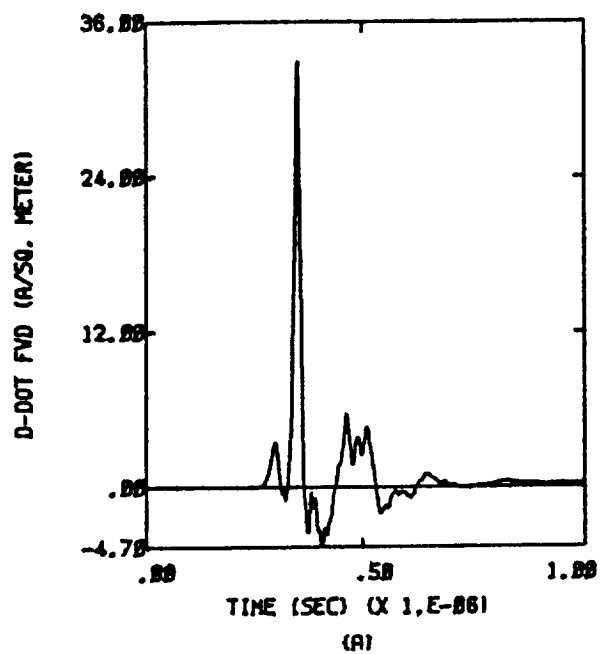


Figure D.1a  $X, Y; Q = 0; E = 2.5 \times 10^5$  Volts per meter

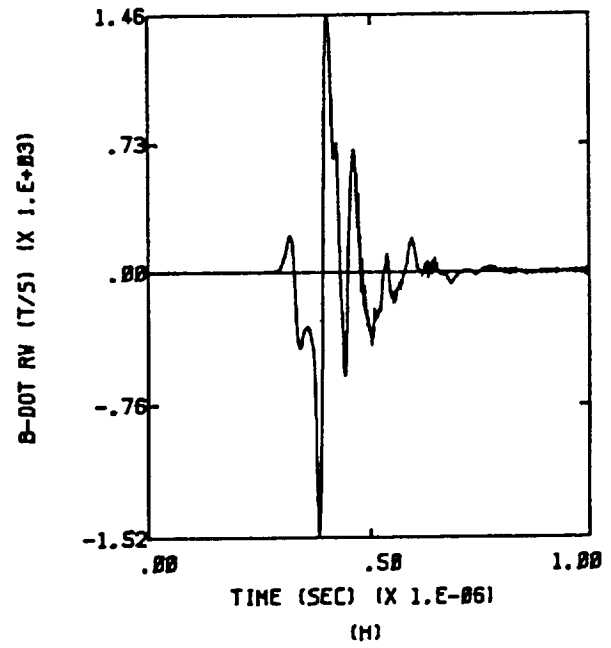
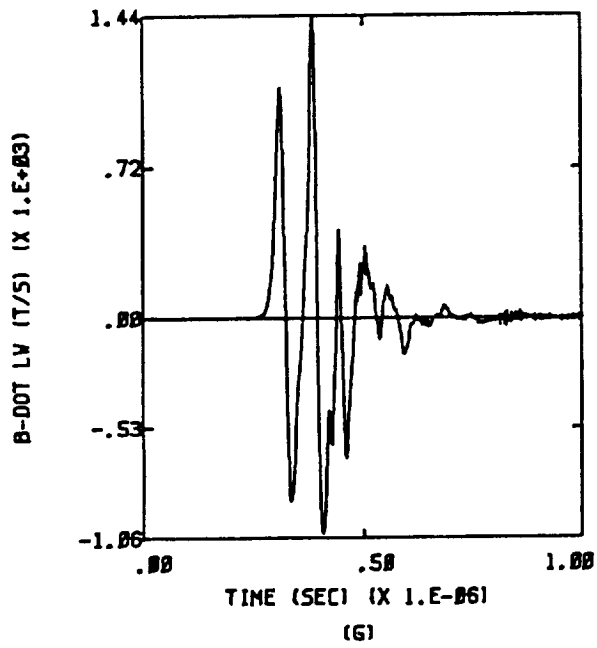
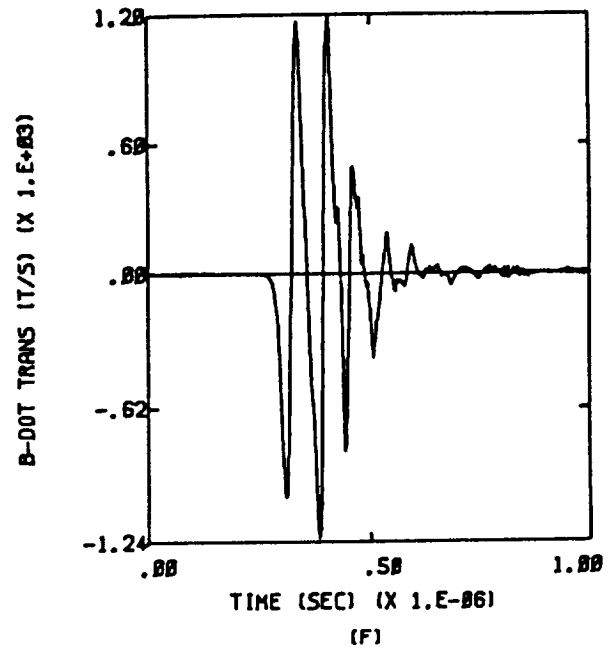
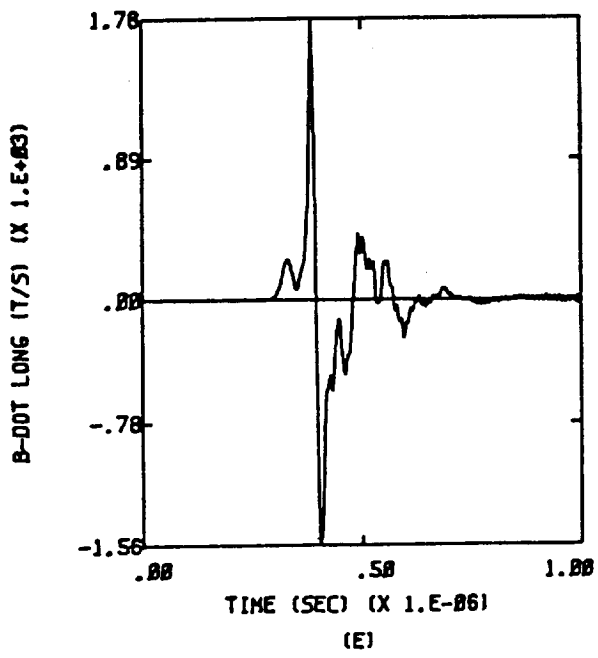


Figure D.1b X,Y; Q = 0; E =  $2.5 \times 10^5$  Volts per meter

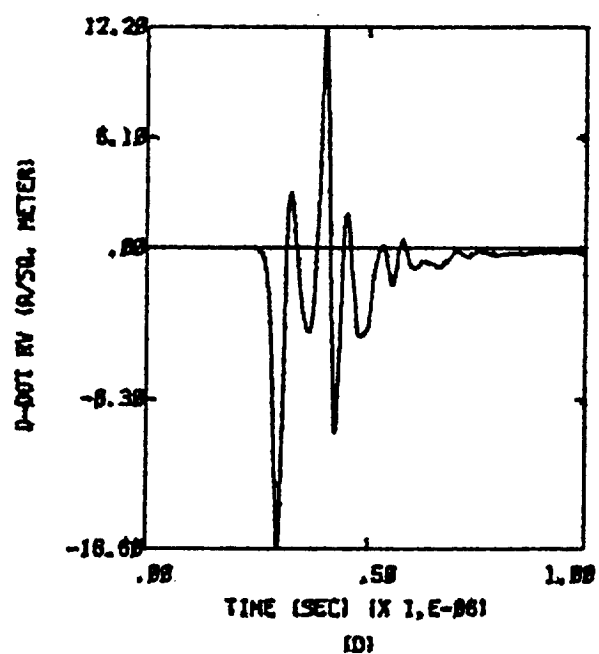
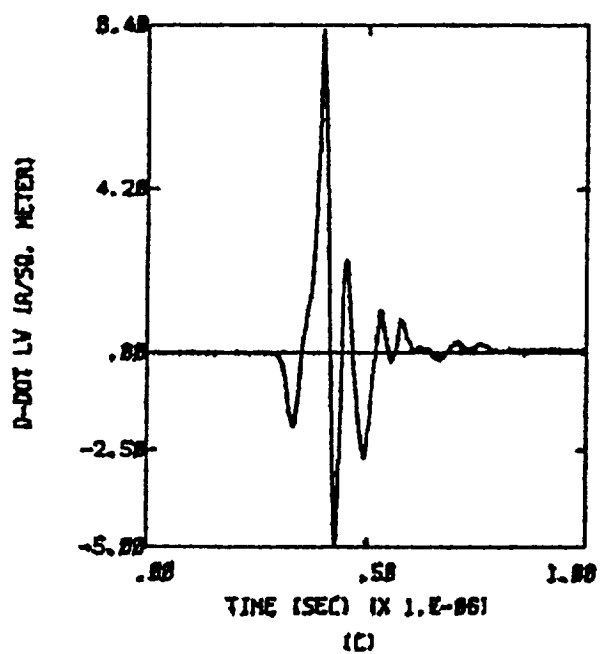
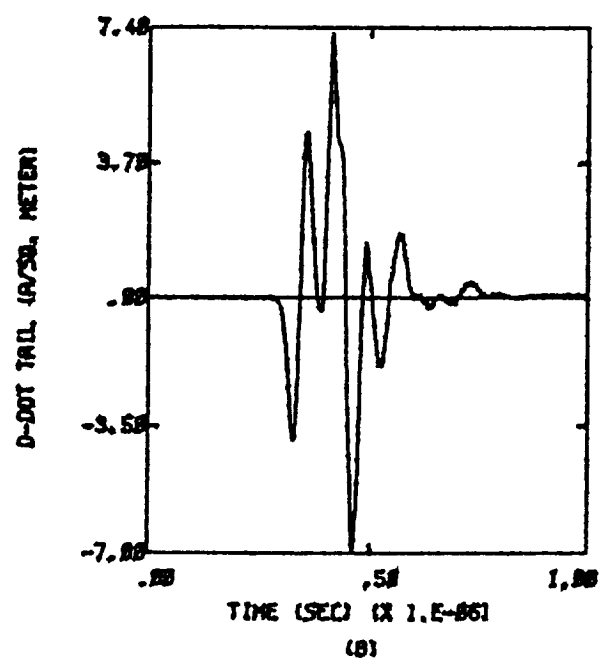
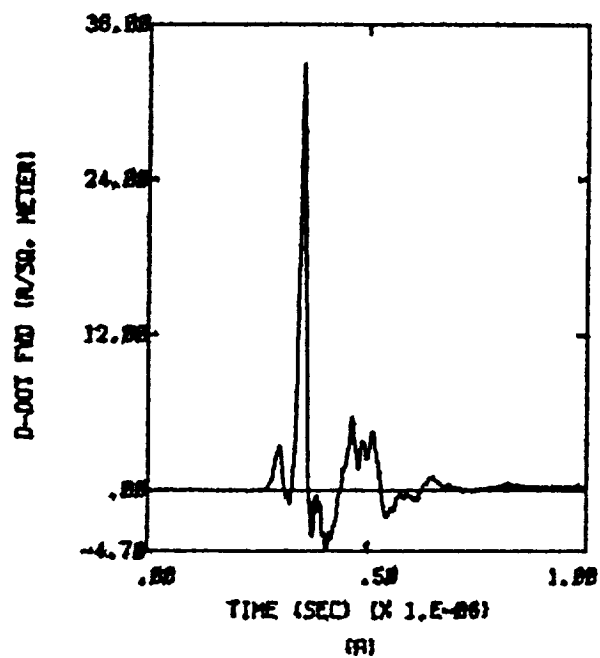


Figure D.2a X,-Y; Q = 0; E =  $2.5 \times 10^5$  Volts per meter

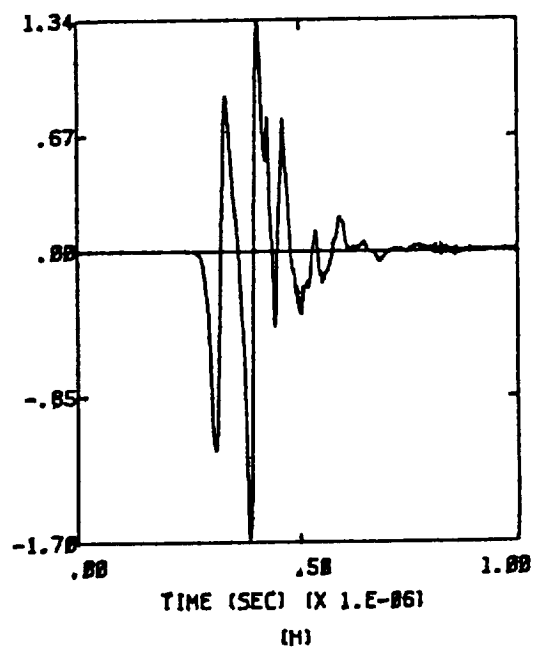
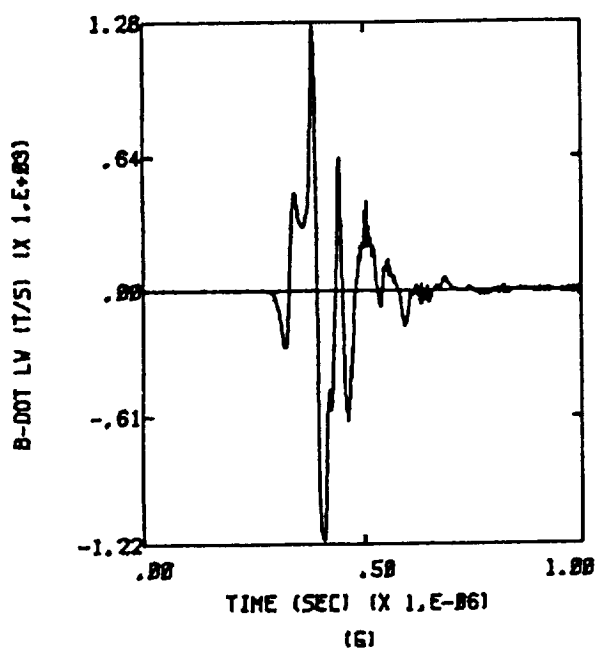
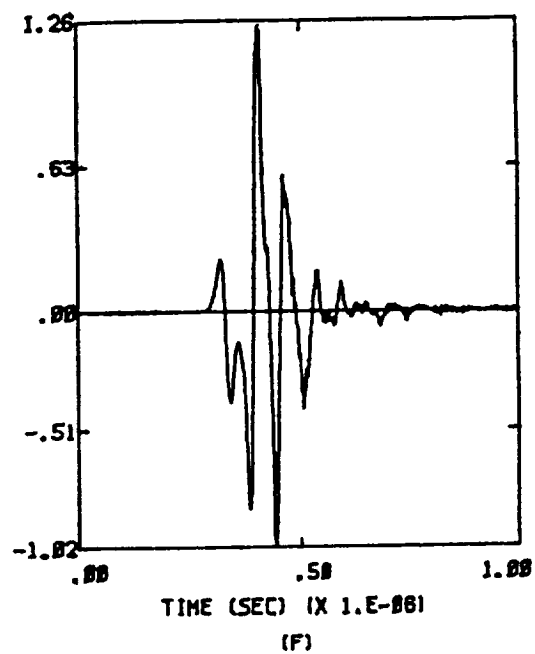
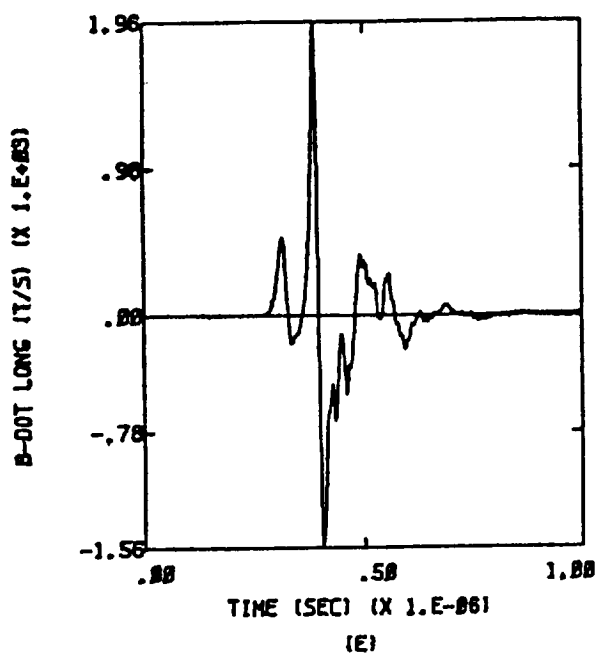


Figure D.2b X,-Y; Q = 0; E =  $2.5 \times 10^5$  Volts per meter

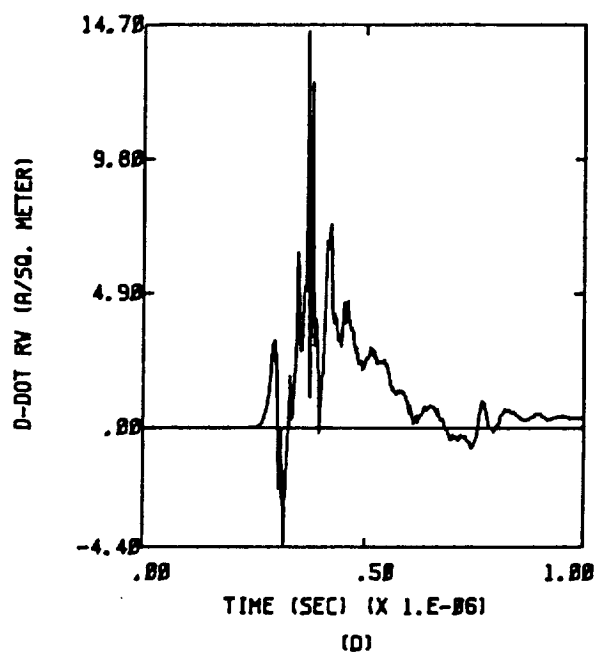
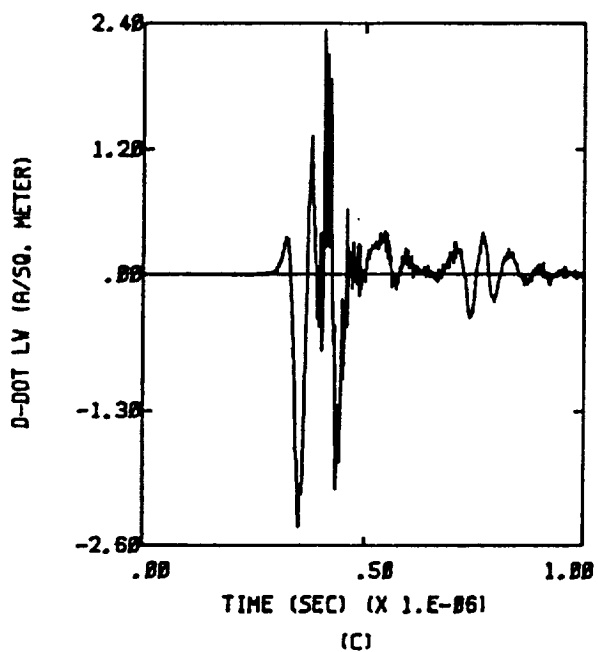
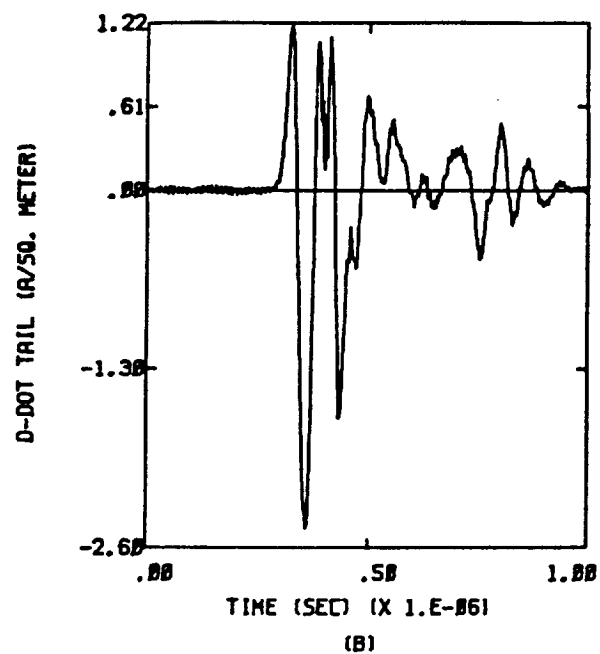
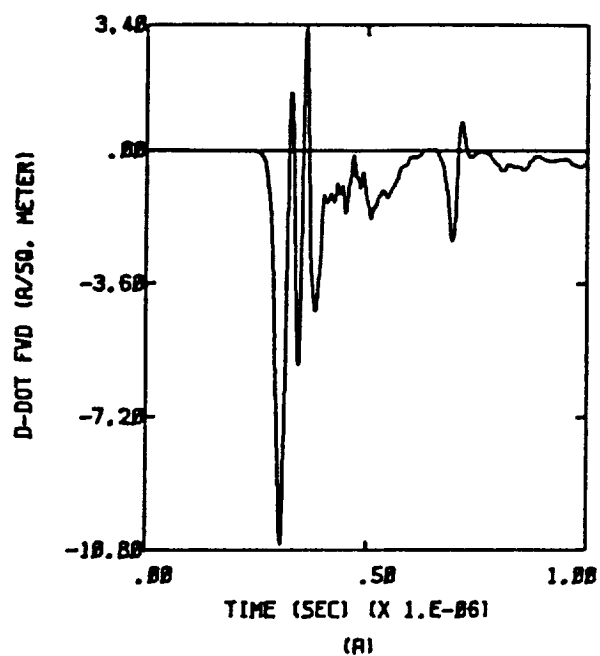


Figure D.3a  $-X, Y; Q = 0; E = 2.5 \times 10^5$  Volts per meter



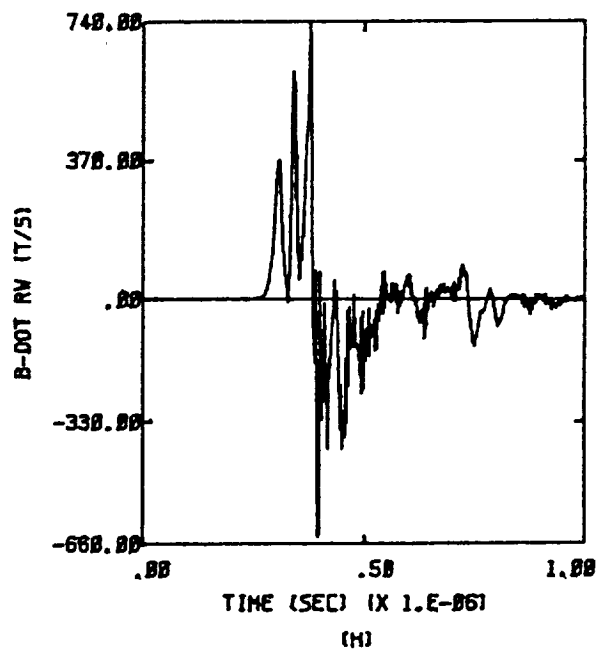
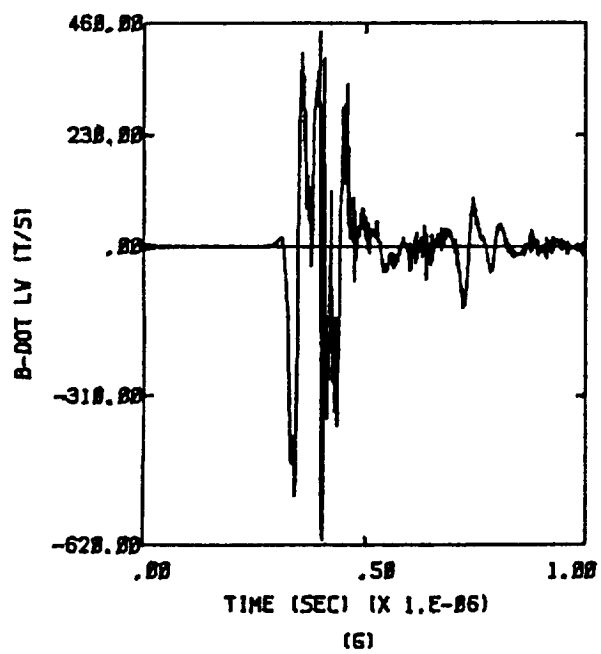
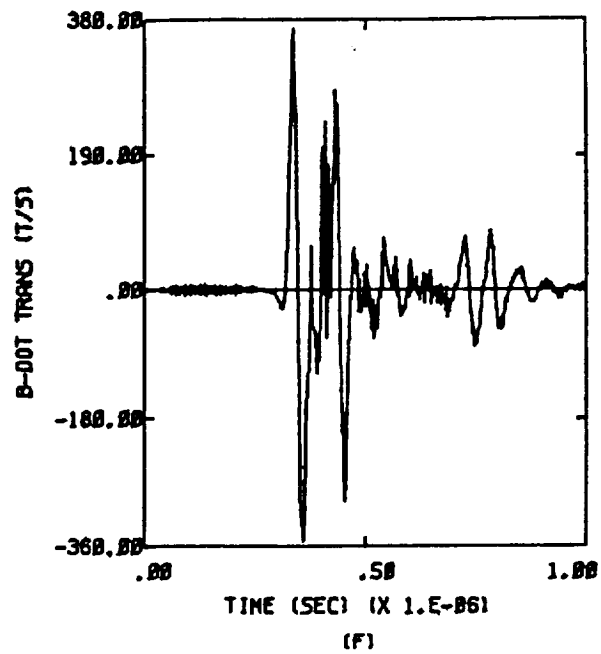
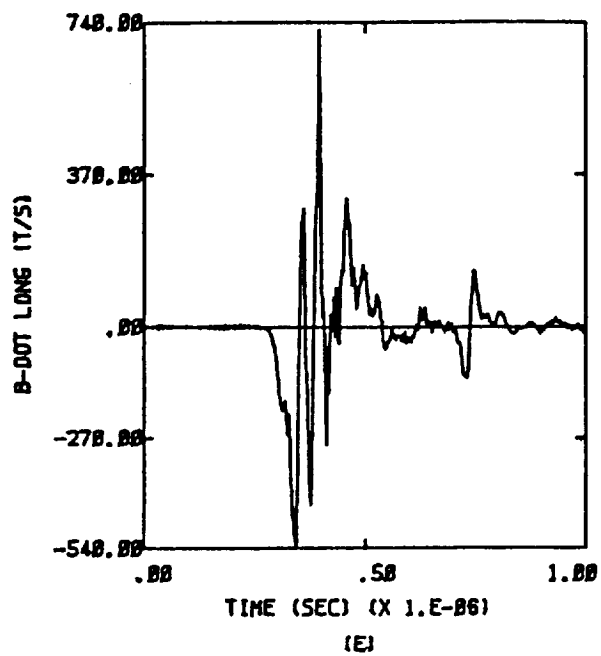


Figure D.3b -X,Y;  $Q = 0$ ;  $E = 2.5 \times 10^5$  Volts per meter

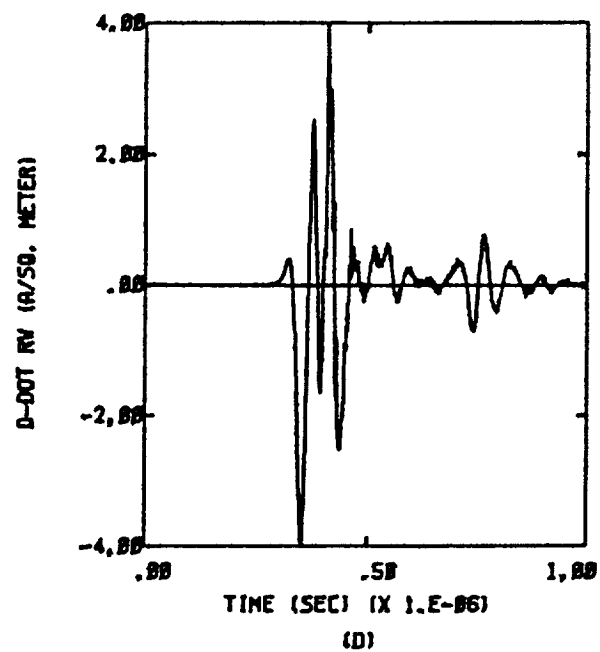
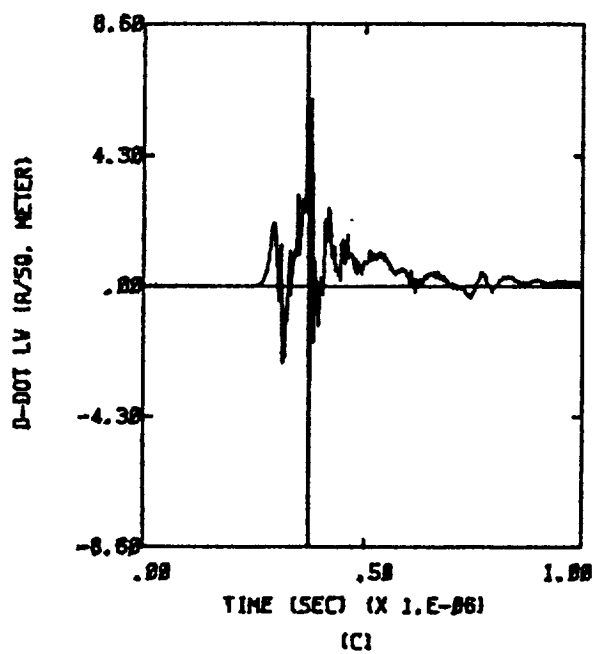
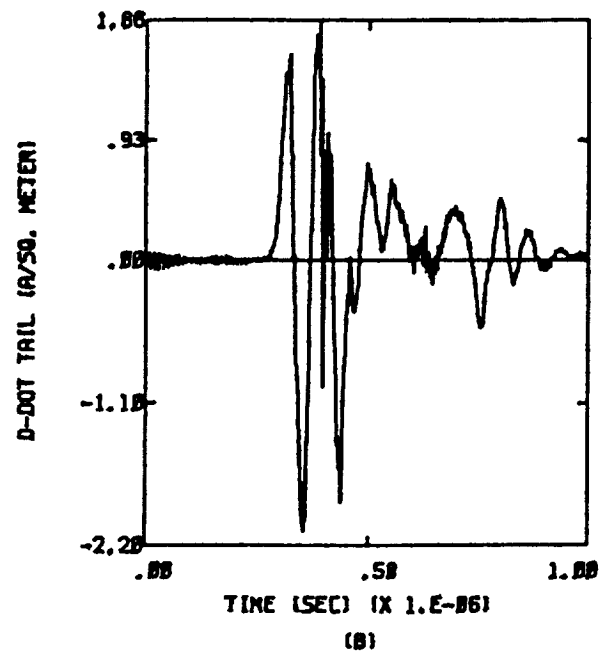
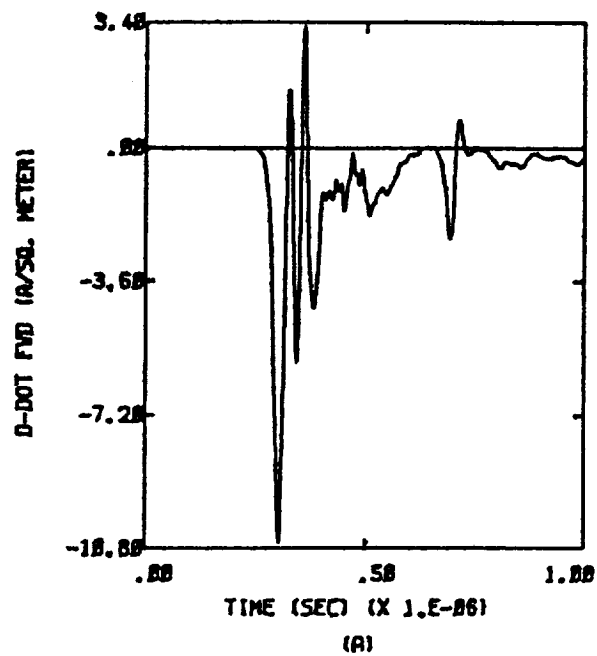


Figure D.4a -X,-Y;  $Q = 0$ ;  $E = 2.5 \times 10^5$  Volts per meter

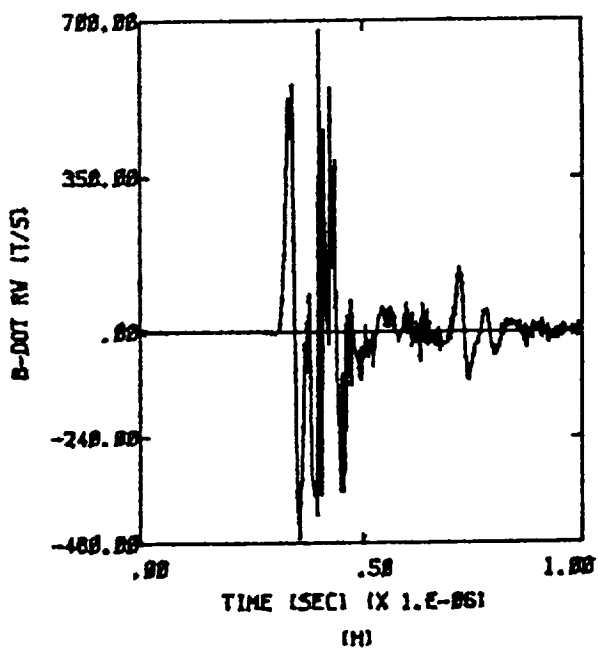
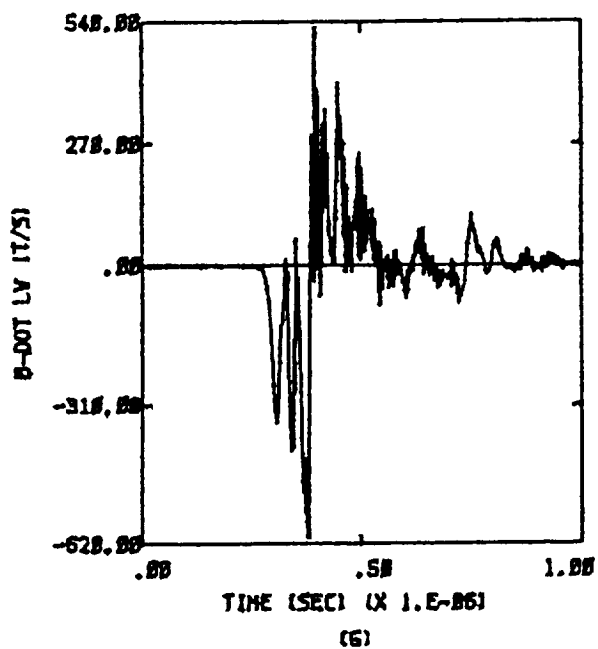
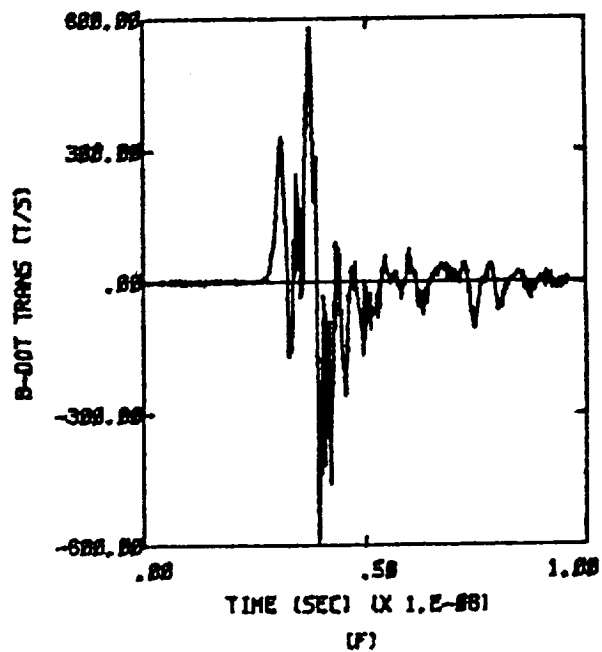
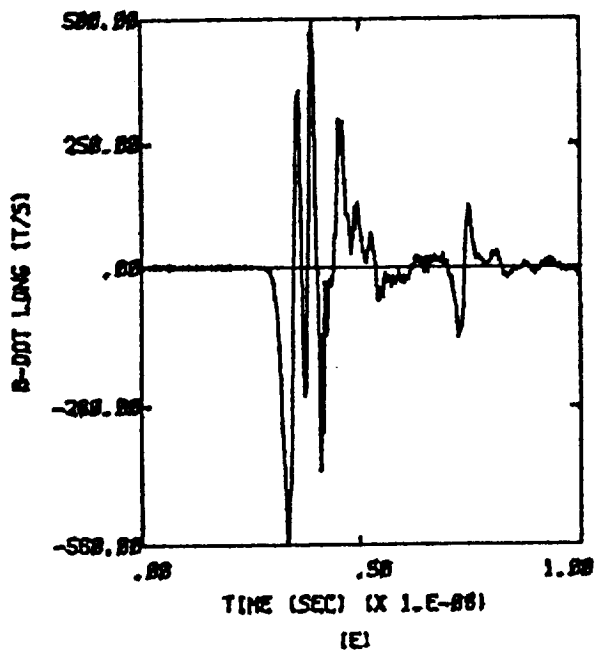


Figure D.4b -X,-Y;  $Q = 0$ ;  $E = 2.5 \times 10^5$  Volts per meter

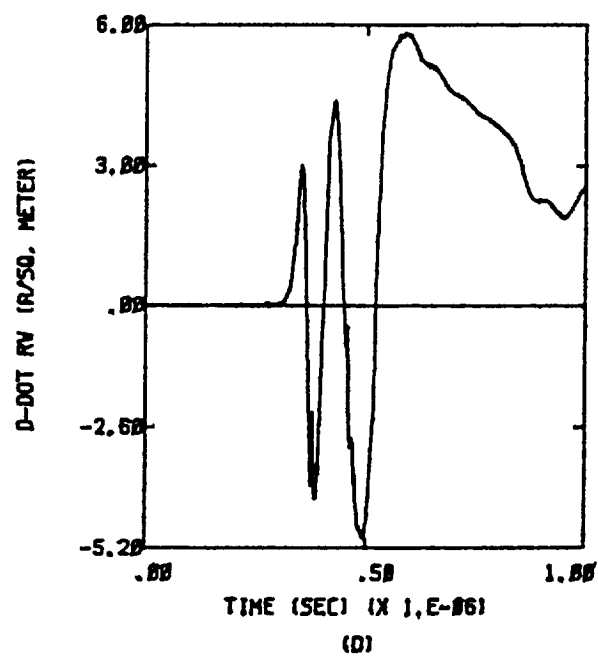
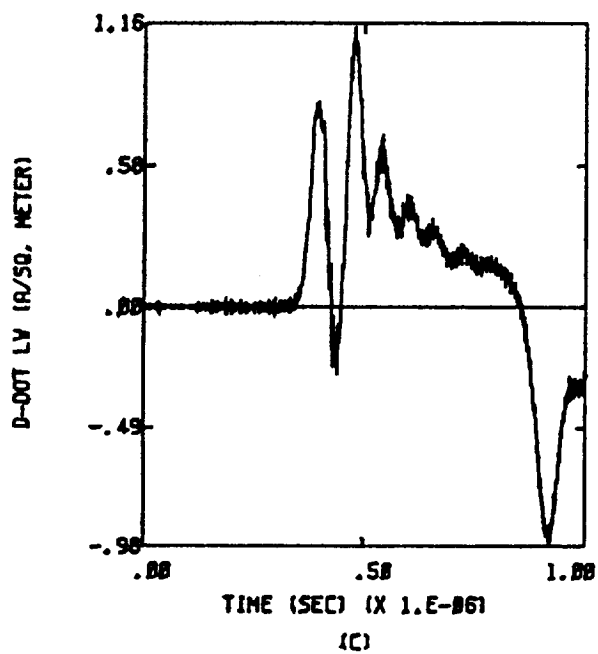
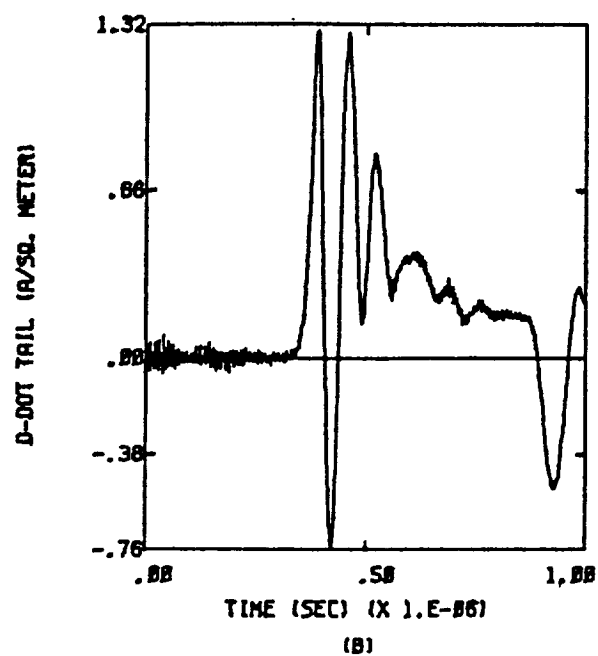
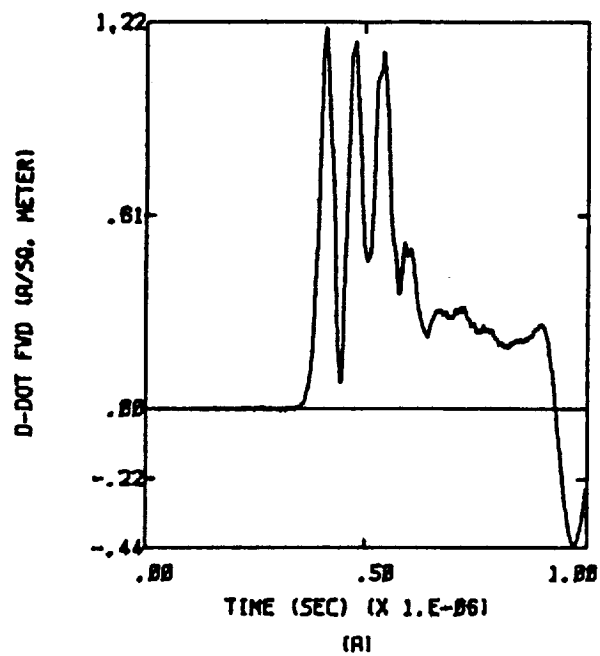


Figure D.5a Y,-Z;  $Q = 0$ ;  $E = 3.7 \times 10^5$  Volts per meter

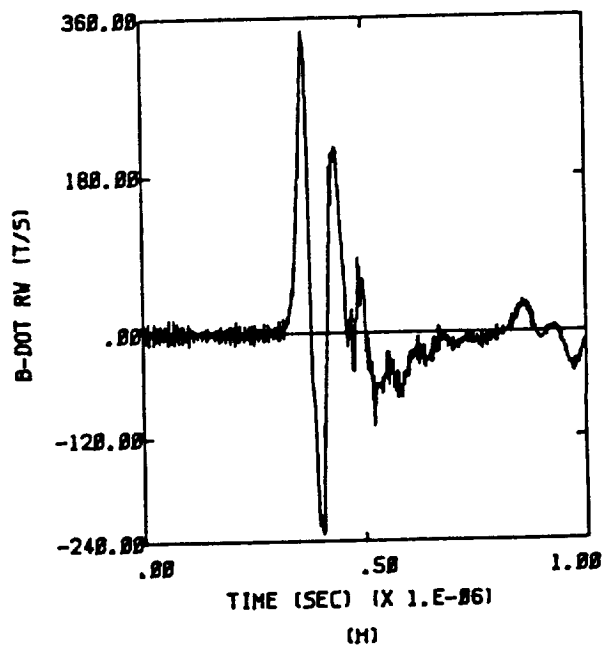
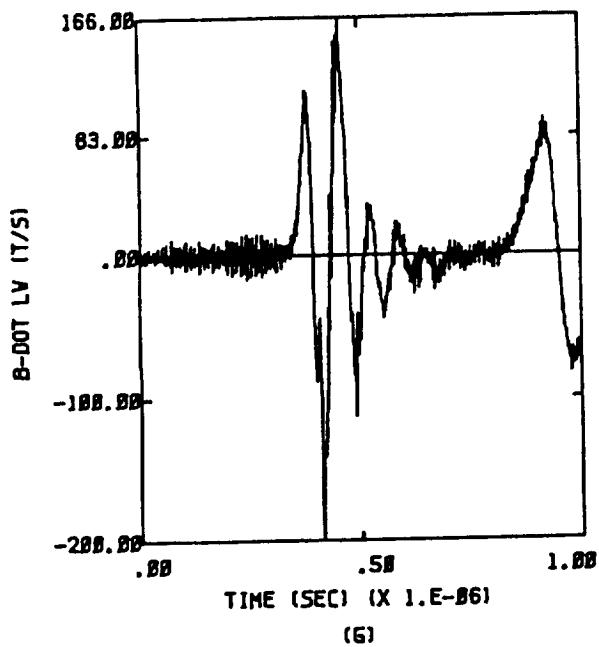
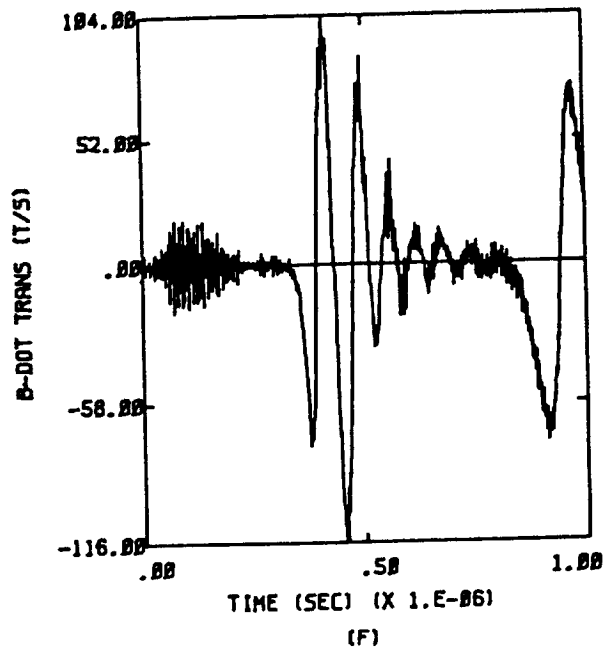
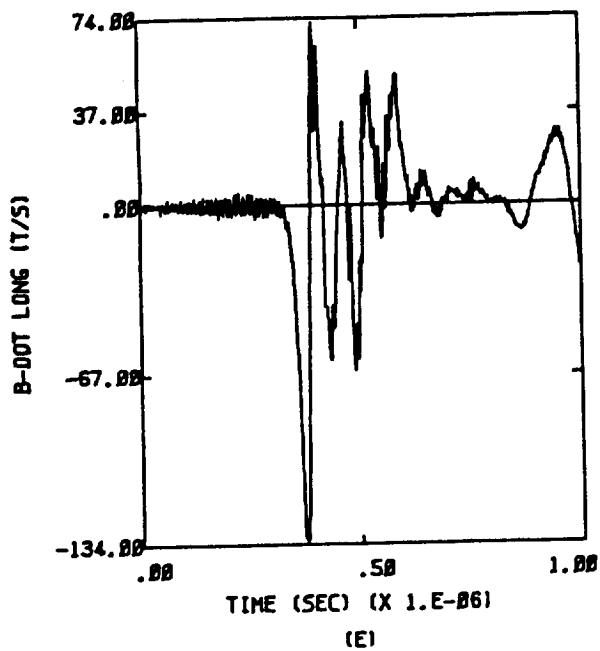


Figure D.5b Y,-Z; Q = 0; E =  $3.7 \times 10^5$  Volts per meter

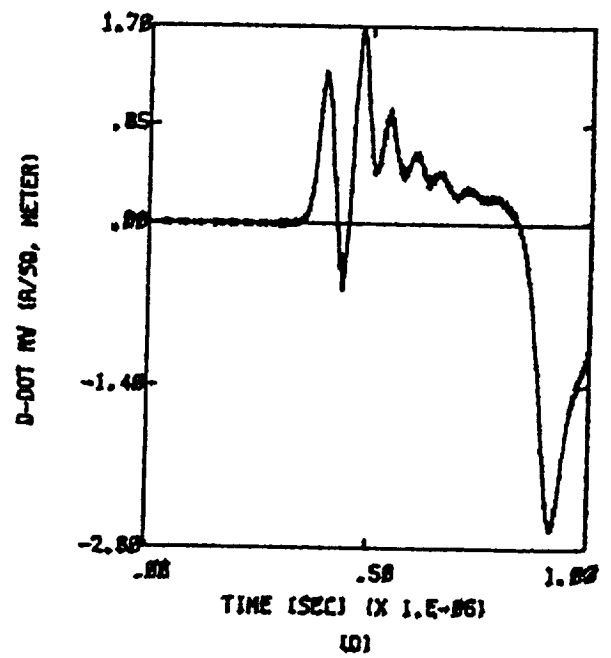
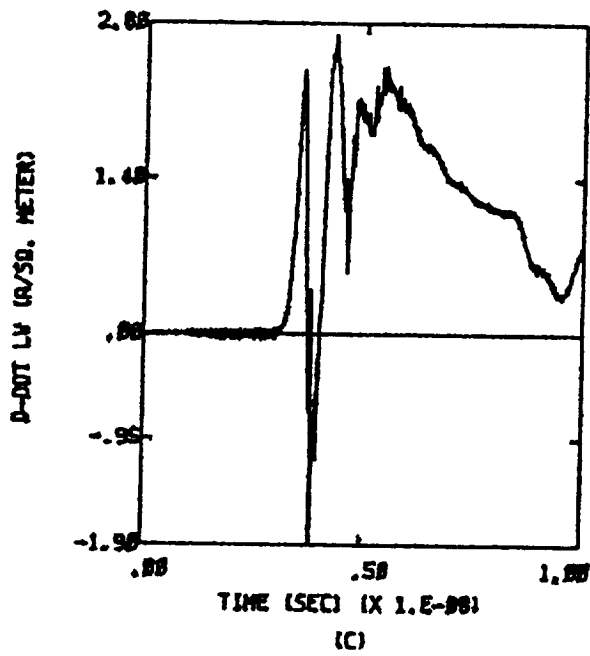
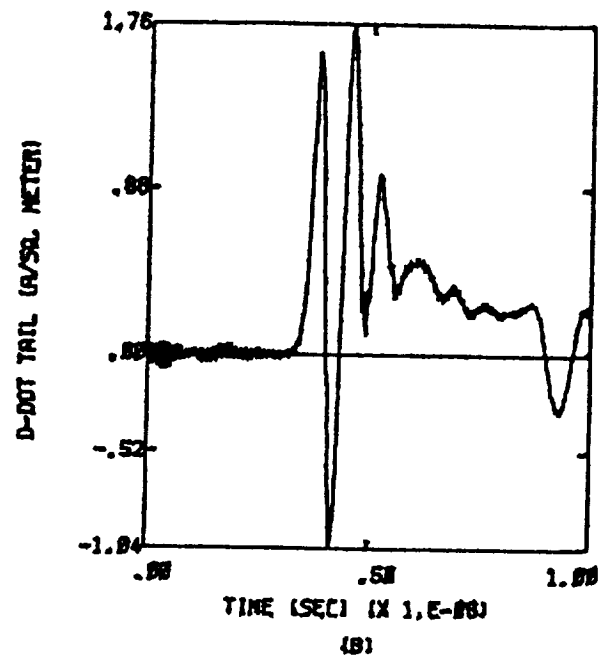
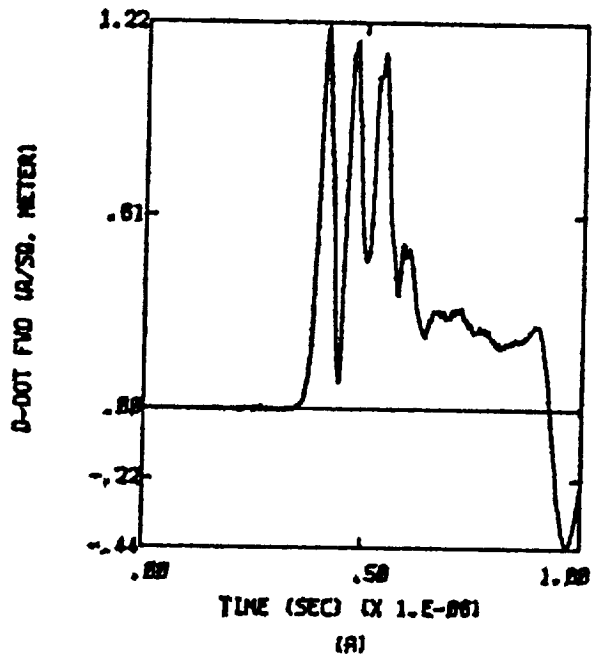


Figure D.6a  $-Y, -Z; Q = 0; E = 3.7 \times 10^5$  Volts per meter

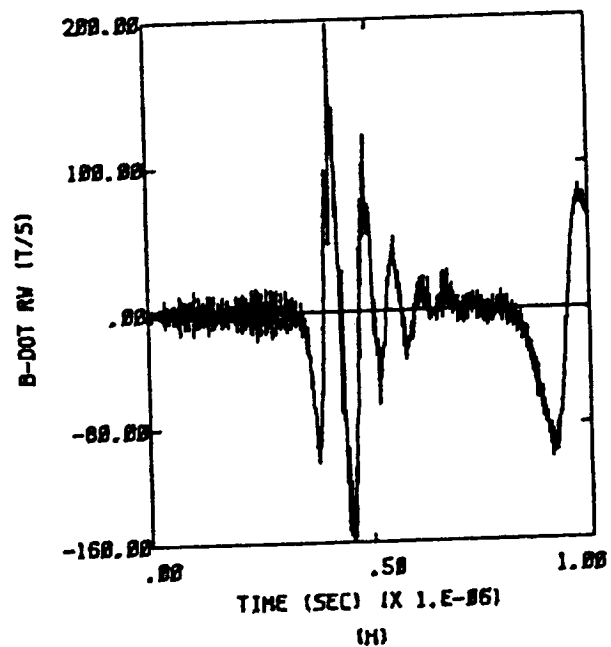
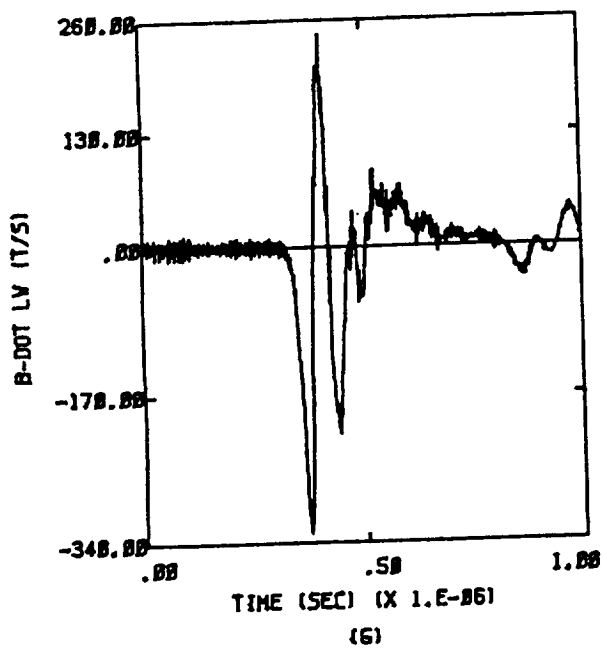
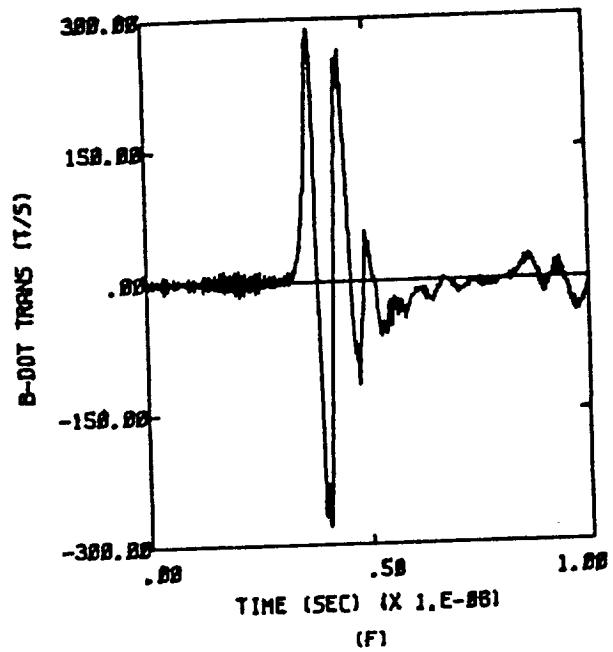
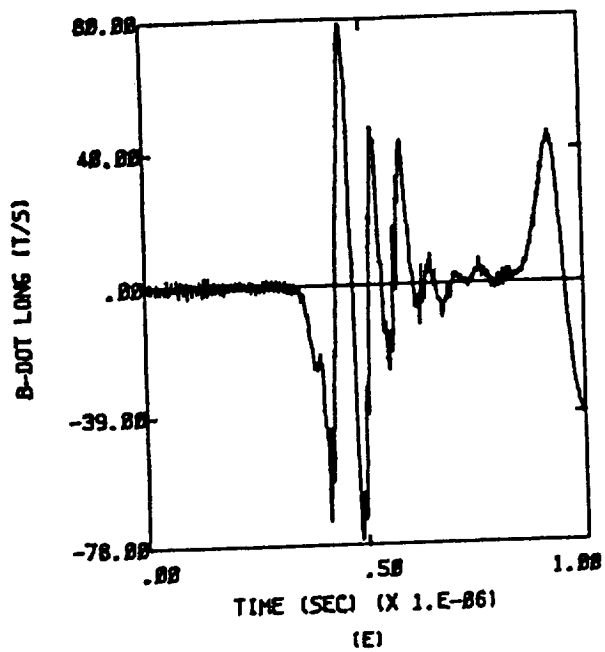


Figure D.6b  $-Y, -Z; Q = 0; E = 3.7 \times 10^5$  Volts per meter

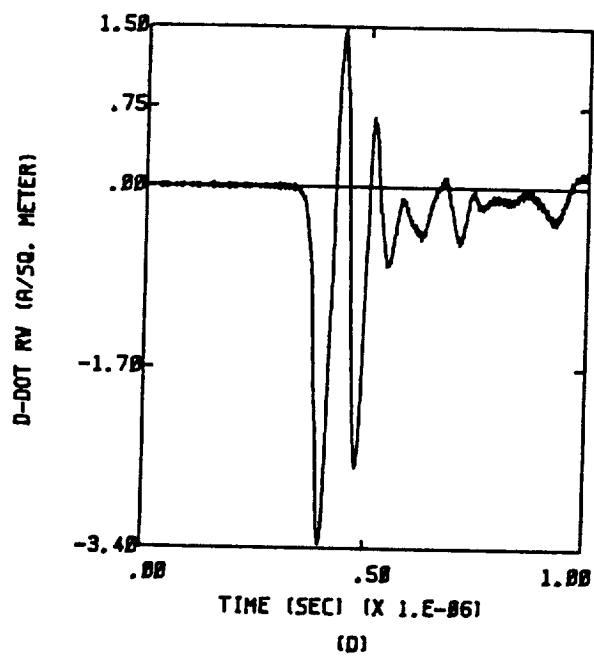
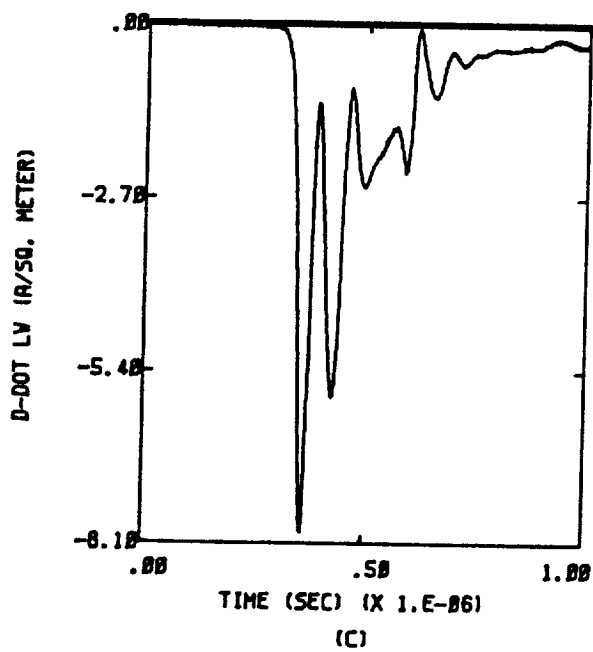
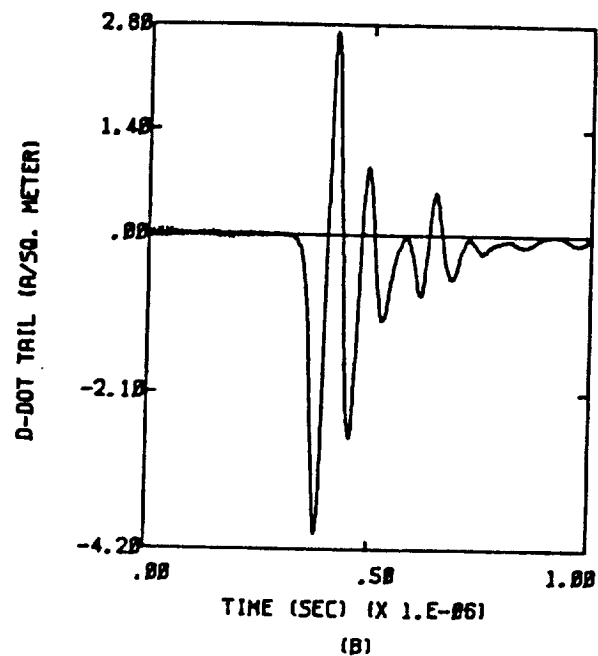
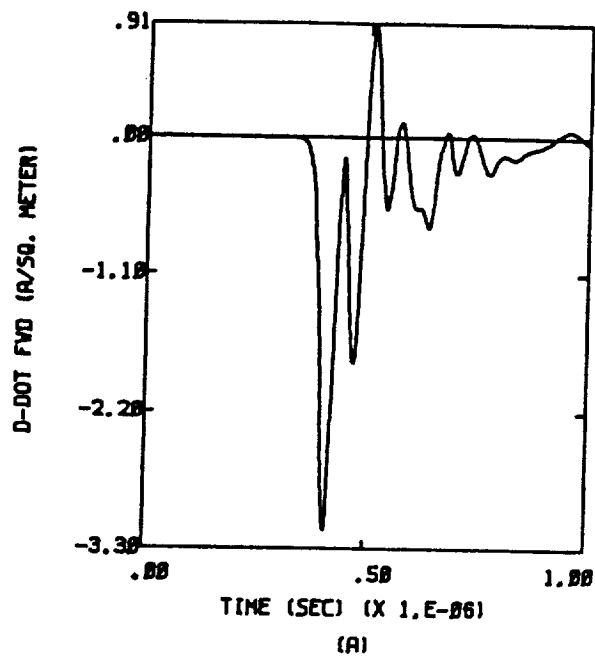


Figure D.7a Y,Z;  $Q = 0$ ;  $E = 3.7 \times 10^5$  Volts per meter



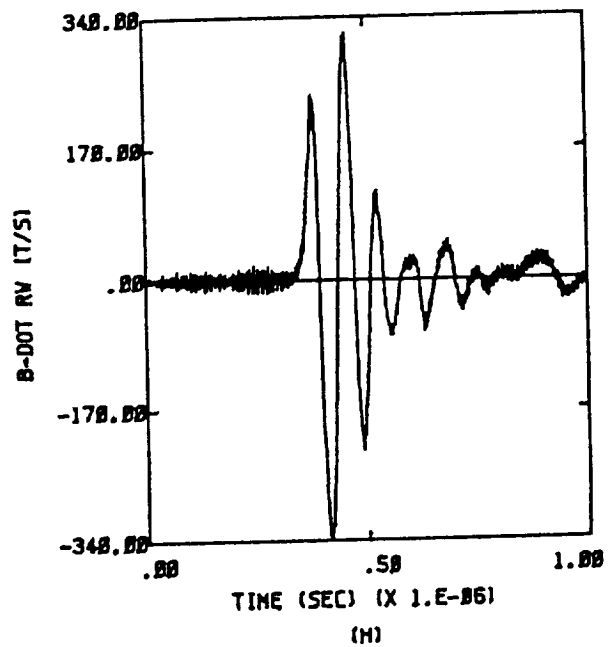
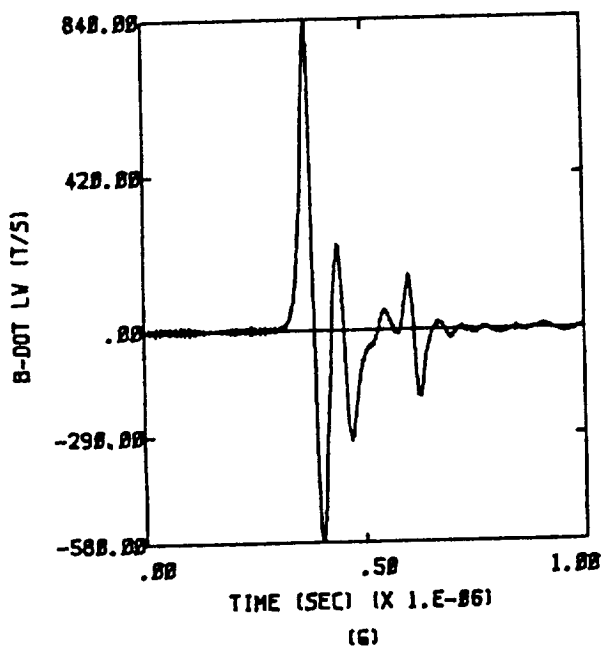
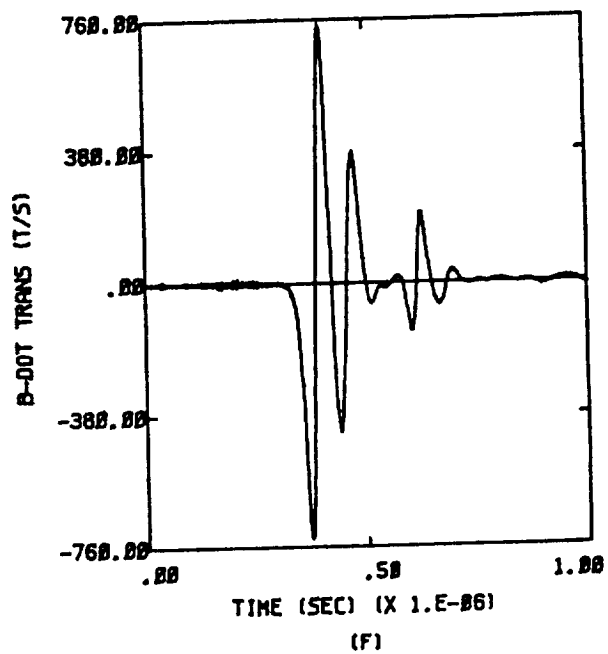
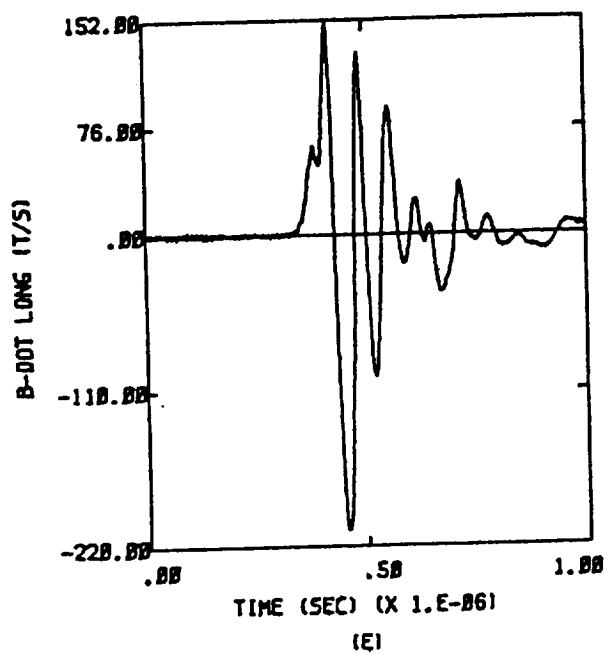


Figure D.7b Y,Z;  $Q = 0$ ;  $E = 3.7 \times 10^5$  Volts per meter

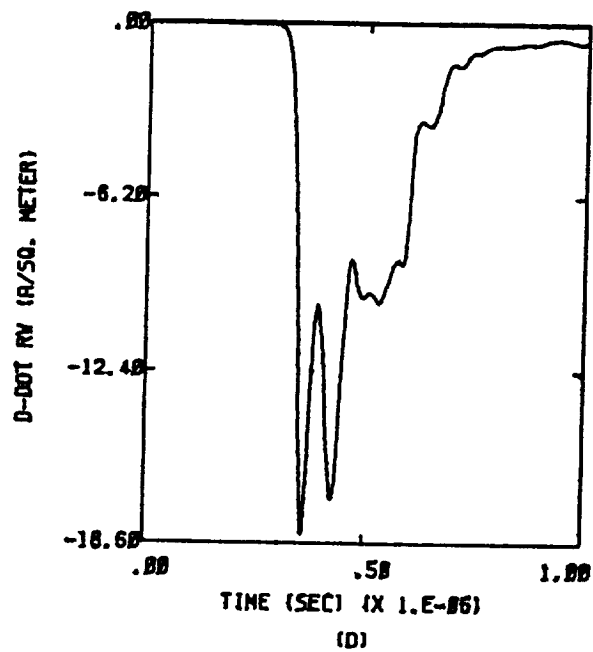
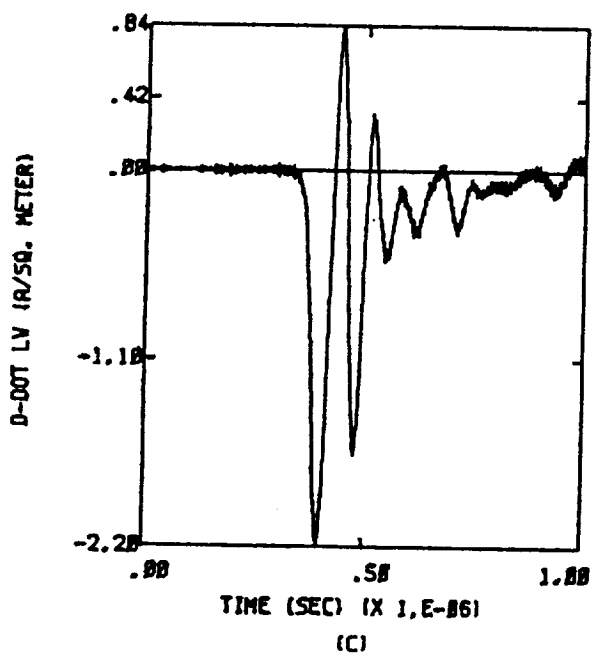
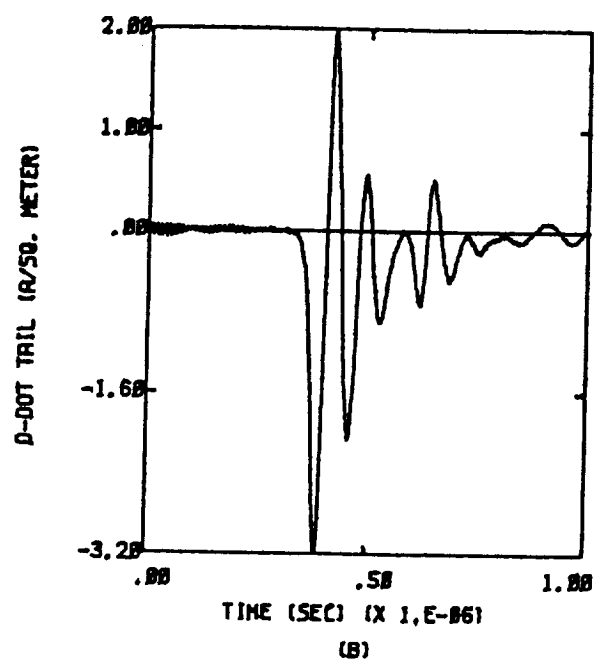
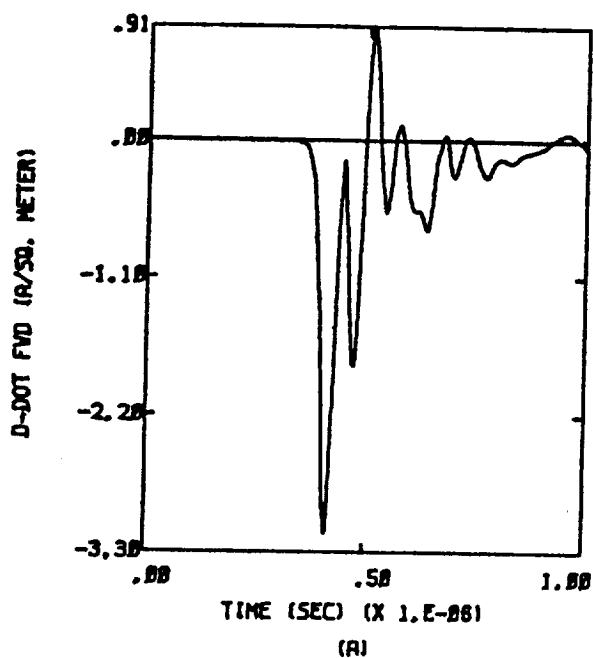


Figure D.8a -Y,Z;  $Q = 0$ ;  $E = 3.7 \times 10^5$  Volts per meter

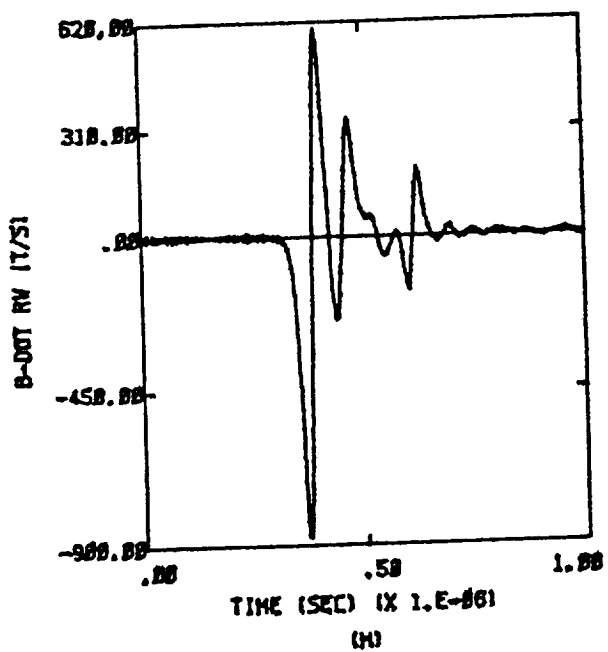
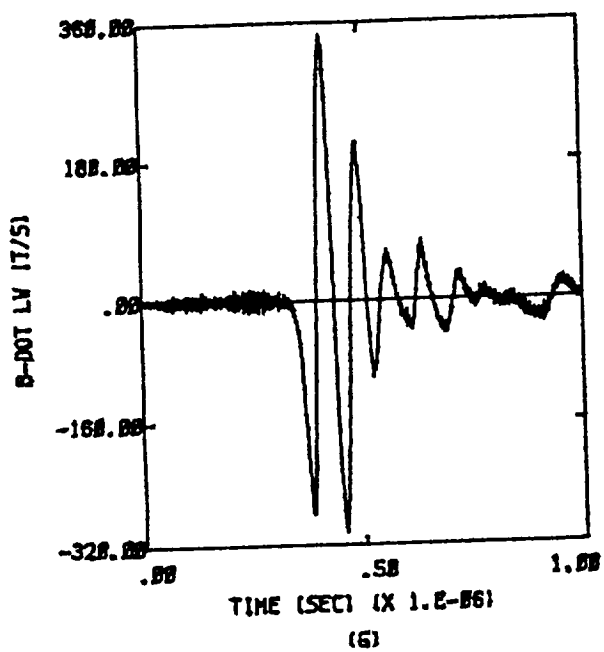
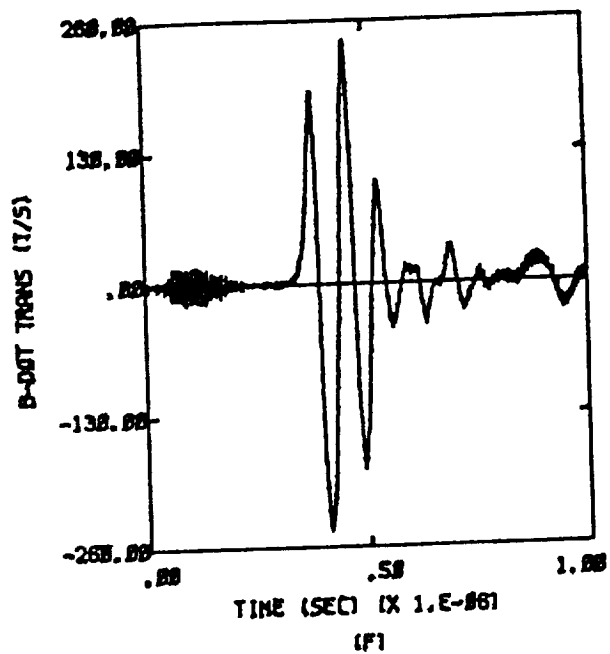
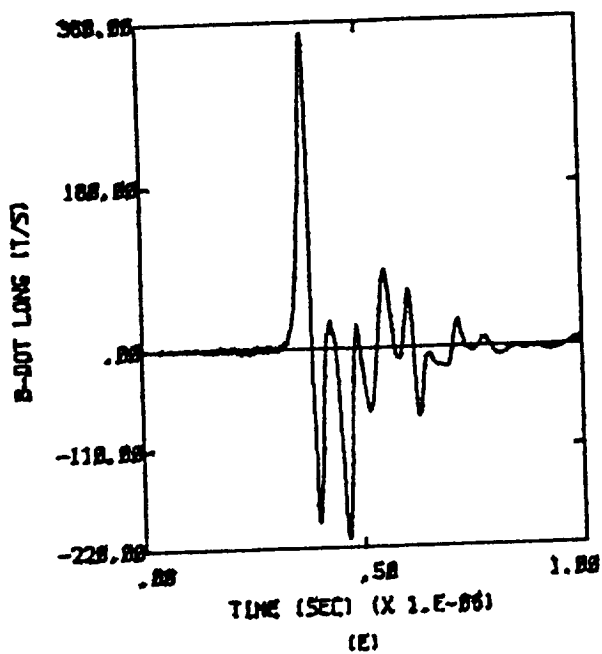


Figure D.8b -Y,Z;  $Q = 0$ ;  $E' = 3.7 \times 10^5$  Volts per meter

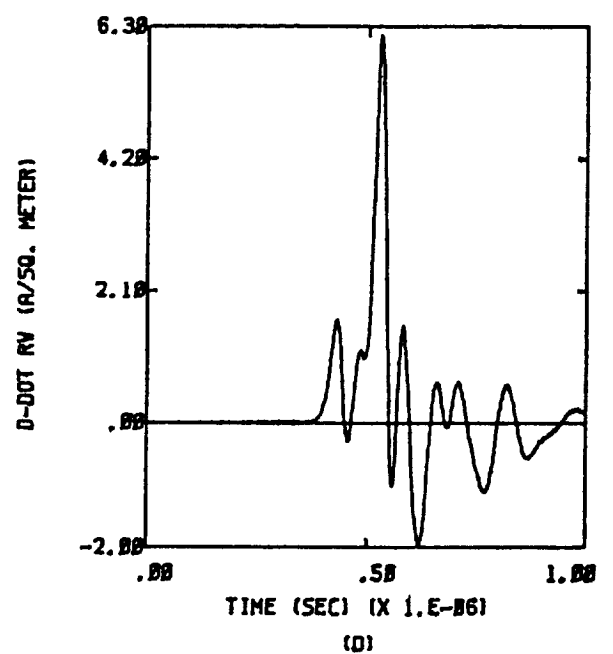
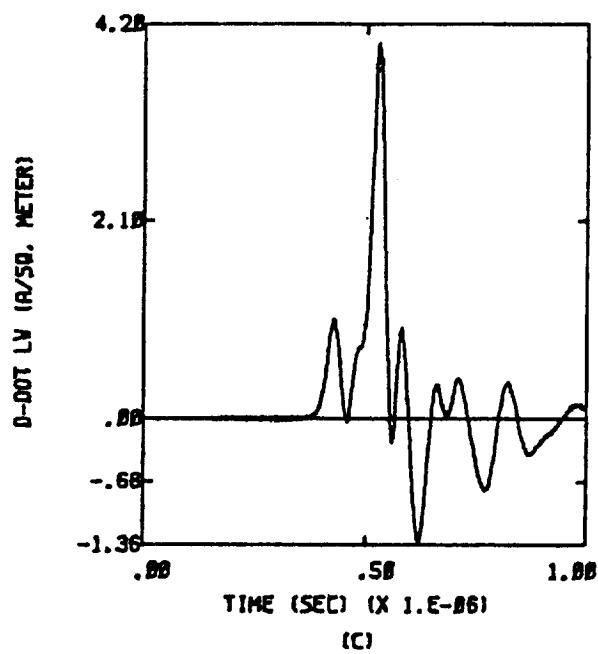
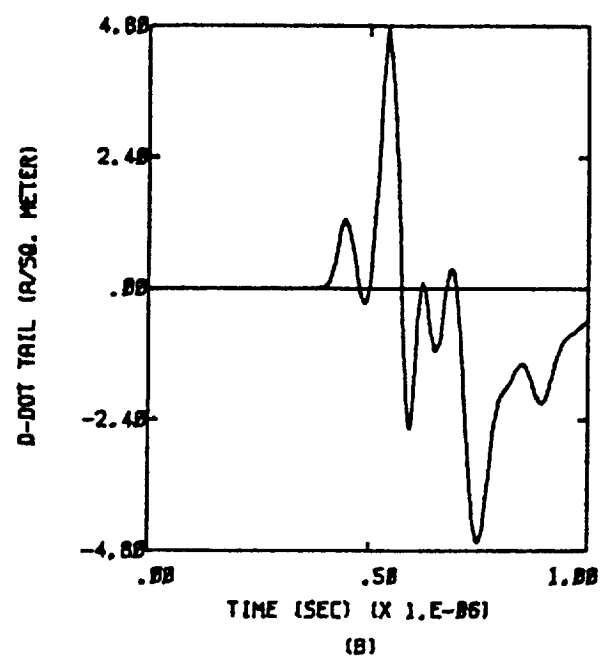
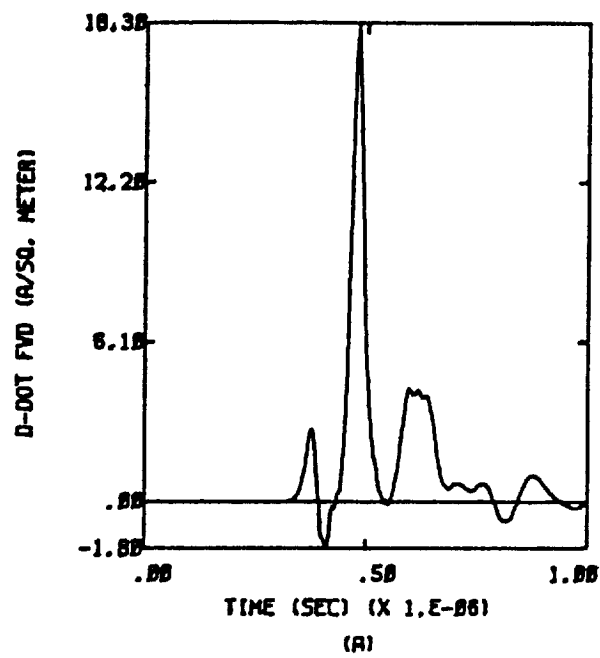


Figure D.9a  $X, -Z$ ;  $Q = 0$ ;  $E = 2.2 \times 10^5$  Volts per meter

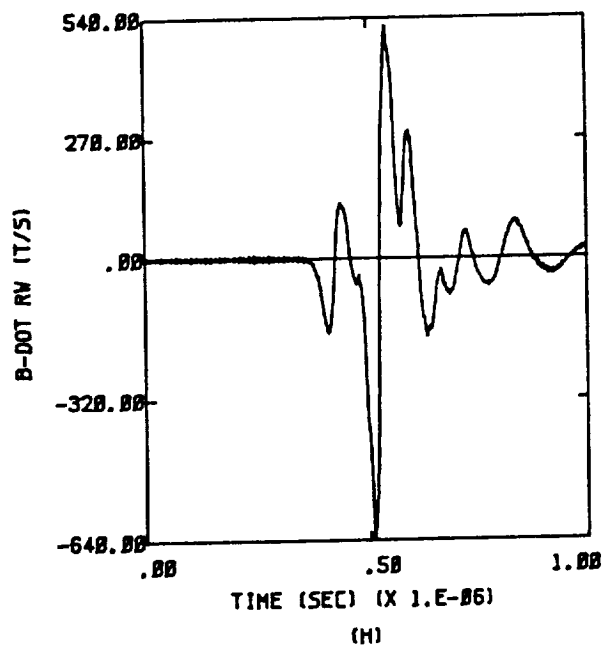
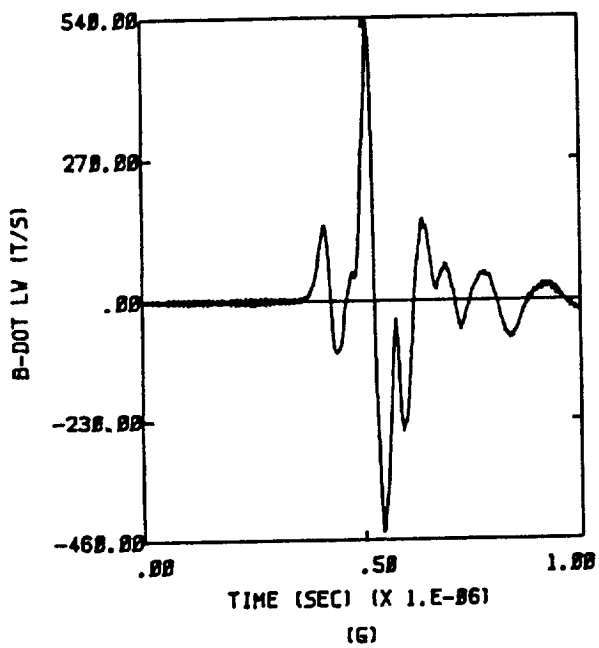
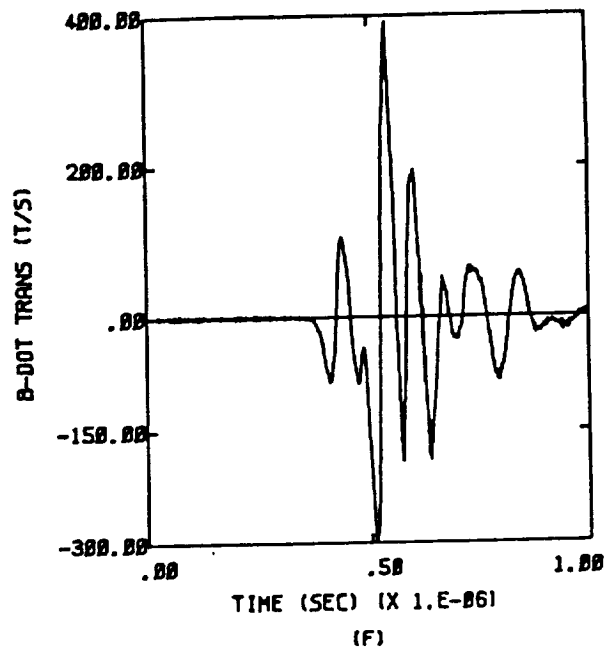
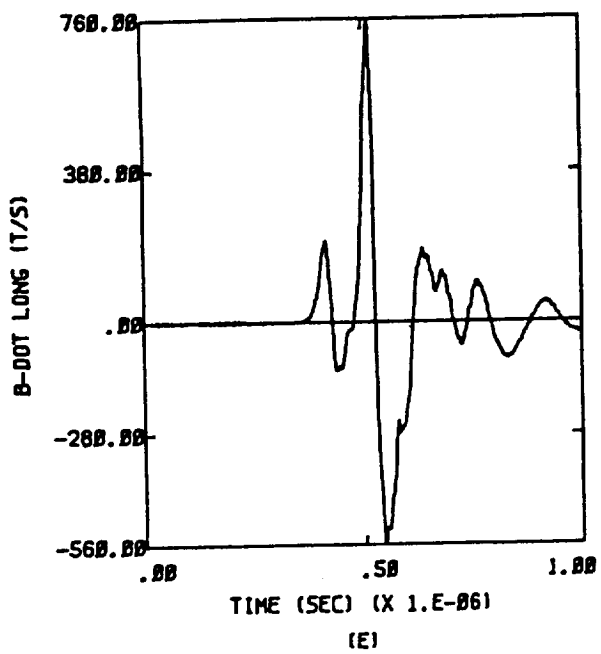


Figure D.9b  $X, -Z$ ;  $Q = 0$ ;  $E = 2.2 \times 10^5$  Volts per meter

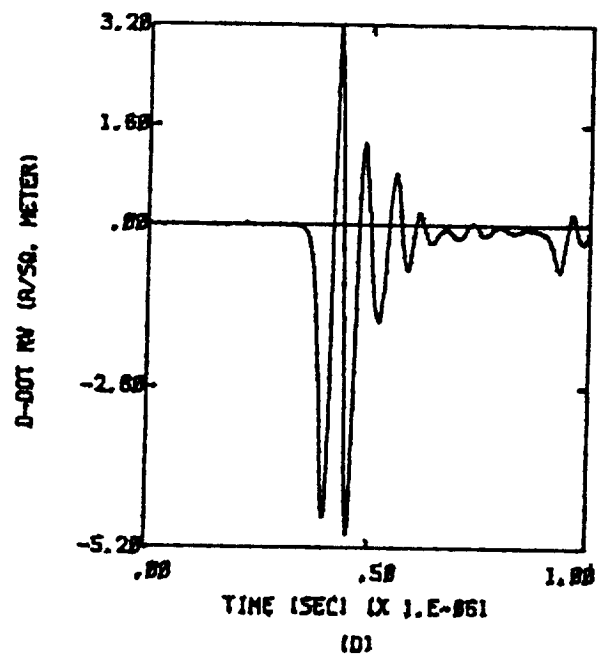
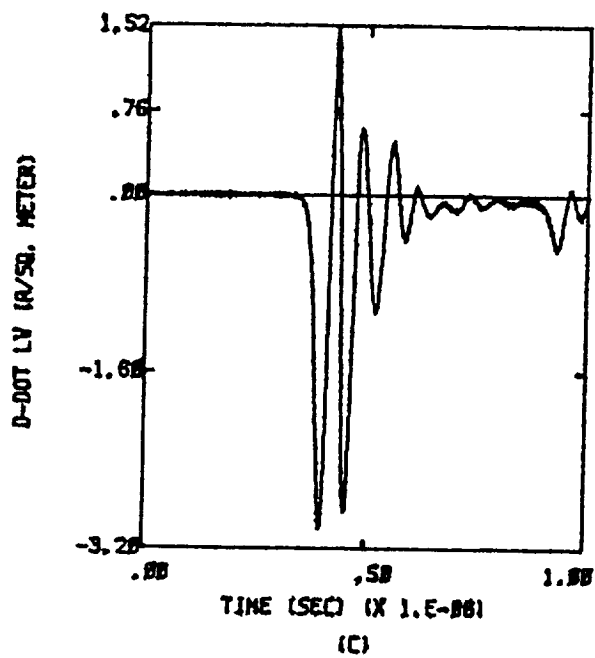
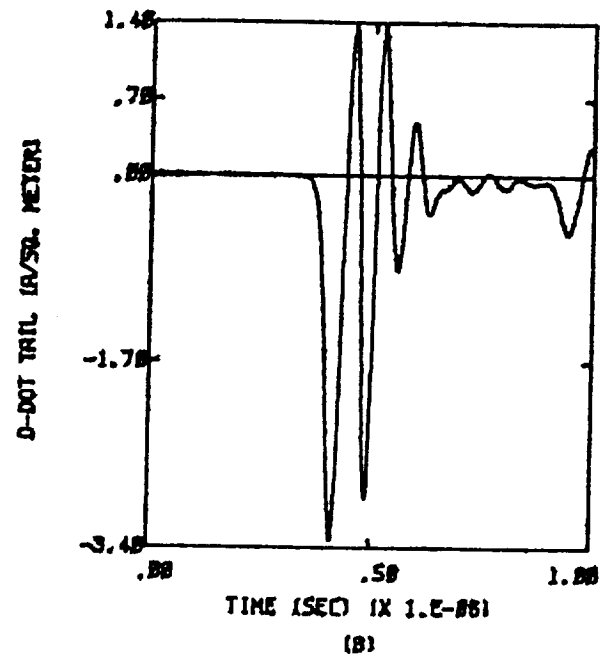
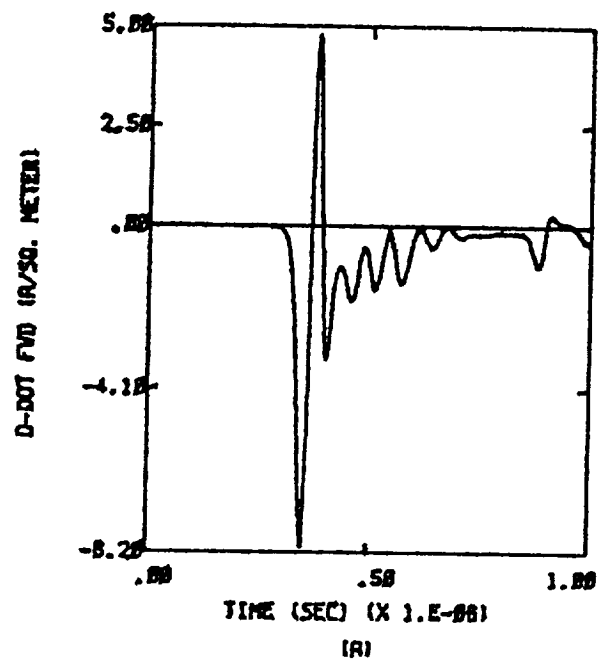


Figure D.10a  $-X, -Z; Q = 0; E = 2.7 \times 10^5$  Volts per meter

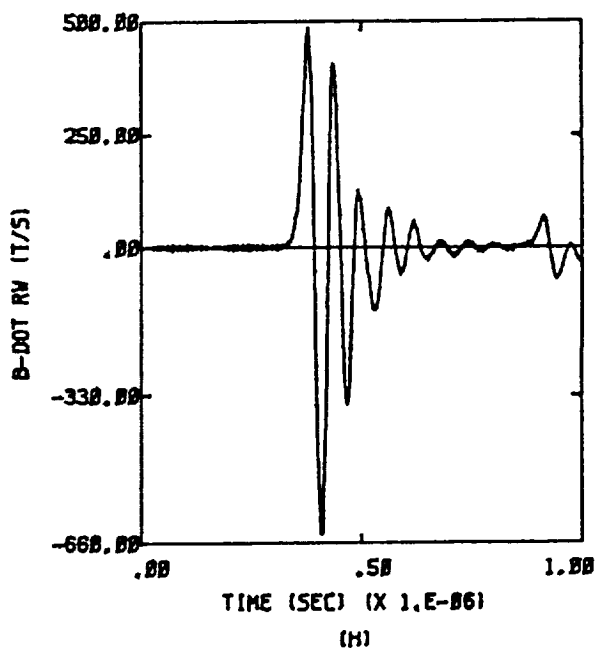
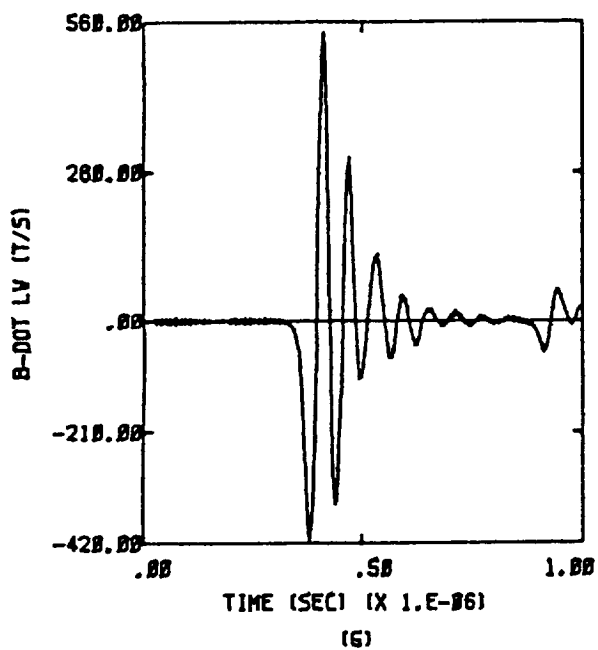
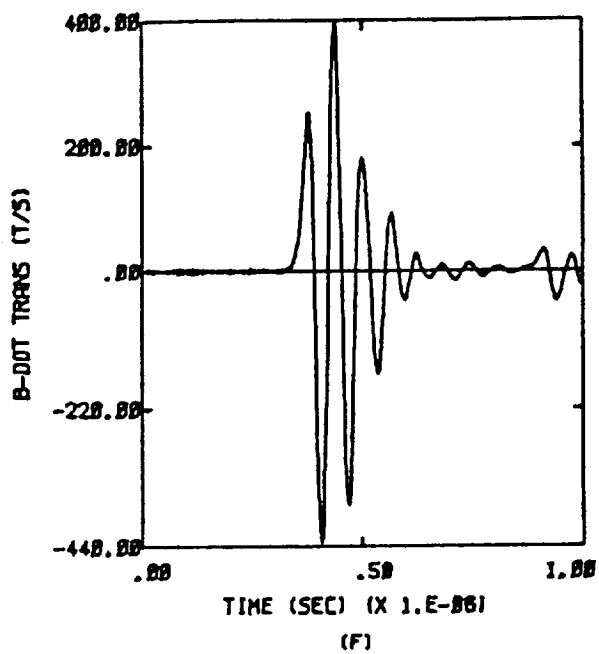
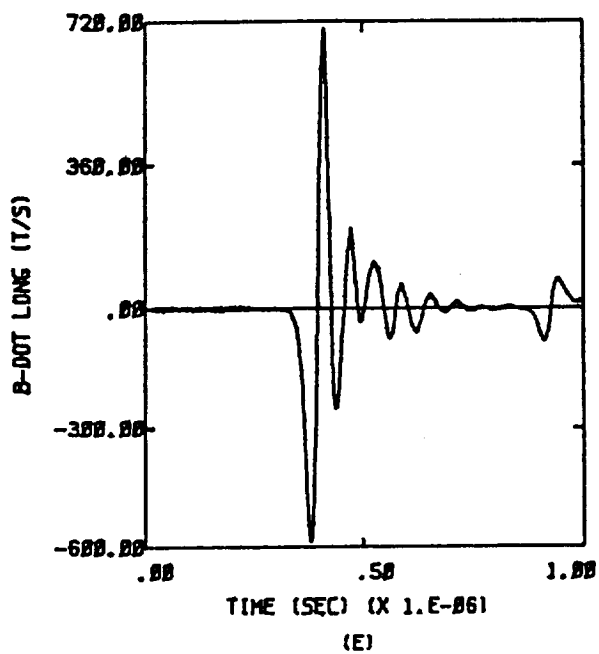


Figure D.10b -X,-Z;  $Q = 0$ ;  $E = 2.7 \times 10^5$  Volts per meter

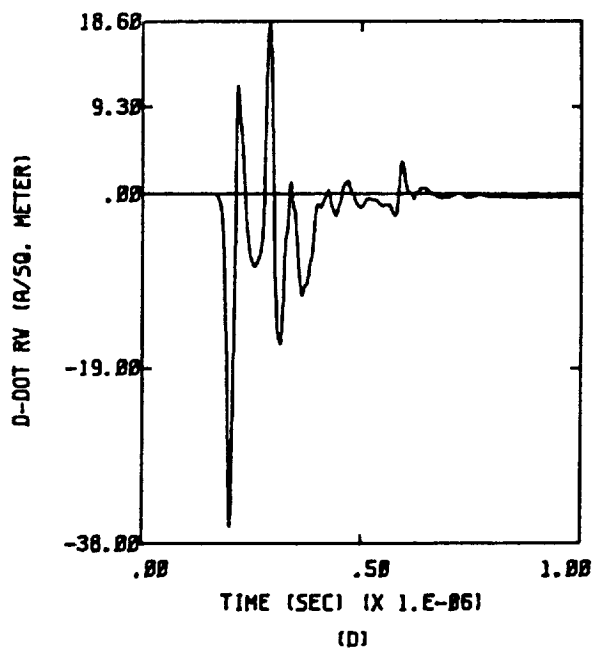
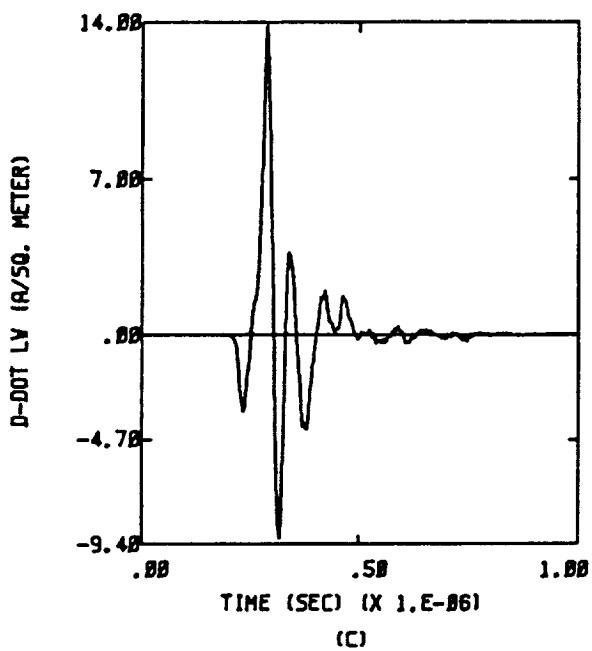
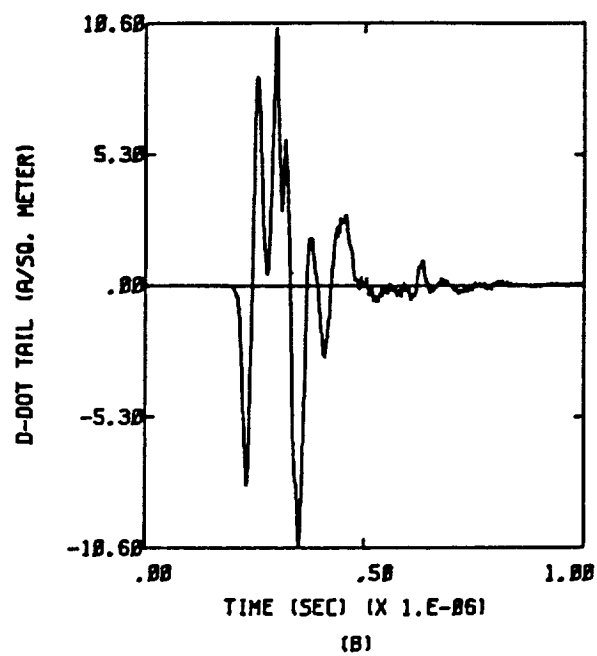
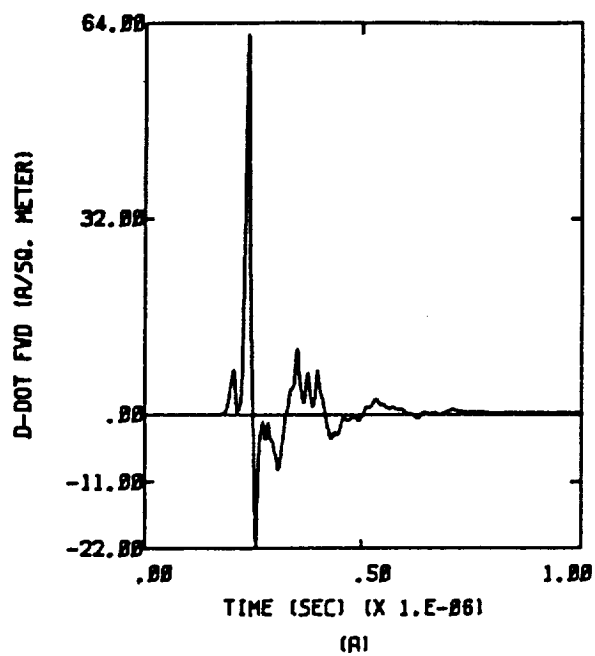


Figure D.11a X,Z;  $Q = 0$ ;  $E = 2.7 \times 10^5$  Volts per meter



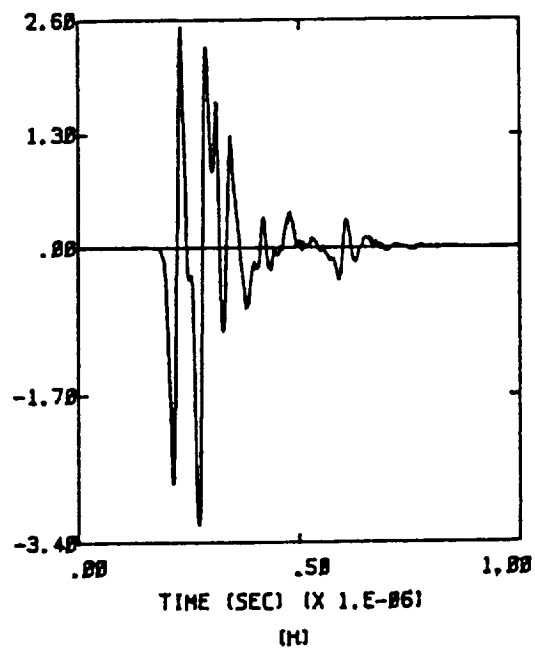
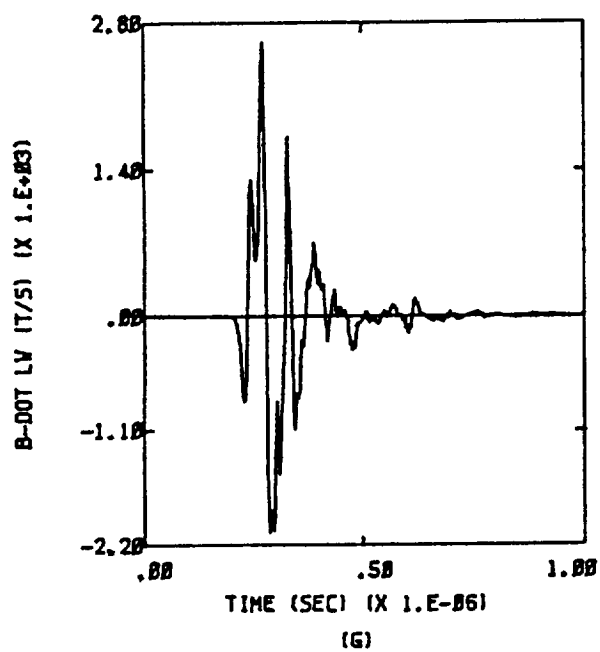
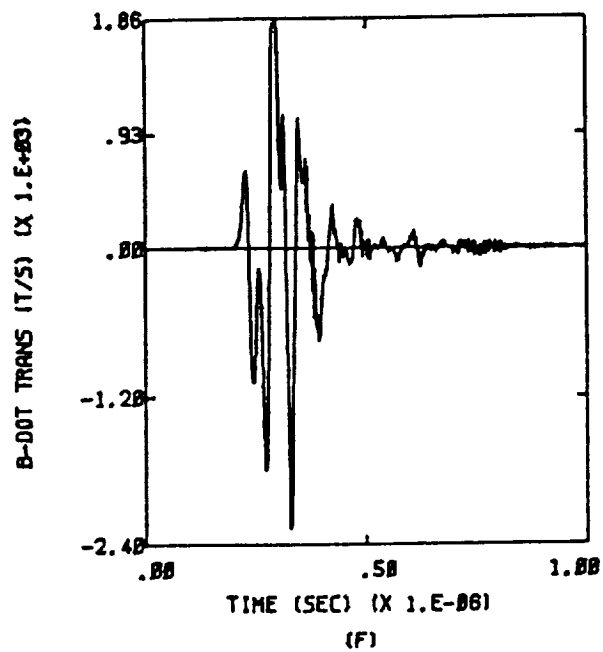
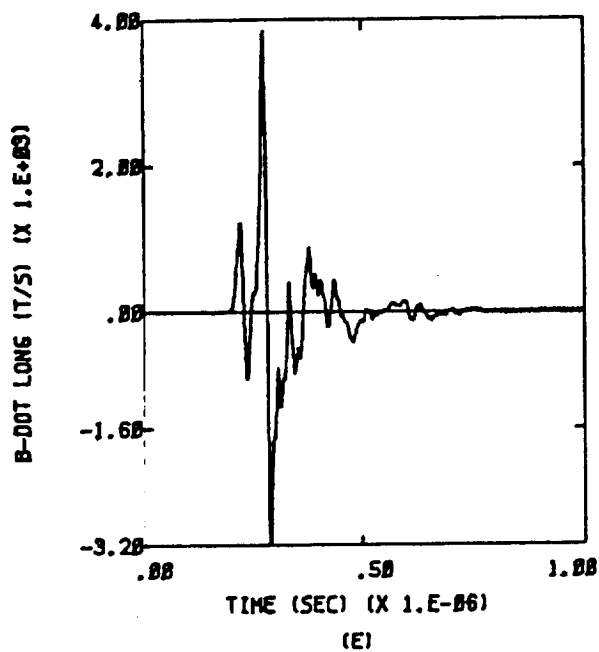


Figure D.11b X,Z;  $Q = 0$ ;  $E = 2.7 \times 10^5$  Volts per meter

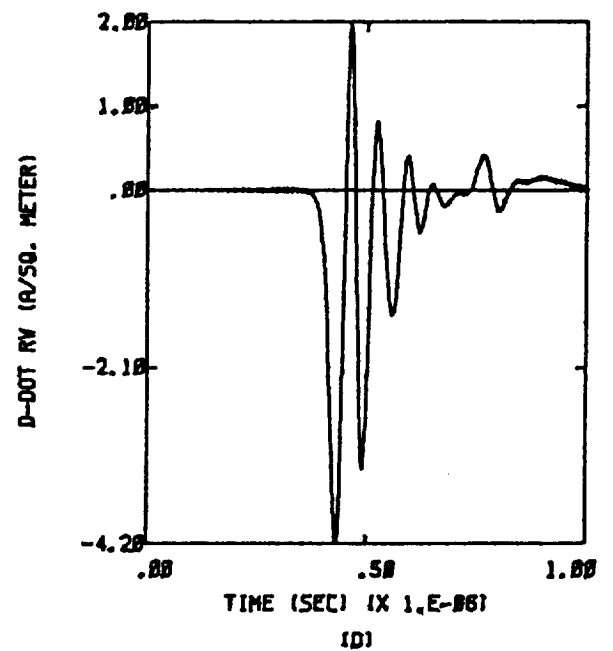
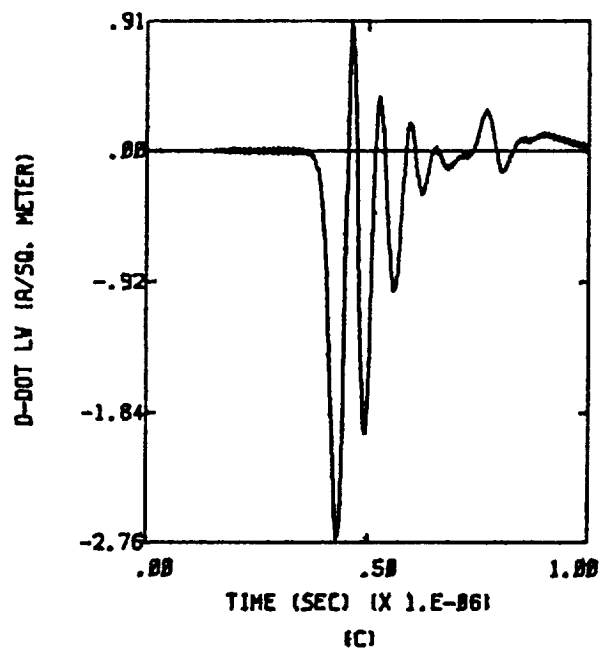
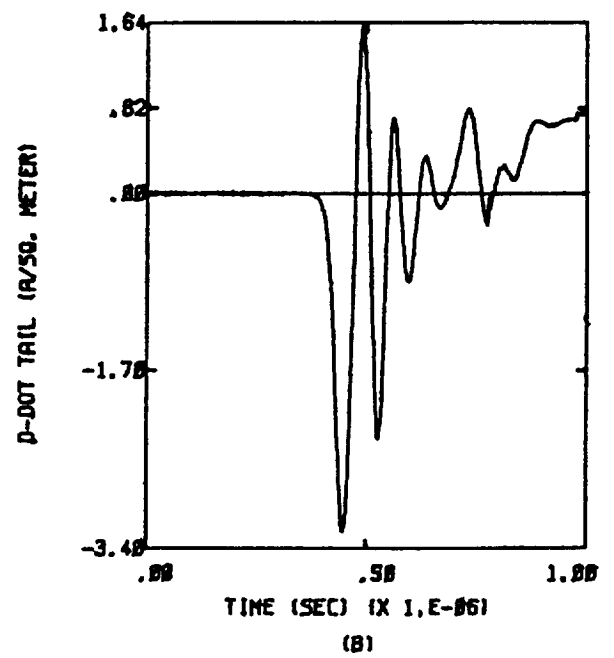
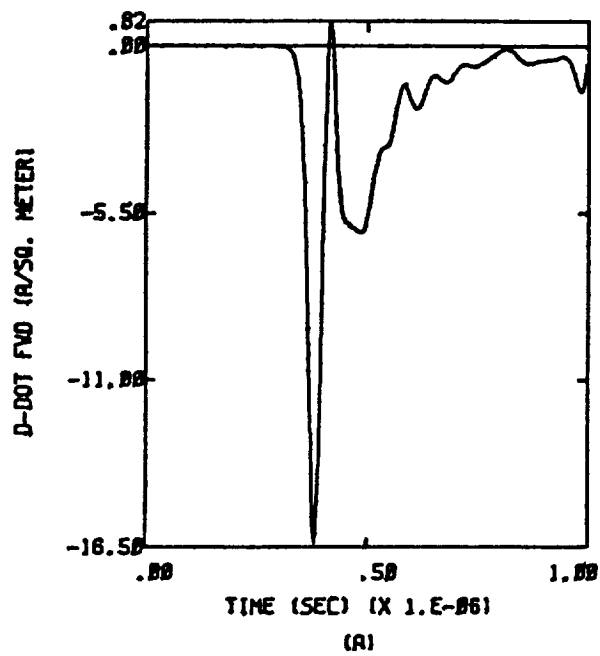


Figure D.12a  $-X, Z$ ;  $Q = 0$ ;  $E = 2.2 \times 10^5$  Volts per meter

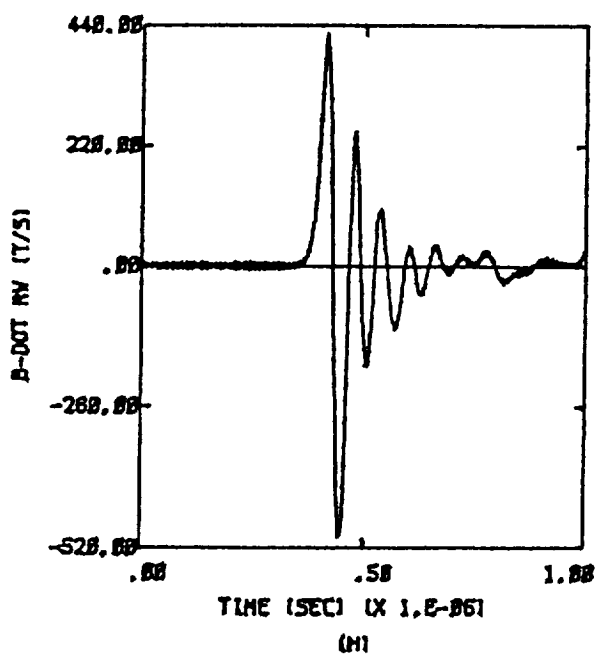
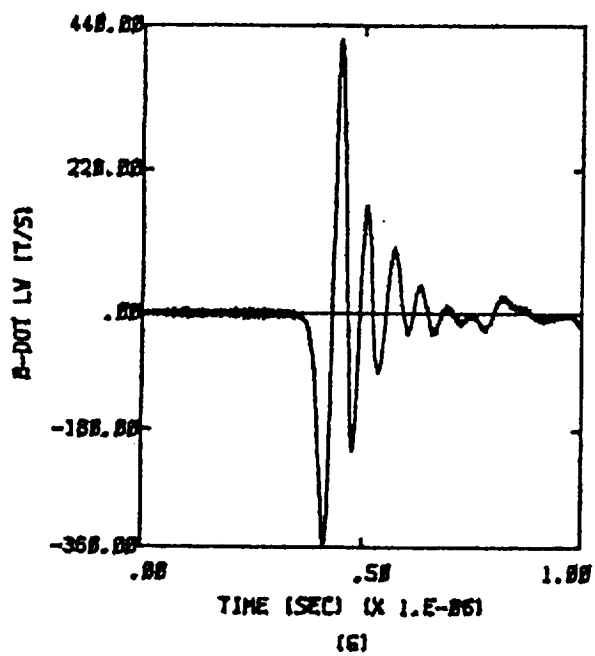
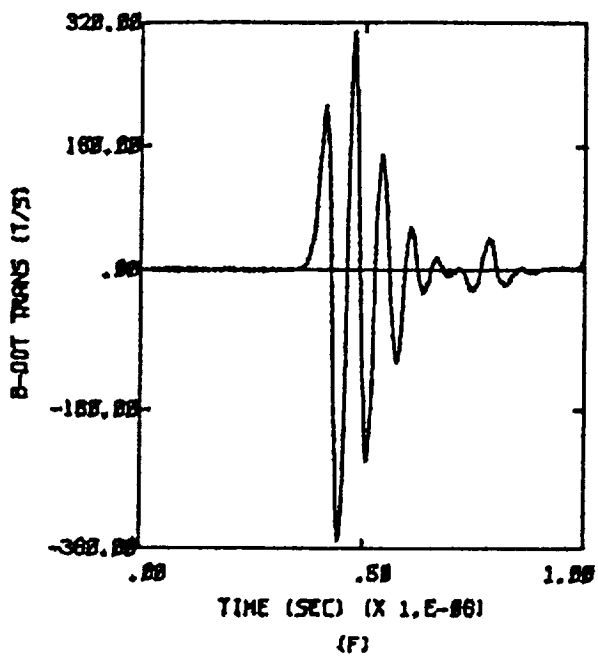
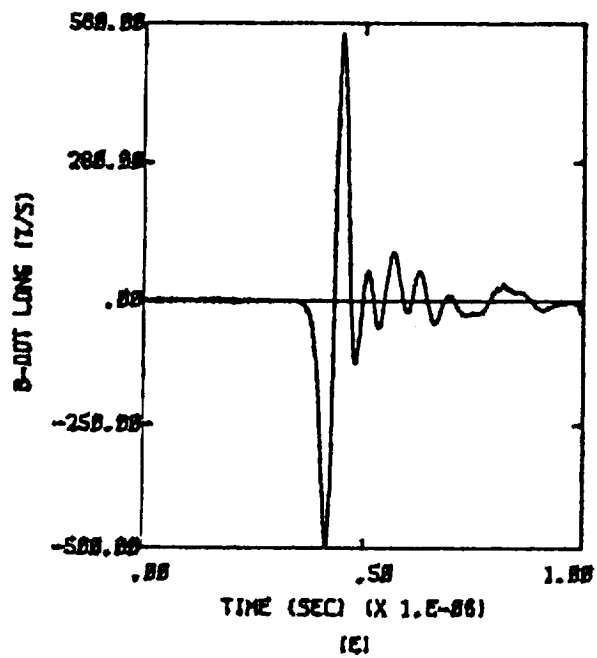


Figure D.12b -X,Z;  $Q = 0$ ;  $E = 2.2 \times 10^5$  Volts per meter

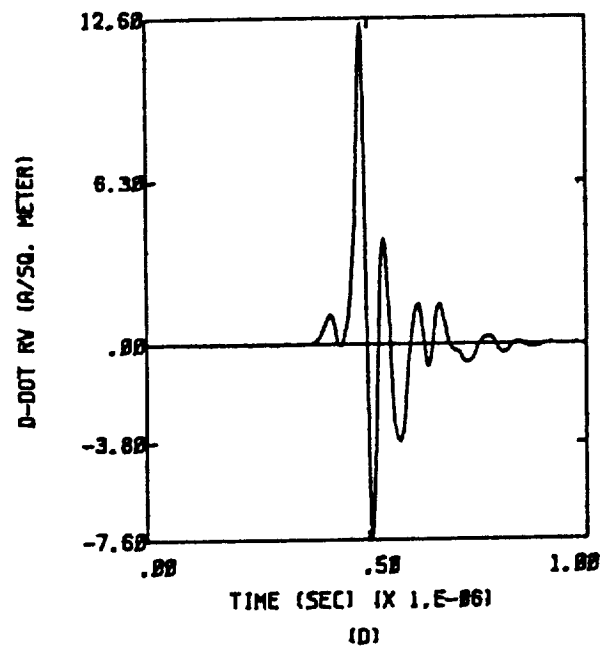
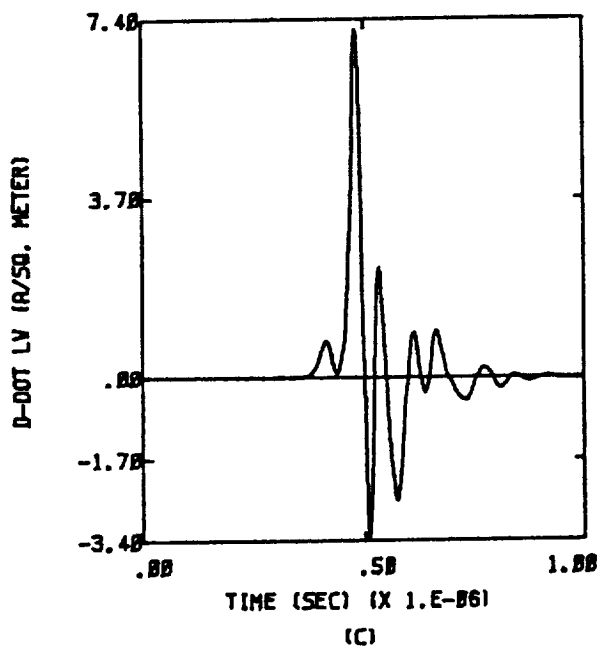
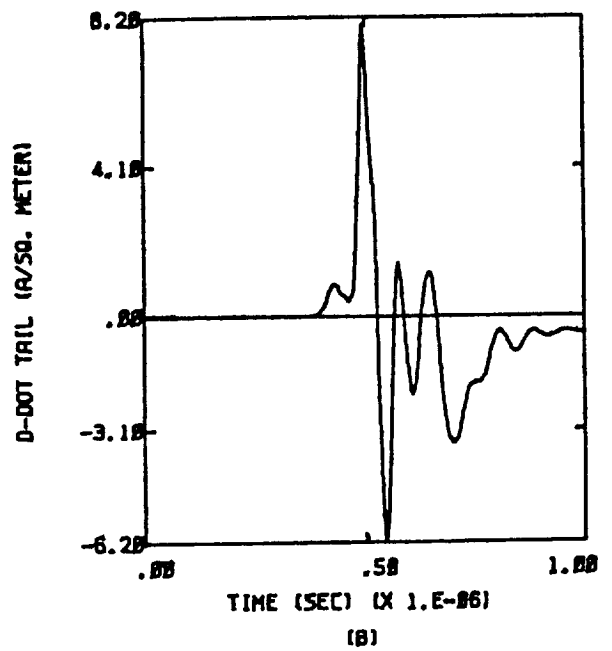
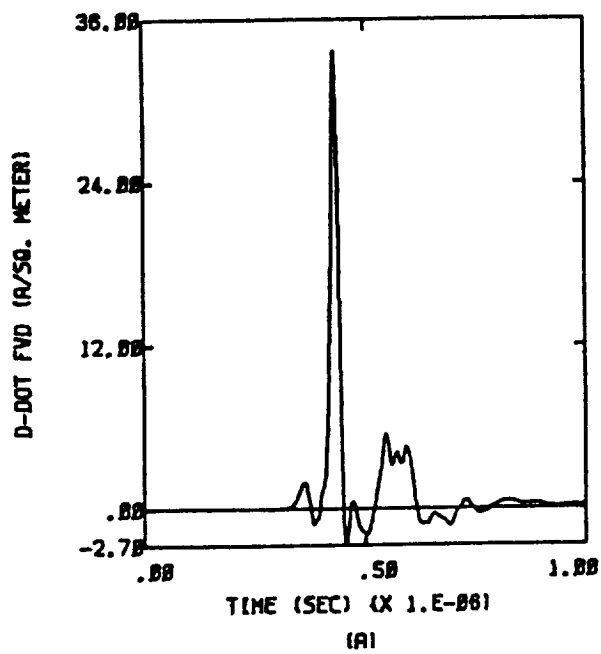


Figure D.13a  $X, Y, -Z; Q = 0; E = 2.6 \times 10^5$  Volts per meter

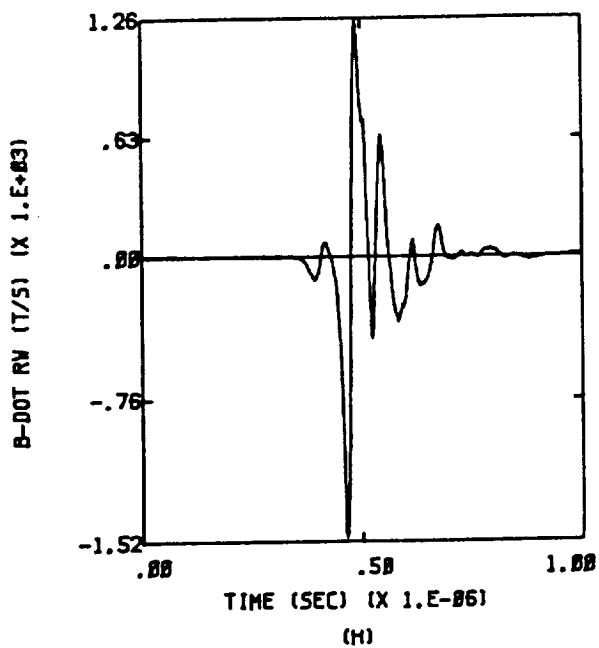
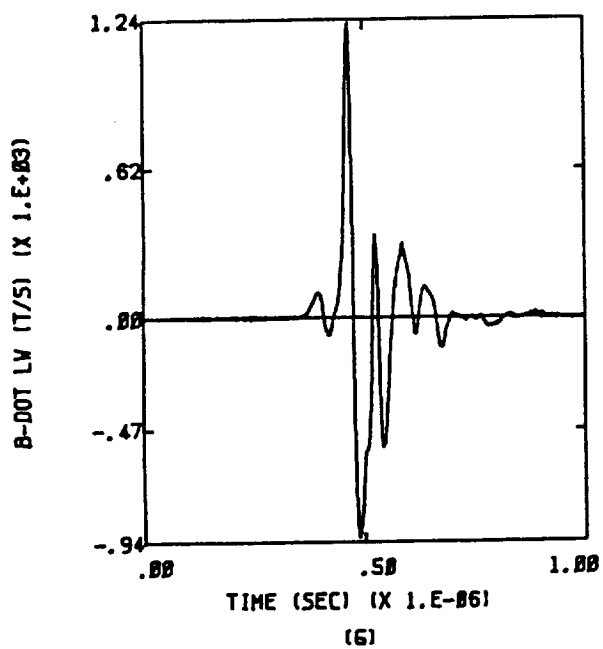
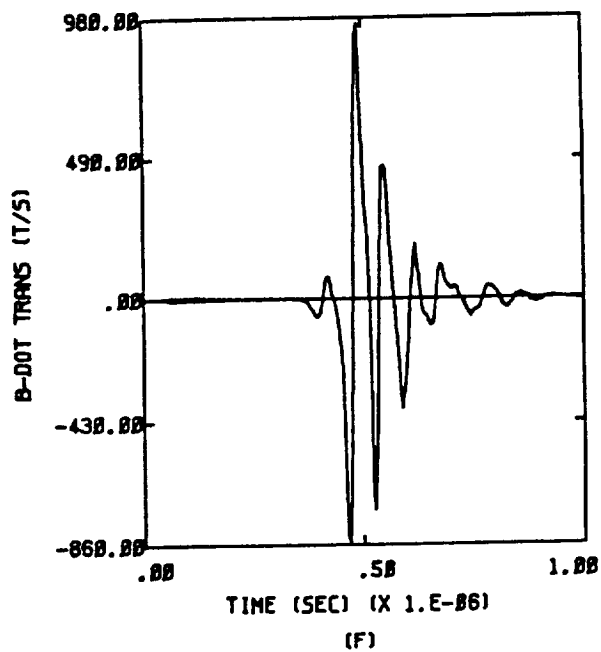
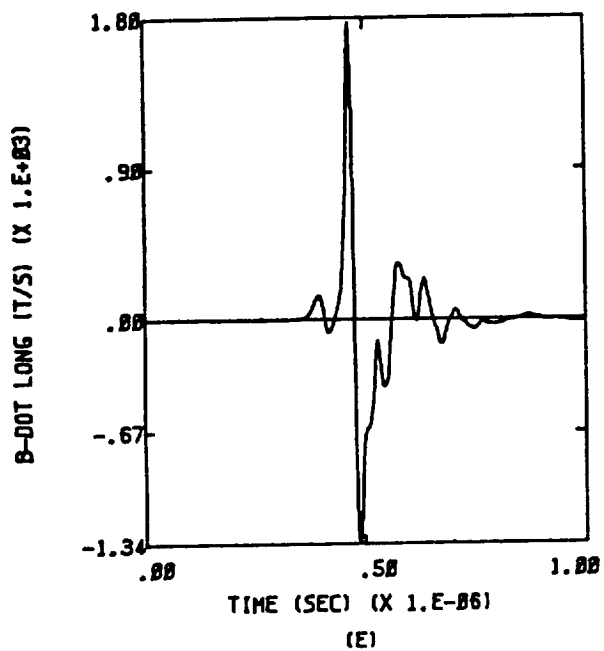


Figure D.13b X,Y,-Z;  $Q = 0$ ;  $E = 2.6 \times 10^5$  Volts per meter

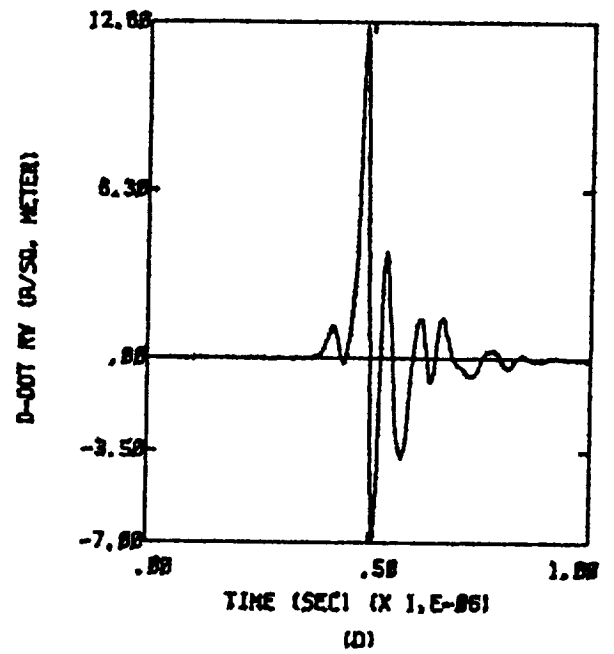
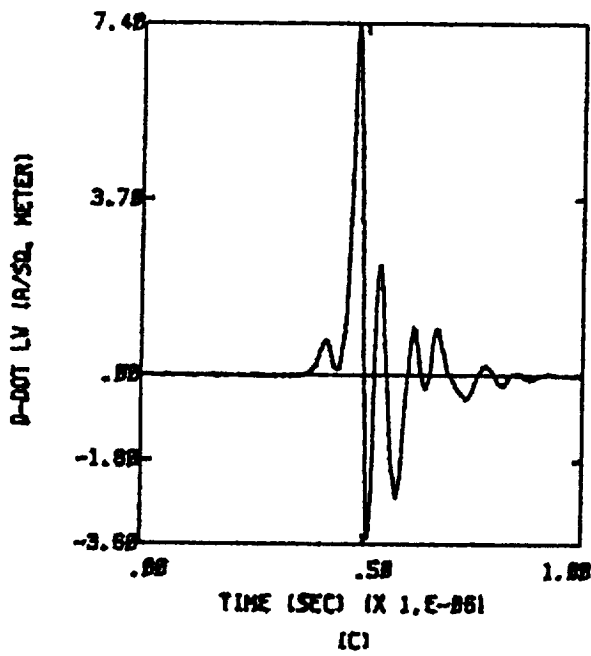
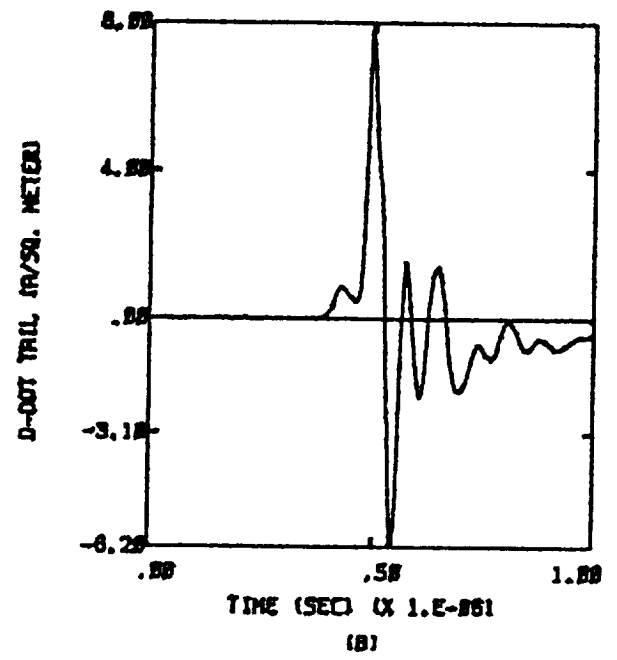
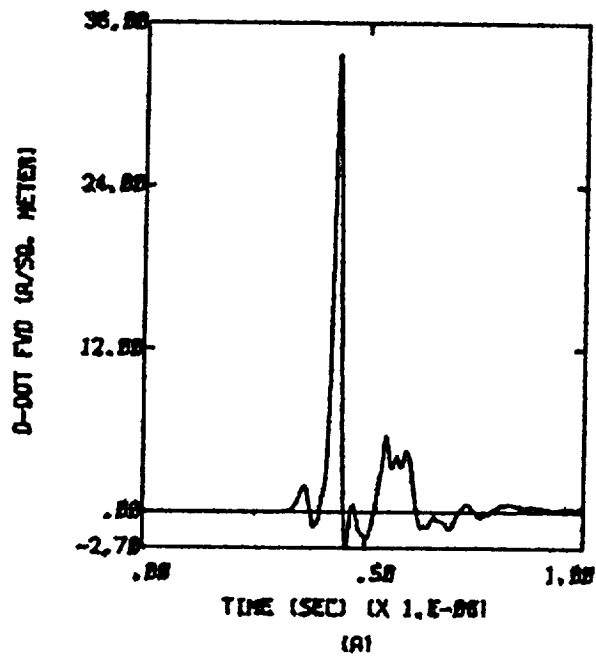


Figure D.14a X,-Y,-Z;  $Q = 0$ ;  $E = 2.6 \times 10^5$  Volts per meter

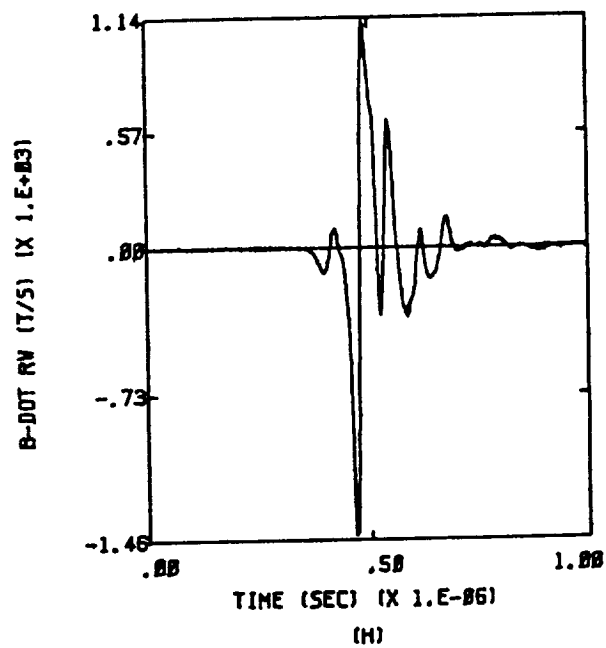
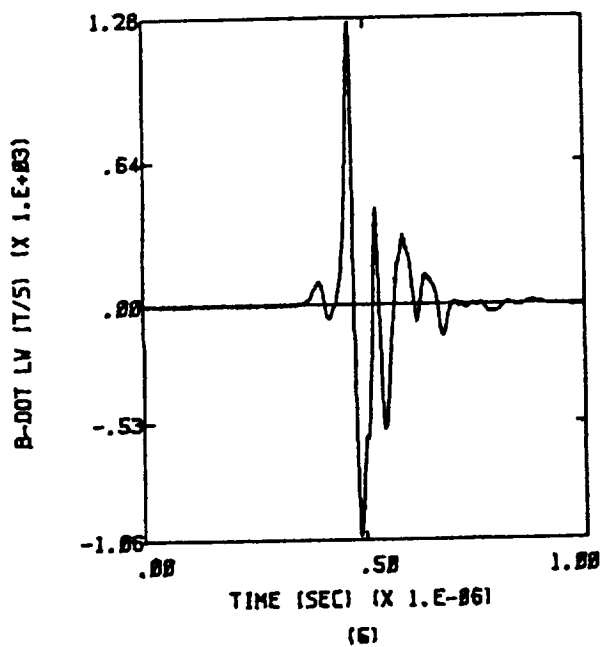
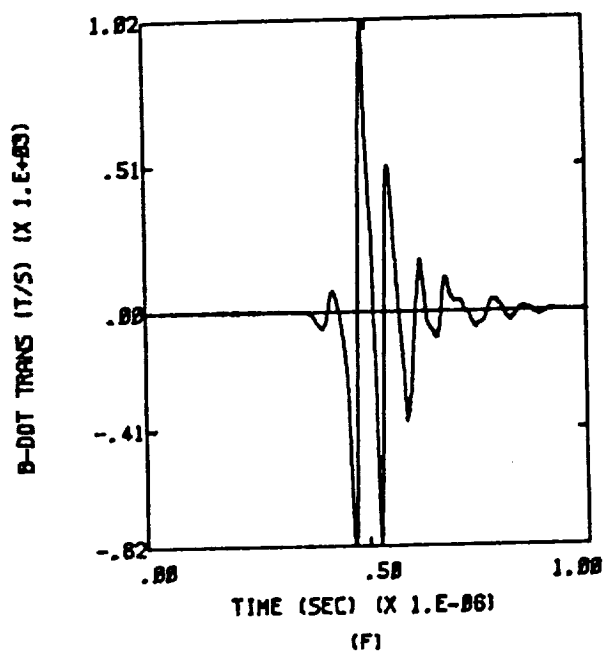
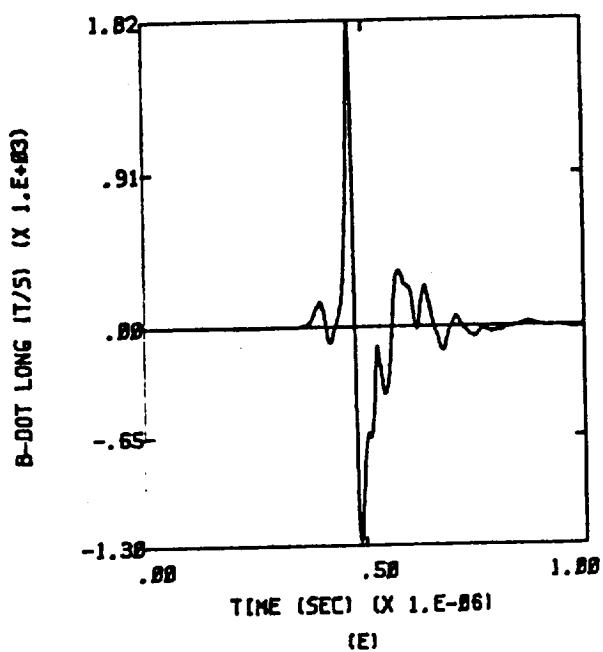


Figure D.14b X,-Y,-Z; Q = 0; E =  $2.6 \times 10^5$  Volts per meter

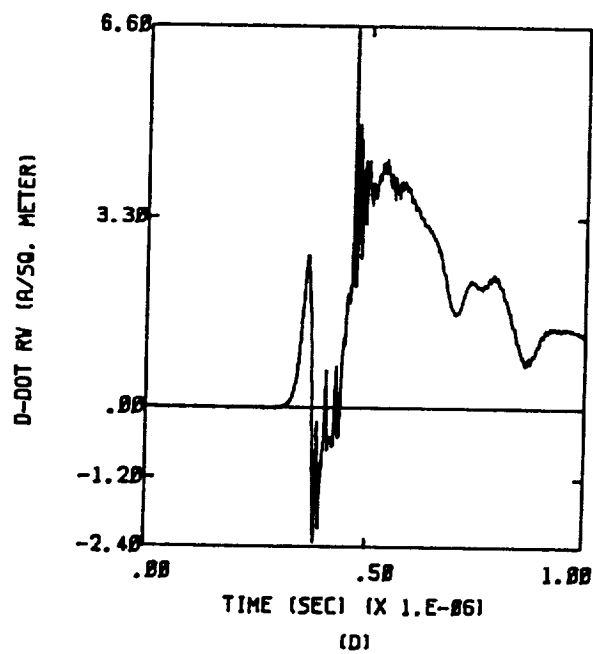
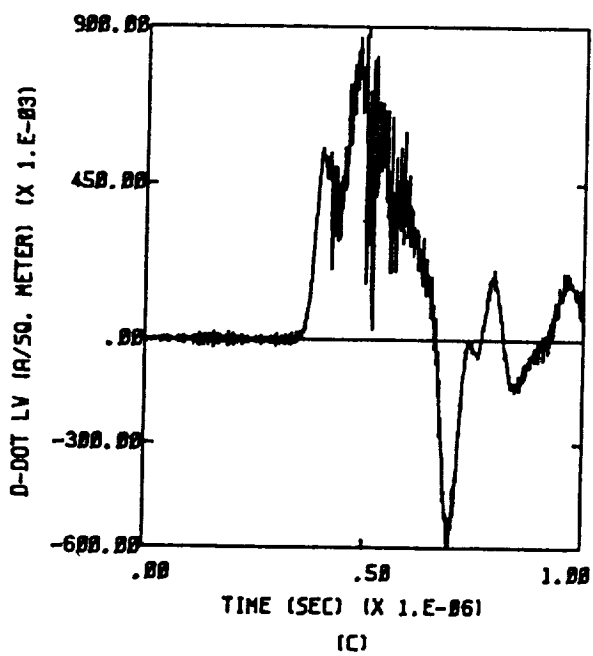
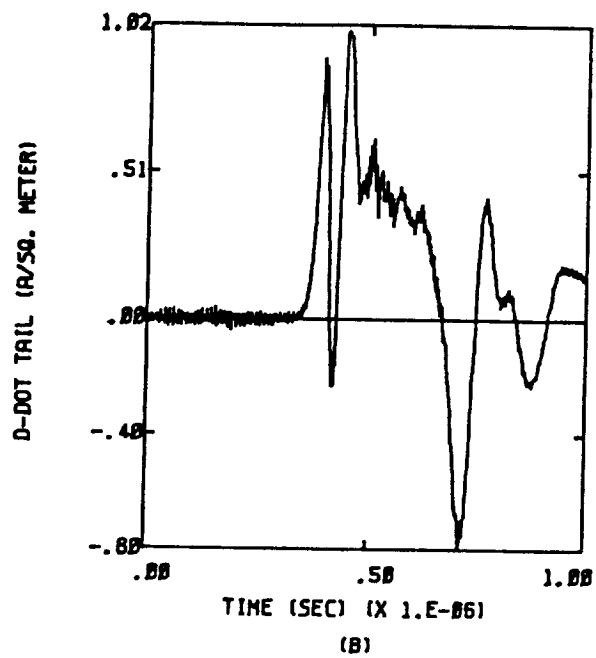
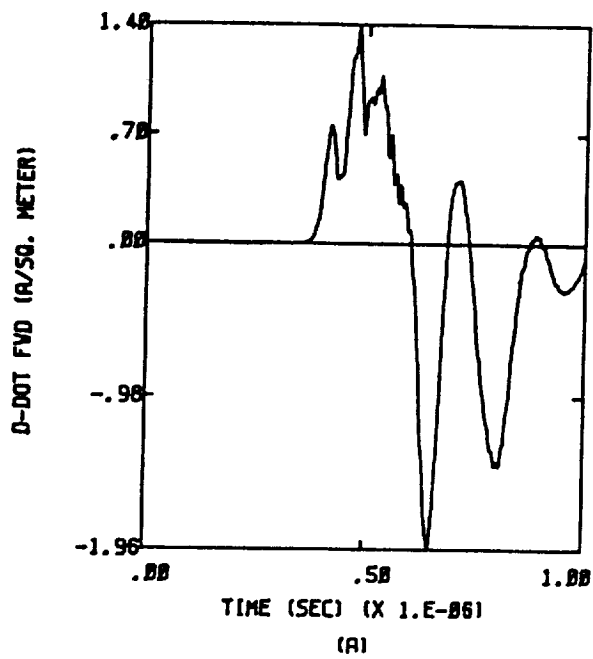


Figure D.15a -X,Y,-Z; Q = 0; E =  $2.8 \times 10^5$  Volts per meter



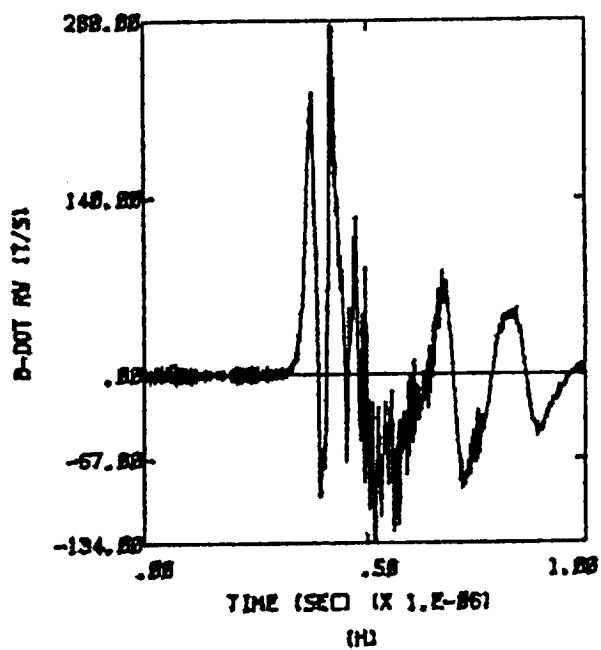
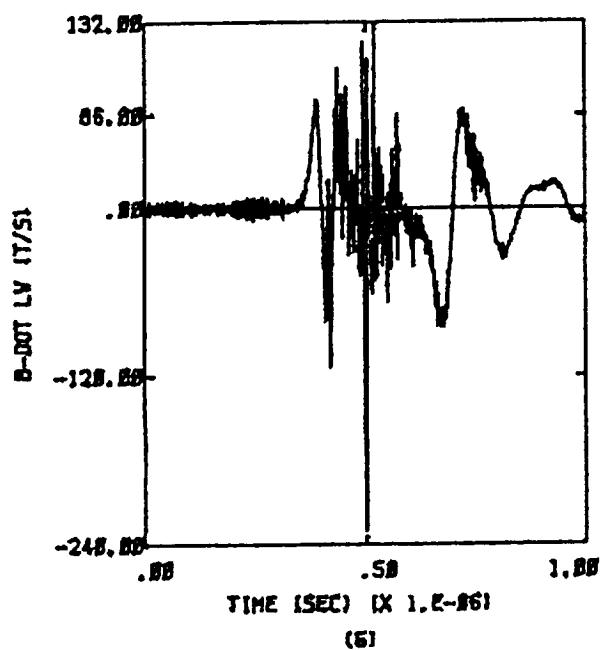
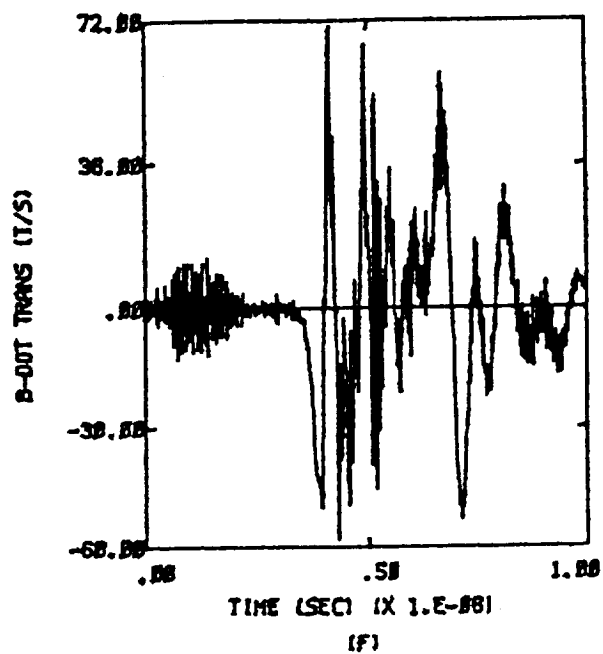
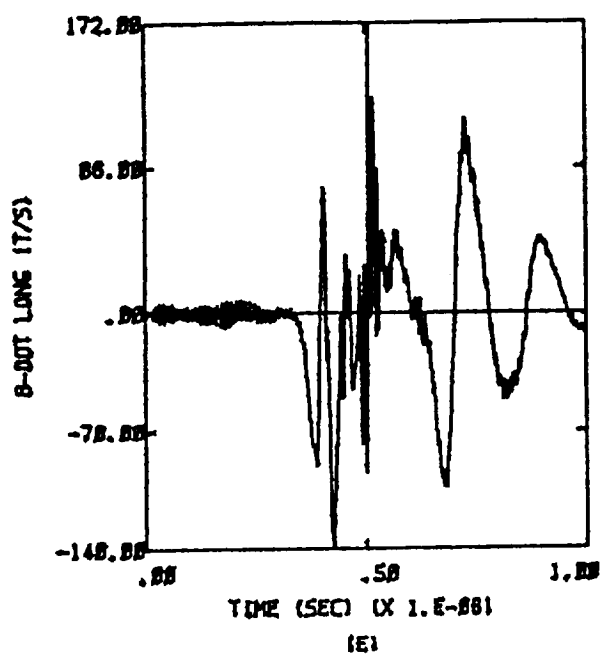


Figure D.15b -X,Y,-Z;  $Q = 0$ ;  $E = 2.8 \times 10^5$  Volts per meter

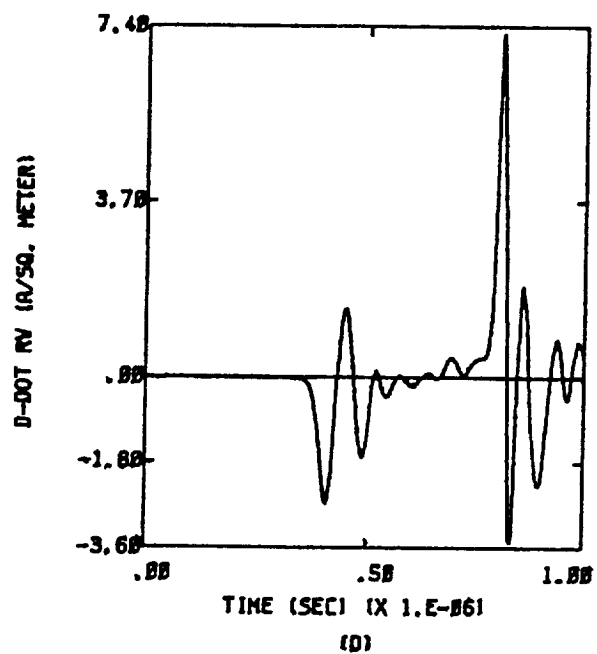
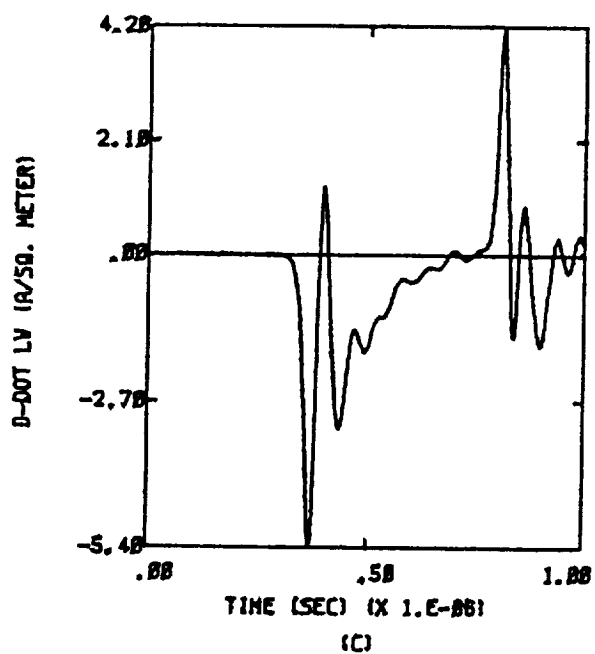
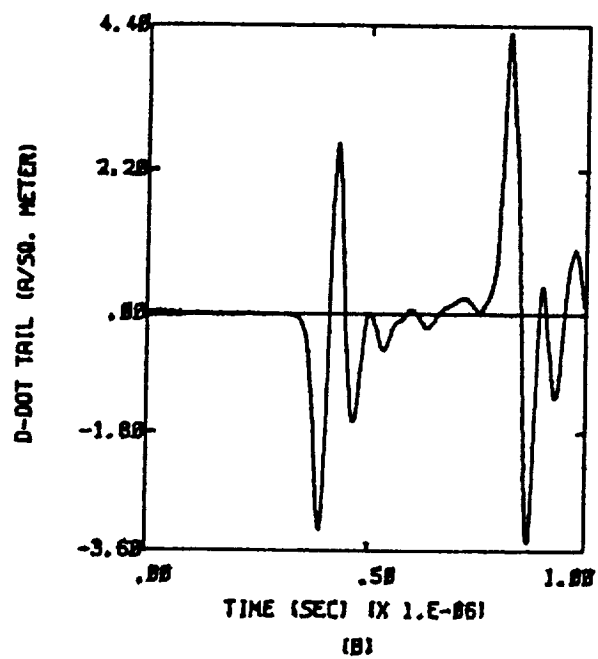
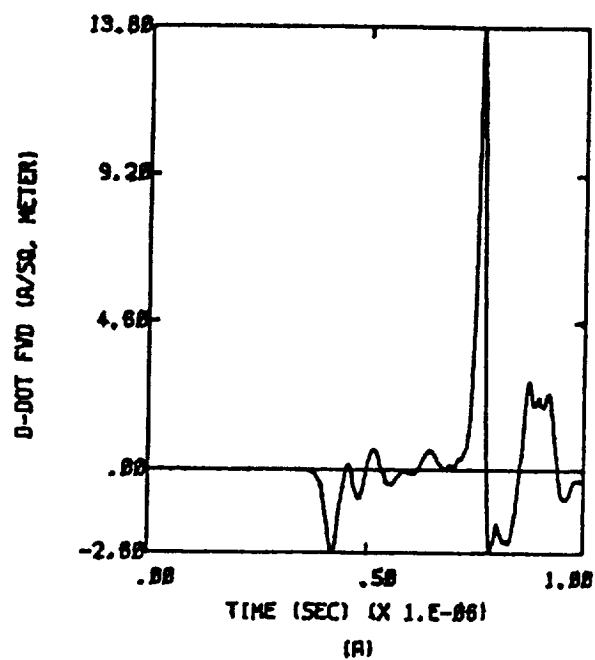


Figure D.16a X,Y,Z;  $Q = 0$ ;  $E = 2.8 \times 10^5$  Volts per meter

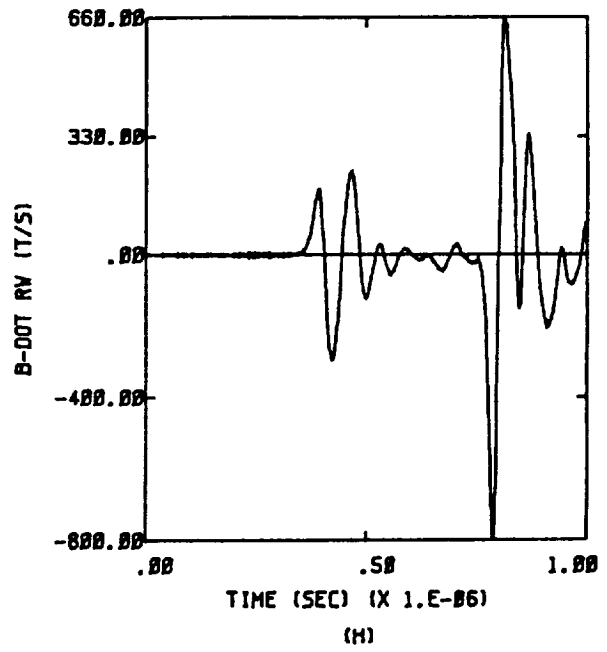
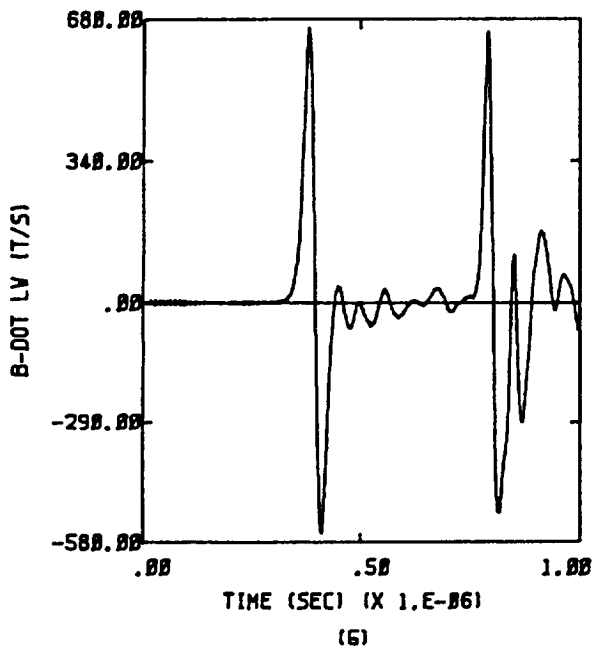
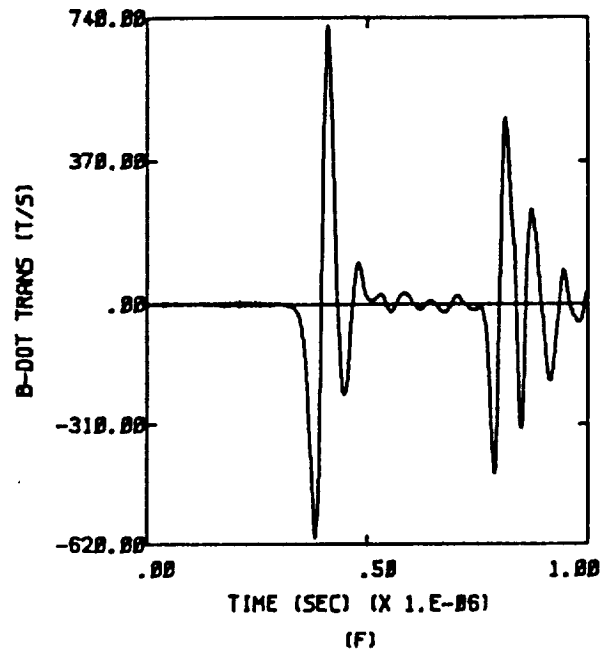
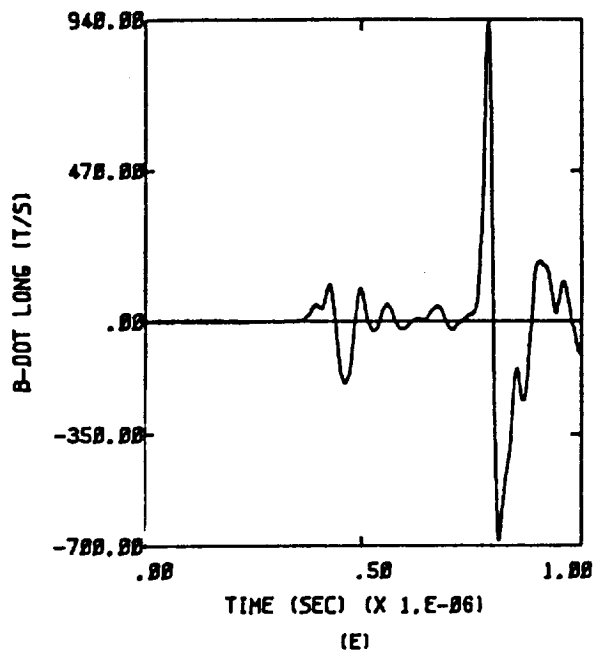


Figure D.16b X,Y,Z;  $Q = 0$ ;  $E = 2.8 \times 10^5$  Volts per meter

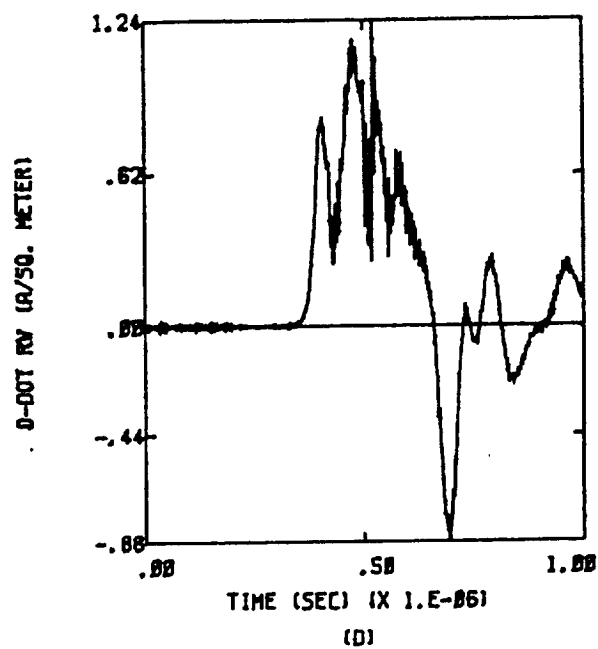
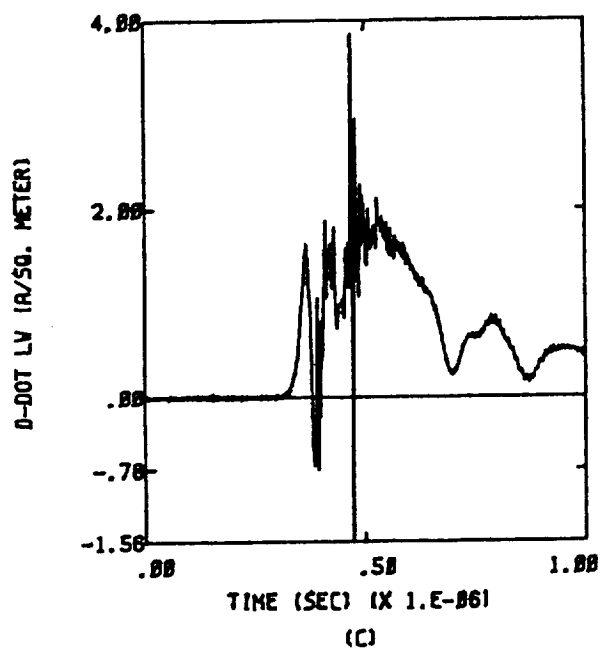
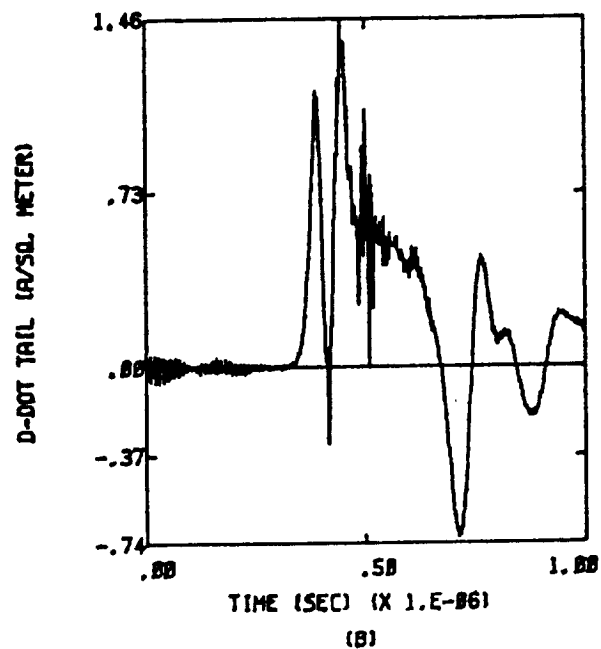
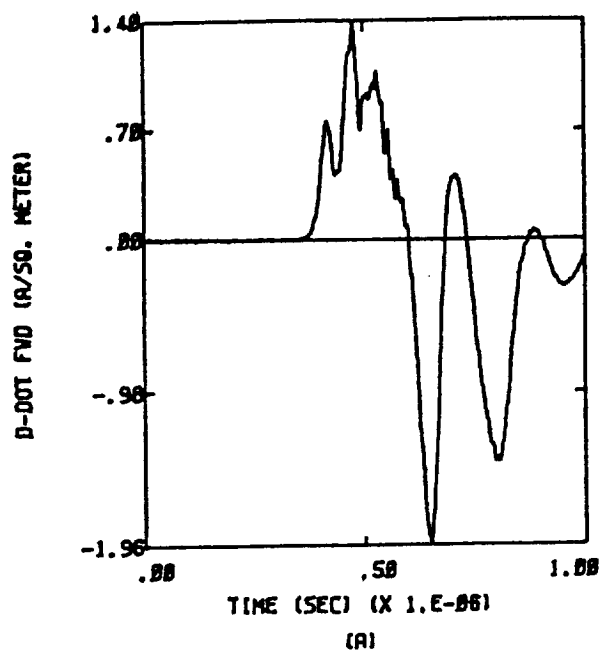


Figure D.17a  $-X, -Y, -Z; Q = 0; E = 2.8 \times 10^5$  Volts per meter

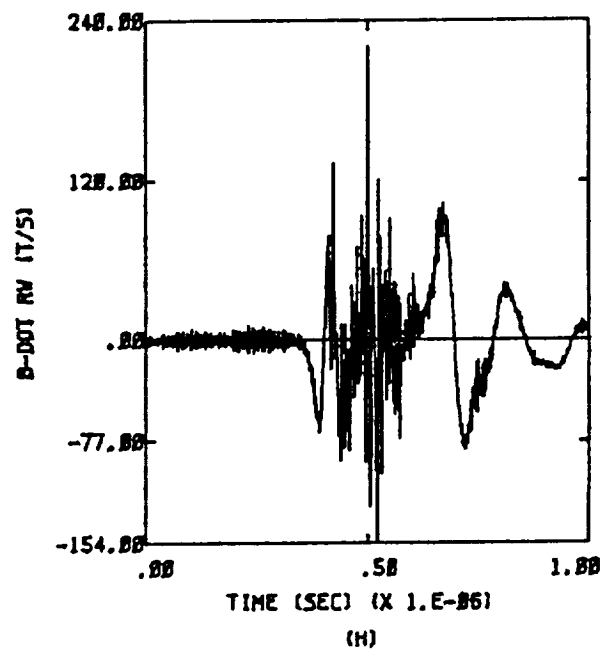
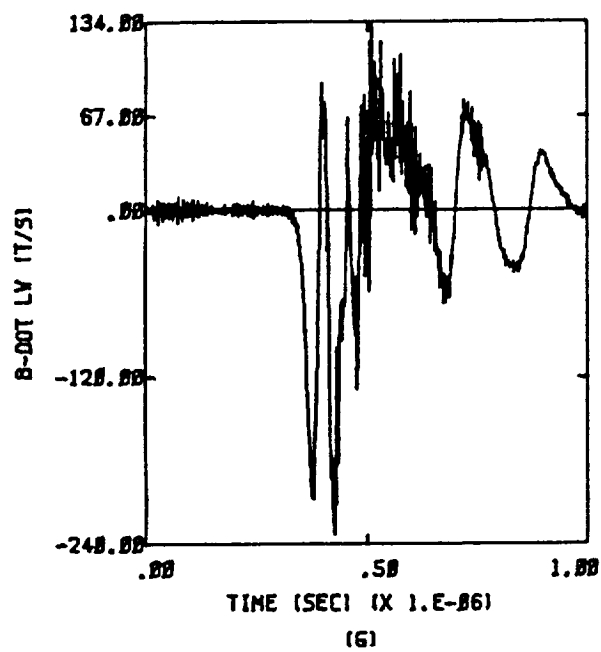
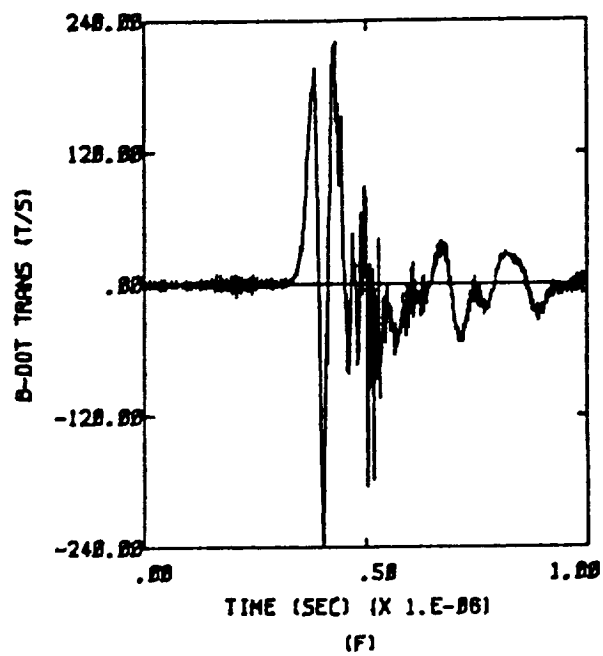
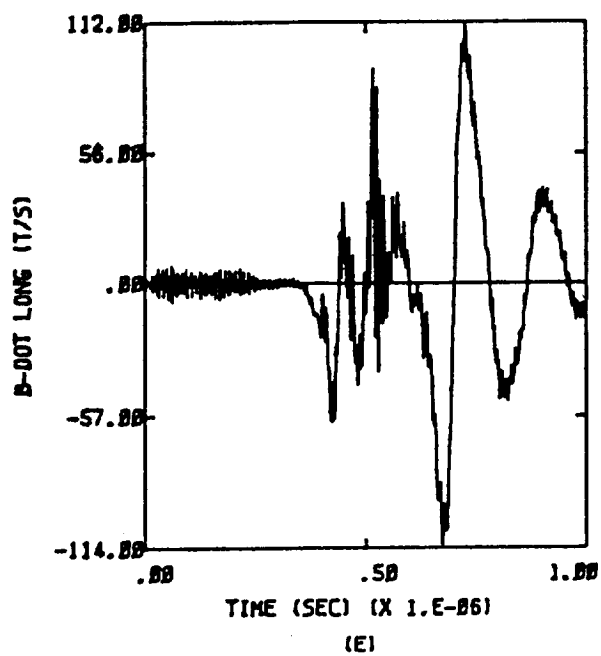


Figure D.17b  $-X, -Y, -Z; Q = 0; E = 2.8 \times 10^5$  Volts per meter

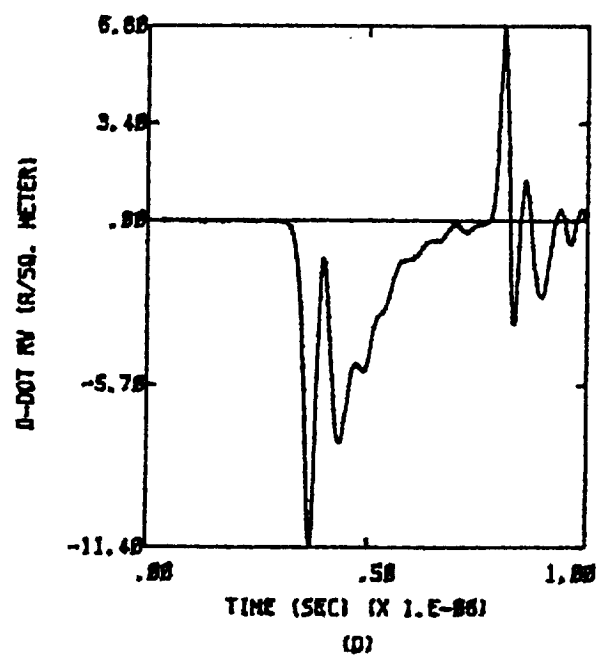
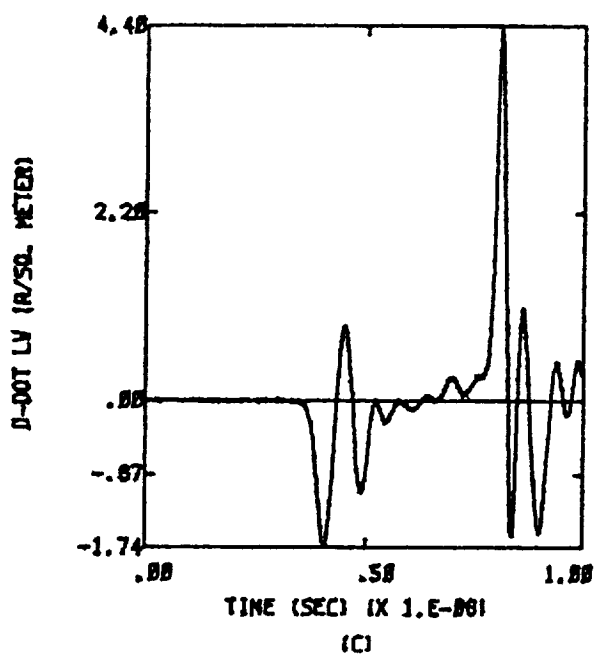
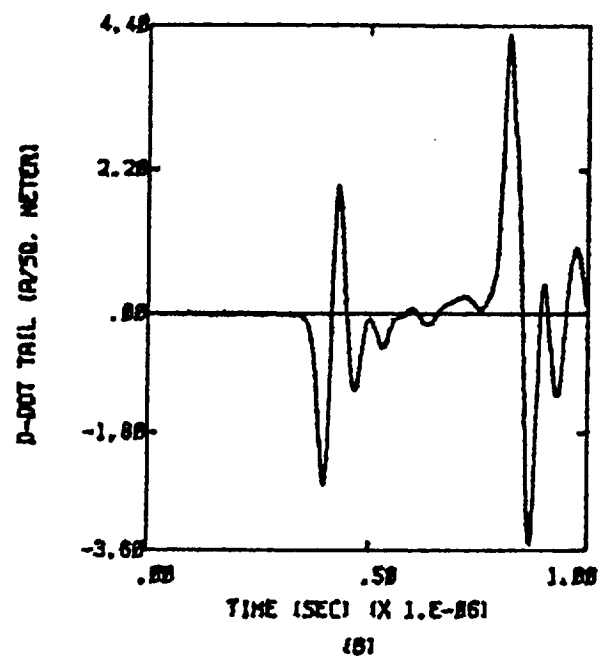
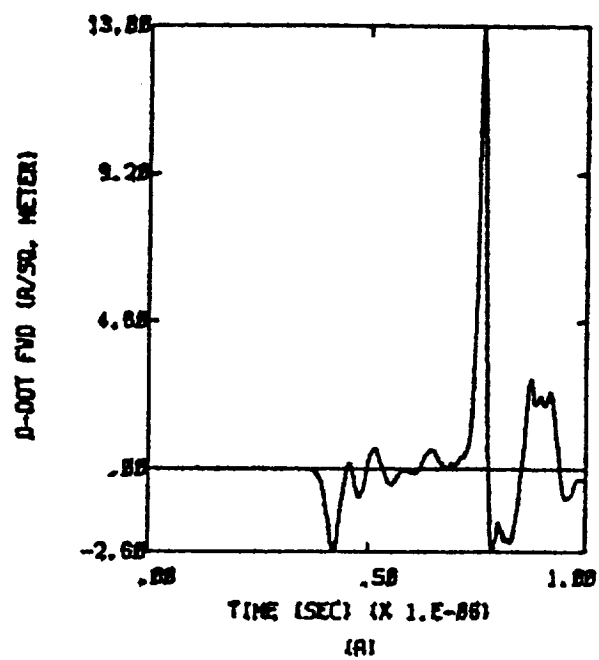


Figure D.18a X,-Y,Z;  $Q = 0$ ;  $E = 2.8 \times 10^5$  Volts per meter

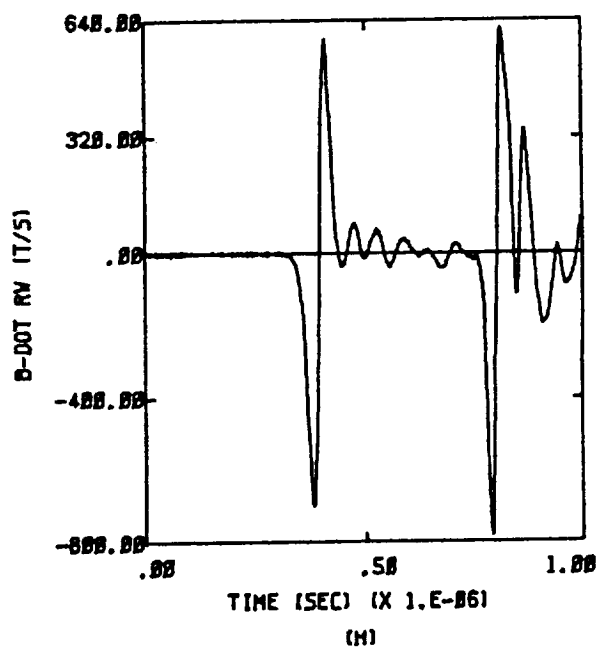
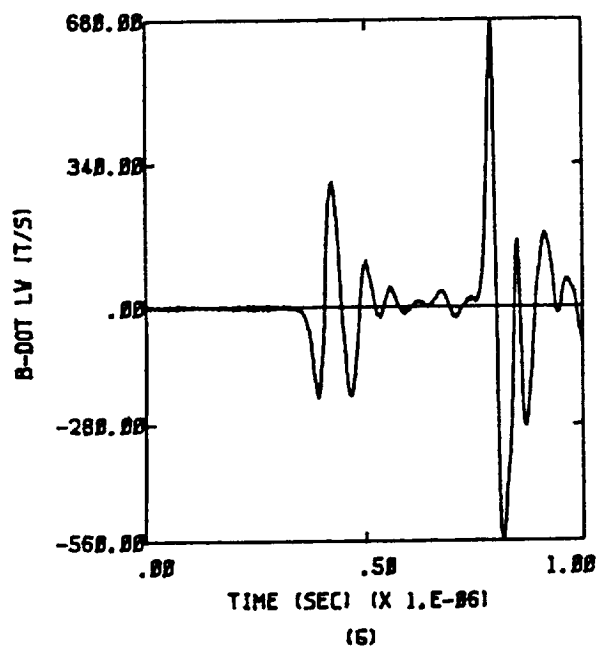
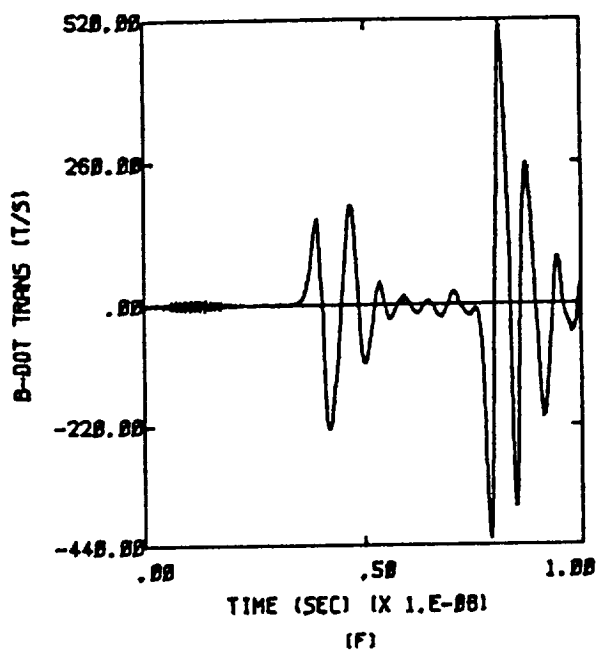
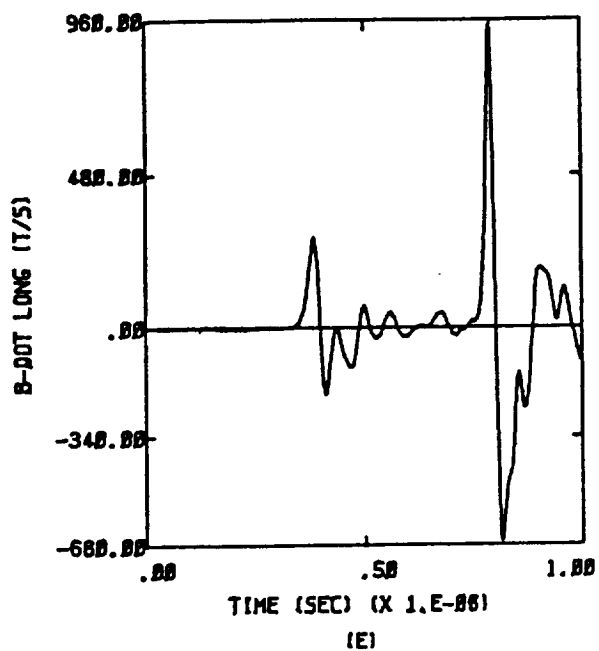


Figure D.18b X,-Y,Z;  $Q = 0$ ;  $E = 2.8 \times 10^5$  Volts per meter

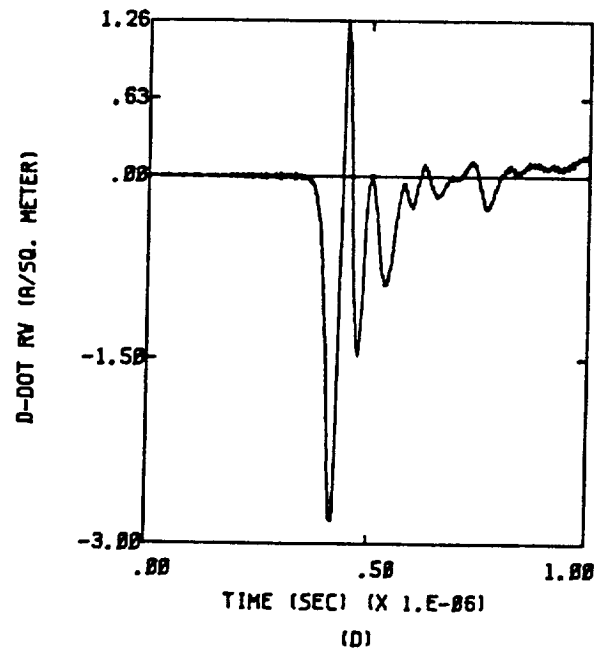
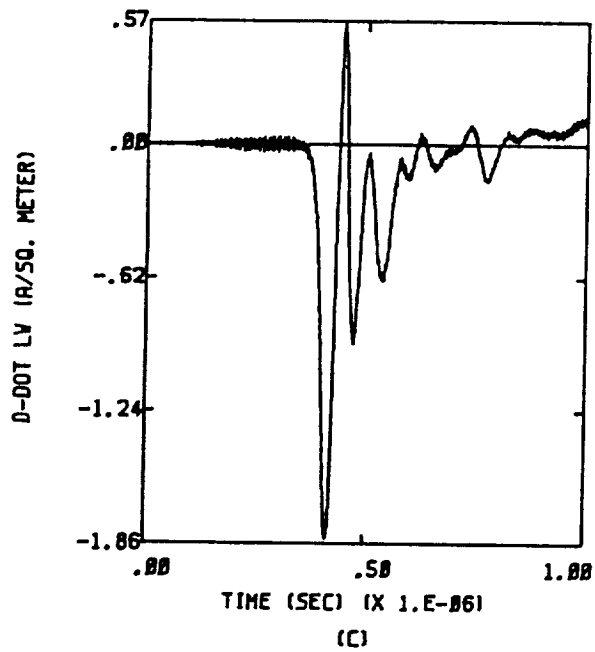
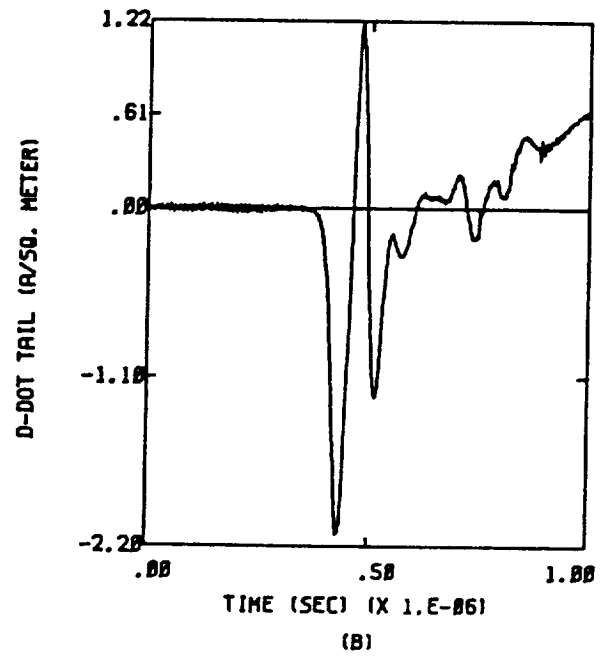
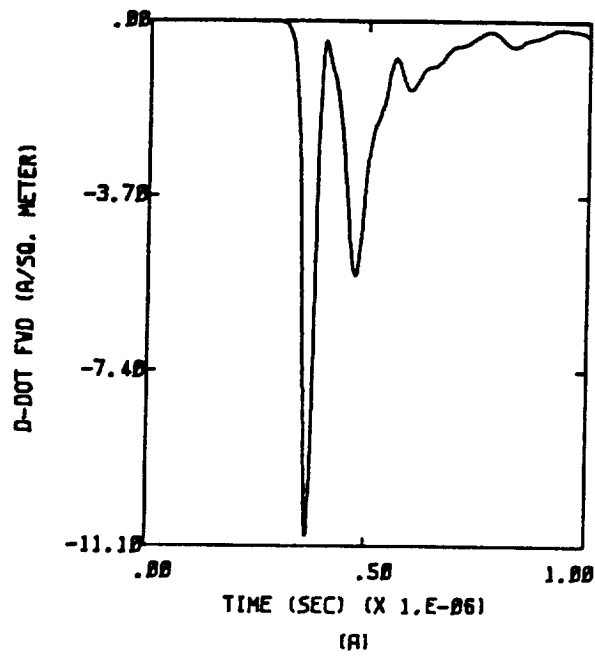


Figure D.19a -X,Y,Z;  $Q = 0$ ;  $E = 2.6 \times 10^5$  Volts per meter



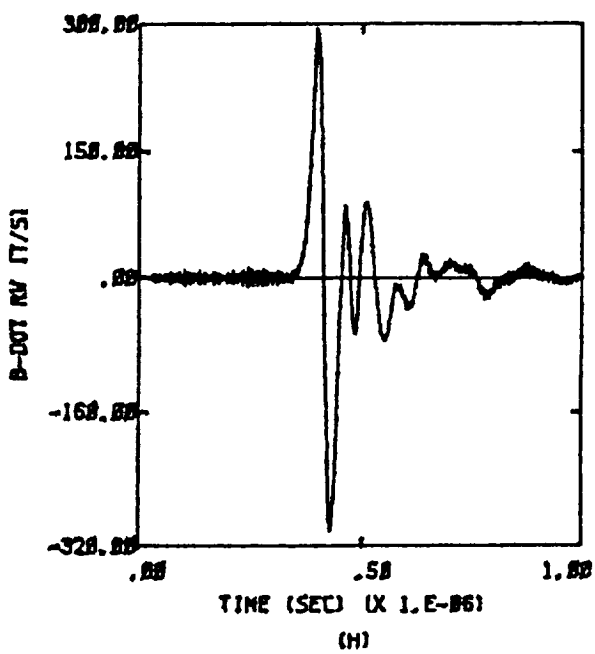
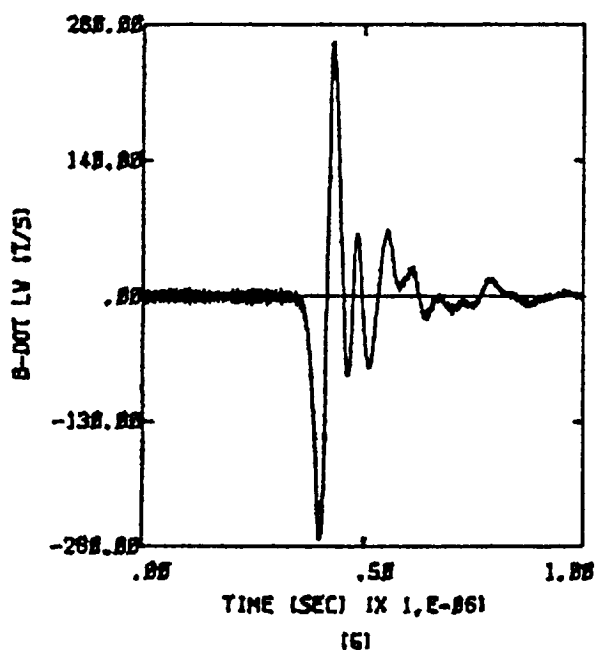
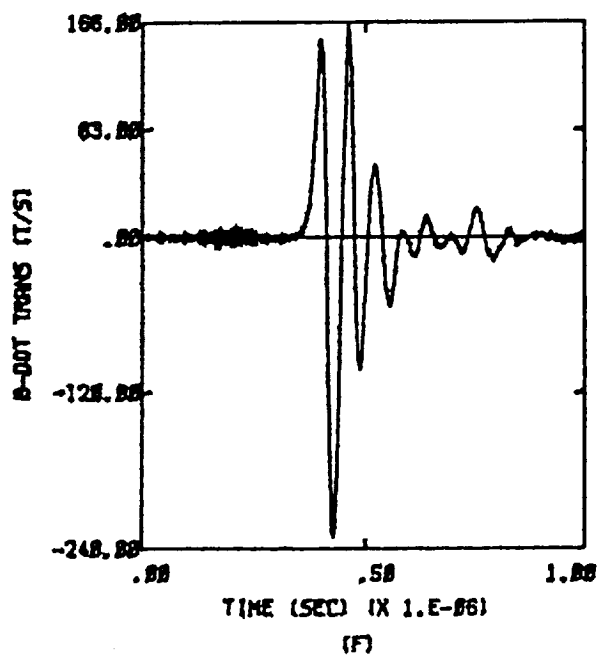
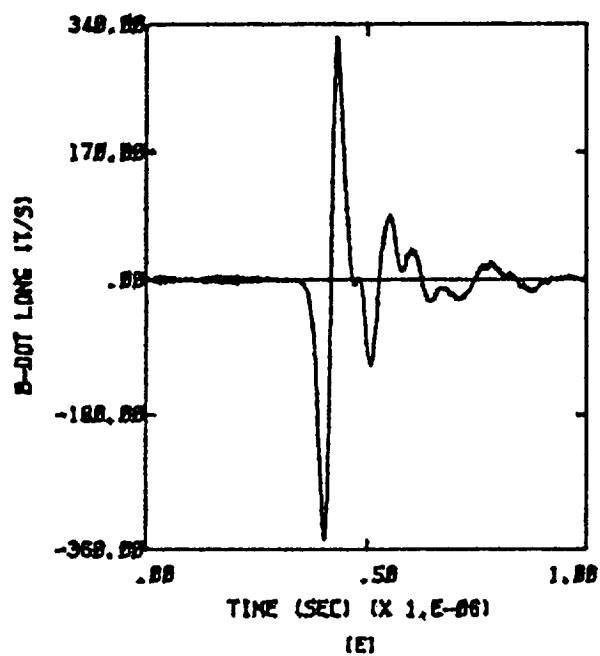


Figure D.19b -X,Y,Z;  $Q = 0$ ;  $E = 2.6 \times 10^5$  Volts per meter

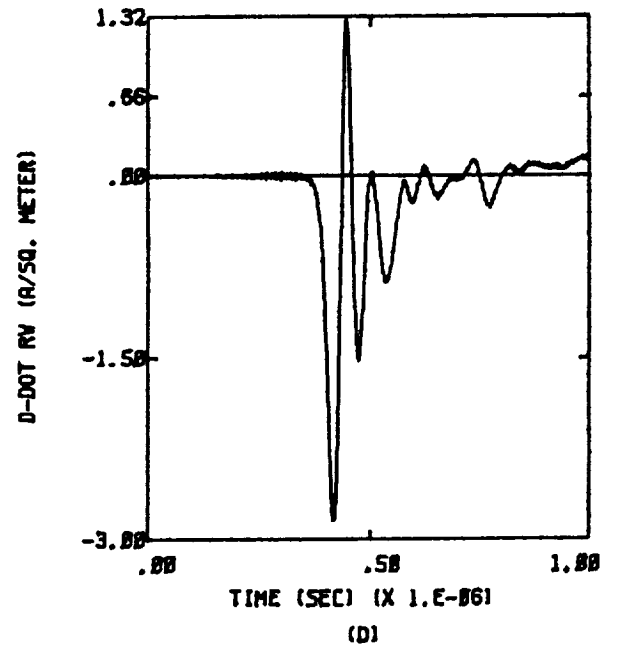
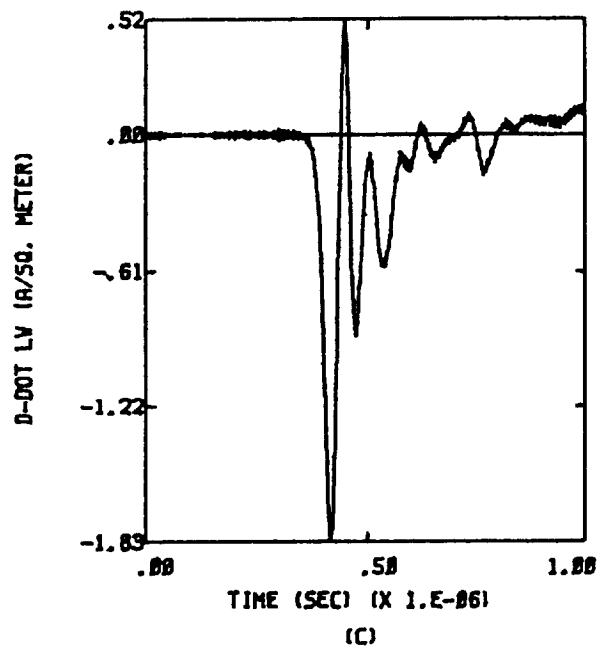
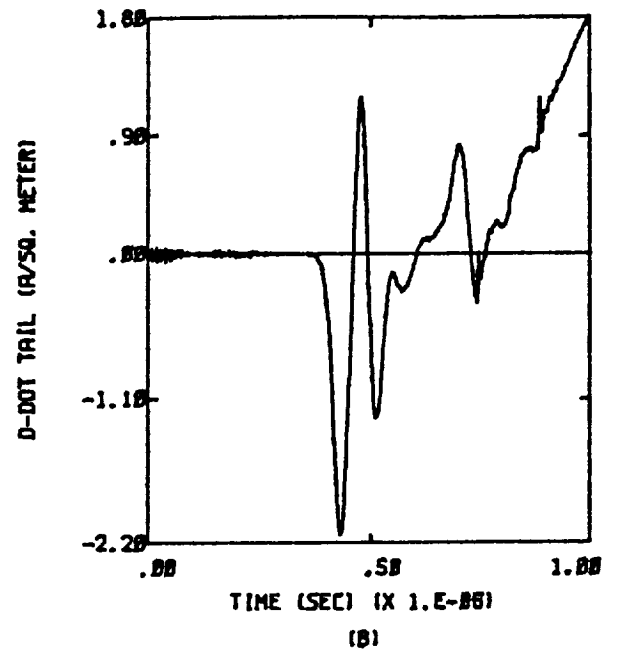
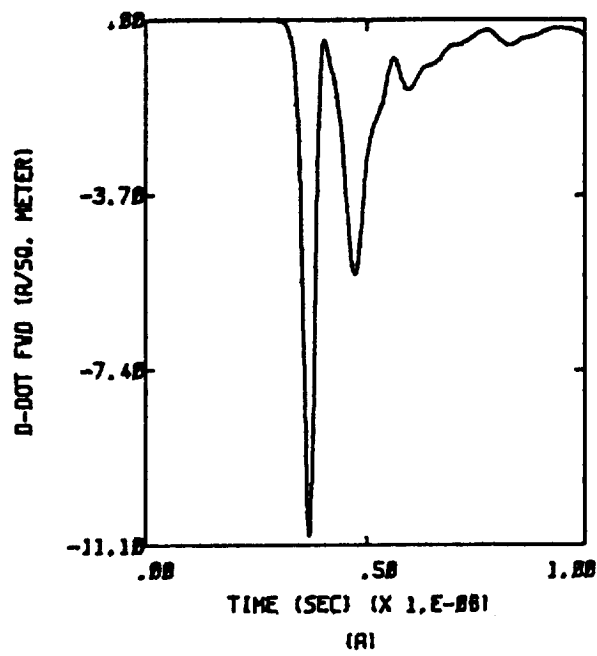


Figure D.20a -X,-Y,Z;  $Q = 0$ ;  $E = 2.6 \times 10^5$  Volts per meter

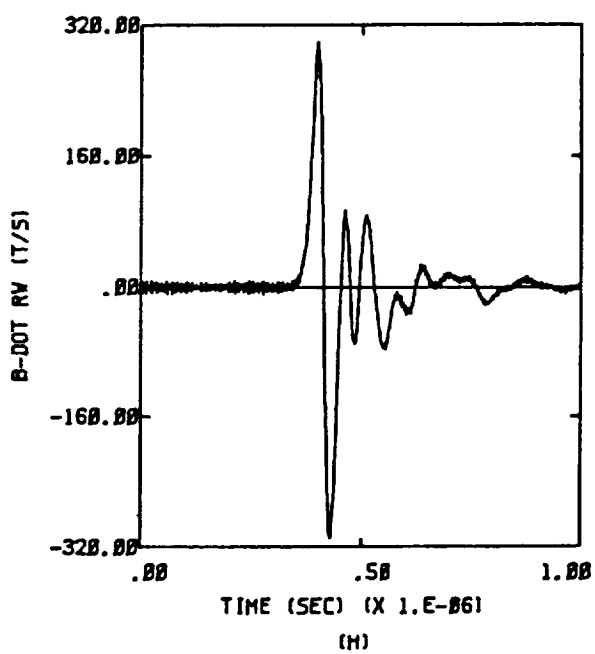
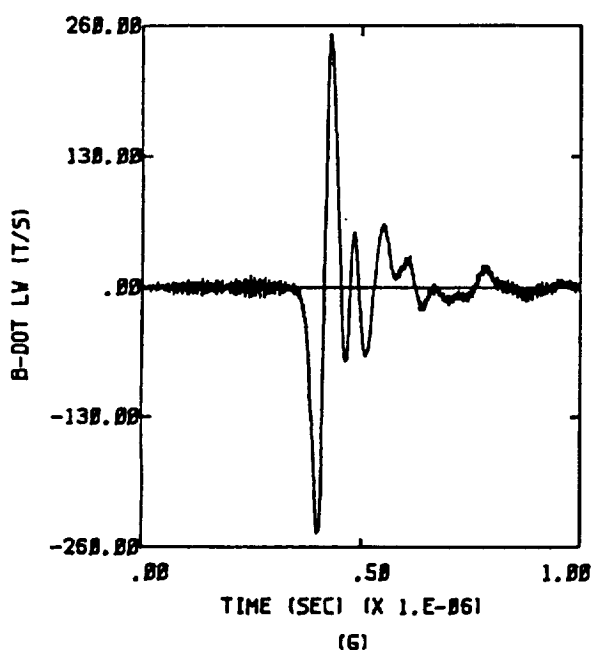
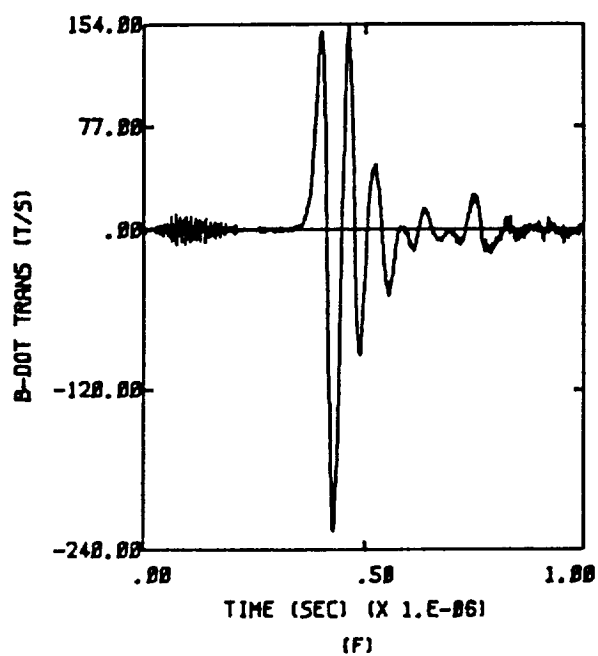
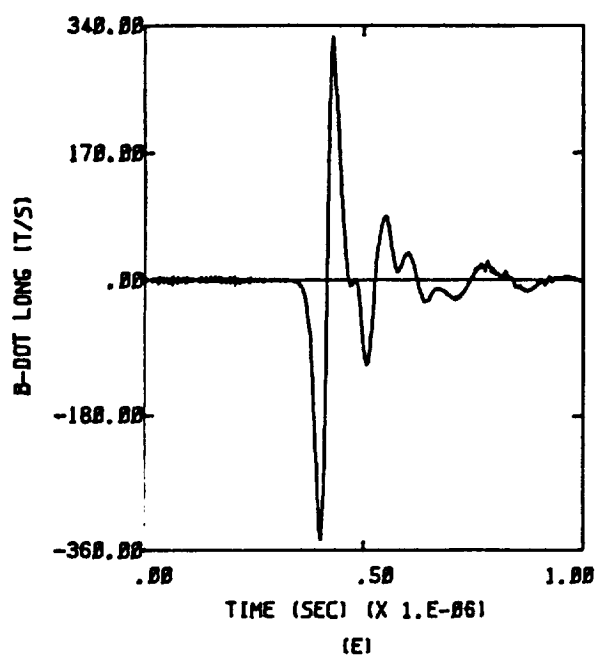


Figure D.20b  $-X, -Y, Z$ ;  $Q = 0$ ;  $E = 2.6 \times 10^5$  Volts per meter

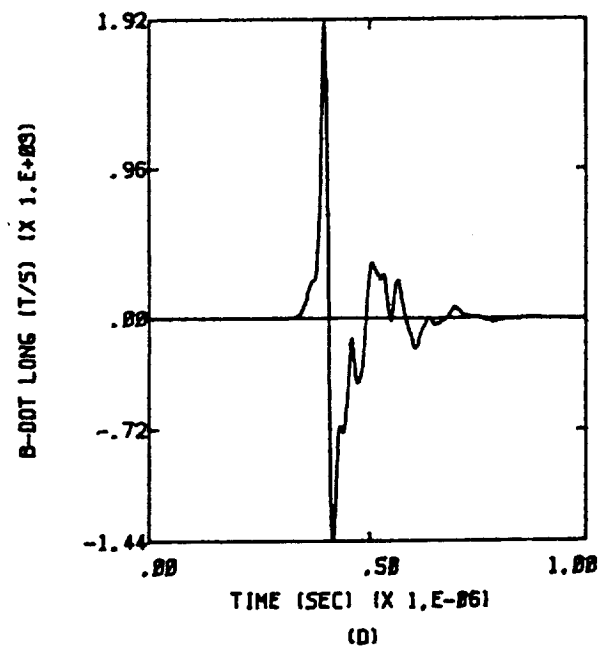
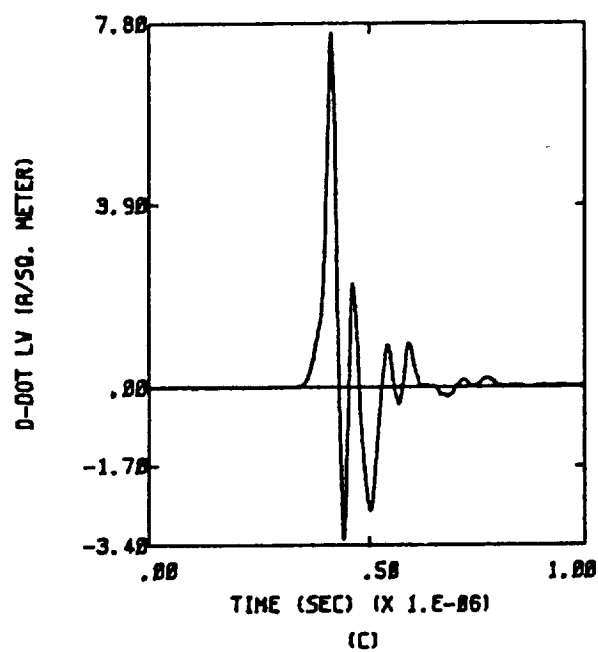
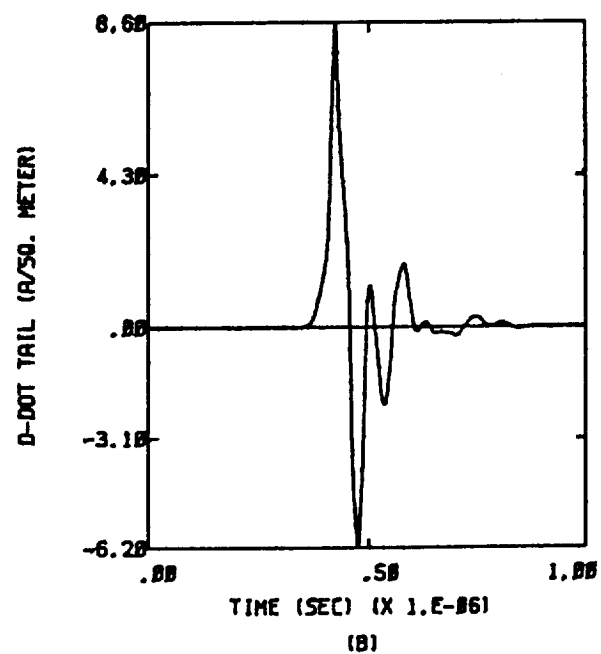
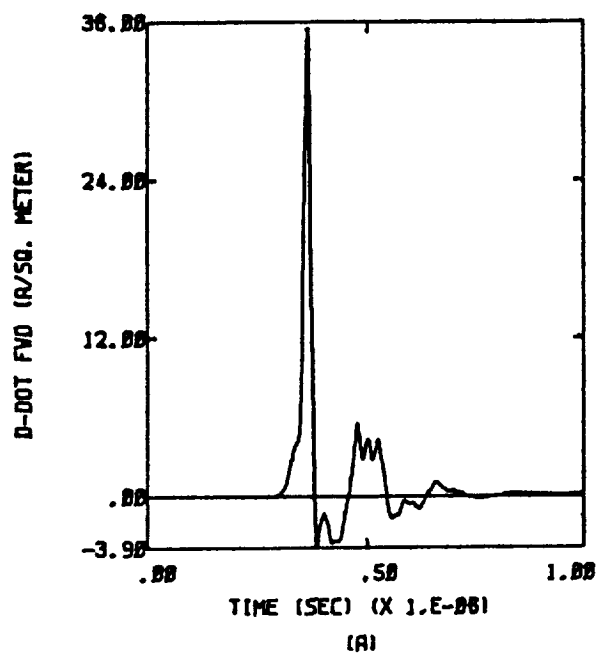


Figure D.21  $X, Y; Q = -1/2 Q_m; E = 1.4 \times 10^5$  Volts per meter

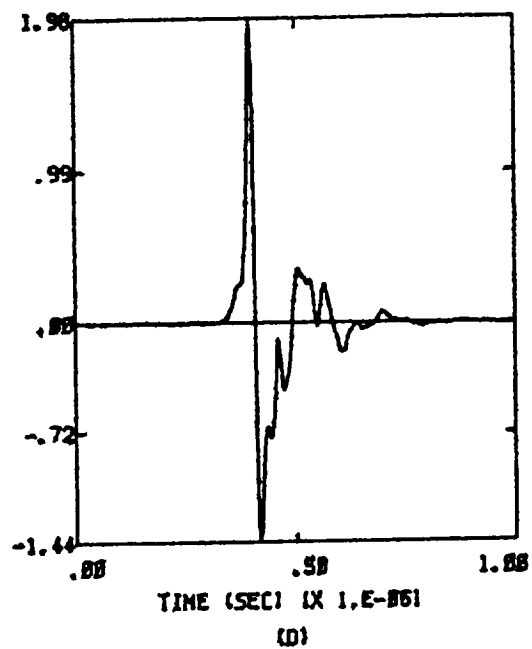
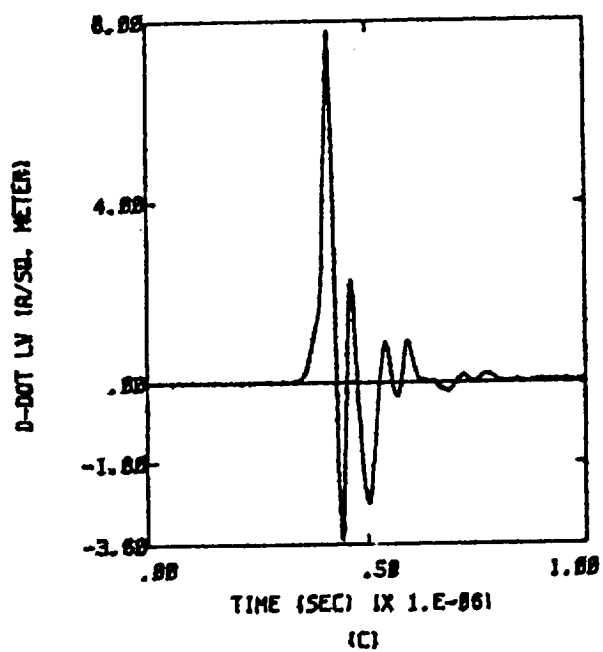
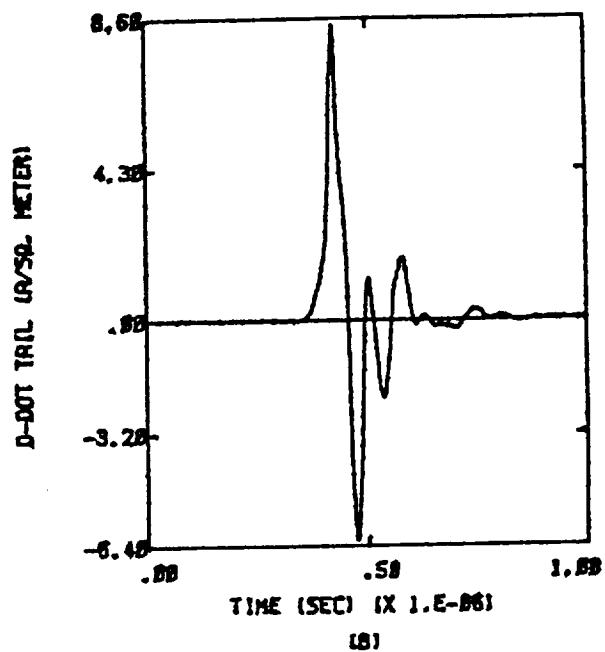
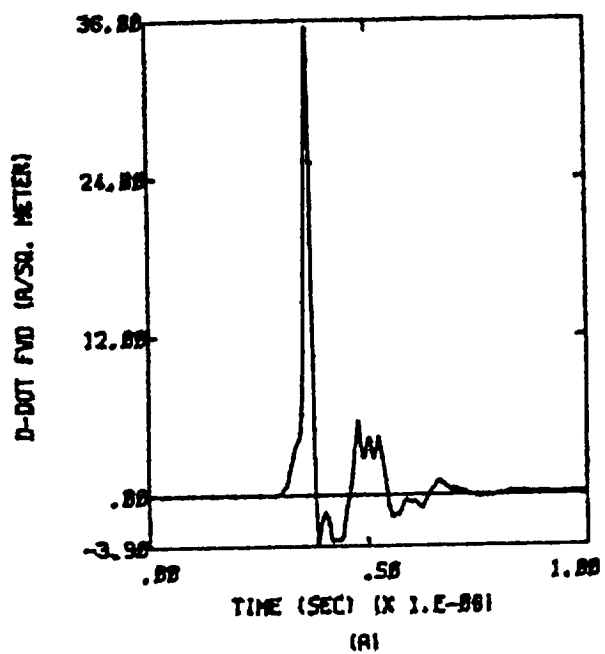


Figure D.22 X,-Y;  $Q = -1/2 Q_m$ ;  $E = 1.4 \times 10^5$  Volts per meter

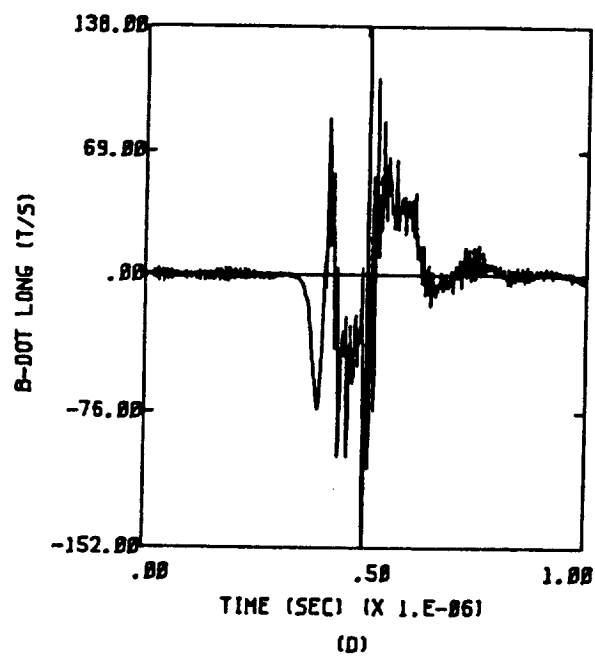
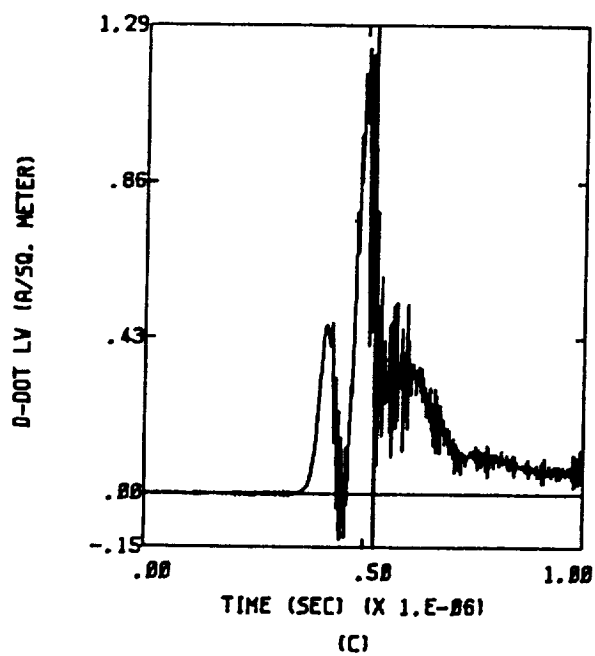
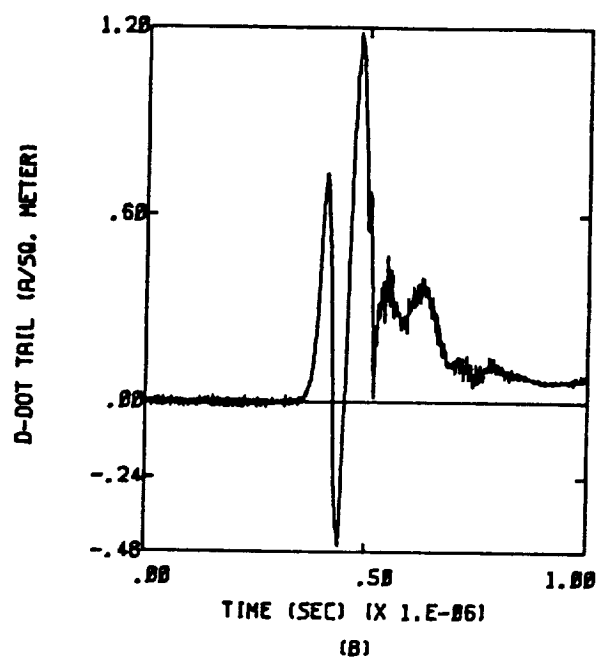
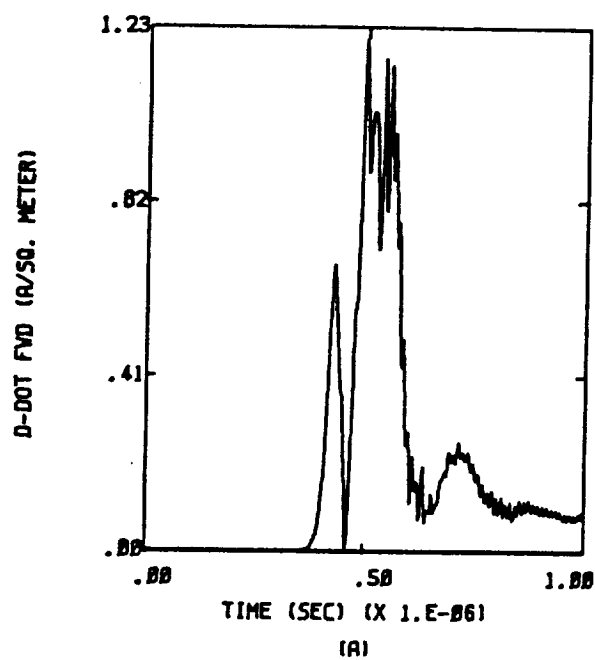


Figure D.23  $-X, Y; Q = -1/2 Q_m; E = 1.3 \times 10^5$  Volts per meter

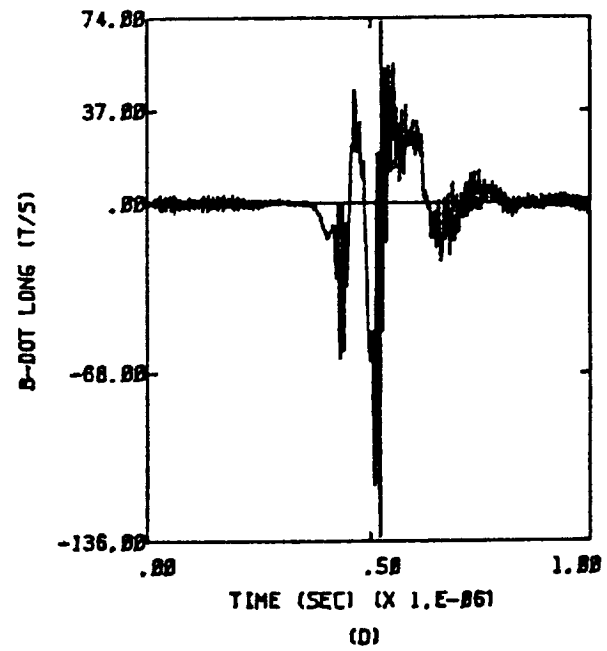
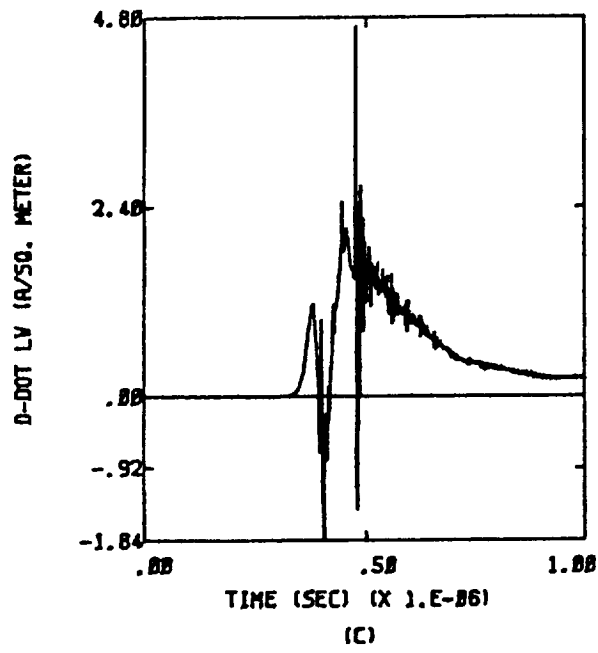
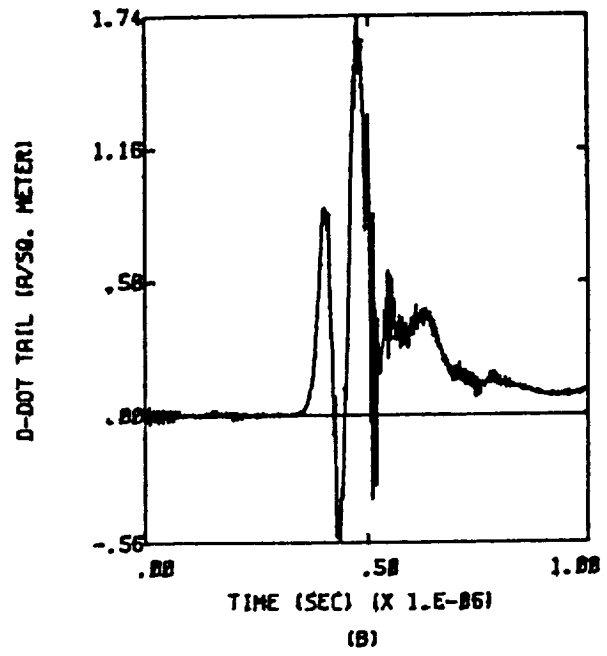
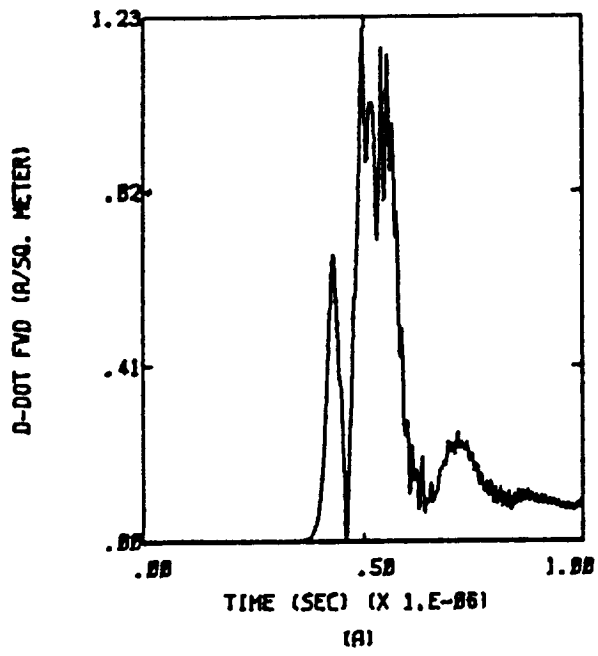


Figure D.24  $-X, -Y; Q = -1/2 Q_m; E = 1.3 \times 10^5$  Volts per meter

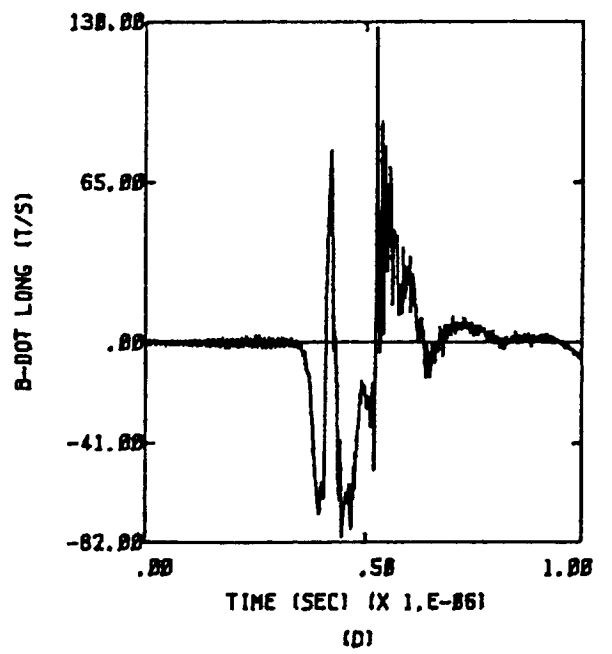
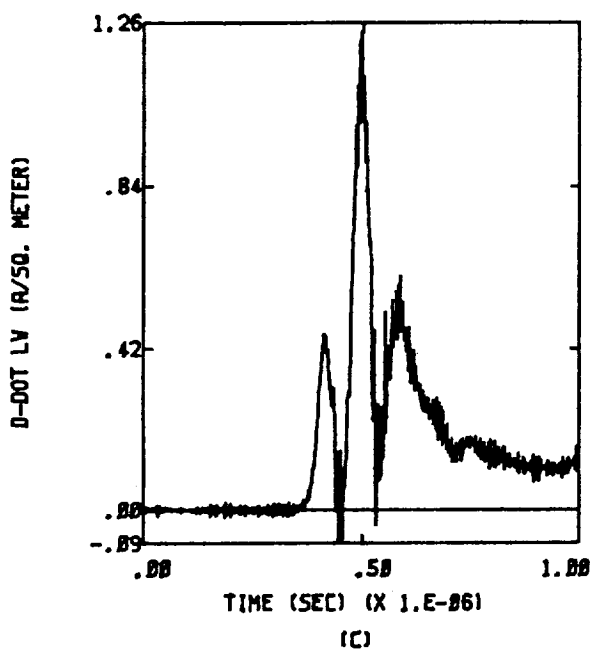
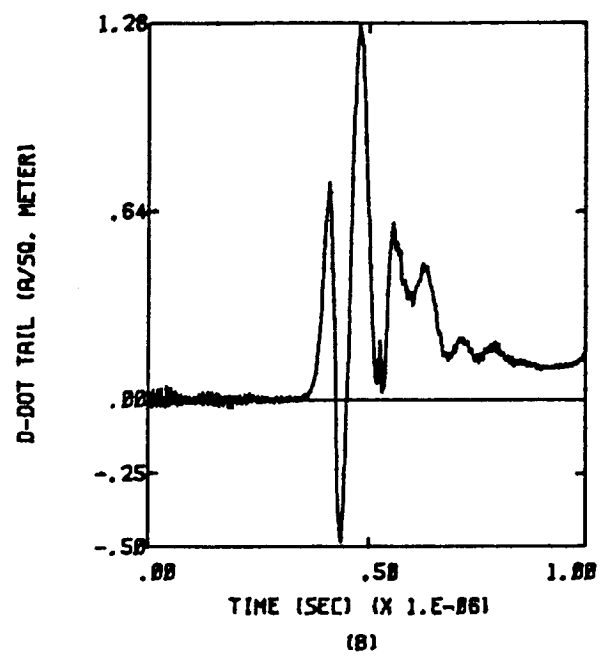
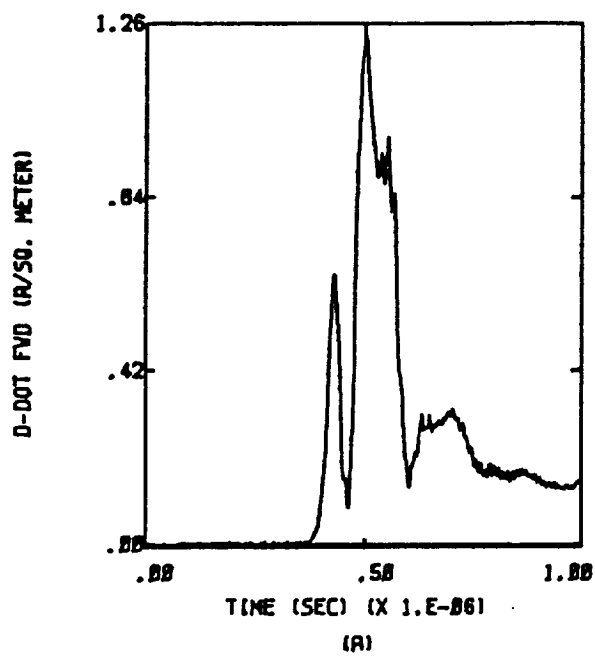


Figure D.25  $Y, -Z; Q = -1/2 Q_m$ ;  $E = 2.0 \times 10^5$  Volts per meter



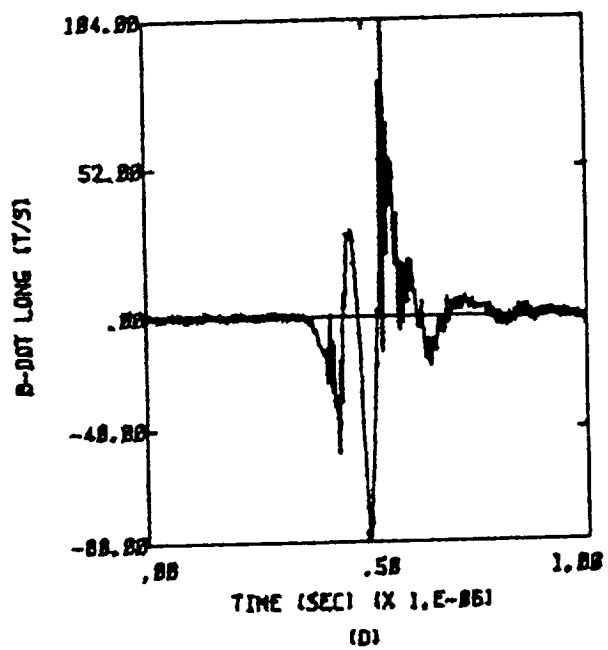
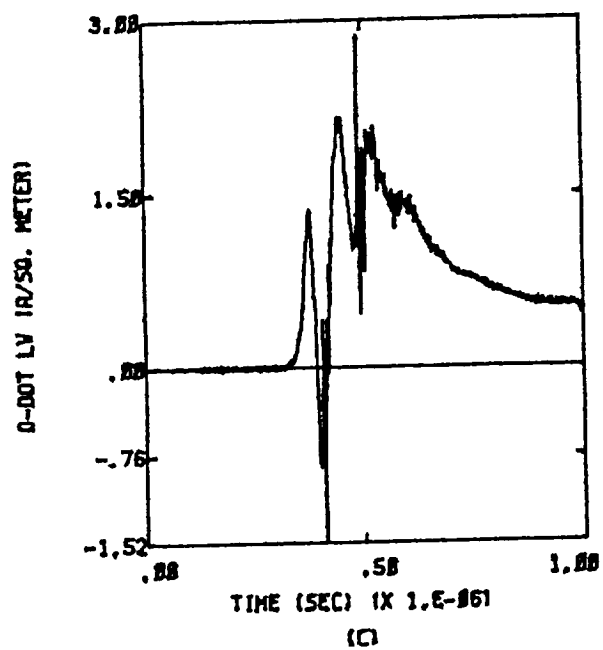
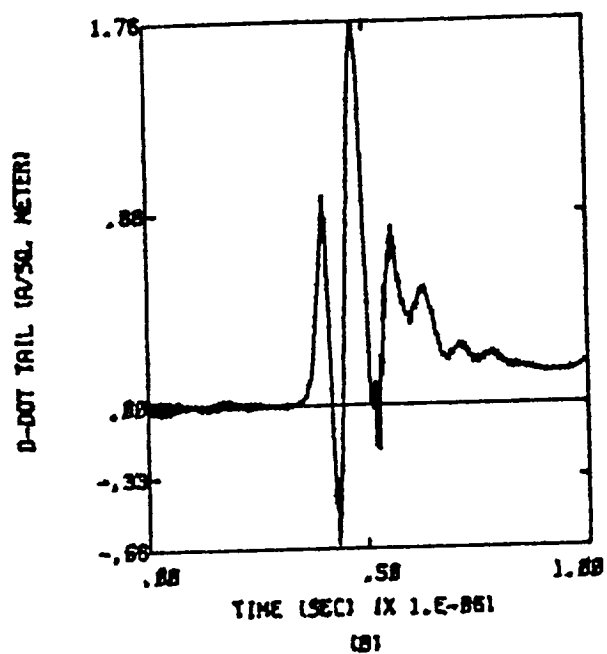
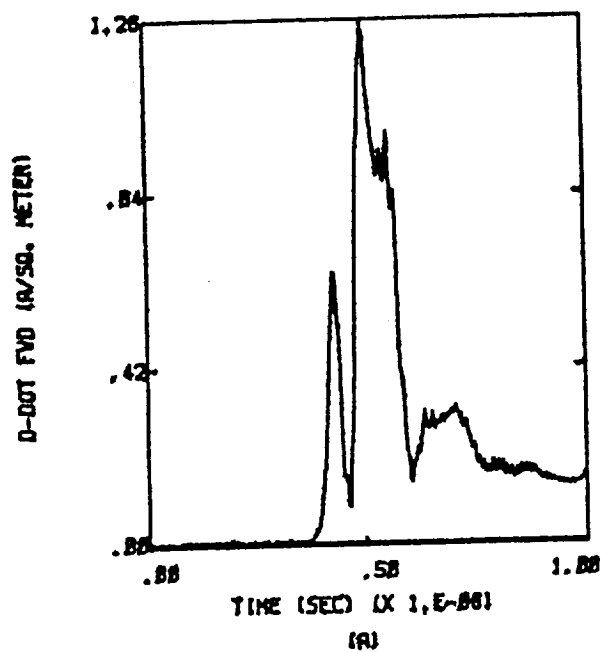


Figure D.26 -Y,-Z;  $Q = -1/2 Q_m$ ;  $E = 2.0 \times 10^5$  Volts per meter

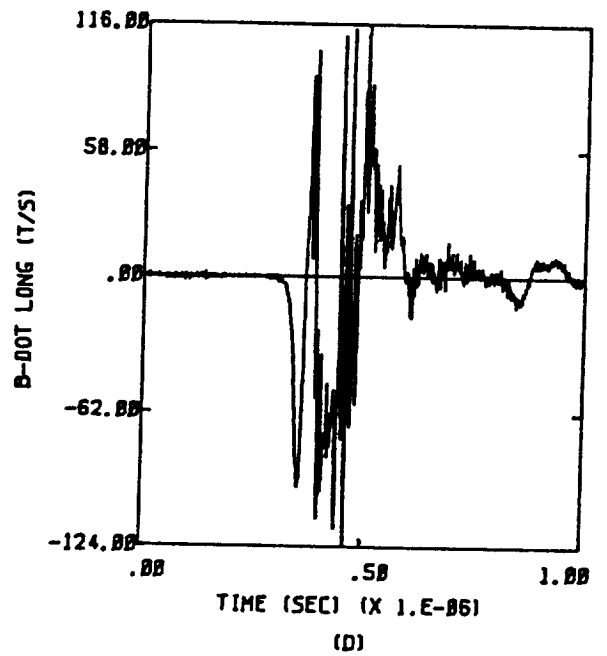
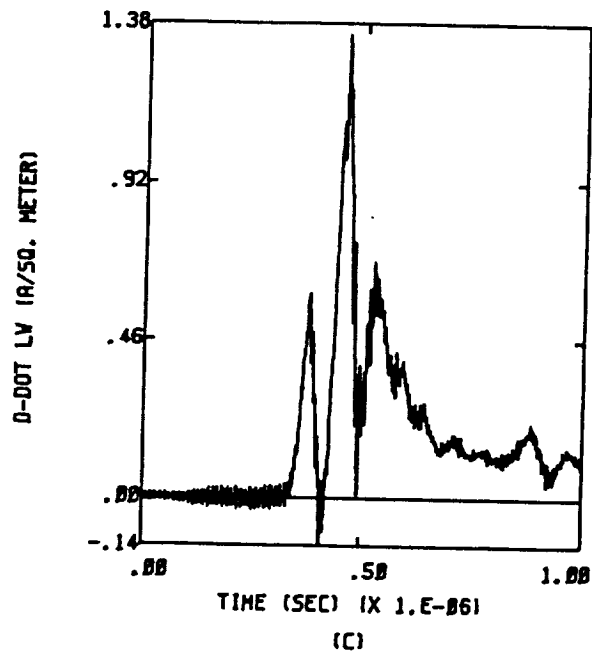
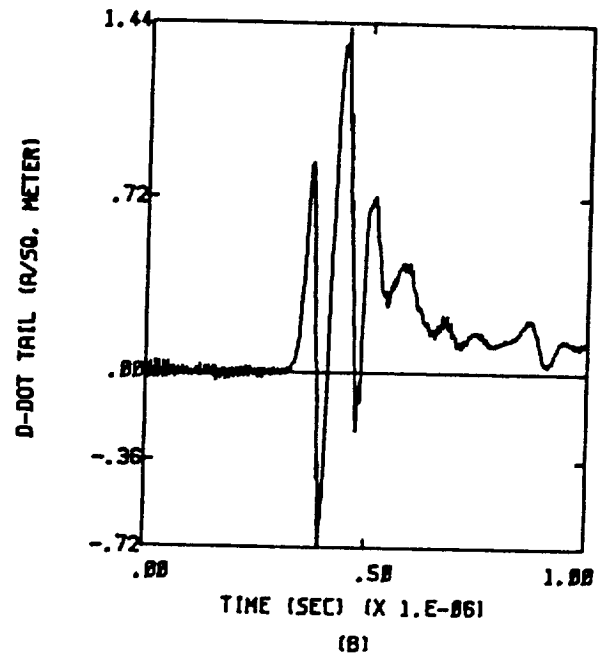
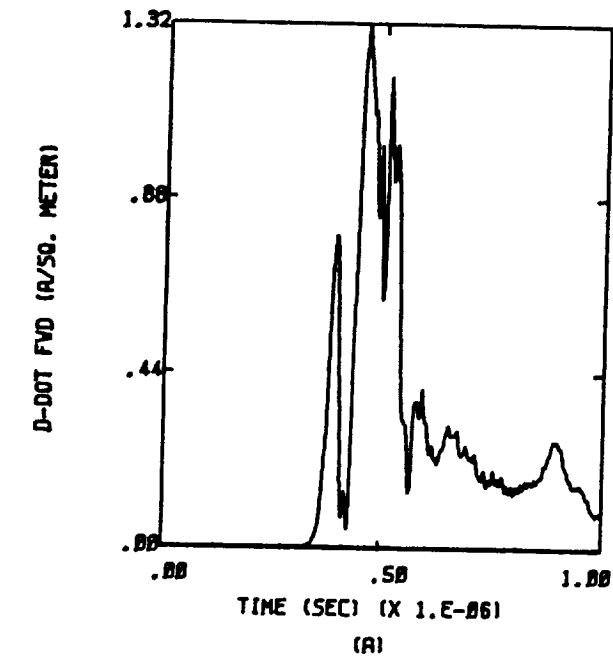


Figure D.27  $Y, Z; Q = -1/2 Q_m; E = 2.4 \times 10^5$  Volts per meter

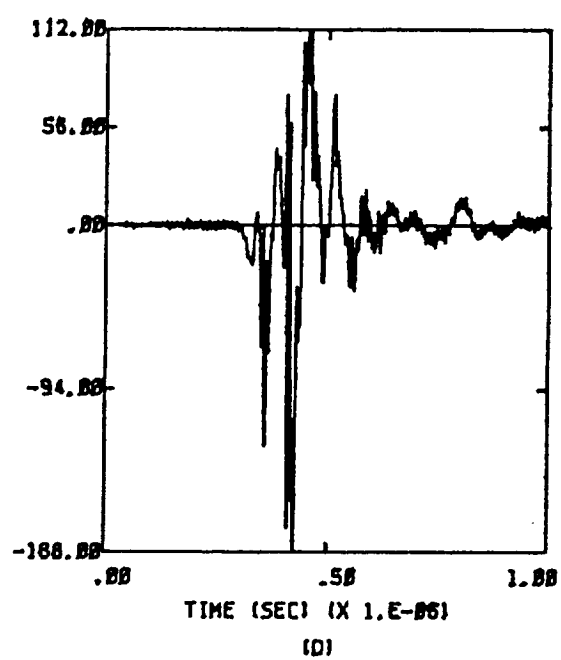
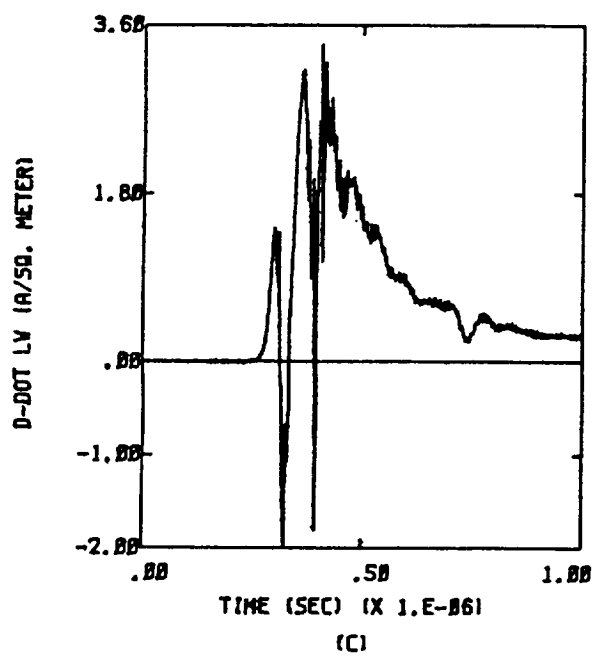
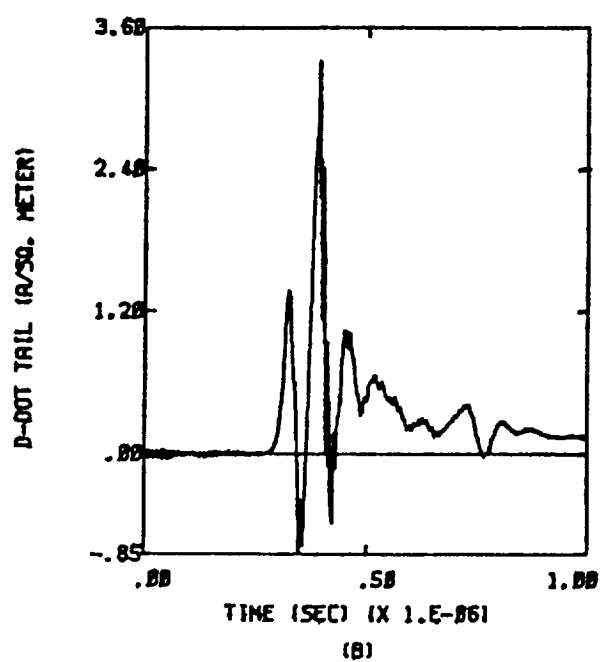
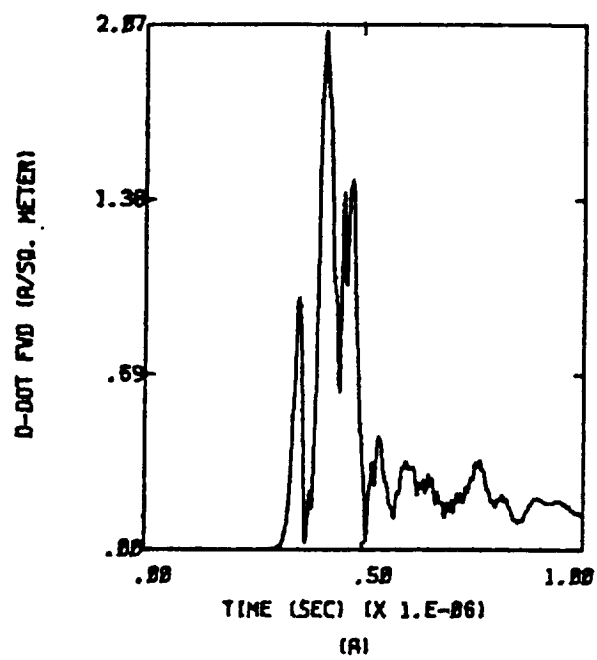


Figure D.28  $-Y, Z$ ;  $Q = -1/2 Q_m$ ;  $E = 2.5 \times 10^5$  Volts per meter

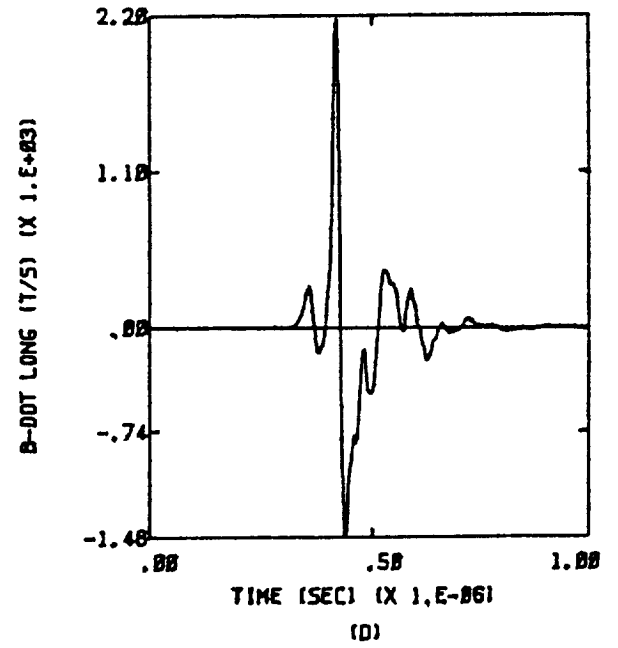
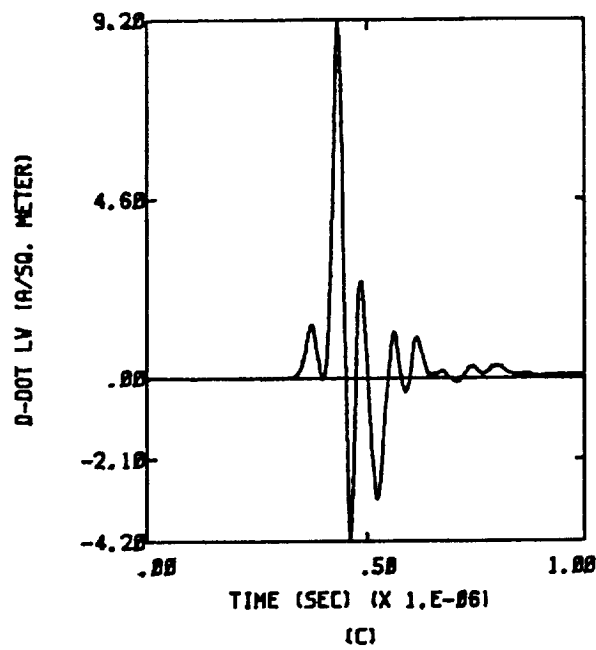
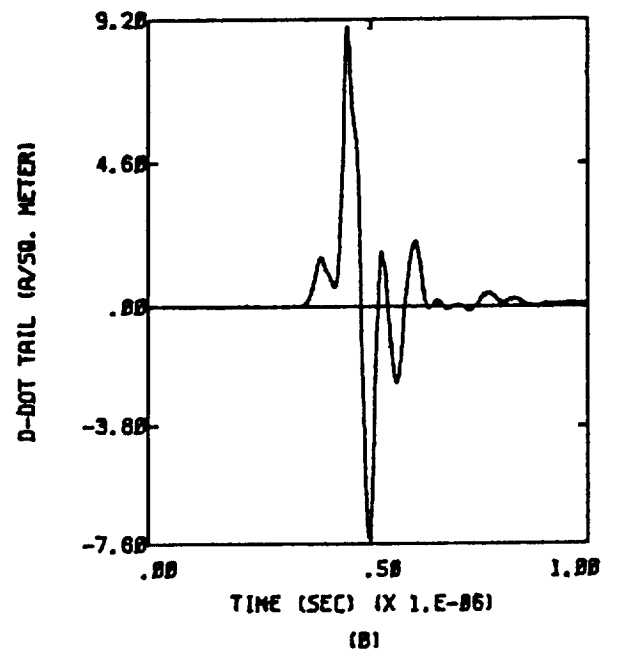
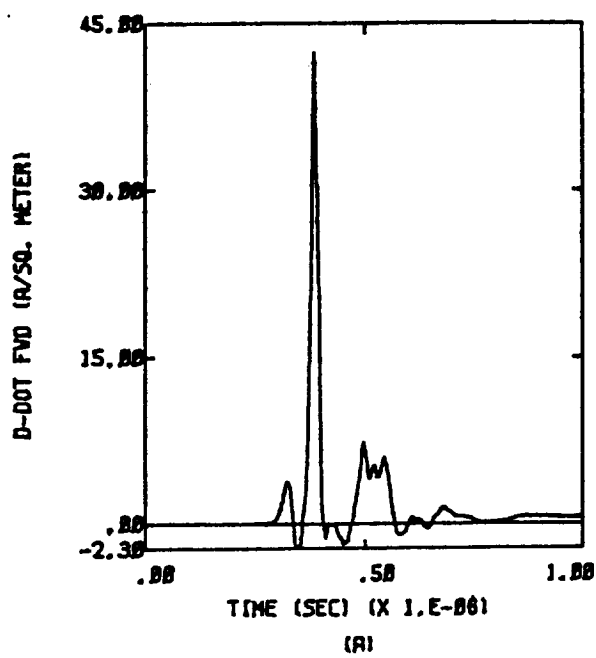


Figure D.29  $X, -Z$ ;  $Q = -1/2 Q_m$ ;  $E = 1.3 \times 10^5$  Volts per meter

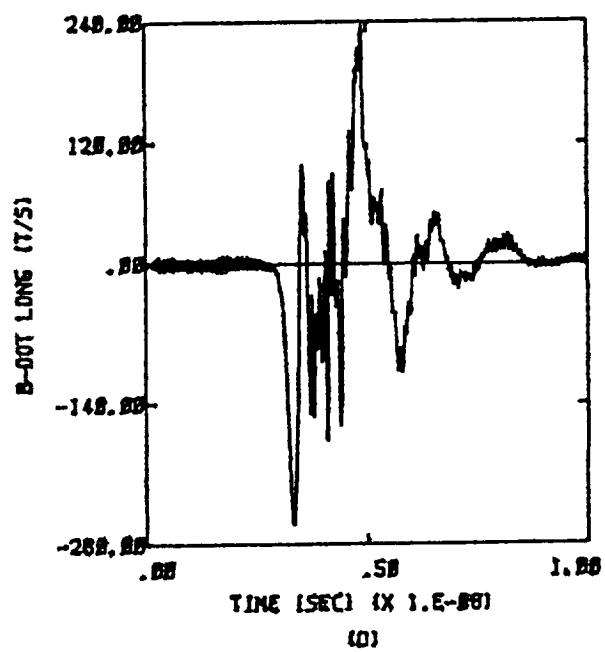
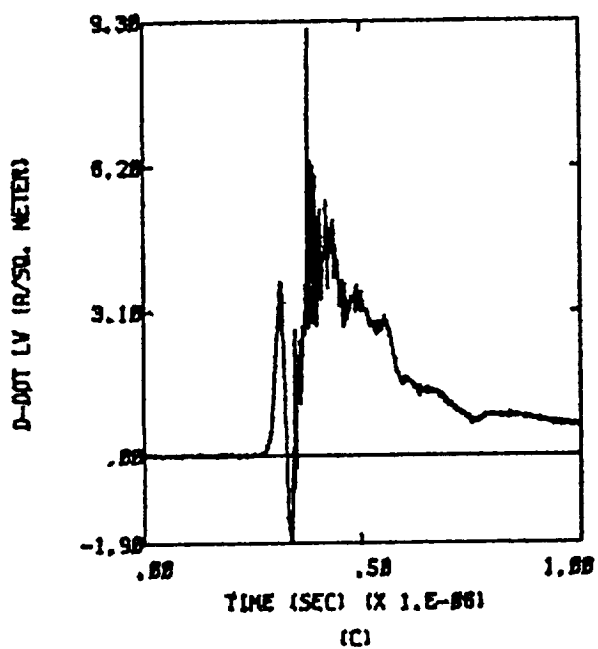
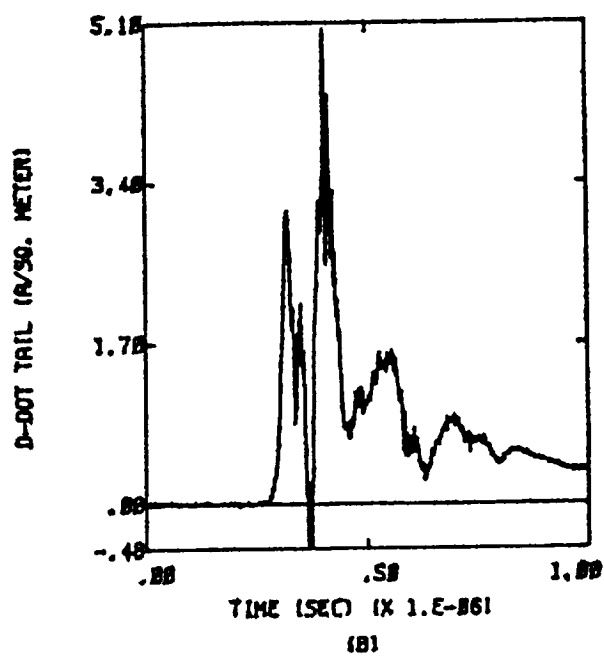
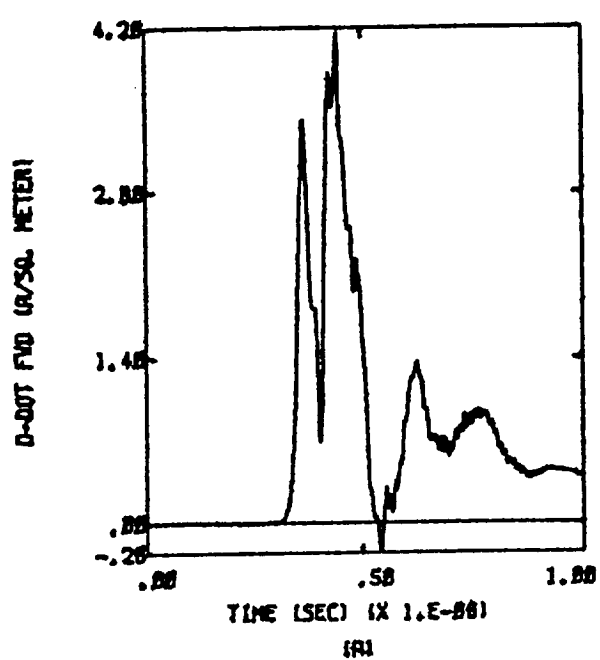


Figure D.30  $-X, -Z; Q = -1/2 Q_m$ ;  $E = 2.7 \times 10^5$  Volts per meter

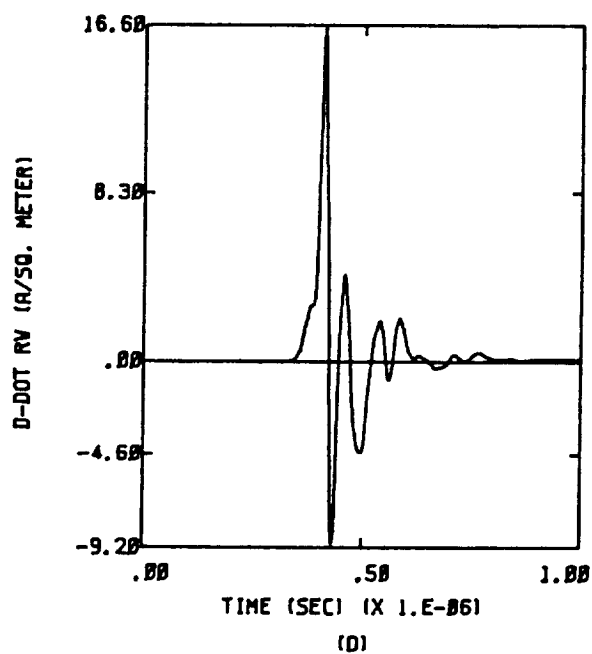
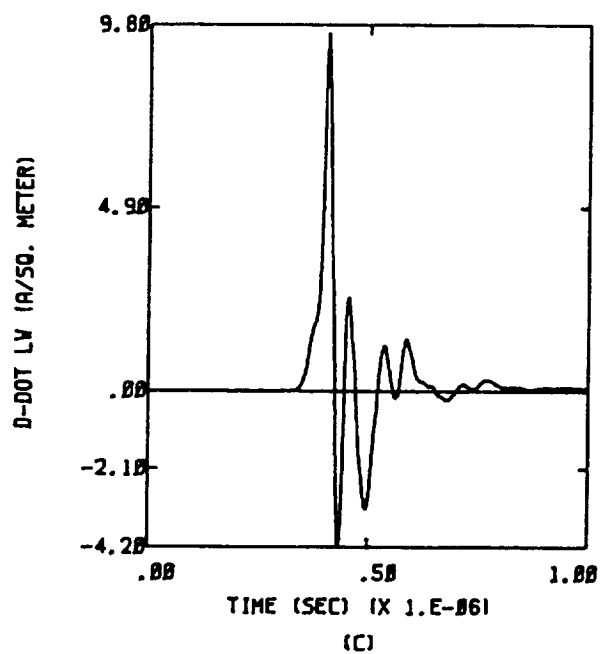
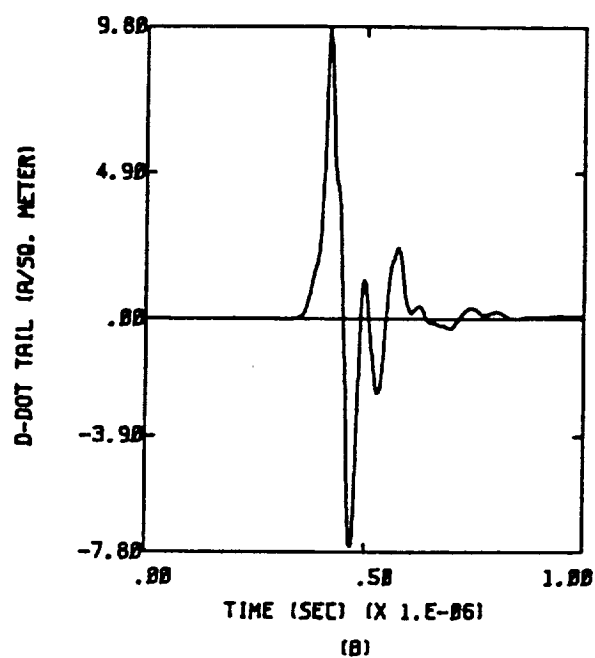
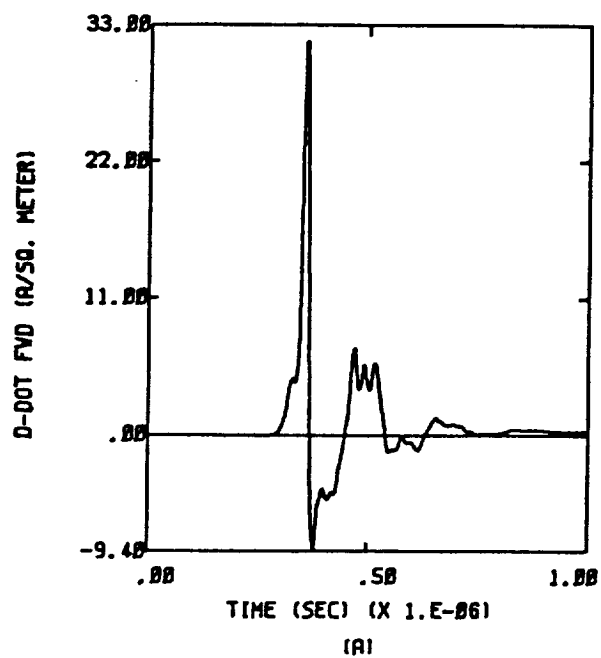


Figure D.31a  $X, Z$ ;  $Q = -1/2 Q_m$ ;  $E = 1.7 \times 10^5$  Volts per meter

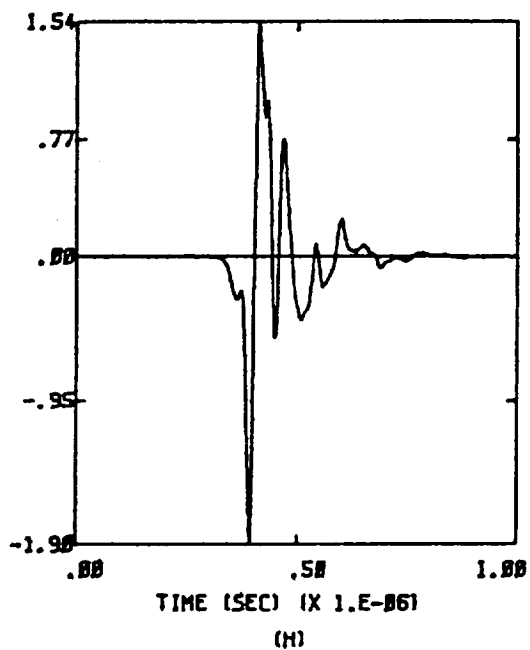
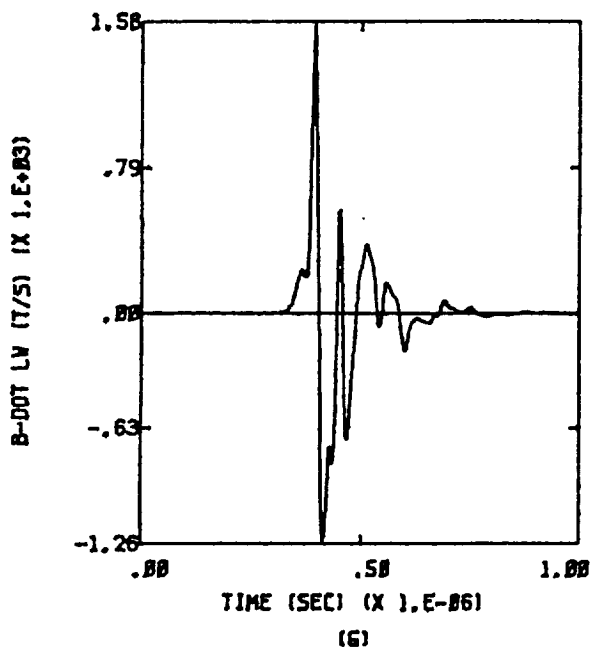
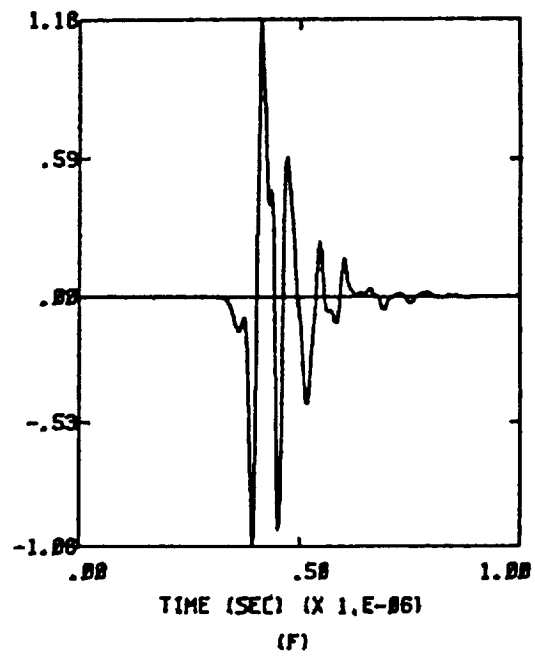
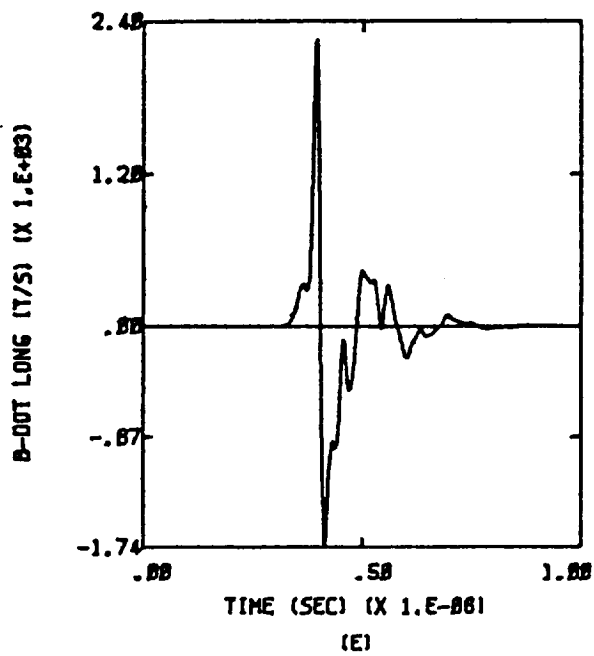


Figure D.31b  $X, Z$ ;  $Q = -1/2 Q_m$ ;  $E = 1.7 \times 10^5$  Volts per meter

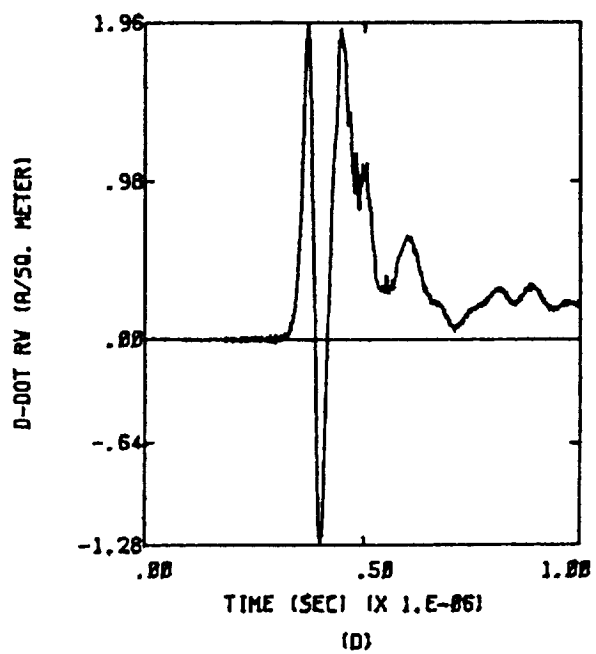
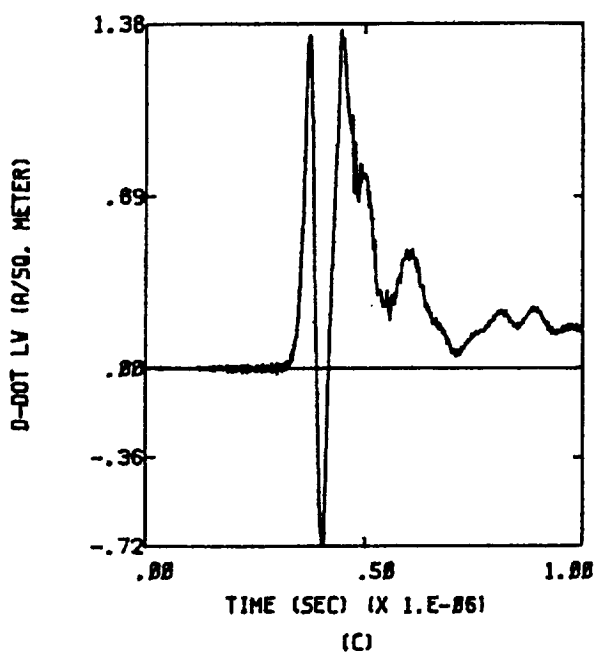
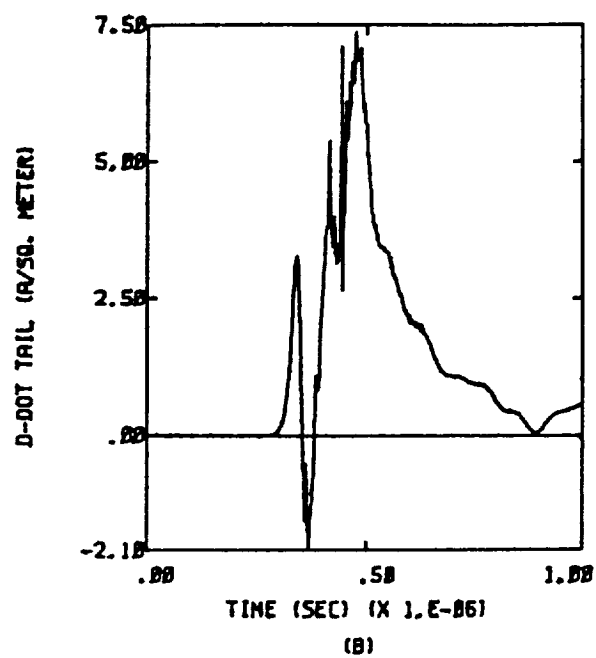
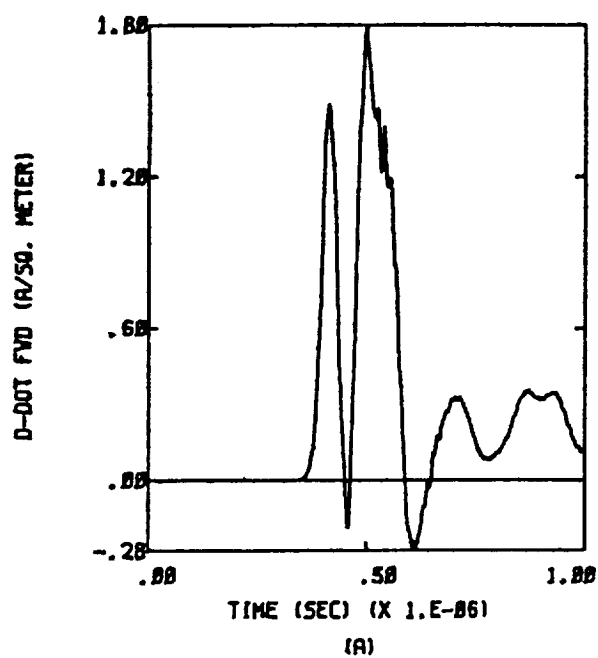


Figure D.32a  $-X, Z$ ;  $Q = -1/2 Q_m$ ;  $E = 1.5 \times 10^5$  Volts per meter



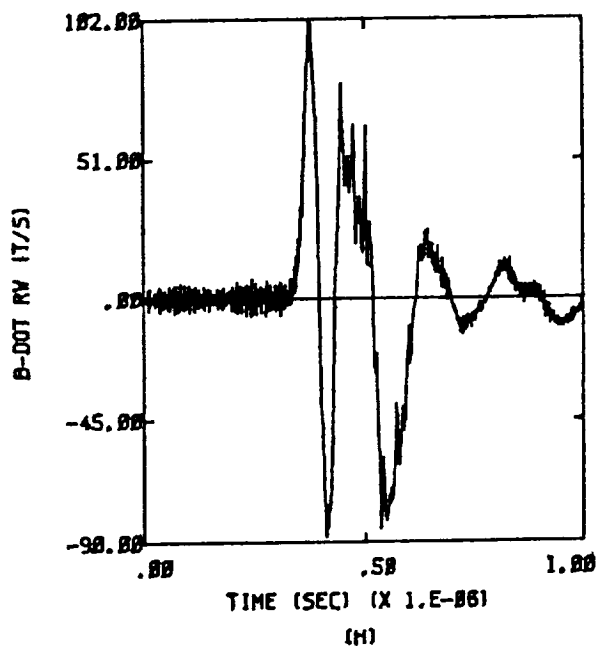
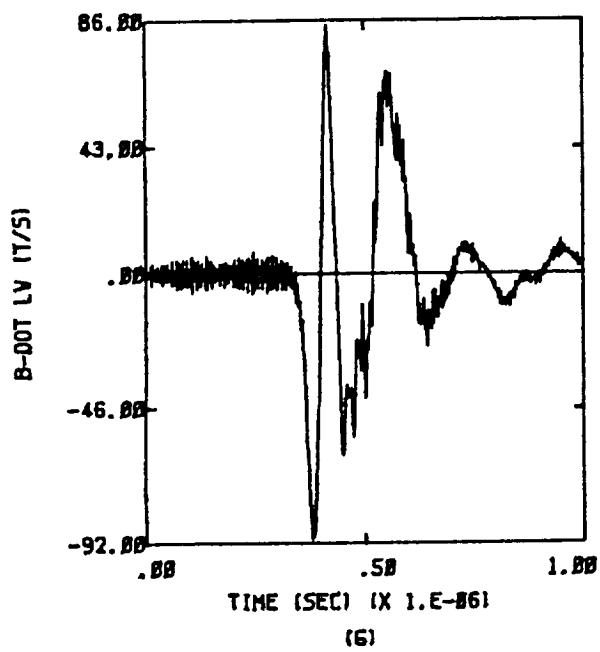
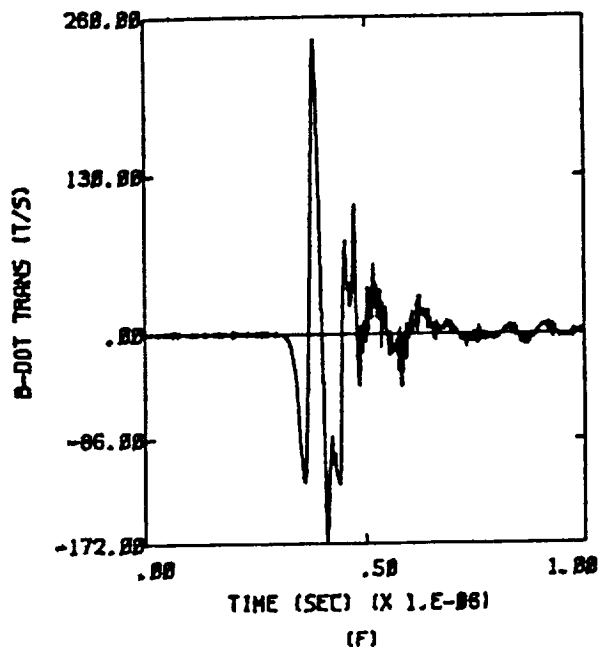
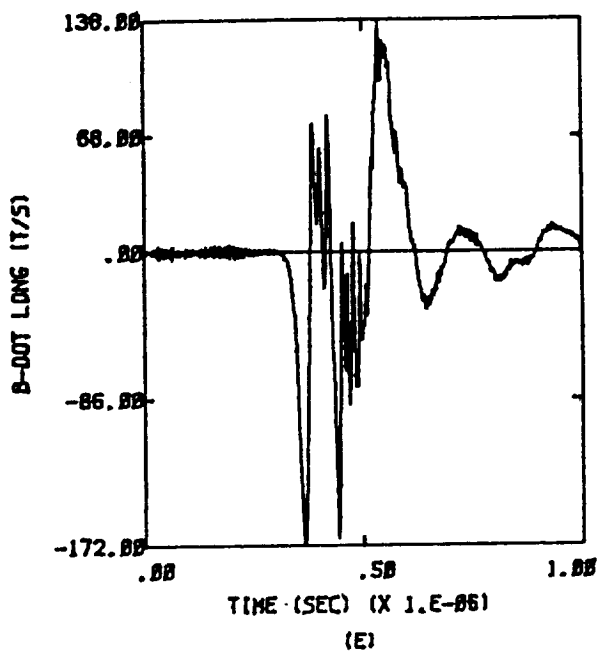


Figure D.32b  $-X, Z$ ;  $Q = -1/2 Q_m$ ;  $E = 1.5 \times 10^5$  Volts per meter

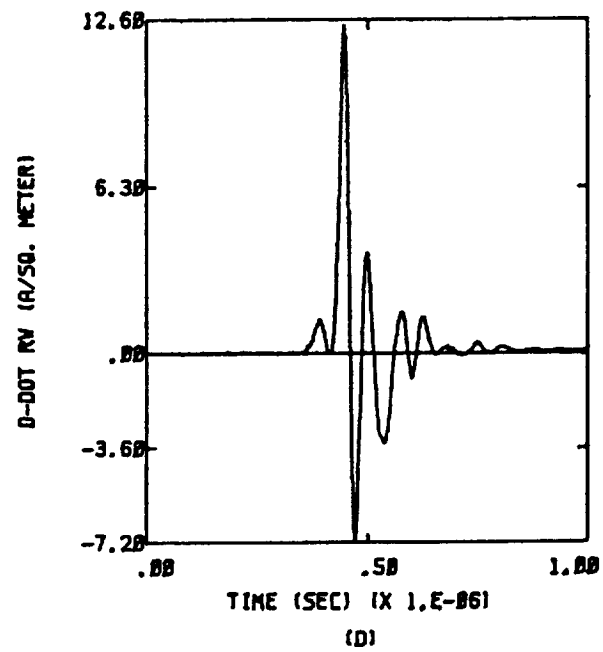
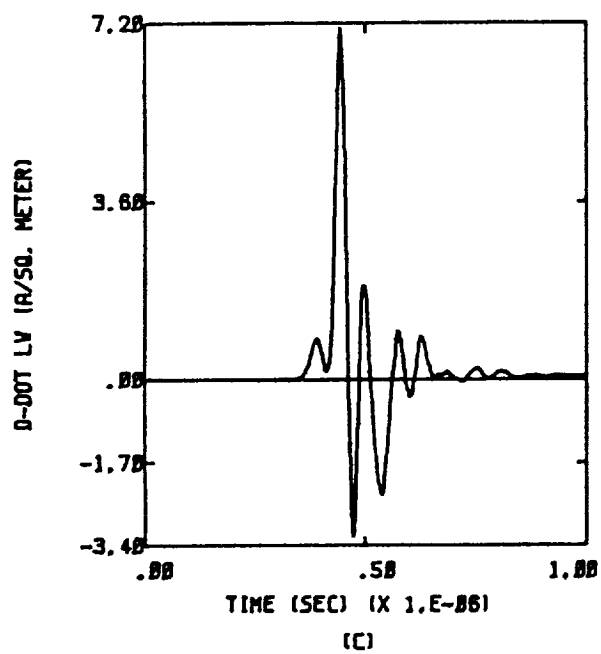
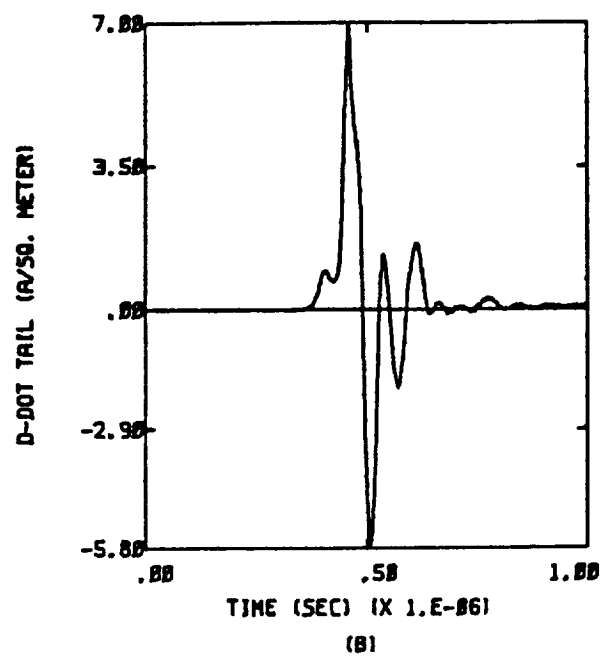
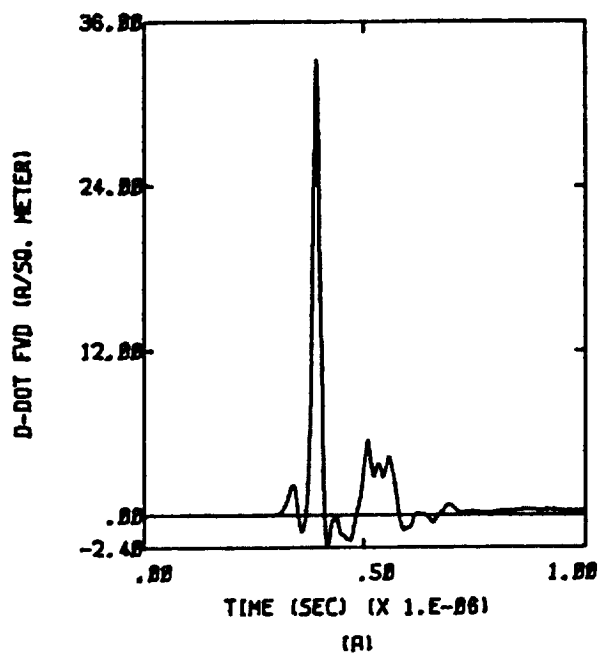


Figure D.33a  $X, Y, -Z; Q = -1/2 Q_m; E = 1.5 \times 10^5$  Volts per meter

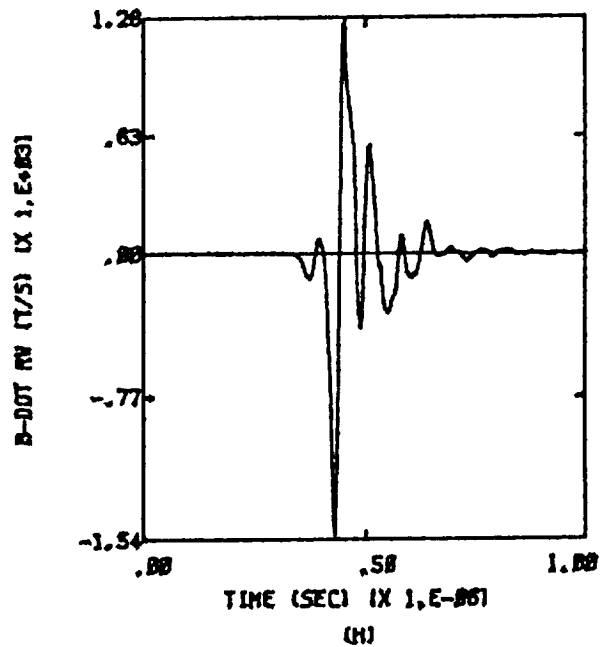
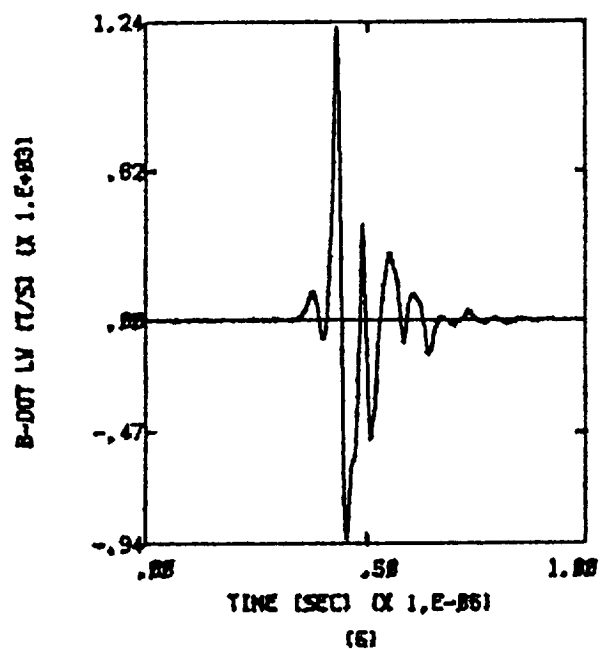
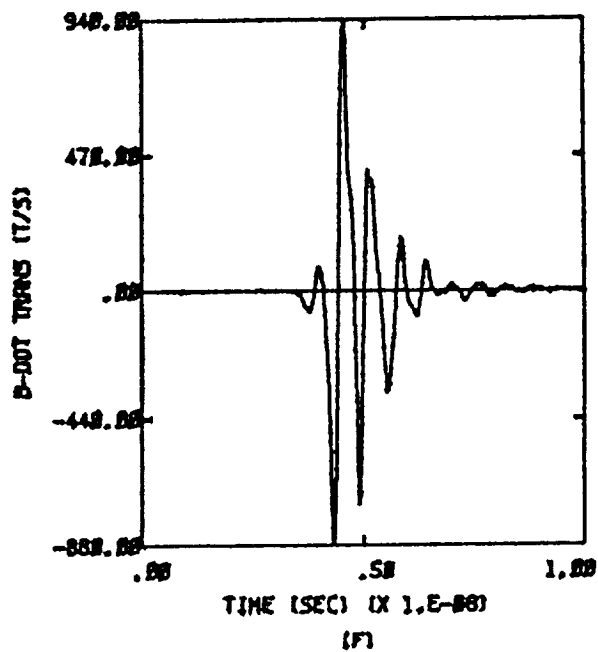
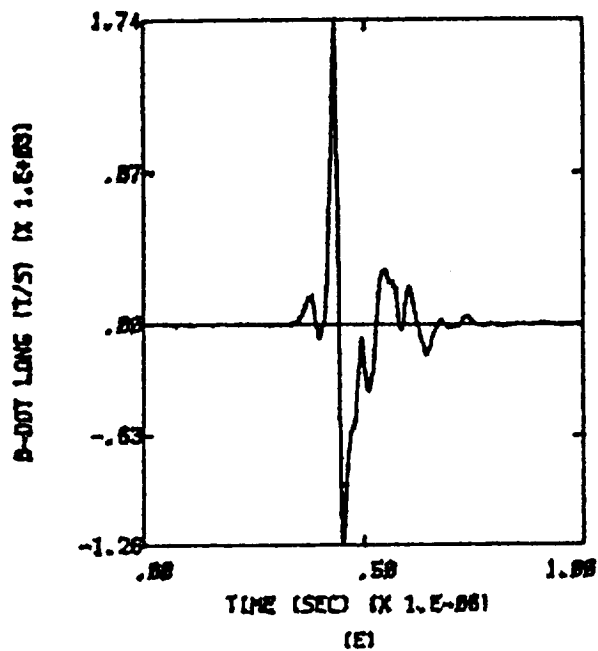


Figure D.33b X,Y,-Z;  $Q = -1/2 Q_m$ ;  $E = 1.5 \times 10^5$  Volts per meter

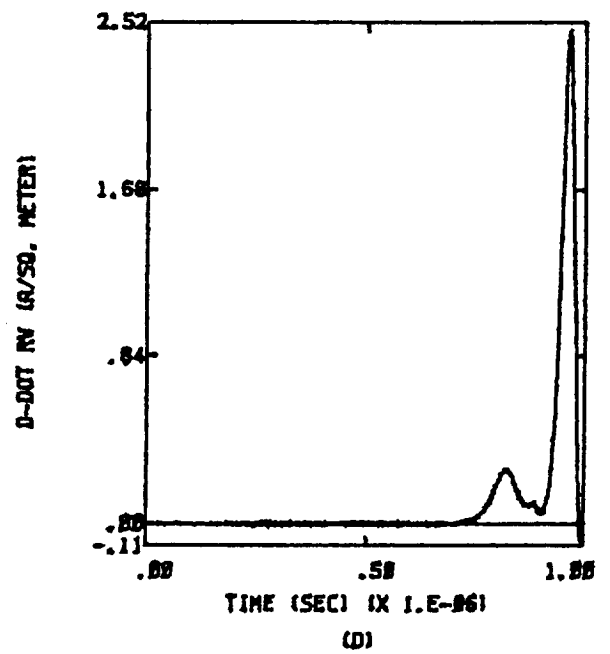
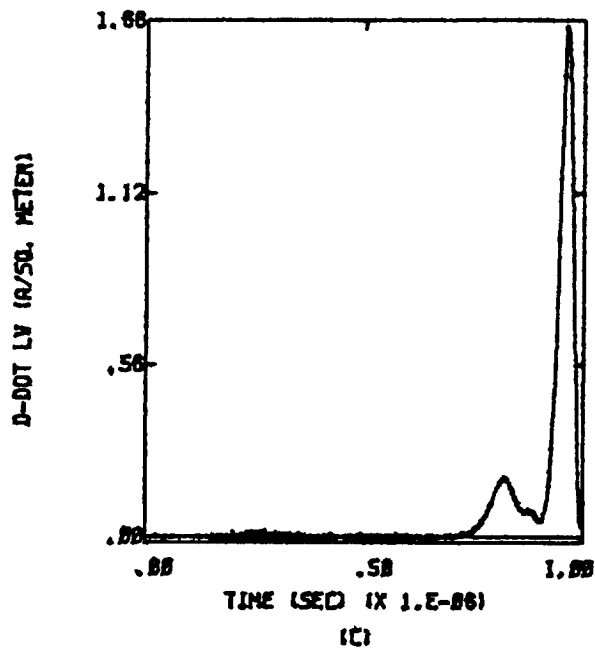
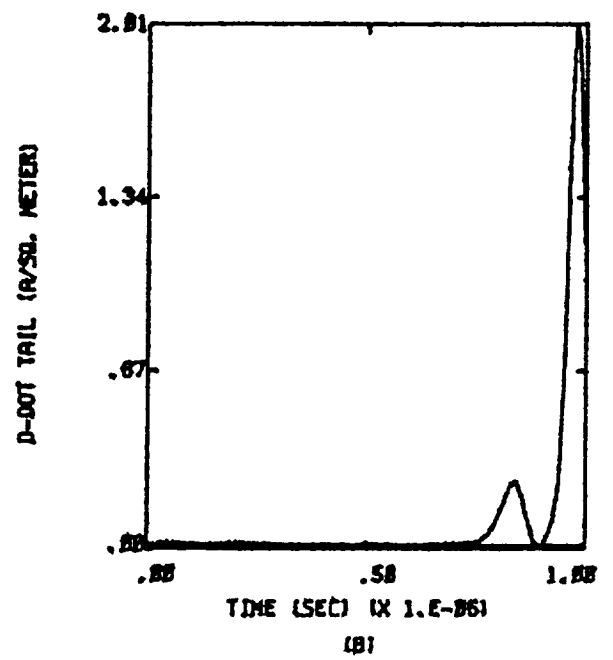
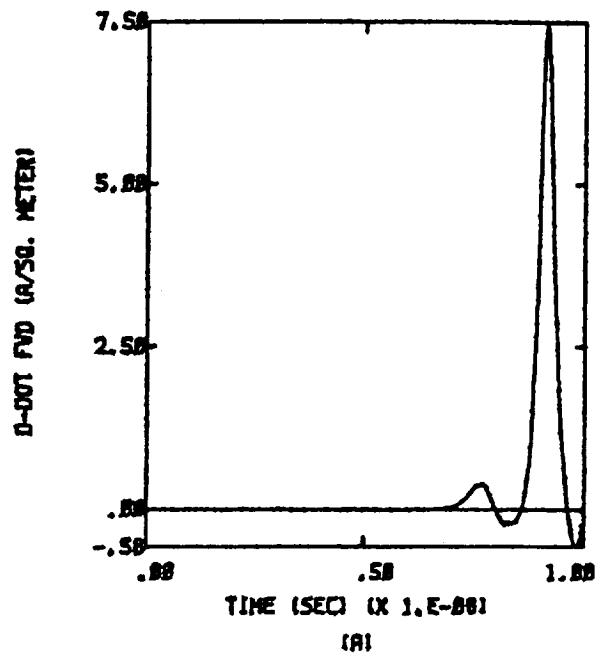


Figure D.34a X,-Y,-Z;  $Q = -1/2 Q_m$ ;  $E = 1.2 \times 10^5$  Volts per meter

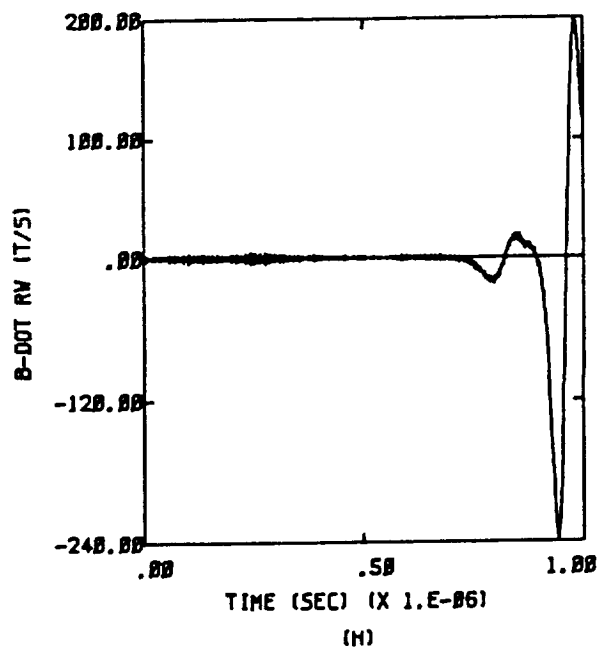
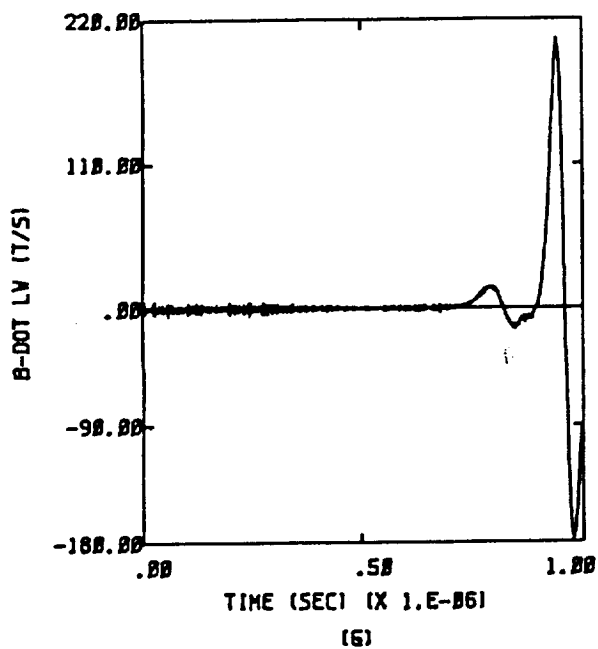
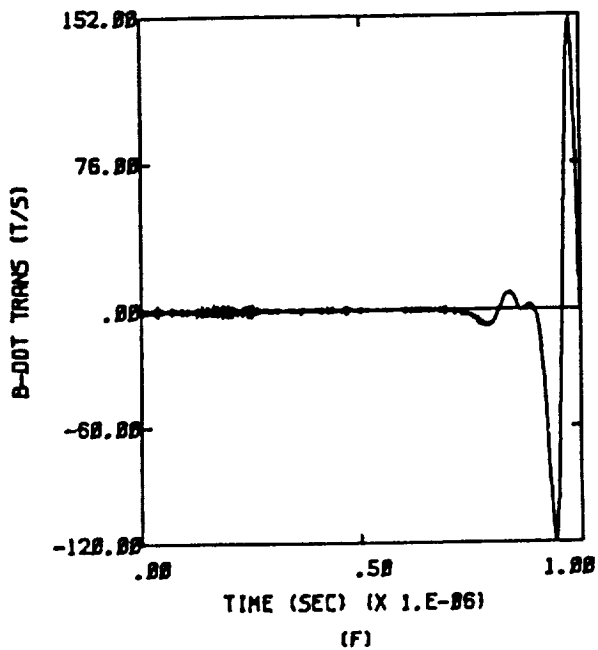
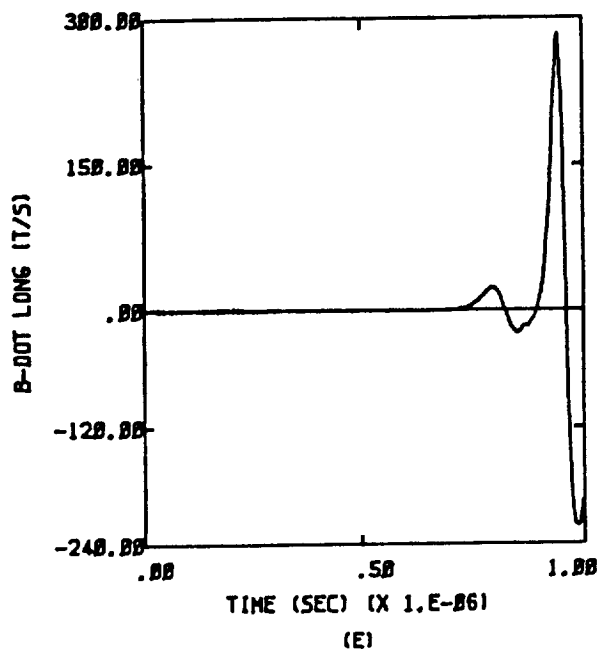


Figure D.34b X,-Y,-Z;  $Q = -1/2 Q_m$ ;  $E = 1.2 \times 10^5$  Volts per meter

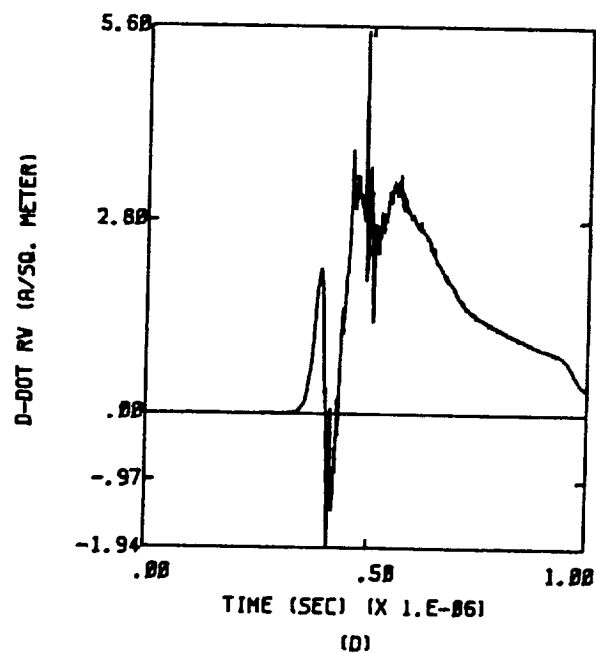
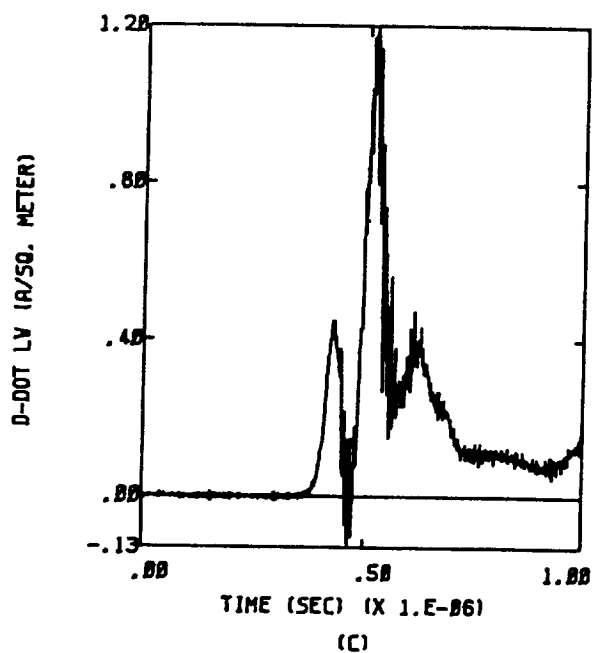
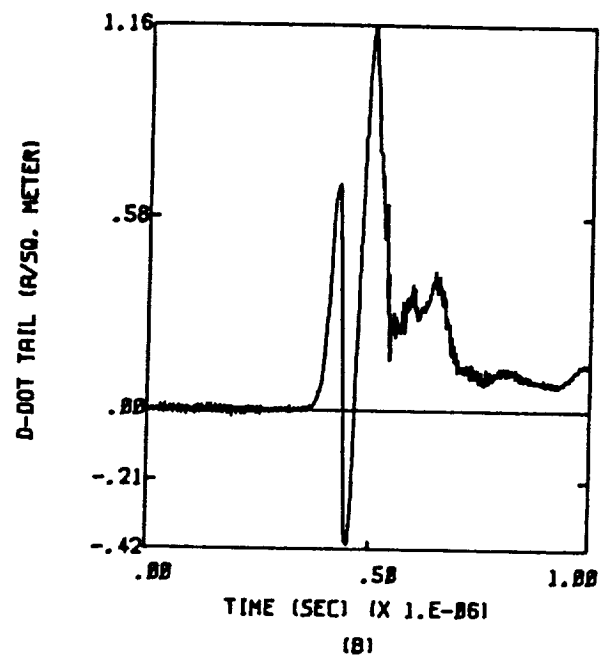
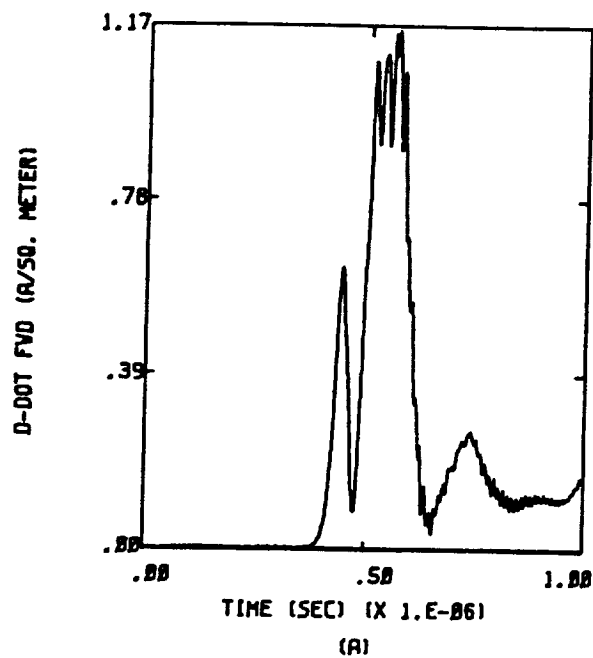


Figure D.35a  $-X, Y, -Z$ ;  $Q = -1/2 Q_m$ ;  $E = 1.5 \times 10^5$  Volts per meter

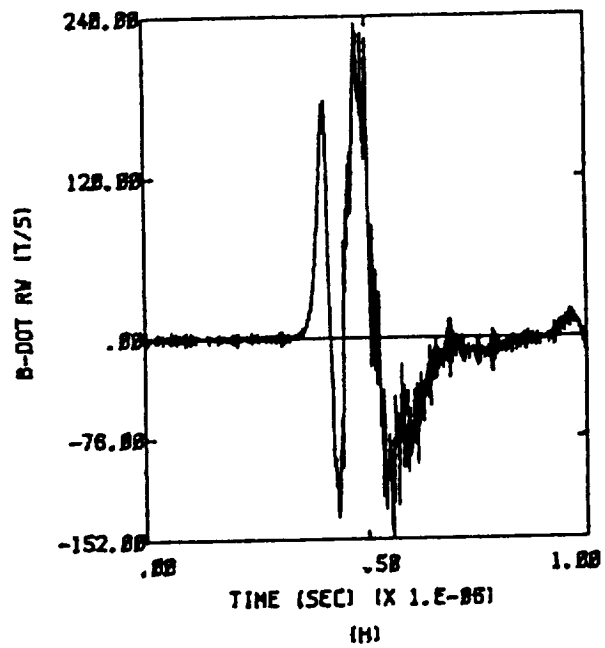
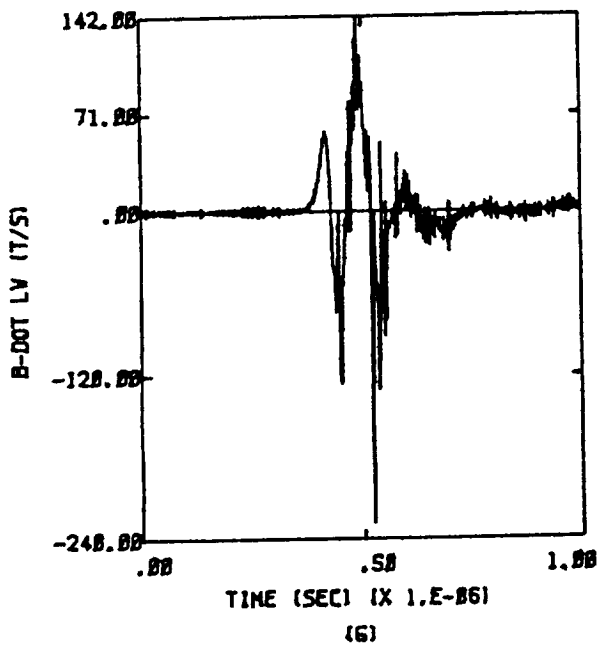
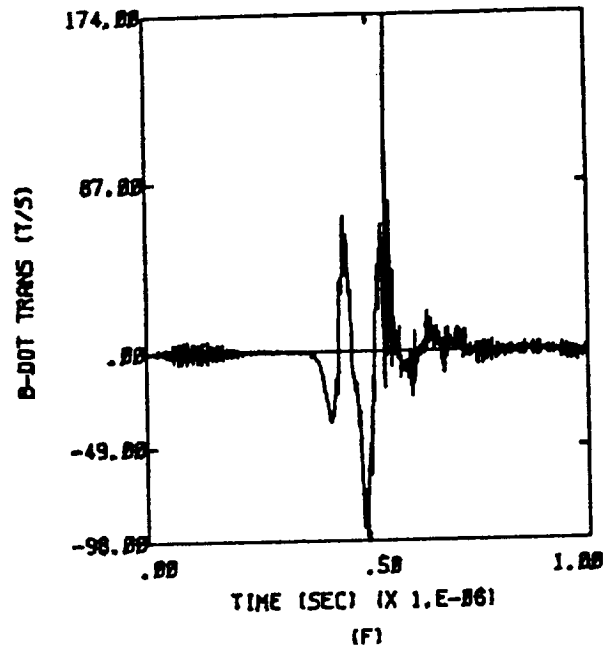
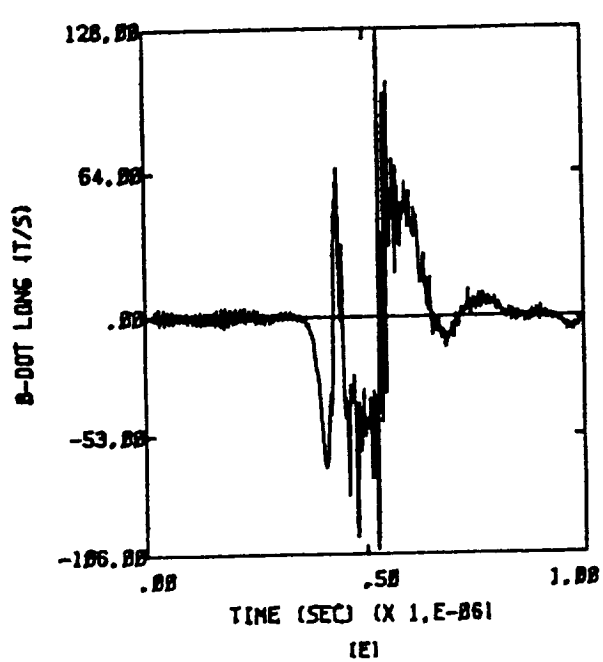


Figure D.35b  $-X, Y, -Z$ ;  $Q = -1/2 Q_m$ ;  $E = 1.5 \times 10^5$  Volts per meter

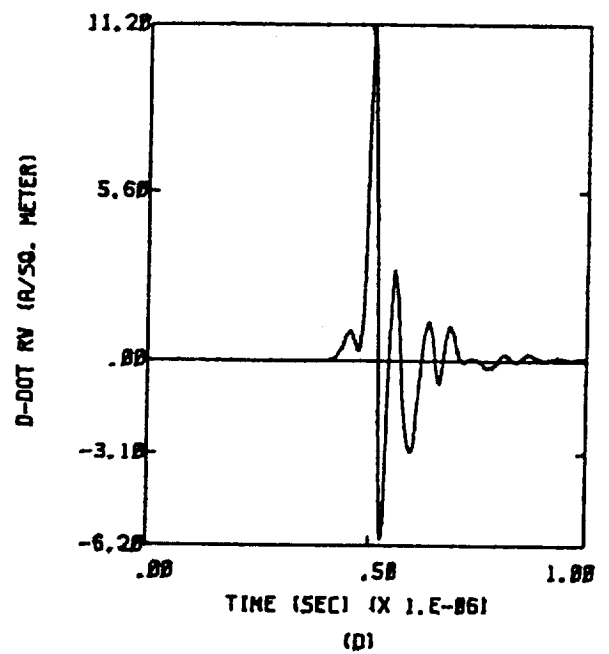
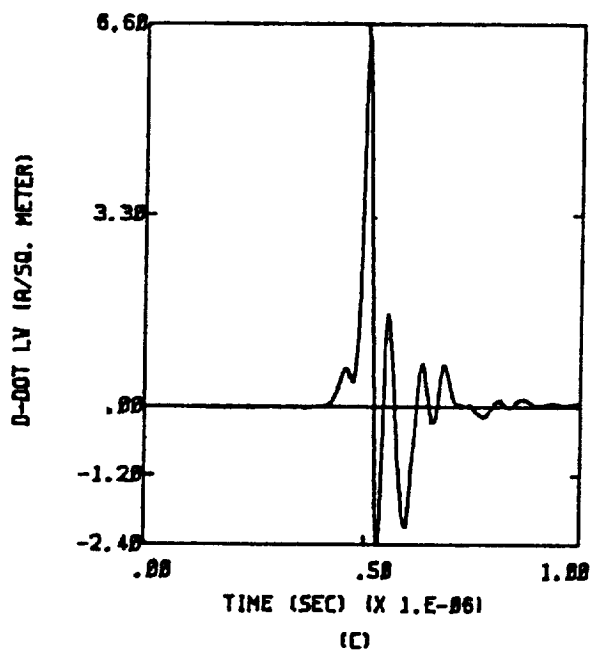
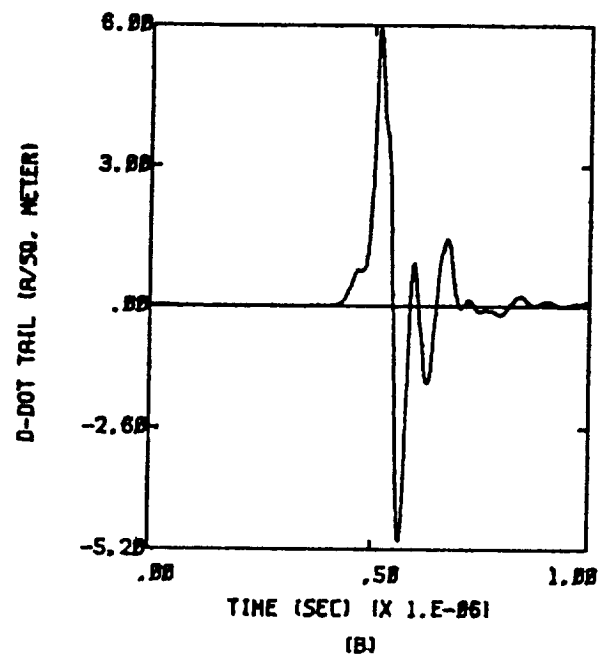
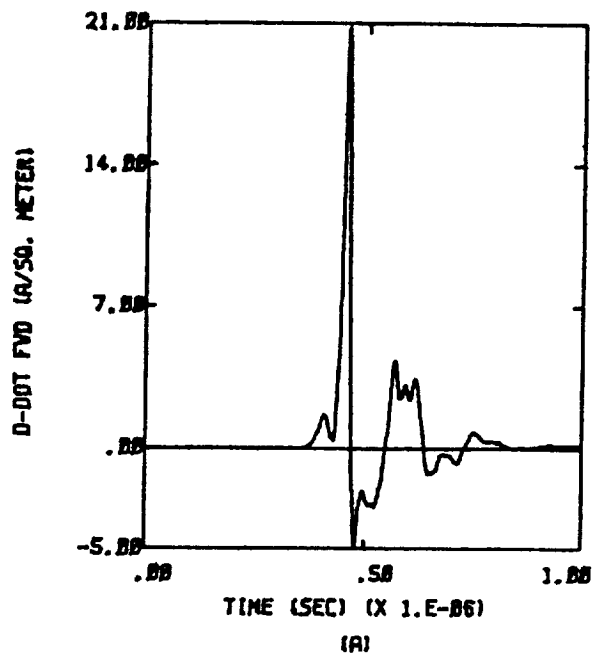


Figure D.36a  $X, Y, Z$ ;  $Q = -1/2 Q_m$ ;  $E = 1.8 \times 10^5$  Volts per meter



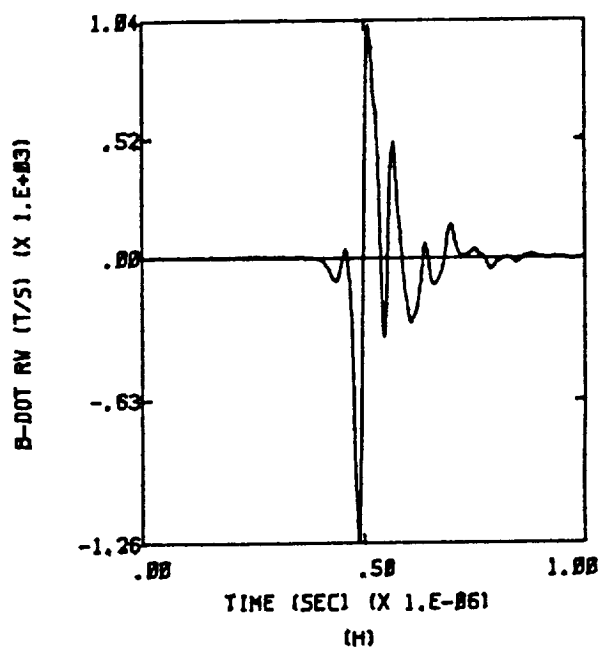
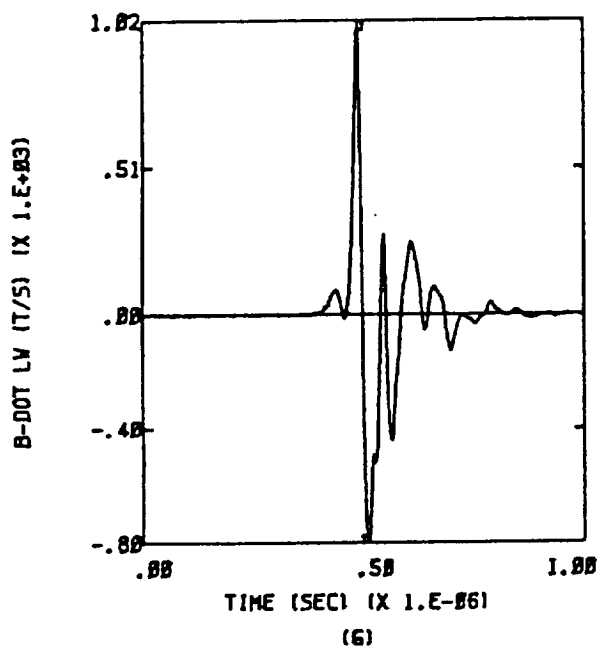
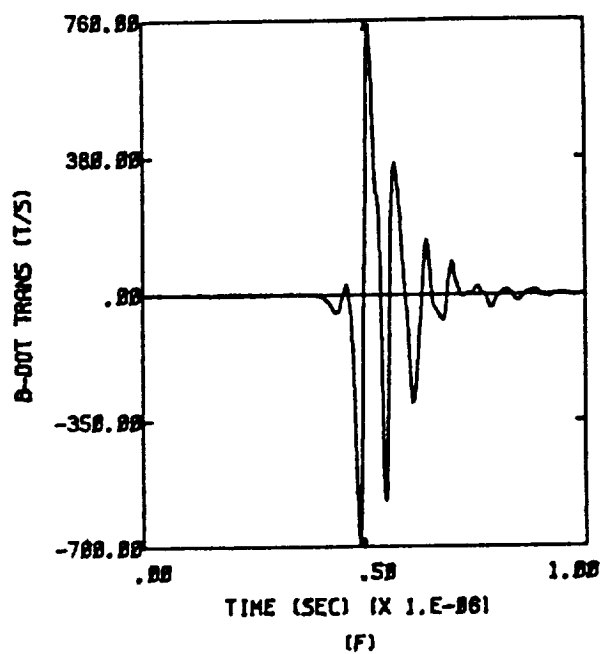
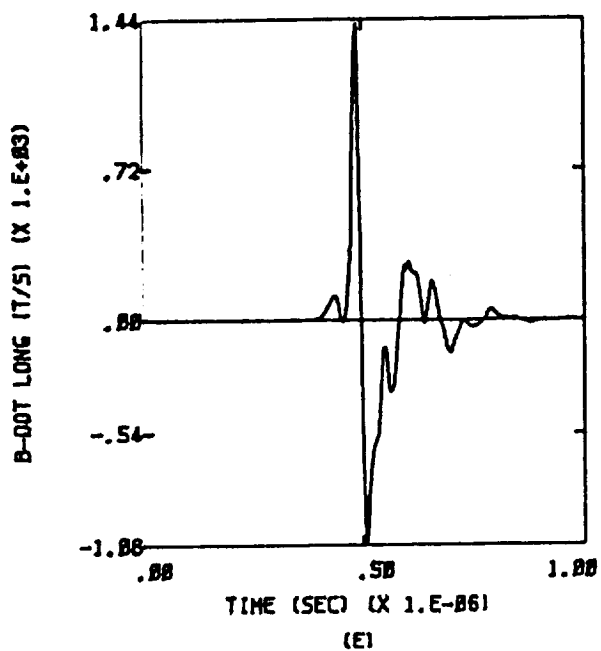


Figure D.36b X,Y,Z;  $Q = -1/2 Q_m$ ;  $E = 1.8 \times 10^5$  Volts per meter

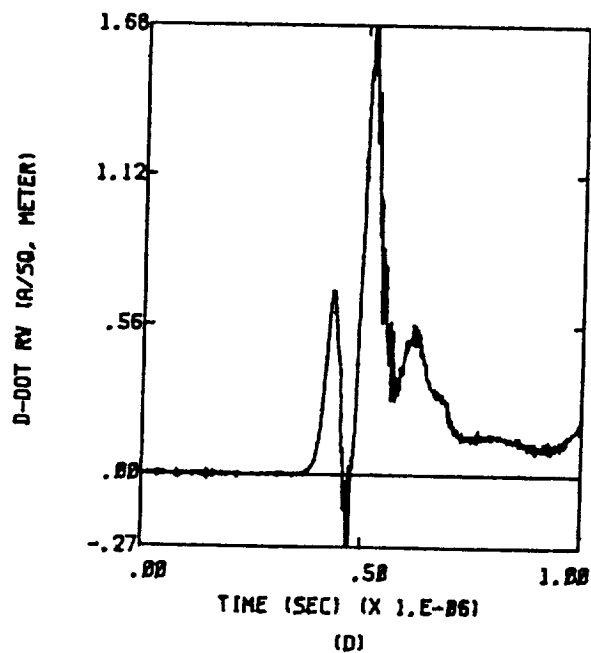
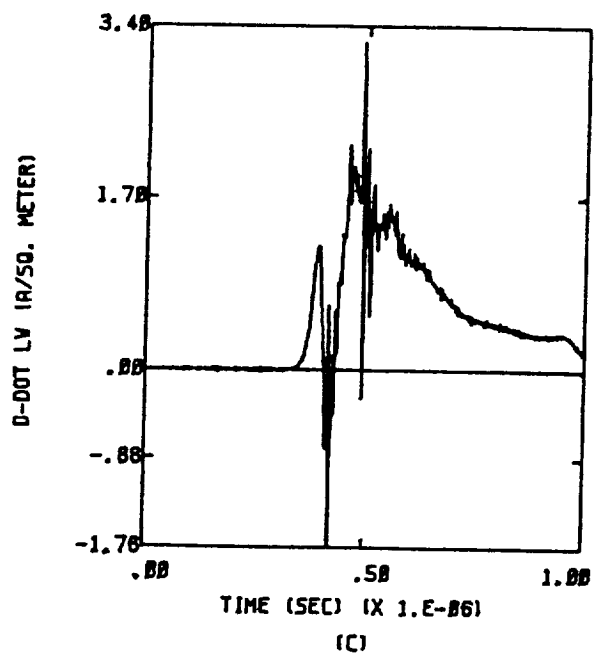
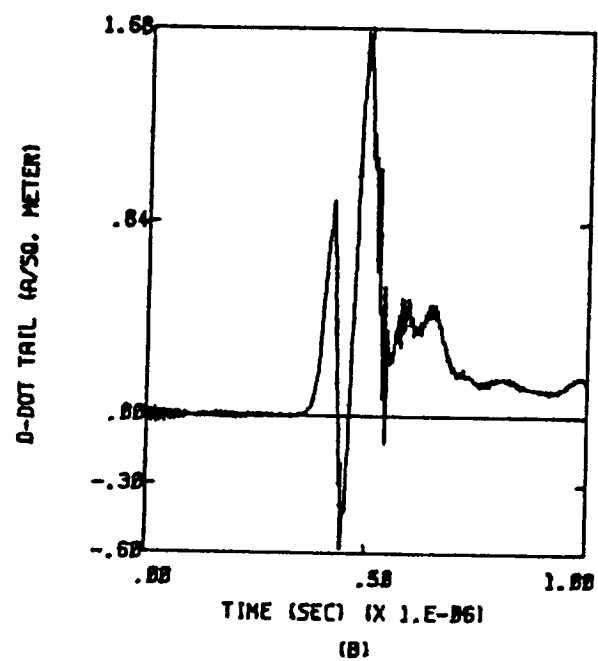
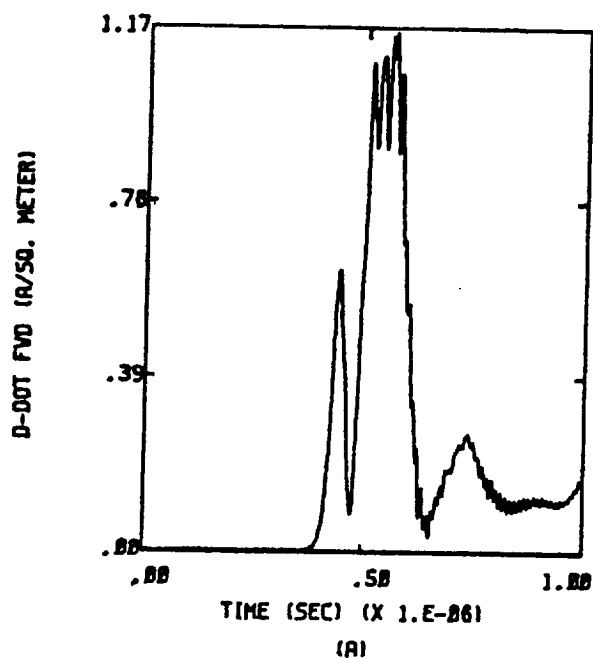


Figure D.37a  $-X, -Y, -Z; Q = -1/2 Q_m; E = 1.5 \times 10^5$  Volts per meter

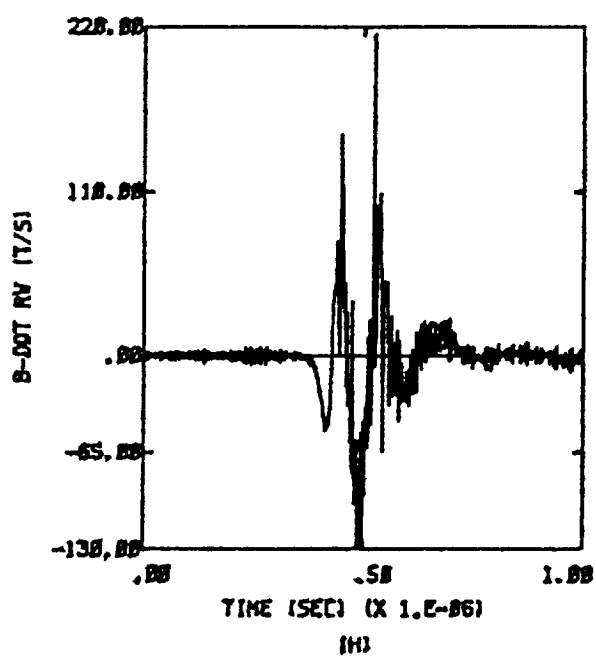
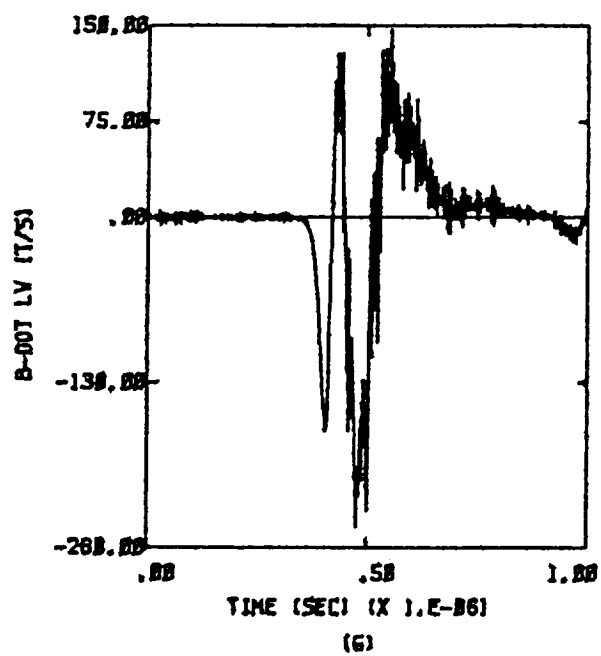
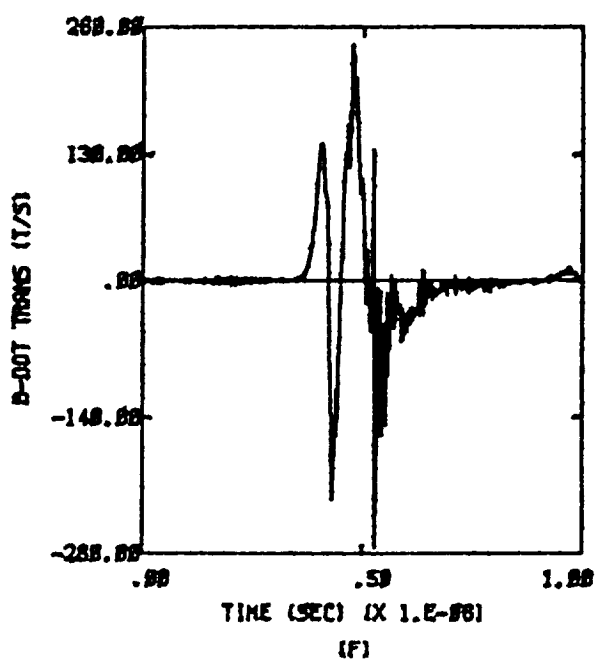
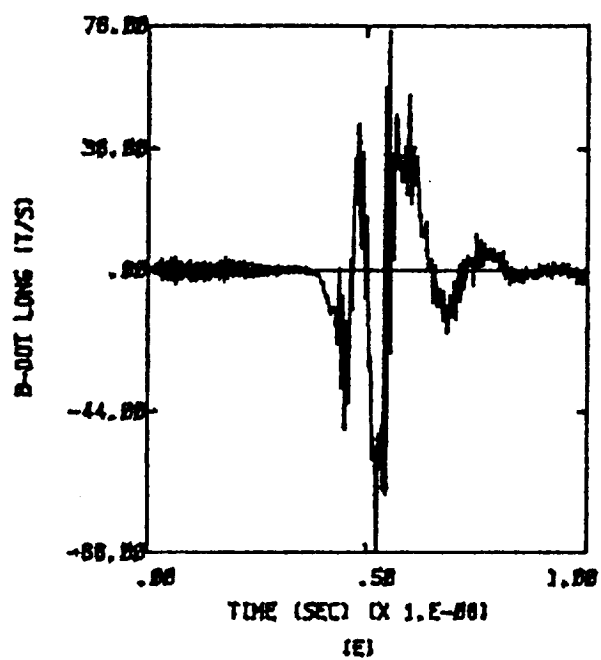


Figure D.37b  $-X, -Y, -Z; Q = -1/2 Q_m; E = 1.5 \times 10^5$  Volts per meter

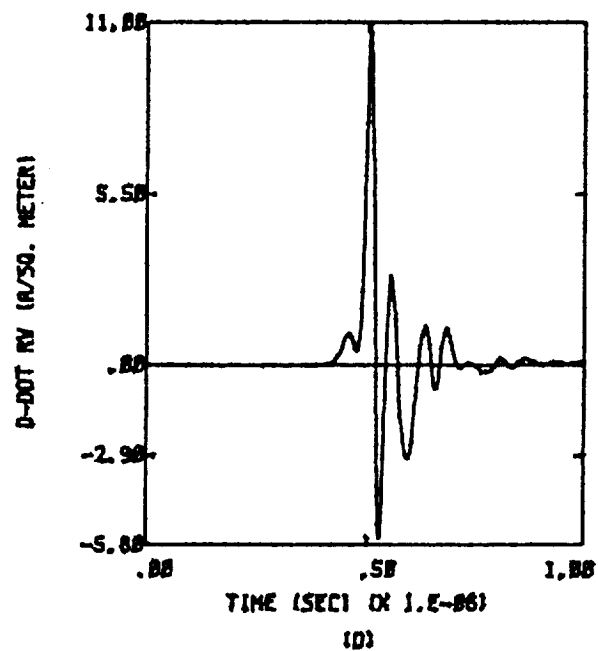
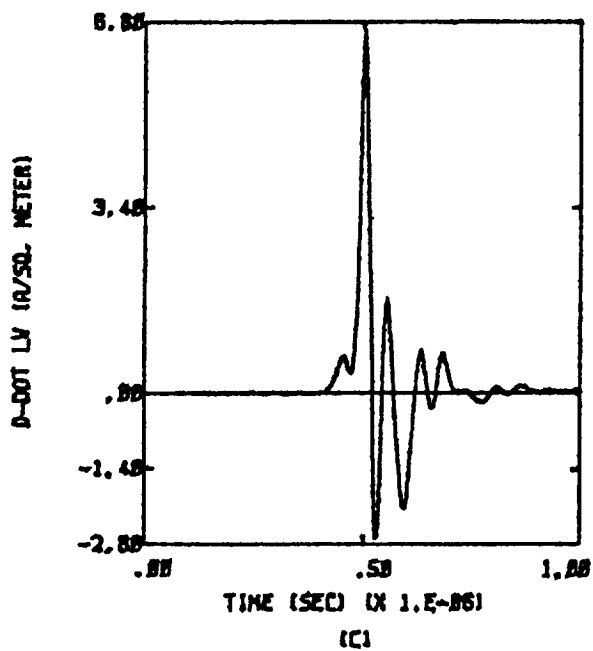
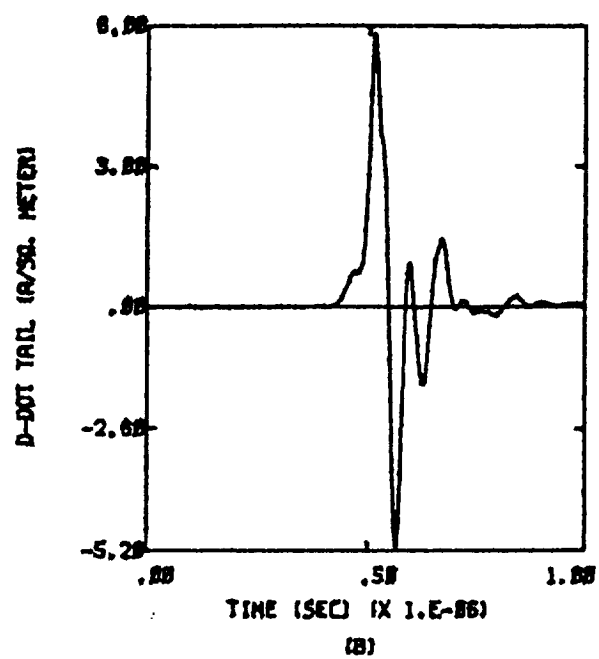
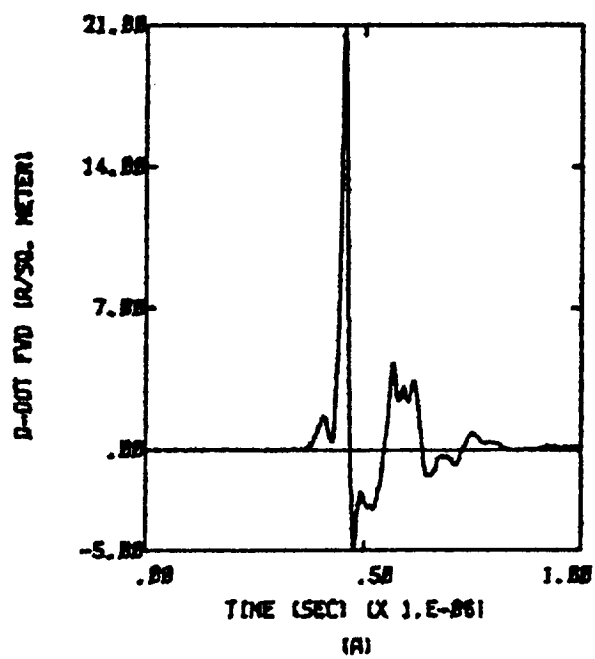


Figure D.38a  $X, -Y, Z$ ;  $Q = -1/2 Q_m$ ;  $E = 1.8 \times 10^5$  Volts per meter

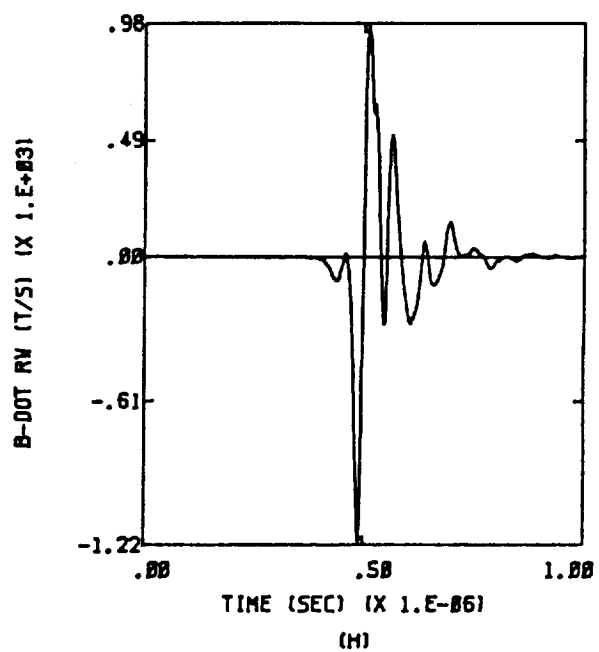
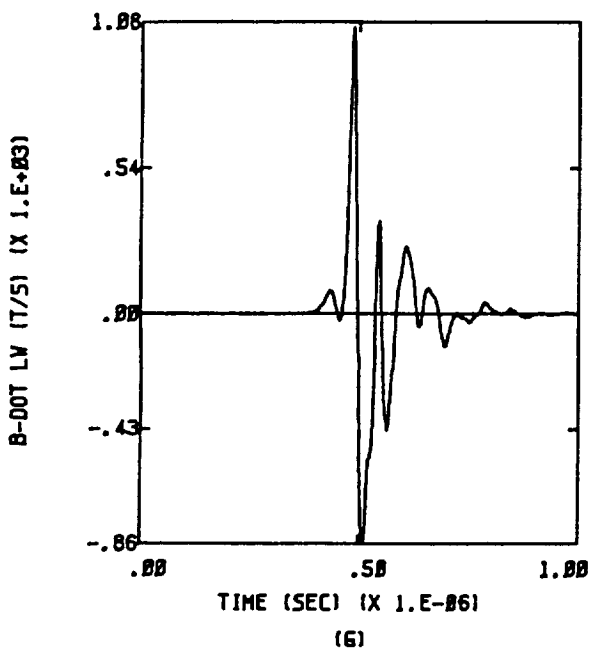
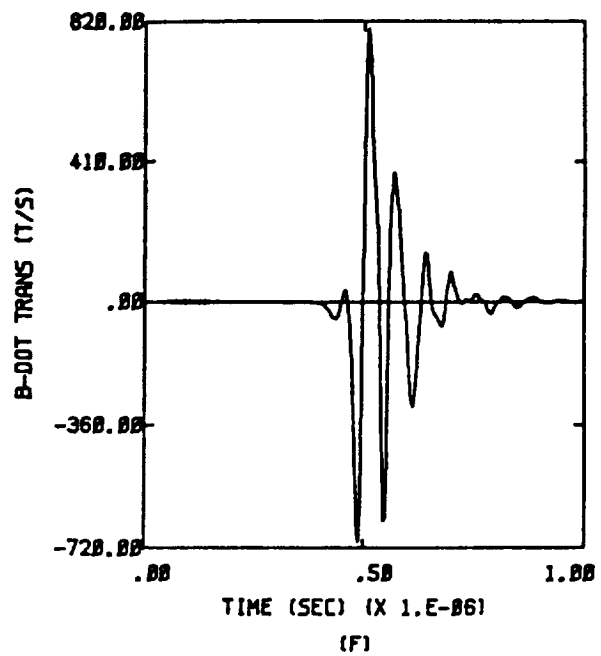
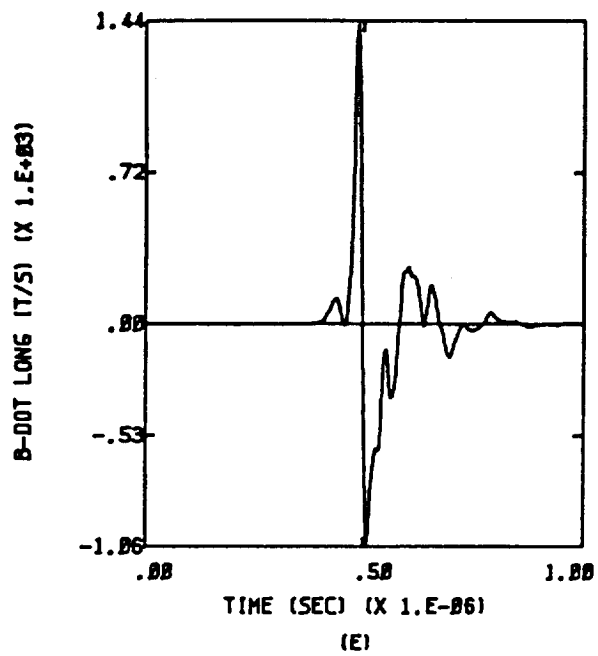


Figure D.38b  $X, -Y, Z$ ;  $Q = -1/2 Q_m$ ;  $E = 1.8 \times 10^5$  Volts per meter

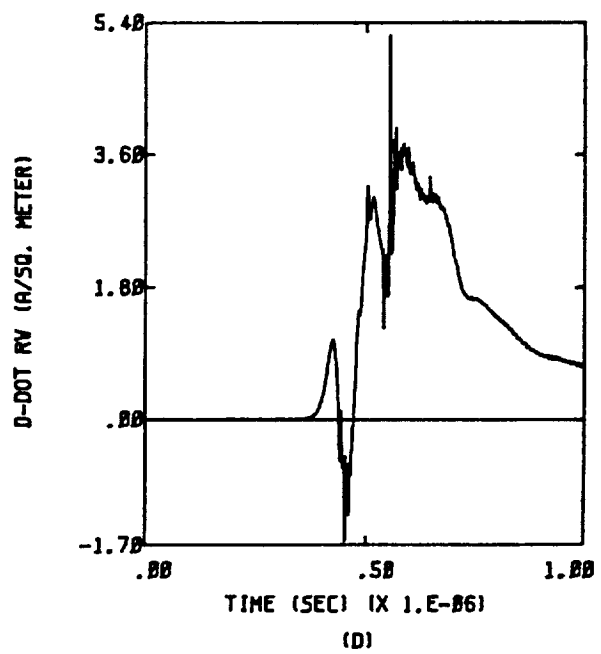
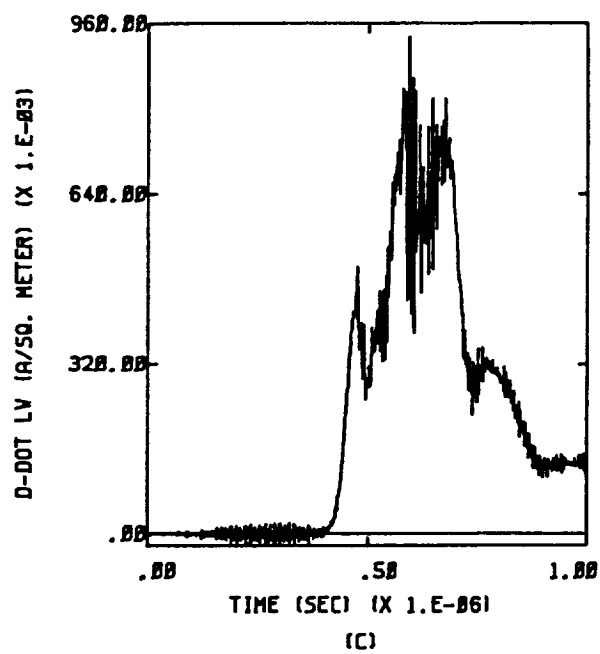
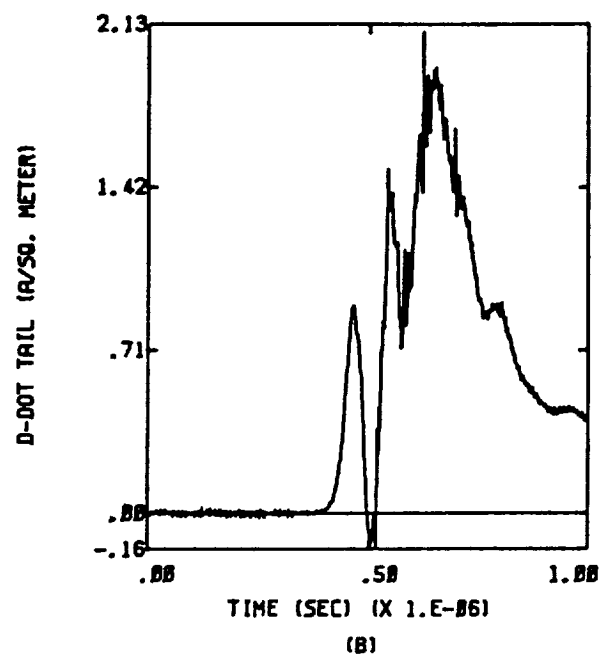
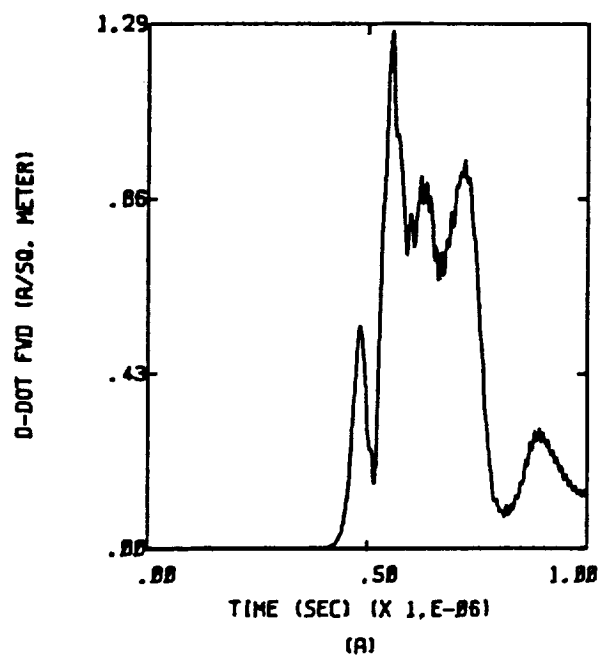


Figure D.39a  $-X,Y,Z$ ;  $Q = -1/2 Q_m$ ;  $E = 1.6 \times 10^5$  Volts per meter

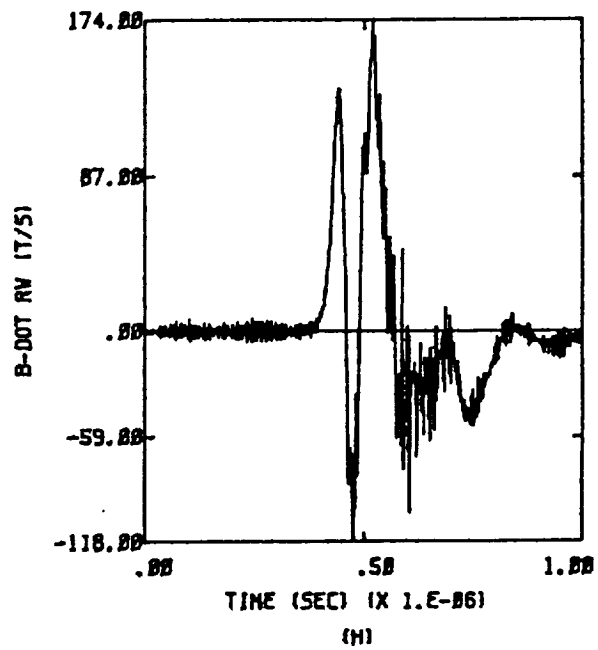
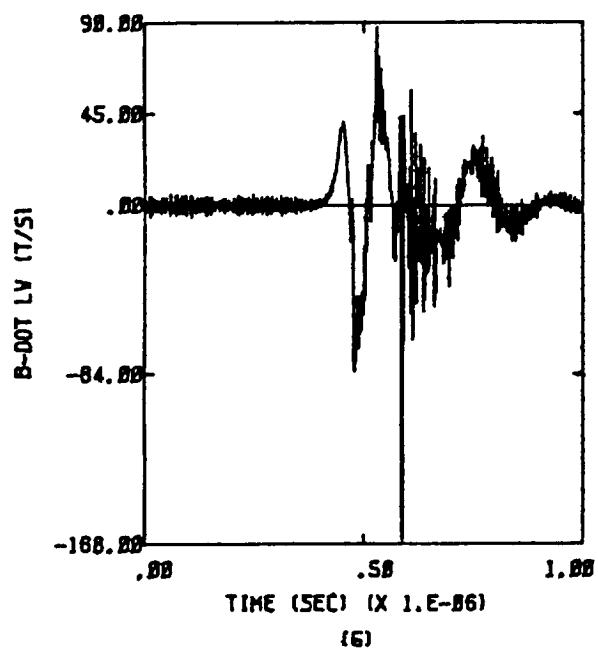
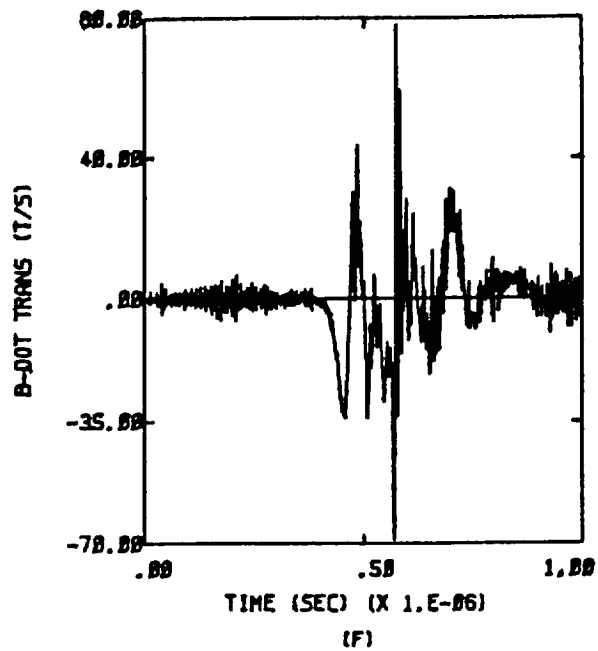
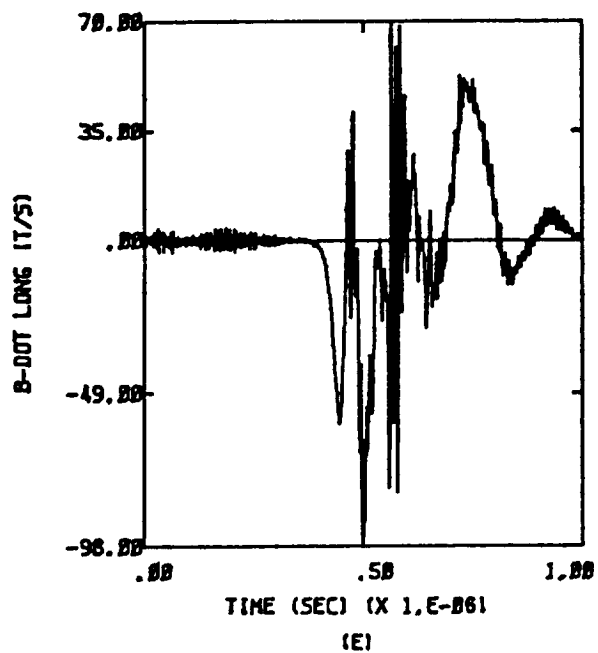


Figure D.39b -X,Y,Z;  $Q = -1/2 Q_m$ ;  $E = 1.6 \times 10^5$  Volts per meter

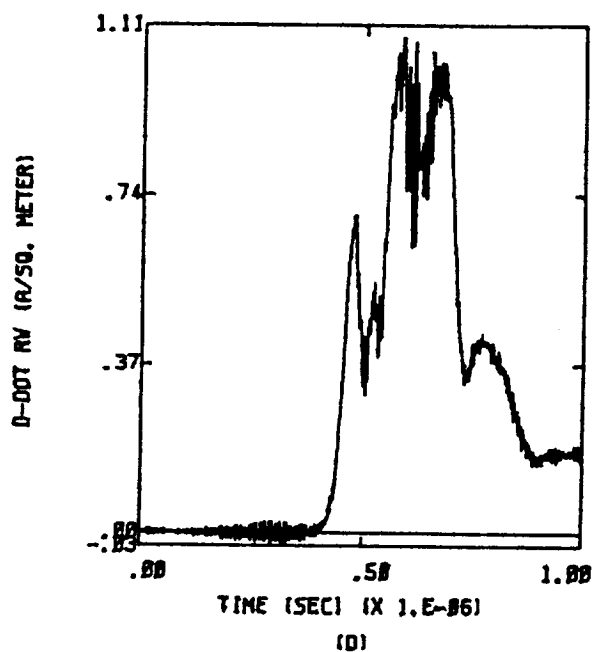
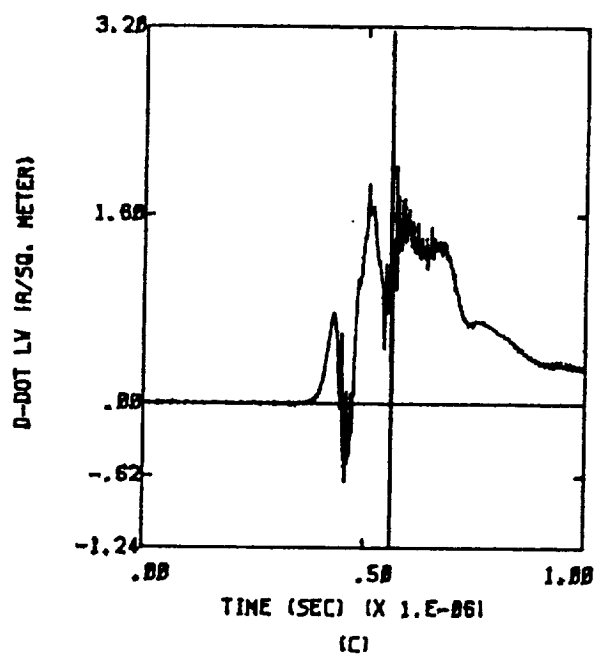
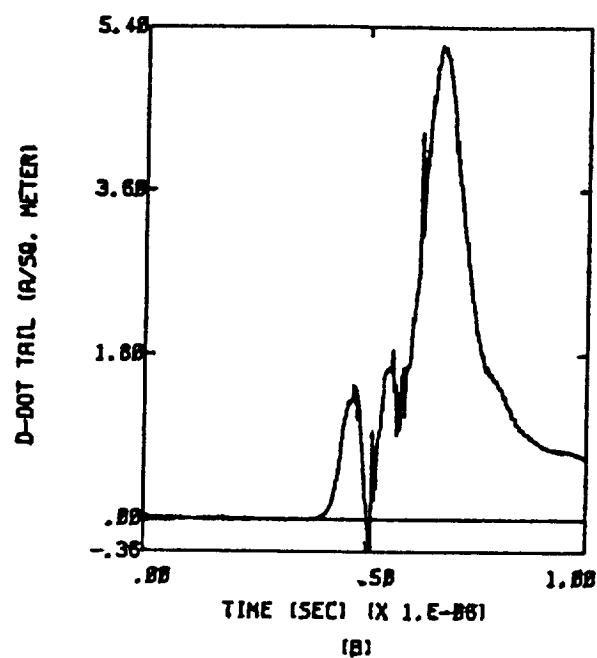
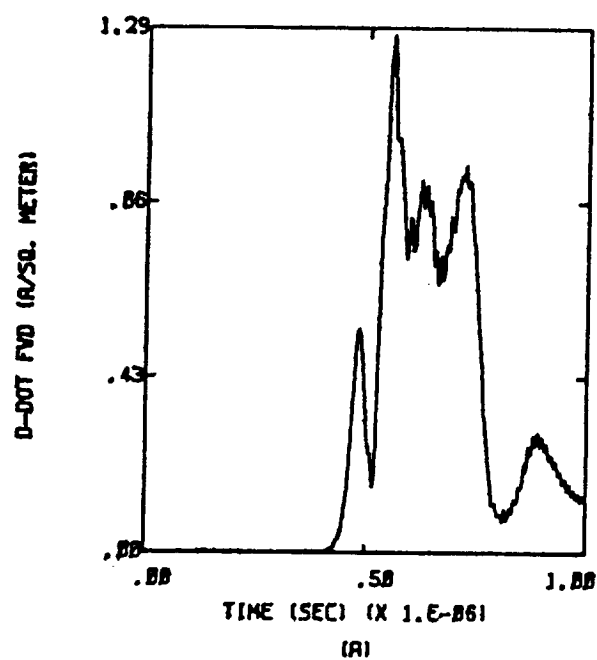


Figure D.40a  $-X, -Y, Z$ ;  $Q = -1/2 Q_m$ ;  $E = 1.6 \times 10^5$  Volts per meter



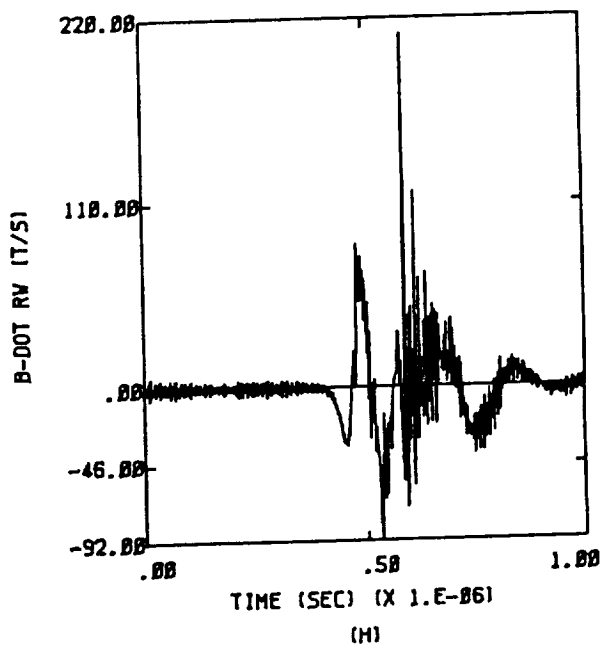
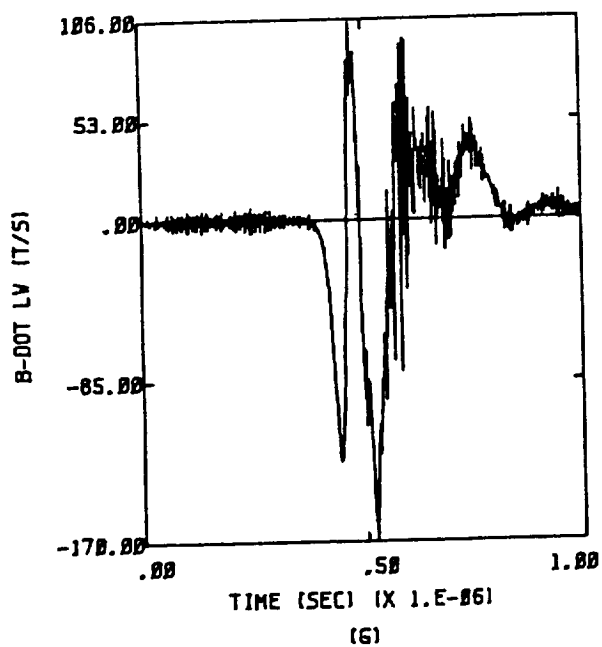
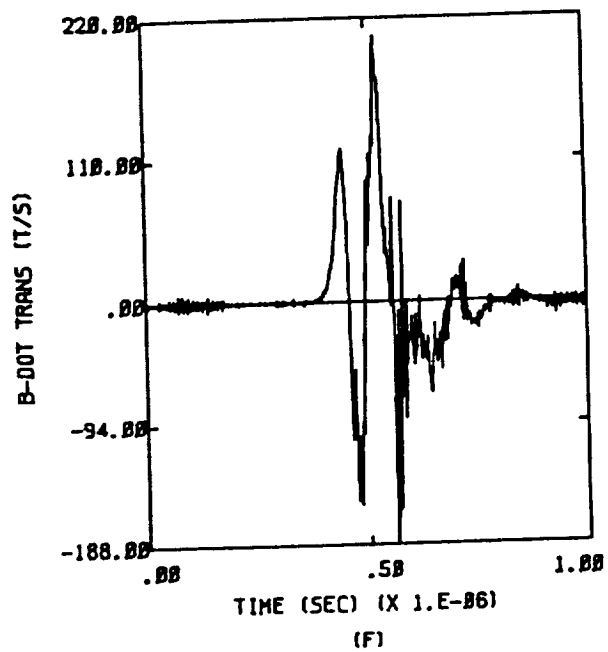
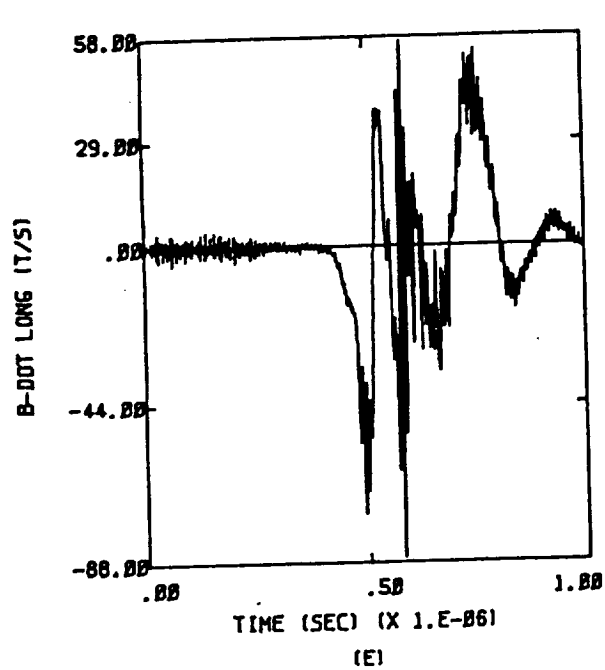


Figure D.40b  $-X, -Y, Z$ ;  $Q = -1/2 Q_m$ ;  $E = 1.6 \times 10^5$  Volts per meter

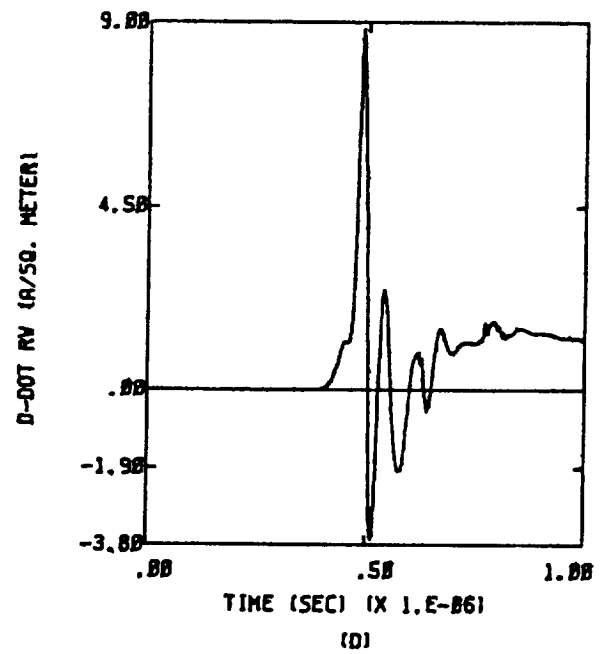
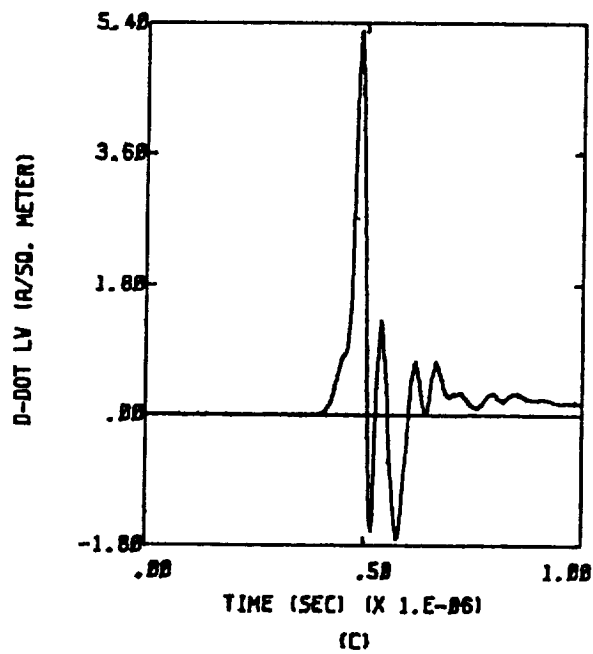
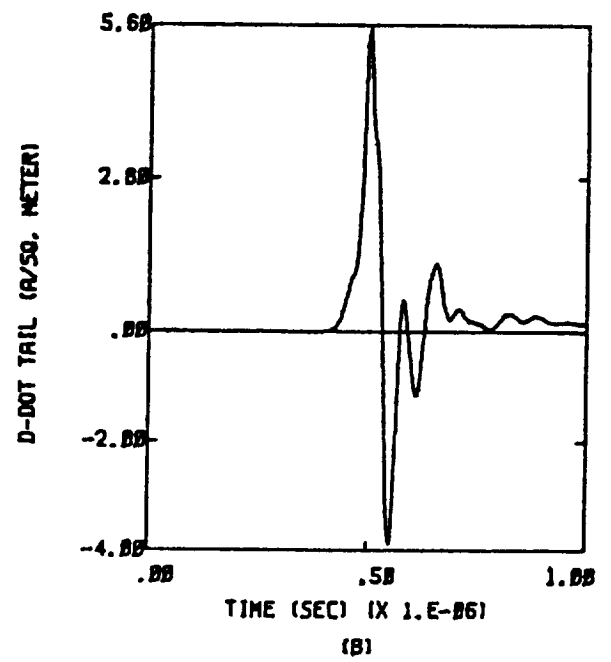
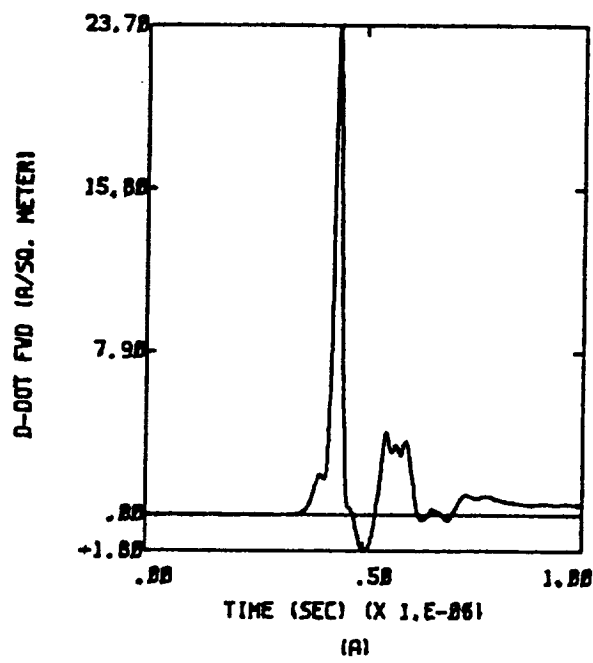


Figure D.41a X,Y;  $Q = -Q_m$ ;  $E = 3 \times 10^4$  Volts per meter

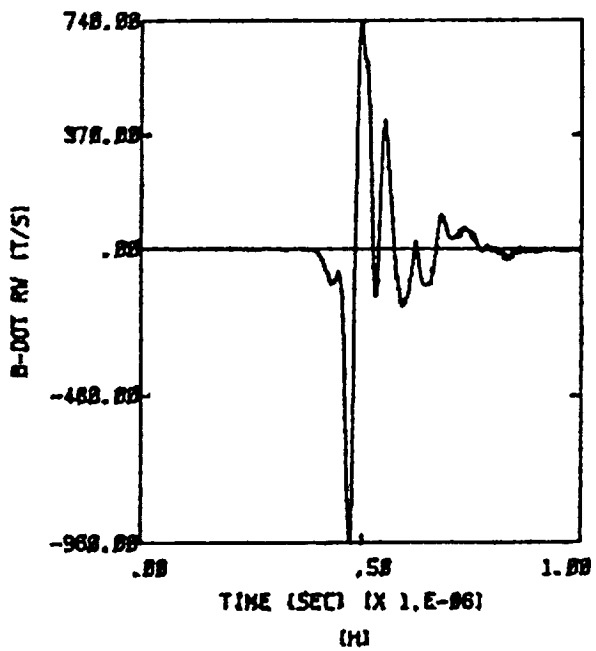
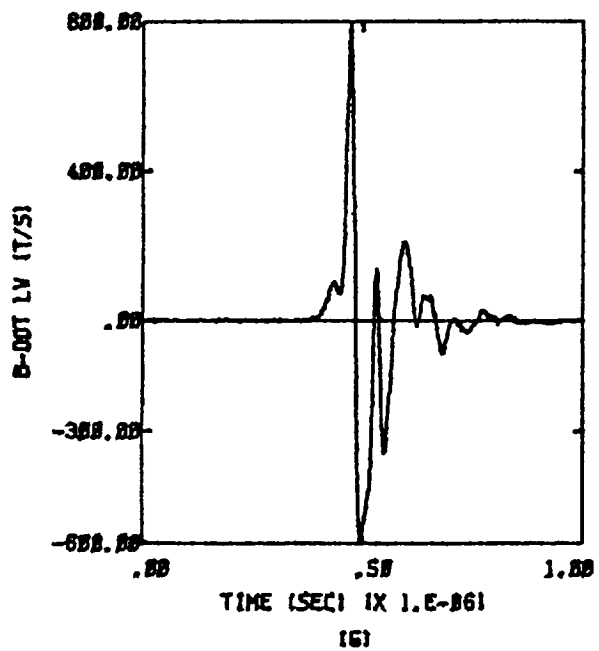
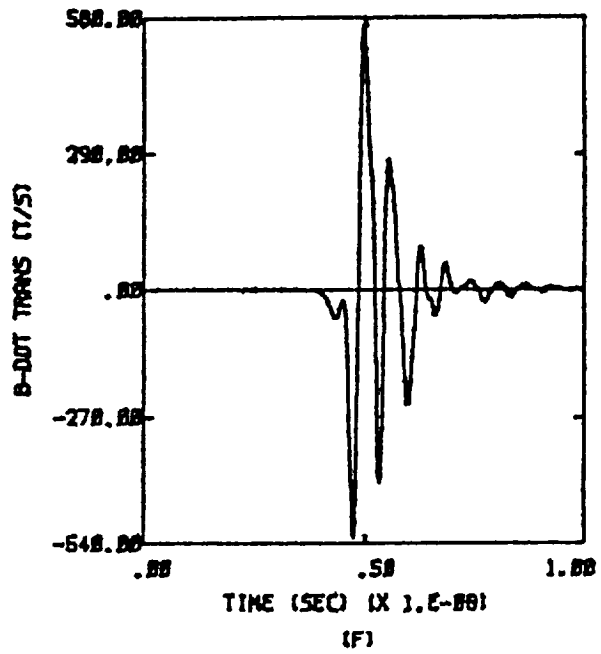
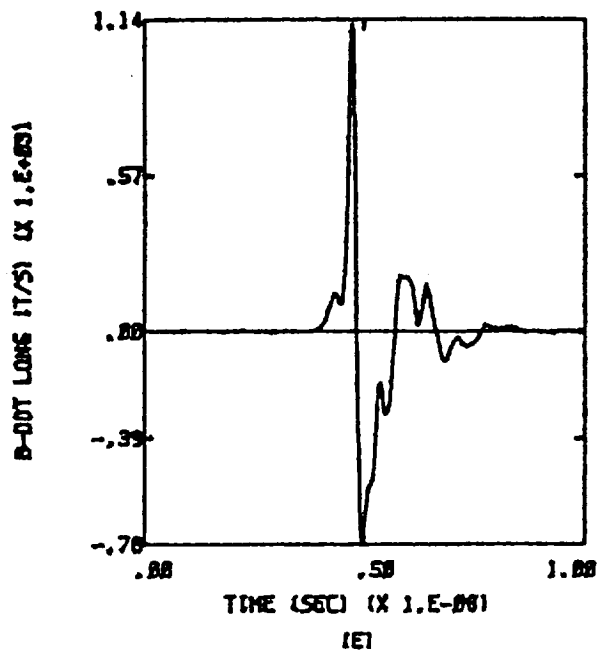


Figure D.41b X,Y;  $Q = -Q_m$ ;  $E = 3 \times 10^4$  Volts per meter

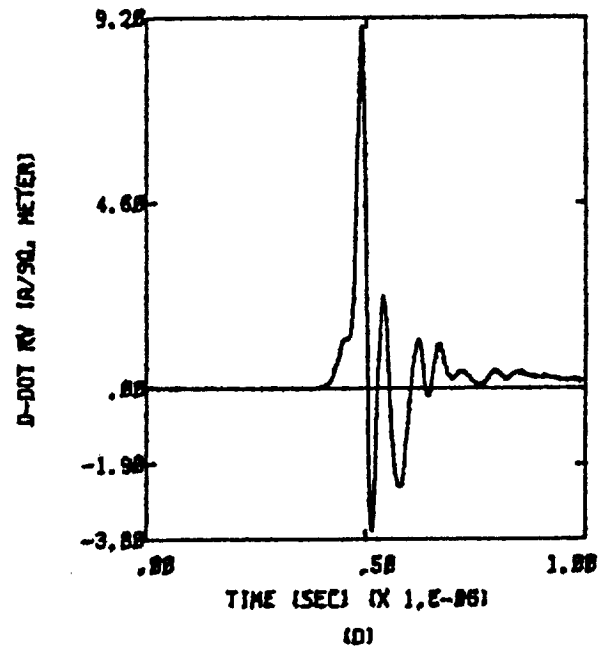
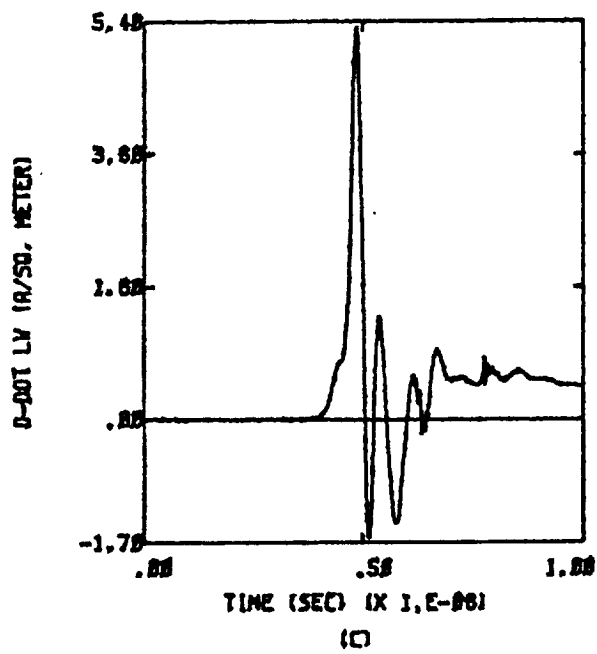
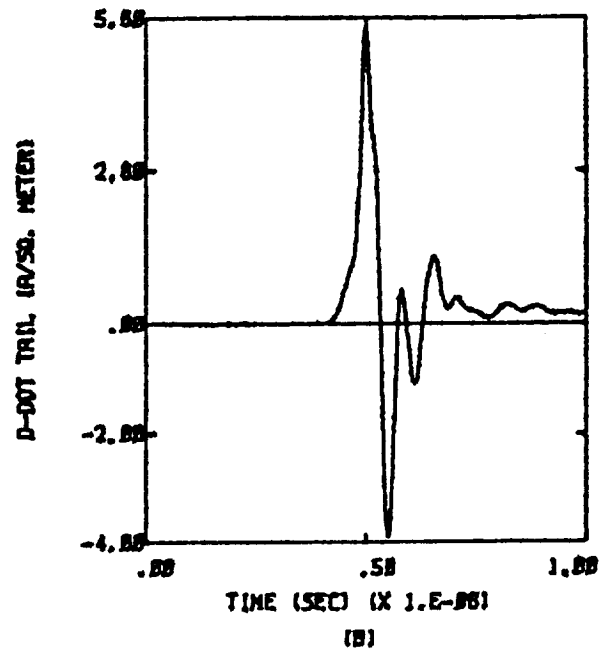
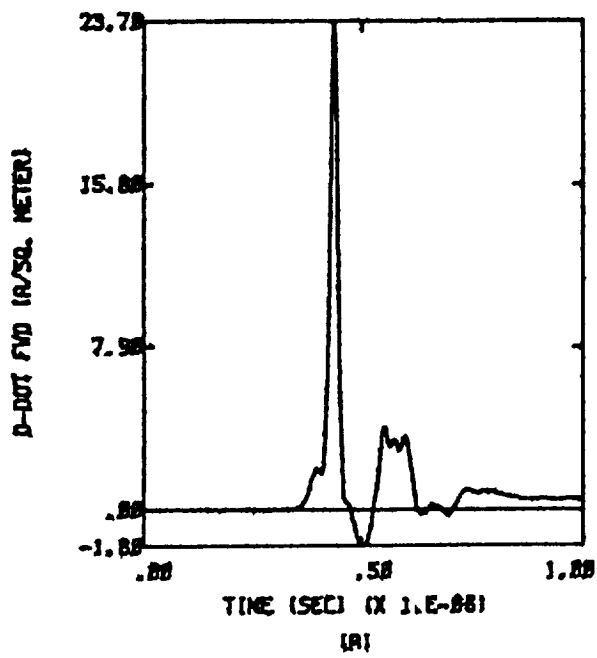


Figure D.42a  $X, -Y; Q = -Q_m; E = 3 \times 10^4$  Volts per meter

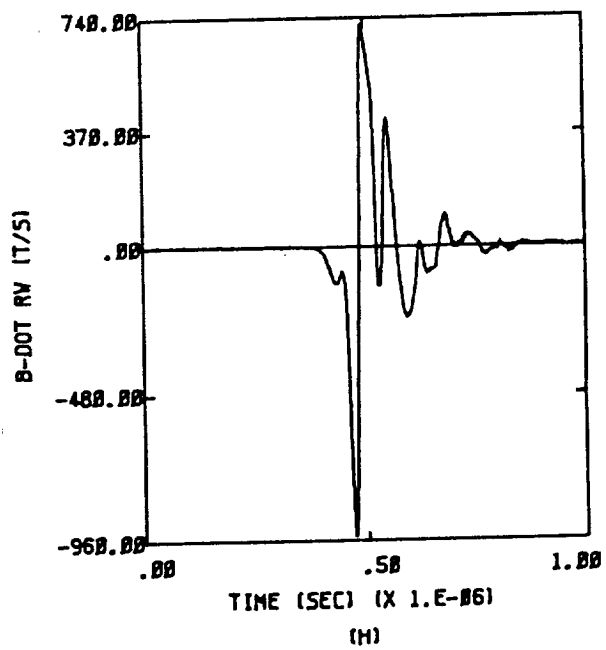
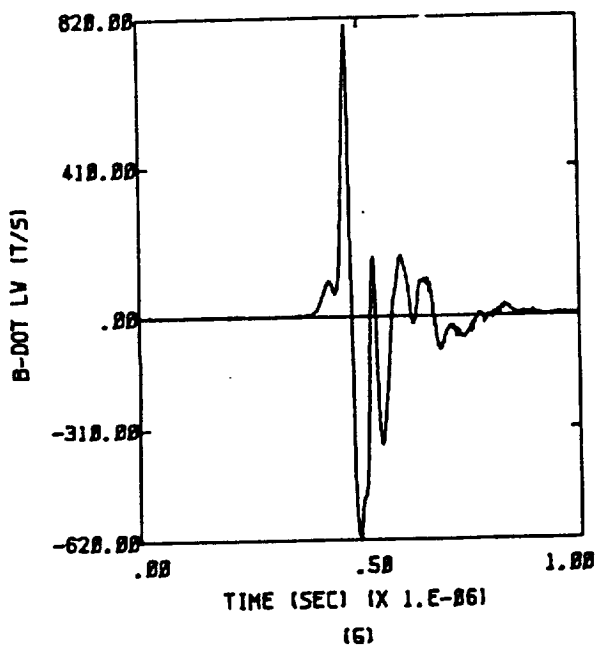
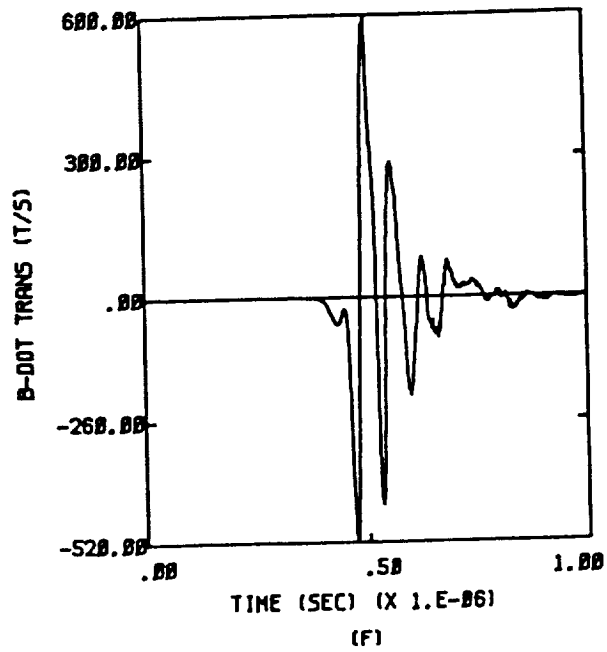
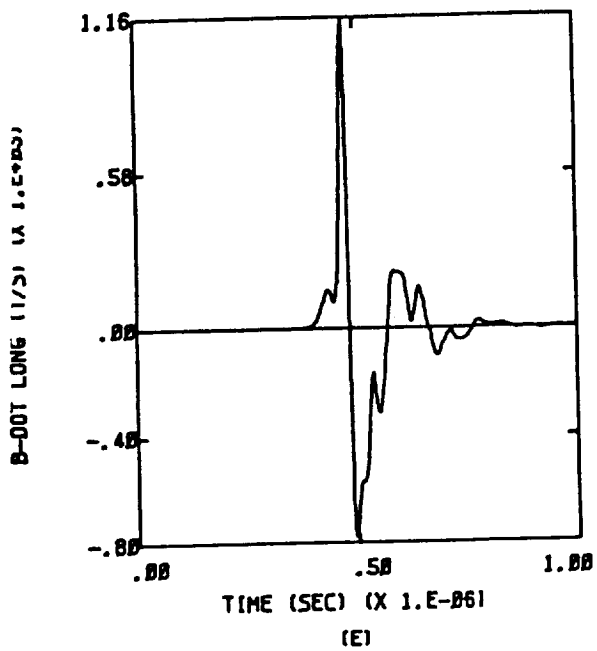


Figure D.42b X,-Y;  $Q = -Q_m$ ;  $E = 3 \times 10^4$  Volts per meter

ORIGINAL PAGE IS  
OF POOR QUALITY

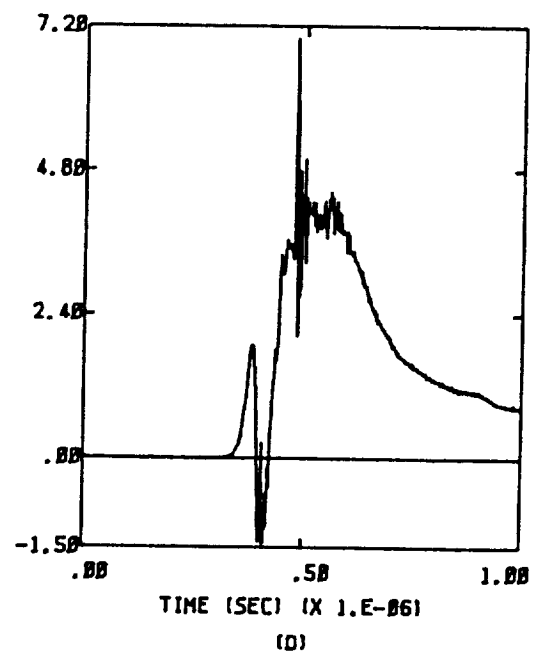
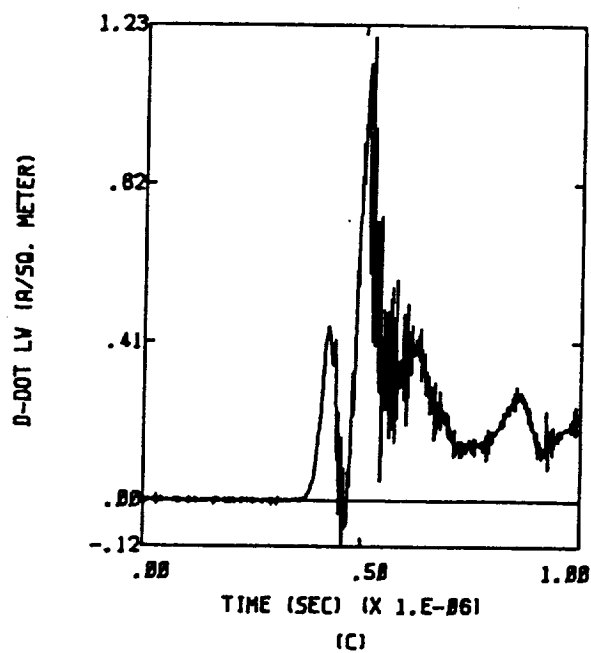
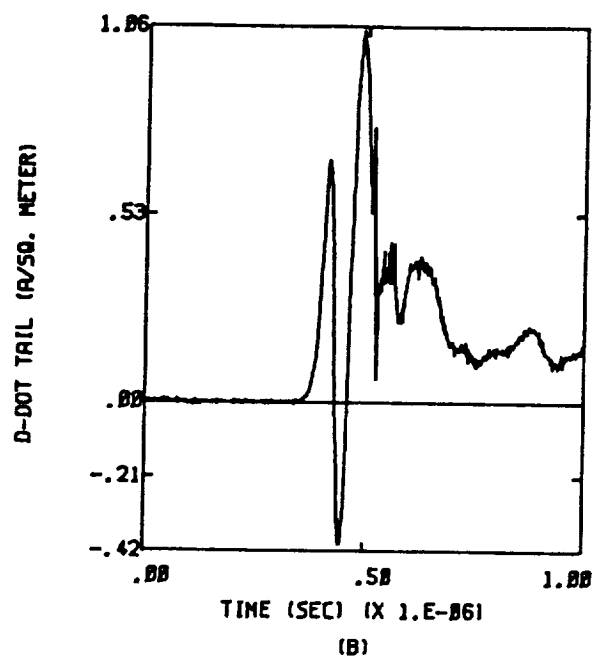
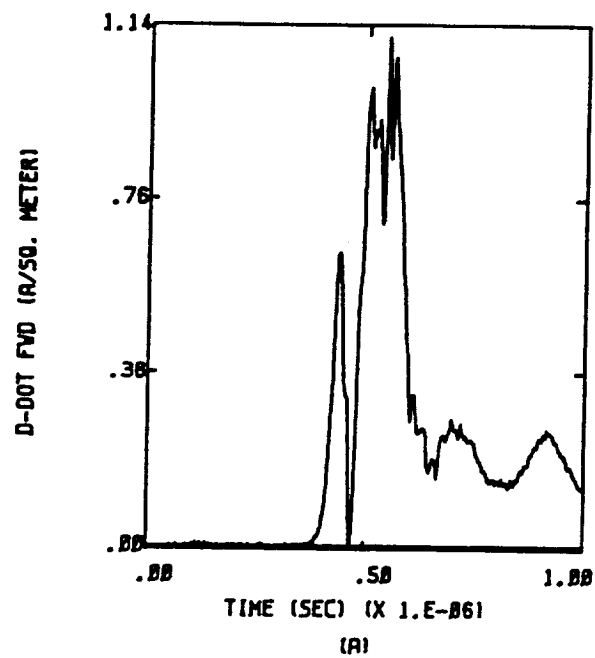


Figure D.43a  $-X, Y; Q = -Q_m; E = 2 \times 10^4$  Volts per meter

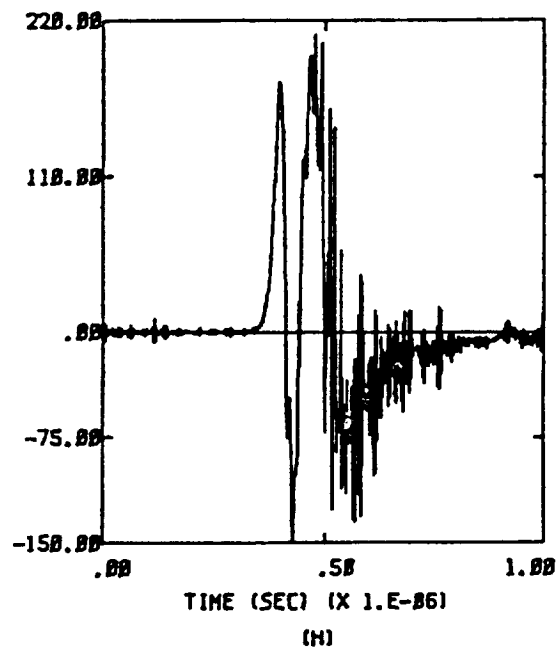
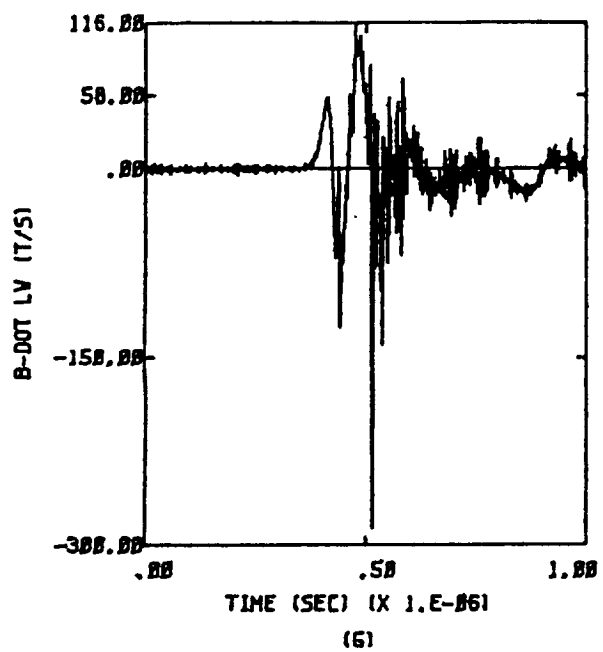
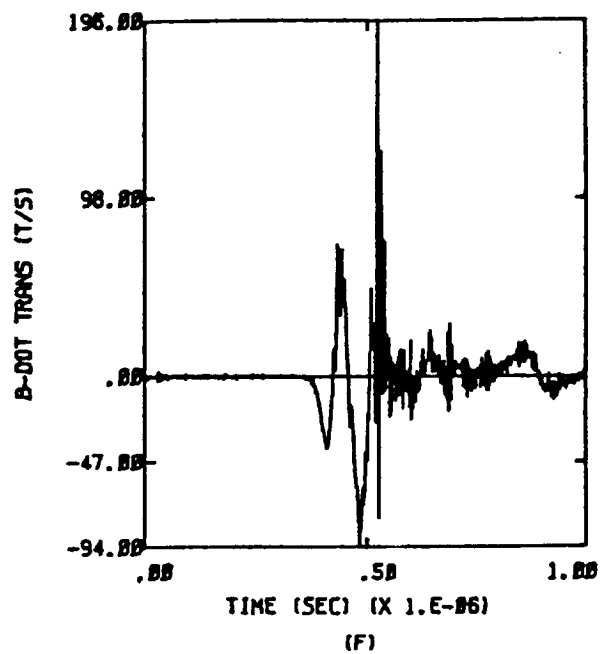
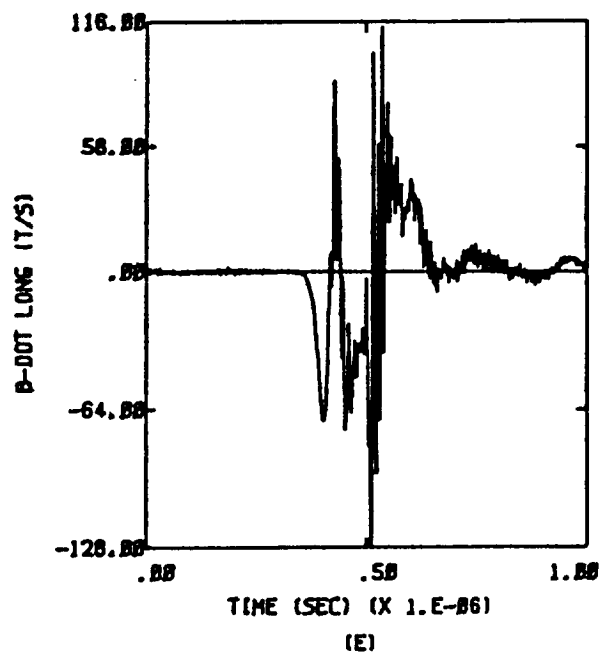


Figure D.43b  $-X, Y; Q = -Q_m; E = 2 \times 10^4$  Volts per meter

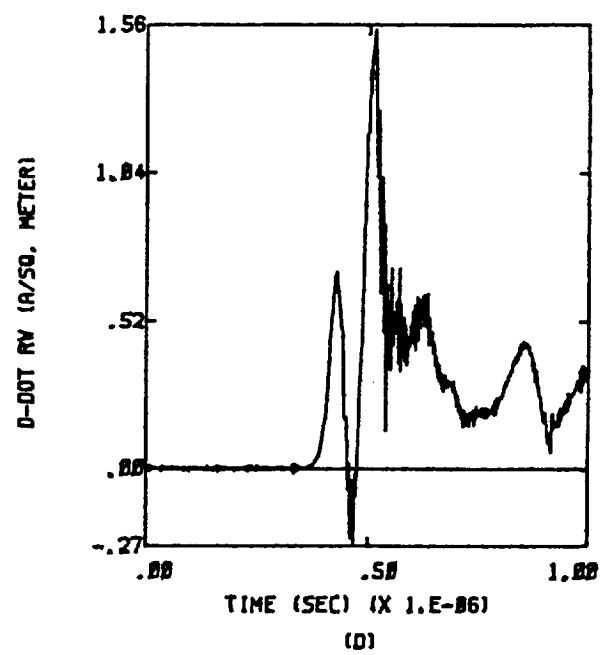
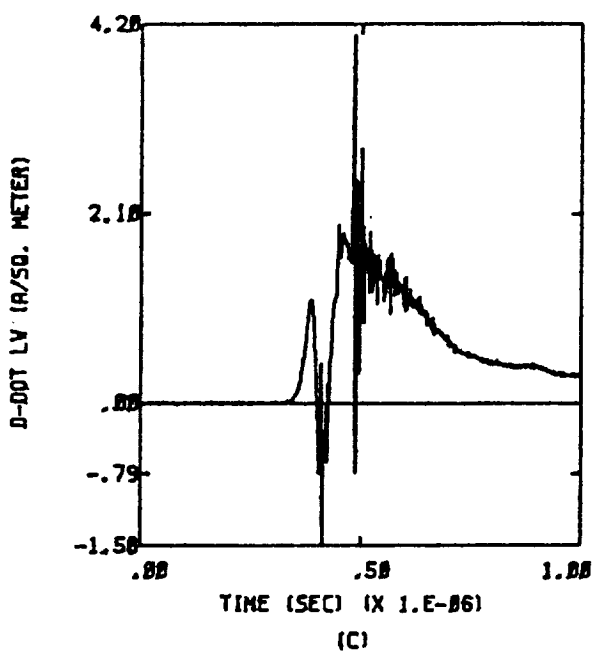
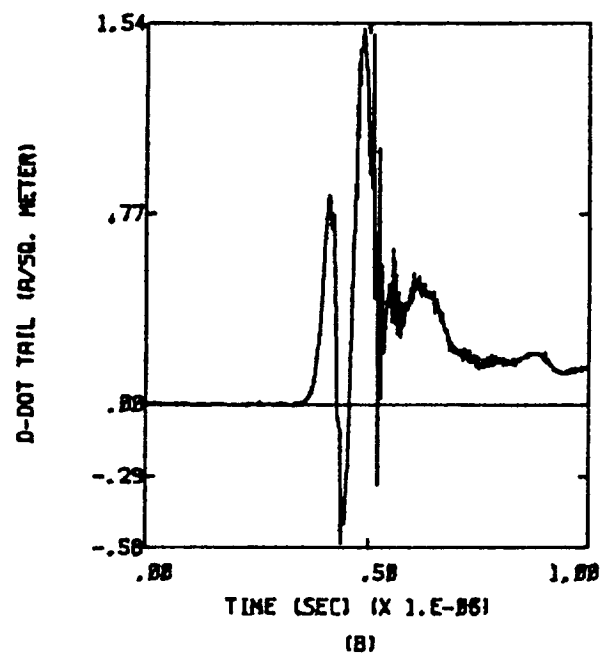
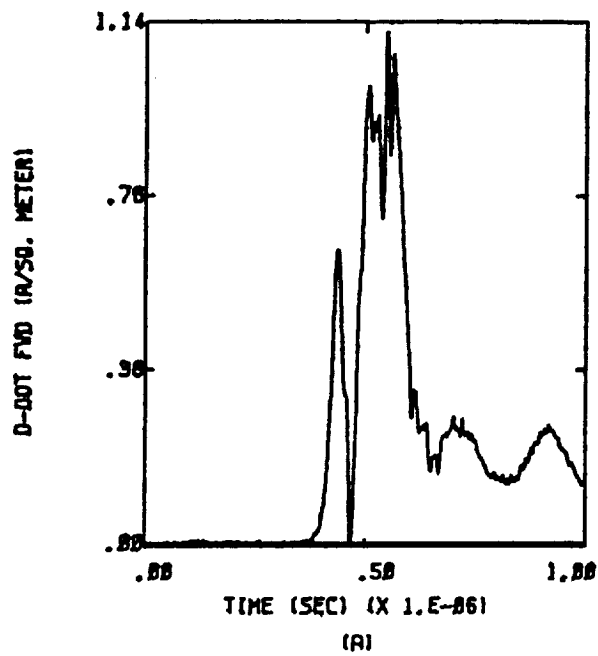


Figure D.44a -X,-Y;  $Q = -Q_m$ ;  $E = 2 \times 10^4$  Volts per meter



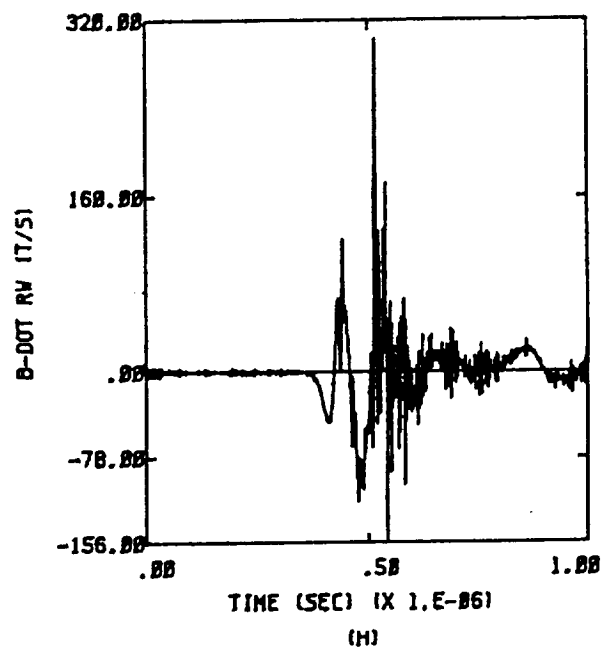
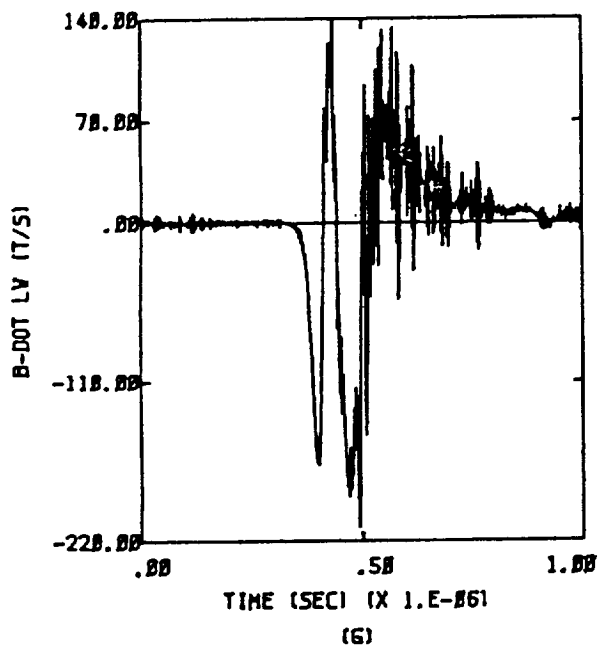
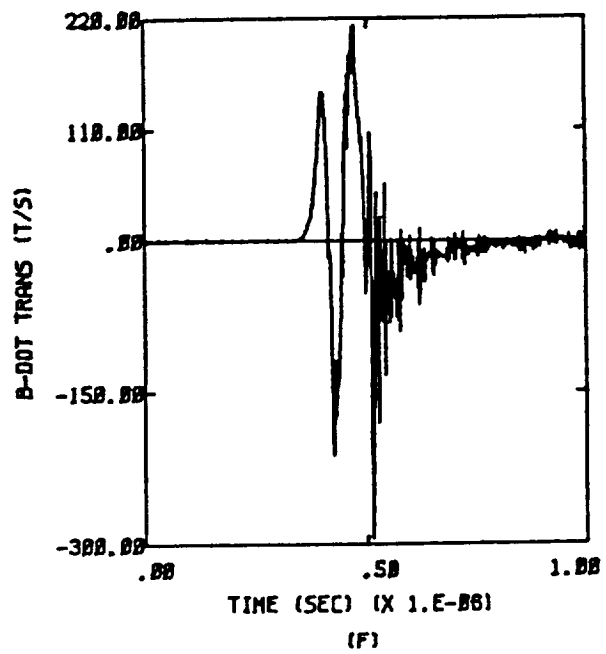
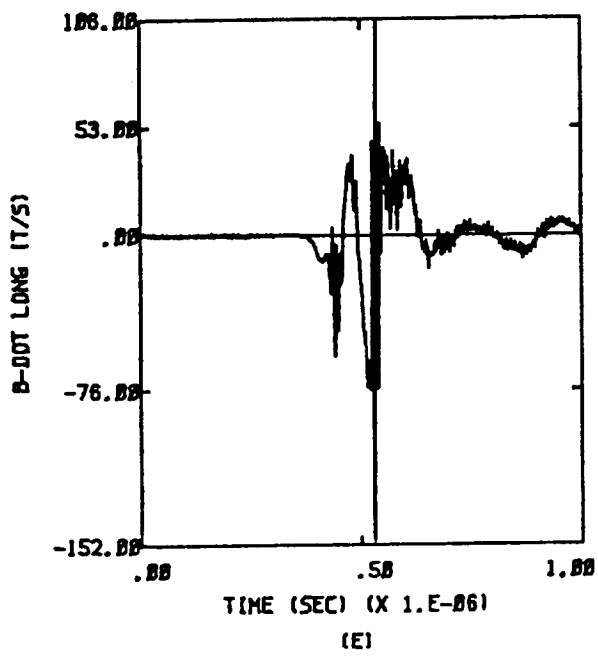


Figure D.44b  $-X, -Y$ ;  $Q = -Q_m$ ;  $E = 2 \times 10^4$  Volts per meter

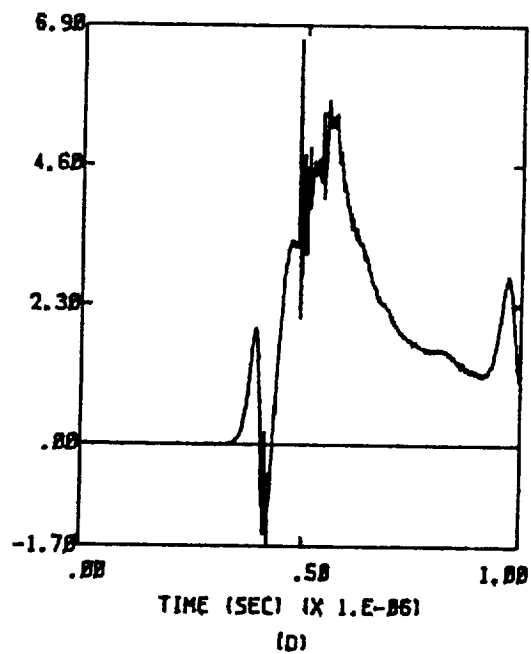
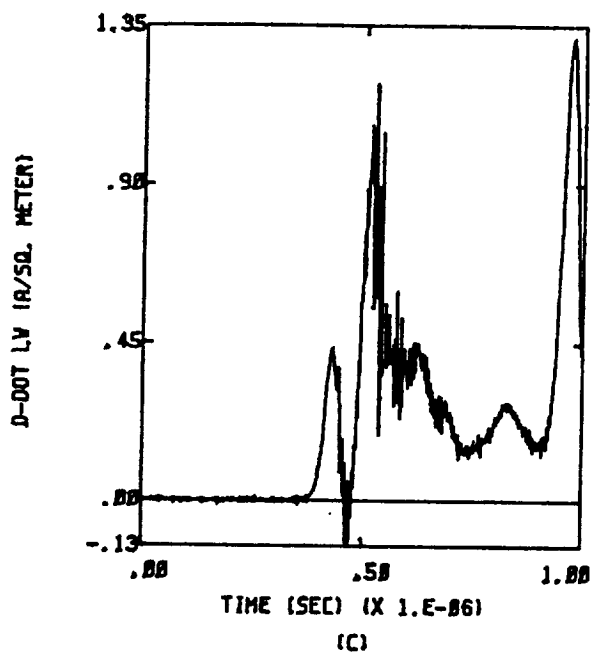
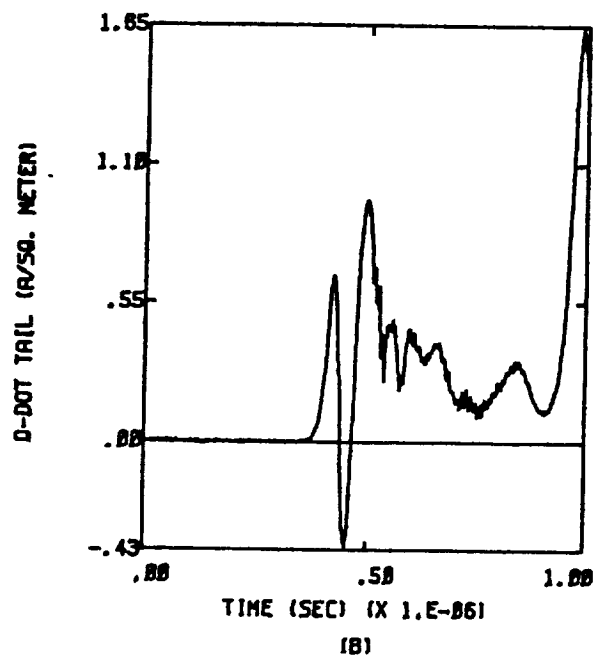
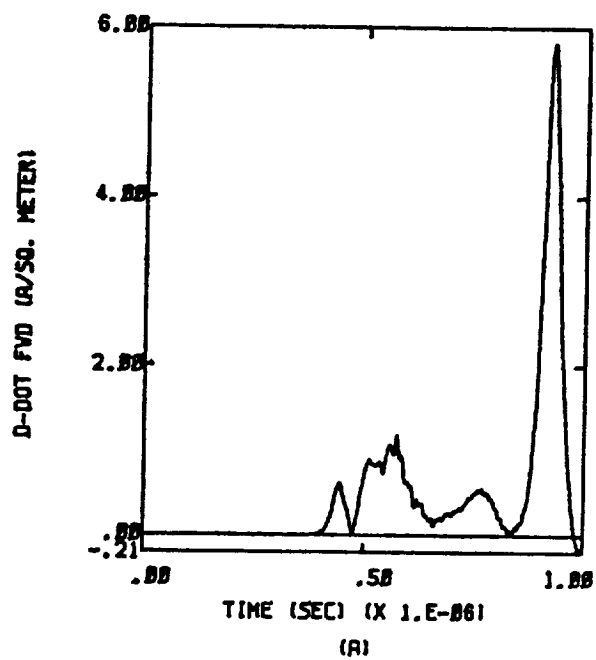


Figure D.45a Y,-Z;  $Q = -Q_m$ ;  $E = 3 \times 10^4$  Volts per meter

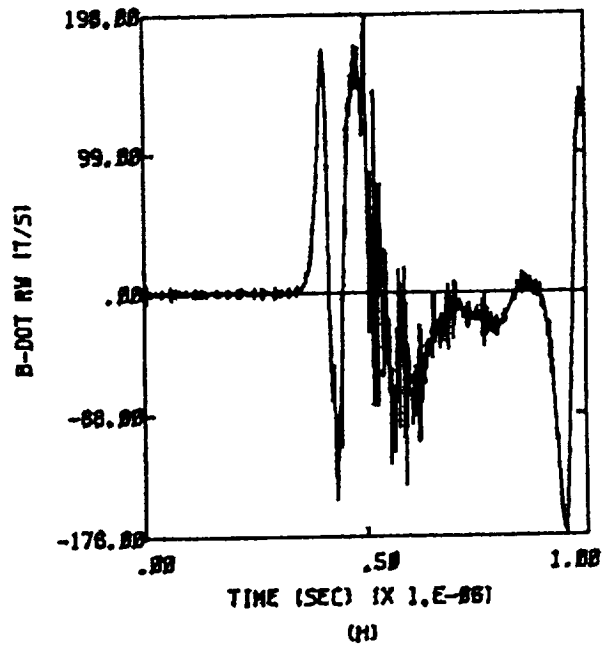
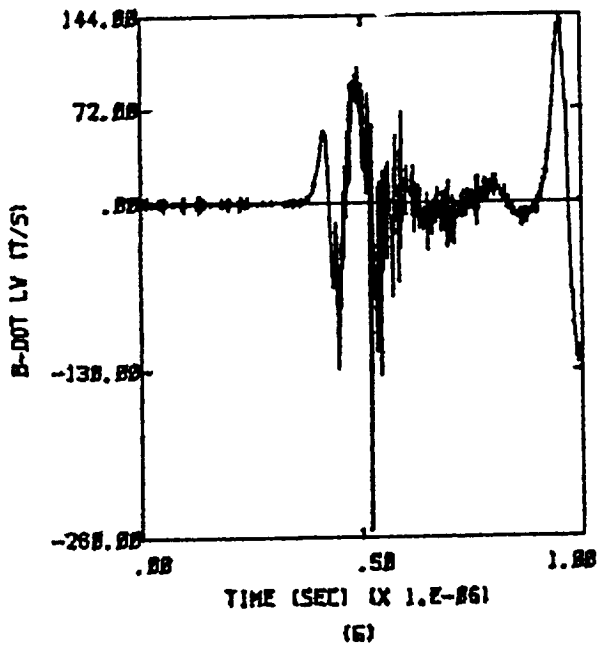
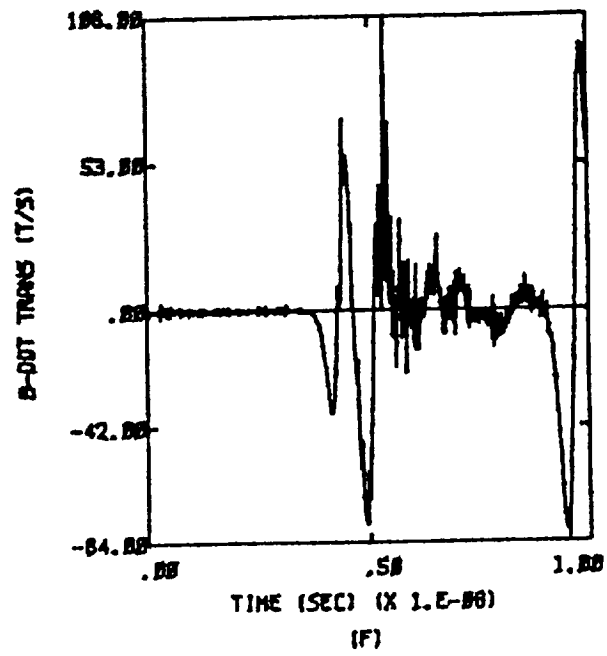
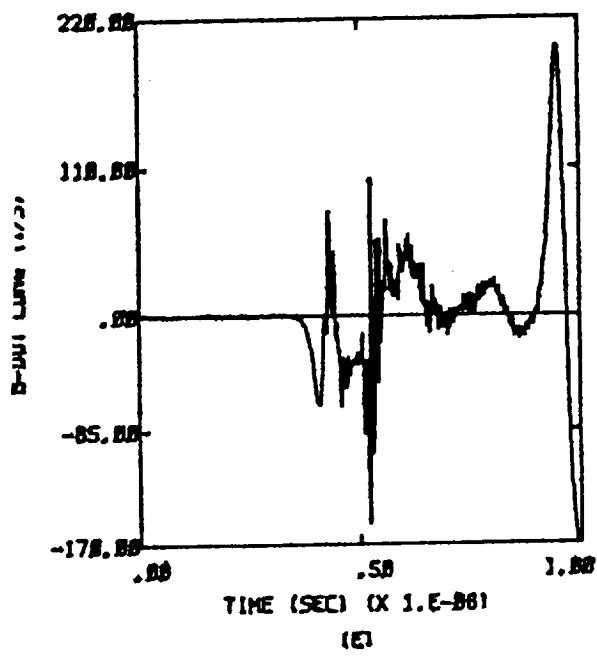


Figure D.45b Y,-Z;  $Q = -Q_m$ ;  $E = 3 \times 10^4$  Volts per meter

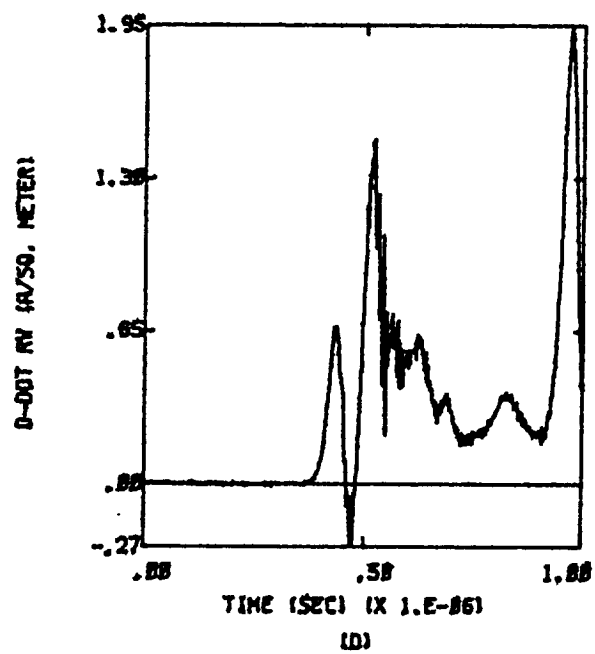
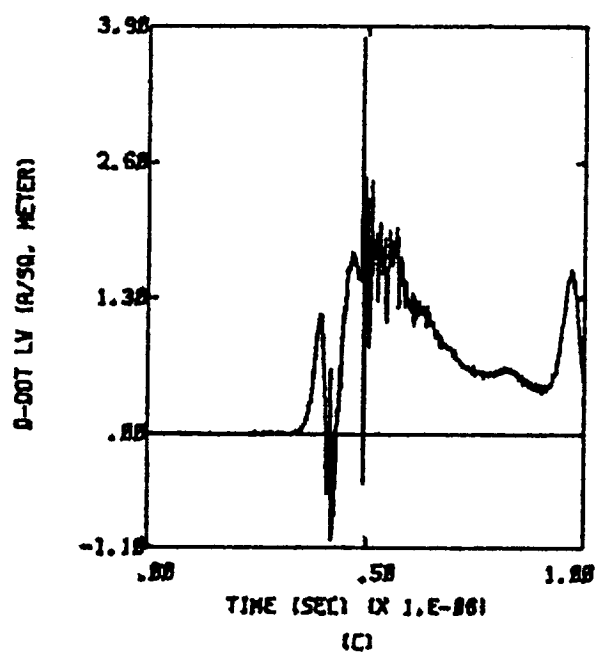
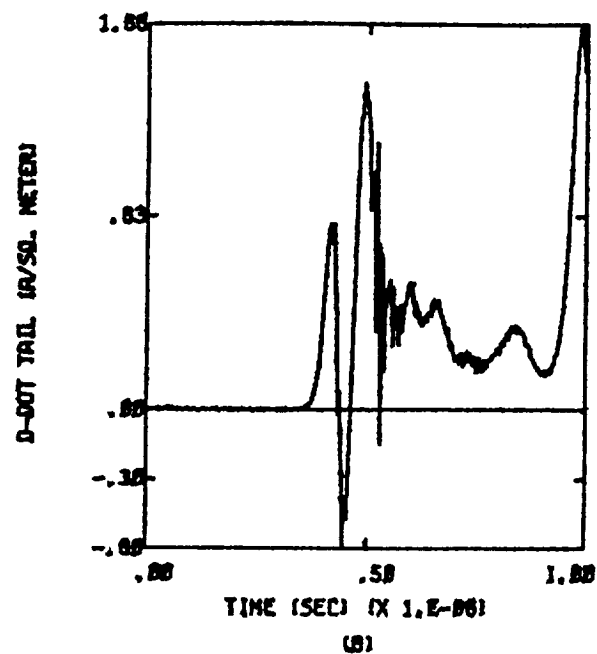
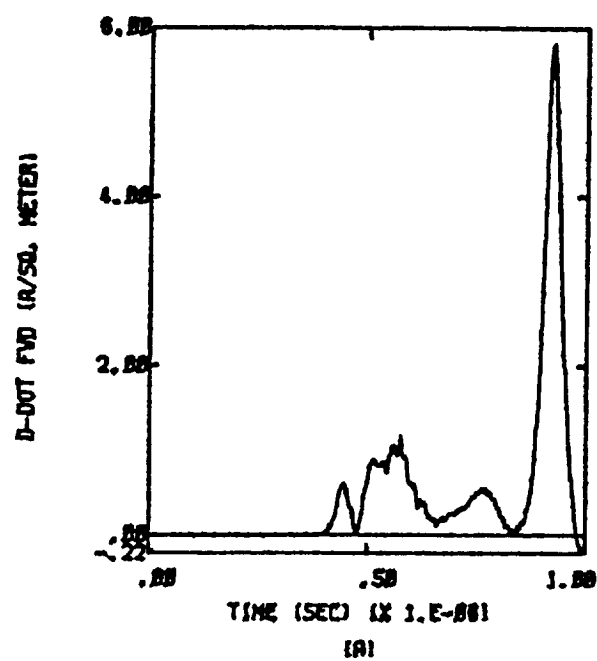


Figure D.46a  $-Y, -Z; Q = -Q_m; E = 3 \times 10^4$  Volts per meter

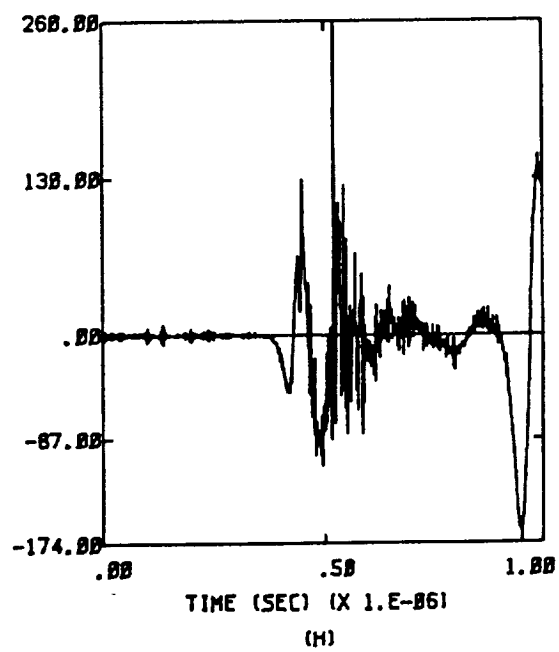
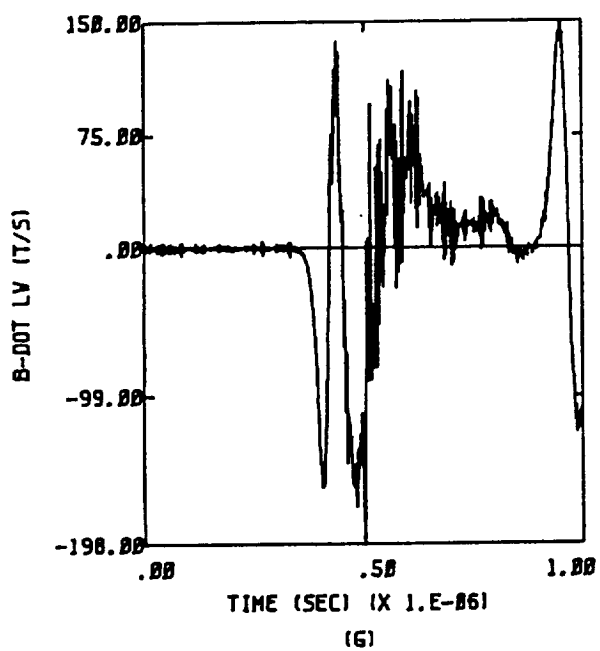
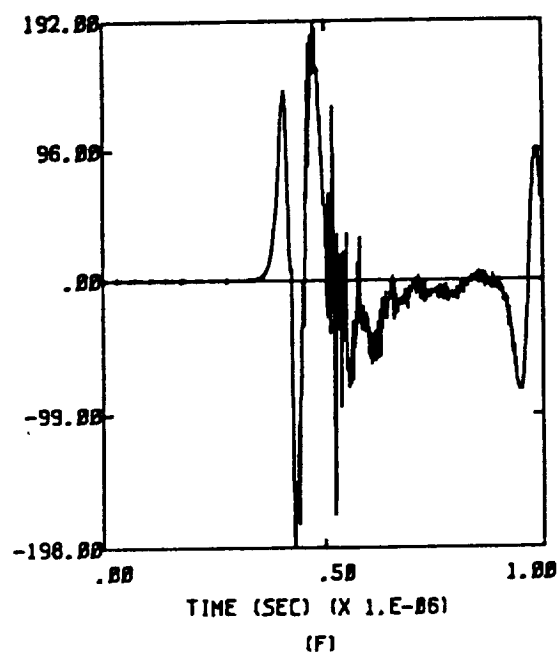
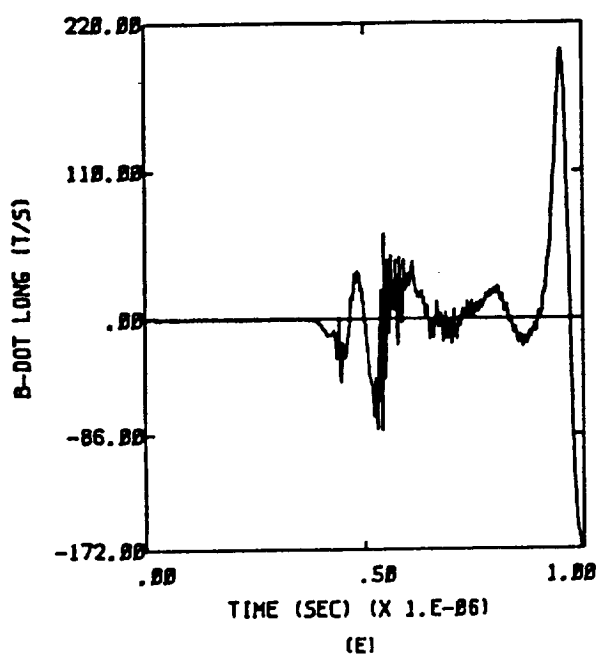


Figure D.46b  $-Y, -Z; Q = -Q_m; E = 3 \times 10^4$  Volts per meter

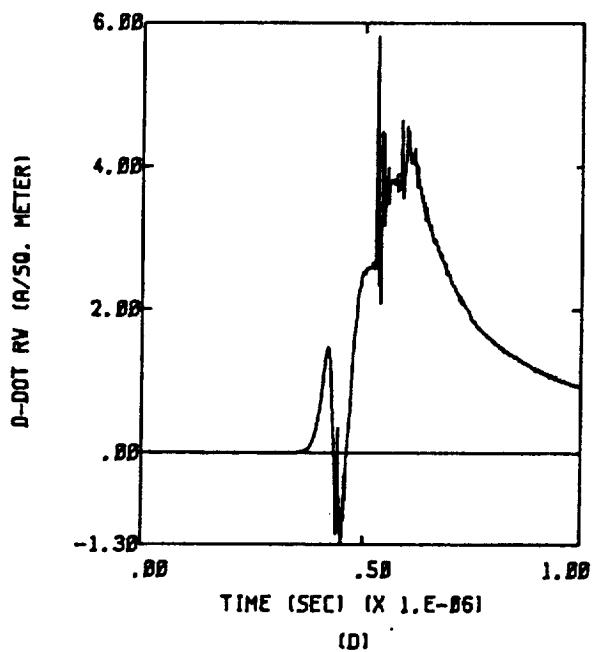
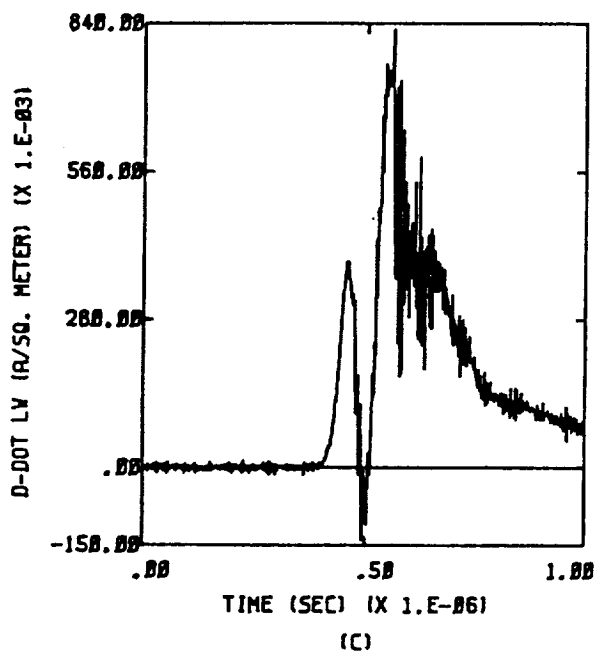
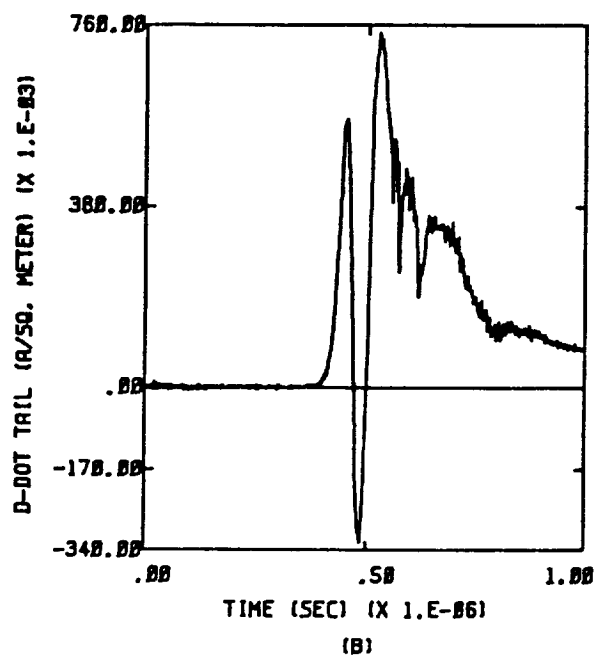
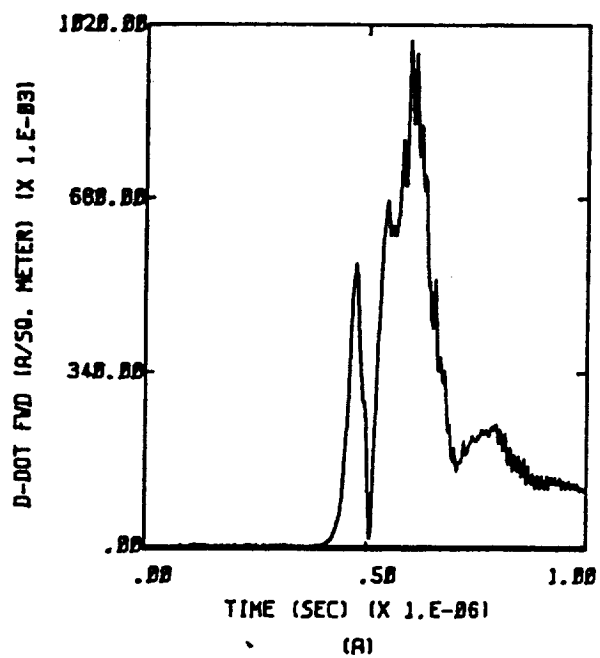


Figure D.47a Y,Z;  $Q = -Q_m$ ;  $E = 3 \times 10^4$  Volts per meter

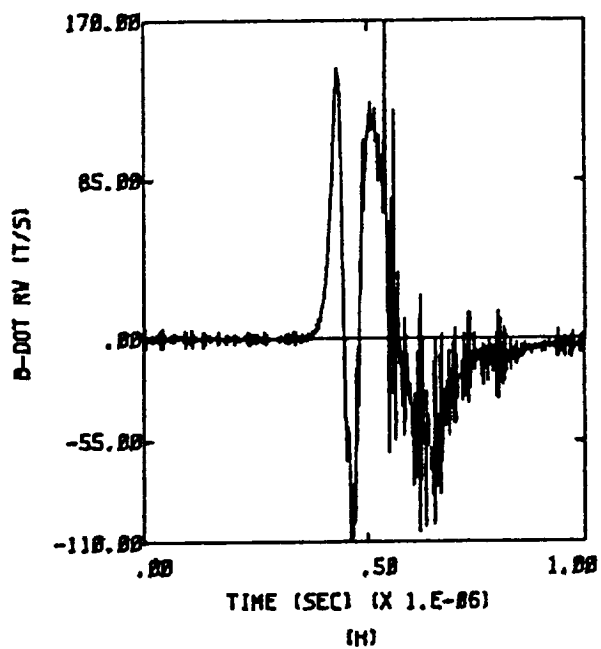
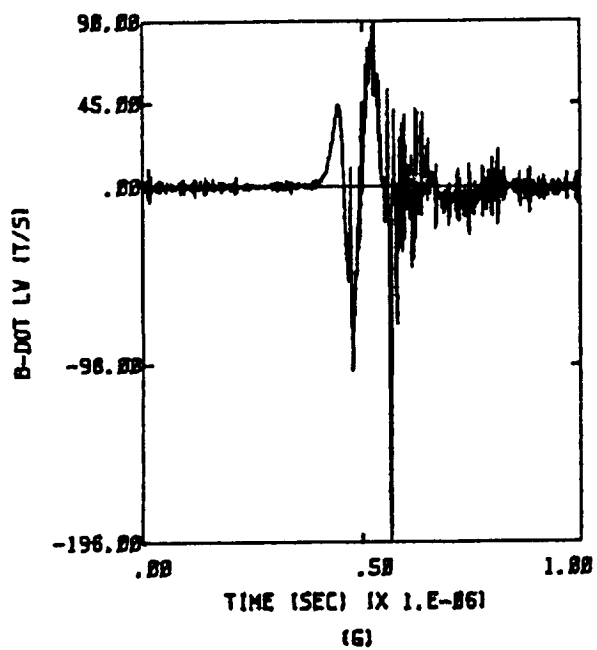
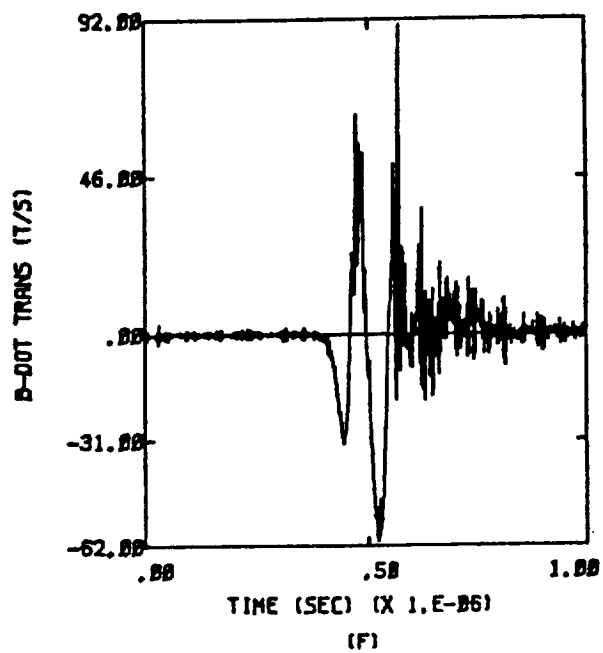
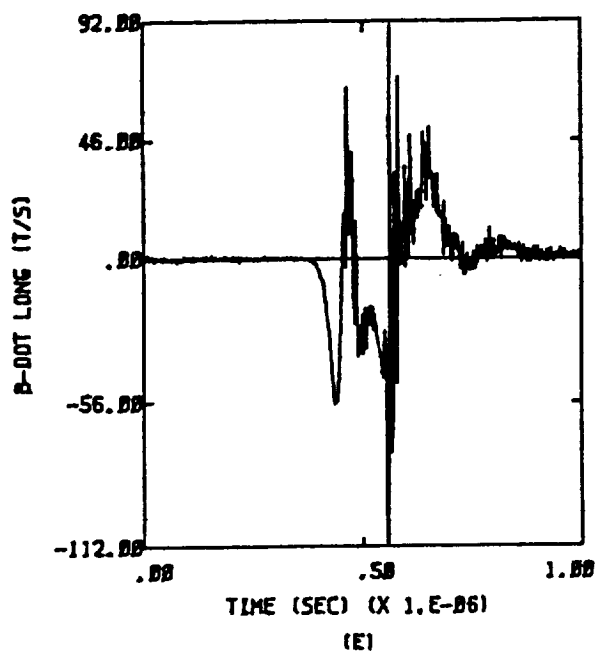


Figure D.47b Y,Z;  $Q = -Q_m$ ;  $E = 3 \times 10^4$  Volts per meter

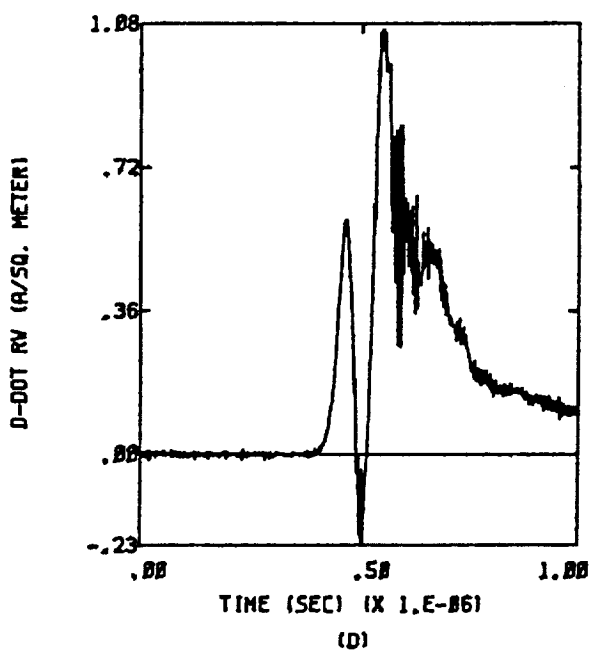
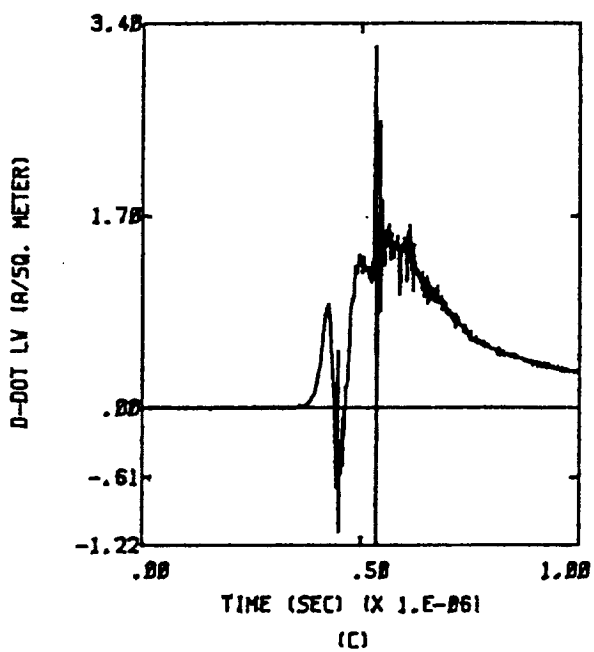
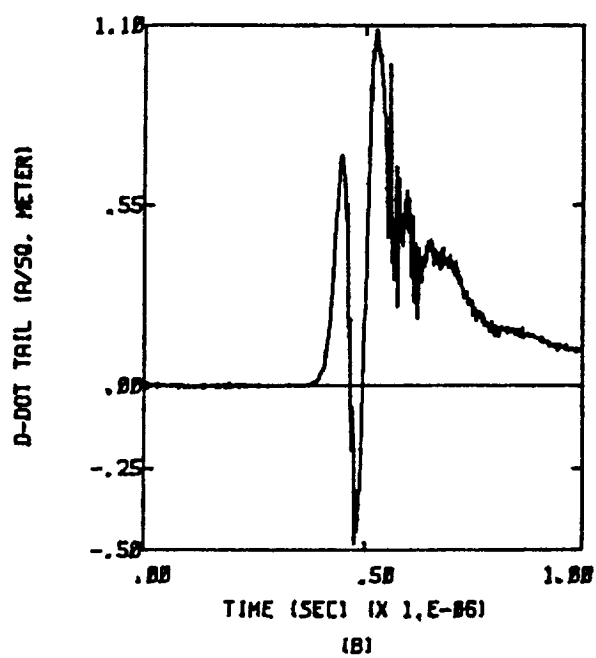
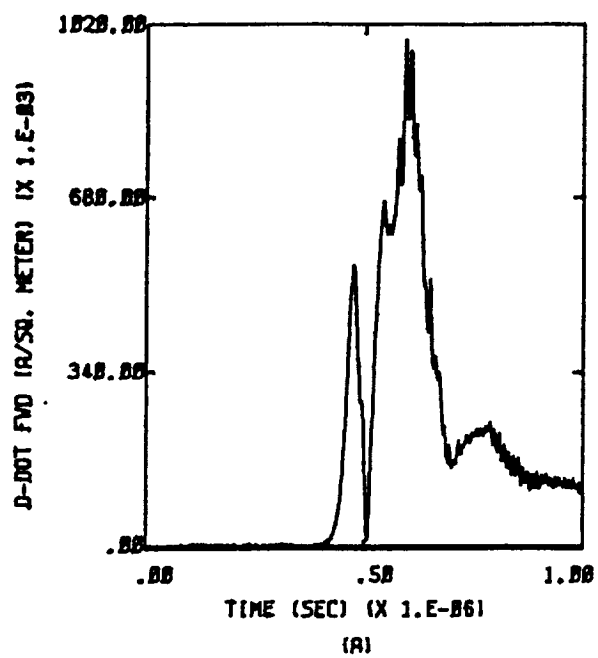


Figure D.48a  $-Y, Z; Q = -Q_m; E = 3 \times 10^4$  Volts per meter



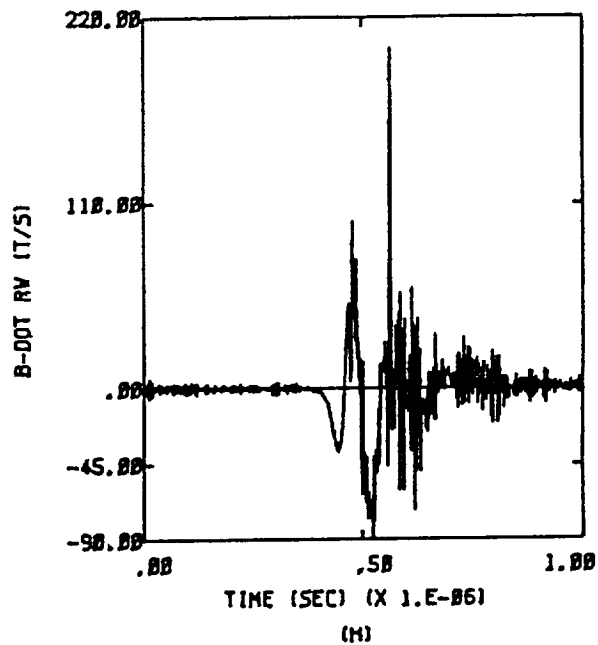
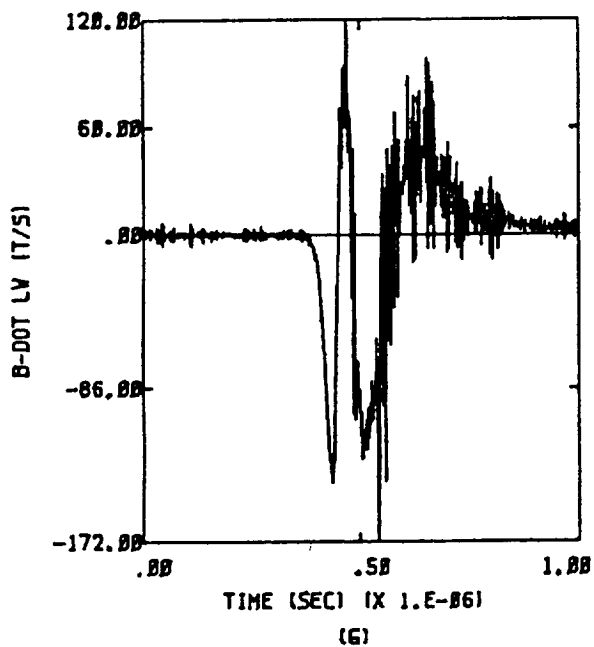
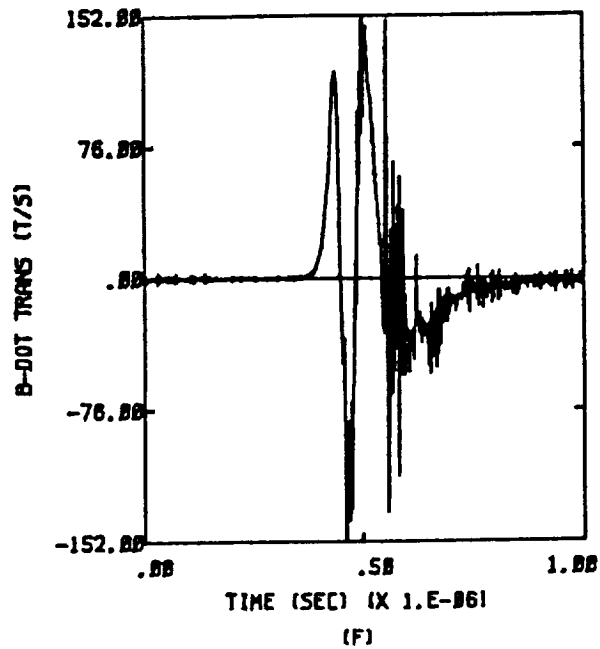
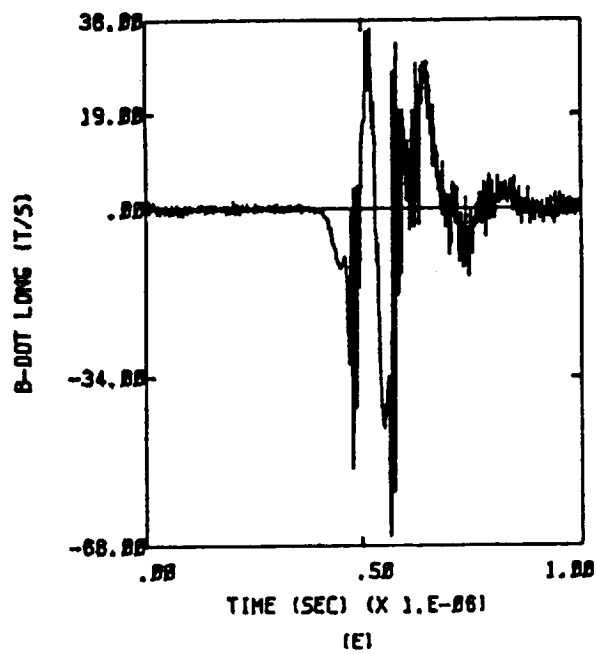


Figure D.48b  $-Y, Z$ ;  $Q = -Q_m$ ;  $E = 3 \times 10^4$  Volts per meter

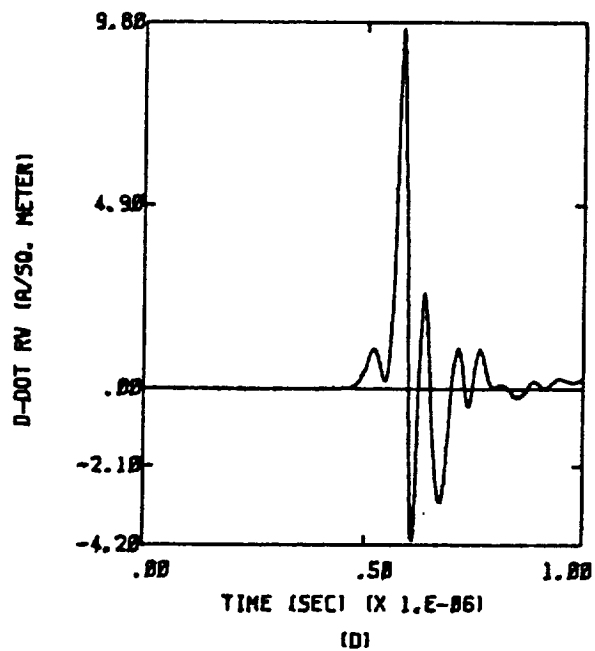
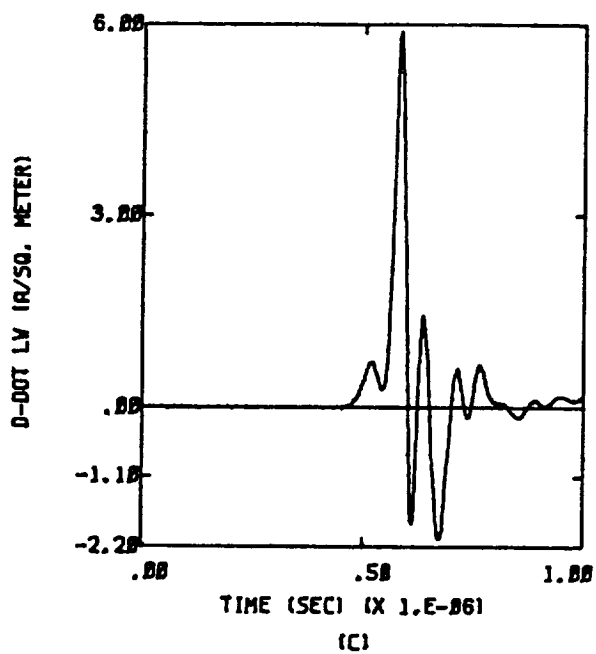
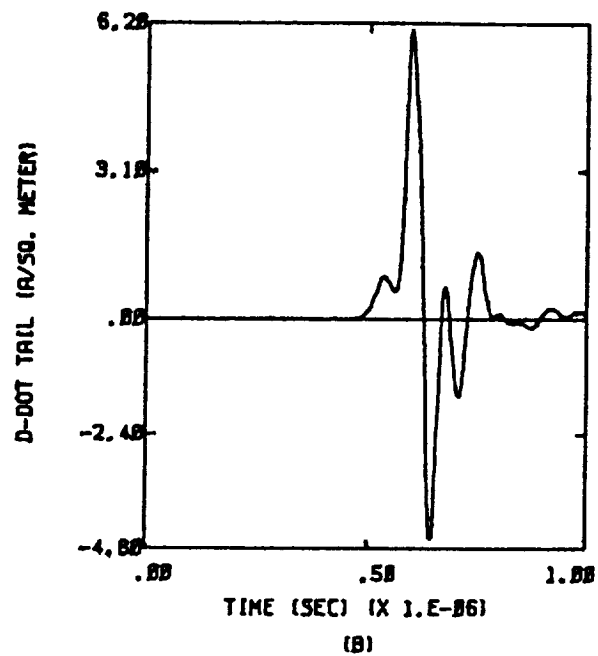
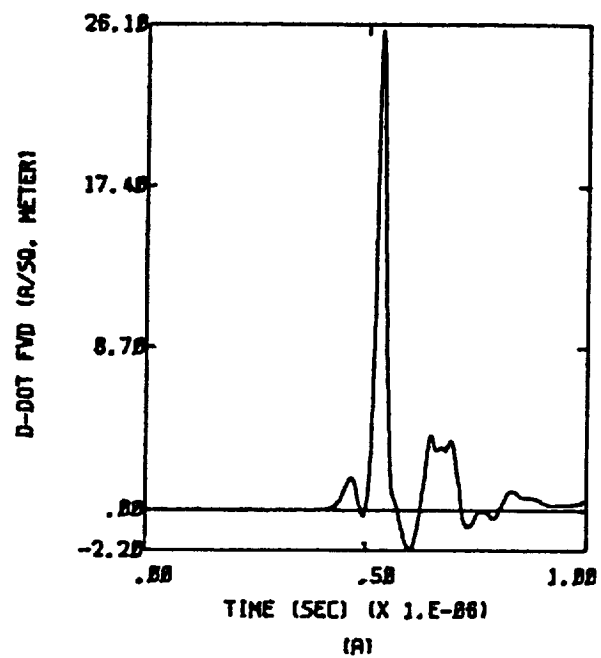


Figure D.49a  $X, -Z$ ;  $Q = -Q_m$ ;  $E = 2 \times 10^4$  Volts per meter

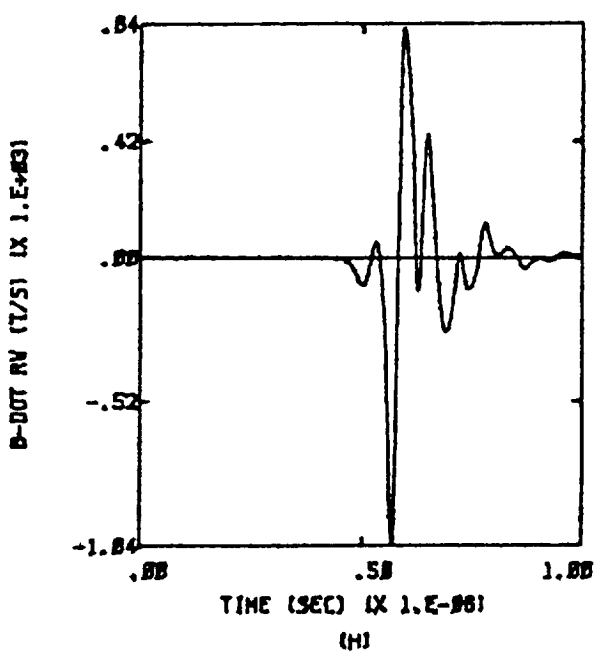
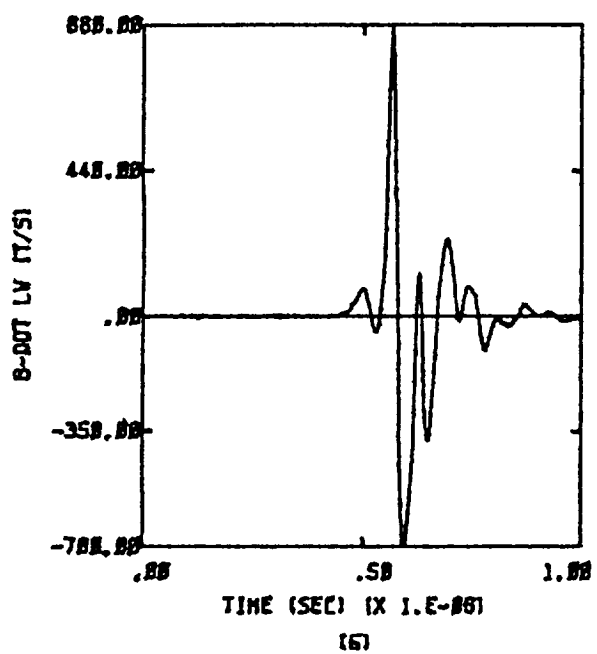
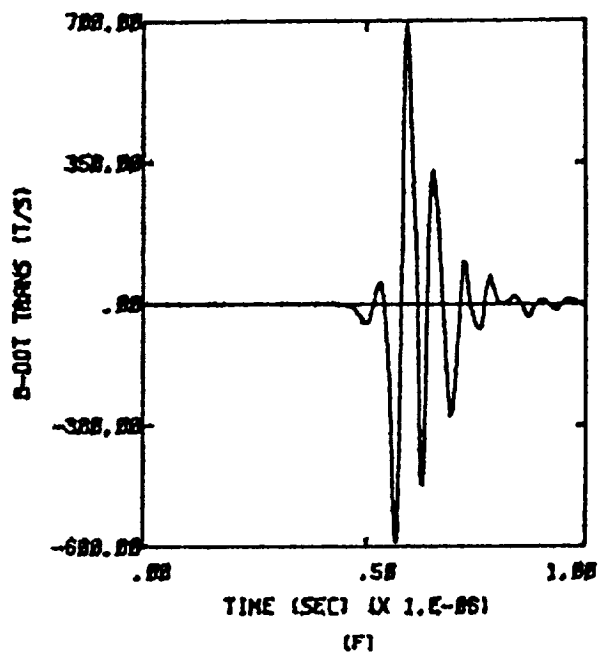
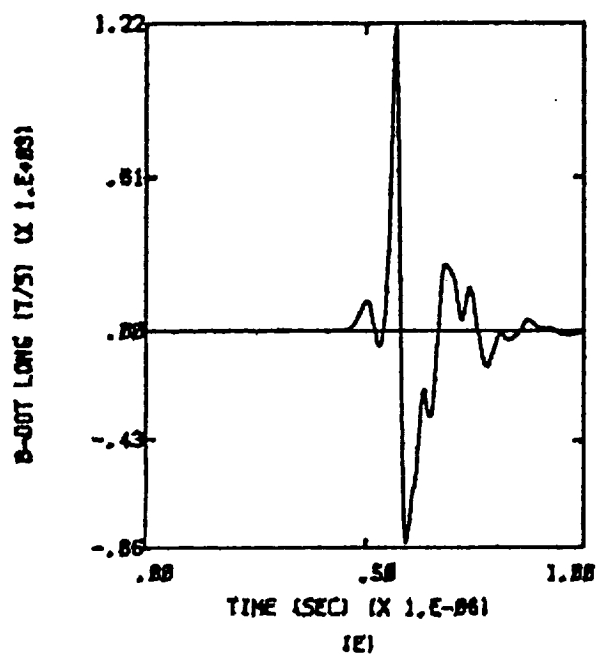


Figure D.49b  $X, -Z$ ;  $Q = -Q_m$ ;  $E = 2 \times 10^4$  Volts per meter

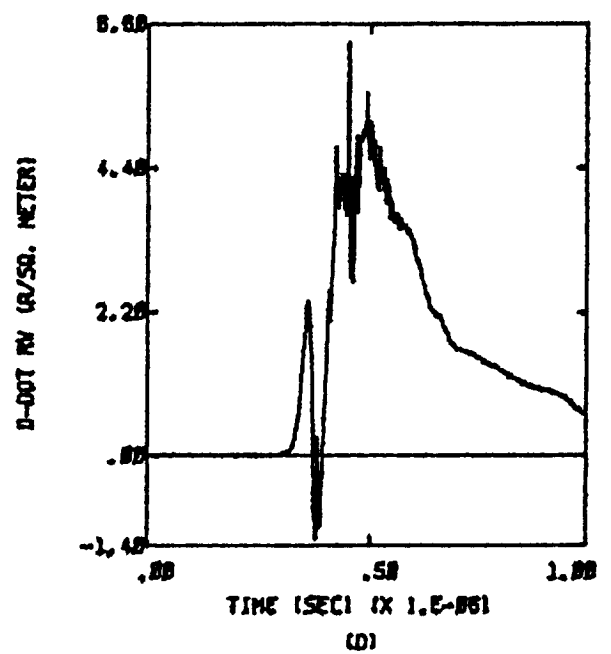
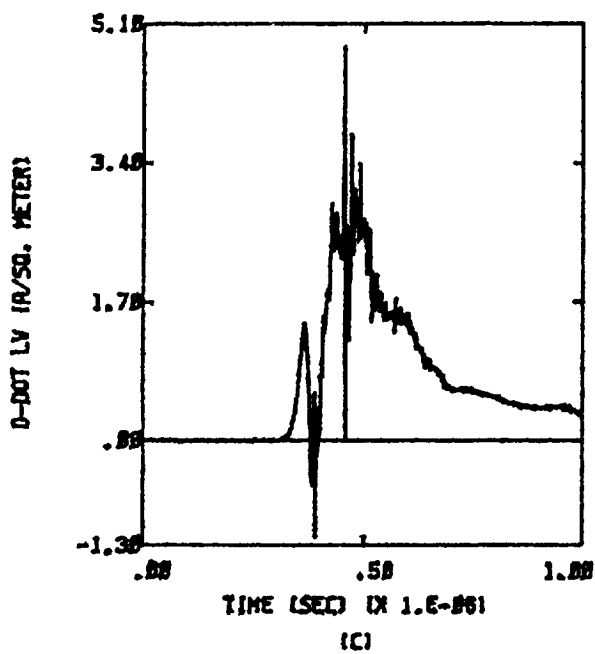
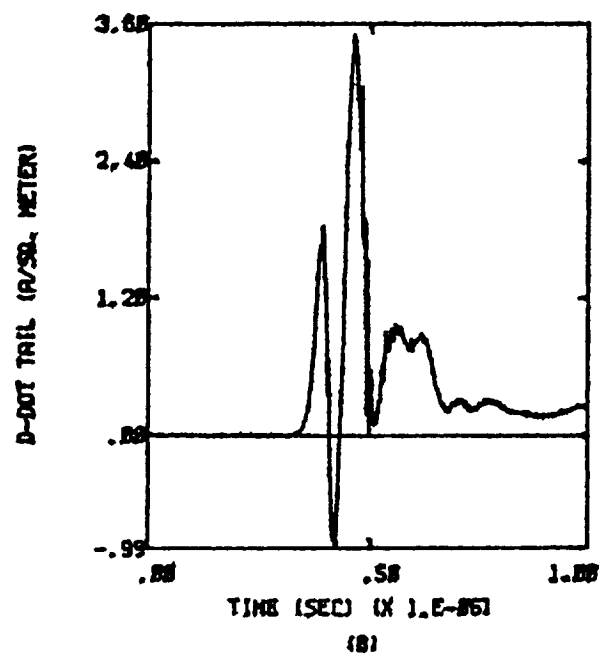
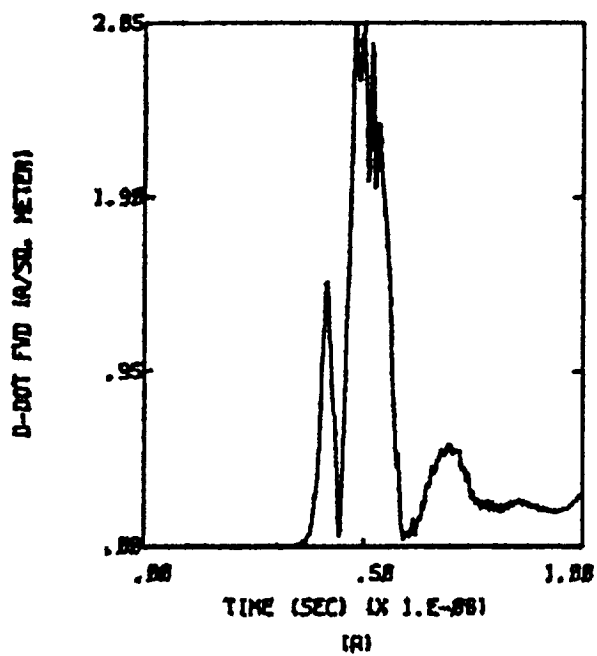


Figure D.50a  $-X, -Z$ ;  $Q = -Q_m$ ;  $E = 5 \times 10^4$  Volts per meter

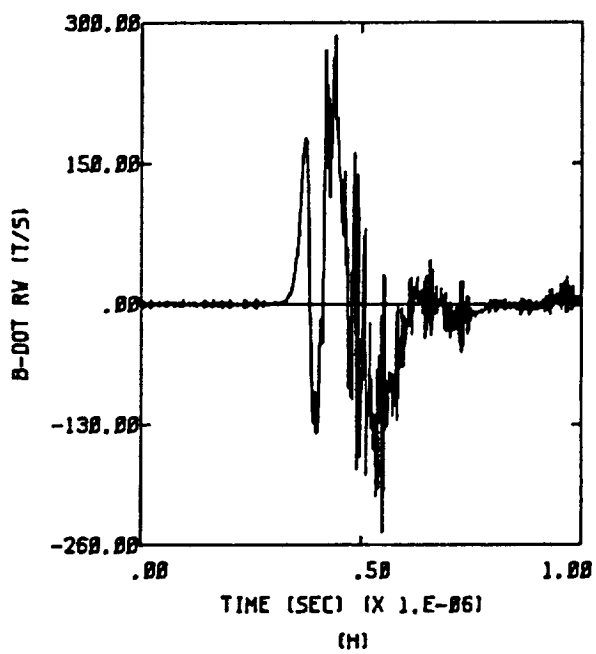
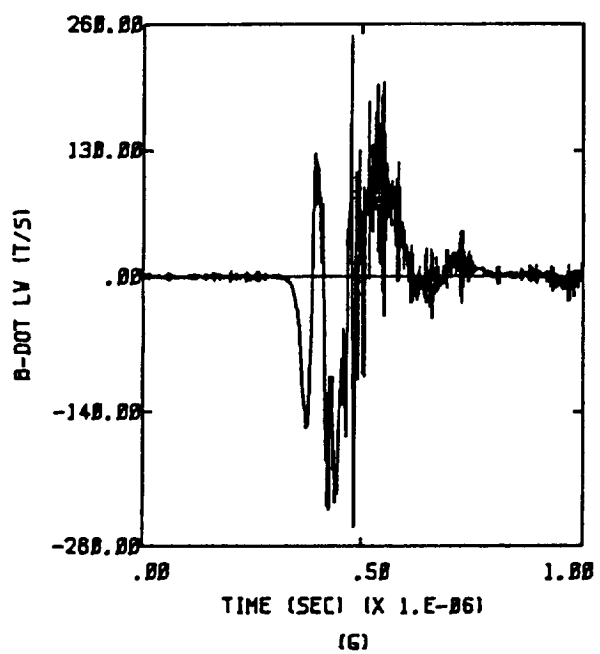
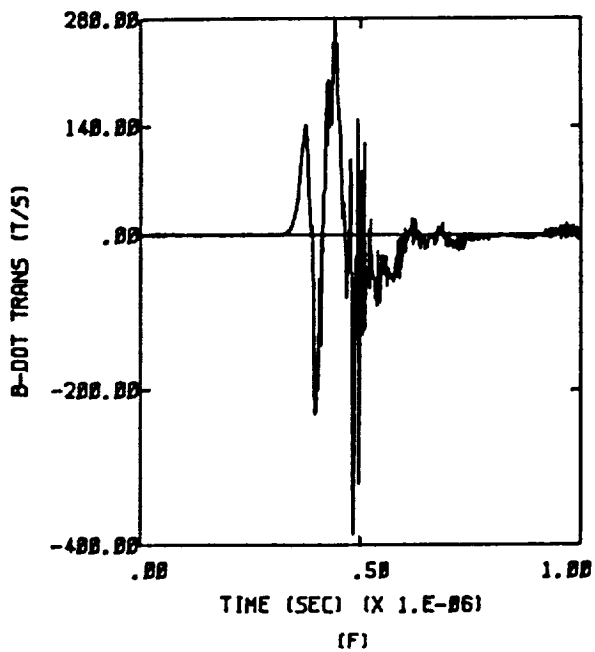
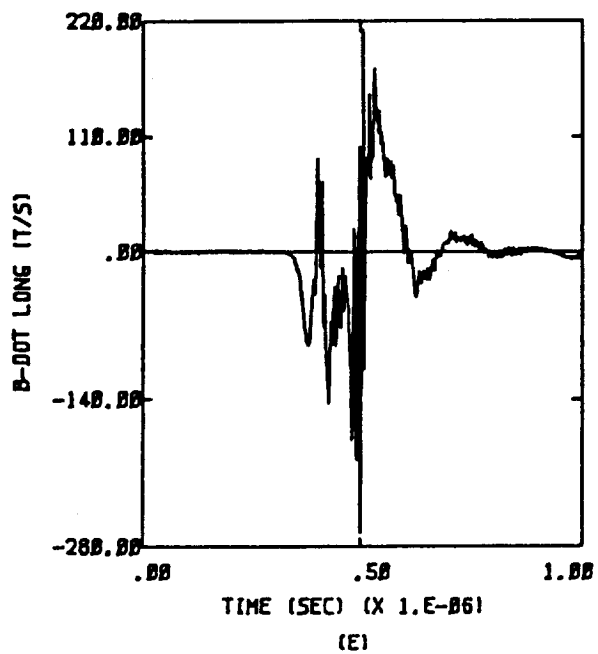


Figure D.50b  $-X, -Z$ ;  $Q = -Q_m$ ;  $E = 5 \times 10^4$  Volts per meter

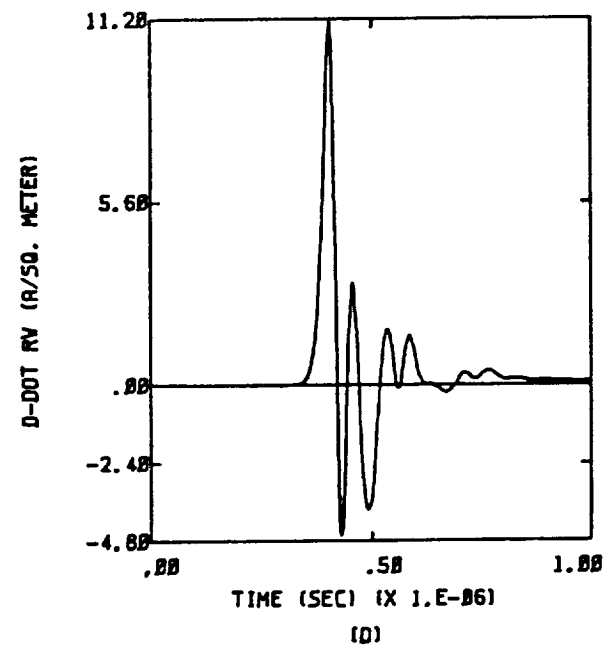
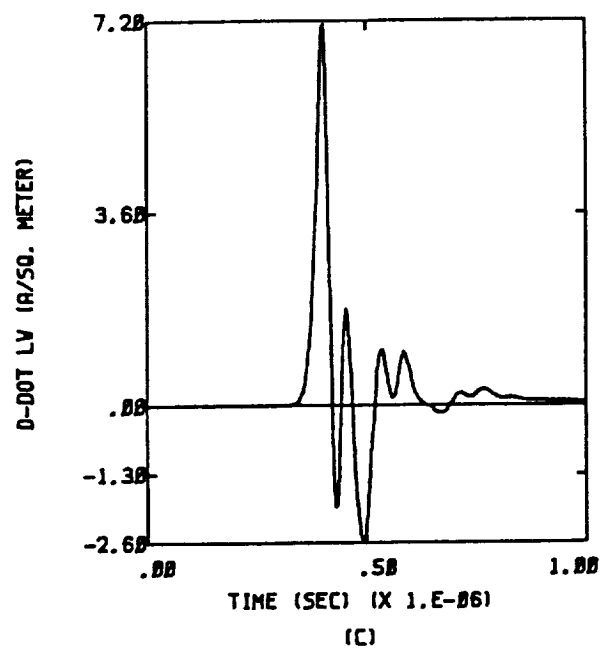
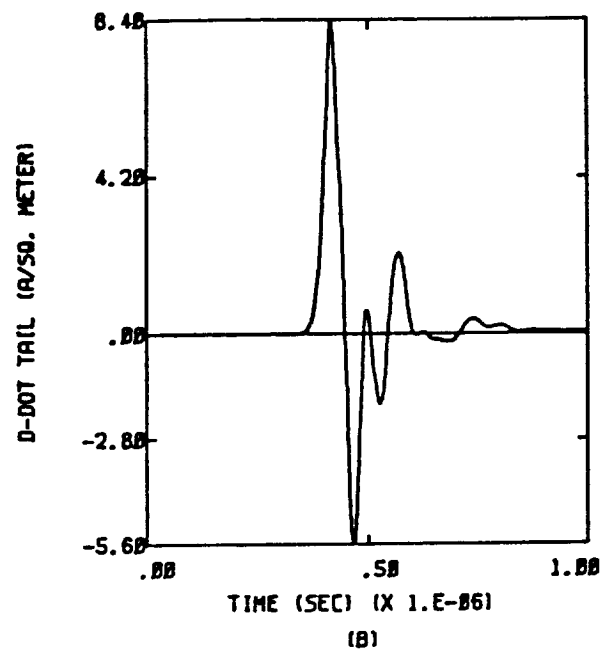
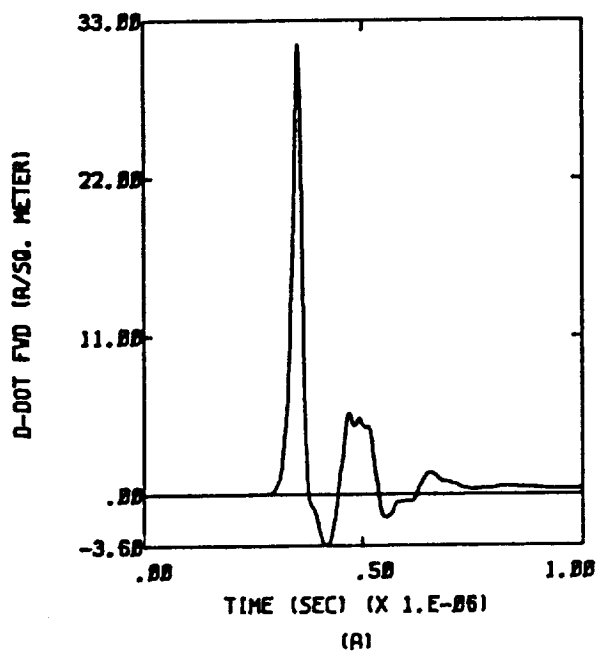


Figure D.51a  $X, Z$ ;  $Q = -Q_m$ ;  $E = 5 \times 10^4$  Volts per meter

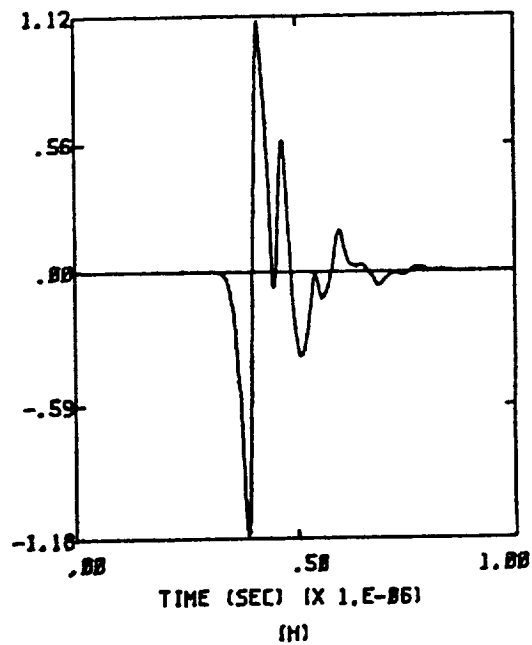
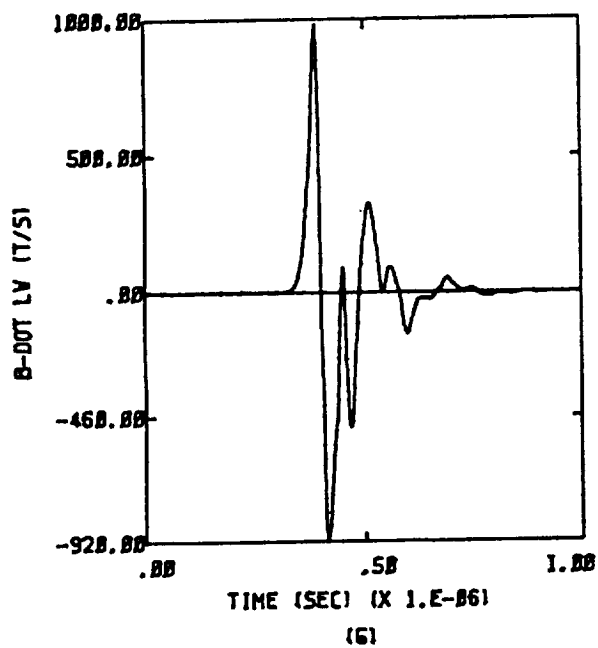
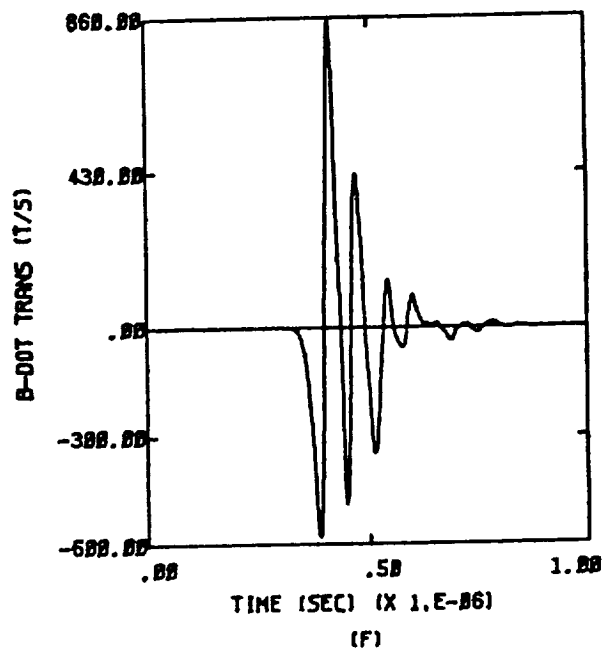
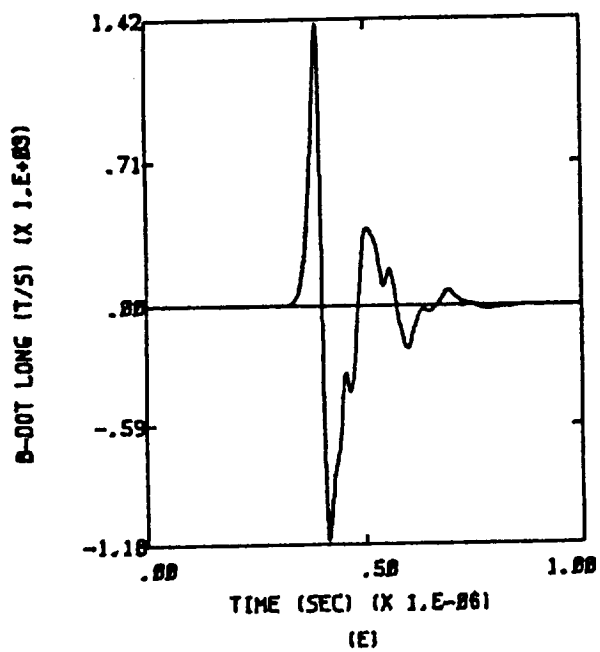


Figure D.51b X,Z;  $Q = -Q_m$ ;  $E = 5 \times 10^4$  Volts per meter

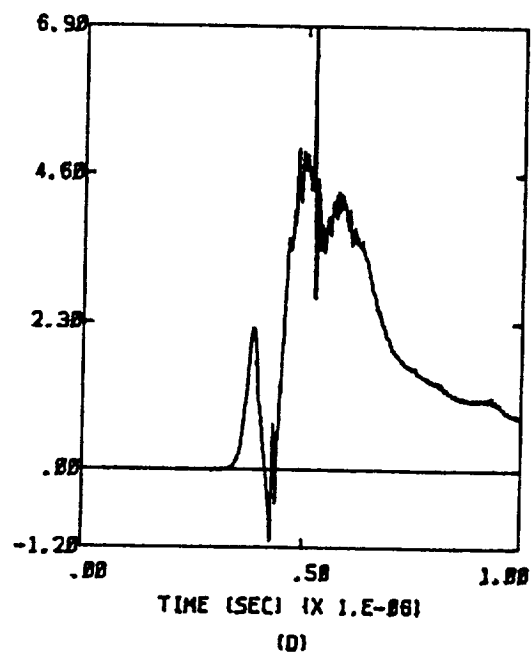
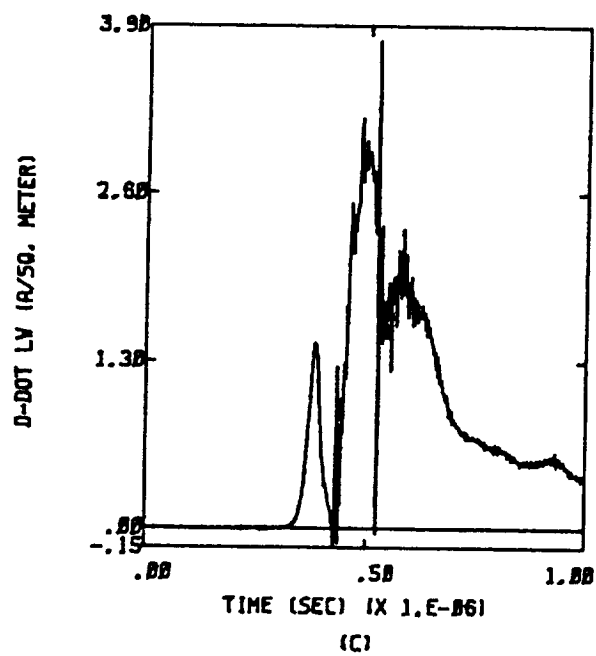
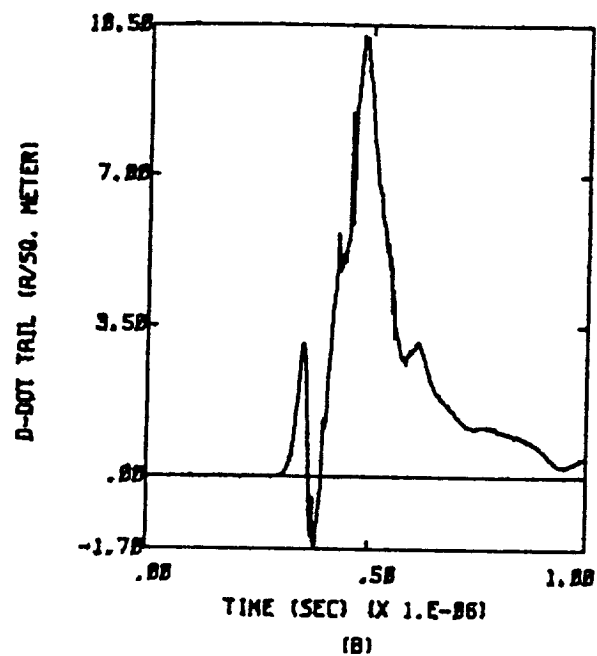
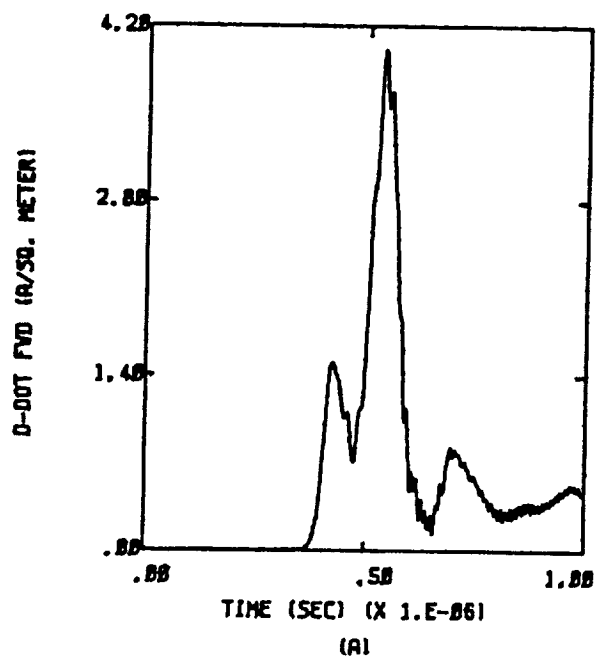


Figure D.52a  $-X, Z$ ;  $Q = -Q_m$ ;  $E = 5 \times 10^4$  Volts per meter



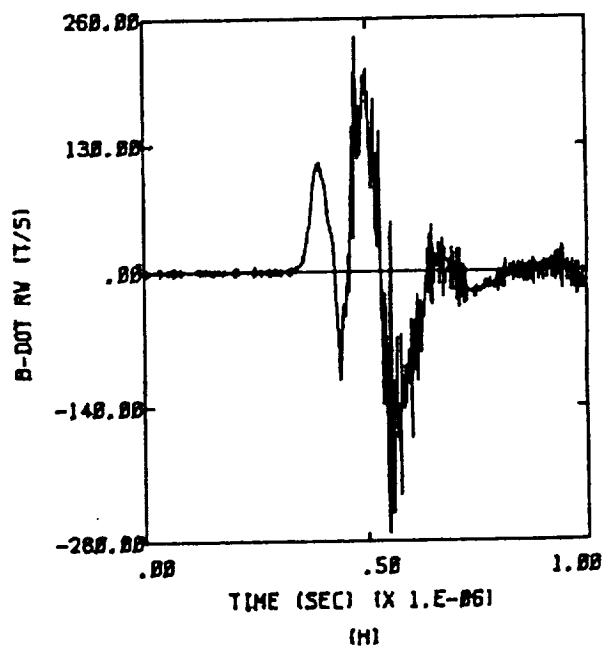
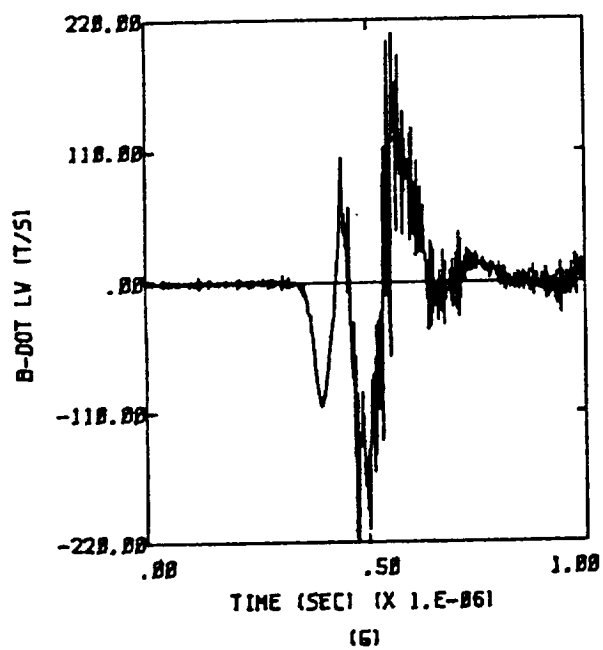
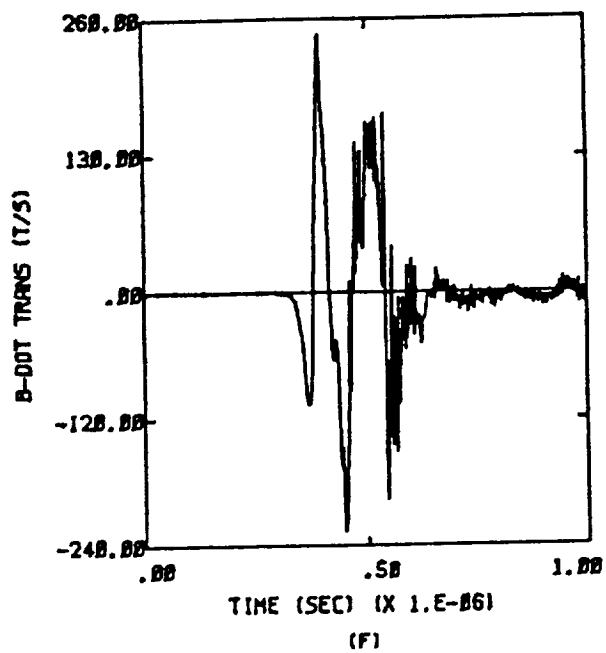
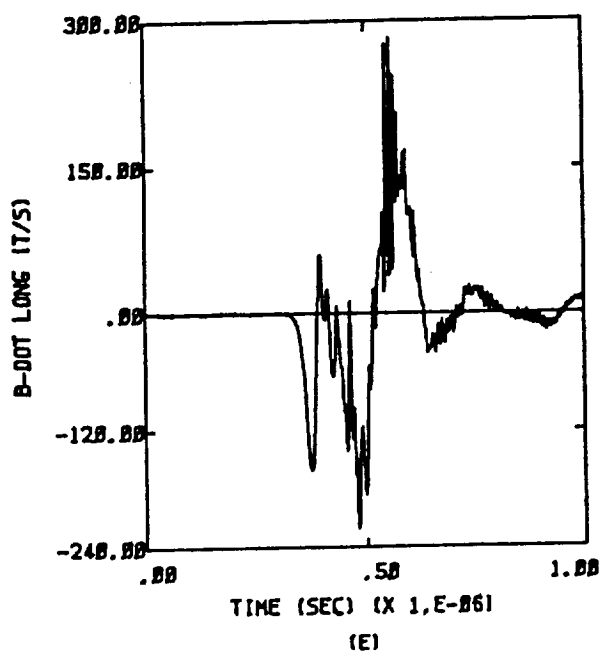


Figure D.52b  $-X, Z$ ;  $Q = -Q_m$ ;  $E = 5 \times 10^4$  Volts per meter

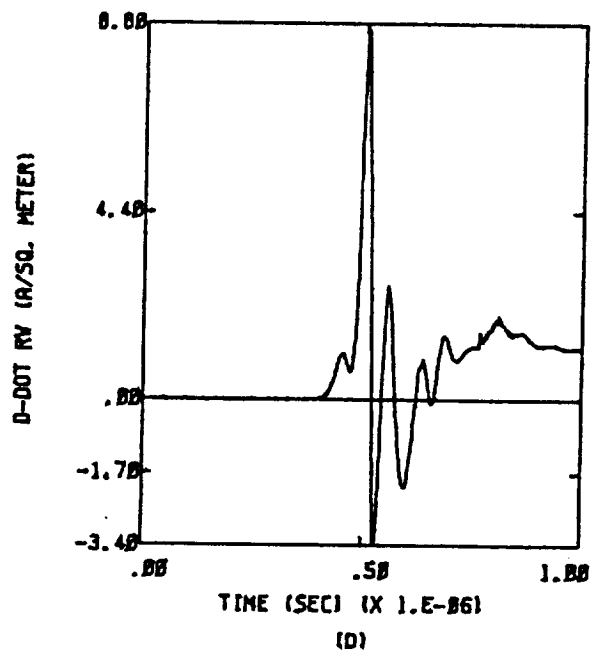
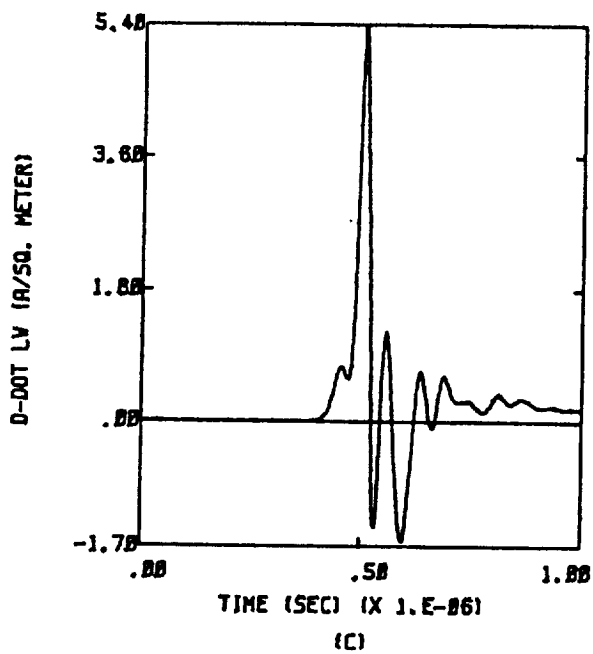
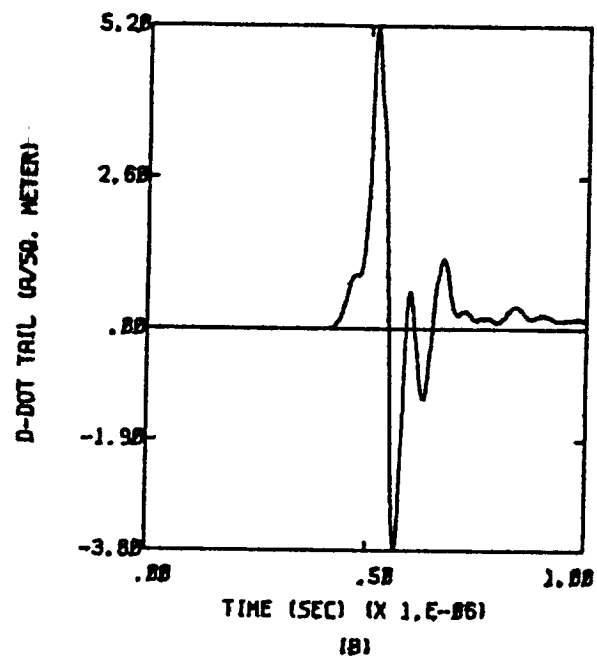
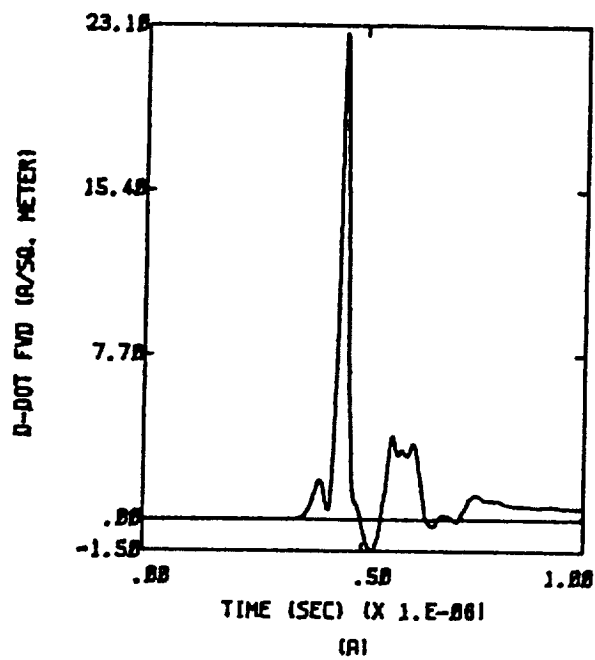


Figure D.53a X,Y,-Z;  $Q = -Q_m$ ;  $E = 3 \times 10^4$  Volts per meter

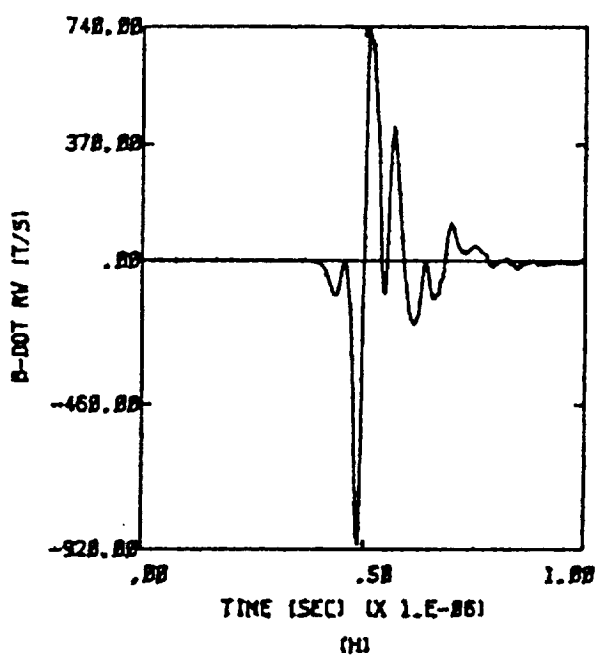
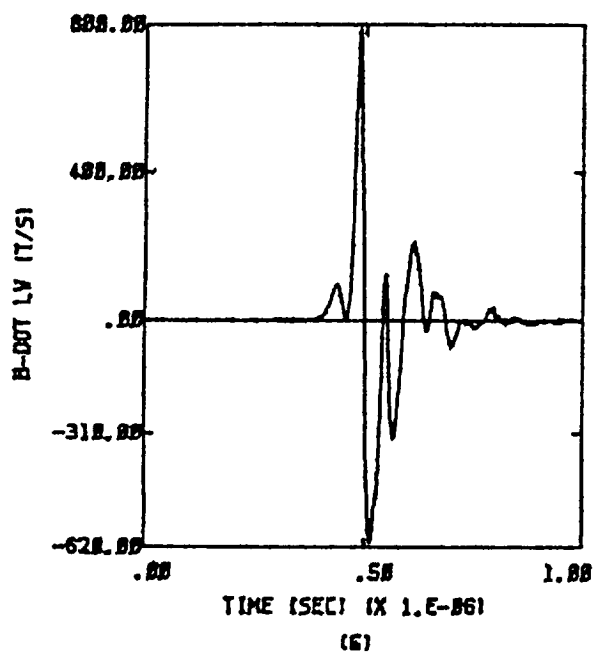
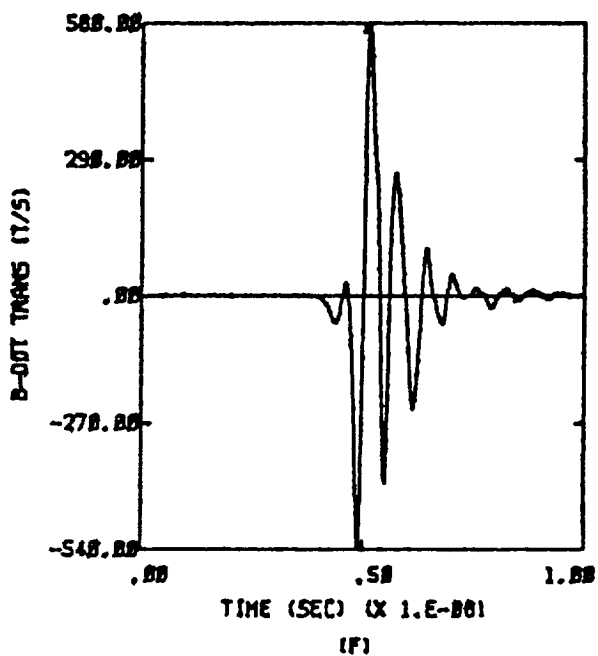
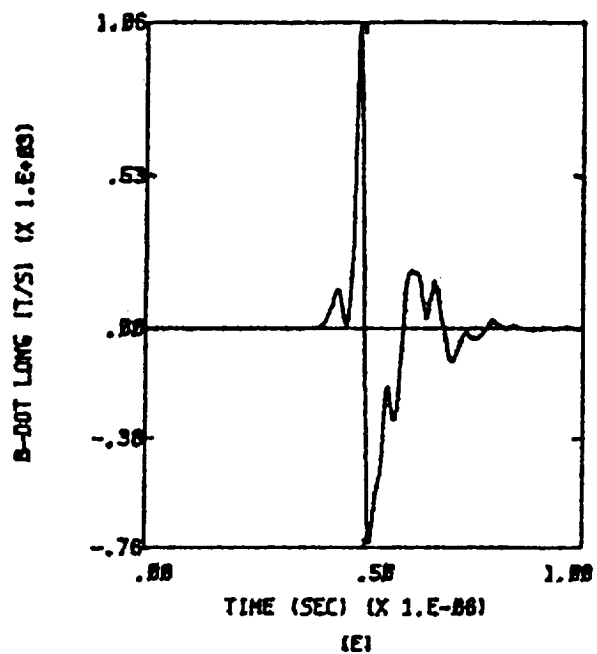


Figure D.53b X,Y,-Z;  $Q = -Q_m$ ;  $E = 3 \times 10^4$  Volts per meter

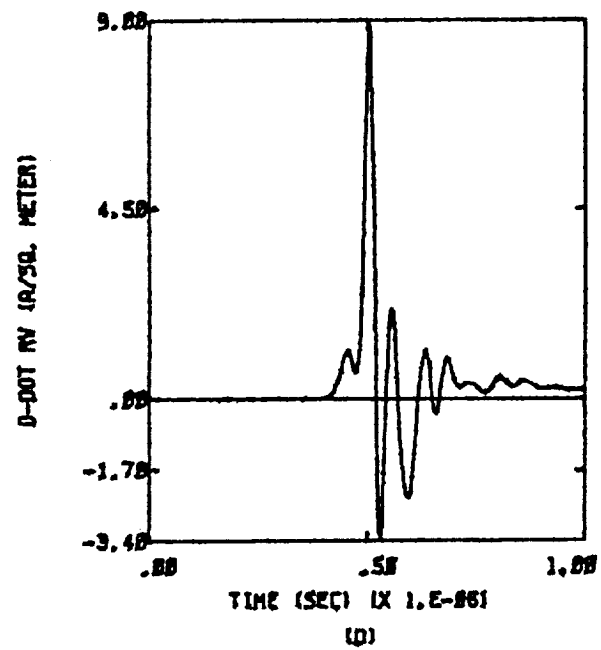
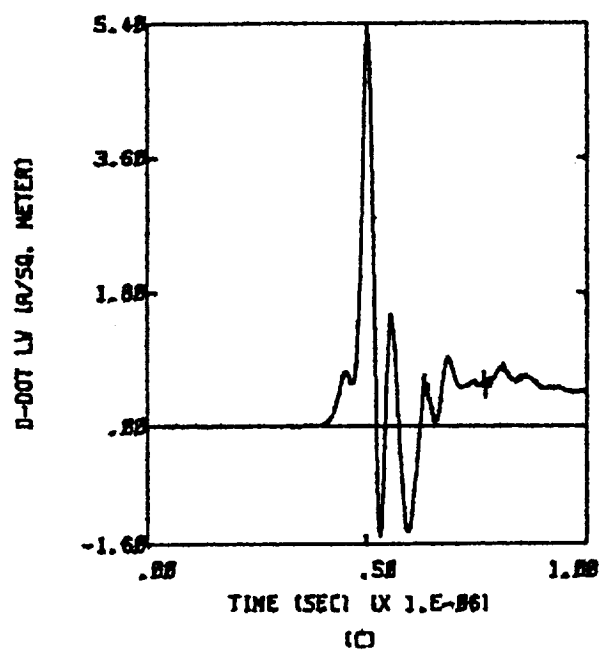
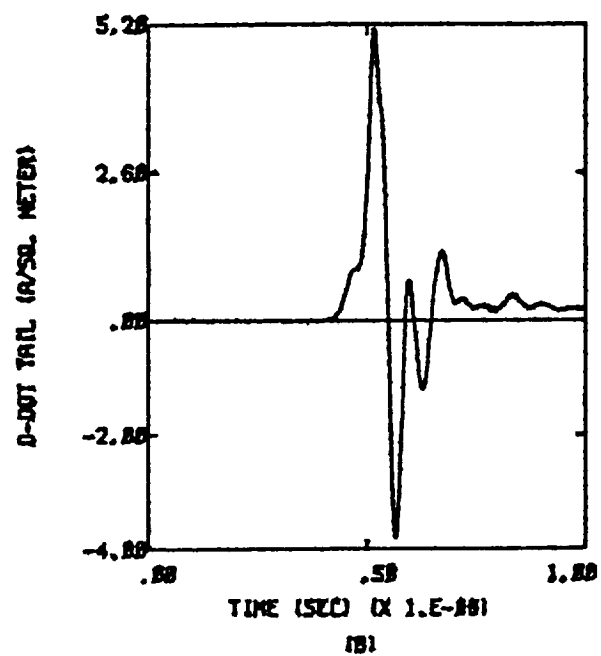
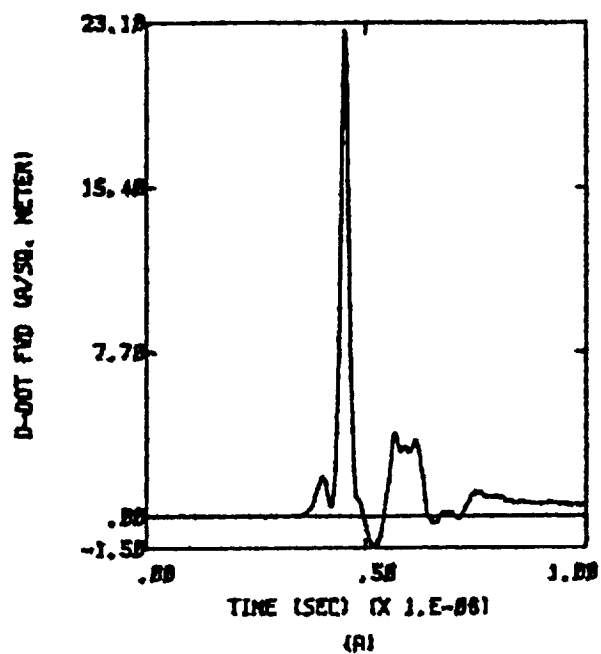


Figure D.54a  $X, -Y, -Z; Q = -Q_m; E = 3 \times 10^4$  Volts per meter

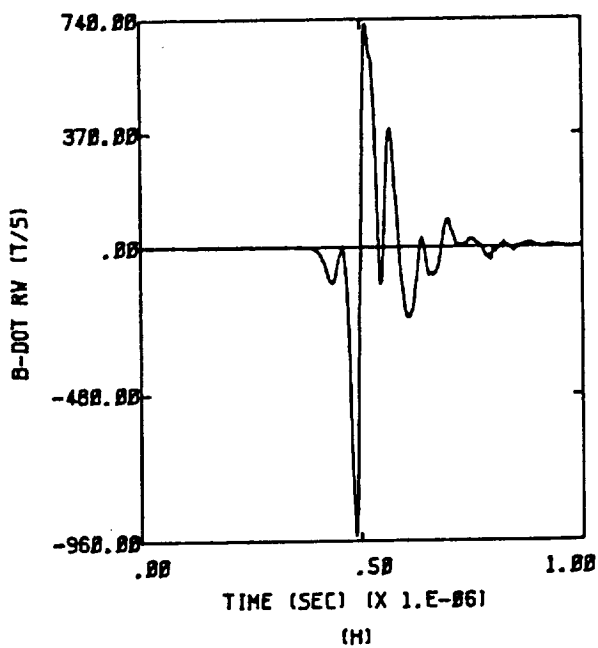
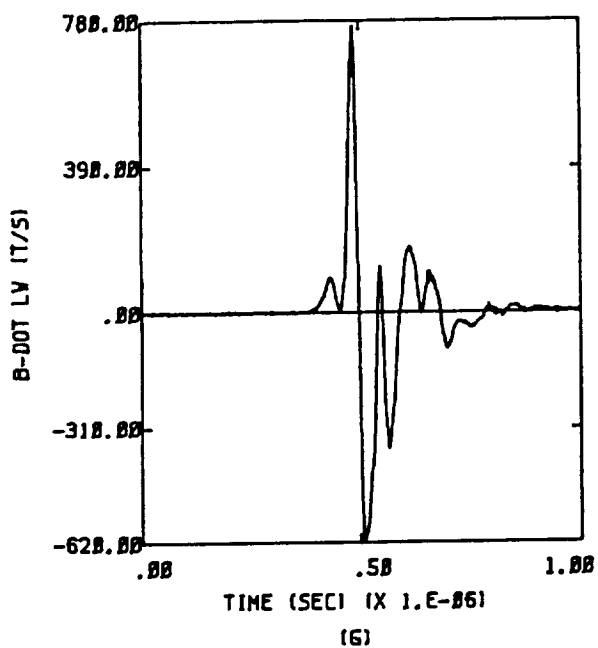
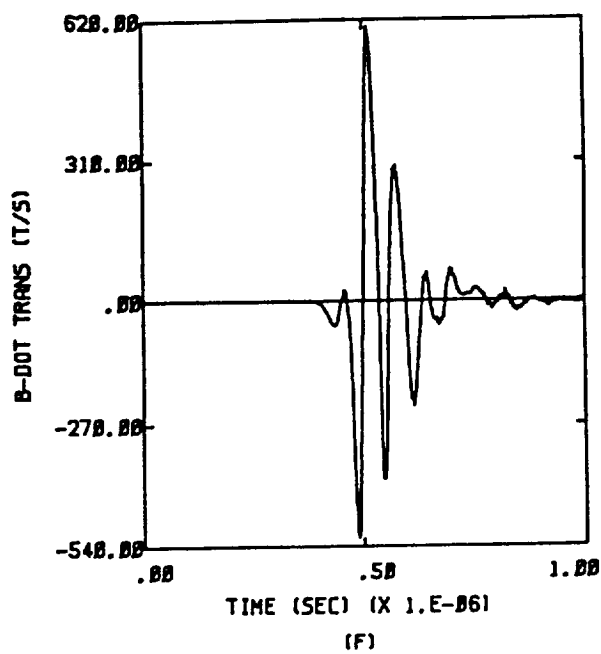
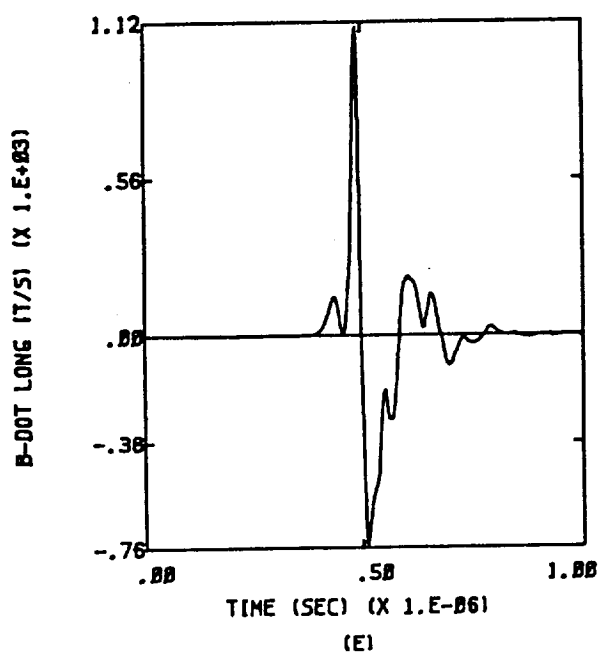


Figure D.54b X,-Y,-Z;  $Q = -Q_m$ ;  $E = 3 \times 10^4$  Volts per meter

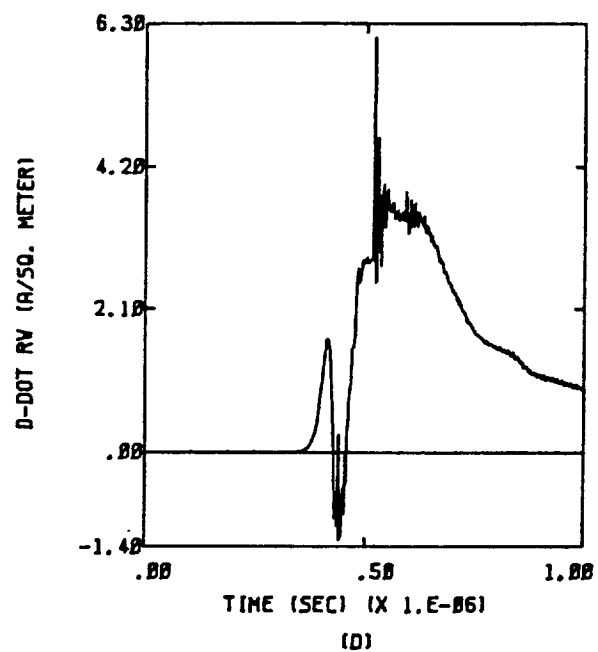
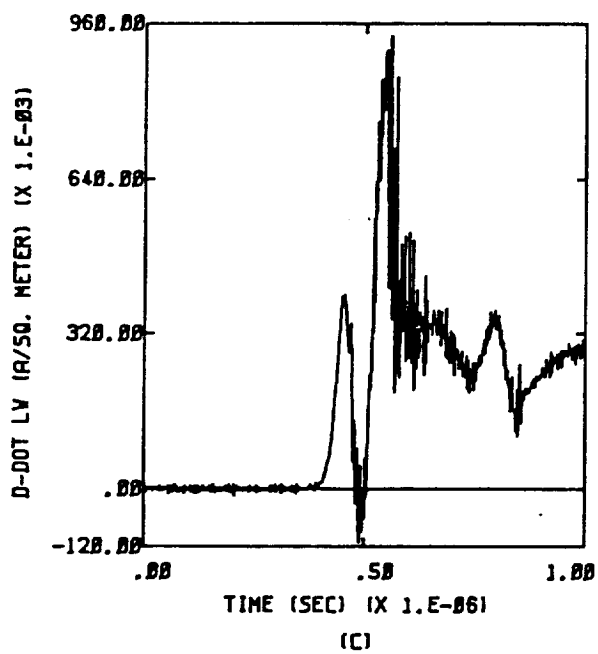
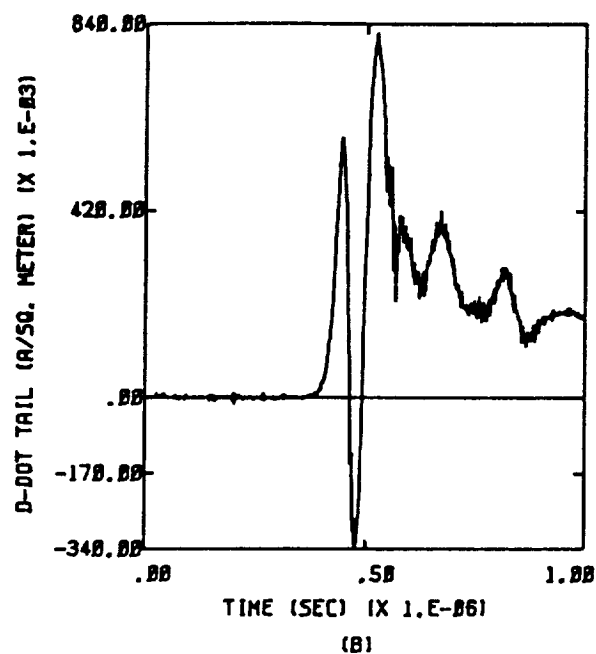
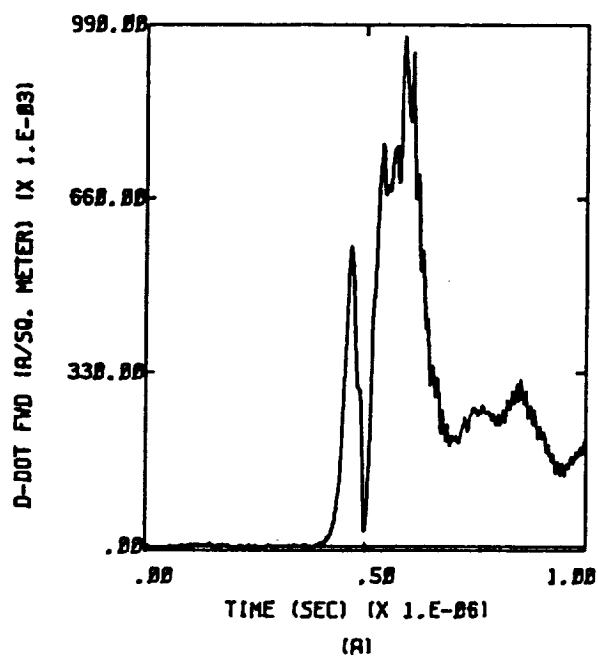


Figure D.55a  $-X, Y, -Z$ ;  $Q = -Q_m$ ;  $E = 2 \times 10^4$  Volts per meter

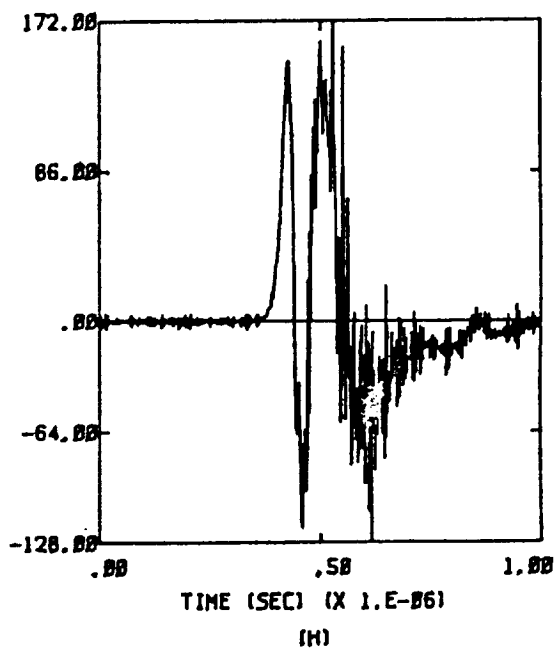
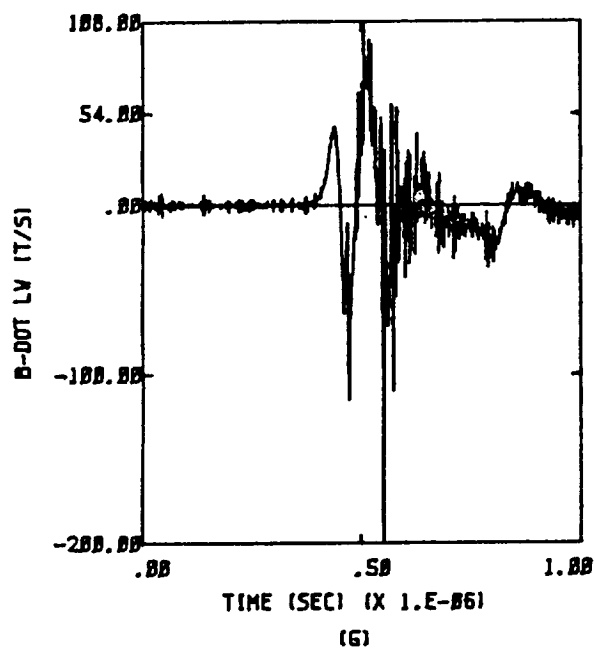
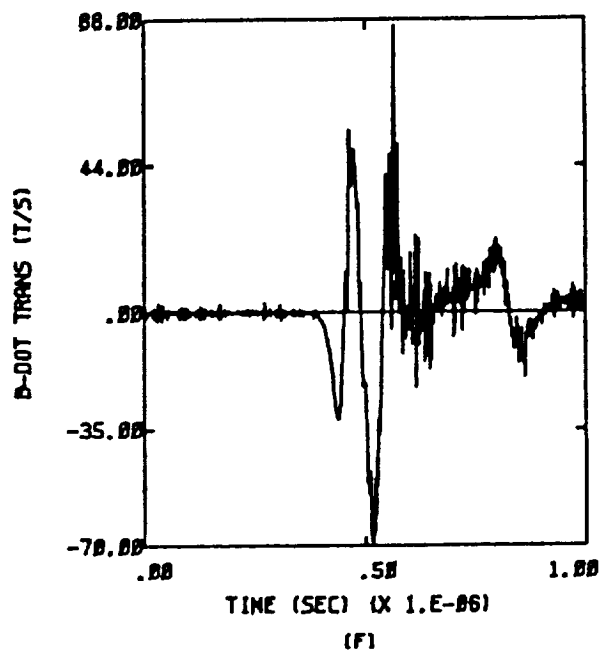
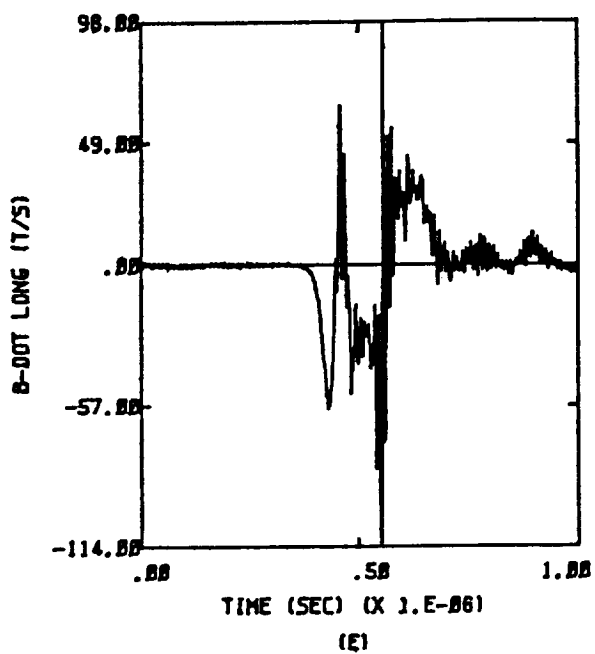


Figure D.55b -X,Y,-Z;  $Q = -Q_m$ ;  $E = 2 \times 10^4$  Volts per meter

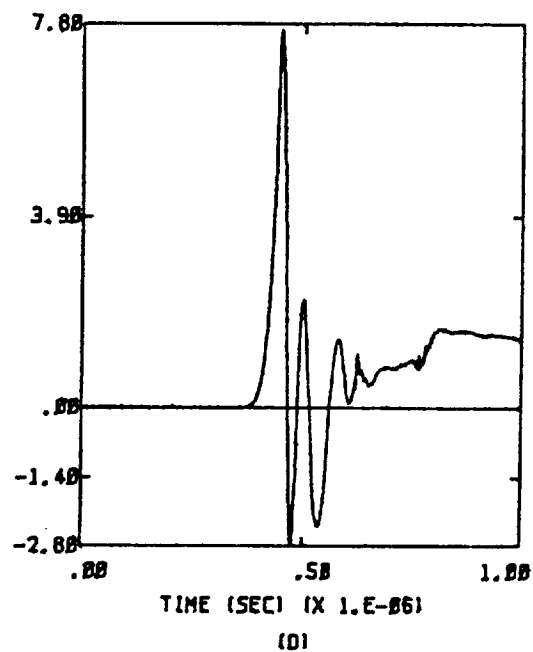
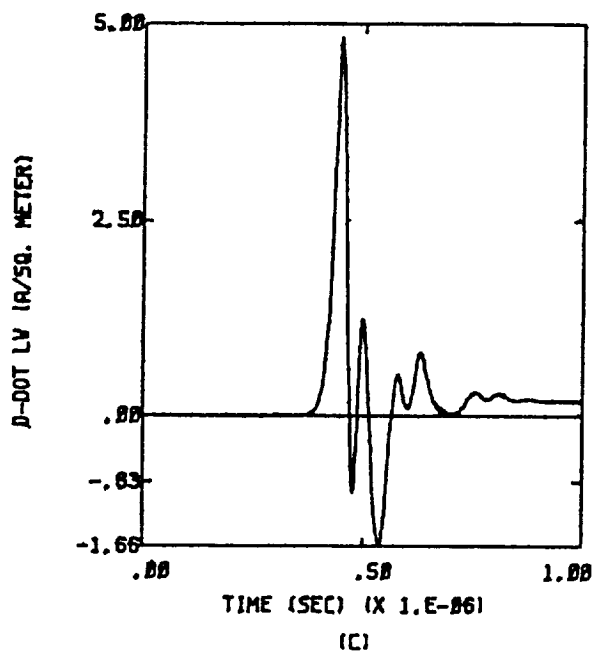
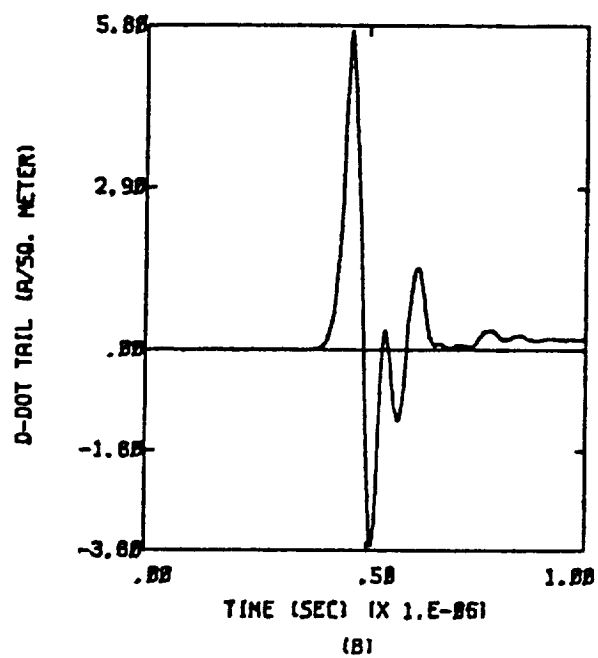
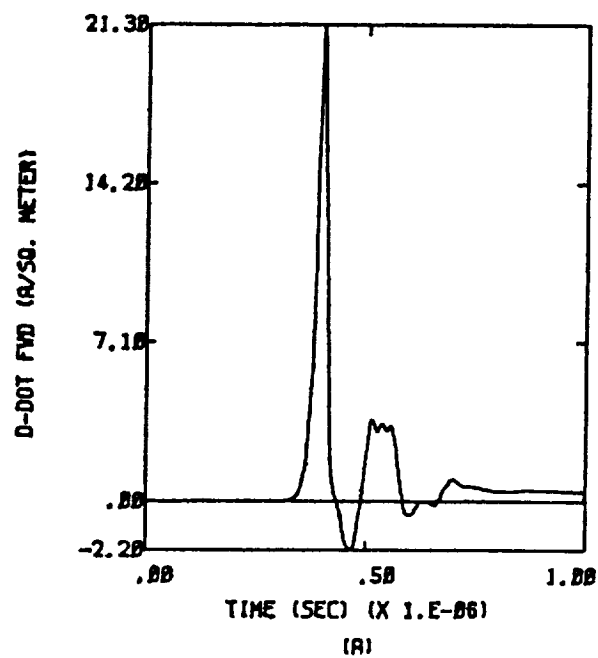


Figure D.56a X,Y,Z;  $Q = -Q_m$ ;  $E = 5 \times 10^4$  Volts per meter



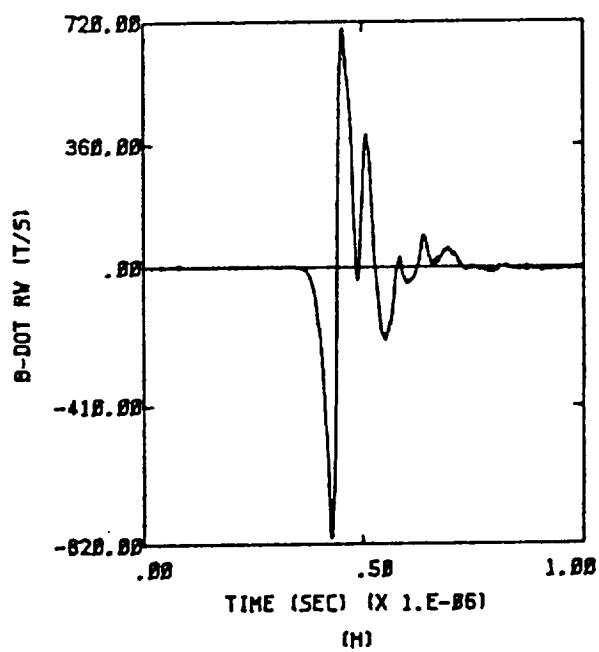
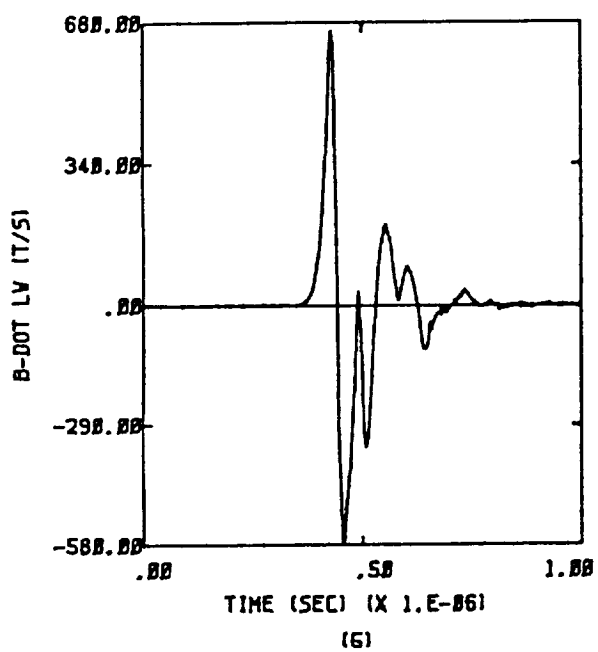
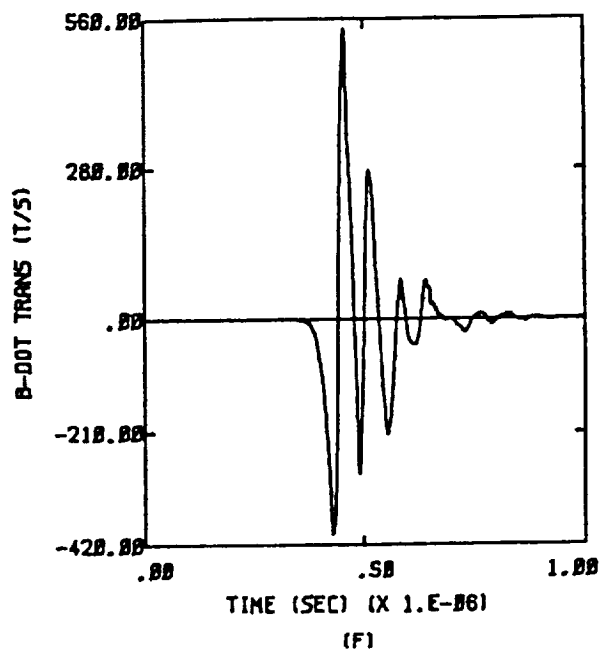
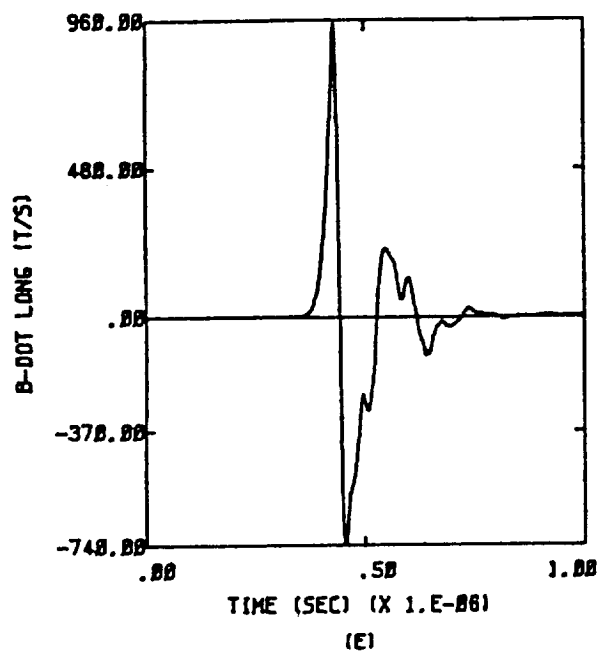


Figure D.56b X,Y,Z;  $Q = -Q_m$ ;  $E = 5 \times 10^4$  Volts per meter

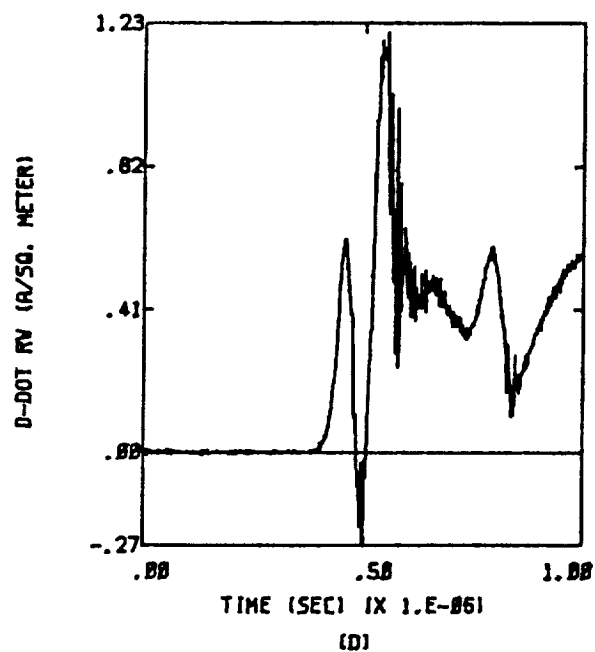
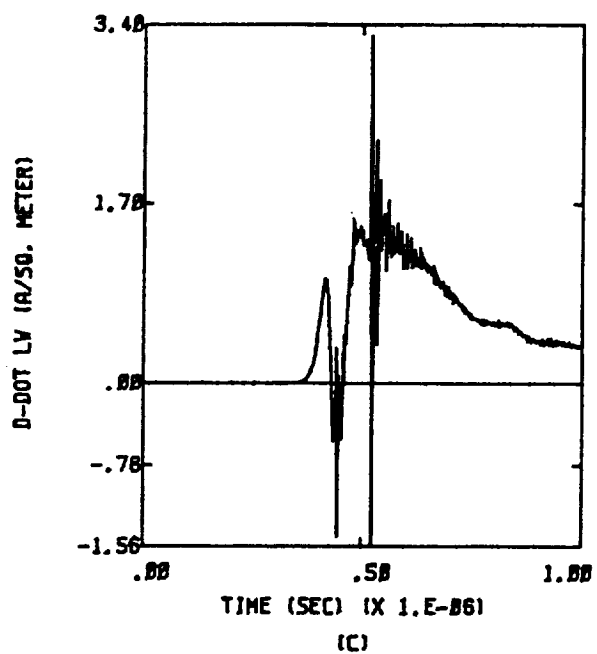
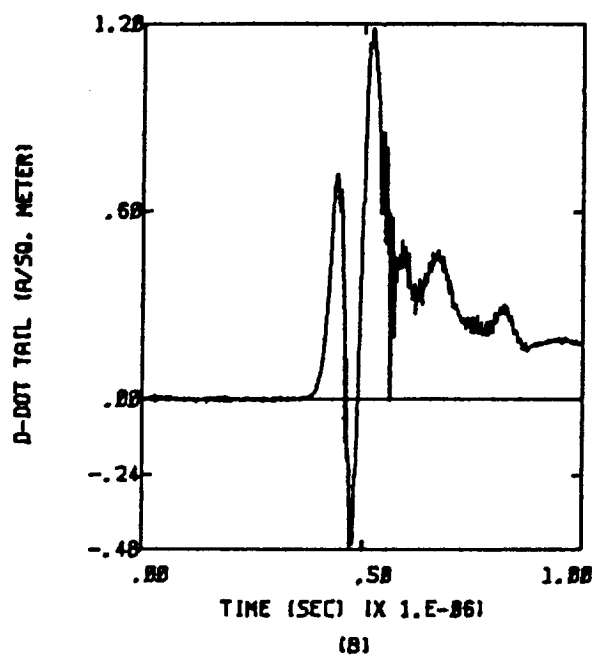
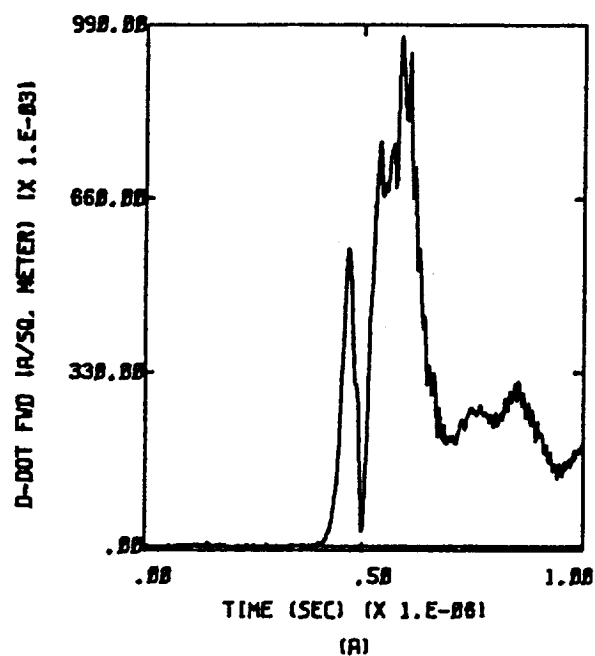


Figure D.57a -X,-Y,-Z;  $Q = -Q_m$ ;  $E = 2 \times 10^4$  Volts per meter

ORIGINAL PAGE IS  
OF POOR QUALITY

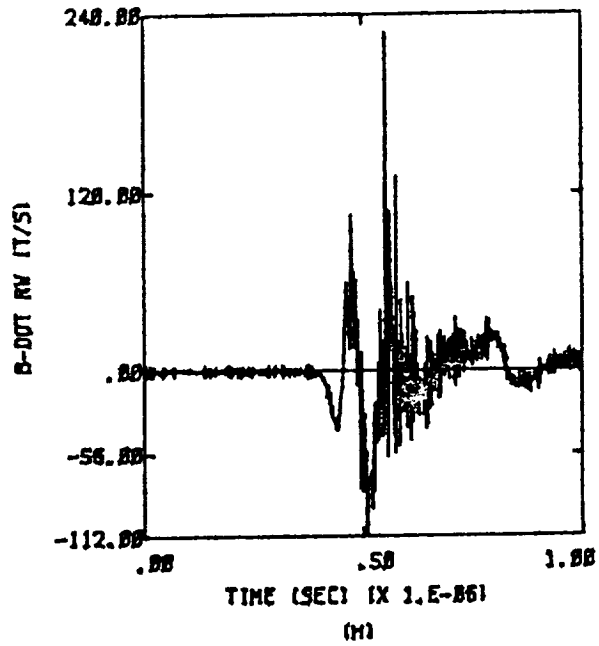
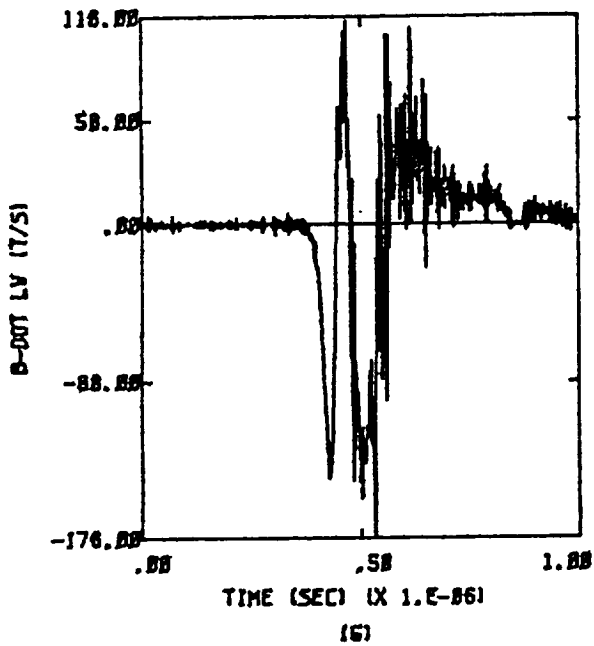
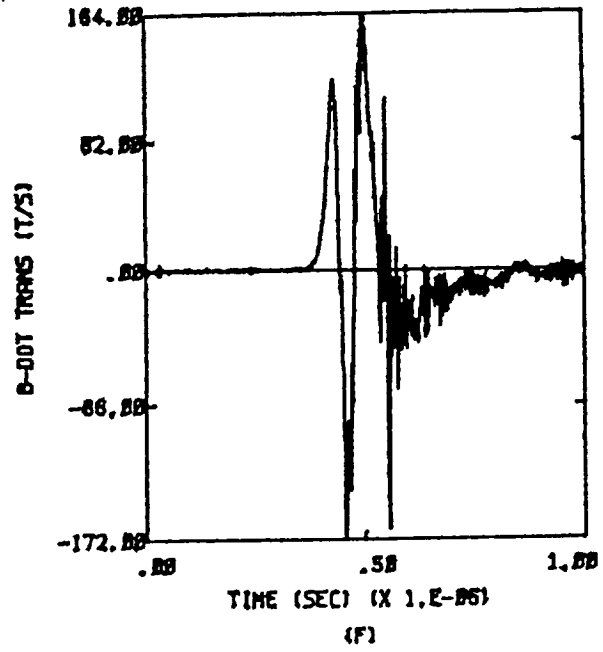
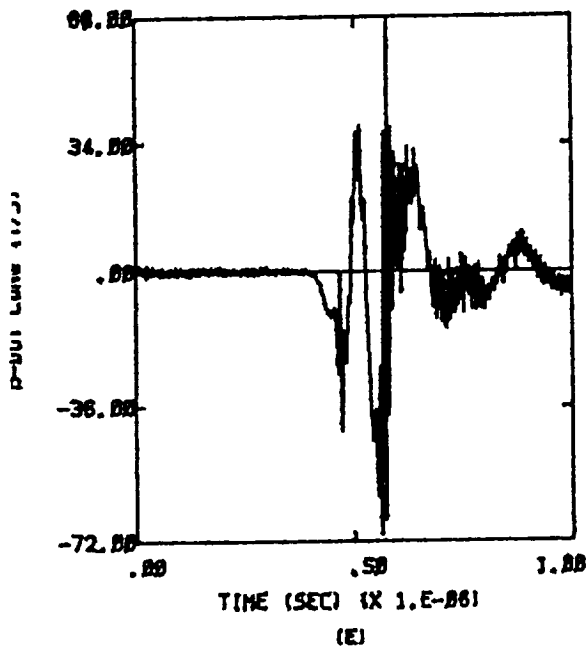


Figure D.57b  $-X, -Y, -Z; Q = -Q_{in}; E = 2 \times 10^4$  Volts per meter

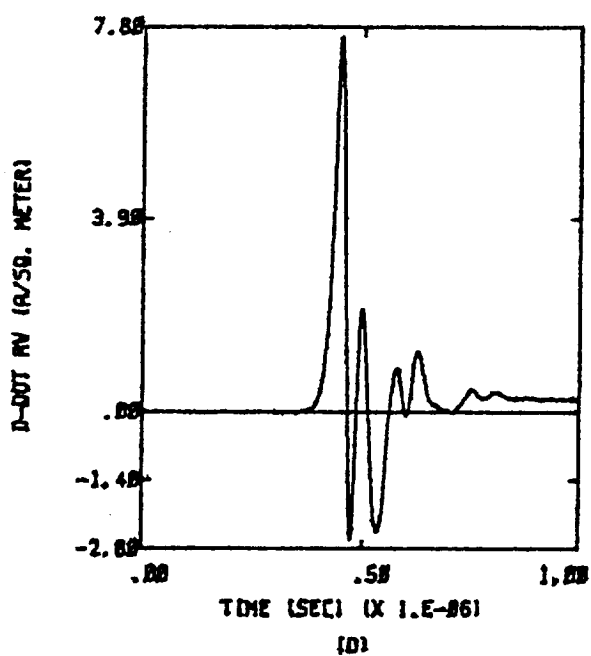
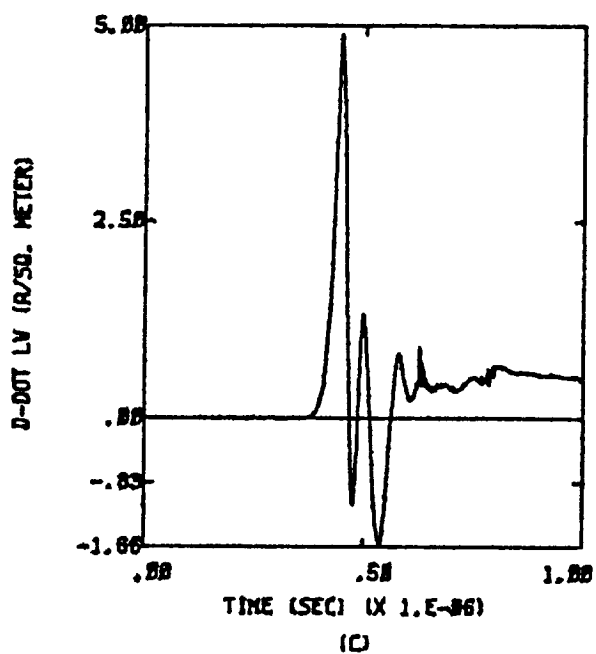
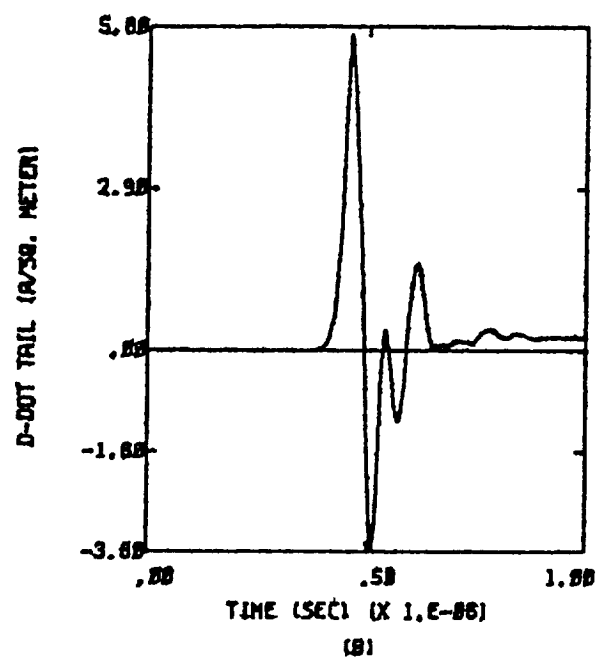
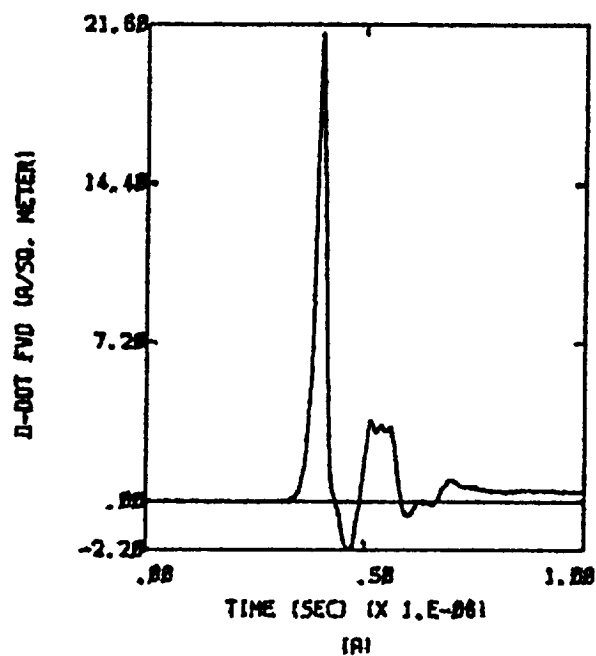


Figure D.58a X,-Y,Z;  $Q = -Q_m$ ;  $E = 5 \times 10^4$  Volts per meter

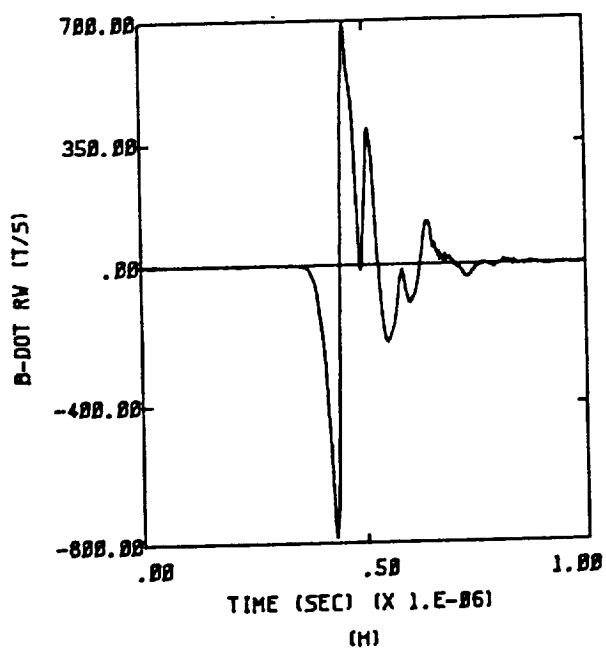
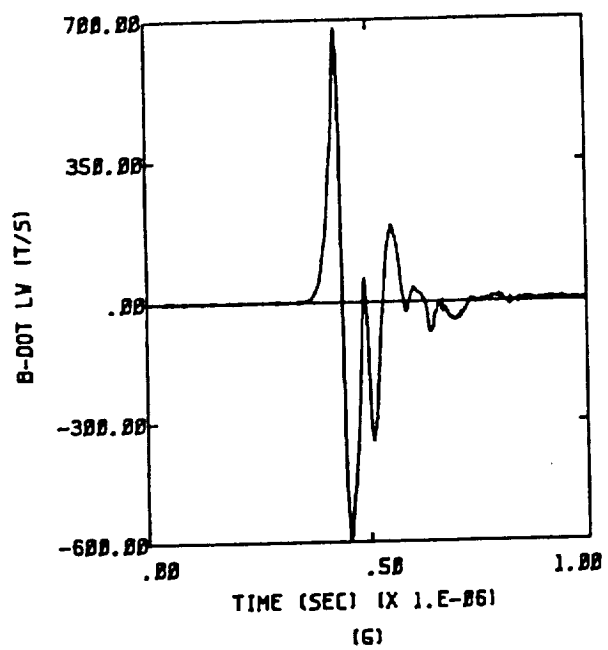
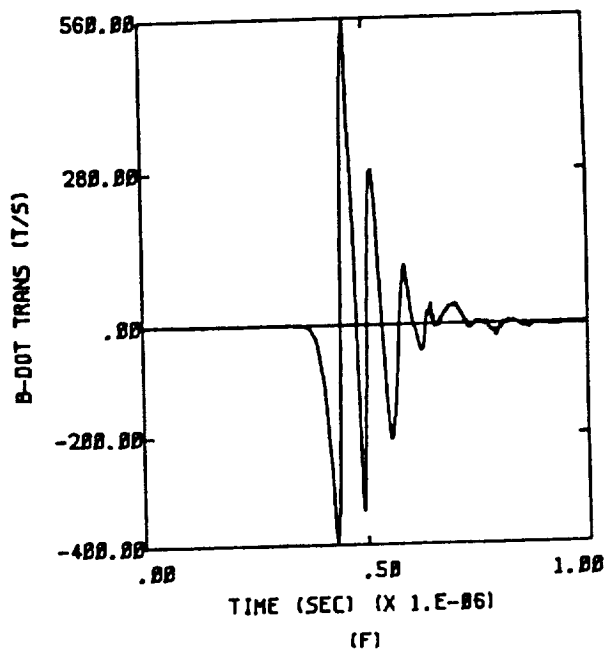
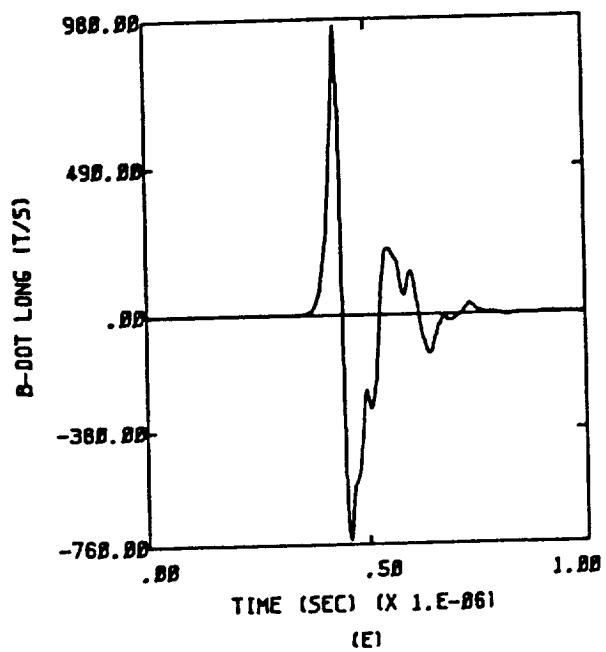


Figure D.58b X,-Y,Z;  $Q = -Q_m$ ;  $E = 5 \times 10^4$  Volts per meter

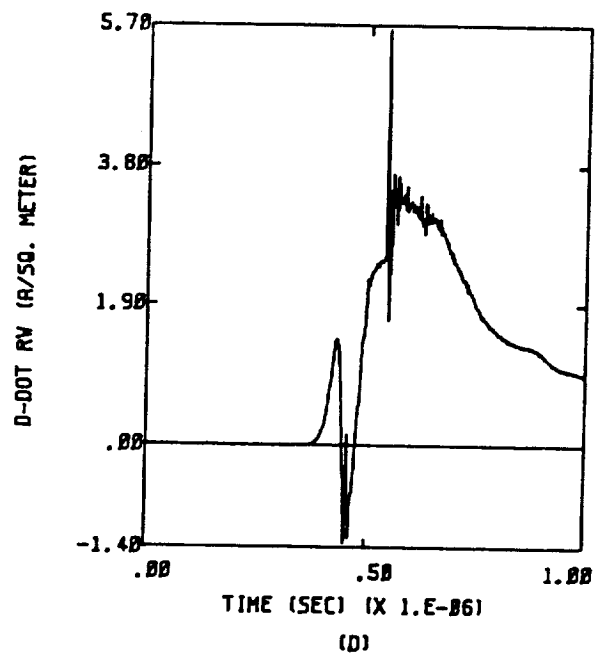
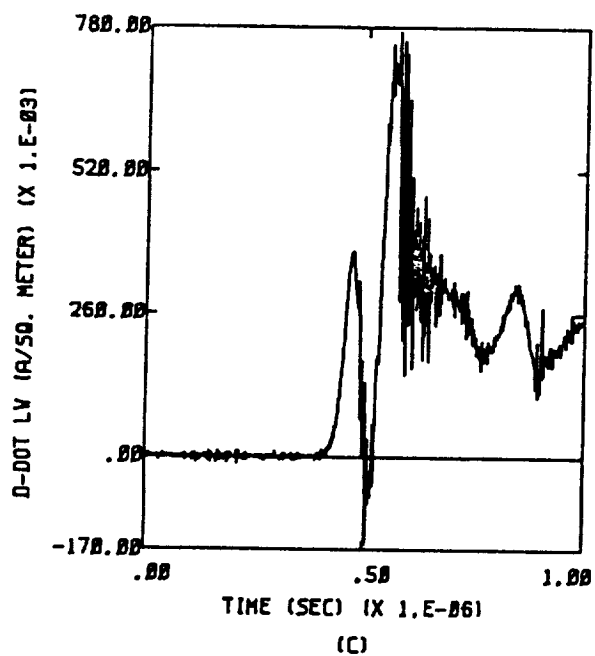
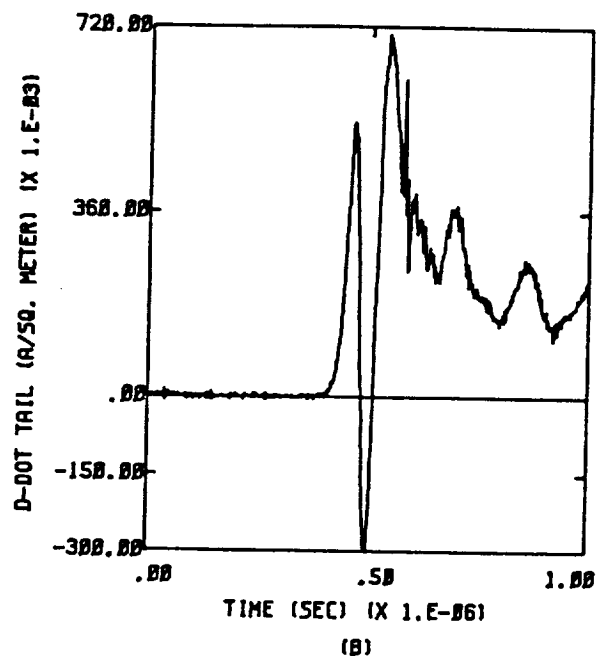
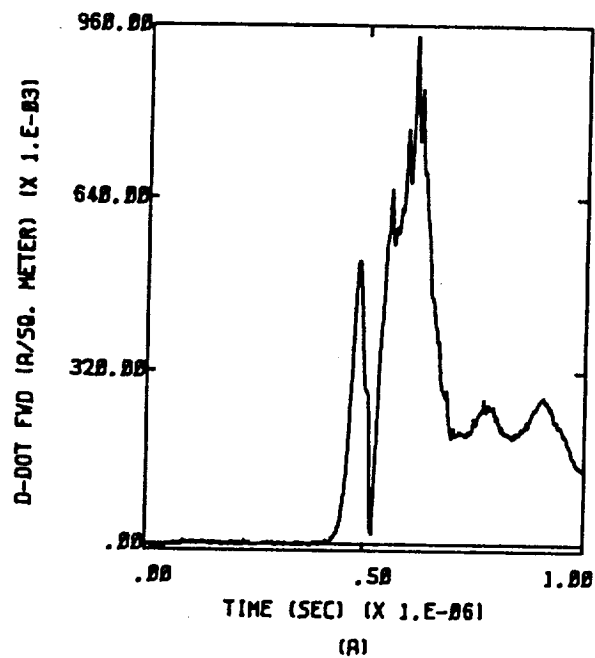


Figure D.59a -X,Y,Z;  $Q = -Q_m$ ;  $E = 2 \times 10^4$  Volts per meter

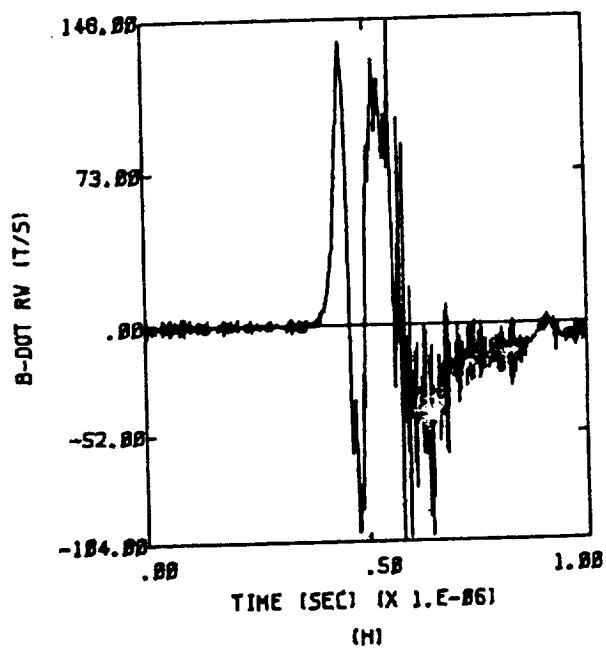
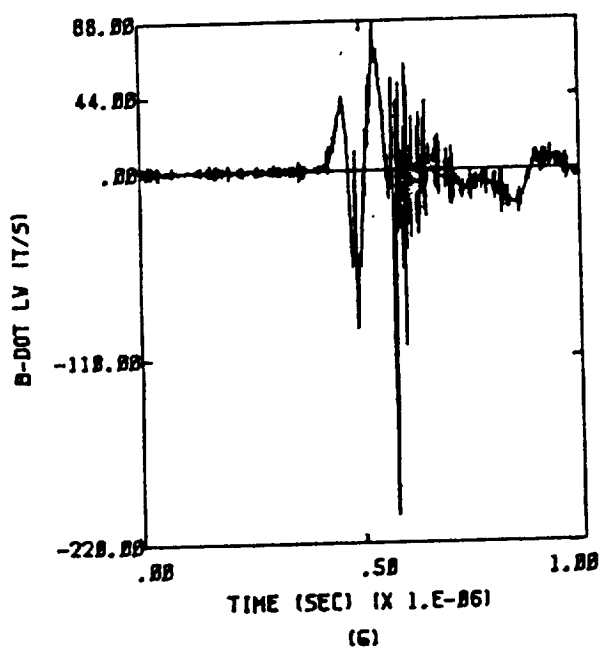
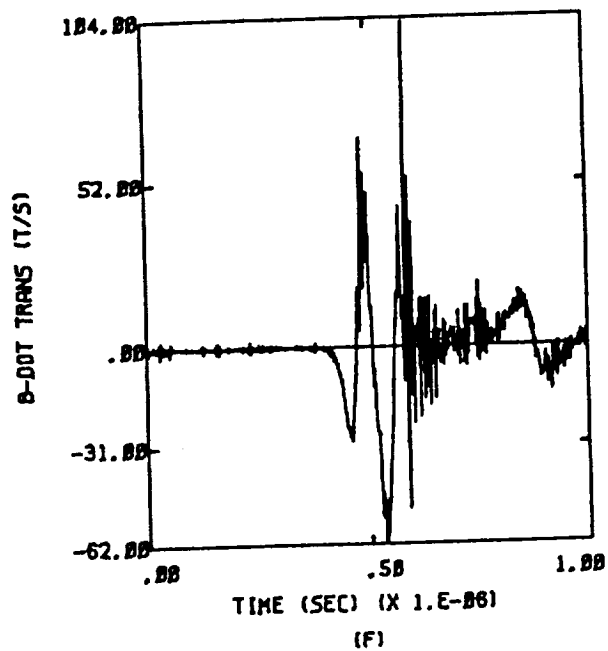
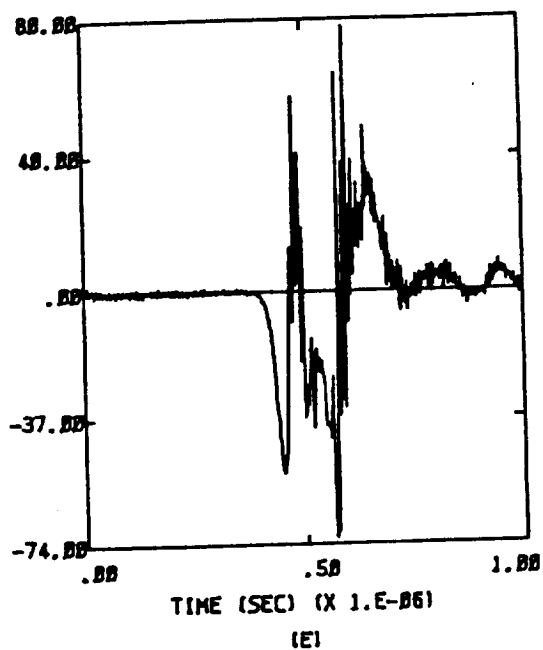


Figure D.59b -X,Y,Z;  $Q = -Q_m$ ;  $E = 2 \times 10^4$  Volts per meter

ORIGINAL PAGE IS  
OF POOR QUALITY

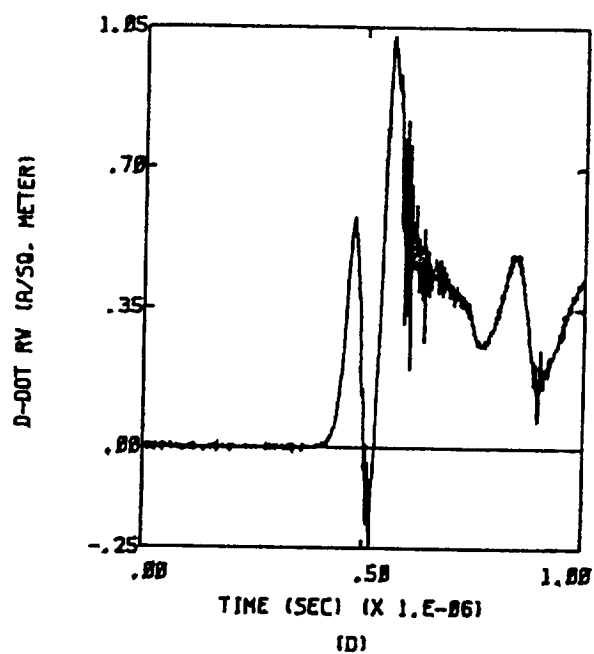
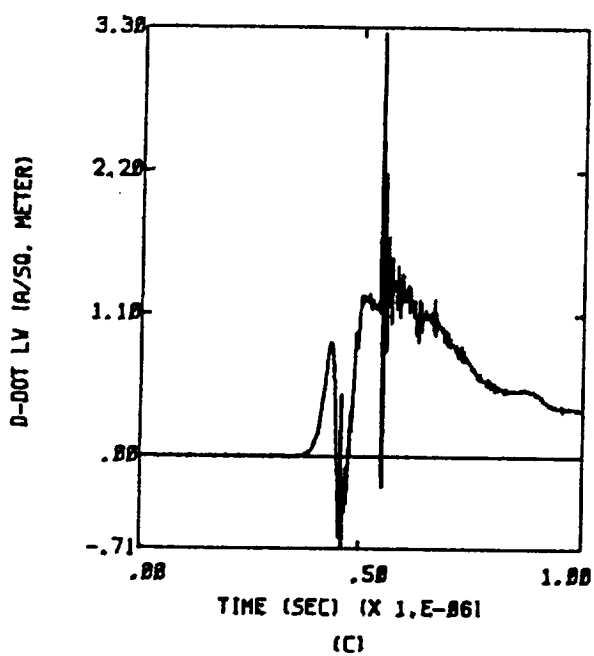
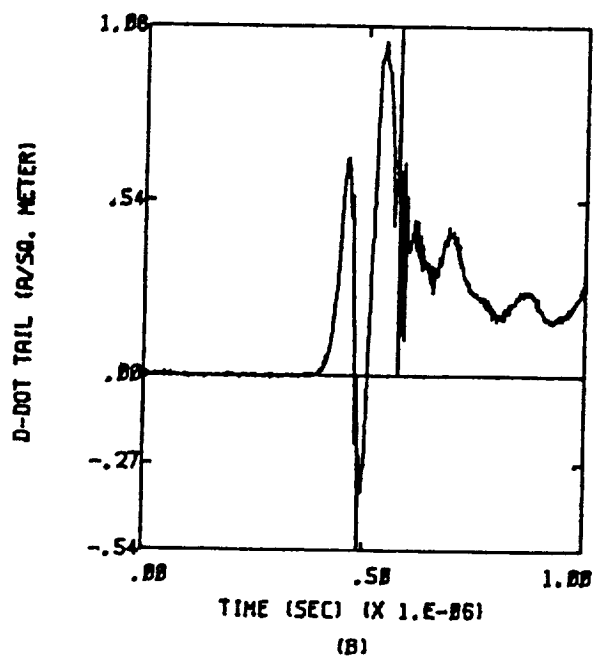
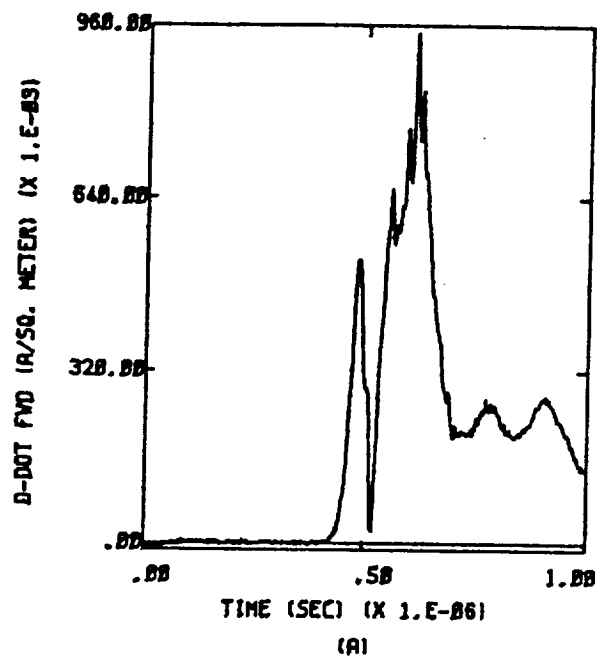


Figure D.60a -X,-Y,Z;  $Q = -Q_m$ ;  $E = 2 \times 10^4$  Volts per meter



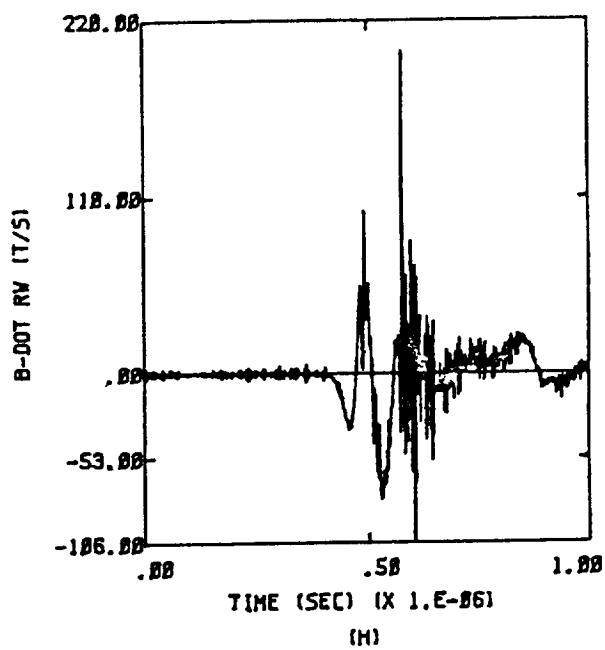
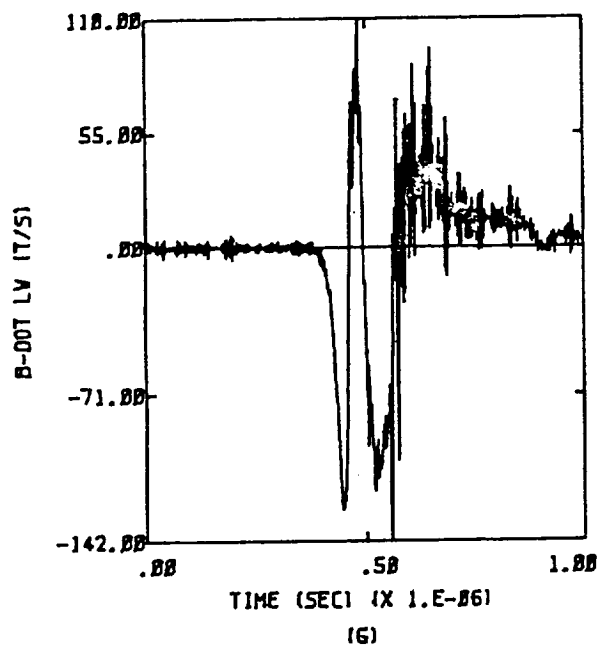
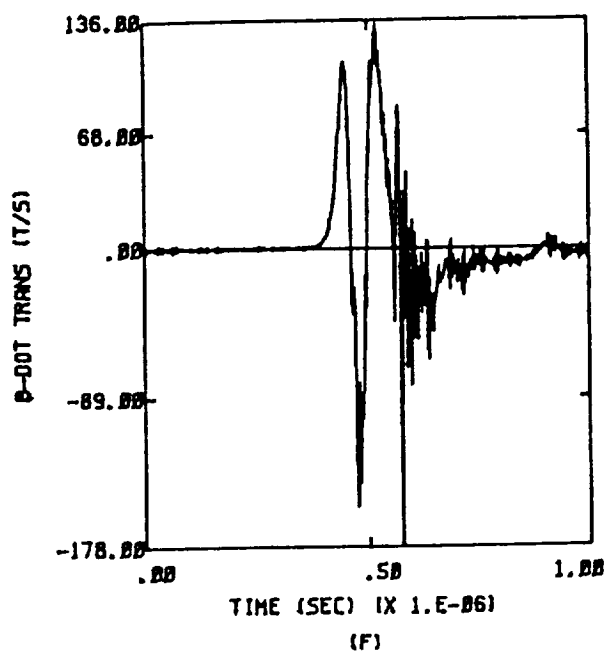
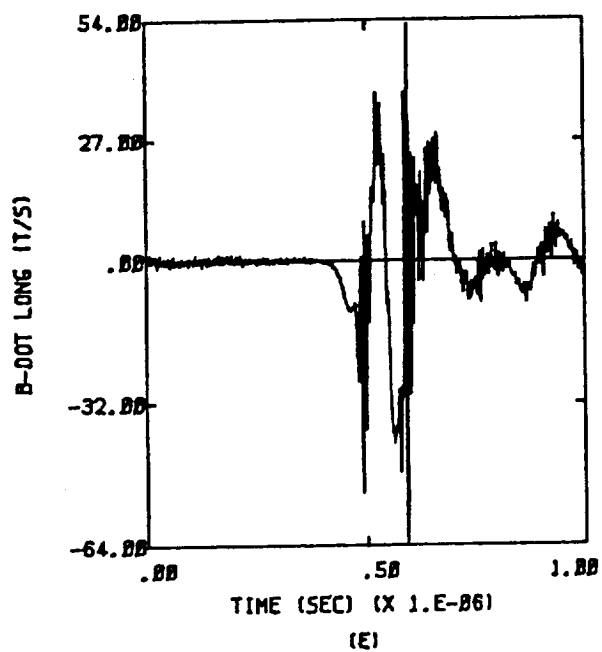


Figure D.60b -X,-Y,Z;  $Q = -Q_m$ ;  $E = 2 \times 10^4$  Volts per meter



## **APPENDIX E**

### **PARTIAL PRINCIPAL ANGLE OF INCIDENCE PARAMETER STUDY**

The plots in this appendix are replacements for part of the principal angle of incidence parameter study published previously in Reference 5. They were generated on the NASA Langley VPS computer. The cases were redone because of uncharacteristic results calculated in the original study.

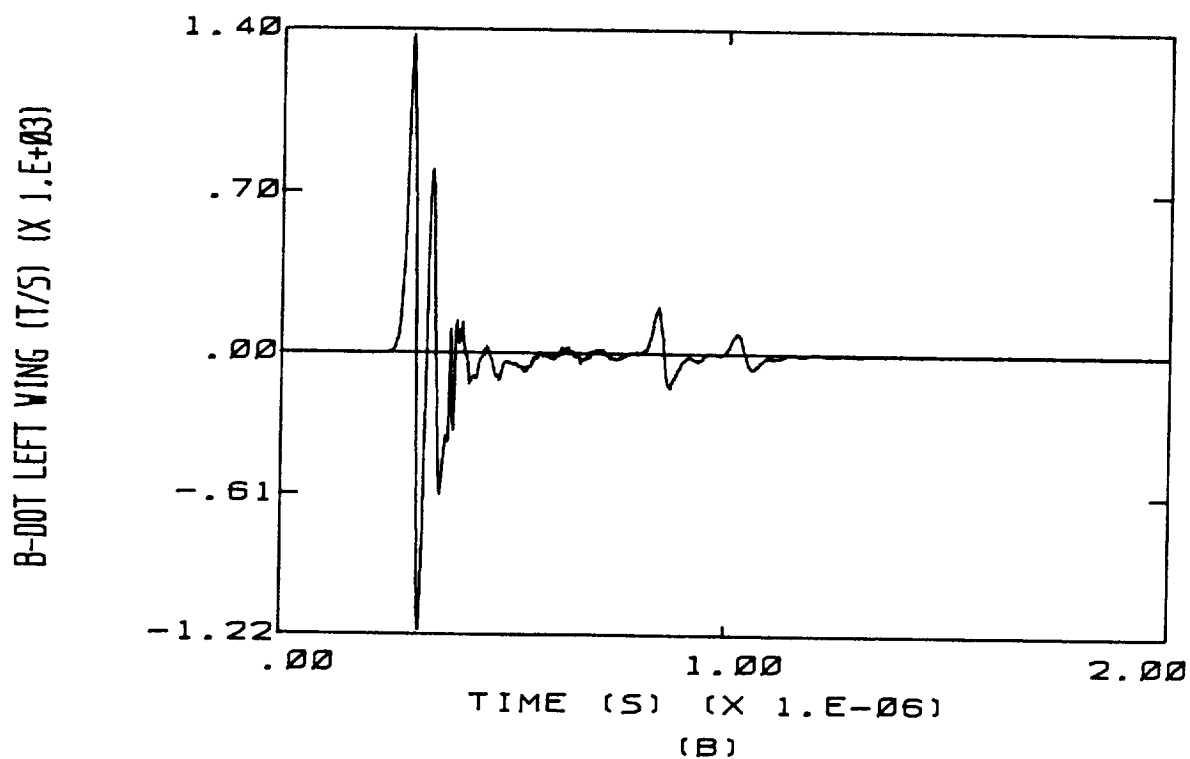
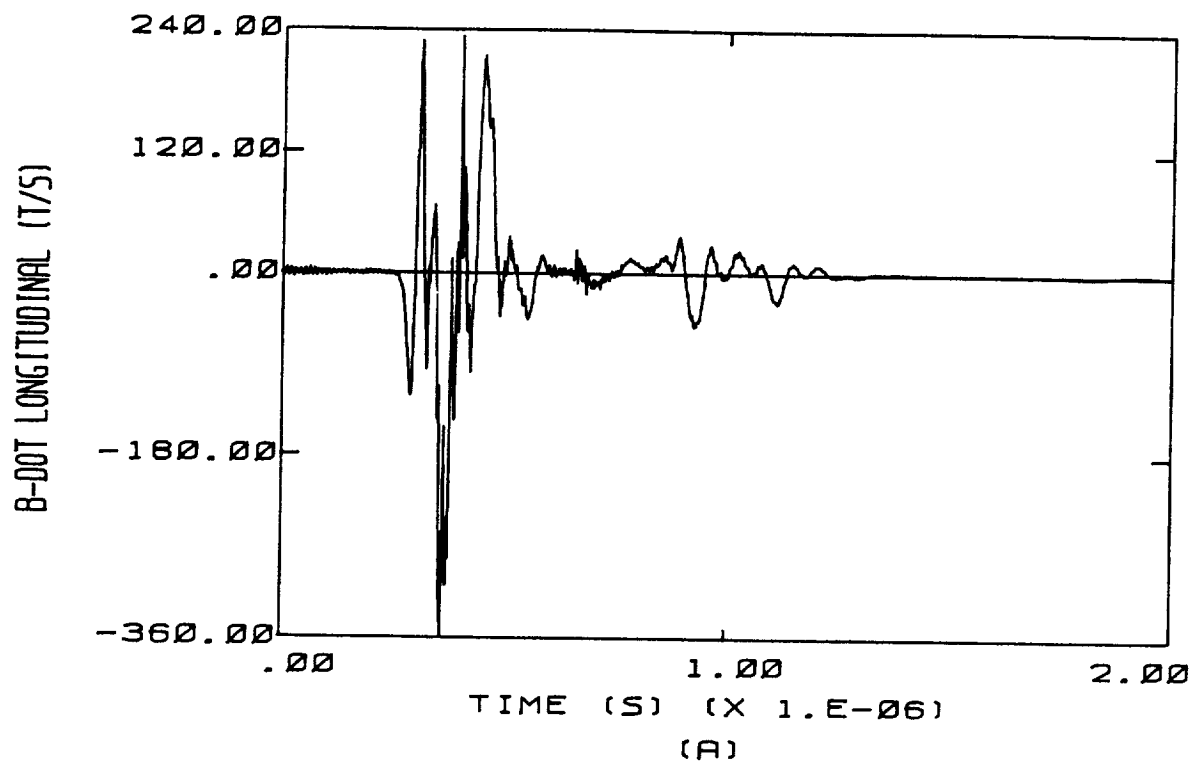
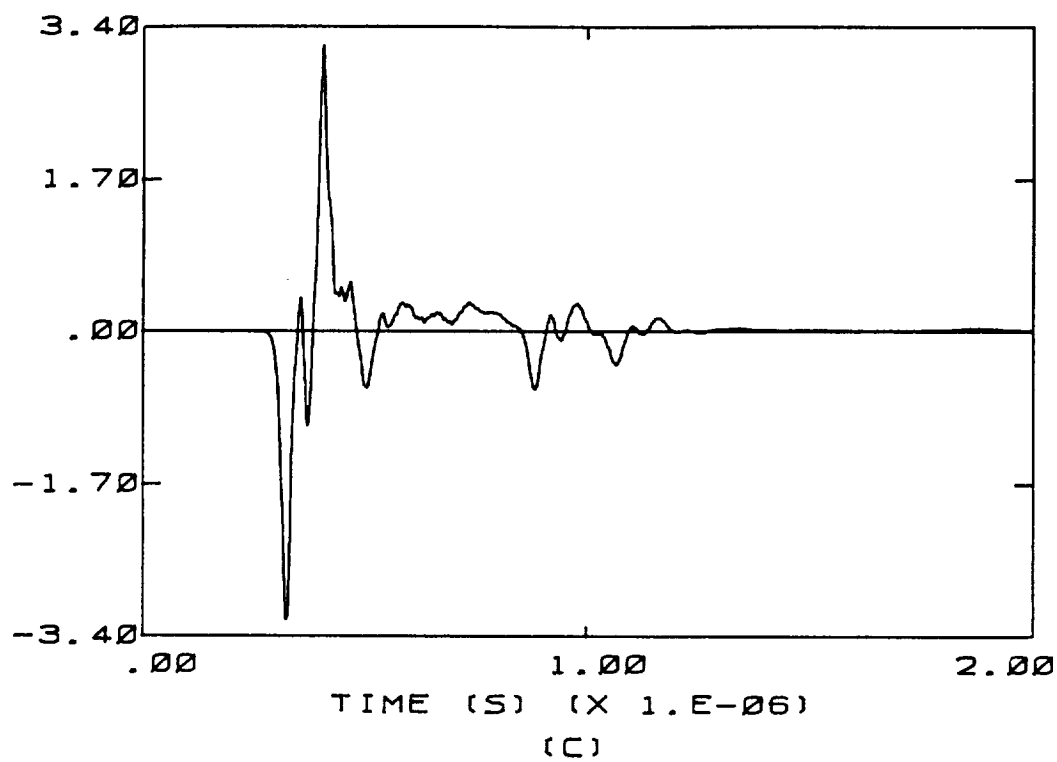


Figure E.1 High Altitude, Right to Left, No Charge

D-DOT FORWARD (A/SQ. METER)



D-DOT LEFT WING (A/SQ. METER)

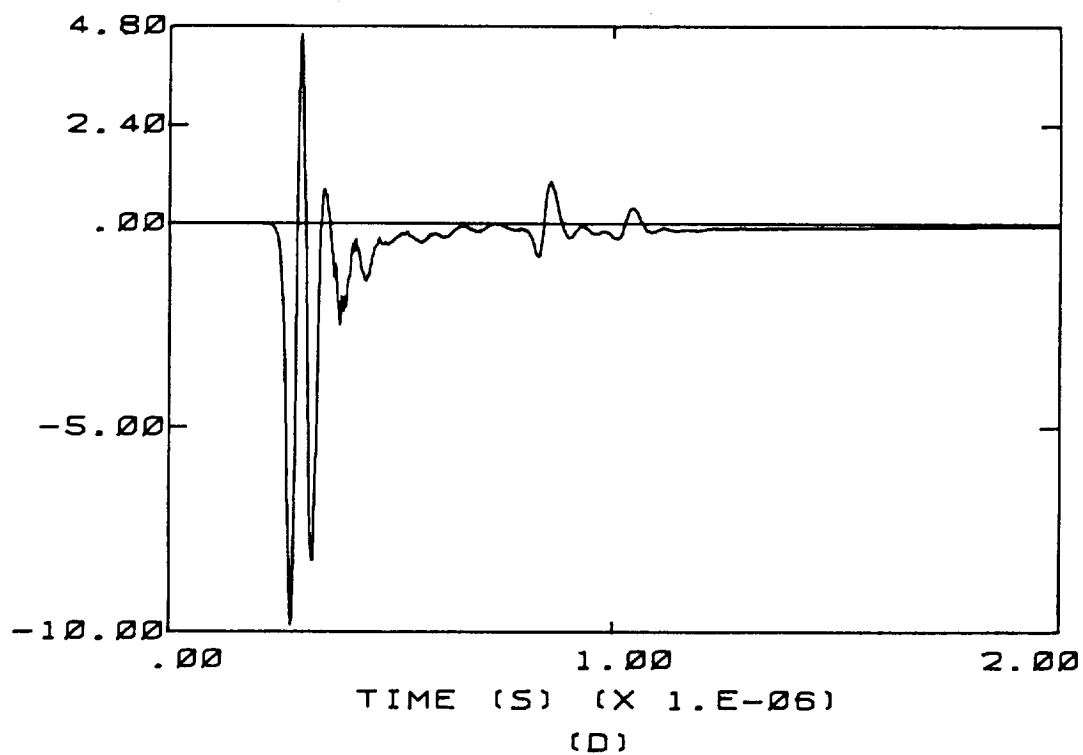


Figure E.1 (continued)

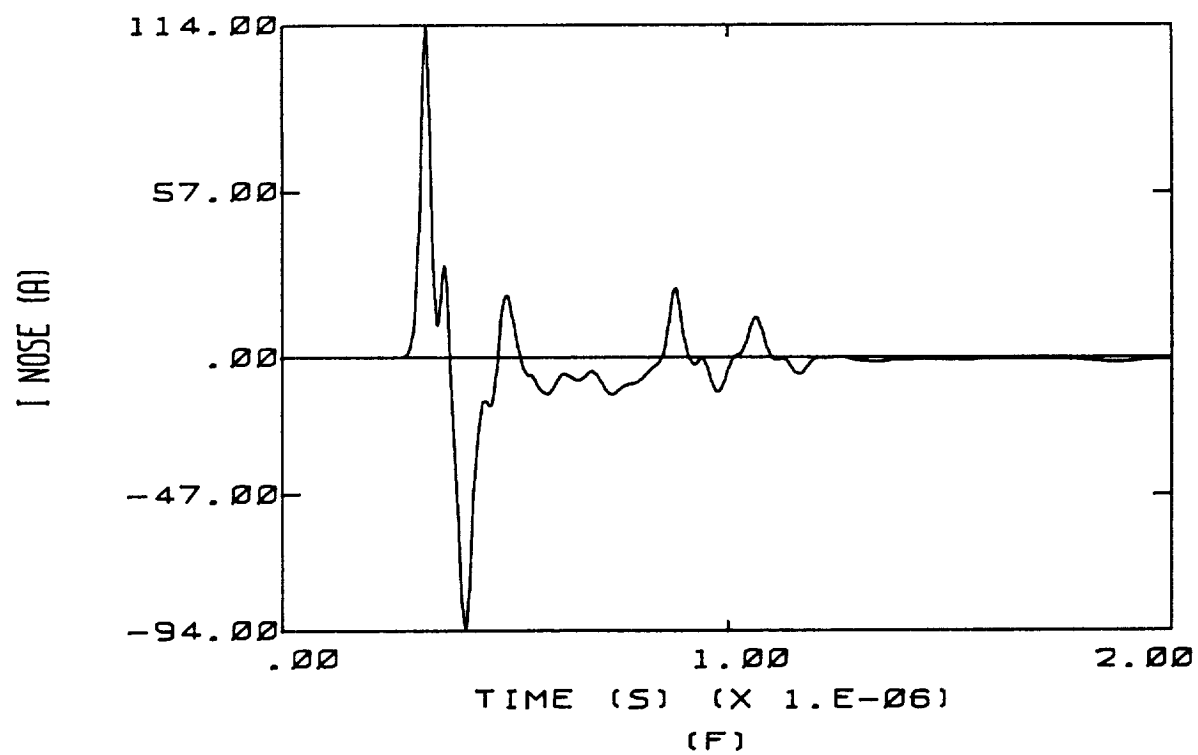
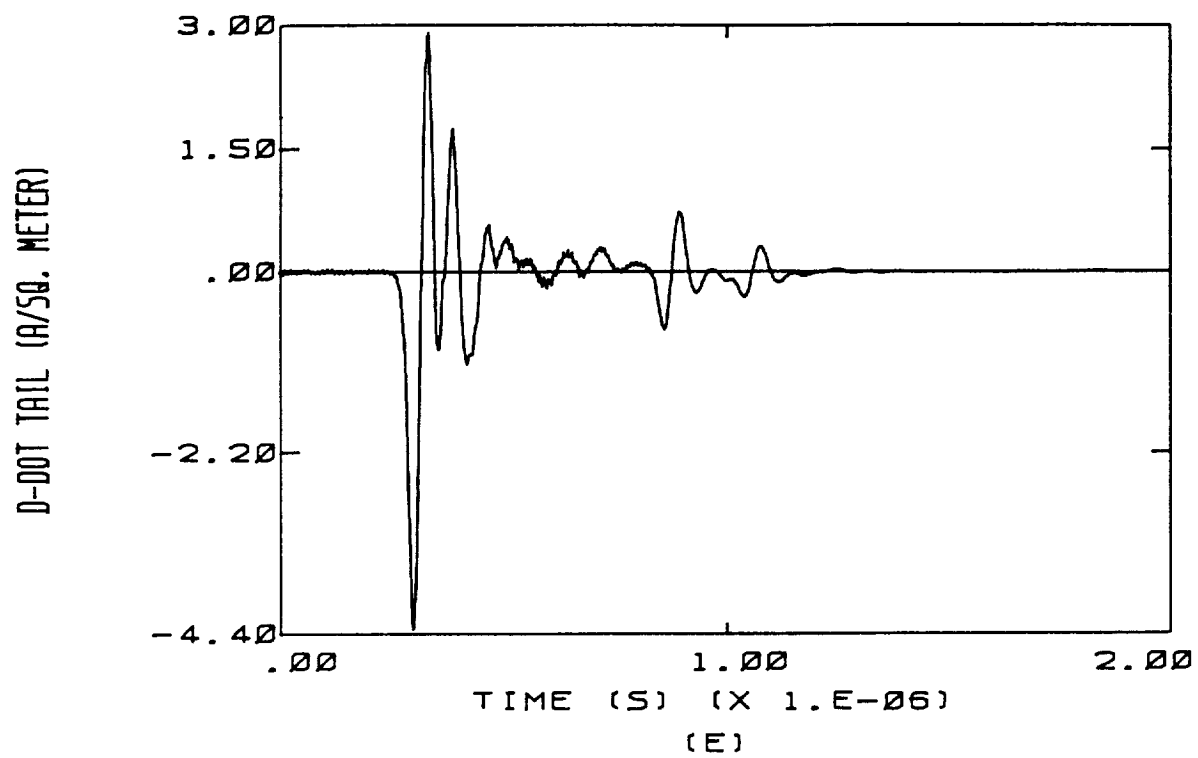


Figure E.1 (continued)

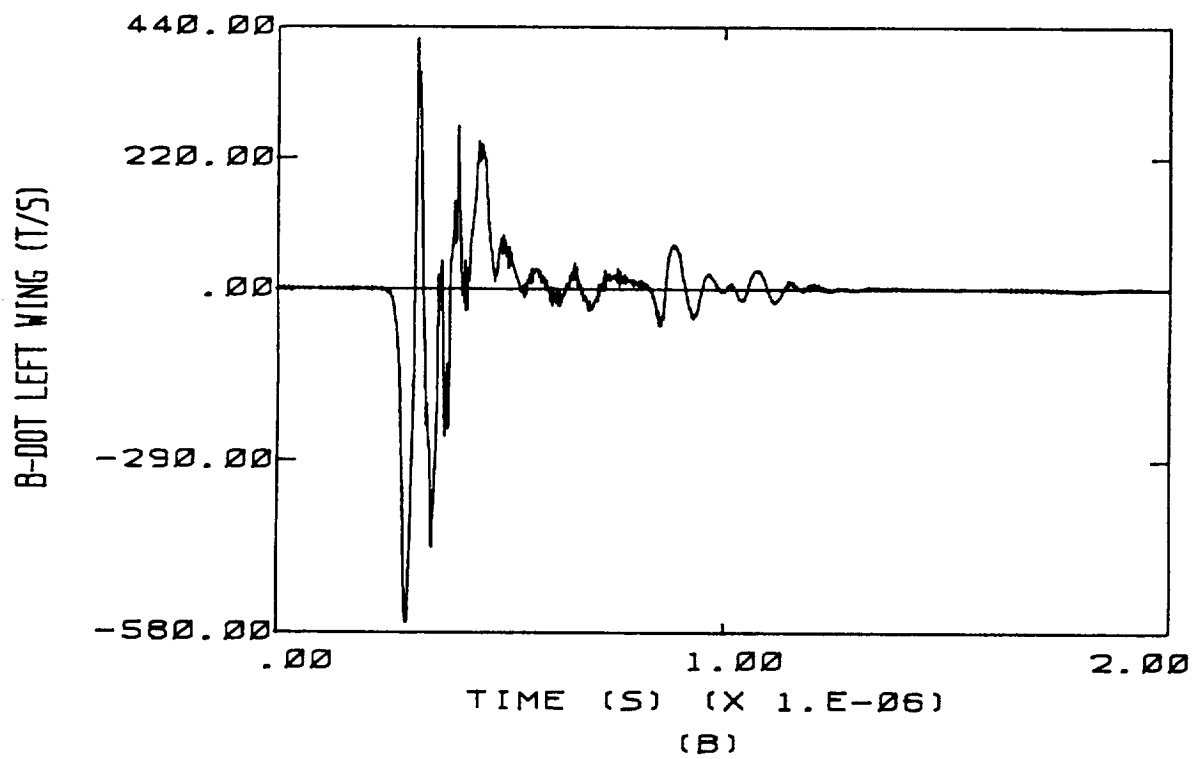
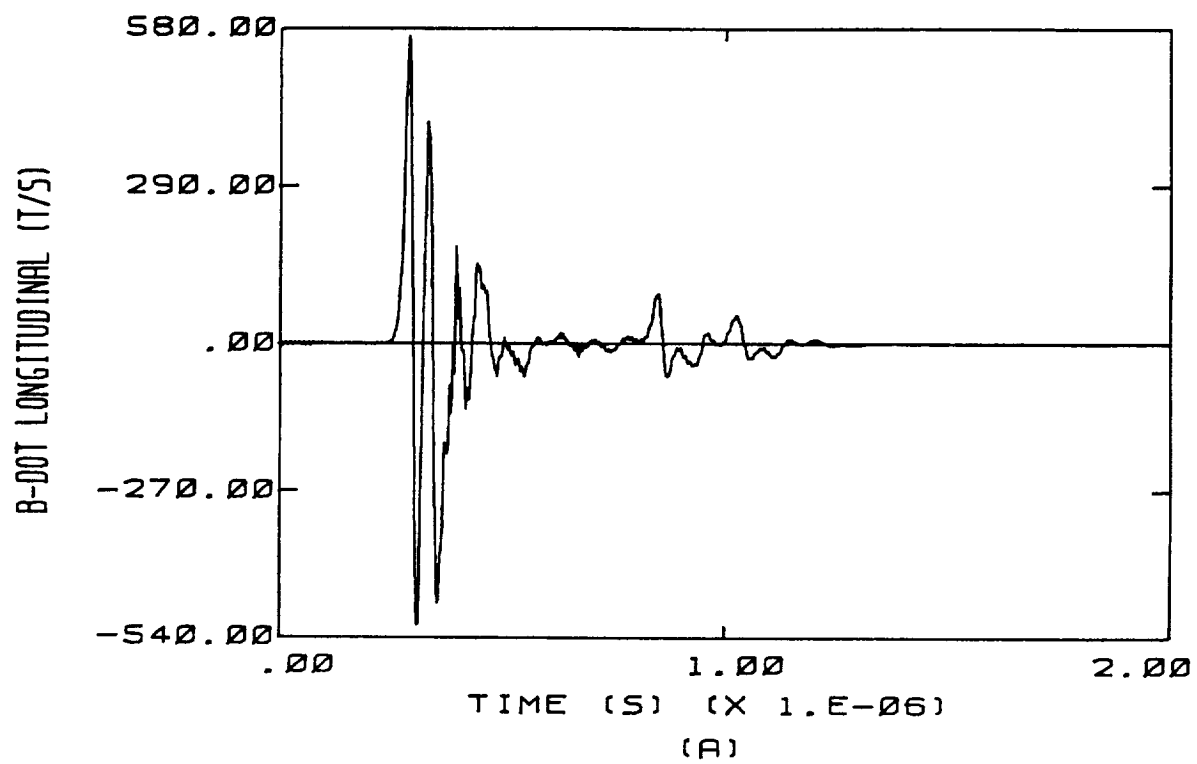
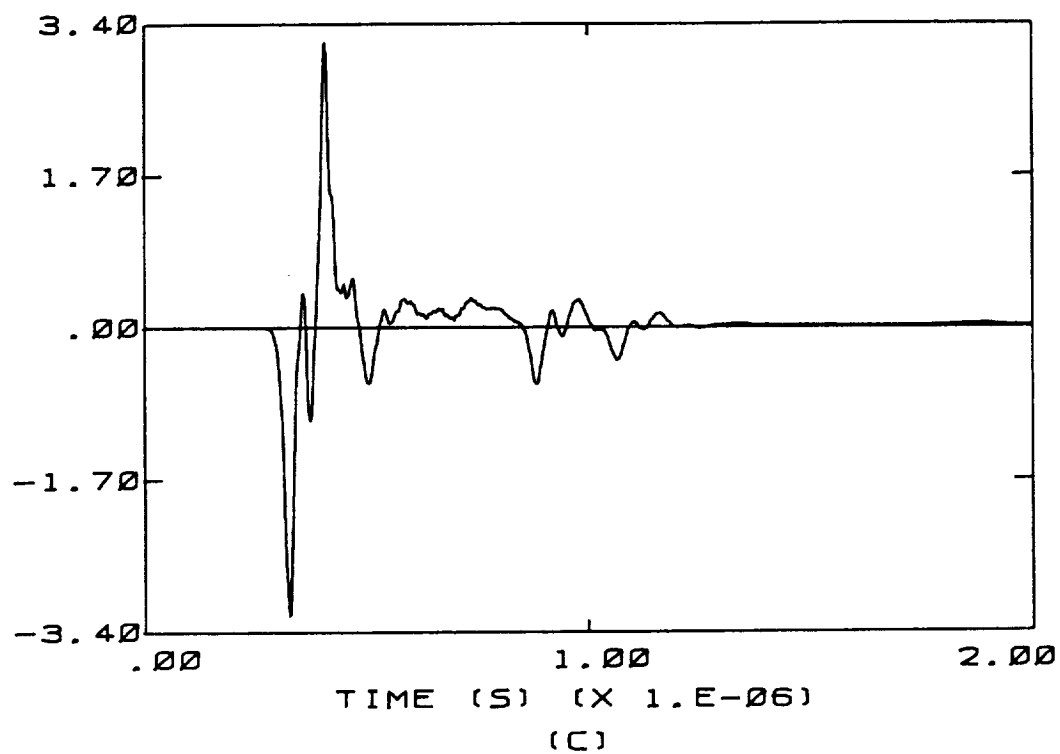


Figure E.2 High Altitude, Left to Right, No Charge

D-DOT FORWARD (A/SQ. METER)



D-DOT LEFT WING (A/SQ. METER)

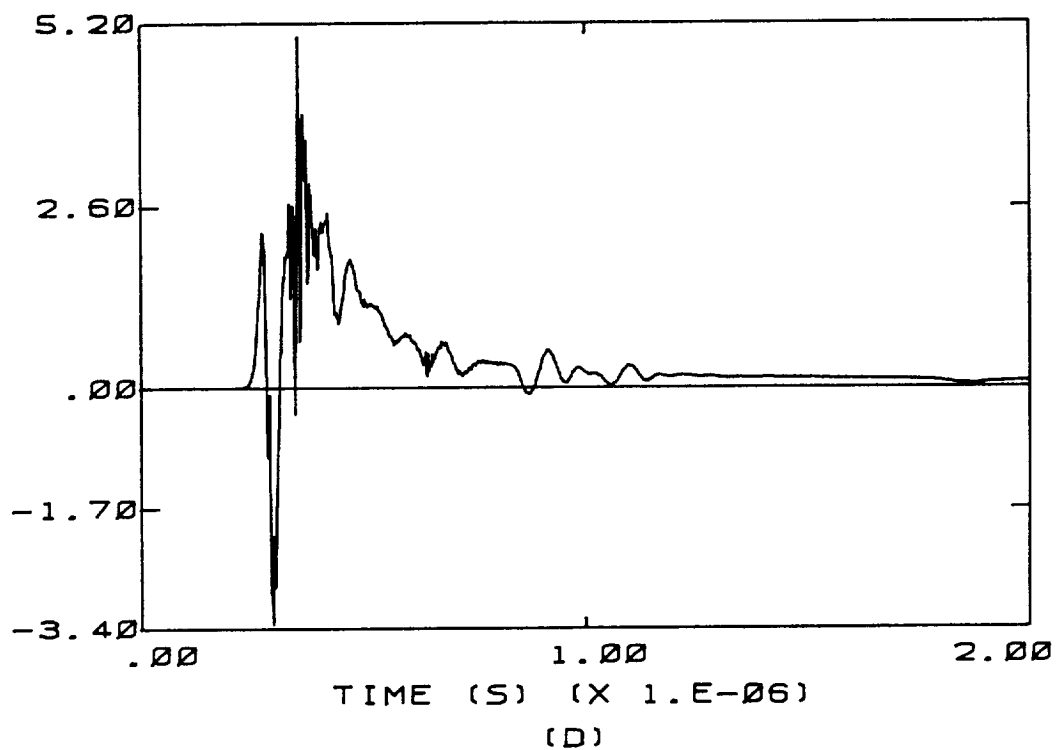


Figure E.2 (continued)



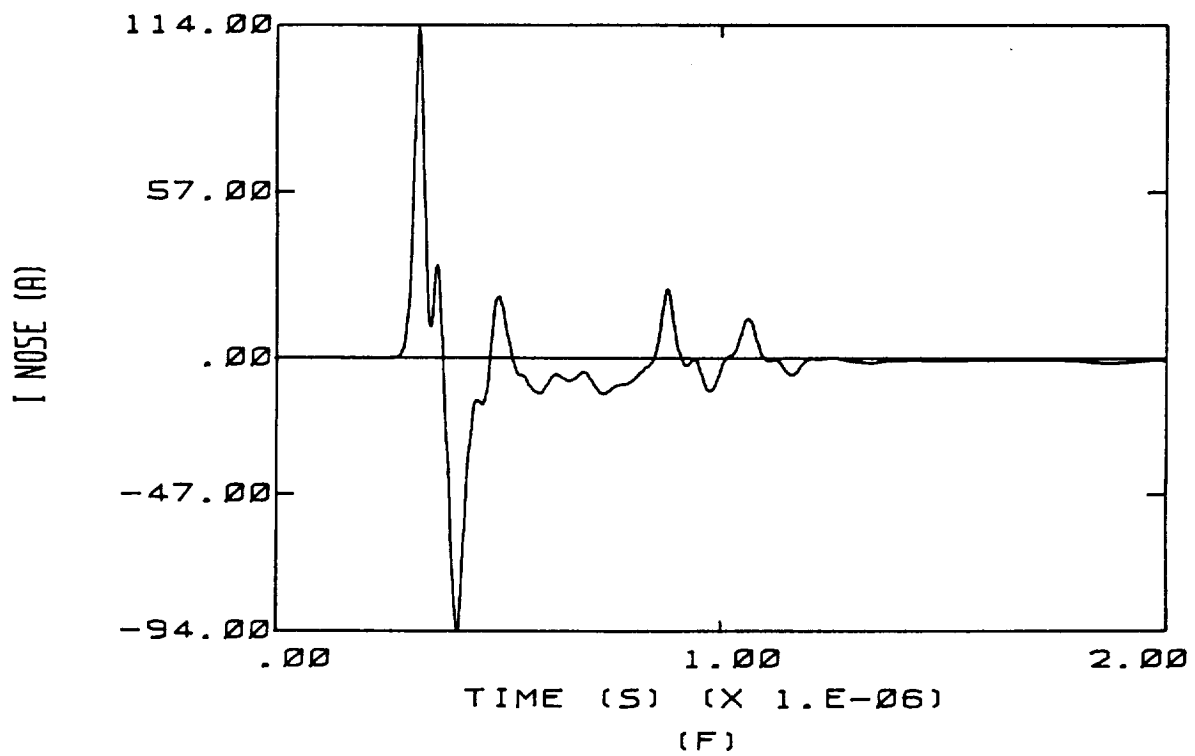
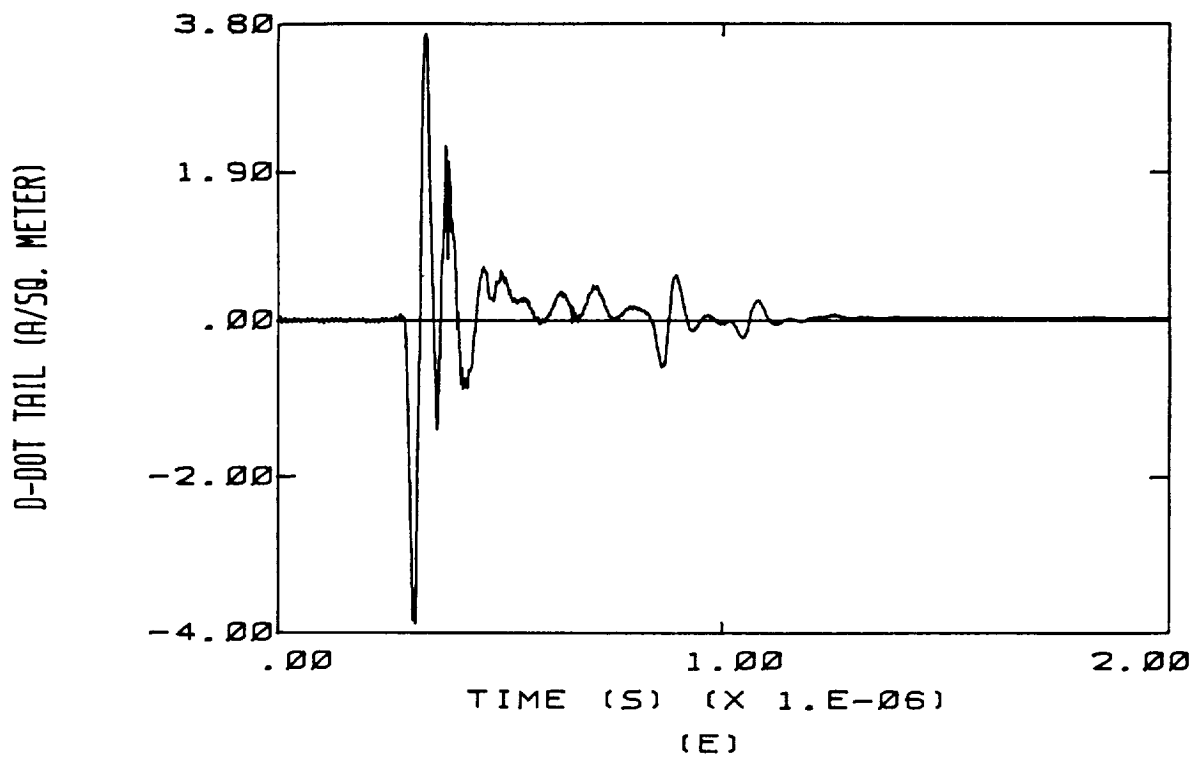


Figure E.2 (continued)

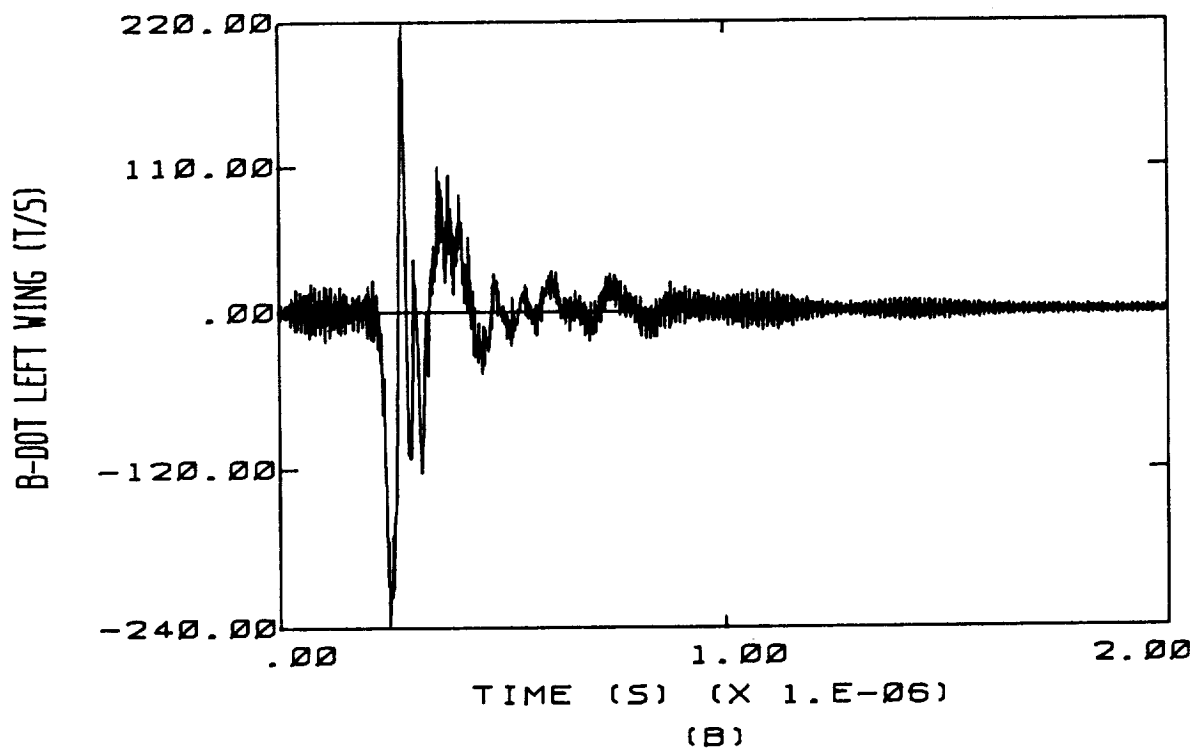
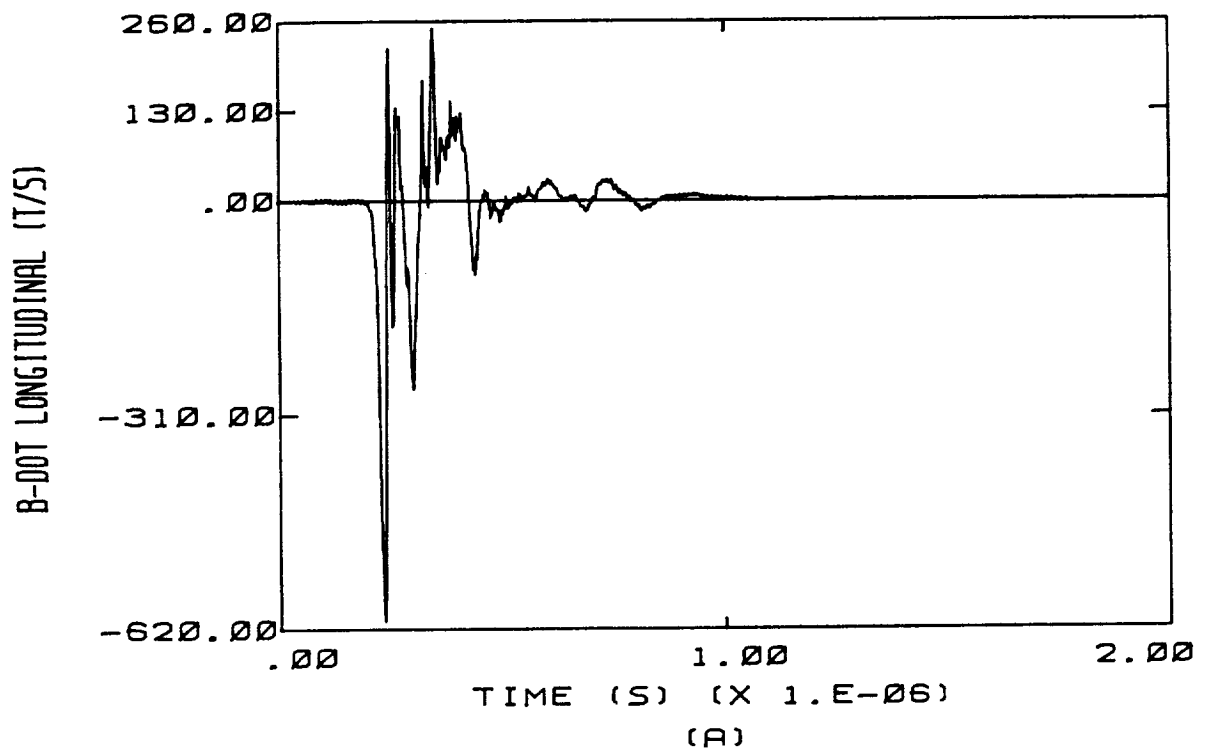
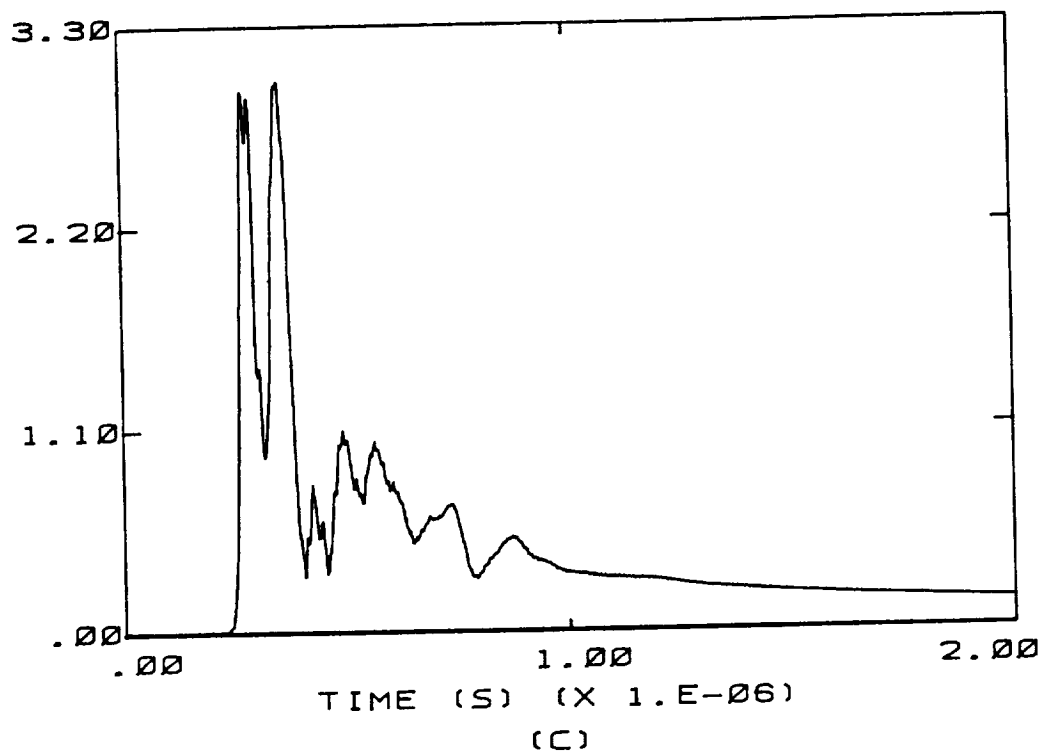


Figure E.3 High Altitude, Top to Bottom, No Charge

D-DOT FORWARD (A/SQ. METER)



D-DOT LEFT WING (A/SQ. METER)

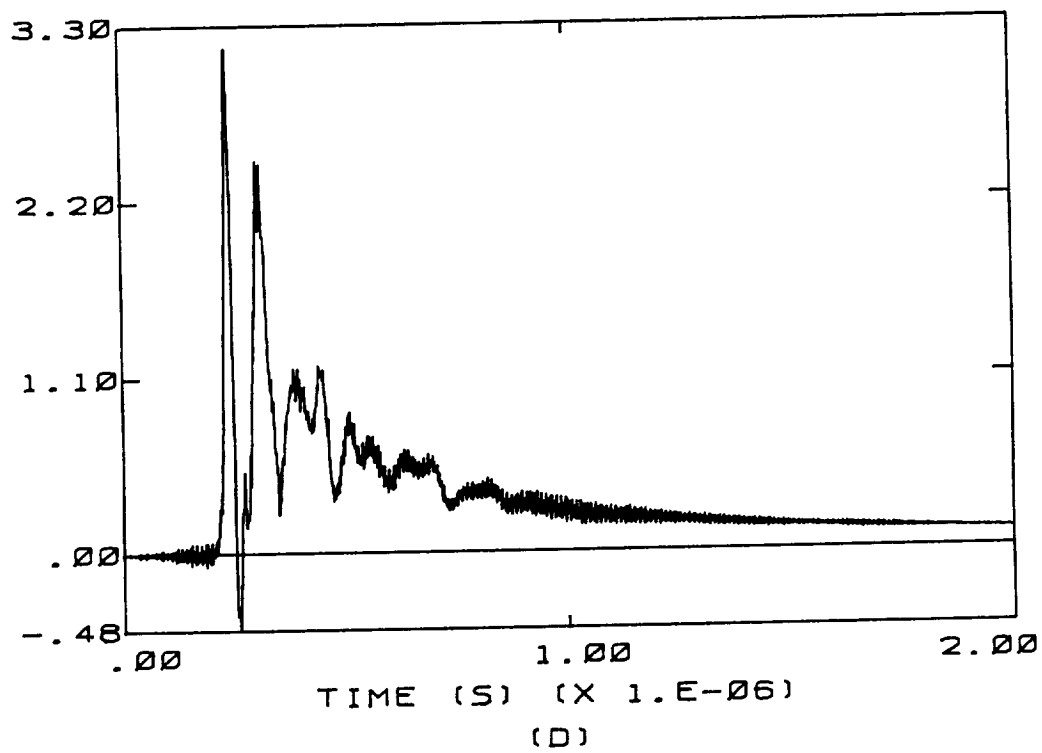


Figure E.3 (continued)

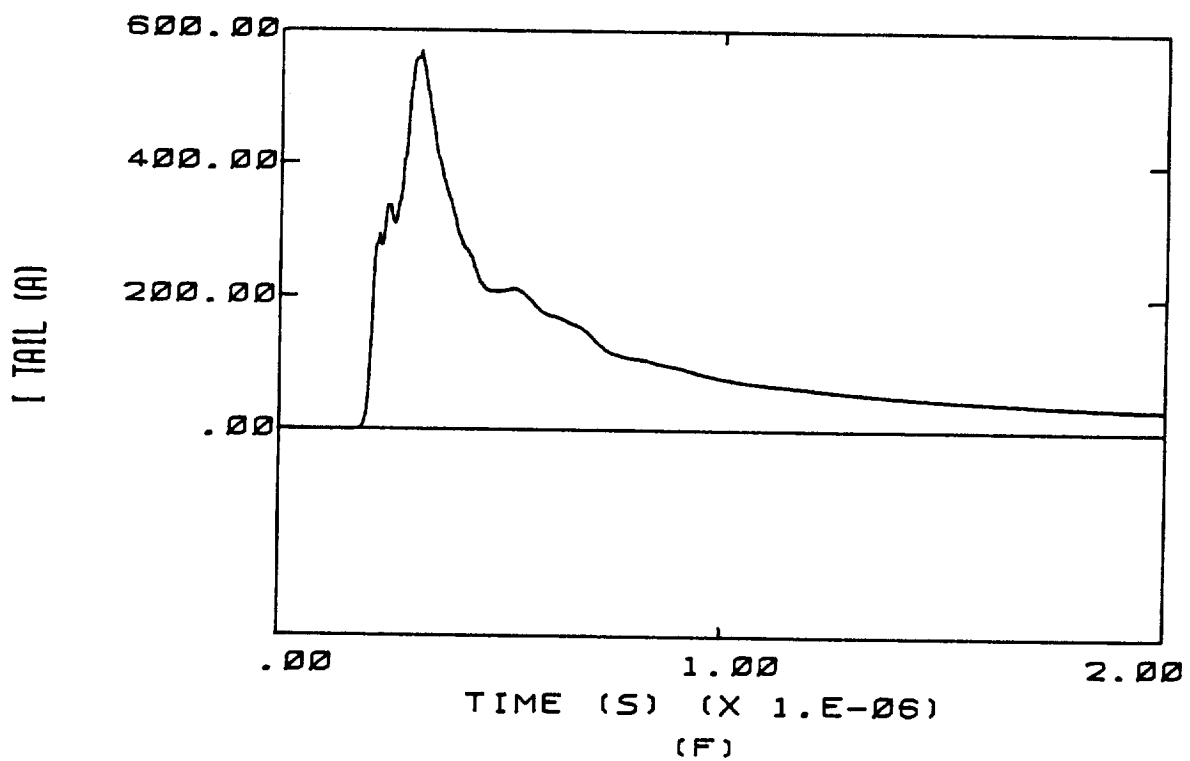
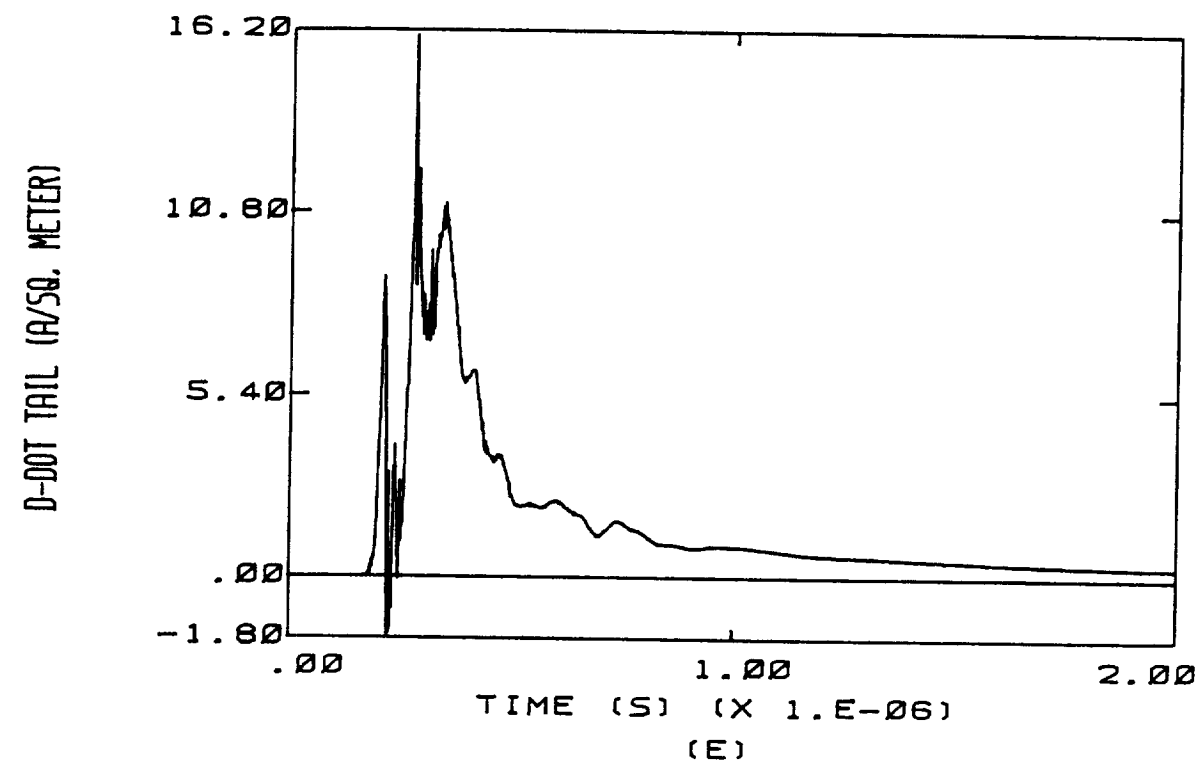


Figure E.3 (continued)

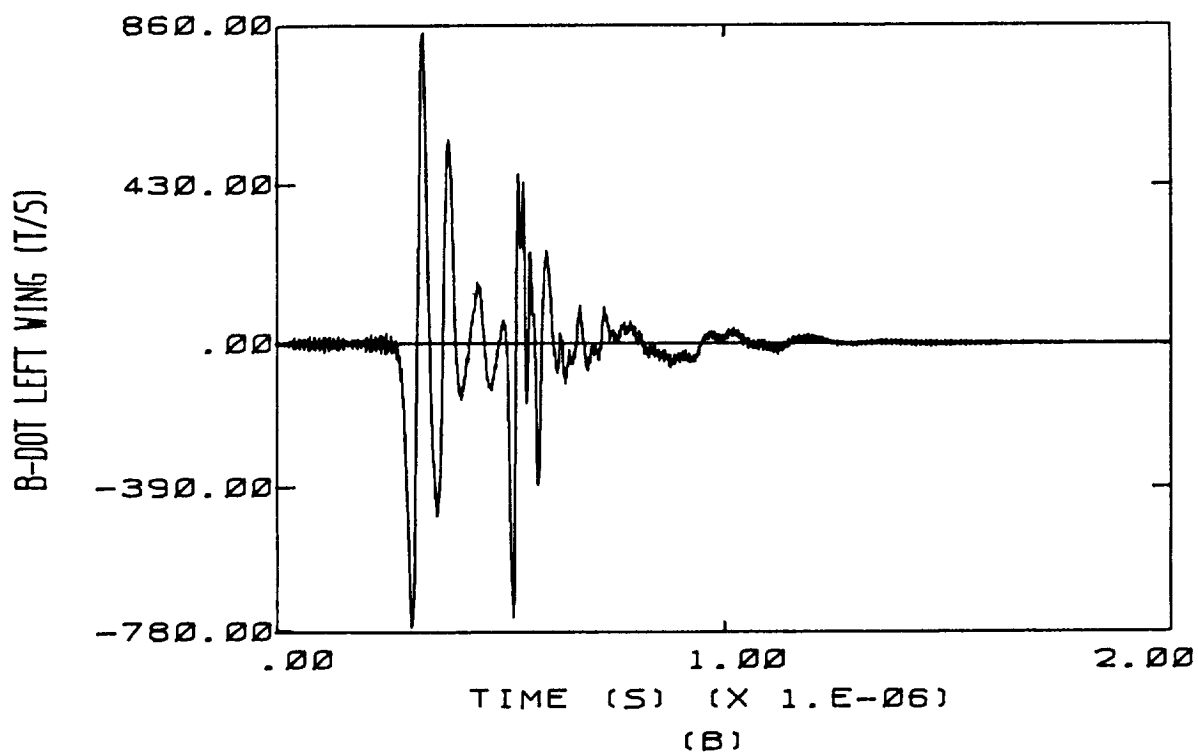
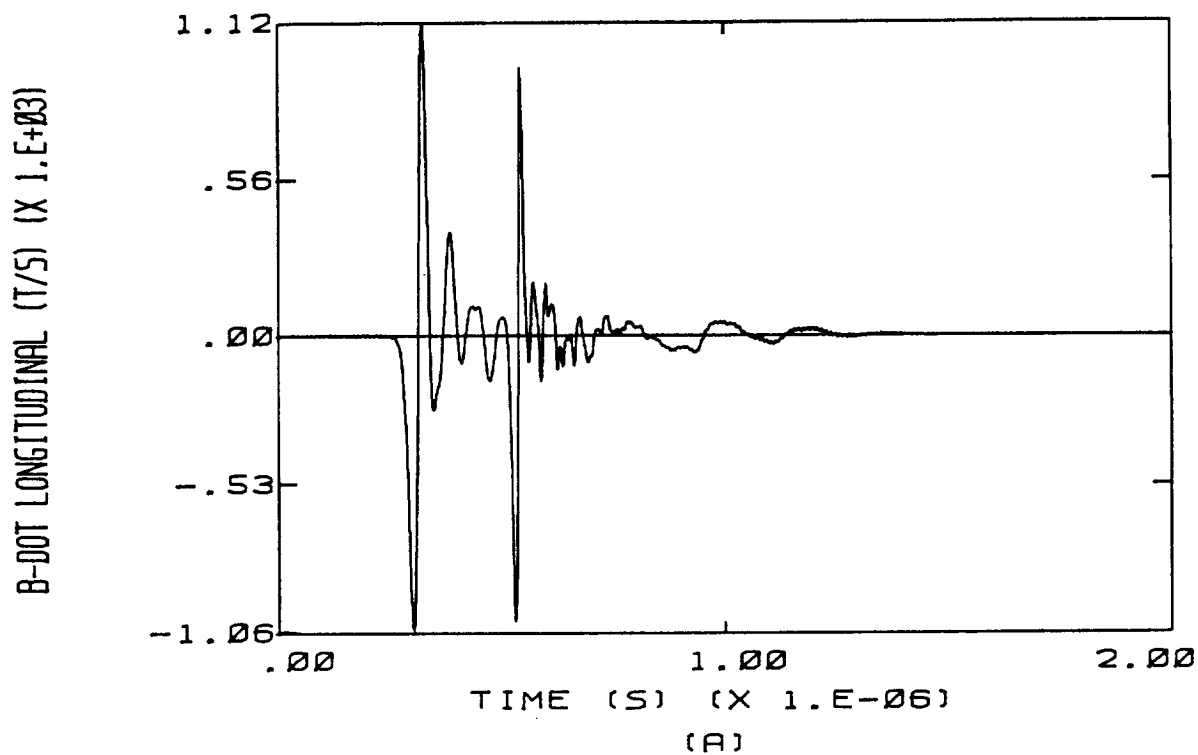
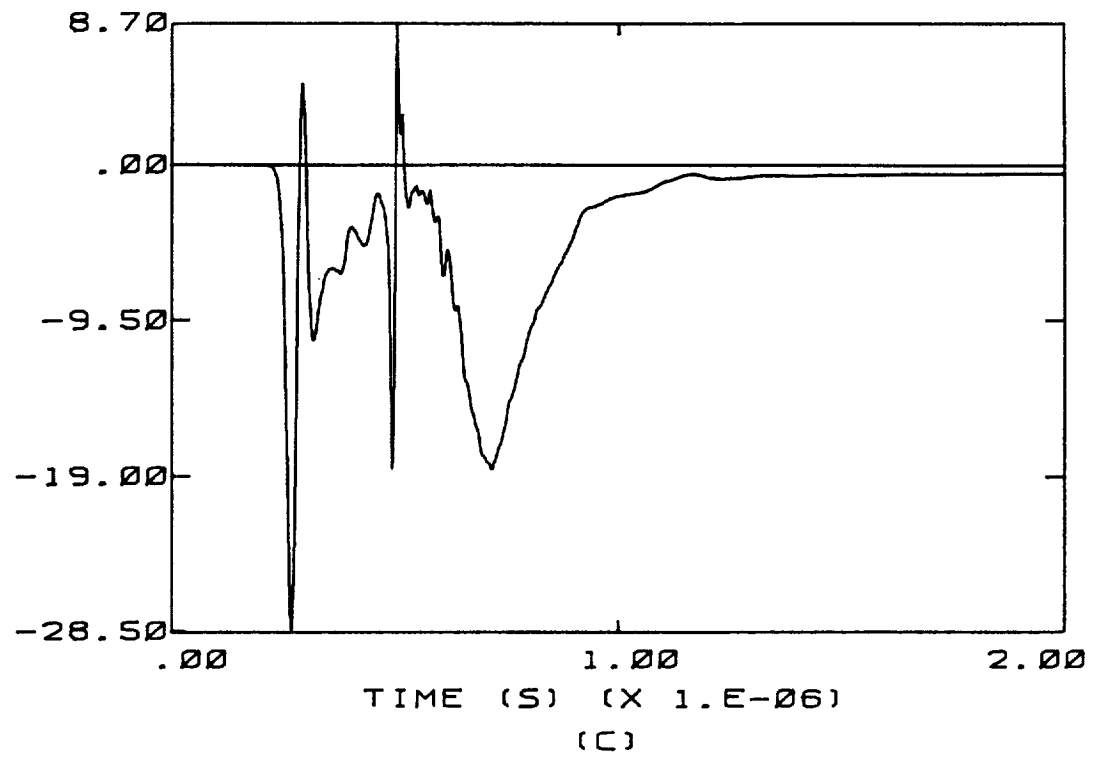


Figure E.4 High Altitude, Top to Bottom, + 1/2 Qm

D-DOT FORWARD (A/SQ. METER)



D-DOT LEFT WING (A/SQ. METER)

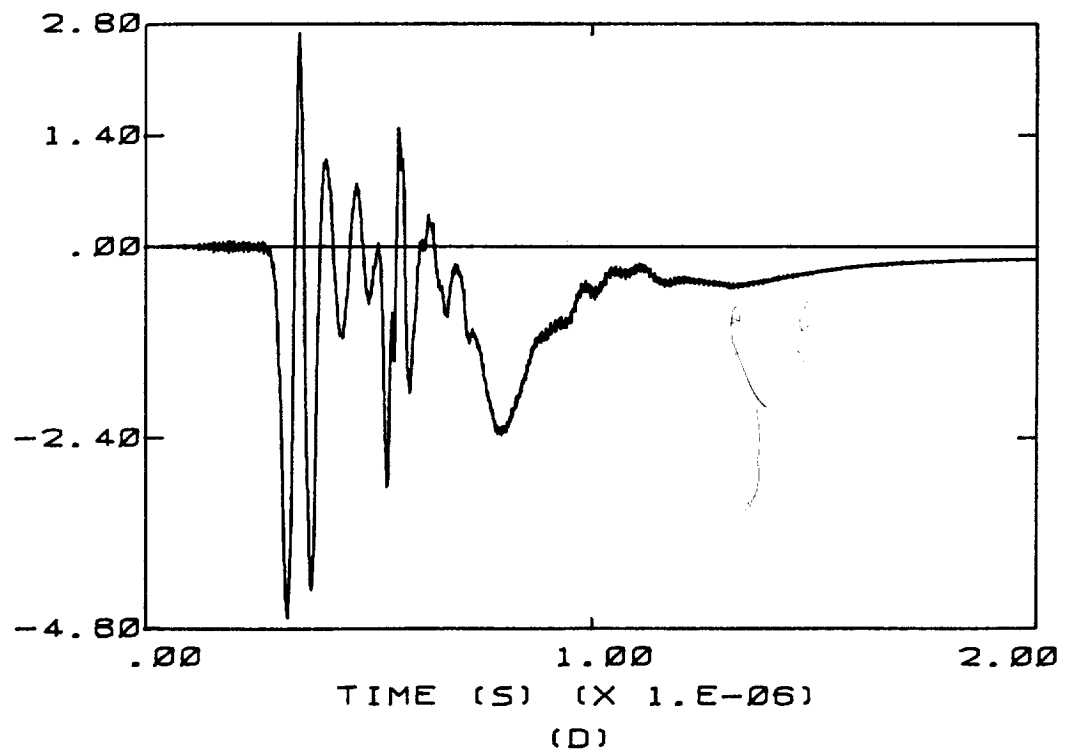


Figure E.4 (continued)

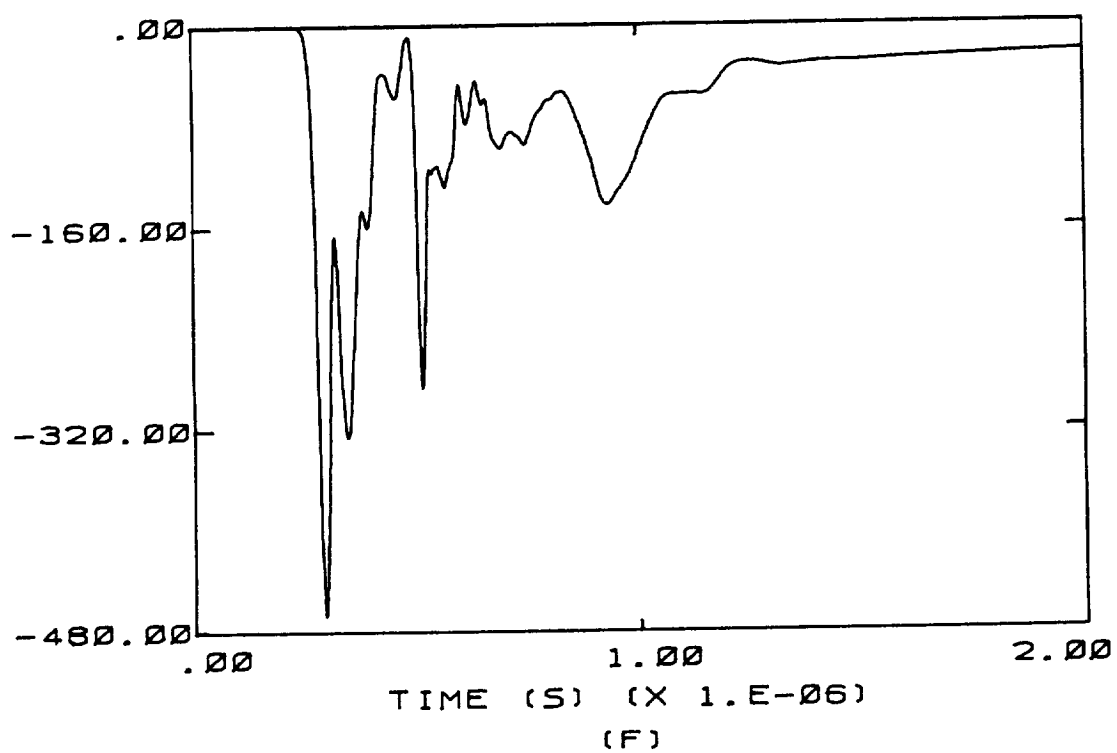
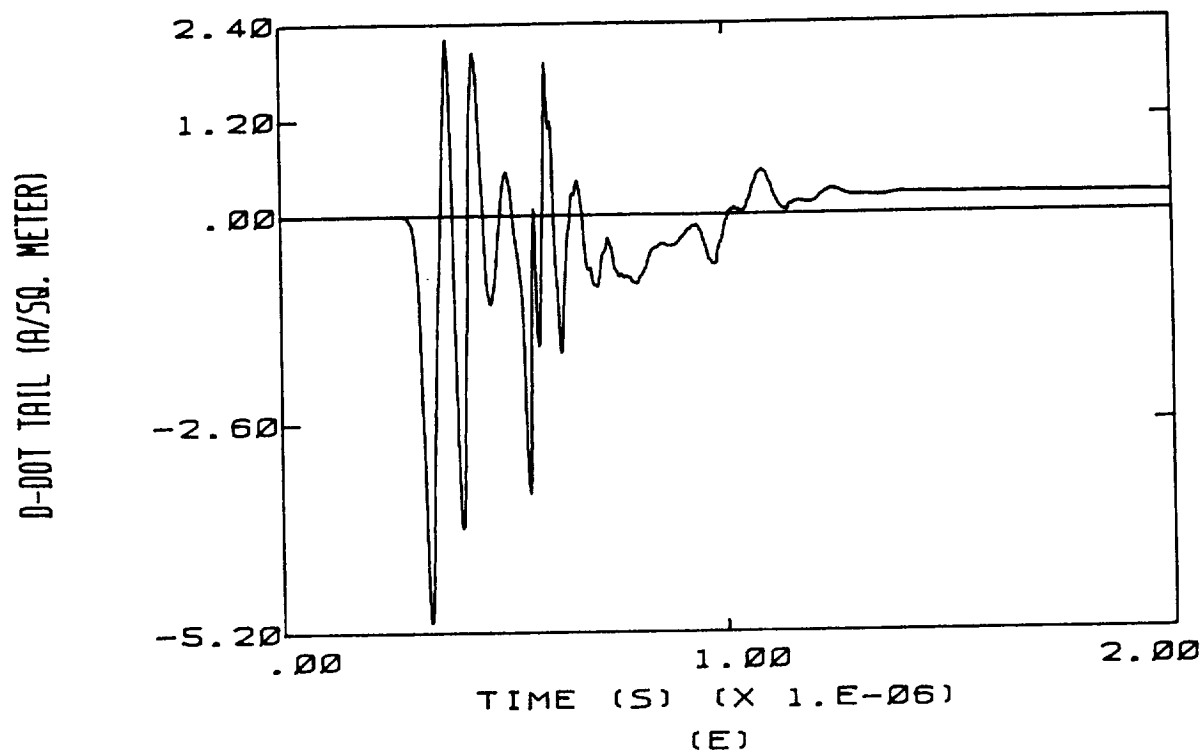


Figure E.4 (continued)

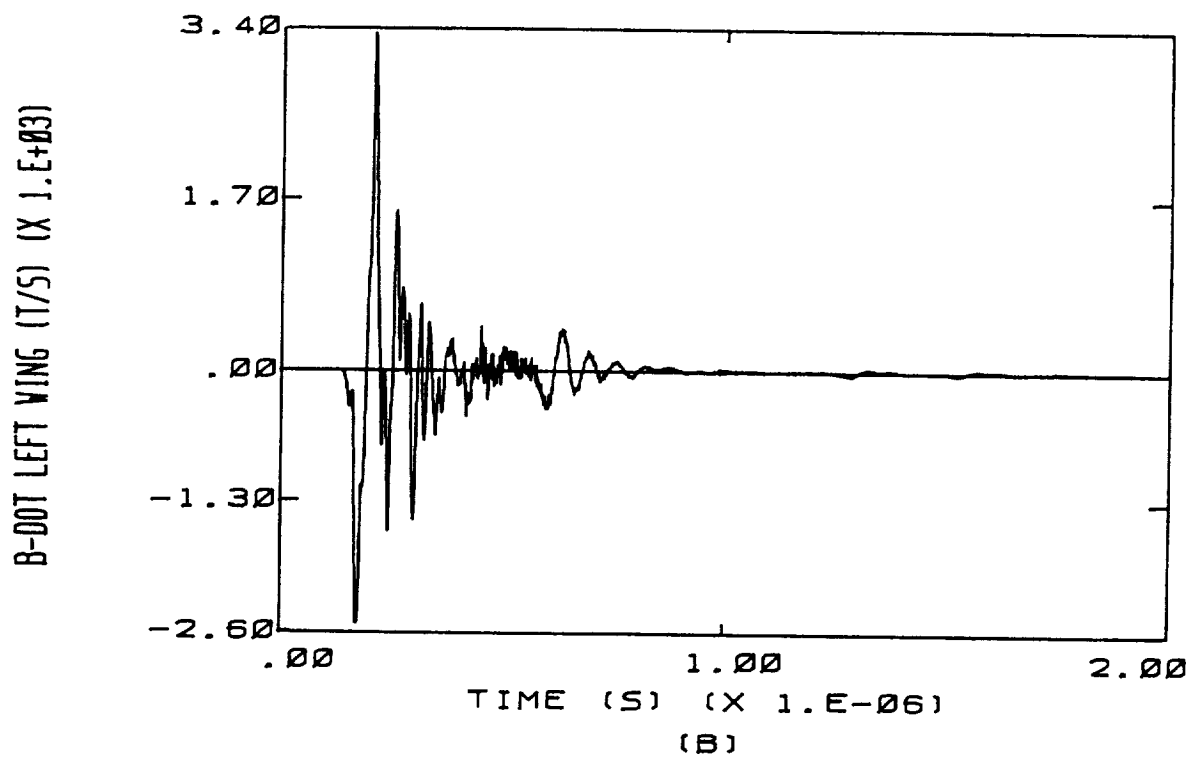
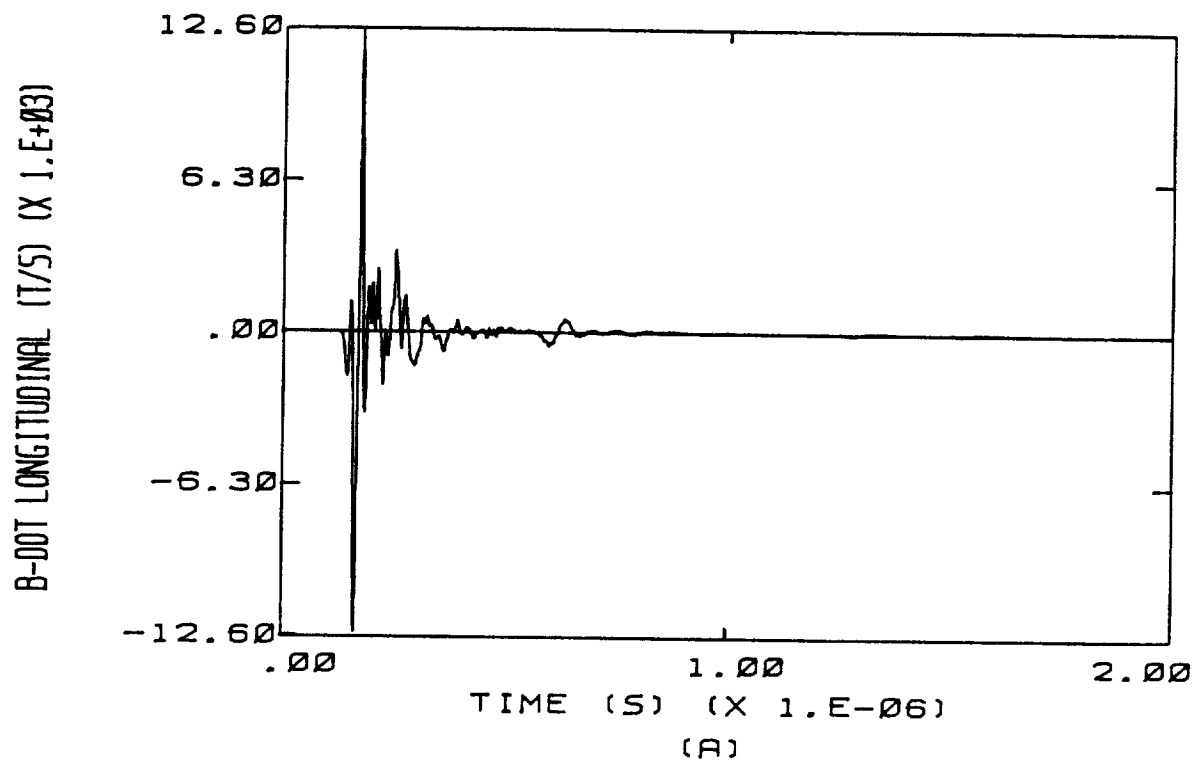
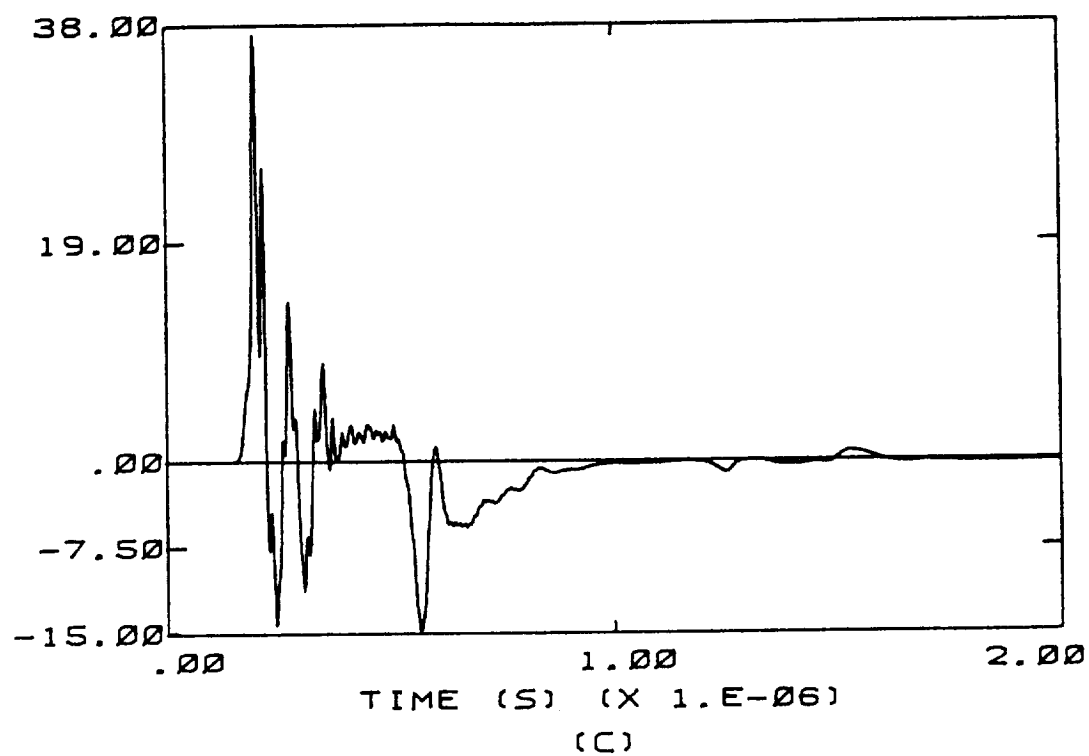


Figure E.5 High Altitude, Back to Front, - 1/2 Qm



D-DOT FORWARD (A/50. METER)



D-DOT LEFT WING (A/50. METER)

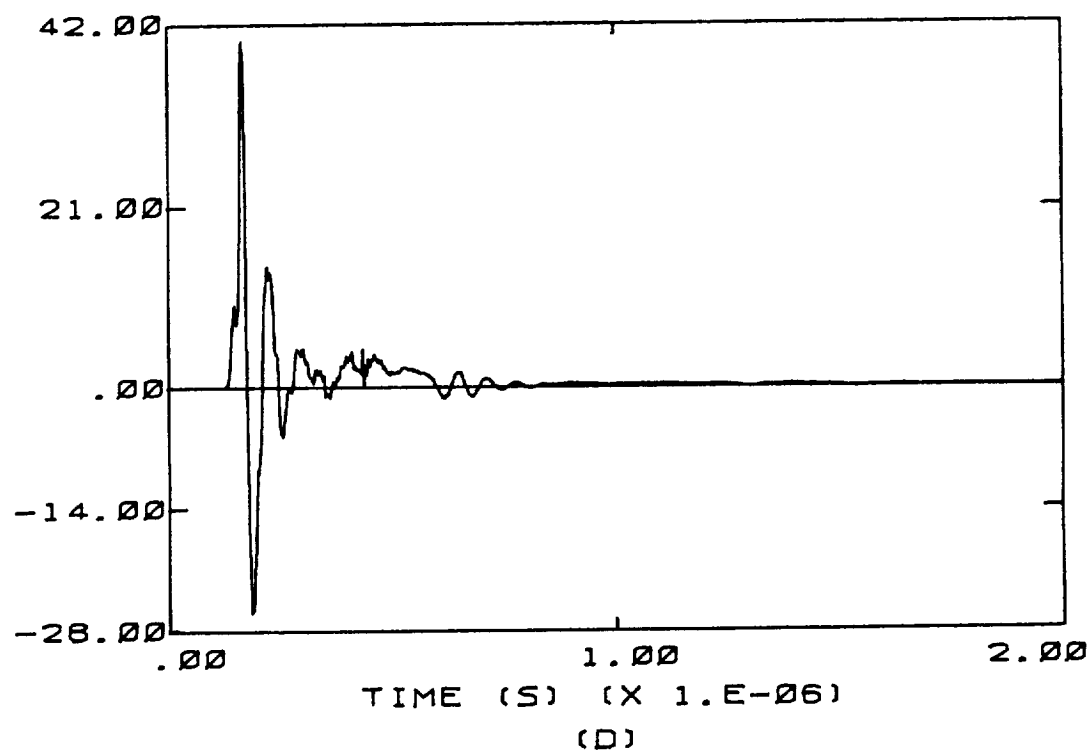


Figure E.5 (continued)

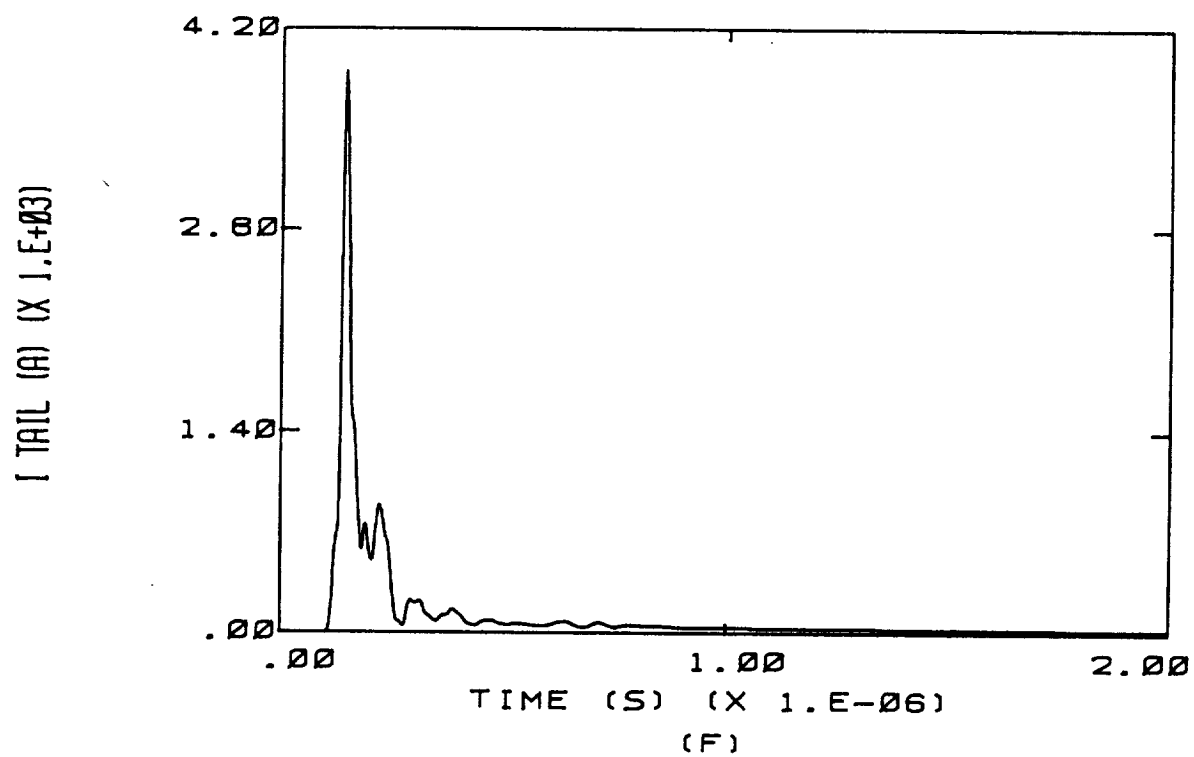
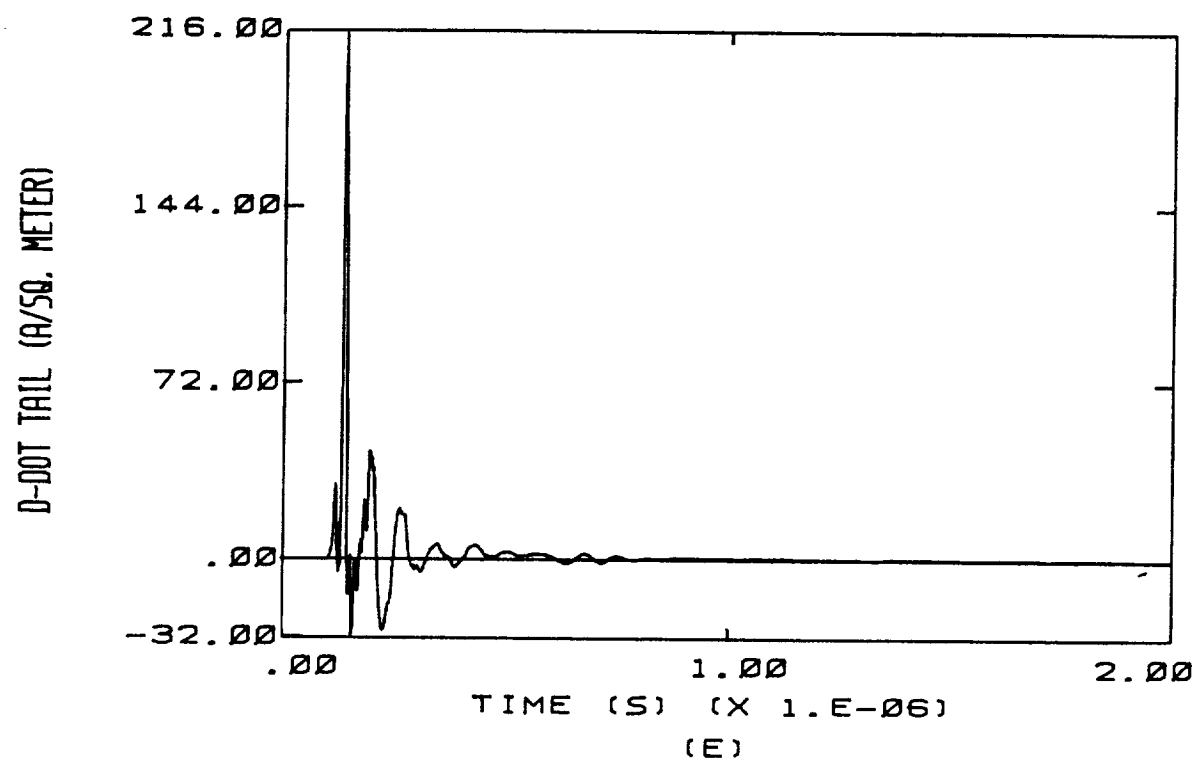
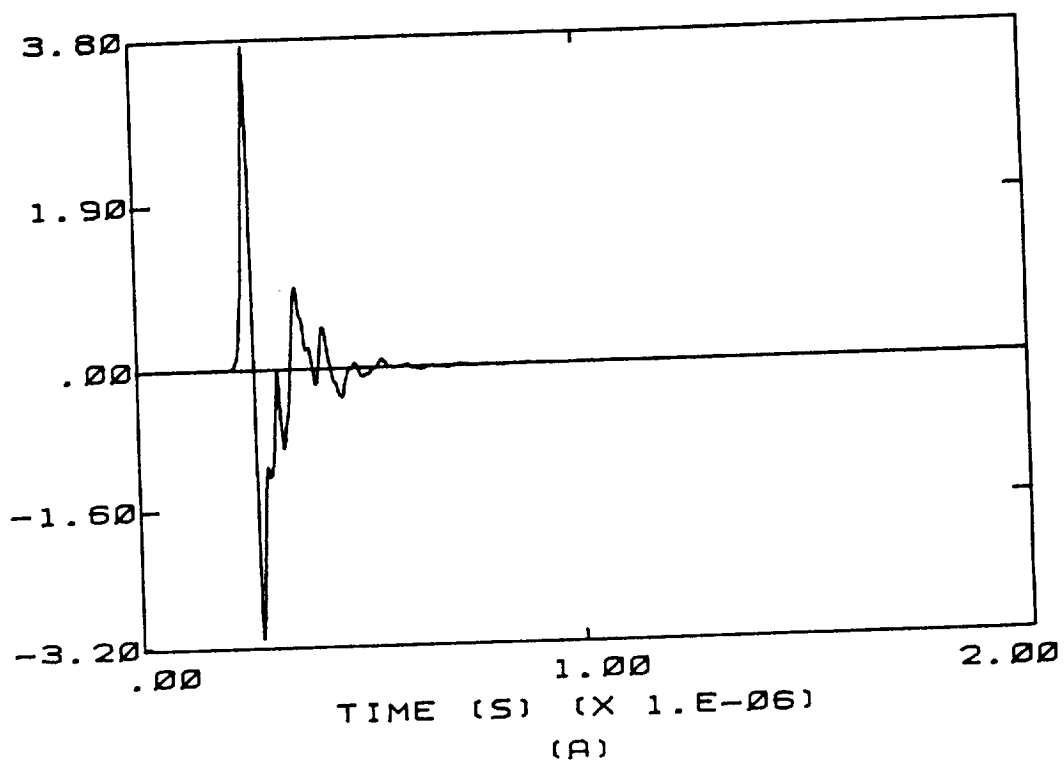


Figure E.5 (continued)

B-DOT LONGITUDINAL (T/S) (X 1.E+03)



B-DOT LEFT WING (T/S) (X 1.E+03)

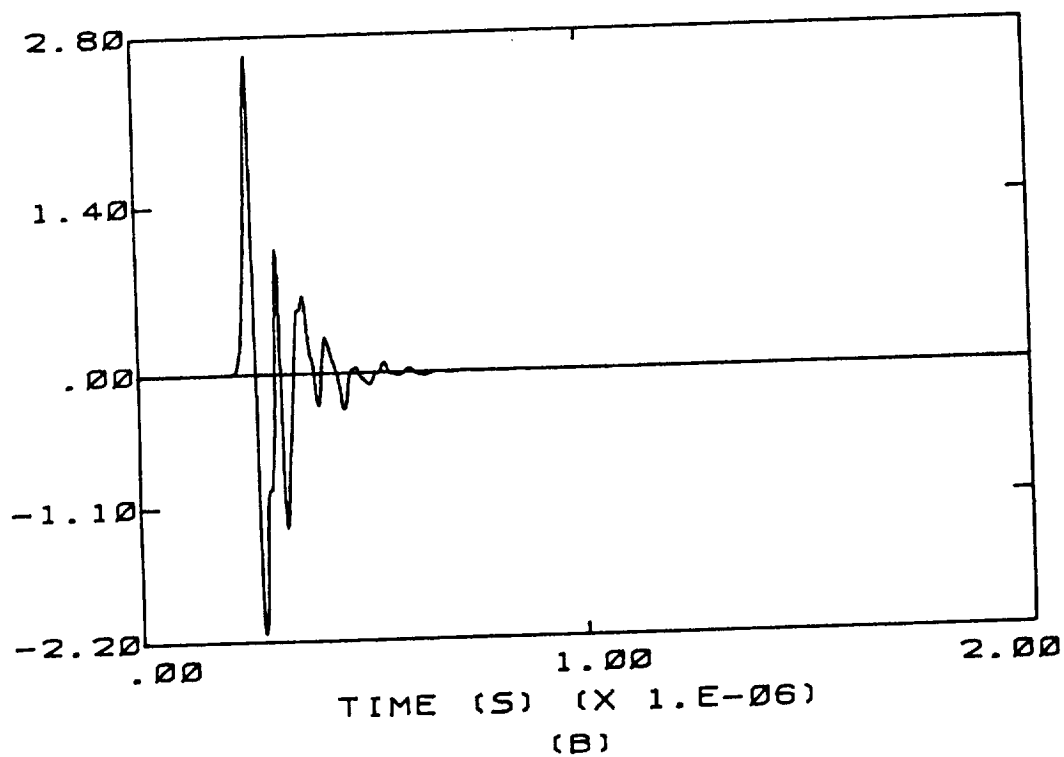


Figure E.6 High Altitude, Front to Back, - 1/2 Qm

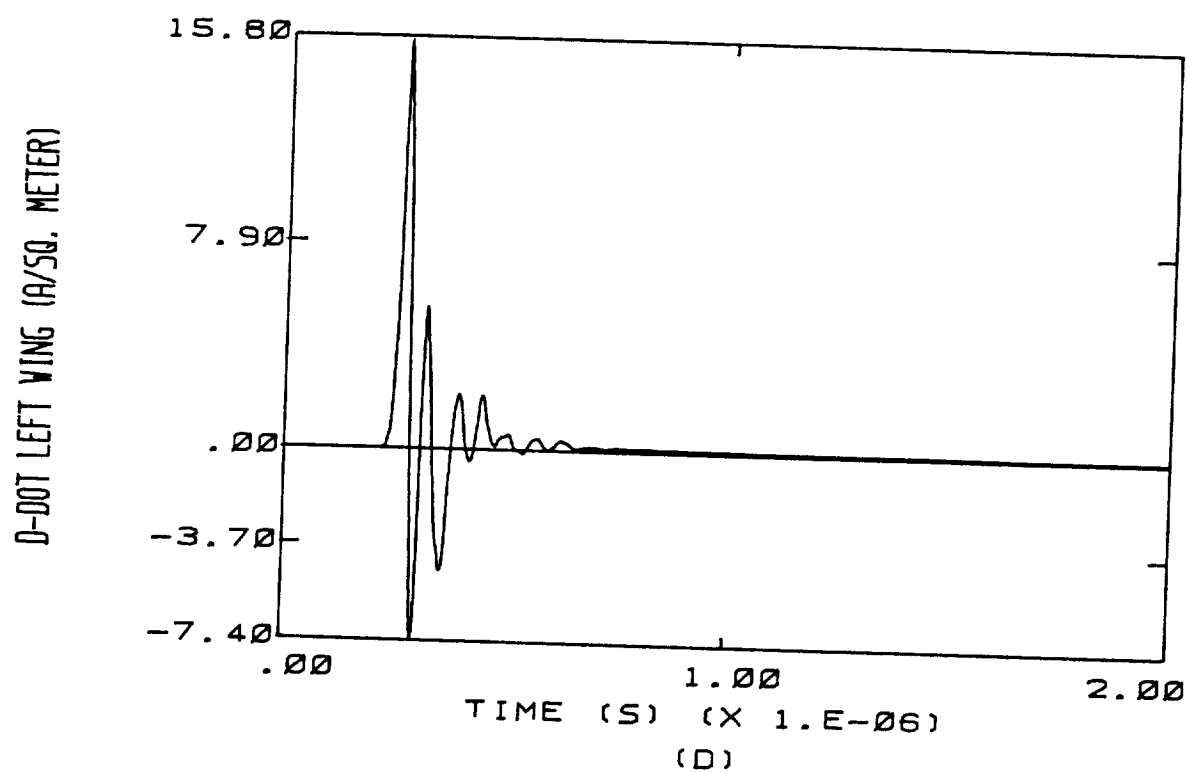
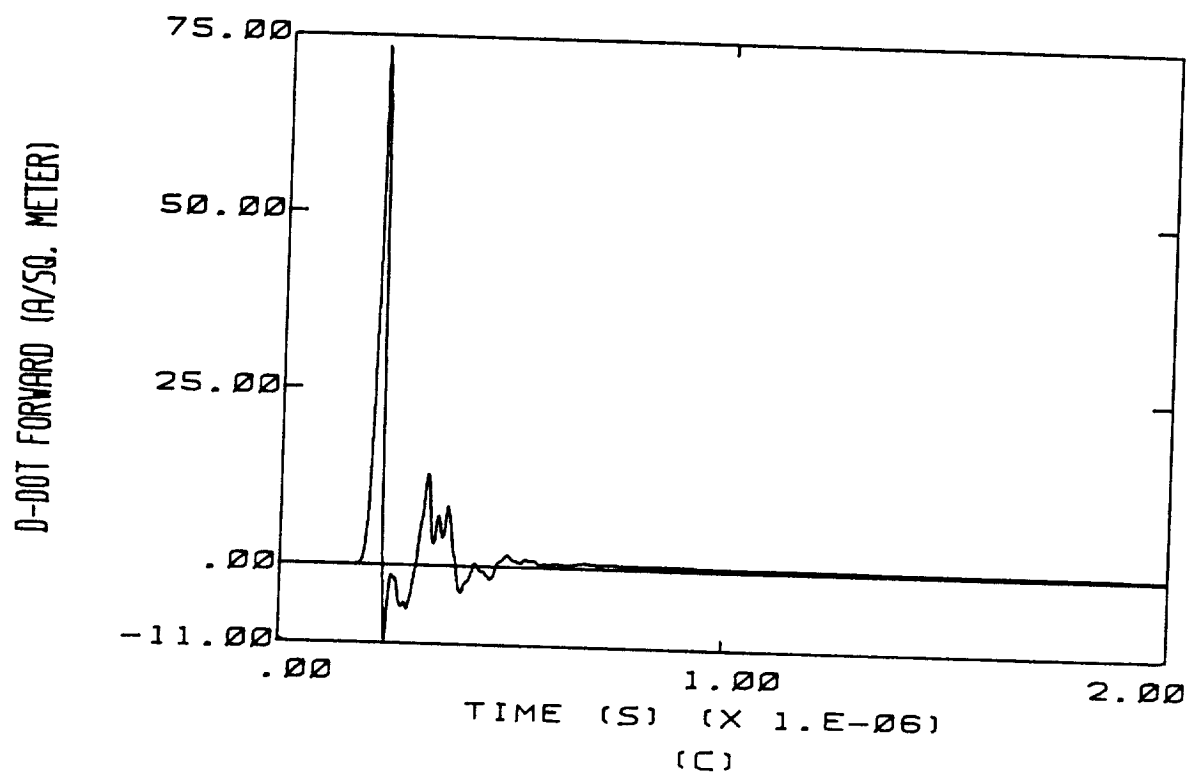
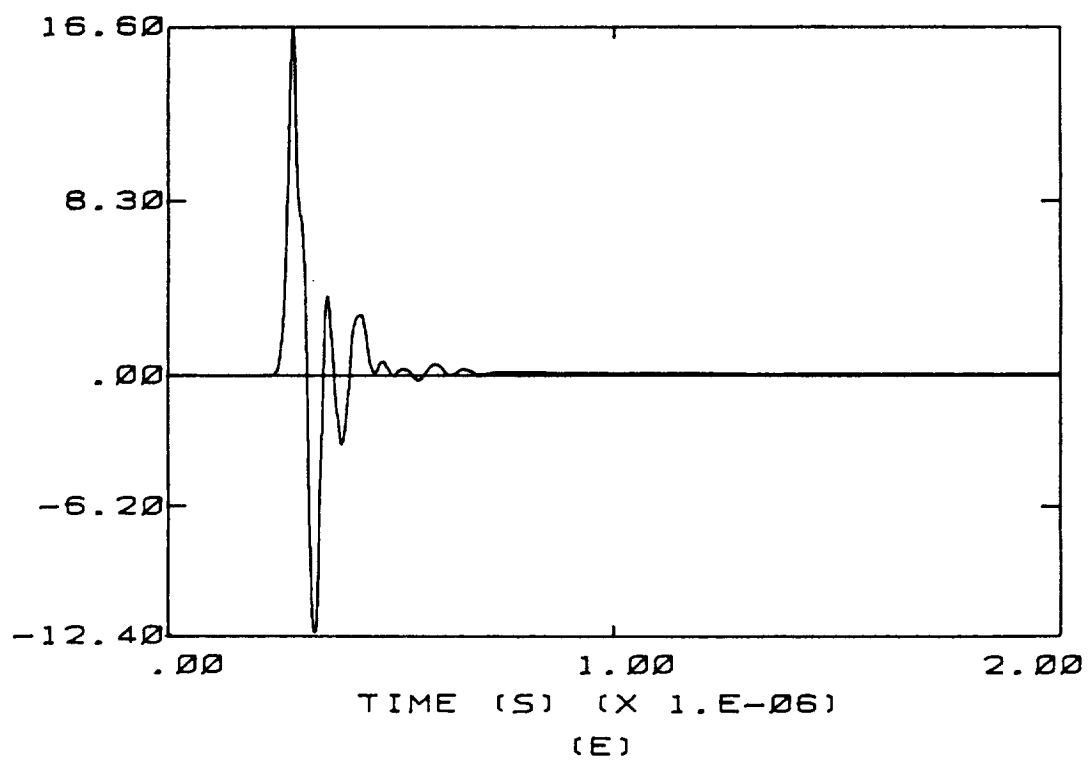


Figure E.6 (continued)

D-DOT TAIL (A/50, METER)



I NOSE (A) (X 1.E+03)

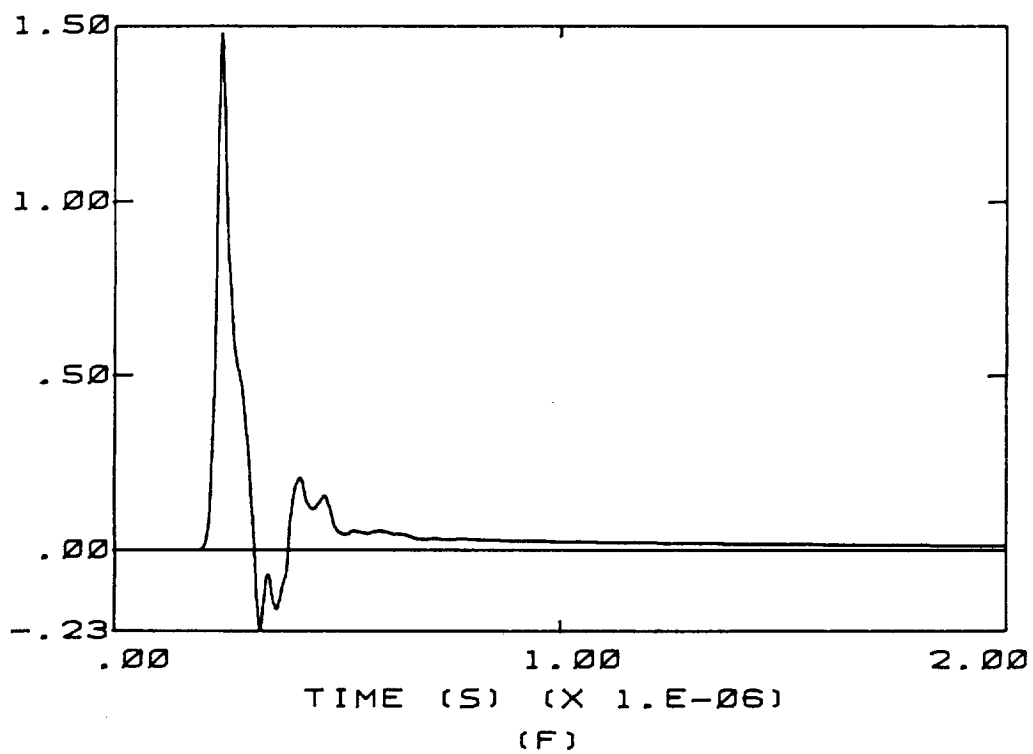


Figure E.6 (continued)

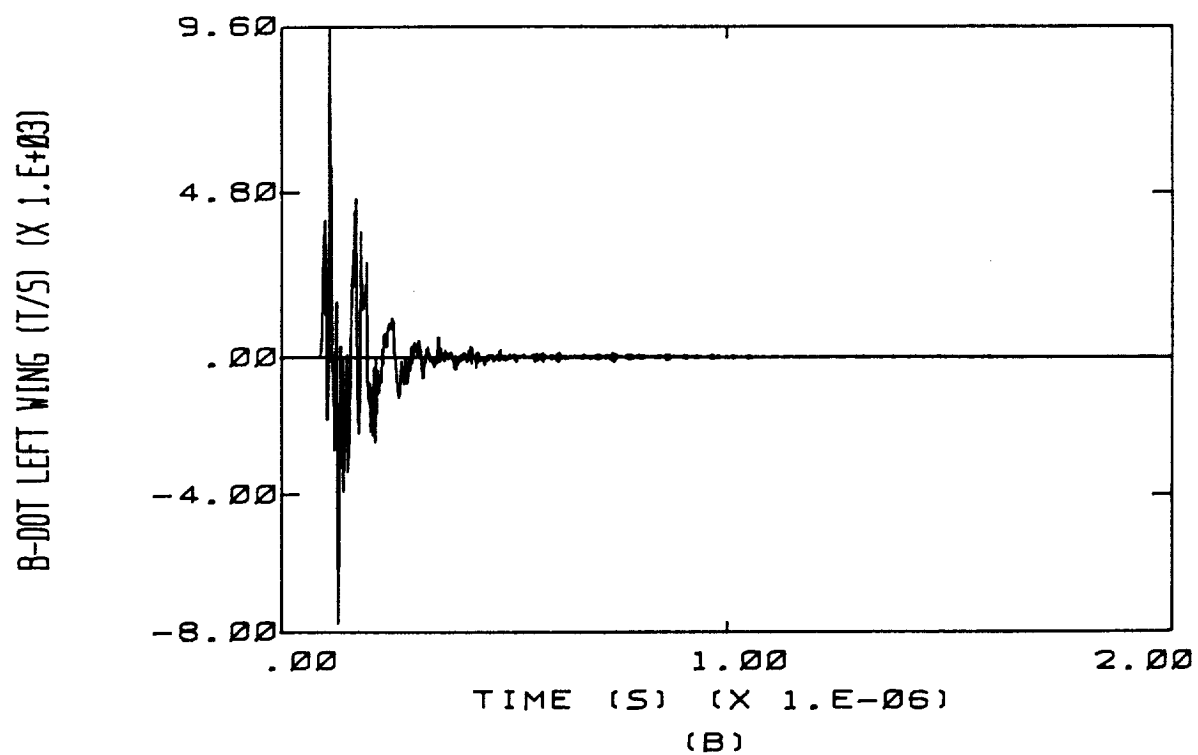
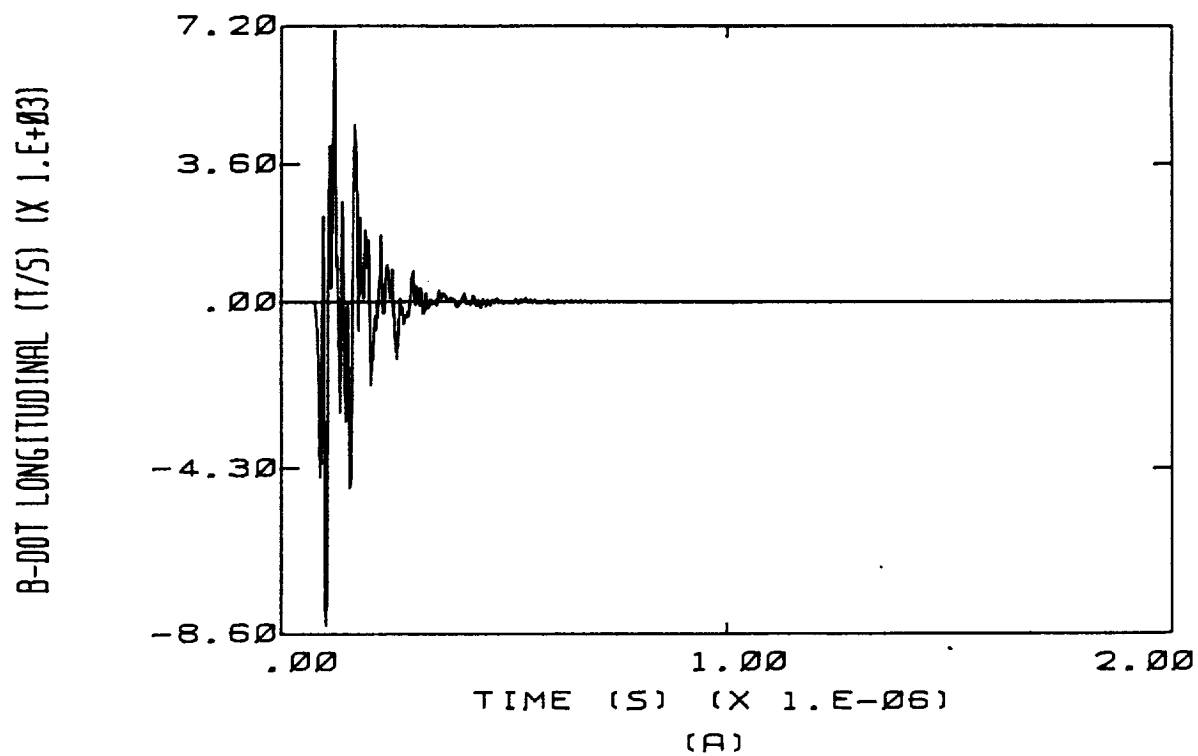
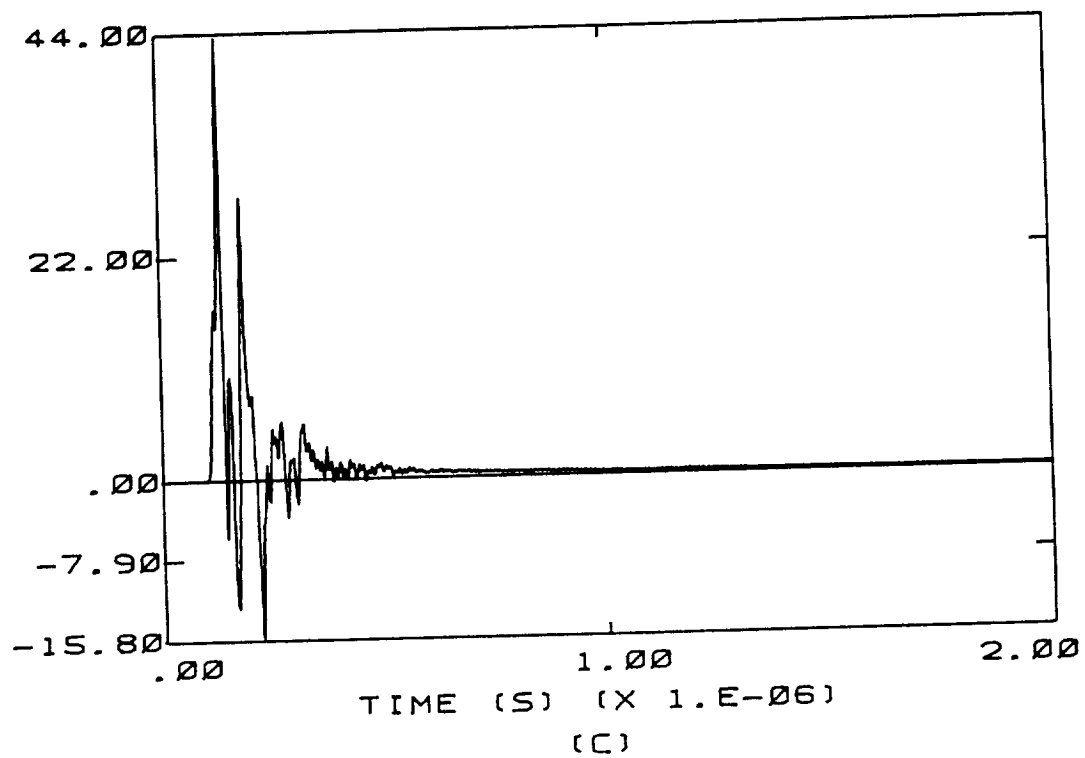


Figure E.7 High Altitude, Right to Left, - 1/2 Qm

D-DOT FORWARD (A/SQ. METER)



D-DOT LEFT WING (A/SQ. METER)

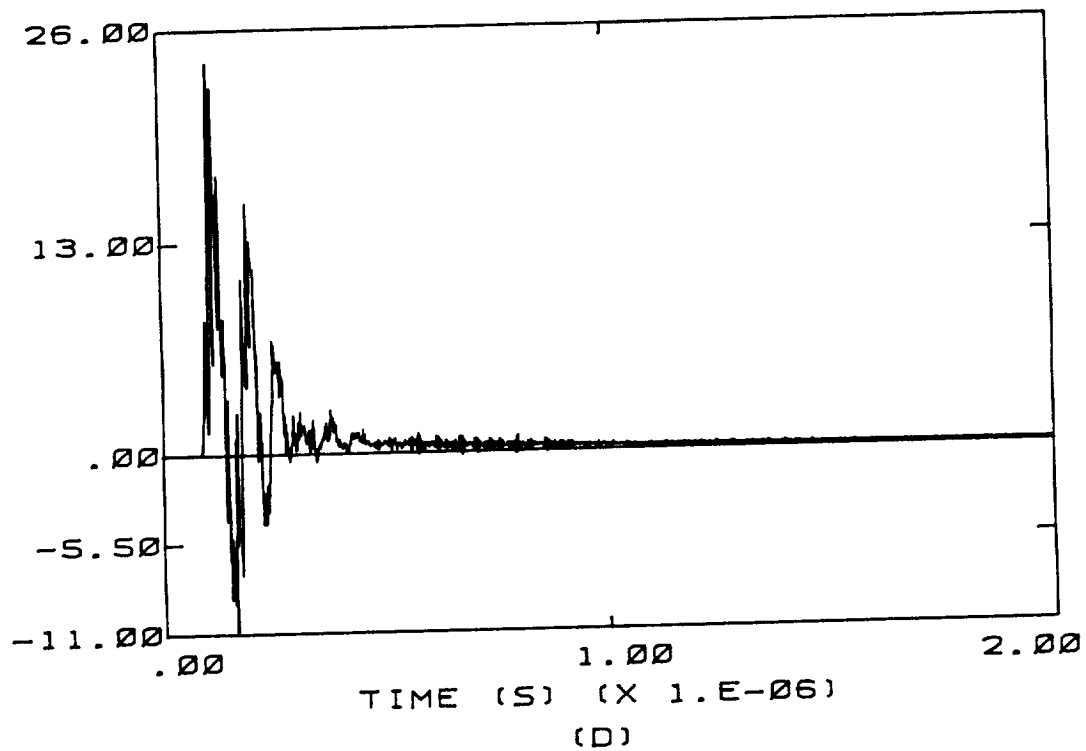


Figure E.7 (continued)

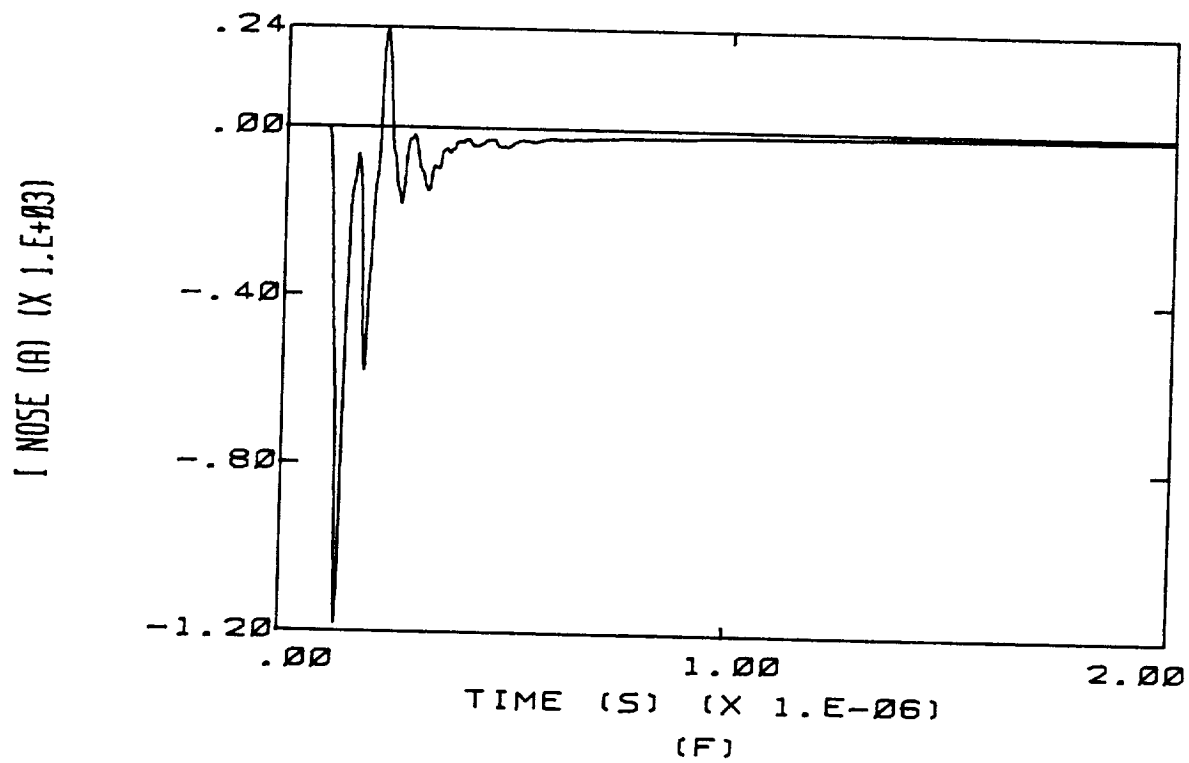
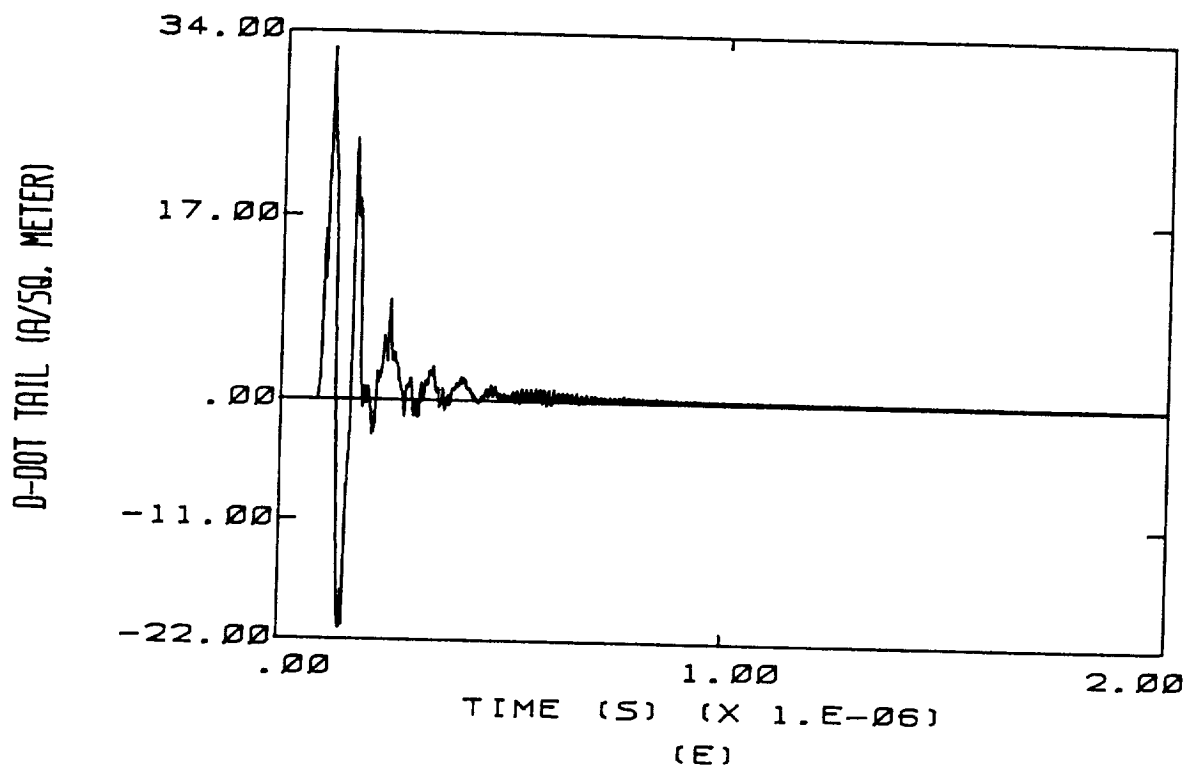


Figure E.7 (continued)



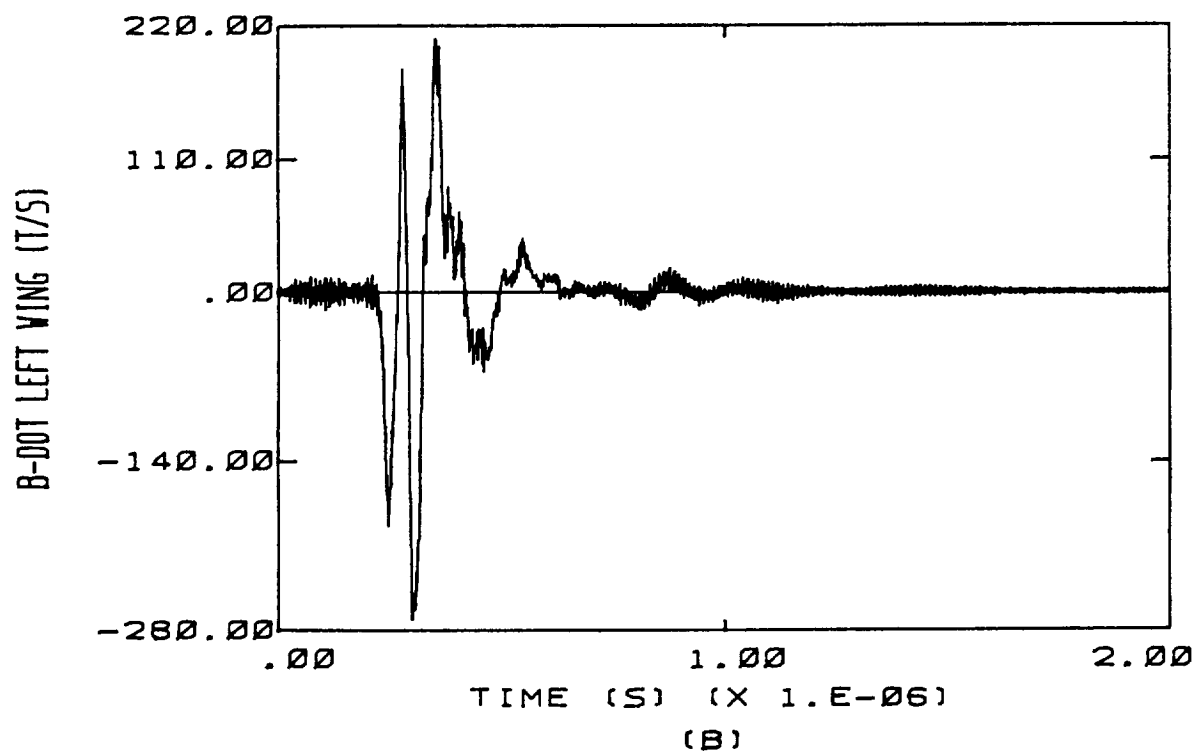
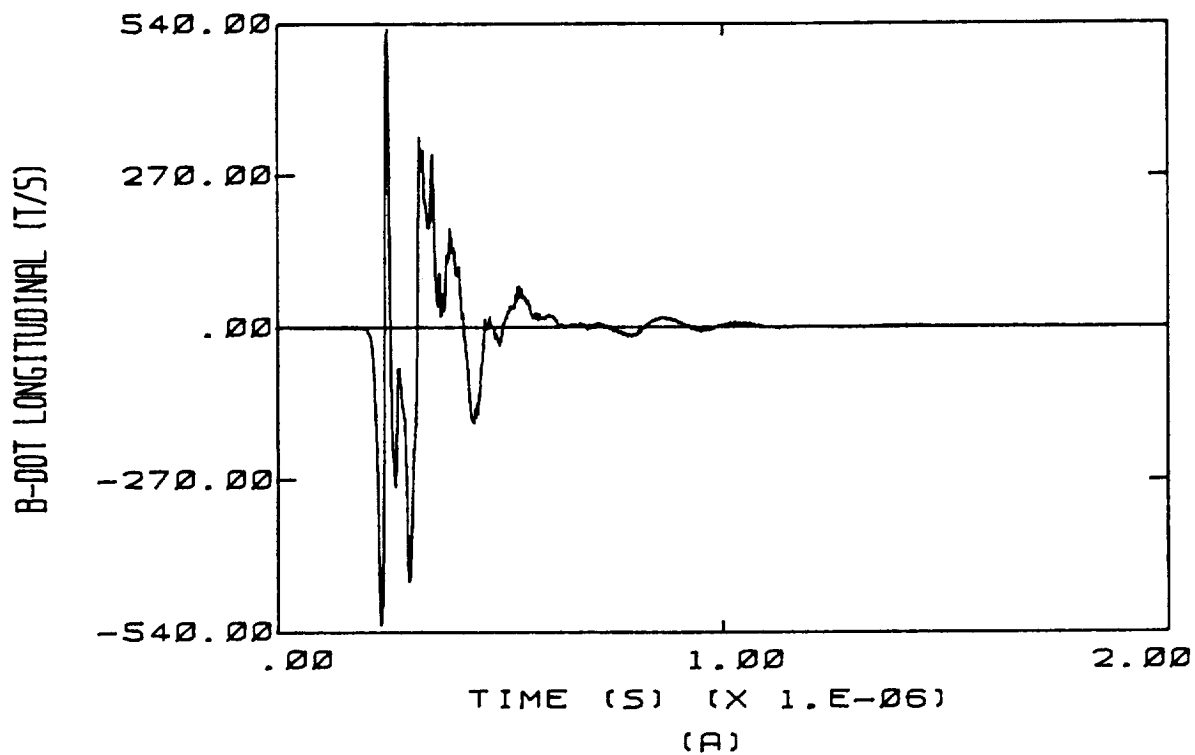
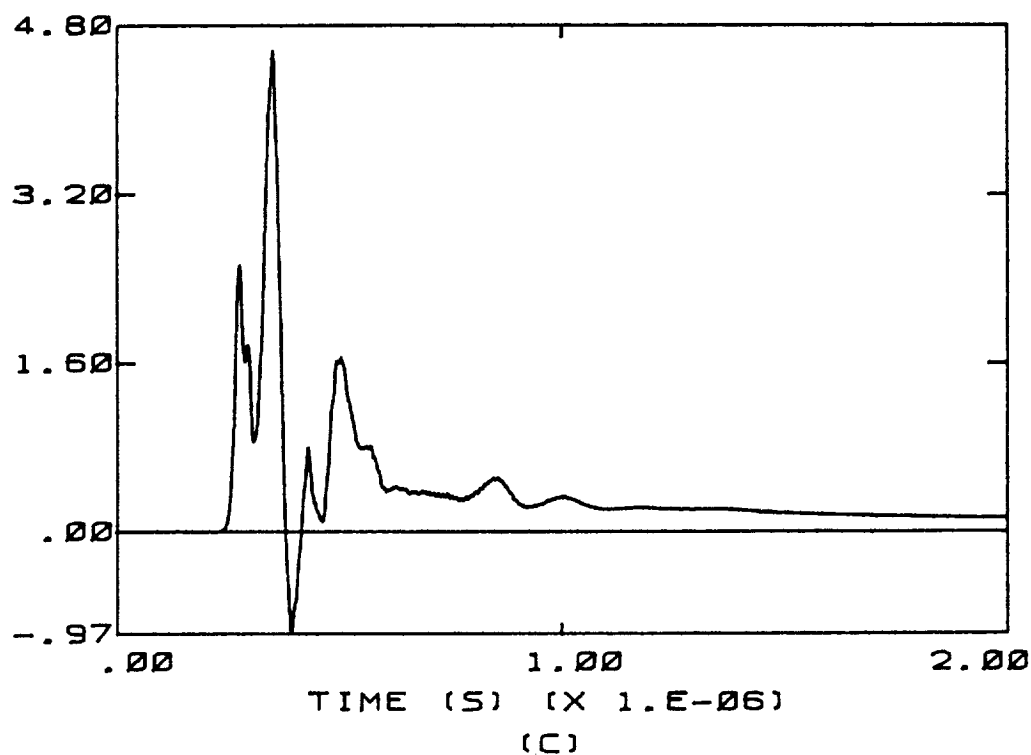


Figure E.8 High Altitude, Top to Bottom, -  $1/2 Q_m$

D-DOT FORWARD (A/50. METER)



D-DOT LEFT WING (A/50. METER)

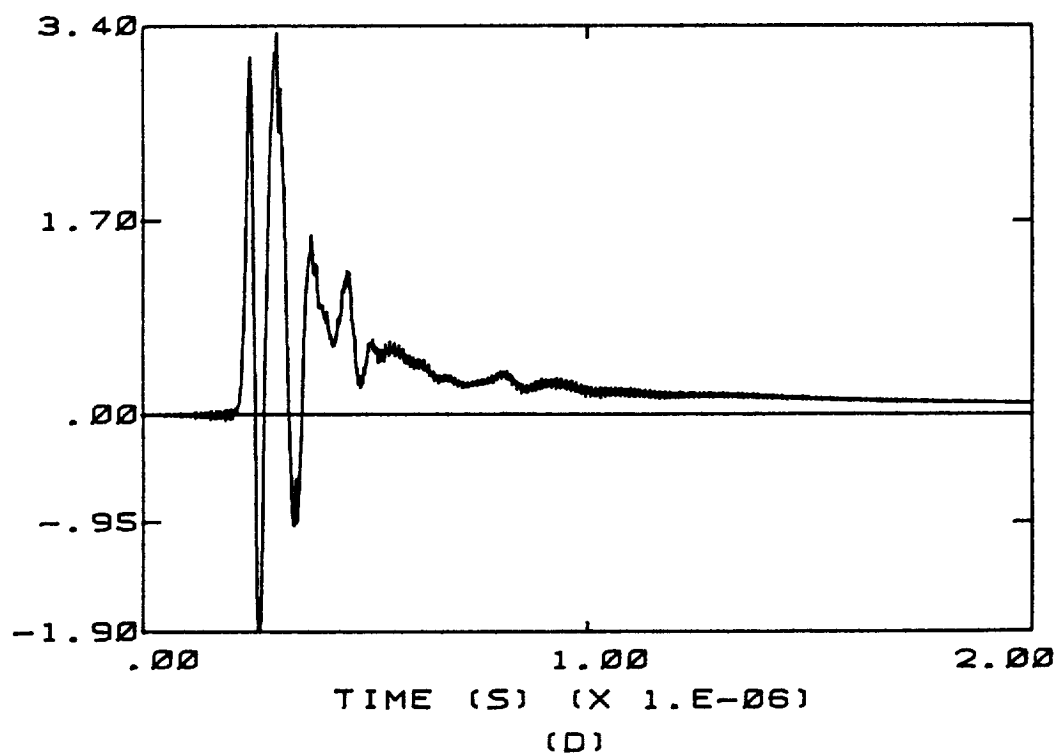


Figure E.8 (continued)

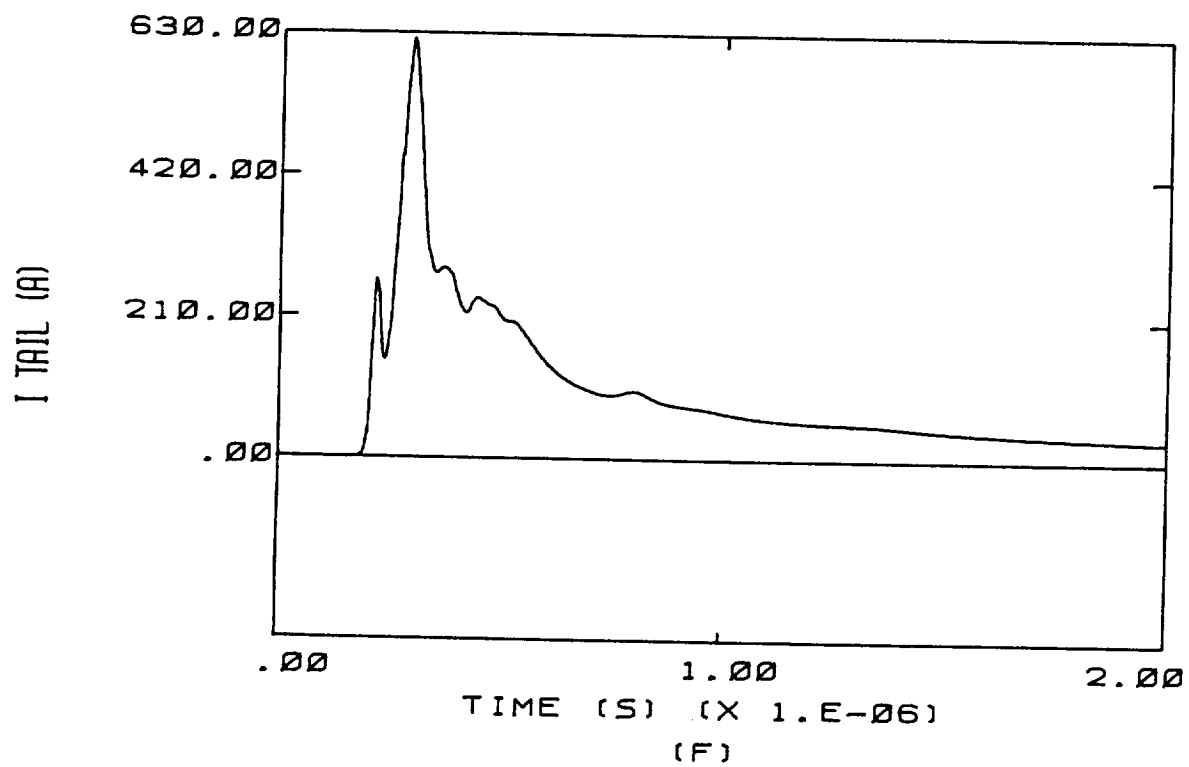
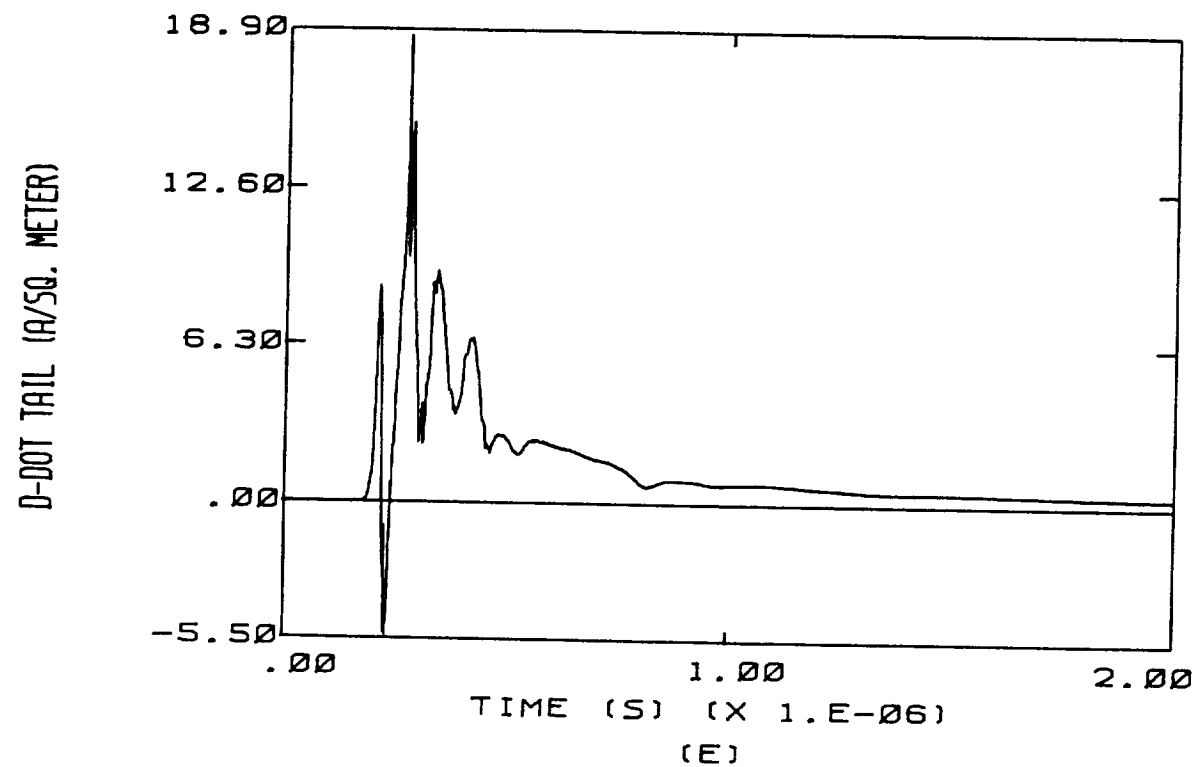


Figure E.8 (continued)

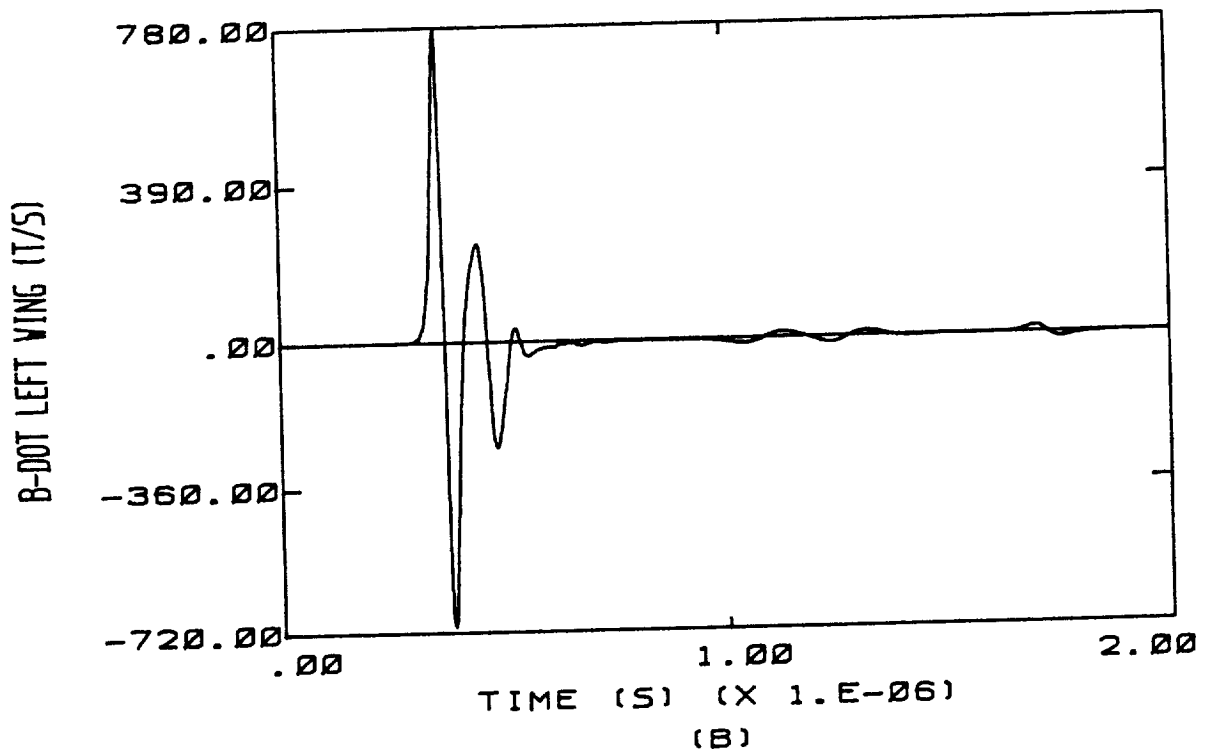
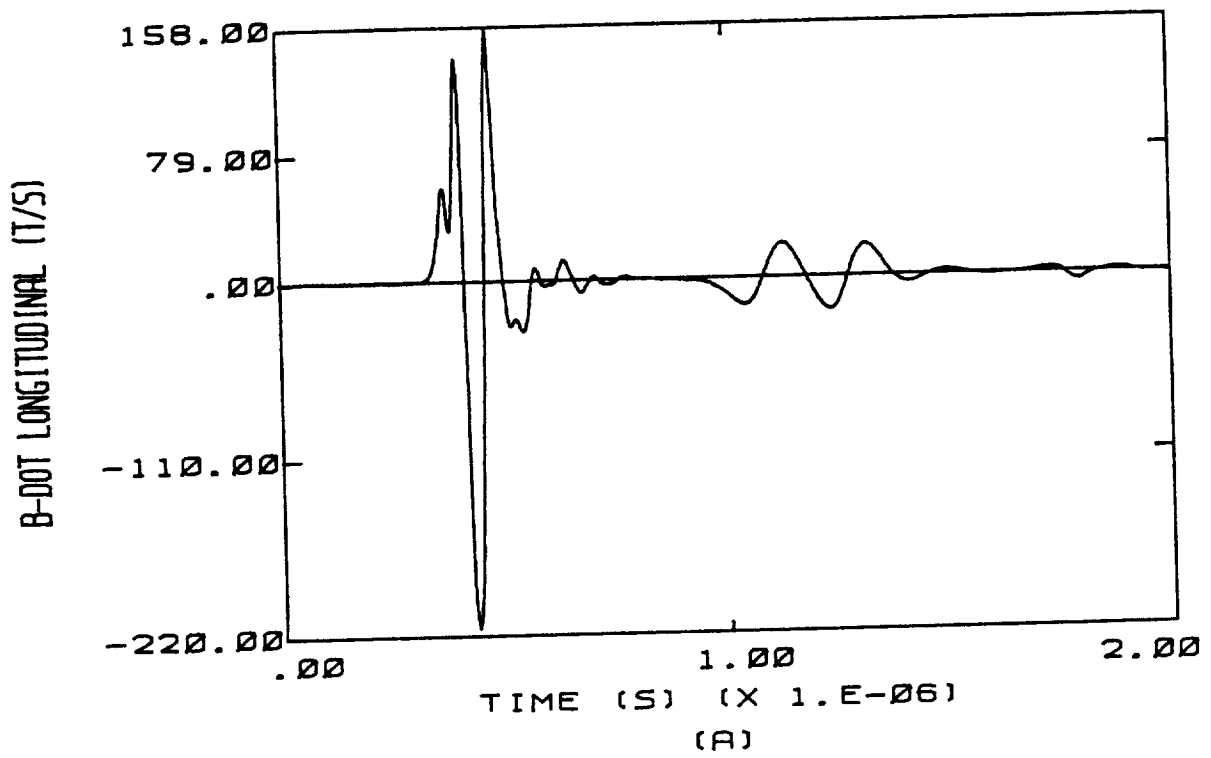
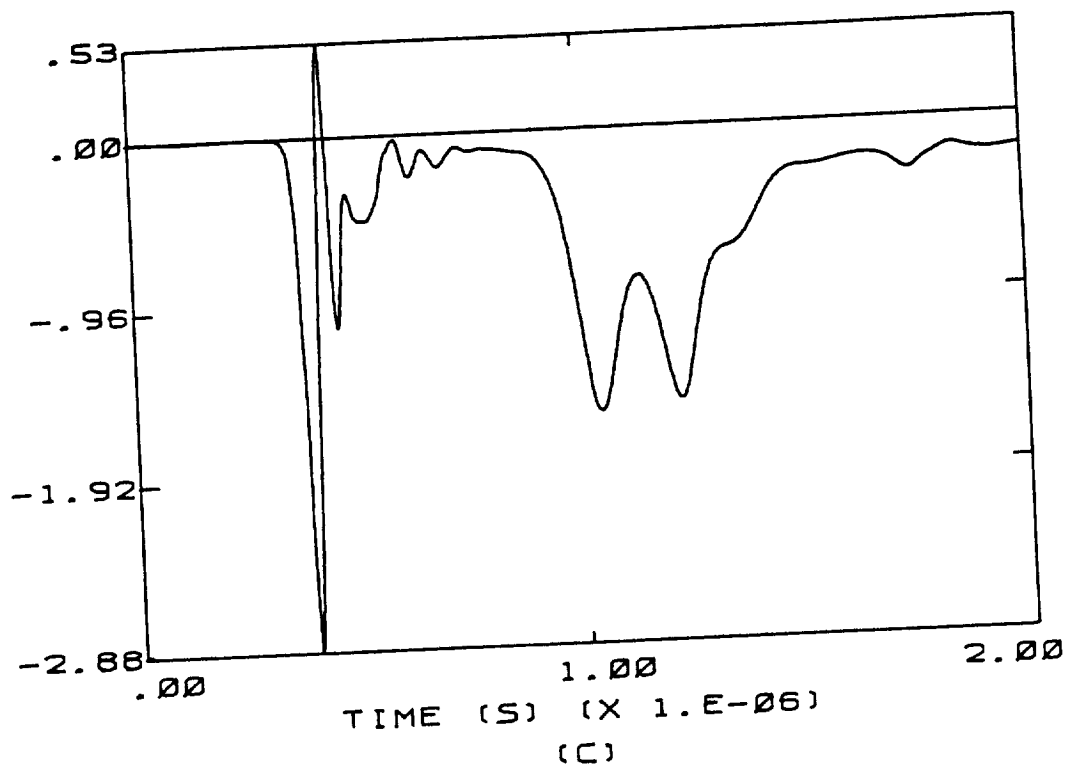


Figure E.9 High Altitude, Right to Left, + Qm

D-DOT FORWARD (A/50. METER)



D-DOT LEFT WING (A/50. METER)

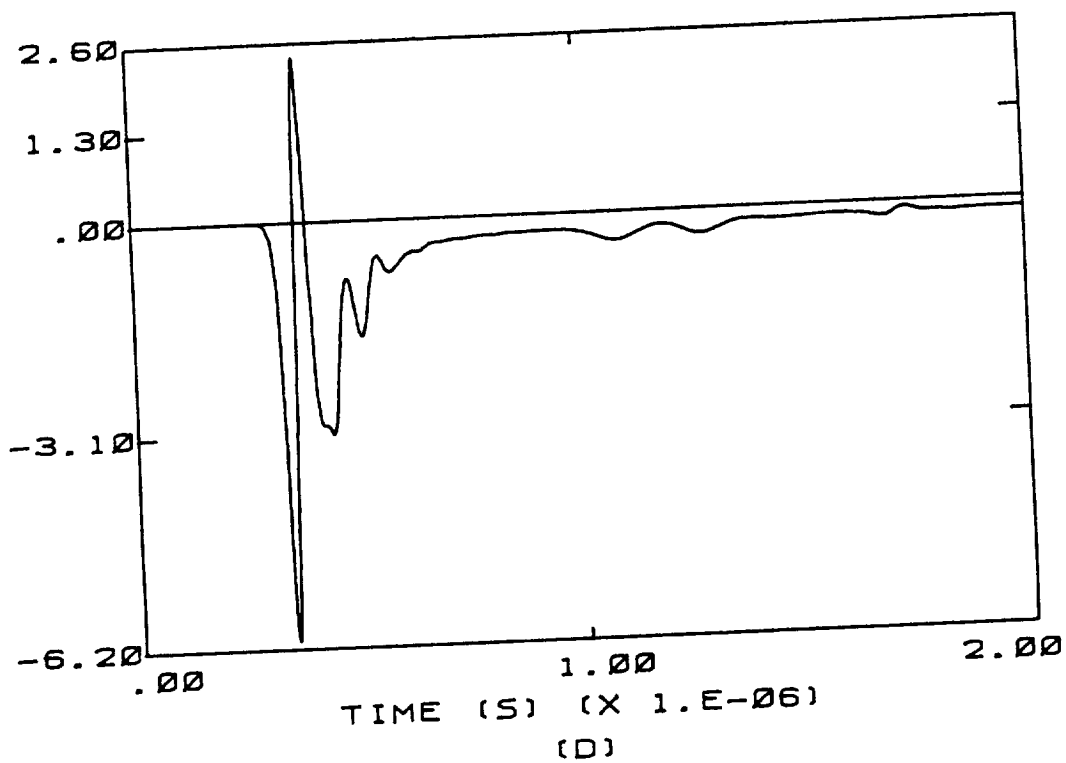


Figure E.9 (continued)

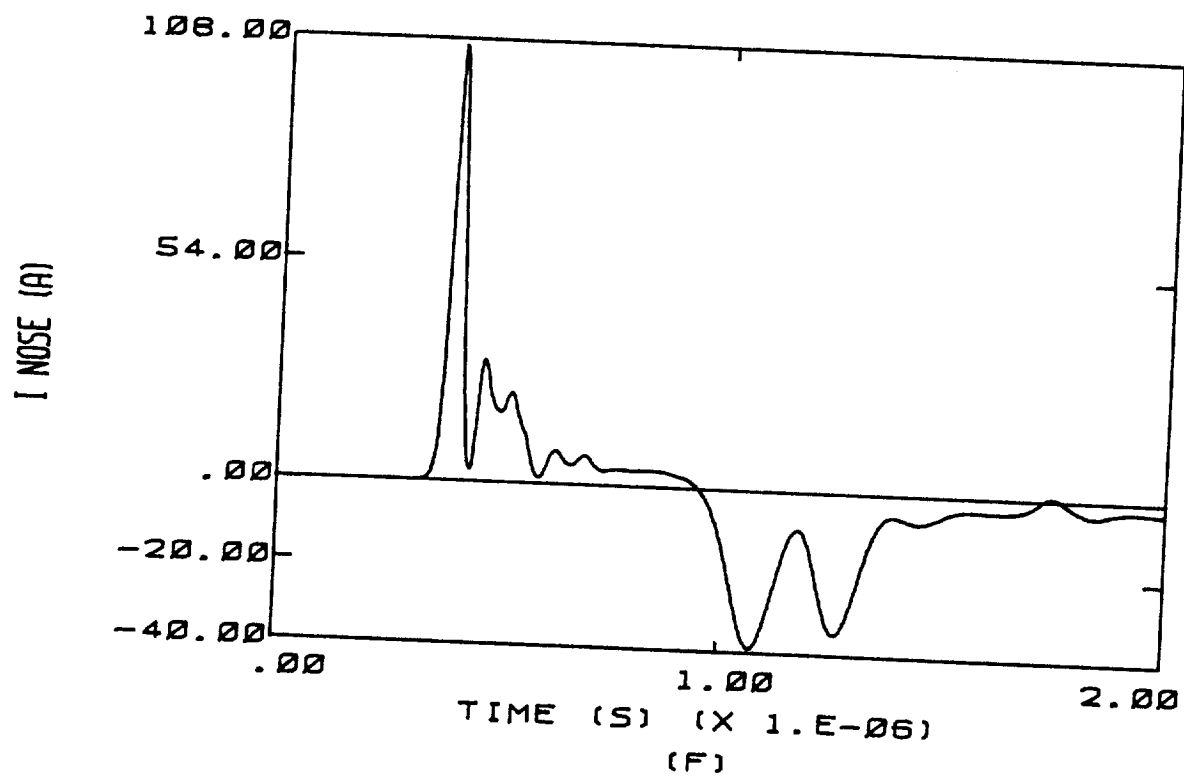
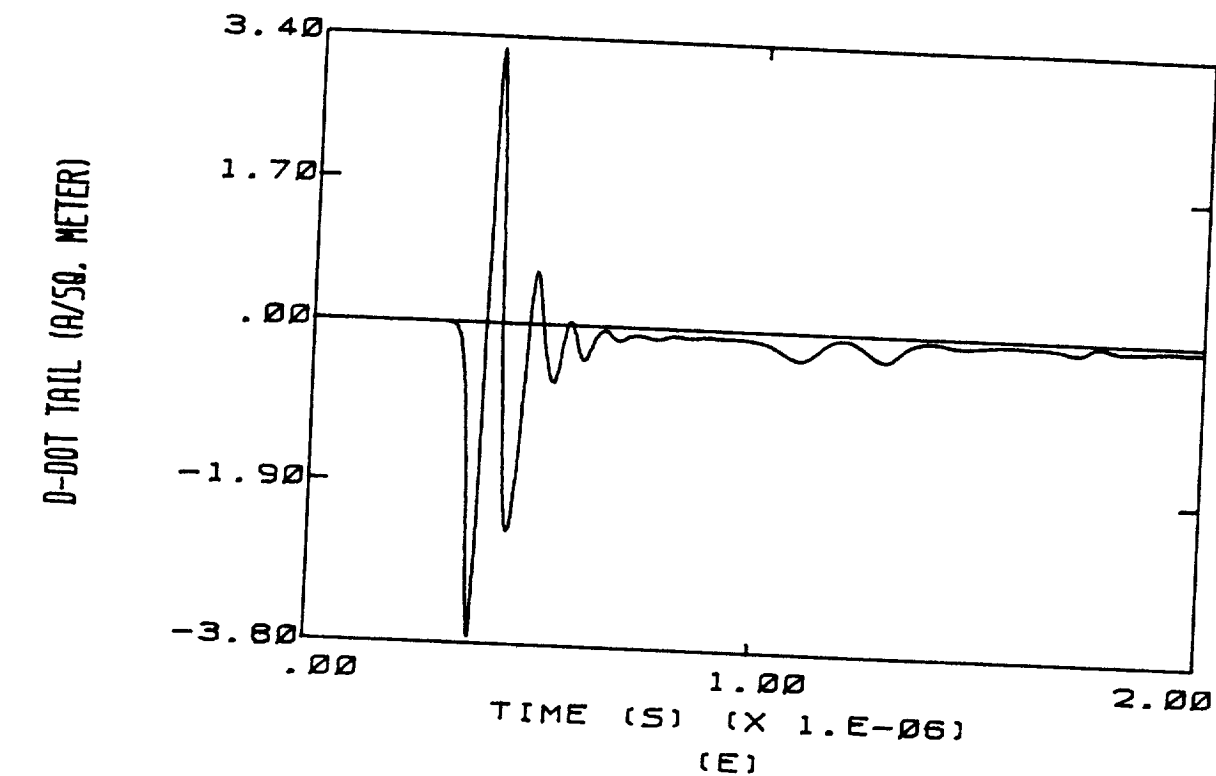


Figure E.9 (continued)

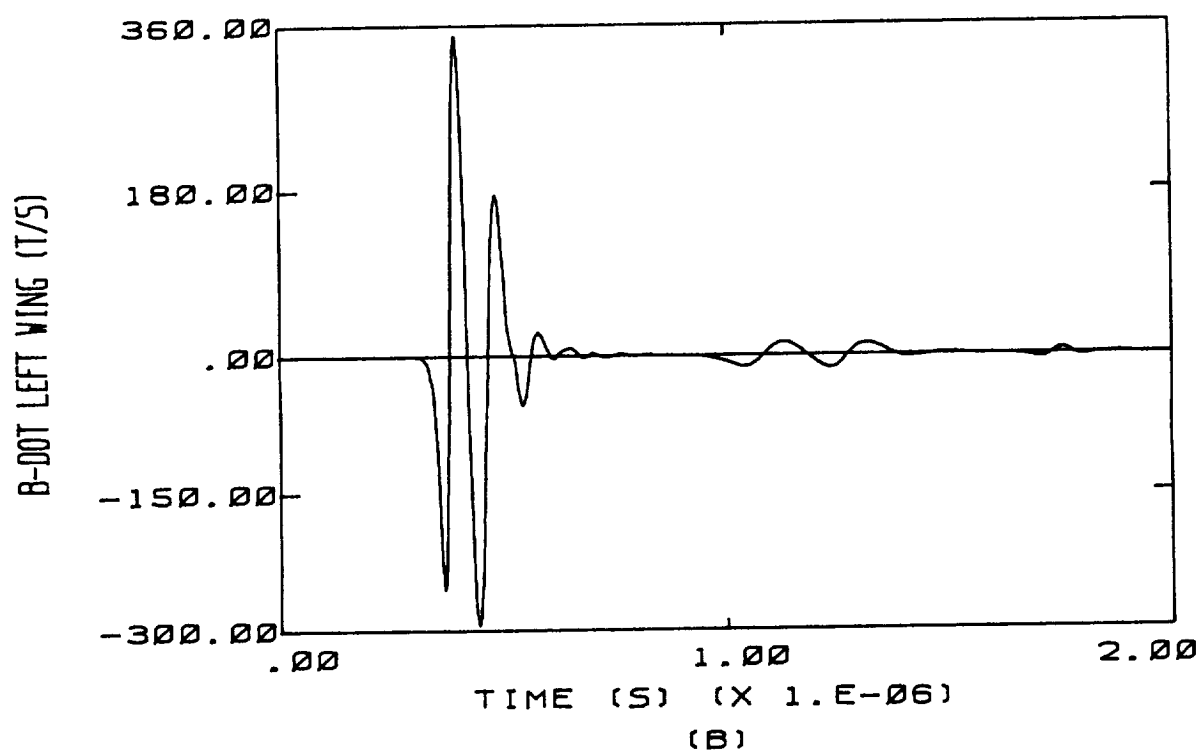
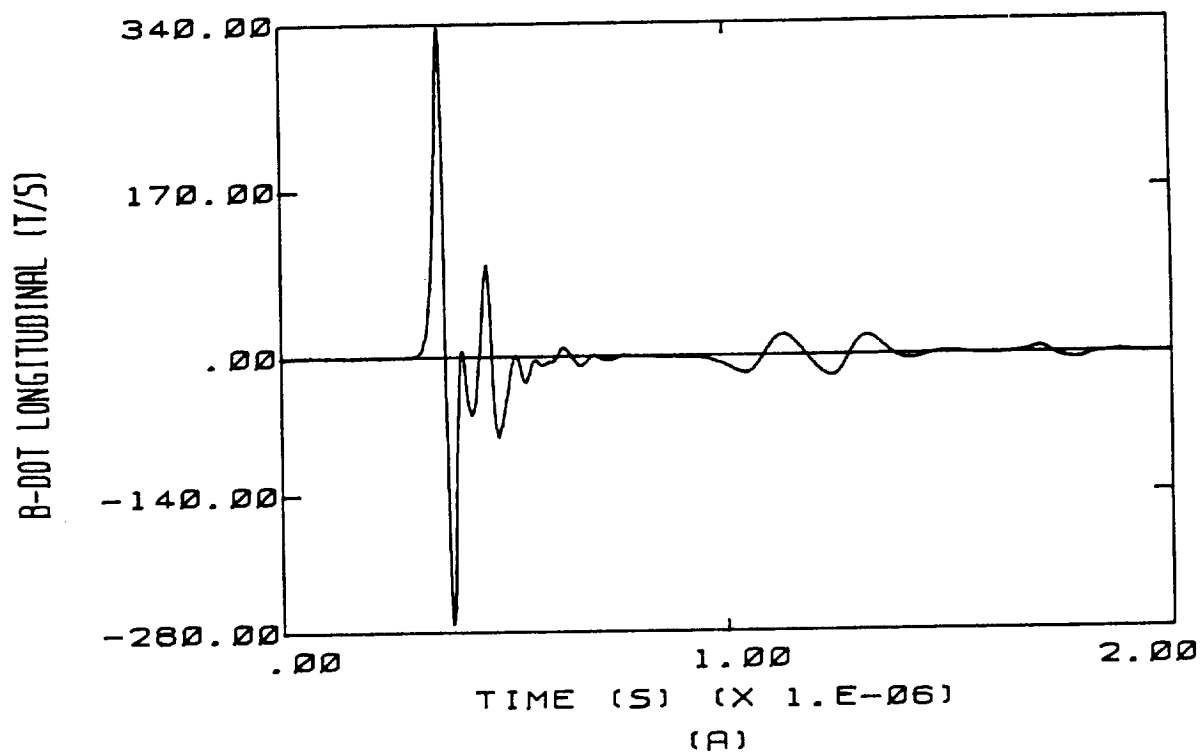
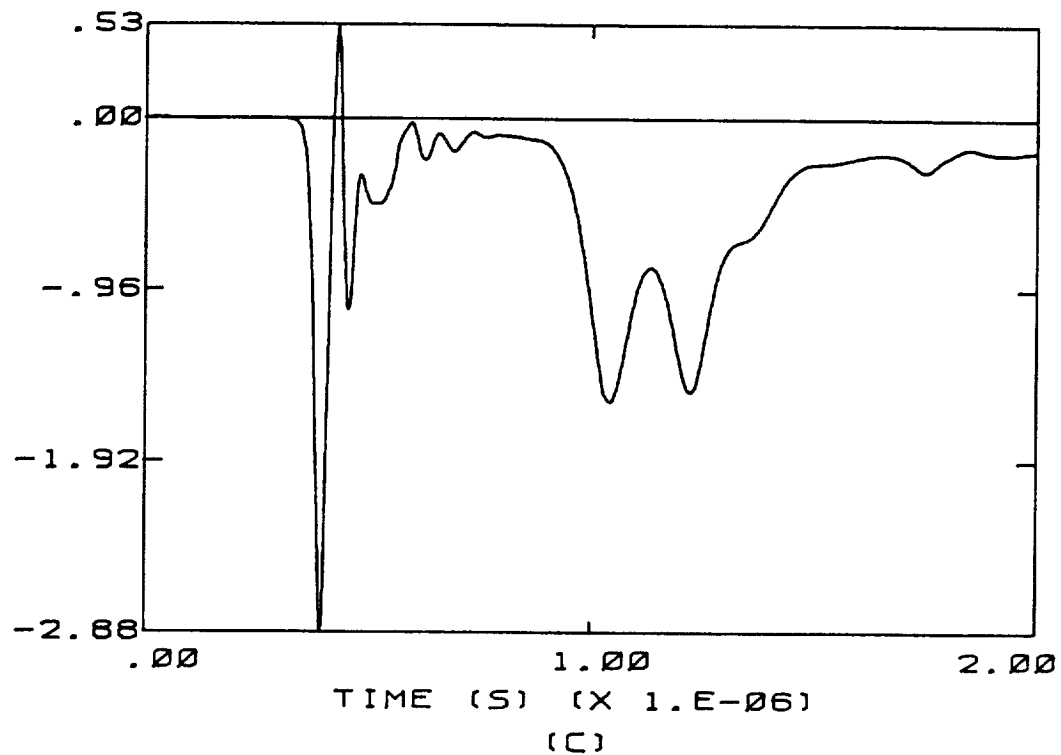


Figure E.10 High Altitude, Left to Right, + Qm

D-DOT FORWARD (A/SQ. METER)



D-DOT LEFT WING (A/SQ. METER)

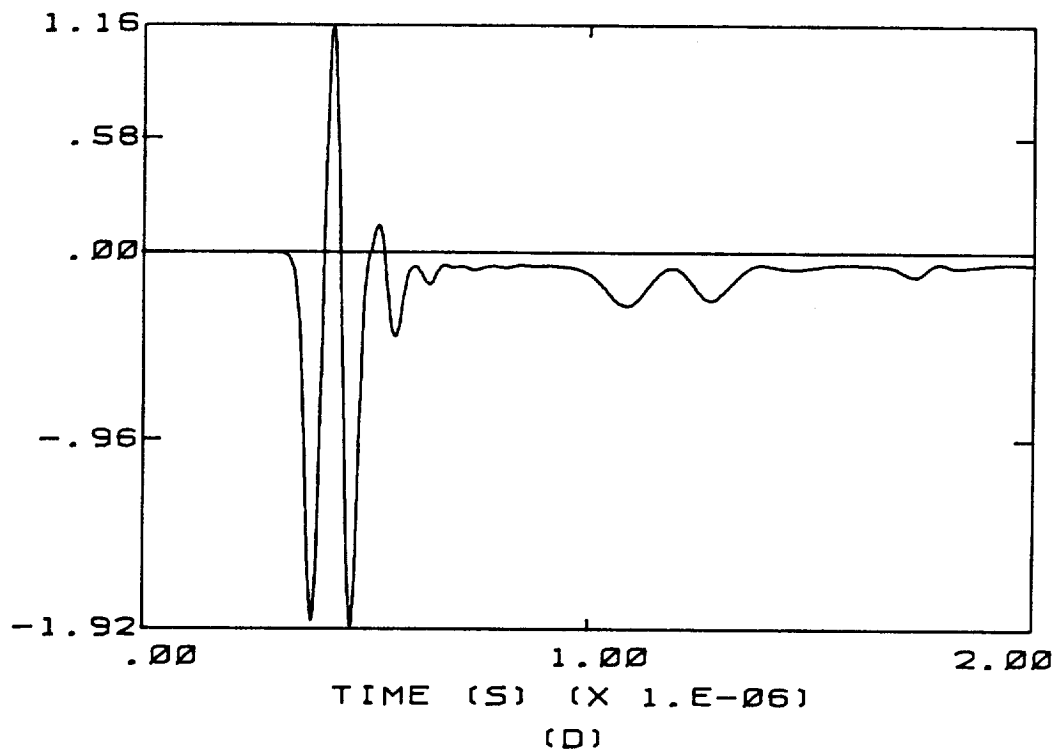
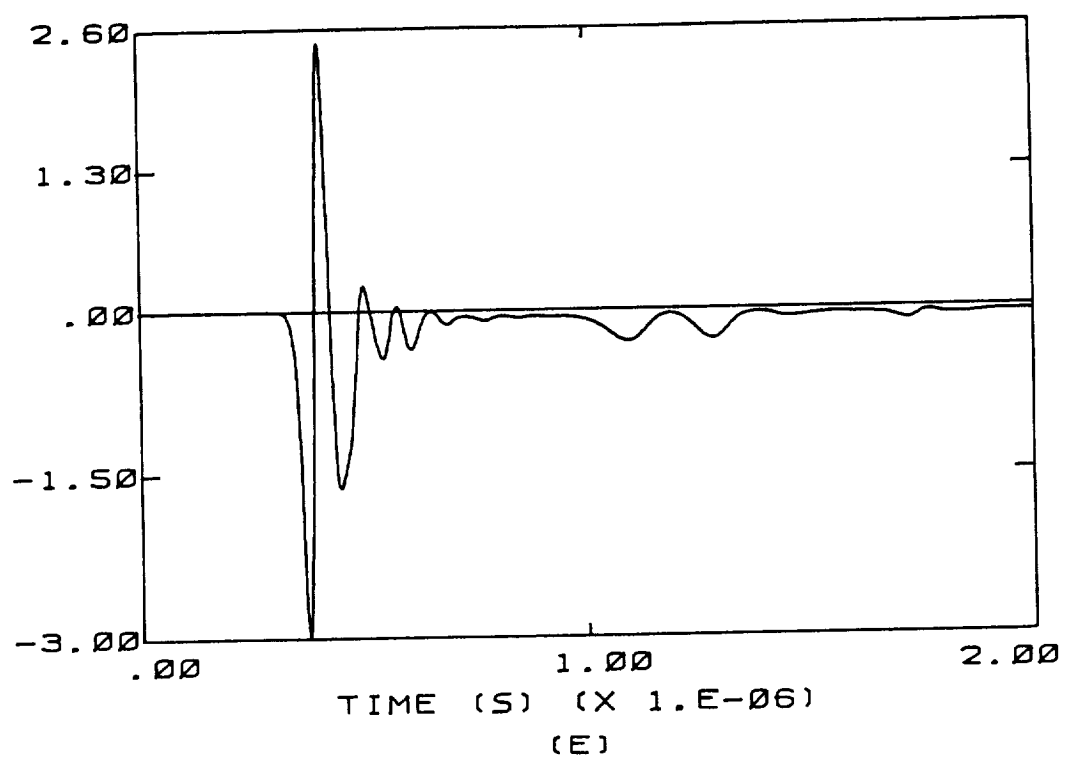


Figure E.10 (continued)



D-DOT TAIL (A/50. METER)



I NOSE (A)

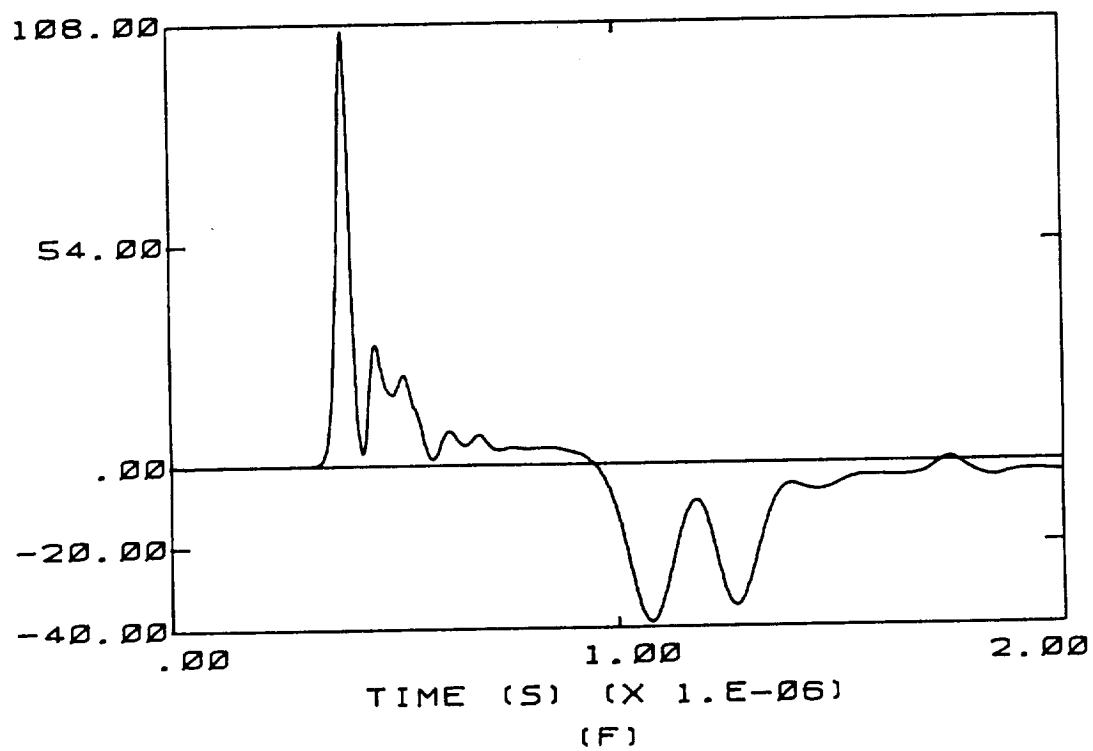


Figure E.10 (continued)

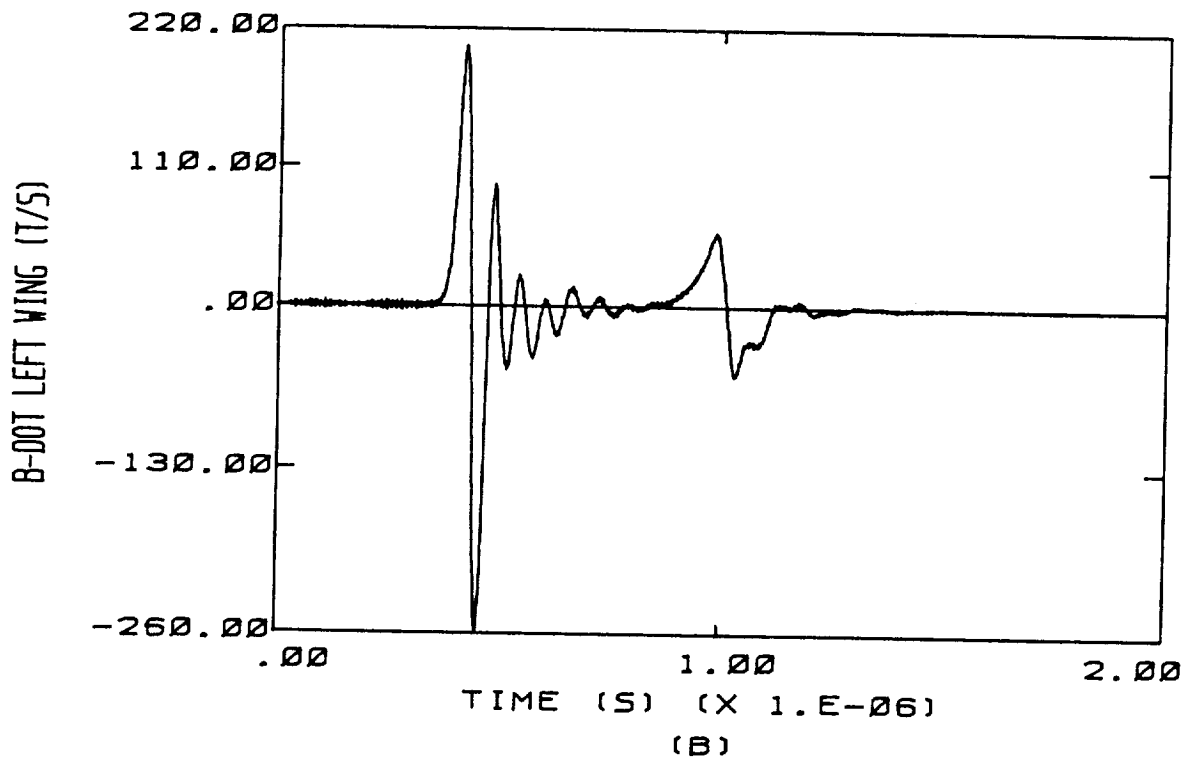
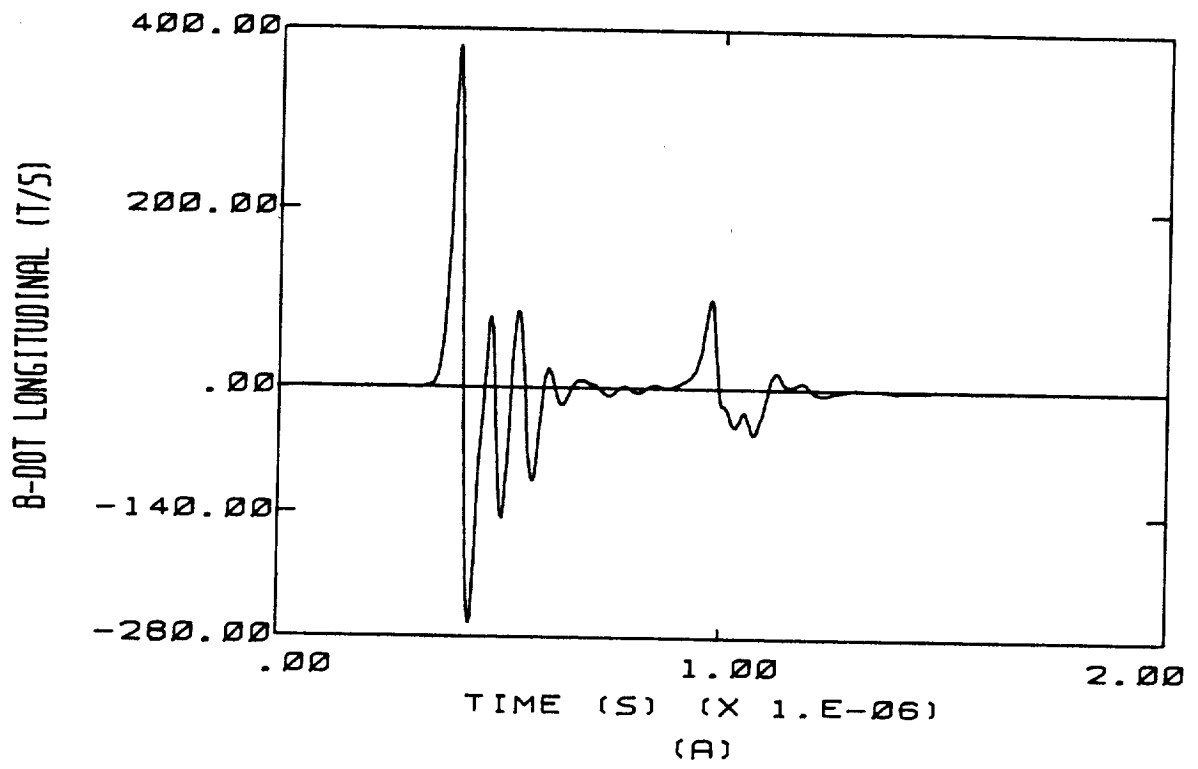
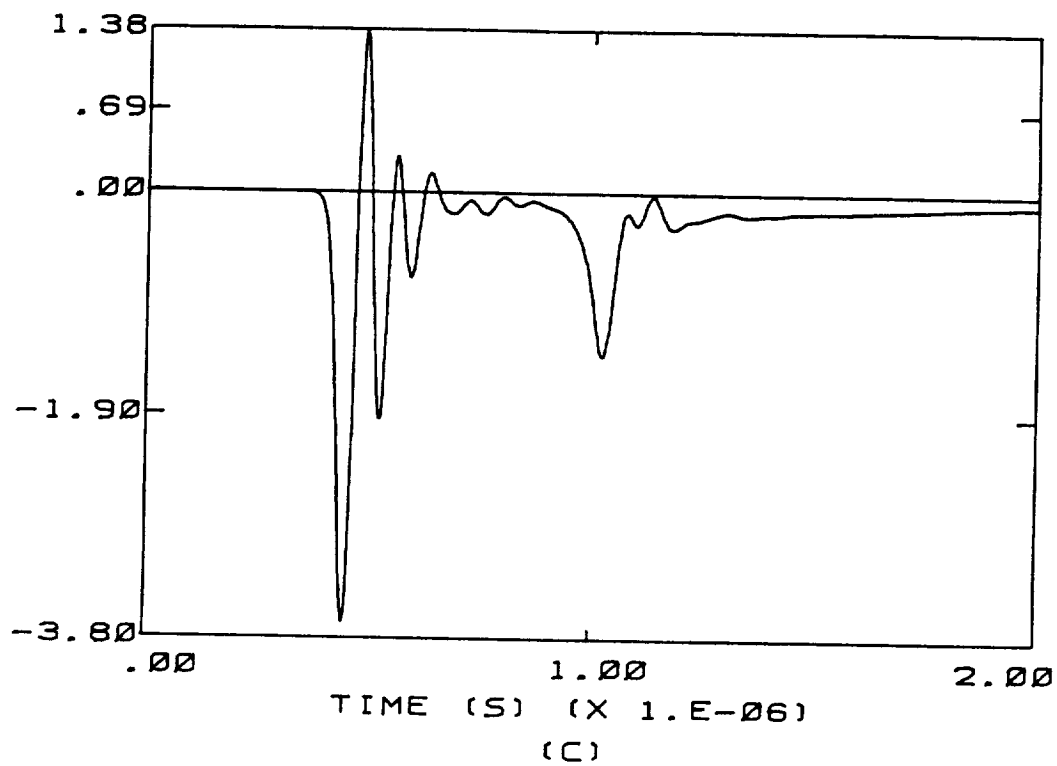


Figure E.11 High Altitude, Bottom to Top, + Qm

D-DOT FORWARD (A/SQ. METER)



D-DOT LEFT WING (A/SQ. METER)

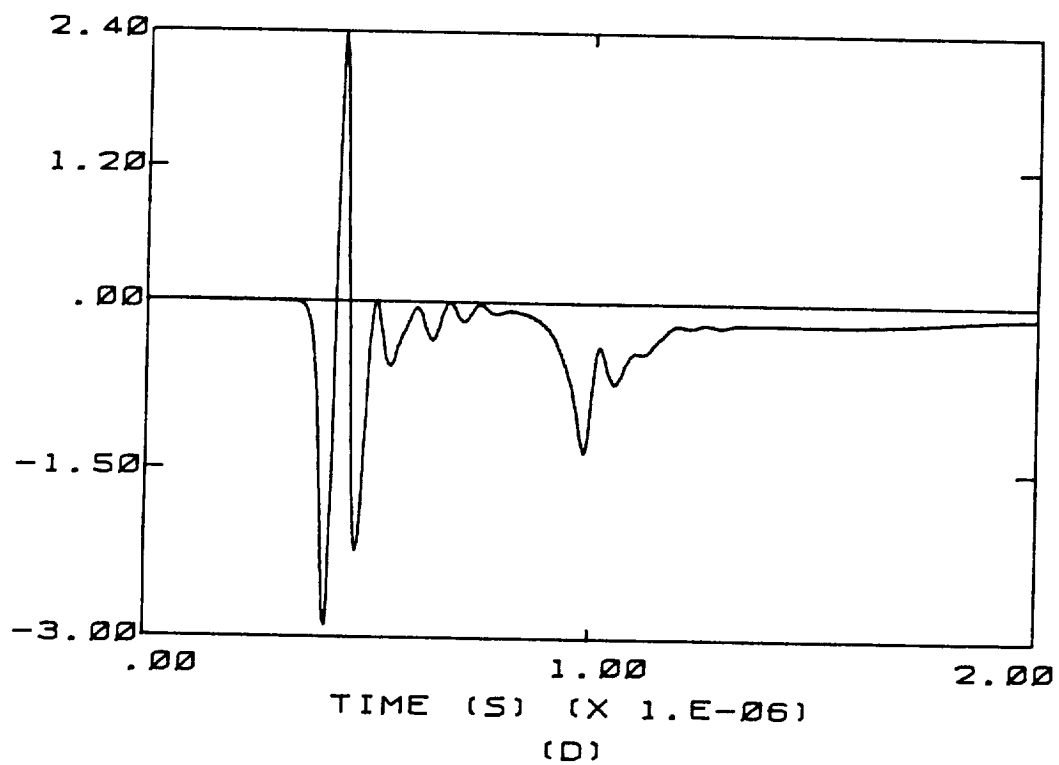


Figure E.11 (continued)

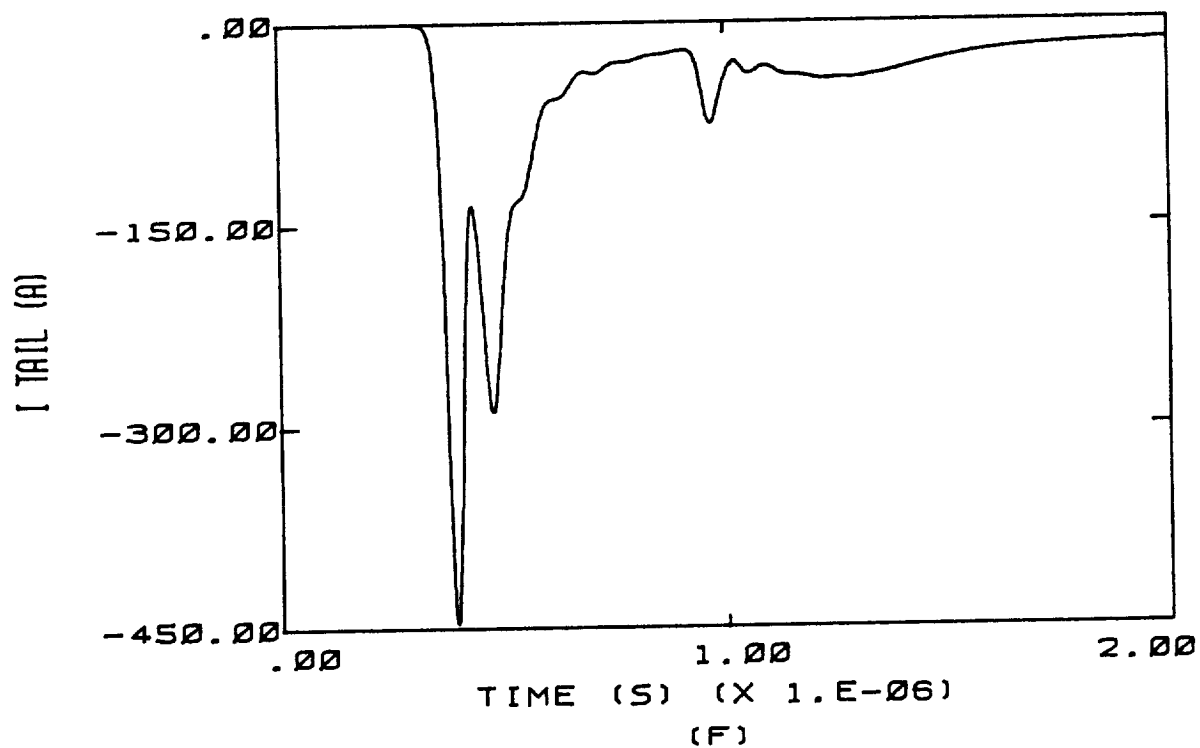
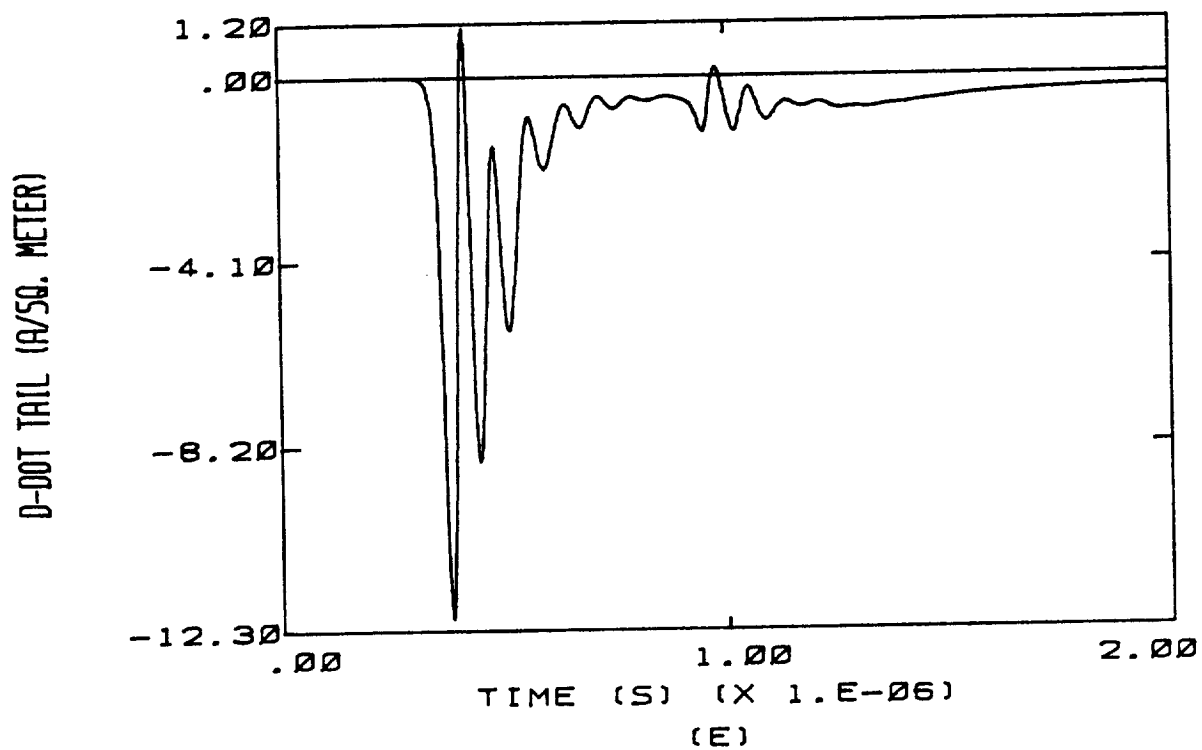


Figure E.11 (continued)

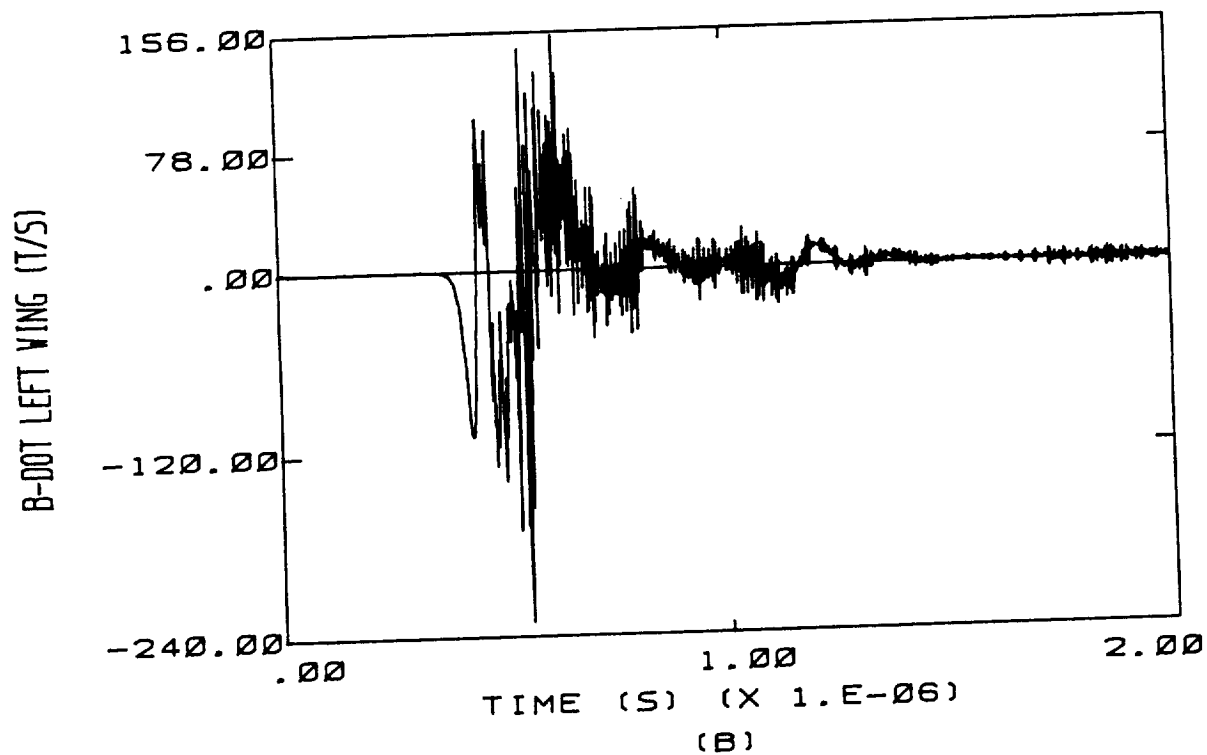
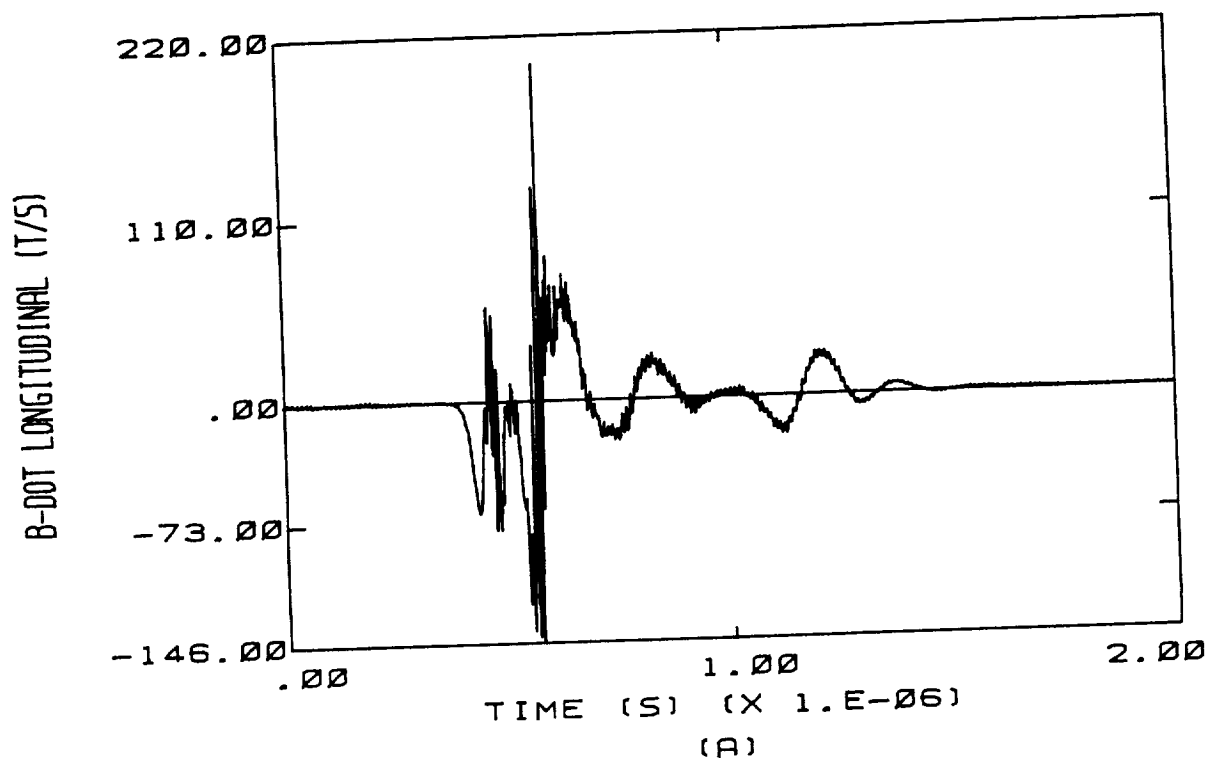


Figure E.12 High Altitude, Back to Front, - Qm

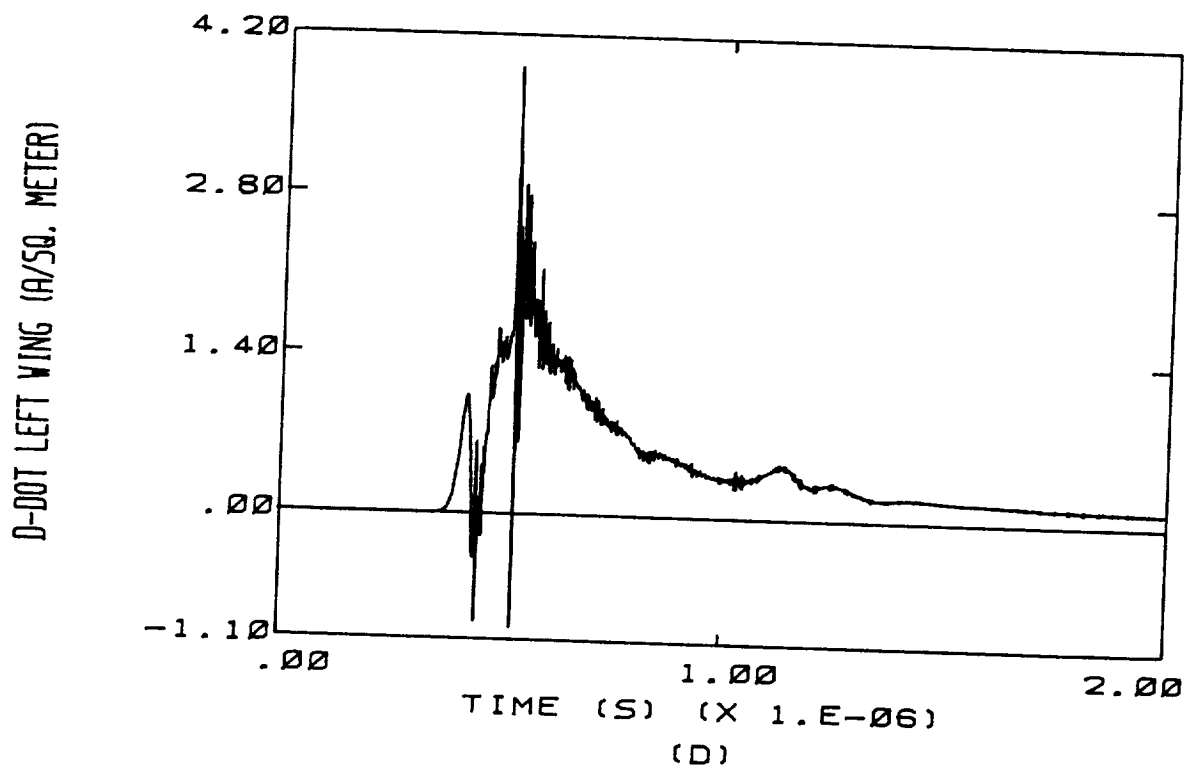
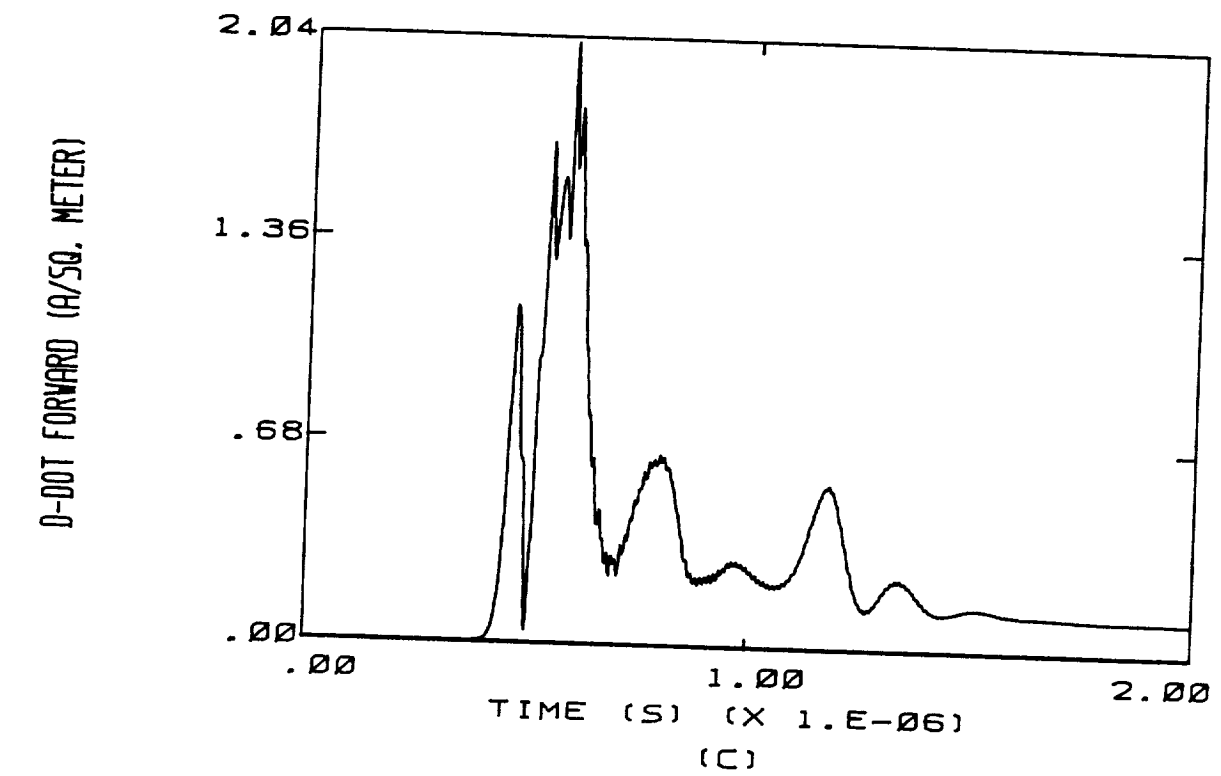


Figure E.12 (continued)

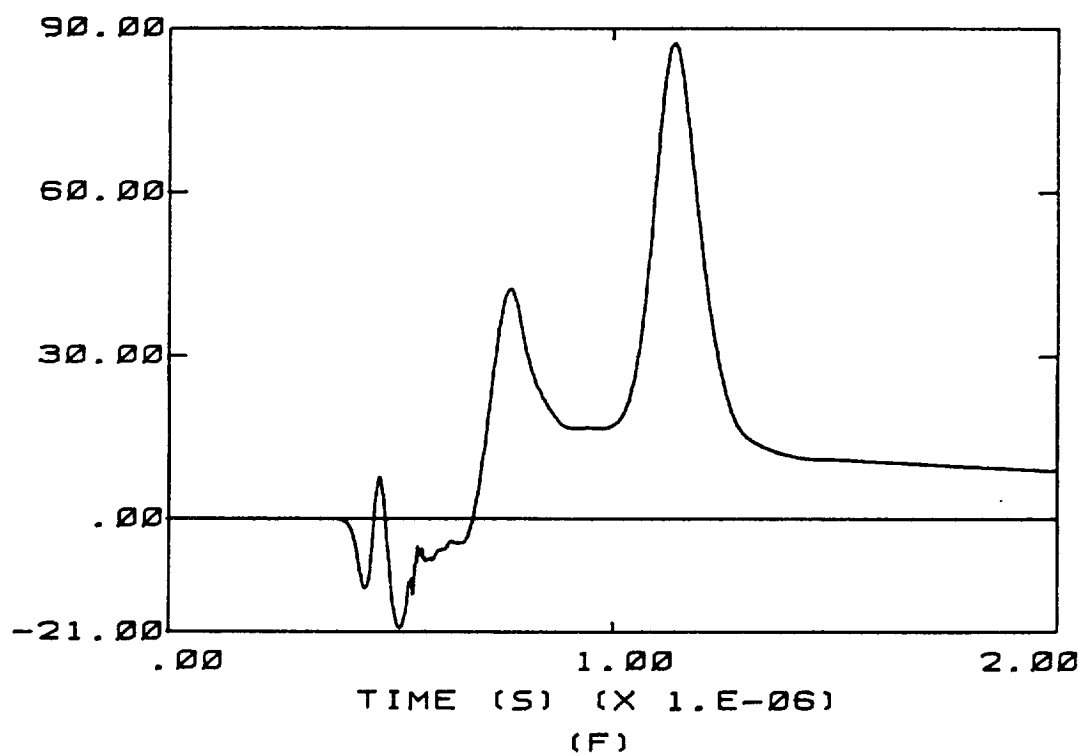
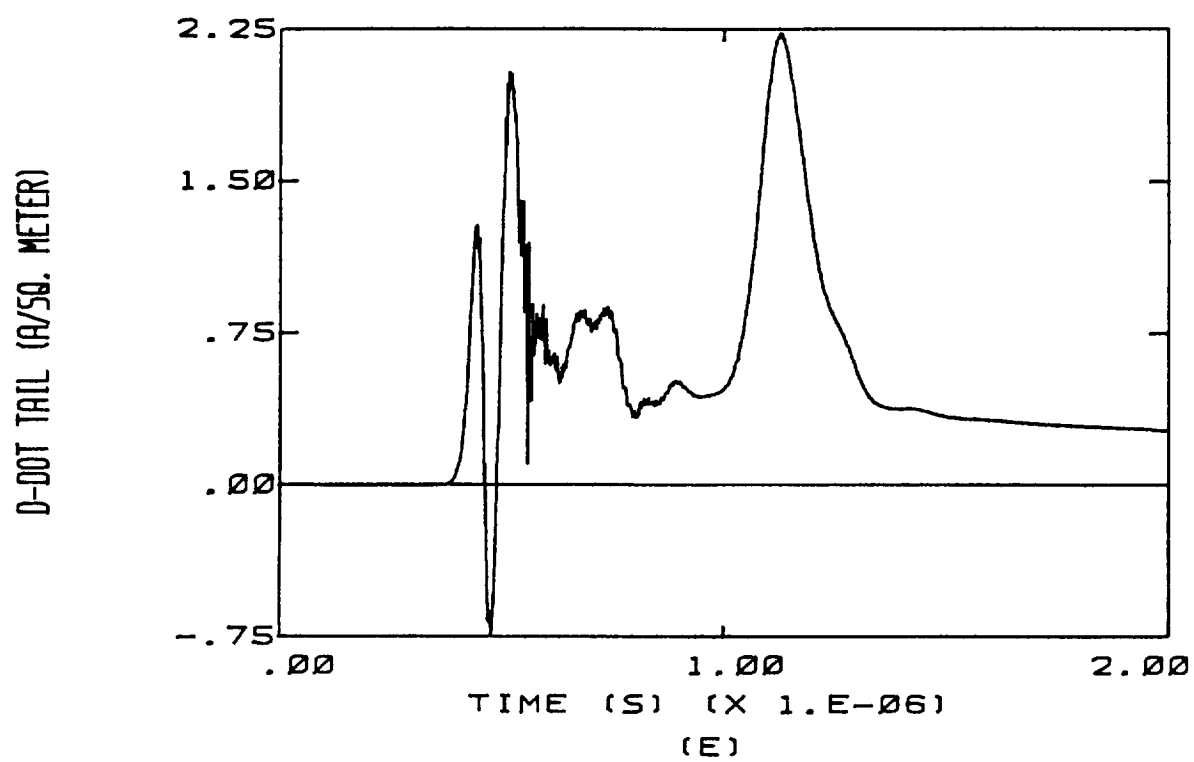


Figure E.12 (continued)

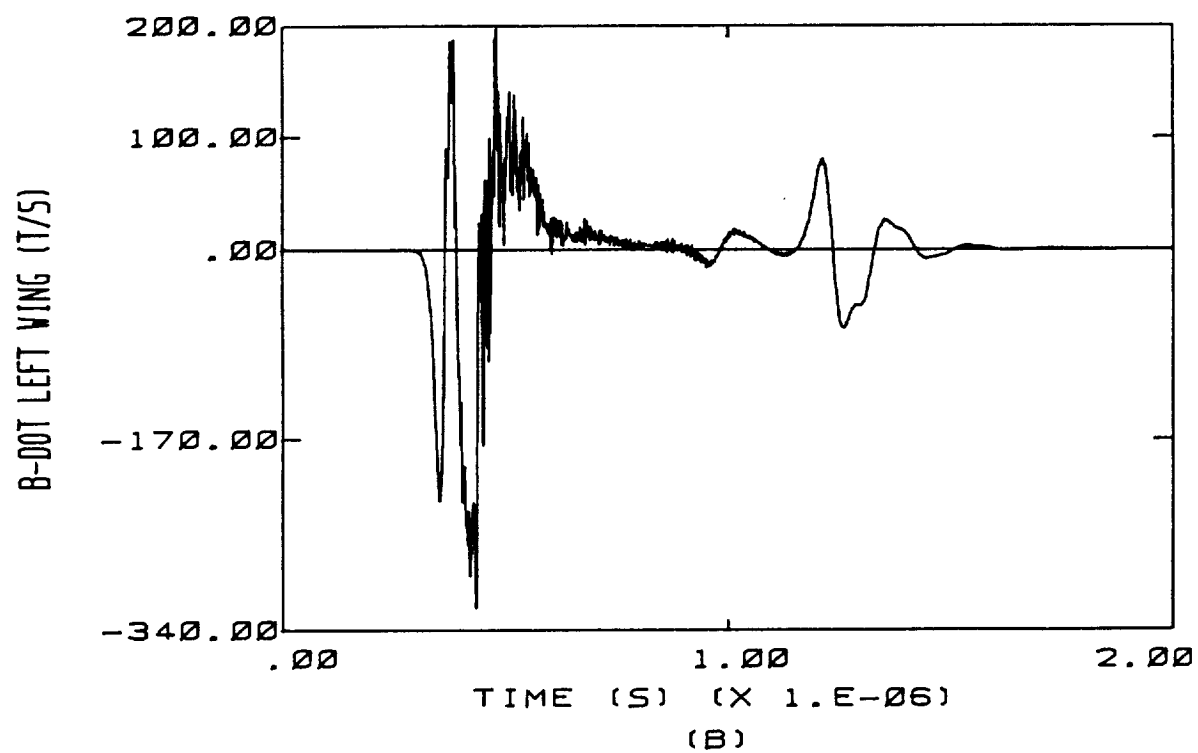
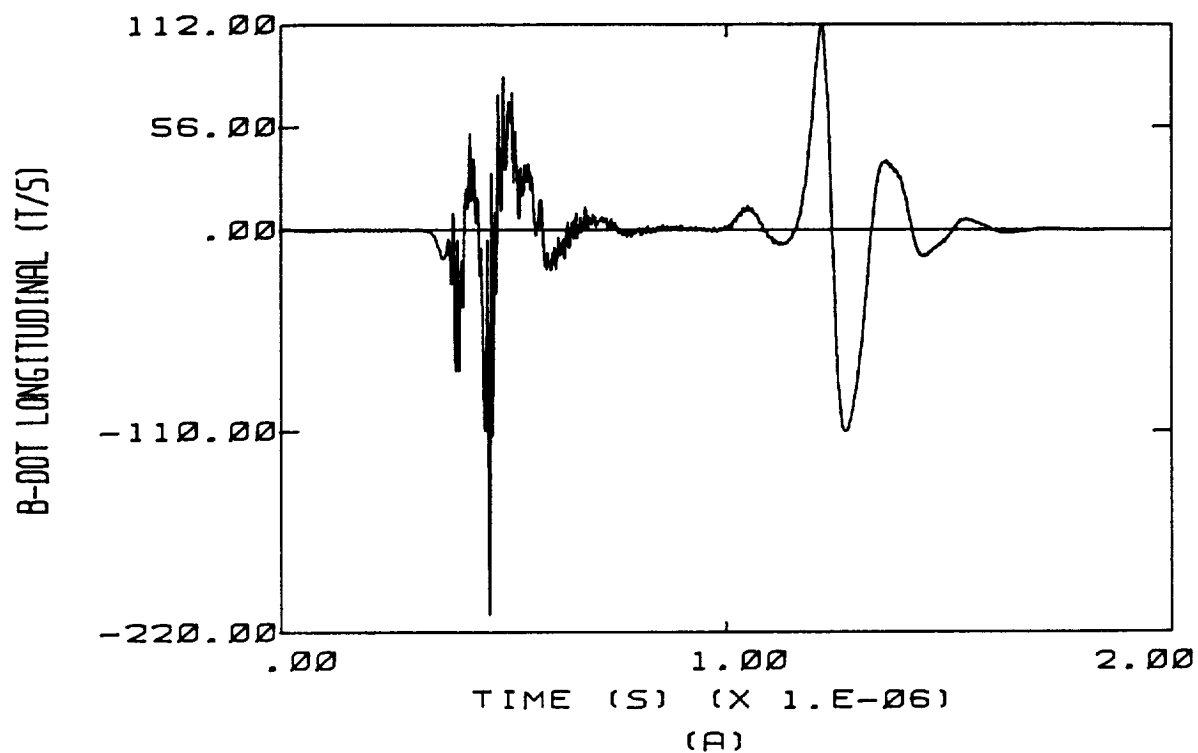
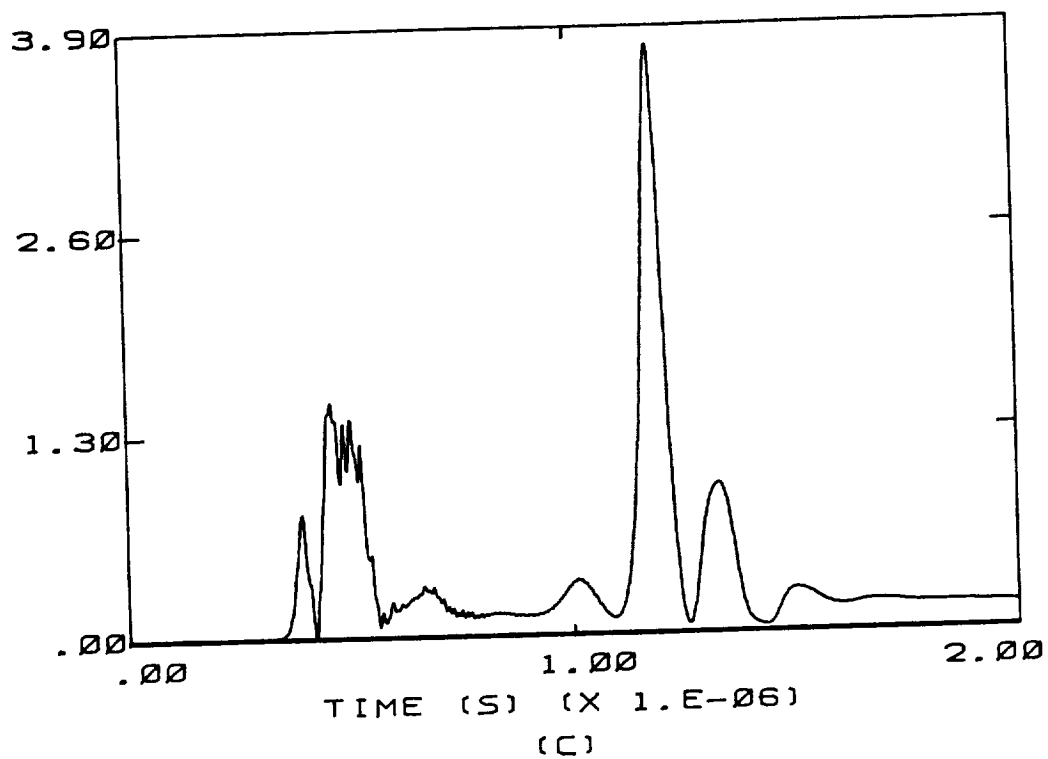


Figure E.13 High Altitude, Left to Right, - Qm



D-DOT FORWARD (A/50. METER)



D-DOT LEFT WING (A/50. METER)

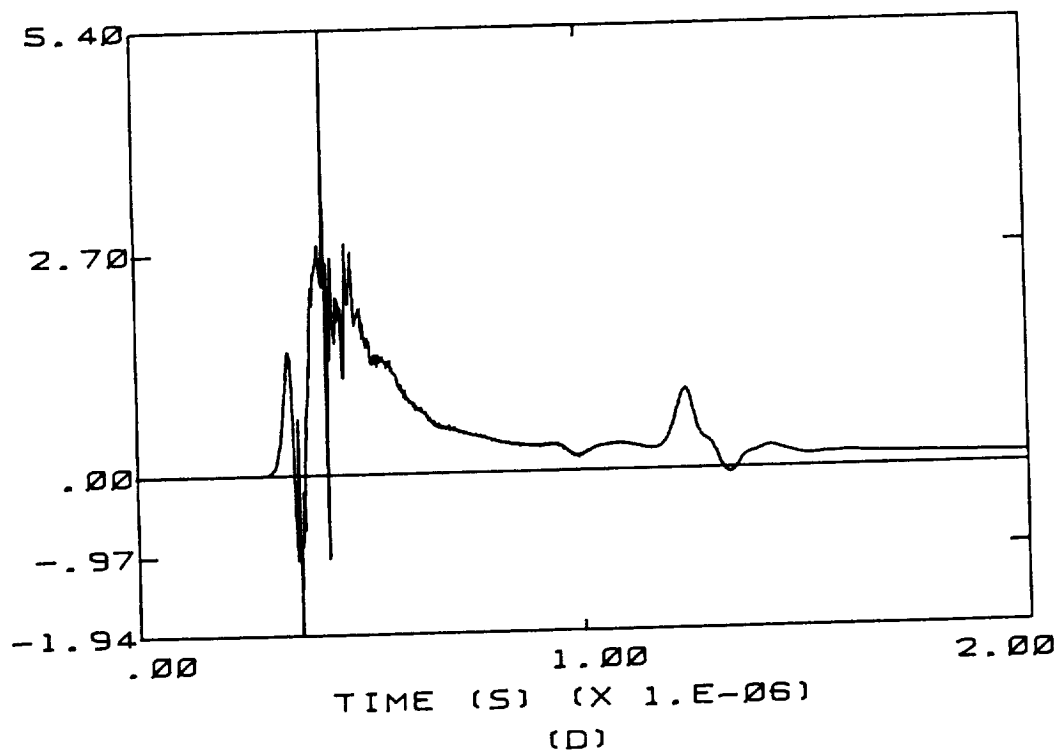


Figure E.13 (continued)

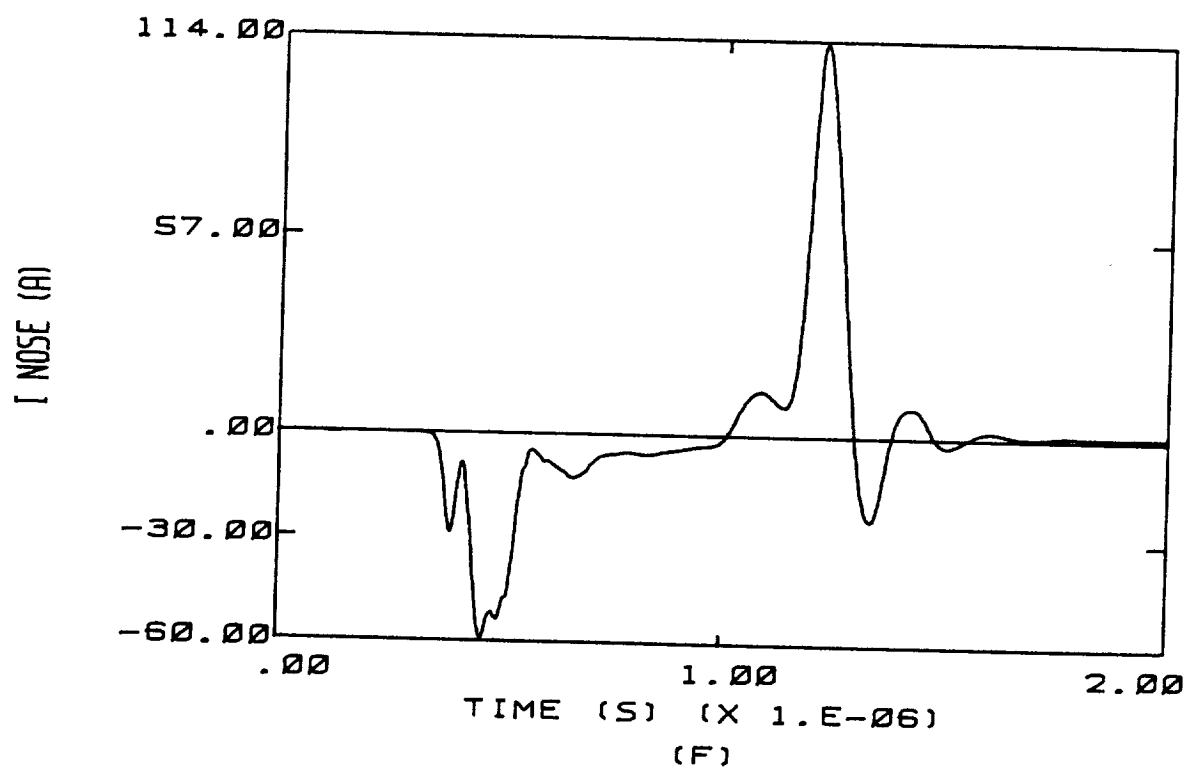
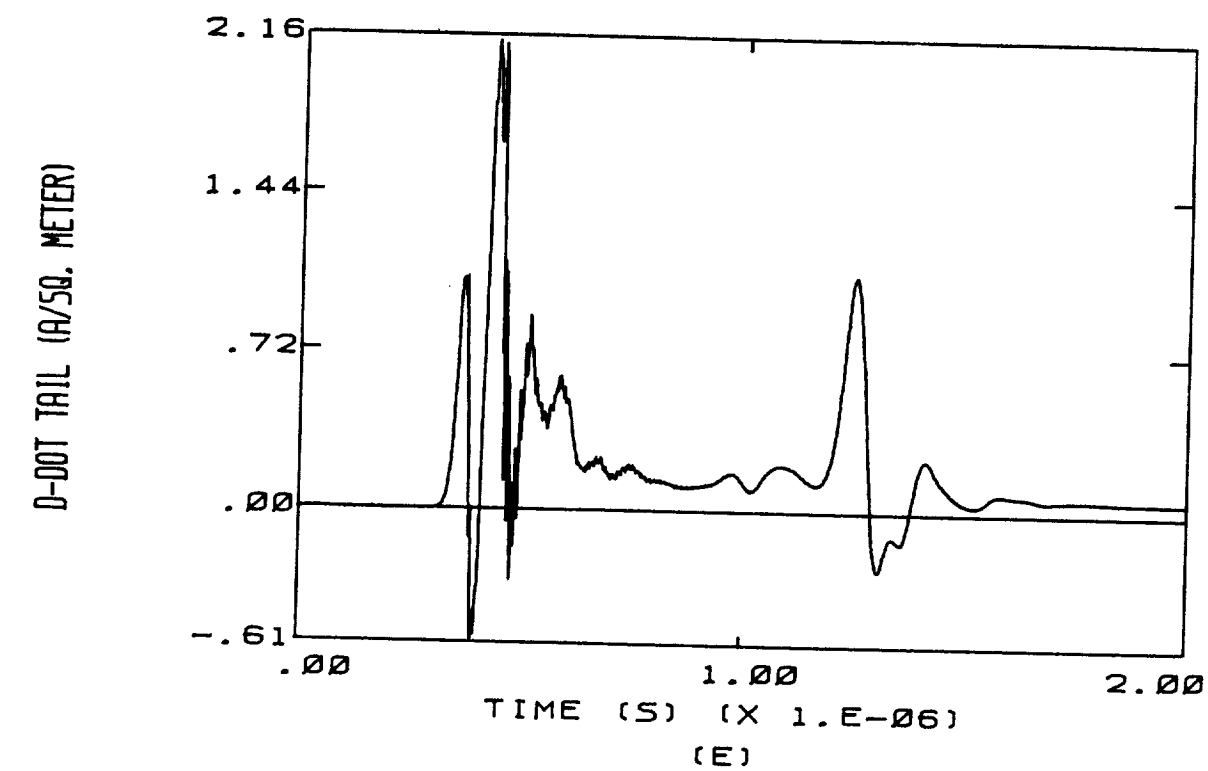


Figure E.13 (continued)

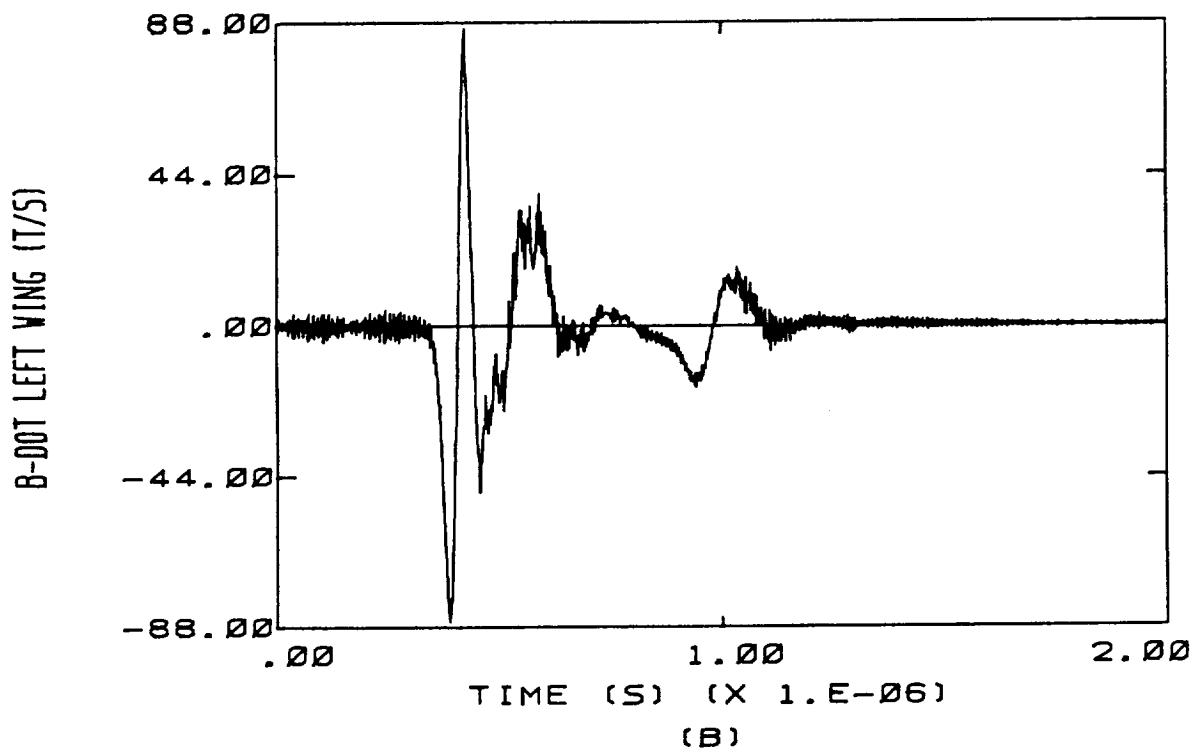
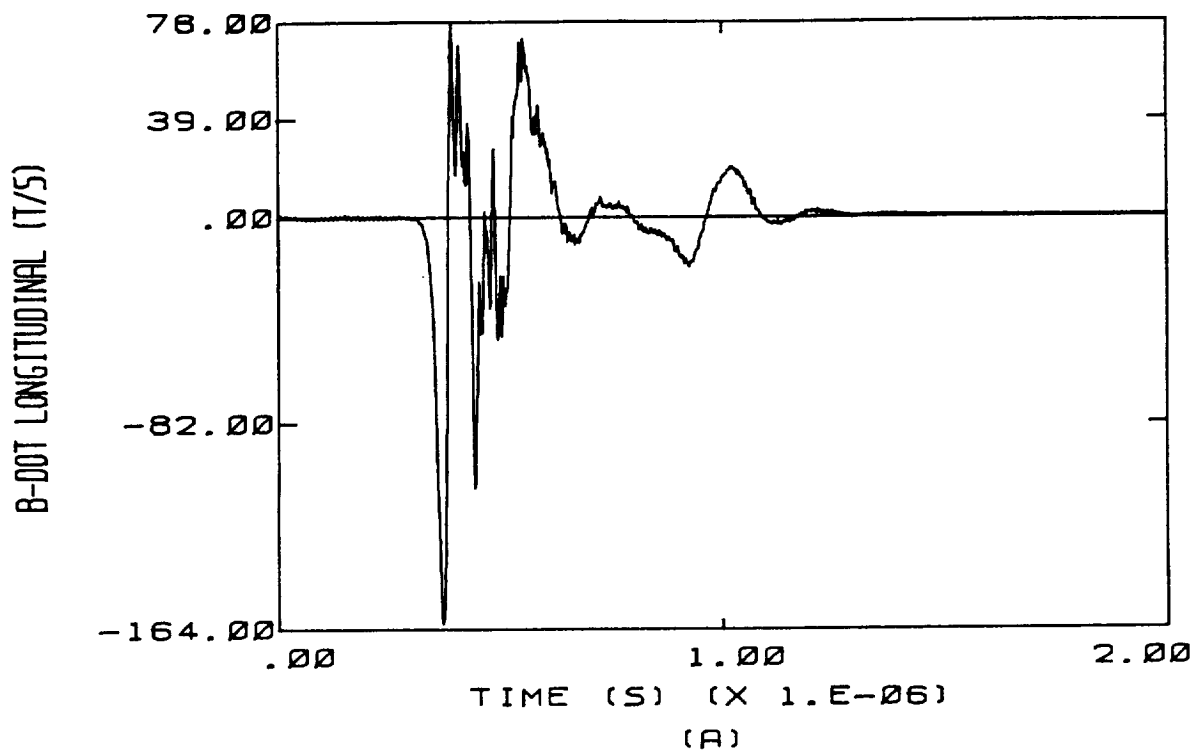
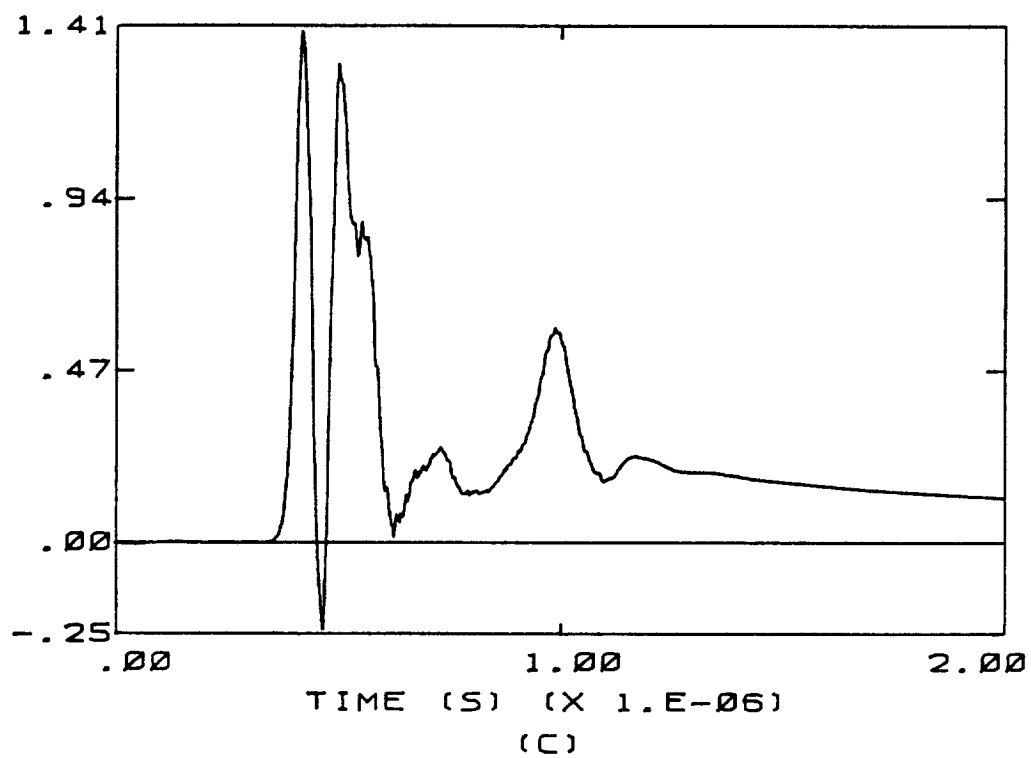


Figure E.14 High Altitude, Top to Bottom, - Qm

D-DOT FORWARD (A/50. METER)



D-DOT LEFT WING (A/50. METER)

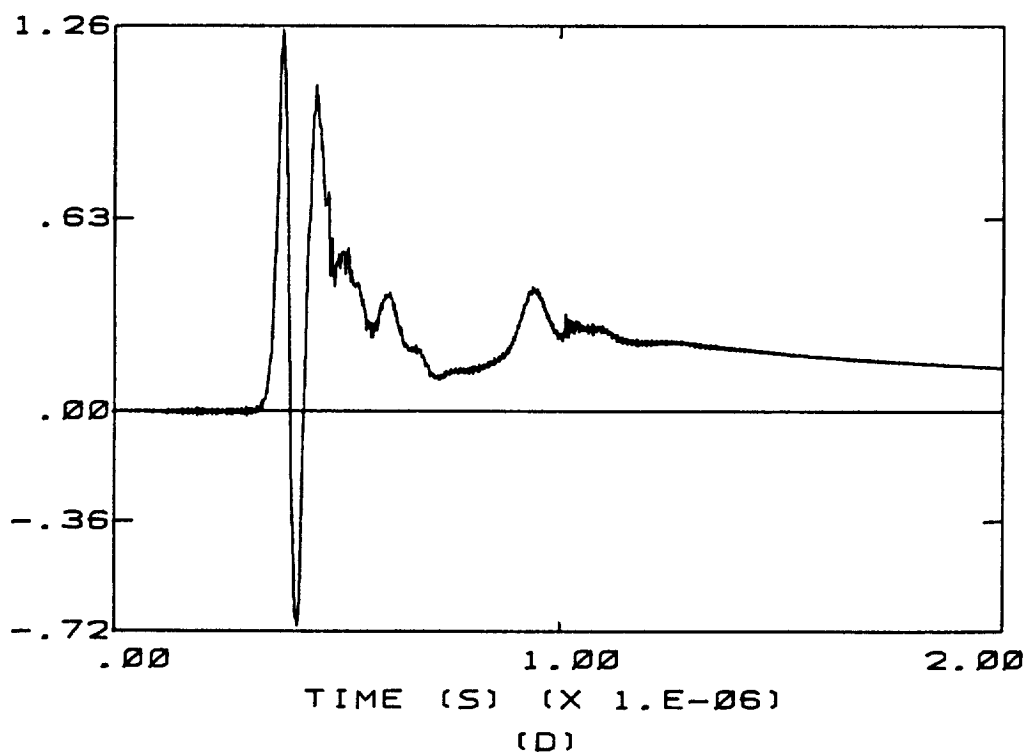


Figure E.14 (continued)

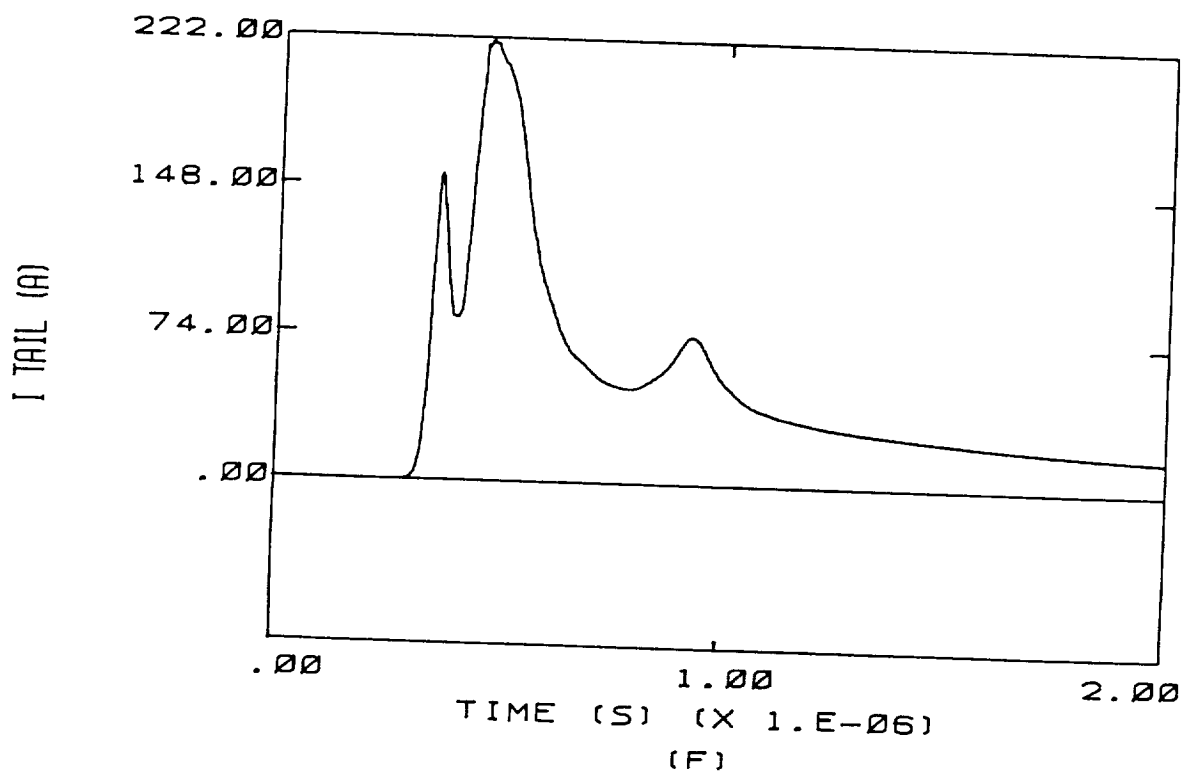
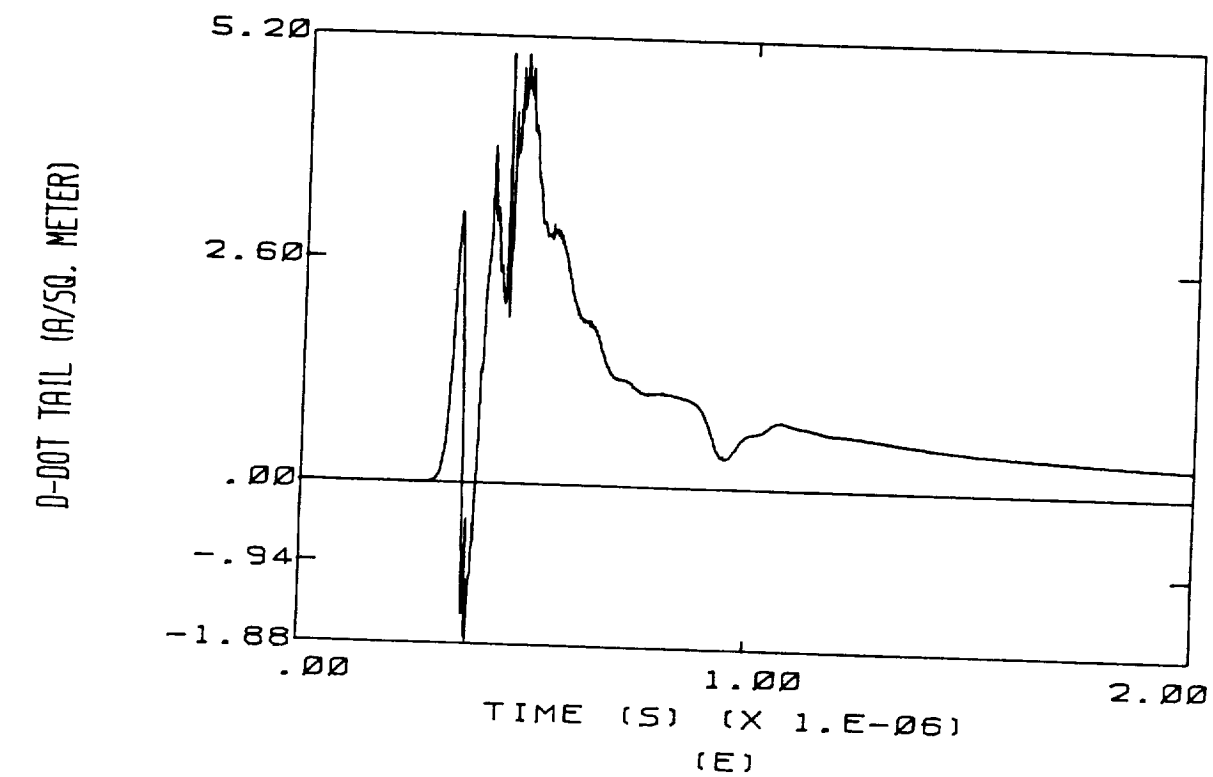


Figure E.14 (continued)



## **APPENDIX F**

### **BIBLIOGRAPHY OF THE THUNDERSTORM ENVIRONMENT LITERATURE SEARCH**

## BIBLIOGRAPHY

### PRECIPITATION CHARGING AND STORM ELECTRIFICATION

1. Acker, F.E., and G.W. Penney, "Some Experimental Observations of the Propagation of Streamers in 'Low Field' Regions of an Asymmetrical Gap," *Journal of Applied Physics*, Vol. 40, No. 6, May 1969.
2. Barreto, E., "The Gas Heating Phase in Electrical Breakdown," VII International Conference on Atmospheric Electricity, June 3-8, 1984.
3. Barreto, E., and S.I. Reynolds, "The Formation of Spark Channels," VI International Conference on Atmospheric Electricity, Manchester, England, 1980.
4. Bennetts, D.A., P. Ryder, and J. Latham, "The Electric Field Structure of Convective Cloud," VI International Conference on Atmospheric Electricity, Manchester, England, 1980.
5. Bicknell, J.A., and R.W. Shelton, "Some Possible Energy Requirements of a Corona Triggered Lightning Stroke," VII International Conference on Atmospheric Electricity, American Meteorological Society, June 3-8, 1984.
6. Bicknell, J.A., and B.M. Humood, "Bipolar Corona and Aircraft Triggered Discharges," International Aerospace and Ground Conference on Lightning and Static Electricity, Orlando, Florida, June 1984.
7. Bicknell, J.A., A.S. Sadik and T. Tang, "The Growth of a Positive Streamer System," VI International Conference on Atmospheric Electricity, Manchester, England, 1980.
8. Boulay, J.L. and S. Larigaldie, "Comparison Between Long Air-Gap Breakdowns, Gliding Surface Discharges and Lightning Leaders," International Aerospace and Ground Conference on Lightning and Static Electricity, June 1984.
9. Braham, R.R., Jr., "The Water and Energy Budgets of the Thunderstorm and Their Relation to Thunderstorm Development," *J. Meteorol.*, 4, 1952.
10. Brook, M., and C.B. Moore, "Lightning in Volcanic Clouds," *Journal of Geophysical Research*, Vol. 29, No. 3, January 20, 1974.
11. Caranti, J.M., W. Gaskell and A.J. Illingworth, "Charge Transfer Accompanying Individual Collisions Between Ice Particles, Surface Potential Steps and Their Role in Thunderstorm Electrification," VI International Conference on Atmospheric Electricity, Manchester, England, 1980.
12. Caranti, J.M., A.J. Illingworth and S.J. Marsh, "The Charging of Ice by Differences in Contact Potential," VII Conference on Atmos. Electricity, Albany, N.Y., AMS, June 1984.



13. Cheng, L., and M. English, "Hailstone Concentration and Size at the Ground and at the Melting Level, "Conf. on Cloud Physics, Chicago, Illinois, Nov. 1982.
14. Cherna, E.V., E.J. Stansbury and E. Ballantyne, "Lightning In Relation To The Precipitation Pattern of a Thunderstorm," VII International Conference on Atmospheric Electricity, June 3-8,. 1984.
15. Chiu, Chin-Shan, "Numerical Study of Cloud Electrification in an Axisymmetric, Time-Dependent Cloud Model," Journal of Geophys. Research, Vol. 83, No. C10, October 20, 1978.
16. Chiu, Chin-Shan, and J.D. Klett, "Convective Electrification of Clouds," Journal of Geophysical Research, Vol. 81, No. 6, Feb. 20, 1986.
17. Christian, H., et al, "Airborne and Ground-based Studies of Thunderstorms in the Vicinity of Langmuir Laboratory," Quarterly Journal of the Royal Meteorological Society, 1980, 106, pp. 159-174.
18. Colgate, Stirling A., "Differential Charge Transport in Thunderstorm Clouds," Journal of Geophys. Research, Vol. 77, No. 24, August 20, 1972.
19. Cotton, William R., G.J. Tripoli and R. Blumenstein, "The Simulation of Orographic Clouds with a Nonlinear, Time-Dependent Model," Conf. on Cloud Physics, Chicago, Illinois, Nov. 1982.
20. Crabb, J.A., and J. Latham, "Corona from Colliding Drops as a Possible Mechanism for the Triggering of Lightning," Journal of the Royal Meteorological Society, 100, 1974.
21. Dawson, G.A., "Pressure Dependence of Water-Drop Corona Onset and Its Atmospheric Importance," Journal of Geophysical Research, Vol. 74, No. 28, December 20, 1969, pp. 6859-6868.
22. Domens, P., J. Dupuy, and A. Gibert, "Positive Streamer Behaviour in Atmospheric Air: Theoretical Approach and Experimental Results," VII International Conference on Atmospheric Electricity, June 3-8, 1984.
23. Endoh, Tatsuo, "An Electrification Mechanism of Ice Crystals in the Atmosphere," VI Int. Conf. on Atmos. Electricity, Manchester, England, 1980.
24. Fisher, Bruce D., J.A. Plumer, and J. Anderson, "Lightning Attachment Patterns and Flight Conditions Experienced by the NASA F-106B Airplane," Proc. Eighth Inter. Aero. and Ground Conference on Lightning and Static Electricity, Fort Worth, TX, June 1983, DOT/FAA/CT-83/25 Supplement.
25. Fisher, B.D., and J.A. Plumer, "Lightning Attachment Patterns and Flight Conditions Experienced by the NASA F-106B Airplane from 1980 to 1983," AIAA 22nd Aerospace Sciences Meeting, January 9-12, 1984.
26. Foster, Michael P., J.C. Pflaum, S.P. Nelson, "The Sensitivity of Hailstone Growth to Variations in Microphysical Parameters," Conf. on Cloud Physics, Chicago, Illinois, Nov. 1982.

27. Fowler, Richard G., "Lightning," Applied Atomic Collision Physics, Vol. 5, 1982, Academic Press, New York.
28. Gardiner, B., D. Lamb, R. Pitter and J. Hallett, "Measurements of Initial Electric Field and Particle Charges in a Montana Summer Thunderstorm," Desert Research Institute, Atmospheric Science Center, Reno, Nevada, 1984.
29. Gaskell, W., A.J. Illingworth, J. Latham, and C.B. Moore, "Airborne Studies of Electric Fields and The Charge and Size of Precipitation Elements in Thunderstorms," Journal of the Royal Meteorological Society, 1978, 104, pp. 447-460.
30. Griffiths, R.F., and J. Latham, "The Emission of Corona from Falling Drops," Journal of the Meteorological Society of Japan, Vol. 50, No. 5, 1972.
31. Griffiths, R.F., and J. Latham, "Electrical Corona from Ice Hydrometeors," Journal of Royal Meteorological Society, 100, 1974.
32. Griffiths, R.F. and C.T. Phelps, "A Model for Lightning Initiation Arising From Positive Corona Streamer Development," Journal of Geophysical Research, July 20, 1976.
33. Griffiths, R.F., J. Latham and V. Myers, "The Ionic Conductivity of Electrified Clouds," J. Roy. Met. Soc. 100, 1974.
34. Gross, G.W., "Role of Relaxation and Contact Times in Charge Separation During Collision of Precipitation Particles with Ice Targets," Journal of Geophysical Research, Vol. 87, No. C9, pp. 7170-7178, August 20, 1982.
35. Gunn, Ross, "The Non-Equilibrium Electrification of Raindrops by the Association of Charged Cloud Droplets," Journal of Meteorology, Vol. 14, p. 326-331, August, 1957.
36. Hallett, J., and C.P.R. Saunders, "Charge Separation Associated with Secondary Ice Crystal Production," J. Atmos. Sci., 36, 1979.
37. Helsdon, J.H., Jr., "Chaff Seeding Effects in a Dynamical-Electrical Cloud Model," Journal of Applied Meteorology, Vol. 19, No. 9, September 1980.
38. Heymsfield, A.J., "Utilization of Aircraft Size Spectra Measurements and Simultaneous Doppler Radar Measurements to Determine the Physical Structure of Clouds," Proceedings, 17th Conference on Radar Meteorology, Seattle, WA., 1976.
39. Heymsfield, A.J., "Case Study of a Hailstorm in Colorado: Graupel and Hail Production Mechanisms," Conf. on Cloud Physics, Chicago, Illinois, Nov. 1982.

40. Heymsfield, A.J., "Initiation Mechanisms and Rates of Development of Graupel Particles and Hailstones in High Plains Storms: A Numerical Evaluation," Conf. on Cloud Physics, Chicago, Illinois, Nov. 1982.
41. Illingworth, A.J., and J.M. Caranti, "Ice Conductivity Restraints on the Inductive Theory of Thunderstorm Electrification," AMS Preprints: VII Conf. on Atmos. Electricity, Albany, N.Y., June 1984.
42. Ishii, M., J. Hojo, and T. Kawamura, "The Polarity of Ground Flashes and Possible Charge Structure in a Thundercloud," VII International Conference on Atmospheric Electricity, 1984.
43. Jayaratne, E.R., J. Hallett and C.P.R. Saunders, "Electrification During Riming and Ice Crystal Collisions," VI International Conference on Atmospheric Electricity, Manchester, England, 1980.
44. Jones, J.J., W.P. Winn, and J.E. Dye, "Early Electrification in a Cumulus," VII International Conference on Atmospheric Electricity, 1984.
45. Jurenka, H. and E. Barreto, "A Fluid Dynamical Analysis of the Observed Wave Propagation in the Electrical Breakdown of Gases," VII International Conference on Atmospheric Electricity, June 3-8, 1984.
46. Kamra, "Effect of the Inclination of the Electric Field on the Inductive Charging Mechanism in Thunderclouds," Journal of the Atmospheric Sciences, Vol. 34, April 1977.
47. Kasemir, H.W., and F. Perkins, "Lightning Trigger Field of the Orbiter," National Oceanic and Atmospheric Administration, Final Report, KSC Contract CC 69694A, October 1978.
48. Kasemir, Heinz, W., "Energy Problems of the Lightning Discharge," VII International Conference on Atmospheric Electricity, June 3-8, 1984.
49. Khemani, L.T., S.K. Sharma, A.S.R. Murty and Bh. V. Ramana Murty, "A Simple Gadget for Collection of Cloud/Rain Water From Aircraft," Conf. on Cloud Physics, Chicago, Illinois, Nov. 1982.
50. Knight, Nancy C., A.J. Heymsfield, "Measurement and Interpretation of Hailstone Density and Terminal Velocity," Conf. on Cloud Physics, Chicago, Illinois, Nov. 1982.
51. Krehbiel, Paul R., "Corona Electrification: A Possible Mechanism for Enhancing and Sustaining the Electrification of Thunderstorms," AMS Preprints: VII Conf. on Atmos. Elect., Albany, N.Y., June 1984.
52. Kunkel, W., "Growth of Charged Particles in Clouds," Journal of Applied Physics, Vol. 19, November, 1948.
53. Latham, J., and R. Warwicker, "Charge Transfer Accompanying the Splashing of Supercooled Raindrops on Hailstones," Quart. J. Roy. Meteor., Soc., 106, 1980.

54. Latham, J., and B.J. Mason, "Generation of Electric Charge Associated with the Formation of Soft Hail in Thunderclouds," Proc. Roy. Soc., A260 1961.
55. Levin, Z., and W.D. Scott, "The Effect of Electrical Conductivity on the Growth of the Electric Field in a Thunderstorm," Tellus, Vol. 27, May 1975.
56. Lin, Yuh-Lang, R.D. Farley and H.D. Orville, "Bulk Parameterization of the Snow Field in a Cloud Model," Journal of Climate and Applied Meteorology, Vol. 22, No. 6, June 1983.
57. Lin, Xin-Sheng and P.R. Krehbiel, "The Initial Streamer of Intracloud Flashes," VII International Conference on Atmospheric Electricity, June 3-8, 1984.
58. Lin, Yuh-Lang, Richard D. Farley, and Harold D. Orville, "Bulk Parameterization of the Snow Field in a Cloud Model," J. Climate and Applied Meteorology, 22, No. 6, June 1983.
59. MacGorman, D.R., W.L., Taylor, and W.D. Rust, "Some Characteristics of Lightning in Severe Storms on the Great Plains of the United States," VII International Conference on Atmospheric Electricity, American Meteorological Society, June 1984.
60. Marshall, T.C., W.D. Rust, and W.P. Winn, "Screening Layers at the Surface of Thunderstorm Anvils," VII International Conference on Atmospheric Electricity, June 1984.
61. Magono, C., and C.W. Lee, "Classification of Natural Snow Crystals," J. Fac. Sci., Hokkaido University, Ser. 7, 2, No. 4, 1966.
62. Martell, E.A., "Ion Pair Production in Convective Storms by Radon and Its Radioactive Decay Products," VII Conference on Atmospheric Electricity, June, 1984.
63. Martner, B.E., "Radar and Aircraft Observations of Generating Cells," Conf. on Cloud Physics, Chicago, Illinois, Nov. 1982.
64. Mazur, V., O.K. Norman, B.D. Fisher and J.C. Gerlach, "Conditions for Lightning Strikes to an Airplane in a Thunderstorm," AIAA 22nd Aerospace Sciences Meeting, January 1984.
65. Muhong, Yan, and G. Zhengmo, "Electrification Process with Ice Phase in Hail Cloud," VII Int. Conf. on Atmospheric Electricity, Manchester, England, 1980.
66. Musil, Dennis J., "Cloud Physics Observations Near Times of Lightning Strikes to a Storm Penetrating Aircraft," South Dakota School of Mines and Technology under Grant ATM-7827018 from Division of Atmospheric Sciences, National Science Foundation.
67. Nelson, Stephan P., "The Influence of Storm Flow Structure on Hail Growth," Conf. on Cloud Physics, Chicago, Illinois, Nov. 1982.

68. Oetzel, G.N., "Computation of the Diameter of a Lightning Return Stroke," *Journal of Geophysical Research*, Vol. 73, No. 6, March 15, 1968.
69. Orville, H.D., "The Numerical Simulation of Severe Convective Storms," *SIAM-AMS Proceedings*, Vol. 11, 1978.
70. Orville, Harold D., and Fred J. Kopp, "Numerical Simulation of the Life History of a Hailstorm," *J. Atmos. Sci.* 34, No. 10, October 1977.
71. Paluch, I.R., and J.D. Sartor, "Thunderstorm Electrification by the Inductive Charging Mechanism: I. Particle Charges and Electric Fields," *J. Atmos. Sci.*, Vol. 30, 1973.
72. Paluch, I.R., and J.D. Sartor, "Thunderstorm Electrification by the Inductive Charging Mechanism: II. Possible Effects of Updraft on the Charge Separation Process," *J. Atmos. Sci.*, Vol. 30, 1973.
73. Parker, L.W., "Breakdown Waves in Return-Stroke and Leader-Step Channels," VII International Conference on Atmospheric Electricity, June 3-8, 1984.
74. Pflaum, J.C. and N.C. Knight, "New Clues for Decoding Hailstone Structure," *Conf. on Cloud Physics*, Chicago, Illinois, Nov. 1982.
75. Phelps, C.T., "Field-Enhanced Propagation of Corona Streamers," *Journal of Geophysical Research*, August 20, 1971.
76. Pislser, E., and W.R. Atkinson, "Atmospheric Electrical Discharges in the Presence of Water and Ice Particles," *Journal of Geophysical Research*, Vol. 76, No. 12, April 20, 1971.
77. Pruppacher, Hans R., and James D. Klett, "Microphysics of Clouds and Precipitation," D. Reidel Publishing Co., Boston, 1980.
78. Sartor, J.D., "Non-Lightning Related Radio Noise from Clouds as a Source of Cloud Physics Information,"
79. Sartor, J.D., "Calculations of Cloud Electrification Based on a General Charge Separation Mechanism," *J. Geophys. Res.*, 66, 1961.
80. Saunders, C.P.R., M.F.S. Wheeler, N. Jallo and E.R. Jayaratne, "Ice Crystal Interaction with a Riming Target: Charge Transfer and Collection Efficiencies," VII International Conference on Atmospheric Electricity, American Meteorological Society, June 1984.
81. Shi, Wen Quan, "Analysis and Research of Hailstone Micro-Structure," *Conf. on Cloud Physics*, Chicago, Illinois, Nov. 1982.
82. Shio, H., "Frictional Electrification of Ice and Snow," International Aerospace and Ground Conference on Lightning and Static Electricity, June 26-28, 1984.


ORIGINAL PAGE IS  
OF POOR QUALITY

83. Spahn, J.F., and P.L. Smith, Jr., "Some Characteristics of Hailstone Size Distributions Inside Hailstorms," Proceedings, 17th Conference on Radar Meteorology, Seattle, WA., 1976.
84. Srivastava R.C. and David Atlas, "Growth, Motion and Concentration of Precipitation Particles in Convective Storms," J. Atmos. Sci. Vol. 26, No. 3, May 1969, pp. 535-544.
85. Stow, C.D., "Atmospheric Electricity," Reports on Progress in Physics, Vol. 32, Part 1, 1969.
86. Strawe, D.F., W.P. Geren, and D.G. Chapman, "A Self-Consistent Model for Return Stroke Currents and Fields," The Boeing Company.
87. Takahashi, T., "Physical Mechanisms of Riming Electrification," Preprints, VII Conf. on Atmos. Electricity, Albany, N.Y., AMS, June 1984.
88. Takahashi, T., "Chemical Composition of Snow in Relation to Their Crystal Shapes," J. Met. Soc. Japan, Vol. 41, No. 6, 1963.
89. Telford, J.W., and P.B. Wagner, "Electric Charge Separation in Severe Storms," Pure Appl. Geophys., 117, 1979.
90. Weber, M., A. Weinheimer, and A. Few, "Possible Influences of Hydrometeor Corona on the Propagating Cloud Streamer," VI International Conference on Atmospheric Electricity, Manchester, England, 1980.
91. Wilkening, M., "Characteristics of Atmospheric Ions in Contrasting Environments," VII Conference on Atmospheric Electricity, Albany, N.Y., June 1984.
92. Willett, J., "Implications of  $^{222}\text{Rn}$  Daughter Deposition on Vegetated Ground," VII Conference on Atmospheric Electricity, June 1984.
93. Williams, E.R., C.M. Cooke, and Kenneth A. Wright, "Electrical Discharge Propagation In and Around Space Charge Clouds," VII International Conference on Atmospheric Electricity, June 1984.
94. Williams, E.R., and R.H. Lhermitte, "Radar Tests of the Precipitation Hypothesis for Thunderstorm Electrification," Journal of Geophysical Research, Vol. 88, No. C15, Dec. 20, 1983, pp. 10,984-10,992.
95. Wilson, C.T.R., "Some Thundercloud Problems," J. Franklin Institute, 208, 1929.
96. Winn, W.P., G.W. Schwede, and C.B. Moore, "Measurements of Electric Fields in Thunderclouds," Journal of Geophysical Research, Vol. 79, No. 12, April 20, 1974.
97. Workman, E.J., and S.E. Reynolds, "A Suggested Mechanism for the Generation of Thunderstorm Electricity," Phys. Rev., 74, 1948.

98. Ziegler, Conrad L., P.S. Ray and N.C. Knight, "Hail Formation in an Oklahoma Multicell Storm," Conf. on Cloud Physics, Chicago, Illinois, Nov. 1982.

[REDACTED]

# Standard Bibliographic Page

1. Report No. NASA CR-3974		2. Government Accession No.		3. Recipient's Catalog No.	
4. Title and Subtitle Development and Application of Linear and Nonlinear Methods for Interpretation of Lightning Strikes to In-Flight Aircraft				5. Report Date September 1986	
				6. Performing Organization Code	
7. Author(s) Terence Rudolph, Rodney A. Perala, Calvin C. Easterbrook, and Steven L. Parker				8. Performing Organization Report No. EMA-85-R-37	
				10. Work Unit No.	
9. Performing Organization Name and Address Electro Magnetic Applications, Inc. P.O. Box 26263 Denver, Colorado 80226-0263				11. Contract or Grant No. NAS1-17748	
				13. Type of Report and Period Covered Contractor Report	
12. Sponsoring Agency Name and Address National Aeronautics and Space Administration Washington, DC 20546				14. Sponsoring Agency Code 505-34-13-34	
15. Supplementary Notes  Langley Technical Monitor: Felix L. Pitts					
16. Abstract  Since 1980, NASA has been collecting direct strike lightning data by flying an instrumented F106B aircraft into thunderstorms. The continuing effort to interpret the measured data is reported here. Both linear and nonlinear finite difference modeling techniques are applied to the problem of lightning triggered by an aircraft in a thunderstorm. Five different aircraft are analyzed to determine the effect of aircraft size and shape on lightning triggering. The effect of lightning channel impedance on aircraft response is investigated. The particle environment in thunderstorms and electric field enhancements by typical ice particles are also investigated.					
17. Key Words (Suggested by Authors(s))  Triggered lightning F106B Nonlinear modeling Linear modeling Data Interpretation			18. Distribution Statement   Until September 1988  Subject Category 47		
19. Security Classif.(of this report) Unclassified		20. Security Classif.(of this page) Unclassified		21. No. of Pages 438	
22. Price					